Treatment of Pharmaceutical Wastewater Using Hibiscus Sabdariffa

Aw Kea Hang[1*], Nurhazwani Ismail[2]

[1]*School of Engineering, Taylor's University Lakeside Campus, Malaysia*

[*]keahangaw@ymail.com

Abstract
Pharmaceutical Wastewater is one the most toxic industry waste as it contains high chemical oxygen demand (COD), biological oxygen demand (BOD), total suspended solid and other hazardous chemical substances. This wastewater has to be treated before it is discharged to the environment. Coagulation process is commonly applied in pharmaceutical industry to remove the pollutant substances from wastewater. Aluminium sulphate is the common chemical coagulant used in wastewater treatment. However, recent studies found that residual aluminium in treated water causes Alzheimer's disease and other environmental problems. Natural coagulant is developed as an alternative source to replace the chemical coagulant in wastewater treatment process. The aim of this research work is to study the performance of *Hibiscus Sabdariffa* as a natural coagulant to treat synthetic pharmaceutical wastewater that contained paracetamol. Coagulation process is conducted by using the jar test equipment. Three working parameters are tested in the coagulation process such as pH, coagulant dosage and initial paracetamol concentration. The working parameters are optimized using Response Surface Methodology (RSM). The reduction of COD and the TSS removal are analyzed as the response. The pH of the wastewater is the main parameter that has a large significant effect on the coagulation process. At the optimum working conditions, pH 3, coagulant dosage of 260mg/l and initial concentration at 75mg/l, the COD reduction percentage and TSS removal percentage can achieve to 68% and 56%. It was also been identified that the performance of natural coagulant is almost closer to the chemical coagulant. From the result obtained the aluminium sulphate result in COD reduction of 75.5% and TSS removal of 72%. Thus, the *Hibiscus Sabdariffa* seed can be used as a natural coagulant to replace alum which has been used in coagulation process for a long time. By using *Hibiscuss Sabdariffa* seed as coagulant, the negative impacts of using chemical coagulant related to health and environmental can be prevented

Keywords: *Hibiscus Sabdariffa*, Natural Coagulant, Paracetamol, Coagulation, Wastewater Treatment.

1. Introduction

Wastewater is known as the water that has been utilized in some processes and caused the negative impacts to the quality of the water. This kind of water is not suitable for human consumption due to the water contained high impurities substances and dissolved compound. The presence of these impurities substances in water making it is unsuitable for use and may cause health hazard and pollution to the environment. Commonly, the wastewater is discharged from households, public building and manufacturing industries such as the production of textile, chemical, pharmaceutical and petrochemical[1].

Recently, pharmaceutical industry consumes large volume of water for the production of drugs and pharmaceutical processes. The wastewater is contained toxic and hazardous chemicals such as anilines, steroids, organic solvents and other pollutants[2]. The presence of high concentration of biological oxygen demand (BOD), chemical oxygen demand (COD) and total suspended solid (TSS) is causes the pharmaceutical wastewater as one of the most toxic industry waste. Thus, this wastewater cannot directly discharge to the environment as it can caused serious trace pollution problems to environment[3].

In pharmaceutical industry, there are different kinds of pharmaceutical compounds are developed and marketed such as paracetamol, aspirin and ibuprofen[4]. Paracetamol is the most common medical drug which is used for pain reliver and fever reducer for humans[5]. Paracetamol is not easy for biodegradable and will retain their chemical structure long enough to do their therapeutic work[6]. Due to the persistence characteristic and resistance to biodegradation, the residual of paracetamol could remain in the environment for a long time and impose toxicity. Therefore, a proper treatment process is required to apply in the industry to avoid the pollutions to environment.

Several technologies have been developed to treat the pharmaceutical wastewater before it is discharged to the environment such as coagulation process, adsorption, advanced oxidation process and so on[3], [7]. Coagulation is the most common physiochemical treatment process that currently is applied in pharmaceutical industry to remove the impurities and turbidity from the wastewater. Coagulation process have been found to be cost effective, high efficient, simple and easy to control[7, 8]. It is a process to neutralize the negative charge colloid and dissolved solid present in wastewater, and remove them from the wastewater. It is effective for removing high concentration pollutants and dissolved compounds using different coagulants. Coagulant is a substance that contains positive charged ions and used to neutralize the negative charged colloid particles[9, 10]. Aluminium sulphate and ferric sulphate are the most common chemical coagulant used in the wastewater treatment process[11]. However, there are several of negative effects are found in the chemical coagulant when it is applied in the treatment process. For example, the residual alum in treated water causes Alzheimer's disease and other environmental problems[12]. In addition, the aluminium sulphate has low working efficiency in low temperature of solution. Hence, natural coagulant is developed and implemented in wastewater treatment to overcome the problems.

The main advantage of using a natural coagulant instead of chemical coagulant for wastewater treatment is environmental friendly and no harmful to human. In the finding of [13], the natural coagulant is extracted from the animals and plants which are high biodegradable, non-toxic and safe for human consumption [14]. There are several natural coagulants have been discovered and studied for wastewater treatment including *Moringa Oleifera, Nirmali seeds* and *Jatropha Curcas.* Some researchers have found that the presence

of the protein inside these plant seeds can be used as a coagulant in the coagulation process[15,16]. The proteins are able to be dissolved in the solution and released positive charged ions. These positive charged ions will neutralize the negative charge of colloid particles and form into large particles. The large particles will suspend in the wastewater and can be removed by sedimentation. *Hibiscus Sabdariffa* also known as one of the potential natural coagulants that can be applied in wastewater treatment[16].

In this research, *Hibiscus Sabdariffa* (Roselle) is selected as a natural coagulant to treat pharmaceutical wastewater. This plant is widely used in food and medical purpose due to it contains high quality of nutrition. The seed of this plant is usually as the byproduct for disposal purpose. Recently, scientists have found out the seed is contains high protein which is 31.02% and it could be used as a potential source of proteins[17,18]. Hence, the seed of this plant is expected to have the ability for coagulation. But there is lack of study of the *Hibiscus Sabdariffa* seed as a natural coagulant for pharmaceutical wastewater treatment. Therefore, this research will study about the performance of *Hibiscus Sabdariffa* seed as natural coagulant for pharmaceutical wastewater treatment

2. Methodology

2.1 Preparation of Natural Coagulant

The *Hibiscus Sabdariffa* was purchased from the NSL market in Klang, Selangor, Malaysia. The seeds were taken out from the capsules. The *Hibiscus Sabdariffa* seeds were washed with the water to remove the impurities substances. According the previous studies by Himanshu Patel[14], the seeds were dried at temperature of 60 ± 2˚C by using an oven. Then, the dried seeds were pulverised into fine powder by using a grinder. The coagulant agent was extracted by adding the 5g of seed powder into a 100ml of 0.5M sodium chloride (NaCl) and blended the mixture solution for 2 minutes with a food blender. NaCl solvent has the high efficient in the extraction of coagulant agent from the natural seeds [15,16]. Next, the coagulant was filtered through a filter paper in order to remove the impurities. The solution was keep in refrigerator to avoid ageing effects such as change in pH, and coagulation activity [14].

2.2 Preparation of Synthetic Pharmaceutical Wastewater

Synthetic pharmaceutical wastewater was prepared by mixing the paracetamol ($C_8H_9NO_2$, 151.2 g/mol) with distilled water to a concentration of 1000 mg/l. Different concentration of pharmaceutical wastewater (20mg/l, 60mg/l and 100mg/l) was prepared for the jar test experiment by diluting the wastewater with distilled water. The pH value of the wastewater was adjusted by adding the 1.0 M concentrated hydrochloric acid (HCl) or 1.0 M sodium hydroxide (NaOH) into the wastewater solution.

2.3 Jar Test Experiment

This jar test experiment was used to evaluate the performance for a coagulant in wastewater treatment process. The natural coagulant extracted, *Hibiscus Sabdariffa* was mixed with the 500 ml of synthetic wastewater. The mixture solution was then undergoes rapid mixing (100 rpm) for 4 minutes and slows mixing (40 rpm) for 25 minutes. After the agitation process was done, the mixture solution is then settled for 30 minutes [17]. The sample was collected for Chemical Oxygen Demand (COD) test and total suspended solid (TSS) test.

2.3.1 Optimization of Coagulation Process

In this experiment, three types of parameters were tested which are pH, coagulant dosage and initial concentration of wastewater. The coagulation experiment was carried out using Response Surface Methodology (RSM). RSM is known as the optimization of analytical method to evaluate the parameters for a process and form a best set of factor level combination [17]. This is help the researches and scientist to identify the significant factor and the best set of factor level combination for a process.

Three factors and three level Box-Behnken design was applied in this experiment in order to investigate the optimum working condition of *Hibiscus Sabdariff*a in coagulation process. Box-Behnken design is suitable for exploration of quadratic response surface and constructs a second-order polynomial model. It is used to optimize the performance of natural coagulant in coagulation process by a small number of experimental runs. In addition, this design can ensure all the experimental runs fall within the safe operating zone.

The experiment detail is shown in Table 1. The reduction for the COD and the TSS removal were analysed as the response. Design Expert Version 10 programme software was used in this experiment. A total of 17 experiments were generated by the programme software. The result obtained was analyse by using the analysis of variance (ANOVA) in order to find out the main factor that affect the performance of the coagulation process [18].

Table 1 Experimental Detail for the Coagulation Process

Factors	Low (-1)	Medium (0)	High (1)
pH	3	7	11
Coagulant Dosage (mg/l)	100	250	400
Initial Paracetamol Concentration (mg/l)	20	60	100

Table 2: The run of experiment using Box-Behnken Design

Run of Experiment	X_1	X_2	X_3
1	0	1	1
2	0	-1	-1
3	1	1	0
4	1	0	-1
5	0	0	0
6	0	0	0
7	1	0	1
8	0	0	0
9	-1	-1	0

10	-1	1	0
11	1	-1	0
12	0	1	-1
13	-1	0	-1
14	-1	0	1
15	0	-1	1
16	0	0	0
17	0	0	0

2.3.2 Chemical Oxygen Demand Test

COD reagent such as sulphuric acid reagent, standard ferrous ammonium sulphate titrant (FAS) (0.1M), standard potassium dichromate digestion solution (0.01667M) and Ferroin indicator solution was prepared. Next, 2.5ml sample was mixed with 1.5ml of potassium dichromate digestion solution and 3.5ml of sulphuric acid reagent. The mixture solution was then heated for 2 hours at temperature of 150˚C. After that, the mixture was cooled to room temperature. 1 or 2 drops of ferroin indicator was added into the mixture. Then, the mixture was titrated with 0.1M FAS until the color changes from blue-green to reddish brown. Blank sample (distilled water) was prepared in the same manner as sample. The COD value was calculated by using the equation:

$$Moloarity\ of\ FAS(M) = \frac{volume\ 0.0167\ M\ K_2Cr_2O_7\ \ solution\ titrated\ (ml)}{volume\ FAS\ used\ in\ titration\ (ml)} \times 0.10 \qquad (1)$$

$$COD\ \left(\frac{mg}{l}\right) = \frac{(A-B)\times M\times 8000}{ml\ of\ sample} \qquad (2)$$

Where,
A = ml of FAS used for blank, B = ml of FAS used for sample, M = molarity of FAS, 8000 = milliequivalent weight of oxygen × 1000 mL/L

For the COD reduction percentage was calculated by using the following equation:

$$COD\ Reduction\ (\%) = \frac{C_i - C_f}{C_i} \times 100\% \qquad (3)$$

Where,
C_i = initial COD value, C_f = final COD value

2.3.3 Total Suspended Solid Test

The weight of a filter paper was measured. The sample was filtered to obtain the suspended solid by using the filter paper. The filtrate was dried together with the filter paper in oven at temperature of 105˚C for 1 hour. After 1 hour, the weight of the dried filter paper was measured. The TSS value was calculated by using the equation (4).

$$TSS\ \left(\frac{mg}{l}\right) = \frac{(A-B)\times 1000\ mg/l}{ml\ of\ sample} \qquad (4)$$

Where,

A = weight of filter paper + weight of filtrate (g), B = weight f filter paper (g)

For the TSS removal percentage was calculated by using the following equation:

$$TSS\ Removal\ (\%) = \frac{TSS_f - TSS_i}{TSS_i} \times 100\% \quad (5)$$

Where,
TSS_i = initial TSS value, TSS_f = final TSS value

2.2.4 Comparison for the Performance between Natural Coagulant and Chemical Coagulant

A comparison between natural coagulant and chemical coagulant was conducted by using the jar test equipment after optimum working condition was identified. The efficiency of the coagulation for *Hibiscus Sabdariffa* was compared with commercial chemical coagulant, aluminium sulphate (alum). The purpose of this experiment is to prove the coagulation ability of the natural coagulant and it can be used for the wastewater treatment process. According to the finding from[20], the optimum condition for aluminium sulphate in coagulation process is pH 7 with coagulant dosage of 100mg/L.

3. Results and Discussion

3.1 ANOVA analysis

The performance of the natural coagulant in the coagulation process can be affected by some parameters such as pH, coagulant dosage and paracetamol concentration in wastewater. Response surface methodology is used for the optimization of the working condition for the natural coagulant in wastewater treatment process. Box-Behnken design is implemented in this research project and total 17 runs of experiment is generated. There are two responses for the experiment, namely COD reduction percentage and TSS removal percentage.

The ANOVA analysis result for the COD reduction is shown in the Table 3.0. The Figure 1.0 is shown that the result obtained from experiment is similar with the predicted result and the R^2 value for COD reduction is 0.9848. The main effect of pH, coagulant dosage and initial paracetamol concentration, and the second-order effect of pH are significant model terms. The result obtained from experiment (COD reduction) is correlated by using the second-order polynomial shown in Equation 6.

$$COD\ Reduction(\%) = 24.11 - 12.27A + 5.39B - 6.85C + 19.27A^2 \quad (6)$$

Where,
A = pH, B = coagulant dosage, C = initial paracetamol concentration

Based on the Table 3.0, the pH value is the most significant parameter that affected the COD reduction percentage in the coagulation process. The P value for this parameter is less than 0.001 which indicates the pH value of wastewater is significant at 95% confidence level. This result is proves that the efficiency of *Hibiscus Sabdariffa* seed as natural coagulant in the coagulation process is highly dependent on the pH value of wastewater.

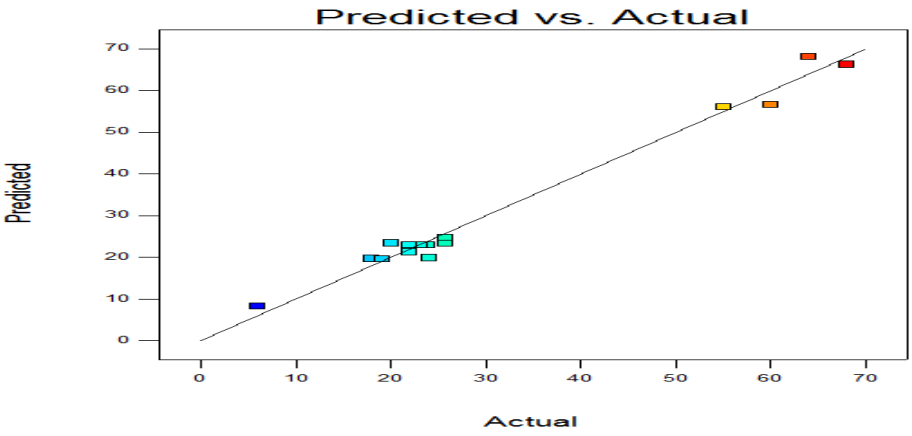


Figure 1.0: Predicted vs. actual result for COD reduction (%)

On the other hand, the ANOVA analysis result for TSS removal is shown in Table 4.0. From the Table 4.0, the ANOVA analysis is states the pH of wastewater is the significant factor that affect the performance of the coagulation process. Figure 2.0 is shows the different between the predicted result and experiment result for TSS removal (%). There are some points do not fit with the linear line while the others are acceptable. The R^2 value for TSS removal (%) is 0.9469. The main effect of pH, coagulant dosage and initial paracetamol concentration, and the second-order effect of pH and coagulant dosage are significant model terms. The result obtained from experiment (TSS removal) is correlated by using the second-order polynomial shown in Equation 7.

$$TSS\ removal(\%) = 24.92 - 13.74A + 3.23B - 6.10C + 22.86A^2 - 5.20B^2 \quad (7)$$

Where,
A = pH, B = coagulant dosage, C = initial paracetamol concentration

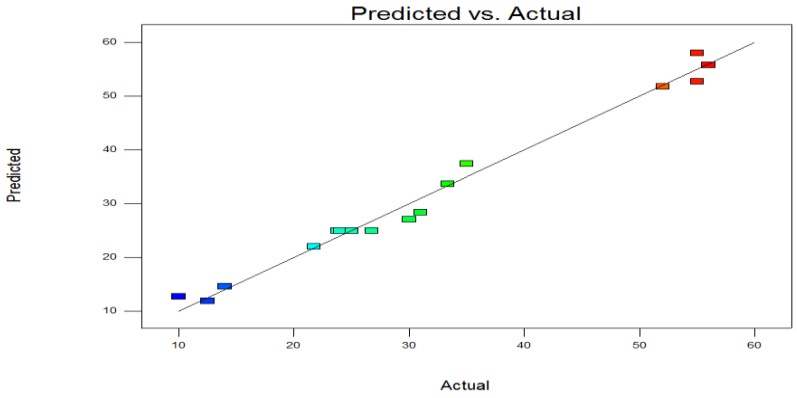


Figure 2.0: Predicted vs. actual result for TSS removal (%)

Table 3.0: ANOVA analysis for COD reduction (%)

Source	Sum of Squares	Degree of Freedom	Mean Square	F Value	Prob >F	
Model	5362.89	9	595.88	52.25	<0.001	Significant
A-pH	3169.27	1	3169.27	277.88	<0.001	Significant

B-coagulant dosage	139.70	1	139.70	12.25	0.0100	
C-initial concentration	88.84	1	88.84	7.79	0.0269	
AB	13.07	1	13.07	1.15	0.3199	
AC	9.00	1	9.00	0.79	0.4039	
BC	21.81	1	21.81	1.91	0.2092	
A^2	1905.39	1	1905.39	167.06	<0.0001	Significant
B^2	17.91	1	17.91	1.57	0.2504	
C^2	31.95	1	31.95	2.80	0.1381	
Residual	79.84	7	11.41			
Lack of Fit	77.14	3	25.71	38.16	0.0021	Significant
Pure Error	2.70	4	0.67			
Cor Total	5442.73	16				

Table 4.0: ANOVA analysis for TSS removal (%)

Source	Sum of Squares	Degree of Freedom	Mean Square	F Value	Prob >F	
Model	4226.76	9	469.64	35.44	<0.0001	Significant
A-pH	1510.58	1	1510.58	114.01	<0.0001	Significant
B-coagulant dosage	83.40	1	83.40	6.29	0.0405	
C-initial concentration	297.19	1	297.19	22.43	0.0021	
AB	0.027	1	0.027	0.0021	0.9651	
AC	0.017	1	0.017	0.0013	0.9725	
BC	52.56	1	52.56	3.97	0.0867	
A^2	2200.96	1	2200.96	166.11	<0.0001	Significant
B^2	113.71	1	113.71	8.58	0.0220	
C^2	34.06	1	34.06	2.57	0.1529	
Residual	92.75	7	13.25			
Lack of Fit	87.25	3	29.08	21.10	0.0065	
Pure Error	5.51	4	1.38			
Cor Total	4319.51	16				

3.2 Respond Surface Plotting and Optimization

3D response surface plot are drawn as a function of two factors while holding other factor at fixed level, normally at the zero level. Those plots are helpful to in understanding both the main and interaction effects of these two factors [21]. For example, for the interaction between pH and coagulant dosage, the initial paracetamol concentration will locate at zero level which is 60mg/l. Then, the effect of this interaction on COD reduction and TSS removal will be analysed and discussed. There are three set of interactions will be discussed which are pH and coagulant dosage, pH and initial paracetamol concentration, coagulant dosage and initial paracetamol concentration.

3.2.1 Effect of pH and Coagulant Dosage on COD reduction & TSS removal

The 3D response surface plot for the effect of pH of wastewater and coagulant dosage at initial paracetamol concentration at 60mg/l is shown in the Figure 3.0 and Figure 4.0. The COD reduction percentage and TSS removal percentage is reached 68% and 56% respectively when the pH of wastewater is in acid condition. The COD reduction and TSS removal percentage is started decreases as the pH value is increases from 3 to 9. After that, a slight increment for the COD reduction and TSS removal percentage from pH 9 to 11. The maximum COD reduction and TSS removal percentage can be achieved when the pH value of wastewater is located at 3 and the coagulant dosage is about 260mg/l. From the Table 3.0 and Table 4.0, the pH is shown in the high significant effect from the ANOVA analysis result. This shows that coagulation process is highly pH dependent.

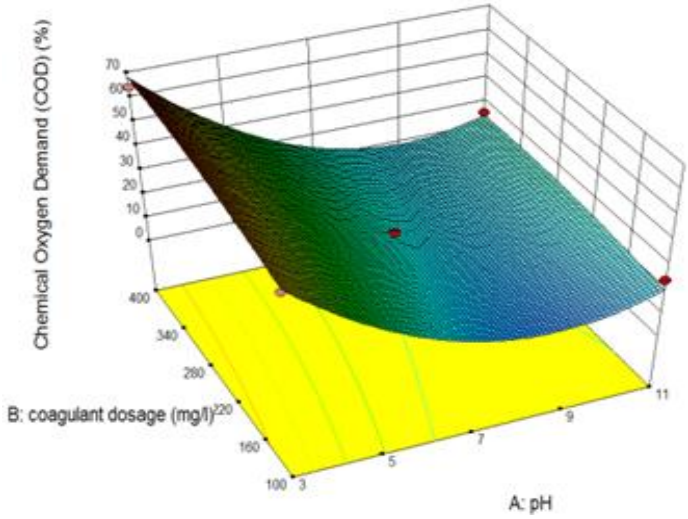


Figure 3.0: Effect of pH and Coagulant Dosage on COD reduction

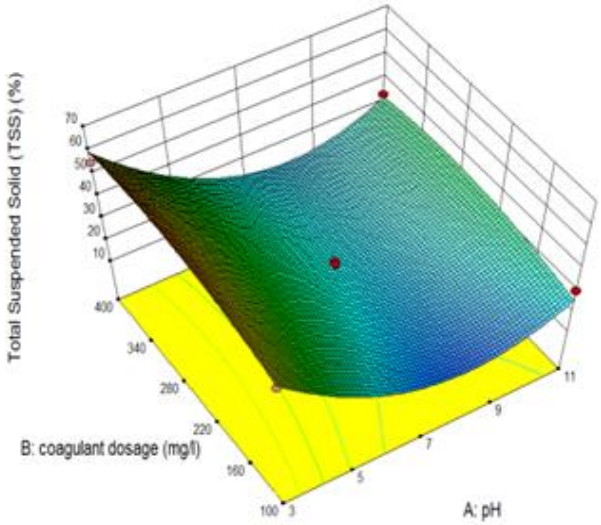


Figure 4.0: Effect of pH and Coagulant Dosage on TSS removal

The proteins of the natural coagulant are made up from amino acids which contain amine group and carboxylic acid. The change of the net charged for the amine group is depended on the pH value of a solution [20]. At the pH 7 (neutral), the amine group is

protonated while the carboxylic acid is deprotonated. If the pH value of a solution is at acidic condition (pH 3), the amine group will be protonated which mean more positively charged ions are produced. Then, the positive charged ions will neutralize the negatively charged colloids in the wastewater during the coagulation process [11,19]. Conversely, the amine group is deprotonated and produced negatively charged ions when there is wastewater in alkali condition (pH 11).

When the pH value of the wastewater is located in acidic condition, the glutamic acid and aspartic acid (cationic amino group) are favour for acidic condition will generate more positively charged ions. These positively charged ions will trap the negative charged particles in the paracetamol wastewater. Thus, the coagulation process has a best efficiency in wastewater with low pH value. A slight increment for the COD reduction and TSS removal in the alkali condition, because there is some anionic amino group such as arginine acid which is more favour for alkali condition is produced. Arginine acid contains about 10.13% protein presence in *Hibiscus Sabdariffa* seed. It will generate negatively charged ions in the high pH value of wastewater [22]. Then, these negatively charged ions are also able to neutralize some of the positively charged particles and perform the coagulation process. Thus, there is small increasing in the COD reduction and TSS removal percentage for the wastewater with high pH value.

3.2.2 Effect of pH and Initial Paracetamol Concentration on COD reduction & TSS removal

Figure 5.0 and Figure 6.0 are show the effect of initial paracetamol concentration and pH on COD reduction. Initial paracetamol concentration is also known as one of the important parameters that affect the performance of coagulation process. If the concentration of paracetamol is exceeds the optimum concentration would result a poor performance for the coagulation process due to the formation of inter-particles bridging is destructed[23]. As mentioned in Section 2.5.3, an increasing of initial paracetamol concentration in wastewater will increase the negatively charged of colloid particles. If there are no sufficient positively charged ions are able to serve as the bridge to attract the colloid particles, the efficiency of coagulation will decrease.

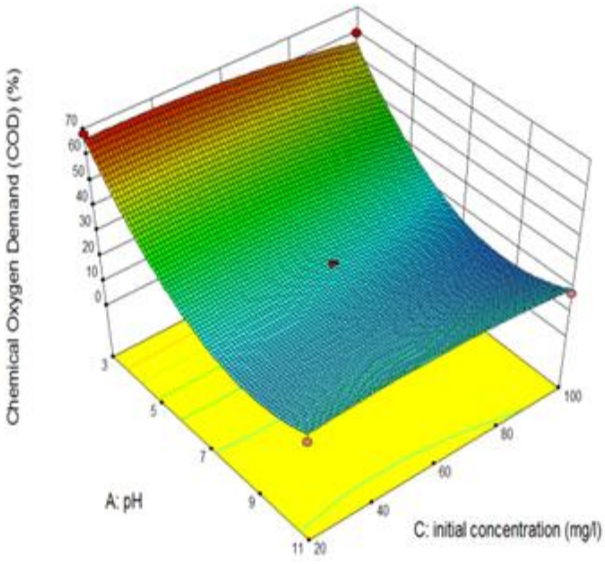


Figure 5.0: Effect of pH and Initial Paracetamol Concentraiton on COD reduction

From the Figure 5.0, the coagulation process is performed within the initial paracetamol concentration range from 20 mg/l to 100 mg/l. Based on the Figure 4.4, the best result is obtained at the pH 3 and initial concentration of 75mg/l. At that condition, the COD reduction percentage can achieves to 60%. When the concentration of paracetamol is beyond 75mg/l, the efficiency of the coagulant is reduced. This mean that the 75mg/l is the saturation point, the paracetamol concentration is saturated at this point. Due to negatively charged particles presence in wastewater is more than the positively charged ions that generated by coagulant. The positively charged ions are not able to completely neutralized the negatively charged ions. Thus, the COD reduction percentage of the coagulation process is decreases.

By comparing the 3D response surface plot between the Figure 3.0 and Figure 5.0, it can clearly see that the patterns on the plots are similar. The best result is obtained from these two 3D response surface plots in the low pH value of wastewater. This means that pH value is play the main parameter in this coagulation process. Based on the result obtained, it shows that the pH has the great affect between these two relationships. This is because more positively charged ions can be generated by the coagulant in the acidic condition.

For the TSS removal, 56% of TSS removal percentage is obtained from the 3D response surface plot (Figure 6.0). Similar to the COD reduction result, the maximum TSS removal percentage is obtained in the wastewater with low pH value and initial paracetamol concentration of 75mg/l. The efficiency of coagulation process is reduced as the initial concentration beyond 75mg/l. Same as the previous discussion, the paracetamol concentration is saturated at 75mg/l. The inter-particles bridge between the negatively and positively charged ions is not able to form beyond the saturation point. Hence, the efficiency of coagulation process is decreases as the initial paracetamol concentration in wastewater above the saturation point.

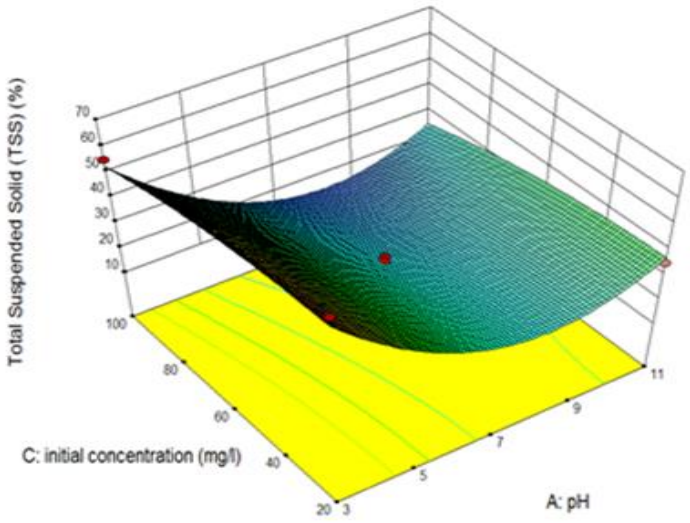


Figure 6.0: Effect of pH and Initial Paracetamol Concentraiton on TSS removal

3.2.3 Effect of Coagulant Dosage and Initial Paracetamol Concentration on COD reduction & TSS removal

The relationship between the coagulant dosage and initial paracetamol concentration is studied in this research study. The mechanism of coagulation will occur once there is sufficient coagulant added to the wastewater to achieve the optimum destabilization of colloid particles and formed into larger flocs. In this research study, coagulant dosage is studied in order to identify the optimal coagulant dosage for this coagulation process. Overdosing or insufficient coagulant dosage can lead to a poor performance of coagulation process [24]. The insufficient coagulant dosage in a coagulation process can causes the neutralisation process between the positive and negative charged particles inside wastewater does not perform well. The reason is same as mentioned before, unbalancing positive and negative charged ions in a solution will cause the inter-particles bridge devastate. Then, the particles will not able to coagulate together and poor result will be obtained. Similar to the overdosing coagulant, more positively charged particles are generated from the coagulant can cause the particles to re-disperse during the coagulation process [21]. Therefore, identifying the optimum coagulant dosage is important for optimum performance with minimum coagulant dosage. This can reduce the cost of a coagulant in the wastewater treatment process and reduce the sludge formation.

From the Figure 7.0, the maximum COD reduction can be achieved at the initial paracetamol concentration of 75mg/l and natural coagulant dosage at 260mg/l. The maximum COD reduction percentage obtained from this combination is 65%.When the initial concentration of paracetamol is beyond the 75mg/l with coagulant dosage at 260mg/l, the percentage for COD reduction is decreases. On the other hands, the performance of coagulation process is decreases when the dosage of coagulant is increasing from the 260mg/l to 400mg/l with the initial paracetamol concentration at 75mg/l. Based on Figure 8.0, the TSS removal percentage is increases as the coagulant dosage increases from 100mg/l to 260mg/l. When the coagulant dosage is above 260mg/l, the TSS removal is decreases. Thus, the higher TSS removal percentage is obtained at the coagulant dosage of 260mg/l and initial paracetamol concentration of 75mg/l.

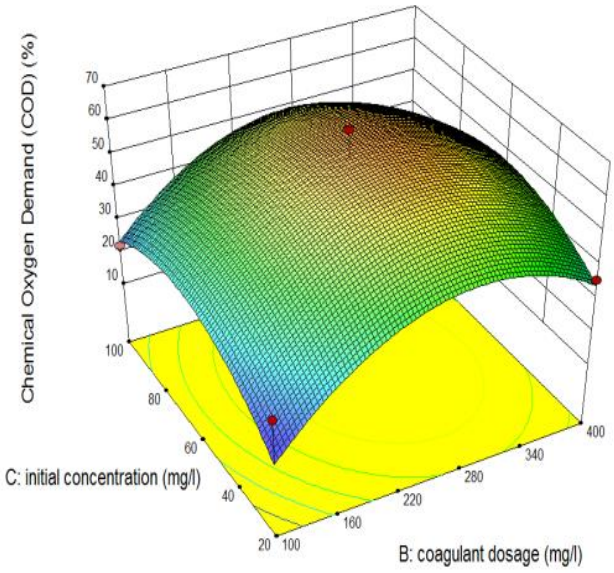


Figure 7.0: Effect of Coagulant Dosage and Initial Paracetamol Concentration on COD reduction

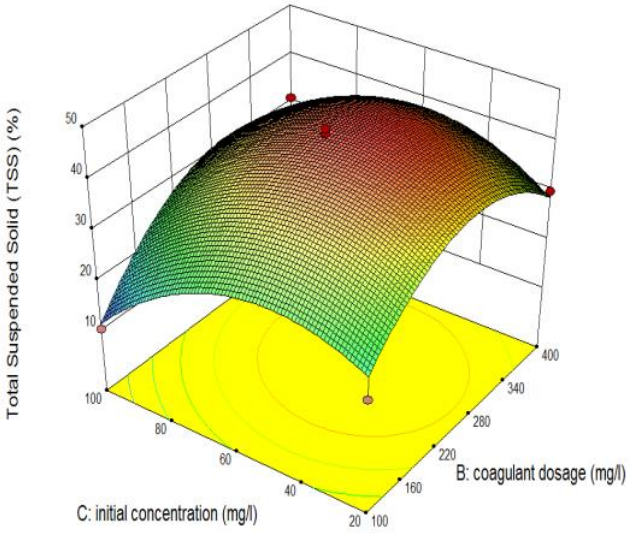


Figure 8.0: Effect of Coagulant Dosage and Initial Paracetamol Concentration on TSS removal

3.2.4 Optimum Working Condition for Hibiscus Sabdariffa seed

In this research study, optimum working condition for *Hibiscus Sabdariffa* seed as natural coagulant is determined. The aim to determine the optimum working condition is to identify the maximum efficiency of the natural coagulant in pharmaceutical wastewater treatment process. The working condition is optimized by using Design Expert (version 10) based on the experimental results obtained. From Section 3.2.1, the higher COD reduction percentage is achieved at pH 3 and coagulant dosage of 260mg/l. On the Section 3.2.2, a best result is obtained when the pH value is 3 (acidic condition) and initial paracetamol concentration at 75mg/l. For the Section 3.2.3, at the initial concentration of 75mg/l and dosage of coagulant with 260mg/l, a maximum COD reduction for the coagulation process is able to achieve. Hence, the maximum COD reduction percentage which is 68% is obtained at pH 3, initial paracetamol concentration of 75mg/l and coagulant dosage of 260mg/l. Similar to the TSS removal, the TSS removal percentage is about 56% at the optimum condition.

4.3 Comparison of Natural Coagulant and Chemical Coagulant

The coagulation process is conducted by using the chemical coagulant, aluminium sulphate (alum). The result obtained from this experiment is used to compare with the *Hibiscus Sabdariffa* seed. Figure 9.0 shows the result of both natural and chemical coagulant in the coagulation process.

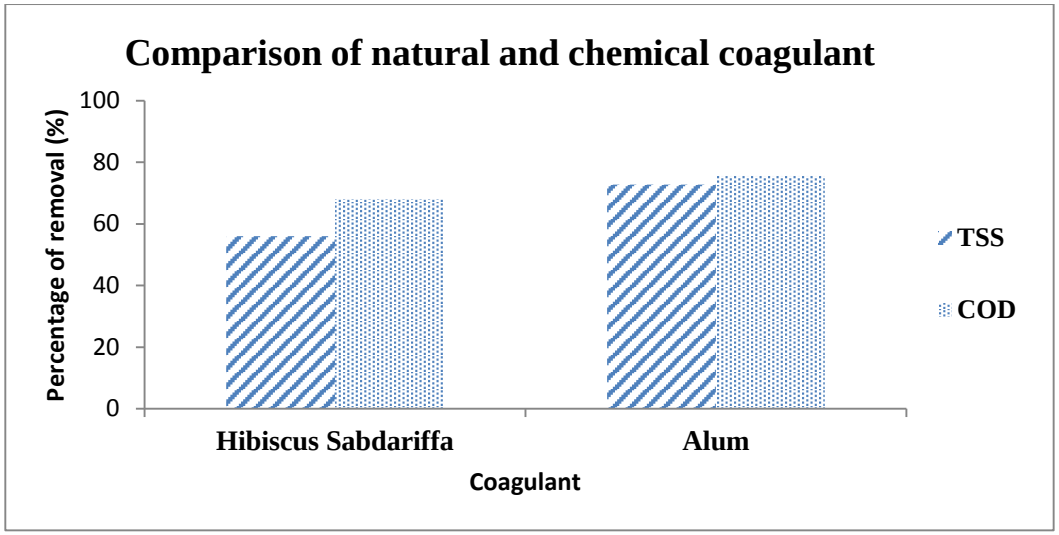


Figure 9.0: Performance Comparison of both Natural and Chemical Coagulant

From the result obtained the alum result in COD reduction of 75.5% and TSS removal of 72%. On the other hand, 68% of COD reduction and 56% of TSS removal is achieved by the natural coagulant, *Hibiscus Sabdariffa* seed. According to Figure 9.0, the performance of *Hibiscus Sabdariffa* seed in COD reduction and TSS removal is closer to the alum. This is shows that the *Hibiscus Sabdariffa* seed can be used as a natural coagulant to replace alum which have been used in coagulation process for a long time. By using *Hibiscuss Sabdariffa* seed as coagulant, the negative impacts of using chemical coagulant related to health and environmental can be prevented. Other than that, cost of using chemical coagulant is more expensive than natural coagulant. This is because the *Hibiscus Sabdariffa* is widely available in local area.

4. Conclusions

In conclusion, this study shows that Hibiscus Sabdariffa seed is found as a natural coagulant that can reduce the COD value and TSS of paracetamol wastewater. The presence of the protein such as amino acid group such as glutamic acid, aspartic acid and arginine are the key components that contributed to the coagulation process. Three parameters such as pH of solution, initial paracetamol concentration and coagulant dosage are evaluated by response surface methodology, and the pH has high significant effect in the coagulation process. This is because the net charged of protein components will change depend on the pH of wastewater. At the optimum working conditions, pH 3, coagulant dosage of 260mg/l and initial concentration at 75mg/l, the COD reduction percentage and TSS removal percentage can achieve to 68% and 56%. Besides that, the performance of Hibiscus Sabdariffa seed is found comparable to chemical coagulant, alum. Therefore, it can be considered an alternative for chemical coagulant which use for the pharmaceutical wastewater treatment process.

References

[1] T. D. Babarao and S. Verma, “Coal Washery Waste Water Treatment using Natural Coagulants and Chemical Precipitation,” vol. 4, no. 6, pp. 1877–1881, 2015.

[2] X. Li and G. Li, “A Review : Pharmaceutical Wastewater Treatment Technology and Research in China,” no. Ap3er, pp. 345–348, 2015.

[3] C. Gadipelly and A. Pérez-González, “Pharmaceutical Industry Waste Water: Review of the Technologies for Water Treatment and Reuse,” *Ind. Eng. Chem. Res.*, vol. 53, no.

April 2016, pp. 11571–11592, 2014.

[4] M. Irfan, T. Butt, N. Imtiaz, N. Abbas, R. A. Khan, and A. Shafique, "The removal of COD, TSS and colour of black liquor by coagulation-flocculation process at optimized pH, settling and dosing rate," *Arab. J. Chem.*, 2013.

[5] M. Jozwiak-Bebenista and J. Z. Nowak, "Paracetamol: Mechanism of action, applications and safety concern," *Acta Pol. Pharm. - Drug Res.*, vol. 71, no. 1, pp. 11–23, 2014.

[6] M. Klavarioti, D. Mantzavinos, and D. Kassinos, "Removal of residual pharmaceuticals from aqueous systems by advanced oxidation processes," *Environ. Int.*, vol. 35, no. 2, pp. 402–417, 2009.

[7] N. D. Tzoupanos and a I. Zouboulis, "Coagulation-Flocculation Processes in Water / Wastewater Treatment : the Application of New Generation of Chemical Reagents," *6th IASME/WSEAS Int. Conf. HEAT Transf. Therm. Eng. Environ.*, pp. 309–317, 2008.

[8] J. Q. Jiang, "The role of coagulation in water treatment," *Curr. Opin. Chem. Eng.*, vol. 8, pp. 36–44, 2015.

[9] M. I. Ashraf, M. Ateeb, M. H. Khan, N. Ahmed, Q. Mahmood, and Zahidullah, "Integrated treatment of pharmaceutical effluents by chemical coagulation and ozonation," *Sep. Purif. Technol.*, vol. 158, pp. 383–386, 2016.

[10] N. Vieno, T. Tuhkanen, and L. Kronberg, "Removal of pharmaceuticals in drinking water treatment: effect of chemical coagulation.," *Environ. Technol.*, vol. 27, no. 2, pp. 183–192, 2006.

[11] Z. L. Yang, B. Y. Gao, Q. Y. Yue, and Y. Wang, "Effect of pH on the coagulation performance of Al-based coagulants and residual aluminum speciation during the treatment of humic acid-kaolin synthetic water," *J. Hazard. Mater.*, vol. 178, no. 1–3, pp. 596–603, 2010.

[12] S. Malaysiana, P. Aluminium, and A. Minum, "Removal of Aluminium from Drinking Water," vol. 39, no. 1, pp. 51–55, 2010.

[13] Y. C. Sook, M.N.P.Krisha, Y.W.Ta, E.R.Mavinakere, and N.R.Ramakrishnan, "Utilization of plant-based natural coagulants as future alternatives sustainable water clarification.",J. Environmental Sciences vol 26, no 11, pp. 2178-2189.

[14] M. Asrafuzzaman, A. N. M. Fakhruddin, and M. A. Hossain, "Reduction of Turbidity of Water Using Locally Available Natural Coagulants," *ISRN Microbiol.*, vol. 2011, pp. 1–6, 2011.

[15] K. L. Nyam, S. Y. Leao, C. P. Tan, and K. Long, "Functional properties of roselle (Hibiscus sabdariffa L.) seed and its application as bakery product," *J. Food Sci. Technol.*, vol. 51, no. 12, pp. 3830–3837, 2014.

[16] E. Approach, "NaturaL Coagulants for Water Purification : AN," vol. 5, no. 5, pp. 1177–1185, 2016.

[17] T. Kazi, A. Virupakshi, and M. T. Scholar, "Treatment of Tannery Wastewater Using Natural Coagulants," *Int. J. Innov. Res. Sci. Eng. Technol.*, vol. 2, no. 8, pp. 4061–4068, 2013.

[18] G. Muthuraman, S. Sasikala, and N. Prakash, "Proteins from Natural Coagulant for Potential Application of Turbidity Removal in Water," *Ijeit*, vol. 3, no. 1, pp. 278–283,

2013.

[19] D. Montgomery, “Design and analysis of experiments.” p. 699, 2001.

[20] J. T. Alexander, F. I. Hai, and T. M. Al-aboud, “Chemical coagulation-based processes for trace organic contaminant removal: Current state and future potential,” *J. Environ. Manage.*, vol. 111, pp. 195–207, 2012.

[21] a L. Ahmad, S. Ismail, and S. Bhatia, “Optimization of coagulation-flocculation process for palm oil mill effluent using response surface methodology.,” *Environ. Sci. Technol.*, vol. 39, no. 8, pp. 2828–2834, 2005.

[22] H. Patel and R. T. Vashi, “Removal of Congo Red dye from its aqueous solution using natural coagulants,” *J. Saudi Chem. Soc.*, vol. 16, no. 2, pp. 131–136, 2012.

[23] A. Mishra and M. Bajpai, “Flocculation behaviour of model textile wastewater treated with a food grade polysaccharide,” *J. Hazard. Mater.*, vol. 118, no. 1–3, pp. 213–217, 2005.

[24] T. K. F. S. Freitas, V. M. Oliveira, M. T. F. de Souza, H. C. L. Geraldino, V. C. Almeida, S. L. Fávaro, and J. C. Garcia, “Optimization of coagulation-flocculation process for treatment of industrial textile wastewater using okra (A. esculentus) mucilage as natural coagulant,” *Ind. Crops Prod.*, vol. 76, pp. 538–544, 2015.

Control of Pollutants from Non-Point Source using Adsorption Process

Chan Huann Yu[1]*, Rajesh Rajasekaran[2]
School of Engineering Taylor's University, Malaysia
*Corresponding email of author**: chanhuannyu@sd.taylors.edu.my

Abstract
In this study, the main objective is to investigate the adsorption rate of a natural adsorbent, rice husk. Two pre-treatment methods were used to increase the adsorption ability of rice husk. The first method is to treat the rice husk with tartaric acid and the second method is to treat the rice husk with hydrochloric acid and sodium hydroxide. The condition of the adsorption processes is simulated to a running vehicle which has an exhaust gas flow rate of 5L/min. The result shows that the rice husk treated with hydrochloric acid and sodium hydroxide can adsorb more gas pollutant than the tartaric acid treated rice husk. Besides that, it also shows that the presence of sodium hydroxide gives a better result on pre-treatment. This gives a very good further study direction although the result is not compatible with the artificial adsorbent.

Keywords: Rice husk, adsorption, gas pollutants, natural adsorbent, sodium hydroxide.

1.0 Introduction

Pollution can be divided into two categories which are the point source pollution and the non-point source pollution. Besides that, there are two main kinds of pollutants which are the water pollutants and the air pollutants.

Point source water pollution is the pollution which coming from a single point which is the same as point source air pollution. The only difference between point source water pollution and air pollution is that the pollutants are in gas phase [1]. For example, municipal water treatment plants, factories and confined animal feedlots can be categorized as point source pollution [2].

Non-point source pollution is that the source of the pollutant is not able to be determined. For example, the acid rain from the air that able to enters the water cycle which will harm the aquatic creatures or even the life on land. Besides that, the pollutants that emitted from the vehicles such as sulphur oxides, nitrogen oxides and carbon monoxide are also non-point source pollutants [1].

In September 15, 2015, NYU Langone Medical Center published that the same association between particular matter exposure and increase in risk of death from all non-accidental causes and from cardiovascular disease [3]. Besides that, it also states that the most harmful particulate matters are from auto exhaust, chemical plants and coal-burning power plants [3]. This shows that the pollutants from the vehicles exhaust really need to be controlled. To control the air pollutants, adsorption process has shown a great result on reducing the pollutant concentration. Adsorption is a process that uses solids the remove substances from either gaseous or liquid solutions. The molecules are attracted to the surface but not enter to the solid's minute space [4]. This phenomenon has become a useful tool for separation and purification.

Research Question:

Which treated natural adsorbent will adsorb most pollutants from the exhaust gas under a condition of fixed adsorption column, fixed flow rate, uncontrolled temperature and uncontrolled pressure of polluted gas?

Objective:

To determine the efficiency of adsorption of different natural adsorbents to reduce the pollutants in polluted gas from vehicle exhaust under a condition of fixed flow rate, uncontrolled temperature and uncontrolled pressure. This is to simulated the condition of a car is running.

Scope:

- The efficiency of adsorption of natural adsorbent with different type of pre-treatment.
- The effect of gas temperature and pressure to the adsorption efficiency.

2.0 Methodology

The natural adsorbent that been used in this research is rice husk. It is used to do adsorption on removing heavy metals such as lead (Pb), zinc (Zn) and nickel (Ni). As rice husk is insoluble in water, having good chemical stability, structural strength due to high silica content, some researchers are using it to treat the heavy metal from the ground water and surface water [18]. But it has been treated before it is used as adsorbent. It is stated in the study of Sneh Lata (2014) that treated rice husk preformed a better adsorption rate on heavy metal than an untreated rice husk. This shows that it has a huge potential on treating the air pollutants as well.

2.1 Material preparation

Rice has been given free from a local rice mill named Mutiara Kita SDN. BHD. located in Kedah, Malaysia. Tartaric acid has been purchased from Evergreen Engineering & Resources. The hydrochloric acid and sodium hydroxide are provided by Engineering Laboratory of Taylors University.

2.2 Pre-treatment of rice husk (tartaric acid)

The rice husk is first rinsed with tab water then followed by distilled water to remove dust and ash. Then, it is dried in an oven for 15 hours at a temperature of 50^0C. After that, it is mixed with a 1.2M tartaric acid. The mixture is stirred continuously until homogenous and then again dried in an oven under same condition. Then, the treated rice husk is rinsed with distilled water until neutral and then dried in an oven under the same condition stated above [18].

2.3 Pre-treatment of rice husk (hydrochloric acid and sodium hydroxide)

The rice husk is first wash and rinsed with tab water then followed by distilled water to remove dust and ash. After that, it is dried in an oven for 15 hours at a temperature of 50^0C. The dried rice husk is then soaked in 5mol% hydrochloric acid solution (HCl) for an hour under room temperature. The followed by soaking it into 50mol% of sodium hydroxide solution (NaOH) for an hour under temperature of 90^0C. Finally, it is rinsed with distilled water until neutral and dried in an oven under the same condition stated above [19].

2.4 Experiment set up

A batch adsorption experiment was conducted to identify the efficiency of pre-treated rice husk to adsorb carbon monoxide (CO), nitrogen oxide (NO) and sulphur dioxide (SO_2). This process is run in a Perspex column as shown in Figure 1 filled with the treated rice husk.

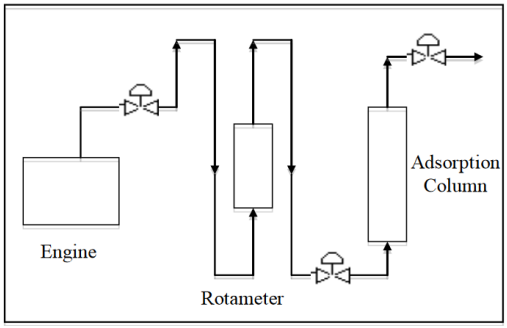


Figure 1: Experimental set up for adsorption process.

The process for each pre-treated rice husk is run for 30 minutes and the concentrations of pollutants (ppm) are collected for every 5 minutes by using gas analyser and gas detector which are shown in Figure 2.



Figure 2: Gas analyser and Gas detector

After the data was collected, the percentage of pollutant adsorbed will be calculated using a formula of:

$$\frac{m_2 - m_1}{m_1} \times 100\% = Percentage\ of\ pollutant\ adsorbed$$

Where:

m_1 = mass of adsorbent before adsorption

m_2 = mass of adsorbent after adsorption

3.0 Result and Discussion

3.1 Adsorption process using rice husk treated with tartaric acid

The adsorption process using this adsorbent has been repeated three times to provide a most accurate data. The data are shown in Table 1, Table 2 and Table 3

Table 1: Concentration of gas pollutant during adsorption process using tartaric acid treated rice husk (set 1)

Time (min)	**Concentration (ppm)**		
	CO	NO	SO_2
0	10000	153	8
5	7950	140	10
10	8500	144	11
15	9260	150	9
20	9720	152	10
25	9830	155	9
30	9910	154	7

Table 2: Concentration of gas pollutant during adsorption process using tartaric acid treated rice husk (set 2)

Time (min)	**Concentration (ppm)**		
	CO	NO	SO_2
0	9990	154	8
5	7900	142	10
10	8450	146	10
15	9300	156	11
20	9780	155	10
25	9820	153	9
30	9900	151	7

Table 3: Concentration of gas pollutant during adsorption process using tartaric acid treated rice husk (average)

Time (min)	**Concentration (ppm)**		
	CO	NO	SO_2
0	9995	154	8
5	7925	141	10
10	8475	145	11
15	9280	153	10
20	9750	154	10
25	9825	154	9
30	9905	153	7

Table 4: Reduction of gas pollutant concentration during adsorption process using tartaric acid treated rice husk (average)

Time (min)	**Reduction percentage (%)**		
	CO	NO	SO_2
0	0.0	0.0	0.0
5	20.7	8.4	-25.0
10	15.2	5.8	-37.5
15	7.2	0.6	-25.0
20	2.5	0.0	-25.0
25	1.7	0.0	-12.5
30	0.9	0.6	12.5

3.2 Adsorption process using rice husk treated with hydrochloric acid (HCl) and sodium hydroxide (NaOH)

The data of adsorption process using this adsorbent have been tabulated in Table 5, Table 6 and Table 7.

Table 5: Concentration of gas pollutant during adsorption process using HCl and NaOH treated rice husk (set 1)

Time (min)	**Concentration (ppm)**		
	CO	NO	SO_2
0	9995	175	9
5	7000	150	8
10	7400	155	7
15	8000	162	11
20	9000	170	10
25	9200	169	11
30	9400	170	12

Table 6: Concentration of gas pollutant during adsorption process using HCl and NaOH treated rice husk (set 2)

Time (min)	**Concentration (ppm)**		
	CO	NO	SO_2
0	9980	169	10
5	7500	153	10
10	7200	155	8
15	7900	160	9
20	8800	169	7
25	8900	167	9
30	9200	168	9

Table 7: Concentration of gas pollutant during adsorption process using HCl and NaOH treated rice husk (average)

Time (min)	**Concentration (ppm)**		
	CO	NO	SO_2
0	9988	163	10
5	7250	152	9
10	7300	155	8

15	7950	161	10
20	8900	170	9
25	9050	168	10
30	9100	169	11

Table 8: Reduction of gas pollutant concentration during adsorption process using HCl and NaOH treated rice husk (average)

Time (min)	**Reduction percentage (%)**		
	CO	NO	SO_2
0	0.0	0.0	0.0
5	27.4	6.8	10.0
10	26.9	4.9	20.0
15	20.4	1.2	0.0
20	10.9	-4.3	10.0
25	9.4	-3.1	0.0
30	8.9	-3.7	-10.0

3.3 Comparison between tartaric acid treated rice husk and HCl, NaOH treated rice husk

From the data above shows that the rice husk that treated with HCl and NaOH is able to adsorb more gas pollutant than tartaric acid treated rice husk. The tabulated reduction percentage data of both the adsorbent are used to formulate 3 graphs for each pollutant. The graph are shown in Figure 3, Figure 4 and Figure 5.

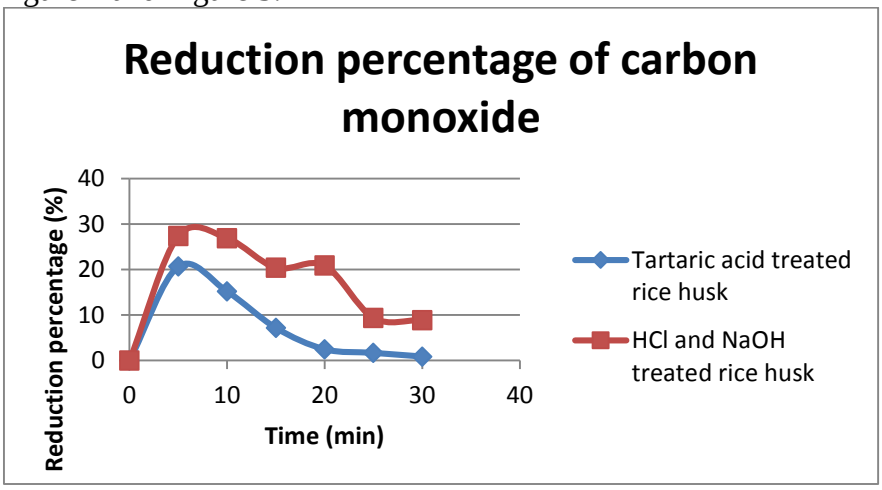


Figure 3: Reduction percentage of carbon monoxide

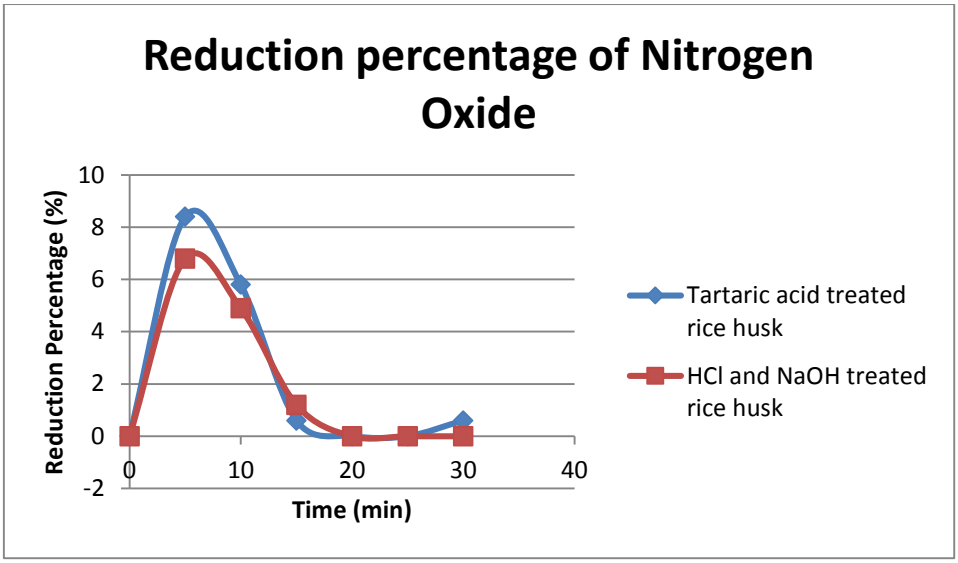


Figure 4: Reduction percentage of nitrogen oxide

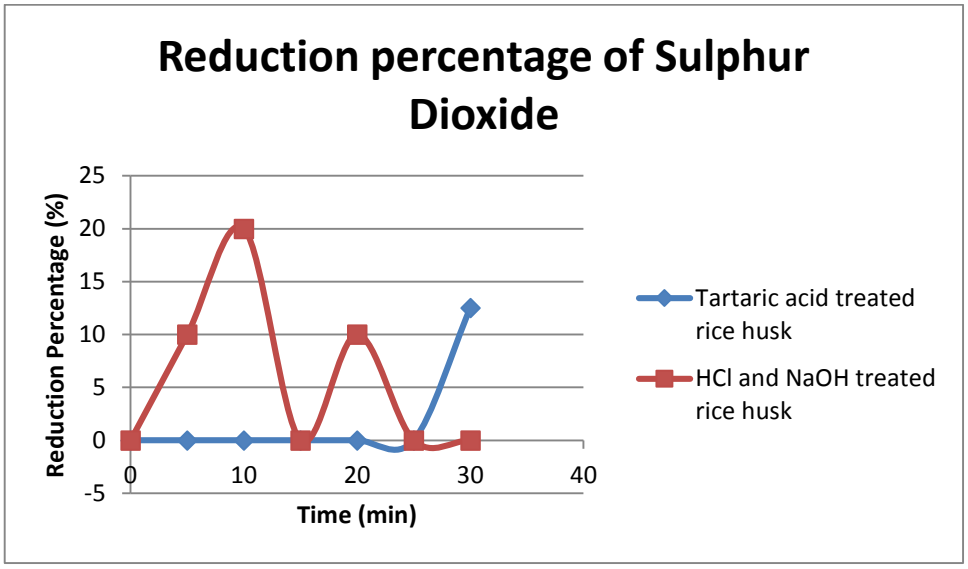


Figure 5: Reduction percentage of nitrogen oxide

From the figures above, they showed that the rice husk a small ability to adsorb carbon monoxide but not nitrogen oxide and sulphur dioxide. Besides that it also shows that the HCl and NaOH treated rice husk performed better than tartaric acid treated rice husk. But still, it is not compatible to the artificial adsorbent such as activated carbon.

3.4 The effect of NaOH

From the data collected, it shows that the rice husk treated with NaOH has a better efficiency to adsorb gas pollutant. This is because rice husk is composed of lignin, cellulose, hemicellulose and siliceous ash. The outer layer of the husk is also covered with a layer of wax and pectin and they are hydrophobic [5]. Thus, the alkali treatment can remove the protective wax on the outer layer of the husk and let the remaining acid (HCl) to create more surface area on the rice husk.

3.5 The effect of flow rate

The flow rate of the polluted gas has been controlled by manipulate the rpm of the combustion engine. This is to simulate the condition of polluted gas coming out from a running vehicle. The normal rpm of the engine for a running vehicle is assumed to be 3000rpm. This rotation of engine will provide a 5L/min exhaust gas. By using the rotary meter, the flow rate is also been fixed. From previous studies that done by Ranila. S. A (2013), it shows that a low flow

rate and a suitable adsorbent bed height will provide a best adsorption process. In the study, they used a 5L/min flow rate of polluted gas and a 30cm height of bed to get the best result in their research [6]. Thus, this condition is also applied in this research.

3.6 The effect of temperature and pressure

In this research, the condition created has no much change in temperature and pressure. The pressure of the adsorption process is near to the atmospheric pressure and the temperature is around 40^0C. This is the condition of a running vehicle. Thus, the pressure and temperature do not affect the result of the adsorption processes. But if the pressure increases or temperature decreases, it will increase the adsorption rate of a physisorption process. For chemisorption, it only occurs at low pressure and the adsorption rates will increases when the temperature increases.

4.0 Conclusion

In this study, the rice husk treated with HCl and NaOH is more effective on adsorbing gas pollutants compared to rice husk treated with tartaric acid. Besides that, it also shows that it only capable on adsorbing carbon monoxide but not nitrogen oxide and sulphur dioxide. Furthermore, the pressure and temperature do not give much effect due to the condition of simulating a running car.

The pre-treated rice husk adsorbents are still not compatible with the artificial adsorbents. But it shows that the alkali treatment of rice husk will boost up the effect of acid to the husk surface. This is a very good direction for a further research on pre-treatment of rice husk.

Reference

[1] Hu, J., Ying, Q., Wang, Y. and Zhang, H. (2015). Environment International.*Characterizing multi-pollutant air pollution in China: Comparison of three air quality indeces*, 1(84).

[2] Kean.edu, (2015). *Point Source and Non-Point-Source Pollution*. [online] Available at: http://www.kean.edu/~fosborne/resources/ex12j.htm [Accessed 12 Nov. 2015].

[3] Fuertes, E., Bracher, J., Flexeder, C., Markevych, I., Klumper, C., Hoffman, B., Kramer, U., Berg, A., Bauer, C., Koletzko, S., Berdel, D., Heinrich, J. and Schulz, H. (2015). International Journal of Hygiene and Environmental Health. *Long-term air pollution exposure and lung function in 15 year-old adolescents living in an urban and rural area in Germany: The GINIplus and LISA plus cohorts*, 1(218).

[4] The American Heritage® Dictionary of Student Science, Second Edition. Copyright © 2014 by Houghton Mifflin Harcourt Publishing Company. Published by Houghton Mifflin Harcourt Publishing Company. All rights reserved.

[5] Bazargan, Alireza et al. "The Effect Of Alkali Treatment On Rice Husk Moisture Content And Drying Kinetics". *Biomass and Bioenergy* 70 (2014): 468-475. Web.

[6] Akbar, Ralina Shirin, Christopher M. K. Chew, and Nurhazwani Ismail. "Adsor Ption Of Gaseous Pollutants (SO 2 & CO) Onto Palm Shell Activated Carbon". *EURECA 2013* (2013): n. pag. Print.

Pretreatment of Oil Palm Mesocarp Fibre for the Application as Fuel Source in DCFC

Elven Cho Man How, Veena Doshi Arun Kumar
School of Engineering, Taylor's University, Malaysia

veenaADoshi.ArunKumarDoshi@taylors.edu.my

Abstract
Direct Carbon Fuel Cell (DCFC) using biomass carbon source to produce energy is capable of producing sustainable energy that can replace the traditional fossil fuel energy source. With the energy demand rising, the depletion of fossil fuel with high environmental contamination becomes a major challenge face globally. Mesocarp fibre with high carbonaceous contents has shown its potential as solid fuel source in DCFC. The raw oil palm mesocarp fibre is alkaline pretreated with NaOH at concentration of 0.5%wt/vl, 2%wt/vl and 4%wt/vl and goes through pyrolysis treatment at 600°C with holding time 1hr with N_2 flowrate at 0.5L/min. The research study used a DCFC with anode consists of Nickel-Yttria stabilized zirconia (Ni-YSZ), cathode consistes of Lanthanum strontium manganite (LSM) and cell electrode is Yttria-stabilized zirconia (YSZ) with the operating parameter at 800°C with N_2 purge gas at flowrate of 0.2L/min and purified air supply at 0.6L/min. The TGA analysis shows that the alkaline and pyrolysis pretreatment has enhance the thermal stability of the mesocarp fibre. The FTIR analysis shows that the cellulose structure of the sample treated by 0.5%wt/vl NaOH did not alter much. The 2%wt/vl and 4%wt/vl NaOH pretreated sample on has shown a complete degradation of the hemicellulose and disruption of lignin. XRD analysis of the sample shows that 2%wt/vl NaOH treated mesocarp fibre has the higherst degree of graphitization which is preferable as fuel source for DCFC. Through DCFC analysis, PMF2.0 sample gives a higher maximum OCV of -842mV compare to PMF0.5 which shows a maximum OCV of -835mV. This shows that the PMF2.0 gives a better performance of DCFC.

Keywords: Direct Carbon Fuel Cell, Biochar, Oil Palm Mesocarp Fibre, Pyrolysis, Alkaline pretreatment

1. Introduction

Forecast from the global energy demand shows that the demand of energy usage globally will be increase due to the growing of population globally and also the modernization of society along with technology. In current technology, the main source of energy that is supply to global is generated by coal and oil. The usage of coal has been a traditional and efficient method in providing energy which supply approximately 1250 million tons oil equivalent of energy per year [1]. The coal is categorized as a non-renewable energy sources which now faces a rapid depletion.

This has been a major challenges faced by global welfare [2]. Therefore, due to the properties coal which contains a slow regeneration rates, the dependent of coal as the major energy sources may not fulfill the demand of energy needed in the future. In addition to that, coal and oil contains acidic composition such as sulphur composition which is not compatible to the green environment causing air contaminations. The sulphur composition reacting with open air will produce harmful toxicological effect to both the environment and society health.

In order to solve the major challenges faced, there are several proposed solutions to replace the coal energy source with a renewable energy source as part of a sustainable solution. One of the major findings has led to the usage of Direct Carbon Fuel Cell (DCFC) application to generate energy from biochar fuel source. DCFC is definse as a type of electrochemical cells which is capable in converting carbonaceous fuels to electricity sources. The potential biomass which is best used for the fuel source of DCFC requires a high percentage of carbonaceous content and low ashes content [3]. Biomass is a renewable components which contains high carbonaceous content and can be easily obtained globally. DCFC functions by oxidizing the carbon at the anode releasing free negatively charge electron which flows to the cathode. The overall fuel cell reaction in a working DCFC is as follows:

Cathode: $O_2\,(air) + 4e \longrightarrow 2O^{2-}$ [4] (1)

Anode: $C + 2O^{2-} \longrightarrow CO_2 + 4e$ [4] (2)

The fuel source for a DCFC is in term of a biochar which is obtained after pretreatment of biomass. The solution of the replacing the coal as the largest fuel source of energy has already been implemented in plant design now. The usage of variety types biomass in producing energy has been rapidly increases which makes the biomass in third largest energy source globally after coal and oil in production of low-grade fuel [5]. There are many previous study of variety of biomass used in DCFC in previous study.

Biomass contains three major layers which make up the biomass. The three later is categorized as the cellulose, hemicellulose and lignin. Upon the three layers, the lignin contains the highest carbonaceous composition. From the carbonaceous composition, the content is pretreated with thermal degradation to be decomposed to biochar which act as fuel source for DCFC utilities. Hence, it concludes that with higher carbonaceous content, the yield of biochar produced will increases. On the other hand, biomass contains undesired properties and composition which prevent the exploitation of the carbonaceous source such as low energy density, hygroscopic nature (tendency to absorb moisture from air) and low bulk density[6]. In order to fully utilize the biomass, pretreated of the biomass is usually perform to enhance the performance of the biomass in DCFC. Pretreatment of the biomass functions to disrupt the lignin structures which enable the pyrolysis process to easily reach out to the carbon

compositions. This prevents the high temperature needed for the process which may disrupt the carbonaceous compositions in the biomass.

The pyrolysis is an established technology to yield carbon content in the biomass that can be used to fuel DCFC [7]. During pyrolysis, the thermal decomposition treatment allows the biomass to decompose and breaks down to short carbon structure providing no oxygen to the process. During the process, the cellulose and hemicellulose will be burn off due to the high volatile matter and high temperature which then leaves out the decomposed lignin which contributes to the production of biochar product.

In year 2020, Malaysia palm oil plantation has forecast to produce an average annually production of palm oil of 15.4 million tonnes [1]. From this huge production, there is a total of 10.9million tons of palm oil mesocarp fibre that was produced every year which contribute to the agriculture waste [8]. This result in placing palm oil wastes in the major disposal waste complication to the country [9]. The proposed solution of using the potential palm oil wastes, oil palm mesocarp fiber as DCFC fuel source to generate energy is one a major aspects in providing Malaysia a renewable and sustainable energy source. The potential of oil palm mesocarp fibre can be observe at the characteristics of fuel-proximate analysis[10] in Table 1.0 below.

Table 1.0: Characteristics of Fuel-proximate Analysis

Biomass	**Moisture**	**CV (MJ/kg^{-1})**	**Ash**	**Volatiles**	**FC**
EFB	66.26±1.55	18.60±0.32	5.50±2.11	84.61	9.89
MCF	45.23	18.66	7.1	81.52	11.38
PKS	17.5	20.4	4.1	81.03	14.87
OPF	71.43	15.59±0.67	3.90±1.26	83.19	12.91
RSK	18.37	15.94	6.1	81.82	12.08
SD	16.30±0.89	18.19±2.02	5	78.8	16.2
SCR	52.20±0.41	15.25±0.22	3.90±2.32	80.19	15.91
RH	13.08±0.61	14.79±1.52	22.00±1.44	59.97	18.03
PS	8.47±0.33	13.74±1.12	18.30±2.02	72.48	9.22
CF	24.51	21.17	6.7	80.24	13.06
CS	18.50±0.89	18.18±2.33	5.52	75	19.48

* CV-Caloric Value, FC- Fixed Carbon, EFB- Empty Fruit Bunch, MCF- Mesocarp Fibre, PKS- Palm Kernel Shell, OPF- Oil Palm Frond, RSK- Rubber Seed Kernel, SD- Sawdust, SCR- Sugarcane residue, RH- Rice Husk, PS- Paddy straw, CF- Coconut Fibre, CS- Coconut shell

Observing Table 1.0, the focus point was given to the caloric value of the oil palm mesocarp fibre (MCF) which has the highest value of 18.66 MJ/kg^{-1}. Comparing to the rest of the biomass, the MCF is proposed as a new fuel source for DCFC application as the MCF does not have any other function in the palm oil plant and only contribute as the plant waste. The other potential biomass such as Palm Oil Kernel Shell (PKS) and the Empty Fruit Bunch (EFB) has already been exploited various energy field to produce energy through combustion in reboiler. The research gap is to propose a pretreatment to the MCF to be able optimized the potential MCF as fuel source for DCFC. The effectiveness of oil palm mesocarp fibre as DCFC fuel source is dependent on the fixed carbon composition, the porous surface area and the sulphur content. The biomass will go through pyrolysis to be converted to biochar as fuel source of DCFC. The high value of fixed carbon (FC) and low level of volatiles matter will

contribute to a higher yield of biochar. The biochar is the decomposition of carbonaceous element that is present in the mesocarp fibre. The challenge faced by DCFC application is that pyrolysis takes place in extreme high temperature and cause the high volatile carbonaceous element in the mesocarp fibre to be burn off [11]. In addition to that, the ash content will cause complication to the electrochemical cells. In modern DCFC function, there are many pretreatment methods before going through thermal decomposition process to increase the yield of the biochar and reduce the ash content. The pretreatments are such as ammonia hydrolysis, chemical pretreatment, carbon dioxide (CO_2) explosion, ammonia pretreatment and combined approach. It takes place to lower down the activation energy and sulphur content in order to recover more carbonaceous element after pyrolysis.

In the research finding, the chemical pretreatment effect the physicochemical properties to the biochar derived from the palm oil mesocarp fibre is studied. The objectives for the research are:

1. To investigate the effect of alkaline pre-treatment to the physicochemical properties of the biochar derived from oil palm mesocarp fibre.
2. To propose an optimum concentration pretreatment to enhance the effectiveness of palm oil mesocarp fibre as an alternative fuel source for the application of DCFC.

The physicochemical property of the biochar derived from the oil palm mesocarp fibre is to observe the effect of the alkaline pretreatment to the mesocarp fibre structure and the changes of properties affecting the performance of the biochar in the application of DCFC.

2. Methodology

In the research, three different concentration of alkaline pretreated and a raw sample of untreated oil palm mesocarp fibres were used. The pretreated mesocarp fibres go through pyrolysis process for the conversion of biochar and labeled based on the concentration of the alkaline pretreatment. The untreated mesocarp fibre is labeled as UMF along with the pretreated mesocarp fibre labeled as PMF0.5, PMF2.0, and PMF4.0 respectively.

2.1 Sample Preparation

The oil palm mesocarp fibre is obtained at a palm oil plant in Sri Ulu Langat in Dengkil. One kilogram of oil palm mesocarp fibre is collected and manually segregated to ensure only the raw mesocarp fibre is left after segregation. The raw mesocarp fibre then goes through a standard drying process according to the ASTM D2867-09 standard for biomass. The standard state that the required temperature and holding time to remove biomass moisture is by drying the biomass at 105°C with holding time of 24 hours in the oven. It is neccesery to remove the moisture from the mesocarp fibre as, high moisture content mesocarp fibre will easily grow mold which will affect the purity of the raw materials. The dried mesocarp fibre will then be milled and sieved into 0.5mm to decrease it to smaller size enable an easy storage and handling [12]. The sieved mesocarp fibre is extracted as the UMF sample.

The PMF samples were prepared by immersing the mesocarp fibre into the alkaline solution. For alkaline pretreatment of mesocarp fibre, sodium hydroxide, NaOH alkaline solution is used [13]. The alkaline solution is prepared by dissolving the sodium hydroxide pellets with distilled water to produce three NaOH solution at 0.5wt/vl%, 2wt/vl% and 4wt/vl%. 20g of palm oil mesocarp fibre is then immersed into the three concentration alkaline solutions and heated with a temperature of 121°C with reaction time of 30 minutes. After the reaction

time, the alkaline solution is slowly poured out to prevent the pretreated mesocarp fibres from leaving the beaker. Distilled water is then used to rinse the pretreated mesocarp fibre till it shows a pH value of 7. Once the pretreated mesocarp fibre is clarify, it then left to dry under standard ASTM D2867-09 condition for 24hrs. The three pretreated samples then goes through pyrolysis at operating condition of 600°C at 1hr holding time with nitrogen flowrate of 0.5L/min [14]. The pretreated samples, PMF0.5, PMF2.0 and PMF4.0 are prepared.

2.2 Biochar Characterization and Analysis

2.2.1 Thermogravimetry Analysis (TGA)

Thermogravimetry analysis was done to study the moisture content, volatile matter and fixed carbon in the samples. The analysis result is obtained from the data of weight loss of sample with increasing temperature. The analysis was conducted with Perkin Elmer STA6000. Approximately 10mg of samples was prepared and heated at 25°C to 950°C at a heating rate of 10.00°C/min with nitrogen gas.

2.2.2 Fourier Transform Infared Spectroscopy (FTIR)

The FTIR analysis was conducted to study the functional groups compositions of the biochar using infared (IR) spectra. The analysis was conducted with Perkin Elmer FTIR Spectrometer (Spectrum 100). The method of FTIR used to scan the sample is the attenuatted total reflectance (ATR) method with the range of wavelength from 4000 λ to 650λ.

2.2.3 X-Ray Diffraction (XRD)

The XRD analysis was conducted to study the atomic and molecular structure of the palm oil mesocarp fibre after pretreatment. The analysisallows a closer view of the biochar atoms position in their crystal structure. The parameter set for XRD is set to measure from 10-90° at step size of 0.02°(2Θ).

2.3 Direct Carbon Fuel Cell Testing (DCFC)

The DCFC testing is perform using apparatus such as DCFC, furnace and electrochemical workstation (Gamry Reference 600 Potentialstat). The solidwork diagram of the fuel cell is shown in Figure 1. The anode of the fuel cell consists of Nickel-Yttria stabilized zirconia (Ni-YSZ) and the cathode is consisted of Lanthanum strontium manganite (LSM). The cell electrode used is Yttria-stabilized zirconia (YSZ) [15]. In order to perform the DCFC testing, 0.1g of biochar is placed on an activated button cell with a circular silver wire sieve placed above it to prevent the sample to blow away. The button cell is activated by heating the button cell with the presence of nitrogen till 800°C with holding time of 30mins. The furnace is set to run from room temperature till it reaches 800°C with holding time of 2hrs[16].

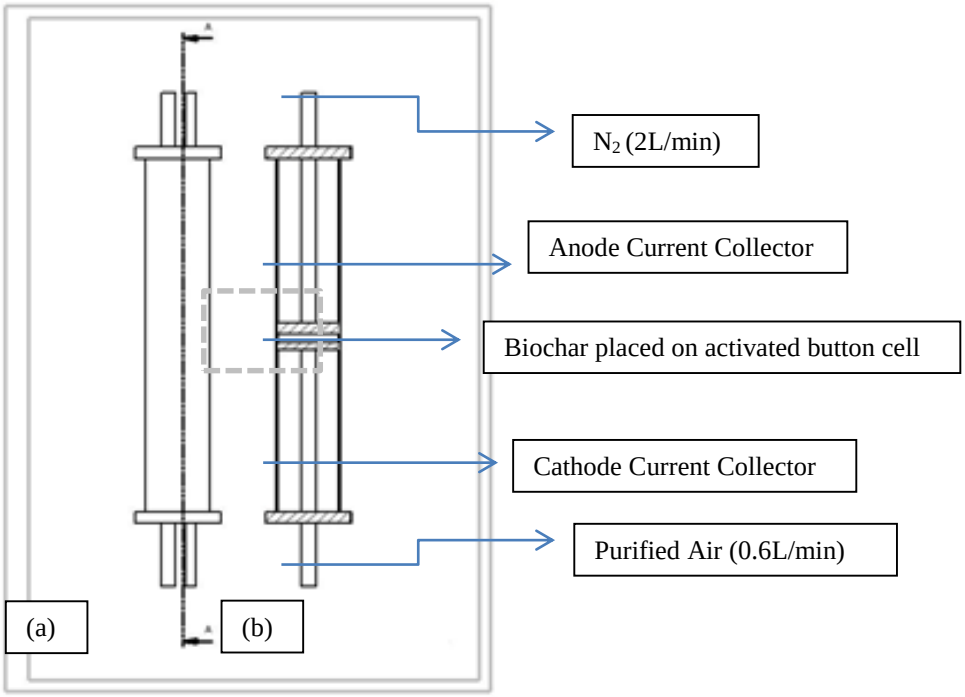


Figure 1: (a) Front view and (b) Internal view of the Direct Carbon Fuel Cell

The anode and cathode chamber were purged with nitrogen (N_2) gas till the furnace heated up to 750°C. The nitrogen flowrates are 0.2L/min at the anode and 0.6L/min at the cathode. When the furnace reaches 750°C, the cathode N_2 gas is switch with purified air, O_2 to provide the oxygen gas to the system to enhance the oxidation and reduction process [17]. During the holding time, the electrochemical workstation is connected to test the Open Circuit Voltage (OCV).

3. Result and Discussion

3.1 Thermogravimetry Analysis (TGA)

The TGA curves and analysis of UMF, PMF0.5%, PMF2.0% and PMF4.0% are shown in Figure 3.0 and Table 3.0. It can be observed that each of the TGA curve contains the first mass drop within the first 20mins. The mass drop show the elimination of the moisture contents in the samples which occurred at temperatures within 0°C to 200°C. From the study of thermal behavior of oil palm mesocarp fibre, the mesocarp fibre loses moisture at 53.4°C [12].

From this point onwards, the moisture is completely removed from the samples. The next mass drop is will be the volatile matter. Obesrving Figure 3.0 (a), there is a massive drop after the moisture elimination. In contra with it, Figure 3.0 (b, c, d) shows a slight mass drop after the moisture is removed. The drop that occurred is due the devolatilisation process. The difference in weigh percentage drop of the untreated mesocarp fibre and alkaline pretreated mesocarp fibre is due to the volatile matter presence in the biomass. From Table 3.0, the untreated mesocarp fibre shows the highest percentage of volatile matter with 62.915%. The volatile matter of untreated mesocarp fibre is higher than the alkaline pretreated biochar is due to the thermal pretreatment process. The alkaline pretreated oil palm mesocarp fibre undergoes thermal pretreatment using pyrolysis process where the organic composition is drastically

devolatilized under high temperature [18]. From previous study of the properties of oil palm mesocarp fibre, 80% of the biomass is occupied by volatile fraction hence during devolatilisation process for the raw oil palm mesocarp fibre, there will be significant drop [19]. The change of mass percentage is supported with the sudden drop of the derivatives graphs along with the TGA curve. The volatile matter drop for biomass is at approximately 200°C to 400°C [12][20]. Hence it can be conclude that the alkaline pretreatment and pyrolysis treatment has altered the thermal behavior of the mesocarp fibre. Besides that, the mass drop is contributed by the hemicellulose and cellulose which decompose at 220-300°C and 300-340°C respectively [12]. The lignin on the other hand, decompose at 750-900°C [19]. At that time range of 80mins to 140mins, it can be observed that the UMF has a slight mass drop. In comparison with the pretreated sample, PMF0.5, PMF2.0 and PMF4.0 show a larger mass drop. This is cause by the degradation of fixed carbon and disruption of lignin.

From Table 3.0, it can be observed that the fixed carbon of pretreated mesocarp fibre is much higher than the untreated mesocarp fibre. By having most of the volatile matter devolatilized during thermal pretreatment, it allows the alkaline pretreated mesocarp fibre to contain abundant of fixed carbon percentage. Finally, the last drop of the TGA curve shows the ash content. The ash content has increases with the thermal pretreatment and alkaline pretreatment. During thermal pretreatment, the volatile matter and the carbonaceous components which go through the high temperature pyrolysis will result in high ash remaining in solid matrix form [18]. During alkaline pretreatment, sodium hydroxide, NaOH alkaline solution was used. The NaOH solution contributes sodium ions where it will diffuse into the porous structure of the oil palm mesocarp fibre and contribute to ash formation.

Table 3.0: TGA Approximate Analysis

	Moisture content	**Volatile matter**	**Fixed Carbon**	**Ash Content**
UMF	7.226	62.915	4.554	4.784
PMF0.5	4.299	18.114	32.33	14.894
PMF2.0	6.86	13.174	33.715	16.195
PMF4.0	7.719	21.486	44.464	15.148

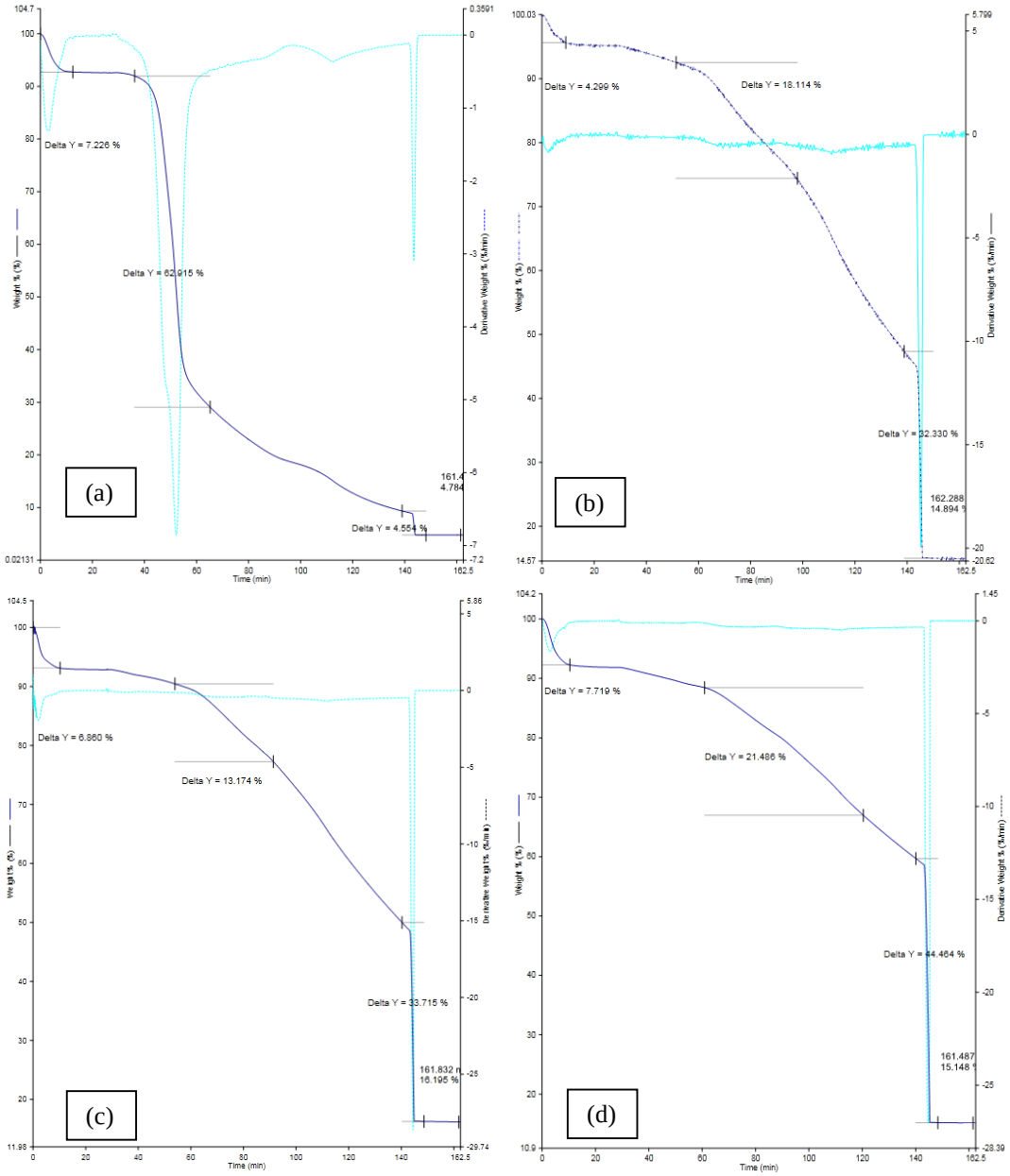


Figure 3.0: TGA curve for (a) UMF, (b) PMF0.5, (c) PMF2.0 and (d) PMF4.0

Comparing all the TGA approximate analysis in Table 3.0, PMF 2.0 sample contains the least volatile matter percentage of 14.174% but contain the highest value of ash content percentage of 16.195%. PMF 4.0 sample contains the highest fixed carbon percentage of 44.464%. In theoretical, PMF 4.0 should give the best performance as fuel source of DCFC with the high carbon contents but the high ash content from PMF 2.0 may enhance catalyst action in the biomass to improve its performance in DCFC.

3.2 Fourier Transform Infared Spectroscopy (FTIR)

The IR spectra of the UMF, PMF0.5, PMF2.0 and PMF 4.0 are shown in Figure 3. From Figure 3, the PMF FTIR spectra show a slight different with the UMF FTIR spectra which shows that the alkaline pretreatment has affect the cellulose structure of the biomass.

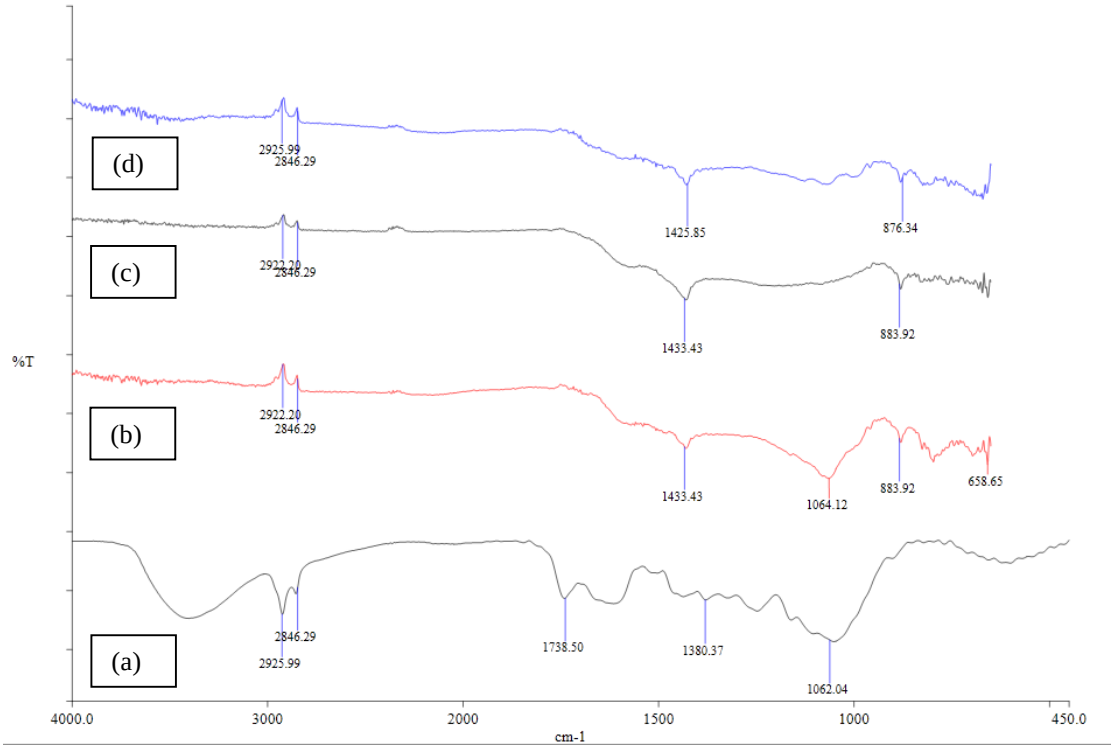


Figure 3: FTIR spectra of (a) UMF (b) PMF0.5 (c) PMF2.0 (d) PMF4.0

Figure 3(a) possesses a strong IR absorbance compare to the pretreated samples which is due to the higher volatile matter that present in the UMF sample. Comparing the FTIR spectra of the UMF sample with the PMF sample, it can be observed that there is a peak at Figure 3(a) at wavelength of 3600-3200cm^{-1}. The peak occurred within the wavelength shows the crystalline cellulose that is strong for the UMF sample. For the PMF samples on the other hand, the crystalline cellulose does not appeared in the samples as the cellulosic content is loss during pyrolysis process. When the band reaches to 2880-2940cm^{-1}, it shows that the samples is associated with C-H stretching of aromatics [21]. It can be observed that each sample FTIR spectra has a peak within the wavelength. At the wavelength of 1738.50cm^{-1}, Figure 3(a) shows a peak which shows that the raw oil palm mesocarp fibre is from a carbohydrate origin. This shows that the samples still contain uronic ester groups which are the hemicellulose and lignin-hemicellulose complexes. Similar peak is not obvious with the pretreated mesocarp fibre as the carbohydrate structure may have decomposed along with the alkaline pretreatment and pyrolysis. The peak at approximately 1422-1594cm^{-1} shows the aromatic skeletal vibrations of the lignin fraction[22]. The peak appeared in Figure 3(b, c, d) which show the possibility of the disruption of lignin after alkaline pretreatment. At 1380.7cm^{-1}, Figure 3(a) shows a peak which is associated with the CH deformation of cellulose and hemicellulose. The peaks are not clear with the pretreated samples as most of the hemicellulose and cellulose has been completely degrade during pyrolysis. Figure 3(a) and Figure 3(b) shows a similarity peak at wavelength 1062-1064cm^{-1} which shows that the UMF and PMF0.5 have similar structural features of cellulose and hemicelluloses[23]. At approximately 897cm^{-1}, Figure 3(b, c, d) shows clear peaks which indicate the present of β-glycosidic linkage. The present of β-glycosidic linkage prove that there is a disruption and removal of hemicellulose and lignin using the alkaline pretreatment[21]. Hence it can be concluded that using alkaline pretreatment; it can enhance the disruption of the carbohydrate components that protecting the carbon contents. The 0.5%wt/vl NaOH is able to disrupt the carbohydrate components in the raw mesocarp fibre but the alkaline pretreatment is not able enhance the complete disrupt on the

hemicellulose and cellulose after pyrolysis. Whereas, the pretreatment using 2.0%wt/vl and 4.0%wt/vl has shown a complete disruption of the hemicellulose and cellulose which is preferable for the oxidation of carbon compositions which gives the better performance of DCFC.

3.3 X-Ray Diffraction (XRD)

The XRD curves of PMF0.5%, PMF2.0% and PMF4.0% are shown in Figure 4. Y.B.Xing study state that crystallinity sample will increase when the lignin removal gradually removed [24]. Hence, the alkaline pretreatment meets its function in partially degrading the lignin for better retrieve of carbonaceous content from the biochar in DCFC. From Figure 4, it can be observed that Figure 4(b) shows an extra peak compare to Figure (a) and Figure (c) which shows that the PMF 2.0 sample possesses an extra phase and higher degree of graphitization compare to PMF0.5 and PMF4.0 [4]. In support with that, Figure 4(b) shows a graph with a lot of noise where the graph is not smooth. The noise is caused by the high degree of graphitization which shows a complex crystalline structure that enhances the intensity of light diffraction during analysis.

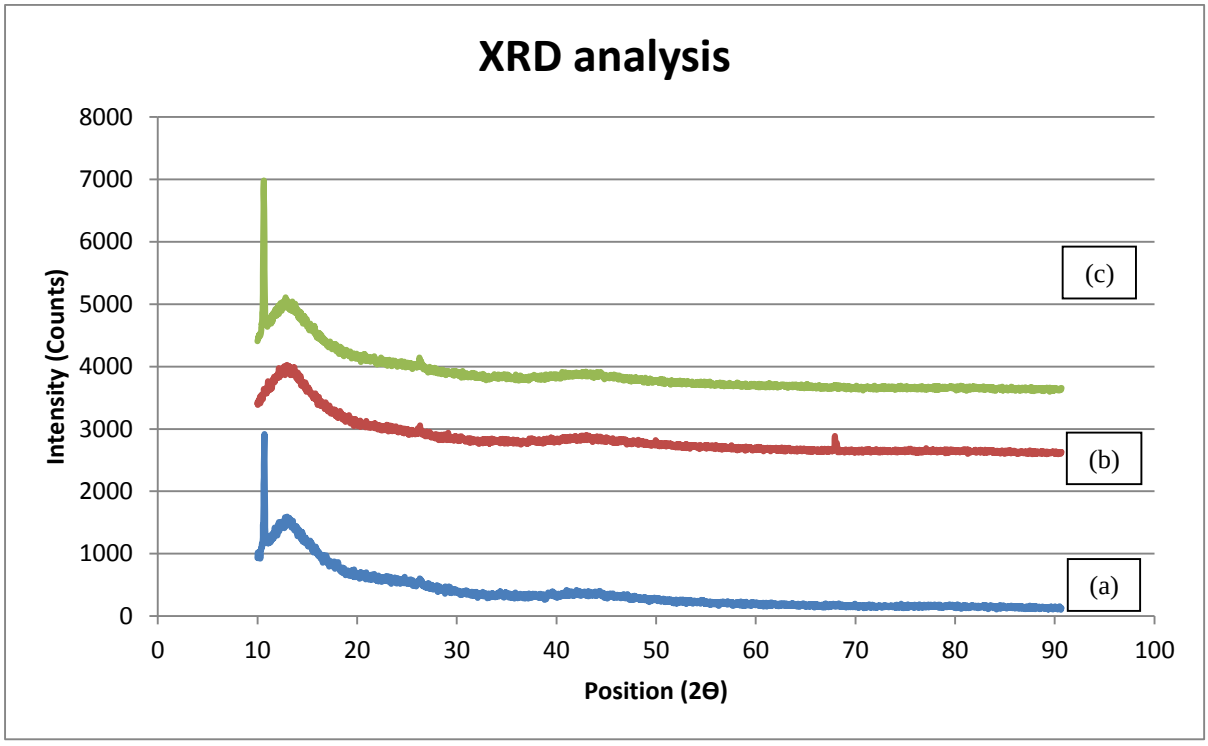


Figure 4: XRD graph of (a) PMF0.5, (b) PMF2.0 and (c) PMF4.0

With higher degree of graphitization, the oxidation rate is higher which allows better oxidation process to occur at the DCFC. It is believe that the sample PMF2.0 which possesses the highest degree of graphitization should give the best result in DCFC analysis.

In order to further support the conclusion, the Brubauer-Emmett-Teller (BET) analysis and the elemental analysis (CHNS) will be conducted to observe the effect of carbon composition and the surface area on the performance of DCFC [21].

3.4 Direct Carbon Fuel Cell Analysis

The Open Circuit Voltage (OCV) of the experimental results and reference are shown in Table 3.1.

Table 3.1: Open Circuit Voltage analysis

Conc	OCV value	Reference
PMF0.5 at 850°C of DCFC	0.8350 - 0.7848	Experimental
PMF2.0 at 850°C of DCFC	0.8452 - 0.8149	Experimental
PMF4.0 at 850°C of DCFC	0.8459 - 0.8083	Experimental
Carbon black at 850°C of DCFC	0.8327 - 0.7514	Experimental
UMF at 750-900°C	0.8800 – 0.6900	[19]
0.5% HCL pretreated mesocarp fibre at 750°C of DCFC	0.6400 - 0.7900	[19]
1% HCL pretreated mesocarp fibre at 750°C of DCFC	0.7300 - 0.3700	[19]
Charcoal at 850°C of DCFC	0.982	[7]

From the Table 3.1, it can be observed that the PMF4.0 sample gives the highest OCV of 845.9mV follow by PMF2.0 with OCV value of 845.2mV and lastly PMF0.5 with the highest OCV value of 835mV. By comparing the three alkaline pretreated OCV, PMF2.0 and PMF4.0 gives approximately the same highest OCV value whereas PMF0.5 gives a low OCV value. Using NaOH alkaline pretreatment of 2% or higher concentration will gives the same amount of OCV due to the abundant of sodium ions presence in the pretreatment solutions. During the alkaline pretreatment, the NaOH alkaline solution provides the sodium ions which diffuse into the porous of the mesocarp fibre solid structure due to the concentration gradient. The OCV value does not vary using 2% and 4% concentration alkaline pretreatment may due to the sodium ions that presence at 2% concentration of NaOH solution has completely interact with the biomass components [18].

In comparison for acidic pretreatment and alkaline pretreatment using oil palm mesocarp fibre biomass, the alkaline pretreated biochar gives a higher OCV value. This is cause by the major disruption using acidic pretreatment [25]. The lignin structure of the biomass contains a high percentage of carbonaceous contents which gives the carbon component for the oxidation reaction. On the other hand, the alkaline pretreatment disrupt mostly on the hemicellulose and cellulose structure of the biomass. When compare with untreated mesocarp fibre, the alkaline pretreatment gives a lower maximum OCV value. The NaOH alkaline solution provides sodium ions which contribute to the formation of ash contents. The high ash contents will disrupt the performance of electrochemical cells which justify the lower maximum OCV value compare to untreated mesocarp fibre. Although the alkaline pretreatment contains a lower maximum OCV, the OCV range for alkaline pretreated biochars is smaller than the untreated mesocarp fibre. This shows that oil palm mesocarp fibre without alkaline pretreated gives a rapid voltage drop. The rapid voltage drop is not ideal for the application of Direct Carbon Fuel Cell as the caloric energy from the biomass is used up quickly.

From the findings of J.Jewulski, the pretreated biochars obtain from experimental has a lower maximum OCV value when compare with charcoal. Charcoal is a product from combustion of wood which contain a higher carbonaceous contents compare oil palm mesocarp fibre. The high carbonaceous contents of charcoal allow it to content high-energy density particles [26]. When the pretreated biochars is compare with carbon black sample, the

pretreated biochars show a higher maximum OCV value. This shows that pretreated oil palm mesocarp fibre provide a potential replacement of carbon black as fuel source in application of DCFC.

7. Conclusions

Oil palm mesocarp fibre has a promising potential as source of solid fuel cell for the application of DCFC. The alkaline chemical and pyrolysis pretreatment was conducted to enhance the performance of mesocarp fibre.

From TGA analysis findings, it shows that the alkaline and pyrolysis pretreatment has alter the thermal behavior of the oil palm mesocarp fibre. It has increase the thermal stability of the mesocarp fibre. The pyrolysis pretreatment has removed most of the moisture in the mesocarp fibre.

Through FTIR analysis, the alkaline and pyrolysis pretreatment has enhance the degradation of the cellulose and hemicellulose. The presence of β-glycosidic linkage prove that there is a disruption and removal of hemicellulose and lignin using the alkaline pretreatment. On the other hand, it can be observed that with low concentration of alkaline pretreatment, the cellulose structure of the mesocarp fibre did not alter much. The missing gap at wavelength 1062-1064cm^{-1} for the PMF2.0 and PMF4.0 samples shows that with NaOH pretreatment and pyrolysis above 2.0%wt/v concentration, the cellulose and hemicellulose of the mesocarp fibre is completely deform.

For XRD analysis, the PMF2.0 sample shows the highest degree of graphitization with more peaks and sounds to the graph. The higher the degree of graphitization will leads to higher the rate of oxidation. Hence it is conclude that at concentration of 2%wt/vl the alkaline pretreatment using NaOH shows the optimum concentration along with pyrolysis treatment of 600°C using holding time of 1hr with 0.5L/min nitrogen flowrate.

Through electrochemical performance analysis, PMF4.0 sample gives a highest maximum OCV of 0.8459V follow by PMF2.0 sample with maximum OCV value of 0.8452V and lastly, PMF0.5 sample with maximum OCV value of 0.8350V. All the alkaline pretreated samples give a higher OCV value than activated carbon with OCV value of 0.8327V. This shows the potential of alkaline pretreated oil palm mesocarp fibre in replacing activated carbon as a fuel source for DCFC application.

References

[1] Y. Uemura, W. N. Omar, T. Tsutsui, S. B. Yusup, Friends of the Earth, Y. Basiron, W. Pei, Q. Ng, H. Loong, F. Yuen, M. Kamal, J. Heng, E. Lim, N. Abdullah, F. Sulaiman, A. Geng, J. Zheng, L. Rehmann, Sime Darby, A. Idi, S. E. Mohamad, T. Shahzadi, S. Mehmood, M. Irshad, Z. Anwar, A. Afroz, N. Zeeshan, U. Rashid, K. Sughra, S. H. a Rahman, J. P. Choudhury, a. L. Ahmad, P. Kernel, S. Pks, T. Biomass, L. Axelsson, M. Franzén, M. Ostwald, G. Berndes, G. Lakshmi, N. H. Ravindranath, B. I. Na, Y. H. Kim, W. S. Lim, S. M. Lee, H. W. Lee, J. W. Lee, M. Sharma, F. Sulaiman, N. Abdullah, H. Gerhauser, a. . . Shariff, D. Piarpuzán, J. a. Quintero, C. a. Cardona, M. Rozario, R. Bott, Wbdi, N. Abdullah, F. Sulaiman, C. Riber, R. Waste-to-energy, C. M. Lewandowski, N. Co-investigator, C. M. Lewandowski, A. Embrandiri, M. H. Ibrahim, R. P. Singh, R. Abas, V. Menon, M. Rao, K. L. Chin, P. S. H, S. H. Shuit, K. T. Tan, K. T. Lee, a. H. Kamaruddin, L. Meng Hon, Joseph, A. Sasekumar, S. Yusoff, a. C. Er, R. R. M. Nor, K. Rostam, M. a. . Abdullah, M. S. . Nazir, and B. a. . Wahjoedi, "Oil palm biomass as a sustainable energy source: A Malaysian case study,"

Biomass and Bioenergy, vol. 3, no. 1, pp. 97–103, 2013.

[2] P. Kumar, D. M. Barrett, M. J. Delwiche, P. Stroeve, P. Kumar, D. M. Barrett, M. J. Delwiche, and P. Stroeve, "Methods for Pretreatment of Lignocellulosic Biomass for Efficient Hydrolysis and Biofuel Production Methods for Pretreatment of Lignocellulosic Biomass for Efficient Hydrolysis and Biofuel Production," 2009.

[3] A. Arenillas, J. A. Menéndez, G. E. Marnellos, M. Konsolakis, V. Kyriakou, K. Kammer, C. Jiang, and A. C. J. T. S. Irvine, "Why combining coal and Direct Carbon Fuel Cells?," 2013.

[4] J. Zondlo, P. D. Co-chair, and W. Virginia, "Direct Carbon Fuel Cell (DCFC): Performance and Degradation Mechanisms Borja Cantero-Tubilla Master of Science In Chemical Engineering Department of Chemical Engineering," 2012.

[5] A. Saddawi, J. M. Jones, A. Williams, and C. Le Coeur, "Commodity Fuels from Biomass through Pretreatment and Torrefaction : Effects of Mineral Content on Torrefied Fuel Characteristics and Quality," 2011.

[6] T. E. O. Y. U. Xun, "DEVOLATILIZATION STUDIES OF OIL PALM PLANTATION RESIDUES VIA TORREFACTION PROCESS," no. January, 2015.

[7] J. Jewulski and M. Skrzypkiewicz, "Direct carbon fuel cells based on solid oxide electrolyte technology," no. 7, pp. 268–270, 2013.

[8] N. I. Iberahim, J. M. Jahim, S. Harun, M. T. M. Nor, and O. Hassan, "Sodium Hydroxide Pretreatment and Enzymatic Hydrolysis of Oil Palm Mesocarp Fiber," *Int. J. Chem. Eng. Apl.*, vol. 4, no. 3, pp. 101–105, 2013.

[9] S. M. Nomanbhay, R. Hussain, K. Palanisamy, and E. T. Al, "Microwave-Assisted Alkaline Pretreatment and Microwave Assisted Enzymatic Saccharification of Oil Palm Empty Fruit Bunch Fiber for Enhanced Fermentable Sugar Yield," vol. 2013, no. March, pp. 7–17, 2013.

[10] S. and S. Y. Shahidah Abdullah, "Method of Screening of Malaysia Biomass.pdf." 2010.

[11] Z. Z. Chowdhury, R. Hasan, and B. Abd, "RSC Advances Catalytic pretreatment of biochar residues derived from lignocellulosic feedstock for equilibrium studies of manganese , Mn (II) cations from aqueous solution," pp. 6345–6356, 2015.

[12] M. Sean and V. Doshi, "Palm Oil Waste as Fuel Source in a DCFC," pp. 1–2, 2014.

[13] M. Nikzad, "Comparative Studies on Effect of Pretreatment of Rice Husk for Enzymatic Digestibility and Bioethanol Production," *Int. J. Eng.*, vol. 26, no. 5 (B), pp. 455–464, 2013.

[14] A. C. Lua, F. Y. Lau, and J. Guo, "Influence of pyrolysis conditions on pore development of oil-palm-shell activated carbons," *J. Anal. Appl. Pyrolysis*, vol. 76, no. 1–2, pp. 96–102, 2006.

[15] A. Kacprzak, R. Kobyłecki, R. Włodarczyk, and Z. Bis, "Efficiency of non-optimized direct carbon fuel cell with molten alkaline electrolyte fueled by carbonized biomass," *J. Power Sources*, vol. 321, pp. 233–240, 2016.

[16] M. Steinberg and J. F. Cooper, "High Efficiency Direct Carbon Fuel Cell for Co 2 Emission and Sequestration," vol. 47, no. Dcc, pp. 85–87, 2002.

[17] C. and S. S. Rayment, "Introduction to Fuel Cell Technology," *Univ. Notre Dame*, p. 156, 2003.

[18] A. A. Rahman, F. Sulaiman, and N. Abdullah, "Influence of Washing Medium Pre-treatment on Pyrolysis Yields and Product Characteristics of Palm Kernel Shell," vol. 27, no. 1, pp. 53–75, 2016.

[19] S. Reen, "Performance of Mesocarp Fibre as a Fuel Source in Direct Carbon Fuel Cell," no. 2, pp. 1–14, 2016.

[20] N. Abdullah and F. Sulaiman, "The properties of the washed empty fruit bunches of oil

palm," *J. Phys. Sci.*, vol. 24, no. 2, pp. 117–137, 2013.
[21] S. H. Lim, S. T. Yong, C. W. Ooi, S. P. Chai, V. Doshi, and W. R. W. Daud, "Pyrolysis of Palm waste for the application of direct carbon fuel cell," *Energy Procedia*, vol. 61, pp. 878–881, 2014.
[22] Paul T.Williams and Serpil Besler, "The Influence 0f Temperature and Heating Rate 0n The Slow Pyrolysis 0f Biomass," vol. 1481, no. 96, pp. 6–7, 1996.
[23] Md.Suruzzaman, "An Alkaline Pretreatment of Biomass for Subsequent Pyrolysis," vol. 4, no. 6, pp. 354–358, 2014.
[24] Y. . B. Xing X.; Wang, K.; JIANG, J.X., "Pretreatment of furfural residues with alkaline peroxide to improve cellulose hydrolysis. Characterization of isolated lignin," *Cellul. Chem. Technol.*, vol. 46, pp. 249–260, 2012.
[25] J. Akhtar, A. Idris, C. L. Teo, L. W. Lai, and N. Hassan, "Comparison of delignification of Oil Palm Empty Fruit Bunch (EFB) by Microwave assisted alkali / acid pretreatment and Conventional Pretreatment Method," vol. 1, no. 2, pp. 155–157, 2014.
[26] M. Dudek, P. Tomczyk, R. Socha, M. Skrzypkiewicz, and J. Jewulski, "Biomass fuels for direct carbon fuel cell with solid oxide electrolyte," *Int. J. Electrochem. Sci.*, vol. 8, no. 3, pp. 3229–3253, 2013.

Effect of Pyrolysis Temperature on DCFC Performance of Rubber Wood Sawdust-derived Biochar

Fabian Goh Kian Choong[1*], Veena Doshi[1], Wai Yin Wong[2]

[1]*School of Engineering, Taylor's University, Malaysia*

[2]*Fuel Cell Institute, University Kebangsaan Malaysia, Bangi, 43600, Selangor Malaysia*

[*] fabian_goh@hotmail.com

Abstract

In Malaysia, an agricultural-based country, the abundancy of agricultural waste such as rubber wood sawdust, corn cob, rice husk and mesocarp fibre has created a huge opportunity for the nation to utilize these waste as a source of energy. Combustion which was used for generating these energy creates a major issue on the greenhouse gas emission. A new advanced technological device which was recently found, called direct carbon fuel cell which uses electrochemical reaction with carbon fuel source seems to be a promising alternative to this challenge. This study is aimed to utilize the rubber wood sawdust biomass as a source of energy after converting it to biochar which will then be used as a potential fuel source in the direct carbon fuel cell. Heating rate and temperature of the pyrolysis was studied as the main factors to investigate the performance of the biochars in DCFC. The pyrolysis was performed at temperature 650°C, 750°C and 850°C with heating rates of 3°C/min and 5°C/min. The proximate content of the rubber wood sawdust derived biochar was characterized by using thermogravimetric analysis (TGA). TGA indicates that the degradation of lignin only happens at high temperature which is 950°C. It also indicates that there is low-to-nothing moisture content at the end of pyrolysis. BET has also indicates that when temperature or heating rate increases, the surface area increases which will lead to good performance in DCFC. FTIR has demonstrated the reduction of functional groups such as phenol, lactonic and carboxylic acid and existence basic groups like quinone and carbonyl at high temperatures. It is shown that temperature of rubber wood sawdust at 850°C gives a higher OCP value when comparing with 750°C.

Keywords: Direct Carbon Fuel Cell; rubber wood sawdust; pyrolysis temperature, thermogravimetric analysis, x-ray diffractogram

1. Introduction

In this century, greenhouse gas emission reduction and increasing renewable energy production have been paid with a lot of attention. However, emission of CO_2 is still rising due to energy demands required for current economy. The global energy source that is constantly used would be coal and biomass. With coal as a non-renewable source, professionals would like to focus more on biomass as a main energy source. By combining a fuel cell system and biomass, it is an eco-friendly technology which is suitable for power generation. Fuel cells have been studied since 1960s. The fundamental concept was suggested by Grove in year 1839[1]. There are a lot of types of fuel cells that has been developed, but the common few that are being studied or used in industry would include alkaline fuel cell (AFC), polymer electrolyte fuel cell (PEFC), molten carbonate fuel cell (MCFC), phosphoric acid fuel cell (PAFC), solid oxide fuel cell (SOFC) and lastly, direct carbon fuel cell (DCFC). Each of this fuel cell varies in their own operating systems, which includes their operation temperatures, catalysts, electrolytes, performance and costs. The studies on this subject would be based on direct carbon fuel cell (DCFC). Direct carbon fuel cell is a recent developed technology which has the potential to convert chemical energy of a solid carbon into electricity without the need of reforming process. A DCFC system does not requires combustion, gasification or even machinery moving with electrical generators which proves to be more economically cheaper compared to solid oxide fuel cell

DCFC contains a few type of assemble such as tubular, planar and button. Tubular and planar are used industries, however button are used for experiment purpose only. Planar DCFC contains cell which are made of rectangular or square disk. The connection of cells are done by interconnecting plates in series. Tubular DCFC contains electrodes where one is a long tube with porous wall. Surrounding the electrodes on the outer layer would be another electrode with the electrolyte. Planar DCFC are easier to fabricate and obtaining power density. Tubular DCFC cost lower to fabricate and has a high thermal stability that gives easy sealing. However, button DCFC, although are never used in industries, is the easiest to use for experiments due to its carbon fuels can be placed directly on the anode of the button cell. Furnace is used to aid in the heating process of the DCFC. The common electrolyte that is used in DCFC is 8YSZ with Ni-YSZ as anode and LSM-YSZ as cathode.

Energy is very important in the current society. Society depends on uninterrupted supply of energy in order to work or live their daily life. In country like Malaysia, problems such as natural resources are the least concern due to their availability. Nevertheless, these natural resources are still exhaustible. Therefore, energy security and sustainability are simultaneously important. Five main energy consumptions by fuel type are natural gas, petroleum products, coal and coke, biodiesel and electricity. Malaysia consumes electricity around 51583ktoe in the year 2013. Out of these 51583 ktoe, natural gas contributes 10076ktoe, petroleum products 29190ktoe, coal and coke 1539ktoe, biodiesel 188 and lastly, electricity 10590ktoe. From Figure 1, by comparing the energy on 2013 with year 1993 which only consume 17728ktoe, the difference has increase greatly [2].

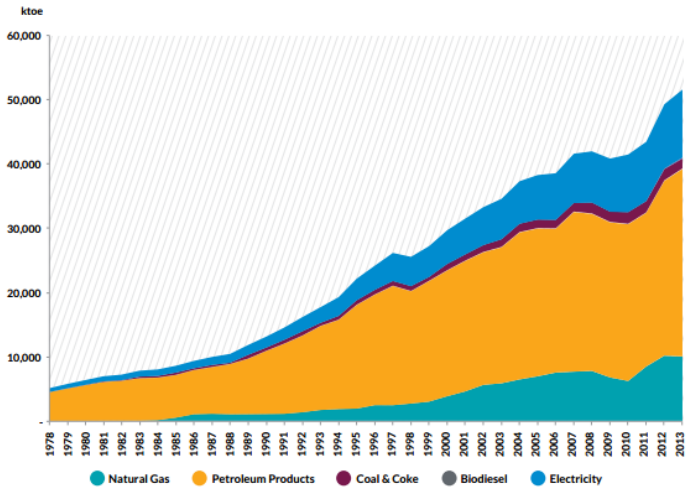


Figure 1: Energy consumption in Malaysia

Climate change is now a global issue due to high levels of greenhouse gases. Fossil fuels that are constant burnt contributes to the increase of carbon dioxide in the atmosphere. An effort to find a renewable and alternative fuels are ongoing to find a solution for these challenges. Lignocellulosic biomass such as saw dust, wood waste and bio char are seen as a promising option. These biomass are considered to be carbon-neutral resource and does not increase emission of carbon dioxide. It is also known to be high volatile matter content with low ash, sulfur and nitrogen content. In Malaysia, rubber-wood are one of the main plantation corps. Malaysia has an estimated plantation area of 1.82 million hectares [3]. After their latex yielding period which last around 25 years, they can be chopped and these woods can be use in a lot of processes. The saw dust produced from cutting the wood has potential in being used as a raw material for energy.

With potential biomass found, DCFC was focused as a technology which will utilize rubber sawdust which would be converted into biochar and serve as fuel for DCFC. DCFC has a higher achievable efficiency which is around 80% when comparing to other fuel cells such as molten carbonate and solid oxide. The emissions produced are also less than conventional-cost power plants [4]. To obtain biochar, pyrolysis is required. In general, there are three types of pyrolysis which are slow, moderate and fast. The properties of biochar that consist of surface area, pore structures, and surface chemical functional group can be customized by changing the pyrolysis properties which is the heating temperature, heating rate, holding time, type of gas and flow rate [1]. A process with lower temperature would be better for the environment.

Therefore, the objectives of this project is:

1. To synthesis biochar derived from rubber wood sawdust using pyrolysis process with different operating conditions
2. To investigate on physicochemical properties and electrochemical performance of direct carbon fuel cell using the as-prepared biochar.

2.0 Methodology

2.1 Materials

Rubber wood is obtained from a rubber wood plantation which is located in Melaka, Malaysia.

2.2 Preparation of Rubber Wood Sawdust

Upon obtaining the rubber wood, the rubber wood is cut using a band saw machine. Rubber wood sawdust will be obtained when cutting of rubber wood is being performed. Rubber wood sawdust is collected and sieved to 0.5mm to make sure lumps were removed. The sawdust are placed in a tray and placed in the oven at 105°C for 24 hour to remove the moisture content. Sawdust was then sieved into particles of 0.5mm using a sieve shaker (RX-812-1, Tyler). Sieved sawdust was placed in a sealed container.

2.3 Pyrolysis

Pyrolysis of rubber wood sawdust was performed using laboratory scale furnace (Carbolite model PM-1008). Two alumina crucibles were used to hold 5g of the rubber wood sawdust biomass samples which were then placed inside the furnace. Before starting pyrolysis, nitrogen was used to purge the oxygen to ensure the environment is oxygen-free. Pyrolysis was then carried out at temperature 650°C,750°C and 850°C with heating rate of 3°C/min and 5°C/min in an oxygen-free environment by using a purge gas with flow rate of 0.5L/min. The holding time was fixed at 60 minutes [5]. The biochar produced was collected after the cooling down of the furnace.

2.4 Characterisation of Biochar

2.4.1 Thermogravimetric Analysis (TGA)

Thermogravimetric Analysis (TGA) was carried out to observe the changes in the weight loss of samples. The analysis was carried using thermogravimetric analyser (STA 6000, Perkin Elmer). The samples were heated from room temperature at 25°C to 950°C at a heating rate of 10°C/min with nitrogen flow at 20mL/min.

2.4.2 X-Ray Diffraction (XRD)

XRD diffractrogram was carried out to study crystallinity of the material. Crystalline atoms will cause the beam of incident X-rays to diffract into many specific directions. Density of electrons can be obtained by measuring the angles and intensities of these beams. Density of electrons is then used to determine the mean positions of the atoms in the crystals including their chemical bonds[6].

2.4.3 Fourier Transform Infrared Spectroscopy (FT-IR)

FTIR is performed to determine the various functional groups on the biochars surface that is produced at the different temperatures and heating rate[6]. The analysis was performed using Perkin Elmer FTIR spectrometer. (Spectrum 100)

2.5 DCFC Setup

A fuel cell stack as shown in Fig. 2 is used to conduct experiment to measure the electrochemical performance of rubber wood sawdust derived biochar. A button cell was placed in the fuel stack. The area of the button cell is 1.25 cm^2. The fuel stack is divided to cathode and anode.

0.1g of sawdust biochar was placed on the button cell to start the experiment. Furnace (HST 12/400, Carbolite) was used to assist in provide heating to the fuel stack. Temperature at constant 800°C was set with heating rate of 10°C/min and holding time 2h.

During the experiment, anode chamber is purged with nitrogen gas at flow rate 0.2L/min to ensure an oxygen-free environment. However, for cathode, the nitrogen gas with flow rate 0.6L/min was used from the start of experiment until temperature 750°C and switched to purified air with flow rate 0.6L/min at cathode till the end of the experiment.

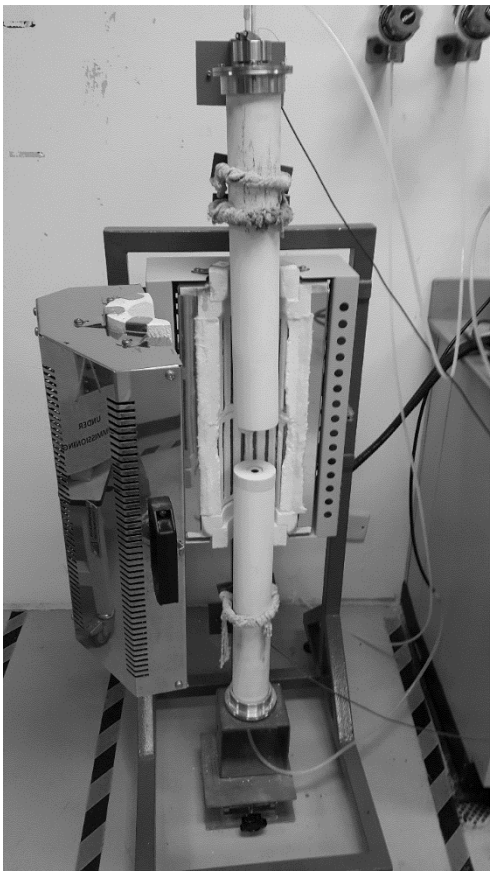


Figure 2: Direct Carbon Fuel Cell

3.0 Results and Discussion

3.1 CHNS elemental analysis

CHNS analysis is an analysis that determines the carbon, hydrogen, nitrogen and sulphur. Based on the readings, it is seen that the when rubber wood sawdust is pyrolyzed, the amount of carbon

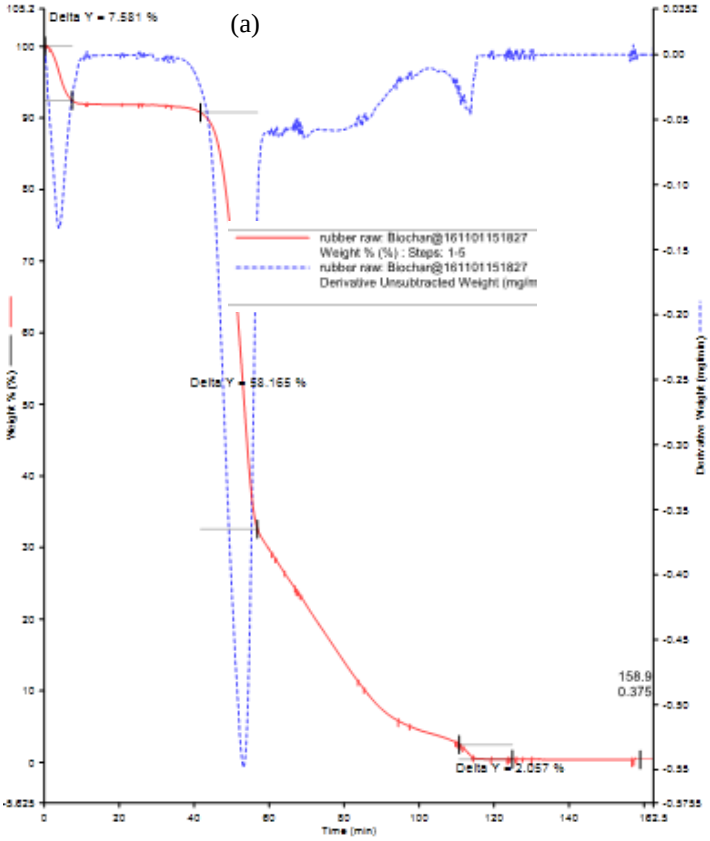
content increases. Carbon is a very important element that is needed for this project as carbon is the important fuel source in DCFC to produce electricity. Hydrogen , nitrogen and sulfur served as impurities in the biocharr. Biomass are generally known for their low content of these elements. Table 2 shows the analysis reading obtained at different operating conditions

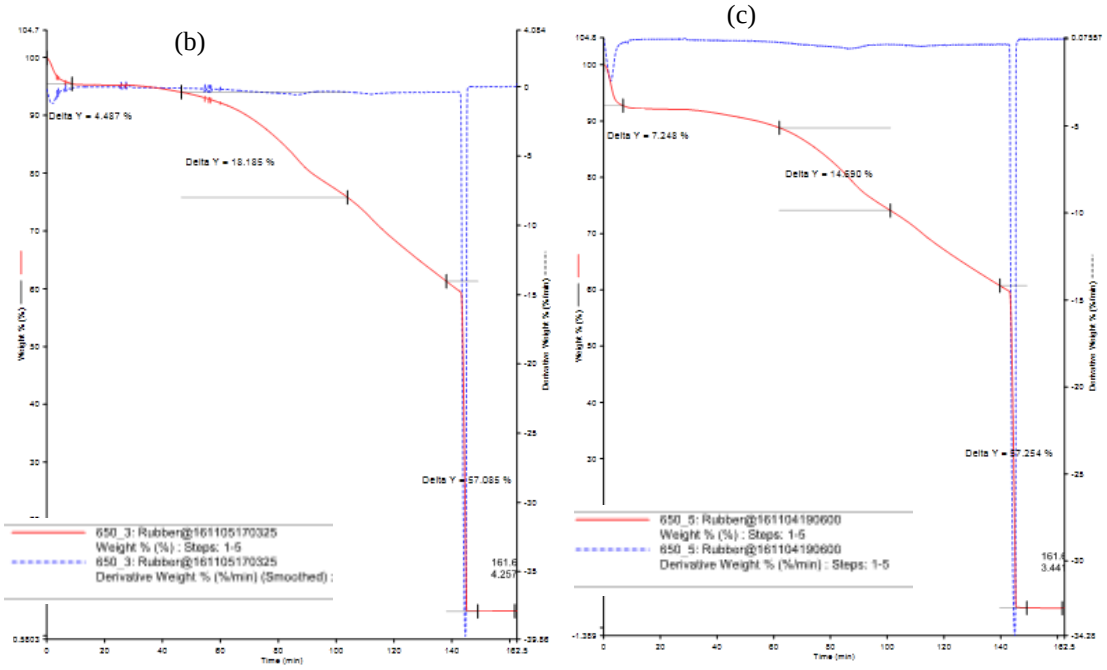
Table 2: CHNS analysis

	Raw	**650/5**	**750/3**	**750/5**	**850/5**
Carbon	43.27	86.21	87.002	88.466	88.685
Hydrogen	6.83	1.554	0.734	0.806	0.557
Nitrogen	0.39	6.583	8.074	4.118	2.486
Sulfur	-	0.028	0.027	0.048	0.05
Ref	[7]	This Study	This Study	This Study	This Study

According to Wan Azlina et al, the produced biochars using CHNS shows increasing trend of carbon when temperature increases [8]. The trend is also shown in this study. Table 2 shows that the highest temperature which is 850°C with 5C°/min is able to produce the highest amount of carbon content. The increasing trend is due to carbon being locked in the soil from biochar produced at lower pyrolysis temperatures. At high temperature, the heat is able to decompose the layer locking the carbon[8]. The readings also show drastic drop for the amount of hydrogen. The very low H/C ratio ratios that is obtained for the biochar indicated that carbon is predominantly unsaturated especially biochar that is formed at 850°C with 5°C/min.

3.2 Thermogravimetric Analysis (TGA)


(a)
Delta Y = 7.581 %
Delta Y = 68.165 %
Delta Y = 2.057 %
rubber raw: Biochar@161101151827
Weight % (%) : Steps: 1-5
rubber raw: Biochar@161101151827
Derivative Unsubtracted Weight (mg/m
Weight % (%)
Derivative Weight (mg/min)
Time (min)


(b)
Delta Y = 4.487 %
Delta Y = 18.185 %
Delta Y = 57.085 %
650_3: Rubber@161105170325
Weight % (%) : Steps: 1-5
650_3: Rubber@161105170325
Derivative Weight % (%/min) (Smoothed) :
Time (min)
(c)
Delta Y = 7.248 %
Delta Y = 14.690 %
Delta Y = 57.254 %
650_5: Rubber@161104190600
Weight % (%) : Steps: 1-5
650_5: Rubber@161104190600
Derivative Weight % (%/min) : Steps: 1-5
Time (min)

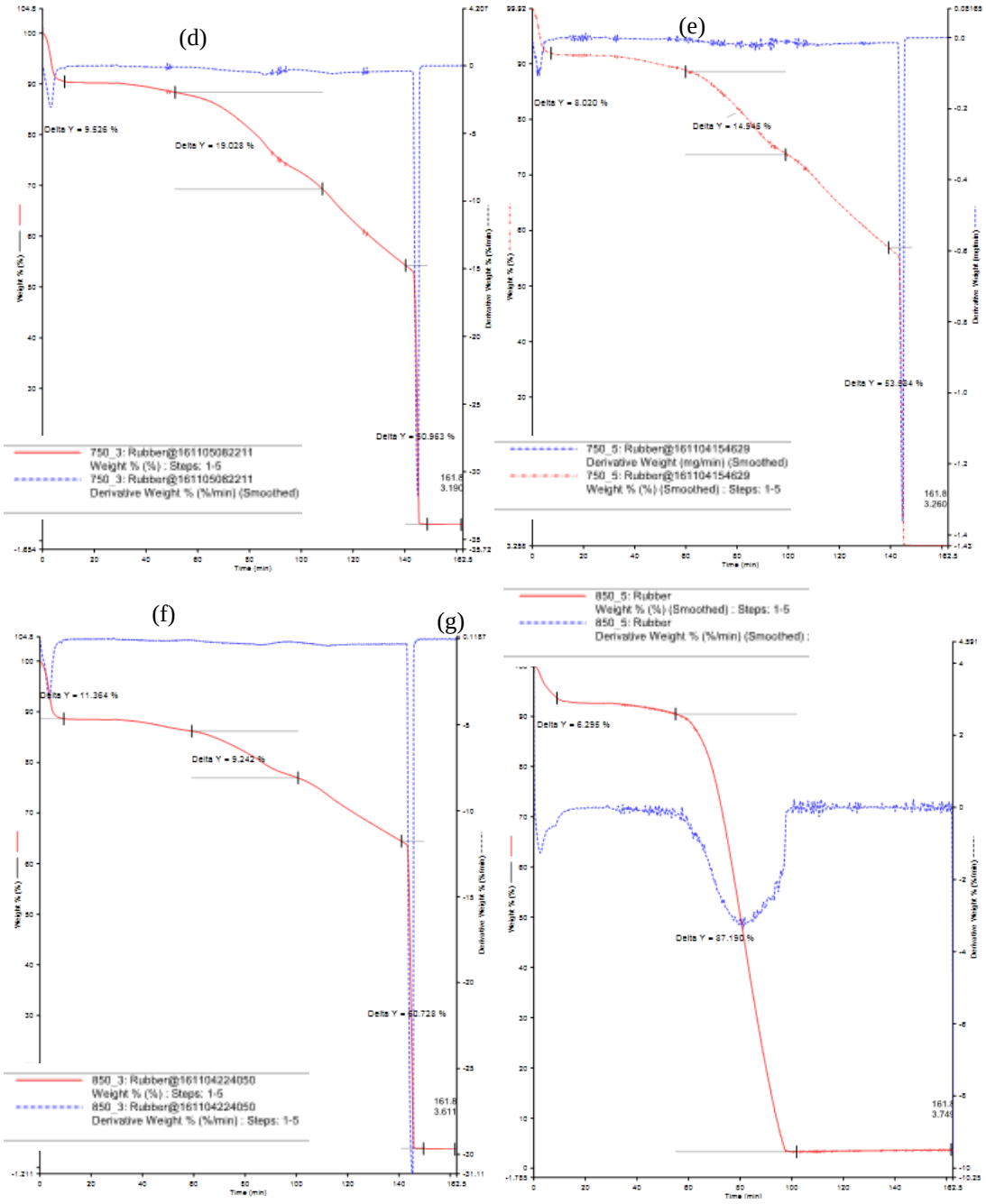


Figure 3 : TGA curve for (a) Raw, (b) Char 650°C 3°C/min , (c) Char 650°C 5°C/min , (d) Char 750°C 3°C/min, (e) Char 750°C 5°C/min, (f) Char 850°C 3°C/min, (g) Char 850°C 5°C/min

Table 3 gives a clear value of the TGA curves shown in Figure 3.

Table 3: TGA curves value in Figure 3

Pyrolysis condition	Moisture	Volatile matter	FC	ASH
Raw	7.581	58.165	2.057	0.375
650/3	4.487	18.185	57.085	4.257
650/5	7.248	14.690	57.254	3.441
750/3	9.526	19.028	50.913	3.190
750/5	8.020	14.945	53.584	3.260
850/3	11.364	9.242	60.728	3.611
850/5	8.295	0.000	87.190	3.749

Figure 3(g) which is sample at 850°C with 5°C/min has a unique degradation stage compared to the others. There are only 2 degradation stages which are shown in the curve. The first stage is the moisture which is followed by the fixed carbon content. This is because the volatiles matter is known to decompose fully at the pyrolysis stage due to high temperature and high heating rate. When comparing Figure 3(a) with Figure 3(b),(c),(d),(e),(f) and (g), it is shown that pyrolysis is able to reduce the amount of volatile matter which is not important and increase the amount of fixed carbon which is a very important element.

According to Wan Azlina et al, the increasing temperature will show the increasing trend of fixed carbon, which is also shown in this project therefore supporting the reading shown. This is due to higher temperature being able to decompose the lignin which will give high amount of fixed carbon[8]. According to Zhezi Zang et al, the increase of heating rate will also give a slight increase of fixed carbon, which is shown in this project. This is due to the residual volatile that is present in the biochar produced at low temperature. At high heating rate, the carbon structure become more ordered with depletion of residual volatile or hydrocarbon molecules deposited on the biochar surface.From the readings show in Table 3, it is seen that the sawdust char at pyrolysis temperature of 850°C with 5°C/min is the best sample due to its fixed carbon content being very high compared to the other samples.

3.3 X-Ray Diffraction (XRD)

XRD is used to study the crystallinity of the material. Fig. 4.2 shows the diffractogram for 3 biochar at temperature of 750°C with 3°C/min, 750°C with 5°C/min and 850°C with 5°C/min. These 3 samples are chosen based journal reference [7] which are supposedly to give the best reading compared to the other samples. Two peaks are seen from each of the curve where one is at the value around $2\theta=12°$ and another one can be seen at around $2\theta=41°$. This broadened peak explains it has a highly disordered crystalline structure which enhances electrochemical activity. This disordered structure helps in enhancing the electrochemical activity which make it very prominent to be applied in fuel cell such as direct carbon fuel cell [9].

Accorrding to A. Shaaban et al, there are two broad peaks that is shown at $2\theta=16°$ and $2\theta=22°$ for raw rubber wood sawdust.This is due to the crystallinity in lattice spacing of cellulose that arranged orderly[6]. However, hemicellulose and lignin are both amorphous in nature. Similar report by Wang et al shows the same trend for raw pine wood [10].

A. Shaaban et al reported that cellulose is decomposed at 315°C, and increase of pyrolysis will lead to volatilities of the cellulose structure. It is stated that temperature that are above 500 are virtually amorphous because of the volatilities of the cellulose structure. And due to temperature 750 and 850 is being used, all the samples shows distinctive characters of amorphous material because as pyrolysis temperature increases, the diffractogram display a distinctive character of amorphous material. Therefore, XRD curves that are shown in Figure 4 show similar pattern[9].

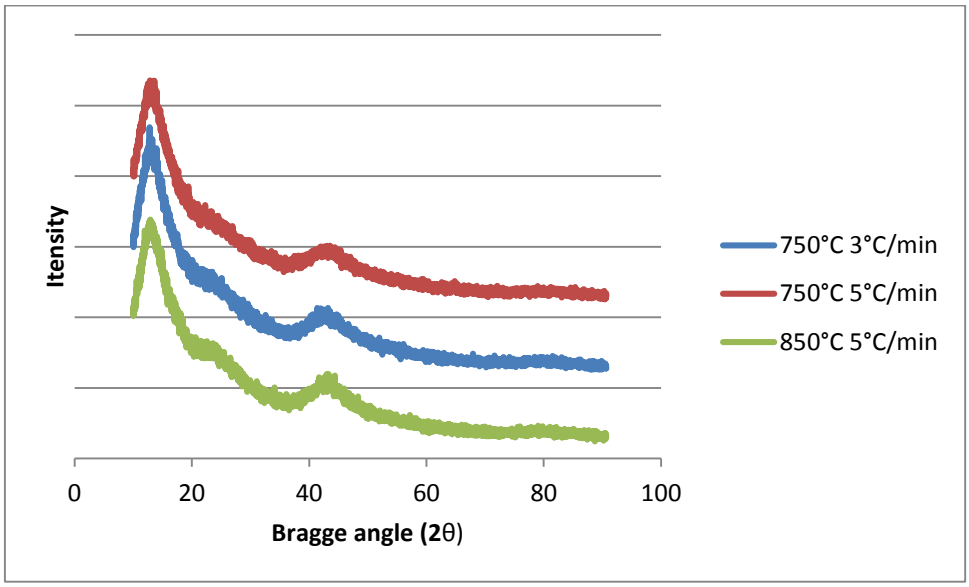


Figure 4. X-Ray diffractogram of sawdust char 750°C with 3°C/min, 750°C with 5°C/min and 850°C with 5°C/min

3.4 FTIR Analysis

FTIR is used to determine the various functional groups on the biochar produced at different conditions. Based on Figure 5, it is seen that raw rubber wood sawdust contains a small peak at the highest wavelength which is around 3200-3600cm^{-1}. The peak indicates that the crystalline cellulose for the raw rubber wood sawdust is very strong. It is observed that at wavelength of around 2900cm^{-1}, all the samples has a peak which shows C-H stretching in methyl and methylene groups. At wavelength of around 1580cm^{-1} , all the samples except for 850°C with 3°C/min shows peaks which indicates that samples undergoes aromatic skeletal vibration with C=O stretching. For raw, at wavelength of 1034cm^{-1}, a peak was clearly shown and at this wavelength, it indicates aromatic C-H in plane deformation, C-O deformation; primary alcohol. At wavelength around1245cm^{-1}, 650°C with 3°C/min and 650°C with 5°C/min shows peaks due to C = stretch in lignin and xylan. This happens due to their low temperature. For higher temperature biochars, they have peaks at wavelength around 1034 cm^{-1} which shows they undergoes C-H in plane deformation, C-O deformation; primary alcohol. At approximately 850cm^{-1}, all the readings except for raw and 850°C with heating rate 3°C/min, gives a peak which indicates the presence of β- glycosidic linkage. It is shown that pyrolysis does disrupt the carbohydrate components in the raw rubber wood sawdust [5].

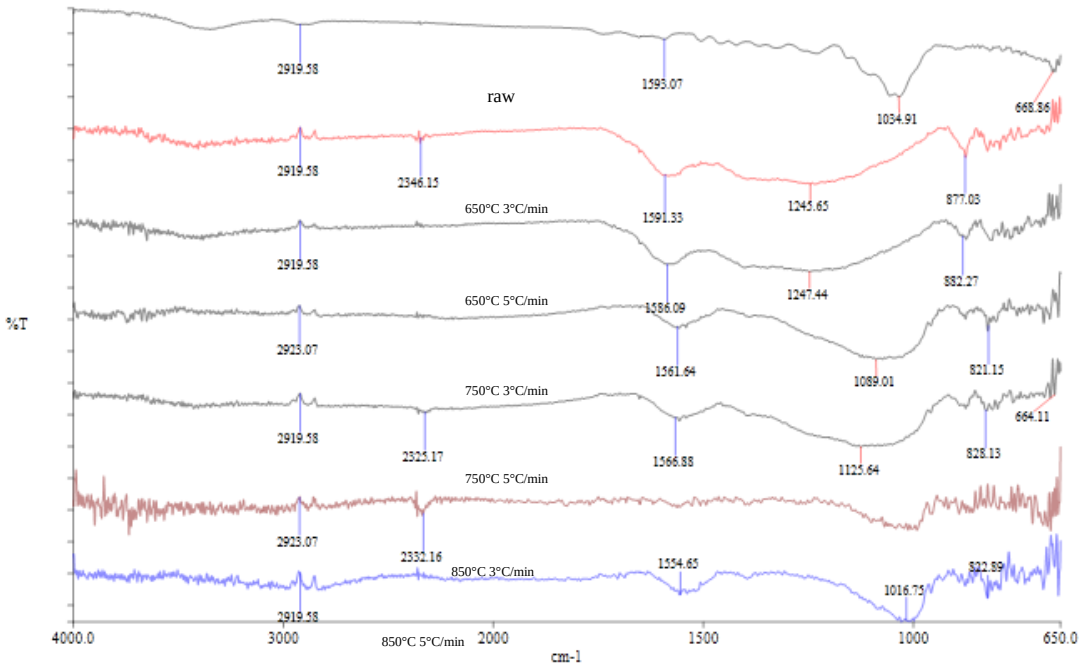


Figure 5. FTIR results of sawdust char.

3.5 Surface area analysis BET

Table 4 shows the BET surface area and total pore volume for raw sawdust and sawdust char at temperature of 650°C with heating rate of 5°C/min and two sample at temperature 750°C with heating rate of 3°C and 5°C respectively.

Table 4 :Surface area readings for biochar at different operating condition [This study]

	BET surface area (m^2/g)	**Total pore volume x10^3 (cm^{-3}/g)**
Raw	0.5832	0.789
650/5	0.9186	1.499
750/3	0.9091	1.25
750/5	0.9339	1.06

It was found out that 650°C with 5°C/min has slightly higher BET surface area when compared to 750°C with 3°C/min. This is probably due to lower heating rate that has caused the sample to partially carbonized as shown in TGA section which is at Table 4. The heating rate is also shown when char sawdust at temperature of 750°C with 3°C/min heating rate is compared with 750°C with 5°C/min.

Secondly, the temperature affects the surface area too. It is observed in Table 4 that as temperature increases, the BET surface area increases. This is because the higher temperature has increased the volatilities of organic compounds and contributed to larger surface area. Higher surface area are usually preferable as it helps in better performance of DCFC due to enlarged reactive region. A. Shaaban has also shown a similar report that shows when temperature is increased, the BET surface area will also increase [6].

3.6 Open Circuit Potential (OCP)

Temperature affects the OCP that is obtained from direct carbon fuel cell. By using sawdust char with their respective pyrolysis conditions shown in Table 2, the OCP that is obtained is compared with several biochar that is used as a fuel source in direct carbon fuel cell.

Table 5 : Comparison of several biochars

Type of fuel	Operating temperature (°C)	Heating rate (°C/min)	OCP(V)	Ref
Corn Cob char	650	10	1.04	[11]
	700	10	1.02	[11]
	750	10	1.05	[11]
Almond shell char	650	5	1.04	[12]
	700	5	1.05	[12]
	750	5	1.07	[12]
Coconut char	800	5	1.04	[13]
	850	5	1.07	[13]
Ash free coal	650	3	0.85	[14]
	750	3	1.08	[14]
	850	3	1.09	[14]
Carbon black	750	10	0.89	[15]
	800	10	0.91	[15]
	850	10	0.89	[15]
Rubber Wood Sawdust	650	3	0.78	This study
	650	5	0.80	This study
	750	3	0.79	This study
	750	5	0.78	This study
	850	3	0.72	This study
	850	5	1.1	This study

It is observed that as the temperature increase, the OCP of most of the sample will increase too. However, some research suggested that temperature that is too high will ended up burning the carbon content in the biochar , therefore reducing the carbon content that is required for direct carbon fuel cell [11]. Based on the studies, the highest temperature with the highest heating rate which is 850°C with 5°C/min is able to give the highest OCP. By comparing 850°C with 5°C/min heating rate and 850°C with 3°C/min which has relatively low OCP, the reason is because the carbon content in 850°C with 3°C/min has burnt off during pyrolysis that is due to the low heating rate. This has caused extended experimental time which causes the burning off of carbon [1]. The high OCP is also due to the amount of fixed carbon that is available in the element which is shown in the TGA curve in Figure 4.1. The amount of fixed carbon present in 850°C with 5°C/min heating rate is the highest.

Not only heating rate and temperature are affecting the OCP, but the YSZ electrolyte is also one of the factors of the high OCP. YSZ is able to perform well in such high temperature is due to the high temperatures that are able to maintain the high ionic conductivity of YSZ [15].

.

4.0 Conclusion

Several analysis of rubber wood sawdust biochar have been researched. It is shown that temperature of rubber wood sawdust at 850°C gives a higher OCP value when comparing with 750°C. However, when comparing to other biomass, the OCP value is lower. XRD analysis shows that rubber wood sawdust biochars broadened peak between the readings that gives highly disordered crystalline structure. The structure aids in enhancing electrochemical activity which proves that rubber wood sawdust is suitable in direct carbon fuel cell. TGA indicates that the degradation of lignin only happens at high temperature which is 950°C. It also indicates that there is low-to-nothing moisture content at the end of pyrolysis. BET has also indicates that when temperature or heating rate increases, the surface area increases which will lead to good performance in DCFC. FTIR has demonstrated the reduction of functional groups such as phenol, lactonic and carboxylic acid and existence basic groups like quinone and carbonyl at high temperatures [6].

References

[1] A. Shaaban, S. M. Se, M. F. Dimin, J. M. Juoi, M. H. Mohd Husin, and N. M. M. Mitan, "Influence of heating temperature and holding time on biochars derived from rubber wood sawdust via slow pyrolysis," *J. Anal. Appl. Pyrolysis*, vol. 107, pp. 31–39, 2014.
[2] Energy Commission, "Malaysia Energy Statistics 2014," p. 84, 2014.
[3] W. A. W. A. K. Ghani, A. Mohd, G. da Silva, R. T. Bachmann, Y. H. Taufiq-Yap, U. Rashid, and A. H. Al-Muhtaseb, "Biochar production from waste rubber-wood-sawdust and its potential use in C sequestration: Chemical and physical characterization," *Ind. Crops Prod.*, vol. 44, pp. 18–24, 2013.
[4] D. Cao, Y. Sun, and G. Wang, "Direct carbon fuel cell: Fundamentals and recent developments," *J. Power Sources*, vol. 167, no. 2, pp. 250–257, 2007.
[5] P. T. Williams and S. Besler, "The Influence of Temperature and Heating Rate on the Slow Pyrolysis of Biomass," *Renew. Energy*, vol. 7, no. 3, pp. 233–250, 1996.
[6] a. Shaaban, S.-M. Se, N. M. M. Mitan, and M. F. Dimin, "Characterization of Biochar Derived from Rubber Wood Sawdust through Slow Pyrolysis on Surface Porosities and Functional Groups," *Procedia Eng.*, vol. 68, pp. 365–371, 2013.
[7] A. Shaaban, S. M. Se, I. M. Ibrahim, and Q. Ahsan, "Preparation of rubber wood sawdust-based activated carbon and its use as a filler of polyurethane matrix composites for microwave absorption," *Xinxing Tan Cailiao/New Carbon Mater.*, vol. 30, no. 2, pp. 167–175, 2015.
[8] W. A. W. A. K. Ghani, A. Mohd, G. da Silva, R. T. Bachmann, Y. H. Taufiq-Yap, U. Rashid, and A. H. Al-Muhtaseb, "Biochar production from waste rubber-wood-sawdust and its potential use in C sequestration: Chemical and physical characterization," *Ind. Crops Prod.*, vol. 44, no. May, pp. 18–24, 2013.
[9] X. Li, Z. Zhu, R. De Marco, J. Bradley, and A. Dicks, "Evaluation of raw coals as fuels for direct carbon fuel cells," *J. Power Sources*, vol. 195, no. 13, pp. 4051–4058, 2010.
[10] Z. Wang, J. Cao, and J. Wang, "Pyrolytic characteristics of pine wood in a slowly heating

and gas sweeping fixed-bed reactor," *J. Anal. Appl. Pyrolysis*, vol. 84, no. 2, pp. 179–184, 2009.
[11] J. Yu, Y. Zhao, and Y. Li, "Utilization of corn cob biochar in a direct carbon fuel cell," *J. Power Sources*, vol. 270, pp. 312–317, 2014.
[12] A. Elleuch, A. Boussetta, J. Yu, K. Halouani, and Y. Li, "Experimental investigation of direct carbon fuel cell fueled by almond shell biochar: Part I. Physico-chemical characterization of the biochar fuel and cell performance examination," *Int. J. Hydrogen Energy*, vol. 38, no. 36, pp. 16590–16604, 2013.
[13] C. Munnings, A. Kulkarni, S. Giddey, and S. P. S. Badwal, "Biomass to power conversion in a direct carbon fuel cell," *Int. J. Hydrogen Energy*, vol. 39, no. 23, pp. 12377–12385, 2014.
[14] D.-L. Vu and C.-G. Lee, "Effect of temperature on the electrochemical oxidation of ash free coal and carbon in a direct carbon fuel cell," *Korean J. Chem. Eng.*, vol. 33, no. 5, pp. 1606–1611, 2016.
[15] R. Liu, C. Zhao, J. Li, F. Zeng, S. Wang, T. Wen, and Z. Wen, "A novel direct carbon fuel cell by approach of tubular solid oxide fuel cells," *J. Power Sources*, vol. 195, no. 2, pp. 480–482, 2010.

Preparation and Characterisation of Bentonite-filled Polylactic Acid (PLA) Composites

Guhen Raj A/L Rajandran[1*], Pang Ming Meng[1], Albert Tshai Kim Yeow[2]

[1]*School of Engineering, Taylors's University, Malaysia*
[2]*Depart of Mechanical, Materials and Manufacturing Engineering, University of Nottingham, Malaysia*

*guhenrajrajandran@sd.taylors.edu.my

Abstract
The rise in environmental, economical and safety challenges in this era has encouraged the use of biodegradable polymers, mainly polylactic acid (PLA) as packaging material instead of the more common petrochemical based polymers. The properties of the PLA has to be enhanced to overcome it's several disadvantages, and the addition of nano filler loading in the PLA overcomes the this problem. The nano filler used in this research is the inorganic mineral clay, bentonite. This research is aimed to study and investigate the effects of different loadings of bentonite on the mechanical, thermal and morphological properties of the bentonite-PLA composites. The challenge is to determine the optimum loading of bentonite that would yield the best result of the characterization tests. The bentonite-PLA composites (with bentonite loading of 1, 3, 5, 7 and 9wt%) are prepared by using the melt-blending process, which then undergoes a compression moulding and cutting of the samples to the desired dimensions. These samples are then tested for the change in the thermal and mechanical properties. The thermal test conducted was the Thermo-Gravimetric Analysis (TGA), the mechanical test conducted is the tensile testing and the third test is the water absorption test. Based on the findings of this research, the addition of 1wt% of bentonite enhances the thermal stability of the composite. The mechanical test conducted determined that the increasing addition of bentonite into PLA decreases the tensile strength and elongation at break, which reduces the composite's elasticity, while increasing the Young's Modulus, where the stiffness is increased. The water absorption was carried out for 1, 3, 5, 24 and 168 hours, and none of the composite samples showed a significant increase in weight after each tests and was deduced that almost no water was absorbed. In conclusion, bentonite can be used as mineral filler for PLA in the industry, and incorporation of 1wt% of bentonite into PLA is enough to increase thermal degradability and overall stiffness.

Keywords: Polylactic acid (PLA), bentonite, Thermo-Gravimetric Analysis (TGA), water absorption, tensile test

1. Introduction

Synthetic polymers are commonly used in all industrial sectors, including packaging, medical appliances and agriculture [1]. These synthetic polymers are usually synthesized from non-renewable and non-biodegradable petrochemcials, which causes serious environmental problems [2]. The drawbacks and difficulties in disposing these polymers have prompted researches to discover other alternatives as an effort to conserve and protect the safety of the environment and society.

Polylactic acid (PLA) has been regularly used in the packaging industry, gradually replacing the use of synthetic polymer. It is synthesised from natural fruit and vegetable extracts such as kenaf, coconut, bamboo and palm oil husks [3]. Being made from natural products, PLA is both organic and renewable. It is biodegradable, being able to decompose naturally into harmless substances [1]. This adheres to the need of protecting and conserving the society and environment. Despite this, PLA has several undesired properties, such as low melting temperature, thermal stability and tensile properties. Researches found that adding fillers (organic or inorganic) into the PLA helps overcome these drawbacks. This research studies the effect of bentonite, an inorganic (mineral) filler on the PLA's thermal and tensile properties.

Bentonite is an inorganic (mineral) phyllosilicate clay [4]. It is a member of the montmorillonite (MMT) group [5]. The MMT is a group of mineral clays with an expanding lattice. These mineral clays are made up of 2 tetrahedral layers, with one central octahedral layer [9, 10]. Bentonite is typically comprised of 70-80% MMT, including other compounds such as carbonites, pyrites, feldspar and quartz [7]. In this study, the bentonite NANOLIN DK® is used.

The objective of paper involved preparing the bentonite-PLA composites, by incorporating 1, 3, 5, 7 and 9 wt% of bentonite fillers into the PLA by the melt blending technique. Next, characterization tests (thermal and mechanical) were carried out to compare the different wt% of bentonite fillers on the composite's thermal and mechanical properties. The thermal test carried out is the TGA analysis, where the composite's thermal stability (weight loss with increase in temperature) is investigated. According to Byeong-Uk Nam et al [8] and Harintharavimal et al [9], adding of mineral filler increases the composite's thermal stability, and the reason for this involves the formation of char in the PLA matrix, which reduces the diffusion of oxygen into the matrix. The tensile test carried out determined the composites tensile strength, elongation at break and Young's modulus. According to W.L. Ngo et al [3] and Alicja et al [10], addition of fillers decreases the tensile strength and elongation at break, but increases the Young's modulus. This is due to the presence of agglomerates in the PLA matrix. Water absorption test was carried out to determine the percentage water uptake of each composite. PLA 3051D and bentonite NANOLIN® DK is used for this research. The properties of PLA 3051D [10] and crystal structure of MMT are shown in Table 1 and Figure 1 respectively. At the end of this research, it can be known whether bentonite is a good and suitable mineral filler to be used in PLA, and the best composition of bentonite needed for this.

Table 1: Properties of PLA 3051D [10]

Physical properties	
Specific Gravity	1.24
Melt Index	10-30°C
Viscosity	3.0-3.5
Melting temperature	145-200°C
Glass transition temperature	55-65°C
Clarity	Transparent
Mechanical properties	
Tensile yield strength	48 MPa
Tensile elongation	2.5%
Flexural strength	83 MPa
Flexural modulus	3828 MPa

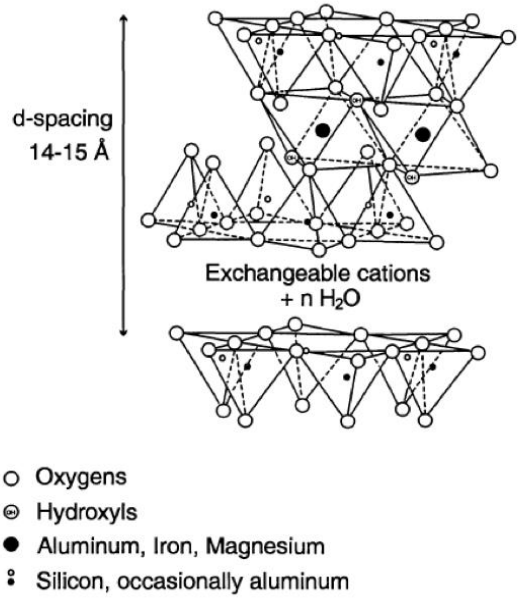


Figure 1: Crystal Structure of an MMT group compound [11]

2. Methodology

2.1 Bentonite-PLA Composite Preparation

Five samples of different composition of the composites are prepared. The total weight of each composite sample is 80g. Different weight percentages (wt%) of bentonite are mixed with the PLA. The wt% of bentonite used in this study is 1, 3, 5, 7 and 9 wt% respectively. Table 3 shows the weight of bentonite and percentage composition of the composites.

Table 3: Weight of Composite Preparation

No.	Percentage composition	Weight of bentonite/ g	Weight of PLA/ g	Total weight of nano-composite/ g
1	1.0 wt% bentonite + 99.0 wt% PLA	0.8	79.2	80
2	3.0 wt% bentonite + 97.0 wt% PLA	2.4	77.6	80
3	5.0 wt% bentonite + 95.0 wt% PLA	4.0	76.0	80
4	7.0 wt% bentonite + 93.0 wt% PLA	5.6	74.4	80
5	9.0 wt% bentonite + 91.0 wt% PLA	7.2	72.8	80

2.2 Melt Blending Process

Firstly, the PLA and bentonite are dried in a vacuum oven for a period of four hours, at a temperature of 80°C and at atmospheric pressure [12]. This step is carried out to remove any moisture or contaminants that maybe present on the composites, as these impurities may alter and harm the results of the subsequent tests [1]. The temperature and pressure are chosen as such as it is determined that these operating conditions will not damage the PLA and bentonite. Next, the melt blending process is carried out, where the bentonite is blended with the PLA in a twin-screw extruder or internal mixer (Machine model: Haake Polylab System E93). The twin-screw extruder is pre-heated at 180°C before the materials are processed. The conditions of the melt-blending process (speed, mixing temperature and time) are set at 150rpm, 180°C and 20 minutes respectively. Once the mixture is well mixed and homogeneous, the melted bentonite-PLA composite is then scrapped and placed on an aluminium foil. The composite is then pressed and cut into small pieces as a preparation for the compression moulding process.

2.3 Compression Moulding

The compression moulding process is carried out to produce a polymer sheet [13]. A hot press machine will be used (Machine model: Moore E53), and is preheated for about 3 minutes. The cut pieces of the bentonite-PLA composite are filled in a mould to shape the sheet, where it is then compressed by the hot press machine at a temperature of 185°C, under a pressure of 150 bar for a period of 5 minutes. The machine is then cooled to 60 °C. The mould is then removed from the machine, and the sheet is carefully peeled from the mould. The sheet has a dimension of 12 X 15cm, with a thickness of 0.2cm. A total of 2 sheets are produced for each sample.

2.4 Cutting

One sheet is required for the tensile test. To address the tensile test requirement (ASTM D638-10), the sheet is cut into a dumb bell shape (Type IV). A total of 3 dumb bell shapes can be obtained from each sheet.

2.5 Characterisation and Analysis of Bentonite-PLA Composite

2.5.1 Water Absorption Test

The water absorption test was conducted to better understand the hydrophilic/phobic properties of the bentonite-PLA composites. 15 square samples, measuring 2 X 2cm, were cut from the polymer sheet and numbered accordingly. The weights of each sample are measured using a digital weighing balance and recorded. Five 100 ml beakers are prepared and filled with distilled water at room temperature, and labelled 1, 3, 5, 24 and 168 hours respectively. 3 samples of each composite are placed in each beaker. At the end of the respected time, all the samples are removed from the beaker and the weights of each sample are measured. The percentage water content, M_t, is calculated using Eq. (1) shown below.

$$M_t(100\%) = \left(\frac{W_f - W_i}{W_i}\right) \times 100 \qquad \text{Eq. (1)}$$

Where W_i is the initial weight of sample (before immersion) and W_f is the final weight of sample (after immersion).

2.5.2 Tensile Test

The tensile test is used to measure the tensile strength of the composites. This test helps to determine the maximum tensile strength, tensile strength at break, elongation at break and tensile modulus. The test is carried out in Texchem Polymers Sdn. Bhd., and the machine used is the Instron 3366 (Serial number: 3366U2438). The requirement of the test is ASTM D638-10, with Type IV dumb bell shape cut from the polymer sheet. The test is carried out under room temperature and pressure, with an average cross speed of 0.00833 cm/s.

2.5.3 Thermo-Gravimetric Analysis (TGA)

The TGA analysis is carried out to examine the weight loss of the samples with the increase in temperature. This test was carried out on a Perkin Elmer STA6000. Each sample of the composite (0.005 to 0.01g) were heated from a temperature range of 30 °C to 600 °C, with a maximum temperature of 1000 °C, at a heating rate of 20°C/ min, under nitrogen environment [14].

3. Results and Discussion

3.1 Water Absorption Test

Table 4 details the percentage water absorbed with increased immersion time. The percentage water absorbed is calculated using Eq. (1). By analysing the results in the table, it is observed that the weight of the composite samples before immersion in water are relatively the same after immersion in water, which indicates little to no water is absorbed into the composites. The difference in weight of some samples is very small (± 0.0001), and is accounted as measurement error during in the weighing process and could be negligible. This is probably due to the superior hydrophobic nature of the PLA used [15]. Next, possible dispersion of the bentonite particles into the polymer matrix could hinder the access of water molecules into the PLA molecule's polar oxygen linkage, hence decreasing the wettability between the PLA fibres [20]. Absorption of water into the polymer may cause degradation and a loss of mass for the polymer, and could cause the mechanical properties to deteriorate as well.

Table 4 Percentage of water absorbed

Samples	Percentage water absorbed (%)				
	1 hour	3 hours	5 hours	24 hours	168 hours
Pure PLA	0	0	0	0.0176	0
1wt%	0	0.0364	0	0	0
3wt%	0	0.0343	0.0175	0.0176	0.0177
5wt%	0	0.0184	0	0.0171	0
7wt%	0.0175	0.0352	0.0173	0	0
9wt%	0	0.0176	0	0	0

3.2 Tensile Test

The results obtained from the tensile test are tabulated in Tables 10-14 and plotted in a chart (Figure 3). By interpreting these results, it is observed that the maximum tensile strength for the samples decreases with the addition of the bentonite. Pure PLA, which has no addition of bentonite, exerts the highest maximum tensile strength and elongation at break, with the lowest tensile modulus. The 7wt% composite, the sample with the second highest amount of bentonite added, displays the lowest the maximum tensile strength and elongation at break, with the highest tensile modulus. The results indicate that pure PLA is the most elastic, and the 7wt% composite is the most brittle. In fact, the tensile test could not be carried out on the 9wt% composite, as the material was too brittle to cut into the standard Type IV dumb bell shape. The reason for this occurrence can be explained by the presence of agglomerates in the polymer matrix [16]. The agglomerates behave as stress concentrators instead of enhancers, and cause a strong adhesion in the interfacial region between the PLA and bentonite particles [17]. This causes the composites to become stiffer and less elastic [18], which are seen the results obtained. The decrease in maximum tensile strength shows the composite are losing its elasticity, and the increase in the tensile (Young's) modulus indicates the composites are becoming stiffer.

Table 5 Tensile properties of pure PLA and bentonite-PLA composites

Sample	Tensile Strength, MPa	Elongation at break, %	Tensile Modulus, MPa
Pure PLA	39.40 ± 0.76	3.45 ± 0.3350	1239 ± 76.0
1% Bentonite	25.40 ± 3.68	1.99 ± 0.24	1294 ± 56.0
3% Bentonite	18.23 ± 0.902	1.38 ± 0.125	1342 ± 62.2
5% Bentonite	13.37 ± 1.32	1.20 ± 0.110	1349 ± 21.5
7% Bentonite	4.00 ± 0.297	0.313 ± 0.00283	1426 ± 222.0

3.3 TGA Analysis

Figure 2 shows the TGA traces of weight loss as a function of temperature. Table 6 shows the tabulation of the onset degradation temperature and residual weight. Based on Figure 2, it can be observed that all the compounds start with 100 wt% and gradually decreases, indicating weight loss due to thermal degradation. The bentonite-PLA composite of 1 wt% shows the highest thermal stability, with the highest onset temperature of 346.55 °C, followed by the pure PLA (339.99 °C). The rest of composites (3, 7 and 9 wt%) show a dramatic decrease in their weight with the increase in temperature. This indicates the thermal stability of the composites diminishes greatly with the increase in bentonite loading. According to Byeong-Uk Nam et al [8], the reason for the increase in thermal degradation for the 1wt% composite is probably due to proper dispersion of the bentonite nanosilicates into the PLA's polymer matrix [8]. The stable phase morphology of the composite is compatibilized with the addition of bentonite, increasing its thermal stability. Next, the segmented motions between the PLA and bentonite in the clay/polymer interface are reduced by the intercalated/ exfoliated silicate platelets, where the clay (bentonite) reduces the degradation chain rate by delaying the diffusion of oxygen into the polymer matrix due to char formation [19]. However, composites with more bentonite loading (3, 7 and 9 wt%) show a noticeable decrease in thermal stability. Harintharavimal et al [9] states that this occurrence is possibly attributed to the agglomeration of the nanosilicates in the polymer matrix, rather than proper dispersion [7,9]. The agglomeration hinders the char formation, as the MMT's surface area is greatly reduced, which increases the oxygen diffusion into the polymer matrix and therefore affecting the composite's thermal stability [18]. It is also noted that the composites have residual weights at 600 °C, while pure PLA has the lowest. The PLA is decomposed completely as it is 100% organic polymer, with no mixture of inorganic minerals. Addition of mineral compounds into the PLA, in an increasing amount, gradually increases the residual weight due to the higher melting temperature of mineral compounds compared to organic compounds

Table 4.1 Onset degradation and residual weight

Samples	Onset Degradation (°C)	Residual Weight (%)
Pure PLA	339.99	0
1 wt%	346.55	0-1
3 wt%	327.47	1-2
5 wt%	331.89	2-3
7 wt%	313.30	8-9
9 wt%	309.65	7-8

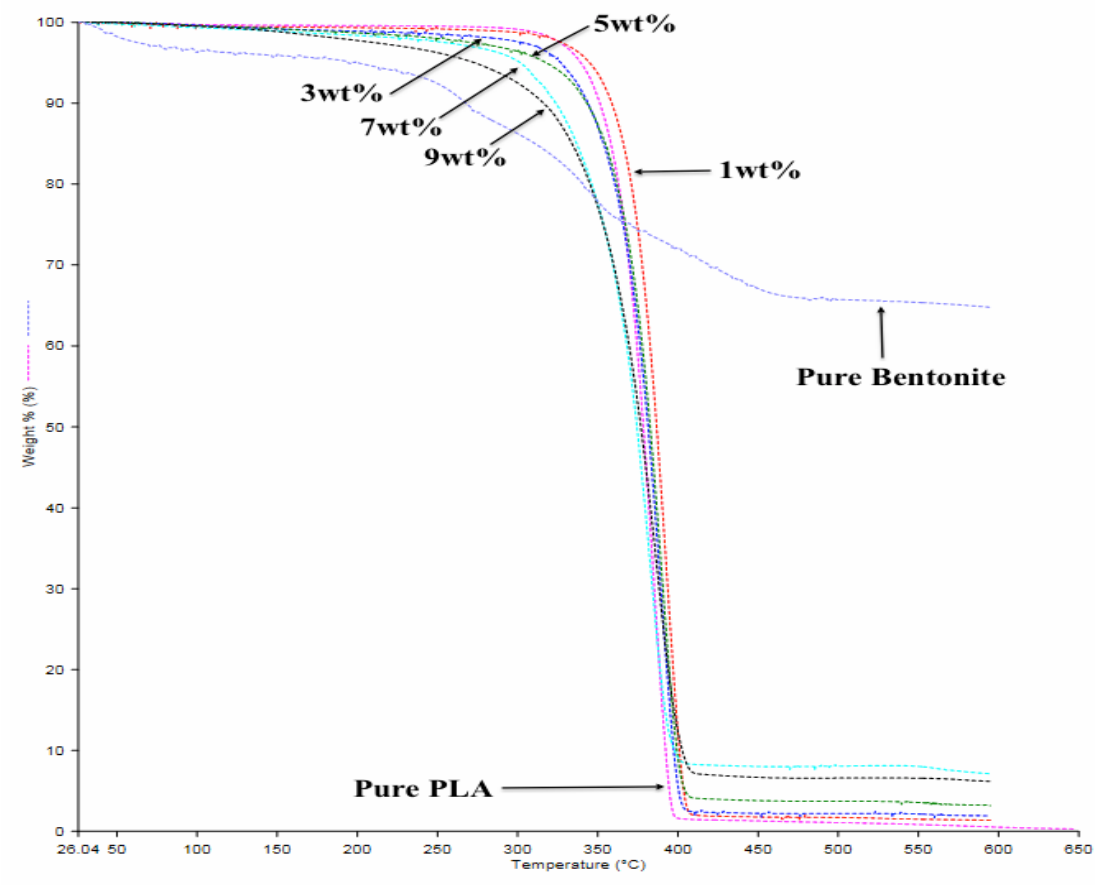


Figure 4.1 Weight loss curve for Pure PLA, bentonite and bentonite-PLA composites

4. Conclusion

PLA was infused with the inorganic nano filler, bentonite, and was prepared using the melt blending and compression moulding process. The composite was then tested for it's mechanical and thermal properties. The mechanical test conducted was tensile test, while the thermal test conducted was the TGA analysis. Based on the findings, addition of 1wt % bentonite shows an increased thermal stability. It also determined that none of the samples absorb any significant amount of water in the water absorption test, which indicates the composites have very low water uptake properties. Next, the increase of bentonite compound in the PLA shows a decrease in elasticity and an increase in overall stiffness. With these research findings, it can be concluded that 1wt% of bentonite-PLA composite is has the most satisfactory results on mechanical, thermal and water absorption properties, and thus can be used in the packaging industry as a safer alternative to synthetic polymers.

Acknowledgement

I would to like to express my gratitude to Dr. Pang Ming Meng, Ms. Eunice Phang Siew Wei, Ms. Lithnes and Ms. Farihah for their help, guidance and supervision throughout this research process.

References

[1] J.-W. W. Rhim, H.-M. M. Park, and C.-S. S. Ha, “Bio-nanocomposites for food packaging

applications," *Prog. Polym. Sci.*, vol. 38, no. 10–11, pp. 1629–1652, 2013.
[2] L.-T. Lim, R. Auras, and M. Rubino, "Processing technologies for poly(lactic acid)," *Prog. Polym. Sci.*, vol. 33, no. 8, pp. 820–852, 2008.
[3] K. Y. T. W.L. Ngo, M.M. Pang, L.C. Yong, "Mechanical Properties of Natural Fibre (Kenaf , Oil Palm Empty Fruit Bunch)," *Adv. Environ. Biol.*, vol. 8, no. 1, pp. 2742–2747, 2014.
[4] S. O. Obaje, J. I. Omada, and U. A. Dambatta, "Clays and their Industrial Applications : Synoptic Review," *Int. J. Sci. Technol.*, vol. 3, no. 5, pp. 264–270, 2013.
[5] J. Nones, J. Nones, A. Poli, A. G. Trentin, H. G. Riella, and N. C. Kuhnen, "Organophilic Treatments of Bentonite Increase the Adsorption of Aflatoxin B1 and Protects Stem Cells Against Cellular Damage," *Colloids Surfaces B Biointerfaces*, vol. 145, pp. 555–561, 2016.
[6] Y. Guo, Z. Gong, P. Li, W. Zhang, and B. Gao, "Preparation, characterization and enhancement of the visible-light photocatalytic activity of In2O3/Na-bentonite composite," *Ceram. Int.*, vol. 42, no. 7, pp. 8850–8855, 2016.
[7] S. S. Metwally and R. R. Ayoub, "Modification of natural bentonite using a chelating agent for sorption of 60Co radionuclide from aqueous solution," *Appl. Clay Sci.*, vol. 126, pp. 33–40, 2016.
[8] B. U. Nam, K. D. Min, and Y. Son, "Investigation of the nanostructure, thermal stability, and mechanical properties of polylactic acid/cellulose acetate butyrate/clay nanocomposites," *Mater. Lett.*, vol. 150, pp. 118–121, 2015.
[9] H. Balakrishnan, A. Hassan, M. U. Wahit, A. A. Yussuf, and S. B. A. Razak, "Novel toughened polylactic acid nanocomposite: Mechanical, thermal and morphological properties," *Mater. Des.*, vol. 31, no. 7, pp. 3289–3298, 2010.
[10] A. RAPACZ-KMITA, S.-Z. Ewa, M. DUDEK, B. SZARANIEC, A. ROZYCKA, and MOSIALEK, "Degradation of Nanoclay-Filled Polylactide Composites," *Physicochem. Probl. Miner. Process.*, vol. 49, no. 1, pp. 91–99, 2013.
[11] A. G. Clem and R. W. Doehler, "Industrial Applications of Bentonite," *Clays Clay Miner.*, vol. 10, no. 1, pp. 272–283, 1961.
[12] M. Murariu and P. Dubois, "PLA composites: From production to properties," *Adv. Drug Deliv. Rev.*, 2016.
[13] S. Jain, M. Misra, A. K. Mohanty, and A. K. Ghosh, "Thermal, Mechanical and Rheological Behavior of Poly(lactic acid)/Talc Composites," *J. Polym. Environ.*, vol. 20, no. 4, pp. 1027–1037, 2012.
[14] O. Gordobil, I. Egüés, and J. Labidi, "Modification of Eucalyptus and Spruce organosolv lignins with fatty acids to use as filler in PLA," *React. Funct. Polym.*, vol. 104, pp. 45–52, 2016.
[15] K. Piekarska, P. Sowinski, E. Piorkowska, M. M. U. Haque, and M. Pracella, "Structure and properties of hybrid PLA nanocomposites with inorganic nanofillers and cellulose fibers," *Compos. Part A Appl. Sci. Manuf.*, vol. 82, pp. 34–41, 2016.
[16] K. Issaadi, A. Habi, Y. Grohens, and I. Pillin, "Effect of the montmorillonite intercalant and anhydride maleic grafting on polylactic acid structure and properties," *Appl. Clay Sci.*, vol. 107, pp. 62–69, 2015.
[17] F. E. Gunawan, H. Homma, S. S. Brodjonegoro, A. B. B. Hudin, and A. B. Zainuddin, "Mechanical Properties of Oil Palm Empty Fruit Bunch Fiber," *J. Solid Mech. Mater. Eng.*, vol. 3, no. 7, pp. 943–951, 2009.
[18] B. K. Chen, C. C. Shih, and A. F. Chen, "Ductile PLA nanocomposites with improved thermal stability," *Compos. Part A Appl. Sci. Manuf.*, vol. 43, no. 12, pp. 2289–2295, 2012.
[19] A. Sarı, "Thermal energy storage characteristics of bentonite-based composite PCMs with enhanced thermal conductivity as novel thermal storage building materials," *Energy Convers. Manag.*, vol. 117, pp. 132–141, 2016.

A Study of Deep Eutectic Solvent (DES) in Chitosan Bio-Membrane for Proton Exchange Membrane Fuel Cell (PEMFC) Application

Jason Gan Boon Hoe[1*], Wai Yin Wong[2], Rashmi Gangasa Walvekar[3]

[1]*Taylor's University Lakeside Campus, Jalan Taylor's, Subang Jaya, 47500, Selangor, Malaysia;*

[2]*Fuel Cell Institute, Universiti Kebangsaan Malaysia, Bangi, 43600, Selangor, Malaysia;*

[3] *Taylor's University Lakeside Campus, Jalan Taylor's, Subang Jaya, 47500, Selangor, Malaysia*

[*]jasongboonhoe93@gmail.com

Abstract

Fuel cell has been regarded as a promising energy conversion device with great potential to alleviate the ever-growing demand for power. Proton Exchange Membrane Fuel Cell (PEMFC) has garnered predominant interest among the various type of fuel cells due to its high energy density, environmental friendliness and high efficiency. The polymer electrolyte membrane (PEM) is the gateway for proton transfer in a PEMFC that governs the performance and functionality of the fuel cell. With the arising challenge of the commercially utilised synthetic polymer, Nafion membrane as PEM due to its high cost, natural polymers such as chitosan are being investigated and established as materials in synthesising PEM is reported herein. Formation of natural polymeric film requires plasticiser to cross link natural polymers in improving the mechanical strength. Ionic liquid which is currently utilised as plasticiser in PEM synthesis is with the challenge of high toxicity and high cost. Thus, an investigation of the potential of choline chloride (ChCl) and urea based deep eutectic solvent (DES) as plasticiser in polymeric film is reported herein. The novelty and innovative of this work lies within the investigation of utilising natural polymers as materials to synthesis PEM and the study of the potential of DES as plasticiser in natural polymeric film to strengthen the plasticising effect and enhanced the flexibility of the membrane. It was found that addition of DES improves the homogeneity of the membrane film besides increasing the plasticising effect of the film that improves the flexibility of the membrane. This subsequently enhances the ionic conductivity of the membrane whereby plasticising effect promotes the amorphous nature of the membrane that is paramount in ionic conduction of the membrane. The water uptake is significantly improved as well in chitosan biopolymer membrane film with the addition of DES.

Keywords: Polymer Electrolyte Membrane (PEM), chitosan, fuel cell, Deep Eutectic Solvent (DES), plasticiser

1. Introduction

The environmental demands associated with energy production have focused our attention towards the development of the fuel cell and the application of fuel cells have gained strong interest contributed by its advantages of increasing fuel efficiency and virtually pollution-free operation [3, 4]. Fuel cells which convert chemical energy directly into electrical energy, have been considered as a promising energy conversion device with the great potential to alleviate the ever-growing demand for power [1 - 3]. Proton Exchange Membrane Fuel Cell (PEMFC) has received widespread interest among the various types of fuel cells that are available due to its advantages in terms of high energy density, easy fuel handling, environmental friendliness, higher efficiency, lower maintenance cost and feasibility of mobile and transport applications [1, 4, 5]. The conventional structure of a PEMFC consists of an anode (fuel supply), a cathode (oxidant supply) and an electrolyte (which allows the flow of ions between anode to cathode) [4, 6]. This is illustrated in the Fig1.1 shown below.

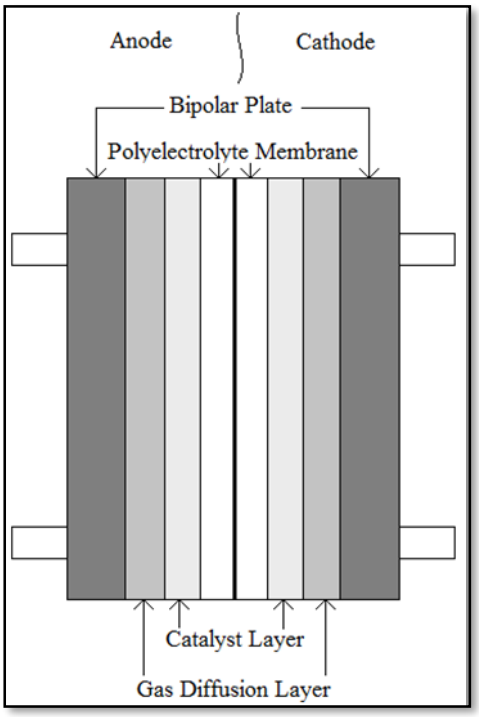


Figure 1.1 The structure of a PEMFC [4, 6]

As shown in Fig 1.1, the PEMFCs are constructed symmetrically with a PEM separating both cathode and anode side. The outest layer of the PEMFCs are known as bipolar plate, it is a conductive plate that appeared to be anode on one side and cathode on following side. The objective of a bipolar plate is to ensure uniform distribution of the process gasses (H_2 or O_2) across both sides of PEM [7]. Then, there are gas diffusion layers on both side that are sandwiched between the bipolar plates. The gas diffusion layer is responsible to homogeneously redistribute the incoming gas phase (H_2 or O_2) to the reaction plane of PEM and promote electric conduction [8].

Lastly, it would be the PEM that are situated between the catalyst layer which is to improve and optimise the performance of PEMFCs [4]. PEM is the main component in a PEMFC, whereby it serves as the electrolyte itself by providing an ion conductive gas barrier to allow only protons to pass through it [4]. Nafion-117 membrane is the commercialised PEM utilised in fuel cell application. The conventional and commercially utilised polymer electrolyte membrane (PEM) in

the PEMFC is the Nafion membrane [4 - 10]. Wang et al. [22] shown that the Nafion consists of a polytetrafluoroethylene backbone and perfluorinated side chains with terminating sulfonic acid group (-SO_3H) that is readily for the proton transfer mechanism [11]. The mechanism takes place in the presence of aqueous phase with rapid hydrogen bond breaking and forming processes on the sulfonic acid group of Nafion. However, Liu et al. [1] and Wan et al. [10] highlighted that researchers have studied the properties of Nafion membrane and intended to search for an alternative due to the drawbacks of Nafion membrane especially contributed by the high cost, high methanol permeability and low proton conductivity at high temperature (>120°C) [24] of this material. With that being said, recent study that are conducted have discovered that biopolymer materials are to be the potential candidate in synthesising the polymer electrolyte membrane as an alternative to Nafion membrane in addressing the current challenge encountered when utilising the commercial membrane in PEMFC applications [4, 9].

Biopolymer materials are able to comply with the mechanical and physicochemical properties of a polymer electrolyte membrane and has gained multiple interest and attention due to its advantages which include low cost, biodegradability, sustainability, environmentally friendly and abundant sources (high availability) [4, 12 ,13]. Therefore, cost effective and eco-friendly polymer electrolyte membrane can become a promising alternative to conventional ones. As mentioned by Ma and Sahai [9], natural polymers are the best candidates as it is available in abundance in the environment. Chitosan is one of the examples of natural polymers it is obtained by further treatment on shrimp or any crustaceans' shells that are being investigated and established as materials in synthesising PEM [9, 12].

Chitosan is a primary derivative from chitin and is commercially available basic polysaccharides [14]. The basicity of chitosan responsible for singular and chemical biological characteristic, biocompatibility, hydrophilicity, affinity to proteins and good membrane forming capability [14]. The following Table 1.1 shows the type of PEM with its respective thickness and proton conductivity.

Table 1.1 The type of polymer electrolyte membrane with its respective thickness and proton conductivity [4, 15, 16]

Types of PEM	Thickness (μm)	Proton Conductivity (S/cm)
Nafion-117	120	8.6×10^{-2}
Chitosan/Silica (doped with H_2SO_4)	55	2.9×10^{-2}
Chitosan / Nafion triple layer	150	8.8×10^{-2}
Chitosan/ PVA (doped with Organophosphorus acids	117	3.5×10^{-2}

Based on Table 1.1, it can be observed that natural polymers such as chitosan, does possess encouraged results in terms of proton conductivity when compared to the proton conductivity of the currently commercially used membrane in PEMFC application, Nafion-117 membrane. With that, this shows the potential of biopolymeric film of PEM in achieving significant performance and results in terms of proton conductivity. Fig 1.2 shows the monomer segments of chitosan.

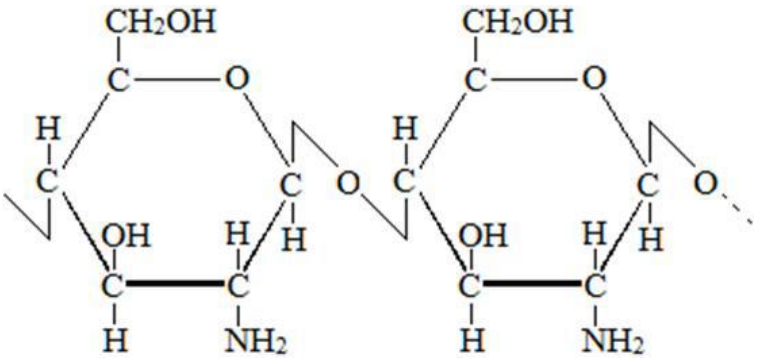


Figure 1.2 The monomer segment of chitosan [4]

Moreover, recent developments have shown that the addition of ionic liquid (IL) in the synthesis of the polymer electrolyte membrane as plasticiser resulted in providing plasticising effect to the PEM synthesised [17, 18, 19]. The plasticising effect generated on the synthesised PEM contributes to increase ionic conductivity [18]. Ionic liquids are organic salts combination of salt and hydrogen bond donor (HBD) with melting points below or equal to room temperature. They have attractive properties such as negligible volatility, non-flammability, high thermal and electrochemical stability and outstanding ionic conductivity even under anhydrous conditions [17, 19]. It is stated by Diaz et al. [19] that the ionic liquid is incorporated in the synthesis of PEM as plasticiser as the plasticising effect of ionic liquid would increase the ionic conductivity. Diaz et al. [19] added that the increased ionic conductivity is due to the strong plasticising effect of the ionic liquid; this effect softens the polymer backbone, increasing the flexibility of the polymer chain that is important in order to improve Grotthus transport mechanism because this type of mechanism must be supported by short-distance transport of ions and it is promoted when the polymer chains have enough mobility. The ionic liquid also acts as a carrier of protons improving the ionic conduction through vehicular mechanism [19].

Nevertheless, the disadvantage of ionic liquid is the high cost and potential toxicity of the material which are not economically feasible and environmentally friendly respectively [17]. These disadvantages of the application of ionic liquid as plasticiser paves the way for the research project objective in addressing the potential of deep eutectic solvent (DES) as an alternative to ionic liquid as plasticiser [17, 19, 21]. DES is referred to as the new ‘green solvent’ that possesses similar characteristic to ionic liquid, at the same time, it is cost effective, environmentally friendly and biodegradable [4]. Therefore, this research will highlight the potential of DES as an alternative to ionic liquid as plasticiser in the synthesis of PEM.

DES is the next promising green solvent to replace the current usage of ILs. The term “green solvents” define that it will not or less likely to cause any environmental impact while in use. DES is a mixture of HBD systems with simple salts to produce liquids which consist of physicochemical properties similar to ILs [4]. Based on the study of DES types, Abbott et al [32] discovered there is 3 different types of DES with a general formula of R1R2R3R4N+X-Y-.

Type I DES: Y = MClx, where M = Zn, Sn, Fe, Al, Ga
Type II DES: Y = MClx•yH2O, where M = Cr, Co, Cu, Ni, Fe
TYPE III DES: Y = R5Z, WHERE Z = -CONH2, -COOH, -OH

In this research, ONE set of type III DES combinations are being discussed which consist of (a) ChCl and Urea, whereby ChCl is the simple salt while urea is the HBD, the combination set of mixture will then prepare for the synthesising of DES solvent. Based on the research conducted by other researchers, the mixture of choline chloride and urea, named reline, at the molar ratio of 1:2 will has a melting point of 12°C, which is considerably low [11, 22 & 23]. This relatively low

melting point makes DES as an ideal replacement for ILs due to its high thermal stability characteristics.

Therefore, in this study, the effects of choline chloride and urea based deep eutectic solvent (DES) added in the synthesis of chitosan biopolymer membrane film will be reported herein.

2. Experimental

2.1 Materials

Chitosan (low-molecular weight) was received in the form of powder from Sigma-Aldrich Corporation with a claimed viscosity of 20-300 cP for 1 wt% of chitosan in 1 wt% of acetic acid. The following chemicals were all obtained and used as reagent grades from Merck Sdn Bhd: choline chloride, urea (99.5%) and acetic acid. Deionized water with a pH level of 7.4 was used for all the samples.

2.2 Synthesising Deep Eutectic Solvent (DES)

The choline chloride (ChCl) and urea based DES is prepared according to the procedure describe by Wong [4] whereby the choline chloride and urea are measured with a molar ratio of 1:2. The measured choline chloride and urea needed is then added into a 100 ml Schott Duran Laboratory bottle utilising a spatula. The bottle is then closed tightly and sealed with paraffin film (parafilm) to prevent any water vapour from entering. The mixture then undergoes heating and continuous stirring utilising magnetic hot plate at the temperature of 120°C with a speed of 300 rpm for 4 hours or until a homogenous liquid (transparent viscous liquid) is obtained. This is executed in the fumehood.

2.3 Dissolution of Biopolymer

1 wt% of Chitosan is dissolved in 100 ml of 0.1M acetic acid where the measured mass of chitosan required is added to a 100 ml Schott Duran Laboratory bottle containing 100 ml of 0.1 M acetic acid. The bottle is then sealed with paraffin film (parafilm) and it is heated at 47°C under continuous stirring at 500 rpm for 4 hours utilising a magnetic hot plate. This is executed in a fumehood. A homogenous solution of chitosan will be obtained.

2.4 Preparation of Chitosan-Bio Membrane

The chitosan solution prepared in Section 2.3 is then added with 1 wt% of the prepared choline chloride and urea based DES. The mixture of chitosan solution and DES solvent is added into a 100 ml Schott Duran Laboratory bottle which is then sealed with paraffin film (parafilm). The mixture undergoes mixing at room temperature of 25°C with a stirring speed of 500 rpm for 4 hours utilising a magnetic hot plate. This is carried out in the fumehood. A homogenous mixture of chitosan solution with DES solvent is obtained. 50 ml of the prepared mixture of solution is then casted on a glass petri dish and left in the fumehood for 10 days for the acetic acid to be evaporated before placing into the oven for drying at 60°C for 24 hours. In this step, the volume of DES added to the chitosan solution is varied with 0 ml, 1 ml, 3 ml and 5 ml. This will allow the study and investigation into the effects of DES in chitosan bio-membrane with and without the addition of DES.

2.5 Membrane Film Thickness Measurement

The thickness of the synthesised biopolymer membrane film is measured utilising the Mitutoyo Digital Vernier Caliper with the sensitivity of 0.01 mm.

2.6 Fourier Transform Infrared Spectroscopy (FT-IR) Analysis

The Fourier Transform Infrared Spectroscopy (FT-IR) (PerkinElmer, Spectrum 100 FT-IR Spectrometer) was used to identify the chemical functional groups of the chitosan biopolymer membrane film. The analysis is driven by the software namely, 'Spectrum' to plot and analyse the data generated. The wavenumber of the analysis was executed between the range of 4000 cm^{-1} to 650 cm^{-1} [4]. Attenuated total reflectance (ATR) sampling techniques were conducted on all samples.

2.7 Scanning Electron Microscope (SEM)

Scanning Electron Microscopy (SEM) (Ultra 55 FESEM from Chicago, USA) with accelerating voltage of 20 kV and low vacuum is used to estimate the thickness of the synthsised chitosan-CMC biopolymer composite membrane. It also provides a study on the cross-sectional areas and surface morphology of the membrane film. [4]. The magnifications utilised to observe the biocomposite blend film include 240x, 600x, 5000x and 10000x.

2.8 Electrochemical Impedance Spectroscopy (EIS)

Electrochemical Impedance Spectroscopy (EIS) (Gamry Interface 1000 Potentiostat) provides information regarding the electrical properties of the biopolymer membrane and its interface with conducting electrodes [4]. The biopolymer membrane is sandwiched between two stainless steel electrodes in a measurement cell through alternating current (AC) mode and measures the impedance of the membrane with a frequency ranged from 1000 kHz to 50 Hz with 10 points/decade at the AC voltage of 10 mV rms [4, 24]. The resistance of the membrane is generated by the Gamry Analyst software from the Nyquist plot through electrochemical circle fit (Fuel Cell model). The EIS testing to measure the impedance is conducted three times for each sample of membranes and the average reading is tabulated. The standard deviation of the readings obtained is determined as well. The conductivity is then calculated by using Eq. (1) in the following:

$$Conductivity = \frac{l}{RA} \quad (1)$$

where l is the thickness of the biopolymer membrane (cm), R is the membrane resistance (Ω) and A is the cross sectional area of the membrane (cm^2).

2.9 Ion Exchange Capacity (IEC)

The ion exchange capacity (IEC) testing is to measure the ability and capability of the synthesiSed biopolymer PEM in ion exchange which is related to the proton conductivity of the PEM and performance of the PEMFC. In IEC testing, the PEM are oven dried at 60°C for 24 hours, then weighed. The membranes were immersed in 20 ml of 2.5 M NaCl solutions for 5.5 hours to ensure exchange of all the protons, H+ with sodium ions, Na+ [25]. The proton content in the salt solution was subsequently determined by titration with 0.05 M sodium hydroxide, NaOH solution to neutralise all the exchanged protons using phenolphthalein as the endpoint indicator [25]. The IEC is conducted once for all membrane samples and the values are then calculated using the Eq. (2) as shown below:

$$IEC = \frac{a \times b}{m} \quad (2)$$

where IEC is the ion exchange capacity (mmol/g); a is the added titrant volume at the equivalent point (mL); b is the molar concentration of the titrant; m is the dry membrane weight (g).

2.10 Water Uptake

Water uptake is an important parameter to identify the suitability of chitosan-CMC biocomposite membrane in fuel cell application. Water uptake rate is a measure of interaction between the biocomposite membrane and liquid. In a PEMFC, the proton conductivity will increases with the decrease in water uptake rate. The membrane should possess with adequate water uptake and dimensional swelling in order to reduce the stress acting towards it throughout the operation [4, 26].

The mass of the dry chitosan biopolymer membrane is weighed, followed by soaking it in distilled water for 5.5 hours. Then, the wet membrane is removed with the excess water tapped dry utilising a tissue paper and immediately weighed to estimate the amount of water absorbed [4]. Eq. (3) is used to calculate the percentage sorption or water uptake rate in term of percentage (%).

$$Water\ Uptake\ (\%) = \frac{W_{wet} - W_{dry}}{W_{dry}} \times 100\% \quad (3)$$

where;

W_{wet} is the mass of wet biopolymer membrane in gram, g
W_{dry} is the mass of dry biopolymer membrane in gram, g

3. Results and Discussion

3.1 Thickness of the chitosan biopolymer film

The thickness of the chitosan biopolymer membrane film synthesised is measured utilising the the Mitutoyo Digital Vernier Caliper with the sensitivity of 0.01 mm. The following Table 3.1 illustrate the thickness of all the chitosan biopolymer membrane synthesised.

Table 3.1 The thickness of the chitosan biopolymer membrane films

Samples	Thickness (mm)
Pure Chitosan without DES	0.08 ± 0.01
Pure Chitosan with 1 ml DES	0.21 ± 0.03
Pure Chitosan with 3 ml DES	0.19 ± 0.03
Pure Chitosan with 5 ml DES	0.55 ± 0.06

Based on the results shown on the thickness of the chitosan biopolymer membrane films in Table 3.1, it can be observed that chitosan biopolymer membrane films with the addition of DES solvent as plasticiser increases the overall film thickness while offering higher flexibility of the film. This results coincides with the study done by Wong [4] whereby similar observations and trend of results are obtained. The thickness of the chitosan biopolymer membrane with the addition

of DES solvent is generally thicker than those without DES solvent added and in terms of flexibility, samples without the addition of DES solvent is brittle and does not acquire any flexibility as compared to the samples of membrane films with addition of DES solvent. This is illustrated in Fig. 3.1

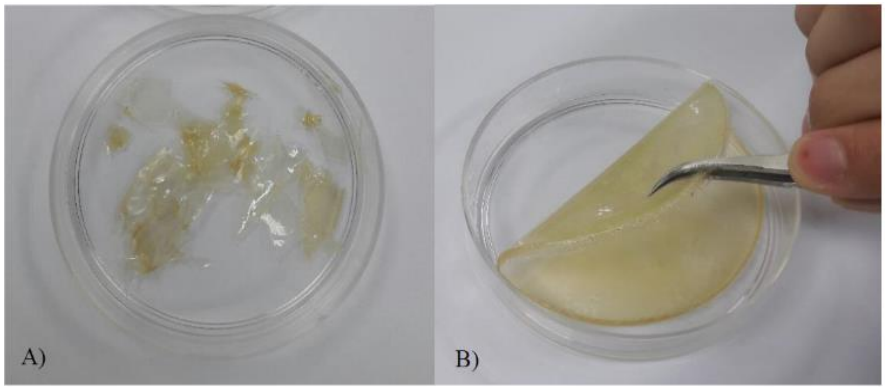


Figure 3.1 (A) The brittle chitosan biopolymer membrane without addition of DES solvent, (B) The flexible chitosan biopolymer membrane with addition of DES solvent

3.2 Fourier Transform Infrared Spectroscopy (FT-IR) Analysis

The formation of the chitosan biopolymer membrane was primarily contributed by the crosslinking between the functional groups of chitosan through hydrogen bonding that enables the formation of a solid biopolymer membrane film. Without the crosslinking of the functional groups, solid film of the membrane will not be formed as it will remain in liquid state. These interactions are determined through the Fourier Transform Infrared Spectroscopy (FT-IR) analysis that depicts the functional groups present in the synthesised membrane and the possible interactions that occurred between the functional groups. Fig 3.2 illustrates the infrared spectra of all the membrane samples synthesised.

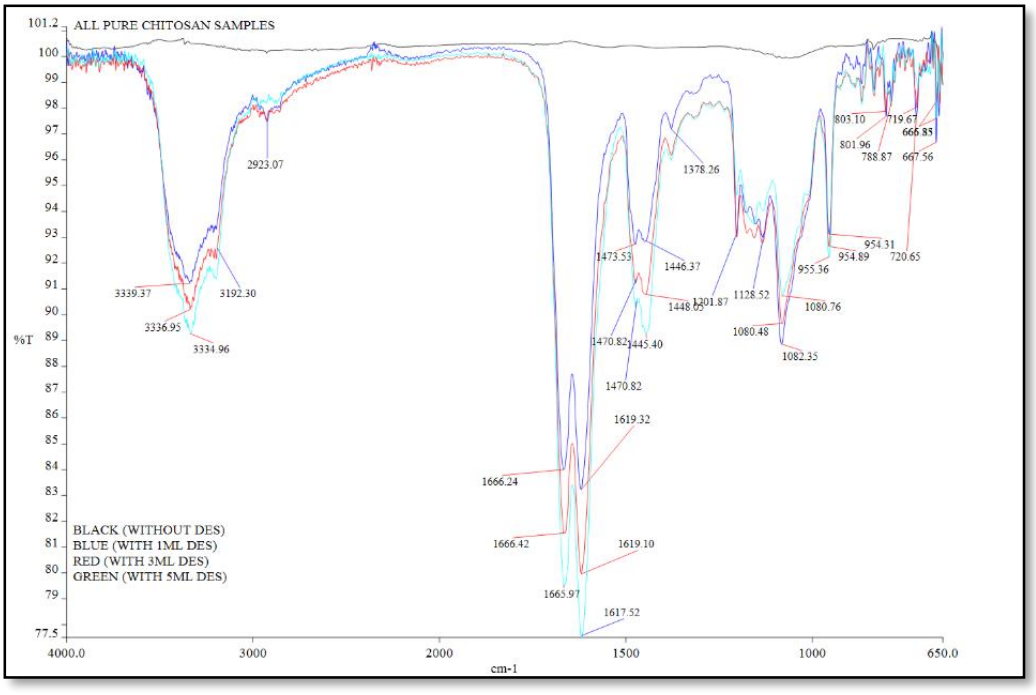


Figure 3.2 The FT-IR spectra for all the chitosan biopolymer samples

It is observed that chitosan biopolymer membrane without the addition of DES solvent has no characteristic peaks between 3300 cm to 3000 cm^{-1} and 1670 cm^{-1} to 1600 cm^{-1} as shown in Figure 3.2. For chitosan biopolymer membrane with the addition of DES solvent, characteristic peaks between 3300 cm^{-1} to 3000 cm^{-1} can be seen across all the samples with DES solvent added, this shows the presence of hydroxyl groups (O-H) contributed by both chitosan and DES solvent. This result is aligned with the study done by Holder et. al. [27] whereby the characteristic peaks within the range of 3581 cm^{-1} to 2401 cm^{-1} is contributed by the hydroxyl characteristic groups (O-H) of chitosan. Peaks formed from the range of 1670 cm^{-1} to 1600 cm^{-1} depicts the presence of carboxyl groups (C=O). The presence of amino groups (N-H), a functional group of chitosan is observed in the membrane with characteristic peak between 1700 cm^{-1} to 1200 $cm^{-}1$ which is similarly reported in the research done by Wong [4].

From the spectra shown in Fig. 3.2, presence of the saccharide ring (C-O-C) is visible through peaks within the range of 1200 cm-1 to 1000 cm-1 which indicates the bonding between two monosaccharides [4, 28]. The presence of the saccharide ring (C-O-C) demonstrates the cross-linking and bonding between chitosan monomers which enable the formation of a solid biopolymer membrane and without this bonding will render the chitosan mixture to be in liquid state [4].

3.3 Scanning Electron Microscope (SEM) Analysis

The SEM micrographs obtained from the pure chitosan biopolymer membrane films (cross-sectional view) measured at a magnification of 600 under the scale of 200 µm were presented in Figure 3.3 to indicate the differences between membrane films with and without DES. The thickness of the pure chitosan polymeric films was measured yielding differences in values due to the presence and absence of DES solvent in the polymer membrane films.

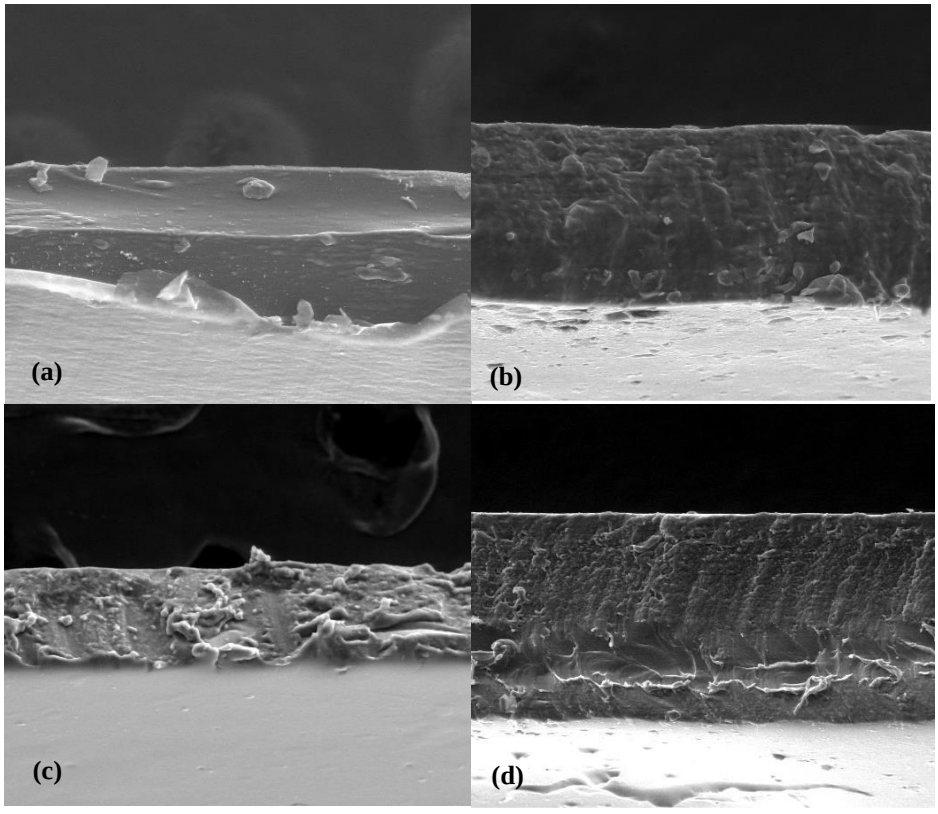


Figure 3.3 Thickness for (a) Pure chitosan without DES; (b) Pure chitosan with1ml DES; (c) Pure chitosan with 3ml DES; (d) Pure chitosan with 5ml DES

Based on the Figure 3.3 depicting the cross-sectional view of the pure chitosan biopolymer membrane whereby the thickness of (a) is 80.82 µm, (b) is 189.10 µm, (c) is 93.10 µm and (d) is 434.20 µm. From the thickness measured through SEM, the chitosan biopolymeric membrane film with addition of DES has greater thickness compared to that of without the addition of DES. The thickness measurement tabulated in Table 3.1 shows similar trend and is comparable with the results obtained from SEM whereby the addition of DES as plasticiser causes an increment on the overall film thickness while offering higher flexibility for the film. This observation and trend of results is aligned with study done by Wong [4].

In order to determine the interaction of DES in the chitosan biopolymeric membrane film, surface morphology of the polymeric membrane film was studied through the SEM micrographs. Fig. 3.4 illustrates the surface morphologies of all the chitosan biopolymeric membrane film with and without the addition of DES under the scale of 10 µm with 10 000 magnification.

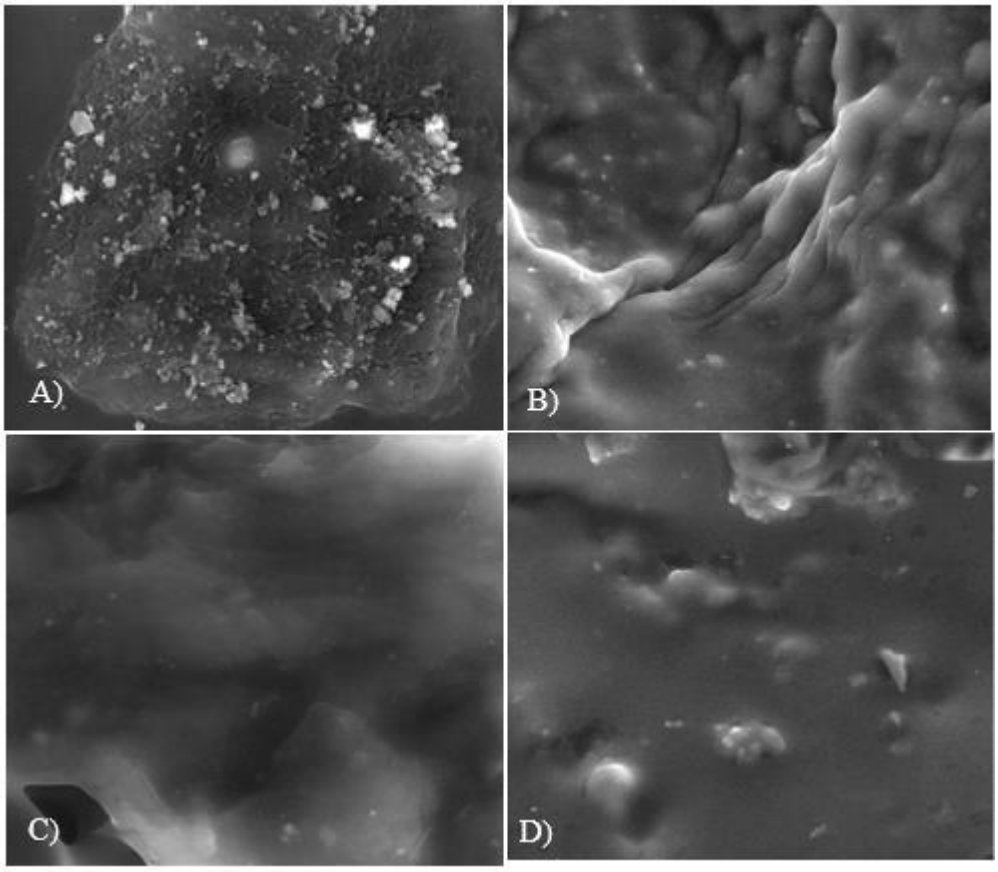


Figure 3.4 Surface morphology (a) Pure chitosan biopolymer membrane without DES; (b) Pure chitosan biopolymer membrane with 1 ml DES; (c) Pure chitosan biopolymer membrane with 3 ml DES; (d) Pure chitosan biopolymer membrane with 5 ml DES

From the surface morphologies of the membrane illustrated in Fig. 3.3, it can be observed that the chitosan biopolymeric membrane film with the addition of DES has the structure of the membrane to be more homogenous and no visible significance of agglomeration as compared to the chitosan biopolymeric membrane without the addition of DES. The addition of choline chloride and urea based DES as plasticicer would enhance the amorphous content of the membrane due to the presence of ammonium salt (choline chloride), subsequently will improve the plasticising effect and ion conductivity of the membrane which is stated in the study by Stefanescu et. al. [9].

3.4 Electrochemical Impedance Spectroscopy (EIS)

The ionic conductivity of the chitosan biopolymer membrane films were measured using complex impedance method. All the samples are performed under both dry and wet state to compare the differences in terms of conductivity. A Nyquist plot of imaginary impedance, -Z'' against the real impedance, Z' was performed for the analysis under the condition of room temperature. Fig. 3.4 demonstrates the sample graphical representation of the Nyquist plot with electrochemical circle fit feature (Fuel Cell model) for the chitosan biopolymer membrane film with 1 ml DES solvent to specify the corresponding high frequency zone. A high frequency zone in the Nyquist plot was referred as the response from grains which is the conduction process through the bulk of the film [4]. The tail of the plot often represents the electrode effect which is determined from the stainless steel electrode sandwiching the polymeric membrane film.

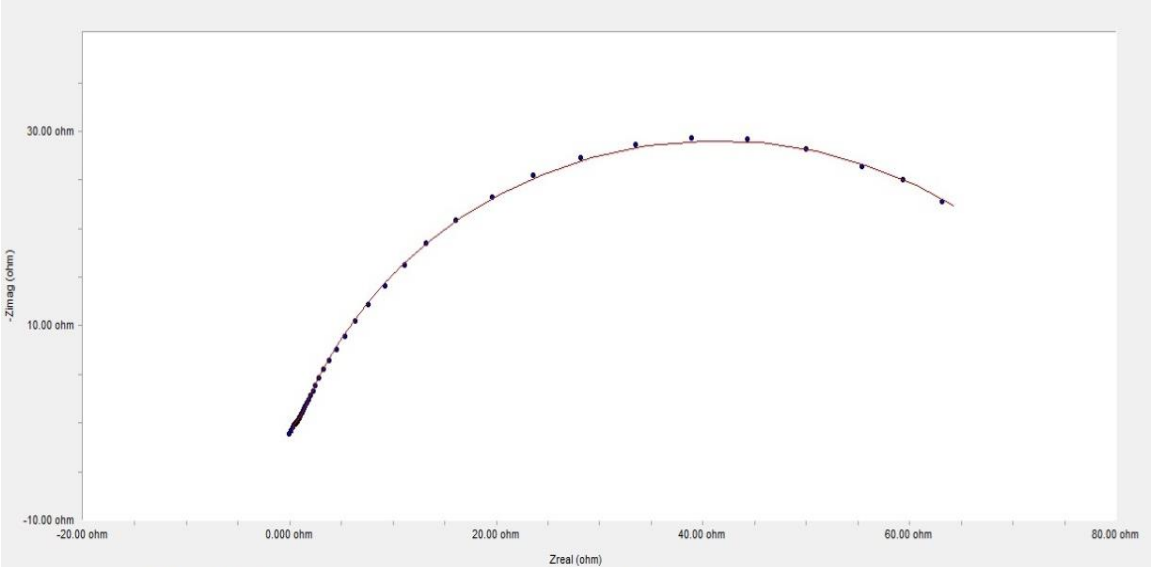


Figure 3.4 The Nyquist plot for pure chitosan biopolymer membrane film with 1 ml DES at wet state

The ionic conductivity of all the samples were calculated by applying Eq. (1) as stated in Section 2.8. The following Table 3.2 demonstrates the conductivity of all membrane samples at both dry and wet states.

Table 3.2 The conductivity of all chitosan biopolymer membrane films

Sample	**Conductivity, S/cm**	
	Dry State	**Wet State**
Pure chitosan without DES	$4.95 \times 10^{-7} \pm 0$	$2.98 \times 10^{-3} \pm 0.00016$
Pure chitosan with 1 ml DES	$4.79 \times 10^{-6} \pm 0.00000116$	$1.23 \times 10^{-2} \pm 0.00268$
Pure Chitosan With 3ml DES	$4.42 \times 10^{-5} \pm 0.00010805$	$6.71 \times 10^{-3} \pm 0.00056$
Pure chitosan with 5 ml DES	$3.14 \times 10^{-7} \pm 0.00000006$	$2.16 \times 10^{-2} \pm 0.00072$

Chitosan in its dry state has a very low electrical conductivity, however, chitosan can be utilised as a polymer matrix for ionic conduction whereby when solvated with lithium salt or proton donor salts such as ammonium salts, ionic conductivity of chitosan will be enhanced as stated in the study done by Stefanescu et. al. [9]. The addition of salt leads to the formation of complexation between salts and chitosan matrix and also enhancement of the amorphous nature [9]. Stefanescu et. al [9] added that the conductivity of the salt-complexed chitosan membrane is dependent on the number of mobile ions and mobility and coulombic interactions between the salt and functional groups of chitosan [9].

As illustrated in Table 3.2, the conductivity of chitosan biopolymer membrane film without DES at dry state is very poor whereas for chitosan biopolymer membrane film with addition of DES at dry state, the conductivity is significantly increased. This is because of the addition of DES as plasticiser and with the presence of ammonium salt (choline chloride) in the DES which improves the ionic conductivity of the membrane. The chitosan sample containing 3 ml DES showed the best conductivity in the dry state.

In the case of wet state, the conductivity of all the samples is higher compared to the respective samples at its dry state. This is due to the presence of moisture that would assist in the mobility of the ions in the membrane that would enhance the conductivity of the membrane. The chitosan sample with 5 ml DES has the highest conductivity (2.16×10^{-2} S/cm) compared to the other samples at wet state. This conductivity is comparable to that of the Nafion membrane (8.6×10^{-2} S/cm). It can be observed as well that the chitosan biopolymer membrane with the addition of DES has better conductivity at both dry and wet state compared to the samples without DES whereby this observation coincide with the research done by Wong [4].

Therefore, the addition of choline chloride and urea based DES as plasticiser in the membrane, strengthens the plasticisation effect in the membrane that enhances the amorphous nature of the film [9]. This subsequently increases the conductivity of the membrane film as the ionic conductivity of polymer electrolytes is dominated by amorphous phase rather than crystalline phase [9].

3.5 Ion Exchange Capacity

The ion exchange capacity is conducted accordingly to the procedure as mentioned in Section 2.9 whereby a measure of the ion exchange capability of the membrane is measured through this analysis. The ion exchange capacity value is calculated using Eq. (2) as stated in Section 2.9. The following Table 3.3 illustrates the ion exchange capacity for all the chitosan samples.

Table 3.3 The IEC value for all the chitosan biopolymer membrane films

Sample	Ion exchange capacity value(mmol/g)
Pure chitosan without DES	1.0870
Pure chitosan with 1 ml DES	0.2066
Pure Chitosan With 3ml DES	0.1000
Pure chitosan with 5 ml DES	0.0270

The ion exchange capacity results shown in Table 3.3 demonstrates that the ion exchange capacity in chitosan samples with addition of DES has a lower performance compared to that of the samples without addition of DES. There is a decreasing trend of ion exchange capacity can observed in the chitosan biopolymer membrane samples with addition of DES, however, as mentioned in Section 3.4, the addition of DES as plasticiser would enhance the conductivity of the membrane film. This is in direct correlation to the ion exchange capacity which determines the performance of the membrane in PEMFC application. The greater the ion exchange capacity, the greater the ionic conductivity, hence, improving the performance of the polymer electrolyte membrane in PEMFC application. Nevertheless, based on the results obtained, excessive volume of DES solvent added will decrease the ion exchange capacity of the membrane film. The pure chitosan biopolymer membrane film with 1 ml DES showed the highest ion exchange capacity value at 0.2066 mmol/g.

3.6 Water Uptake

The water uptake for all the samples are conducted at room temperature and the procedure is done accordingly as mentioned in Section 2.10. The water uptake in terms of percentage is calculated using Eq. (3) as stated in Section 2.10. The following Table 3.4 shows the water uptake for all the chitosan biopolymer membrane films.

Table 3.4 The water uptake for all the chitosan biopolymer membrane films

Sample	Water Uptake (%)
Pure chitosan without DES	698.89
Pure chitosan with 1 ml DES	180.67
Pure Chitosan With 3ml DES	77.78
Pure chitosan with 5 ml DES	8.47

As illustrated in Table 3.4, the water uptake for chitosan sample without DES is extremely high as compared to the water uptake of chitosan samples with the addition of DES. The polymer electrolyte membrane should have sufficient water uptake to a certain percentage to prevent the membrane to over swell and affect its performance. The water uptake of Nafion-117 membrane, the commercialised polymer electrolyte membrane in PEMFC application which acquires a water uptake of 8.74%.

The lowest water uptake percentage is shown by the chitosan biopolymer membrane film with 5 ml DES at 8.47% which shows similar trend as Nafion-117 membrane at 8.74%. In fact, the water uptake of the chitosan biopolymer membrane film with 5 ml DES performed better than that of Nafion-117 membrane. Nevertheless, the conductivity of the chitosan biopolymer membrane film with 5 ml DES is slightly lower compared to that of with chitosan samples with 1 ml and 3 ml DES. It can be observed as well the decreasing trend of water uptake as the volume of DES added increases.

In correlation between the water uptake and ion exchange capacity of the membrane film, as the water uptake of the film decreases, the ion exchange capacity of the membrane film decreases as well as reported by Taghizadeh et. al [28]. This correlation and relationship is observed in the results obtained for both ion exchange capacity (Section 3.5) and water uptake (Section 3.6) whereby the decreasing trend in both the ion exchange capacity and water uptake when the volume of DES solvent added increases for chitosan samples with DES.

4.0 Conclusion

In conclusion, based on the findings of this study, the addition of choline chloride and urea based DES as plasticiser in synthesising the polymer electrolyte membrane improves the homogeneity of the membrane film besides increasing the plasticising effect of the film that improves the flexibility of the membrane. This subsequently enhances the ionic conductivity of the membrane whereby plasticising effect promotes the amorphous nature of the membrane that is paramount in ionic conduction of the membrane.

Moreover, addition of DES as plasticiser significantly improves the water uptake of the chitosan biopolymer membrane which prevents the membrane film from over swelling and affects its conductivity performance. With that, addition of DES has improve the homogeneity,

plasticising effect, flexibility and water uptake of the membrane which consequently improves the proton conductivity and performance of the membrane film in PEMFC application.

Therefore, with the innovative step of discovering natural polymers such as chitosan as the potential material in synthesising PEM and the novelty of incorporating choline chloride and urea based DES as plasticiser that significantly improves the mechanical and physiochemical properties of the membrane, this will lead to a breakthrough in Proton Exchange Membrane Fuel Cell (PEMFC) application.

Acknowledgement

Gratitude and thanks to Dr. Wong Wai Yin, Dr. Rashmi G. Walvekar and Ms. Lithnes Kalaivani for their continuous and relentless guidance and support throughout this research study.

References

[1] Y. Liu, J. Wang, H. Zhang, C. Ma, J. Liu, S. Cao, and X. Zhang, "Enhancement of proton conductivity of chitosan membrane enabled by sulfonated graphene oxide under both hydrated and anhydrous conditions," J. Power Sources, vol. 269, pp. 898–911, 2014

[2] L. B. Braga, J. L. Silveira, M. Evaristo Da Silva, E. B. Machin, D. T. Pedroso, and C. E. Tuna, "Comparative analysis between a PEM fuel cell and an internal combustion engine driving an electricity generator: Technical, economical and ecological aspects," Appl. Therm. Eng., vol. 63, no. 1, pp. 354–361, 2014.

[3] Y.-S. Ye, J. Rick, and B.-J. Hwang, "Water Soluble Polymers as Proton Exchange Membranes for Fuel Cells," Polymers (Basel)., vol. 4, pp. 913–963, 2012.

[4] W. C. Yik, "Application of Deep Eutectic Solvent (DES) in Chitosan-Cellulose Blend Film for Proton Exchange Membrane," no. November, 2015.

[5] M. Malinowski, A. Iwan, K. Parafiniuk, L. Gorecki, and G. Pasciak, "Electrochemical properties of PEM fuel cells based on Nafion-polybenzimidazole-imidazole hybrid membranes," Int. J. Hydrogen Energy, vol. 40, no. 1, pp. 833–840, 2015

[6] J. Fang, J. Qiao, D. P. Wilkinson and J. Zhang, Ed., "Electrochemical Polymer Electrolyte Membranes," Taylor & Francis Group, LLC. pp.7, 2015.

[7] Y. Dai, J. van Spronsen, G. J. Witkamp, R. Verpoorte, and Y. H. Choi, "Natural deep eutectic solvents as new potential media for green technology," Anal. Chim. Acta, vol. 766, pp. 61–68, 2013.

[8] X. Yang, Q. Wang, and H. Yu, "Dissolution and regeneration of biopolymers in ionic liquids," Russ. Chem. Bull., vol. 63, no. 3, pp. 555–559, 2014.

[9] C. Stefanescu, W. H. Daly, and I. I. Negulescu, "Biocomposite films prepared from ionic liquid solutions of chitosan and cellulose," Carbohydr. Polym., vol. 87, no. 1, pp. 435–443, 2012.

[10] Y. Wan, K. A. M. Creber, B. Peppley, and V. T. Bui, "Chitosan-based electrolyte composite membranes. II. Mechanical properties and ionic conductivity," J. Memb. Sci., vol. 284, no. 1–2, pp. 331–338, 2006.

[11] T. Chakrabarty, M. Kumar, and V. K. Shahi, "Chitosan Based Membranes for Separation , Pervaporation and Fuel Cell Applications : Recent Developments," pp. 5–8.

[12] J. Ma and Y. Sahai, "Chitosan biopolymer for fuel cell applications," Carbohydr. Polym., vol. 92, no. 2, pp. 955–975, 2013.

[13] N. N. Mobarak, A. Ahmad, M. P. Abdullah, N. Ramli, and M. Y. A. Rahman, "Conductivity enhancement via chemical modification of chitosan based green polymer electrolyte," Electrochim. Acta, vol. 92, pp. 161–167, 2013.

[14] T. Chakrabarty, M. Kumar, and V. K. Shahi, "Chitosan Based Membranes for Separation, Pervaporation and Fuel Cell Applications : Recent Developments," pp. 5–8.

[15] A. Vega-Rios, J. L. Olmedo-Mart??nez, B. Far??as-Mancilla, C. A. Hernanndez-Escobar, and E. A. Zaragoza-Contreras, "Synthesis and electrical properties of polyaniline/iota-carrageenan biocomposites," Carbohydr. Polym., vol. 110, pp. 78–86, 2014.

[16] Q. Zhao, Q. F. An, Y. Ji, J. Qian, and C. Gao, "Polyelectrolyte complex membranes for pervaporation , nanofiltration and fuel cell applications," J. Memb. Sci., vol. 379, no. 1–2, pp. 19–45, 2011.

[17] P. Of and A. Films, "Eutectic-Based Ionic Liquid on Physicochemical," BioResources, vol. 7, no. 4, pp. 4760–4775, 2012.

[18] S. Das and A. Ghosh, "Effect of plasticizers on ionic conductivity and dielectric relaxation of PEO-LiClO4 polymer electrolyte," Electrochim. Acta, vol. 171, pp. 59–65, 2015.

[19] M. Zdanowicz and T. Spychaj, "Ionic liquids as starch plasticizers or solvents," Polimery/Polymers, vol. 56, no. 11–12, pp. 861–864, 201

[20] M. D??az, A. Ortiz, and I. Ortiz, "Progress in the use of ionic liquids as electrolyte membranes in fuel cells," J. Memb. Sci., vol. 469, pp. 379–396, 2014.

[21] Y. Dai, J. van Spronsen, G. J. Witkamp, R. Verpoorte, and Y. H. Choi, "Natural deep eutectic solvents as new potential media for green technology," Anal. Chim. Acta, vol. 766, pp. 61–68, 2013.

[22] *S. Lin, L. Chen, L. Huang, S. Cao, X. Luo, K. Liu, and Z. Huang, "PREPARATION AND CHARACTERIZATION OF CHITOSAN / CELLULOSE BLEND FILMS USING ZnCl 2 •3H 2 O AS A SOLVENT," vol. 7, pp. 5488–5499, 2012.*

[23] M. Hasegawa, A. Isogai, S. Kuga, and F. Onabe, "Preparation of cellulose-chitosan blend film using chloral/dimethylformamide," Polymer (Guildf)., vol. 35, no. 5, pp. 983–987, 1994.

[24] J. Xu, G. Sheng, H. Luo, W. Li, and L. Wang, "Fouling of proton exchange membrane (PEM) deteriorates the performance of microbial fuel cell," Water Res., vol. 46, no. 6, pp. 1817–1824, 2012.

[25] Y. Devrim and A. Albostan, "ScienceDirect Enhancement of PEM fuel cell performance at higher temperatures and lower humidities by high performance membrane electrode assembly based on Nafion / zeolite membrane," Int. J. Hydrogen Energy, vol. 40, no. 44, pp. 15328–15335, 2015.

[26] L. García-cruz, C. Casado-coterillo, J. Iniesta, and V. Montiel, "Chitosan : poly (vinyl) alcohol composite alkaline membrane incorporating organic ionomers and layered silicate materials into a PEM electrochemical reactor," J. Memb. Sci., vol. 498, pp. 395–407, 2016.

[27] S. L. Holder, C. H. Lee, S. R. Popuri, and M. X. Zhuang, "Enhanced surface functionality and microbial fuel cell performance of chitosan membranes through phosphorylation," *Carbohydr. Polym.*, vol. 149, pp. 251–262, 2016.

[28] S. Yu, H. Hsieh, J. Pang, D. Tang, C. Shih, M.Tsai, Y. Tsai and F. Mi, 'Active films from water soluble chitosan/cellulose composite incorporating releasable caffeic acid for inhibition of lipid oxidation in fish oil emulsion,' Food Hydrocolloids, vol. 32, no. 1, pp. 1-19, 2013.

[29] M. T. Taghizadeh and M. Vatanparast, "Journal of Colloid and Interface Science Ultrasonic-assisted synthesis of ZrO 2 nanoparticles and their application to improve the chemical stability of Nafion membrane in proton exchange membrane (PEM) fuel cells," J. Colloid Interface Sci., vol. 483, pp. 1–10, 2016.

Thermophysical Properties of MoS_2 Based Graphene Nanolubricant

Kelly Lee[1*], Rashmi W[1], Author[3]

[1]*Taylor's University Malaysia*

[*]kelly.lee@sd.taylors.edu.my

Abstract

Lubricants play a vital role in many of the industries where the machineries are operated for a longer duration and under extreme conditions which can generate heat, wear and friction between the moving components. Thus a new lubricant is proposed to utilize the potential of graphene and MoS_2 solid lubricants and also blend of vegetable (peanut oil) and naphthenic oils, which can not only provide better lubrication but also act as heat carriers. This study aims to synthesize a hybrid graphene-MoS_2 based nanolubricant dispersed in blend oil. The ratio of peanut oil and naphthenic oil is varied between 1:3 to 3:1. A fixed composition of POME (4.34 wt%) is added to enhance the anti-wear property. Graphene and MoS2 concentration is varied between 1:2 to 5:2, respectively. The mixture is physically mixed using water bath sonication for 4 hours. Stability of the resultant nanolubricants are measured using UV Vis spectrophotometer for 28 days. Thermal conductivity of the nanolubricants are also measured to study the effect of graphene, MoS_2, peanut oil and naphthenic oil concentrations as a function of temperature (25°C-55°C). Results show that combinations of 3:1 naphthalene and peanut oils showed higher stability for all the hybrid and MoS_2 alone lubricants. Stability decreased as the peanut concentration is increased above 25wt%. Similarly, highest thermal conductivity enhancement is observed for 100wt% naphthenic oil with 1:2 ratio of graphene-MoS_2 at 55°C.

Keywords
Nanolubricant; MoS_2; Graphene; Stability; Thermal conductivity; Naphthalene Oil; peanut oil

1. Introduction

In the metal work cutting industry, frictional forces which were created from the sliding motions often results in the wear and tear of components. Hence, lubricants are often applied to reduce the loss of energy and minimize the wearing of machine component parts. Besides that, the use of lubricants would bring along other

positive effects and benefits to both the users and the environment as well. Lubricants act as agents which help to remove heat generated due to friction, and as cleaning agents to remove the particulate matters, which in return reduces the need of operational maintenance in the industry.

The importance of naphthalene has been realized ever since the last century in the industrial fields [1]. Mineral oils generally have lower cost as compared to crude oils where they are being derived from. One of the biggest limitations of mineral oils is that they do not have strict tribological principles, which results in the formation of a wide range of lubricant-sized molecules ranging from good to bad tribological properties, where some of the mineral oils work better in reducing the coefficient of friction [2]. In contrast, there are more advantages in vegetable oils over petroleum based oils. Vegetable oils are known for its renewability and biodegradability, where it is a type of environmentally friendly oil yet the source would not be depleted easily. As compared to petroleum based oils, vegetable oils have relatively higher viscosity index, which means smaller change in viscosity is observed with respect to temperature. This makes them to be conducive to be used as lubricants in various applications, including the metal working field [3].

A recent discovery was done on the research of metallic nanofluids and carbon nanotube (CNT), where the particles come in spherical and cylindrical shapes. A major challenge was found in the industry as there is still no better suggestion on the stable substitution of existing coolants. Graphene, formed by carbon atoms which are hexagonally arrayed in two-dimensional (2D) are governed with various positive characteristics such as its high thermal conductivity behavior and high fracture strength [4]. It is expected that there would be more graphene-based applications emerging in the industry in the future due to its extraordinary traits. Since graphene is known as a good thermal conductor, hence, it is not surprising to expect significant thermal conductivity enhancement from the graphene based nanofluids. Moreover, graphene which comes in the form of thin films, also acts as excellent solid lubricant in reducing friction [5].

Molybdenum disulfide (MoS_2) is a commonly used dry lubricant in the industry for various applications such as machinery services and aircraft engines. It is known for its good lubricating properties which are due to the weak Van der Waals forces between the atoms, hence causing a low coefficient of friction in the fluid [6]. On the other hand, as graphene is also known for its high thermal conductivity and relatively stable atomic structure, therefore, this study aims to investigate the characteristics of the combination of graphene-MoS_2. It is expected that the good traits of the combination of both compounds could be discovered to benefit the applications in the industry.

Palm Oil Methyl Ester (POME) which is a type of vegetable based oil, is produced through the transesterification process of palm oil. The main compositions of POME include triglycerides, glycerides, fatty acids and non-glycerides compounds. It is known that the fatty acids composition in POME portrays effective boundary lubrication property, which makes it to be conducive to be used as an anti-wear additive for most lubricants [7]. There's another recent study proves that POME itself acts as a good anti-wear lubricant additive, where smaller wear scars were found in test runs with the addition of POME [8]. Based on a study done by Masjuki and

Maleque [9], it is shown that 4.34wt% is the optimum concentration of POME in base oil solution that would result in a minimum wear rate.

In this study, naphthalene oil and the peanut oil were blended in various ratios with the presence of graphene-MoS_2 nanoparticles and POME to determine the optimum ratio of the mixture based on the fluid characteristics. The ratio of the mixtures was discussed thoroughly in the research methodology section. It is believed that the synthesis of hybrid graphene-MoS_2 nanoparticles would contribute to the improvement of tribological properties in metal working lubricants in terms of reducing the coefficient of friction and wearing rate etc. Therefore, this research work aims to contribute to the reduction of wearing effect in the metal work industry.

2. Methodology

This research focuses on the study of graphene and MoS_2 which act as solid lubricants to enhance the lubricating effect of nanolubricant in metal cutting work. Naphthalene oil and peanut oil were used as the based fluids in this research study.

2.1 Materials

The materials which were used in the preparation of hybrid nanolubricant include the graphene powdered nanoparticles (diameter: 12nm, purity: 99.2%) from Graphene Supermarket USA, MoS_2 (size: 1cm) from Apar Industries, India, naphthalene oil (refined grade with 95% purity) from Nynas, Sweden, peanut oil (refined grade) from Sunway Cold Storage as well as palm oil methyl ester (POME) (0.1% of free fatty acid) from Excelvite, Malaysia.

2.2 Synthesis of hybrid graphene-MoS_2 nanoparticles

The graphene-MoS_2 compound is formed through the physical mixing process of graphene with molybdenum disulfide (MoS_2). The mass of graphene and molybdenum disulfide were varied in few different mass percentages in order to determine the optimum concentration of graphene-MoS_2 which would help in enhancing the thermophysical properties of base fluids. The ratio of graphene-MoS_2 was being varied between 1:2 and 5:2.

2.3 Samples Preparation

The preparation of the test samples was categorized into few levels whereby different types of solutions were being prepared in each level. In the first level of the samples preparation, two types of fluids which include the peanut oil and the naphthalene base oil were prepared individually. The second level of samples preparation involved the blending of peanut and naphthenic oils in different ratios, with the presence of an optimum concentration of POME (4.34 wt%). The blending ratios of naphthalene oil and peanut oil was being summarized in **Table 1**. The base fluids samples from second level preparation were then being brought forward to the third level where each blending ratio of the base fluids was added with 9 different combinations of graphene-MoS_2 concentration which was illustrated in **Table 2** and **Table 3**. The nanolubricants prepared were being sonicated for 4 hours by using a

water sonication bath at constant room temperature. NL and PL served as base fluids for benchmarking.

Table 1. Composition of Base Fluids Samples for Second Level Samples Preparation.

Base Fluids	Weight percentage, %		Ratio
	Naphthalene oil	Peanut oil	
NL	100	0	1:0
NPL1	75	25	3:1
NPL2	50	50	1:1
NPL3	25	75	1:3
PL	0	100	0:1

Table 2. Composition of Samples (MoS_2 only) for Third Level Samples Preparation.

	Weight (%)			
Samples	**Naphthenic oil**	**Peanut oil**	**POME**	**MoS_2**
NL1	95.66	0	4.34	0.05
NL2	95.66	0	4.34	0.10
NL3	95.66	0	4.34	0.15
NPL1	71.75	23.92	4.34	0.05
NPL2	71.75	23.92	4.34	0.10
NPL3	71.75	23.92	4.34	0.15
NPL4	47.83	47.83	4.34	0.05
NPL5	47.83	47.83	4.34	0.10
NPL6	47.83	47.83	4.34	0.15
NPL7	23.92	71.75	4.34	0.05
NPL8	23.92	71.75	4.34	0.10
NPL9	23.92	71.75	4.34	0.15
PL1	0	95.66	4.34	0.05
PL2	0	95.66	4.34	0.10
PL3	0	95.66	4.34	0.15

Table 3. Composition of Samples (graphene and MoS_2) for Third Level Samples Preparation.

	Weight (%)				
Samples	**Naphthenic oil**	**Peanut oil**	**POME**	**MoS_2**	**Graphene**
NGL1	95.66	0	4.34	0.05	0.075
NGL2	95.66	0	4.34	0.10	0.075
NGL3	95.66	0	4.34	0.15	0.075
NGL4	95.66	0	4.34	0.05	0.010
NGL5	95.66	0	4.34	0.10	0.010
NGL6	95.66	0	4.34	0.15	0.010
NGL7	95.66	0	4.34	0.05	0.015

NGL8	95.66	0	4.34	0.10	0.015
NGL9	95.66	0	4.34	0.15	0.015
NPGL1	71.75	23.92	4.34	0.05	0.075
NPGL2	71.75	23.92	4.34	0.10	0.075
NPGL3	71.75	23.92	4.34	0.15	0.075
NPGL4	71.75	23.92	4.34	0.05	0.010
NPGL5	71.75	23.92	4.34	0.10	0.010
NPGL6	71.75	23.92	4.34	0.15	0.010
NPGL7	71.75	23.92	4.34	0.05	0.015
NPGL8	71.75	23.92	4.34	0.10	0.015
NPGL9	71.75	23.92	4.34	0.15	0.015
NPGL10	47.83	47.83	4.34	0.05	0.075
NPGL11	47.83	47.83	4.34	0.10	0.075
NPGL12	47.83	47.83	4.34	0.15	0.075
NPGL13	47.83	47.83	4.34	0.05	0.010
NPGL14	47.83	47.83	4.34	0.10	0.010
NPGL15	47.83	47.83	4.34	0.15	0.010
NPGL16	47.83	47.83	4.34	0.05	0.015
NPGL17	47.83	47.83	4.34	0.10	0.015
NPGL18	47.83	47.83	4.34	0.15	0.015
NPGL19	23.92	71.75	4.34	0.05	0.075
NPGL20	23.92	71.75	4.34	0.10	0.075
NPGL21	23.92	71.75	4.34	0.15	0.075
NPGL22	23.92	71.75	4.34	0.05	0.010
NPGL23	23.92	71.75	4.34	0.10	0.010
NPGL24	23.92	71.75	4.34	0.15	0.010
NPGL25	23.92	71.75	4.34	0.05	0.015
NPGL26	23.92	71.75	4.34	0.10	0.015
NPGL27	23.92	71.75	4.34	0.15	0.015
PGL1	0	95.66	4.34	0.05	0.075
PGL2	0	95.66	4.34	0.10	0.075
PGL3	0	95.66	4.34	0.15	0.075
PGL4	0	95.66	4.34	0.05	0.010
PGL5	0	95.66	4.34	0.10	0.010
PGL6	0	95.66	4.34	0.15	0.010
PGL7	0	95.66	4.34	0.05	0.015
PGL8	0	95.66	4.34	0.10	0.015
PGL9	0	95.66	4.34	0.15	0.015

2.4 Stability studies of graphene-MoS_2 based hybrid nanolubricant

A UV spectrophotometer (GENESYS 10S UV-VIS, USA) was used to study the dispersion stability of the test samples by observing the absorbance on its wavelength. Visual observation was also performed by monitoring the samples by capturing digital images over a period of 28 days to determine the sedimentation of nanoparticles.

2.5 Viscosity studies

The Brookfield DV-II+ Pro (USA) was used to measure the viscosity of the samples which comes with the LV Spindle tests. The Brookfield viscometer which comes with an enhanced UL adapter has ensured the accuracy of the test results, despite using small volumes of test samples which can be as low as 16ml. UL adapter is a cylindrical spindle which rotates in a machine tube. The spring deflection was also used in measuring the viscous drag of the fluid against the spindle. Auto-zero calibration was done before performing any viscosity tests to ensure the accuracy of the test results. In order to allow zero-calibration to take place on the instrument, the connected spindles were detached accordingly. ULA-40Y water jacket which comes with the UL adapter functioned as a heat exchanger in heating and maintaining the temperature of the samples. The viscosity measurements were taken at 40, 75 and 100°C.

2.6 Thermophysical properties analysis

A thermal conductivity meter (KD2Pro, Decagon device, USA) was being utilized to measure the thermal conductivity properties, which comes with a 5-10% of accuracy range. KD2 Pro comes with a controller and a sensor which was inserted to the testing mediums during the experiment. A standard glycerin was used to calibrate the instrument before conducting any experiment. The KS-1 single-needle sensor (diameter: 1.3mm, length: 60mm) which connects to a microprocessor was used to measure the thermal conductivity of the fluids [10]. The sensor which consists of a heating element and thermo-resistor in its internal surface has an accuracy of $\pm 5\%$. Each sample of 16 ml was placed in a sample bottle, where the bottle was held by a water jacketed glass vessel. The needle probe was placed in the sample bottle to test its thermal conductivity. The samples were being tested at 25°C, 40°C and 55°C.

3. Results and discussion

3.1 Stability analysis of nanofluids

3.1.1 Effect of MoS_2

Visual observations of the test samples were being carried out throughout a period of 28 days. The samples were well sonicated before observing the sedimentation process to occur. Figure 1 shows how well do the samples which are of various concentrations of nanofluids sediment after 4 weeks of observation. Figure 1(a) shows that the sedimentation of nanoparticles is rather significant where nanoparticles and base oils started to be separated into two complete layers. This shows that the nanoparticles are poorly dispersed in this combination of base oils concentration [11]. While observing the samples from Figure 1(b), there was no pristine nanoparticles observed in the base oils. It could be said that the nanoparticles are relatively well dispersed and have high suspension stability [12]. It could be seen in Figure 1 (c), (d) and (e) that the nanoparticles are gradually sedimenting to the bottom of the cuvettes, forming relatively clear base oil solution layers at the top.

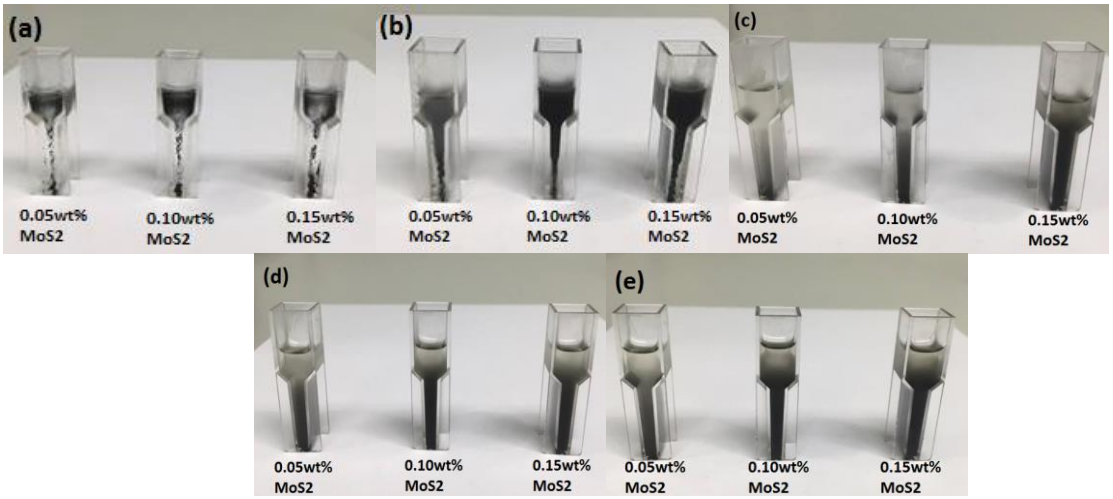
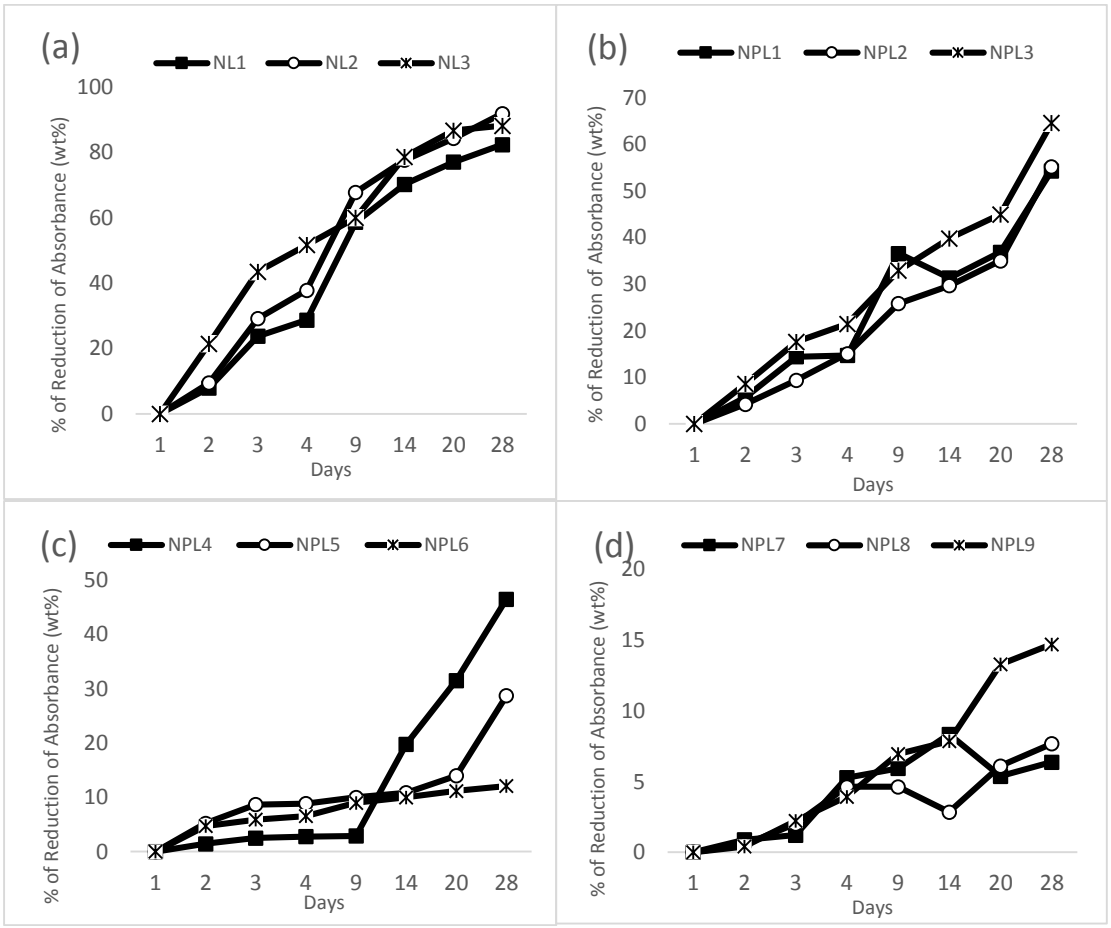


Figure 1. Images of nanofluids of various concentration 28 days after sonication process. (a) NL1-3, (b) NPL1-3, (c) NPL4-6, (d) NPL7-9, (e) PL1-3.

UV spectrophotometer was used to test out the absorbance values of the samples throughout a period of 28 days. The samples could be categorized into 2 main sets, where the first set only consists of MoS_2 nanoparticles and the second set consists of both graphene and MoS_2. These samples were measured at different wavelength as the peak wavelength, λmax obtained for each set of samples varies due to the presence of different nanoparticles (MoS_2 only: 276nm, MoS_2 and graphene: 308nm).



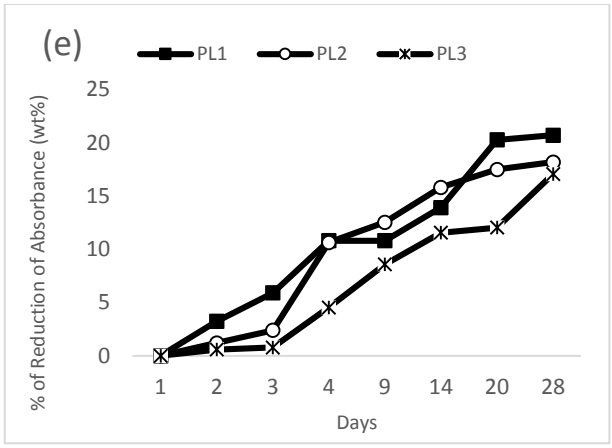


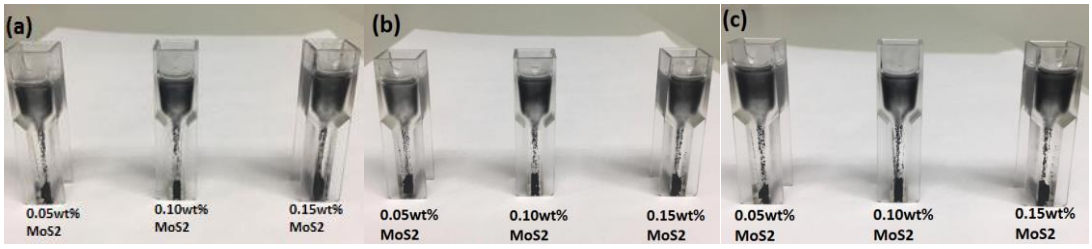
Figure 2. Percentage of absorbance reduction for various concentration of MoS_2 with respect to time. (a) NL1-3, (b) NPL1-3, (c) NPL4-6, (d) NPL7-9, (e)PL1-3.

As time goes by, the absorbance value of the nanofluids reduces due to the sedimentation process that takes place. The percentage of the absorbance reduction was being illustrated as shown in Figure 2. It was shown that 0.1wt% of MoS_2 in 100wt% of naphthalene oil (NL1-3) has the most significant results in reducing the absorbance value, which hits up to 90% of reduction rate. In other words, the occurrence of this phenomenon means that MoS_2 nanoparticles which were blended with 100wt% of naphthalene oil is the least stable combination among all.

3.1.2 Effect of graphene and MoS_2

Since graphene is known for its high stability property, it is expected that the addition of graphene to MoS_2 nanoparticles would form a better dispersion phenomenon in the base fluids [13]. Based on Figure 3, it is shown that the samples from images (d) and (j) have slightly outperformed the others in terms of dispersion rate. The samples from Figure 3(d) formed complete dark solutions as compared to others, where little to no sediments were found. The samples from Figure 3(j) came in a lighter tone of color with no sediments found as well. Hence, it can be said that the combination of MoS_2 nanoparticles with 75wt% of naphthalene oil, 0.075wt% graphene and 25wt% of naphthalene oil, 0.075wt% graphene exhibits the best stability property.

In contrast, sedimentations were found in most of the test samples in Figure 3, where in some cases formation of clusters could be seen. This means that the nanoparticles did not completely adhere to the base fluids during the mixing process, therefore, forming solutions which are relatively unstable.



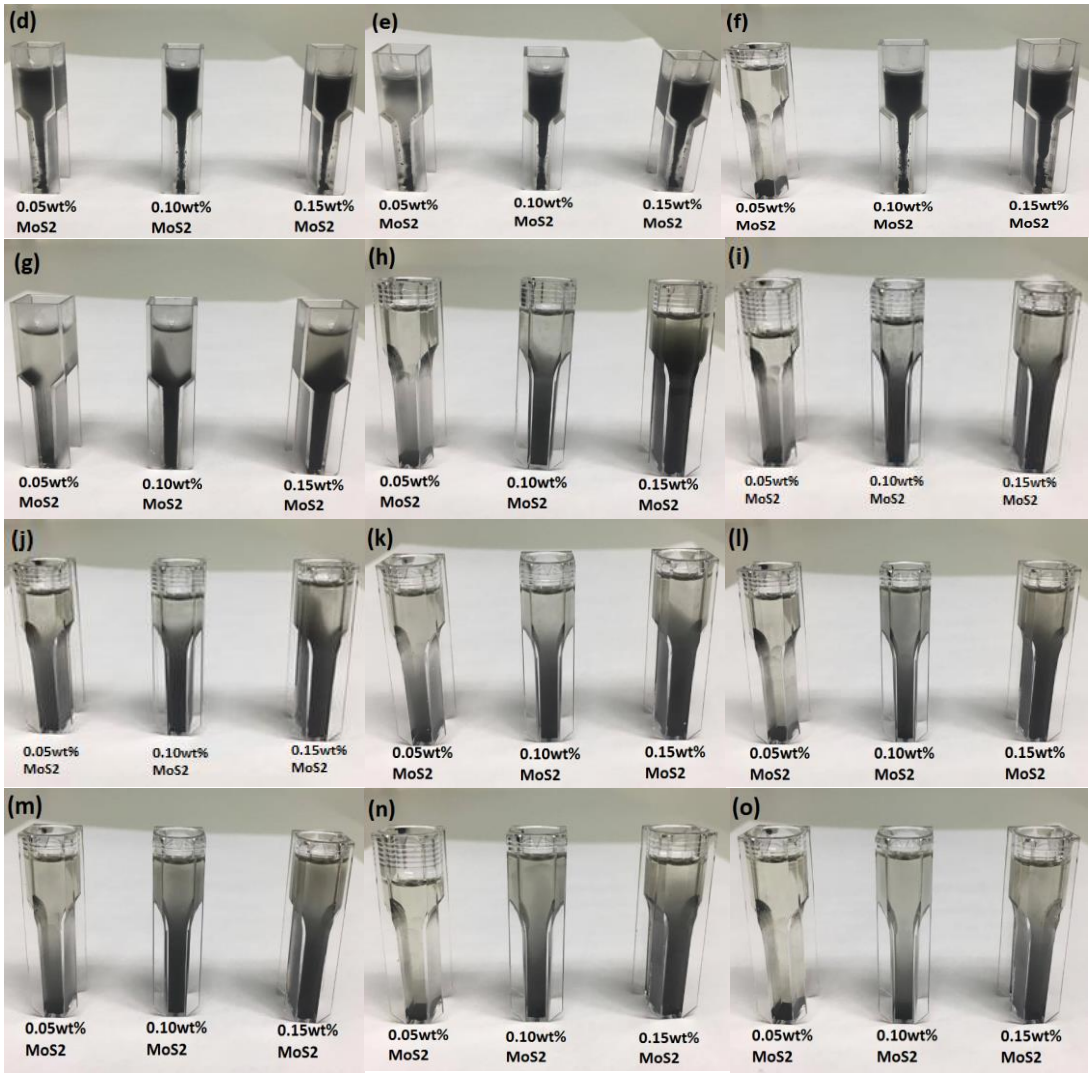


Figure 3. Images of nanofluids of various concentration 28 days after sonication process. (a) NGL1-3, (b)NGL4-6, (c) NGL7-9, (d) NPGL1-3, (e) NPGL4-6, (f) NPGL7-9, (g) NPGL10-12, (h) NPGL13-15, (i) NPGL16-18, (j) NPGL19-21, (k) NPGL22-24, (l) NPGL25-27, (m) PGL1-3, (n) PGL4-6, (o) PGL7-9.

3.2 Thermophysical properties analysis of nanofluids

3.2.1 Effect of temperature

Based on the observation from Figure 4, it could be seen that higher temperature was more conducive in enhancing the thermal conductivity of the nanolubricant. This trend could be well explained by the Brownian motion [14], where the nanoparticles tend to collide with each other more aggressively at higher temperature due to the kinetic energy possessed. However, the results portrayed from Figure 4(e) did not follow the trend which was mentioned earlier. This was due the nature behavior of the peanut oil, where the nanoparticles could not be completely well mixed in the peanut oil as compared to naphthalene oil. It was also noticed that the higher concentration of MoS_2 contributed to a better thermal conductivity enhancement.

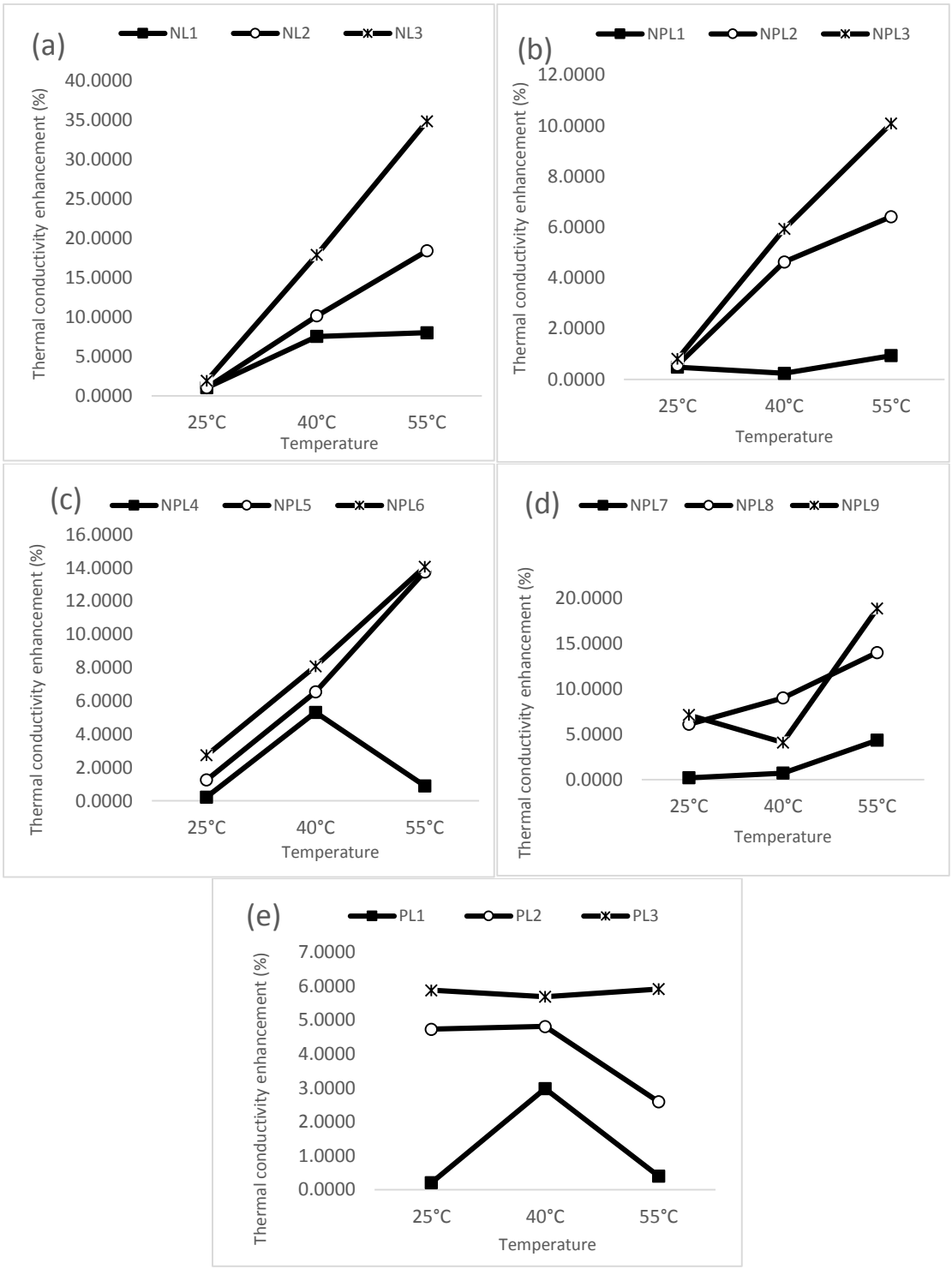


Figure 4.0 Thermal conductivity enhancement of various samples. (a) NL1-3, (b) NPL1-3, (c) NPL4-6, (d) NPL7-9, (e)PL1-3.

4. Conclusions

In this study, the hybrid graphene-MoS_2 was synthesized to enhance the stability and thermal conductivity of the nanolubricant. The thermal conductivity of the nanofluids were successfully being enhanced up to a maximum of 35%. Stability analysis of this research study has also proven that 75wt% of naphthalene oil works best with the graphene and MoS_2 nanoparticles. Further studies are required to test the tribological properties of the lubricants to understand the role of individual component. With these enhanced lubricating properties of the nanofluids, the metal work machines could be well maintained by reducing the occurrence of wearing and tearing component parts at a significant rate. Hence, this research is economically viable to the industry.

References

[1] H. G. Franck, J. W. Stadelhofer, *Naphthalene – production and uses*. Frankfurt: Springer Berlin Heidelberg, 1988. [E-book] Available: springer

[2] A. Jackson, "Synthetic versus Mineral Fluids in Lubrication," *International Tribology Conference*. P. 10, 1987.

[3] I.Gawrilow, "Vegetable oil usage in lubricants," *Inf. – Int. News Fats, Oils Relat. Mater*., vol.15, no. 11, pp. 702-705

[4] Maruyama S. et al. (2013). Thermal conductivity enhancement of liquid and solid with single-walled carbon nanotubes. Ph.D. thesis, Dept. Mechanical Eng., Tokyo Univ., Tokyo, Japan.

[5] Z.J. Zhang, D. Simionesie and C. Schaschke. "Graphite and Hybrid Nanomaterials as Lubricant Additives" *Lubricants,* vol. 2, pp. 44-65, 2014.

[6] Z. He and W. Que*, "Molybdenum disulfide nanomaterials: Structures*, properties, synthesis and recent progress on hydrogen evolution reaction," *Appl. Mater. Today*, vol.3, pp. 23-56, 2016

[7] R. A. Alrawi, N. Norulaini, N. Ab, A. Ahmad, N. Ismail, amd A. K. M. Omar, "Characterization of Oily and Non-Oily Natural Sediments in Palm Oil Mill Effluent," vol. 2013, 2013.

[8] W. Yu and H. Xie. "A Review on Nanofluids: Preparation, Stability Mechanisms, and Applications" *Journal of Nanomaterials,* vol. 2012, p. 17, 2012.

[9] M. A. Maleque, H. H. Masjuki, and A. S. M. A. Haseeb, "Effect of mechanical factors on tribological properties of palm oil methyl ester blended lubricant," pp. 117-125, 2000.

[10] K.S. Hong, T.K. Hong and H.S. Yang. "Thermal conductivity of Fe nanofluids depending on the cluster size of nanoparticles" *Applied Physics Letters,* vol. 88, p. 031901, 2006.

[11] J. Zhao, Y. He, Y. Wang, W. Wang, L. Yan, and J. Luo, "An Investigation on the Tribological Properties of Multilayer Graphene and MoS2 Nanosheets as Additives Used in Hydraulic Applications," *Tribol. Int.*, 2016.

[12] E. Basavaraj, B. Ramaraj, J. H. Lee, and Siddaramaiah, "Polyamide 6/carbon black/molybdenum disulphide composites: Friction, wear and morphological characteristics," *Mater. Chem. Phys.*, vol. 138, no. 2–3, pp. 658–665, 2013.

[13] T. Morimoto, "Effect of molybdenum disulphide upon the friction and wear in ceramic – steel pair," *Tribol. Int.*, vol. 30, no. 12, pp. 871–879, 1998.

[14] Johnson D. W. et al. (2015). A manufacturing perspective on graphene dispersions. Curr. Opin. Colloid Interface Sci., 20(5), 367–382.

Preparation and Characterization of Talc-filled Polylactic Acid Composites

Lee Carmen[1*], Pang Ming Meng[1], Albert Tshai Kim Yeow[2]

[1]*School of Engineering, Taylor's University, Malaysia*

[2]*University of Nottingham Malaysia Campus, Department of Mechanical, Materials & Manufacturing Engineering, Jalan Broga, 43500 Semenyih, Selangor Darul Ehsan, Malaysia*

[*]carmen.lee@sd.taylors.edu.my

Abstract

Over the past few years, high attention has been given to Polylactic acid (PLA) as the potential replacement of polymers with petroleum based. Polylactic acid (PLA)-based composite filled with Talc, a hydrous magnesium silicate mineral with five compositions of 5%, 10%, 20%, 30% and 40% is prepared via melt blending method. Talc is being used as reinforcing agent due to its low cost and high crystallizing efficiency. The objective of this research is to identify the best loading of talc filler targeting for packaging material (i.e. food packing tray) by characterising the properties in thermal, mechanical and morphological of the talc-filled PLA composites. Characterisation studies such as Tensile, Thermo-Gavimetric analysis (TGA), water absorption and Differential Scanning Calorimetry (DSC) and Scanning Electron Microscopy (SEM) were carried out for PLA composites. The polymer sheets were being immersed in distilled water at room temperature to test the water absorption for 168 hours. In order to characterise the thermal and morphological behaviour of PLA composites, DSC was performed with double cycle heating processes as well as TGA thermal test under nitrogen flow. Good dispersion and uniform dispersion of talc lamellae is observed under SEM. However, there is sign of agglomeration when more talc is added. The density of the composites increase with talc loadings. From the water weight loss data, results show that there is no water absorption took place indicating that the composites are hydrophobic material. TGA analysis shows most significant increase in thermal stability for 5 wt% in PLA/talc composite. Degree of crystallinity showed improvement from 23% to 27% after adding talc filler into the composites during heating and cooling respectively resulting in higher nucleation density. Talc has significantly increased the tensile modulus at 40 wt% due to the reinforcing ability of talc. 30 wt% talc filler shows overall improvement in thermal and mechanical properties acting as a reinforcing filler in polymer composites.

Keywords: Poly (lactic acid), talc, PLA composite, mechanical properties

1. Introduction

Wide varieties of petroleum-based synthetic polymers are being produced annually worldwide which exceeds 300 million tons by 2015 [1]. Polymeric materials are commonly applied in many industries like packaging, medical, food, plasticulture and textile [2]. One of the important issues with non-biodegradable plastics is the environmental aspect where soil pollution and blockage of drainage system because of improper disposal. Synthetic polymers are mainly derived from non-renewable fossil fuel resources which contribute significant carbon footprint to the environment [3]. Hence, renewable resources are important for fossil fuels replacement [4]. According to ASTM D6400-12 established by the international organization, the biodegradability of polymeric materials is assured [5]. Some examples of biodegradable polymer that has been introduced to the market to conserve the environment includes polylactic acid (PLA), polyglycolic acid (PGA) and polycaprolactone (PCL) [6].

High attention has been given to PLA as replacement of petroleum based polymers over the past few years. PLA is a bio-based resin that is ultimately made of renewable sources like potato, corn and sugar cane having hydrophobic behavior [2]. Dextrose is being processed and fermented from corn starch to produce lactide acid where further polymerization takes place to produce polylactide. Ring-opening polymerization (ROP) is a typical method used to produce PLA. PLA is commonly applied in packaging industry due to its dominant properties of biodegradability, good processability and biocompatibility [5].

However, due to the inherent weaknesses of PLA, they limit the applications of PLA such as low glass transition temperature (T_g), high brittleness with less than 10% elongation at break, high cost and low crystallization rate [7]. Research efforts have been focusing on blending biodegradable resins or compounding fillers (micro/nano-sized) with PLA in order to improve the desired PLA properties [7,8]. The main purpose of nucleating agent is to enhance the rate of crystallization of semi-crystalline polymers. The crystallization rate can be initiated at high temperature upon cooling by cause of lowering the surface energy barrier on nucleation [9].

Talc having chemical formula of $Mg_3Si_4O_{10}(OH)_2$, is a hydrous magnesium silicate mineral which is normally available in white, gray or colorless. Talc can be found in metamorphic rocks of convergent plate boundaries. The structure is held by weak Van der Waals forces that allows to slip past to one another easily creating higher dispersion. Talc is commonly act as nucleating agent which offers particular advantages of having high performance, eco-friendly and low cost [7]. It increases the stiffness and tensile modulus at loadings of 10-40 wt% [4]. The variables of Talc's end-uses depend on the mineralogical and chemical composition, particle size, hardness and specific gravity [10]. Talc is chemically hydrophobic material which can be dispersed and blended easily with polymers since PLA is also hydrophobic showing the compatibility of talc and PLA. It is being used in many industrial products such as rubbers, ceramics, papers, polymers, paints etc. [11]. Luciana A. Castillo reported that macrocyrstalline talc has higher improvement on mechanical properties when compared to microcrystalline on polypropylene based composites [12]. Talc and Calcium carbonate ($CaCO_3$) are frequently integrated in thermoplastics

to mainly reduce the end product cost. These two fillers enhance properties like hardness, strength and durability. According to Seena Joseph, Talc is found to be having higher crystallizing efficiency being used as filler in PLA composites as compared to calcium carbonate and microcrystalline cellulose (MCC) [13].

Melt compounding method is carried out without presence of organic solvents thus it is highly preferred in context of sustainability and eco-friendly as compared to solvent-based method (solvent casting) [14]. Five different compositions of talc are involved to be compared with pure PLA composite in physical, thermal, mechanical and morphological properties. The polymer sheets undergo various tests such as Thermo-Gavimetric analysis (TGA) & Differential Scanning Calorimetry (DSC), Tensile density, water absorption test, Scanning Electron Microscope (SEM) characterization study. The optimum conditions for each testing are identified from various research to achieve highest performance of PLA/talc composites benchmarking neat PLA for packaging applications which requires moderate mechanical and thermal properties.

A. Shakoor and N.L Thomas has added Talc up to 30 wt% and observed that there is only a slight reinforcing effect on Young's modulus with 5 wt% of mineral contents, where sharp increase is resulted at 30 wt% of talc addition [15]. This paper is further researched on the high loading of talc filler in PLA composites since the highest loading used in previous research is 30 wt%. There are also limited results reported for water absorption test, thus, it is an opportunity to study the water uptake characteristic for this talc-filled PLA composites. Higher rate of water absorption can be obtained for higher loadings of natural fiber but mineral fiber may exhibit opposite water absorption effect [16]. In terms of mechanical properties, with 10 wt% talc added, results showed significant improvement in the composite's Young modulus and increased crystallinity. From differential scanning calorimetry (DSC) thermal testing, the cold crystallization temperature (T_{cc}) has reduced from 127°C to 96°C for PLA/talc composites proving the nucleating effect of Talc [17]. In addition, talc particles are reported to be well dispersed in the matrix based on morphology of talc [4].

In light of above mentioned drawbacks, main objective for this research paper is to identify the best loading focusing on packaging material industry by improving the desired properties (higher crystallinity, thermal stability, glass transition temperature) for packaging material benchmarking the pure PLA. It is important to be biodegradable as the packaging material will be discarded into the environment by the end-users once unpacking the product to be naturally degraded or collected for composting by relevant organization. Therefore, the material has to be recyclable, reusable and biodegradable.

2. Experimental

2.1. Materials

The Polylactide acid 3051D is manufactured by NatureWorks LLC having ratio of 96% L-Lactide to 4% D-Lactide units with the glass transition temperature of 55-65°C and melting temperature of 150-165°C. Talc powder (KM10TC) in micro size is obtained from Kaolin (M) SDN BHD, the manufacturer of refined kaolin.

2.2. Material processing

2.2.1. Sample preparations

Five different compositions of PLA/talc polymer sheets with one pure PLA sheet were prepared. The formulation is tabulated as shown in Table 1:

Table 1. Sample preparations.

No.	Composition	Weight of PLA (g)	Weight of Talc (g)	Total weight (g)
1	100 wt% pure PLA	80	-	80
2	5 wt% Talc + 95 wt% PLA	76	4	80
3	10 wt% Talc + 90 wt% PLA	72	8	80
4	20 wt% Talc + 80 wt% PLA	64	16	80
5	30 wt% Talc + 70 wt% PLA	56	24	80
6	40 wt% Talc + 60 wt% PLA	48	32	80

These formulations were selected based on the limited literature review done on high dosage of talc addition. Low dosage of talc shows improvement in mechanical properties hence, better improvement is expected for higher dosage of talc in comparison with the properties of pure PLA.

2.2.2. Melt Blending

PLA 3051D and micro particle of Talc (KM10TC) were dried at 80°C for at least 4 hours in vacuum oven prior to melt blending process in SIRIM to remove moisture content [7]. Different dose of micro particle Talc (KM10TC) was blended with PLA as well as pure PLA (benchmark) in a twin-screw extruder or internal mixer (Model: Haake Polylab System E93) which is known as melt blending process. The mixing temperature, time and speed will be set at 180°C, 18 minutes and 100 rpm respectively [18]. Preheat at 180°C of twin screw extruder is required before processing the materials [19]. After well mixing of the mixture, it was then taken to compression molding machine to be molded into a sheet form.

2.2.3. Compression Molding

Rectangular polymer sheets were produced from this compression molding process with the size of 12 cm × 15 cm and thickness of 1 mm as this is the thinnest mold available for the ease of cutting. The compound was filled in a mold to shape the sheet before being compressed by a hot press machine (Model: Moore E53) at 185°C in SIRIM. The hot press machine was preheated for 3 minutes before compressing process took place at pressure of 150 bar for 5 minutes [7]. The composite sheets produced were cooled to the temperature of 60°C for the polymer to be harden and shaped [20]. The readily polymer sheet was taken out after undergoing the whole process. The pure PLA sheet was also prepared under the same operating conditions as other composites.

2.2.4. Cutting

The compression sheets were cut into different sizes for various characterization tests. For water absorption, the size is 2 cm × 2 cm, whereas for tensile the specimens need to cut into dumb bell shape (Type IV) as per ASTM D638 requirement.

2.3 Characterizations

2.3.1. Thermo-Gavimetric Analysis (TGA)

TGA thermal test of PLA/Talc composite and pure PLA were carried out with a TA Instruments (Model: Perkin Elmer TGA 8000). The purpose of TGA test is to study the weight loss of compound subjected to heating under inert environment. 10 mg of samples were measured for this test. TGA was carried out with operating conditions: 25-650°C, at heating rate of 10°C/min [21]. The measurement is generally done under nitrogen atmosphere [7].

2.3.2. Differential Scanning Calorimetry (DSC)

DSC thermal test is to characterize the thermal behavior of PLA composites subjected to heating and cooling temperatures which includes crystallization temperature (T_c), glass transition temperature (T_g), melting temperature (T_m), cold crystallization temperature (T_{cc}), crystallization enthalpy (ΔH_c), melting enthalpy (ΔH_m) and cold crystallization enthalpy (ΔH_{cc}). The analysis of DSC was performed using DSC (Model: Perkin Elmer DSC 8500) under nitrogen flow of 20 ml/min. Samples of 5-10 mg were prepared and sealed in a platinum pan. An empty pan was also prepared as reference sample. The heat-cool-heat processes were carried out from 25-220°C at 10°C/min and 220-25°C for cooling cycle at rate of 10°C/min. After the first heating stage, the sample was kept at the highest temperature reached for approximately 2 minutes in order to eliminate previous thermal histories. Each sample test took 1.20 hours to complete. The degree of crystallinity, X_c was be calculated as Eq. (1) below [17,7,22,9]:

$$X_c = \frac{\Delta H}{\Delta H_m^0 (1 - \frac{W_f}{100})} \times 100\% \quad (1)$$

Where ΔH (J/g) includes two stages of cooling at heating as $\Delta H = \Delta H_c$ and $\Delta H = \Delta H_m - \Delta H_{cc}$ and ΔH_m^0 is melting enthalpy for 100% crystalline polymer matrix = 93.1 J/g [23,24] and W_f is the wt% of filler (Talc) added.

2.3.3. Water absorption

Three 2cm × 2cm composite specimens with the same composition were labeled and immersed in a container filled with 50 ml distilled water were tested at room temperature for water absorption test (ASTM D570). The specimens are dried using filter paper and weighed on digital scale to record the initial weight of the samples. It will be re-immersed in the water bath at room temperature. The samples were taken out periodically to weigh at interval of 24 hours for 7 days until it reaches a saturation point. Three samples were measured at each composition so that the

average value can be evaluated. The water content, M_t will be calculated using formula in Eq (2) below:

$$M_t(\%) = \left(\frac{W_t - W_0}{W_0}\right) \times 100 \quad (2)$$

Where W_0 is the initial sample weight and W_t is weight of sample at time t [16,25,26,27].

2.3.4. Tensile

Tensile testing (ASTM D638-10) was carried out to identify the amount of stress prior to failure. Tensile properties of tensile strength at break, tensile modulus and elongation at break can be determined using Instron Tensile Test Machine (Model: Instron 3366). Three samples testing were cut into dumb bell shape (Type IV) for each formulation to obtain the maximum, minimum and mean tensile analysis results. The gauge testing length, gauge width, crosshead speed and load cell of 5 kN at 60-100 mm, 10-15 mm, 5 mm/min respectively [15,21,4].

3. Results and Discussions

3.1. Thermal analysis

3.1.1. Thermo-Gavimetric Analysis (TGA)

The thermal degradation of pure PLA, pure Talc and PLA/talc composites were studied by TGA where Fig. 1 and 2 show the results for typical weight loss curves (TGA) and derivative weight loss curves (DTGA) respectively. From Table 2, it can be seen that 5% Talc exhibited highest onset temperature of thermal degradation as compared to other talc loadings composites. The onset decomposition temperature was seen to be improved by around 5°C in comparison to neat PLA as shown in Fig. 1 showing the improvement in thermal stability as reported in previous research [7,15,21]. In contrast, with addition of talc, the composite degraded inferior to the degradation. All the TGA traces showed weight loss shifts towards higher temperature. Incorporation of filler into polymer matrix results in volatile degradation causing the thermal stability to increase. The residual weight verifies the actual content of the filler [7]. Hence, showing increasing trend of the residual weight.

The maximum temperature of weight loss can be obtained from the DTGA curves in Fig. 2. It can be seen that there is peak shift from 373.94°C to 366.25°C for different talc content indicating the thermal stability change of PLA/talc composites as compared to pure PLA. Thermal stability is one of the key criteria to process PLA in order to eliminate any thermal degradation of the composites as reported by Donald Garlotta [32]. Moderate thermal stability is required for this project targeting packaging industry as it does not require very high thermal degradation temperature as long as it can be thermoformed into various sizes and shapes according to consumer's requirement.

Table 2. Thermal properties of pure PLA and PLA/Talc composites.

Samples	Degradation temperature (°C)			Residual weight % at 648°C	DTG (°C)
	T_{on}	T_{40}	T_{80}		
Pure PLA	293.93	368.24	344.33	0.45	373.94
PLA/Talc 5%	309.21	383.42	363.97	3.07	387.50
PLA/Talc 10%	296.08	374.27	351.45	16.52	376.41
PLA/Talc 20%	303.38	377.25	356.54	15.05	378.63
PLA/Talc 30%	301.49	376.42	354.86	26.37	373.56
PLA/Talc 40%	279.93	368.30	344.94	28.52	366.25

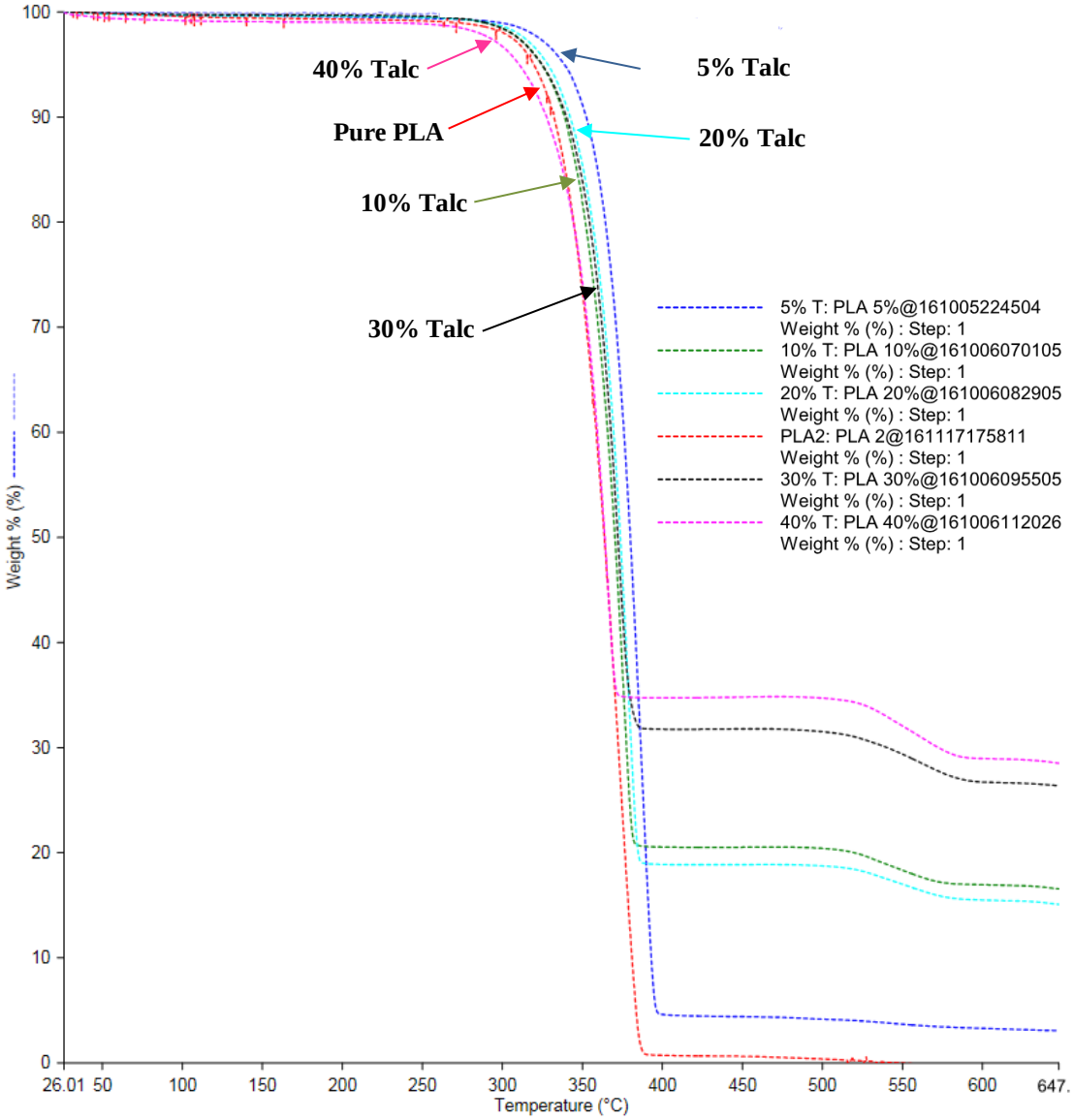


Figure 1.
Weight loss curves of pure PLA, pure Talc and PLA/talc composites from TGA.

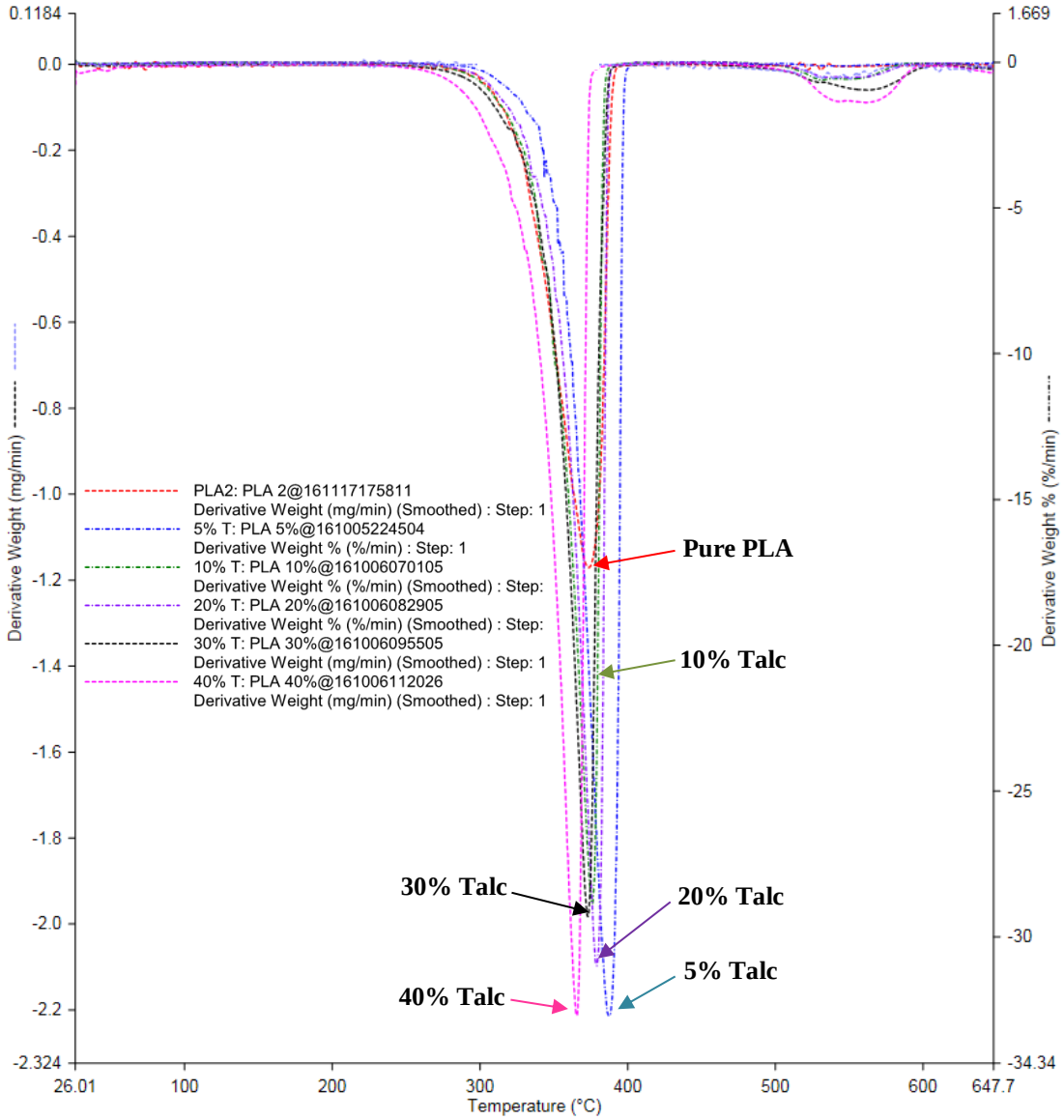


Figure 2. Derivative weight loss curves (DTGA) of pure PLA, pure Talc and PLA/talc composites.

3.1.2. Differential Scanning Calorimetry (DSC)

Second run of heating curves was considered for analysis of thermal behavior during the heat-cool-heat process of DSC test [23]. The results were tabulated in Table 3 and presented in Fig. 3 and Fig. 4. Fig. 3 represents the melting endotherm of the samples from second heating cycle. It is observed that the melting behavior was affected with the addition of talc. The melting peak (T_m) of PLA shifted slightly. The Pure PLA crystallized at 108.36°C which is known as cold crystallization (T_{cc}) behavior showing the amorphous nature of PLA. Mobile chains of PLA become mobile and structuring in regular chain array to form cold crystallization behavior above glass transition temperature (T_g) [15]. From Fig. 3, it can be seen that the PLA/talc composites did not exhibit cold crystallization except for neat PLA showing the amorphous nature of polymer as reported by previous research [15,7,21]. 5% and 40% talc addition show highest glass transition temperature among the PLA/talc matrix due to the chain mobility [33,15,17,7]. With high glass transition temperature,

the mechanical properties can only be desirably justified as mentioned by D. Battegazzore [17].

PLA did not crystallize during cooling exotherm but crystallization occurred after talc addition. Sharp crystallization peak (T_c) appeared at 99.46, 101.48, 102.36 and 102.54°C for 5, 20, 30 and 40 wt% respectively. The crystallization peaks shifted higher with talc content indicating faster crystallization rate for PLA/talc composites enhancing the crystallization kinetics. The results are supported by previous research done by Shikha Jain on lower talc loadings of 1-5% [15,17].

Degree of crystallinity (x_c) was calculated using Eq. (1) and results showed in Table 3. Second cycle of heating in DSC thermogram was taken for analysis in order to eliminate previous thermal histories. The degree of crystallinity increased from 23% to 27% after adding talc filler into the composites during heating. Same pattern showed in cooling cycle. This shows that talc is an efficient nucleating agent that can increase polymer matrix degree of crystallinity resulting in higher nucleation density [28,15].

Table 3. DSC analysis of pure PLA and PLA/talc composites.

Sample	Second Heating				Cooling
	T_g (°C)	T_{cc} (°C)	T_m (°C)	x_c (%)	T_c (°C)
Pure PLA	56.08	108.36	156.42	23.00	-
5% Talc	54.99	-	155.75	25.29	99.46
20% Talc	51.20	-	156.21	27.24	101.48
30% Talc	51.59	-	156.43	26.41	102.36
40% Talc	54.77	-	156.39	14.11	102.54

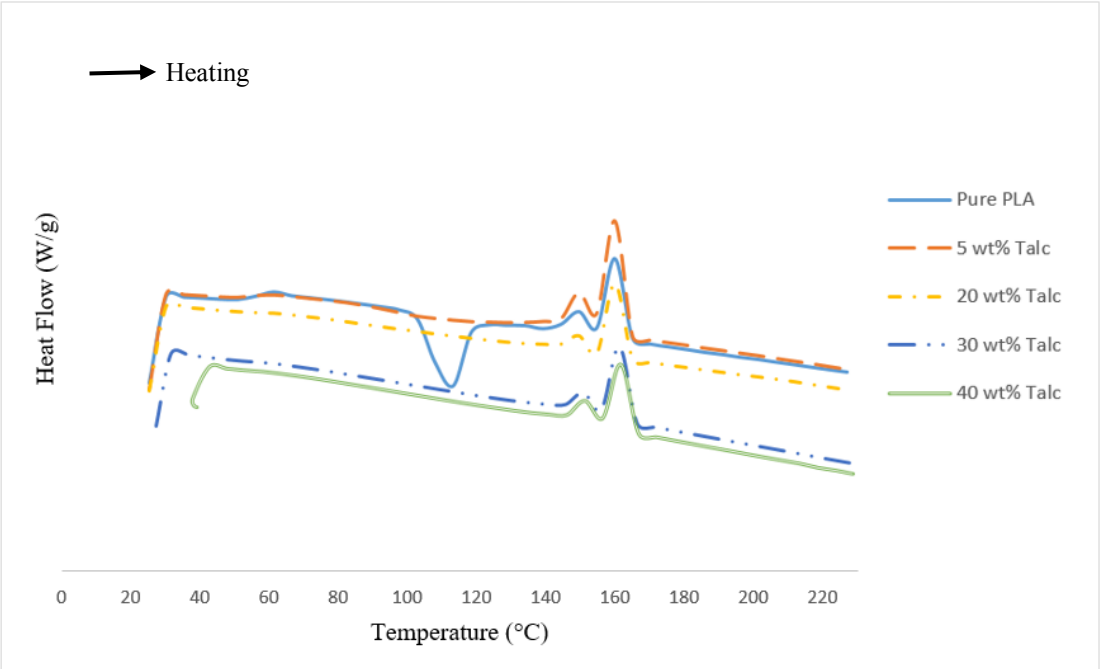


Figure 3. DSC analysis for second heating (10°C/min at 25°C-220°C)

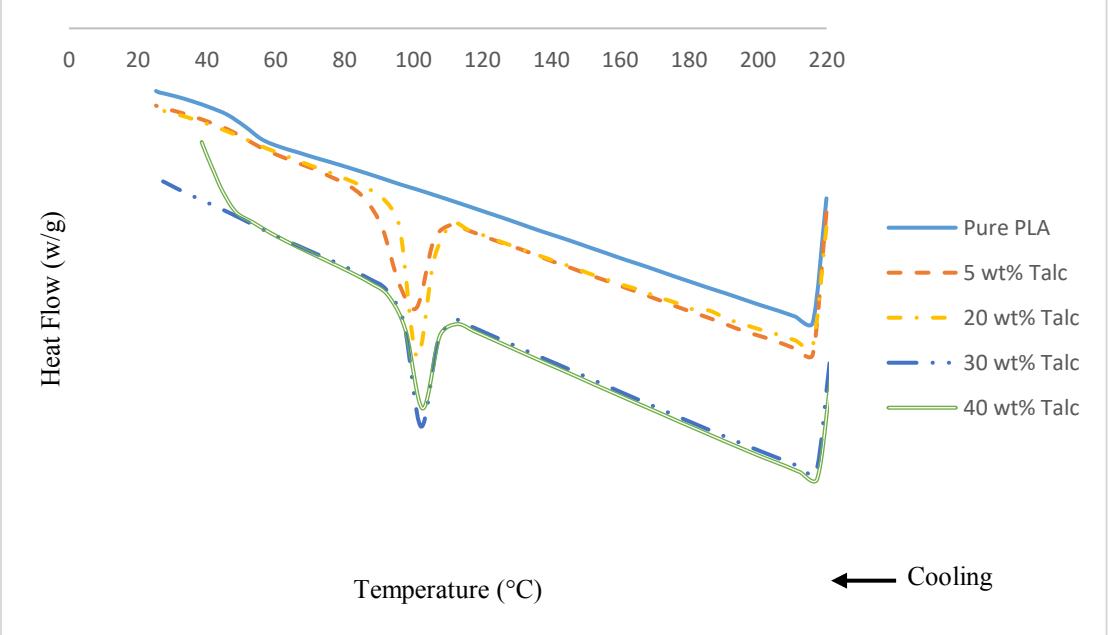


Figure 4. DSC analysis for cooling (10°C/min at 220°C-25°C)

3.2. Water Absorption

The water uptake of the composites was calculated using Eq. 2. The effect of talc loading on the water absorption in PLA composites with increased in immersion time is shown in Fig. 5. It is observed that the percentage weight loss is insignificant and negligible for talc filled PLA. Sample with 20% Talc has the highest weight loss difference as compared to other loadings. The percentage weight loss for 5% and 10% talc addition started to show a slight increasing trend after the samples being immersed in water for 168 hours whereas other PLA composites continue showing consistent trend in percentage weight loss. The hydrophobic behavior of talc and PLA is seen to have superior water absorption resistance as all the composites have very small weight loss percentage. Polymer that absorbs water has the tendency to change its dimension [29]. Mechanical properties of the polymer may be affected negatively with water absorption. Thus, with this results, it is proved that talc is showing high performance acting as a reinforcing filler in polymer composites.

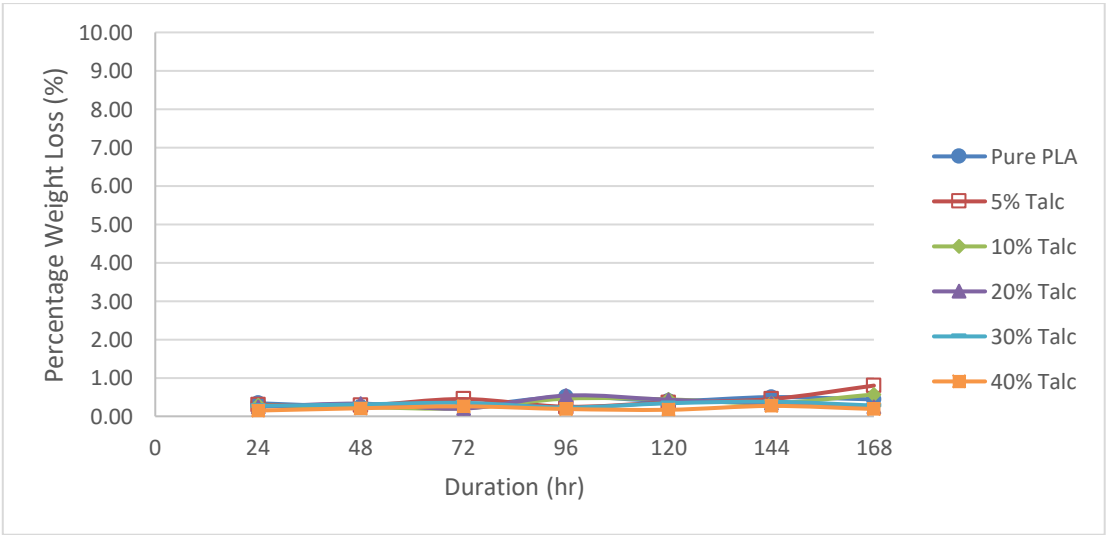


Figure 5. The percentage weight loss of pure PLA and PLA/Talc composites.

3.3. Mechanical Properties

The mechanical properties of PLA composites include tensile strength, elongation at break and tensile modulus are one of the important factors in polymeric film studies [21]. The effect of talc filler in PLA composites was studied and the results are tabulated in Table 4.

Maximum stress a material could withstand before it breaks under tension is known as tensile strength. The tensile strength of PLA composites was observed to increase with talc content as shown in Figure 4.6. However, the pure PLA still has the highest tensile modulus of 39.4 MPa as compared to the 40% talc content with tensile modulus of 35 MPa indicating that higher loadings of talc can be further tested to study the talc filler effect on tensile strength. Material toughness is ultimately determined from the combination of tensile strength and elongation. Similar results had reported by Shikha Jain showing similar trend on tensile strength [15].

The elongation at break is found to be highest at 5% talc filler as compared to the higher talc loadings sample. Further increment in talc content does not improve its elongation most likely due to the addition of talc to a brittle polymer causing stress concentration and crack initiation and thus resulting in toughness reduction [15] as well as research reported by Shakoor [34]. Agglomeration of the filler and PLA may happen where the particles are held by strong bonds which resulted increasing its elongation and at the same time reducing the tensile strength [29]. Fengmei Yu has reported that the tensile strength improved insignificantly and elongation at break decreased when talc loading increases [35]. 5% talc or 40% talc can be said to be more preferable [29,30].

Overall, the tensile result shows deterioration on both tensile strength and elongation at break after the addition of talc. However, the tensile modulus improved with talc percentage as shown in Figure 4.8. This is due to the ability of stress transfer from the matrix to the filler reported by Whaling et al. [31]. 30% talc exhibit the highest tensile modulus in comparison to other talc loadings. Lack of interfacial adhesion between talc and PLA limited the tensile strength and elongation properties of PLA/talc composites.

Table 4. Tensile properties of PLA and PLA/talc composites.

Sample	Tensile Strength, MPa	Elongation at break, %	Tensile Modulus, MPa
Pure PLA	39.40±0.76	3.45±0.3350	1239±76.0
5% Talc	31.90±2.00	2.46±0.1100	1358±52.0
10% Talc	33.00±2.08	1.99±0.1610	1764±34.1
30% Talc	29.10±1.35	1.49±0.1230	2065±70.7
40% Talc	35.00±0.50	2.22±0.0513	1774±33.0

4. Conclusions

PLA/talc composites with different talc content for packaging material was prepared by compression moulding to improve its properties by studying the effect on talc in thermal and mechanical behaviour. In comparison to neat PLA, the addition of talc shows considerable improvements in thermal and mechanical properties. TGA

analysis shows the increase in thermal stability for 5 wt% in PLA/talc composite. Degree of crystallinity showed improvement from 23% to 27% after adding talc filler into the composites during heating and cooling respectively. This proves that talc is an efficient nucleating agent which can increase polymer matrix degree of crystallinity resulting in higher nucleation density. Talc has significantly increase the tensile modulus at 40 wt% due to the reinforcing ability of talc platelets. Tensile strength for 40 wt% show the highest improvement as compared to other talc concentrations. The hydrophobic behavior of talc and PLA is seen to have superior water absorption resistance as all the composites have very small weight loss percentage. It is proved that talc is showing high performance acting as a reinforcing filler in polymer composites. The overall results show that there is a potential to use the talc-filled PLA as a packaging material as higher level of crystallinity contributes to higher density, thermal degradation temperature and chemical resistance. 30% talc addition can be said to be having the best overall results by looking at the compatibility with pure PLA.

References

[1] M. M. Reddy, S. Vivekanandhan, M. Misra, S. K. Bhatia, and A. K. Mohanty, "Progress in Polymer Science Biobased plastics and bionanocomposites : Current status and future opportunities," *Prog. Polym. Sci.*, vol. 38, no. 10–11, pp. 1653–1689, 2013.

[2] E. Castro-Aguirre, F. Iniguiez-Franco, H. Samsudin, X. Fang, and R. Auras, "Poly(lactide acid)-Mass Production, Processing, Industrial Applications and End of Life," *Adv. Drug Deliv. Rev.*, 2016.

[3] J. R. Dorgan, H. Lehermeier, and M. Mang, "Thermal and Rheological Properties of Commercial-Grade Poly (Lactic Acid) s," vol. 8, no. 1, pp. 1–9, 2000.

[4] I. Repository, "Talc as a nucleating agent and reinforcing filler in poly (lactic acid) composites," *Polym. Eng. Sci. 54*, pp. 64–70, 2014.

[5] R. Muthuraj, M. Misra, and A. K. Mohanty, *Studies on mechanical, thermal, and morphological characteristics of biocomposites from biodegradable polymer blends and natural fibers*, Fourteenth Edition. Elsevier Ltd., 2015.

[6] A. A. Shah, F. Hasan, A. Hameed, and S. Ahmed, "Biological degradation of plastics : A comprehensive review," *Dep. Microbiol. Quaid-i-Azam Univ. Islam. Pakistan*, vol. 26, pp. 246–265, 2008.

[7] P. Russo, D. Acierno, and G. Filippone, *Mechanical performance of polylactic based formulations*, Fourteenth Edition., no. 1932. Elsevier Ltd., 2015.

[8] I. Fillers, "Technology Focus Report : Polylactic Acid Containing Fillers and Fibers *," pp. 0–4, 2007.

[9] T. F. Cipriano, A. Lúcia, I. De Macromoléculas, P. Eloisa, M. Ima, A. Henrique, F. Thomé, A. Maria, F. De Sousa, and G. Monteiro, "Thermal, Rheological and Morphological Properties of Poly (Lactic Acid) (PLA) and Talc Composites Technical-Scientific Session," vol. 24, pp. 276–282, 2014.

[10] S. C. Code and M. The, "TALC AND PYROPHYLITE GROUP – 2 : 1 Phyllosilicate," vol. 10, pp. 1–21.

[11] P. Marzbani, H. Resalati, A. Ghasemian, and A. Shakeri, "Talc , a multi-purpose filler : A review of talc ' s features and improvement methods of its efficiency," *Ann. Biol. Res.*, vol. 4, no. 6, pp. 159–162, 2013.

[12] L. A. Castillo, S. E. Barbosa, and N. J. Capiati, "Influence of talc morphology

on the mechanical properties of talc filled polypropylene," 2013.
[13] S. Joseph and E. D. P. A. Mahanwar, "Studies on Melt Processable Biocomposites of Polylactic Acid," 2014.
[14] M. Murariu and P. Dubois, "PLA composites: From production to properties," *Adv. Drug Deliv. Rev.*, 2016.
[15] S. Jain, M. Misra, A. K. Mohanty, and A. K. Ghosh, "Thermal , Mechanical and Rheological Behavior of Poly (lactic acid)/ Talc Composites," *Springer Sci. Media, LLC*, vol. 20, pp. 1027–1037, 2012.
[16] E. Muñoz and J. A. Garcia-Manrique, "Water Absorption Behaviour and Its Effect on the Mechanical Properties of Flax Fibre Reinforced Bioepoxy Composites," *Int. J. Polym. Sci.*, vol. 2015, pp. 1–10, 2015.
[17] D. Battegazzore, S. Bocchini, and A. Frache, "Crystallization kinetics of poly (lactic acid) -talc composites," vol. 5, no. 10, pp. 849–858, 2011.
[18] S. Ouchiar, G. Stoclet, C. Cabaret, E. Georges, A. Smith, C. Martias, and V. Gloaguen, "Applied Clay Science Comparison of the in fluence of talc and kaolinite as inorganic fillers on morphology, structure and thermomechanical properties of polylactide based composites," *Appl. Clay Sci.*, 2015.
[19] K. Oksman, M. Skrifvars, and J. Selin, "Natural fibres as reinforcement in polylactic acid (PLA) composites," vol. 63, pp. 1317–1324, 2003.
[20] A. N. Frone, S. Berlioz, and D. M. Panaitescu, "Morphology and thermal properties of PLA – cellulose nanofibers composites," *Carbohydr. Polym.*, vol. 91, pp. 377–384, 2013.
[21] J. Yang, Y. Qin, M. Yuan, J. Xue, and J. Cao, "Preparation and characterization of poly (l -lactide) -co-poly (trimethylene carbonate)/ talc film," *Int. J. Biol. Macromol.*, vol. 62, pp. 411–417, 2013.
[22] R. Al-itry, K. Lamnawar, and A. Maazouz, "Improvement of thermal stability , rheological and mechanical properties of PLA , PBAT and their blends by reactive extrusion with functionalized epoxy," *Polym. Degrad. Stab.*, vol. 97, no. 10, pp. 1898–1914, 2012.
[23] A. Shakoor, "Development of novel bio-derived polymer composites reinforced with natural bres and mineral llers Doctoral thesis by," *Loughbrgh. Univ. Institutional Repos.*, pp. 1–222, 2013.
[24] L. Lim, R. Auras, and M. Rubino, "Processing technologies for poly (lactic acid)," *Prog. Polym. Sci.*, vol. 33, pp. 820–852, 2008.
[25] R. M. Taib, S. Ramarad, Z. A. M. Ishak, and M. Todo, "Water Absorption and Tensile Properties OF Kenaf Bast Fiber- Plasticized Poly(lactic acid) Biocomposites," pp. 2–5, 2008.
[26] T. Alomayri, H. Assaedi, F. U. A. Shaikh, and I. M. Low, "Effect of water absorption on the mechanical properties of cotton fabric-reinforced geopolymer composites," *Integr. Med. Res.*, vol. 2, no. 3, pp. 223–230, 2014.
[27] H. Deng, C. T. Reynolds, N. O. Cabrera, N. Barkoula, B. Alcock, and T. Peijs, "The water absorption behaviour of all-polypropylene composites and its effect on mechanical properties," *Compos. Part B*, vol. 41, no. 4, pp. 268–275, 2010.
[28] A. M. Harris and E. C. Lee, "Improving Mechanical Performance of Injection Molded PLA by Controlling Crystallinity," no. September, 2007.
[29] S. O. Adeosun, M. A. Usman, and W. A. Ayoola, "Physico-Mechanical Responses of Polypropylene-CaCO3 Composite," vol. 2013, no. July, pp. 145–152, 2013.
[30] P. Taylor, M. S. Rasidi, S. Husseinsyah, and T. P. Leng, "The Effect of Filler Content and UltraPlast TP01 of Nypa Fruticans Fiber-Filled Polylactic Acid /

Recycled Low Density Polyethylene Biocomposites on Tensile Properties and Morphology," no. January, pp. 37–41, 2015.

[31] A. Whaling, R. Bhardwaj, and A. K. Mohanty, "Novel Talc-Filled Biodegradable Bacterial Polyester Composites," pp. 7497–7503, 2006.

[32] D. Garlotta, "A Literature Review of Poly (Lactic Acid)," vol. 9, no. 2, 2002.

[33] M. F. De Sousa, G. Monteiro, and C. Rabello, "Rheological and Morphological Properties of Composites Based on Polylactide and Talc," vol. 3, no. 11, pp. 695–699, 2013.

[34] Shakoor A. and Thomas, N.L., "Talc as a nucleating agent and reinforcing filler in poly (lactic acid) composites", Polymer Engineering and Science, 54(1), pp. 64-70, 2014.

[35] F. Yu, T. Liu, X. Zhao, X. Yu, A. Lu, and J. Wang, "Effects of Talc on the Mechanical and Thermal Properties of Polylactide,", pp.1-11, 2011.

Drying Kinetic of "*Dioscorea Opposita*" *Chinese Yam*

Liong Seng Hao, Chua Bee Lin
School of Engineering, Taylor's University, Malaysia

Beelin.chua@taylors.edu.my

Abstract

Dioscorea Opposita better known as Chinese yam is one of the most common source of medicinal plant available in China. Certain rural region of China such as the Henan Region. *Dioscorea Opposita* is well known as one of the main traditional medicine used to cure diseases. The main objective of this research paper is to study the drying kinetic of *Dioscorea Opposita* and determine the antioxidant bioassay provided by *Dioscorea Opposita*. The *Dioscorea Opposita* undergo a blanching process where the raw material is wash with tap water and store under a temperature of 4□ for 12 hours. The *Dioscorea Opposita* is dried using a moisture analyser under a temperature of 40□ , 50□ and 60□. The initial moisture content and weight of the sample is recorded. The weight of the sample is recorded with an interval of one minute. The sample undergoes ultrasonic assisted extraction using methanol as solvent. The extracted product would be collected using a rotary evaporator. The data from the experiment are used to solve the unknown drying parameter for each thin layer model through the usage of Equation solver incorporated in Microsoft word Excel. The total antioxidant activities of the sample are determined through 2-Diphenyl-1-picrylhrazyl (DPPH) method. The result shows that the total antioxidant would reach its maximum at the lowest for soft drying mode(91%) while the antioxidant for the boost drying mode would reached maximum at the highest temperature (60°C). However in the standard drying mode, the maximum antioxidant activity available would be at 50°C with approximately 88 %. The correlation and coefficient, root mean square error analysis and reduced chi-square are the parameter used to determine the best suited thin layer model. The experimental data for accuracy for standard mode is Modified Henderson and Pabis >Henderson and Pabis >Newton model >Wang & Singh >Midilli et al> Approximation Diffusion> two term model> Logarithmic model> Lewis model. The experimental data for best accuracy for soft drying is two term model> Henderson & Pabis> Newton> Wang & Singh> Midilli et al model> Approximation Diffusion model > Logarithmic model >Modified Henderson & Pabis model>Lewis model.The experimental data for best accuracy for boost drying is Modified Henderson and Pabis >Logarithmic model>Midilli et al >Approximation Diffusion model >Lewis model> two term model> Wang & Singh model >Henderson & Pabis model> Newton model.

Keywords: *Dioscorea Opposita*, thin layer model, 2-Diphenyl-1-picrylhrazyl (DPPH) method, antioxidant activity bioassay

1. Introduction

Plant such as medicinal herbs has been used as a counter measure against diseases in various cultures throughout the world. Malaysia have a diverse variety of medical plant available such as sweet flag, aloe vera, Asiatic Penny, Ceylon cinnamon and many more. Malaysia is known to be a country which contributed a significant portion toward the agriculture sector as Malaysia has a diverse variety of medicinal plant. Based on an article written by Mohd Hafizudin bin Zakaria stated that Malaysia had been ranked as the 12th rank in Asia according to FFTC Agriculture Policy Platform. In the agriculture industry, it had been contributing a significant amount toward the economy of the country. Based on the market survey conducted by Mohd Hafizudin bin Zakaria, the market estimation for the agriculture industry had been predicted to reached approximately RM 32 billion in the year 2020 [1].

In this particular paper, the Chinese Yam will be used as the main specimen in order to study its drying kinetic. The scientific name of Chinese Yam is known to as *Dioscorea Opposita.* The origin of *Dioscorea Opposita* is first discover in China. *Dioscorea Opposita* had been migrated to different country in Asia such as Japan and Korea. The main usage to be found from *Dioscorea Opposita* is to be used as a tonifying spleen and kidney agent. *Dioscorea Opposita* also assist by providing certain degree of nourishment to certain organ of the human body such as the lung [2-4]. Medical researcher state that *Dioscorea Opposita* has other potential which could prove beneficial for human body such as reduce blood fat, regulate the body immune system and also had anti-aging properties [2].

Due to the availability of fresh *Dioscorea Opposita* throughout the year, several techniques had been used in order to preserve *Dioscorea Opposita.* Drying is one of the traditional methods of food preservation technique known to man. Drying process had been classified as one of the most crucial process required in the food industry as the quality of the food are dependent toward the method of preservation.

The main objective for drying process in the agriculture industry is to reduce the moisture content of herbal plant to a specific level which allowed the agriculture product such as herbal plant to be store for an extended amount of time for usage in the future [7]. Drying kinetic of any specimen is greatly affected by two major factors which are air temperature and material characteristic dimension. In this paper, other processes factors are neglected due to several constrain. In order to ensure the optimization of the drying process, two criteria must be strictly ensured which are the restricted consumption of necessary energy and to ensure the safeguard the biological properties of the dried products.

There were numerous information regarding the drying kinetic of selected plant such as lemon grass, sweert potato, Spear mint , olive leaves and many more . However, there was limited information which could be found on several research platforms regarding the specimen *Dioscorea Opposita.* Drying kinetic of herbal plant could be determined through a mathematical modelling .The mathematical modelling selected for this particular specimen is known as thin layer model. In order to describe the thin layer drying of any particular agricultural plant, there are two main groups of model which are frequently found in literature review of multiple journal paper. The first group corresponds toward the empirical models and the second group would correspond toward the diffusion model. The first group of empirical model are important not because it assists to describe the thin later water removed however it assisted to describe the heat of penetration during the removal of water moisture. The heat penetration is identified in the second group known as the diffusion model as it involves around

the drying rate in term of energy. There are numerous empirical mathematical models which correspond toward the thin layer model. The empirical mathematical models which are used in this research paper are shown in Figure 1.1 Empirical Mathematical Models for Thin Layer Model.

Table 1.1 Empirical Mathematical Models for Thin Layer Model

Model Name	Model	Specimen Plant	Unknown Drying Parameter
Lewis	$MR = exp(-kt)$	Grape seeds, Pumpkin	k
Logarithmic	$MR = a\ exp(-kt) + b$	Sweet Potato, Pistachio, Long green pepper, Rambutan	a,k,b
Wang and Singh	$MR = 1+at+bt^2$	Dioscorea Opposita, Sweet Sorghum	a,b
Midilli et al	$MR=a.exp(-kt^n)+bt$	Adathoda vasica, Cymbopogon citratus, SpearMint	a,k,n,b
Modified Page (I)	$MR = exp[-kt^n]$	Mint leaves Basil leaves	k,n
Two term model	$MR=a.exp(k_0t)+b.exp(-k_1t)$	Nuts Fermented sugar cane prickly pear fruit sultana grape	a, k_0,b, k_1
Modified Henderson–Pabis	MR=a.exp(-kt)+b.exp (-gt)+c.exp(ht)	Dika kernels olive leaves	a,k,b,g,c,h
Approximation Diffusion	MR= a.exp(-k_ot)+(1-a)exp(-k_{ob}t)	Banana Amelia , Brooks mangoes	a , k_o,
Newton	MR= exp (-kt)	Lemon grass	

In order to determine the drying kinetic for *Dioscorea Opposita* , the moisture content of the specimen are recorded throughout the experiment with an assumption such as constant relative humidity and drying temperature [8]. The specimens are dried based on the moisture analyser XM-60 Precisa. The normal heating program symbolise the standard oven heating process.

The main objective of this research paper was to describe the thin layer drying kinetic of *Dioscorea Opposita* using the empirical models. Several models were selected as shown in Figure 1.1 Empirical Mathematical Models for Thin Layer Models. The mathematical expression must be obtained through the calculation from the drying rate and the process time. The moisture content of the specimen are calculated based the formula shown in equation 1

$$Initial\ Moisture\ Content: \frac{Initial\ Weight\ of\ the\ specimen - Final\ Weight\ of\ the\ specimen}{Initial\ Weight\ of\ the\ specimen} \times 100 \quad (1)$$

In order to identify the most suitable thin layer models for *Dioscorea Opposita* , three criteria will be used to compare between them which are the reduced chi square ($\chi 2$), coefficient determination(R^2) and root mean square (RSME). These three main criteria is calculated based on equation 2, equation 3 and equation 4.

$$R^2 = 1 - \left[\frac{\sum_{i=1}^{N} \left(MR_{\exp,i} - MR_{pre,i} \right)^2}{\sum_{i=1}^{N} \left(MR_{\exp,i} - \overline{MR_{\exp}} \right)^2} \right] \quad (2)$$

$$RMSE = \left[\frac{1}{N} \sum_{i=1}^{N} \left(MR_{\exp,i} - MR_{pre,i} \right)^2 \right]^{1/2} \quad (3)$$

$$\chi 2 = 1 - \left[\frac{\sum_{i=1}^{N} \left(MR_{\exp,i} - MR_{pre,i} \right)^2}{N - n} \right] \quad (4)$$

There are a total of four parameters which include coefficient determination, root mean square error and reduced chi-square. These parameters were the key parameter in order to determine the goodness fit of the models for the experimental data. The most suitable models which best describe the drying kinetic model were chosen based on the highest coefficient determination and the least for both root mean square and reduced chi-square.

Coefficient determination (R^2) is a statistical measurement of similarity of the experimental data with the fitted regression line. The formula for the coefficient determination is written as shown

$$R^2 = 1 - \left[\frac{\sum_{i=1}^{N} \left(MR_{\exp,i} - MR_{pre,i} \right)^2}{\sum_{i=1}^{N} \left(MR_{\exp,i} - \overline{MR_{\exp}} \right)^2} \right] \quad (5)$$

The root mean square error is the measurement of the differences between the values predicted from the mode. The root mean square error could be calculated based on the equation shown.

$$RMSE = \left[\frac{1}{N} \sum_{i=1}^{N} \left(MR_{\exp,i} - MR_{pre,i} \right)^2 \right]^{1/2} \quad (6)$$

The reduced chi square is the statistical test which is commonly used to used as comparison between the observed data with the predicted value. The reduced chi –square could be determine through the formula below

$$\chi 2 = 1 - \left[\frac{\sum_{i=1}^{N} \left(MR_{\exp,i} - MR_{pre,i} \right)^2}{N - n} \right] \quad (7)$$

The second objective of this research paper was to identify the existing antioxidant activity bioassay which is present in *Dioscorea Opposita*. The amount of antioxidant activity could be identify through the 2,2-diphenyl-1-picrylhydrazyl scavenging method (DPPH). The antioxidant activity are conducted based from 3 different temperature which are 40□ , 50□ and 60 □ and different drying condition which are known as Normal heating program, soft heating program and Boost Heating program which are available in the moisture analyser XM-60 precisa.

METHODOLOGY

3.1 Introduction

The research approach for this particular paper is focused on the drying kinetic of *Dioscorea Opposita* and the antioxidant bio-assay of the *Dioscorea Opposita* under different drying temperature with different drying technique. The process of drying, mathematical modeling and antioxidant bioassay testing would be discussed in this chapter.

The first stage of the experiment was the planning stage, in the planning stage research work was carried out to determine the suitable candidate to be used as the specimen for this research topic and identify the research gap in order to determine the research objective. *Dioscorea Opposita* was chosen to be the research specimen. Moisture analyzer was selected to be used as the drying method in order to determine the drying kinetic of *Dioscorea Opposita*. Further scientific research from various papers were review and studies in order to further understand regarding the drying kinetic of various plant in order to select the possible thin layer model which could be used for this specific specimen.

The second stage of the research was to implement the studies literature review and implement toward the specimen of the research paper. The operating parameter of the experiment is fixed by the different mode available within the moisture analyzer which includes “standard mode”, “soft mode” and “boost mode”. Each mode from the moisture analyzer represent similar scenario which could be used to

simulate different drying technique. Standard mode from the moisture analyzer simulates the oven drying technique as it shows gradual increase of predefined drying temperature and maintained till there are no weight loss after several interval of one minute. The soft drying mode from the moisture analyzer simulate sun-drying technique as the temperature throughout the drying process will slowly increase in a slow and steady state till it reached its predefined temperature. Finally the boost mode would simulate as close to the convective dryer as it start the drying temperature approximately 120 % higher to the predefined temperature and gradually reached to the predefined drying temperature. Several thin layer drying models were selected to compare with the experimental data in order to determine the most suitable drying temperature for different drying mode available in the moisture analyzer. To evaluate the suitable drying kinetic model for each mode, the antioxidant testing were carried out in order to determine the highest antioxidant bioassay present after drying process. The 2-Diphenyl-1-picrylhrazyl (DPPH) method was chosen in order to determine the antioxidant activity available for each specimen from different mode and temperature. After the highest antioxidant from each mode were determined, the mathematical modeling were carried out using the equation solver incorporated in microsoft excel 2007. The correlation and coefficient, root mean square error analysis and reduced chi-square are the key parameters which are used to determine the most suitable thin layer model for each drying mode.

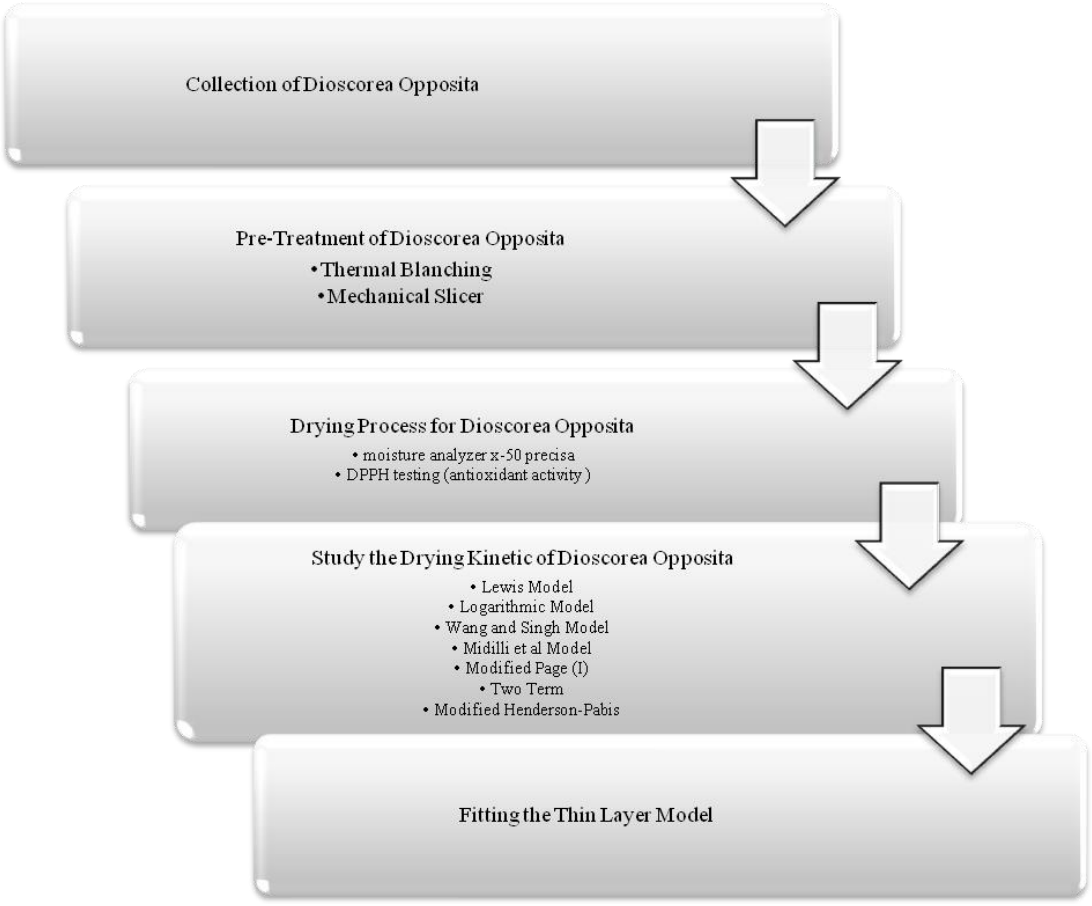


Figure 3.1 Experiment Procedure Flow Diagrams

3.2 Raw material – Chinese Yam Tuber

Chinese yams were purchased and collected from a selected location to ensure a constant supply of *Dioscorea Opposita*.

3.3 Pre-treatment of Dioscorea Opposita

Pre-treatment is required in order to mitigate the quality attributes of degradation of any herbal plant. Pre-treatment method is conducted in order to assist the drying process as it reduce the total drying time significantly while ensuring the quality of the specimen. Blanching technique was chosen as blanching is one of the most common techniques which utilize thermal treatment toward the treatment before processing the herbal plant. Blanching technique assist in removing unwanted enzyme which causes deterioration reaction and undesirable changed in colour. As time passes, *Dioscorea Opposita* would changed from pale yellow to pink colour which signified that the bio-assay of the product starts to deteriorate .Blanching technique assist the drying process through expelling intercellular air from the surface and inner surface of the *Dioscorea Opposita* therefore it would ensure that the surface texture of the specimen to be soften [11].The *Dioscorea Opposita* is sliced approximately 2 centimetre by 2 centimetre before measuring the mass of the specimen. The thickness of the *Dioscorea Opposita* could not be sliced evenly due to limitation.

3.4 Drying Method Moisture Analyzer X-50 Presica

The size for each sample should be approximately around 4 g each. The samples were sliced as thin as possible with a knife until the surface area of each samples are approximately 2 centimeter by 2 centimeter. The surface area of 2 cm by 2 cm was chosen was due to the limitation of the surface area of the drying plate. The average weight of each sample placed on the drying plate was approximately 4g in weight. The samples were placed on the flat surface of the drying plate without minimum contact between each sample. The moisture analyzer was set to the appropriate drying setting such as “standard mode”, “soft mode” and “boost mode” with a temperature of 40°C, 50°C and 60°C for each sample. The duration of the moisture analyzer were switch off in order to ensure that the moisture content of the sample reached equilibrium. The experiment were stopped where there was no sign of weight loss observed on the moisture analyzer. The experiments were conducted in triplicate. With an interval of one minute, the mass of the sample are taken and recorded until it could be observe that there are no mass loss.



Figure 3.4a Slices of *Dioscorea Opposita* (before drying)



Figure 3.4b Slices of *Dioscorea Opposita* (after drying)

1) 3.4.1 Ultrasonic Assisted Extraction

Ultrasound assisted extraction (Elmasonic Model P120H, Singen, Germany) was set at 20kHz in the continuous mode at 50% amplitude or 28 W of thermal energy. The temperature of the water bath was set to the 30°C throughout the sonification process. The total volume of distilled water was filled until the test tube consist of the specimen is fully submerged. Each sample consist of 2g of sample with a mixture of 40 ml of methanol solvent. The samples were removed from the ultrasound assisted extraction after 30 minute of sonification. The samples were filter after sonification process for a total of 3 times. The samples were placed into the rotary vacuum evaporator (Heidolp Model Hei-VAP Precision (HL), Schwabach Germany) in order to remove the solvent in the sample. The setting on the rotary vacuum evaporator were set to 40 °C , 196 mbar and an rpm of 150. The extraction process was halted until crude extract could be observed in the evaporating flask. The experiments were conducted

in triplicate in order to ensure the experiment accuracy. The crude samples were send to antioxidant testing.

2) 3.4.2 Mathematical modeling for drying kinetics

Nine thin layer models are listed in table 3.1 were used for evaluation in order to determine the most suitable model to describe the drying process of each drying mode. The nine thin layer models were selected because they were found to be the most common thin layer models which are applicable for multiple herbal plants. For example two term thin layer model was suitable for plant such as bitter gourd, Amelia brook, mango and sultana grape. For approximation diffusion model , it had been suitable for plant such as tomato, amelie brooks mango, red pepper , *aristolochia cymbifera mart* sand zucc leaf. Modified Henderson and pabis is suitable for plant such as mango, cassava, banana and nuts kernels. Logarithmic model was suitable for apricots. Middili et al were suitable for multiple plant such as spear mint, mint leaves, egg plants, green pepper, olive husk, ximeng and *gundelia tournefortii l.* The Newton model was suitable for lemon grass. The page model was suitable for ginger rhizome, parsley leaves, mint and basil leaves. The Wang and sigth model was suitable for smith apple. The dimensionless moisture ratio is given by

$$MR = \frac{M - M_e}{M_o - M_e} \qquad (3.1)$$

Where M is the moisture content of the specimen

M_o is the initial moisture content of the specimen

M_e is the equilibrium moisture content of the specimen

Table 3.1 Empirical Mathematical Models for Thin Layer Model

Model Name	Model	Reference	Specimen Plant	Unknown Drying Parameter
Lewis	$MR = exp(-kt)$	[15]	Grape seeds, Pumpkin	k
Logarithmic	$MR = a\ exp(-kt) + b$	[14. 21, 23]	Sweet Potato, Pistachio, Long green pepper, Rambutan	a,k,b
Wang and Singh	$MR = 1+at+bt^2$	[20, 24]	Dioscorea Opposita, Sweet Sorghum	a,b
Midilli et al	$MR=a.exp(-kt^n)+bt$	[17, 22]	Adathoda vasica, Cymbopogon citratus,	a,k,n,b

			SpearMint	
Modified Page (I)	$MR = \exp[-kt^n]$	[7]	Mint leaves Basil leaves	k,n
Two term model	$MR=a.\exp(k_0t)+b.\exp(-k_1t)$	[25, 27]	Nuts Fermented sugar cane prickly pear fruit sultana grape	a, k_0,b, k_1
Modified Henderson–Pabis	$MR=a.\exp(-kt)+b.\exp(-gt)+c.\exp(ht)$	[25, 29]	Dika kernels olive leaves	a,k,b,g,c,h
Approximation Diffusion	$MR= a.\exp(-k_ot)+(1-a)\exp(-k_{ob}t)$		Banana Amelia , Brooks mangoes	a , k_o,
Newton	$MR= \exp(-kt)$		Lemon grass	

Note: t is drying time and the notation such as a, b, k, n, g, c, h and k_0 are drying constants

The value of the equilibrium moisture content of the specimen was very small compare to the initial moisture content and moisture content therefore it could be neglected thus the formula would in turn written as shown

$$MR = \frac{M}{M_o} \tag{3.1.2}$$

The regression analysis was performed by using the Equation Solver incorporated into Microsoft excel 2007.The criteria for selecting the best suitable model to describe the drying curve were based on Correlation Coefficient (R^2) , Root mean Square error analysis (RSME) and the reduced chi-square ($\chi 2$). The reduced Chi Square is the deviation between the calculated value and the experimental value in order to determine the good fit among the mathematical model. The RSME value should be close to zero as it shows the deviation of the predicted value and the experimental value. The Correlation Square should be close to 1 in order to shows that the best fit for the drying curve for each empirical model.

$$R^2 = 1 - \left[\frac{\sum_{i=1}^{N} \left(MR_{\exp,i} - MR_{pre,i} \right)^2}{\sum_{i=1}^{N} \left(MR_{\exp,i} - \overline{MR_{\exp}} \right)^2} \right] \tag{3.2}$$

$$RMSE = \left[\frac{1}{N} \sum_{i=1}^{N} \left(MR_{\exp,i} - MR_{pre,i} \right)^2 \right]^{1/2} \quad (3.4)$$

$$\chi 2 = 1 - \left[\frac{\sum_{i=1}^{N} \left(MR_{\exp,i} - MR_{pre,i} \right)^2}{N - n} \right] \quad (3.5)$$

3.5 Chemicals and Reagents

2-diphenyl-2-picrylhydrazyl (DPPH) were purchased from Sigma-Aldrich (M) Sdn. 99 % of Methanol Solvent was purchase from Ever Green Engineering. Other chemical are provided by Taylors University Lakeside.

3) 3.5 2-diphenyl-2-picrylhydrazyl (DPPH) free radical scavenging assay (DPPH assay)

DPPH solution is a stable free radical which is sensitive to light exposure. The DPPH solution colour will be reduce from purple to yellow colour when there is present of free radical antioxidant.

The antioxidant activity of *Dioscorea Opposita* was determined using the DPPH method alter from "Extraction modelling and activities of antioxidant from pomegranate marc. 1.9 mg of DPPH powder was dissolved into 100 ml of methanol to prepared 0.1mM. The DPPH solution was prepared by using a schott bottle wrap by aluminums foil. The DPPH solution was left to settle down in a dark room for 30 minutes before usage.

1 ml of the prepared solution was added into the 3 ml of extract solution. The sample colour alters from purple to yellow. The prepared sample was then left in a dark room for 30 minutes before the sample was measured at the absorbance value of 517 nm with a blank solution using a UV spectrometer (Model Genesys 10S, Massachusetts, United States). 3 ml of pure methanol was used as the blank solution. The absorbance value of each sample was recorded in order to calculate the radical scavenging activity of *Dioscorea Opposita* [30].The radical scavenging activity of *Dioscorea Opposita* is calculated based on the equation:

$$inhibition\,\% = 100 \times \left[1 - \frac{Aco - Aat}{Aco} \right] \quad \textbf{(3.6)}$$

RESULTS AND DISCUSSION

4.1 Introduction

The drying profile of the *dioscorea opposita* is determined through the usage of moisture analyzer X-50 precisa with its multiple drying modes. The standard drying mode represents the oven-drying method. Due to the best of my knowledge regarding the drying mode of the moisture analyzer the soft drying mode represent the sun-drying technique and the boost mode represent the convective drying based from the assumption I concluded. Based on observation from the experimental data, it shows that "boost mode" has the minimum amount of time require for the moisture of the sample to reached equilibrium. Based on the DPPH method conducted for each sample it shows that the antioxidant activity from each drying mode varies. Based on the comparison between the experimental and predicted result, the highest R^2 and the lowest RMSE and X^2 are different in the different drying mode available in the moisture analyzer X-50 precisa. The 9 model for each thin layer drying model would be shown further in this chapter.

4.2 Drying kinetic

4) 4.2.1 Drying curve in term of drying rate

The drying curve of *Dioscorea Opposita* slices are dehydrated by using a moisture analyzer X-50 precisa. The slices of *dioscorea opposite* have been dehydrated in different drying mode. The time taken for slices of *dioscorea opposite* for standard mode and soft mode is approximately close to 1 hour 30 minute, however for boost drying mode it would only take approximately 1 hour 20 minute. Based on the figure 4.4 and figure 4.5, it shows that the data fluctuate a lot for 60 ℃ after exceeding the 65 minute drying process. However for figure 4.2, it shows that the data from 60 ℃ had a high drying rate of 0.039 g/moisture min at the first few minute of the drying process before it slowly increase at a steady state after 8 minute. It shows that data for 60°C for figure 4.5 seems to have inconsistence data which could be due inconsistence drying temperature within the drying process. Based on the drying curve of standard model, it shows significant error for 60°C around 100 to 110 minute where there was a fluctuation of drying rate. The drying rate for standard mode reached equilibrium around the 150 minute.

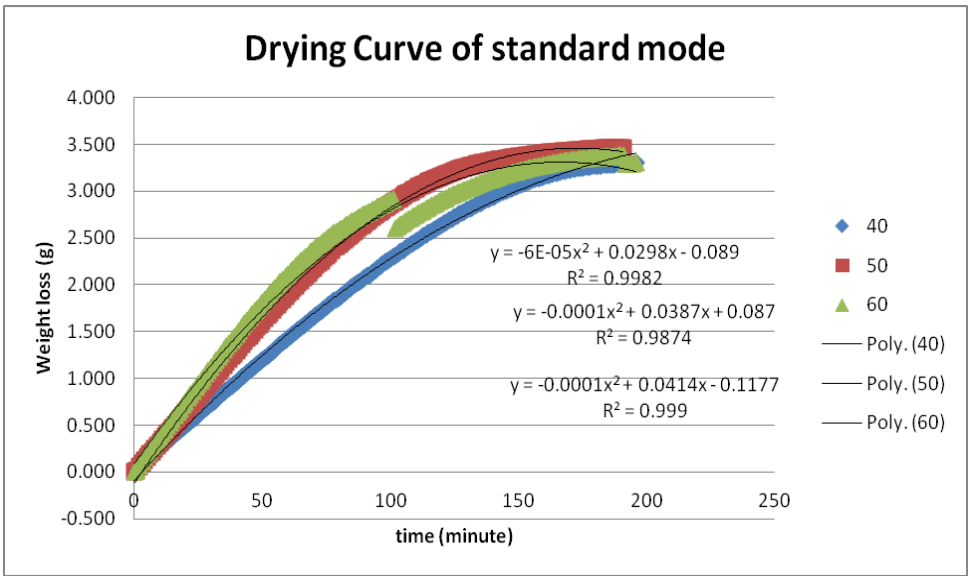


Figure 4.1 Drying Curve Standard mode

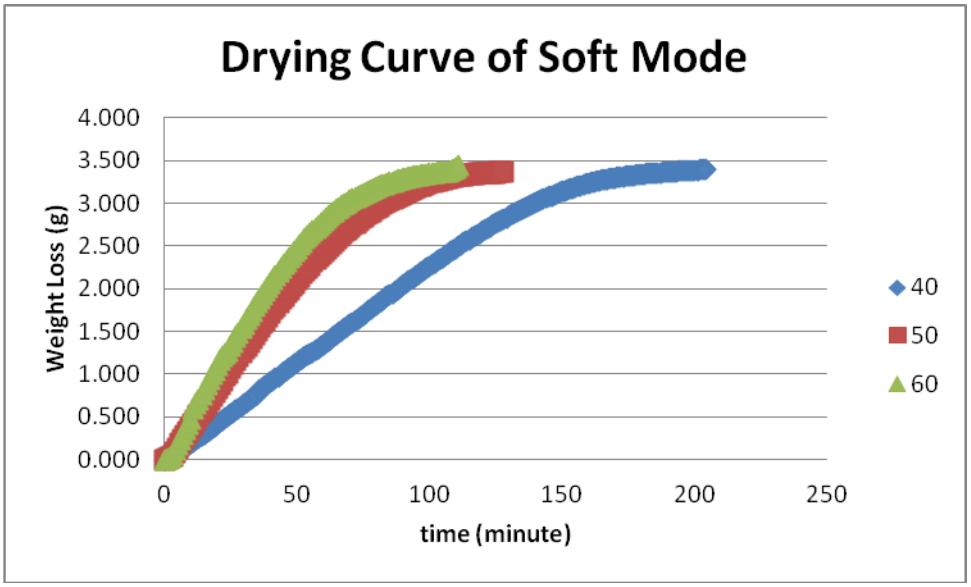


Figure 4.2 Drying Curve of Soft mode

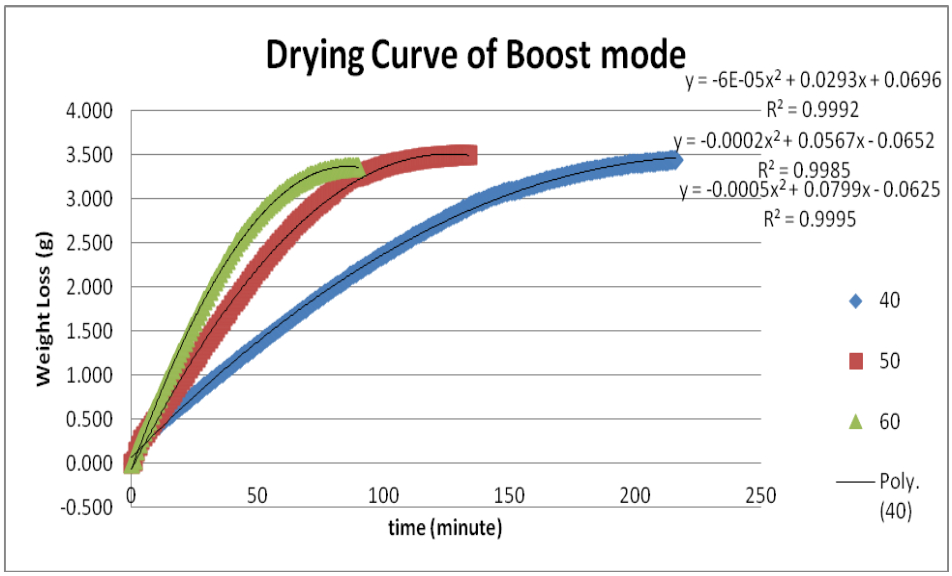


Figure 4.3 Drying mode of boost mode

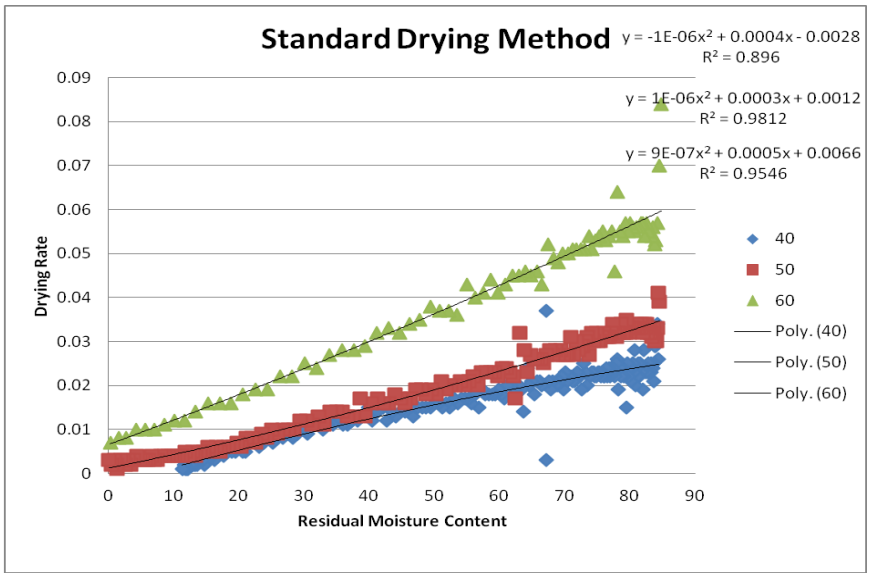


Figure 4.4 Drying rate over Residual moisture content for standard mode

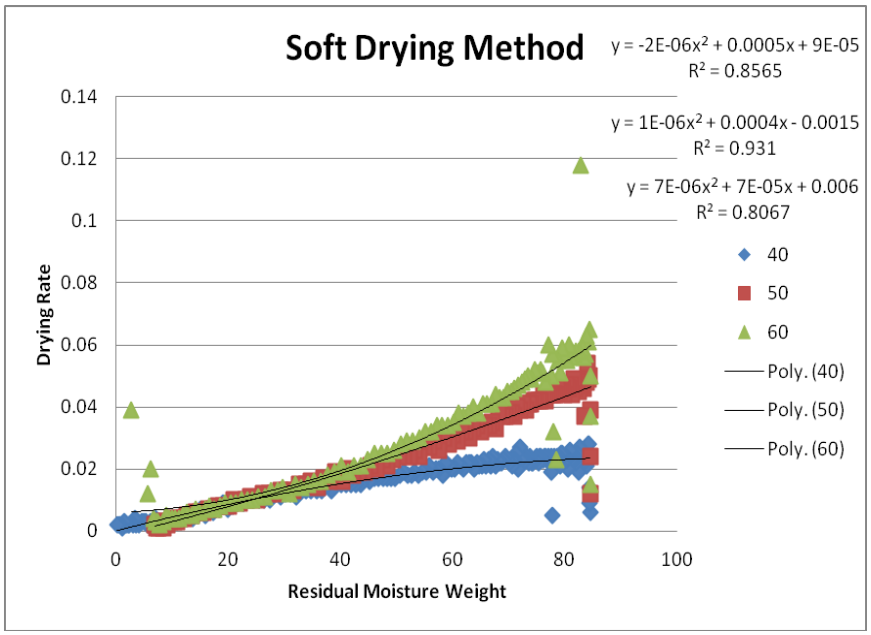


Figure 4.5 Drying rate over Residual moisture content for soft mode

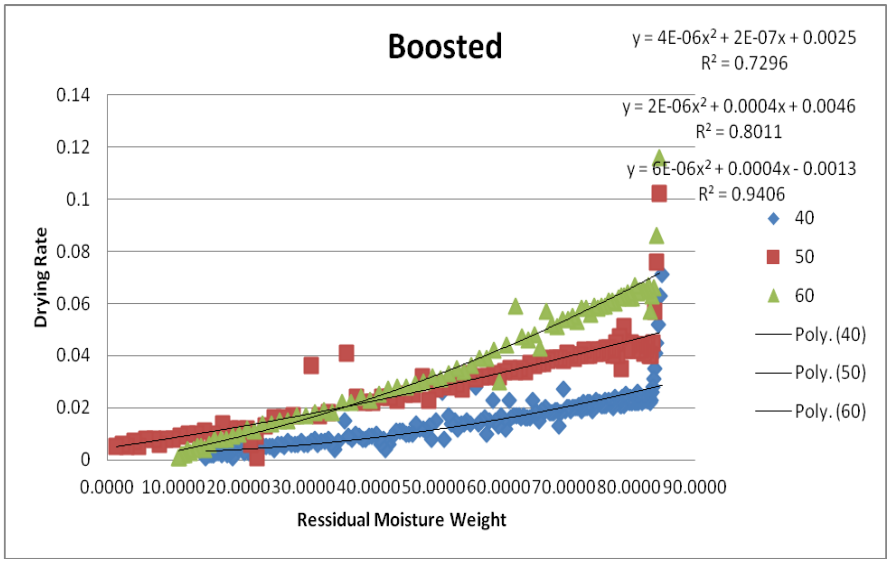


Figure 4.6 Drying rate over Residual moisture content for boost mode

4.3 Effect of Temperature on DPPH Radical Scavenging Activities

Based on the DPPH radical method which had been used to evaluate the free radical scavenging activities of antioxidant bio-assay, the mixture of the sample with DPPH solution would decolorize from purple to pale yellow. The discoloration occurring was due to the present of antioxidant bio-assay present in the mixture. In table 5.1, table 5.2 and table 5.3 it shows the antioxidant activity. The DDPH radical scavenging activities of antioxidant for *dioscorea opposita* vary in different drying process. It could be observed from the result obtained that for standard drying mode, the total antioxidant activity for 50°C appear to be the highest (88.04%) follow with 60°C (84.88%) then 40°C (83.13%). However in soft mode, the highest total antioxidant activity present in 40°C (91.13%) follow up by 50°C (87.96%)

and finally 60°C (87.08%). In this mode, it shows that the total antioxidant increases as the temperature increases. In the boost mode, it also shows that the total antioxidant increases as the temperature increases. The total antioxidant at 60°C (92.64%) follow up to 50°C (92.02%) then 40°C (91.75%)

Figure 5.1 DPPH radical scavenging of *Dioscorea Opposita* at standard mode

Temperature °C	*Radicals scavenging activity (%)*
40	83.13
50	88.04
60	84.89

Figure 5.2 DPPH radical scavenging of *Dioscorea Opposita* at Soft mode

Temperature °C	*Radicals scavenging activity (%)*
40	91.13
50	87.96
60	87.08

Figure 5.3 DPPH radical scavenging of *Dioscorea Opposita* at Boost Mode

Temperature °C	*Radical scavenging activity (%)*
40	91.75
50	92.02
60	92.60

4.4 Comparison of kinetic models

The dimensionless moisture ratio from the sample is fitted into the mathematical models which discussed in chapter 2. In order to investigate the drying kinetic of *Dioscorea Opposita* are plotted as a function of dimensionless moisture ratio against drying time (0 minute 200 minute) and the result is shown in figure 6.1, figure 6.2 and figure 6.3. Based on the objective of the experiment, only the temperature for the highest antioxidant is chosen for the studies.

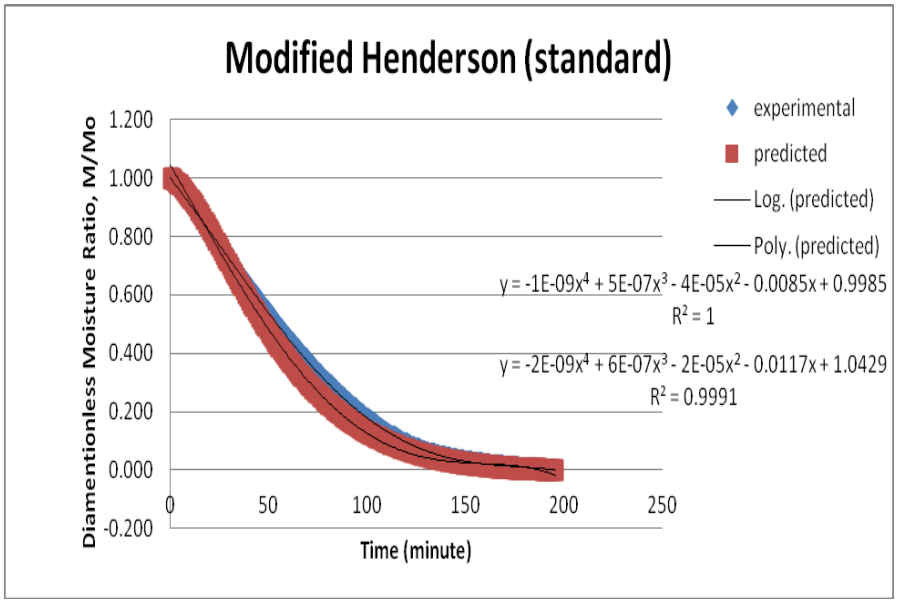


Figure 6.1 Modified Henderson & Pabis

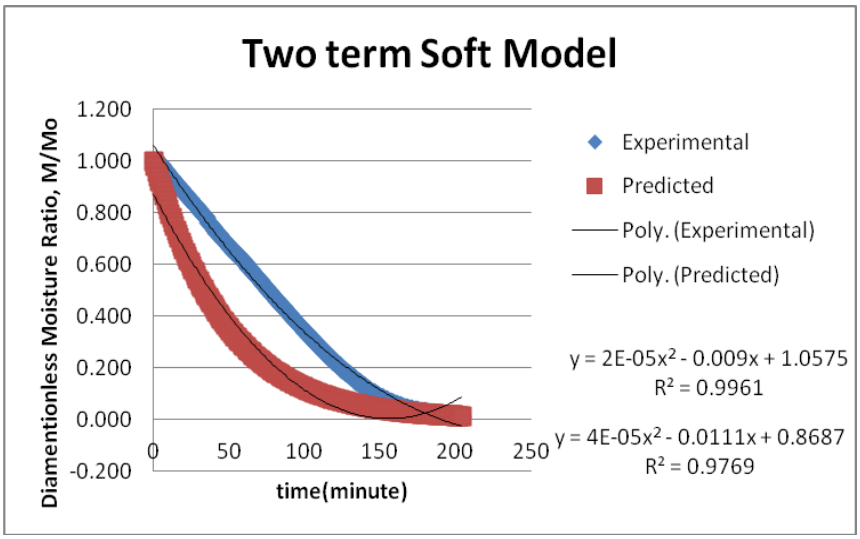


Figure 6.2 Two term (soft mode)

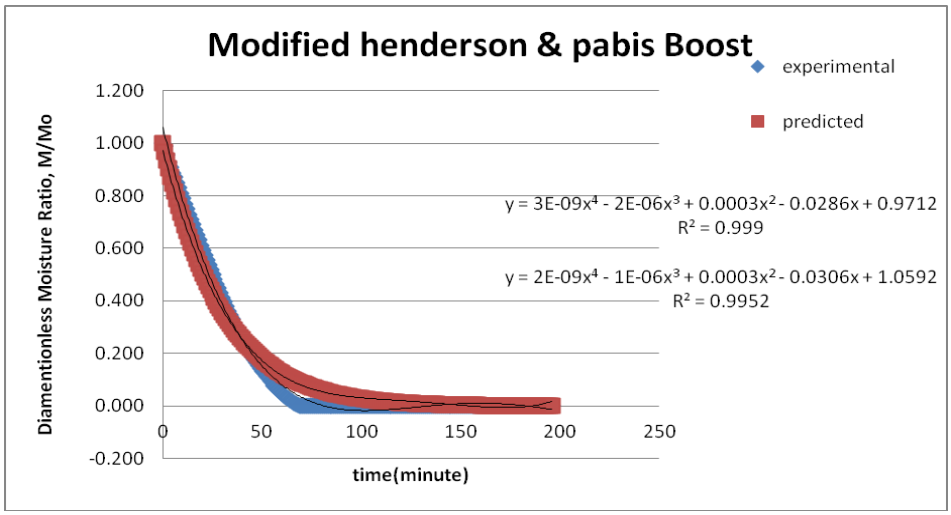


Figure 6.3 Approximation Diffusion (boost)

The value of coefficient determination, root mean square error and reduced chi-square are the main criteria which had been used determine the goodness of fit and to select the most suitable model for a given experimental. A high coefficient determination with a low root mean square error and reduced chi-square indicated the ideal fit. Table 4.1, Table 4.2, and Table 4.3 showed the value for each criteria for selecting the ideal fit. For standard drying mode, the models exhibit good fitting performance for the experimental data. Among the nine model shown in the figure, the best model for standard drying is modified henderson & pabis with a coefficient determination of 0.9861, root mean square error with 8.37E-06 and the reduced chi-square with a value of 0.002886. The experimental data for accuracy for standard mode is Modified Henderson and Pabis >Henderson and Pabis >Newton model >Wang & Singh >Midilli et al> Approximation Diffusion> two term model> Logarithmic model> Lewis model

The best model for soft drying is two term model with a coefficient determination of 1, root mean square error of 6.4E-15 and the reduced chi-square with a value of 0.000773.The experimental data for best accuracy for soft drying is two term model> Henderson & Pabis> Newton> Wang & Singh> Midilli et al model> Approximation Diffusion model > Logarithmic model >Modified Henderson & Pabis model>Lewis model.

The best model for boost drying is Modified Henderson and Pabis with a coefficient determination of 0.998453, root mean square error of 1.39E-06 and the reduced chi-square with a value of 0.001177. The experimental data for best accuracy for boost drying is Modified Henderson and Pabis >Logarithmic model>Midilli et al >Approximation Diffusion model >Lewis model> two term model> Wang & Singh model >Henderson & Pabis model> Newton model.

Table 4.1 thin layer drying model for standard mode

Model	*Temperature (°C)*	*R2*	*RMSE*	*χ2*	*k*	*n*		
Lewis	40	0.974659	9.8E-06	0.003123	0.0096	1.0000		
	50	0.957749	2.55E-05	0.005037	0.0175	1.0000		
	60	0.977197	1.87E-05	0.004311	0.030296	1.0000		
Henderson & Pabis	40	0.998265	6.71E-07	0.000817	0.0024	1.2996		
	50	0.984299	9.48E-06	9.48E-06	0.0017	1.5489		
	60	0.888106	9.17E-05	9.17E-05	0.0017	1.5489		
					a	b		
Wang & Singh	40	0.98546	5.63E-06	0.002366	-0.0068	-0.0029		
	50	0.982477	1.06E-05	0.003244	-0.0123	-0.0061		
	60	0.943944	4.59E-05	0.006759	-0.0158	-0.0078		
					k	n		
Newton Model	40	0.998265	6.71E-07	0.000817	0.0024	1.2996		
	50	0.984299	9.48E-06	0.00307	0.0017	1.5489		
	60	0.359156	0.000525	0.022855	0.8521	1.0323		
					a	b	k_0	k_1
two term	40	0.998446	6.01E-07	0.000773	6.6183	-5.6183	0.0171	0.0194

	50	0.976208	1.44E-05	0.00378	6.6183	-5.6183	0.0108	0.0100		
	60	0.958764	1.63E-05	0.004033	6.6183	-5.6183	0.0246	0.0237		
					a	b	c	k	g	h
Modified Henderson&	40	0.998888	4.3E-07	0.000654	7.0524	-5.6297	-	0.0140	0.0161	-
Pabis							0.42273			0.00634
	50	0.986129	8.37E-06	0.002886	14.6580	-6.2014	-	0.0253	0.0324	-
							7.45659			0.02248
	60	0.992705	5.98E-06	0.002438	14.8385	-6.3575	-	0.0513	0.0630	-
							7.48104			0.04799
					a	b	k			
Logarithmic	40	0.995294	1.82E-06	0.001346	1.4208	-0.4208	0.0055			
	50	0.97406	1.57E-05	0.003947	1.0537	-0.0537	0.0152			
	60	0.918134	6.71E-05	0.008169	1.0639	0.1213	0.0452			
					a	b	k	n		
Midilli et al	40	0.998443	6.02E-07	0.000774	1.0000	-0.0001	0.0028	1.258077		
	50	0.984731	9.22E-06	0.003028	1.0000	0.0000	0.0018	1.534234		
	60	0.993374	5.43E-06	0.002324	1.0000	0.0000	0.0033	1.59166		
					a	b	k			
Approximation	40	0.998453	5.98E-07	0.000772	8.8267	0.0190	0.0174			
Diffusion										
	50	0.976214	1.44E-05	0.003779	8.8267	0.0101	0.0107			

	60	0.980046	1.63E-05	0.004033	8.8267	0.0238	0.0245

Table 4.2 Thin layer drying model for Soft mode

Model	*Temperature (°C)*	R^2	*RMSE*	$\chi 2$	*k*	*n*
Lewis	40	0.935038	3.42E-05	0.005829	0.0114	1.0000
	50	0.95161	2.55E-05	0.005037	0.0175	1.0000
	60	0.977197	1.87E-05	0.004311	0.03029584 3	1.0000
Henderson & Pabis	40	0.99508	2.7E-06	0.001639	0.0007	1.5948
	50	0.984299	9.48E-06	9.48E-06	0.0017	1.5489
	60	0.888106	9.17E-05	9.17E-05	0.0017	1.5489
					a	b
Wang & Singh	40	0.99033	5.31E-06	0.002298	-0.0082	-0.0040

	50	0.982477	1.06E-05	0.003244	-0.0123	-0.0061				
	60	0.943944	4.59E-05	0.006759	-0.0158	-0.0078				
					k	n				
Newton Model	40	0.994865	2.7E-06	0.001639	0.0007	1.5957				
	50	0.984299	9.48E-06	0.003079	0.0017	1.5489				
	60	0.359156	0.000525	0.022855	0.8521	1.0323				
					a	b	k0	k1		
two term	40	1	6.4E-15	7.98E-08	6.6183	-5.6183	0.0186	0.0182		
	50	0.976208	1.44E-05	0.003784	6.6183	-5.6183	0.0108	0.0100		
	60	0.958764	1.63E-05	0.004033	6.6183	-5.6183	0.0246	0.0237		
					a	b	c	k	g	h
Modified Henderson & Pabis	40	0.982364	9.27E-06	0.003037	1785.4606	0.1396	-1784.6	0.0034	0.0134	-0.00337

	50	0.986129	8.37E-06	0.002886	14.6580	-6.2014	-7.45659	0.0253	0.0324	-0.02248
	60	0.992705	5.98E-06	0.002438	14.8385	-6.3575	-7.48104	0.0513	0.0630	-0.04799
					a	b	k			
Logarithmic	40	0.98262	9.14E-06	0.003015	1.3603	-0.3603	0.0065			
	50	0.97406	1.57E-05	0.003947	1.0537	-0.0537	0.0152			
	60	0.918134	6.71E-05	0.008169	1.0639	0.1213	0.0452			
					a	b	k	n		
Midilli et al	40	0.997358	1.39E-06	0.001176	1.0000	-0.0002	0.0012	1.476009		
	50	0.984731	9.22E-06	0.003028	1.0000	0.0000	0.0018	1.534234		
	60	0.993374	5.43E-06	0.002324	1.0000	0.0000	0.0033	1.59166		
					a	b	k			
Approximation Diffusion	40	0.998453	5.98E-07	0.000772	8.8267	0.0190	0.0174			

	50	0.97621 4	1.44E-05	0.00377 9	8.8267	0.0101	0.0107
	60	0.98004 6	1.63E-05	0.00403 3	8.8267	0.0238	0.0245

Table 4.3 Thin layer drying model for Boost mode

Model	*Temperature (°C)*	R^2	*RMSE*	$\chi 2$	*k*	*n*
Lewis	40	0.974659	9.8E-06	0.003123	0.0096	1.0000
	50	0.957749	2.55E-05	0.005037	0.0175	1.0000
	60	0.977197	1.87E-05	0.004311	0.030296	1.0000
Henderson & Pabis	40	0.998265	6.71E-07	0.000817	0.0024	1.2996
	50	0.984299	9.48E-06	9.48E-06	0.0017	1.5489
	60	0.784835	0.000187	0.000187	0.0017	1.5489
					a	b
Wang & Singh	40	0.98546	5.63E-06	0.002366	-0.0068	-0.0029
	50	0.982477	1.06E-05	0.003244	-0.0123	-0.0061
	60	0.938296	5.35E-05	0.007296	-0.0177	-0.0083
					k	n
Newton	40	0.998265	6.71E-07	0.000817	0.0024	1.2996
	50	0.984299	9.48E-06	0.00307	0.0017	1.5489
	60	0.607966	0.00034	0.018389	0.3590	1.0000

					a	b	k0	k1		
two term	40	0.998446	6.01E-07	0.000773	6.6183	-5.6183	0.0171	0.0194		
	50	0.976208	1.44E-05	0.00378	6.6183	-5.6183	0.0108	0.0100		
	60	0.979429	9.88E-06	0.003135	6.6183	-5.6183	0.0291	0.0283		
					a	b	c	k	g	h
Modified Henderson	40	0.998888	4.3E-07	0.000654	7.0524	-5.6297	-0.42273	0.0140	0.0161	-0.00634
	50	0.986129	8.37E-06	0.002886	14.6580	-6.2014	-7.45659	0.0253	0.0324	-0.02248
	60	0.998111	1.64E-06	0.001276	14.6831	-6.2471	-7.43603	0.0525	0.0654	-0.04764
					a	b	k			
Logarithmic	40	0.995294	1.82E-06	0.001346	1.4208	-0.4208	0.0055			
	50	0.97406	1.57E-05	0.003947	1.0537	-0.0537	0.0152			
	60	0.98757	1.08E-05	0.003274	1.0012	-0.0012	0.0345			
					a	b	k	n		
Midilli et al	40	0.998443	6.02E-07	0.000774	1.0000	-0.0001	0.0028	1.258077		
	50	0.984731	9.22E-06	0.003028	1.0000	0.0000	0.0018	1.534234		
	60	0.998394	1.39E-06	0.001177	1.0000	0.0000	0.0066	1.463547		
					a	b	k			
Approximation Diffusion	40	0.998453	5.98E-07	0.000772	8.8267	0.0190	0.0174			
	50	0.976214	1.44E-05	0.003779	8.8267	0.0101	0.0107			
	60	0.988608	9.88E-06	0.003135	8.8267	0.0284	0.0290			

5.1 Conclusion

This research study was conducted to determine the drying kinetic of *dioscorea opposita* through the usage of moisture analyzer x-50 precisa with different drying process. The result shows that the boost mode used the least amount of time to ensure that the specimen reached equilibrium. Based on the result obtained from different mode, it could be seen there would always consist a certain percentage of moisture in the specimen unless a higher drying temperature is used. However through the usage high drying temperature could lead to the degradation of its bio-assay such as the antioxidant activity of the specimen. The result shows that the total antioxidant would reach its maximum at the lowest for soft drying mode(91%) while the antioxidant for the boost drying mode would reached maximum at the highest temperature (60°C). However in the standard drying mode, the maximum antioxidant activity available would be at 50°C with approximately 88 %.

For standard drying mode, the models exhibit good fitting performance for the experimental data. Among the nine model shown in the figure, the best model for standard drying is modified henderson & pabis with a coefficient determination of 0.9861, root mean square error with 8.37E-06 and the reduced chi-square with a value of 0.002886. The experimental data for accuracy for standard mode is Modified Henderson and Pabis >Henderson and Pabis >Newton model >Wang & Singh >Midilli et al> Approximation Diffusion> two term model> Logarithmic model> Lewis model

The best model for soft drying is two term model with a coefficient determination of 1, root mean square error of 6.4E-15 and the reduced chi-square with a value of 0.000773.The experimental data for best accuracy for soft drying is two term model> Henderson & Pabis> Newton> Wang & Singh> Midilli et al model> Approximation Diffusion model > Logarithmic model >Modified Henderson & Pabis model>Lewis model.

The best model for boost drying is Modified Henderson and Pabis with a coefficient determination of 0.998453, root mean square error of 1.39E-06 and the reduced chi-square with a value of 0.001177. The experimental data for best accuracy for boost drying is Modified Henderson and Pabis >Logarithmic model>Midilli et al >Approximation Diffusion model >Lewis model> two term model> Wang & Singh model >Henderson & Pabis model> Newton model.

Acknowledge

I would like to express my gratitude to my supervisor and my fellow friend for fully supporting with my final year project. I would also like to express my gratitude toward the lab assistant for providing me guidance on certain task relating to my final year project

REFERENCES

[1] H. B. Zakaria, "FFTC Agricultural Policy Platform," Economic and Technology Management Research Centre, 20 March 2015.[Online]. Available: http://ap.fftc.agnet.org/ap_db.php?id=395. [Accessed 1 May 2016].

[2] Wang, X. (2016). Influence of development of chenji dioscorea opposita thunb . cv . tiegun series products on economic development in shandong province.

[3] Pingale, T., & Prabhavalkar, K. (2016). Antioxidant Activity of Formulation Containing Mixture of Herbs, *2*(1), 29–32.

[4] Kondo, T., & Fujita, T. (2012). Complete nucleotide sequence and construction of an infectious clone of Chinese yam necrotic mosaic virus suggest that macluraviruses have the smallest genome among members of the family Potyviridae, *3*, 2299–2307. http://doi.org/10.1007/s00705-012-1429-1

[5] Shujun, W., Hongyan, L., Wenyuan, G., & Haixia, C. (2006). Food Chemistry Characterization of new starches separated from different Chinese yam (Dioscorea opposita Thunb .) cultivars, *99*, 30–37. http://doi.org/10.1016/j.foodchem.2005.07.008

[6] M. Umamaheswari and K. Chatterjee, "In Vitro Antioxidant Activities of the Fractiond of Coccinia Grandis L. Leaf Extract.," *Afr J Trad Comp Alter Med*, no. 5, pp. 61-73, 2008.

[7] Akpinar, E. K. (2006). Mathematical modelling of thin layer drying process under open sun of some aromatic plants, 77, 864–870. http://doi.org/10.1016/j.jfoodeng.2005.08.014

[8] Akpinar, E. K., & Bicer, Y. (2008). Mathematical modelling of thin layer drying process of long green pepper in solar dryer and under open sun, *49*, 1367–1375. http://doi.org/10.1016/j.enconman.2008.01.004

[9] Wu, Z., Jiang, W., Nitin, M., & Bao, X. (2016). ScienceDirect Characterizing diversity based on nutritional and bioactive compositions of yam germplasm (Dioscorea spp .) commonly cultivated in China. *Journal of Food and Drug Analysis*, *24*(2), 367–375. http://doi.org/10.1016/j.jfda.2015.12.003

[10] Zhou, Y., Zhou, C., Yao, H., Liu, Y., & Tu, R. (2008). Application of ISSR markers in detection of genetic variation among Chinese yam (Dioscorea opposita Thunb) cultivars *∂*.

[11] Wang, L. (2015). Mathematical modeling and effect of blanching pretreatment on the drying kinetics of chinese yam, 21(4), 511–518. http://doi.org/10.2298/CICEQ140816007F

[12] Dioscorea, L. (2016). Dioscorea oppositifolia Scientific Name, *10*. http://doi.org/10.1007/978-94-017-7276-1

[13] Moisture analyser XM 50 Operating Instructions 350-8150-000. (n.d.).

[14] Midilli, A. (2003). Mathematical modeling of thin layer drying of pistachio by using solar energy, *44*, 1111–1122.

[15] Roberts, J. S., Kidd, D. R., & Padilla-zakour, O. (2008). Drying kinetics of grape seeds, *89*, 460–465. http://doi.org/10.1016/j.jfoodeng.2008.05.030

[16] Akpinar, E. K., & Bicer, Y. (2008). Mathematical modeling of thin layer drying process of long green pepper in solar dryer and under open sun, *49*, 1367–1375. http://doi.org/10.1016/j.enconman.2008.01.004

[17] Simha, P., Mathew, M., & Ganesapillai, M. (2016). Empirical modeling of drying kinetics and microwave assisted extraction of bioactive compounds from Adathoda vasica and Cymbopogon citratus. *Alexandria Engineering Journal*, *55*(1), 141–150. http://doi.org/10.1016/j.aej.2015.12.020

[19] Hashim, N., Daniel, O., & Rahaman, E. (2014). A Preliminary Study : Kinetic Model of Drying Process of Pumpkins (Cucurbita Moschata) in a Convective Hot Air Dryer. *Italian Oral Surgery*, *2*, 345–352. http://doi.org/10.1016/j.aaspro.2014.11.048

[20] **Wang, L. (2015). Mathematical modeling and effect of blanching pretreatment on the drying kinetics of chinese yam, 21(4), 511–518. http://doi.org/10.2298/CICEQ140816007F**

[21] **Transfer, H. M. (2011). Thin-layer drying characteristics of sweet potato slices and mathematical modelling, 277–285. http://doi.org/10.1007/s00231-010-0722-3**

[22] Ayadi, M., Ben, S., Zouari, I., & Bellagi, A. (2014). Kinetic study of the convective drying of spearmint. Journal of the Saudi Society of Agricultural Sciences, 13(1), 1–7. http://doi.org/10.1016/j.jssas.2013.04.004

[23] Nor, S., Syed, F., Rahman, A., Wahid, R., & Ab, N. (2015). Drying Kinetics of Nephelium Lappaceum (Rambutan) in a Drying Oven. *Procedia - Social and Behavioral Sciences*, *195*, 2734–2741. http://doi.org/10.1016/j.sbspro.2015.06.383

[24] Shen, F., Peng, L., Zhang, Y., Wu, J., Zhang, X., Yang, G., Qi, H. (2011). Thin-layer drying kinetics and quality changes of sweet sorghum stalk for ethanol production as affected by drying temperature. *Industrial Crops & Products*, *34*(3), 1588–1594. http://doi.org/10.1016/j.indcrop.2011.05.027

[25] Aregbesola, O. A., Ogunsina, B. S., Sofolahan, A. E., & Chime, N. N. (2015). Mathematical modeling of thin layer drying characteristics of dika (Irvingia gabonensis) nuts and kernels. *Nigerian Food Journal*, *33*(1), 83–89. http://doi.org/10.1016/j.nifoj.2015.04.012

[26] Mazutti, M. A., Zabot, G., Boni, G., Skovronski, A., Oliveira, D., Di, M., Maugeri, F. (2010). Mathematical modeling of thin-layer drying of fermented and non-fermented sugarcane bagasse, *34*, 780–786. http://doi.org/10.1016/j.biombioe.2010.01.021

[27] Lahsasni, S., & Kouhila, M. (2004). Drying kinetics of prickly pear fruit (Opuntia ficus indica), *61*, 173–179. http://doi.org/10.1016/S0260-8774(03)00084-0

[28] Yaldiz, O. (2001). Mathematical modeling of thin layer solar drying of sultana grapes, *26*, 457–465.

[29] Erbay, Z., & Icier, F. (2008). Thin-layer drying behaviors of olive leaves (, *3880110*(2010), 287–308. http://doi.org/10.1111/j.1745-4530.2008.00275.x

[30] Amat, N., Amat, R., Abdureyim, S., Hoxur, P., Osman, Z., & Mamut, D. (2014). Aqueous extract of dioscorea opposita thunb . normalizes the hypertension in 2K1C hypertensive rats, 1–10.

[31] A Prakesh, F Rigelhof and E Miller."Antioxidant Activity" Medallion Laboratories Analysis Progress[Online] Available: Medallion Labs

[32] Ozkan, I. A. (2007). Microwave drying characteristics of spinach, *78*, 577–583. http://doi.org/10.1016/j.jfoodeng.2005.10.026

[33] Gallo, L., Llabot, J. M., Allemandi, D., Bucalá, V., & Piña, J. (2011). In fl uence of spray-drying operating conditions on Rhamnus purshiana (Cáscara sagrada) extract powder physical properties. *Powder Technology*, *208*(1), 205–214. http://doi.org/10.1016/j.powtec.2010.12.021

[34] Drying kinetics of ginger rhizome (. (2013), *38*(June), 301–319.

[35] Xiao, H. W., Yao, X. D., Lin, H., Yang, W. X., Meng, J. S., & Gao, Z. J. (2012). Effect of SSB (Superheated Steam Blanching) time and drying temperature on hot air impingement drying kinetics and quality attributes of yam slices. Journal of Food Process Engineering, 35(3), 370–390. https://doi.org/10.1111/j.1745-4530.2010.00594.x

[36] Shujun, W., Hongyan, L., Wenyuan, G., Haixia, C., Jiugao, Y., & Peigen, X. (2006). Characterization of new starches separated from different Chinese yam (Dioscorea opposita Thunb.) cultivars. Food Chemistry, 99(1), 30–37. https://doi.org/10.1016/j.foodchem.2005.07.008

[37] Yi, W., & Wetzstein, H. Y. (2011). Effects of drying and extraction conditions on the biochemical activity of selected herbs. HortScience, 46(1), 70–7

Jatropha Curcas Powder Manufactured by Hot Air and Freeze Drying for Wastewater Applications

Loh Hon Yeen, Nurhazwani Ismail
School of Engineering, Taylor's University, Malaysia

Nurhazwani.ismail@taylors.edu.my

Abstract
Waste water treatment is one of the most important processes in many chemical engineering industries. Coagulation is one of the main unit operations in waste water treatment. It is a process whereby small colloids form larger flocks of solids in water, making the filtration of water easier. Most typical waste water treatment plants use synthetic substances such as alum as a coagulant. However there has been a rise in demand for natural coagulants since the use of synthetic coagulants have been linked to the cause of Alzheimer's disease. Jatropha curcas seed extract has been identified as a suitable natural coagulant and has a turbidity removal of up to 99.5%. Natural coagulants are extracted and stored as liquid form. Studies have shown that natural coagulants in liquid form have a short shelf life and are prone to bacterial growth due to its high moisture content. Storage of liquid natural coagulants over long periods of time also has a deteriorating effect on its turbidity removal. Drying is a process where water is removed from a substance. When water is removed, the oxidative effects and bacterial growth in liquid can be eliminated. Drying is mainly used in food processing to increase the shelf life of commercially produced goods such as milk powder. The objective of this study is to apply hot air drying and freeze drying techniques to produce a dehydrated form of the Jatropha Curcas extract in powder form. The resulting product has water activity lower than 0.7 which is a threshold for bacterial growth. The coagulation tests using kaolin wastewater also yielded at least 97% turbidity removal at acidic mediums. The highest turbidity recorded was at 99.1% for the sample dried at 75 °C. The hot air drying temperature did not show to have an effect on the coagulation performance. These results strongly suggest that hot air drying and freeze drying are suitable methods to synthesize Jatropha Curcas extract with prolonged shelf life.
Keywords: wastewater; coagulant; Jatropha; freeze drying; hot air drying; coagulation

1. Introduction

Water is one of the most important elements for human life. About 70% of the earth's surface is covered in water. However, only 0.4% of this is usable [1]. Studies conducted by the United Nations have shown that 20% of the world's population does not have access to safe drinking water [1]. Besides that, water pollution is estimated to affect 1.2 billion people and causes deaths to 15 million children under the age of 5 annually[1].

Coagulation is one of the main unit operations in wastewater treatment. In wastewater, there are dissolved solids such as colloids [2]–[4]. These suspensions are too small to be removed via ultrafiltration. In this case, a coagulant is used to form larger flocs of the solids and making it easier to be removed [2]–[4]. There are many types of coagulants and flocculants that are used in wastewater treatment processes such as aluminium and iron (III) salts. However, there have been calls for alternatives as studies have linked the consequences of using aluminium salts to diseases such as Alzheimer's [5]–[8]. The use of the alum salts also affected the pH of water causing low efficiency of coagulation in wastewater under low temperatures [5]. Therefore, to solve this issue, there is a need for natural coagulants derived from natural and renewable sources.

One of the latest natural coagulants used in pollutant removal is *Jatropha curcas* seeds extract [9]. It is mainly used in turbidity removal studies. Turbidity is one of the main parameters in wastewater treatment. It is the measure of light scattering ability due to the presence of suspended solids in wastewater sample [9], [10]. Most wastewater has high levels of turbidity. Hence, turbidity removal can be a suitable parameter to indicate pollutant removal from the treated wastewater.

Most natural coagulants such as *Moringa Oleifera* and *Jatropha Curcas* extracts are often prepared in liquid form. There are several problems with the use of natural coagulants as a liquid extract. For instance, the use of *Jatropha* seed extract in the form of liquid has a limited shelf life for effective use. S. Katayon in 2005 reported that time had an effect on the effectiveness of *Moringa oleifera* seeds as a coagulant in turbidity removal [11]–[13]. When the liquid extract is kept and then tested for 1, 3 and 5 months, it was noted that the best turbidity removal was when the extract was stored for 1 month. In the same study, it was also found that the relationship between the storing temperature and the turbidity was insignificant. In months 3 and 5, the turbidity of the stored extract decreased in terms turbidity removal [11]–[13]. As the extract in *Moringa oleifera* seeds share the same characteristics as the extract of Jatropha curcas seeds (both are plant proteins), there is an opportunity to manufacture a new form of this extract by means of drying so that the extract may be used effectively for longer periods of time. In a similar study involving the use of *Moringa oleifera* seeds extract as coagulant in liquid form, it was also found that the overall bacteriological quality of the treated wastewater had increased [11]–[13]. The resulting water was found to have increased concentration of bacteria when treated with natural coagulant that has been stored for 5 months. This is due to the high moisture content in the extract liquid that encourages growth of microorganisms such as streptococcus and faecal coliforms in the water [11]–[13].

Drying is a process that is used in most food processing industries. It is a unit operation that removes water and moisture from an object. Drying can be done using different temperatures and relative humidity that is the driving factor for removing moisture in an object. Drying not only removes water and moisture but also prevents any growth of microorganisms [14]. There are many types of drying techniques. In this study, a combination of hot air drying and freeze drying is used to prepare *Jatropha* seed extract powder as a coagulant. Studies have shown that a reduction in moisture content to 0.10 ± 0.005 (kg water/kg dry matter) can increase the shelf life and protein extraction of *Jatropha curcas* seeds [15]. As higher temperature gives a higher rate of moisture removal, the effect of temperature on the coagulation effect of *Jatropha curcas* is not known. A range of temperatures (50 °C ,75 °C ,and 105 °C) [15] is

used to dry the seeds before extraction to identify the effect on temperature on the quality of the freeze dried coagulant.

Freeze drying or lyophilisation is one of the most widely used methods for removing water from substances especially in pharmaceuticals where water is removed from probiotics with the intention to enhance the storage life of the product. Freeze drying processes are carried out in batches and usually consist of 3 stages; freezing, primary drying followed by secondary drying [16]. Frozen water is removed under vacuum by means of sublimation [16]. In the secondary drying step, water that is still in liquid form is removed via desorption process. Freeze drying is a relatively expensive and time consuming process and therefore the product usually forms a dry cake [16]. As a result, an additional step is required to break down the press cake into powder [16]. Despite its disadvantages, freeze drying does not cause the proteins in the probiotics to denature [16]. As protein content is an important aspect of *Jatropha* seed extract as a coagulant, freeze drying may produce good quality powder form of the extract.

The first problem with the current use of *Jatropha curcas* extract in liquid form is such that it has a short shelf life and the growth of microorganisms due to the high amount of moisture content. Water activity is the first parameter to be chosen. Water activity is defined as the partial vapour pressure of water in a substance whereby a higher water activity (a_w) supports higher growth of microorganisms [17]. Pure distilled water has a_w of 1 while the a_w needed for bacteria and fungi growths are 0.91 and 0.7 respectively [17]. Therefore it is important that the dried *Jatropha Curcas* freeze dried seed extract powder has water activity level lower than 0.7 upon testing to ensure it does not support growth of microorganisms.

In this research, *Jatropha Curcas* freeze dried seed extract powder is manufactured through hot air drying before extraction, and then freeze drying. Coagulation tests are conducted to compare the effectiveness of the coagulant compared to in liquid form. Water activity is also tested to ensure that the product does not encourage bacterial growth. For hot air drying, the moisture curve is generated to obtain the best time and conditions to reduce the moisture content of the seeds to 0.10 ± 0.005 (kg water/kg dry matter), while at the same time, does not affect the quality of the extract.

2. Methodology

2.1 Determining the Moisture Content of Jatropha Seeds.

A sample of *Jatropha Curcas* seeds (husk removed) of weight W_0 is placed in the hot air oven. The temperature is set at 105 °C. the seeds are dried for 24 hours to obtain the bone dry weight of the seeds (0 % moisture content). The remaining content indicates the weight of dry matter (W_f) in the powder extract. The moisture content of the fresh seeds can be obtained by Eq (1).

$$M = \frac{W_0 - W}{W_0} \times 100\% \quad (1)$$

Whereby:

M $Moisture\ content\ of\ sample, kg$
W_0 $Initial\ weight\ of\ sample, kg$
W $Final\ weight\ of\ sample, kg$

2.2 Hot Air Drying of Jatropha Curcas Seeds

A sample of Jatropha Curcas seeds (husk removed) of weight W_0 is placed in the hot air oven. The temperature is set at 50 °C. The seeds are dried until it reaches a moisture ratio of 0.10 ± 0.005 (kg water/kg dry matter). The relationship between the moisture ratio, *MR* and the moisture content of the sample is shown in Eq. (2). The sample is weighed every 15 minutes

to determine the changes in moisture ratio with time. The samples are removed when the sample reaches moisture ratio of 0.10 ± 0.005 (kg water/kg dry matter).

$$MR = \frac{M - M_f}{W_f} \quad (2)$$

Whereby;
M_f Final moisture content
M Initial Moisture Content
W_f Bone dry weight of the seeds
This process is repeated for temperatures of 75°C and 105°C

2.3 Preparation of Jatropha curcas seed extract powder (JP) from Jatropha seed extract liquid (JL).

The standard preparation method involves blending 20 g of finely ground Jatropha seeds with 100ml of distilled water using a simple food processor. The blending time is 2 minutes for complete extraction of the active compound in the seeds that give coagulating effects. After blending, the suspension is filtered through muslin cloth and the filtrate solution is used as the resulting JL. To prevent effects of oxidation, pH changes, viscosity and coagulation due to prolonged storage, the liquid is placed in the freezer before freeze drying process.

To prepare JP using freeze drying method, a freeze dryer (Thermo Electron MODULYOD freeze dryer) is used. The samples are frozen in 50ml plastic tubes and placed inside the freeze drier. The samples are dried for 24 hours until a dry powder is formed.

2.4 Determining Water Activity of JP Samples

Water activity is measured using a water activity meter (AquaLab LITE, USA) at room temperature. The water activity meter is calibrated using distilled water. The JP samples are placed in a plastic dish used for the water activity meter. The dish is then placed inside the meter and reading can be obtained. The experiment is conducted in triplicates and an average value is obtained.

2.5 Coagulation Tests

Before jar tests are conducted, a stock solution of the synthetic wastewater is prepared. 10g of kaolin is mixed into 1000ml of distilled water. The mixture is mixed at 100rpm for 1 hour for complete dispersion of the kaolin particles. Then the stock solution is kept in a bottle and allowed to set for 24 hours for complete hydration of the kaolin particles [9], [18]. This stock solution is used to prepare water samples of varying turbidities for the coagulation tests. Turbidity is measured using a turbidity meter (Eutech Instruments,USA). It is calibrated using samples of varying turbidities.

To prepare the coagulant, the JP will need to be rehydrated using distilled water. 5g of JP is mixed with 100ml of distilled water. This preparation will yield 50mg/L dosage. To control the dosage of coagulant, Eq. (3) is used.

$$C_1 V_1 = C_2 V_2 \quad (3)$$

Whereby:
C_1 $Coagulant\ dosage$

V_1 $Volume\ of\ water$
C_2 $Desired\ concentration$
V_2 $Volume\ of\ Coagulant$

On top of that, pH of the wastewater is controlled using 1M HCl and 1M NaOH. A pH meter is used to detect the pH of the wastewater while buffer solution is added to achieve desired pH.

2.5.1 Effect of Coagulant Dosage on Turbidity Removal

Jar tests are carried out to determine the concentration of waste in wastewater before and after coagulation. The synthetic waste water being tested for is kaolin suspension in distilled water. To study the effect of coagulant dosage, the pH is kept at 3 and the initial turbidity is kept constant at 500NTU. 3 different dosages, 50mg/L , 250mg/L and 500mg/L are used to treat the wastewater [9], [18]. The coagulation is carried out in a jar floc test (JLT 6 Velp Scientifica, Italy). The flocculator is set at 100rpm for 4 minutes. Once the water is being mixed, the coagulant is added. After 4 minutes, the wastewater is allowed to set for the waste particles to set at the bottom. The wastewater is then filtered using a muslin cloth to remove the sediments. After that, the clarified water is measured for its turbidity. The turbidity removal for each sample is recorded. The experiment is conducted in triplicates and an average value is obtained.

2.5.2 Effect of Wastewater pH on Turbidity Removal

To study the effect of pH, the coagulant dosage is kept at 500 mg/L and the initial turbidity is kept constant at 500NTU. Wastewater at 3 different pH, 3, 7 and 11 are prepared [9], [18]. The coagulation is carried out in a jar floc test (JLT 6 Velp Scientifica, Italy). The flocculator is set at 100rpm for 4 minutes. Once the water is being mixed, the coagulant is added. After 4 minutes, the wastewater is allowed to set for the waste particles to set at the bottom. The wastewater is then filtered using a muslin cloth to remove the sediments. After that, the clarified water is measured for its turbidity. The turbidity removal for each sample is recorded. The experiment is conducted in triplicates and an average value is obtained.

2.5.3 Effect of Initial Turbidity on Turbidity Removal

To study the effect of initial turbidity, the pH is kept at 3 and the coagulant dosage is kept constant at 500 mg/L. Waste water with 3 different initial turbidity, 200NTU, 500NTU and 800NTU prepared [9], [18]. The coagulation is carried out in a jar floc test (JLT 6 Velp Scientifica, Italy). The flocculator is set at 100rpm for 4 minutes. Once the water is being mixed, the coagulant is added. After 4 minutes, the wastewater is allowed to set for the waste particles to set at the bottom. The wastewater is then filtered using a muslin cloth to remove the sediments. After that, the clarified water is measured for its turbidity. The turbidity removal for each sample is recorded. The experiment is conducted in triplicates and an average value is obtained.

2.6 Storage of JP

When not used, the JP samples are stored in vacuum sealed plastic bags and placed in a cool area away from direct sunlight. This is to prevent the oxidative effects of the moisture from air from degrading the coagulant powder.

3.0 Results and Discussion

3.1 Drying Kinetics of Jatropha Curcas Seeds

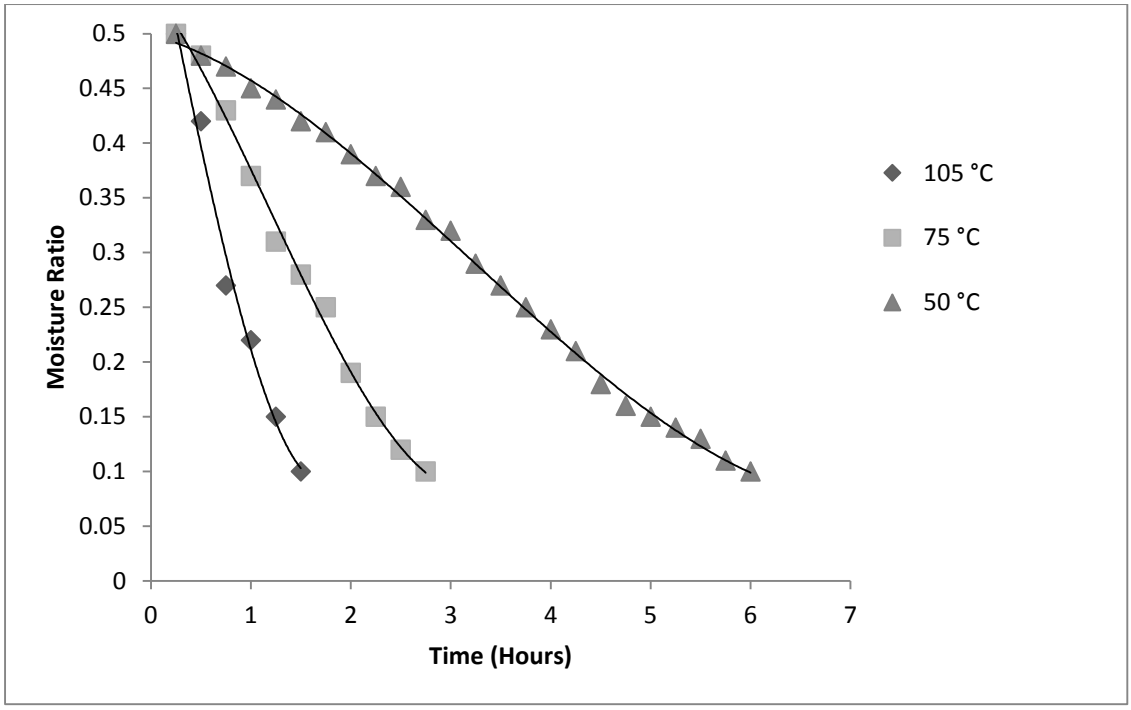


Figure 1: Moisture Ratio change with time

Before freeze drying is conducted, the *Jatropha* seeds undergo hot air drying at 3 different temperatures. The objective of the hot air drying is to reduce the moisture content of the seeds to 0.10 ± 0.005 (kg water/kg dry matter) moisture ratios. This method can increase the protein extraction in order to produce the coagulant [19],[20],[21]. Reduction of seed moisture is a complex process which involves mass and heat transfer. From an economic standpoint, a higher drying temperature gives a faster drying rate to the desired moisture content as depicted in figure 1. When the temperature is at 105°C, the time taken to reduce the moisture ratio from 0.50 ± 0.005 (kg water/kg dry matter) to 0.10 ± 0.005 (kg water/kg dry matter) is significantly shorter at 1.5 hours compared to at 50 °C which requires 6 hours. It can be said that 105 °C is the optimum temperature to reduce the moisture content of the seeds for 1.5 hours for large scale manufacturing of *Jatropha Curcas* powder. The temperature of 105 °C shall not be exceeded as the temperature higher than 130°C can lead to mailard reactions or in other words, burn the sample [22]. On the other hand, temperatures lower than 50°C will not dry the fresh seeds to the desired moisture content. This is because the seeds will be in equilibrium moisture content with the surroundings with no nett transfer of moisture in and out of the seeds. The effect of the temperature on the coagulant performance will be explained in the coagulation tests section

3.2 Water Activity

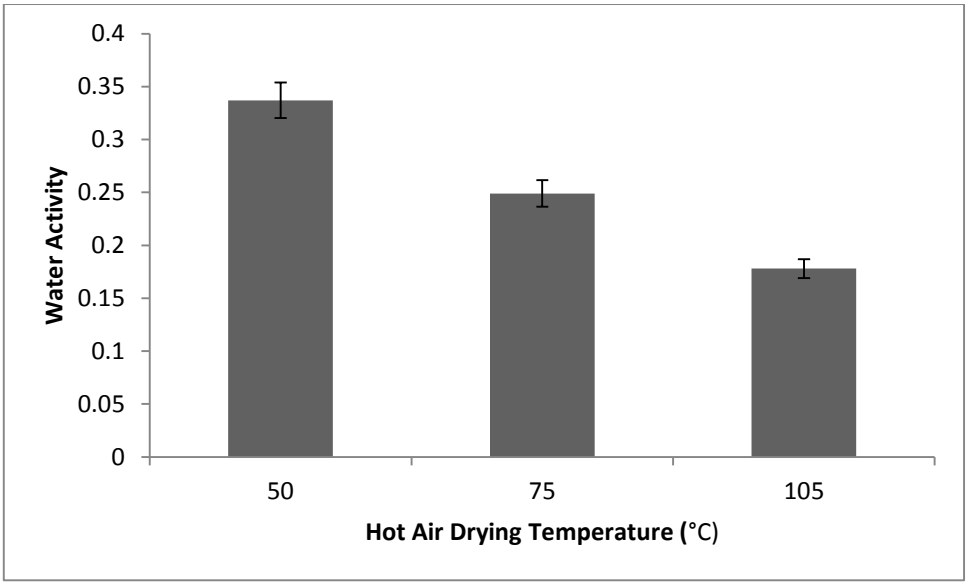


Figure 2. Comparison between Hot Air Drying Temperature and Water Activity

The water activity, a_w values for all samples are below 0.7. This shows that there will be no bacterial activity in the freeze dried JP. However as shown in figure 1, there is a correlation between the temperature and the water activity. When the sample is dried at a higher temperature, the resulting a_w is lower. This is due to the higher temperature drawing out more moisture from the seeds. However the difference in water activity as shown in figure 2 is negligible as they are all below 0.7 which is the threshold for bacterial growth [17], [23].

3.3 Coagulation Tests

3.3.1 Effect of Coagulant Dosage on Turbidity Removal

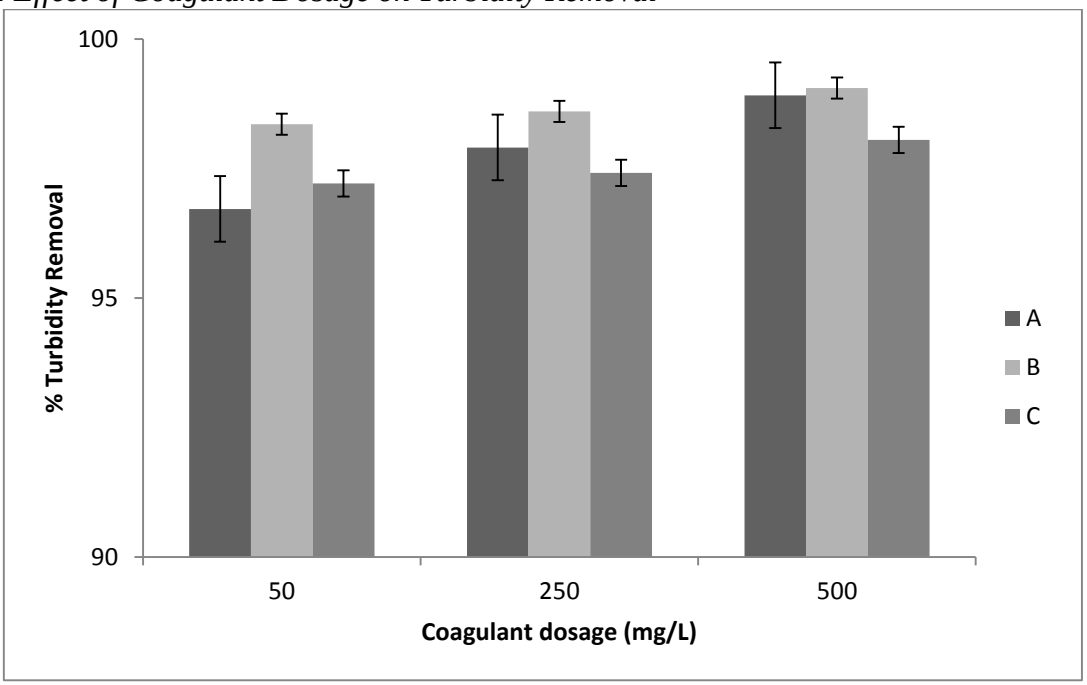


Figure 3. Relationship between coagulant dosage and turbidity removal

In studying the effect of dosage, the pH of each test is set at 3 while the initial turbidity is set at 500 NTU. The dosages were varied from 50 mg/L to 500mg/L. The 3 dosages from all 3 samples yielded above 97% turbidity removal as shown in figure 3. However the best dosage

for the removal of turbidity is 500mg/L from the sample dried at 75°C at 99.1%. It is also observed that at higher dosage, the formation of flocs were faster. This is due to the higher content of coagulant that present during the flocculation. It is observed that the hot air drying temperature has negligible effect on the performance of the coagulant. Comparing the use of this coagulant in powder form to its original liquid without freeze drying, the turbidity removals are almost identical. However when compared to using alum, the volume of sludge produced was considerably lower. Since JP is derived from a plant, it is biodegradable, and thus offer a more environmental friendly alternative to using alum [13].

3.3.2 Effect of Wastewater pH on Turbidity Removal

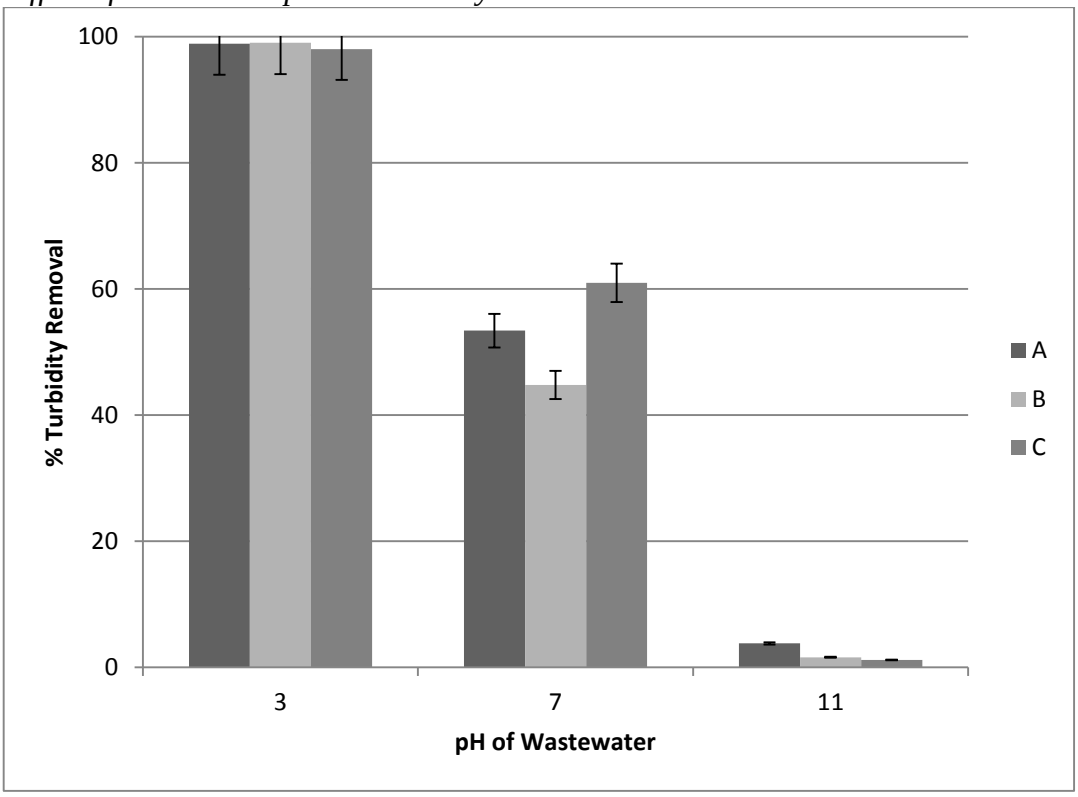


Figure 4. Effect of pH on Turbidity removal

As can be seen in figure 4 the turbidity removal is highest when the wastewater is acidic in nature. At pH 3, the turbidity removals were above 98%. This is because at this pH, the presence of H^+ ions in the acidic wastewater contains positive charges. The protein molecules of the *Jatropha* seed extract now has positive charges that make up the molecule that is in excess [19]. The protein works well as a cationic coagulant agent that brings together negatively charged colloids that repel one another [2].

At pH 7, the wastewater is neutral. The turbidity removal ranges between 44.8 to 61%. At this pH, there is a mixture of positive and negative charged ions. This can hinder the performance of the coagulant given that the protein has a reduced net cationic capability [9]. This reduces the amount of positive charges used to neutralise the negative charge between the colloids and thus reduces turbidity removal.

At pH 11, the wastewater is rich in. It is now filled with negatively charged ions. Therefore above pH 11, the positively charges is most likely to interact with the OH^- ions [19]. This greatly reduces the cationic capability of the coagulant which is responsible in turbidity removal. It can be said that Jatropha works well as a coagulant under highly acidic mediums. However, the hot air drying temperature did not seem to have an effect on the performance of the coagulant for this case.

3.3.3 Effect of Initial Turbidity on Turbidity Removal

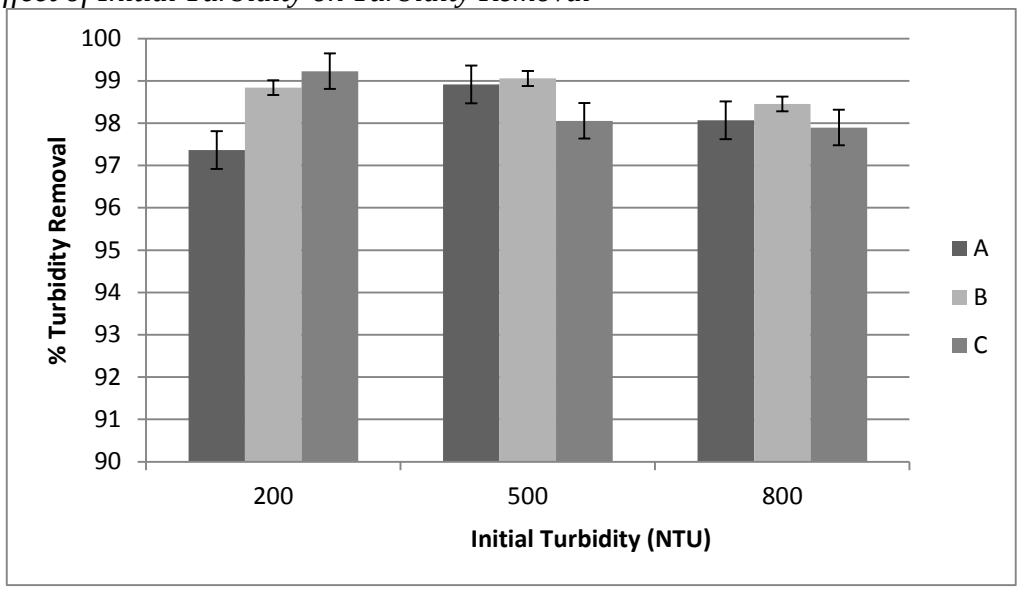


Figure 5. Effect of initial turbidity on turbidity removal

The initial turbidities of the kaolin wastewater sample are varied between 200-800 NTU. For this experiment, the pH is set at 3 and dosage is set at 500 mg/L (best dosage from previous experiment). Figure 5 shows the turbidity removals for samples of kaolin wastewater with different initial turbidities. It can be seen that the turbidity removal increases when the turbidity is at 500NTU and then decreases slightly when at 800NTU. However, the difference is negligible as the turbidity removal across all samples is above 97%. The highest turbidity removal recorded is 99.2%. This suggests that *Jatropha Curcas* is suitable for treating wastewater with large range of turbidity. Furthermore, the hot air drying temperature did not have an effect on the performance of the coagulant in terms of turbidity removal.

4. Conclusion

It can be concluded that *Jatropha curcas* seeds extract in powder form can be synthesized using hot air and freeze drying methods. The resulting product has good coagulation properties in turbidity removal. Moreover, the water activity for all samples is well below the 0.7 threshold. This shows that the product has a good shelf life with low bacterial activity. The best performance can be seen using 500mg/L of coagulant dosage manufactured at 75°C. The coagulant works best at highly acidic wastewaters as the nature of the charges on the amino acid profile is positive charge. The medium will need to be highly acidic in order for the amino acids to provide a cationic capacity to neutralise the charges between the pollutant particles. Besides that, the coagulant is shown to be able to treat water at wide range of turbidities. For the hot air drying, the temperature 105°C can be selected for a faster drying rate and economic reasons. In the coagulation tests, the hot air drying temperatures did not show to have an effect on the coagulant performance in terms of pollutant removal. The sludge produced from the coagulation process is of biodegradable material and therefore offers a more environmental friendly alternative in wastewater treatment technologies.

References

[1] E. H. Mohamed, T. A. Mohammad, M. J. Megat, M. Noor, and A. H. Ghazali, “Influence of extraction and freeze-drying durations on the effectiveness of Moringa oleifera seeds powder as a natural coagulant,” vol. 3994, no. October, 2015.

[2] a Koohestanian, M. Hosseini, and Z. Abbasian, “The Separation Method for Removing

of Colloidal Particles from Raw Water," *Euras. J. Agric. Environ. Sci*, vol. 4, no. 2, pp. 266–273, 2008.

[3] S. Gaffney Jeffrey, A. Marley Nancy, and B. Clark Sue, "Humic and Fulvic Acids and Organic Colloidal Materials in the Environment," *Humic and Fulvic Acids*, vol. 651, no. 651, pp. 2–16, 1996.

[4] Woodard & Curran Inc., *Industrial Waste Treatment Handbook*. 2006.

[5] J. Haarhoff and J. L. Cleasby, "COMPARING ALUMINUM AND IRON COAGULANTS FOR IN-LINE FILTRATION OF COLD WATER.," *J. / Am. Water Work. Assoc.*, vol. 80, no. 4, pp. 168–175, 1988.

[6] K. P. Y. Shak and T. Y. Wu, "Coagulation-flocculation treatment of high-strength agro-industrial wastewater using natural Cassia obtusifolia seed gum: Treatment efficiencies and flocs characterization," *Chem. Eng. J.*, vol. 256, pp. 293–305, 2014.

[7] D. V. Kuki??, M. B. ????iban, J. M. Prodanovi??, A. N. Tepi??, and M. A. Vasi??, "Extracts of fava bean (Vicia faba L.) seeds as natural coagulants," *Ecol. Eng.*, vol. 84, pp. 229–232, 2015.

[8] C. Y. Yin, "Emerging usage of plant-based coagulants for water and wastewater treatment," *Process Biochemistry*, vol. 45, no. 9. pp. 1437–1444, 2010.

[9] Z. Z. Abidin, N. Ismail, R. Yunus, I. S. Ahamad, and a Idris, "A preliminary study on Jatropha curcas as coagulant in wastewater treatment.," *Environ. Technol.*, vol. 32, no. 9–10, pp. 971–977, 2011.

[10] B. Ramavandi, "Treatment of water turbidity and bacteria by using a coagulant extracted from Plantago ovata," *Water Resour. Ind.*, vol. 6, pp. 36–50, 2014.

[11] S. Katayon, M. J. M. M. Noor, M. Asma, L. A. A. Ghani, A. M. Thamer, I. Azni, J. Ahmad, B. C. Khor, and A. M. Suleyman, "Effects of storage conditions of Moringa oleifera seeds on its performance in coagulation," *Bioresour. Technol.*, vol. 97, no. 13, pp. 1455–1460, 2006.

[12] F. K. Amagloh and A. Benang, "Effectiveness of Moringa oleifera seed as coagulant for water purification," *African J. Agric. Res.*, vol. 4, no. 2, pp. 119–123, 2009.

[13] S. a Muyibi, H. M. Salleh, M. R. M. Salleh, and J. Gombak, "Moringa Oleifera Seeds As Natural Coagulant for Water Treatment," *Water Technol.*, vol. 13, no. coagulacion de aguas residuales, pp. 163–168, 2009.

[14] I. Dincer, M. M. Hussain, A. Z. Sahin, and B. S. Yilbas, "Development of a new moisture transfer (Bi-Re) correlation for food drying applications," *Int. J. Heat Mass Transf.*, vol. 45, no. 8, pp. 1749–1755, 2002.

[15] V. C. Siqueira and O. Resende, "Drying kinetics of Jatropha seeds 1," pp. 171–177, 2012.

[16] G. Broeckx, D. Vandenheuvel, I. J. J. Claes, S. Lebeer, and F. Kiekens, "Drying techniques of probiotic bacteria as an important step towards the development of novel pharmabiotics," *International Journal of Pharmaceutics*, vol. 505, no. 1–2. pp. 303–318, 2016.

[17] L. B. Rockland and S. K. Nishi, "Influence of water activity on food product quality and stability," *Food Technol.*, vol. 34, pp. 42–59, 1980.

[18] Z. Z. Abidin, N. S. Mohd Shamsudin, N. Madehi, and S. Sobri, "Optimisation of a method to extract the active coagulant agent from Jatropha curcas seeds for use in turbidity removal," *Ind. Crops Prod.*, vol. 41, no. 1, pp. 319–323, 2013.

[19] I. Food, "Quality assessment profile of Jatropha curcas (L) seed oil from Nigeria," vol. 21, no. 2, pp. 735–741, 2014.

[20] L. Seremet, E. Botez, O. V. Nistor, D. G. Andronoiu, and G. D. Mocanu, "Effect of different drying methods on moisture ratio and rehydration of pumpkin slices," *Food Chem.*, vol. 195, pp. 104–109, 2016.

[21] "EFFECT OF HEAT AND ALKALINE HYDROLYSIS ON THE AMINO ACID," vol. 14, no. 2, pp. 1–13, 2014.

[22] S. Nie, J. Huang, J. Hu, Y. Zhang, S. Wang, C. Li, and M. Xie, "Effect of pH , temperature and heating time on the formation of furan in sugar – glycine model systems," *Food Sci. Hum. Wellness*, vol. 2, no. 2, pp. 87–92, 2013.

[23] R. S. Reddy, C. T. Ramachandra, S. Hiregoudar, U. Nidoni, J. Ram, and M. Kammar, "Influence of processing conditions on functional and reconstitution properties of milk powder made from Osmanabadi goat milk by spray drying," *Small Rumin. Res.*, vol. 119, no. 1–3, pp. 130–137, 2014.

Release Behaviour Study on Controlled-Release P-Fertilizer Encapsulated by Starch-Alginate Superabsorbent Composite

Jia Yee Low[1*], Siew Wei Phang[1, 2*]

[1]School of Engineering, *Taylor's University Lakeside Campus, Malaysia*
[2]Department of Chemical Engineering. Faculty of Engineering and Science, University Tunku Abdul Rahman, Kuala Lumpur, Malaysia

Corresponding author email: SiewWei.Phang@taylors.edu.my

Abstract
Controlled-release fertilizer is used as a promising green technology in preventing excessive application and leaching into undesired places. A hydrogel is a polymer matrix that is able to hold water and release its active ingredient at a controlled pace. This work presents the release behaviour study on the encapsulation of starch and sodium alginate on diammonium hydrogen phosphate (phosphorous) fertilizer using calcium chloride as an effective crosslinker agent. The FTIR peaks showed the successful interaction between O-H stretching bonds in starch with COO^- in alginate. Furthermore, the peak at 3430cm^{-1} verified that crosslinking action was successfully employed. At the same time, the phosphate group was successfully retained in its own form. The amount of phosphorous released into distilled water was measured using HPLC with a mobile phase of water and methanol in the ratio of 80:20 v/v% and a wavelength of 240nm for phosphate compound to be detected. The swelling and dissolution study of hydrogel was carried out using the weighing technique. Microscopy images at magnification of 40X verified that calcium chloride was able to improve the surface morphology of the hydrogel. TGA results of the controlled-release fertilizer showed that hydrogel with high $CaCl_2$ content has low thermal stability. The variation of calcium chloride content showed a more stable trend in release rate, swelling and dissolution in comparison to the variation of starch and alginate. Formulation S13 showed optimum results whereby it released 7wt% phosphorous into distilled water after 30 days with 40% swelling and 80% dissolution. Therefore, it was concluded that the main effect is $CaCl_2$ and sample S13 (12 wt% St, 1 wt% Alg, 3.5M $CaCl_2$) produces the best controlled-release fertilizer.

Keywords: Controlled-release, Hydrogel, Swelling, Starch-Alginate, Phosphorous

1. Introduction

In the agricultural industry, phosphorous is important for the production of nucleotides in plants [1]. One of the main challenges is the loss of nutrient elements resulting in the inefficiency of plant nutrients uptake due to excessive application. Subsequently, phosphorous based fertilizers is the primary cause of excessive algae growth in lakes and rivers which can negatively impact the environment [1]. The formulation of controlled release fertilizers has been vastly used to resolve this challenge whereby nutrients are released at a controlled pace through a polymer matrix for maximum utilization by plants [1]. A polymer hydrogel is a three-dimensional polymeric network having large water retention property that is able to swell without dissolving in water [1]. Thus, the right formulation will produce a controlled release of fertilizer out of the polymer matrix. Therefore, the material of the controlled-release formulation is the key in solving this challenge.

Controlled release formulation has been investigated over the past 50 years to determine the compatibility of various encapsulation materials for fertilizers. There are three broad categories for these formulations which are organic, inorganic and superabsorbent material [2]. More recently, the use of superabsorbent composite is found to be more favorable due to its low cost and biodegradability, hence this is the main research area [2]. A conventional fertilizer without controlled-release formulation gave a full release after 2 days as tested by Y.H. Liu et al [3]. However, R. Liang et al. [4] tested wheat straw as a superabsorbent material which shows a full release after 5 days. A. Rashidzadeh et al. [5] reviewed the formulation of sodium alginate and montmorillonite which showed a more controlled release rate after 60 days. A similar trend was showed by Y. Cao et al. [6] whereby starch matrix was used to coat pesticide and successfully showed a full release of active ingredient after 60 days. In agreement, superabsorbent materials gained high attention in the controlled-release formulation especially starch due to its excellent water retention properties.

However, starch based formulation has a high potential to burst due to high water absorbency. Therefore, researchers are trying to improve the polymer matrix of controlled release fertilizer through addition of another material. A. Roy et al. [7] continued this work by adding alginate to starch using calcium chloride as the cross-linking agent. The combination has reduced the release rate of pesticide by 30%. A similar trend was shown by B. Singh et al. [8] whereby the release rate is further reduced by 35%. This justifies that these superabsorbent composites have the potential to reduce the release rate of encapsulated ingredient. Sodium alginate is a type of copolymer known to be able to hold the matrix together due to its good gelation property [8]. Furthermore, the molecular structure and porosity of the polymer is enhanced by calcium chloride as a crosslinking agent [8].

There are several ways to synthesize controlled release fertilizer such as the coating, extrusion and encapsulation method. It is more economical to use the encapsulation method whereby the active ingredient is loaded into the superabsorbent material to form hydrogel beads [8]. Due to the research findings which demonstrated the good properties of starch, sodium alginate and calcium chloride, it is worth the investigation. The application of these superabsorbent materials were only tested on several active ingredients such as urea, pesticide and fungicide. However, there are currently no research on the application of these materials for phosphorous fertilizer.

Nevertheless, the objective of this project is to study the effect of each material variation on phosphorous release rate for a total of 13 formulations. The project scope includes the release behaviour study which covers the mechanism of swelling, dissolution as well as the

diffusion of phosphorous into distilled water. Physical characterization was also carried out to justify the release behaviour of each formulation.

2. Research Methodology

2.1 Material Specifications

Pharmaceutical grade of sodium alginate (99% purity), anhydrous calcium chloride (93% purity) and diammonium hydrogen phosphate (99.99% purity) were purchased from Sigma-Aldrich Corporation, USA whereas pure cassava starch (99.9% purity, food grade) was purchased from Aeon Supermarket, Malaysia.

2.2 Synthesis of Starch-Alginate Hydrogel Beads

The synthesis method followed the methodology of B. Singh et al. [9, 10]. There are a total of 13 samples under three sets of formulation consisting of variation of starch, sodium alginate and calcium chloride as shown in Table 1. These components were mixed in 100 ml distilled water with constant amount of phosphorous at 5 w/v%. The chemicals were constantly mixed using a hot plate (Thermo Scientific MSH-300, Malaysia) and a magnetic bar stirrer at a temperature of 40°C with stirring speed of 600RPM for 15 – 30 minutes until homogeneity is reached. Cross-linking solution was prepared by dissolving calcium chloride into 100ml of water. This was followed by the dripping of starch-alginate-phosphorous mixture using a 1.2mm diameter syringe into calcium chloride solution for crosslinking action to occur. The hydrogels were then rinsed with distilled water, filtered using 200-mesh stainless steel sphere-shaped net. Then they were dried using tissue paper to remove excess calcium chloride. The beads were dried using microwave oven (Electrolux EMM 1908S, Malaysia) at a temperature of 80°C for 24 hours to provide thermal stability. The dried samples were retrieved from the oven, cooled and stored in bottles sealed with parafilm to prevent moisture.

Table 1. Controlled-release Formulations

Material Variation	Sample	Cassava Starch (w/v) %	Sodium Alginate (w/v) %	Calcium Chloride (M)
Starch	**S1**	3	1	1.5
	S2	6	1	1.5
	S3	9	1	1.5
	S4	12	1	1.5
	S5	15	1	1.5
Sodium Alginate	**S6**	12	0.5	1.5
	S7	12	1.5	1.5
	S8	12	2	1.5
	S9	12	2.5	1.5
Calcium Chloride	**S10**	12	1	2.0
	S11	12	1	2.5
	S12	12	1	3.0
	S13	12	1	3.5

2.3 Fourier Transform Infrared (FTIR)

Fourier Transform Infrared Spectrometer (FTIR Spectrum 100, Perkin Elmer) was used to identify the functional groups of materials used in sample synthesis. Attenuated Total Reflectance (ATR) sampling method was employed with a total of 16 scans under the operating range of 4000 – 650 cm^{-1}.

2.4 Thermogravimetric Analyzer (TGA)

Thermogravimetric Analyzer (TGA 8000, Perkin Elmer) was carried out over a temperature range of 30 – 700°C with a constant heating rate of 20°C/min under nitrogen atmosphere to determine the thermal degradation of the beads.

2.5 Digital Microscope

The surface morphology was visually analyzed using a digital microscope (M10DB-MP, Motic) under a magnification of 40X.

2.6 High Performance Liquid Chromatography (HPLC)

The amount of phosphate released into distilled water was determined through the calibration curve of known concentration of pure phosphate. This was carried out using High Performance Liquid Chromatography (1220 Infinity LC, Agilent Technologies Co.). The mobile phase used consists methanol and water in the ratio of 20:80 v/v. The separation of phosphate group was carried out at a flow rate of 1.0 ml/min on Zorbax Extend-C18 column. The column temperature was set at 30°C with an auto-sampler injection volume of 25 µL. The detection wavelength of Bisep^{TM} – 1100 UV/Vis detector was set at 254nm for phosphate to be detected.

2.7 Release Behaviour Study on Controlled-Release P-Fertilizer

The swelling study consists of setting the initial weight (W_o) of the beads at 5g which was immersed into 100 ml of distilled water over a fixed interval of time (1h, 2h, 4h, 6h, 1 day, 2 days, 7 days, 14 days, 21 days and 30 days) under static conditions and room temperature of 25°C. The swollen weight of the hydrogels were measured at W_{wet} and the swelling percentage was calculated using Eq. (1) by A. Senna et al. [18] as shown below:

$$Swelling\ \% = \frac{W_{wet} - W_o}{W_o}\ x\ 100\% \quad (1)$$

For the dissolution study, the swollen beads were dried using oven under the same temperature of 80°C for 24 hours where the new dried weight was recorded as W_{Dry}. Thus, the dissolution can be determined using Eq. (2) from A. Roy et al. [7] as shown in the following:

$$Dissolution\ \% = \frac{W_o - W_{Dry}}{W_o}\ x\ 100\% \quad (2)$$

3. Results and Discussions

3.1 Material Characterization

3.1.1 Physical shape

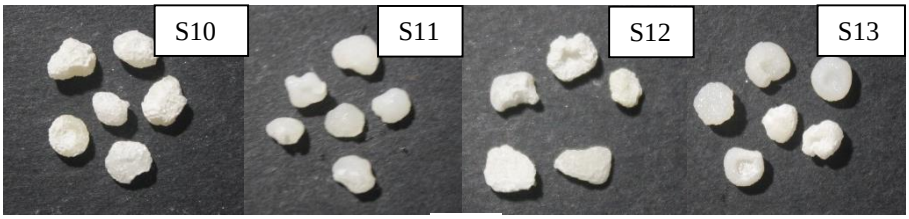
The physical shape of the beads varies with different formulation. The variation of starch content from 3wt% to 15wt% as shown in Fig. 1a demonstrates that starch is responsible for the spherical shape of the hydrogel bead. This is because starch acts as a polymer filler in this formulation. On the other hand, the variation of sodium alginate composition from 0.5wt% to 2.5wt% displays a significant difference in the shape. It is evident from Fig. 1b that viscosity increases due to higher amount of sodium alginate, thus forming tear-drop shape during sample synthesis. Fig. 1c shows that increasing calcium chloride from 2.0M to 3.5M produces convex-shaped beads. The difference in shape was suggested by G. Lozano et al. [17] that an appropriate balance in the formulation is necessary for a more closely packed arrangement to form uniform beads.



(a)



(b)



(c)

Figure 1. Physical images of (a) starch variation, (b) sodium alginate variation and (c) calcium chloride variation

3.1.2 Microscopic morphology

The surface morphologies of the samples were observed using a microscope under a magnification of 40X as shown in Fig. 2. It can be seen from Fig. 2a that the hydrogel surface has a highly porous network with poor mechanical integrity. The porosity of the surface improves with increasing content of calcium chloride as evident from Fig. 2b and Fig.2c. This can be explained through the crosslinking effect whereby the bivalent calcium ion from the $CaCl_2$ is necessary for the formation of tighter cavity network. Therefore, the mesh size of the polymeric hydrogels are reduced as shown in Fig. 2d with highest $CaCl_2$. Similar result was reported by H. Essawy et al. [11].

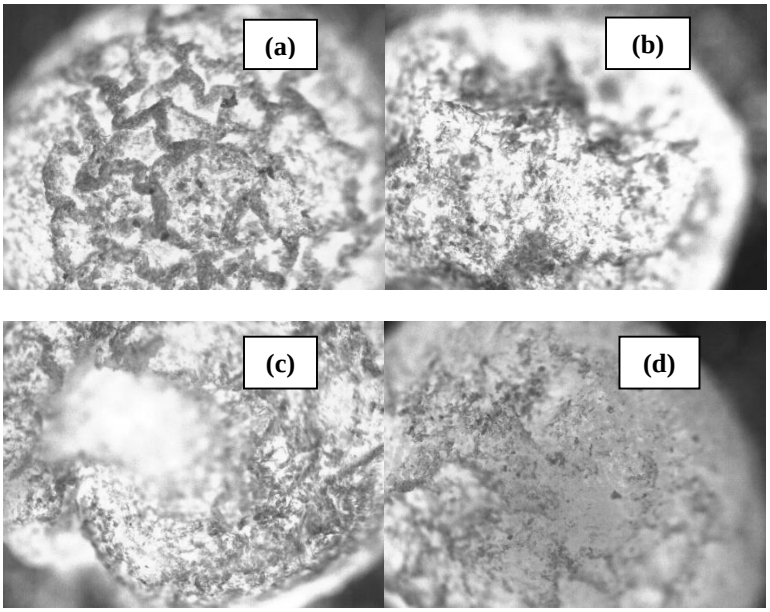


Figure 2. Microscopic images (X40 magnification) for samples with calcium chloride variation: (a) 2.0M, S10 (b) 2.5M, S11 (c) 3.0M, S12 (d) 3.5M, S13

3.1.3 FTIR analyses

FTIR has been used to ensure that the functional group of phosphate remains unchanged as well as to study the interactions between polymer and crosslinking agent. Fig. 3a demonstrates the spectra of pure alginate microparticles whereby the characteristic absorption bands are found at 3430cm^{-1} due to the presence of O-H stretching vibrations, 2934cm^{-1} (C-H stretching vibrations), 1654cm^{-1} and 1464cm^{-1} (COO^- asymmetric stretching vibrations) and 1034cm^{-1} (C-O-C stretching vibration). The combination of starch and alginate caused a decrease in the wave number COO^- from 1464cm^{-1} to 1453cm^{-1}. For the phosphorous-loaded sample as shown by S4 in Fig. 3b, the peak at 1060cm^{-1} indicates the presence of asymmetric stretching vibrations of P-O. Thus, diammonium hydrogen phosphate is present in its own form and shows successful encapsulation within hydrogel. The results are in agreement with the findings regarding the loading of fertilizer into starch-alginate which has been reported by P. Stoch et al. [12]. Additionally, the hydroxyl peak shifted from 3430 to 3411cm^{-1} as seen from Fig. 3c, thus proving the interaction of St-Alg. Similar analysis has been reported by S. Hosseini et al. [13].

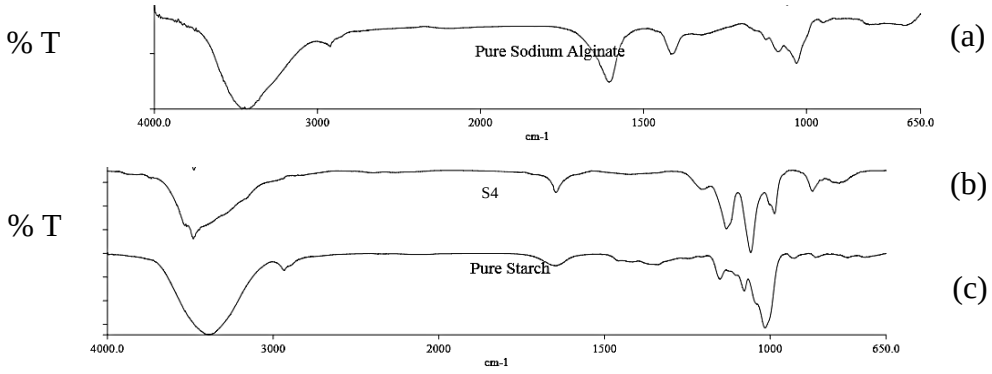


Figure 3. FTIR spectra of (a) Alg microparticles (b) phosphorous loaded Alg-St microparticles (c) and St microparticles

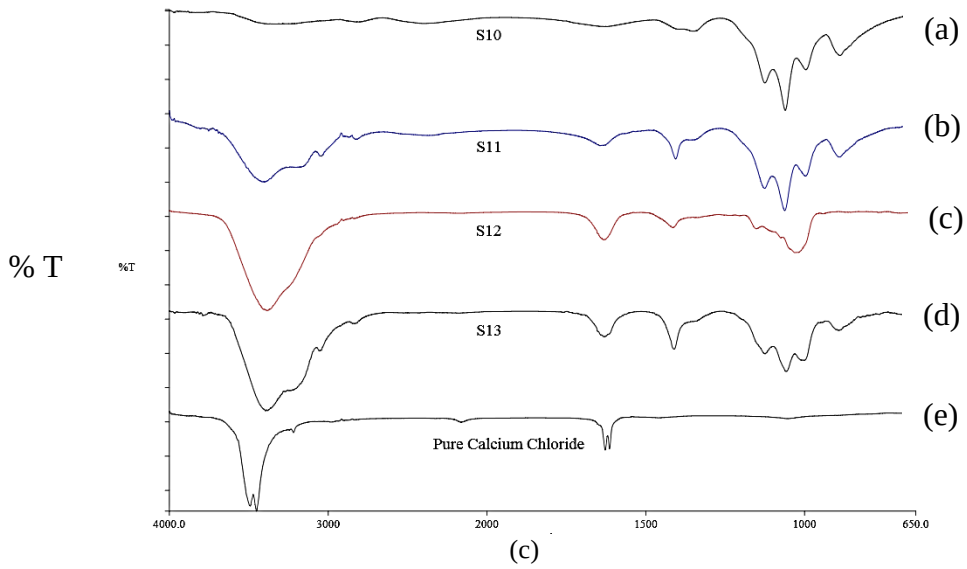


Figure 4. FTIR spectra of sample with $CaCl_2$ variation: (a) 2.0M $CaCl_2$ (b) 2.5M $CaCl_2$ (c) 3.0M $CaCl_2$ (d) 3.5M $CaCl_2$ (e) pure $CaCl_2$

Fig. 4 displays the change in chemical structure of the samples with increasing $CaCl_2$ content. The increasing intensity of the peak at 3430cm^{-1} shows that the crosslinking has been employed effectively. This shift was considered as an additional evidence in support of the crosslinker effect between starch and alginate microparticles as reported by L. Nnamonu [20]. Thus, the formulation with the highest $CaCl_2$ should be further studied to determine the main effect of controlled-release formulation.

3.1.4 Thermogravimetric analysis (TGA)

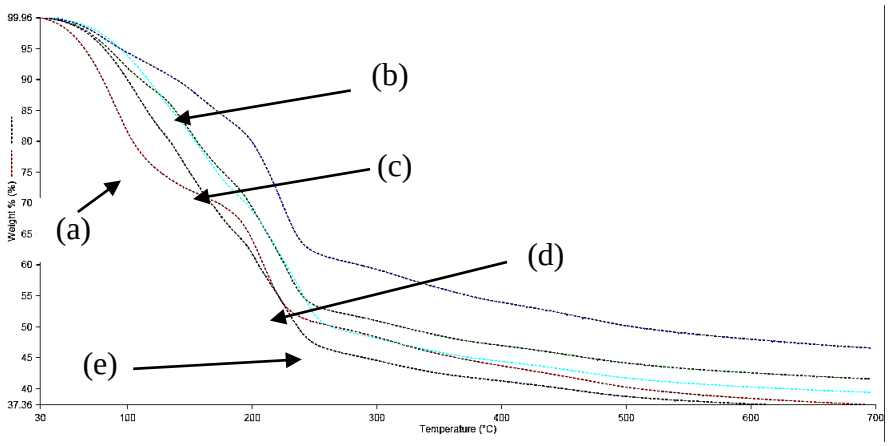


Figure 5. TGA curves for (a) S4, (b) S10, (c) S11, (d) S12, (e) S13

When biomaterial is subjected to high temperature, it usually decomposes into CO, CO_2, NO_x and H_2O. The TGA curves show a heating range of 30 to 700°C for superabsorbent material. The curve of sample S4 was used a standard for comparison as shown by Fig. 5a where its shape is similar to all the other curves except for Fig. 5e. At 700°C, the thermograms of St-Alg and St-Alg-Ca^{2+} have shown more than 38% residual matter, indicating char residue of carbohydrate polymer. The weight loss of St-Alg (Fig. 5a) is 45wt% at 250°C whereas St-Alg-Ca^{2+} (Fig. 5e) has a greater sample loss of 60wt% at the same temperature. This shows

that the thermal stability is better with higher purity of bicomposites in St-Alg in accordance to M. A. et al. [14]. The poor thermal stability of St-Alg-Ca^{2+} is due to higher $CaCl_2$ content, causing its breakdown as a whole crosslinked polymer group which no longer exists as a single component of $CaCl_2$. This indicates that it is worth the current investigation to find out more about the chemical properties of sample S13 in the release behaviour study.

3.2 Release Behaviour Studies

3.2.1 Release rate of phosphorous

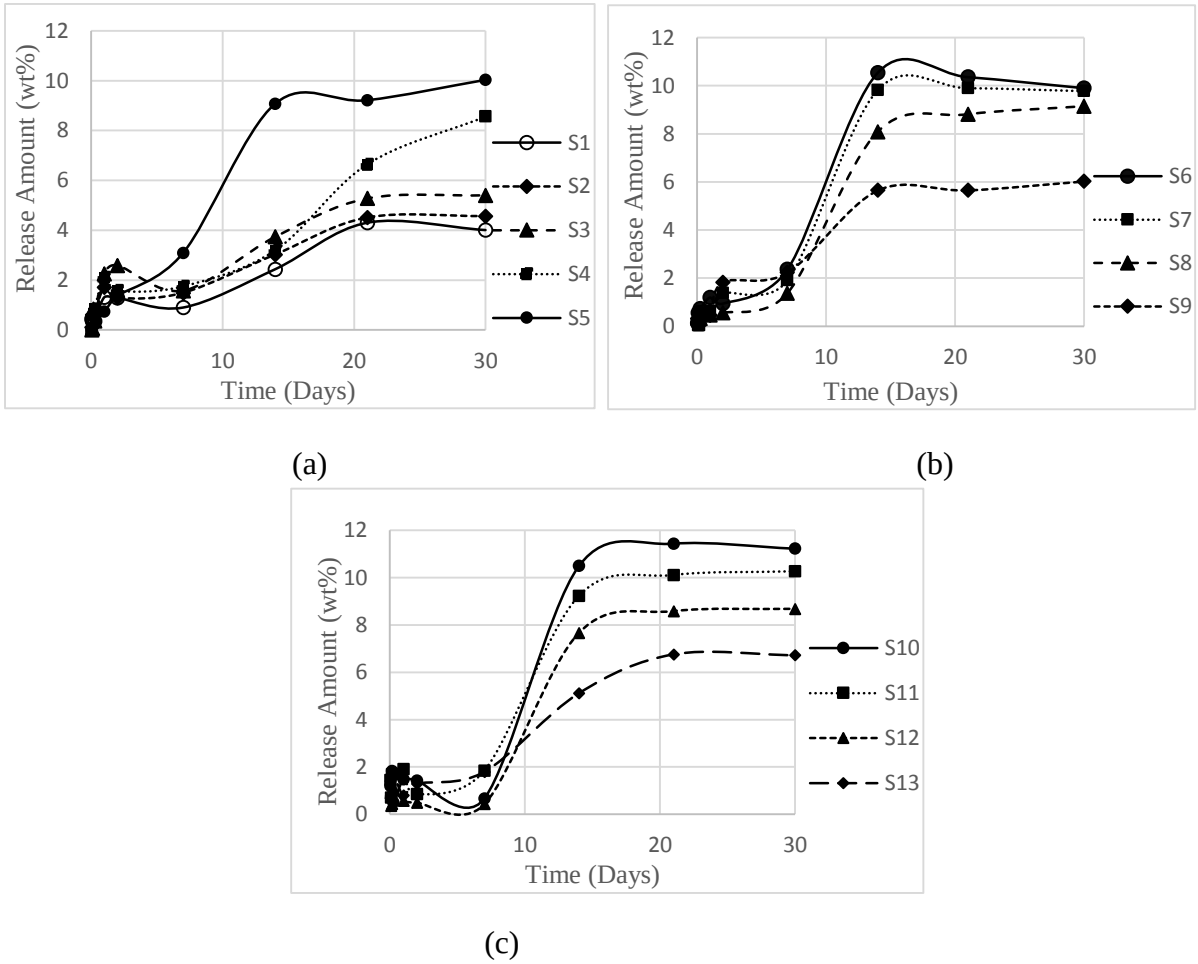


Figure 6. Release amount of phosphorous in wt% for samples: (a) S1 – S5 with starch variation (b) S6 – S9 with NaAlg variation (c) S10 – S13 with $CaCl_2$ variation

Fig. 6 shows a common trend whereby constant release of phosphorous started after 14 days for all graphs. The maximum release is 11wt% shown by S6 and S10 while the minimum is 4wt% by S1. However, no conclusion can be drawn from this as further evaluation needs to be done. Fig. 6a shows that the release rate increases with increasing starch content. Similar result was reported by A. Roy et al. [7] on the controlled-release of pesticide using St-Alg biocomposite whereby the same phenomena was caused by the increase in the hydrophilic nature of starch. At the same time, the non-ionic content of the hydrogel is reduced, thus the crosslinking of calcium chloride became underdeveloped. Therefore, the penetration rate of water into the hydrogel accelerated, causing a higher diffusion rate of phosphorous out of the matrix.

On a contrary, Fig. 6b shows that release rate decreases with increasing sodium alginate content. This is due to the greater polymer fraction which increases the encapsulation efficiency of the hydrogel bead. Thus, the path of diffusion in the matrix is increased as more COO^- from sodium alginate is able to crosslink with Ca^{2+} available in calcium chloride. B. Singh et al. [15] also described the same effect on testing with controlled-release thiram fungicide formulation.

Similarly, from Fig. 6c, the observation shows that the release of phosphorous was well controlled in a sustained manner with increasing calcium chloride content. The decelerated release can be explained due to better crosslinking and tighter cavity on the superabsorbent material as reported by [7, 15]. As an overall comparison among these graphs of release rate, Fig. 6c shows the most stable and gradual release rate with increasing material variation while Fig. 6a and Fig. 6b shows a more unsustain release rate. It is suggested that the main controlling parameter is the amount of crosslinking agent used in the synthesis. Therefore, the formulation of S13 has the potential to be used as agrochemical to solve leaching challenges and will be further evaluated using the swelling and dissolution studies to confirm the hypothesis.

3.2.2 Water absorption evaluation

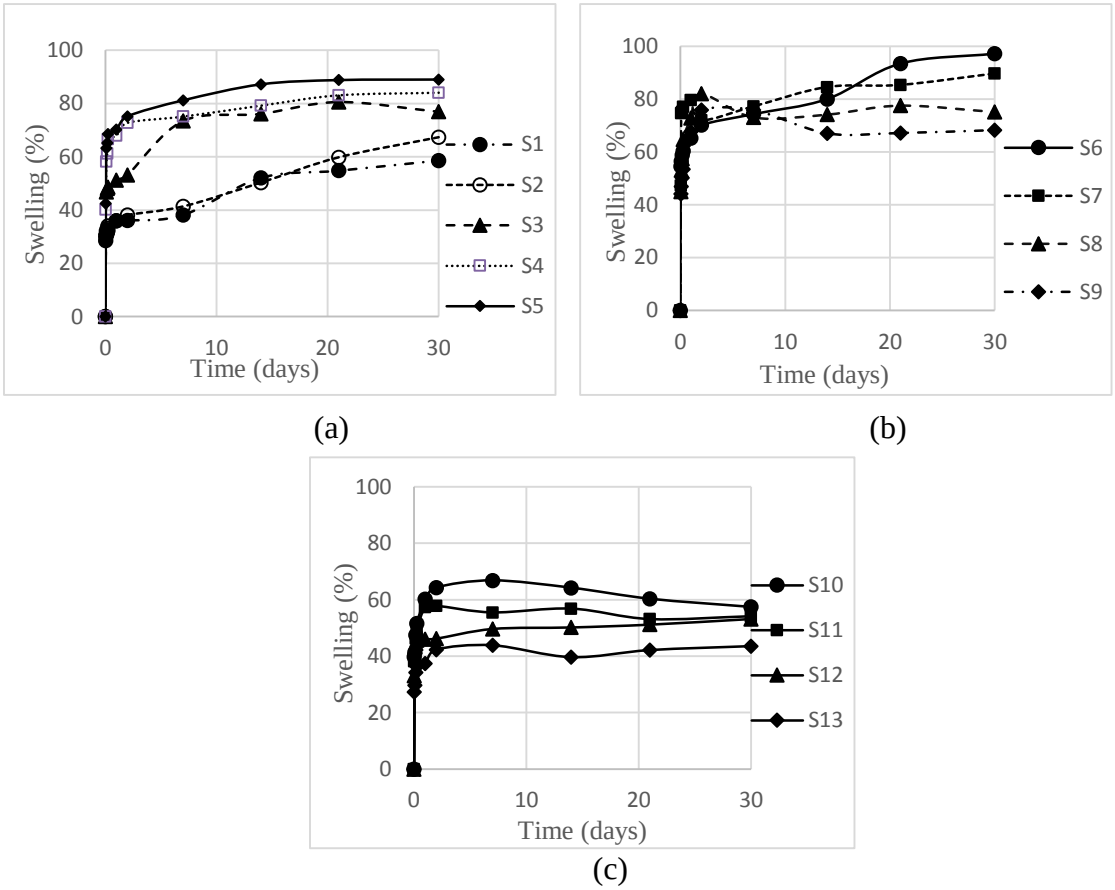


Figure 7. Swelling percentage (%) of hydrogel for samples: (a) S1 – S5 with starch variation (b) S6 – S9 with NaAlg variation (c) S10 – S13 with $CaCl_2$ variation

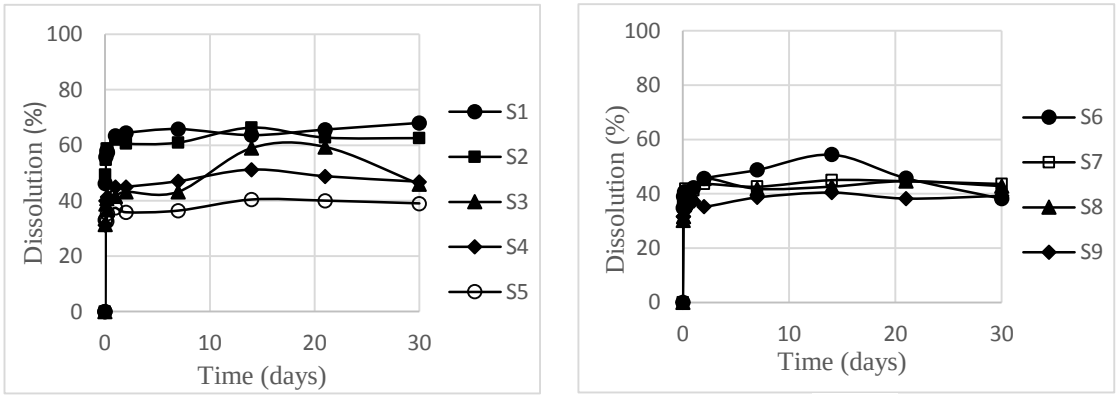
Based on Fig. 7, the graphs show constant swelling over 30 days where the trend is seen to be more volatile for Fig. 7a and Fig. 7b in comparison to a more stable swelling pattern in Fig. 7c. This is mainly due to the variation of material that affects the absorption efficiency by hydrogel beads. The swelling increases with increasing starch content as shown in Fig. 7a. Similar to the release rate trend discussed earlier, the hydrophilic property of starch allows formation of hydrogen bonds with water molecules. This phenomena has been verified by the

FTIR results showing O-H stretching alcoholic group of pure starch and S4 bead. Thus, the same observation has been reported by A. Roy et al. [7] proving the high water absorbency property of starch.

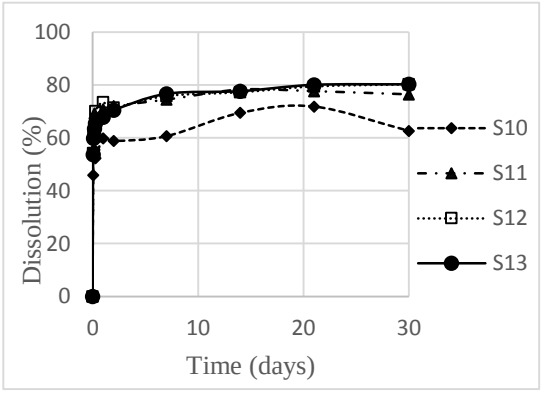
Increasing the sodium alginate content results in a drop of swelling as seen from Fig. 7b due to longer path of diffusion of molecules into and out of the polymeric matrix. The same reason supports the trend for the release of phosphorous previously mentioned during the study of release rate. Similar results were also justified by Z. Wu et al. [16] on controlled-release herb encapsulated by starch-alginate.

Similar to the trend of release rate in this paper, there is a decline in water absorbency from S10 – S13 as seen from Fig. 7c due to the increase of $CaCl_2$ content up to 3.0M $CaCl_2$. This causes the crosslinking density to increase, thus the network becomes more compact and reduces the penetration of water molecules into the hydrogel. This is in line with the reported results by [7, 15] using $CaCl_2$ as crosslinker.

3.2.3 Dissolution evaluation



(b)



(c)

Figure 8. Dissolution percentage (%) for samples: (a) S1 – S5 with starch variation (b) S6 – S9 with NaAlg variation (c) S10 – S13 with $CaCl_2$ variation

Opposing the release rate and swelling trends of controlled-release formulation, the dissolution of phosphorous within the matrix decreases with increasing starch and sodium alginate content as shown in Fig. 8a and Fig. 8b. This effect was reported by A. Roy et al. [7] whereby there are more intermolecular interactions between the starch and alginate molecules.

With this, the polymer matrix becomes more compact, thus hindering the water penetration. There is a high tendency for the hydroxyl group from starch and the carbonyl group from sodium alginate to form strong hydrogen bonds.

On contrary, the dissolution improves with increasing calcium chloride content as shown in Fig. 8c due to its high solubility property. The Ca^{2+} ion readily forms bond with the O-H group from water molecules, thus increasing the interaction for dissolution to occur. This is the same effect as testified by S. I. Ahmad et al. [18]. In addition, higher amount of $CaCl_2$ shows a more constant dissolution at a maximum of 80% exhibited by S13 over 30 days. This shows that S13 has good dissolving property of active ingredient within the hydrogel whereby 80% of the loaded fertilizer was able to be diffuse out of the polymer matrix. Therefore, formulation S13 displays one of the potential good characteristics of controlled-release fertilizer.

As an overall comparison, Fig. 8a and Fig. 8b shows unstable dissolution rate in comparison to Fig. 8c. The same observation in the stability trend provided by the $CaCl_2$ can also be seen from the release rate and swelling studies. Together with the surface morphology of S13 being the best, this further supports the hypothesis whereby the main effect of controlled-release is the variation of calcium chloride.

4. Conclusions

In this research, the encapsulation of phosphorous fertilizer using starch and sodium alginate has been successfully synthesized and tested for release behaviour study for a good controlled-release fertilizer. The results obtained from this research proposed that there are differences in the physicochemical and morphological properties of all the 13 formulations for starch-alginate-Ca^{2+} hydrogel beads. It was found out through surface morphology analysis that $CaCl_2$ was responsible for the porosity of the hydrogel surface. A balanced formulation between starch and sodium alginate was important for the overall shape of the bead. The successful bonding between these functional groups were verified through TGA and FTIR. The swelling and the dissolution studies further explained the effect of each material variation on the release rate. It can be observed that the swelling characteristics of hydrogels are closely associated to the phosphorous release which is the key is determining the chemical structure of the hydrogels. The graphs of phosphorous release, swelling and dissolution rate exhibit volatile pattern for the samples with variation of starch and sodium alginate whereas it is more stable with calcium chloride variation. In conclusion, $CaCl_2$ is the main effect of controlled-release fertilizer whereby S13 shows stable controlled release rate with lowest swelling (40%) with highest dissolution (80%) properties. All experimental work was carried out in replicates of 3.

Future work includes the testing of controlled-release fertilizer in soil for a longer period of study. Another recommendation is to increase the concentration of $CaCl_2$ for a better crosslinking effect. As an alternative approach, it is also recommended to substitute the crosslinker agent with polyacrylic acid to encapsulate phosphorous-fertilizer to improve the surface morphology.

References

[1] N. Xiaoyu et al. (2013). A novel slow-release urea fertiliser: Physical and chemical analysis of its structure and study of its release mechanism. *Biosyst. Eng*., 274–282 vol. 115.

[2] S. Chien et al. (2010). Agronomic and environmental aspects of phosphate fertilizers varying in source and solubility: an update review.

[3] Y. Liu et al. (2008). Urea particle coating for controlled release by using DCPD modified sulfur. *Powder Technolgy*, 88-93, vol. 183.

[4] R. Liang et al. (2009). Synthesis of wheat straw-g-poly(acrylic acid) superabsorbent composites and release of urea from it. *Carbohydr. Polym*., 181-187, vol. 77.

[5] A. Rashidzadeh et al. (2014). Slow-released NPK fertilizer encapsulated by NaAlg-gpoly(AA-co-AAm)/MMT superabsorbent nanocomposite. *Carbohydr. Polym*., 269–78, vol. 114.

[6] Y. Cao et al. (2005). Development of a controlled release formulation based on a starch matrix system. *Int. J. Pharm.*, 108–16, vol. 298.

[7] A. Roy et al. (2009). Dynamics of controlled release of chlorpyrifos from swelling and eroding biopolymeric microspheres of calcium alginate and starch. *Carbohydr. Polym*., 222–231, vol. 76.

[8] M. Trenkel et al. (2010). Slow-and controlled-release and stabilized fertilizers: An option for enhancing nutrient use efficiency in agriculture. *Paris, France: IFA, International fertilizer industry association.*

[9] B. Singh et al. (2009). A study towards release dynamics of thiram fungicide from starch-alginate beads to control environmental and health hazards. *Appl. Clay Sci.*, 76–82, vol. 45.

[10] B. Singh et al. (2009). Controlled release of the fungicide thiram from starch– alginate–clay based formulation. *Appl. Clay Sci.*, 76–82, vol. 45.

[11] H. Essawy et al. (2016). Superabsorbent hydrogels via graft polymerization of acrylic acid from chitosan-cellulose hybrid and their potential in controlled release of soil nutrients. *International Journal of Biological Macromolecule,* 144-151, vol. 89.

[12] P. Stoch et al. (2015). Structure of phosphate and iron-phosphate glasses by DFT calculations and FTIR/Raman spectroscopy. *Journal of Non-Crystalline Solids*, 48-60, vol. 450.

[13] S. Hosseini et al. (2015). Preparation and characterization of alginate and alginate-resistant starch microparticles containing nisin. *Carbohydrate Polymers*, 573-580, vol. 103.

[14] P. Marie et al. (2012). Evaluation of biocomposite films containing alginate and sago starch impregnated with silver nano particles. *Carbohydrate Polymers.* 717-724, vol. 90.

[15] B. Singh et al. (2009). A study towards release dynamics of thiram fungicide from starch-alginate beads to control environmental and health hazards. *J. Hazard. Mater.*, 208–16, vol. 161.

[16] Z. Wu et al. (2014). Characterization of Raoultella planticola Rs-2 microcapsule prepared with a blend of alginate and starch and its release behaviour. *Carbohydrate Polymers*, 259-267, vol. 110.

[17] G. Lozano-Vazquez et al. (2015). Effect of the weight ratio of alginate-modified tapioca starch on the physicochemical properties and release kinetics of chlorogenic acid containing beads. *Food Hydrocolloids*, 301-311, vol. 48.

[18] S. I. Ahmad et al. (2014). Quantitation of urea in urine by Fourier transforms infrared spectroscopy Ibn Sina National College for Medical Studies, *Jeddah, Kingdom of Saudi Arabia*. 90–96, vol. 1.

[19] A. Senna et al. (2015). Synthesis, characterization and application of hydrogel derived from cellulose acetate as a substrate for slow-release NPK fertilizer and water retention in soil. *Journal of Environmental Chemical Engineering,* 996-1002, vol. 3.

[20] L. Nnamonu et al. (2012). Alginate Reinforced Chitosan and Starch Beads in Slow Release Formulation of Imazaquin Herbicide—Preparation and Characterization. *Mater. Sci. Appl.*, 566–574, vol. 2012.

Bioethanol Production Via Simultaneous Saccharification and Fermentation Using Unwashed Pretreated Corncob

Mathen Kupusamy, Yoon Li Wan
School of Engineering, Taylor's University, Malaysia

Liwan.Yoon@taylors.edu.my

Abstract
Maize is one of the main food sources throughout major parts of the world and this leads to large scale of corn cobs being disposed as agrowastes without being utilised for its high cellulosic composition. Large scale bioethanol production utilizing corn cob is a great idea to overcome this issue and in the present study, enzymatic hydrolysis and simultaneous saccharification and fermentation is investigated for feasible bioethanol yield. This study involves pretreatment using 2% NaOH (alkaline) of 1:7 solid to liquid ratio onto corncob. The treated corncobs are prepared as washed and unwashed substrate which undergoes enzymatic hydrolysis with the aid of cellulase from *Trichoderma Longibrachiatum* of concentration 30 FPU/g-corncob and citrate buffer (0.1M citric acid and 0.1M sodium citrate). The washed pretreated corncob is prepared using 1:6 ratio of raw corn cob to rinsing water. The parameters varied in this study are the pH (ranging from pH 4 to 6), temperature (40 to 60°C) and, duration (0 to 48). The expected outcome convinces that unwashed NaOH pretreated corncob gives good rate of fermentable sugar conversion (hydrolysis yield of 10.29%) with not much difference compared to the washed substrate (glucose yield of 10.53%). Besides that, two methods of sugar breakdown and conversion are considered in this thesis; simultaneous saccharification and fermentation (SSF), and separate hydrolysis and fermentation (SHF) with independent factors of pH (4 to 6), incubation temperature (30 to 50°C) and duration (24 to 72 hours). The optimum condition for SSF is evaluated to be at pH 4, 33.71°C and 24 hours giving 6.145% of ethanol yield whereas for SHF, highest predicted yield of 6.677% is noted at pH 4, 30°C and 72 hours. Generally, after studying the effect of SSF and SHF onto corn cob, it is favorable for SSF to be applied because it generates similar ethanol yield compared to SHF (with a small difference of 0.532%) optimally and takes shorter process duration compared to SHF (lower residence time). Water consumption can also be reduced to a greater scale and this signifies that SSF process is the most cost effective sequence with unwashed pretreated corn cob being used as substrate for bioethanol production.

Keywords: Corncob, SSF, unwashed pretreated biomass, NaOH pretreatment, bioethanol.

1. Introduction

Most major industries have been relying on fossil resources such as coal, natural gas and petroleum for decades however, the vast utilisation of these resources resulted in severe global warming issues due to high CO2 accumulation. Implementations of renewable energies to substitute over the fossil resources are being researched for a cleaner world and bioethanol (bioenergy) sourced from cellulosic biomass is included as one of renewable sources.

Lignocellulosic biomass comprises mainly of three compositions which are cellulose, hemicellulose and lignin. The composition percentages vary depending on biomass type. Cellulose is the most important composition in hydrolysis, in which the glucose is then fermented into ethanol. Cellulose and hemicellulose can be made to glucose and xylose respectively by means of chemical or biological process whereas, lignin which is a non-carbohydrate compound, affects the hydrolysis activity [1, 2].

Inhibitors which are degradation products formed during pretreatment and hydrolysis that consists of furfural, 5-hydroxymethylfurfural (HMF), acetic acid and phenols [4]. There are various ways to reduce inhibitor accumulation and washing is the most common as the substrates are only rinsed using finite amount of water to remove the residues and inhibitor. However, this method has higher possibilities of washing off fermentable sugar resulting in significant glucose loss. Moreover, washing is expensive because large amount of water is needed and has to undergo wastewater treatment at the end of the process [3]. There are much higher chances of benefiting from unwashed pretreated cellulosic biomass but, it depends on feedstock selection, type of pretreatment and choice of hydrolysis used.

Hydrolysis also known as saccharification, is a breakdown process converting cellulose to glucose. Acid hydrolysis using H_2SO_4 and HCl is commonly used and neutralization of pH after acid hydrolysis is vital to keep yeast active for fermentation as well as lowering the number of inhibitory compounds formed [5]. Enzymatic hydrolysis eliminates the glycosidic bonds present in the biomass as the hydrogen bonds are difficult to break. Enzymatic saccharification is normally conducted at mild temperature (about 50°C) and pH (4 to 5) for it is optimal for enzyme activity [5]. Cellulase enzymes aids the cellulose saccharification whereas, xylanase enzyme breaks down hemicellulose into xylose. The main factor affecting the rate of hydrolysis is the lignin content of the biomass as it limits the accessible reaction sites of the enzymes. Thus, alkaline (preferably NaOH) pretreatment is considered favorable as lignin solubilization occurs during the biomass structural change due to pretreatment [6]. The low utility cost and high sugar conversion rate makes the enzymatic hydrolysis more feasible to apply.

Fermentation takes place subsequently after the hydrolysis and it allows the transformation of compounds into simpler substance by the enzymes or microorganisms. The breakdown undergone by selected carbohydrate compounds in absence of air (oxygen) can also be referred as fermentation process. The sequence of hydrolysis and fermentation can be done in different units and this step is known as separate hydrolysis and fermentation (SHF). Another alternative configuration can be applied that is the simultaneous saccharification and fermentation (SSF) in which both the hydrolysis and fermentation takes place in a single unit. The unwashed factor in this project might increase the chance of obtaining high presence of inhibitors formed [11]. Therefore, by implementing SSF technique, the buildup rate of inhibitory compounds can be reduced as the residence time of sugar substrate is extremely short

compared to SHF. Besides that, this results in a better rate of sugar conversion through yeast activity so that higher ethanol concentration (end-product) can be achieved.

There are pros and cons of both SSF and SHF hence, this project enable the study about the implications of these saccharification and fermentation configurations in conjunction with its advantages. SSF is selected as the process configuration for this bioethanol production study via corn cob.

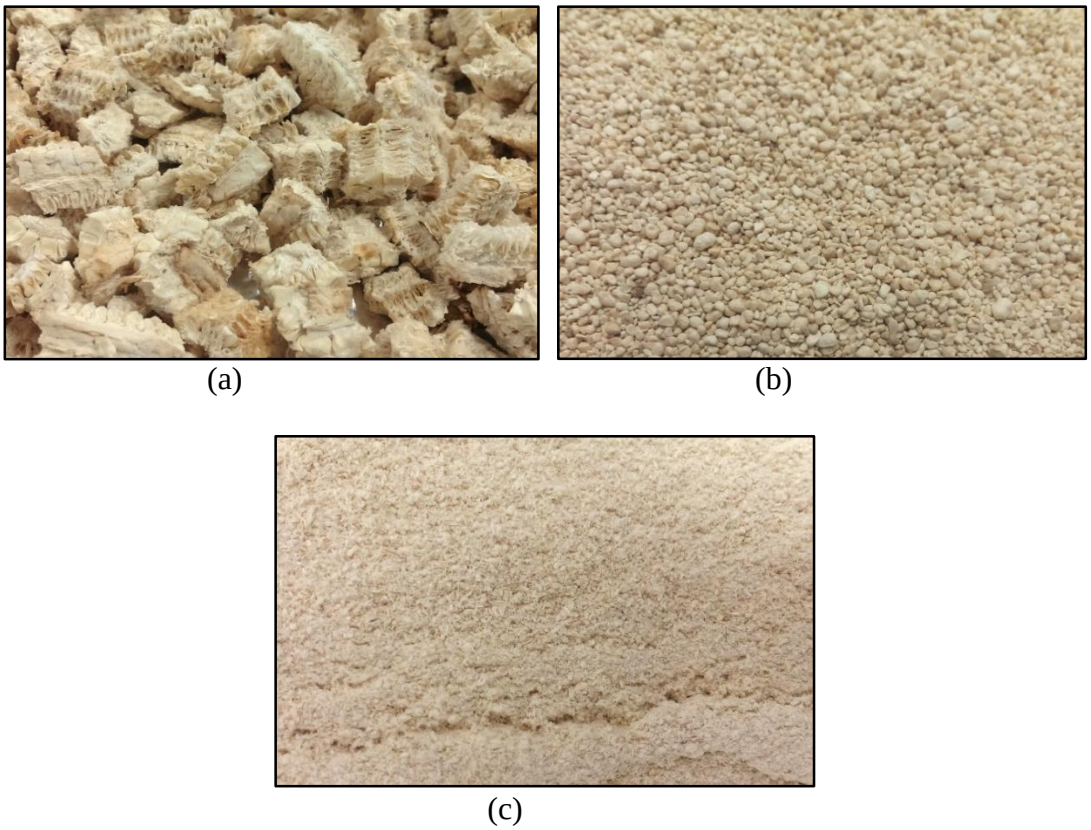
The objectives of this research project are as follows:

1. To investigate the sugar production using washed and unwashed pretreated corn cob in enzymatic hydrolysis by comparing their saccharification yields.
2. To obtain the specific value of factors such as temperature, pH and duration, which can promote optimum condition for the SSF to take place, utilizing unwashed pretreated corn cob.
3. To identify whether efficient hydrolysis and fermentation of unwashed pretreated corn cob in terms of ethanol yield is achievable when these sequences are done separately (SHF) or simultaneously (SSF).

2. Materials and Methods

2.1 Lignocellulosic Material

Corncob was obtained from local market (Perak, Malaysia) and dried in oven at 60°C for 48 hours. The corncob was subjected to pre-milling until reaching particle size less than 1 mm. It is sieved to obtain fine powdered corncob with maximum particle size of 500 µm.



(a) (b)

(c)

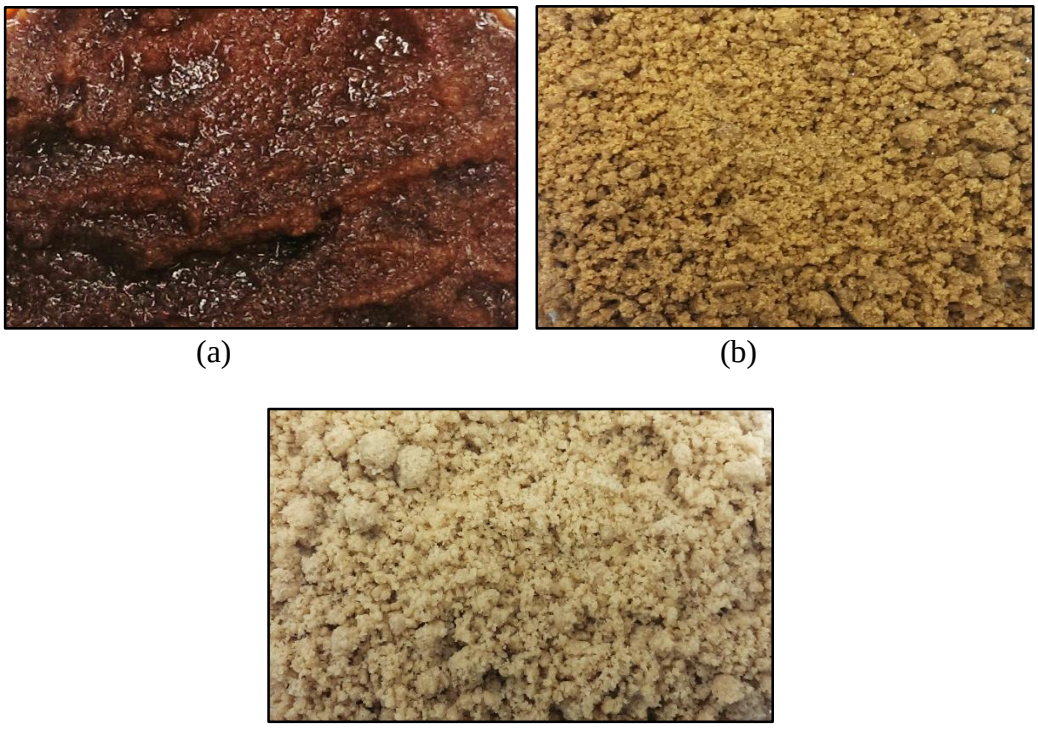
Figure 2.1. Comparison view of (a) initial raw corncob, (b) grinded raw corncob and (c) sieved raw corncob.

2.2 Sodium Hydroxide Pretreatment and Solids Washing

60 g of sieved corncob was treated with 2% (w/v) NaOH using autoclave (WiseClave, Model no. WAC-60) at 121°C for 30 minutes with a ratio of 1g of raw sieved corncob to 7 mL of NaOH solution. Upon completion of NaOH pretreatment, the pretreated slurry was collected and squeezed with a strainer to remove moisture. After the first straining cycle of the substrate, the product obtained was labelled as the unwashed pretreated substrate. For solids washed with one cycle, the unwashed substrate was mixed with 600 mL of UPW using ratio of 1:10 of initial raw corn cob to UPW and stirred thoroughly for 5 minutes, followed by straining method. The washing sequence was repeated to acquire solids washed with two cycles as well.



Figure 2.2. Picture showing the corncob before (left) and after added with 2% w/v NaOH solution (right)



(a) (b)

(c)

Figure 2.3. Comparison view of (a) pretreated corn cob slurry obtained right after pretreatment, (b) strained unwashed pretreated corn cob and (c) strained pretreated corn cob undergone two washing cycles.

2.3 Yeast Inoculum Preparation

Colonial yeast cells were first cultured by adding of *Saccharomyces Cerevisiae* to a YPD agar plate and left for three days in the incubator at 35°C. Four loopful of activated yeast from the agar plate is then inserted into 100 mL of 3% YPD broth (autoclaved at 121°C, 20 minutes for sterilization) and incubated with such conditions for a day: at 35°C and 120 rpm [23]. The yeast inoculum preparation steps were carried out carefully in a laminar flow cabinet (ESCO, Model no. AHC-401) and utilizing UPW as solvent to avoid occurrence of cell contamination.



Figure 2.4. Picture showing the multiple colonial yeast cells cultured on a YPD agar plate

2.4 Design of Enzymatic Hydrolysis

10 g of unwashed pretreated corncob was weighed and placed in three different 250 mL conical flasks. Same steps were repeated for pretreated corncob washed with one cycle and two cycles. Three flasks each containing three different type of substrates, were then buffered with 80 mL of pH4 citrate buffer (0.1 M of citric acid and 0.1 M of sodium citrate) [7]. Two repetitions were done for pH 5 and 6, giving a total of 9 flasks per set of experiment. Cellulase from *Trichoderma Longibrachiatum* (Sigma-Aldrich, C9748-100G) with an activity of 30 U/g substrate was added for 10 mL into each flask and the enzymatic hydrolysis was carried out for 48 hours using orbital incubator shaker (Yihder, Model no. LM-400D) at 50°C (120 rpm) and these steps were repeated using varying temperature of 40°C and 60°C. The flasks were sealed with rubber stopper and a layer of aluminium foil to prevent air contamination. Total of 5 sets of enzymatic hydrolysis were carried out with different combinations of the independent variables considered. At each interval, the samples collected were placed in the freezer at -20°C for 20 minutes to deactivate the enzymes [32].



(a) (b)

Figure 2.5. Comparison view of unwashed (left), pretreated corncob washed once (center) and pretreated corncob washed twice (right): (a) before adding buffer solution and (b) after adding buffer solution.



Figure 2.6. Laboratory orbital shaker incubator used during experiment

2.5 Investigated Parameters for Enzymatic Hydrolysis

Multiple factors do affect the rate and performance of enzymatic saccharification and several were chosen for this study, however due to time constraint, only three were selected as shown in Table 2.1. The factors and levels considered are based on suitable application in industrial scale in terms of cost effectivity.

Table 2.1. Levels of independent variables applied in the enzymatic saccharification comparison test between washed and unwashed pretreated corn cob.

Independent variables	Coding	Units	Levels		
			-1	0	1
pH	A	-	4	5	6
Temperature	B	°C	40	50	60
Washing Frequency	C	-	0	1	2
Duration	D	hours	3 pre-determined intervals (0-48 hours)		

3.5.1 pH

Optimal pH value for saccharification using cellulase from *Trichoderma Longibrachiatum* was investigated and a set point temperature (50°C) was fixed to carry out this part. The optimum temperature for saccharification by cellulase was researched to be at 50°C and the growth tolerant pH for *Trichoderma* species was studied to be in between 3 to 6 [8, 9]. The effect of varying range of pH combined with corn cob substrates of different washing frequency can be further evaluated through this study.

3.5.2 Temperature

Enzymatic saccharification can be performed with temperature held higher compared to fermentation process conditions and stated previously, 50°C is the optimal saccharification temperature. Therefore, due to time limitation, temperature range between 40°C to 60°C is utilized with constant pH value of 5 involving pretreated corn cob with various number of washing cycles.

3.5.3 Washing Frequency

Washing is also a considerable factor that influences the efficiency of enzymatic hydrolysis relating to number of inhibitors present. Lower inhibitory accumulation due to washing can lead to higher hydrolysis rate. However, in industrial scale, it can be considered as not cost productive due to large amount of rinsing water required. In this study, pretreated corn cob with washing frequency ranging between 0 to 2 was investigated to consider the possibility of utilizing unwashed pretreated corn cob as an alternative to washed substrate in industries relevant to bioethanol production.

3.6 Experimental Design of SSF and SHF

For SSF, 10 g of unwashed pretreated corncob was weighed and placed in sterilized 250 mL conical flask. The solids were then buffered with 80 mL of citrate buffer (0.1 M of citric acid and 0.1 M of sodium citrate, pH 4) [7]. Same steps were repeated for pH 5 and 6. 10 mL of cellulase from *Trichoderma Longibrachiatum* with cellulase activity of 30 U/g substrate was added into each flask followed by additional 10 mL of yeast inoculum prepared [*Note: U is defined as cellulase activity in which one unit that will liberate 1.0 micromole of glucose from cellulose in one hour at pH5 and 37°C with two hours of incubation time]. The SSF was carried out for 72 hours using orbital incubator shaker at 40°C (120 rpm) and these steps were repeated using two different temperatures which are 30°C and 50°C. The flasks were sealed with sterilized cotton stoppers, allowing the produced CO^2 to escape.

SHF was carried out with repeating the steps involved in SSF but, with lesser residence time of yeast compared to SSF. Enzymatic hydrolysis was carried out for 48 hours utilizing 30 U/g of cellulase, *Trichoderma Longibrachiatum*. The solids in the conical flasks were filtered and removed to discontinue the enzymatic hydrolysis. Yeast inoculum from *Saccharomyces Cerevisiae* was then added for 10 mL and the fermentation only then took place for 24 hours to have a total duration of 72 hours of experimental period.

Sixteen runs of SSF and SHF respectively were carried out by various combinations of independent variable values based on the optimum conditions of enzymatic hydrolysis and preliminary studies on SSF. Temperature levels of 30, 40 and 50°C were chosen because the yeast ferment at optimal rate within this range.

Table 2.2. Levels of independent variables applied in both SSF and SHF using unwashed pretreated corn cob.

Independent variables	Coding	Units	Levels		
			-1	0	1
pH	A	-	4	5	6
Temperature	B	°C	40	50	60
Duration	C	hours	24	48	72

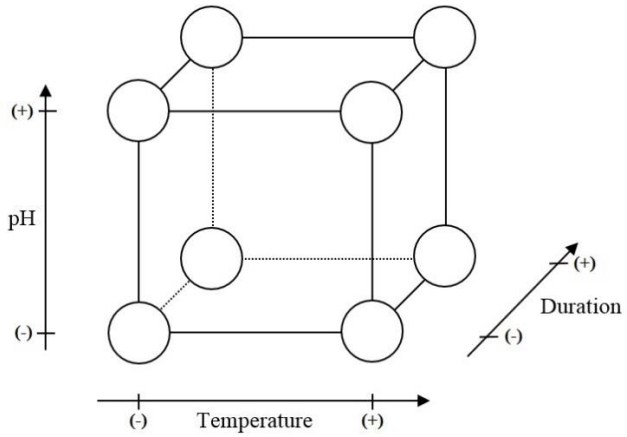


Figure 2.7. Cube diagram of three investigated factors (multiple) experiment and their levels, with center points excluded.

2.7 Regression Analysis and Analytical Methods

2.7.1 Optimization of SSF and SHF

CCD of RSM was applied in quadratic polynomial regression analysis to obtain the optimum conditions of SSF. The results obtained from SSF and SHF respectively were evaluated with the aid of Design Expert 7.0.0 software (STAT-EASE Inc., Minneapolis, USA). The experimental response, *Y* (ethanol yield, %) was fitted into the complete regression model with three factors shown in Eq. (2.1). The α value of 1 was implemented in the analysis and 16 experimental runs were done for SSF optimization.

$$Y = \beta_0 + \beta_1.A + \beta_2.B + \beta_3.C + \beta_{12}.A.B + \beta_{13}.A.C + \beta_{23}.B.C + \beta_{11}.A^2 + \beta_{22}.B^2 + \beta_{33}.C^2 \quad \text{Equation (2.1)}$$

where,

A = coded factor of pH
B = coded factor of temperature
C = coded factor of duration.
β_0 = coefficient of intercept effect
β_i = coefficient of linear effect (one variable)
β_{ij} = coefficient of linear-by-linear interaction (two variable)
β_{ii} = coefficient of quadratic effect (two variable)

2.7.2 HPLC Analysis

HPLC equipment was used for quantitative analysis to determine the concentration of glucose in HPLC standard samples and experimental samples. The mobile phase applied was UPW with flow rate 0.6 mL/min [7]. The column used for this study was Hi-Plex H column (7.7mm x 300, Agilent, USA). Before the sample analysis via HPLC with refractive index detector (Agilent, USA, Model no. 1220-G1362A) was carried out, samples were centrifuged (Multipurpose Centrifuge Scanspeed, Model no. 1236MG) for 15 minutes at 4,500 rpm. Supernatant was then filtered through nylon syringe filter (0.2 µm pore size) and subjected for analysis as 65°C was the set column temperature.



Figure 2.8. Supernatant collected after enzymatic hydrolysis of unwashed (left), one cycle washed pretreated corncob (middle), two cycle washed pretreated corncob (right)

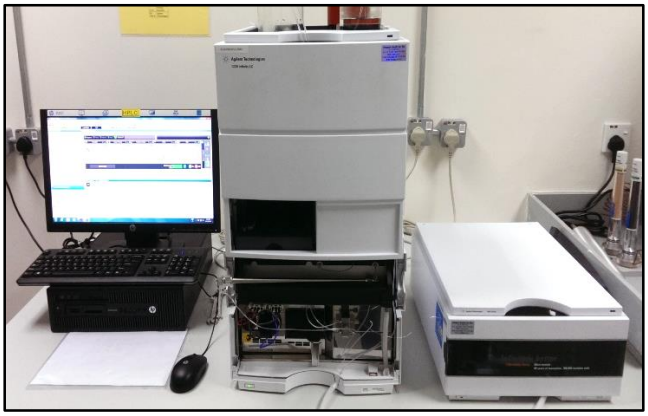


Figure 2.9. Picture showing HPLC equipment setup with DAD (center) and RID (right).

2.7.3 Glucose Yield

The glucose concentration results obtained from the HPLC readings were compared using the results of HPLC standard calibration of pure glucose samples (calibration curve). The area under the peak given by HPLC was converted to amount of glucose (g/L). The glucose (hydrolysis) yield percentages was calculated manually using related formulas Eq. (2.2) and (2.3) below:

$$Hydrolysis\ yield = Concentration\ of\ Glucose\ \left(\frac{g}{L}\right) \times\ 0.11, Total\ amount\ of\ solution\ (L)$$
$$= a\left(\frac{g\ glucose}{10g\ corncob}\right) \times\ 0.1$$
$$= b\left(\frac{g\ glucose}{g\ corncob}\right) \qquad \text{Equation (2.2)}$$

$$Hydrolysis\ yield\ (\%) = b\ \left(\frac{g\ glucose}{g\ corncob}\right) \times\ 100\% = X\ (\%) \qquad \text{Equation (2.3)}$$

2.7.4 Ethanol Yield

The concentration values extracted from HPLC results were compared to the results of pure ethanol (HPLC grade) standard calibration curve in which the area under the peak was then converted to ethanol amount produced (g/L). The ethanol (fermentation) yield percentages for SSF and SHF was calculated relating to formulas given in Eq. (2.4) and (2.5):

$$Fermentation\ yield = Concentration\ of\ Ethanol\ \left(\frac{g}{L}\right) \times\ 0.12\ (Total\ amount\ of\ solution, L)$$
$$= d\left(\frac{g\ ethanol}{10g\ corncob}\right) \times\ 0.1$$
$$= e\left(\frac{g\ ethanol}{g\ corncob}\right) \qquad \text{Equation (2.4)}$$

$$Ethanol\ yield\ (\%) = e\left(\frac{g\ ethanol}{g\ corncob}\right) \times\ 100\% = Y\ (\%)$$ Equation (2.5)

3. Results and Discussion

In this study, the enzymatic hydrolysis is considered the vital process in simultaneous saccharification and fermentation (SSF) to produce bioethanol from lignocellulosic biomass, which is corncob. Since glucose is converted to ethanol during fermentation, the glucose yield from saccharification is to be the contributing factor for a better ethanol yield. However, selection between washed or unwashed pretreated biomass is said to have an effect onto the sugar yield derived from lignocellulosic biomass (Yu-Shen Cheng et.al.,2010). Hence, this study determines the productivity comparison of washed and unwashed pretreated corn cob in hydrolysis yield as it gives better understanding of feasibility using unwashed pretreated lignocellulosic biomass. The main reason the unwashed factor is being focused due to effect of reduced water consumption throughout the process. Bioethanol production requires large amount of water throughout and by implementing this, the production cost can be reduced as less wastewater needs to be treated.

3.1 Enzymatic Hydrolysis

3.1.1 Effect of pH

The optimal pH value for saccharification using cellulase from Trichoderma Longibrachiatum is investigated and a set point temperature is selected to carry out this part. The optimum temperature for saccharification by cellulase is researched to be at 50°C and the growth tolerant pH for Trichoderma species is between 3 to 6 [8, 9]. So, this experiment was done using three different pH variables which is 4, 5 and 6 at a constant incubation temperature of 50°C. For the result, the highest final concentrations of glucose yield using unwashed and pretreated corn cob washed once and twice are obtained at pH 5 which are 9.95 g/L, 10.59 g/L and 10.22 g/L respectively. A small concentration difference between washed once (highest) and unwashed substrate is observed through this experiment and the difference calculated is 0.638 which is less than 1. This insignificant value difference resembles the high potential of unwashed pretreated corn cob to be utilised in major bioethanol production. Besides that, the concentration values obtained for the saccharification between pH 4 till 6 gradually increases with time (0-24 hours) and stops increasing when the duration is at 24~25 hours. The substrate is noted to experience only a small increase in glucose concentration at pH 6 compared to the concentrations at pH 4 and 5.

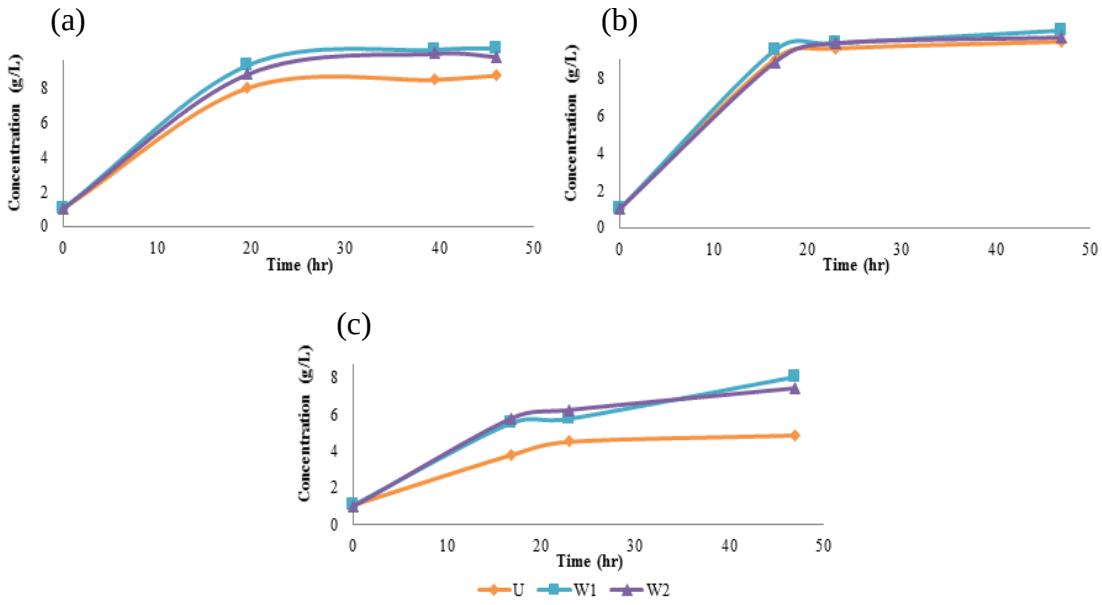


Figure 3.1 Glucose concentration-time curve for (a) pH 4, (b) pH 5 and (c) pH 6 at 50 °C with different pretreated corn cob samples: U = unwashed, W1 = washed once, W2 = washed twice.

3.1.2 Effect of Temperature

The hydrolysis rate of cellulose is also affected by the incubation temperature. Hence, an ideal temperature is to be confirmed at the optimal pH obtained previously and this experiment allows the study of sugar concentration produced from hydrolyzed corn cob with constant pH value of 5 but, varying incubation temperature of 40°C and 60°C since the results for 50°C has been noted. Based on results obtained at the end of experiment, the final highest concentration is noted at 40°C (46.92 hours ~ 47 hours) for unwashed pretreated corn cob which is 10.3933 g/L whereas for substrate washed once and twice, they are 10.5914 g/L and 10.2161 which are at 50°C (47 hours). The difference in concentration between both washed once and unwashed substrates is calculated to be 0.1981 which is negligible. The glucose concentration values are comparable with other experiment (Ouyang et al. 2009) that utilizes washed pretreated corn cob with T.reesei cellulase at 8 FPIU/g substrate, pH 4.8 and 50°C, giving maximum resultant glucose concentration of 7.38 g/L.

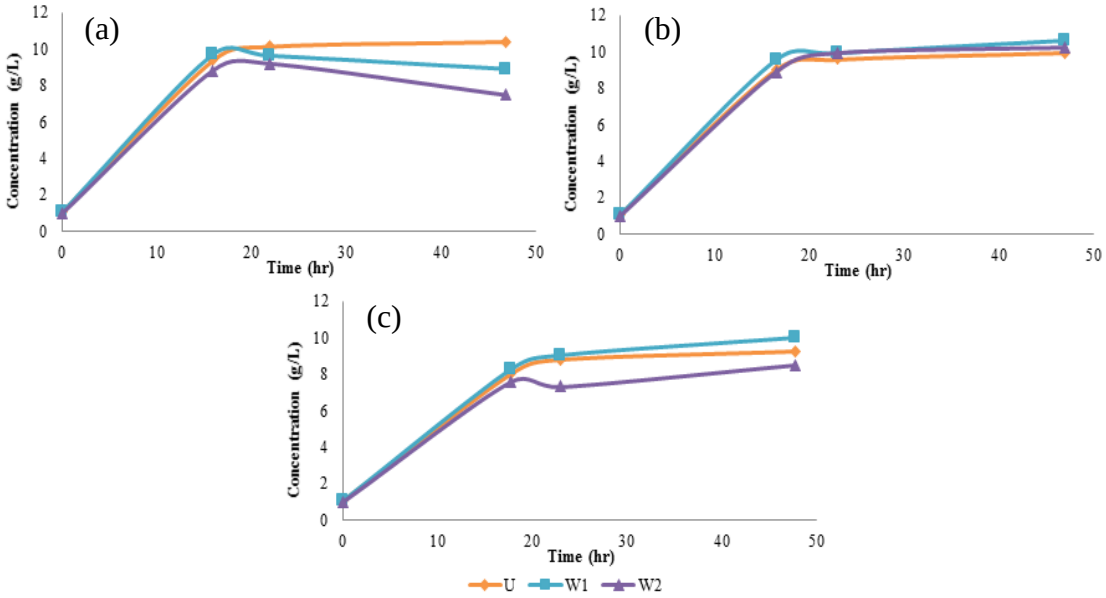


Figure 3.2 Glucose concentration-time curve for (a) 40 °C, (b) 50 °C and, (c) 60 °C at pH 5 with different pretreated corn cob samples: U = unwashed, W1 = washed once, W2 = washed twice.

3.1.3 Influence of Washing Frequency on Glucose Yield

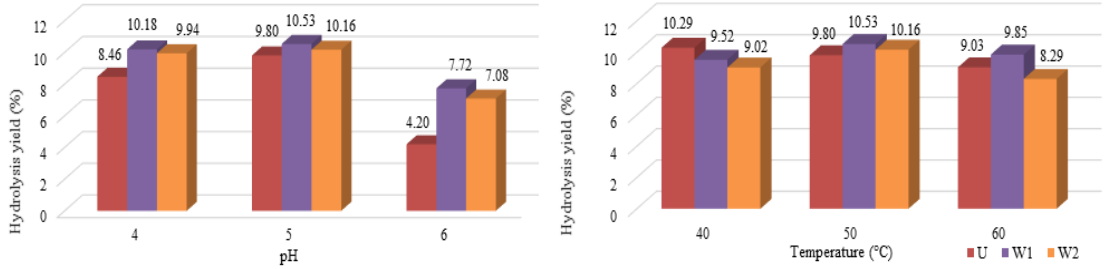


Figure 3.3 Glucose yield (%) from enzymatic hydrolysis for (a) varying pH and, (b) varying temperature using different pretreated corn cob samples: U = unwashed, W1 = washed once, W2 = washed twice

According to the results shown in the Figure 3.3, the optimum condition for unwashed pretreated corncob is at pH 5 and 40 °C as the highest hydrolysis yield recorded shows 10.29 % is obtained during the 48 hours period. The highest sugar yield values achievable using washed pretreated corn cob are 10.53% (one cycle washing) and 10.16% (two cycle washing) at conditions of pH 5 and 50 °C. The unwashed pretreated corn cob gives a higher glucose yield compared to substrate washed twice. This is because more fine unreacted corn cob is washed away compared to the amount of inhibitor accumulated due to the rinsing effect utilizing large amount of water. Therefore, the yield percentages are compared between the substrates of unwashed and washed with one cycle, giving a difference of 0.24 %. This shows that the unwashed pretreated corn cob can give a similar hydrolysis yield (negligible difference) as the washed lignocellulosic biomass, indicating a better choice of hydrolysis substrate as water consumption can be cut down significantly. The glucose yield percentages obtained are comparable with the experimental hydrolysis values obtained by M. Yu et al. (2015), which the unwashed 10g of solid residue (sweet sorghum bagasse) gives maximal sugar yield of 65.14%

whereas, same amount of substrate which are washed once and twice delivers glucose yield of 61% and 58% respectively. This proves that pretreated corn cob is ideal for delivering maximized glucose yield when the substrate does not undergo washing sequence nevertheless, saving cost and energy.

3.2 Regression Analysis of SSF

3.2.1 Analysis of Variance (ANOVA)

The experimental design matrix with 16 runs (including 4 center points per block) and the corresponding response, Y_{SSF} (ethanol yield from SSF using unwashed pretreated corn cob), which is the main study of this research is presented in Table 3.1. A quadratic polynomial equation was used to fit the response which is shown in Eq. (2.1). The coefficients of β_0, β_i, β_{ij}, β_{ii} were obtained using the Design Expert 7.0.0 software and the insignificant model terms were eliminated. This results to a final regression model equation in terms of the coded factors as shown in Eq. (3.1):

$$Y_{SSF} = 4.73 - 0.45\,A - 1.56\,B - 0.4\,C + 0.23\,BC - 1.42\,B^2 \qquad \text{Equation (3.1)}$$

where,

A = coded factor of pH
B = coded factor of temperature
C = coded factor of duration

Table 3.1. SSF experimental design matrix and results

Run	pH, A	Temperature, B (°C)	Duration, C (hours)	Glucose yield, X_{SSF} (%)	Ethanol yield, Y_{SSF} (%)
1	4	50	48	9.96	1.95
2	6	40	24	0.82	4.34
3	5	40	48	0.37	4.97
4	6	50	48	2.54	1.58
5	5	30	24	0.42	5.45
6	5	40	48	0.37	4.68
7	5	50	72	9.64	1.68
8	4	30	48	0.54	5.3
9	4	40	72	0.31	4.43
10	6	30	48	0.66	4.3
11	5	40	48	0.37	4.92
12	5	40	48	0.4	5.09
13	5	30	72	0.64	4.43
14	5	50	24	9.06	1.8
15	6	40	72	0.41	3.63
16	4	40	24	0.61	5.79

Table 3.2 Analysis of variance for SSF of unwashed pretreated corn cob.

Source	Sum of Squares	DF	Mean Square	F-value	Probability > F	
Model	30.63178	5	6.126355	77.64708	< 0.0001	significant
A	1.63805	1	1.63805	20.76109	0.0010	
B	19.43761	1	19.43761	246.3576	< 0.0001	
C	1.288013	1	1.288013	16.32462	0.0024	
BC	0.2025	1	0.2025	2.56654	0.1402	
B^2	8.0656	1	8.0656	102.2256	< 0.0001	
Residual	0.789	10	0.0789			
Lack of Fit	0.7001	7	0.100014	3.37506	0.1728	not significant
Pure Error	0.0889	3	0.029633			
Total	31.42078	15				
R^2 = 0.9749 or 97.49%				Adj R^2 = 0.9623 or 96.23%		
Q^2 = 0.9354 or 93.54%				Adeq Precision = 24.911		

The result from the ANOVA for the reduced model with ethanol yield as response is shown in Table 3.2. Under 90% confidence level, *A*, *B*, *C*, *BC* and B^2 are the significant model terms and this clearly states that the variation in temperature of linear and quadratic terms has the greatest influence on ethanol yield. However, the temperature x duration (B*C*) has the least effect on ethanol yield based on its large Probability > F value. In addition, the model has a F-value of 77.65 implied that this model investigated is significant under the confidence level of 90%. The Lack of Fit with F-value of 3.38 shows that it is not significant relative to the variation in the response as its probability value of 0.1728 > 0.1, which further indicates that the model accurately fits the data. Besides that, the large values of both coefficient of determination and predictability, R^2 = 97.49% and Q^2 = 93.54% respectively, indicates a good fit of data to the regression model. The difference between the two coefficients (R^2 and Q^2) is less than 0.5 and the Q^2 value is more than 0.9, which also proves that it is an excellent model.

The model developed was also tested for its validity by comparing the experimental ethanol yield with predicted ethanol yield. The comparison results are tabulated as shown in Table 3.3. Error percentages were tabulated using the difference between the predicted and experimental response values and from the table, it states that the predicted ethanol yields are compatible with the experimental values with less than 0.4 % error.

Table 3.3. Model validity check

Run	Experimental ethanol yield (%)	Predicted ethanol yield (%)	Error (%)
1	1.95	2.205	0.255
2	4.34	4.68	0.340
3	4.97	4.731	0.239
4	1.58	1.3	0.280
5	5.45	5.271	0.046
6	4.68	4.731	0.051
7	1.68	1.351	0.104

8	5.3	5.322	0.022
9	4.43	4.782	0.352
10	4.3	4.417	0.117
11	4.92	4.731	0.189
12	5.09	4.731	0.359
13	4.43	4.469	0.186
14	1.8	2.154	0.129
15	3.63	3.877	0.248
16	5.79	5.585	0.205

3.2.2 Model Analysis of SSF

The response surface 3-D graphs and contour plots were observed by varying two variables according to the respective experimental ranges while maintaining one variable at zero level as shown in Figure 3.4 and 3.5. The quadratic term of temperature (B^2) causes the rise (quadratic effect) of the surface response at the temperature axis whereas, linear effect on ethanol yield is observed on the pH axis as illustrated in Figure 3.4. Increase in ethanol yield is observed at a lower SSF temperature with shorter duration as shown in Figure 3.5. In addition, prolonged SSF period would result in ethanol yield reduction even at lower temperature because of loss in accessible surface area of enzymes relative to inhibitor accumulation and residues present [13]. Besides that, ethanol is highly volatile and this attributes to the loss in observed ethanol yield since possibility of ethanol vaporization increases with time. High incubation temperature (> 40°C) do contribute to low ethanol yield even at varying SSF duration from short to long period. Hence, operating conditions with shorter process (SSF) time and low incubation temperature is considered optimal for SSF. From Figure 3.4 also, when the incubation temperature drops too low (< 31°C), the ethanol yield is observed to decline regardless of period. The contributing factor to this effect is the yeast cell activity, which is optimal at temperature range of 30 to 40°C [10].

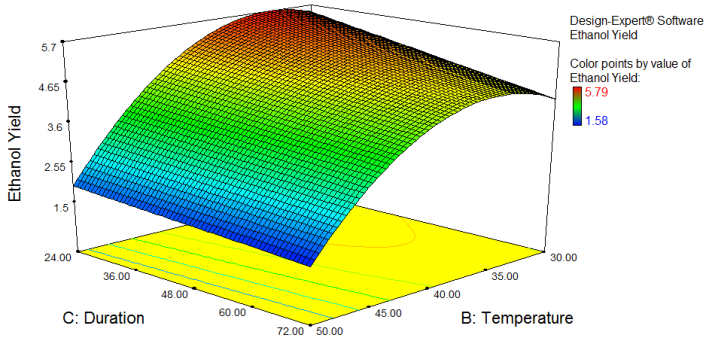


Figure 3.4. Surface response plot of the influence of temperature and duration on ethanol yield at pH 5

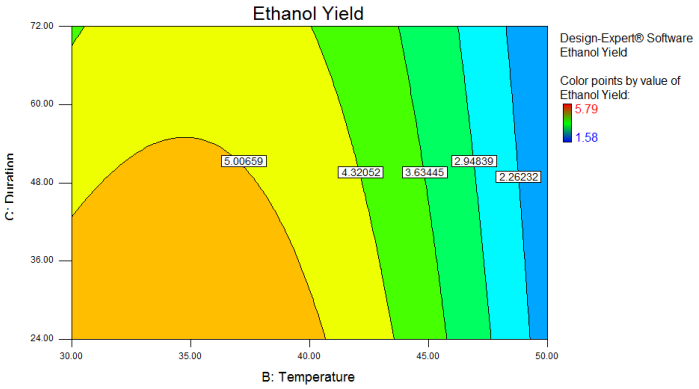


Figure 3.5. Contour plot of temperature and duration variation responding to ethanol yield at pH 5

Figure 3.6 and 3.7 clearly shows that the ethanol yield increases as lower pH is implemented in low temperature-SSF. However, pH is not considered as a major contributing factor in ethanol yield as the linear effect at the pH axis is noted to have a slight gradient at various incubation temperature values. From the response plot, ethanol yield at low temperature (30 - 40°C) and low pH results in increase of ethanol yield via SSF. Furthermore, the interactive effect of SSF temperature and pH is weaker compared to the incubation temperature-duration interaction as the *BC* term has greater significance with lower P-value.

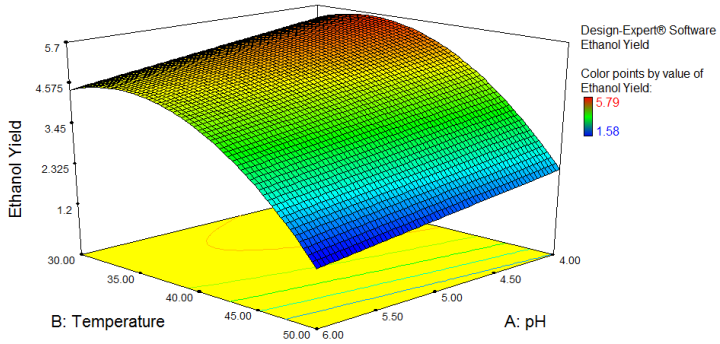


Figure 3.6. Surface response plot of pH-temperature relation on ethanol yield at 48 hours

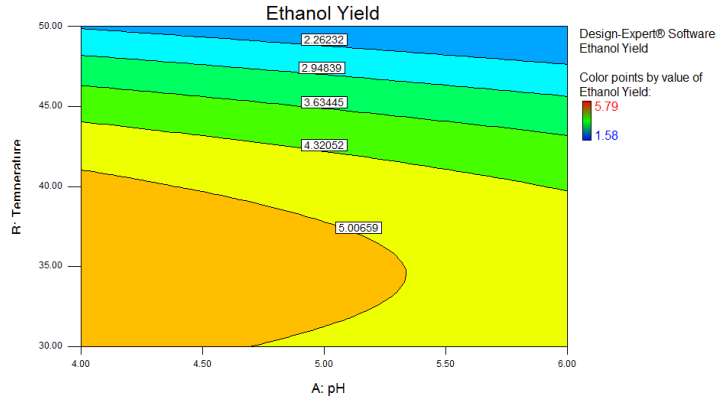


Figure 3.7. Contour plot of temperature and pH variation responding to ethanol yield at 48 hours

Moreover, the linear relation of pH and duration can be evaluated using Figure 3.8 and 3.9. Both coefficients of the *A* and *C* are negative meaning that a decrease in ethanol yield is noted when pH is increased from 4 to 6 as SSF incubation period increases too. A slightly steeper gradient is observed at the pH axis indicating that a change in pH has more influence onto ethanol yield compared to SSF duration as cellulase deactivates rapidly at higher pH [12]. The relative low pH provides acidic condition which prevents bacterial contamination during fermentation (Olofsson *et al*., 2008). Yeast cells do have reduced activity rate over time and it is favorable for SSF to be carried out at shorter duration (24 hours) [11].

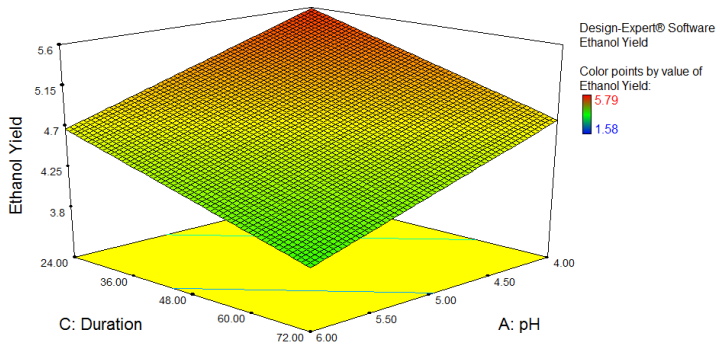


Figure 3.8. Surface response plot of the influence of pH and duration on ethanol yield at 40°C

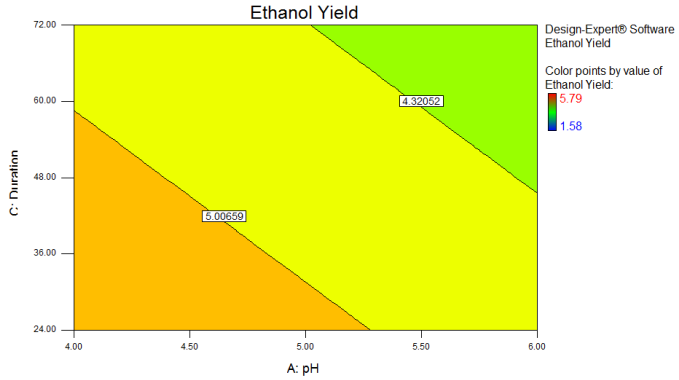


Figure 3.9. Contour plot of duration-pH interaction responding to ethanol yield at 40°C

The highest SSF ethanol concentration observed, 4.828 g/L is compared with other research with similar biomass source. Zakpaa *et.al*.,2009 obtained highest ethanol concentration of 0.642 g/L after 24 hours fermentation period with following conditions; pH 5, room temperature, 6 g of initial corn cob, 10 mL of inoculated cellulase from *Aspergillus niger* and 10 mL of yeast inoculum from *Saccharomyces cerevisiae.*

3.2.3 Optimum Conditions of SSF

The optimum conditions for simultaneous saccharification and fermentation using unwashed pretreated corn cob is determined via optimization feature from Design Expert 7.0.0 software used. The criteria selected is ethanol yield and the goal is to attain maximized response value. The predicted optimum condition identified for SSF of unwashed pretreated corn cob in relevant to the response model is at pH 4, 33.71°C, and incubation period of 24 hours, which gives the highest predicted ethanol yield of 6.145% as per illustrated in Figure 3.10 and this

value exceeds the highest observed experimental ethanol yield (pH4, 40°C and 24 hours) by 0.355%.

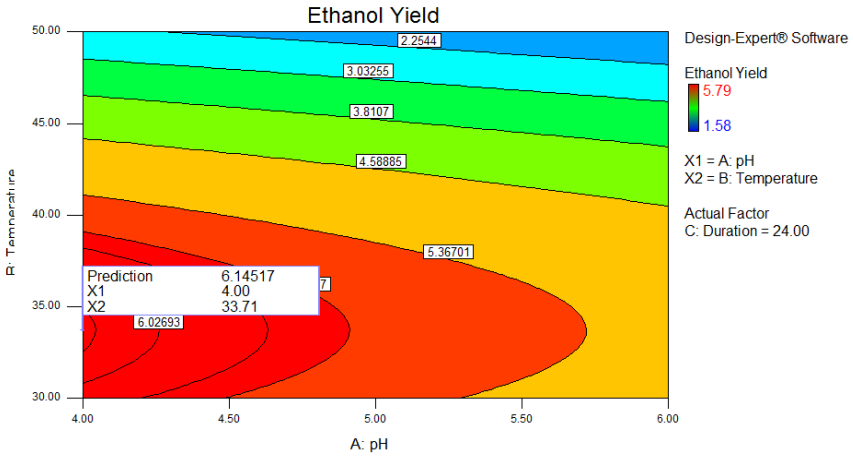


Figure 3.10. Contour plot of optimum conditions predicted at 24 hours.

3.3 Regression Analysis of SHF

3.3.1 Analysis of Variance (ANOVA)

The experimental design matrix with 16 runs (including 4 center points per block) and the corresponding response, Y_{SHF} (ethanol yield from SHF using unwashed pretreated corn cob), purposed for comparison study in this research is presented in Table 3.4. The response model is fitted using a quadratic polynomial equation written in Eq. (2.1). The coefficients of β_0, β_i, β_{ij}, β_{ii} obtained is placed into the equation as the insignificant model terms is eliminated, giving a final regression model equation in terms of the coded factors shown in Eq. (3.2):

$$Y_{SHF} = 0 - 0.61\,A - 0.33\,B + 2.26\,C - 1.22\,AC + 2.26\,BC^2 \qquad \text{Equation (4.2)}$$

where,

A = coded factor of pH
B = coded factor of temperature
C = coded factor of duration

Table 3.4. SHF experimental design matrix and results

Run	pH, A	Temperature, B (°C)	Duration, C (hours)	Hydrolysis yield, X_{SHF} (%)	Ethanol yield, Y_{SHF} (%)
1	4	50	48	12.03	0.00
2	6	40	24	5.89	0.00
3	5	40	48	12.06	0.00
4	6	50	48	3.10	0.00
5	5	30	24	10.34	0.00
6	5	40	48	11.76	0.00
7	5	50	72	11.27	1.91
8	4	30	48	10.19	0.00
9	4	40	72	0.29	8.24

10	6	30	48	2.80	0.00
11	5	40	48	11.73	0.00
12	5	40	48	11.75	0.00
13	5	30	72	0.26	4.56
14	5	50	24	10.45	0.00
15	6	40	72	0.47	3.34
16	4	40	24	12.20	0.00

Table 3.5 Analysis of variance for SHF of unwashed pretreated corn cob.

Source	Sum of Squares	DF	Mean Square	F-value	Probability > F	
Model	70.90184	5	14.18037	11.65165	0.0007	significant
A	2.991776	1	2.991776	2.458267	0.1480	
B	0.881436	1	0.881436	0.724254	0.4147	
C	40.69672	1	40.69672	33.43947	0.0002	
AC	5.983551	1	5.983551	4.916533	0.0509	
C^2	20.34836	1	20.34836	16.71973	0.0022	
Residual	12.17026	10	1.217026			
Lack of Fit	12.17026	7	1.738609			
Pure Error	0	3	0			
Total	83.07211	15				
R^2 = 0.8535 or 85.35%				Adj R^2 = 0.7802 or 78.02%		
Q^2 = 97.82 %				Adeq Precision = 10.789		

The result from the ANOVA for the reduced model with ethanol yield as response is shown in Table 3.5. Under 90% confidence level, *A*, *B*, *C*, *AC* and C^2 are the significant model terms and this clearly states that the variation in duration of linear and quadratic terms has the greatest influence on ethanol yield. However, the temperature (*B*) has the least effect on ethanol yield based on its large Probability > F value. In addition, the model has a F-value of 11.65165 implied that this model investigated is significant under the confidence level of 90%. In addition, the large values of both coefficient of determination and predictability, R^2 = 85.35% and Q^2 = 97.82 % respectively, indicates a good fit of data to the regression model. The Q^2 value is more than 0.9, which also proves that it is an excellent model.

The model developed was also tested for its validity by comparing the experimental ethanol yield with predicted ethanol yield. The comparison results are tabulated as shown in Table 3.6. Error percentages were tabulated using the difference between the predicted and experimental response values and from the table, it states that the predicted ethanol yields are compatible with the experimental values with less than 2.3 % error.

Table 3.6. Model validity check

Run	Experimental ethanol yield (%)	Predicted ethanol yield (%)	Error (%)
1	0	0.28	0.28
2	0	0.612	0.612
3	0	0	0
4	0	-0.943	0.943
5	0	0.332	0.332
6	0	0	0
7	1.905	4.179	2.274
8	0	0.943	0.943
9	8.235	6.346	1.889
10	0	-0.28	0.28
11	0	0	0
12	0	0	0
13	4.561	4.843	0.282
14	0	-0.332	0.332
15	3.343	2.676	0.667
16	0	-0.612	0.612

3.3.2 Model Analysis of SHF

The response surface 3-D graphs and contour plots were observed by varying two variables according to the respective experimental ranges while maintaining one variable at zero level as shown in Figure 3.11 and 3.12. The quadratic term of duration (C^2) causes the rise (quadratic effect) of the surface response at the duration axis whereas, linear effect on ethanol yield is observed on the pH axis as illustrated in Figure 3.11. Increase in ethanol yield is observed at a lower SHF pH with longer duration shown in Figure 3.12. In addition, shorter incubation period would result in ethanol yield reduction especially at high pH because of the fermentation process which is performed only for the final 24 hours. Hence, operating conditions with longer incubation time and low pH is considered optimal for SHF. The contributing factor to this effect is also the yeast cell activity, which is optimal at pH range of 4.5 to 5.5 [10].

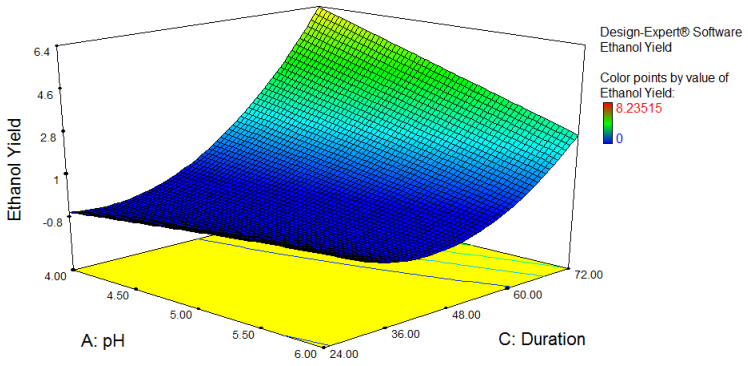


Figure 3.11. Surface response plot of the influence of pH and duration on ethanol yield at 40°C

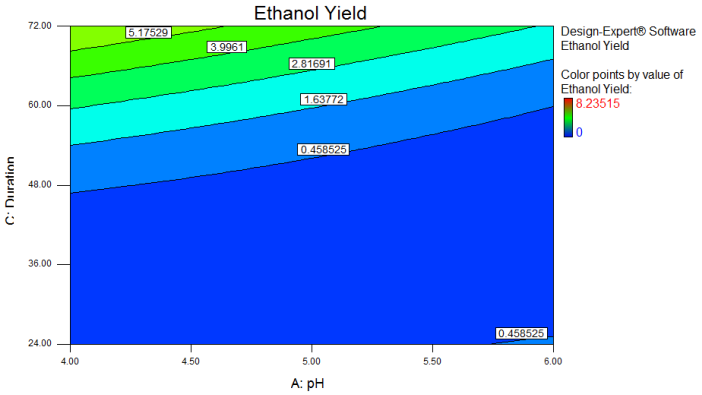


Figure 3.12. Contour plot of pH and duration variation responding to ethanol yield at 40°C

Figure 3.13 and 3.14 clearly shows that the ethanol yield increases as higher duration is implemented in low temperature-SHF. However, temperature is not considered as a major contributing factor in ethanol yield as the linear effect at temperature axis do have a low gradient slope when duration varies. From the response plot, ethanol yield at low temperature (30 - 35°C) and high incubation period (48-72 hours) results in increase of ethanol yield via SHF. Furthermore, the interactive effect of SHF temperature and duration is weaker compared to the pH-duration interaction as the *AC* term is more significant since it has lower P-value.

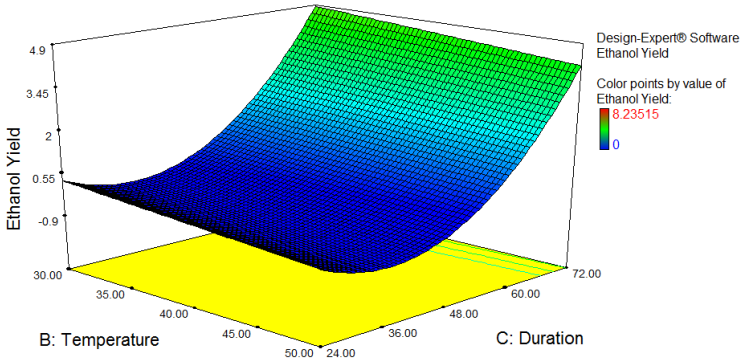


Figure 3.13 Surface response plot of temperature-duration relation on ethanol yield at pH 5

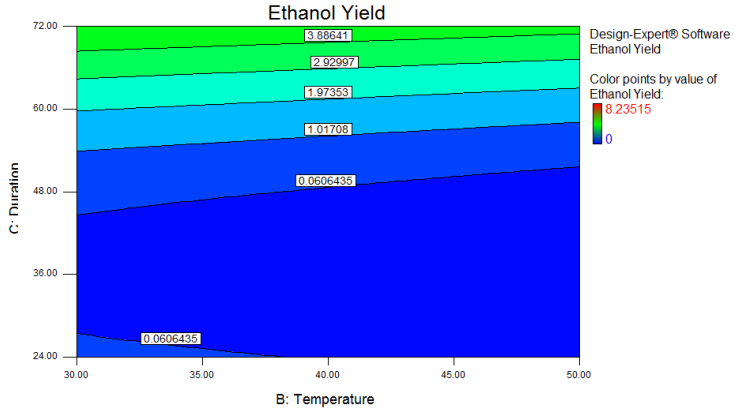


Figure 3.14. Contour plot of temperature and duration variation responding to ethanol yield at pH 5

The linear relation of pH and temperature can be deduced using Figure 3.15 and 3.16. Both coefficients of the *A* and *B* are negative in value meaning that a decrease in ethanol yield is noted when pH is increased from 4 to 6 together with SHF incubation temperature. A slightly

steeper gradient is observed at the pH axis indicating that a change in pH has more effect onto ethanol yield compared to SHF temperature. The maximum ethanol yield is found in one of the corners of the model (pH at level -1) as no curvature occurs.

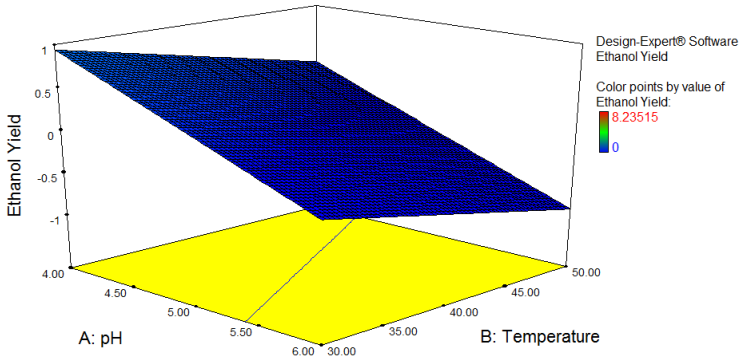


Figure 3.15. Surface response plot of the influence of pH and temperature on ethanol yield at 48 hours

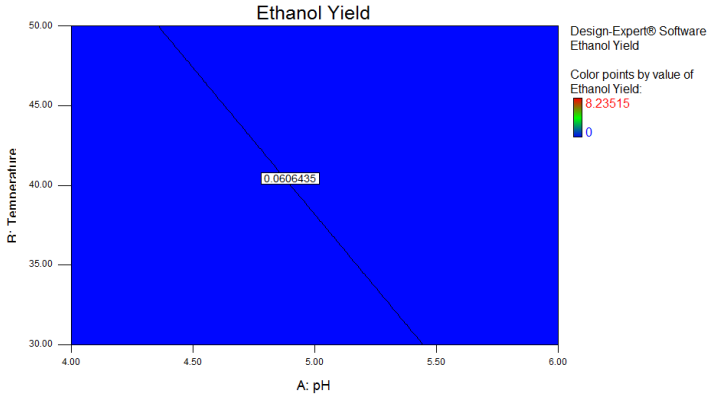


Figure 3.16. Contour plot of temperature-pH interaction responding to ethanol yield at 48 hours

3.3.3 Optimum Conditions of SHF

The optimum conditions for separate hydrolysis and fermentation using unwashed pretreated corn cob is determined via Design Expert 7.0.0 software used. The criteria selected is ethanol yield and the goal is to attain maximized response value with high desirability value. The predicted optimum condition identified for SHF of unwashed pretreated corn cob according to the response model is at pH 4, 30°C, and incubation period of 72 hours, which gives the highest predicted ethanol yield of 6.677% (0.811 desirability) as tabulated in Table 3.7.

Table 3.7. Desirability results with highest predicted ethanol yield at optimum conditions generated by Design Expert software.

Number	pH	Temperature	Duration	Ethanol Yield	Desirability
1	4	30	72	6.677390932	0.810840463
2	4	30.33	72	6.663884554	0.809200373
3	4	30.66	72	6.655429028	0.808173613
4	4	30.86	72	6.648887081	0.807379219
5	4	31.54	72	6.626167695	0.804620388

6	4	32.81	72	6.58412047	0.799514562
7	4	30	71.68	6.569940141	0.797792635
8	4	33.9	72	6.548018687	0.795130697
9	4.08	30.16	72	6.527829663	0.792679129
10	4	35.19	72	6.505274626	0.789940254

3.4 Comparison of SSF and SHF

The optimum condition for SSF using unwashed pretreated corn cob is at pH 4, 33.71°C and 24 hours whereas for SHF, it is noted to be pH 4, 30°C, and incubation period of 72 hours. Both conditions signify the utilization of low temperature and pH but, varying process duration. The predicted optimum ethanol yields are 6.145% and 6.677% for SSF and SHF respectively. SHF gives better results in ethanol yield due to the solids removal before the insertion of yeast for fermentation. This allows more accessible surface of the active sites of the yeast cell resulting in higher conversion rate of glucose to ethanol. SHF allows production of glucose without disturbance via enzymatic hydrolysis first before yeast is added hence, allowing the activated yeast to readily convert the highly-accumulated glucose product, giving higher ethanol yield. In other words, the SSF fermentation yield is lower in value due to low glucose concentration as fermentable sugars are converted to ethanol without delay (less residence time allowed for glucose to gather) thus, preventing the yeast to perform at active rate. So, if extra glucose is prepared and added at the initial stage of SSF (Josefin Axelsson *et al*. 2011), there is high possibility of obtaining greater end-product (ethanol yield) compared to SHF. The optimum condition of SSF requires only 24 hours, which is 48 hours less than SHF optimal duration, this proves that SSF contributes better in acquiring high ethanol yield at lower incubation duration. Since the difference between the highest ethanol yields that can be attained at the optimum conditions of SSF and SHF is 0.532%, which is assumed to be negligible (< 1.0%), it can be concluded that SSF is more feasible to be used due to the lower quantity requirements of water supply. Hence, if this method is applied in large scale bioethanol plant, a profitable and cost effective production rate can be guaranteed. In addition, the cost of expenses in terms of heat generation can also be narrowed as both SSF and SHF not needing high incubation temperature due to the structural characteristics of enzyme and yeast, which might get destroyed when in contact with high temperature.

4. Conclusion

Corn cob was used as lignocellulosic feedstock in the enzymatic hydrolysis carried out in order to determine the optimal conditions. The conditions recorded are necessary to be applied for simultaneous saccharification and fermentation using unwashed pretreated corn cob where hydrolysis yield plays a major role in bioethanol production (ethanol yield). In comparison between the glucose yield analyzed, unwashed pretreated corncob has a slightly lower rate of sugar yield due to the presence of inhibitors as no rinsing is done. However, the concentration difference between both washed and unwashed substrates are very small and this proves that it is feasible to utilize unwashed pretreated lignocellulosic biomass in large scale bioethanol production. Moreover, based on the analysis graphs, the graph line increases gradually from time to time at early stages referring to active hydrolysis rate however, the concentration value stays at a constant upon reaching a certain period. This is due to factors such as inaccessible surface area of enzyme and depletion of cellulose content affecting glucose conversion rate. This also proves that the enzymatic hydrolysis by cellulase Trichoderma Longibrachiatum requires not more than 30 hours according to parameters set in this study.

Olofsson et al. (2008) reported that enzymatic hydrolysis of the solid fraction has a large control over the total rate of ethanol production in SSF. Optimum condition for SSF is at 33.71°C, pH 4 and 24 hours whereas, for SHF, it is 30°C, pH 4 and 72 hours. Hence, it is more feasible to implement SSF for bioethanol production using unwashed pretreated corn cob since lower water usage and incubation period is required as the predicted highest ethanol yield difference between SSF and SHF involving same independent factors is just 0.53 %, assumed to be negligible.

Acknowledgment

Sincere gratitude and thanks are to Dr. Yoon Li Wan for all the guidance and supervisions throughout the entire project. I would also like to thank the Faculty of Chemical Engineering of University Malaya for allowing me to use their equipment in order to complete this research.

References

[1] D. Lee, V. Owens, A. Boe, and P. Jeranyama. *Composition of Herbaceous Biomass Feedstocks*.

[2] R. Benson, C. Bradt, R.O. Benech, R.R. Lehoux, and G.E. Inc (2012). *Patent US8287651 - cellulose pretreatment process*.

[3] B. Marshall (2007). *Gas From The Grass, Field & Stream* (pp.40).

[4] Harmsen, P.F.H. (2010). *Literature Review Of Physical And Chemical Pretreatment Processes For Lignocellulosic Biomass*. Wageningen UR, Food & Biobased Research.

[5] K. Otulugbu (2012). *Production of Ethanol from Cellulose (Sawdust).*

[6] A. Raspolli Galletti and C. Antonetti (2011). *Biomass pre-treatment: separation of cellulose, hemicellulose and lignin. Existing technologies and perspectives.* University of Pisa.

[7] H. Zakpaa, E. Mak-Mensah and F. Johnson (2009). *Production of bio-ethanol from corncobs using Aspergillus niger and Saccharomyces cerevisae in simultaneous saccharification and fermentation*. African Journal of Biotechnology, vol. 8, no. 13.

[8] Zhang YHP, Lynd LR (2004). *Toward an aggregated understanding of enzymatic hydrolysis of cellulose: noncomplexed cellulase systems*. Biotechnol Bioeng (88: pp.797–824)

[9] Tao F, Miao JY, Shi GY, Zhang KC (2005). *Ethanol fermentation by an acid-tolerant Zymomonas mobilis under non-sterilized condition*. Process Biochem (40: pp.183–187)

[10] Y.-S. Cheng, Y. Zheng, C. W. Yu, T. M. Dooley, B. M. Jenkins, and J. S. VanderGheynst (2010). *Evaluation of high solids alkaline pretreatment of rice straw*. Applied Biochemistry and Biotechnology (vol. 162, no. 6, pp. 1768–1784)

[11] Lin, Y, Lee, W (2011). *Simultaneous Saccharification And Fermentation Of Alkali Pretreated Cogongrass For Bioethanol Production*. Bioresources, North

America.

[12] R. Su (2012). *Ethanol production from high-solid SSCF of Alkaline-Pretreated Corncob using recombinant Zymomonas mobilis CP4*. BioEnergy Research (vol. 6, no. 1, pp. 292–299)

[13] A. Pandey, C.-G. Dussap, and E. Gnansounou (2011). *Biofuels: Alternative feedstocks and conversion processes.* Oxford: Elsevier Science.

Ultrasound Assisted Extraction of Pectin from Dragon Fruit Peels

Ng Yee Kai[1*], Chua Bee Lin[2], Rebecca Lim Xiao Yien[3]

[1,2,3]*School of Engineering, Taylor's University*

[*]jordangyeekai93@gmail.com

Abstract

Pectin has increasingly gained importance as it is largely employed in different industry such as food industry, pharmaceutical industry and others due to its gelling capability. Studies have shown that dragon fruit peel was an ideal source of pectin but there was limited study about pectin extracted by Ultrasound Assisted Extraction (UAE) method. The main focus of this research is to study the effect of various parameters (temperature, time and liquid-solid ratio) on the pectin yield and optimise the extraction process. Determination of a most suitable extraction kinetic model is one of the objectives in this study. In this study, UAE method was selected to extract pectin from red dragon fruit (*Hylocereus polyrhizus*) peels by using a sonicator (Elmasonic P 120 H). Central Composite Design (CCD) was used to study and optimise the effect variables on pectin yield. Analysis of variance (ANOVA) was performed to study the significant of independent variable on pectin yield. The pectin yield in this study was significantly affected by extraction temperature and time but not significantly affected by liquid-solid ratio (LSR). Pectin yield increased with the extraction temperature and time. The optimised conditions in this study were extraction temperature of 71.8 °C, extraction time of 25 minutes and LSR of 35.6:1 ml/g with the maximum pectin yield of 7.49%. This condition was confirmed by validation experiments. Five existing common used extraction kinetic models (First Order Kinetic Model, Peleg's Model, Second-order Rate Equation, Logarithmic Model and Power Law Equation) were compared based on determination of coefficient (R^2) in order to select the one with best-fitted to the experimental data. Peleg's Model with highest determination of coefficient (R^2) value (0.9642) was the most suitable model to describe the extraction process of pectin from studied fruit peels. From this study, dragon fruit peel demonstrated as an ideal alternative source of pectin. An efficient UAE process had been established to extract pectin from dragon fruit peel and this could bring contribution to the future pectin industry.

Keywords**:** pectin, dragon fruit peels, ultrasound assisted extraction, central composite design

1. Introduction

A treasured byproduct that can be obtained from fruit wastes is pectin, a naturally occurring polysaccharide [1]. It is a complex polysaccharide that consists of a backbone of a-1,4 linked D-galacturonic acid units which interrupted by α-1-2-L- rhamnose units with the attached side chain of neutral sugar [2]. In addition, pectins can be esterified with the methyl ester at carbon six or acetylated at positions two or three [2]. The name, pectin comes from the Greek word 'pektos' with the definition of hard and firm, indicating the capability of pectin to form gel [3].

Pectin has increasingly gained importance recently. It is largely employed in food industry, pharmaceutical industry and health promotion due to its gelling capability [4]. In 2011, around 60% of the pectin produced is used in food industry as gelling agent [3]. Pectin's best-known use is in jams as it is the only permitted gelling agents in these products [3]. On the other hand, approximately 25% of pectin in the market is used in beverages as thickening agent to give texture to soft drinks or juices [3]. Another 4% of pectin is contributed in dairy products as stabiliser by forming electrostatic interaction with casein particles [3]. This will prevent alteration of casein particles and unstable dispersion caused by heat treatment and acidification [3]. Furthermore, the use of pectin in pharmaceutical industry is growing due to its potential drug delivery properties [3]. Recently, pectin is also applied in improving the shelf life of vegetables and fruits as it can reduce the oxygen and water transfer by forming a barrier [3].

The major source of pectin in current market is from citrus peels and apple pomace which are by-products obtained from the manufacture of juice or cider [2], [5]. High pectin content in both fruit peels make them an important source of pectin. Apple pomace contains 10–15% of pectin on a dry matter basis while citrus peel contains 20–30% [6]. Due to the high demand of pectin in health and pharmaceutical industry, more investigations are carried out to evaluate the pectin content from other fruit sources such as lychee, mango, papaya, banana (Musa sp.) and others [2].

Dragon fruit (*Hylocereus polyrhizus*) are widely grown in Asian countries such as Malaysia, Vietnam, Thailand, the Philippines and Taiwan [7]. In Malaysia, the average production of dragon fruit in 2014 was about 3,835 tons [8]. Besides, the peel constitutes about a quarter of the fruit mass [9]. The peels of dragon fruit are the waste from fruit processing industry which in turn leads to environmental problem. Thus, pectin extraction from the peels of dragon fruit can add a value to the waste and minimise the waste disposal [10]. Additionally, dragon fruit is chosen in this study due to the potential of becoming important source of pectin in the future. In a study by Rahmati et al. proved that dragon fruit had a great potential in food industry as the extracted pectin exhibit a high quality of properties (67.5% of galaturonic acid (GA) content and 49.84% degree of esterification (DE)) which were comparable to citrus pectin (53.62% DE) [10]. Besides, another study showed the yield of pectin from dragon fruit peels was 11 – 13% which was equivalent to apple pomace [5]. Furthermore, there are limited investigations on dragon fruit from the perspective of pectin extraction. Therefore, dragon fruit is selected in this study.

There are several types of pectin extraction method such as conventional extraction, microwave-assisted extraction (MAE) and ultrasound-assisted extraction (UAE). From extensive literature, it was found that only a few fruits have been studied using UAE such as, grapefruit [11], yellow passion fruit (Passiflora edulis Sims f. flavicarpa) [12], grape pomace

of (Cabernet Sauvignon) [13], pomegranate fruit (Punica granatum) [14], fresh grapefruit (Citrus paradisi Macf) [15] and apple [16]. To the best of our knowledge, no UAE method has been performed for pectin extraction from dragon fruit peels. UAE is a less expensive method where acoustic energy is subjected to solvent to perform pectin extraction from sample [17]. Ultrasound can assist the penetration of solvent into sample and cause the solute to be leaked out from sample thereby increased the extraction yield [17]. Furthermore, previous studies showed shorted extraction time and higher yield in UAE as compared to other methods [11], [18]. With regards to this, UAE was performed in this study.

Extraction parameters such as extraction temperature, extraction duration and liquid-solid-ratio can affect the yield of pectin. Therefore, a response surface methodology (RSM) using central composite design (CCD) was applied in this study to evaluate the variables. Three independent variables (extraction temperature, extraction duration and liquid-solid-ratio) were evaluated by CCD with the yield of pectin in order to get the optimum extraction condition. The extraction kinetic of pectin from studied fruit peels was also studied and the experimental data were fitted to 5 kinetic models namely, first order kinetic model, Peleg's model, second-order kinetic, logarithimic kinetic and power law equation to evaluate the applicability. A suitable extraction model that can explain the kinetic extraction of pectin (best fit to the experimental data) from studied raw material was determined.

In this research, pectin extracted by UAE method from dragon fruit peels is studied. The first objective was to study the effect of temperature, duration of ultrasound-assisted extraction (UAE) and liquid-solid ratio (LSR) on the yield of pectin from dragon fruit peels and to study the optimum condition for pectin extraction through response surface methodology (RSM). Second objective was to select the best fitted extraction kinetic model to represent the extraction progress based on the highest coefficient of determination (R^2) using Solver that incorporated in Excel.

2. Methodology

2.1 Preparation and Pre-treatment of dragon fruit peels

2.1.1 Material Collection

Raw material of the target waste fruit, red dragon fruit *(Hylocereus polyrhizus)* peels were collected from local fruit juice vendor "Vitamin Factory" in Taylor's Lakeside University, Selangor.

2.1.2 Drying and Grinding

The peels were washed with running tap water and distilled water to remove impurities on surface. Then they were cut into smaller pieces by using a knife to improve the air contact in drying oven for faster drying purpose. Drying was carried out at moderate temperature, 50 °C until constant weight was attain in order to completely remove moisture to prevent spoilage [19]. The dried peels were sent to a grinder followed by sieving into 500micron to produce dragon fruit peel powder [10], [20]. The sieved dried powder was stored in a seal bag kept dry in desiccator.

2.2 Ultrasound-Assisted Extraction (UAE)

Sonicator (Elmasonic P 120 H) was used. Weak organic citric acid was selected as the solvent in the mixing process. The dried fruit powder (1 g) was first place in a scott bottle and mix with 0.1M citric acid solution of pH 2 with the LSR set at 30:1 ml/g. The powder-acid solution was then placed in an ultrasonic device with to carry out the ultrasound assisted extraction. In the extraction process, time was selected at 5 minutes interval, LSR was constant at 30:1 ml/g, whereas temperature was chosen at 50, 60 and 70°C. A total of 45 samples were prepared and 15 samples for each extraction temperature (50, 60 and 70°C) at 75 min extraction. One sample from each temperature condition was taken out every 5 minutes. The frequency will set at 37 kHz with continuous ultrasonic. Each experiment will carry out thrice to ensure the result reliability.

2.3 Pectin Precipitation and Pectin Yield Determination

The pectin precipitation was modified from Tang et al. (2011) [5]. The extracted mixture was filter using vacuum filtration the filtrate was precipitated with 95% of ethanol at equal volume (ER=1) for 2 hrs. The mixture was then centrifuged at 6000 rpm for 30 min. The filtrate was discharged whereas the pellet from previous step was collected to rinse with 95% of ethanol three times to remove impurities such as monosaccharide, disaccharides and phenolic compounds. The wet pectin was dried in the oven again at 60 °C until constant weight is obtained. Pectin yield (%) was expressed as the ratio of dried pectin mass (Wp) obtained after extraction to the initial mass of dried peel powder (Wt) used for extraction [21]:

$$Yield\ (\%) = \frac{W_p}{W_t} \times 100 \quad (1)$$

2.4 Kinetic Extraction (Preliminary Study)

30 ml of dragon fruit solution was extracted every 5 minutes (total 45 samples) and the dried weight was weighted by using a digital balance (Ohaus PA4102, U.S.A) [22]. The pectin yield was calculated as shown in section 3.4 and a graph of pectin yield (%) against time (mins) was plotted to show the extraction pattern of pectin from dragon fruit peels. The extraction temperature condition that produced the highest pectin yield was selected as the central point of CCD.

2.5 Optimisation of Response Surface Methodology (RSM) and Experimental Validation

RSM was employed to optimise the extraction condition of pectin from the studied fruit waste. Hence, a five level CCD in Design Expert software with three independent variables (extraction temperature, extraction time and LSR) was applied. The five experimental levels in CCD were coded as -α (-1.682), -1 (low), 0 (medium), +1 (high), +α (1.682) [23], [24], where 0 implies the central point [25]. Meanwhile, three independent variables were coded; extraction temperature, extraction time and LSR were coded as X_1, X_2 and X_3. The extraction temperature that produce highest yield in previous kinetic extraction study was 70°C. Thus, the temperature range in CCD was set as 60 – 80°C. Meanwhile, the range of other two variables, extraction time and LSR were chosen based on the previous studies. The range of optimum extraction time was 10 – 30 minutes [19], [14], [18], [26], [15], [27], [21]. On the other hand, the optimum range of LSR was 15:1 to 45:1 ml/g [28], [19], [14], [26], [15]. Table 1 shows the three variables in regards of their actual and coded values.

Table 1. Experimental range and levels of the independent variables

Independent Variables	**Code**	**Independent Variables Level**				
		-α (-1.68)	**-1**	**0**	**+1**	**+α (+1.68)**
Extraction temperature (°C)	X_1	60	64	70	76	80
Extraction time (min)	X_2	10	14	15	26	30
Liquid-solid ratio (LSR)(ml/g)	X_3	15:1	21	30	39	45:1

After inserting the independent variables and the experimental range, CCD generated the combinations of design parameters with their respective responses. Table 2 represents the CCD for the extraction yield of pectin.

Table 2. Central Composite Design (CCD) for the extraction yield of pectin

Std	**Run**	**Temperature (X_1)(°C)**	**Time (X_2)(min)**	**Lsr (X_3)(ml/g)**	**Response (yield)(%)**
1	2	64	14	21	
2	9	76	14	21	
3	6	64	26	21	
4	12	76	26	21	
5	13	64	14	39	
6	8	75	14	39	
7	17	64	26	39	
8	3	76	26	39	
9	1	60	20	30	
10	16	80	20	30	
11	4	70	10	30	
12	10	70	30	30	
13	7	70	20	15	
14	20	70	20	45	
15	5	70	20	30	
16	11	70	20	30	
17	15	70	20	30	
18	18	70	20	30	
19	14	70	20	30	
20	19	70	20	30	

A total of combination set was generated from CCD and each run was conducted in triplicates to obtain the average yield. A mathematical model - second order (quadratic) polynomial equation which can estimate the relationship between independent variables and

response was built. Optimisation of the extraction parameters were then performed by using response optimiser to find the optimum values for each independent variables that give the optimum pectin yield. After obtaining the optimum condition from the software, experimental validation was carried out thrice.

2.6 Analysis of Variance (ANOVA)

ANOVA with 95% of confidence level (CI) was used to analysis the data from RSM in order to determine the significance of independent variables. The significance level was set as $P < 0.05$. In other words, for each terms (independent variable) in the model, a P-value less than 0.05 indicates a significant effect of variable on the response [29]. The adequacy of the regression model was evaluated by F-value, P-value and coefficient of determination (R^2) value [24], [29], [30]. The F-value indicates the ratio of mean square error to the pure error whilst the P-value represent the significance of the variables [30]. The R^2 value defines as the degree of fit and it is used to describe how close the experimental data to the fitted regression line [24]. In general, the term with larger F-value and smaller P-value is regarded as more significant on the response [31]. The range of coefficient of determination (R^2) is between 0 – 1 and the larger value is desirable [24]. Additionally, coefficient of determination (R^2) > 0.75 implies the aptness of the regression model [12].

2.7 Mathematical Modeling for Solid-Liquid Extraction (SLE) of Pectin from Dragon Fruit Peels

In this study, five existing kinetic extraction models were used to study the kinetic extraction process of pectin from dragon fruit peels. These models are first order kinetic model, Peleg's model, second order rate equation, logarithmic model and power law equation.

2.7.1 First Order Kinetic Model

A study on extraction of polyphenol from jamum seeds by Balyan & Sarkar (2016) demonstrated that first order kinetic model was the best model to describe the extraction process [32]. The first order kinetic model based on Fick's Law can be used to study the mass transfer rate of extracted solute into liquid phase from its solid [33]:

$$C_t = C_\propto(1 - e^{-kt}) \qquad (2)$$

where C_t is the concentration of solute in bulk liquid phase at time t (mg solute/g of solid material), $C_\propto$ is concentration of solute at equilibrium at the solid-liquid interface (mg solute/ g of solid material), k is the overall volumetric mass transfer coefficient (min^{-1}), and t is the extraction time.

2.7.1 Peleg's Model

A well-known kinetic model that depict the food material sorption isotherms was introduced by Peleg, 1988 [33]:

$$C_t = C_0 + \frac{t}{k_1 + k_2 \cdot t} \qquad (3)$$

where C_t is the concentration of solute at time t (mg solute/g of solid material), C_0 is the initial concentration of solute in liquid solvent, t is the extraction time, K_1 is the Peleg's rate constant (min g/mg) whereas K_2 is Peleg's capacity constant (min g/mg).
However, C_0 was omitted from the equation due to the initial concentration of solute in liquid solvent was zero. Thus, the modified Peleg's equation can be written as:

$$C_t = \frac{t}{(k_1 + k_2 t)} \tag{4}$$

Peleg's model is extensively used by researches to explain the extraction curves of biological compound from various plants with modification owing to the similarity to the sorption curves shape. In addition, this model was used by Jokic et al. (2010) to represent the extraction process of total polyohenol from soybean [34].

2.7.1 Second Order Rate Equation

This model was applied by researches to explain the extraction of antioxidant from pomegranate marc [35]. The general second order kinetic model is as shown below:

$$\frac{dC_t}{dt} = k(C_e - C_t)^2 \tag{5}$$

Where k is the rate constant (L/g min), C_e is the concentration of solute at equilibrium in liquid phase (g/L) and C_t is the solute concentration in liquid phase at time t (g/L).

The integrated rate law for this model under the boundary conditions t = 0 to t and C_t = 0 to C_t, the equation is as below:

$$C_t = \frac{C_e^2 kt}{1 + C_e kt} \tag{6}$$

The initial extraction rate when t approaches zero can be presented as:

$$h = kC_e^2 \tag{7}$$

By rearranging equation 6 and 7, the C_t can be expressed as:

$$C_t = \frac{t}{\left(\frac{1}{h}\right) + \left(\frac{t}{C_e}\right)} \tag{8}$$

2.7.1 Logarithmic Model

Jokic et al. (2010) had successfully applied logarithmic model to describe the extraction process of polyphenol compound from soybean [34].
The model was used as follows:

$$c(t) = a \log t + b \tag{9}$$

where c(t) is the concentration of solute at time t, a and b are the constant of logarithmic model.

2.7.1 Power Law Equaion

Power law is another useful model to depict the solid- liquid extraction process. The successful example were extraction of rutin from chinese scholar-tree flower [36], water soluble compunds and polysaccharides from medicinal fungus [22] and vanilla extraction from vanilla palifolia Andrews [37]. Cheung et al. (2013) had made some general assumption with regards to Power Law equation [22]:
1. All solid particles are uniform size with spherical shape
2. The extractable material are uniformly distributed within the solid
3. The extractable material have constant diffusion coefficient
4. The solid particles are well dispersed in the liquid extracting solvent

The Power Law equation can be written as:

$$C_t = Bt^n \quad (10)$$

where C_t represents the solute concentration (mg g^{-1}) at time t, t is the extraction time (min), B is the extraction rate constant (g $mg^{-1}min^{-1}$), t is the extraction time (min) and n is the power-law exponent (n<1).

2.8 Extraction Kinetic Model Fitting

The five kinetic models mentioned in section 3.8 were solved by using SOLVER which incorporated in Microsoft Excel 2010. The coefficient of determination (R^2) was chosen to determine the applicability of the model to the experimental data and the models were solved for R^2 close to unity. The R^2 formula is as shown below:

$$R^2 = 1 - \frac{\sum_{i=1}^{n}\left(C_{exp,i} - C_{pre,i}\right)^2}{\sum_{i=1}^{n}\left(C_{exp,i} - \bar{C}\right)^2} \quad (11)$$

where n represents the number of samples, $C_{exp,i}$ indicates the experimental pectin concentration, $C_{pre,i}$ is the predicted pectin concentration and $\bar{C}$ symbolises the mean value of experimental data.

3. Result and Discussion

3.1 Preliminary Study

The result of the preliminary study of pectin yield from dragon fruit peels is shown in figure 1.

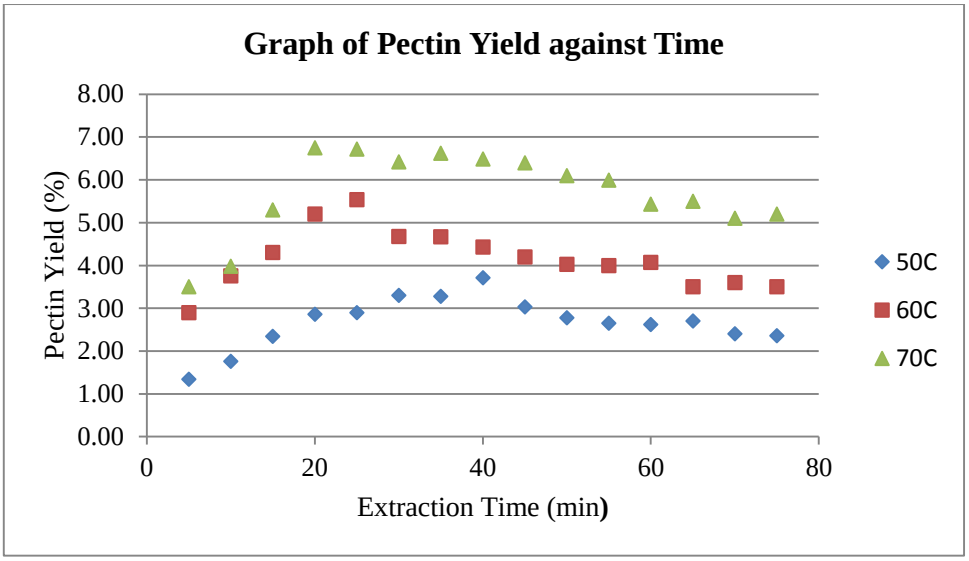


Figure 1. Graph of Pectin Yield against Time

From figure 1, it was found that the extraction temperature with 70°C gave the highest yield compared to 50°C and 60°C. This can be supported by a study that comparing pectin yield from grapefruit under three different temperature (50, 60 and 70°C) and the optimum temperature was 70°C too [11]. Similarly, the method of pectin extraction in that study was UAE [11]. Besides, it can be observed that the pectin yield is increasing with extraction time (sonication time) until reaching 20 – 40 minutes. The pectin yield started to decrease after 20 minutes under temperature 70°C; 25 minutes under temperature 60°C and 40 minutes under temperature 50°C. In addition, previous studies that extracted pectin by UAE mean demonstrated that the extraction time that produce highest yield of pectin ranged from 20 – 60 minutes [11], [19], [13], [18], [21]. Pectin is susceptible to heat degradation [38]. Bahgerian et al. (2011) stated that the reduction of pectin yield over extraction period may be the consequence of thermal degradation of the extracted pectin [11]. The higher the temperature, the more the cavitation bubbles produced [11]. This will increase the shear stress in order to break these bubbles. As a result, the event of pectin chain degradation into smaller components happened and pectin yield decreased [11].

The temperature of 70°C was then selected to be the center point in CCD to produce different experimental conditions (as shown in Table 3) in order to find optimum condition for pectin extraction from studied fruit peel.

Table 3. Central Composite Design with Experimental and Predicted Pectin Yield

Std	Run	Temp (°C)	Time (min)	Lsr (ml/g)	Pectin Yield (%)	
					Experimental	Predicted
9	1	60	20	30	1.98	0.85
1	2	64	14	21	1.83	3.28
8	3	76	26	39	6.75	6.66
11	4	70	10	30	4.89	4.07
15	5	70	20	30	6.65	7.03
3	6	64	26	21	3.15	3.75
13	7	70	20	15	7.14	5.52
6	8	75	14	39	3.69	4.53
2	9	76	14	21	4.38	4.68
12	10	70	30	30	7.65	6.50
16	11	70	20	30	7.18	7.03
4	12	76	26	21	3.42	4.86
5	13	64	14	39	1.89	1.75
19	14	70	20	30	6.29	7.03
17	15	70	20	30	6.69	7.03
10	16	80	20	30	4.59	3.84
7	17	64	26	39	3.42	4.49
18	18	70	20	30	7.65	7.03
20	19	70	20	30	7.389	7.03
14	20	70	20	45	6.10	5.75

3.2 Optimisation of Response Surface Methodology (RSM)

3.2.1 Experimental Design

Optimisation of extraction process was performed by using CCD in Design Expert software 7.0 [23], [39]. CCD with quadratic model was employed to determine the effect of variables on the yield of pectin in this study. After the selection independent variables (temperature, time and LSR) and the range, CCD generated a table with different combinations of extraction condition. Each run was performed trice to acquire the average pectin yield. Table 4 represents the experimental design with the predicted and experimental result.

Table 4. Central Composite Design (CCD) with experimental and predicted pectin yield

Std	**Run**	**Temp (°C)**	**Time (min)**	**Lsr (ml/g)**	**Pectin Yield (%)**	
					Experimental	**Predicted**
9	1	60	20	30	1.98	0.85
1	2	64	14	21	1.83	3.28
8	3	76	26	39	6.75	6.66
11	4	70	10	30	4.89	4.07
15	5	70	20	30	6.65	7.03
3	6	64	26	21	3.15	3.75
13	7	70	20	15	7.14	5.52

Std	Run	Temp (°C)	Time (min)	Lsr (ml/g)	Pectin Yield (%)	
					Experimental	Predicted
6	8	75	14	39	3.69	4.53
2	9	76	14	21	4.38	4.68
12	10	70	30	30	7.65	6.50
16	11	70	20	30	7.18	7.03
4	12	76	26	21	3.42	4.86
5	13	64	14	39	1.89	1.75
19	14	70	20	30	6.29	7.03
17	15	70	20	30	6.69	7.03
10	16	80	20	30	4.59	3.84
7	17	64	26	39	3.42	4.49
18	18	70	20	30	7.65	7.03
20	19	70	20	30	7.39	7.03
14	20	70	20	45	6.10	5.75

From table 4, the experimental pectin yield in this study was range from 1.89 to 7.65%. Result showed the experiment 10 with extraction temperature of 70°C, extraction time of 20 minutes and LSR of 30:1 ml/g produced highest pectin yield whilst experiment 13 with temperature 64°C, time of 14 minutes and LSR of 39:1 ml/g produced the least pectin. The effect of independent variables on the pectin yield was discussed in the following section.

3.2.2 Analysis of Variance (ANOVA)

A multiple regression analysis with respect to the experimental results that retrieved from the CCD was performed. It was observed that a quadratic polynomial model produced a satisfactory fitting of the experimental data with regard to the total pectin yield. ANOVA was used to evaluate the adequacy of the model to exhibit the extraction of pectin from dragon fruit peel in this study. The result in table 5 shows that the quadratic model was able to explain most of the variation in the response due to high F value (F value = 5.0333) and low P-value (P = 0.0094) [14]. The final equation in terms of coded factors was presented in Eq. 12.

$$\begin{aligned} Pectin\ Yield = & -234.4883 + 6.60334X_1 + 0.64843X_2 - 0.17540X_3 \\ & - (2.03643 \times 10^{-3})X_1X_2 + (4.94096 \times 10^{-3})X_1X_3 \\ & + 0.010508X_2X_3 - 0.046869{X_1}^2 - 0.017496{X_2}^2 \\ & - (6.21610 \times 10^{-3}){X_3}^2 \end{aligned} \quad (12)$$

The quality of the fitted model was checked by R^2, adjusted R^2 and adequate precision as shown in table 4.2. High value of R^2 (0.8192) and adjusted R^2 (0.6564) indicated the model could represent the actual relationship between independent variables and response (pectin yield). In this study, the R^2 implying that only 18.08% of the total variation could not be explained by the model [40]. Adequate precision measures the signal to noise ratio and it is desirable if the ratio is > 4 [41]. As shown in table 4.3, the adequate precision of the developed model was 7.275 which showed the best fitness of the model.

Furthermore, the statistical significance of each variable was determined by F value and P-value including the interaction between each variable. From table 4.2, linear effect of extraction temperature (X_1), extraction time (X_2) and quadratic term of extraction temperature

(X_1^2) were found as the significant model terms in this case (P < 0.05). The variable with larger F value and smaller P-value indicated it has more significant effect than others. Therefore, quadratic term of extraction temperature (X_1^2) had greater effect on the pectin yield followed by linear term of extraction temperature (X_1) and extraction time (X_2). The result demonstrates that the pectin was not significantly affected by linear term of LSR (X_3), quadratic effect of extraction time (X_2^2), quadratic effect of LSR (X_3^2) and interaction effect of these three independent variables (X_1X_2, X_1X_3 and X_2X_3) (P > 0.05).

Table 5. Analysis of variance (ANOVA) for the surface quadratic model

Source	**Sum of Squares**	**df**	**Mean Square**	**F Value**	**p-value (Prob > F)**
Model	65.3510	9.0000	7.2612	5.0333	0.0094
A-Temperature	10.5843	1.0000	10.5843	7.3367	0.0220
B-Time	7.1693	1.0000	7.1693	4.9696	0.0499
C-LSR	0.0645	1.0000	0.0645	0.0447	0.8368
AB	0.0411	1.0000	0.0411	0.0285	0.8693
AC	0.5449	1.0000	0.5449	0.3777	0.5525
BC	2.5704	1.0000	2.5704	1.7817	0.2115
A^2	39.3352	1.0000	39.3352	27.2661	0.0004
B^2	5.5557	1.0000	5.5557	3.8510	0.0781
C^2	3.5502	1.0000	3.5502	2.4609	0.1478
Residual	14.4264	10.0000	1.4426		
Lack of Fit	13.1008	5.0000	2.6202	9.8826	0.0126
Pure Error	1.3256	5.0000	0.2651		
Cor Total	79.7774	19.0000			

Std. dev.	1.20	**R^2**	0.8192
Mean	5.14	**Adj-R^2**	0.6564
C.V.%	23.38	**Pred-R^2**	-0.3144
Press	104.86	**Adequate Precision**	7.275

3.3 Effect of Variables on Pectin Yield

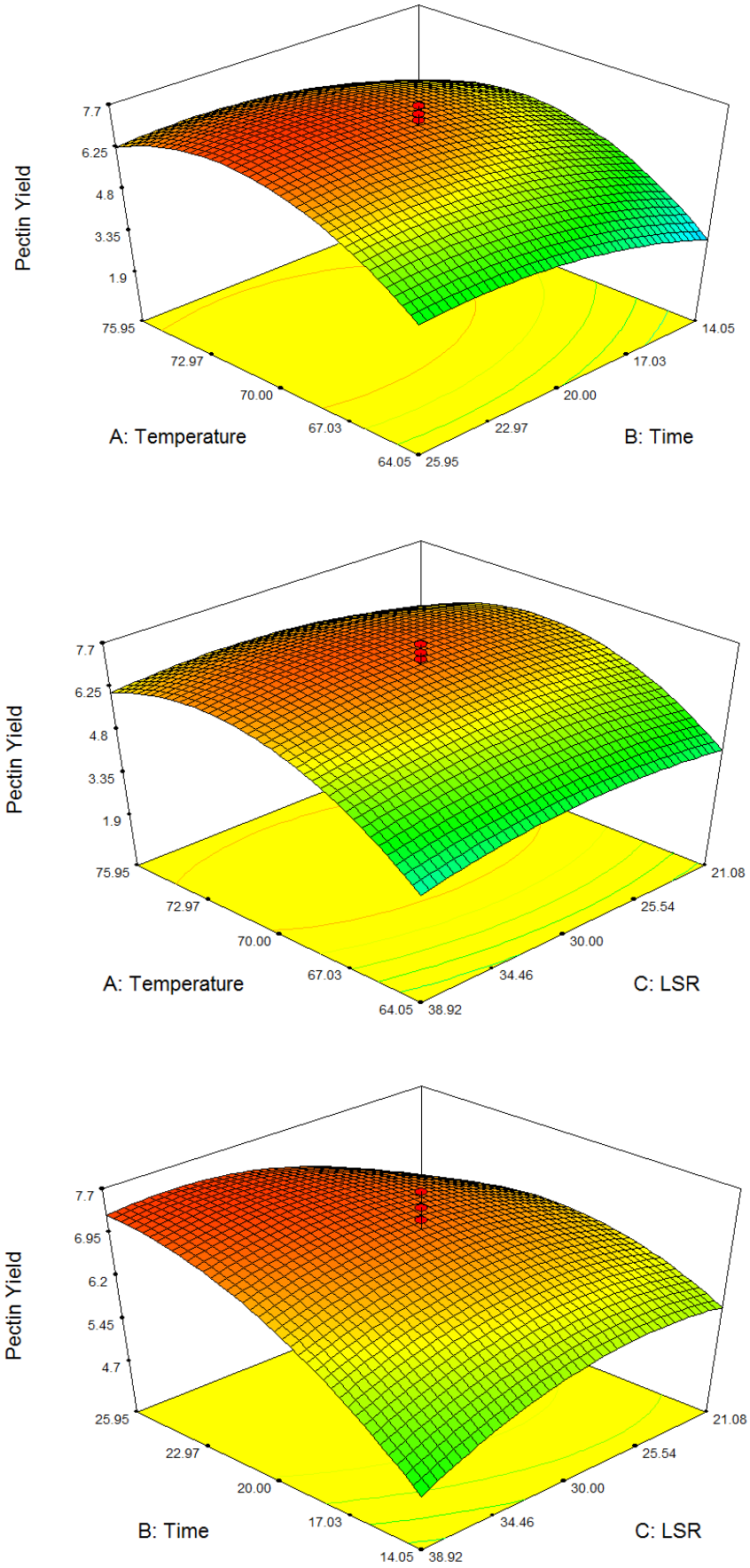


Figure 2. Effect of variables on pectin yield

3.3.1 Effect of temperature on Pectin Yield

The extraction temperature was significantly affecting the pectin yield in this study. From figure 2, the pectin yield increased with extraction temperature until 71.8°C but dropped when further increment. This phenomena (pectin yield increased drastically at early extraction phase) happened because the solubility and diffusivity of solid from the plant materials will increase when temperature increased [14]. Increased in temperature may cause disruption of the ester linkage and hydrogen bond which favor the pectin extraction from material [13]. Nevertheless, solvent surface tension and viscosity will reduce with increased temperature [14]. This may cause some disruptions to the characteristics of ultrasonic cavitation and intensity of mass transfer enhancement [14]. Besides, thermal degradation of pectin can occur which lead to further loss of pectin yield [11], [14].

3.3.2 Effect of extraction time on Pectin Yield

Pectin yield in this study was significantly affected by extraction time. Figure 2 shows that the pectin yield increased drastically initially but slowed down at later extraction phase. This result was in accordance to the study by Freitas et al. (2016) who reported the pectin yield slowed down for longer period of extraction time [12]. Long extraction time is not preferred due to the possibility of pectin degradation which lead to reduced pectin yield [18]. Wang et al. (2015) stated that the shorter extraction time can prevent pectin side chain from degradation [18]. Furthermore, Xu et al. (2014) also stated that the exposure of ultrasound for a long period will lead to pectin degradation [15].

Moorthy et al. (2015) reported that the yield increased initially due to the swelling and hydration of the material which caused by cavitation effect of ultrasound wave [14]. Disruption of cell wall and penetration of solvent into the plant matrix were enhanced which enhanced the extraction process [14]. Nevertheless, the decomposition and destruction of pectin could be happened if prolong the extraction time (prolong the exposure to ultrasound) which reduces the pectin yield [14]. These explanations justified why the rate of pectin yield increased significantly at early phase of extraction but slowed down during the later phase.

3.3.3 Effect on Liquid-Solid Ratio (LSR) on Pectin Yield

Although LSR was not significantly affecting the pectin yield in this study, it was found that the pectin yield increased as the LSR increased up to 30ml/g. The pectin yield decreases when LSR is beyond 30:1 ml/g. This could be explained as LSR increased, the contact area between material and solvent also increased [28]. This cause polysaccharide fully dissolved out from the material [28]. However, when the LSR keep increasing (beyond 30:1 ml/g), the distribution of ultrasonic energy density in the solution decreased [28]. As a result, polysaccharide yield decreased by hindering the dissolution of polysaccharide [28].

3.4 Determination and Validation of Optimum Condition

Optimum condition for extraction to produce the highest pectin yield of 7.49% generated by the Design Expert 7.0 obtained were extraction temperature of 71.78°C, extraction time of 25.04 min and LSR of 35.57:1 ml/g with the desirability of 0.785. After performed the experiment thrice based on the optimum condition (as mentioned above) for validation, the actual experimental mean pectin yield acquired was 7.75% whereas the error

percentage is 3.5%. The results showed that using RSM optimization, the pectin yield had successfully improved by 0.26%.

3.5 Comparison of Existing Solid-liquid Extraction (SLE) Kinetic Models

Table 6. Model's constant and coefficient of determination () of different models for solid-liquid extraction

Model	Model's constants	R^2
First-order Kinetic Model	k_1=0.1461	0.9537
Peleg's Model	k_1=0.4305; k_2=0.1259	0.9642
Second-order Rate Equation	h=3.0745	0.9415
Logarithmic Model	a=2.1186; b=3.8101	0.9256
Power Law Equation	B=4.4573; n=0.1290	0.9177

Table 6 shows the constant and coefficient of determination (R^2) of each model. Peleg's Model was shown to be the most suitable model used to describe the kinetic extraction of pectin from dragon fruits in this study because the coefficient of determination (R^2) value was the highest and closest to 1 among the models.

4.0 Conclusion

In this study, UAE was a good approach to extract pectin from red dragon fruit peels. The result revealed that pectin yield was significantly affected by extraction temperature and time but not significantly affected by LSR. Pectin yield increased with the extraction temperature and time. The application of RSM by using CCD in this study had successfully developed an optimum condition with extraction temperature of 71.8, extraction time of 25 minutes and LSR of 35.6:1 ml/g with the maximum pectin yield of 7.49% in which the condition was confirmed by validation experiments. The most suitable kinetic model that can represent the extraction of pectin from studied raw material was Peleg's Model with the highest coefficient of determination (R^2) 0.9642.

Although dragon fruit could be an ideal pectin source, there is still lacking of studies on the properties of pectin extracted from dragon fruit. Therefore, research on properties of extracted pectin from dragon fruit peels can be performed in the future and it is best if compared to other raw materials such as banana. In addition, optimisation process can be done not only based on the yield but also the properties of pectin for quality and quantity purpose.

References

[1] A. Madhav and P. B. Pushpalatha, "Characterization of Pectin Extracted From Different Fruit Wastes," *J. Trop. Agric.*, vol. 40, pp. 53–55, 2002.
[2] L. Wicker and Y. Kim, "Pectin and Health," *Encycl. Food Heal.*, pp. 289–293, 2016.
[3] B. De Cindio, D. Gabriele, and F. R. Lupi, "Pectin : Properties Determination and Uses," *Encycl. Food Heal.*, pp. 294–300, 2016.
[4] P. Sriamornsak, "Chemistry of pectin and its pharmaceutical uses: a review," no. 28/06/2007, pp. 207–228, 2007.
[5] P.-Y. Tang, T.-S. Kek, C.-Z. Gan, C.-Y. Hee, C.-H. Chong, and K.-K. Woo, "Yield and some chemical properties of pectin extracted from the peels of dragon fruit [Hylocereus polyrhizus (Weber) Britton and Rose]," *Philipp. Agric. Sci.*, vol. 94, no. 3,

pp. 307–311, 2011.
[6] C. D. May, “Industrial Pectins : Sources , Production and Applications,” *Carbohydr. Polym.*, vol. 12, no. December 1988, pp. 79–99, 1990.
[7] Y. Mizrahi, A. Nerd, and P. . Nobel, “Cacti as crops. Horticulture Reviews,” 1997. .
[8] L. . Cheah and M. Z. Wan, “Status of pitaya cultivation in Malaysia,” Putrajaya, 2008.
[9] B. Jamilah, C. E. Shu, M. Kharidah, M. A. Dzulkily, and Noranizan, “Physico-chemical characteristics of red pitaya (Hylocereus polyrhizus) peel,” *Int. Food Res. J.*, vol. 1, no. 18, pp. 279–286, 2011.
[10] S. Rahmati, A. Abdullah, E. Momeny, and O. L. Kang, “Optimization studies on microwave assisted extraction of dragon fruit (Hylocereus polyrhizus) peel pectin using response surface methodology,” *Int. Food Res. J.*, vol. 22, no. 1, pp. 233–239, 2015.
[11] H. Bagherian, F. Zokaee Ashtiani, A. Fouladitajar, and M. Mohtashamy, “Comparisons between conventional, microwave- and ultrasound-assisted methods for extraction of pectin from grapefruit,” *Chem. Eng. Process. Process Intensif.*, vol. 50, no. 11–12, pp. 1237–1243, 2011.
[12] C. of pectin from passion fruit peel assisted by ultrasound Freitas de Oliveira, D. Giordani, R. Lutckemier, P. D. Gurak, F. Cladera-Olivera, and L. D. Ferreira Marczak, “Extraction of pectin from passion fruit peel assisted by ultrasound,” *LWT - Food Sci. Technol.*, vol. 71, pp. 110–115, 2016.
[13] R. Minjares-Fuentes, A. Femenia, M. C. Garau, J. A. Meza-Vel??zquez, S. Simal, and C. Rossell??, “Ultrasound-assisted extraction of pectins from grape pomace using citric acid: A response surface methodology approach,” *Carbohydr. Polym.*, vol. 106, no. 1, pp. 179–189, 2014.
[14] I. G. Moorthy, J. P. Maran, S. M. Surya, S. Naganyashree, and C. S. Shivamathi, “Response surface optimization of ultrasound assisted extraction of pectin from pomegranate peel,” *Int. J. Biol. Macromol.*, vol. 72, pp. 1323–1328, 2015.
[15] Y. Xu, L. Zhang, Y. Bailina, Z. Ge, T. Ding, X. Ye, and D. Liu, “Effects of ultrasound and/or heating on the extraction of pectin from grapefruit peel,” *J. Food Eng.*, vol. 126, pp. 72–81, 2014.
[16] L. Zhang, X. Ye, T. Ding, X. Sun, Y. Xu, and D. Liu, “Ultrasound effects on the degradation kinetics, structure and rheological properties of apple pectin,” *Ultrason. Sonochem.*, vol. 20, no. 1, pp. 222–231, 2013.
[17] M. A. Rostagno, M. Palma, and C. G. Barroso, “Ultrasound-assisted extraction of soy isoflavones,” *J. Chromatogr. A*, vol. 1012, no. 2, pp. 119–128, Sep. 2003.
[18] W. Wang, X. Ma, Y. Xu, Y. Cao, Z. Jiang, and T. Ding, “Ultrasound-assisted heating extraction of pectin from grapefruit peel : Optimization and comparison with the conventional method,” *Food Chem.*, vol. 178, pp. 106–114, 2015.
[19] J. P. Maran and B. Priya, “Ultrasound-assisted extraction of pectin from sisal waste,” *Carbohydr. Polym.*, 2014.
[20] Oliveira, M. F. Rosa, F. L. Cavalcante, H. F. Pereira, G. K. Moates, N. Wellner, S. E. Mazzetto, K. W. Waldron, and H. M. C. Azeredo, “Optimization of pectin extraction from banana peels with citric acid by using response surface methodology,” *Food Chem.*, 2015.
[21] A. N. Grassino, M. Brnčić, D. Vikić-topić, S. Roca, M. Dent, and S. R. Brnčić, “Ultrasound Assisted Extraction and Characterization of Pectin from Tomato Waste,” *Food Chem.*, 2015.
[22] Y. C. Cheung, K. C. Siu, and J. Y. Wu, “Kinetic Models for Ultrasound-Assisted Extraction of Water-Soluble Components and Polysaccharides from Medicinal Fungi,” *Food Bioprocess Technol.*, vol. 6, no. 10, pp. 2659–2665, 2013.

[23] E. R. Pinheiro, I. M. D. A. Silva, L. V. Gonzaga, E. R. Amante, R. F. Teófilo, M. M. C. Ferreira, and R. D. M. C. Amboni, "Optimization of extraction of high-ester pectin from passion fruit peel (Passiflora edulis flavicarpa) with citric acid by using response surface methodology," *Bioresour. Technol.*, vol. 99, no. 13, pp. 5561–5566, 2008.
[24] C. Rai, G. C. Majumdar, and S. De, "Optimization of Process Parameters for Water Extraction of Stevioside using Response Surface Methodology," *Sep. Sci. Technol. 1014-1022 2012*, vol. 47, no. 7, pp. 1014–1022, 2012.
[25] R. M. Banik and D. K. Pandey, "Optimizing conditions for oleanolic acid extraction from Lantana camara roots using response surface methodology," *Ind. Crops Prod.*, vol. 27, no. 3, pp. 241–248, 2008.
[26] K. Thirugnanasambandham, V. Sivakumar, and J. P. Maran, "Process Optimization And Analysis Of Microwave Assisted Extraction Of Pectin From Dragon Fruit Peel," *Carbohydr. Polym.*, 2014.
[27] H. Chen, X. Fu, and Z. Luo, "Properties and extraction of pectin-enriched materials from sugar beet pulp by ultrasonic-assisted treatment combined with subcritical water," *Food Chem.*, vol. 168, pp. 302–310, 2015.
[28] J. P. Maran and B. Priya, "Ultrasound-assisted extraction of polysaccharide from Nephelium lappaceum L. fruit peel," *Int. J. Biol. Macromol.*, vol. 70, pp. 530–536, 2014.
[29] M. Bouras, M. Chadni, F. J. Barba, N. Grimi, O. Bals, and E. Vorobiev, "Optimization of microwave-assisted extraction of polyphenols from Quercus bark," *Ind. Crops Prod.*, vol. 77, pp. 590–601, 2015.
[30] M. K. Khan, M. Abert-Vian, A. S. Fabiano-Tixier, O. Dangles, and F. Chemat, "Ultrasound-assisted extraction of polyphenols (flavanone glycosides) from orange (Citrus sinensis L.) peel," *Food Chem.*, vol. 119, no. 2, pp. 851–858, 2010.
[31] L. Mei, W. Zhen-Chang, D. Hao-Jie, C. Li, X. Qing-Gang, and L. Jing, "Response surface optimization of polysaccharides extraction from liriope roots and its modulatory effect on sjogren syndrome," *Int. J. Biol. Macromol.*, vol. 45, no. 3, pp. 284–288, 2009.
[32] U. Balyan and B. Sarkar, "Aqueous extraction kinetics of phenolic compounds from jamun (*Syzygium cumini* L.) seeds," *Int. J. Food Prop.*, vol. 2912, no. March, p. 10942912.2016.1163266, 2016.
[33] E. Karacabey, L. Bayindirli, N. Artik, and G. Mazza, "Modeling solid-liquid extraction kinetics of trans-resveratrol and trans-??-viniferin from grape cane," *J. Food Process Eng.*, vol. 36, no. 1, pp. 103–112, 2013.
[34] S. Jokic, D. Velic, M. Bilic, Ana Bucic-Kojic, M. Planinic, and S. Tomasa, "Modelling of the process of solid-liquid extraction of total polyphenols from soybeans," *Czech J. Food Sci.*, vol. 28, no. 3, pp. 206–212, 2010.
[35] W. Qu, Z. Pan, and H. Ma, "Extraction modeling and activities of antioxidants from pomegranate marc," *J. Food Eng.*, vol. 99, no. 1, pp. 16–23, 2010.
[36] J. Xi and S. Luo, "Pressure-enhanced solid-liquid extraction of rutin from Chinese scholar-tree flower: Kinetic modeling of influential factors," *Sep. Purif. Technol.*, vol. 156, pp. 809–816, 2015.
[37] Z. Dong, F. Gu, F. Xu, and Q. Wang, "Comparison of four kinds of extraction techniques and kinetics of microwave-assisted extraction of vanillin from Vanilla planifolia Andrews," *Food Chem.*, vol. 149, pp. 54–61, 2014.
[38] B. R. Thakur, R. K. Singh, A. K. Handa, and M. A. Rao, "Chemistry and Uses of Pectin — A Review," *Crit. Rev. Food Sci. Nutr.*, vol. 37(1), no. March 2013, pp. 47–73, 2009.
[39] E. Kliemann, K. N. De Simas, E. R. Amante, E. S. Prudêncio, R. F. Teófilo, M. M. C.

Ferreira, and R. D. M. C. Amboni, “Optimisation of pectin acid extraction from passion fruit peel (Passiflora edulis flavicarpa) using response surface methodology,” *Int. J. Food Sci. Technol.*, vol. 44, no. 3, pp. 476–483, 2009.

[40] J. P. Maran, “Statistical optimization of aqueous extraction of pectin from waste durian rinds,” *Int. J. Biol. Macromol.*, pp. 1–7, 2014.

[41] J. P. Maran and K. A. Prakash, “Process variables influence on microwave assisted extraction of pectin from waste Carcia papaya L . peel,” *Int. J. Biol. Macromol.*, vol. 73, pp. 202–206, 2015.

Physical Properties Investigation on Controlled-Released N-Fertilizer Encapsulated by Alginate-Bentonite Nanocomposite Hydrogel

Ngu Chew Ping, Eunice Phang Siew Wei
School of Engineering, Taylor's University Lakeside Campus, Malaysia

chewping.ngu@sd.taylors.edu.my, SiewWei.Phang@taylors.edu.my

Abstract
Controlled-released fertilizers refers to fertilizers that are stored in capsules of different sizes to achieve a steady release rate into the soil. This state-of-the-art development in the field of fertilizer has an advantage over the standard, quick release fertilizer in which it is able to preserve and maintain the nutrients until it is released at the right time, in the right place with the right amount. In this research project, encapsulation of N-fertilizer (Urea) will be done by using Sodium Alginate-Bentonite nanocomposite hydrogel. The physical properties such as rate of swelling, solubility as well as release rate of the urea will be studied and investigated. The encapsulation will be done by combining a mixture of bentonite, sodium alginate, urea and water under 10 different composition formulations. The mixture will be mechanically stirred with a homogenizer to achieve a homogenous state. Finally, a cross-linking agent which is Calcium Chloride solution of 0.1M will be used so that the fertilizer can be produced in beads form. The nanocomposite hydrogel encapsulation that is made up of sodium alginate and bentonite mixture acts like a cell wall so as to provide a controlled release mechanism to ensure that the fertilizer is supplied at a controlled rate. The release rate of the nitrogen fertilizer under such encapsulation will be determined. The rate of release of the nitrogen-fertilizer depends on the contents of sodium alginate, bentonite and urea in the composition formulation. It is concluded that, the lower the content of sodium alginate in the composition formulation, the lower the rate of release of the encapsulated urea; meanwhile the higher the content of bentonite, the lower the rate of release of the encapsulated urea. The swelling and solubility rate of the produced fertilizer depends on the mass of sodium alginate, bentonite and urea in the fertilizer's composition formulation; the higher the mass of sodium alginate, the higher the swelling and solubility rate of the fertilizer produced. The higher the mass of bentonite, the lower the swelling and solubility rate of the fertilizer produced.

Keywords: Alginate, Bentonite, Controlled-Released Fertilizer, Nanocomposite hydrogel, Urea.

1. Introduction

According to Gerbens-Leenes et al [1], a United Nation studies shows that world's population will experience a rapid increment of population from 5.7 billion in 1995 up to a staggering 9.4 billion in 2050. The issue stated above leads to calls for an immediate solution to solve the resultant rapid rise in global food consumptions. In order to sort out the issue, it is imperative that the agricultural sector increases its crop output. This will then be followed by ensuring a sustainable yet intensified crop production on a land which is currently under cultivation, while securing ecosystem services and mitigate further land degradation [2].

Traditionally, quick release fertilizer has been used to solve the rising issue of increasing food demand where crops are being fed with these fertilizers and experience a normal growth rate. However, according to Mikkelson et al, the right amount of fertilizer has to be applied with the right rate, at the right time and in the right place. Controlled-released fertilizer (CRF) is a type of fertilizer by which its nutrient's release rate and duration is carefully controlled when applied [3]–[5]. This state-of-the-art development in the agriculture sector contributes hugely towards meeting the continuously increase in demand for food. In this research, sodium alginate and bentonite were chosen to form the nanocomposite hydrogel to encapsulate the nitrogen fertilizer (urea) so as to achieve the required controlled-released mechanism.

According to various researchers, hydrogel is defined as hydrophilic polymers that are able to form a cross-linked network and swells under presence of water [6], [7]. Sodium alginate is selected to fulfill this role as the main building block of the hydrogel due to its superior ability in gel formation, biodegradability as well as its ease of production. Bentonite is added to the hydrogel formation as a nanocomposite support in order to provide mechanical strength for the encapsulation. Bentonite, in its nanocomposite form provides coverage to the cross-linked network formed when sodium alginate is exposed to water, thus it reduces the leakage of nutrients in order to achieve the desired controlled-release mechanism. On top of that, addition of bentonite improves the overall solid content of the CRF and it enhances the stability of the encapsulation [8].

In this research however, limitations of the project includes the inability to conduct the research by using soil as well as the lack of parameters to illustrate the biodegradability of the produced fertilizer. This is because of the time constraint of the project which results in several parameters being investigated is done with using water as a medium instead of soil. The parameters, or the physical properties that will be investigated includes the degree of swelling and solubility of the produced CRF beads and the rate of release of urea from the produced CRF beads.

In a nutshell, this research aims to investigate on the usage of sodium alginate and bentonite on the production of CRF. The objectives of this research is shown below:

1. To investigate the rate of release of the produced CRF under the encapsulation of sodium alginate-bentonite nanocomposite hydrogel.
2. To investigate the degree of swelling as well as the rate of solubility of the produced CRF.

2. Methodology

In this research, there will be multiple factors that determine the outcome of the physical properties investigation. Thus, as per the objective of this research, the physical properties investigation will be conducted by only manipulating the mass of sodium alginate, bentonite and urea in the composition formulation while keeping the water content, the sample's drying time and the concentration of cross-linking agent constant. This is because of the time constraint

2.1 Sample Preparation

Table 1 shows the composition of alginate and bentonite in different samples that are produced.

Table 1: The composition formulations of alginate-bentonite nanocomposite hydrogel fertilizer.

Sample	Mass of Alginate, g	Mass of Bentonite, g	Mass of Urea, g	Volume of Water, ml	Concentration of $CaCl_2$, M	Drying time, hr
1	3.0	3.0	2.5	150	0.1	24
2	2.5	3.0	2.5	150	0.1	24
3	2.0	3.0	2.5	150	0.1	24
4	1.5	3.0	2.5	150	0.1	24
5	3.0	2.5	2.5	150	0.1	24
6	3.0	2.0	2.5	150	0.1	24
7	3.0	1.5	2.5	150	0.1	24
8	3.0	3.0	3.0	150	0.1	24
9	3.0	3.0	2.0	150	0.1	24
10	3.0	3.0	1.5	150	0.1	24

Sample preparation begins with measuring the required amount of sodium alginate with the electronic balance, followed by the required amount of bentonite and the amount of urea in grams. This will be followed by the preparation of the cross-linking agent, 0.1M of calcium chloride solution.

In order to produce the required concentration of calcium chloride, we will make use of the equation shown below.

$$n = \frac{MV}{1000}$$

By which,

n = Number of moles of calcium chloride
M = Desired molarity of calcium chloride solution
V = desired volume of calcium chloride solution

As M = 0.1M and V = 1000 ml,
Number of moles of calcium chloride required = $\frac{0.1\ x\ 1000}{1000}$ = 0.1 mol.

Thus, from the calculated required number of moles of calcium chloride, the actual mass of calcium chloride is obtained by using the equation below

$$Required\ mass\ of\ Calcium\ chloride, in\ g = number\ of\ moles\ of\ calcium\ chloride\ x\ Molecular\ Weight\ of\ calcium\ chloride$$

Therefore, required mass of calcium chloride to produce 1000ml of 0.1M calcium chloride solution = 0.1 x 110.98 = 11.098 g

Where molecular weight of calcium chloride is given as 147.02g [9].

Next, the measured amount of sodium alginate, urea and bentonite will be mixed in a clean beaker filled with 150 ml of distilled water. In this step, the homogenizer will be used so as to improve the mixing and allows the mixture to reach a homogenous state. The mixture will be added dropwise to the calcium chloride solution by using a standard laboratory syringe with the needle of diameter 1.2mm to allow the controlled-release fertilizer to form in a beads shape. Then, the newly formed CRF beads will then be extracted from the cross-linking solution and are rinsed once with distilled water. The surface water of the newly produced CRF beads will be removed followed by the drying of the bead in the chemical oven for 24 hours at 80°C.

2.2 Sample Testing

2.2.1 Swelling test

The swelling test is conducted by immersing 0.3g of produced CRF beads in 100 ml of distilled water by using a 100ml Schott bottle. The bottled is then tightly sealed by using the plastic film on the openings to prevent further air and moisture from seeping into the bottle. The sample is then left in the bottle for a few different set time interval from 1 day up to 1 month. The main purpose of this swelling test is to observe the effect of different composition of sodium alginate, bentonite and urea in the composition formulation as well as its effect on achieving optimum controlled-release mechanism. The degree of swelling of the controlled-released fertilizer beads is measured by using the equation stated below:

$$Degree\ of\ swelling, \% = \frac{W_{WS} - W_{DS}}{W_{DS}}\ x\ 100\%$$

Where by,
W_{WS} = Weight of wet samples, g
W_{DS} = Weight of dried samples, g

2.2.2 Solubility test

On the other hand, the solubility test is conducted by taking the wet and swelled samples from the swelling test and a secondary drying operation will be conducted. The wet and swelled samples will be oven dried at a high temperature of 120 degree Celsius for 4 hours to ensure total moisture removal from the samples. The dried samples were then immediately have its weight measured by using an electronic balance. The degree of solubility of the samples were estimated by using the mass difference between the produced samples and the secondary dried samples. The equation that governs the degree of solubility is given as shown below:

$$Degree\ of\ solubility, \% = \frac{W_{DS} - W_{DS2}}{W_{DS}}\ x\ 100\%$$

Where by,
W_{DS} = initially produced dried samples, g
W_{DS2} = Secondary dried samples, g

2.2.3 Rate of release test

The rate of release test is an important test in which it highlights the core objective of this research. Through the rate of release test, the function of sodium alginate as the main building block of the hydrogel and the function of bentonite as the nanocomposite support is investigated and the overall effectiveness of the sodium alginate and bentonite nanocomposite hydrogel is determined.

The rate of release of urea is calculated by conducting the Ultraviolet-Visible (UV-Vis) spectrophotometry. Fix concentrations of urea solutions from 0.1M to 0.5M is prepared and the corresponding solutions is inserted to the UV-Vis spectrophotometer. The absorbance value is obtained at a wavelength of 570nm where the presence of urea in the solution can be detected [10]. This results in a calibration graph where the urea concentration is plotted against its corresponding absorbance value.

Next, the samples that are stored in the Schott bottle as per the swelling test is removed after its designated time interval to obtain the results for swelling test. On the other hand, the liquid in the Schott bottle is extracted and then subjected to UV-Vis Spectrophotometry where the absorbance value will be taken and recorded. The concentration of urea in the solution will be determined by referring to the calibration graph produced earlier. This concentration of urea directly reflects the release of the urea in the water and it shows the ability of CRF to release the nutrients when exposed to water.

3. Results and Discussion

3.1 Swelling test results and discussions

Table 2: Swelling test results based on 1 day sample.

Sample	Weight of Dried Samples, WDS/g			Weight of Swelled Samples, WSS/g		
	WDS 1	WDS 2	WDS 3	WSS 1	WSS 2	WSS 3
1	0.3000	0.3000	0.3000	0.4142	0.4158	0.4140
2	0.3000	0.3000	0.3000	0.4000	0.3988	0.4025
3	0.3000	0.3000	0.3000	0.3870	0.3894	0.3853
4	0.3000	0.3000	0.3000	0.3710	0.3691	0.3657
5	0.3000	0.3000	0.3000	0.4005	0.4001	0.3998
6	0.3000	0.3000	0.3000	0.3925	0.3920	0.3931
7	0.3000	0.3000	0.3000	0.3885	0.3880	0.3877
8	0.3000	0.3000	0.3000	0.4075	0.4072	0.4074
9	0.3000	0.3000	0.3000	0.4065	0.4060	0.4062
10	0.3000	0.3000	0.3000	0.4055	0.4057	0.4054

Table 3 below shows the analysis on the swelling test on 1 day sample.

Table 3: Swelling Test Analysis (1 day sample)

Sample	Percentage of swelling, PS/%			Average percentage of swelling, %
	PS 1	PS 2	PS 3	
1	38.0667	38.6000	38.0000	38.2222
2	33.3333	32.9333	34.1667	33.4778
3	29.0000	29.8000	28.4333	29.0778
4	23.6667	23.0333	21.9000	22.8667
5	33.5000	33.3667	33.2667	33.3778
6	30.8333	30.6667	31.0333	30.8444
7	29.5000	29.3333	29.2333	29.3556
8	35.8333	35.7333	35.8000	35.7889
9	35.5000	35.3333	35.4000	35.4111
10	35.1667	35.2333	35.1333	35.1778

Table 4 below shows the results for swelling test on samples that was immersed in distilled water inside a Schott bottle for 7 days.

Table 4: Swelling test results based on 7 days sample.

Sample	Weight of Dried Samples, WDS/g			Weight of Swelled Samples, WSS/g		
	WDS 1	WDS 2	WDS 3	WSS 1	WSS 2	WSS 3
1	0.3000	0.3000	0.3000	0.4309	0.4314	0.4303
2	0.3000	0.3000	0.3000	0.4126	0.4118	0.4115
3	0.3000	0.3000	0.3000	0.4034	0.4067	0.4059
4	0.3000	0.3000	0.3000	0.3961	0.3899	0.3915
5	0.3000	0.3000	0.3000	0.4195	0.4187	0.4129
6	0.3000	0.3000	0.3000	0.4093	0.4097	0.4118
7	0.3000	0.3000	0.3000	0.3994	0.3967	0.3985
8	0.3000	0.3000	0.3000	0.4198	0.4206	0.4213
9	0.3000	0.3000	0.3000	0.4165	0.4189	0.4175
10	0.3000	0.3000	0.3000	0.4135	0.4146	0.4137

Table 5 below shows the analysis on the swelling test on 7 days sample.

Table 5: Swelling Test Analysis (7 days sample)

Sample	Percentage of swelling, PS/%			Average percentage of swelling, %
	PS 1	PS 2	PS 3	
1	43.6333	43.8000	43.4333	43.6222
2	37.5333	37.2667	37.1667	37.3222
3	34.4667	35.5667	35.3000	35.1111
4	32.0333	29.9667	30.5000	30.8333
5	39.8333	39.5667	37.6333	39.0111
6	36.4333	36.5667	37.2667	36.7556
7	33.1333	32.2333	32.8333	32.7333
8	39.9333	40.2000	40.4333	40.1889
9	38.8333	39.6333	39.1667	39.2111
10	37.8333	38.2000	37.9000	37.9778

Table 6 below shows the results for swelling test on samples that was immersed in distilled water inside a Schott bottle for 30 days.

Table 6: Swelling test results based on 30 days sample.

Sample	Weight of Dried Samples, WDS/g			Weight of Swelled Samples, WSS/g		
	WDS 1	WDS 2	WDS 3	WSS 1	WSS 2	WSS 3
1	0.3000	0.3000	0.3000	0.4531	0.4495	0.4516
2	0.3000	0.3000	0.3000	0.4321	0.4254	0.4219
3	0.3000	0.3000	0.3000	0.4159	0.4167	0.4189
4	0.3000	0.3000	0.3000	0.4059	0.3994	0.4016
5	0.3000	0.3000	0.3000	0.4315	0.4295	0.4265
6	0.3000	0.3000	0.3000	0.4278	0.4193	0.4168
7	0.3000	0.3000	0.3000	0.4132	0.4107	0.4111
8	0.3000	0.3000	0.3000	0.4351	0.4401	0.4365
9	0.3000	0.3000	0.3000	0.4276	0.4326	0.4293
10	0.3000	0.3000	0.3000	0.4201	0.4233	0.4254

Table 7 below shows the analysis on the swelling test on 30 days sample.

Table 7: Swelling Test Analysis (30 days sample)

Sample	Percentage of swelling, PS/%			Average percentage of swelling, %
	PS 1	PS 2	PS 3	
1	51.0333	49.8333	50.5333	50.4667
2	44.0333	41.8000	40.6333	42.1556
3	38.6333	38.9000	39.6333	39.0556
4	35.3000	33.1333	33.8667	34.1000
5	43.8333	43.1667	42.1667	43.0556
6	42.6000	39.7667	38.9333	40.4333
7	37.7333	36.9000	37.0333	37.2222
8	45.0333	46.7000	45.5000	45.7444
9	42.5333	44.2000	43.1000	43.2778

10	40.0333	41.1000	41.8000	40.9778

Based on the results displayed above in table 2-7 respectively, the results obtained provided an insight to the physical properties of the produced alginate-bentonite nanocomposite hydrogel.

Firstly, on the fixed model composition formulation in which it is represented by Sample 1, the percentage of swelling for 1-day sample, 7-days sample and 30-days sample are 38.2222%, 43.6222% and 50.4667% respectively. This shows that the swelling rate of this sample increases with time. As per discussed earlier in the Background Section of this thesis report, the increment in swelling represents the ability of the fertilizer to absorb water and experience an expansion in size. As the swelling percentage increases, the nutrient release will also be increased. However, it is to be noted that, in 30 days of constantly immersed in distilled water, 0.3g of sample only achieved about 50% of swelling rate in which that the nutrient release of the urea in the alginate-bentonite nanocomposite hydrogel is somehow controlled.

Secondly, the physical properties investigation on the alginate-bentonite nanocomposite hydrogel urea fertilizer is determined when the mass percentage of alginate is decreased in the composition formulation as represented in sample 2-4 where the mass of alginate is decreased from 3g to 2.5g, 2.0g and 1.5g respectively. The comparison in 1-day sample shows that the average percentage of swelling of sample 2, 3 and 4 are 33.4778%, 29.0778% and 22.8667% respectively. The decrease in alginate content in the composition formulation results in a decrease in swelling of the produced fertilizer. This is due to the lack of alginate in the composition formulation leads to lesser gel-enhancing properties as per described in sodium alginate's properties and thus the resulting fertilizer formed will have less water absorbent tendency. The literature review that is done on alginate showed that at increasing alginate content, swelling rate will be decreased at a certain mass content of sodium alginate. This is because of the outer matrix that leads to a more complex path for water to travel before it is absorbed by the fertilizer. This condition however, did not exist as the amount of alginate used is too little. Based on table 5 and table 7, for sample 2-4 where the decrease in alginate sample stay immersed in water for up to 7 and 30 days, the average percentage of swelling increases as the number of days increases but the trend of decreasing alginate results in decreasing swelling rate remains the same. Overall, the swelling rate of sample 2-4 showed a trend in which it is always lower than the swelling rate of sample 1. This proves that, under the influence of bentonite, the produced fertilizer remained its core function of providing the desired controlled-release mechanism despite a decrease in alginate content.

Furthermore, the physical properties investigation on the alginate-bentonite nanocomposite hydrogel urea fertilizer is determined when the mass percentage of bentonite is decreased in the composition formulation as represented in sample 5-7 where the mass of bentonite is decreased from 3g to 2.5g, 2.0g and 1.5g respectively. The comparison in 1-day sample shows that the average percentage of swelling of sample 5, 6 and 7 are 33.3778%, 30.8444% and 29.3556% respectively. Similarly to the effect of decreasing alginate content, the decrease in bentonite content in the composition formulation results in a decrease in swelling of the produced fertilizer. The effect of lesser bentonite under constant sodium alginate content leads to smaller rate of swelling is unexpected as bentonite's core function in the produced fertilizer would be providing mechanical support and improves the overall structure and strength of the fertilizer. The lack of bentonite in the composition formulation should lead to the produced fertilizer having lesser mechanical strength properties as per described and thus the resulting fertilizer formed will have higher water absorbent tendency. The literature review that is done on bentonite showed that at increasing bentonite content, swelling rate will be decreased. As more bentonite is added into the formulations, its water repelling properties will be exerted

onto the fertilizer, this condition clearly did not showed in the results obtained. The reasoning behind this can be explained by bentonite's distribution in the produced fertilizer beads may not be even. As there are no methods available to check on the bentonite distribution, the justification to that proof is not available. Based on table 5 and table 7 for sample 5-7 where the decrease in alginate sample stay immersed in water for up to 7 and 30 days, the average percentage of swelling increases as the number of days increases but the trend of decreasing alginate results in decreasing swelling rate remains the same. Overall, the swelling rate of sample 2-4 showed a trend in which it is always lower than the swelling rate of sample 1. This proves that, under the influence of bentonite, the produced fertilizer remained its core function of providing the desired controlled-release mechanism despite a decrease in alginate content. Moreover, the overall results of swelling properties that are shown by sample 5-7 clearly are higher than sample 2-4. This proves that, the decrease of bentonite does not affect the swelling properties of the fertilizer as compared to the effect of decreasing alginate. This too proves to be a justification towards alginate's hydrophilic properties to bentonite's hydrophobic properties.

Last but not least, the effect of urea content also affected the swelling properties of the produced fertilizer. This is because, at higher or lower content of urea than the model sample, as shown in sample 8 (3.0g of urea), sample 9 (2.0g of urea) and sample 10 (1.5g of urea), the swelling rate decreases slightly. The reasoning behind the lower swelling rate when the urea content is lower is due to urea being able to be dissolved in water provides an additional water absorbency properties to the fertilizer, hence the lower the urea content, the lower the amount of water being able to be absorbed by the produced fertilizer under similar mass content of sodium alginate and bentonite as compared to sample 1. However, as the mass of urea is increased, the resultant swelling rate is decreased remains unexplained as there are no proof to support this unexpected yield in results. However, it is assumed that, similarly to the sodium alginate's swelling properties as explained in the literature review section, urea has a certain limit in absorbing water in which if the water absorbing limit is achieved, there would be no longer any increment in its swelling rate.

3.2 Solubility test results and discussion

Table 8 below shows the results for solubility test on samples that was immersed in distilled water inside a Schott bottle for 1 day.

Table 8: Solubility test results based on 1 day sample.

Sample	Weight of Dried Samples, WDS/g			Weight of Secondary Dried Samples, WDS'/g		
	WDS 1	WDS 2	WDS 3	WDS' 1	WDS' 2	WDS' 3
1	0.3000	0.3000	0.3000	0.1875	0.1934	0.1988
2	0.3000	0.3000	0.3000	0.2245	0.2356	0.2259
3	0.3000	0.3000	0.3000	0.2306	0.2264	0.2351
4	0.3000	0.3000	0.3000	0.2379	0.2354	0.2394
5	0.3000	0.3000	0.3000	0.2180	0.2157	0.2169
6	0.3000	0.3000	0.3000	0.2070	0.2048	0.2099
7	0.3000	0.3000	0.3000	0.2080	0.2015	0.2033
8	0.3000	0.3000	0.3000	0.2450	0.2395	0.2356
9	0.3000	0.3000	0.3000	0.2400	0.2314	0.2411
10	0.3000	0.3000	0.3000	0.2350	0.2328	0.2271

Table 9 below shows the analysis on the solubility test on 1 day sample.

Table 9: Solubility Test Analysis (1 day sample)

Sample	Percentage of swelling, PS/%			Average percentage of swelling, %
	PS 1	PS 2	PS 3	
1	37.5000	35.5333	33.7333	35.5889
2	25.1667	21.4667	24.7000	23.7778
3	23.1333	24.5333	21.6333	23.1000
4	20.7000	21.5333	20.2000	20.8111
5	27.3333	28.1000	27.7000	27.7111
6	31.0000	31.7333	30.0333	30.9222
7	30.6667	32.8333	32.2333	31.9111
8	18.3333	20.1667	21.4667	19.9889
9	20.0000	22.8667	19.6333	20.8333
10	21.6667	22.4000	24.3000	22.7889

Table 10 below shows the results for solubility test on samples that was immersed in distilled water inside a Schott bottle for 7 days.

Table 10: Solubility test results based on 7 days sample.

Sample	Weight of Dried Samples, WDS/g			Weight of Secondary Dried Samples, WDS'/g		
	WDS 1	WDS 2	WDS 3	WDS' 1	WDS' 2	WDS' 3
1	0.3000	0.3000	0.3000	0.1713	0.1729	0.1738
2	0.3000	0.3000	0.3000	0.2019	0.2067	0.2052
3	0.3000	0.3000	0.3000	0.2033	0.2054	0.2071
4	0.3000	0.3000	0.3000	0.2179	0.2051	0.2061
5	0.3000	0.3000	0.3000	0.2001	0.2014	0.1983
6	0.3000	0.3000	0.3000	0.1968	0.1994	0.1977
7	0.3000	0.3000	0.3000	0.1951	0.1915	0.1920
8	0.3000	0.3000	0.3000	0.2295	0.2167	0.2064
9	0.3000	0.3000	0.3000	0.2185	0.2171	0.2043
10	0.3000	0.3000	0.3000	0.2106	0.2149	0.2087

Table 11 below shows the analysis on the solubility test on 7 days sample.

Table 11: Solubility Test Analysis (7 days sample)

Sample	Percentage of swelling, PS/%			Average percentage of swelling, %
	PS 1	PS 2	PS 3	
1	42.9000	42.3667	42.0667	42.4444
2	32.7000	31.1000	31.6000	31.8000
3	32.2333	31.5333	30.9667	31.5778
4	27.3667	31.6333	31.3000	30.1000
5	33.3000	32.8667	33.9000	33.3556
6	34.4000	33.5333	34.1000	34.0111

7	34.9667	36.1667	36.0000	35.7111
8	23.5000	27.7667	31.2000	27.4889
9	27.1667	27.6333	31.9000	28.9000
10	29.8000	28.3667	30.4333	29.5333

Table 12 below shows the results for solubility test on samples that was immersed in distilled water inside a Schott bottle for 30 days.

Table 12: Solubility test results based on 30 days sample.

Sample	Weight of Dried Samples, WDS/g			Weight of Secondary Dried Samples, WDS'/g		
	WDS 1	WDS 2	WDS 3	WDS' 1	WDS' 2	WDS' 3
1	0.3000	0.3000	0.3000	0.1645	0.1604	0.1679
2	0.3000	0.3000	0.3000	0.1901	0.1895	0.1874
3	0.3000	0.3000	0.3000	0.1978	0.1901	0.1955
4	0.3000	0.3000	0.3000	0.1989	0.1994	0.1967
5	0.3000	0.3000	0.3000	0.1751	0.1775	0.1799
6	0.3000	0.3000	0.3000	0.1704	0.1741	0.1725
7	0.3000	0.3000	0.3000	0.1686	0.1621	0.1716
8	0.3000	0.3000	0.3000	0.2008	0.2043	0.2167
9	0.3000	0.3000	0.3000	0.2085	0.2012	0.2029
10	0.3000	0.3000	0.3000	0.2029	0.2041	0.2005

Table 13 below shows the analysis on the solubility test on 30 days sample.

Table 13: Solubility Test Analysis (30 days sample)

Sample	Percentage of swelling, PS/%			Average percentage of swelling, %
	PS 1	PS 2	PS 3	
1	45.1667	46.5333	44.0333	45.2444
2	36.6333	36.8333	37.5333	37.0000
3	34.0667	36.6333	34.8333	35.1778
4	33.7000	33.5333	34.4333	33.8889
5	41.6333	40.8333	40.0333	40.8333
6	43.2000	41.9667	42.5000	42.5556
7	43.8000	45.9667	42.8000	44.1889
8	33.0667	31.9000	27.7667	30.9111
9	30.5000	32.9333	32.3667	31.9333
10	32.3667	31.9667	33.1667	32.5000

With regards to table 9, table 11 and table 13, it is concluded that the produced fertilizer in model sample (represented by sample 1) experienced increasing solubility as the number of days that it was immersed in distilled water increases. On top of that, generally the model sample obtains the highest solubility rate (35.5889%, 42.4444% and 45.2444%) when compared to 9 other samples in which it justifies that the particular formulation is the most

suitable formulation to be used to produce the sodium alginate-bentonite nanocomposite hydrogel urea fertilizer with optimum performances.

For samples with decreasing sodium alginate content (represented by samples 2 – 4), the solubility rate decreases with decreasing sodium alginate in the composition formulation. This is due to the lack of sodium alginate which it results in the decreasing water absorbency of the fertilizer. As sodium alginate can be readily dissolve in water to form a gel-like substance for easier encapsulation, the lack of it can cause the overall fertilizer to lose the water absorbency properties. On top of that, the presence of macrospores in the outer matrix of the produced hydrogel fertilizer due to presence sodium alginate is also reduced as the mass of sodium alginate is decreased. This results in lesser paths for water to be fully absorbed into the fertilizer and for the urea within to diffuse out from the fertilizer. As the time of the samples spent immersed inside the distilled water in the Schott bottle increases, the solubility rate increases. This shows that the lack of sodium alginate does not affect the solubility rate to be increased over time. Besides that, the overall solubility rate of samples 2-4 are lower than sample 1 which shows that with decreasing sodium alginate content, the produced sodium alginate-bentonite nanocomposite hydrogel urea fertilizer has less than optimum performances.

On the other hand, for samples with decreasing bentonite content (represented by samples 5 - 7), the solubility rate increases with decreasing bentonite in the composition formulation. This is due to the lack of bentonite which it results in the increasing water absorbency of the fertilizer. As bentonite cannot be readily dissolve in water due to its hydrophobic nature, the lack of it can cause the overall water absorbency properties of the fertilizer to play its role thanks to the presence of sodium alginate. On top of that, the presence of bentonite produced hydrogel fertilizer will lead to the fertilizer's overall mechanical strength to be improved. This results in higher difficulty for water to be fully absorbed into the fertilizer and for the urea within to diffuse out from the fertilizer through the macrospores provided by sodium alginate. The lack of bentonite causes the macrospores to be easily expanded when immersed in water. As the time of the samples spent immersed inside the distilled water in the Schott bottle increases, the solubility rate increases. This shows that the lack of bentonite does not affect the solubility rate to be increased over time. Besides that, the overall solubility rate of samples 5-7 are lower than sample 1 which shows that with decreasing bentonite content, the produced sodium alginate-bentonite nanocomposite hydrogel urea fertilizer has less than optimum performances. Nonetheless, the overall solubility rate of samples with decreasing bentonite showed higher value when compared to samples with decreasing alginate. This shows that, sodium alginate plays a more important role in producing fertilizer with optimum solubility rate but the contribution of bentonite towards achieving a desired controlled release medium is equally essential.

Lastly, the effect of urea in the samples also affected the solubility rate of the produced fertilizer. As shown in sample 8 (3.0g urea), sample 9 (2.0g urea) and sample 10 (1.5g urea), the lower the urea content, the lower the solubility rate. This is due to urea being able to be dissolve in water contributes to the solubility of the fertilizer itself in general. On top of that, presence of sodium alginate at its optimum level allows maximum diffusion of urea out of the fertilizer. Hence, when the urea content is lower, the amount that is able to diffuse out is also lower. Nonetheless, there is one scenario in which when the urea content in the composition formulation is increased as shown in sample 8, the overall solubility rate decreases as compared to the model sample. This can be explained in which similar scenarios are encountered by other researchers as described in the Literature review section where similarly to sodium alginate reached its peaked swelling rate value, urea too reached a peak value in solubility in a fixed

amount of distilled water. Once again this justifies the model sample choice as the most optimum formulation out of the 10 samples.

3.3 Rate of release test results and discussion

In order to determine the rate of release of urea, a calibration graph is produced in order to determine the concentration of urea in M by using absorbance value in A through performing UV-VIS spectrophotometry. Figure 1 below shows the calibration graph created by running 0M to 0.8M of urea solution through the UV-VIS spectrophotometry at 570nm wavelength.

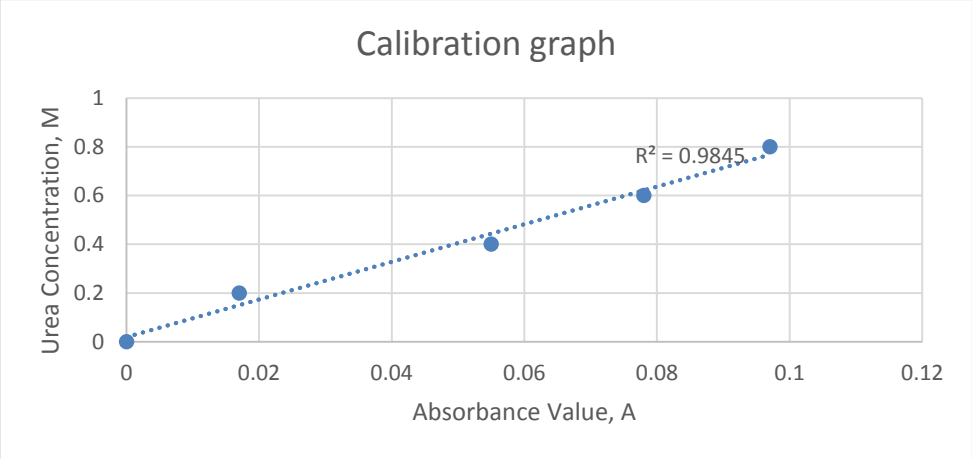


Figure 1: Calibration graph on determination of urea concentration

From the 10 samples that was produced according to the composition formulation displayed above, 0.3g was taken from each sample and are placed in 100 ml of distilled water in a Schott bottle for 1 day. After 1 day, the fertilizer will be extracted from the storing water and the water will be subjected to UV-VIS spectrophotometry absorbance test in order to determine how much urea diffused out in term of concentration. Table 14 below shows the results obtained from each samples in the 1 day test.

Table 14: Rate of urea release test results

Sample	Absorbance, A	Resulting concentration, M
1	0.008	0.47
2	0.009	0.53
3	0.002	0.12
4	0.006	0.35
5	0.005	0.29
6	0.006	0.35
7	0.006	0.35
8	0.007	0.41
9	0.003	0.18
10	0.001	0.06

As shown above in table 14, the overall urea release is noticeable in all of the sample that are produced. This justifies that under presence of water, the fertilizer will be able to produce its core function of releasing nutrients. The rate of release of urea is generally high on the model sample in which it implies that the suggested model sample is achieving the desired optimum performance albeit its rate of release is slightly lower when compared to sample 2. As for the rate of release for decreasing alginate samples, the rate decreases when the content of sodium alginate is decreased. This is once again due to the hydrophilic properties provided by the sodium alginate is lacking as the mass of sodium alginate is decreased across the 3 samples. As the fertilizer loses the hydrophilic properties, the urea from the fertilizer itself faces a tougher condition towards optimum diffusion. Thus, the rate of release is generally decreased as mass of sodium alginate is decreased. Similarly, as the mass of bentonite is decreased in the composition formulations a shown in samples 5-7, the rate of release is generally increased. However, the results obtained in sample 7 implies that there might be a slight error when conducting the experiment. As explained earlier in the previous section, bentonite provides mechanical strength and improves the overall controlled-release mechanism to the fertilizer. This leads to an expected general increment in rate of release in decreasing bentonite content samples. However, the expected condition did not take place in sample 7 leads to the conclusion that there might be some experimental error that are conducted when the UV-VIS spectrophotometry is conducted. Nonetheless, the general increasing trend towards decreasing bentonite content proves that the above suggested theory still applies. Lastly, the effect of decreasing urea showed a decreasing trend in rate of release of urea. This is because as the concentration of urea in the fertilizer decreases, it results in lesser urea being able to diffuse out from the encapsulation of sodium alginate and bentonite. However, the results in sample 8 shows that the urea concentration obtained from the water is slightly lower than the model sample. This shows that the optimum amount of urea that should e included in the formulation is as per the model sample's formulation in which only 2.5g of urea is sufficient to achieve the optimum performance.

4. Conclusions

In conclusion, it is found that sodium alginate and bentonite are suitable to be used as the building component for the controlled-released fertilizer. The optimum composition that is suggested through various testing and characterization showed that at mass of sodium alginate = 3.0 g, mass of bentonite = 3.0 g, mass of urea = 2.5g, volume of water used = 150ml and concentration of cross-linking agent (calcium chloride at 0.1M), the fertilizer produced has the

best swelling rate, best solubility rate and fairly good rate of release for urea as compared to 9 other proposed samples. On top of that, through this research, it is known that the thermal stability of the produced fertilizer is above average as it is able to withstand up to a temperature of 200°C before it experience weight reduction. In a nutshell, the research of producing a controlled-released mechanism is also a successful one as the fertilizer is able to achieve the desired core function.

References

[1] P. W. Gerbens-Leenes, S. Nonhebel, and W. P. M. F. Ivens, "A method to determine land requirements relating to food consumption patterns," *Agric. Ecosyst. Environ.*, vol. 90, no. 1, pp. 47–58, 2002.

[2] P. Heffer, H. Magen, R. Mikkelsen, and D. Wichelns, "Managing Water and Fertilizer for Sustainable Agricultural Intensification," *Int. Fertil. Ind. Assoc.*, 2015.

[3] M. E. Trenkel, "Improving Fertilizer Use Efficiency Controlled-Release and Stabilized Fertilizers in Agriculture."

[4] X. Han, S. Chen, and X. Hu, "Controlled-release fertilizer encapsulated by starch/polyvinyl alcohol coating," *Desalination*, vol. 240, no. 1–3, pp. 21–26, 2009.

[5] G. C. Sharma, "Controlled-release fertilizers and horticultural applications," *Sci. Hortic. (Amsterdam).*, vol. 11, no. 2, pp. 107–129, 1979.

[6] M. A. Abed, A. M. Haddad^, A. J. Hassen, and S. M. Sultan, "Preparation and evaluation of new hydrogels as new fertilizer delivery system," *Basrah J. Scienec*, vol. 2424, no. 11, pp. 103–1149, 2006.

[7] E. M. Ahmed, "Hydrogel: Preparation, characterization, and applications: A review," *J. Adv. Res.*, vol. 6, no. 2, pp. 105–121, 2015.

[8] Y. He, Z. Wu, L. Tu, Y. Han, G. Zhang, and C. Li, "Encapsulation and characterization of slow-release microbial fertilizer from the composites of bentonite and alginate," *Appl. Clay Sci.*, vol. 109–110, pp. 68–75, 2015.

[9] "Molarity Basic Concepts of Preparing Solutions."

[10] Z. Filutowicz, K. Łukaszewski, and K. Pieszyński, "REMARKS ON SPECTRA-PHOTOMETRIC MONITORING OF UREA IN DIALYSATE," *J. Med. INFORMATICS Technol.*, vol. 8, pp. 1642–6037, 2004.

Accelerated Enzymatic Hydrolysis of Lignocellulose using Membrane Separation

Phang Zhen Fei, Rajesh Rajasekaran
School of Engineering, Taylor's University, Malaysia

Rajesh.rajasekaran@taylors.edu.my

Abstract

Pretreatment of cellulose technology has been receiving a considerable amount of attention worldwide due to its potential as an alternative energy source to biofuel. Many efforts have been made over the past decade to improve the bioethanol conversion process to be more cost-effective and feasible for large-scale production. The incentive of this effort is due to the renewable capability of bioethanol as an energy and also the small amount of pollutant bioethanol produced during combustion (clean energy). Hence, new technology to cellulose pretreatment is needed to increase the bioethanol production capability. Research on adding membrane separation technique during hydrolysis have shown promising results in recent studies, but it is only limited to ionic dissolution pretreatment process. This research emphasized on improving enzymatic hydrolysis of both acidic H_2SO_4 and alkaline NaOH solution pretreated lignocellulose biomass by implementing 10 kDa cutoff ultrafiltration membrane to reuse enzyme in hydrolysis process for subsequent sugar recovery. An additional membrane separation technique is attached at the end of a tube connecting with a pump to glucose storage container to filter enzyme from sugar so that the enzyme will retain in the hydrolysis container. The combination of 1M diluted H_2SO_4 and 1M diluted NaOH pretreatment, enzymatic hydrolysis using optimum 3% dosage of Trichoderma Viride enzyme cellulases and membrane separation using 10 kDa cutoff ultrafiltration membrane are to be evaluated for sugar recovery efficiency. The hydrolysis process will produce sugar versus time profile within four hours of the process with predicted significant increase of sugar yield after implementing the membrane separation technique. Total reducing sugar quantification test of the samples will be done using HPLC for sugar concentration analysis after enzymatic hydrolysis process. A preliminary result from similar studies suggests that the ultrafiltration membrane has high potential in retaining the enzyme inside the hydrolysis container which leads to high sugar yield from hydrolysis process.

Keywords: Enzymatic hydrolysis, pretreatment of lignocellulose, membrane separation, sugar inhibition.

1. Introduction

Pretreatment of cellulose technology has been receiving a considerable amount of attention worldwide due to its potential as an alternative energy source to biofuel. Many efforts have been made over the past decade to improve the bioethanol conversion process to be more cost-effective and feasible for large-scale production. The incentive of this effort is due to the renewable capability of bioethanol as an energy and also the small amount of pollutant bioethanol produced during combustion (clean energy). Hence, new technology to cellulose pretreatment is needed to increase the bioethanol production capability. Most of the conventional crops like rice, wheat, corn and sugarcane are ideal for the production of bioethanol, however, it has become highly debatable on fuel over food due to the negative impacts and regional economic factor. Therefore, non-food lignocellulose feedstock (agriculture waste such as empty fruit bunches and corn stover) are favored in the production of bioethanol [1 - 2]. Furthermore, converting agricultural waste to bioethanol takes a huge leap in helping environmental sustainability and makes biodiesel price more competitive.

There are three main processes involved in the production of bioethanol which starts from i) the cellulose pretreatment to break down the lignin structure , ii) hydrolysis of the lignocellulose to recover sugar and iii) sugar fermentation and product purification. Many types of research have been done on these three processes in order to improve the economic feasibility of this technology so that the production of bioethanol can be more affordable [3]. Pretreatment process is primarily mean to remove lignin from the lignocellulose and decrease the polymerization of the cellulose component, thus making it susceptible to the enzyme attack in the hydrolysis stage [4]. Recovering sugar from lignocellulose biomass usually done by enzymatic hydrolysis. However, the lignin structure in cellulose biomass exhibits resistance to the enzyme to recover sugar from the cellulose. Therefore, a pretreatment process needs to break down the recalcitrant structure of the cellulose biomass. Hence, it is essential to study the effect of various pretreatment method has on the lignocellulose [5]. Studies show that only about 20% of total cellulose are recovery as glucose without cellulose pretreatment [6]. There is currently 4 common type of pretreatment used by the bioethanol production industry to pretreat cellulose biomass and there are an ionic dissolution, microwave-assisted pretreatment, and acidic/alkaline solutions pretreatment. Pretreatment method is chosen depending on the type of cellulose feedstock, availability and economic factor, the degree of polymerization and so on. This paper intends to use acidic (sulfuric acid) and alkaline solutions (sodium hydroxide) pretreatment due to resources constraint. Both acidic and alkaline solutions pretreatment work towards the same goal, to break down lignin wall from cellulose biomass so that enzyme can recover sugar from cellulose during hydrolysis. However, there are 2 challenges that obstruct enzymatic hydrolysis which is the accessibility of enzyme inhibition on cellulose biomass and by-product inhibition on the enzymes.

To overcome these 2 issues, research needs to be conducted with 2 approaches. Firstly, pretreating the cellulose biomass with strong solvent (acidic and alkaline solvent in this case) to decrease the crystallinity and break down the lignin structure of cellulose hence improving enzyme accessibility to cellulose. Secondly, reducing by-product inhibition in sugar recovery process during hydrolysis. This research will focus more on the second approach in reducing by-product inhibition.

Studies have shown that the application of ultrafiltration membrane in separating the enzyme from sugar process proved to be rather effective, especially with ultrafiltration membrane 10 kDa cutoff where 1 Da is equivalent to 1 g/mol. [10][11]. Large molecular like enzyme cellulases which can weight from 30 kDa to 60 kDa is unable to pass through the membrane thus retaining inside the hydrolysis tank while glucose molecule with the weight of 150 – 180 Da will penetrate through the membrane [12]. In other words, the enzyme is retained inside the hydrolysis tank and being reused to recover more glucose. This lead to cost saving in subsequent separation due to less enzyme consumption and certainly cause the overall bioethanol production more cost-effective. So far, research on membrane separation is only done on the separating product from unwanted substance, and none has been done on hydrolysis pretreatment. Hence, this paper will evaluate minor modification on the sugar recovery process from biomass by adding ultrafiltration membrane separation technique to enzymatic saccharification.

This research is looking at a future possibility to make use of sugar baggase as a potential source of bio-ethanol production. In Malaysia, there are countless sugar baggase generated per day from sugar cane vendor but none of the sugar baggase is being utilized as a biofuel. Therefore, the biomass selected for this study is mainly on sugar baggase. The objectives of this research will be as follow:

1. To compare the total sugar recovery of acidic/alkaline pretreatment, hydrolysis with and without ultrafiltration membrane technique.

2. To reduce sugar inhibition on enzyme with ultrafiltration membrane, thus reusing enzyme solution for subsequent sugar recovery.

2. Methodology

2.1 Pretreatment

Sugarcane bagasse was dry in a food-grade oven at 70ºC for 6 hours to remove any water content. The dry sugarcane bagasse is then ground into powder form and sift through a 2 mm holes sifter. 10 grams of powder sugarcane bagasse was placed inside a mesh pouch and soaked inside a 500 ml beaker containing 1 M sodium hydroxide with a solid loading of 4% (w/v). The beaker was covered and placed on a hot plate stirrer at 110ºC for 3 hours. The mesh pouch was retrieved and carefully washed with distilled water after pretreatment. Before subjecting the pretreated biomass to enzymatic hydrolysis, the pretreated biomass was filtered with Whatman filter paper. For acid solution pretreatment, 1 M of sulfuric acid was used instead of 1 M sodium hydroxide.



Figure 2.1: Sugarcane bagasse (powder)



Figure 2.2: Mesh pouch

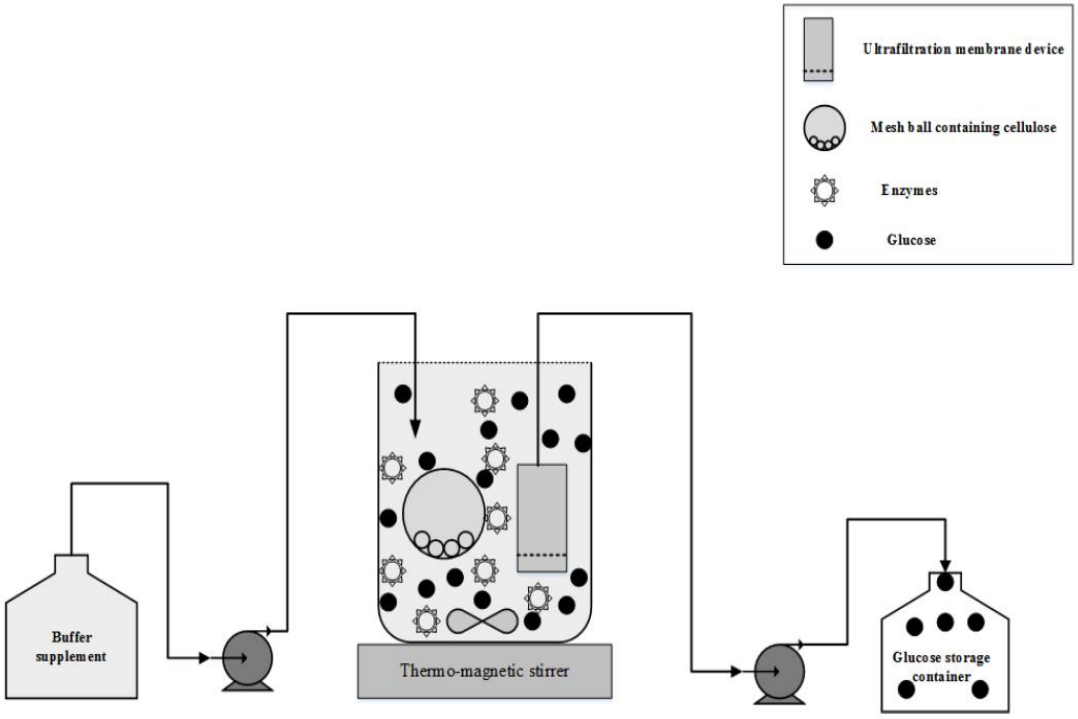
2.2 Enzymatic Hydrolysis

The pretreated sugarcane bagasse cellulose is recommended by R&M Chemical to be hydrolyzed with 30 FPU g^{-1} of Trichoderma Viride enzyme cellulose. Hydrolysis of the cellulose is to be carried out in a 500 mL polypropylene beaker with pH 5.0 citrate buffer at room temperature. An additional amount of buffer is to be supplemented to achieve 5% (w/v) solid loading of the cellulose mass (g/ml). Samples are taken from sugar storage container every 1 hours after the first hour for a total of 4 hours of hydrolysis. Each sample is taken three times for accuracy purposes.

2.3 Ultrafiltration Membrane

To apply ultrafiltration membrane separation technique, a minor modification to the normal experimental setup was done. Two peristaltic pumps and tubes were added to the hydrolysis setup (Figure 3.6). A 10 kDa cutoff ultrafiltration membrane are to be attached at the end of the tube leading towards glucose storage container. The membrane function as a separator to separate the glucose from enzyme so that the enzyme retain inside the hydrolysis beaker to recover more sugar

Figure 2.3: Experiment setup for Enzymatic Saccharification.



3. Results and Discussion

The above experiments were mainly divided into three parts. Firstly, the sugarcane bagasse biomass was either pretreated with sodium hydroxide or sulfuric acid. Secondly, the biomass undergoes enzymatic hydrolysis without ultrafiltration membrane with 30 FPU g^{-1} of Trichoderma Viride and lastly, the pretreated biomass undergoes the same enzymatic hydrolysis process with 10 kDa cutoff ultrafiltration membrane.

3.1 Glucose Content Analysis Using High-Performance Liquid Chromatography

In order to measure the sugar concentration from the sample taken from the experiments, a glucose calibration curve is needed. A sugar concentration range of 0.5 mg/ml to 9 mg/ml samples were prepared to generate the needed calibration curve using High-Performance Liquid Chromatography (HPLC) machine. It is

found that the time need for the HPLC to read glucose content lies between 8 to 9 minutes from running testing sampler. A graph with peaks are generated from the HPLC machine and through those results, sugar concentration can be analyzed and measured which can be found in the Appendix.

3.2 Sugar Concentration Evaluation

Glucose recovered from hydrolysis process was measured in sugar concentration (mg/ml) every two hours inside the glucose storage container. Both peristaltic pumps have a flow rate of 2 ml/min to ensure that the buffer solution inside the reactor does not run out. Since additional buffer solution was added onto the required amount needed inside the reactor due to the peristaltic pump, dilution factor needs to be considered when measuring the sugar concentration inside the storage container. It can be observed that all the sugar concentration in figure 4.1 share the same trend, which is lower sugar concentration at 4 hours compare to 2 hours. This is mainly because the amount of buffer solution accumulates at the end of 4 hours are much higher than the amount in 2 hours. This makes the solution more diluted and hence lower sugar concentration. However, this does not mean that sugar recovered is less in 4 hours because if it is, the sugar concentration at 4 hours should be half the value measured in 2 hours since the amount of buffer solution at 4 hours is double.

Table 3.1 Sugar Concentration of both Acid and Base Pretreatment without Ultrafiltration

Without Ultrafiltration		
Time	**Acid Pretreatment**	**Base Pretreatment**
2	2.15 mg/ml	2.46 mg/ml
3	1.97 mg/ml	2.11 mg/ml
4	1.92 mg/ml	1.94 mg/ml

Table 3.2 Sugar Concentration of both Acid and Base Pretreatment with Ultrafiltration

With Ultrafiltration		
Time	**Acid Pretreatment**	**Base Pretreatment**
2	3.21 mg/ml	6.23 mg/ml
3	2.86 mg/ml	5.78 mg/ml
4	2.31 mg/ml	4.14 mg/ml

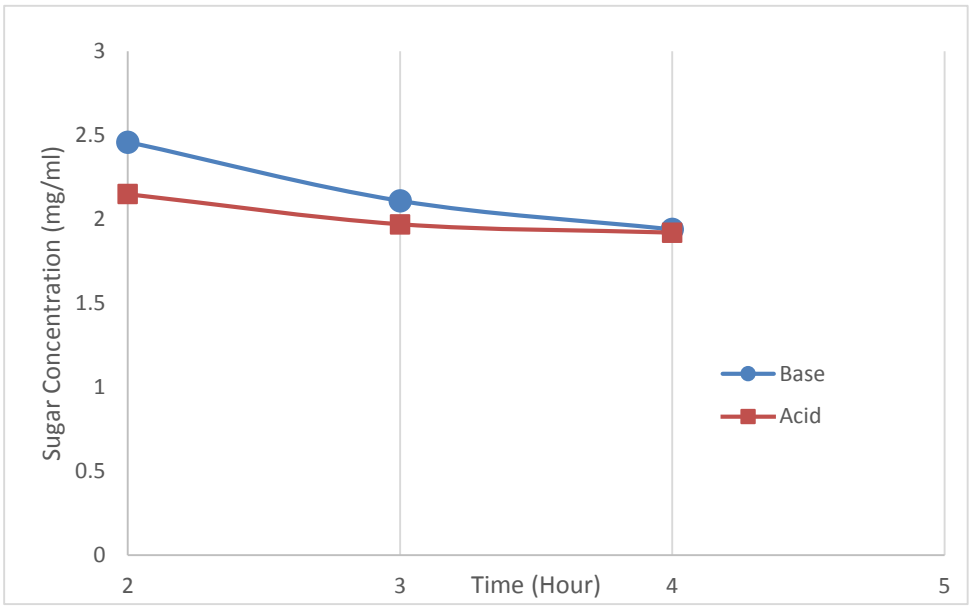


Figure 3.1 Time profile of Sugar Concentration without Ultrafiltration.

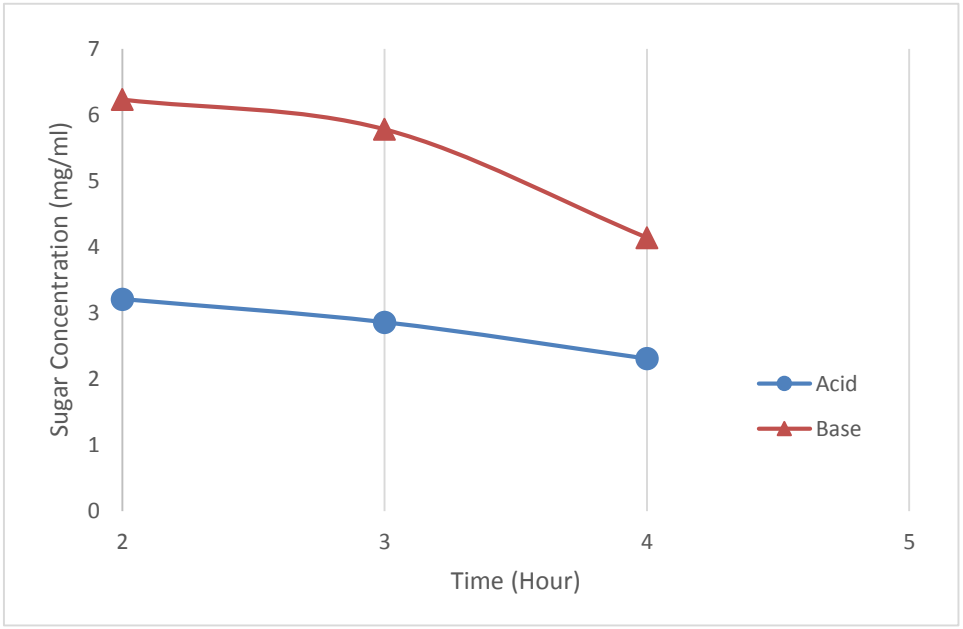


Figure 3.2: Time profile of Sugar Concentration with Ultrafiltration.

In this research experiment, it shows that 1 M dilute sodium hydroxide is a better pretreatment agent as the sugar concentration of the biomass pretreated with sodium hydroxide post-hydrolysis is higher than the biomass pretreated with sulfuric acid. It is very likely that sulfuric acid breaks the sugar polymer chain along with the lignin wall during pretreatment as suggested by Asyraf Kassim's group, causing lower sugar yield during hydrolysis process [24]. It is also clear that ultrafiltration membrane technique is effective in retaining the enzyme inside the reactor based on the given results. Byproducts caused by hydrolysis reaction is a big factor in causing enzyme inhibition and causing that enzyme unable to further recover sugar from the cellulose biomass. By implementing a peristaltic pump and ultrafiltration technique, the membrane is able to separate the enzyme from byproducts so that the enzyme can be reused to continue the hydrolysis process to recover more sugar.

By comparing this experiment results to Wyman's et Al enzymatic hydrolysis of cellulose biomass that did not apply ultrafiltration membrane, the setup could only handle a low range of solid loading (2 to 3%) to achieve 91% sugar conversion from cellulose. When a higher solid loading was applied, the sugar recovery

significantly drops to almost no sugar conversion whereas in this experimental work, was able to handle 5% solid loading and 2 ml/min constant buffer flow rate.

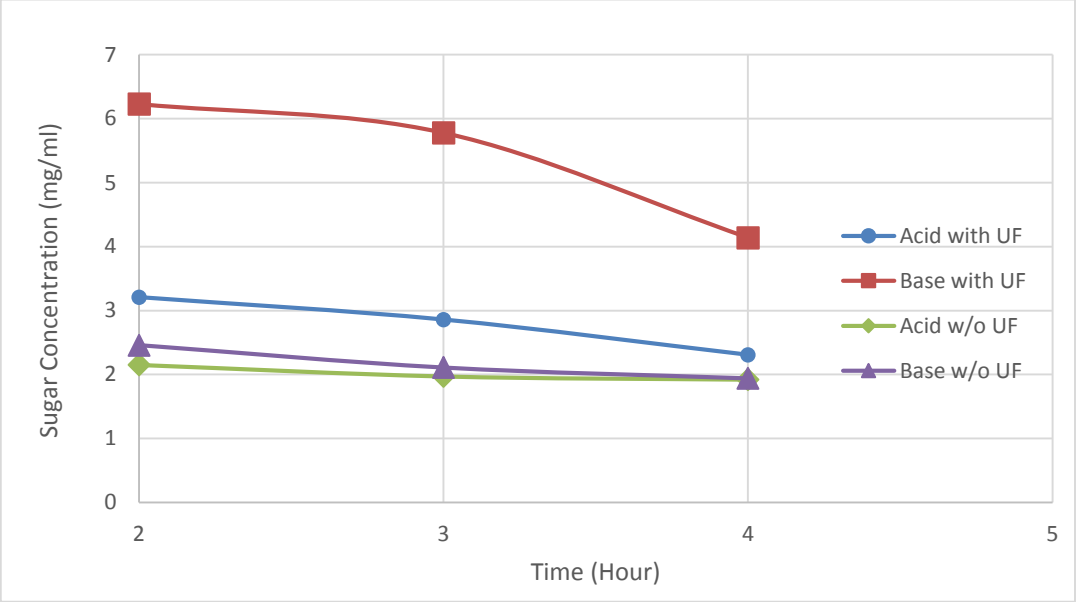


Figure 3.3: Comparison of Sugar Concentration with and without Ultrafiltration Membrane Separation.

4.3 Error Analysis and Limitation

In this research project, errors and uncertainties still exist during some of the experiments. First of all, the powder form of sugarcane bagasse might still be able to leak out from the mesh pouch, causing weight losses. However, the enzyme concentration, as well as other dosage, are still base on the initial value of the cellulose biomass. Secondly, some of the sugar concentration analysis done by the HPLC machine give huge value difference on the same sample. Though each sample have been taken thrice to obtain an average value, this can probably cause inaccuracy during sugar concentration measurements.

4.4 T-test for Sugar Concentration Results.

Statistical analysis is a good way to determine if there is a significant difference in means value and T-test is the common method to perform such analysis. The means value in this research project is inevitably be the sugar concentration in both hydrolysed with and without membrane separation. From table 4.3, the p values are less than 5% which conclude that the sugar concentration in both hydrolyses is significantly different from each other.

Table 3.3: T-test for Enzymatic Hydrolysis for both configuration

Pretreatment Type	**Acid**	**Base**
	Without Ultrafiltration	With Ultrafiltration
Mean	2..09	4.088
p value	0.007	

7.0 Conclusion

This research highlighted the feasibility of adding ultrafiltration membrane separation technique to enzymatic hydrolysis process. The technique aims to remove glucose byproduct continuously so that it does not stay inside the reactor to cause enzyme inhibition. Sodium hydroxide solution is the preferred pretreatment agent in this study, together with 30 FPU g^{-1} Trichoderma Viride and 10 kDa cutoff ultrafiltration membrane from

Sartorius were able to work coherently in a whole integrity. Based on the above results and findings, it is clear to state that sugar concentration from hydrolysis with ultrafiltration membrane was much higher than the hydrolysis without ultrafiltration. On top of that, this setup is able to handle a higher range of solid loading (5%) in enzymatic hydrolysis. The main difference of this research is that the direct application of ultrafiltration membrane on the tube to retain enzyme inside the reactor while pumping sugar products out. This method of applying ultrafiltration membrane may be the new way of fractionating sugar in hydrolysis process. One possible future work would be to determine the sugar conversion percentage and the feasibility of applying ultrafiltration method in scale up industry.

Acknowledgement

Many thanks to Dr. Rajesh Rajasekaran for the guidance and supervision throughout the entire research and Ms. Lithnes Kalaivani for the training on HPLC machine.

References

1. J. S. Lim, Z. Abdul Manan, S. R. Wan Alwi, and H. Hashim, "A review on the utilization of biomass from rice industry as a source of renewable energy," Renewable and Sustainable Energy Reviews, vol. 16, no. 5, pp. 3084–3094, 2012.
2. H. Y. Yoo, S. B. Kim, H. S. Choi, K. Kim, C. Park, and S. W. Kim, "Optimization of sodium hydroxide pretreatment of canola agricultural residues for fermentable sugar production using a statistical method," in Proceedings of the International Conference on Future Environment and Energy (IPCBEE '12), vol. 28, 2012.
3. Z. Anwar, M. Gulfraz, M. Imran, et al., "Optimization of dilute acid pretreatment using response surface methodology for bioethanol production from cellulosic biomass of rice polish," Pakistan Journal of Botany, vol. 44, no. 1, pp. 169–176, 2012.
4. A. Avci, B. C. Saha, B. S. Dien, et al., "Response surface optimization of corn stover pretreatment using dilute phosphoric acid for enzymatic hydrolysis and ethanol production," Bioresource Technology, vol. 130, pp. 603–612, 2013.
5. V. Menon and M. Rao, "Trends in bioconversion of lignocellulose: biofuels, platform chemicals & biorefinery concept," Progress in Energy and Combustion Science, vol. 38, no. 4, pp. 522–550, 2012.
6. A. Li, B. Antizar-Ladislao, and M. Khraisheh, "Bioconversion of municipal solid waste to glucose for bio-ethanol production," Bioprocess and Biosystems Engineering, vol. 30, no. 3, pp. 189–196, 2007.
7. C. Li, B. Knierim, C. Manisseri et al., "Comparison of dilute acid and ionic liquid pretreatment of switchgrass: biomass recalcitrance, delignification and enzymatic saccharification," Bioresource Technology, vol. 101, no. 13, pp. 4900–4906, 2010.
8. M. Ioelovich and E. Morag, "Study of enzymatic hydrolysis of mild pretreated lignocellulosic biomasses,"BioResources, vol. 7, no. 1, pp. 1040–1052, 2012.
9. E. Arvaniti, A. B. Bjerre, and J. E. Schmidt, "Wet oxidation pretreatment of rape straw for ethanol production," Biomass and Bioenergy, vol. 39, pp. 94–105, 2012.
10. Y. Kim, A. Yu, M. Han, G.-W. Choi, and B. Chung, "Enhanced enzymatic saccharification of barley straw pretreated by ethanosolv technology," Applied Biochemistry and Biotechnology, vol. 163, no. 1, pp. 143–152, 2011.
11. N. Guragain, J. De Coninck, F. Husson, A. Durand, and S. K. Rakshit, "Comparison of some new pretreatment methods for second generation bioethanol production from wheat straw and water hyacinth," Bioresource Technology, vol. 102, no. 6, pp. 4416–4424, 2011.
12. N. Muhammad, Z. Man, M. A. Bustam, M. I. A. Mutalib, C. D. Wilfred, and S. Rafiq, "Dissolution and delignification of bamboo biomass using amino acid-based ionic liquid," Applied Biochemistry and Biotechnology, vol. 165, no. 3-4, pp. 998–1009, 2011.

13. X.-F. Tian, Z. Fang, D. Jiang, and X.-Y. Sun, “Pretreatment of microcrystalline cellulose in organic electrolyte solutions for enzymatic hydrolysis,” Biotechnology for Biofuels, vol. 4, article 53, 2011.\
14. J. S. Van Dyk and B. I. Pletschke, “A review of lignocellulose bioconversion using enzymatic hydrolysis and synergistic cooperation between enzymes-Factors affecting enzymes, conversion and synergy,”Biotechnology Advances, vol. 30, no. 6, pp. 1458–1480, 2012.
15. Y. Sun and J. Cheng, “Hydrolysis of lignocellulosic materials for ethanol production: a review,”Bioresource Technology, vol. 83, no. 1, pp. 1–11, 2002.
16. M. Galbe and G. Zacchi, “Pretreatment: the key to efficient utilization of lignocellulosic materials,”Biomass Bioenergy, vol. 46, pp. 70–78, 2012.
17. C. E. Wyman, B. E. Dale, R. T. Elander et al., “Comparative sugar recovery and fermentation data following pretreatment of poplar wood by leading technologies,” Biotechnology Progress, vol. 25, no. 2, pp. 333–339, 2009.
18. Badiei, M., Asim, N., Jahim, J. M., & Sopian, K. (2014). Comparison of Chemical Pretreatment Methods for Cellulosic Biomass. *APCBEE Procedia*, *9*, 170–174. http://doi.org/10.1016/j.apcbee.2014.01.030
19. Abels, C., Thimm, K., Wulfhorst, H., Spiess, A. C., & Wessling, M. (2013). Membrane-based recovery of glucose from enzymatic hydrolysis of ionic liquid pretreated cellulose. *Bioresource Technology*, *149*, 58–64. http://doi.org/10.1016/j.biortech.2013.09.012
20. Alvira, P., Tomás-Pejó, E., Ballesteros, M., & Negro, M. J. (2010). Pretreatment technologies for an efficient bioethanol production process based on enzymatic hydrolysis: A review. *Bioresource Technology*, *101*(13), 4851–4861. http://doi.org/10.1016/j.biortech.2009.11.093
21. Al-Zuhair, S., Al-Hosany, M., Zooba, Y., Al-Hammadi, A., & Al-Kaabi, S. (2013). Development of a membrane bioreactor for enzymatic hydrolysis of cellulose. *Renewable Energy*, *56*, 85–89. http://doi.org/10.1016/j.renene.2012.09.044
22. Asim, N., Syuhami, M. F., Badiei, M., & Yarmo, M. A. (2014). WO3 Modification by Synthesis of Nanocomposites. *APCBEE Procedia*, *9*, 175–180. http://doi.org/10.1016/j.apcbee.2014.01.031
23. Avci, A., Saha, B. C., Kennedy, G. J., & Cotta, M. A. (2013). Dilute sulfuric acid pretreatment of corn stover for enzymatic hydrolysis and efficient ethanol production by recombinant Escherichia coli FBR5 without detoxification. *Bioresource Technology*, *142*, 312–319. http://doi.org/10.1016/j.biortech.2013.05.002
24. Badiei, M., Asim, N., Jahim, J. M., & Sopian, K. (2014). Comparison of Chemical Pretreatment Methods for Cellulosic Biomass. *APCBEE Procedia*, *9*, 170–174. http://doi.org/10.1016/j.apcbee.2014.01.030
25. Li, X., Mupondwa, E., Panigrahi, S., Tabil, L., Sokhansanj, S., & Stumborg, M. (2012). A review of agricultural crop residue supply in Canada for cellulosic ethanol production. *Renewable and Sustainable Energy Reviews*, *16*(5), 2954–2965. http://doi.org/10.1016/j.rser.2012.02.013
26. Mandels, M., Kostick, J., & Parizek, R. (2007). The use of adsorbed cellulase in the continuous conversion of cellulose to glucose. *Journal of Polymer Science Part C: Polymer Symposia*, *36*(1), 445–459. http://doi.org/10.1002/polc.5070360133
27. Ooshima, H., Burns, D. S., & Converse, A. O. (1990). Adsorption of cellulase fromTrichoderma reesei on cellulose and lignacious residue in wood pretreated by dilute sulfuric acid with explosive decompression. *Biotechnology and Bioengineering*, *36*(5), 446–452. http://doi.org/10.1002/bit.260360503

28. Riedel, K., & Bronnenmeier, K. (2002). Intramolecular synergism in an engineered exo-endo-1,4-β-glucanase fusion protein. *Molecular Microbiology*, *28*(4), 767–775. http://doi.org/10.1046/j.1365-2958.1998.00834.x
29. Saloheimo, M., Paloheimo, M., Hakola, S., Pere, J., Swanson, B., Nyyssönen, E., … Penttilä, M. (2002). Swollenin, a Trichoderma reesei protein with sequence similarity to the plant expansins, exhibits disruption activity on cellulosic materials. *European Journal of Biochemistry*, *269*(17), 4202–4211. http://doi.org/10.1046/j.1432-1033.2002.03095.x
30. Lee, J.-W., & Jeffries, T. W. (2011). Efficiencies of acid catalysts in the hydrolysis of lignocellulosic biomass over a range of combined severity factors. *Bioresource Technology*, *102*(10), 5884–90. http://doi.org/10.1016/j.biortech.2011.02.048

Extraction Kinetic of *Ziziphus jujuba* Fruit Using Solid-liquid Extraction

Poh Jingwen[1*], Chua Bee Lin[2]

[1,2]*School of Engineering, Taylor's University*

[*]nicolepjw@gmail.com

Abstract

Ziziphus jujuba is one of the most common Chinese traditional herbs and it is one of the five most valuable herbal plants in China due to the high nutritional and nutraceutical values of bioactive compounds. The main aim of this research work is to study the effect of extraction temperature on the kinetic extraction of *Z. jujuba* fruit by ethanol solvent extraction to obtain high antioxidants of *Z. jujuba* fruit and the best extraction model for *Z. jujuba* fruit. The *Z. jujuba* fruit is dried by using an oven at a temperature of 60°C for 24 hours. The extraction process is carried out with three different temperatures (40 °C, 50 °C and 60 °C) while other extraction parameters of *Z. jujuba* fruit such as extraction time, ultrasound power and ratio of *Z. jujuba* fruit (g): ethanol (ml) are 90 minutes, 70 W and 1:20 respectively. The results indicated that the concentration of crude extract from *Z. jujuba* fruit increase with the increased of extraction temperature but the concentration of crude extract from *Z. jujuba* fruit decreased when the extraction temperature of 60 °C. The antioxidants extracted from the whole *Z. jujuba* fruit has higher yield (93.64%) at 50 °C. The yield of antioxidants in *Z. jujuba* fruit increase with the increased of temperature but the antioxidants decreased when the extraction temperature is 60 °C. Six different existing extraction kinetic models, including First-order Kinetic Model, Second-order Rate Equation, Peleg's model, Power Law Equation, Page's Model and Logarithmic Model are used to study the extraction process. First-order Kinetic Model is the best model for the kinetic extraction of *Z. jujuba* fruit as a good agreement between the experimental and fitted data from model is obtained.

Keywords: *Ziziphus jujuba*, Extraction kinetic, Ultrasound-assisted Extraction, Antioxidant, Mathematical modelling

1. Introduction

A medicinal plant is a plant that has similar properties with pharmaceutical drugs and it has been discovered and used since ancient times [1]. Spices are commonly used by the human as they content high essential oil which helps to keep foods from becoming diseased by bacteria [2]. These herbs and spices have their own special compounds in order to prevent disease. Today, most of the herbal plants remedies are used to treat health problems with scientific reports proven on the success in treating the diseases.

Ziziphus jujuba Mill. is one of the most common Chinese traditional herbs and it is one of the five most valuable herbal plants in China. *Z. jujuba* fruit is well-known and recognized as one of the valuable herbal plants due to it contains high nutritional and nutraceutical values of bioactive compounds [2]. Dried *Z. jujuba* fruit is commonly used as food additive and flavouring because of their high nutritional value. The dried *Z. jujuba* fruit is frequently used in the traditional Chinese medicine for the treatment on anorexia, fatigue and the syndromes of the spleen and hysteria of women. Besides, it has various effects including antimicrobial, anticancer, antioxidant and anti-inflammatory [3, 5]. There are scientific proven on it has been used to improve sleep, nourish the heart and soothe the nerves. Because of these benefits of *Z. jujuba*, the interest develops on extract the *Z. jujuba* fruit [5].

There are study had been done on the antioxidant activities of the crude extract of *Z. jujuba* fruit but all of them are mainly focused on the antioxidant activity for the seeds, fruiting bodies, peels and leaves of *Z. jujuba* fruit individually. Therefore, it is worth to study the total antioxidant activity for the whole *Z. jujuba* fruit (fruiting bodies and peel) in order to use this herbal plant for a development of therapeutics that could be prevent diseases such as cardiovascular disease and cancer.

Extraction of *Z. jujuba* fruit may be accomplished using Ultrasonic-assisted extraction (UAE). This is due to the traditional solvent extractions have several drawbacks, time consuming, have low selectivity and low extraction yield [4]. UAE is widely used in the extraction of herbal plants as it enables to destroy the cell walls of plants causes the contact between solvent and compounds in plants increases [6]. Ethanol acts as solvent for the extraction of *Z. jujuba* fruit. Organic solvent are usually costly, environmentally hazardous and require expensive disposal procedures. However, ethanol has relatively low impact to the environment, has a positive net energy balance and it is recognised as Generally Recognised as Safe (GRAS) solvent [7].

There are lots of researches had been done on the solid-liquid extraction of *Z. jujuba* fruit. However, there is no report available in the literature regarding the extraction kinetics of *Z. jujuba* fruit. Therefore, there is a need for mathematical modelling of this extraction process and herbal plant. Mathematical modelling is a very useful engineering tool as it helps to explain a system and to study the effects of different parameters and make predictions about the behaviours [8]. Thus, the objective of this research work is to evaluate on the kinetic extraction of *Z. jujuba* fruit by ethanol solvent extraction to obtain high antioxidants of *Z. jujuba* fruit and the fit the unknown parameters to obtain the best extraction model for *Z. jujuba* fruit.

2. Methodology

2.1 Chemical Reagents

Ethanol (99.8% AR grade) and 2, 2-Diphenyl-1-Picrylhydrazyl (DPPH) were purchased from Chemolab Supplies Sdn. Bhd.

2.2 Preparation and Pre-treatment of *Z. jujuba* Fruit

Dried *Z. jujuba* fruit were purchased from NSK Trade City, Kuchai Lama, Kuala Lumpur. 1 kg of dried *Z. jujuba* seedless fruit was washed with distilled water to remove the dirt. The dried *Z. jujuba* fruit was cut into slices. The dried *Z. jujuba* fruit was further dried in a drying oven (Model UFE-800, Memmert, Germany) at 60 °C for 48 hours followed by grounding them into fine powder using a cutting mill (Model SM–100, Retsch, Germany) [9]. The powder form of the *Z. jujuba* fruit was passed through a 500 µm sieve mesh to remove the chunk particles to ensure the particles size was uniform. The powder form of *Z. jujuba* fruit was sealed in a plastic container and stored in dry cabinet for further usage.

2.3 Ultrasound-assisted Extraction (UAE) of *Z. jujuba* Fruit

The UAE of *Z. jujuba* fruit was conducted according to the procedure presented by Jin-wei et al [9]. Ethanol was used as solvent for the extraction of *Z. jujuba* fruit with the ratio of solid to solvent was 1:20 (g/mL). 18 g of *Z. jujuba* fruit powder was mixed with 360 ml of 99.8% ethanol in a beaker. The sample was immersed in an ultrasonic bath (Elmasonic Model P120H, Singen, Germany) at 40 °C, ultrasonic input power of 70 W and frequency of 37 kHz with occasional swirling during extraction period, each with three replicates to ensure the sample mixed well and uniform throughout the extraction process. The extraction was carried out at three different temperatures (40 °C, 50 °C and 60 °C). The extract was sampled at every 5 minutes for 90 minutes. The sample was filtered using Whatman filter paper no. 1 in a rotary flask to obtain supernatants of the sample. The supernatants of filtrate (20 mL) was dried in a rotary vacuum evaporator (Heidolph Model Hei-VAP Precision (HL), Schwabach, Germany) to remove ethanol at 40 °C until crude extracts were observed [9].

According to previous findings, the optimum conditions were adopted for this research work using UAE technique and performed under the conditions shown Table 2.1 by varied the extraction temperature.

Table 2.1: Optimum extraction parameters for Solid-liquid Extraction (SLE) of *Z. jujuba* fruit using UAE [10]

Ultrasound power (W)	Type of solvent	Ratio of solid to solvent	Extraction time (mins)
70	Ethanol	1:20	90

2.4 Extraction Kinetic Data Collection of *Z. jujuba* fruit

20 ml of *Z. jujuba* fruit was extracted every 5 minutes and the extraction solution was filtered to remove the supernatant from the residue. The resulting filtrate was concentrated to dryness under the temperature of 40 °C in a rotary evaporator to remove the solvent. Then, the dried extract was weighted using a digital balance (Ohaus PA4102, U.S.A). The extraction yield of *Z. jujuba* fruit was presented in the term of concentration. The concentration of *Z. jujuba* fruit extract was calculated using the weight of a dried extract and volume of *Z. jujuba* fruit extract. The concentration of the crude extract was calculated based on the Eq. (1). The change of solute concentration in the liquid phase with respect to time during the extraction of *Z. jujuba* fruit was clearly indicated by plotting graph to study the behaviour of extraction of *Z. jujuba* fruit [9, 10].

$$C_A = \frac{W_d}{V_e} \quad (1)$$

where C_A is the concentration of crude extract (g/mL), W_d is the weight of dried extract (g) and V_e is the volume of filtrate of each sample (mL).

2.5 Antioxidant assay of *Z. jujuba* Fruit by using DPPH Radical Scavenging Capacity

The antioxidant activity of *Z. jujuba* fruit was determined using the DPPH according to the procedure of Himaja *et al* [11]. 1.9 mg of DPPH was dissolved in 100 ml of ethanol in order to produce 0.1mM of DPPH solution. The solution was prepared in a schott bottle wrapped with aluminium foil to minimise light exposure. The DPPH solution was left for 30 minutes to complete the reaction before it was used for analysis. Then, 1 ml of DPPH solution was added into 3 ml of crude extract and the sample was observed to change from purple to yellowish. The prepared sample was then left in a dark room for 30 minutes before the sample absorbance value at 517 nm was measured against a blank using UV spectrometer (Model Genesys 10S, Massachusetts, United States). This test was performed triplicate to ensure the results were not offset. 3 mL of pure ethanol was used as the blank solution for this test and ethanolic solution of DPPH was used as positive control [12]. The absorbance value of sample was recorded to calculate the radical scavenging activity of *Z. jujuba* fruit. The lower absorbance of sample mixture indicates higher free radical scavenging activities. The equation of calculate the DPPH scavenging activity of *Z. jujuba* fruit was using Eq. (2):

$$\text{Scavenging activity } (\%) = [1 - (\frac{A_{sample}}{A_{control}})] \times 100\% \quad (2)$$

where $A_{control}$ is the absorbance of control DPPH solution at 0 minutes and A_{sample} is the absorbance in the presence of test sample at exaction time.

2.6 Mathematical Modelling of SLE of *Z. jujuba* Fruit

In this research work, six mathematical models that were commonly applied in modelling in the recovery of solutes from different type of solid materials were used to fit the experimental data and evaluate the entire extraction process, namely, First-order

Kinetic Model, Peleg's Model, Second-order Rate Equation, Power Law Equation, Page's Model and Logarithmic Model. These models were compared in order to determine the closest mathematical model that best fits the experimental data.

2.6.1 First-order Kinetic Model

The first-order kinetic model was commonly used in extraction kinetic for herbal plants [1]. Therefore, this mathematical model was used to describe the extraction kinetic model of *Z. jujuba* fruit. A kinetic approach based on Fick's law can be used [13]:-

$$\frac{dC_A}{dt} = k_L A[C_e - C_t] \quad (3)$$

where $\frac{dC_A}{dt}$ is the rate of mass transfer of *Z. jujuba* fruit (g/min), k_L represents mass transfer coefficient (cm/min), A is the total surface area of solid (cm^3), C_e represents the solute concentration at equilibrium in the liquid phase (g solute $A.cm^{-3}$) and C_t is the solute concentration in the bulk liquid (g solute $A.cm^{-3}$).

After further derivative, the equation of extraction process of solute from solid into bulk liquid is as below:-

$$C_t = C_e[1 - e^{(-k.t)}] \quad (4)$$

$$k = k_L \alpha$$

where C_t is the solute concentration in the bulk liquid (g solute $A.cm^{-3}$), C_e represents the solute concentration at equilibrium in the liquid phase (g solute $A.cm^{-3}$), k_L represents mass transfer coefficient (cm/min), and α is specific surface area of the solid ($cm^3\ g^{-1}$).

2.6.2 Second-order Rate Equation

The second-order rate law equation provides satisfactory representation of the solid-liquid extraction process [13, 14]. Therefore, this mathematical model was suitable to use in this research work on the extraction of *Z. jujuba* fruit. The second-order rate equation can be written as:

$$\frac{dC_t}{dt} = k(C_e - C_t)^2 \quad (5)$$

where $\frac{dC_t}{dt}$ is the rate of extraction (g cm^{-3} min^{-1}), k is the rate constant of extraction process, C_e and C_t are the concentration of solute in equilibrium state and at extraction time t respectively (g cm^{-3}).

When the t = 0, the initial rate of extraction, h can be expressed as:

$$h = kC_e^2 \quad (6)$$

After integrated under the initial and boundary conditions of t = 0, and $C_t = 0$ to C_t and rearranging the equation can be written as:

$$C_t = \frac{t}{\left(\frac{1}{h}\right)+\left(\frac{t}{C_e}\right)} \quad (7)$$

2.6.3 Peleg's Model

Peleg is widely used to explain the extraction curve for bioactive compounds from medicinal plants due to the shape of sorption curves is similar [7]. The equation was as below:-

$$C_t = C_0 + \frac{t}{k_1 + k_2 t} \quad (8)$$

where C_0 is the initial concentration of solute at time t (g/g powder), C_t is the concentration of solute at time t (g/g powder), t is the extraction time (min), k_1 is Peleg's rate constant (min g/mg) and k_2 is the Peleg's capacity constant (g/mg).

The C_0 can be omitted when the initial concentration of solute is zero and this equation now is named as modified Peleg's equation which is shown as below:

$$C_t = \frac{t}{k_1 + k_2 t} \quad (9)$$

where C_t is the concentration of solute at time t (g/g powder), t is the extraction time (min), k_1 is Peleg's rate constant (min g/mg) and k_2 is the Peleg's capacity constant (g/mg).

2.6.4 Power Law Equation

Power law model is one of the useful empirical equations for SLE and has been successfully used for extraction of polysaccharides from a medicinal fungus [16]. The power law equation can be written as:

$$C_t = Bt^n \quad (10)$$

where C_t is the concentration of solute at extraction time t (g cm^{-3}), B represents the rate constant of extraction process, t is extracted time (min) and n is Power-law component (<1).

2.4.5 Page's Model

Page's model is commonly used in drying kinetic, however, there is satisfactory representation of solid-liquid extraction process [17]. The Page's model equation can be written as:

$$C_t = e^{(-kt^n)} \quad (11)$$

where C_t is the concentration of solute at extraction time t (g cm^{-3}), k and n are the Page's constant and t is the extracted time (min).

2.4.6 Logarithmic Model

Logarithmic model was not only can be used for drying process but also SLE process as β-carotene extraction from dried carrot and polyphenols from soybeans are the successful examples of Logarithmic model for SLE process [17, 18]. The Logarithmic model can be written as below:

$$C_t = a \log t + b \tag{12}$$

where C_t is the concentration of solute at extraction time t (g cm^{-3}), a and b represent the logarithmic model constants and t is the extraction time (min).

2.7 Statistical Analysis and Model Validation

All the experiments were performed triplicate and the results were represented in the form of their mean $\pm$ standard deviation (SD). The values of model parameters had been calculated with GRG Nonlinear solving method using SOLVER incorporated in Microsoft Excel 2010. Four parameters, coefficient determination (R^2), root mean square error (RMSE), reduced chi-square (χ^2) and mean absolute error (MAE) were used to determine the goodness of fit of the models to the experimental data. The best model describing the SLE characteristics of *Z. jujuba* fruit was chosen with the one has highest value of $R^2$and the least value RMSE, $\chi^2$and MAE.

Coefficient determination (R^2) is a statistical measure of how close the experiment data are to the fitted regression line [20]. The formula for R^2 is written as below:

$$R^2 = 1 - \frac{\sum_{i=1}^{n}(C_{exp,i} - C_{pre,i})^2}{\sum_{i=1}^{n}(C_{exp,i} - \bar{C})^2} \tag{13}$$

where n is number of samples, $C_{exp,i}$ and $C_{pre,i}$ represent experimental and predicted concentration of *Z. jujuba* fruit respectively and $\bar{C}$ is the mean value of all experimental data.

The root mean square error (RMSE) is used to measure the differences between data predicted by a model and the experimental data [21]. Eq. (2.15) was used to calculate the RMSE of the experiment data.

$$RMSE = \sqrt{\frac{1}{N}\sum_{i=1}^{N}(C_{pre,i} - C_{exp,i})^2} \tag{14}$$

where N represent the number of observations, $C_{exp,i}$ and $C_{pre,i}$ represent experimental and predicted concentration of *Z. jujuba* fruit respectively.

Reduced Chi-square (χ^2) is a statistical test commonly used to compare experimental data with the data that obtain from models [22]. Eq. (15) is the equation used to obtain the value of χ^2.

$$\chi^2 = \sum \frac{(C_{exp,i} - C_{pre,i})^2}{N-n} \tag{15}$$

where $C_{exp,i}$ and $C_{pre,i}$ represent experimental and predicted concentration of *Z. jujuba* fruit respectively, N is the number of observations and n is number constants.

Mean absolute error (MAE) is a measure of prediction accuracy of a forecasting method in statistics. In another words, it is the average over the verification sample of the absolute values of the differences between forecast and the corresponding observation. MAE is one of the useful measures which widely used in model evaluations [21]. The equation of MAE was shown as below:

$$MAE = \frac{1}{n}\sum_{i=1}^{N}\left|C_{exp,i} - C_{pre,i}\right| \quad (16)$$

where $C_{exp,i}$ and $C_{pre,i}$ represent experimental and predicted concentration of *Z. jujuba* fruit respectively and n indicates the number of model constants.

3. Results and Discussion

3.1 Effect of Extraction Temperature on Concentration of Crude Extract from *Z. jujuba* Fruit

The temperature of extraction was varied in the range from 40°C to 60 °C to evaluate the effect of extraction temperature on the concentration of crude extract from *Z. jujuba* fruit. The extraction temperature had significant effects on the concentration of crude extract from *Z. jujuba* fruit and it was presented in Figure 3.1. The concentration of crude extract from *Z. jujuba* fruit increased rapidly almost linear within the first 15 minutes and then exhibits a slow extraction until reaching equilibrium. As the temperature increased, the concentration of crude extract from *Z. jujuba* fruit also increases, this may due to the higher temperature causes the tissues of *Z. jujuba* fruit to be soften and thus increased the diffusion rate of solutes from cell into extracting solvent [12]. However, the figure shows that elevation of temperature to 60 °C has lower concentration of solute and the concentration at equilibrium only reached 0.0224 g/mL. This shown that the compounds in *Z. jujuba* fruit were degraded due to the high extraction temperature during the process of SLE. [17, 22]. This was proven by Durling *et al*, the inactive compounds were extracted from *Z. jujuba* fruit during the extraction process at high extraction temperature causes decreased in concentration of crude extract from *Z. jujuba* fruit [24].

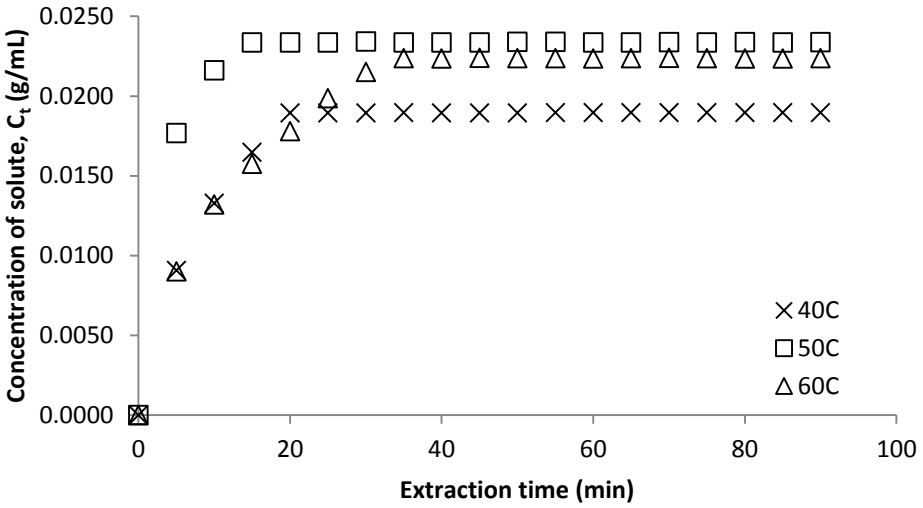


Figure 3.1: Effect of temperature on concentration of crude extract from *Z. jujuba* fruit.

3.2 Effect of Temperature on DPPH Radical Scavenging Activities

DPPH radical method was widely used to evaluate the free radical scavenging activities with the change in colour of DPPH reagent from purple to yellow. The discoloration of DPPH reagent denoted the potential of free radical scavenging of the sample antioxidant [25]. Table 3.1 shown the temperature varied from 40 °C to 60°C and the resulting DPPH radical scavenging activities of antioxidant for *Z. jujuba* fruit. The DPPH radical scavenging activities of antioxidant in *Z. jujuba* fruit increased with the increased of extraction temperature from 40 °C to 50 °C. This might be due to the increased in solubility and diffusion coefficient of antioxidants compounds in *Z. jujuba* fruit [26]. However, with further elevation of temperature to 60 °C, the DPPH radical scavenging activities of antioxidant in *Z. jujuba* fruit decreased. This was due to the antioxidant compounds in *Z. jujuba* fruit was thermo-sensitive and thus reduce their activities at high temperature [4, 18, 19] .

Table 3.1: DPPH scavenging activities of antioxidant in *Z. jujuba* fruit. [a]

Temperature (°C)	**Radical Scavenging activity (%)**
40	90.38 ± 0.15
50	93.64 ± 0.15
60	92.44 ± 0.24

[a] Values are expressed as percentage mean of triplicate determination (n=3) ± standard deviation.

Based on the results in Table 3.1, the highest DPPH radical scavenging activities (93.64%) was achieved for *Z. jujuba* fruit with the extraction temperature of 50 °C and extraction time of 15 minutes. It was observed that the absorbance of this DPPH sample is low (0.035 nm). The low absorbance of sample was mainly because of the high radical scavenging by the hydrogen donation [25].

3.3 Comparison of Kinetics Models

The experimental concentration of crude extract from *Z. jujuba* fruit was fitted into the mathematical models which discussed in section 2.6. In order to study the extraction kinetics of *Z. jujuba* fruit, the concentration of crude extract from *Z. jujuba* fruit were plotted as a function of the extraction time (from 0 to 90 minutes) and the results were shown in Figure 3.2. Figure 3.2 demonstrated the experimental data and the predicted data which obtained from the mathematical models and the accuracy of fitting each model was also compared with the experimental data. Based on Figure 3.2, it showed First-order Kinetic Model is the best fitted extraction model for *Z. jujuba* fruit. Thus, First-order Kinetic Model is best model for describing the extraction kinetic of *Z. jujuba* fruit in this research work.

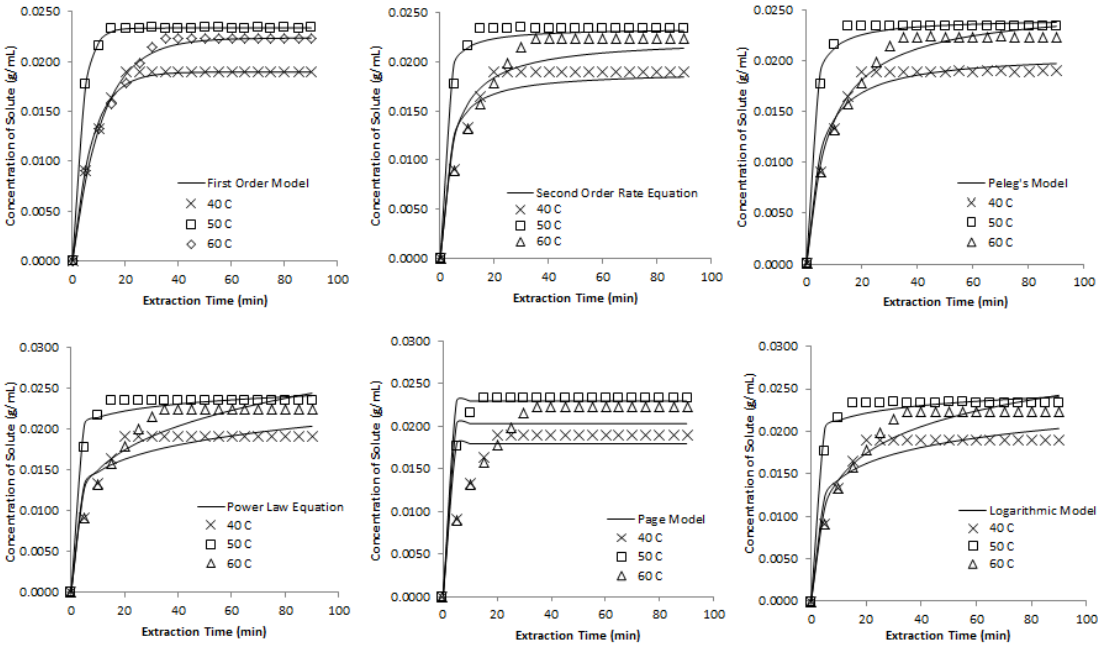


Figure 3.2: Comparison of kinetic extraction of *Z. jujuba* fruit fitted to the First-order Kinetic Model, Second-order Rate Equation, Peleg's Model, Power Law Equation, Page's Model and Logarithmic Model respectively. (Symbols – experimental data, lines – model fitting curves)

The goodness od fit and best model for a given experimental data is commonly evaluate from the values of coefficient determination (R^2), root mean square error (RMSE), reduced chi-square (χ^2) and mean absolute error (MAE). A high value of R^2 and a low value of RMSE, χ^2 and MAE indicate good fit. Table 3.2, 3.3 and 3.4 showed the R^2, RMSE, χ^2 and MAE values for First-order Kinetic Model, Second-order Rate Equation, Peleg's Model, Power Law Equation, Page's Model and Logarithmic Model at extraction temperature of 40 °C, 50 °C and 60 °C respectively. Only a few models exhibit good fitting performance for the experimental data. First-order Kinetic Model is the best fitted model with the experimental data at 50 °C and show high accuracy by showing the highest value of R^2 is 0.9995 and the lowest values of RMSE, χ^2 and MAE are $5.01 \times 10^{-27}, 1.95 \times 10^{-26}$ and 4.26×10^{-26} respectively among the mentioned models. The fitting accuracy of experimental data is in the order of: First-order Kinetic Model > Peleg's Model > Second-order Rate Equation > Logarithmic Model > Power Law Equation > Page's Model.

Table 3.2: Modelling of Solid-Liquid Extraction of *Z. jujuba* fruit at 40 °C

Model	Model Constants	R^2	χ^2	RMSE	MAE
1	k = 0.1348; C_e = 0.019	0.9935	6.19E-16	2.41E-15	5.26E-15
2	h = 0.0070; C_e = 0.019	0.9227	1.63E-08	6.36E-08	1.39E-07
3	k_1 = 221.7122; k_2 = 48.2493; C_0 = 0	0.9658	8.51E-07	3.32E-06	7.24E-06
4	B = 0.0104; n = 0.1476	0.8978	2.55E-06	9.93E-06	2.16E-05
5	k = 4.0197; n = 0.0010	0.7082	7.27E-06	2.84E-05	6.18E-05
6	a = 0.0063; b =0.0080	0.9139	2.14E-06	8.37E-06	1.82E-05

1: First-order Kinetic Model, 2: Second-order Rate Equation, 3: Peleg's Model, 4: Power Law Equation, 5: Page's Model and 6: Logarithmic Model.

Table 3.3: Modelling of Solid-Liquid Extraction of *Z. jujuba* fruit at 50 °C

Model	Model Constants	R^2	χ^2	RMSE	MAE
1	k = 0.2790; C_e = 0.0234	0.9996	5.01E-27	1.95E-26	4.26E-26
2	h = 0.0246; C_e = 0.0234	0.9818	2.98E-09	1.16E-08	2.53E-08
3	k_1 = 58.1056; k_2 = 41.4335; C_0 = 0	0.9906	2.95E-07	1.15E-06	2.51E-06
4	B = 0.0188; n = 0.0543	0.9709	9.12E-07	5.09E-06	7.75E-06
5	k = 3.7741; n = 0.0543	0.9311	2.15E-06	8.40E-06	1.83E-05
6	a = 0.0029; b =0.0184	0.9722	8.70E-07	3.39E-06	7.40E-06

1: First-order Kinetic Model, 2: Second-order Rate Equation, 3: Peleg's Model, 4: Power Law Equation, 5: Page's Model and 6: Logarithmic Model.

Table 3.4: Modelling of Solid-Liquid Extraction of *Z. jujuba* fruit at 60 °C

Model	Model Constants	R^2	χ^2	RMSE	MAE
1	k = 0.0902; C_e = 0.0224	0.9934	2.63E-12	1.03E-11	2.24E-11
2	h = 0.0051; C_e = 0.0224	0.9187	5.93E-08	2.31E-07	5.04E-07
3	k_1 = 318.4472; k_2 = 39.2443; C_0 = 0	0.9805	7.45E-07	2.91E-06	6.33E-06
4	B = 0.0089; n = 0.2235	0.9213	3.00E-06	1.17E-05	2.55E-05
5	k = 3.8964; n = 0.0010	0.5886	1.57E-05	6.12E-05	1.33E-04
6	a = 0.0104; b =0.0039	0.9471	2.02E-06	7.86E-06	1.71E-05

1: First-order Kinetic Model, 2: Second-order Rate Equation, 3: Peleg's Model, 4: Power Law Equation, 5: Page's Model and 6: Logarithmic Model.

4. Conclusions

This research work investigated the effect of extraction temperature on the concentration of crude extract from *Z. jujuba* fruit. The results showed that the concentration of crude extract from *Z. jujuba* fruit increase with the increased of extraction temperature whereas the concentration of crude extract decrease when the elevation of extraction temperature to 60 °C. This shows that the compounds in *Z. jujuba* fruit were degraded due to the high extraction temperature during the process of SLE.

The antioxidants of *Z. jujuba* fruit had higher yield (93.64%) at extraction temperature of 50 °C. The result of research showed that the yield of antioxidants increase with the increased of extraction temperature but the yield of antioxidant

decrease when the extraction temperature at 60 °C. Since all the antioxidants have similar results, this proved that *Z. jujuba* fruit is a good source of producing antioxidants.

Kinetic modelling was used to study the effect of temperature on the SLE of *Z. jujuba* fruit. First-order Kinetic Model, Second-order Rate Equation, Peleg's Model, Power Law Equation, Page's Model and Logarithmic Model were used to fit the experimental data. The results shown that temperature have significant effects on the concentration of crude extract from *Z. jujuba* fruit. SLE of *Z. jujuba* fruit has high concentration of crude extract at 50 °C temperature. Based on the extraction models, First-order Kinetic Model is the best fitted model for the experimental data with the high value of R^2 (0.9995) and low values of RMSE (5.01×10^{-27}), χ^2 (1.95×10^{-26}) and MAE (4.26×10^{-26}) compared to other models.

References

[1] B. S. Musli, B. L. Chua, Z. Abdullah, K. Y. Pin, L. C. Abdullah, T. Shean, Y. Choong, and U. K. Yusof, "Isolation , Structure Elucidation , Identification and Quantitative Analysis Of Di (2-Ethylhexyl) Phthalate (DEHP) from the Roots of Chlorophytum September - October," *Res. J. Pharm. Biol. Chem. Sci.*, vol. 6, no. 1090, pp. 1090–1095, 2015.

[2] Q. H. Gao, C. Sen Wu, and M. Wang, "The Jujube (Ziziphus Jujuba Mill.) fruit: A Review of current knowledge of fruit composition and health benefits," *J. Agric. Food Chem.*, vol. 61, no. 14, pp. 3351–3363, 2013.

[3] S. Guo, Y. Zheng, J.-G. Joung, S. Liu, Z. Zhang, O. R. Crasta, B. W. Sobral, Y. Xu, S. Huang, and Z. Fei, "Transcriptome sequencing and comparative analysis of cucumber flowers with different sex types.," *BMC Genomics*, vol. 11, p. 384, 2010.

[4] J. Chen, C. Y. Q. Du, K. Y. C. Lam, W. L. Zhang, C. T. W. Lam, A. L. Yan, P. Yao, D. T. W. Lau, T. T. X. Dong, and K. W. K. Tsim, "The standardized extract of Ziziphus jujuba fruit (jujube) regulates pro-inflammatory cytokine expression in cultured murine macrophages: suppression of lipopolysaccharide-stimulated NF-κB activity," *Phytother. Res.*, vol. 28, no. 10, pp. 1527–1532, 2014.

[5] P. Tripathi and S. Tripathi, "Ziziphus jujuba: A Phytopharmacological Review," *Int. J. Res. Dev. Pharm. Life Sci.*, vol. 3, no. 3, pp. 959–966, 2014.

[6] D. Y. Zhang, Y. Wan, J. Y. Xu, G. H. Wu, L. Li, and X. H. Yao, "Ultrasound extraction of polysaccharides from mulberry leaves and their effect on enhancing antioxidant activity," *Carbohydr. Polym.*, vol. 137, pp. 473–479, 2016.

[7] S. Das and D. Bera, "Mathematical Model Study on Solvent Extraction of Carotene From Carrot," *Int. J. Res. Eng. Technol.*, vol. 2, no. 9, pp. 343–349, 2013.

[8] G. D. Wright, "Mathematical Modeling of the Solid-Liquid Extraction of Phenolic-Rich Compounds from Pinus contorta Bark by Mathematical Modeling of the Solid-Liquid Extraction of Phenolic-Rich Compounds from Pinus contorta Bark," 2015.

[9] J. w. Li, S. dong Ding, and X. l. Ding, "Optimization of the ultrasonically assisted extraction of polysaccharides from Zizyphus jujuba cv. jinsixiaozao," *J. Food Eng.*, vol. 80, no. 1, pp. 176–183, 2007.

[10] C. Qu, S. Yu, L. Luo, Y. Zhao, and Y. Huang, "Optimization of ultrasonic extraction of polysaccharides from Ziziphus jujuba Mill. by response surface methodology.," *Chem. Cent. J.*, vol. 7, no. 1, p. 160, 2013.

[11] M. Himaja, A. Ranjitha, M. V Ramana, M. Anand, and K. Asif, "Phytochemical Screening and Antioxidant Activity of Rhizome Part of Curcuma Zedoaria," *Int. J. Res. Ayurveda Pharm.*, vol. 1, no. 2, pp. 414–417, 2010.

[12] W. Qu, Z. Pan, and H. Ma, "Extraction modeling and activities of antioxidants from pomegranate marc," *J. Food Eng.*, vol. 99, no. 1, pp. 16–23, 2010.

[13] M. Ly, A. Margaritis, and B. Jajuee, "Extraction and Identification of Di (2-Ethylhexyl) Phthalate from Safed Musli (Chlorophytum Borivilianum L.)," *Biotechnol. Bioeng.*, vol. 96, no. 1, pp. 67–79, Jan. 2007.

[14] J. Xi and S. Luo, "Pressure-enhanced solid–liquid extraction of rutin from Chinese scholar-tree flower: Kinetic modeling of influential factors," *Sep. Purif. Technol.*, vol. 156, pp. 809–816, 2015.

[15] A. D. Handayani, Sutrisno, N. Indraswati, and S. Ismadji, "Extraction of astaxanthin from giant tiger (Panaeus monodon) shrimp waste using palm oil: Studies of extraction kinetics and thermodynamic," *Bioresour. Technol.*, vol. 99, no. 10, pp. 4414–4419, 2008.

[16] Y.-C. Cheung, K.-C. Siu, and J.-Y. Wu, "Kinetic Models for Ultrasound-Assisted Extraction of Water-Soluble Components and Polysaccharides from Medicinal Fungi," *Food Bioprocess Technol.*, vol. 6, no. 10, pp. 2659–2665, Oct. 2013.

[17] S. Jokic, D. Velic, M. Bilic, Ana Bucic-Kojic, M. Planinic, and S. Tomasa, "Modelling of the process of solid-liquid extraction of total polyphenols from soybeans," *Czech J. Food Sci.*, vol. 28, no. 3, pp. 206–212, 2010.

[18] C. H. Su, C. S. Liu, P. C. Yang, K. S. Syu, and C. C. Chiuh, "Solid-liquid extraction of phycocyanin from Spirulina platensis: Kinetic modeling of influential factors," *Sep. Purif. Technol.*, vol. 123, pp. 64–68, 2014.

[19] M. Ly, A. Margaritis, and B. Jajuee, "Effect of solvent concentration on the extraction kinetics and diffusivity of Cyclosporin A in the fungus Tolypocladium inflatum," *Biotechnol. Bioeng.*, vol. 96, no. 1, pp. 67–79, Jan. 2007.

[20] K. Sinha, S. Chowdhury, P. Das Saha, and S. Datta, "Modeling of microwave-assisted extraction of natural dye from seeds of Bixa orellana (Annatto) using response surface methodology (RSM) and artificial neural network (ANN)," *Ind. Crops Prod.*, vol. 41, no. 1, pp. 165–171, 2013.

[21] T. Chai and R. R. Draxler, "Root mean square error (RMSE) or mean absolute error (MAE)? -Arguments against avoiding RMSE in the literature," *Geosci. Model Dev.*, vol. 7, no. 3, pp. 1247–1250, 2014.

[22] I. Doymaz, "Thin-layer drying of spinach leaves in a convective dryer," *J. Food Process Eng.*, vol. 32, no. 1, pp. 112–125, 2009.

[23] R. Chaiklahan, N. Chirasuwan, and B. Bunnag, "Stability of phycocyanin extracted from Spirulina sp.: Influence of temperature, pH and preservatives," *Process Biochem.*, vol. 47, no. 4, pp. 659–664, 2012.

[24] M. Dent, V. Dragovi, M. Peni, and M. Brn, "The Effect of Extraction Solvents , Temperature and Time on the Composition and Mass Fraction of Polyphenols in Dalmatian Wild Sage (Salvia officinalis L .) Extracts," *Ftb*, vol. 51, no. 1, pp. 84–91, 2013.

[25] M. F. et al. bd Ghafar, "Effect of temperature and extraction process on antioxidant activity of various leaves crude extracts of Thymus vulgaris," *J. Coast. Life Med.*, vol. 1, no. 2, pp. 130–134, 2013.

[26] G. Spigno and D. M. De Faveri, "Antioxidants from grape stalks and marc : Influence of extraction procedure on yield , purity and antioxidant power of the extracts," vol. 78, pp. 793–801, 2007.

[27] M. Miranda, H. Maureira, K. Rodríguez, and A. Vega-Gálvez, "Influence of temperature on the drying kinetics, physicochemical properties, and antioxidant capacity of Aloe Vera (Aloe Barbadensis Miller) gel," *J. Food Eng.*, vol. 91, no. 2, pp. 297–304, 2009.

[28] C. Liyana-Pathirana and F. Shahidi, "Optimization of extraction of phenolic compounds from wheat using response surface methodology," *Food Chem.*, vol. 93, no. 1, pp. 47–56, 2005.

eureca 2016- Conference Paper
Paper Number 2CE17

Devulcanization of Waste Rubber Tyre Utilizing Deep Eutectic Solvent and Ultrasonic Energy

Ricky Saputra, Rashmi G. Walvekar, Mohammad Khalid Siddiqui & Kaveh Shahbaz

rickysaputra070894@gmail.com
rashmi.walvekar@gmail.com
khalidchem@gmail.com
shahbaz.kaveh@gmail.com

Abstract
Tyre belongs to a polymer group which is known for its ability to degrade within thousands of years and little efforts were made to recycle them where it eventually becomes source of pollution. This research aims to study the devulcanization of waste rubber tyres utilizing ultrasonic method to minimize environmental impacts. In particular, effect of deep eutectic solvent (DES) – ChCl:Urea as new class of green solvent on devulcanization was studied through its ability in cleaving sulphur crosslink-network. DES characterization proved that it is suitable to be used at 180^{o}C which has water content of 1.55 wt%, freezing point of 285.15 and degradation temperature of 501.83 K. Devulcanization study was done using mass ratio formulation of 1:20 to 1:40 at temperature variation of 5-30 minutes. Increasing trend on degree of devulcanization was observed from 5 to optimum value of 15 minutes in EDX analysis. Beyond 15 minutes, bond reformation due to rubber active chains prevails and degree of devulcanization decreases. Furthermore, the degree of devulcanization increases as the mass ratio increases. For rubber with DES, FTIR analysis was performed and shows that no significant change in main rubber organic chain but indicates changes at –S-S- bond that shows at 15 minutes bond intensity increases but decreases beyond 15 minutes. Morphological study through FESEM also shows similar result where smooth surface is observed at optimum time of 15 minutes and rough surface at 5 minutes. Research proven that ultrasonic devulcanization with DES increases the efficiency to 74.44% compared to any current existing technology.

Keywords: Deep Eutectic Solvents, Devulcanization, Bond Reformation, Sulphur-Crosslink-Network, Ultrasonic.

1. Introduction

Special type of elastomer called rubber is a substance that possesses the capability to elastically deform by applying forces to it. It can be made naturally from a plant called *Hevea Brasiliensis* which then is called natural rubber or it can be made synthetically. However, before it is usable for commercial purposes, raw rubber needs to be treated and processed whereby various additives, industrial oils, carbon black fillers are mixed together with raw rubbers for the purpose of increasing the rubber's strength, life and cut the processing cost [2]. Next, the rubber undergoes vulcanization process for it to manifest its full potential and suitable to be used commercially.

Throughout the course of years, the demand for rubber has increased significantly around the globe from normal household to industrial applications such as shoes' soles, electrical insulators, industrial conveyor-belts, tiles or flooring, railway and especially on automotive part which is tyre. Vulcanization reaction is shown in Fig. 1 which defined as a chemical reaction that involves complex cross-links formation between all rubber compounds in order to produce rubber that is infusible, hard, insoluble and robust but increases its mechanical properties at the consequences of having low recyclability and subjection to landfill [1, 2].

Figure 1. Vulcanization chemical reaction [1]

Within recent years, consumption of vulcanized elastomers specifically in tyre industries keep growing and has reached 17.20 million tons globally whereby 39% of it is based on natural rubber and the remaining 61% comes from synthetic rubber. This growth phenomenon impacts the market prices of raw materials and causes them to increase. Despite the tremendous demand upon vulcanized elastomer, there are lacks of efforts upon recycling it even after they have ended their life cycle. Thus, these scrap tyres eventually turn out to be wastes that have continuously caused serious issues on environment, economic and social.

To resolve such sustainability issue, recycling scrap tyres through a reclaiming process called devulcanization is one of the solutions to minimize risks upon environment and return the tyres back to virgin rubbers that can be reused for re-vulcanization process or may be utilized for other applications such as for soil amending materials, rubberized-asphalt or concrete, plastic enhancing materials, reef to control erosion and others. Devulcanization reaction is shown in Fig. 2 as follow.

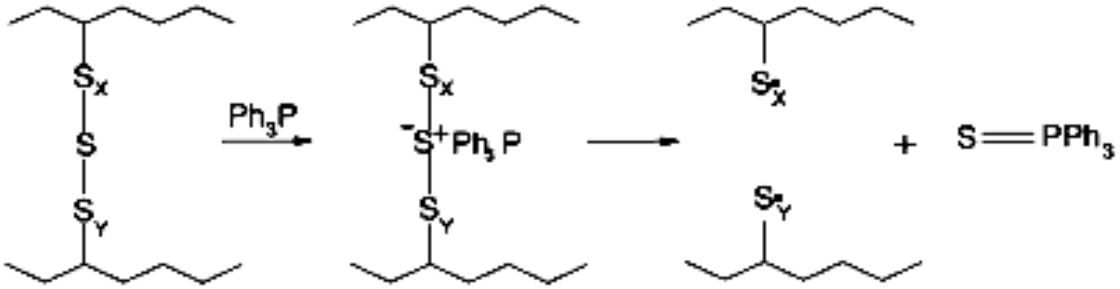


Figure 2. Devulcanization chemical reactions [10]

In accordance to devulcanization technology from various studies, there are various methods and techniques that had been used to devulcanize the waste rubber such as chemical, thermo-chemical, mechano-chemical, high-power microwave energy and many more [3]. Although these methods capable to devulcanize rubber, the product obtained has poor mechanical property which is not suitable for re-vulcanization [3] and materials or solvent used are either too expensive or not green enough to build the three pillars of sustainability.

Devulcanization of rubber tyre is a rather complicated process due to its complex composition that are blended together during production as shown in Table 1 whereby each of them has their own specific properties and characteristics. In addition to that, rubber tyre also has complex structure with three-dimensional networks arrangement that is formed through crosslinking process with sulphur of which makes it non-melting and insoluble.

Table 1. Typical tyre composition for passenger car [4]

Compounds	Amount (phr)
Polymer Base	100
Natural Rubber (NR)	30
Styrene Butadiene Rubber (SBR)	40
Butadiene Rubber (BR)	20
Butyl & Halogenated Butyl Rubber	10
Active Filler – Carbon Black	34 ± 2
Textile Fabric	2

One of the recent studies done by [3] shows an innovative experimental analysis where devulcanization of waste rubber tyre is done through the usage of ionic liquid (IL) combined with microwave treatment and result in a good outcome – 50% sulphur removal. Indeed many experimental analyses have been performed through the usage of IL due to its unique ability that can be tuned as desired and resulted in a satisfying outcome. However, [3, 5] proven that IL will not be very convenient to be used in terms of industrial scale due to its various drawbacks such as high level of toxicity, not economically viable, high viscosity and non-biodegradable. Thus, a more suitable candidate is required to be introduced to overcome these drawbacks.

Recently, an alternative solution has been found which provide a similar feature to IL. This solution also has the capability to be synthesized in such way that it has the desired property for particular application; this solution is called deep eutectic solvent (DES) [5]. DES consists of mixture of two or more components that has a melting point below of its make-up components whereby it is normally made out of quaternary ammonium halide salt and hydrogen bond donor (HBD). Based on study done by [3], it has been proven that IL has the capability to devulcanized and recycle back waste tyres. Hence, DES that is a substitute or derivative solvent of IL which has the similar feature can be used to devulcanize rubber in a similar manner providing that it is made from the correct mixture.

In addition to that, similar area of research was performed in a petrochemical industry where DES was used in desulphurization process which defined as removal of sulphur from petrochemical products, normally oil. From study made by [6-8], removal of sulphur through the usage of DES is indeed producing a satisfactory result at ± 99.48% and it is proven to be suitable for sulphur removal process.

Thus, with respect to the study that has been done, in order to reutilise back the waste tyre rubber, a new approach through impregnation of DES alongside with treatment by means of ultra-sonication irradiation energy is introduced to improve the process' recovery efficiency, simultaneously decrease the consumption of energy during the treatment as well as through the usage of cheaper and greener solvent.

In this particular research of interest, the DES proposed to be coupled with ultrasonic devulcanization of rubber is ChCl:Urea at molar ratio of (1:2) whereby the objectives of this research are as follows:

1. To synthesize and characterize the different types of DES in terms of water content, freezing point and thermal degradation temperature,
2. To study the effect of heating time and rubber to DES mass ratio on devulcanization of waste rubber tyre, and
3. To compare the performance of recycled rubber tyre in terms of structure and chemical bonding.

2. Methodology

In this particular research, in order to achieve the objectives seeks, quantitative types of research will be implemented whereby analysis and justification made will be based on the DES properties that is for suitable devulcanization environment, the amount of sulphur removed by means of measuring sulphur content at initial & final stage and structure of the rubber. Thus, validations and verifications will be performed in accordance to the experimental and numerical results.

2.1 Preparation of DES

Chemicals used to synthesize the DES are choline chloride as the halide salt and Urea as the HBD that was purchased from Merck Sdn. Bhd. Malaysia at 99.0% purity. The solvent is prepared at 1:2 molar ratio of salt and HBD.

The procedure of synthesizing the DES which was used in the research is through the guidance from publication of [9, 10]. With respect to the study, the salt and HBD at 1:2 molar ratio was added into a 100 mL schott bottle alongside with 30 mm magnetic bar. The bottle was then closed and tightly sealed with parafilm to minimize the chances of having contact with moisture that might cause crystallization. Next, the sample was placed on a hot plate at 393.15 K with speed of agitation at 300 rpm in a fume-hood. The synthesis process only will come to an end when a clear and homogeneous liquid is achieved.

2.2 Characterization of DES

To ensure that the synthesized DES is appropriate and suitable to be used as devulcanizing solvent, three types of analysis will be performed upon the synthesized DES which are Karl Fischer titration (KFT), thermogravimetric analysis (TGA) and differential scanning calorimetric (DSC).

2.2.1 Karl-Fischer Titration

Purpose of DES analysis through KFT is to determine the moisture content presents in the solvent whereby it is must not be more than 3 wt% as described by [10, 11]. In addition to that, to check the accuracy and precision of the equipment, 1.00 mg/g of Hydranal-water standard was used which was supplied by Sigma-Aldrich Malaysia. The following Fig. 3 shows the Karl Fischer instrument.

2.2.2 Thermogravimetric Analysis

Thermal analysis through the usage of thermogravimetry analyser was performed to determine the degradation temperature of the solvent. The analysis was performed on a Perkin Elmer - TGA 8000. DES sample was placed on a sample pan and weighted to 5–10 mg. Then it is placed in the instrument. Under the influence of constant nitrogen purge gas which is at 40 mL/min, the sample was heated from 30 to 500^{o}C at the rate of 10 K/min until complete degradation is achieved [10].

2.2.3 Differential Scanning Calorimetric

The freezing point of the DES was determined using DSC. The instrument which was used is Perkin Elmer DSC 8000. DES sample was prepared in an aluminium pan and weighted to about 5-10 mg. Under the influence of constant nitrogen purge gas which is at 40 mL/min, the sample was heated from 30 to 60^{o}C at the rate of 10 K/min, then cooled from 60 to -70^{o}C at a rate of 5 K/min and was heated again from -70 to 60^{o}C at a rate of 2 K/min [10].

2.3 Rubber Sample Preparation

In this particular research of interests, the rubber to DES mass ratio was varied at 1:20, 1:30 and 1:40 with the total mass of 50 gram [3]. Such ratio was chosen in order to avoid the mixture of rubber and solvent from becoming very sluggish which will be ineffective for devulcanization purposes as the solvent cannot cater or is not equally distributed over the sample rubber.

In addition to that, all the rubber and DES mixture was initially exposed to Elma-ultrasonic-bath treatment for 1 hour at 37 kHz [12] for extraction purposes before it was heated at 180^{o}C on a hot plate in a fume-hood where the heating time was varied from 5 to 30 minutes. Such heating temperature was chosen due to the fact that according to [3-5], the flash point of the rubber is approximately around 205^{o}C. Hence, for safety purposes, a temperature below the flash point is recommended to be chosen. Hence, for clearer understanding upon the experimental formulation described, the following Table 2 is provided.

After extraction process which includes ultrasonic treatment and heating process finishes, the mixture will be filtered using gravity filtration method [13]. The filtered rubbers were then thoroughly washed clean by means of distilled water for three times as suggested by [3], to ensure no DES presents in the rubber. Lastly, the washed rubber was dried in oven for 24 hours at 70^{o}C.

Table 2. DES and rubber mixture formulation

Rubber : DES Mass Ratio	Heating Time [min]	Sample Name
1:20	5	1A
(2.38 gr Rubber : 47.62 gr DES)	15	2A
	30	3A
1:30	5	4A
(1.61 gr Rubber : 48.39 gr DES)	15	5A
	30	6A
1:40	5	7A
(1.22 gr Rubber : 48.78 gr DES)	15	8A
	30	9A

2.4 Rubber Sample Characterization

After the rubber sample has been completely dry due to it was left overnight in the oven, analysis upon the rubber can be performed. Since analysis revolved around the concentration of sulphur presents and upon the bonding phenomenon as per described in research objectives, the analyses that will be done are Fourier transform infrared spectroscopy (FTIR), field emission scanning electron microscope (FESEM) and energy dispersive x-rays (EDX).

2.4.1 Fourier Transform Infrared Spectroscopy

FTIR which was used is FTIR-ATR Spectrum 100. The purpose of its usage is to determine and identify the structural change that may or may not happen during devulcanization process [14]. In addition to that, FTIR also can help to identify what chemical bondages that are being affected by the process of devulcanization [15] through spectra analysis. It was expected that disulphide (S-S) and (C-S) bonds that presents in original rubber will reduce upon completion of devulcanization process.

2.4.2 Field Emission Scanning Electron Microscope and Energy Dispersive X-Rays

Such analysis was done by sending out sample to Nottingham University Malaysia. FESEM technology which was used is Ultra 55 FESEM from Chicago, USA with accelerating voltage of 20kV. This particular analysis is done to study the morphological structure of the rubber before and after devulcanization process. For EDX, the equipment that will be used is EDX-Zeis Supra 35 VP. The purpose of EDX analysis is to determine rubber's elemental composition before and after the process of devulcanization.

3.0 Results and Discussion

With respect to the methodology described, analysis of the result will be divided into two parts which will be regarding the devulcanizing solvent and regarding the results of devulcanization process.

3.1 Analysis of DES' Physicochemical Characteristics

In this particular research, a quaternary ammonium salt which is choline chloride with HBD which is urea was selected for the preparation of type I eutectic solvent. Such DES was obtained through mixing the HBD with quaternary ammonium salt at molar ratio of (1:2). The end product will be a homogeneous and colourless liquid which has supremely high viscosity when it is at room temperature. Accordingly, its physicochemical properties were to be determined which includes the water content, degradation temperature and freezing point.

The moisture content that presents in the DES is one of the most important parameter that requires to be determined to ensure the effectiveness and efficiency of the solvent during its application whereby it is limited to maximum of 3 wt% due to the fact that the moisture content significantly affects its physical properties [17]. Hence, to have sufficient amount of DES to cater the formulation describes in Table 2, six batches of the same DES were synthesized and their individual moisture content is shown in Table 3. Such repetition is required due to the fact that DES must only be synthesized at maximum of 60 mL per batch as recommended by [13, 16]. All the moisture content of DESs shown have been proven to be less than the maximum allowable, hence they are suitable to be used.

Table 3. Moisture content of ChCl:Urea (1:2) DES

Batch Number	Water Content [%]	Freezing Point [K]	Abbreviation
1	0.81	285.7	DES 1A
2	1.45	285.8	DES 2A
3	1.55	286.3	DES 3A
4	1.46	284.3	DES 4A
5	1.71	286.1	DES 5A
6	1.52	285.9	DES 6A

The melting or freezing point of DESs is another important parameter that needs to be defined to illustrate the solvent range of liquidity. Its value corresponds to the batch of the DES prepared is also reported in Table 3 whereby it is determined and measured through the usage of temperature programme declared earlier in section 2.2.3. With respect to the freezing point value obtained, it is then compared to other related literature such as [18, 19]. In general, DES which is made out of ammonium salt with Urea has a melting point below 291.15 K [19]. Such behaviour characteristic indeed declares that the values of freezing point obtained in this research are valid and hence DES synthesized is suitable to be used. The following Table 4 shows some of the available freezing point data for ammonium salt with urea based DES.

Table 4 Freezing point of ammonium with salt with HBD based DES [19]

Ammonium Salt	HBD	Ammonium Salt to HBD Ratio	Freezing Point [°C]
Choline Fluoride	Urea	1 : 2	1
Choline Nitrate	Urea	1 : 2	4
Choline Acetate	Urea	1 : 2	18
Trithylethanaminium Chloride	Urea	1 : 2	14.7

The degradation temperature of the DES is the utmost importance parameter that requires to be determined to ensure that the solvent does not degrades at devulcanization operating temperature which is at 180°C. Its measurement is done through the usage of temperature programme declared in section 2.2.2 and the following Fig. 3 display the percentage of weight loss of ChCl:Urea DES as a function of temperature.

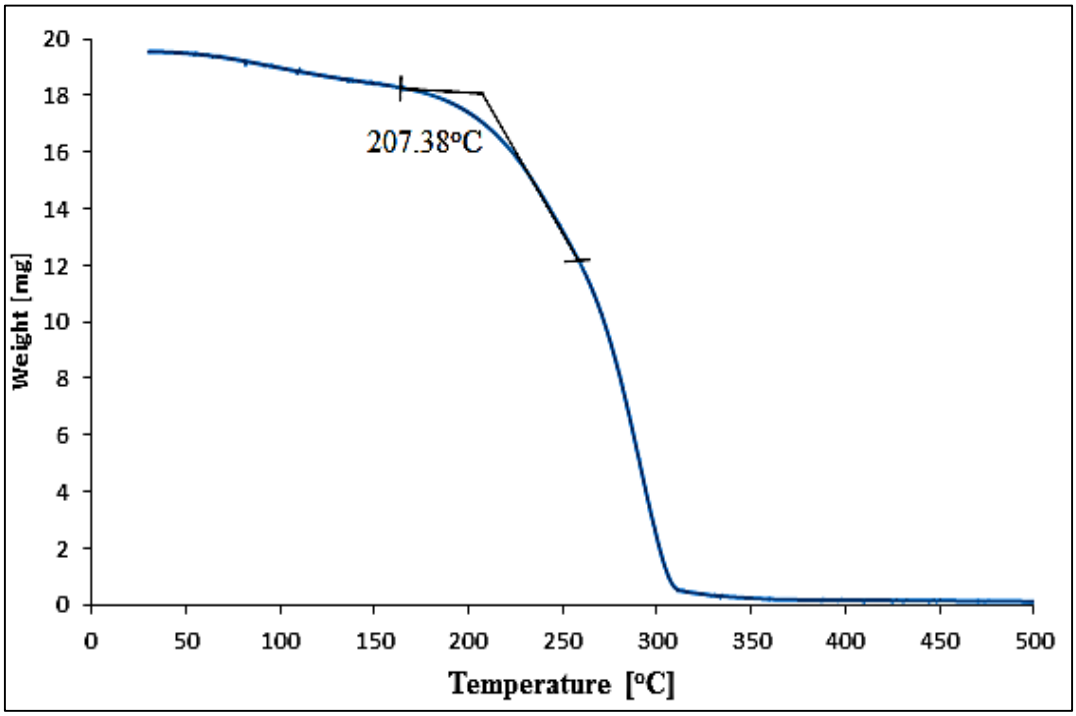


Figure 3. Degradation curve of ChCl:Urea (1:2) DES

In accordance to Fig. 3, the degradation temperature was evaluated by means of tangent line at the point where there is a sudden drop in weight percentage and the temperature was found to be ~228.68. This value clearly indicates that the devulcanization temperature must not reach such temperature to avoid the degradation of the DES. Hence, the selected temperature as well as the DES is both suitable to be used for this particular devulcanization research.

3.2 Analysis of Devulcanized Rubber

Evaluation upon devulcanized rubber with ChCl:Urea DES is to be analysed in terms of its initial and final Sulphur content presents as well as its structural bond(s) which was done through the usage of EDX and FTIR respectively.

3.2.1 Energy Dispersive X-Ray Analysis

The result obtained from composition analysis of devulcanized rubber by means of XRD in this research is shown in Fig. 4. Such analysis gives the initial and final rubber composition whereby the percentage removal was determined. It is clearly illustrated that DES has the potential in extracting Sulphur. In accordance to [4, 20-22], the rise in the degree of devulcanization indicates that the rubber network's crosslink density are reduced and its soluble fraction increases which marks successful devulcanization process.

During the process, the energy that is being released is mostly utilized for the breakage of disulphide and C-S bond present in the rubber. Such phenomenon happened due to the fact that the amount of energy needed to break -S-S- and -C-S- bond is much lower which is 227 and 273 kJ/mole [21] respectively while the main organic carbon chain bonds have much higher energy. Hence, the tendency for breaking -S-S- and -C-S- bond or in other increases of degree of devulcanization is expected to be high at high temperature for a short period of devulcanization time. In addition to that, [4] declares that degree of devulcanization will be reducing back at certain point as time increases due to the fact that the crosslink density increases back.

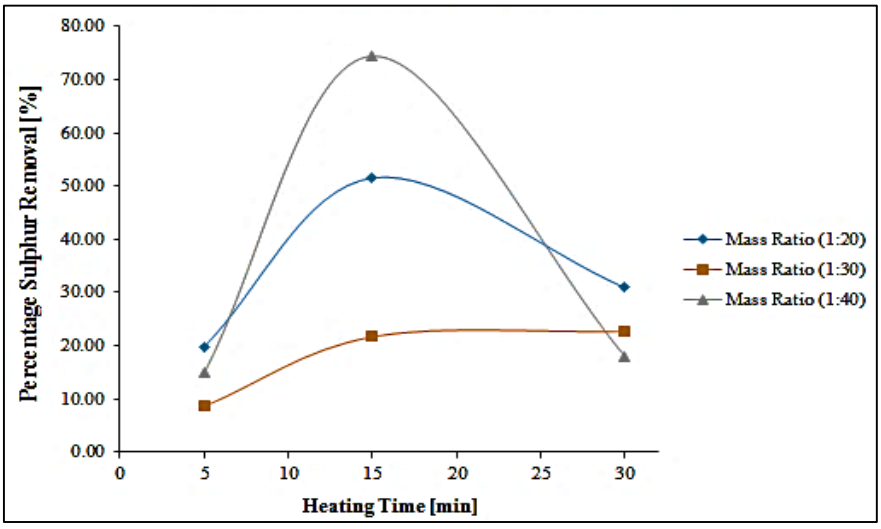


Figure 4. XRD analysis of devulcanized rubber at various mass ratios

With respect to the theoretical practice described, observation from Fig. 4 clearly indicates such phenomenon where with the increases of time for a certain period, the degree of devulcanization increases but reaches maximum at 15 minutes for all rubber to DES ratio and then after 15 minutes the degree of devulcanization decreases. Hence, the observation obtained describes that 15 minutes is the optimum devulcanization time for this research which is tally with the result presented by [4, 21-22] whereby their optimum recommended devulcanization time is in range of 5-15 minutes at 370^{o}C.

Such interesting phenomena happens because during continuation of devulcanization process, two types of reaction may occur which is the cleavage of the -S-S- and -C-S- bond as well as reformation of -S-S- and -C-S- bond back due to the chain segment of rubber that is active. Hence, it is critical to ensure the correct time to stop devulcanization process to prevent reformation process of the sulphur bond back from the fragments of active chains in becoming the prevailing occurrence, but at the same time, achievement of highest -S-S- and -C-S- breakage must be ensured at that particular time. Thereby, time for devulcanization process should be as short as possible and for this particular research, reforming reaction prevails at devulcanization time greater than 15 minutes.

In terms of mass ratio evaluation upon devulcanization process, Fig. 2 indicates that the higher the amount of DES added to the rubber during devulcanization process, the greater the degree of Sulphur bond cleavage will be. This phenomenon happens because the capacity of DES of which able to extract or break the bondage increases. Hence, the degree of devulcanization is directly proportion to the mass ratio whereby in this particular research the ratio 1:40 gives the best outcome. However, irregular trend can be observed from sample 1:30. Such behaviour can be explained that during the process, the rubber is may not be completely soaked by the DES and formed a two layer mixture where impregnation and contact of solvent to the rubber is minimized. More detail characterization on immiscibility of rubber in ChCl:Urea DES at this particular ratio is suggested for further research.

3.2.2 Fourier Transform Infrared Spectroscopy Analysis

Analysis by means of FTIR emphasized on the structural changes that happens with the rubber before and after devulcanization processes upon all nine samples prepared as well as analysing what bond(s) is actually cleaved during such treatment process. The following Fig. 5 and Fig.6 describes the FTIR spectra for samples at various mass ratios selected at 15 and 30 minutes heating respectively.

With respect to the shown figures, it has been identified that above 3,000 and 1,700 cm^{-1}, there are no significant appearance of any peak other than the broad peak above 3,000 cm^{-1} which indicates the presence of water which may still remain in the sample. Hence, it can be conclude that there is an averagely low percentage amount of rubber degradation that contains the group of –C=O and -OH [23]. The occurrence of degradation generally happens due to the existence of free radicals which presents because the breakage of -S-S- and -C-S- bonds which will then reacts with the oxygen from the surrounding to form either –OH or –C=O functional group that has a wavelength in a range above 3,000 and 1,700 cm^{-1} respectively.

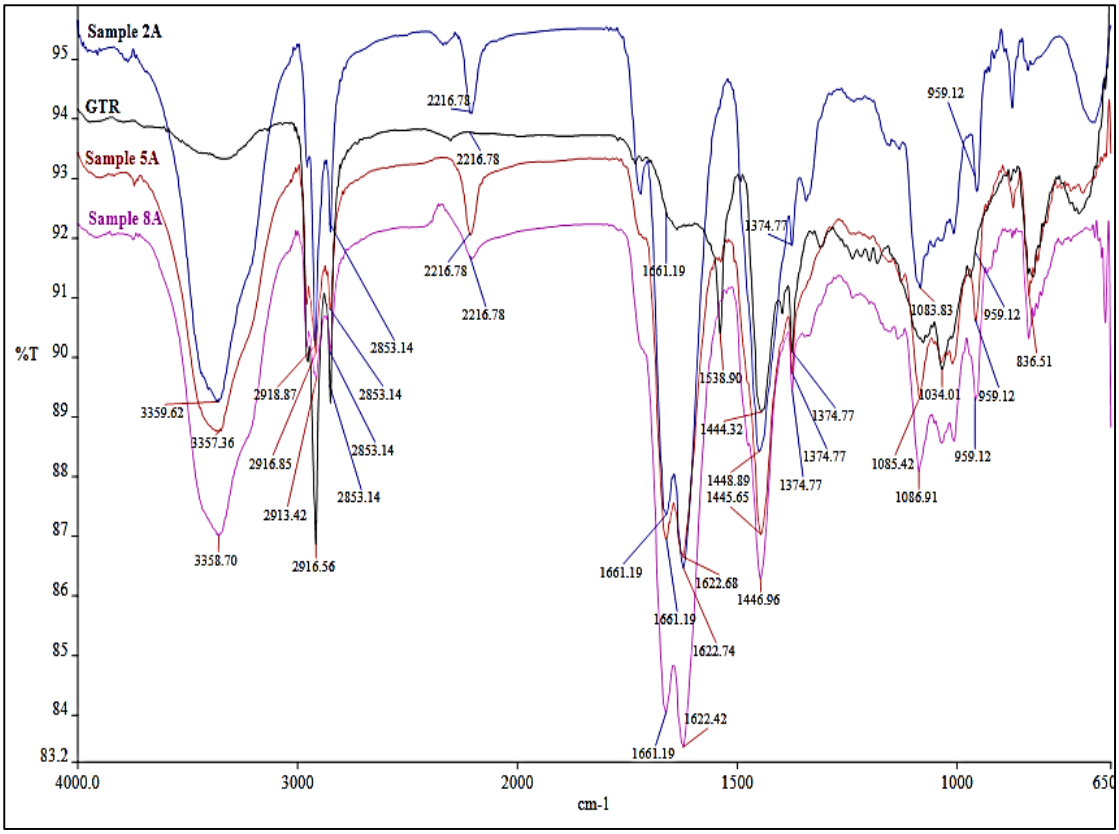


Figure 5. FTIR spectrum for sample of various ratios for 15 minutes devulcanization

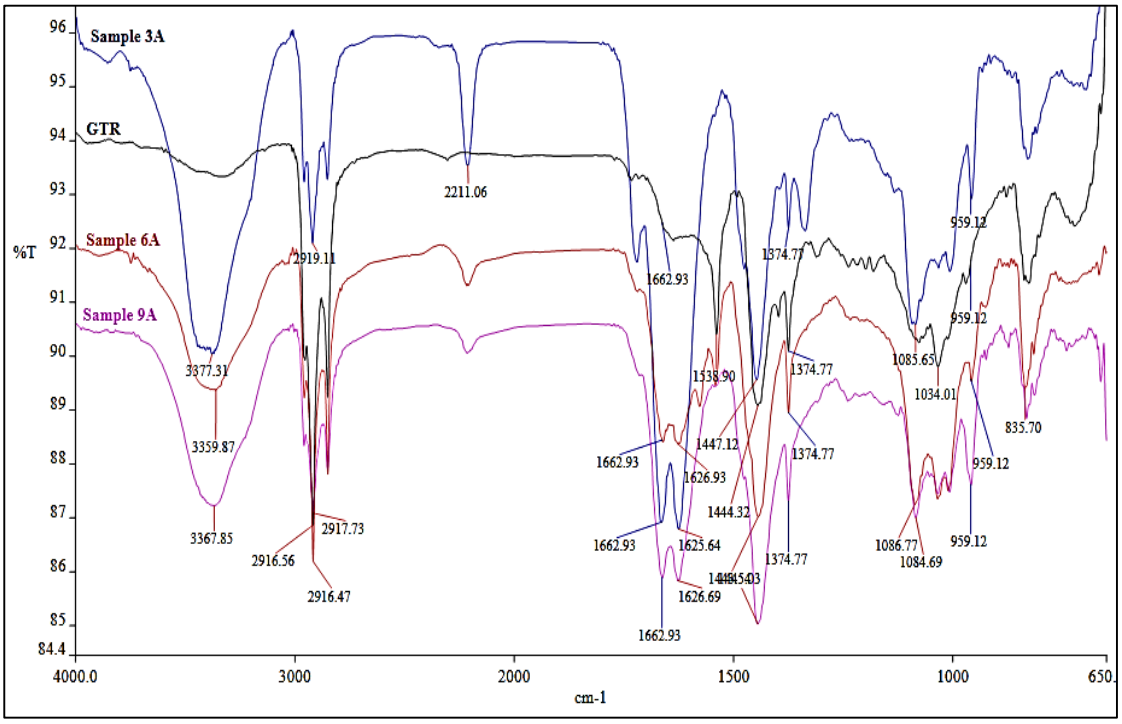


Figure 6. FTIR spectrum for sample of various ratios at 30 minutes devulcanization

The spectrum wavelength for $–CH_3$ appears in the region of 1374.77 cm^{-1} and its value with respect to treatment mass ratio did not significantly change for 15 minutes sample. However, for 30 minutes sample, a structural change is seen. Similarly, -CH- bond stretching also appears at the wavelength of 2916.56 whereby at 15 minutes sample, the difference in percentage of transmission between sample at different treatment time does not give any significant difference. But again, for 30 minutes sample, a slight greater of difference in percentage transmission is seen. Then –S-S- bond is also analysed at 700-550 cm^{-1}. From Fig. 5 and 6, it can be compared that sample 2A, 5A and 8A which operated at 15 minutes do not have any peak appearance while sample 3A, 6A and 9A which operated at 30 minutes experience the reappearance of peak which indicating reformation. Lastly, -C-S- bond which falls in the region of 720-570 cm^{-1} is also analysed whereby in both Fig. 5 and 6, the peak still present which indicating the bonds were not cleaved. Hence, the treatment did not cleave any bond(s) that has higher energy than -S-S- which indicating the main carbon backbone chain is not damaged and being retained.

From this analysis, it can be concluded that during devulcanization process performed in this research, it does not harm any bond that has higher energy than disulphide bond and the DES used selectively breaks only the S-S bonds. However, as the devulcanization time increases, the S-S bond will be reformed again. Hence, both FTIR and EDX analyses are tally with each other and validation has been made.

3.2.3 Field Emission Scanning Electron Microscope

Display for rubber's FESEM analysis is shown in Fig. 7 and 8 as follow at 1500x of magnification. The treated rubber selected for evaluation is sample at mass ratio of 1:40 for heating time at 5, 15 and 30 minutes.

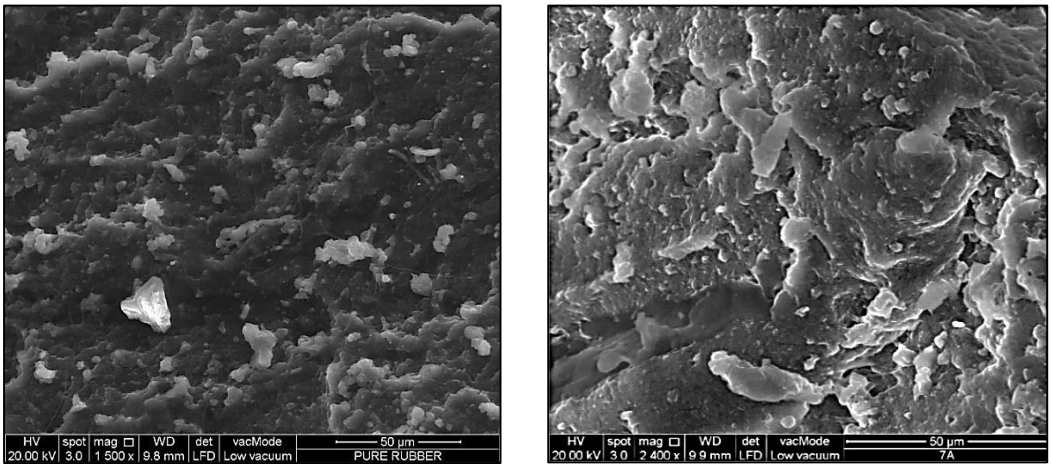


Figure 7. Initial rubber (left) and rubber at 1:40 mass ratio for 5 minutes (right)

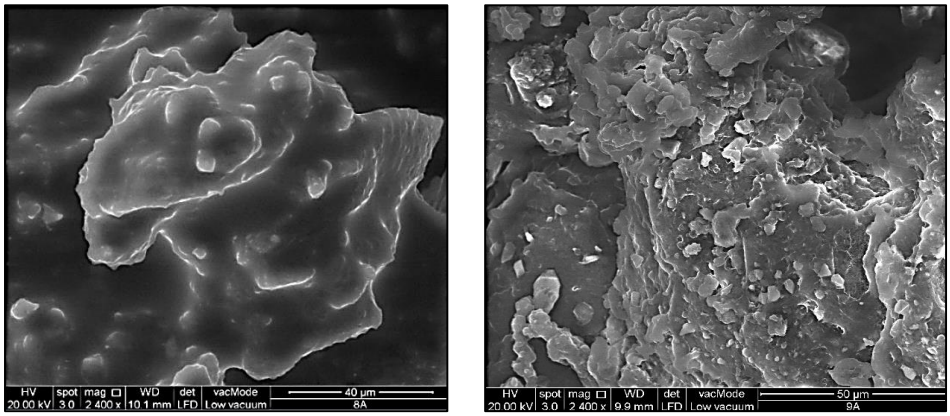


Figure 8. Rubber at 1:40 mass ratio for 15 (left) and 30 minutes (right)

In accordance to Fig. 7 and 8, it can be seen that rubber after devulcanization gives various type of structure which is different from its initial. For 5 minutes treatment, it can be seen that the rubber surface clearly shows a rough surface with the existence of holes and pores. During this particular time, rubber under subjection of ultrasonic and heating begins to degrade and partially break or remove some of the components presents which illustrated by the degree of roughness. For treatment at 15 minutes, a clearer and smoother surface is shown due to the fact that devulcanization process has reached its maximum and the required bonds have been removed. As for 30 minutes sample, the surface of the rubber becomes bubbly and rough, this indicates that the reformation of bond is likely to take place as discussed due to active chain that presents in the rubber.

4.0 Conclusion

Deep eutectic solvent which was utilized in recycle process called devulcanization for waste rubber tire has been studied. Initial characterization of DES was performed through Karl Fischer, DSC and TGA was conducted. Based upon the finding, the water content presents is 1.55 wt% in average with freezing point of 285.15 K and degradation temperature of 501.83 K. Since the operating temperature selected for devulcanization process is 180^{o}C, the selected DES is suitable to be used.

The potential of this particular DES to perform devulcanization process of which is coupled with ultrasonic treatment has been proven. The increase of sulphur removal with time from 5 to 15 minutes and decrease when above 15 minutes regardless of the mass ratio is testifying that there is a certain time for devulcanization process to reach its optimum condition and once the optimum time exceeded, reformation of the bond prevails. In addition to that, it was also observed that devulcanization process favours higher mass ratio between the rubber to DES due to the fact that, the capacity of DES to break the bond(s) increases.

In fact, such conclusion was also withdrawn from FTIR analysis where the disulphide bond disappears at 15 minutes and reappears at 30 minutes which indicating reformation phenomenon. The outcome of such observation indicates that very low deformation percentage upon the main polymer chain which in turn may result in good mechanical property if the rubber were to be vulcanized back. Lastly, similar outcome was also drawn from FESEM analysis through the degree of roughness of rubber structure and texture.

As a primary conclusion for this research, the usage of DES exhibits high potential towards effective, successfully and efficient devulcanization process of rubber that gives 74.44% effectiveness and provides better and environmental friendly solvent for industrial usage.

Acknowledgement

Throughout the process of research, the author would like to give a token of appreciation to Dr. Rashmi G. Walvekar, Prof. Dr. Mohammed Khalid Siddiqui, Dr. Kaveh Shahbaz, Ms. Lithnes Kalaivani and Ms. Nur Farihah A. Malek for their kind support and guidance that enables this research to reach its completion..

References

[1] B. Rodgers, *Rubber Compounding: Chemistry and Applications, 2nd ed.*, United States: CRC Press: Taylor & Francis Group, 2016, pp. 1-15, 33-40 and 523-535.

[2] T. Liang, "Continuous Devulcanization of Ground Tire Rubber of Different Particle Sizes Using an Ultrasonic Twin-Screw Extruder," M. S. thesis, Dept. Science., University of Akron, Ohio, United States, 2013.

[3] S. Seghar, N. A. Hocine, V. Mittal, S. Azem, B. Schmaltz, and N. Poirot, "Devulcanization of styrene butadiene rubber by microwave energy : Effect of the presence of ionic liquid," vol. 9, no. 12, pp. 1076–1086, 2015.

[4] R. U. N. D. Anwendungen, "Devulcanization of Whole Passenger Car Tire Material," pp. 20–25, 2013.

[5] P. S. Garcia, F. D. B. De Sousa, J. A. De Lima, S. A. Cruz, and C. H. Scuracchio, "Devulcanization of ground tire rubber : Physical and chemical changes after different microwave exposure times," vol. 9, no. 11, pp. 1015–1026, 2015.

[6] G. Garcia, S. Aparicio, R. Ullah, and M. Atilhan, "Deep Eutectic Solvents : Physicochemical Properties and Gas Separation Applications," vol. 10, no. 29, pp. 2616–2644, 2015.

[7] C. Supercapacitors, W. Zaidi, J. Jacquemin, and L. Timperman, "Deep Eutectic Solvents Based on N- Methylacetamide and a Lithium Salt as Electrolytes at Elevated Temperature for Activated Carbon- Based Supercapacitors," vol. 10, no. 1021, pp. 4033–4042, 2014.

[8] S. Hosseinnezhad, "Investigating effect of amine based additives on asphalt rubber rheological properties," vol. 3, no. 138, pp. 921–931, 2016.

[9] Q. Zhang, K. De Oliveira Vigier, S. Royer, and F. Jerome, "Deep eutectic solvents: syntheses, properties and applications," *Chemical Society Reviews*, vol. 41, pp. 7108-7146, 2012.

[10] C. Acids, C. Florindo, and A. M. Fernandes, "Insights into the Synthesis and Properties of Deep Eutectic Solvents Based on Cholinium Chloride," *ACS Sustainable Chemistry* Engineering, vol. 2, pp. 2416-2425, 2014.

[11] K. Shahbaz, F. S. Mjalli, M. A. Hashim, and I. M. AlNashef, "Using Deep Eutectic Solvents Based on Methyl Triphenyl Phosphunium Bromide for the Removal of Glycerol from Palm-Oil-Based Biodiesel," *Energy & Fuels*, vol. 25, pp. 2671-2678, 2014/04/20.

[12] A. I. Isayev, S. P. Yushanov, S.-H. Kim, and V. Y. Levin, "Ultrasonic Devulcanization of Waste Rubbers: Experimentation and modeling," *Rheol. Acta*, vol. 35, no. 6, pp. 616–630, 1996.

[13] K. Shahbaz, F. S. Mjalli, M. A. Hashim, and I. M. AlNashef, "Eutectic solvents for the removal of residual palm oil-based biodiesel catalyst," Separation and Purification Technology, vol. 81, pp. 216-222, 2011.

[14] S. Poyraz, Z. Liu, Y. Liu, and X. Zhang, "Devulcanization of Scrap Ground Tire Rubber and Successive Carbon Nanotube Growth by Microwave Irradiation," Curr. Org. Chem., vol. 17, no. 20, pp. 2243–2248, 2013.

[15] F. K. Aksaray, "Characterization of styrene butadiene rubber and microwave devulcanized ground tire rubber composites Characterization of styrene butadiene rubber and microwave devulcanized ground tire rubber composites," vol. 34, no. 4, pp. 543-554, 2014.

[16] F. S. Ghareh, K. Shahbaz, F. S. Mjalli, M. A. Hashim, and I. M. Alnashef, "Zinc (II) chloride-based deep eutectic solvents for application as electrolytes : Preparation and characterization," vol. 204, pp. 76–83, 2015.

[17] K. Shahbaz, F. S. Mjalli, M. A. Hashim, and I. M. Alnashef, "Fluid Phase Equilibria Prediction of the surface tension of deep eutectic solvents," *Fluid Phase Equilib.*, vol. 319, pp. 48–54, 2012.

[18] F. Endres, D. McFariane and A. Abbot, *Electrodeposition from Ionic Liquid*, Germany: Wiley-VCH, 2008.

[19] G. Garc, S. Aparicio, R. Ullah, and M. Atilhan, "Deep Eutectic Solvents : Physicochemical Properties and Gas Separation Applications," 2015.

[20] F. Karabork, E. Pehlivan, and A. Akdemir, "Characterization of styrene butadiene rubber and microwave devulcanized ground tire rubber composites," vol. 34, no. 6, pp. 543–554, 2014.

[21] S. Rooj, G. C. Basak, P. K. Maji, and A. K. Bhowmick, "New Route for Devulcanization of Natural Rubber and the Properties of Devulcanized Rubber," 2011.

[22] F. Danielli, B. De Sousa, C. H. Scuracchio, and C. De Engenharia, "The Role of Carbon Black on Devulcanization of Natural Rubber by Microwaves," vol. 18, no. 4, pp. 791–797, 2015.

[23] S. Rodsuk, S. Ritsuar, and K. Wattanakul, "Characterization the Effect of Disulfide Compound on the Devulcanization of Thermoplastic Vulcanizate," vol. 245, pp. 240–245, 2012.

Effect of Torrefaction and Pyrolysis on the Electrochemical Reaction Mechanisms in Direct Carbon Fuel Cells

Donald Thong Weng Hung [1],. Veena Doshi [2]
School of Engineering, Taylor's University, Malaysia

Veenaadoshi.arunkumardoshi@taylors.edu.my

Abstract
Direct carbon fuel cells (DCFC) is a device capable of producing high electrical efficiency by converting chemical energy stored in biomass at high temperatures. To justify that cause, this research will attempt the thermal treatments of biomass to improve the performance of DCFC. Thermal treatment methods applied such as pyrolysis and torrefaction can enhance carbon compositions and energy densities of biomass by conversion into biochar. This research analyses the operation of a DCFC powered by thermally treated sustainable oil palm mesocarp fibre. This fibre is a biomass waste abundant from oil palm processing. This research will investigate the performance of DCFC fuelled by torrefied oil palm mesocarp fibre at 230,260 and 290°C and samples undergoing pyrolysis at 650 °C. Treated biochar will be analysed by analytical methods such as Thermogravimetric analysis, Fourier-transform (FTIR) analysis and x-ray diffraction (XRD) analysis. This is in order to obtain the physicochemical characteristics of the treated biomass. The performance of the operational fuel cell will be evaluated via peak power density and impedance demonstrations using electrochemical impedance spectroscopy and open circuit testing. DCFC fuelled by torrefied biomass is estimated to show better peak power densities compared to biomass treated with pyrolysis. This would be the cause of higher carbon constituents that remain after torrefaction treatment as compared to pyrolysis. Biochar derived from torrefied biomass at 260 °C can highly be suggested for storage purposes while preserving fuel properties in a DCFC. Further study into fuel cell configurations should can be done to simulate a more commercialized DCFC operation.

Keywords: Direct Carbon Fuel Cells, Torrefaction, Oil Palm Waste, Mesocarp Fibre

1.0 Introduction

Consumption of electrical energy from recent history has shown an increase in demand for electrical energy with the incremental human population. However, energy generation has begun to see gradual depletion of non-renewable fuels with developing countries such as Malaysia draw 93% of its energy consumption from non-renewable methods. These methods are non-sustainable with the depletion of the natural gas reserves in addition to emission of greenhouse gases from the power generation [1]. Leveraging the energy requirement by new technologies and innovations with a sustainable mind-set will in turn provide a stable economic, socialistic and environmental platform in the future. Fuel cell technology is among the more beneficiary in terms of carbon emission when commissioning modern sustainable energy generation. The technology itself has pioneered energy generation with the credibility to have electrical efficiencies of above 80% in addition to be powered by waste compounds [2]. Key business drivers are keen on the chemical reactivity potential of fuel cells to sustain low emission methods of generating energy with high fuel efficiency. Inadvertently this seeks potential of using a form of renewable waste source as fuel to power the fuel cells.

Direct Carbon Fuel Cells (DCFC) are a form of newly improvised fuel cells that is fuelled by chemical decomposition of carbon compounds. This shows high potential in applying waste forms of organic material from industrial processing and commercial bio-degradable waste. The high fuel efficiency of the technology is sometimes applied with non-renewable carbon compounds such as coal which is often set as a benchmark to be followed by renewable bio-energy fuels such as biomass [3]. DCFC do come with a compromise of operating at temperatures between 600 °C to 900 °C in order to successfully perform the carbon oxidation and reduction respectively shown in Equations 1 and 2[4]. However, commercial applications of fuel cells are reliant on none renewable sources such as coal.

Anode Reaction: $C + 2O^{2-} \rightarrow CO_2 + 4e^-$ (1)
Cathode Reaction: $O_2 + 4e^- \rightarrow 2O^{2-}$ (2)

Henceforth, one of the more abundantly generated forms of biomass in the South East Asian region is palm oil. Malaysia which leads the production and exportation of palm oil has conducted several sustainable implementations for the prolonged supply of palm oil production. This includes the formation of the Roundtable of Sustainable Palm Oil assigned in monitoring the developing 4.3 million hectares committed to palm oil in Malaysia [5]. Thus, palm oil waste derived from commercial processing can then be credible for use as fuels for DCFC. Palm oil waste are mainly constituent of lignocellulosic biomass that shows high energy densities required for fuel cell operations. Palm oil mesocarp fibre (PMF) is the likeliest candidate for fuelling DCFC chemical operations as it shows high calorific values and is the least utilised palm oil derived waste due to high moisture issues [6].

Prior to being utilized as the fuel source for DCFC, the lignocellulosic biomass would have to be subjected to thermal treatment via torrefaction and later converted into biochar with pyrolysis. Torrefaction was introduced as a thermal treatment originally to reduce moisture for logistic and pelletization purposes [7]. However, the lower held oxygen to carbon ratios from torrefaction can improve gasification to potentially increase the performance in DCFC [8]. Pyrolysis is proven to remove

volatile matter composition and ash metal content of the biomass while improving surface areas of biomass [9]. No previous publications attempting the use of thermally treated palm oil mesocarp fibre biochar as fuel for DCFC. This was the investigated criteria of the research.

2.0 Methodology

This research composes the effect of torrefaction and pyrolysis on Mesocarp Fibre to be used as fuel for DCFC. The fuel is characterized by the torrefaction temperatures pre-pyrolysis (#A), direct torrefaction of sample (#B) and direct pyrolysis of sample (#C).

2.1 Thermal Treatment

The mesocarp fibre was collected from post production of palm oi mill processing from Seri Ulu Langat plant located in Dengkil. 2kg of the raw fibre was later sundried for 6 hours to remove lingering odours. The biomass was then subjected to oven drying at 105 °C for 24 hours to evaporate unbound moisture. The biomass was then mechanically grinded and sieved to a particle under 5 mm.

The mesocarp fibre was then torrefied at 230, 260 and 290 °C for 1 hour under low oxygen conditions. The torrefaction was performed in a sealed cylindrical muffle furnace with 15 g of mesocarp fibre loaded. Nitrogen gas (99%) was flown into the furnace at 100 ml/min throughout the period of ramping and torrefaction. The furnace was set to ramp at 10 °C/min until desired temperatures were reached. Torrefied samples were then stored under standard room conditions of 25 °C with a relative humidity of 84% for a duration of 7 days.

2.1.1 Biochar Preparation

After the storage duration, one sample of raw mesocarp fibre of 15 g and the remaining torrefied biomass of their respective temperatures will undergo pyrolysis at 650 °C with a ramping rate of 10 °C/min to produce the biochar. Similarly, pyrolysis was performed with low oxygen conditions with high purity nitrogen gas (99%) channelled into the furnace volume at 100 ml/min.

2.2 Fuel Characterisation and Analysis

2.2.1 Thermogravimetric Analysis

Thermogravimetric analysis was performed to analyse the mass loss of the respective samples as the temperature was increased. This analysis was carried out with the Perkin Elmer TGA 8000 model. The biomass samples of 10 mg was heated from 30 °C to 950 °C with a ramping rate of 10 °C/min. High purity nitrogen (99%) was

channelled into the analysis chamber at 20 ml/min during this period. The sample was then allowed to dwell for 7 minutes at 950 °C with a 20 ml/min flowrate of oxygen.

2.2.2 Fourier-Transform-Infra-Red

The apparatus utilised for performing FTIR analysis was the Spectrum 100 issued by Perkin Elmer. The scans is carried out at 16 scans at a resolution of 4 cm^{-1} with a wave number range of 400 cm^{-1} – 4000 cm^{-1}. Given the biomass samples are in a powder like substance, the testing was performed with potassium bromide pelletization, KBr. A ratio of 4 to 1 was used for KBr to sample and relatively 20 mg of KBr was used.

2.2.3 X-Ray Diffraction

X-Ray Diffraction is performed to show amorphous structural differences for PMF after being subjected to torrefaction and pyrolysis. The analysis was done externally by faculty of Monash University, Selangor. Scans was collected for 2θ from 10° to 90° with a step size of 0.05 and 15 seconds per step.

2.3 Direct Carbon Fuel Cell Performance

Compressed button cells were used as the reaction medium for the DCFC operations with the high temperature conditions. The composition and configuration of the button cell was comprised of Nickel-yttria-stabilized zirconia (Ni-YSZ), lanthanum strontium manganite (LSM), and Yttria-stabilized zirconia (YSZ) for the anode, electrolyte and cathode respectively. The performance of the DCFC was analysed with a potentiostat model Gamry Interface 1000 with two electrode configuration. The positive anode end is connected to the working (W) and working sense (WS) while the negative cathode end is connected to the reference (R) and counter (c) electrodes.

The button cell is supported on perforated ceramic plate sandwiched between two equivalent diameter ceramic cylinders to house the cell in a sealed volume. PMF derived biochar of 0.1 mg was loaded onto an exposed button cell surface area of 1.743 cm^2 as the fuel. The furnace was then programmed to ramp at 10 °C/min until the desired temperature of 800 °C before remaining at that temperature for 2 hours. While the temperature is increasing, nitrogen was flowing into the anode and cathode ends of the DCFC at 200 and 600 ml/min respectively. The gas supply to the cathode end was switched with oxygenated air before 800 °C is reached with a flowrate of 600 ml/min. Open circuit voltage and peak power densities are determined a linear sweep voltammetry method.

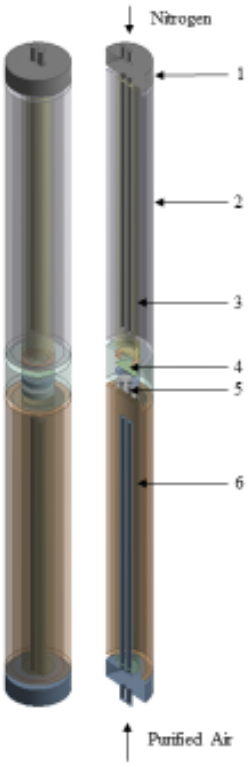


Figure 1. Isometric and cross section view of DCFC.1: flange, 2: ceramic cylinder, 3: anode wiring, 4: button cell, 5: button cell platform, 6: cathode wiring

3.0 Results and Discussions

3.1 Fuel Analysis

3.1.1 Mass Analysis

The overall mass characterizations of the biomass through stages of torrefaction and pyrolysis is shown in Table 3.1. General mass yield of the mesocarp fibre samples demonstrates a detrimental trend with a higher torrefaction temperature. The decrease of mass is credited from the release of moisture and thermal decomposition to form volatile matter. The higher mass loss seen from temperatures of 260 and 290 °C show more devolatisation of hemi-cellulose compared mass losses at 230 °C attributed mainly from moisture. The decomposition rate of the PMF was also seen to have increased at the temperature of 290 °C attributing to complete devolatisation of cellulose composition. This is in agreement with findings from other research works [10][11]. The overall mass yields between the ranges of 28 wt% to 31wt% are representative of rapid decomposition of cellulose. This indicates the high cellulose composition nature of PMF[10]. Therefore, torrefaction can improve the logistic and storage capabilities of PMF before being converted into biochar.

Table 1: Mass characterization for thermally treated PMF.

Biomass Characteristic	Initial Mass (g)	Final Mass (g)	Mass Yield (wt %)	Pyrolysis at 650 °C			Overall Yield (wt %)
				Initial Mass (g)	Final Mass (g)	Mass Yield (wt %)	
Torrefied at 230 °C	15.004	12.736	86.166	13.030	4.260	32.693	28.390
Torrefied at 260 °C	15.003	10.708	73.490	11.591	4.484	38.685	29.888
Torrefied at 290 °C	15.000	8.429	57.204	9.023	4.411	48.883	30.751
Raw				4.342	10.635	29.135	29.135

3.1.2 Thermogravimetric Analysis

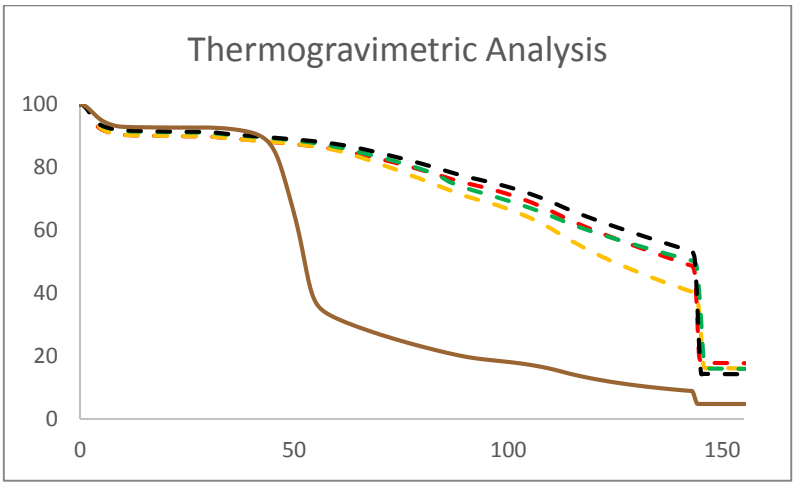
The TGA curves of thermally treated PMF via torrefaction and pyrolysis are shown in Figures 3.1(a) and 3.1(b). It can be seen that the pyrolysis process heavily influences the mass loss trend of the biomass. All curves show an initial weight lost step contributing to the moisture content of the sample. This is compared further in detail in Table 3.1. The moisture content for samples that have undergone pyrolysis demonstrates a moisture content that is above 9% with raw mesocarp fibre having a moisture content of 7.952%. The directly torrefied sample at 260 °C shows the lowest moisture content at 5.536%. This demonstrates that torrefaction is a susceptible method for storage and palletization of Mesocarp Fibre similar to other works [7].

The shallow degradation of the post-pyrolysis curves after 150 °C demonstrates the lower volatile matter composition and would suggest a higher percentage of lignin in the biomass. This can be supported by the tendency of hemicellulose to deconstruct at a lower temperature due to a short chain polymer structure [12]. Whereas lignin is credited with a more complex chemical composition that enables thermal stability at higher temperatures. In accordance with other works, biomass samples rich in lignin generically demonstrates gradual mass loss past 300 °C followed by an observable mass loss at 750 °C representing the decomposition of lignin [13]. In addition, the yields of char from the analysis is evidence of high lignin biomass [14].

Mesocarp Fibre torrefied at 260 °C and raw mesocarp fibre can be seen undergoing rapid devolatisation respectively at 280 °C and 240 °C. The rapid devolatisation can be analysed as the fast decomposition and liberation of hemicellulose and cellulose evident by the heavy mass drop of both samples. This relates to a respective mass drop of 70.011% and 52.910% for raw and torrefied mesocarp fibre at 260 °C. Observably, this temperature is where the biomass sample is reduced to below 50% of original weight. This is supported by typical biomass composing of 80 wt% volatile fraction with the remaining 20 wt% representing solid carbonaceous residue [15]. This corresponds to a lower fixed carbon weight composition for torrefied and raw mesocarp fibre.

Table 2. Moisture and volatile matter content of mesocarp fibre torrefied at 260 °C (260A) and 290 °C (290A) before pyrolysis at 650 °C, directly torrefied at 260 °C (260B) and directly pyrolysed at 650 °C.

Biomass Sample	Moisture Content (%)	Volatile Matter Content (%)
Raw	7.952	70.011
260A	9.036	4.745
290A	8.519	4.287
260B	5.536	52.910
650C	9.116	4.001



Figures 2. TGA curve against time for PMF; Raw (brown), direct torrefaction at 650 °C (black), direct pyrolysis (black), torrefied at 230 °C (red), 260 °C (orange) and 290 °C (green) before pyrolysis.

Comparatively, the temperature of torrefaction shows differences only on the fixed carbon and ash composition noticed by the gradients of mass drop. This ranks biomass that is directly pyrolysed to show a lesser fixed carbon percentage followed by

the sample thermally treated at 290 °C and 260 °C. This is similarly observed in research works whereby higher torrefaction temperatures can prematurely decompose lignin compositions in biomass [10]. Hence, torrefied biomass exhibit good thermal stability which can support their performance in DCFC.

3.1.3 Fourier-Transform-Infra-Red

The IR spectra for the mesocarp fibre exposed to thermal treatment via torrefaction and pyrolysis is shown in Figure 3.2. The spectra of the biomass samples shows distinctive peaks that corresponds to cellulose, hemi-cellulose and lignin compositions in biomass.

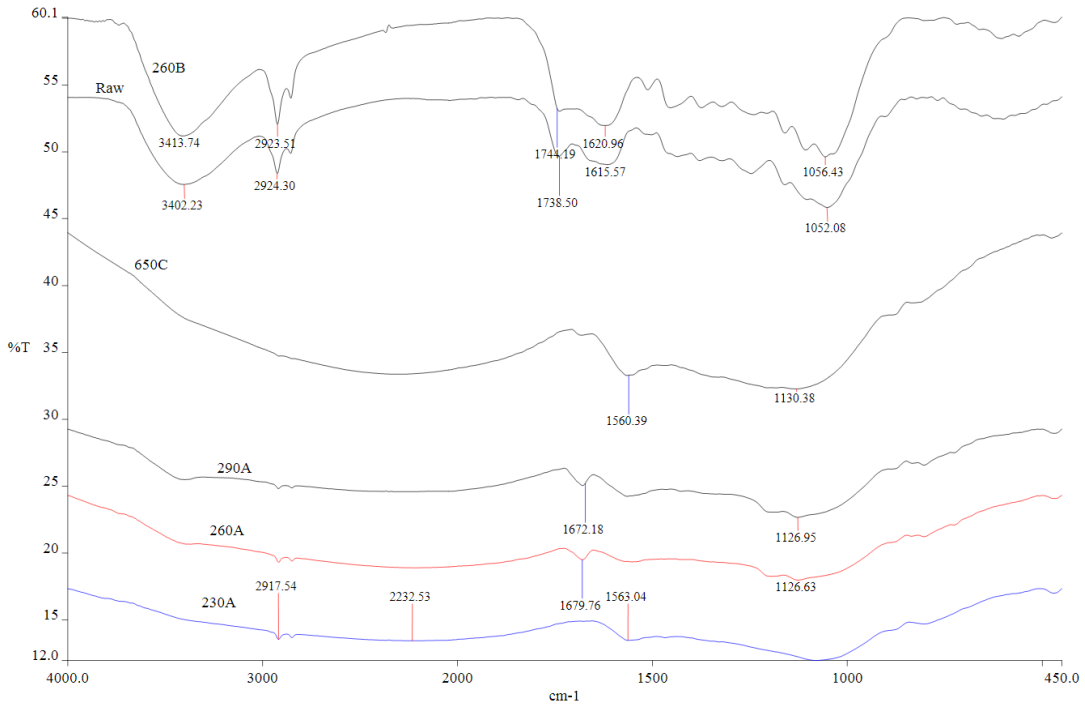


Figure 3. FTIR for PMF; raw, direct torrefaction (260B), direct pyrolysis (650C), torrefied at 260 °C (260A) and 290 °C (290A) before pyrolysis.

As indicated in Figure 3.2, Mesocarp Fibre that has not undergone pyrolysis exhibit peaks around the 3400 cm^{-1} which demonstrates O-H stretching common in phenolic compounds. This is trait commonly associated with lignin rich biomass [13]. Peaks around the band of 2900 cm^{-1} indicate C-H stretching in the compound. These peaks attributes to the alkane and alkene functional groups associated with presence of cellulose. Additionally, this shows successfully decomposition of lignin and cellulose via pyrolysis of the biomass.

Peaks shown between the wavelengths of 1560 cm^{-1} and 1620 corresponds to C=O axial deformation that indicates the presence of various acids, aldehydes, esters and ketones related to the presence of aromatic ring models. This observation is normally associated with presence of hemicellulose and cellulose. Peaks observed in the range of 1130 cm^{-1} and 1500 cm^{-1} are assigned as O-H deformation and C-O stretching of oxygenated compounds such as alcohols, phenols and ethers. The aromatic C-O stretching of methoxyl and phenyl propane structure and aromatic ring vibration

in lignin correspond to the peaks that occur between 1500 cm^{-1} and 1000 cm^{-1} indicating degradation of lignin. This supports the decomposition of lignin during pyrolysis of the mesocarp fibre.

3.1.4 X- Ray Diffraction

The XRD patterns for the thermally treated PMF are presented in Figure 4. High intensity peaks detected at 15 θ° for the biomass torrefied at 260 °C. This peak phenomenon is remained after the sample is subjected to pyrolysis at 650 °C which is representative of cellulosic material such as rubber wood sawdust [9].

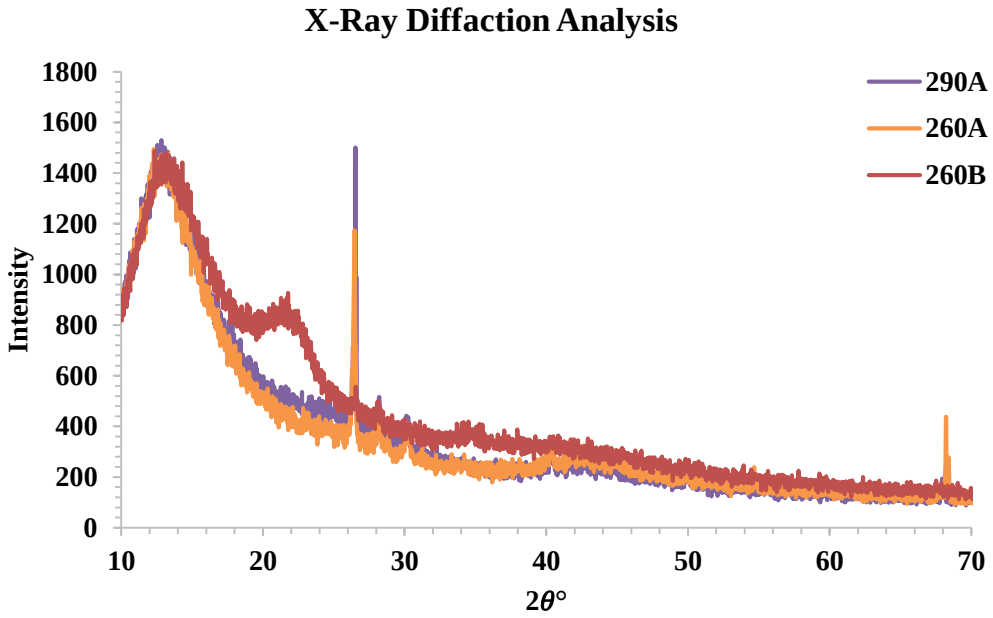


Figure 4. XRD analysis of PMF torrefied at 260 °C (orange), biochar torrefied at 260 °C (green) and 290 °C (yellow) before pyrolysis at 650 °C (260A) and

PMF torrefied at 260 °C also demonstrate composition of cellulose from broad peak patterns at 21 θ°. This peak is shifted to the right to 26 θ° after pyrolysis indicating a loss of crystal structure in cellulose attributed to a devolatisation of cellulose composition. This is in accord with research of pinewood heat treatment [16]. The peak transformed becoming narrower indicating possible formation and evolution of turbostratic crystallites [17].

Non-discriminative peaks detected at 68 θ° show possibility of ash formation from the pyrolysis process. However, the better degree of graphitization shown for treating PMF with pyrolysis can support performances in DCFC [18].

3.2 Fuel Performance in DCFC system

The performance of the PMF subjugated to different methods of thermal treating can be seen in Figure 3.3. Thermal treatment via torrefaction and pyrolysis show significance from one another based on their Open circuit voltage (OCV) and peak power density. The highest OCV of 0.82 obtained was from the biochar torrefied at 230 °C. Lowest observed OCV of 0.74 was detected from the biomass subjected to torrefaction at 260 °C before being pyrolysed at 650 °C. The range of generated OCV values are in accord with research concerning activated carbon and waste coffee grounds [3]. This supports credibility for the PMF to be used as a fuel when compared to other forms of biomass. The high OCV value is possibly credited to the presence of CO originated from decomposition of ash components containing oxygen or alternatively reaction with CO_2 subsequently released from the fuel cell reaction. CO has a higher tendency to form in lignocellulosic biomass where substances of impurities in the form of Ca, K and Fe could catalyse the formation [19]. This can be observed from works of torrefied PMF shown in Table 4. The lowest shown OCV was demonstrated by PMF torrefied at 260 °C which could be credited to the targeted decomposition of biomass constituents for impurity and moisture reductions. The more rapid linear decrease of the voltage for the PMF is likely credited to the ash formation degrading the performance of the DCFC for temperatures of 230 °C.

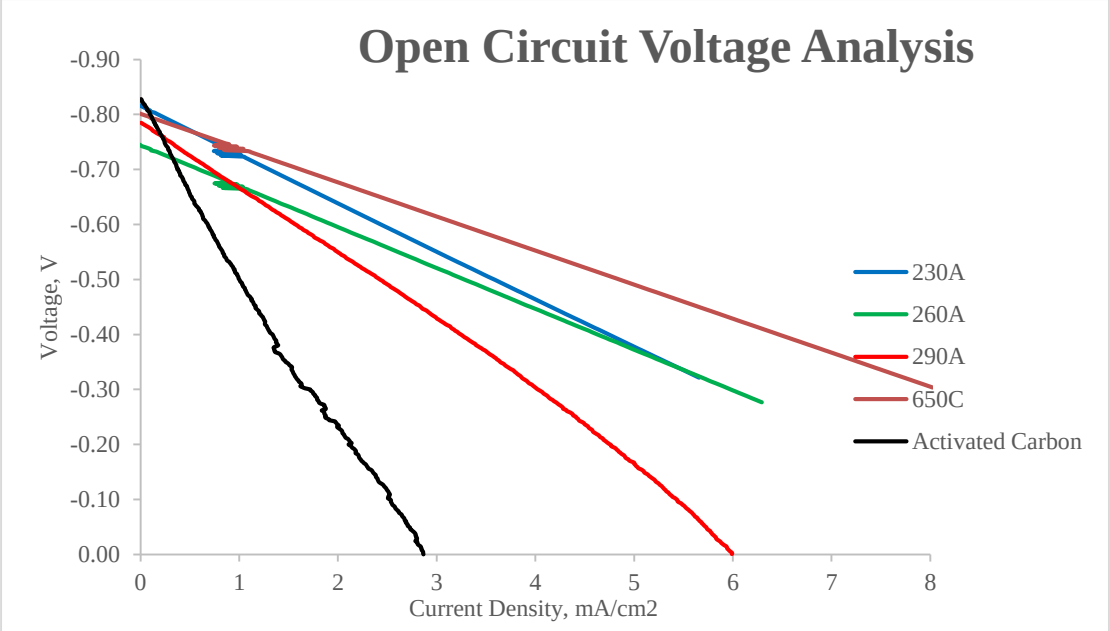


Figure 5. Open Circuit Voltage for PMF biochar torrefied at 230 °C (red), 260 °C (green) and 290 °C (blue) before pyrolysis, activated carbon (black).

Table 3. Ultimate analysis of PMF thermally treated via torrefaction.

Temperature	Ultimate Analysis (Weight %)			Source
	C	H	O	
260	50.50	4.27	43.59	[10]
260	57.08	4.85	14.63	[7]
250	47.70	5.20	40.18	[20]

The highest peak power densities obtained was 2.5 mW/cm^2 from the directly pyrolysed PMF at 650 °C. This can be credited to a more amorphous carbon structure, better thermal reactivity and higher compositions of impurities [21]. Torrefaction temperatures of 230 °C and 260 °C showed similar peak power densities. This follows the original intent to reduce hemi-cellulose and cellulose components. Targeted devolatisation temperatures from torrefaction thermal treating ultimately provided more thermal stability that demote DCFC performance. The highest torrefaction temperature of 290 °C targeted to reduce lignin components in the biomass ultimately provided the thermal stability which demonstrates its low peak power density. This shows similarity for low current density operations of DCFC with woody biomass crediting low current density performance to surface functional groups [22].

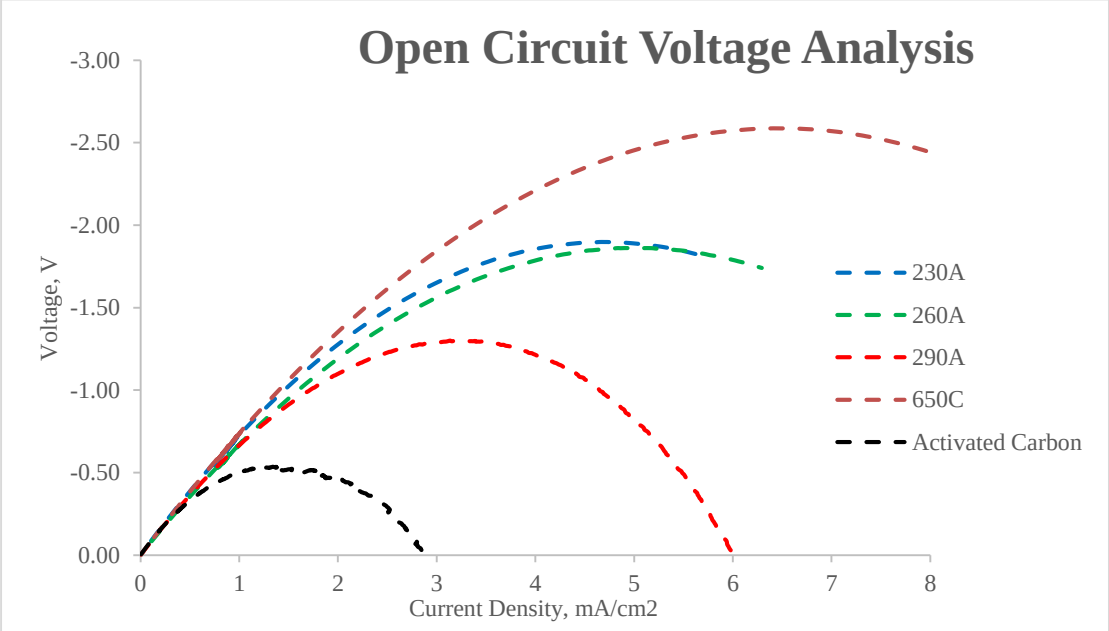


Figure 6. Peak Power Density for PMF biochar torrefied at 230 °C (red), 260 °C (green) and 290 °C (blue) before pyrolysis, activated carbon (black).

4.0 Conclusions

Thermally treated mesocarp fibre was utilized as a fuel in DCFC operations in this work. Thermal treatments were done using selective temperatures targeted for volatile matter decomposition. The findings of this research show that torrefaction of mesocarp fibre that show release of volatiles can improve the carbon composition of the biomass from fixed carbon. Torrefaction of PMF with a temperature of 290 °C can cause lignin degradation that ultimately increase thermal stability of the biomass.

The capability of the fuel cell performance for low current density regions favoured direct pyrolysis of mesocarp fibre. Subjecting biomass to torrefaction temperatures that are too high ultimately jeopardizes its performance in a DCFC credited from the loss of surface functional groups and increased ash. If the biomass were to be torrefied for logistic and storage purposes, a temperature of 260 °C would be recommended as it shows a lesser potential for ash generation in DCFC. In addition, the peak power density and OCV of the biochar previously torrefied at 260 °C shows similar performances to those performed at minor torrefaction temperatures.

Acknowledgements

Sincere gratitude and thanks are well-deserved from Dr. Wong Wai Yin, Ms. Nida Jafri, Ms. Lithnes and research partners Elven Cho and Fabian Goh for their unselfish supervision, mentoring and guidance over the course of this research project.

5.0 References

[1] A. H. Shamsuddin, "Development of Renewable Energy in Malaysia-Strategic Initiatives for Carbon Reduction in the Power Generation Sector," *Procedia Eng.*, vol. 49, no. 0, pp. 384–391, 2012.

[2] O. Z. Sharaf and M. F. Orhan, "An overview of fuel cell technology: Fundamentals and applications," *Renew. Sustain. Energy Rev.*, vol. 32, pp. 810–853, 2014.

[3] H. Jang, J. D. Ocon, S. Lee, J. K. Lee, and J. Lee, "Direct power generation from waste coffee grounds in a biomass fuel cell," *J. Power Sources*, vol. 296, pp. 433–439, 2015.

[4] S. Giddey, S. P. S. Badwal, A. Kulkarni, and C. Munnings, "A comprehensive review of direct carbon fuel cell technology," *Prog. Energy Combust. Sci.*, vol. 38, no. 3, pp. 360–399, 2012.

[5] K. T. Tan, K. T. Lee, A. R. Mohamed, and S. Bhatia, "Palm oil: Addressing issues and towards sustainable development," *Renew. Sustain. Energy Rev.*, vol. 13, no. 2, pp. 420–427, 2009.

[6] S. S. Idris, N. A. Rahman, and K. Ismail, "Combustion characteristics of Malaysian oil palm biomass, sub-bituminous coal and their respective blends via thermogravimetric analysis (TGA)," *Bioresour. Technol.*, vol. 123, pp. 581–591, 2012.

[7] B. I. Na, Y. H. Kim, W. S. Lim, S. M. Lee, H. W. Lee, and J. W. Lee, "Torrefaction of oil palm mesocarp fiber and their effect on pelletizing," *Biomass and Bioenergy*, vol. 52, pp. 159–165, 2013.

[8] B. Sen Chiou, D. Valenzuela-Medina, C. Bilbao-Sainz, A. K. Klamczynski, R. J. Avena-Bustillos, R. R. Milczarek, W. X. Du, G. M. Glenn, and W. J. Orts, "Torrefaction of pomaces and nut shells," *Bioresour. Technol.*, vol. 177, pp. 58–65, 2015.

[9] A. Shaaban, S. M. Se, M. F. Dimin, J. M. Juoi, M. H. Mohd Husin, and N. M. M. Mitan, "Influence of heating temperature and holding time on biochars derived from rubber wood sawdust via slow pyrolysis," *J. Anal. Appl. Pyrolysis*, vol. 107, pp. 31–39, 2014.

[10] K. M. Sabil, M. A. Aziz, B. Lal, and Y. Uemura, "Effects of torrefaction on the physiochemical properties of oil palm empty fruit bunches, mesocarp fiber and kernel shell," *Biomass and Bioenergy*, vol. 56, pp. 351–360, 2013.

[11] S. W. Park, C. H. Jang, K. R. Baek, and J. K. Yang, "Torrefaction and low-temperature carbonization of woody biomass: Evaluation of fuel characteristics of the products," *Energy*, vol. 45, no. 1, pp. 676–685, 2012.

[12] P. K. Kanaujia, Y. K. Sharma, M. O. Garg, D. Tripathi, and R. Singh, "Review of analytical strategies in the production and upgrading of bio-oils derived from lignocellulosic biomass," *J. Anal. Appl. Pyrolysis*, vol. 105, pp. 55–74, 2014.

[13] C. Quan, N. Gao, and Q. Song, "Pyrolysis of biomass components in a TGA and a fixed-bed reactor: Thermochemical behaviors, kinetics, and product characterization," *J. Anal. Appl. Pyrolysis*, vol. 121, pp. 84–92, 2016.

[14] C. Q. Dong, Z. F. Zhang, Q. Lu, and Y. P. Yang, "Characteristics and mechanism study of analytical fast pyrolysis of poplar wood," *Energy Convers. Manag.*, vol. 57, pp. 49–59, 2012.

[15] S. Abdullah, S. Yusup, M. Ahmad, a Ramli, and L. Ismail, "Thermogravimetry Study on Pyrolysis of Various Lignocellulosic Biomass for Potential Hydrogen Production," *Int. J. Chem. Biol. Eng.*, vol. 3, no. 3, pp. 137–141, 2010.

[16] Z. Wang, J. Cao, and J. Wang, "Pyrolytic characteristics of pine wood in a slowly heating and gas sweeping fixed-bed reactor," *J. Anal. Appl. Pyrolysis*, vol. 84, no. 2, pp. 179–184, 2009.

[17] M. Keiluweit, P. S. Nico, M. Johnson, and M. Kleber, "Dynamic molecular structure of plant biomass-derived black carbon (biochar)," *Environ. Sci. Technol.*, vol. 44, no. 4, pp. 1247–1253, 2010.

[18] N. J. Cherepy, R. Krueger, K. J. Fiet, a F. Jankowski, and J. F. Cooper, "Direct conversion of carbon fuels in a molten carbonate fuel cell," *J. Electrochem. Soc.*, vol. 152, pp. A80–A87, 2005.

[19] C. Munnings, A. Kulkarni, S. Giddey, and S. P. S. Badwal, "Biomass to power conversion in a direct carbon fuel cell," *Int. J. Hydrogen Energy*, vol. 39, no. 23, pp. 12377–12385, 2014.

[20] Y. Uemura, W. N. Omar, T. Tsutsui, and S. B. Yusup, "Torrefaction of oil palm wastes," *Fuel*, vol. 90, no. 8, pp. 2585–2591, 2011.

[21] W. Hao and Y. Mi, "Evaluation of waste paper as a source of carbon fuel for hybrid direct carbon fuel cells," *Energy*, vol. 107, pp. 122–130, 2016.

[22] S. Y. Ahn, S. Y. Eom, Y. H. Rhie, Y. M. Sung, C. E. Moon, G. M. Choi, and D. J. Kim, "Utilization of wood biomass char in a direct carbon fuel cell (DCFC) system," *Appl. Energy*, vol. 105, pp. 207–216, 2013.

eureca 2016 – Conference Paper
Paper Number 2EE01

Application of Image Processing for Password Protection using the Eye

Chong Chen Yow, Chew Wei Jen
Electrical & Electronic Engineering
Taylor's University

Ccyoyo92@gmail.com

Abstract

The purpose of the research of this self developed security system using eye gaze tracking as password input is to improve the level of security without lowering the usability or the ergonomics aspect of the security system. This eye gaze security system uses MATLAB software with Image Processing an Computer Vision add-on installed to develop the coding and user interface. This project employs Viola-Jones method and Hough transform algorithms for the development of the detection system. The level of security include the protection against a few notable technique such as shoulder surfing and brute force hacking. The process testing and analyzing will involve multiple testing human personal to prove the usability and security protection level. The anticipated outcome of this program is the identification of the eye gaze tracking security system is the more viable and reliable option of security system compare to existing security system. The data and information of the design process and testing phase can be used for future development and improvement. The eye position detection of the project currently were capable to achieve a detection rate of 86% and the success rate of able to track changes of gaze position is 70% under stable light. A GUI was created for the project for user friendliness.

Keywords: **e**ye gaze tracking, security, MATLAB, Image processing.

1. Introduction

Encryption has been introduced since ancient time to encode messages or information where only authorized parties able to access the encrypted messages or information. It is important that the encrypted will not fall on to unauthorized parties to prevent losses such as financial information or military information. Therefore, the importance of a strong yet simple security system is very crucial for the current century where the flow amount of messages and information are enormous[1].

As the current technologies grow and shifting towards robotic and software based technologies, the demand of a new and reliable cyber security is always growing due to the active crackdown of the older security system. The main challenge is to design a cyber security system that is able to eliminate the possibility of the most simple form of "hacking" such as shoulder surfing where a person obtaining password by shoulder peeking the user without his/her knowledge.

Currently, code/text input methods are the most vulnerable against shoulder surfing, the latest approaches to reduce this attack technique is using various graphical or advanced method of password input to replace the previous mention code input method. These graphical are mostly effective but always in the cost of the usability of the system which often require users to use security token or additional steps to take prevention of shoulder-surfing.[2] In addition, the more sophisticated graphical method such as iris scanning method can be very costly compare to normal password authentication methods.

In this paper, a new graphical method for password input authentication is proposed. This proposed method operate by using a camera device to capture a live feed of the face of the user and obtaining frames which will be processed by the computer. The proposed method can separate into three stages which started with eye detection where the position of the user's eyes are detected, tracked and bounded by a box. The processing stage will crop out the image of an user's eye bounded in the box previously mentioned which will be processed to determine the position of the eye gaze. Lastly, the authentication stage will take in the inputs from the user and decide whether if the password is correct before authentication.

The proposed system in this project uses MATLAB software 2014b to code the detection, recognition of gaze position and the authentication system due to MATLAB software has a constant updated resources and libraries to perform complex computations. During the detection phase, the software uses Viola-Jones algorithms based program to detect the feature of a human face with efficiency and reasonable accuracy. In the processing phase where the program undergo the process to recognize the position of the gaze, it uses Hough Transform algorithm based computation to process the image to find the iris.

This paper consists of 5 sections where section 1 is the introduction of the topic. Section 2 contains the type of existing password authentication methods to tackle shoulder surfing attacks. Section 3 presents the design concept of the new graphical method and Section 4 will show the discussion of the proposed method. Lastly, Section 5 is the conclusion of this paper.

2.1 Introduction of Existing Authentication System to counter Shoulder surfing

Authentication System is a system process of authentication and authorization where the system receive credentials provided by users are compared to the documents regarding the information of the authorized users that are stored in the database and make the decision of authorization for access depending to the information input. Hacking is a method developed to counteract or bypass the process of an authentication system and always been a major issue in cyber security industry due to the advancement of hacking methods are always nearly on par with the most advanced security system. Shoulder surfing is one of the simplest and oldest method of hacking.

2.2 Biometric Based Authentication

Bio-metric scanning system is an advanced type of security system where the system uses human's unique body parts such as retina and fingerprint as process of authentication and authorization. Both of these mentioned securities system are considered as high ended and the most secure type of authentication methods this is due to human body parts contain countless of unique patterns such as the blood vessels in the retina which is obtained through a high definition camera and convert into a set of unique data then allowing the user to use them as a password and since it is unique, it is one of the most secure way to set a password for authentication for some high value information or items. It is proven to be safe from both shoulder-surfing attacks as it is almost impossible to duplicate the pattern without the means of advanced techniques and the false acceptance rate where the chances of two or more person having the same bio-metric data in the world by coincidence is very low [3] as shown in the figure 2 below.

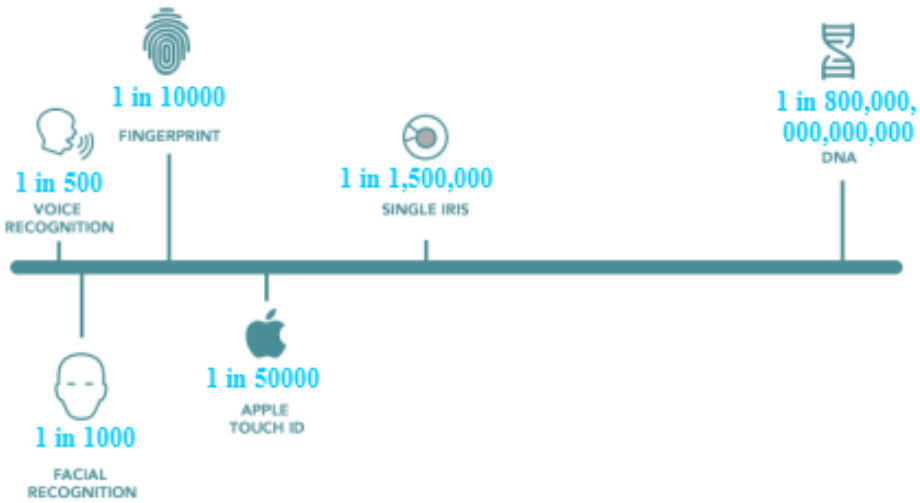


Figure 1: The probability of bio-metric false acceptance rate. [3]

2.2.1 Fingerprints

Finger prints are the "friction skin" at the tip of fingers where the ridges of the rough skin have a definite pattern for each human being which made them unique throughout a human lifetime.[3] Finger prints of a human being are one of the most reliable and rather common high level security system in current technology which

the latest common application is on smart-phones as a fast authentication system. The authentication system of fingerprints can be separate into manual verification and advanced verification system using optical sensors. Manual verification is processed by having an individual smudge his/her fingertip with ink which he/her then stamping their fingerprints onto a piece of paper. The fingerprints will later be checked by administrator manually to confirm the similarities which is time consuming and chances of human error is very high. On the other hand, advanced system which used optical sensors and computers to process the feature matching process shown in Figure 2 and 3 will significantly improve the process time, accuracy and able to completely eliminate the chance of shoulder surfing attack but in the expense of high equipment and maintenance cost.

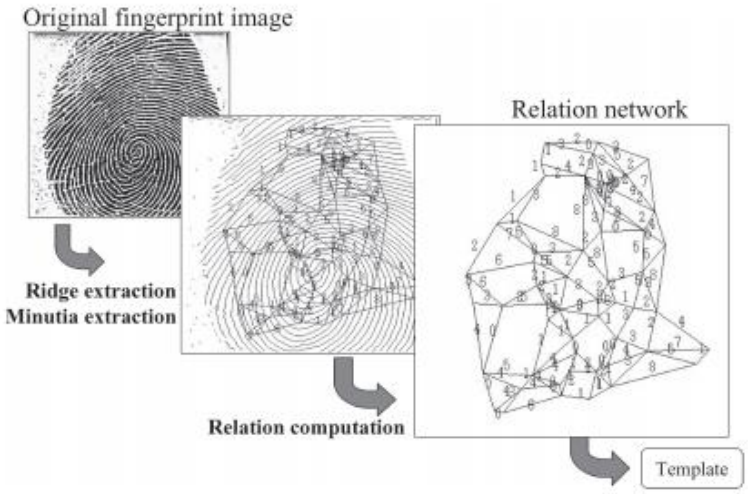


Figure 2 : Fingerprint using Ridge and Minutia extraction to convert into computation data for password. [4]

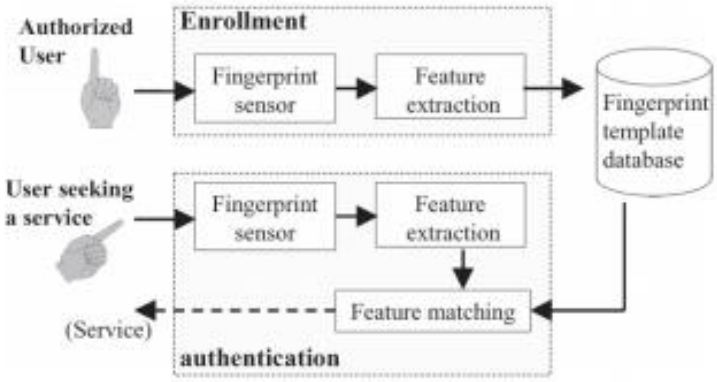


Figure 3: The process of fingerprint authentication system [4]

2.2.2 Retina Scanning

Retina is the layer of the back of an eyeball containing light sensitive cells and a unique pattern wall of blood vessels shown in Figure 5. A retina scanning system uses these definite pattern of blood vessels of the human eye for verification and similar to fingerprints, it will remain unique throughout a human's lifetime. [10] The

process of retina authentication have multiple methods to undergo verification such as vessel segmentation or features extraction from the obtained retinal images in figure 4 where the first mentioned method is a complex algorithms which need a high amount of computational time while the latter require a lesser computational due to its lesser complexity in algorithms but comprising accuracy in pattern detection. [8]

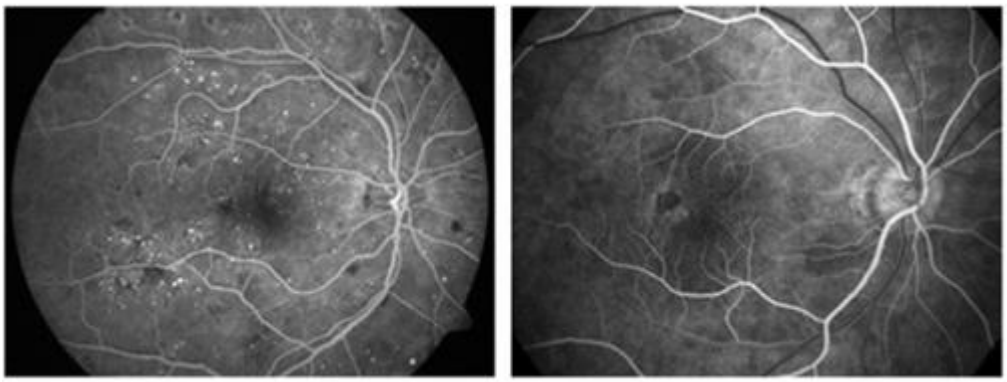


Figure 4 : Blood vessel of a retina wall of a human eye [8]

2.2.3 Others

Face and voice recognition are types of biometric authentication that uses the distinctive features of the individual to identify and authenticate the user. In face recognition, the system obtain the feature of captured image or video and compare against the database stored. It is able to overcome shoulder surfing attacks but this method need a constant update of database due to facial features changes with age or injuries. Voice recognition system is where the system obtain the frequency of sound of the user speech and compare to the database stored in order to undergo authentication. This method is unreliable due to shoulder surfing attackers could be able to record one's voice to pass the authentication system.

2.3 Existing methods to counter shoulder surfing

2.3.1 Puzzle Authentication Method

This authentication method is a creative approach by Kanagawa Institute of Technology [12] to counter shoulder surfing and still using code/text input method. The process of this puzzle is to scramble the usual 1 to 9 digit in a 3x3 formation shown in figure 5 which present everyday devices such as ATM and mobile phones into larger number of row and columns formation such as 4x4 shown in the figure 6 below or scrambling any text input system which are usually qwerty keyboard format by default into different format.

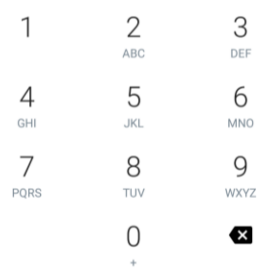


Figure 5: Digit Input in 3x3 formation. [11]

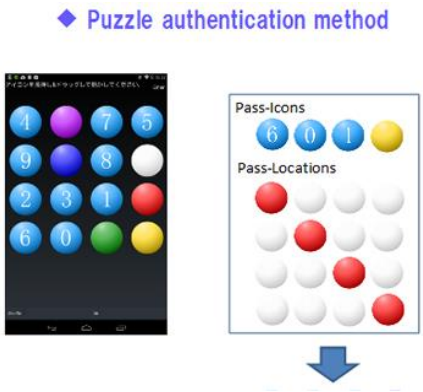


Figure 6: Digit input in puzzle authentication method. [12]

2.3.2 Rhythm Authentication Method

Another creative approach by Kanagawa Institute of Technology [12] to overcome shoulder surfing attacks which will effectively eliminate the possibility of shoulder surfing. With this approach, user tap the device screen with a distinctive rhythm for example Morse code like tapping to undergo the authentication and authorization. The process is done by user without looking at the screen of the device by keeping the device in a concealed place while unlocking the system as shown in figure 7.



Figure 7: User able to undergo authentication without looking at the screen. [12]

2.4 Summary

In order to prevent shoulder surfing attacks, bio-metric methods are the best in terms of protection and processing time with the expense of very expensive equipment cost as these methods doesn't require a screen for visual feedback of what the user have entered as password. By using rhythm authentication method, it achieved the similar level of prevention as bio-metric method but reducing the user friendliness as user might struggle to input their password correctly. By evaluating the advantages of each existing authentication system, this project proposes an gaze tracking based program which will be able to counter shoulder surfing attacks while keeping the cost of equipment low.

3. Design of the Proposed Authentication Method

Firstly, the steps of designing an authenticate method to counter shoulder surfing is to understand how shoulder surfing attack can be successfully used to obtain password without the knowledge of the user.A normal human field of sight is approximately 120-130 degree in a cone-shaped area illustrated in figure 8.[6] Shoulder surfing attacker used this limitation of our human body to their advantage by observing the password input process from area outside of the field of sight of the user as shown as Figure 9.

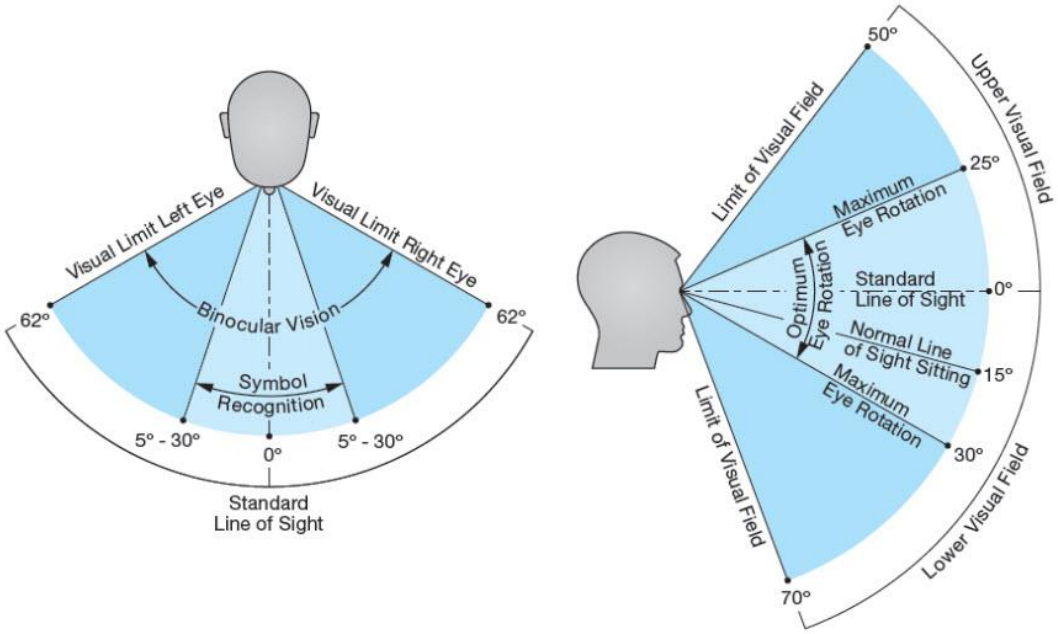


Figure 8: Human field of sight measured in angle degree. [6]

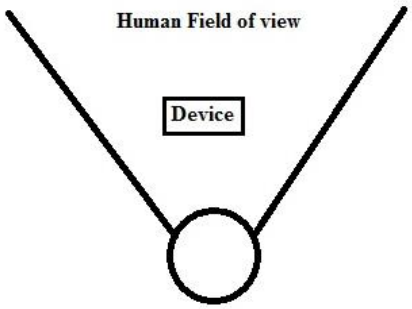


Figure 9: Device user field of view during usage

Therefore, the method to eliminate the possibility of shoulder surfing must allow the user to undergo the authentication and authorization process without losing the awareness outside the human field of view.
Eyes the main tool of detection of a human body. By using human eyes' gaze movement as input to the authentication system, shoulder surfer will unable to

observe the password input process by positioning themselves outside of the field of view of the user and will be detected if they attempt to observe the authentication process. This method allow the user to safely input their password while still able to detect shoulder surfers and abort their authentication process if a shoulder surfer is present.

The gaze movement authentication method designed in the sense the device is able to detect the movement of a human gaze by using the iris of human eye as a reference point. This method required a camera device as the input device such as a laptop webcam. In this paper, the authentication system is coded in MATLAB format and used Image Processing and Computer Vision add-on provided by MATLAB program as shown in figure 10. The program is coded in the concept as shown in the figure 20 and various important function including vision.CascadeObjectDetector function which used a database of images used in the Training Image Labeler tool provided in the Image processing and computer vision add-on as references to detect similar object which possess similar features as labeled in the database and imfindcircles function which used Mathematical model Hough transform to detect outline of object in the input images.

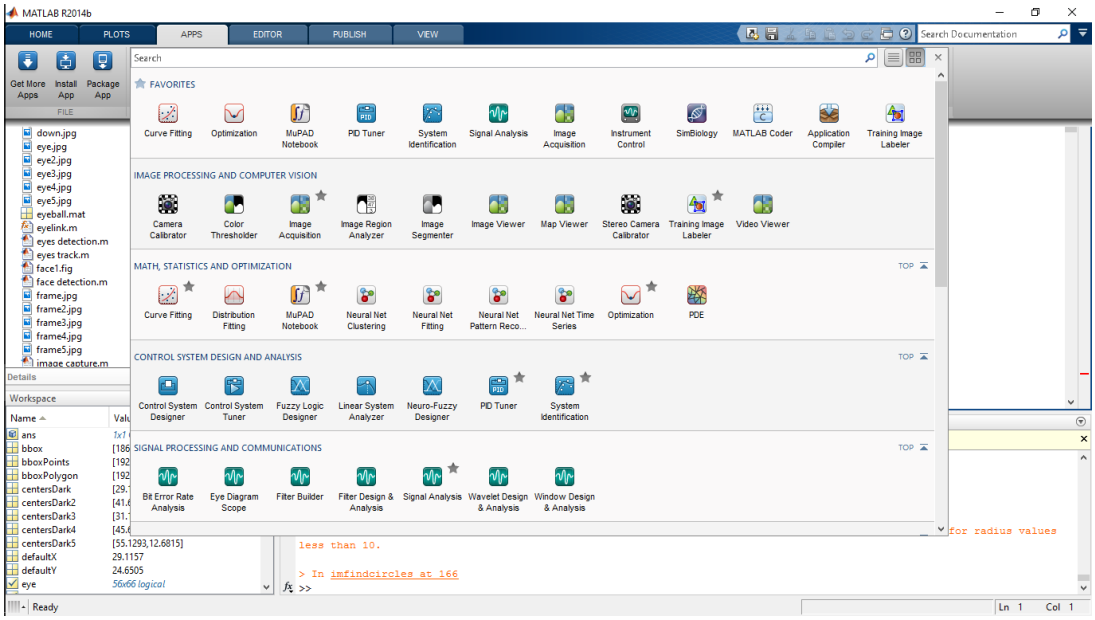


Figure 10: MATLAB program with Image processing and computer vision add on installed

3.2 Eye detection

Firstly, Training Image Labeler Tool shown in Figure provided in the MATLAB's image processing toolbox is used to create a database of eyes by labeling pictures containing eyes for the MATLAB function "vision.CascadeObjectDetector".

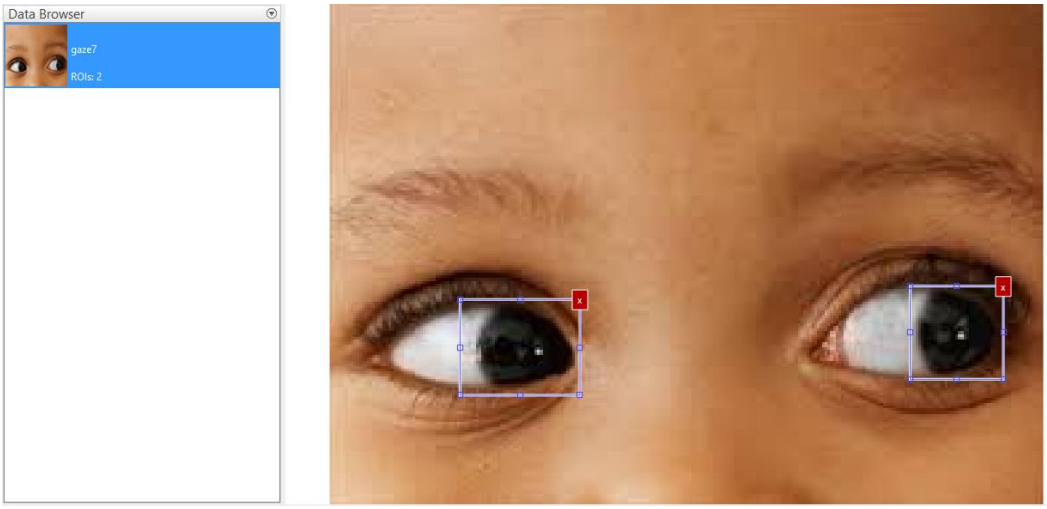


Figure 11: Training Image Labeler Tool. [7]

Once the database of eyes are processed and stored, the eye detection process can begin. A webcam feed can inserted into MATLAB program by using webcam() function as input provided the image processing tool and can be called to show the preview of the webcam feed by using the function “vision.VideoPlayer”.

In the next step, a single frame from the webcam feed is captured and converted into gray scale image using the MATLAB function “rgb2gray” which the gray scale image will be used as the input data for the function ”vision.CascadeObjectDetector” to initiate Viola-Jones feature detection system. The detected region will be bounded in a box to show in the video player by using the functions “estimateGeometricTransform” and “transformPointsForward” to determine the approximately detected eyes feature.



Figure 12: Result of successful detection using visionCascadeObjectDetector function

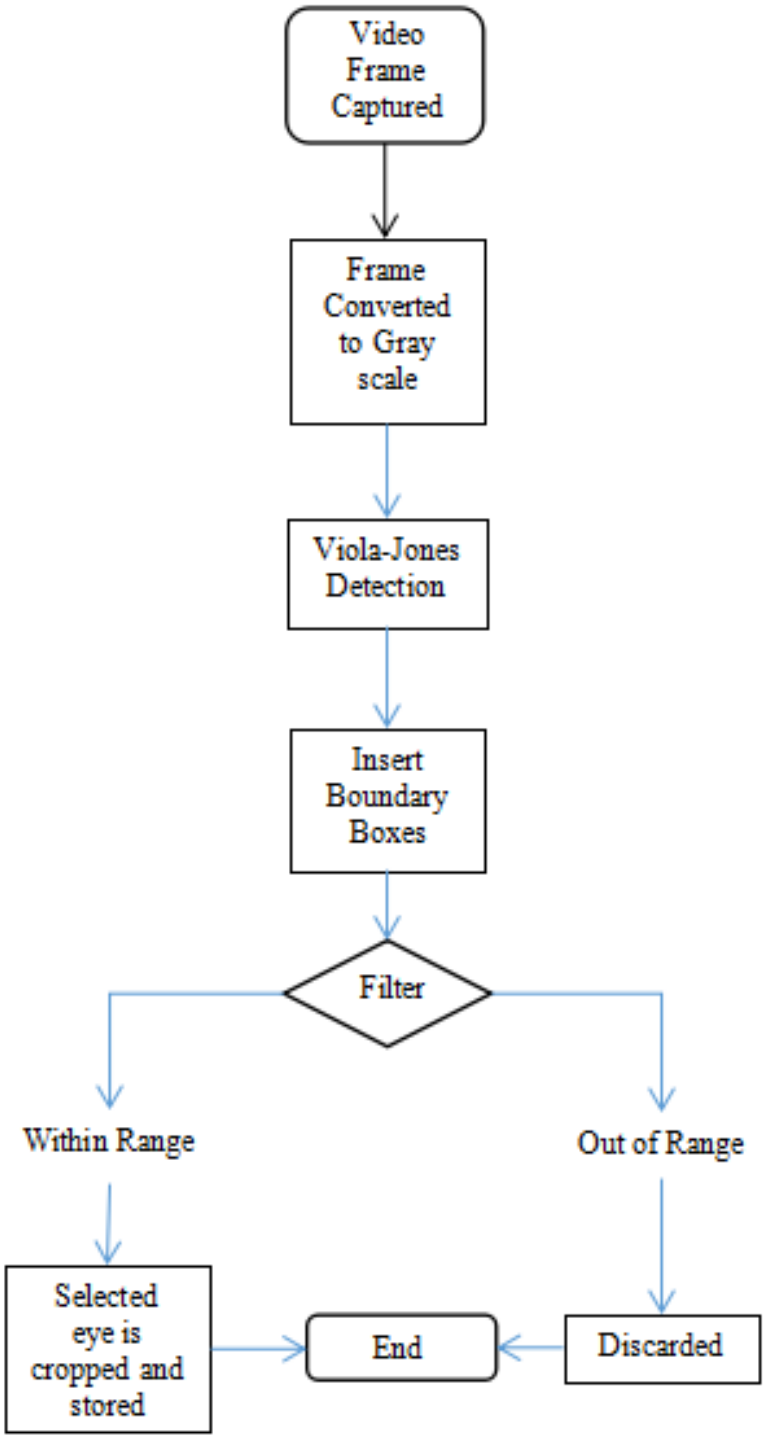


Figure 13: Flow chart of Eye Detection

3.3 Gaze Detection

A human iris move when he/she gaze in a different direction which changes in the center point coordinate of the iris in an image can be used to determine the direction of an eye gaze. When the frame from eye detection is obtained and stored,

the bounded region shown in figure 14 is cropped into a selected 75x55 image of the left eye by using the coordinates of the right upper corner of the bounding box of figure 14 as a reference point. This step will increase the accuracy and rate of detection significantly as less unnecessary objects in the image will process in the gaze detection.

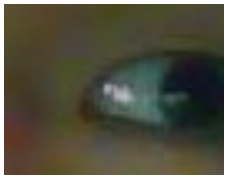


Figure 14: The cropped image of the left eye

The cropped image is then converted from RGB format into binary format using the MATLAB function “im2bw” which intensity will be adjusted according to the brightness of the image. This step allow the image to remove noises and further increasing the feature of an circle of the human iris.



Figure 15 : The cropped image is converted from RGB to binary format.

In the last step of gaze detection, MATLAB function “imfindcircles” which used Hough transform algorithms to detect the circle shape of an human iris in the cropped image in binary format as shown in figure 16 below. The circle detected must be set to detect within a certain radius and bounded in lines to show detection.



Figure 16 : Circle shape of a human iris detected

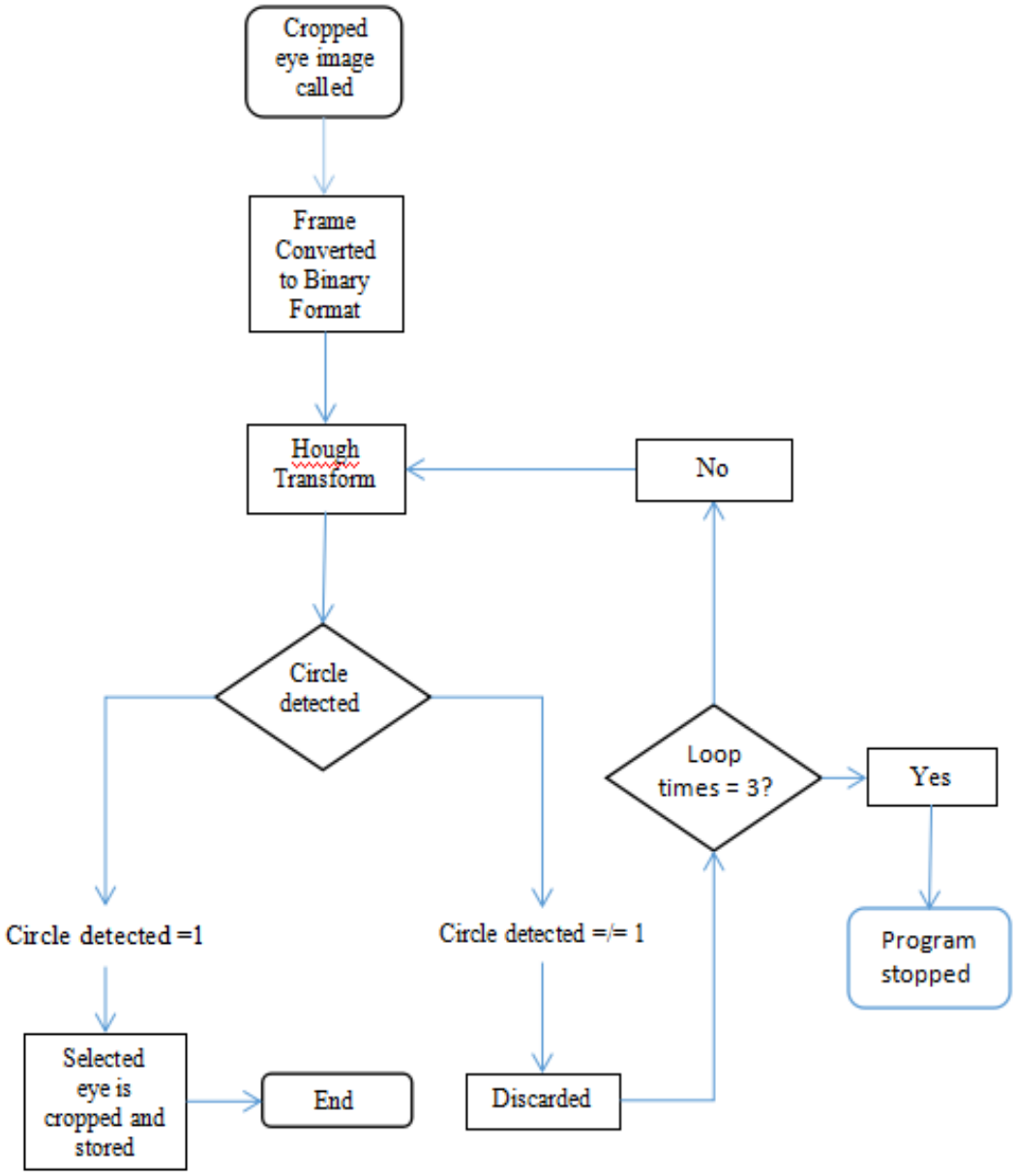


Figure17: Flowchart of Gaze Detection

3.4 Gaze Direction and Authentication

Once the the gaze position is detected, the center point of the plotted circle shown in figure 16 will be stored as input data. The eye and gaze detection process is repeated for each of the initial position of a straight gaze and four other direction of gaze as password input. All of the directional gazes' center points is then compared with the initial position of a straight gaze in a developed programmed algorithm to determine the direction of a gaze by using the changes in X and Y axis of their coordinates. Examples from authentication session is shown in the figure 18 and figure 19 below:

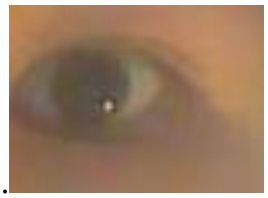



Figure 18: Pre- Processed Image and Detected Iris of a straight gaze

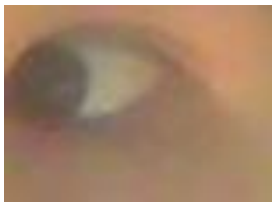



Figure 19: Pre-Processed Image and Detected Iris of gazing to the right.

As shown in both figure, the center point of the circles detected in each image have a specific difference from the center point of the straight gaze. When the center point X-axis value of the gaze is lower than the center point X-axis value of the straight gaze, it will be recorded as gazing right.

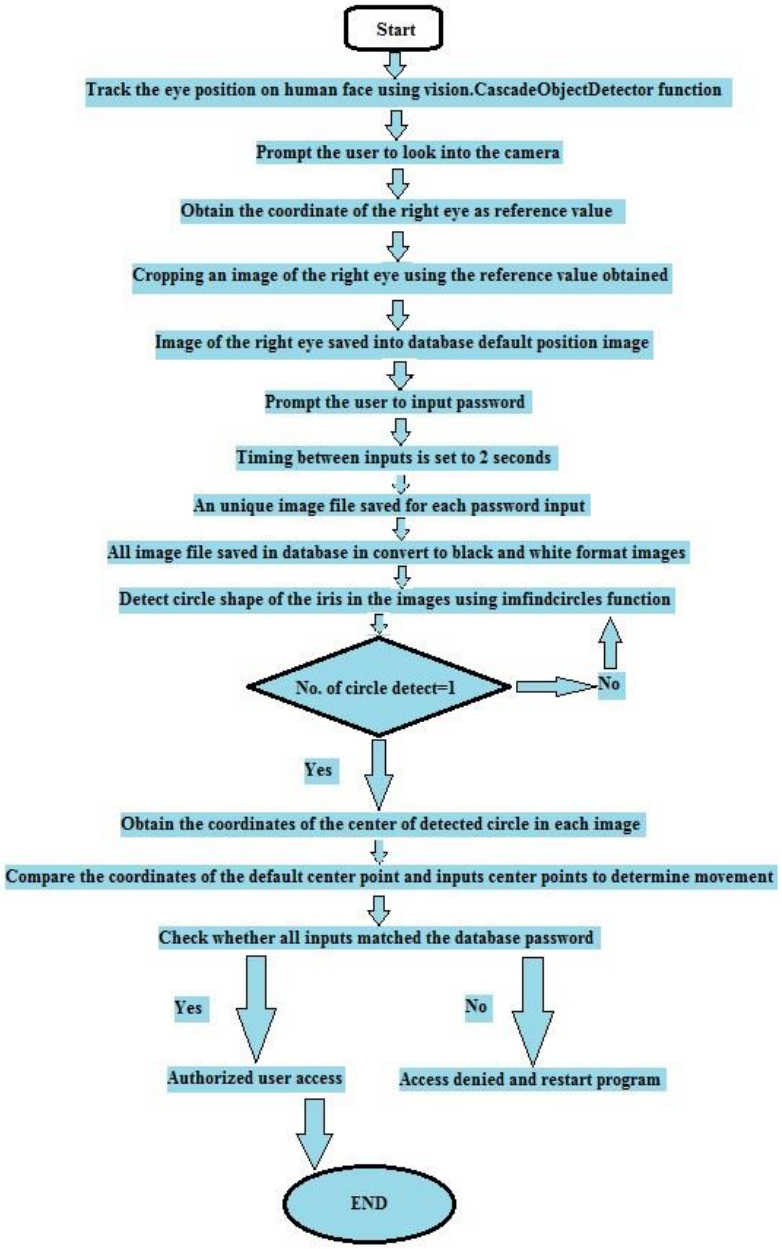


Figure 20 Proposed authentication method programming flow chart.

Table 1. Specification for the computer

Characteristic	Values
System Compatibility	Windows 10 64 bit
Software Compatibility	MATLAB ver. 2014b or newer version Image Processing and Computer Vision add-on installed Updated Program Driver for MATLAB installed
Hardware Compatibility	Webcam/camera devices connected

4. Comparison between Existing and Proposed methods and Discussion

To ensure the developed method is a good authentication system, the system must be able to effectively prevent shoulder surfing attacks and have advantage compare to existing authentication methods.

Table 2. Comparison of existing methods with proposed method

	Authentication System			
	Bio-metric scanning	Puzzle Method	Rhythms method	Eye Gaze
Security Level	High level of security is achieved as bio-metric data is unique for almost every person and unable to be easily duplicate by attackers	Low level of security as it is still vulnerable to shoulder surfers who is well trained.	Provide a medium level of security as attackers will be unable to obtain the password if device is hidden. Cannot be used on visible devices such as ATM.	It is specially designed to tackle shoulder surfing and can be fuse into bio-metric scanning program to provide the best level security.
User Friendly	It is very user friendly as the user does not need to do any additional steps other than having their eyes scanned.	User friendliness is great as it is used for everyday electronic applications. The password input method is very simple and easily recall by user.	Moderate user friendliness as user might have some difficulties tap the correct rhythm consistently especially in emergency situation	Eye gaze tracking as password input obtain the user friendliness of graphical pattern password and can be use with camera/webcam that are available to all electronic devices.
Budget	Very expensive as the equipment is very hard to obtain and budget needed to develop the server storage for the database is expensive.	Low budget is needed to develop this system.	Low budget is needed to develop this system.	Low budget as the budget will only be used on the development of the program and user interface due to its usage of webcam/camera which is present in most devices.

Shown in Table 2, the proposed method retain most advantages of the low budget existing authentication method as low budget system can developed by free source developer.

As mentioned in the section 3 design of the proposed authentication method, the designed program function as a effective prevention of shoulder surfing attack as users is able to be aware of any shoulder surfing attempted by other attackers. By conducting a small test with a user and several person posing as attackers and user are unaware of the identity of the attackers, the user is able to spot shoulder surfing attempts 8 out of 10 times and attackers had given feedback that although their attempt may be undetected, they have harder times to observe the movement of eye gaze clearly.

5. Conclusions

The proposed authentication method using gaze movement of the human eye as password input shows a great potential to contribute into the Engineering Grand Challenge of cyber security by being able to counter the attacks of shoulder surfing effectively with limited budget required and able to gain slight advantage over existing authentication methods. The performance of this proposed method can be further improved as development continues in terms of detection and movement accuracy and including encoding system into the proposed designed method.

References

[1] M. ., 'Count Based Hybrid Graphical Password to Prevent Brute Force Attack and Shoulder Surfing Attack', *International Journal of Research in Engineering and Technology*, vol. 03, no. 19, pp. 405-411, 2014.

[2] Naveed Khan Balcoh, M. Haroon Yousaf, Waqar Ahmad and M. Iram Baig . "Algorithm for Efficient Attendance Management: Face Recognition based approach." IJCSI International Journal of Computer Science Issues, Vol. 9, Issue 4, No 1, July 2012

[3] Y. M. Mustafah, T. Shan, A. W. Azman, A. Bigdeli, and B. C. Lovell, "Real-Time Face Detection and Tracking for High Resolution Smart Camera System." IEEE computer society international conference Digital Image Computing Techniques and Applications, pp- 387-393, 2007.

[4] K. Manu, G. Tar, B. Dan and W. Terry, 'Reducing shoulder-surfing by Using Gaze-based Password Entry', *Reducing shoulder-surfing by Using Gaze-based Password Entry*, p. Page 1, 2007.

[5] www.eyelock.com, 'EyeLock - Myris', 2015. [Online]. Available: http://www.eyelock.com/index.php/products/myris. [Accessed: 16- Nov- 2015].

[6] M.Edwin O'Neill, " Fingerprints in Criminal Investigation", Journal of Criminal Law and Criminology, Vol. 30, Issue 6, Article 8, pg. 929-940, March-April, 1940.

[7] Kaoru Uchida, "Fingerprint Identification" , *Special Issue on Security for Network Society, NEC Journal of Advance Technology*, Vol.2 , No.1, page 19-27, 2005.

[8] Boris I Gramatikov, "Modern Technologies for Retinal Scanning and Imaging: An Introduction for The Biomedical Engineer" , Biomedical Engineering OnLine, Vol. 13, No. 1, 2014

[9] Zsolt MikloÂs KovaÂcs-Vajna, "A Fingerprint Verification System Based on Triangular Matching and Dynamic Time Warping." IEEE TRANSACTIONS ON PATTERN ANALYSIS AND MACHINE INTELLIGENCE, VOL. 22, NO. 11, NOVEMBER 2000

[10] Amin Dehghani, Zeinab Ghassabi,Hamid Abrishami Moghddam and Mohammad Shahram Moin, "Human recognition based on retinal images and using new similarity function."EURASIP Journal on Image and Video Processing 2013, 2013:58

[11] Screenshot from Dropbox mobile app.

[12] Broadhurst, R. G., Maller, R. A. (1991). *Sex offending and recidivism* (Tech. Rep. No. 3). Nedlands, Western Australia: University of Western Australia, Crime Research Centre.

[13] Http://buildmedia.com/portfolio-items/what-are-survey-accurate-visual-simulations/ [Online] [Accessed : 17 - Oct - 2016]

[14] MATLAB software ver. 2014b, Training Image Labeler tool.

[15] S. Edmund, 'Biometric Scanning Technologies: Finger, Facial and Retinal Scanning', *Sans.org*, 2003. [Online]. Available: https://www.sans.org/reading-room/whitepapers/authentication/biometric-scanning-technologies-finger-facial-retinal-scanning-1177. [Accessed: 07- Oct- 2015].

[16] A. Jain, *Fundamentals of Digital Image Processing*, Prentice-Hall, 1989, Chap. 9.

[17] R. Boyle , R. Thomas *Computer Vision:A First Course,* Blackwell Scientific Publications, 1988, Chap. 5.

[18]AK Jain, A Ross and S Prabhakar, "An introduction to biometric recognition." IEEE Trans. Circuits Syst. Video Technol. 14(1), 4–20 (2004)

eureca 2016 – Conference Paper
Paper Number 2EE02

Motoring and Generating Capability in Hybrid Electric Vehicle with Outer Rotor Electrical Machine

Katrina Marie Fernandez[1], Aravind CV[1,*], Charles R Sarimuthu[1], A Suresh[2]
[1]School of Engineering, Taylor's University, Malaysia.
[2]Department of Electrical and Electronics, S.A Engineering College, Chennai, India.
[*]*aravindcv@ieee.org*

Abstract

Hybrid Electric Vehicles (HEV) have been known to be the most promising means of solving the myriad of environmental issues that are present today due to the emission of harmful gasses, which is mainly caused by the use of Internal Combustion Engines (ICE) in vehicles. The electric machine in a HEV work by converting electrical energy into mechanical energy to power the drive of the vehicle. HEVs also have the added advantage of converting mechanical energy back into electrical energy during the braking or decelerating phase of the vehicle. This system is also known as regenerative braking which reduces the energy wastage of the vehicle during its braking phase as it stores the mechanical energy in a battery storage system in the vehicle. Due to the process in which an HEV works, it is important to ensure that the power flow of the HEV during charging and discharging is efficient to reduce any power losses. There has been numerous research conducted to improve the power flow of a HEV. However, these researches are mainly focused on the improvement of the batteries in the EV/HEV which would lengthen the battery capacity. This project highlights the algorithm proposed to improve the power flow of a proposed redesigned machine which was able to operate as an electric motor and a generator. The algorithm used the HEV drivetrain system to work out how the power split should divide the power coming from two different sources at specific drive characteristics. The results show different range in velocities that depicted various drive characteristics which were early start, normal speed, acceleration, high speed, deceleration and stop. The algorithm showed that the two types of energy sources, typically a petrol engine and an electric motor would function in a 3:2 ratio. This meant that at each of the drive modes, the maximum ratio that the power split would divide its energy in is 3:2 in the favor of either the petrol engine or the electric motor.

Keywords: Electric Vehicles, Magnetic Gear, Power Flow Management, Generator, Motor

1. INTRODUCTION

A study that was conducted by the United Nation Environmental Program (UNEP) showed that the third largest contributor to the production of harmful gases in the environment come from motored vehicles powered by Internal Combustion Engines (ICE) [1]. The same study stated that the estimated amount of carbon dioxide produced by ICE vehicles was 1.7 ~ 2.5 Gigatonne in the year 2012 alone [1]. Scientists, researchers and engineers have brought forward a new means of powering up vehicles by using electricity instead of exhausting the earth's fossil fuel remains in order to alleviate the harmful effects of ICE vehicles on the environment. These vehicles are known as Electric Vehicles (EV) or Hybrid Electric Vehicles (HEV).

EVs and HEVs have come a long way since its early days. Many of the giant car manufacturing companies such as Tesla, Nissan, BMW and Toyota to name a few, understand the need to take this leap into manufacturing these vehicles as it not only assists in the improvement of the overall environment but its technologies have significant effects on the betterment of the fossil fuel crisis [2]. In the present day, there are significantly higher benefits to owning an EV/HEV compared to an ICE vehicle. Comparatively, EVs/HEVs emit less noise when running, demands lesser maintenance and does not produce any harmful gasses. They also outperform ICE in terms of torque as it is able to yield a higher maximum torque on the first revolution making them more efficient in terms of torque compared to ICE vehicles [3]. Figure 1 shows a study conducted by the University of Malaya in 2102 showing the percentage of people in Malaysia that are aware of the types of EVs available in the market [4]. Since Malaysians are more prone to buying a HEV, this paper studied the power flow management emphasizing particularly on HEVs.

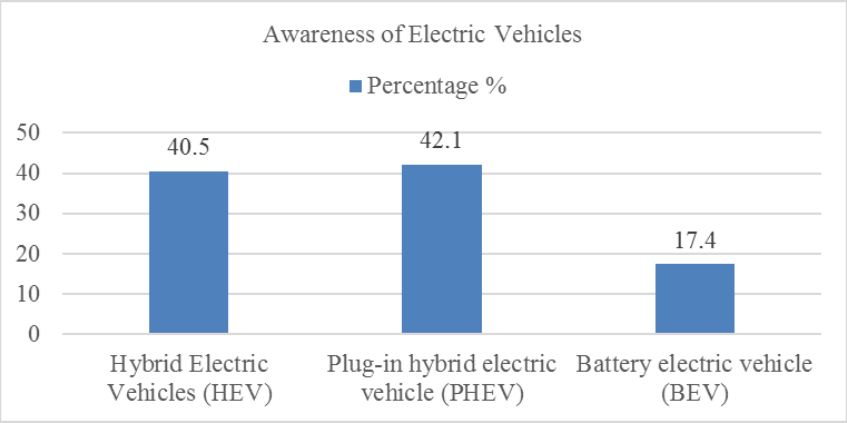


Figure 1. Malaysian Awareness of EV [4]

The objectives of this paper were to study and understand the power flow in an electric vehicle and hybrid electric vehicles at various drive conditions, to investigate the impact of an ORPM machine on the overall performance of the vehicle and the power flow demands required, to create an algorithm that can be used to improve the power flow management in electric vehicles particularly, hybrid electric vehicles. The main contribution of this research project is the finding of the ratio of power needed between two different sources of energy in a Hybrid Electric Vehicle to ensure that the electric motor is performing at its optimum level.

2. Operating Principle

There are many different types of EVs depending on how the vehicle is configured, it could be a HEV, plug-in hybrid electric vehicle (PHEV) or fuel cell electric vehicle [5]. Regardless of the configuration of these models, the underlying principle of how an HEV works is the same. When the vehicle is stopped, the electric motor is not active. When the vehicle begins its motion, the electric motor functions using direct current from the main power [6, 7]. An added advantage that HEVs have over ICE vehicles is its ability to produce maximum torque during starting. During acceleration the torque decreases as the speed of the car increases. When the vehicle begins braking, the electric motor shifts to generator mode. The wheels transfer the kinetic energy through the drivetrain to the generator [7]. From its rotation, the generator converts a percentage of the kinetic energy into electrical energy which is stored in a high voltage battery. The generative braking torque of the electric motor decelerates the vehicle. At low speeds, shortly before the vehicle comes to a complete stop, the electric motor can no longer supply sufficient generative braking torque and the friction brake is activated [8]. To maintain the required deceleration, the braking torque from the friction brake is adapted to the generative braking torque which is called torque blending.

The characteristics of how the electric motor works in a HEV can be described using a four-quadrant speed torque graph. The first quadrant shows that the torque and speed produced are both positive, this indicates that the electric motor is in forward motoring operation causing the vehicle to be in motion. In the second quadrant, electric torque is in the negative side of the x-axis while the speed is in positive of the y-axis. The electric torque is in the reverse direction of motion indicating that the vehicle is in forward braking. The third quadrant shows both electric torque and speed to be having negative signs, exhibiting reverse motoring. Lastly, electric torque is seen to be in positive side of the x-axis and speed is in the negative side of the y-axis in the fourth quadrant, this indicates that the electric drive is in reverse braking which is responsible for the regenerative braking characteristics of an EV [9].

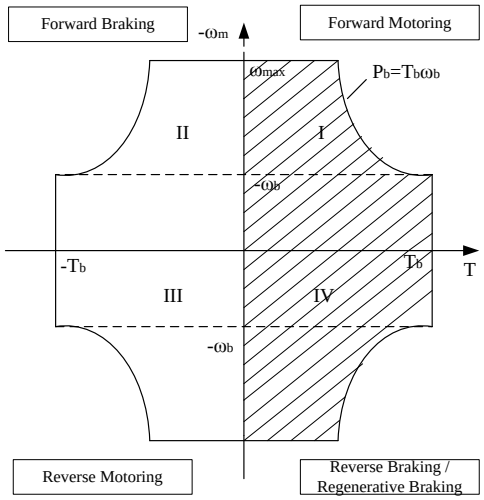


Figure 2. Four Quadrant Speed Torque Characteristics

3. Design Concept

This paper was centered around the power flow in HEVs as they need not be connected to the grid to recharge its batteries as it is able to recharge the battery through regenerative braking and by siphoning off excess energy that comes from the generator which is run by the petrol engine in the vehicle [10]. Hence, the need for power flow management in HEVs between the electric motor, petrol engine and the batteries is more desirable compared to a full EV. Any vehicle that uses the functions of two types of energy source to power the vehicle drive is known as a hybrid vehicle. Essentially, a fully EV vehicle using two different types of battery sources would also adhere to the algorithm that was devised in this project.

The HEV was analyzed during different drive conditions and the demands that the vehicle requires during these conditions. The drive conditions that were considered in this project were early start, normal speed conditions, acceleration, deceleration and when the HEV comes to a complete stop. The development of the ORPM focused on improving the efficiency of the electric motor when it is run during the various aforementioned drive conditions and improve the overall torque performance of the electric motor [11]. The hybrid system in Figure 3 shows a system that maximizes the use of the energy sources available. This system has both generator and motor as two separate electric machines. The system utilizes both the electric motor and the petrol engine depending on the vehicle need. It is able to function solely on the electric motor or when needed on both electric motor and petrol engine. The power split device as seen in Figure 3, functions to split the power from the petrol engine between generator and the drive wheels [7]. The power flowing through the generator fed by the engine functions to charge the battery, moreover, the drive wheels in this system are also able to charge the battery through regenerative braking.

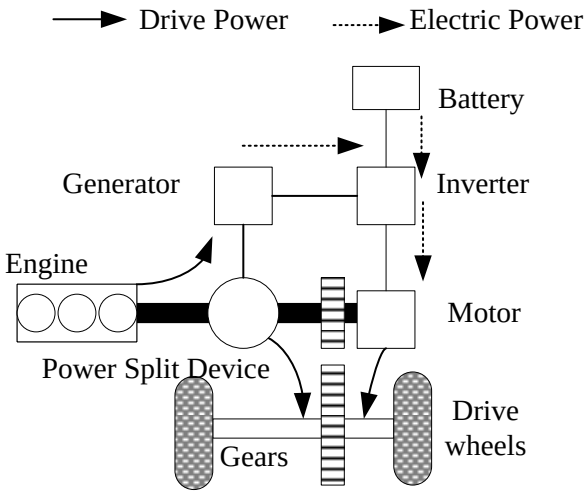


Figure 3. Hybrid System

4. Structural Configuration

Figure 3 shows a motor that was used for an electric bicycle. This motor is a single stator, single rotor permanent magnet machine [11]. It has 18 slots and 20 poles. The machine was remodeled to an 18 slots and 16 poles machine using JMAG®. The 18 slots 16 poles configuration of the structure showed better flux performance when compared to the 18 slots 20 poles structure. The structure was designed so that the flux linkage is maximized between the stator and rotor [12]. and Figure 3 shows its isometric view of the PM machine while Table 1 shows the parameters at which the 18 slots and 16 poles machine was modeled.

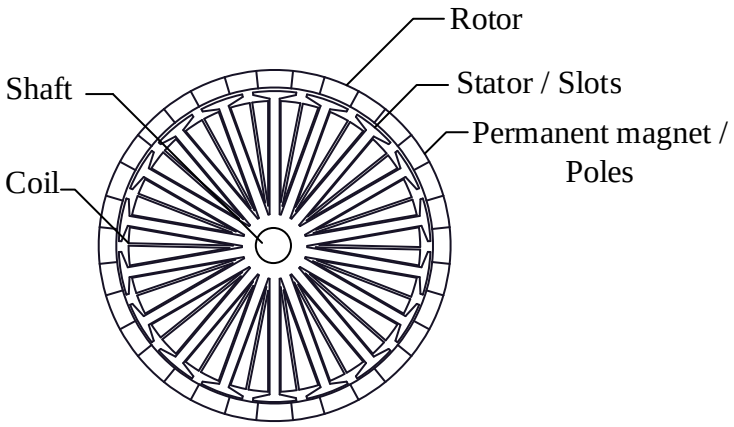


Figure 4. 2D JMAG® 18 slots 16 poles model

Table 1. Design Parameters of the PM Machine

Parameter	Symbol	Value
Outer Diameter of Rotor	R_{od}	70mm
Inner Diameter of Rotor	R_{id}	63mm
Outer Diameter of Permanent Magnet	M_{od}	70mm
Inner Diameter of Permanent Magnet	M_{id}	63mm
Width of Stator Pole	W_{s1}	5mm
Width of Stator Teeth	W_{s2}	6.97mm
Length of Stator Pole	L_s	23mm
Diameter of Shaft	Sft_d	5mm
Length of Air Gap	L_{ag}	0.5mm
Stack Length	Stk_l	100mm
Outer Diameter of Stator	S_{od}	62mm
Inner Diameter of Stator	S_{id}	5mm
Outer Diameter of Coils	C_{od}	58mm
Inner Diameter of Coils	C_{id}	17.8mm
Permanent Magnet Pole Arc	A_p	2 degrees
Rotor Pole Arc	A_r	16 degrees
Stator Teeth Pole Arc	A_s	13 degrees

5. Magnetic Transient Analysis of PM Machine

The entirety of the performance of the proposed machine was analyzed through the he magnetic transient analysis FEA tool in JMAG®. The objective of running this analysis was to show the machine structure characteristics in the magnetic flux linkage over time distribution. Hence, to attain such speed-torque characteristics the electric motor was studied in different cases where the starting angle of

rotation and the current fed to the source were varied. In terms of the machine acting as a generator, the machine was analyzed at different rotational speed to show the voltage produced.

5.1 Motor Analysis

To analyze the machine as a motor, the torque-speed characteristics was needed to be found. In order accurately graph the torque-speed graph, the machine was needed to be analyzed at different armature currents during varying angles of 0°, 10°, 20°, 30°, 40°, 50°, 60°, 70° and 80°. The first step in doing this was to find the varying armature currents. Equation (1) was used to find the armature current.

$$Armature\ Current, I_a \quad \frac{J_a \times \alpha \times S_c}{N_t} \times 3 \times \sqrt{2} \tag{1}$$

Where J_a is the current density, α is the coil filling factor, S_c is the coil slot area and N_t is the number of turns in the coils per phase.

The motor armature current was analyzed at 0A, 15.41A, 30.82A, 46.23A, 61.64A, 77.05A, 92.46A.

5.2 Generator Analysis

To analyze the machine as a generator, the voltage produced by the generator at different varying speeds were simulated. However, the speeds simulated here had to coincide with the speed range capabilities of the machine when it was analyzed as a motor. This was done in order to obtain accurate representation of the generator characteristics of the same machine design. The machine as a generator was analyzed at rotational speeds of 300rpm, 0rpm, 1300rpm, 1350rpm, 1400rpm, 1450rpm, 1500rpm, 1550rpm, 1600rpm, 1650rpm, 1700rpm, 1750rpm. Table 3.7 shows the cases that were run for generator analysis.

6. Results and Discussions

This chapter highlights the results attained from the overall analysis of the machine as well as how the machine functions as both an electric motor and a generator in a HEV system. The initial parts of this section emphasize on the performance of the machine as a motor and a generator evaluating the speed-torque characteristics and the voltage produced by the machine. Then the algorithm of the power flow was discussed when using the proposed machine capabilities at different drive characteristics.

6.1 Machine Performance as an Electric Motor

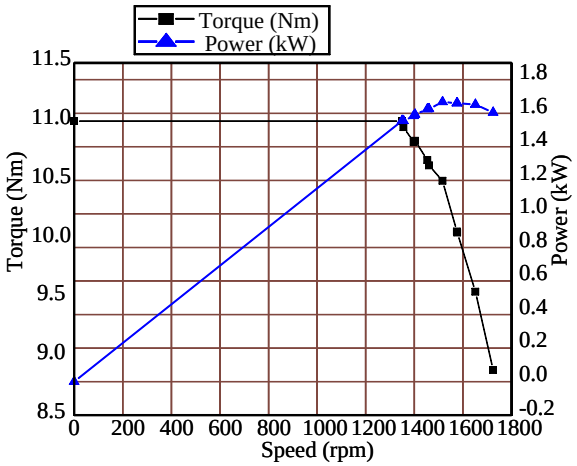


Figure 5. Speed-Torque Characteristics

Figure 5 shows the speed torque characteristics of the PM machine when analysed as a motor. From the graph, it is seen that the maximum torque produced is 11Nm; The graph also indicates that the PM machine is able to produce its maximum torque on its first revolution. This is essential for HEVs as initial start of the vehicle runs on the electric motor alone. Hence, producing a high torque from the start due to the current flowing through the motor causes the rotor to begin rotation [13, 14]. As the motor reaches its maximum speed, the torque decreases. Bear in mind that the torque and speed in this analysis is small for fabrication purposes

6.2 Machine Performance as a Generator

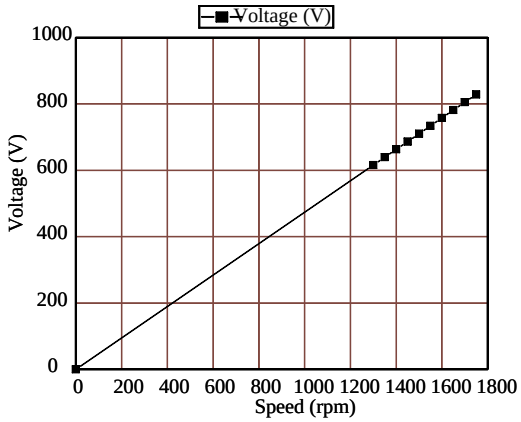


Figure 6. Graph of Voltage against Speed

Figure 6 depicts the voltage generated by the generator. This graph shows that the voltage produced by the generator increases as the rotational speed of the machine increases. Essentially the function of the generator in a HEV system is to siphon excess energy from the engine to generate electricity and charge the vehicle batteries and to run the electric motor. Therefore, from the graph it can be deduced

that as the excess energy from the petrol engine reaches a value high enough to rotate the generator shaft, the amount of voltage produced to drive the vehicle increases.

6.3 Power Flow Characteristics

In order to evaluate the overall capabilities of the proposed machine design in the application of EVs and HEVs, the graph of velocity against time was plotted. The velocity was calculated because the speed in rpm only represents the rotational speed in which the electric motor and the generator functions. Analyzing the machine in terms of its linear velocity would produce a more accurate depiction on how the machine functions on the EV as a motor and as a generator as linear velocity shows the speed of the motion of the vehicle with time. To convert the speed in rpm to velocity in ms^{-1}, the Equation (2) was used. Hence the graph shown in Figure 7 was produced.

$$Linear\ Velocity, ms^{-1} \quad \frac{rev}{min} \times \frac{1min}{60s} \times \frac{2\pi r}{1rev} \tag{2}$$

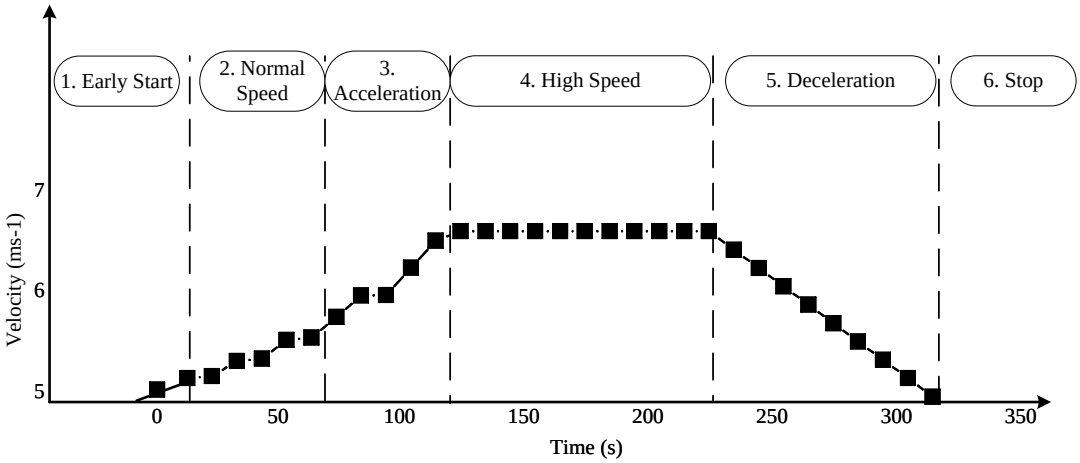


Figure 7. Driving modes based on the velocity-time graph

Figure 6 demonstrates the velocity-time graph gathered from the simulations of the proposed machine. This velocity-time graph shows how the machine functions during different drive characteristics. The scope of this project was to understand power flow in an EV but more particularly in Hybrid EVs. The reasons behind emphasizing on the power flow in HEVs was because HEVs need not be connected to the grid to recharge its batteries as it is able to recharge the battery through regenerative braking and by siphoning off excess energy that comes from the generator which is run by the petrol engine in the vehicle. Hence, the need for power flow management in HEVs between the electric motor, petrol engine and the batteries was more desirable compared to a full EV.

Therefore, based on the capabilities of the proposed machine to be applied as a EV/HEV machine, an algorithm was devised to show the amount of energy needed between the two energy sources in a series-parallel hybrid system. As shown in the research methodology, the two types of hybrid studies that were conducted were full-hybrid and mild-hybrid. Hence it should be known that the ratio of the energy supply from the two energy sources would be different in a full-hybrid and a mild-hybrid. Any vehicle that uses the functions of two types of energy source to power the vehicle drive is known as a hybrid vehicle. Essentially, a fully EV vehicle using two different types of battery sources would also adhere to the algorithm that was devised in this project.

Table 2 depicts how the proposed electric motor and generator would perform in the different drive modes of the Full-Hybrid Vehicle. In Full-Hybrid vehicles, the vehicle is heavily dependent on the electric motor. As shown in the motoring analysis, the maximum power that the proposed electric vehicle would be able to produce should the vehicle demand such power is 1.67kW. Hence, any extra

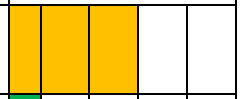
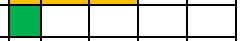
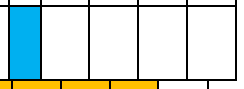
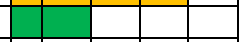
energy demanded by the vehicle would have to be supported by the petrol engine. The power split device is responsible for monitoring the amount of power each energy source is supplied to the drive wheels. Full-hybrids are able to provide regenerative braking which is crucial to any EV/HEV. Both mild-hybrids and full-hybrids need not be plugged into the grid for battery recharging as commonly conceived because the batteries are capable of being fully charged on regenerative braking and through drawing off excess energy from the engine during acceleration. One of the most popular fully hybrid cars in the market today is the Toyota Prius [7].

A mild-hybrid vehicle would rely more on the petrol engine rather than the electric motor. The petrol engine would have to work continuously throughout the drive and would only stops working when the speed of the vehicle is at significantly low speeds which would bring the vehicle to a halt. Essentially, the electric motor in a mild-hybrid vehicle would only function to provide support to drive the vehicle forward during acceleration. Table 3 shows the energy demands in mild hybrid vehicles with proposed machine. The most important feature of the electric motor in this system is to provide the regenerative braking properties which are not present in internal combustion engine vehicles. Some examples of vehicles currently in the market that use the mild-hybrid systems are the Honda's Civic Hybrid, Jazz Hybrid, Insight, and CR-Z [6].

Table 2 Energy Demands in Full Hybrid Vehicles with Proposed Machine

Drive Mode	Description	Energy Sources	Energy Source Supply Needed
Early Start	In the early start mode, the electric motor would function using the direct current from the main motor. Because the vehicle in this drive mode would be in low speeds, it is sufficient for the vehicle to run only on the electric motor.	Petrol Engine	
		Electric Motor	
		Vehicle Battery	
Normal Speed	At normal speeds, the vehicle would be cruising at speed above the speed ranges in which lonesome operation of the electric motor can function optimally. Therefore, in a full-hybrid system this driving mode would require the support of the petrol engine. However, the excess energy would be significant to be siphoned from the engine to charge the batteries during this mode.	Petrol Engine	
		Electric Motor	
		Vehicle Battery	
Acceleration	The gradient of the graph in accelerating mode is steeper than that of the normal speed mode. Therefore, to push the vehicle forward, any excess energy that the petrol engine would produce would be used to increase the power of the vehicle during acceleration. The electric motor would function at maximum operations. Charging of the battery would not take place during this mode to fully optimize the petrol engine to drive the vehicle.	Petrol Engine	
		Electric Motor	
		Vehicle Battery	
High Speed	At high speeds, the vehicle is in cruising mode and would require the work of both petrol engine and electric motor. However, as shown in the speed-torque characteristics of the motor, the power drops at maximum speeds. Hence, during this mode the petrol engine would be required to produce the bulk of the energy to meet the demands of the vehicle.	Petrol Engine	
		Electric Motor	
		Vehicle Battery	
Deceleration	During deceleration, the petrol engine would cease to work and as the vehicle can be controlled by the electric motor alone. The motor would not need to produce any power. Here, kinetic energy generated by the car is converted into electrical power in regenerative braking in order to recharge the battery. As seen from the voltage time graph, produced by the generator, the voltage produced by machine decreases as the vehicle slows down to come to a complete stop.	Petrol Engine	
		Electric Motor	
		Vehicle Battery	
Stop	When the vehicle stopped the engine and the electric motor in a position of inactivity. However, since the vehicle would still be active in this mode, the air conditioning of the vehicle would still be able to function using the batteries.	Petrol Engine	
		Petrol Engine	
		Vehicle Battery	

Table 3 Energy Demands in Mild Hybrid Vehicles with Proposed Machine

Drive Mode	Description	Energy Sources	Energy Source Supply Needed
Early Start	In a mild-hybrid system, the early start of the vehicle at low to mid-range speed would require the use of both petrol engine and electric motor.	Petrol Engine	
		Electric Motor	
		Vehicle Battery	
Normal Speed	During the normal speed mode, the mild-hybrid system would rely solely on the petrol engine while siphoning off its excess power in order to charge the batteries.	Petrol Engine	
		Electric Motor	
		Vehicle Battery	
Acceleration	In a mild hybrid system, the electric motor functions only as a support to the petrol engine, hence during acceleration, the petrol engine would have to produce the bulk of the energy compared to the electric motor in order to drive the vehicle forward.	Petrol Engine	
		Electric Motor	
		Vehicle Battery	
High Speed	At high speed levels, the mild hybrid functions solely on the petrol engine to drive the vehicle forward. Hence, fuel consumption would be at the highest in mild-hybrids when functioning at full speeds.	Petrol Engine	
		Electric Motor	
		Vehicle Battery	
Deceleration	During deceleration, there would be some form of regenerative braking. Although, the amount of energy that would be able to be stored in the batteries would be far lesser in comparison to a full-hybrid. The petrol engine would still work to bring the vehicle to a complete stop.	Petrol Engine	
		Electric Motor	
		Vehicle Battery	
Stop	In the stop position, the engine remains active in order for the air conditioning to remain functional.	Petrol Engine	
		Petrol Engine	
		Vehicle Battery	

6.2 Power Flow Algorithm

By studying the energy demands that were needed by the vehicle during different drive conditions, the following algorithm was devised. Table 4 shows the proposed optimum manner in which the power split should be to divide power from the two energy sources.

Table 4 Proposed Algorithm on the Percentage of Usage of the Energy Sources

Speed Range (ms^{-1})	Motor (%)	Engine (%)	Battery (%)
0 – 5	60% - motor is run via the charge stored in the battery	0%	60% - discharge to run the motor at low to medium speed range.
5 – 5.3	40%	60% - 40% to power the drive wheels while the other 20% is used to charge the batteries	20% - of power is siphoned from the petrol engine to charge the battery
5.3 – 5.6	100% (maximum power)	100% (maximum fuel consumption)	0%
5.6 – 6.4	40%	60%	0%
6.4 – 5	100% - the proposed electric motor in this decelerating speed ranges would function as a high output generator to charge the batteries through regenerative braking	0%	100% - charged through regenerative braking

7. Conclusions

It was found that the energy demand of the HEVs change according to their drive characteristics. Ensuring the proposed electrical motor was able to meet the said demands, an algorithm was created. In this algorithm, it showed that the ratio in which the electric motor and the engine should function was 3:2. This meant that for the vehicle to function as a full hybrid system, the electric motor would have to produce the bulk of the power however. In a mild hybrid system, the ratio would favor the engine as mild hybrid system only uses the motor as a form of support. However, the proposed machine showed that it could function optimally for a full hybrid system and a mild hybrid system.

References

[1] N. UNEP 2014, “The Emissions Gap Report 2014. United Nations Environment Programme (UNEP),” The Emissions Gap Report 2014: A UNEP synthesis Report. 2014.

[2] C. Mi, M.A Masrur, D.W Gao, “Hybrid Electric Vehicles: Principles and Applications with Practical Perspectives,” United Kingdom: John Wiley & Sons Ltd, 2011. [Online] Available: Google books

[3] Roberto Cipollone, David Di Battista, Matteo Marchionni, Carlo Villante, “Model Based Design and Optimization of a Fuel Cell Electric Vehicle,” IEEE Trans. On Energies, vol. 45, pp. 71-80, 2014.

[4] Afroz. R, Rahman. A, Akhtar. R, "Malaysian Perception and Attitude Towards Electric Vehicle," 2nd International Conference on Mechanical, Automotive and Aerospace Engineering, pp. 1-5, 2013.

[5] A. Panday and H. Bansal, "A Review of Optimal Energy Management Strategies for Hybrid Electric Vehicle," International Journal of Vehicular Technology, vol. 2014, pp. 1-19, 2014.

[6] Honda Emergency Response Guide for Hybrid Vehicles, 1st Ed. American Honda, pp. 1-32, 2012.

[7] Toyota Hybrid System THSII, 1st Ed. Tokyo: Toyota Motor Corporation Public Affairs Division, pp. 1-21, 2003.

[8] J.S. Hsu and G.W.Ott, "Evaluation of 2004 Toyota Prius Hybrid Electric Drive System Interim Report," Oak Ridge National Library, 2004.

[9] C. Musardo, G. Rizzoni, Y. Guezennec and B. Staccia, "A-ECMS: An Adaptive Algorithm for Hybrid Electric Vehicle Energy Management", European Journal of Control, vol. 11, no. 4-5, pp. 509-524, 2005.

[10] Y. Riffonneau, S. Bacha, F. Barruel and S. Ploix, "Optimal Power Flow Management for Grid Connected PV Systems with Batteries", IEEE Trans. Sustain. Energy, vol. 2, no. 3, pp. 309-320, 2011.

[11] Aravind C.V, Kamalini Raj, Raja Nor Firdaus, "Design and Development of a Novel Outer Rotor Permanent Magnet Machine", Journal of Engineering Science and Technology, EURECA, pp. 1-11, 2014.

[12] K. Chau, C. Chan and Chunhua Liu, "Overview of Permanent-Magnet Brushless Drives for Electric and Hybrid Electric Vehicles", IEEE Transactions on Industrial Electronics, vol. 55, no. 6, pp. 2246-2257, 2008.

[13] C. Chan and K.T. Chau, "An advanced permanent magnet motor drive system for battery-powered electric vehicles," IEEE Transactions on Vehicular Technology, vol. 45, no. 1, pp. 180-188, 1996.

[14] C. Chan, K. Chau, J. Jiang, W. Xia, M. Zhu and R. Zhang, "Novel permanent magnet motor drives for electric vehicles," IEEE Transactions on Industrial Electronics, vol. 43, no. 2, pp. 331-339, 1996.

The Application of Image Processing for Hand Gesture Recognition Using Microsoft Kinect

Liew Wai Lin[1]*, Chew Wei Jen[1]

[1]School of Engineering Taylor's university, Malaysia

wailinnyu@gmail.com

Abstract

Most people with impaired hearing will learn sign language to aid them in communication throughout their daily lives. Learning a new language is not easy, likewise teaching. This study proposes an American Sign Language (ASL) Alphabet Recognition System for education purposes to assist both deaf and non-deaf people in learning ASL alphabets. This system will be taking advantage of the Kinect for Xbox One capability to capture depth images and also perform body tracking. MATLAB will be used as the programming software for the ASL recognition system. As for the recognition part, Principle Component Analysis (PCA) will be used. PCA is statistical technique commonly used image compression, gesture recognition, and for finding patterns in data with many dimensions. The algorithm needed for this system was separated into 5 stages for simulation. This includes: Hand Segmentation, Normalization, ASL Alphabet Database, Gesture Recognition, Graphical User Interface (GUI). The sign recognition algorithm using PCA was efficient as it is capable of producing a recognition rate of 91.45%. The GUI was created successfully as a .exe file so that people without MATLAB is also able to use the system.

Keywords: American Sign Language, Microsoft Kinect, Principle Component Analysis, Depth Image.

1. Introduction

Hand gestures are widely used in various forms of non-verbal communication, ranging from communication between two individuals to human-machine interaction. This is especially true for deaf people as sign language is their native language. An approximate of 360 million people has disabling hearing loss. Hearing loss greater than 40 decibels (dB) for adults and 30 dB in children in the better hearing ear is considered disabling. Most people with impaired hearing will learn sign language to aid them in communication throughout their daily lives. Learning a new language is not easy, likewise teaching. Deaf children with parents who are also deaf will easily pick up sign language naturally as how hearing children learn to speak from their hearing parents. However, more than 90 percent of deaf children are born to parents who are able to hear. Hearing parents may face difficulties in teaching sign language to their deaf children as the language is new to both of them.

Various types sign language recognition system such as vision and glove based are currently being used. The most common approach for Sign Language (SL) recognition is vision based with more leaning towards Two-Dimensional (2D) based system as they are relatively low cost due to webcams that are already built into almost every existing laptop. In order to detect the signing hand from 2D RGB images, the system has to pre-process the images to remove noise and then only detect and extract skin colored pixels using methods like hue, saturation, value (HSV) color space [1-2]. As for hand detection, A. S. Konwar et al. applied uncanny edge detection algorithm on 2D RGB images with skin pixels extracted to extract the hand gesture [2]. Due to geometric variations and uneven background light conditions, the system has only a detection rate of 65%. In J. R. Pansare and M. Ingle's work, an Edge Orientation Histogram (EOH) algorithm was use to achieve a recognition rate of 88.26% under proper lighting conditions in complex background while 87.82% under mixed lighting condition in static background [1].

Since lighting condition and background affects the recognition rate of 2D RGB image based system, glove based methods are introduced. M. Aarthi and P. Vijayalakshmi have developed a flex sensor-based gesture recognition module to recognize sign language [3]. Based on the voltage values returned by the flex sensor, it could determine the corresponding sign. Additional sensors such as a gyroscope is need for non-static signs to determine movement [4]. Although glove based methods are generally more accurate under all lighting conditions and background, it is necessary for the signers to wear them at all times in order to use the system.

As for depth image processing systems, M. Geetha et al has presented a study on a Vision Based Dynamic Gesture Recognition of Indian Sign Language on Kinect based Depth Images [5]. The author proposed a new trajectory based feature extraction using method using the concept of Axis of Least Inertia for global feature extraction. These extracted features are then combined with a local feature extraction using PCA to identity unknown signs. The combination of both global and local features presented a very high accuracy of recognition rate. Other than than, R. Erdefi et at proposed a study on combining Depth Image and Skeleton Data from Kinect for Recognizing Words in the Sign System for Indonesian Language [6]. An accuracy of 96.67% was obtained in one of the different scenarios tested.

Therefore, a depth image based Hand Gesture Recognition System (HGRS) for ASL Alphabet Recognition System that is able to work under all lighting and background condition without the usage of gloves is proposed. Instead of using the traditional 2D images, the usage of 3D depth images is proposed. This is because depth images stores information of the distance between the object and camera. This allows the signing hand to be easily segmented out from any background compared to 2D RGB images and also use the depth values for recognition purposes. The objective of this project is to create a working system that can detect ASL alphabets signed by a person and determine if it was performed correctly or not. This will be extremely helpful for anyone trying to learn sign language. The system is to be integrated into a GUI for easy access for the user.

2. Research Methodology

This thesis proposes an ASL Alphabet Recognition System through the use of a Kinect for Xbox One sensor, a relatively low cost but high-performance sensing device. Figure 1 illustrates the various sensors that can be found on the Kinect [12]. This project will be taking advantage of the Kinect's ability to capture depth images. The Kinect's infrared (IR) depth sensor records at a maximum of 512 x 424 resolution with a depth space range of 0.5 to 4.5 meters [12].

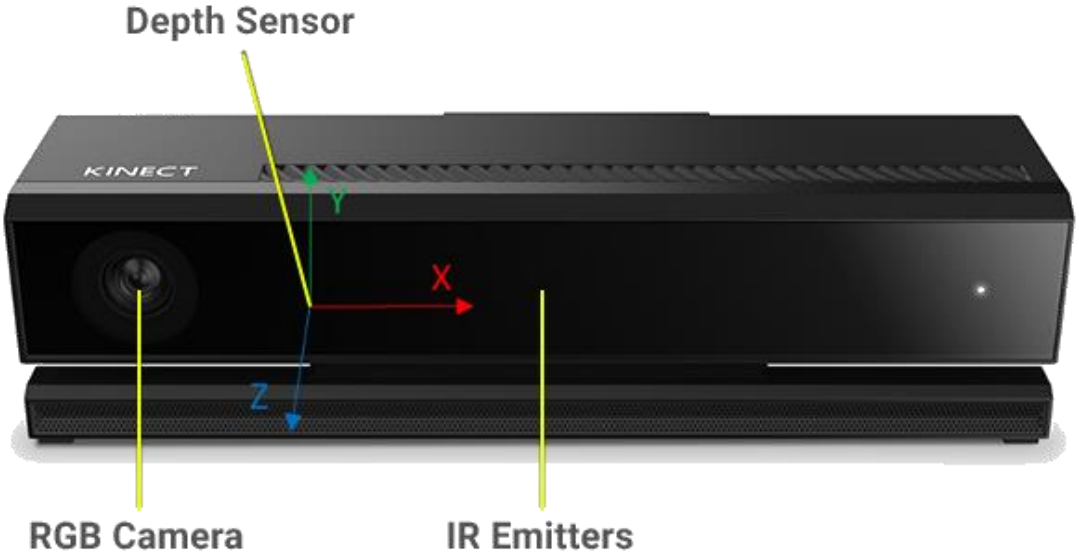


Figure 1. Kinect for Xbox One sensor components [12].

The system's algorithm was written entirely using the MATLAB language in the MATLAB Integrated Development Environment (IDE). The algorithm needed for this system was separated into 5 stages for simulation. This includes: Hand Segmentation, Normalization, ASL Alphabet Database, Gesture Recognition and GUI. The condition set for the input depth image is that the signing hand must be the closes object within the cropped area which will be further explained under the Hand Segmentation and Normalization stage. Figure 2 shows the flowchart on how the system works as an application.

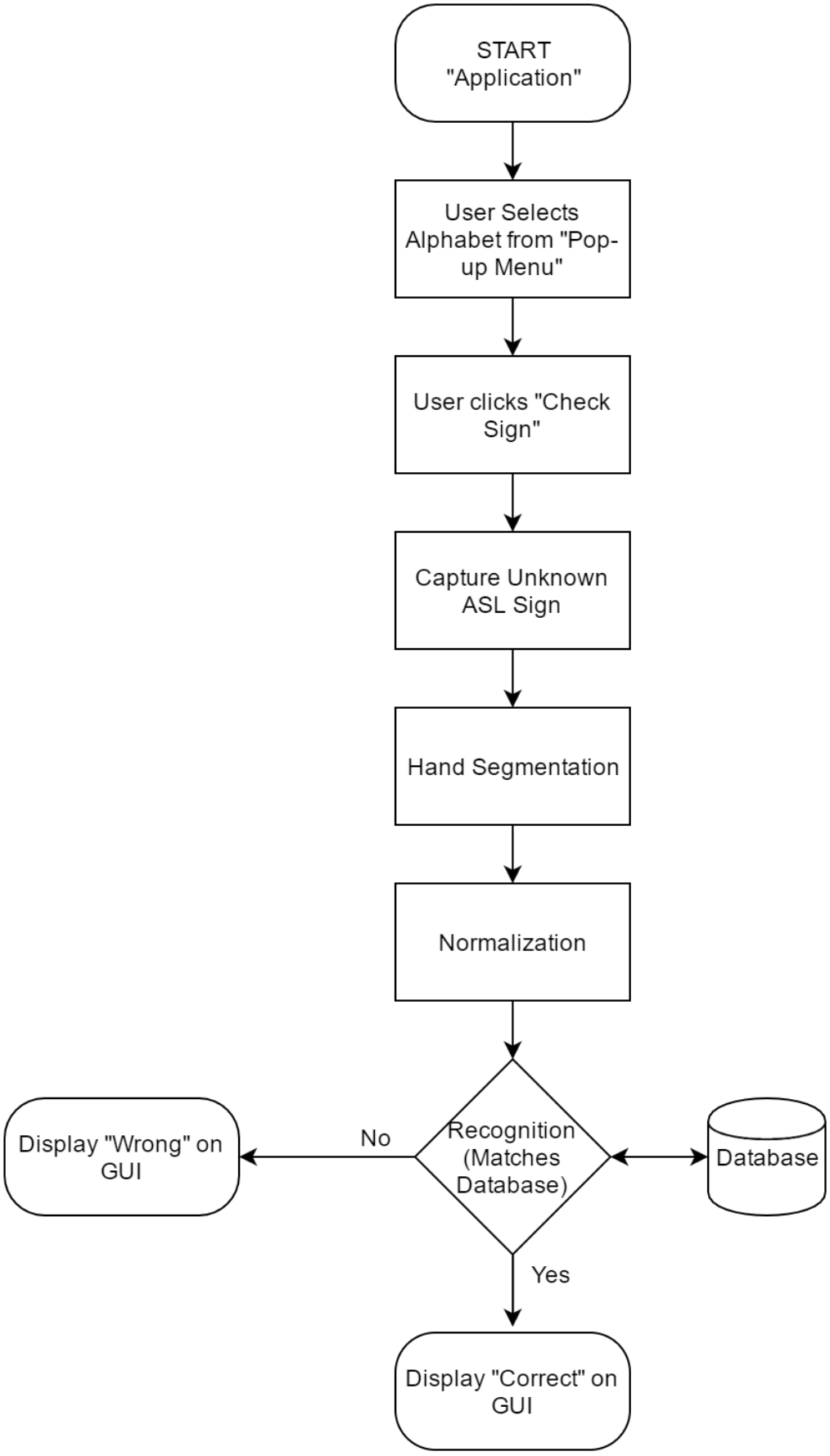

START
"Application"
User Selects Alphabet from "Pop-up Menu"
User clicks "Check Sign"
Capture Unknown ASL Sign
Hand Segmentation
Normalization
Recognition (Matches Database)
No
Display "Wrong" on GUI
Database
Yes
Display "Correct" on GUI

Figure 2. Flowchart for ASL Alphabet Recognition System.

2.1 Hand Segmentation

Figure 3 displays the captured image of ASL alphabet 'G' through the Kinect's RGB camera while Figure 4 is the depth image representation of Figure 3 that was captured through the Kinect's IR depth sensor. These images are captured through the Kinect interfacing with MATLAB using the function "savefig". The depth images are presented in grayscale for objects that are within the field of view of the depth sensor and uses the maximum resolution available on the Kinect depth sensor, which is 512 x 424 pixels. Depth images stores data in each pixel which contains the Cartesian distance represented in millimeters from the camera plane to the objects within the depth space range at a particular (X, Y) coordinate shown in Figure 5.



Figure 3. ASL alphabet 'G' RGB Image captured through the RGB camera.



Figure 4. ASL alphabet 'G' Depth image captured through Kinect's IR depth sensor.



Figure 5. Stored Cartesian distance (Index) and the (X, Y) coordinates.

The closer the object is to the IR depth sensor, the darker the object, opposite if the object is further. In order to segment out the hand, the function "EnableBodyTracking" was set to on for the Kinect. This allows the tracking of individual parts of the body, specifically the hands. The current design of the system will be using the right signing hand of the user, so "DepthJointIndices(12)" will be called in the system to obtain the (X, Y) coordinates metadata for the right hand.

Once the right signing hand position is obtained, a border of 160 x 160 pixels will be drawn over the hand to signify that the signing hand is being detected. A depth threshold will be determined to tell the system when to crop and save signing hand image data based on the border drawn. Furthermore, "HandRightState" was also called to identify whether the hand state is open or closed. This data was also saved for separating the open and closed hands used in Normalization, ASL Alphabet Database and Recognition stage.

2.2 Normalization

This section will consist of the following 3 steps to normalize the image: IR shadow removal, depth normalization, cropping and resizing. Since we are designing the system under the condition where the signing hand is the closes object to the IR depth sensor within the segmented area, in order to normalize out the hand we must first eliminate the IR shadow. Figure 6 illustrates how the IR shadow is formed. Since there is a physical offset between the IR lamp and the IR camera, the object in the foreground cast a shadow which blocks the IR, subsequently preventing the IR camera from picking up the IR which result in an Index = 0. The IR shadow is eliminated by finding all the Index = 0 values in the image and setting it to the furthest value possible, Index = 4000.

With the IR shadow removed, the signing hand can be normalized out by finding the minimum value of the new depth Image which represents the closest point of the hand to the IR depth camera. The function "min()" was called on the depth image array to find the closest point of the hand to the IR depth camera within the segmented image, labelled as ImgHandStart. In order to obtain the full range of values of the signing hand, an offset, ImgOffset of Index = 90 (90 millimeter) from ImgHandStart was assigned to ImgHandEnd. Thus, consistency will be maintained in the system as all signing hands will have a common start point of Index = 0 and end point of Index = 90 and a background of Index = 4000.

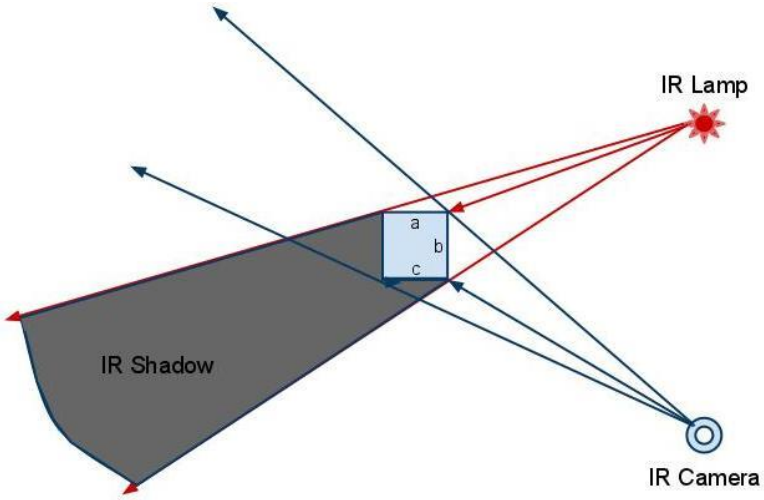


Figure 6. IR shadow due to physical offset between IR lamp and IR camera.

Next, after normalizing the depth of the segmented depth image, the depth image will be cropped and resized again using the function "imresize()". The cropping algorithm will be determined based on the first non-4000 pixel from the left and right corner of the image with a fixed height based on the "HandRightState" value obtained during the segmentation stage. Since the width of each alphabet will be different, the width of image is set to a fixed length of 50 pixels. If the signing hand is in an open state, the corresponding images will be resized to a new resolution of 80 x 50 pixels; whereas for closed state, corresponding images will be resized to a new resolution of 40 x 50 pixels. This consistent size is necessary in order to store the data into a single array variable. The normalization algorithm flowchart is shown in Figure 7.

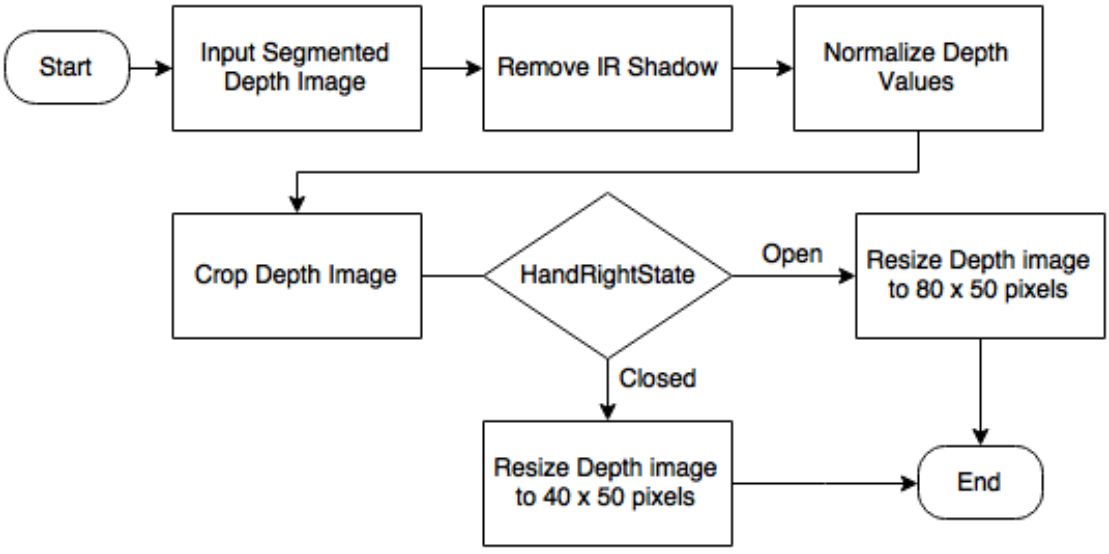


Figure 7. Flowchart of normalization algorithm.

2.3 ASL Alphabet Database

In In order to create an ASL Alphabet Database, a set of training depth images must be obtained for each ASL alphabet. A total of 10 variations for each ASL alphabet are captured and these depth images will then be segmented and normalized. A total of 10 x 24 = 240 images will be stored to create a consistent database. The resultant depth images will be stored into two separate MATLAB array variables labelled as "DatabaseOpen" and "DatabaseClosed" using a MATLAB function called "reshape()" depending on the "HandRightState". This function reshapes either an 80 by 50-pixel depth image into a 4000 by 1-pixel depth image and saves in databaseOpen or a 40 by 50-pixel depth image into a 2000 by 1-pixel depth image and saves it in databaseClosed. Figure 8 displays the flowchart for ASL Alphabet Database algorithm.

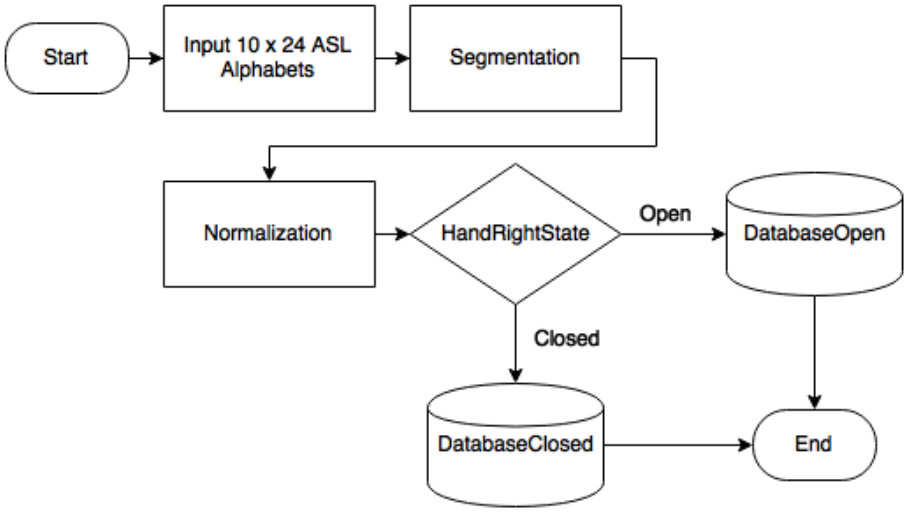


Figure 8. Flowchart of ASL Alphabet Database algorithm.

2.4 Recognition

As for the recognition part, Principle Component Analysis (PCA) will be used. PCA is statistical technique commonly used in gesture recognition, image compression, and for finding patterns in data with many dimensions. PCA consist of 5 steps:

I. Obtain data samples.

The ASL Alphabet database was created and will be used as our data sample.

II. Find the mean of each data set and subtract them from the original data produce a data set whose mean is zero.

Each column $col(x)$ with "x" as the position of the column represents a data set where the mean of each column given as $\overline{col(x)}$.

$$\overline{col(x)} = \frac{\sum_{i=1}^{n} col(x)_i}{n} \quad (1)$$

The new zero mean dataset is derived as *DatabaseAdjust(x)* by taking the original dataset, *Database(x)* and subtract it with the mean $\overline{col(x)}$. With each column subtracted with the mean of their respective self, we will obtain a new array called *DatabaseAdust*.

$$DatabaseAdjust(x) = Database(x_i) - \overline{col(x)} \tag{2}$$

III. Calculate the covariance matrix of the new zero mean data set.

The covariance for the DatabaseAdjust(x_1) and DatabaseAdjust(x_2) is given as below:

$$cov(DA(x_1), DA(x_2)) = \frac{\sum_{i=1}^{n}(DA(x_1)-\overline{DA(x_1)})(DA(x_2)-\overline{DA(x_2)})}{(n-1)} \tag{3}$$

The covariance matrix for more than 2 dimensions (m x n) matrix is then formed based on the equation below:

$$covMat = \begin{bmatrix} cov(DA(x_1), DA(x_1)) & cov(DA(x_1), DA(x_2)) & \cdots & cov(DA(x_1), DA(x_n)) \\ cov(DA(x_2), DA(x_1)) & cov(DA(x_2), DA(x_2)) & \cdots & cov(DA(x_2), DA(x_n)) \\ \vdots & \vdots & \ddots & \vdots \\ cov(DA(x_m), DA(x_1)) & cov(DA(x_m), DA(x_2)) & \cdots & cov(DA(x_m), DA(x_n)) \end{bmatrix} \tag{4}$$

IV. Calculate the eigenvalues and eigenvectors of the covariance matrix.

The eigenvalue, λ and eigenvector, $coeff$ is given by the formula below:

$$covMat \cdot coeff = \lambda \cdot coeff \tag{5}$$

V. Derive the new data set by taking the transpose of eigenvector and multiple the transposed of the zero mean data.

$$score = coeff^{T} \times DatabaseAdjust^{T} \tag{6}$$

PCA will be performed on the ASL Alphabet Database array variable by calling the built-in MATLAB function “PCA” to obtain the corresponding new data set, labeled as “score”. Likewise, PCA is also performed on the unknown sample to identify the corresponding data for recognition. The unknown sample’s data is compared with the PCA variable to recognize which ASL alphabet it belongs to by checking the lowest difference in value of each set of alphabet.

2.5 GUI

After the completion of Hand Segmentation, Normalization, ASL Alphabet Database and Gesture Recognition, these algorithms are then applied to create a single system to for a GUI. The algorithm design in MATLAB are just a means to test and validate the system. It would be inconvenient for the user to type commands through the MATLAB terminal, so a GUI was created to permit higher productivity for those who are not well versed in using MATLAB.

MATLAB's built in GUI creator, GUI development environment (GUIDE) was used to design user interfaces for the ASL Alphabet Recognition System. "Axes" are used to display the RGB camera feed from the Kinect and also the corresponding ASL alphabets illustrations to teach the user how to sign. A "Pop-up Menu" was used to list out all the selectable ASL alphabets in the system. In order to check whether the user's sign is correct, a "button" labeled as "Check Sign" is added into the GUI for the user to click. A "Text view" was added to display the status of the system.

Once the GUI is completed, an Application Compiler App in MATLAB was used to convert the GUI into an executable (.exe) file. Once the details and name of the application was specified. The necessary MATLAB files were included into the main application. The size of the application depends on whether the runtime was included while compiling. The web version will be selected to reduce the file size as the users can go to the MATLAB website to download the runtime necessary for running the application.

3. Results and Discussion

Upon completing the design of the algorithm, a database was created from a set of training depth images. Then, the database created was used in the recognition stage for simulation. The performance and accuracy of the system will be tested based on different individuals signing. The results for each stage proposed in the methodology are thoroughly discussed below.

3.1 Hand Segmentation

Hand segmentation plays an important role for this system as this stage determines the type and size of image the system will be using for both database and recognition. The hand segmentation part is done in real time while recording where the image is updated frame by frame to inform the user that the hand is being tracked. First, EnableBodyTracking" was enabled for the Kinect and the (X, Y) coordinates for the right hand, "HandRight(12)" and right thumb, "ThumbRight(25)" was called using functions "DepthJointIndices".

In order to maintain consistency throughout all inputted depth images, the system only crops and saves the depth image when a threshold distance of 60 to 70cm is reached. To notify the user at what distance will the system capture the sign, the rectangle will display in yellow for the signing hand being too far, red for the signing hand being too close and green within threshold. The corresponding images for ASL alphabet 'B' are shown in Figure 9 (a) for too far, Figure 9 (b) too close and Figure 9 (c) within threshold. Figure 10 shows the captured depth image cropped from Figure 9 (c) using "imcrop" function.



(a) (b) (c)

Figure 9. Rectangle border color for varying distances of ASL alphabet ‘B’



Figure 10: Captured ASL alphabet ‘B’ depth image from Figure 9 (c).

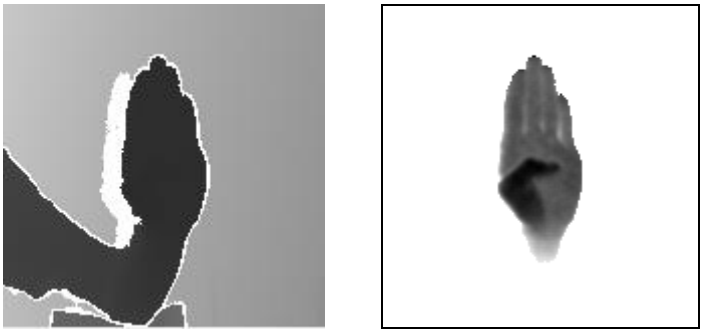
Furthermore, the “handRightState” for each alphabet is recorded down in Table 1 in order to separate the database for open and closed states, namely “DatabaseOpen” and “DatabaseClosed”. Alphabet ‘E’ appears in both open and closed states due to the size of the hand when signing. The larger the hand, the more likely for the Kinect to detect it as open, likewise the opposite.

Table 1. Alphabets open and closed state

HandRightState	**Alphabets**
Open	B, C, D, E, F, G, H, I, K, L, O, P, Q, R, U, V, W, X, Y
Closed	A, E, M, N, S, T

3.2 Normalization

After segmentation, the IR shadow must be removed in order to normalize the depth image. Figure 30 displays the ASL alphabet ‘B’ depth image from Figure 11(a) with IR shadow removed by setting all Index = 0 values to Index = 4000. With the IR shadow removed, we are now able to find the true minimum value of the signing hand in the depth image by offsetting the minimum point to zero as shown in Figure 11(b).



(a) (b)

Figure 11. ASL alphabet ‘B’ Depth image with IR shadow removed and normalized.

The background noise will be further reduced through cropping again. Two different cropping algorithm are designed for “DatabaseOpen” and “DatabaseClosed” Figure 12 shows ASL alphabet ‘B’, ‘G’ and ‘Y’ with the cropping algorithm for “DatabaseOpen” with varying horizontal width and a fixed height of 80 pixels. Figure 13 shows ASL alphabet ‘A’, ‘M’ and ‘T’ with the cropping algorithm for “DatabaseClosed” with varying horizontal width and a fixed height of 50 pixels. These alphabets are picked to illustrate the differences between varying width signs. The cropped images are resized into 50 by 80 pixel image for “DatabaseOpen” and 50 by 40 pixel for “DatabaseClosed” by calling the MATLAB function “imresize”.



Figure 12: ASL alphabet ‘B’, ‘G’ and ‘Y’ using “DatabaseOpen” cropping algorithm.



Figure 13: ASL alphabet ‘A’, ‘M’ and ‘T’ using “DatabaseClosed” cropping algorithm.

3.3 ASL Alphabet Database

All the 24 ASL alphabets of 10 different variations each have been captured and saved into a folder called “raw”. A script was created to normalize and arrange each of the 10 x 24 ASL alphabets in the “raw” folder into 2 separate array variables, “DatabaseOpen” and “DatabaseClosed” using the function “reshape()” as shown in table 2 and 3.

Table 2. “DatabaseOpen” segmented and normalized images.

Alphabet	Segmented	Normalized

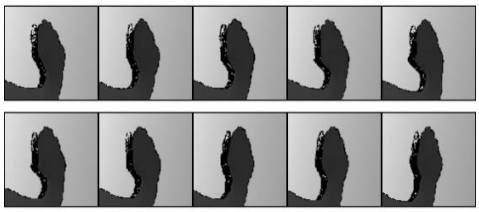
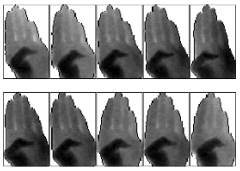
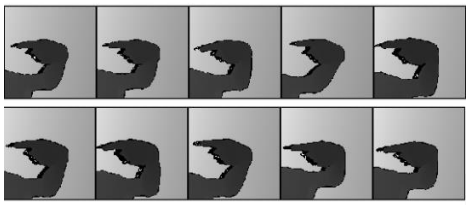
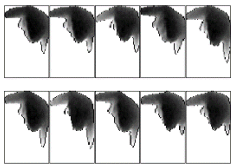
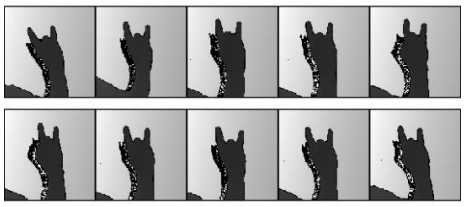
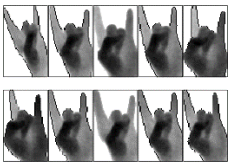
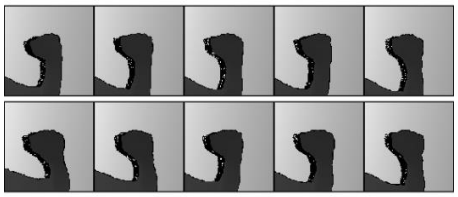
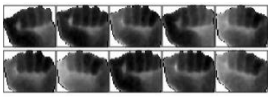
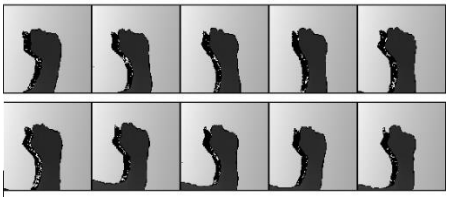
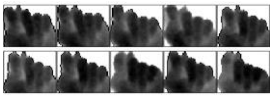
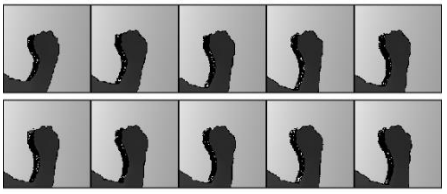
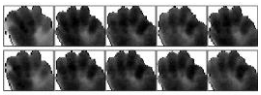
B		
G		
Y		

Table 3. “DatabaseOpen” segmented and normalized images.

Alphabet	Segmented	Normalized
A		
M		
T		

3.4 Recognition

The depth image system was tested across 4 different users with 5 samples for each alphabet. Alphabets “J” and “Z” are not included due to the refresh rate being too slow for motion tracking when “EnableBodyTracking” was enabled. Table 11 displays the recognition rate for each user.

Table 4: Recognition Rate for Users 1 to 4.

User	1	2	3	4
Recognition Rate	90.8%	93.33%	91.67%	90.0%

A mean recognition rate of 91.45% is achieved based on the 4 users in Table 4. Further testing of the recognition algorithm was also carried out on the corresponding RGB images captured together with the depth images while creating the database. The recognition rate of the RGB images are 75.82% with a plain background and 40.78% with a normal background. This shows that 3D image processing is better than 2D due to better segmentation and normalization.

3.5 GUI

After verifying that the GUI is working properly, the GUI along with the required MATLAB files were then compiled into a .exe file using the built-in Application Compiler App in MATLAB shown in Figure 14. The final version of the American Sign Language Recognition System application is illustrated in Figure 15. The ASL alphabet image will be shown to the user depending on what the user selects. When "Check Sign" button is clicked, the TextView display texts changes to "Analyzing", "Correct" or "Wrong" depending on whether the system is analyzing, correct or wrong sign detected.

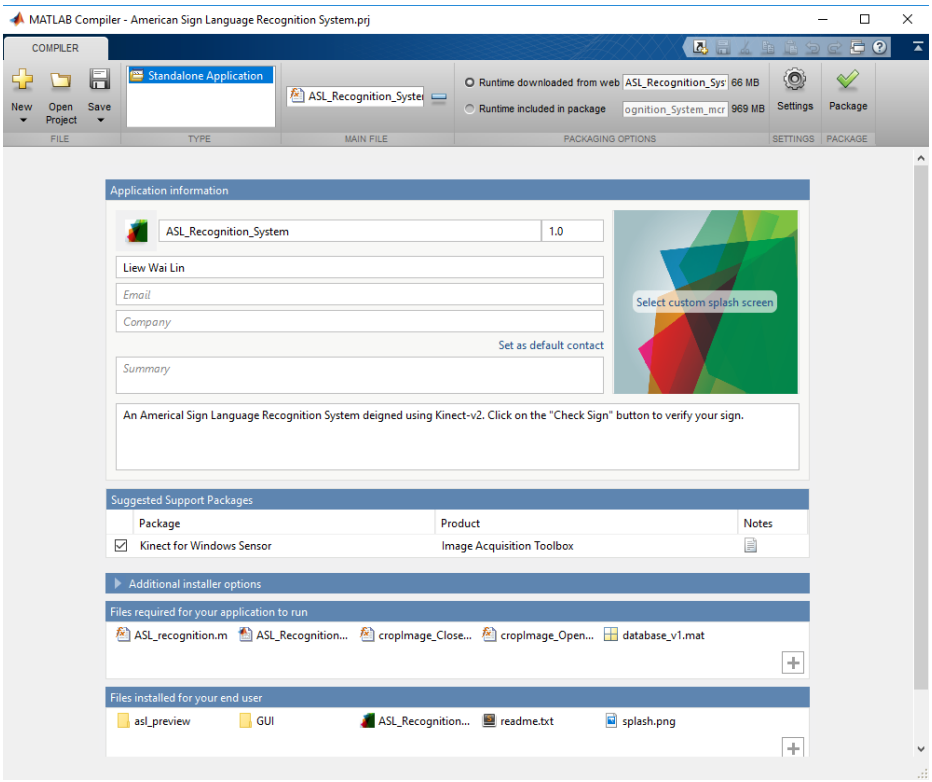


Figure 14. MATLAB Application Compiler.

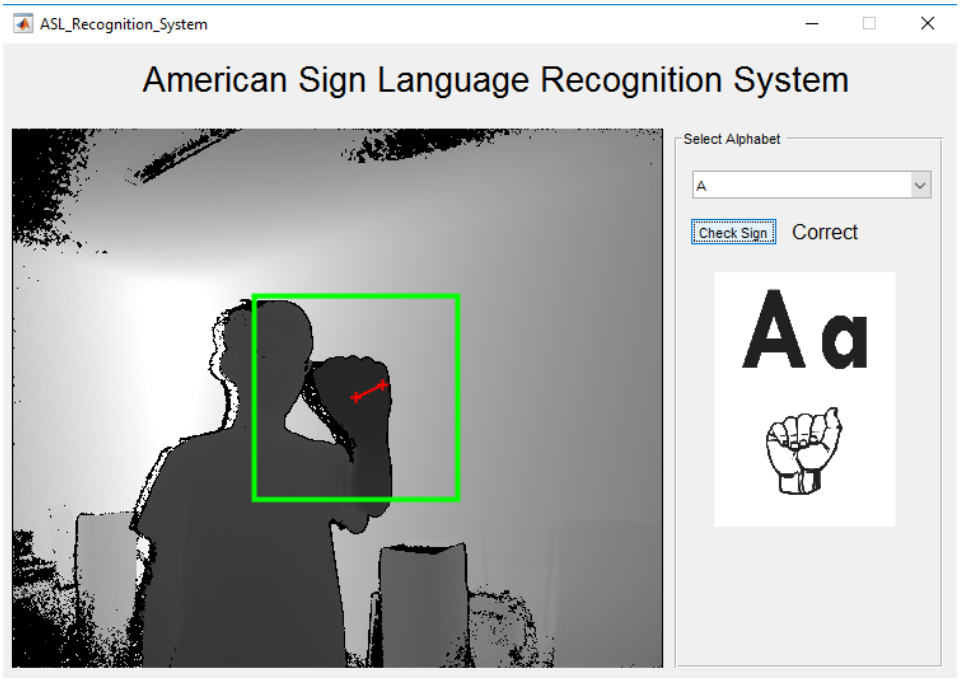


Figure 15. Finalized American Sign Language Recognition System application.

4. Conclusions

This project presents an ASL Alphabet Recognition System using MATLAB interfacing with a Kinect. All objectives such as designing an algorithm for segmentation, normalization and recognition of ASL Alphabets using depth images from the Kinect, designing a GUI and create an executable file for the system and determining the accuracy of the ASL Alphabet Recognition System compared to 2D image processing is achieved. The ASL Alphabet recognition, segmentation and normalization algorithm were constructed using a MATLAB. The ASL Alphabet Recognition System was capable of producing a recognition rate of 91.45% which demonstrates that the recognition algorithm is accurate.

References

[1] J. R. Pansare, M. Ingle, " Vision-Based Approach for American Sign Language Recognition Using Edge" in *2016 International Conference on Image, Vision and Computing*, 2016, DOI: 10.1109/ICIVC.2016.7571278.

[2] A. S. Konwar *et al*, "An American Sign Language detection system using HSV color model and edge detection" in *International Conference on Communication and Signal Processing*, 2014, DOI: 10.1109/ICCSP.2014.6949942.

[3] P. Vijayalakshmi, M Aarthi, "Sign language to speech conversion" in *2016 International Conference on Recent Trends in Information Technology (ICRTIT)*, 2016, DOI: 10.1109/ICRTIT.2016.7569545.

[4] P. Das *et al*, "Analytical study and overview on glove based Indian Sign Language interpretation technique" in Michael Faraday IET International Summit 2015, 2015, DOI: 10.1049/cp.2015.1650.

[5] M. Geetha *et al.*, "A vision based dynamic gesture recognition of Indian Sign Language on Kinect based depth images," in *Emerging Trends in Communication, Control, Signal Processing & Computing Applications (C2SPCA)*, 2013, DOI: 10.1109/C2SPCA.2013.6749448

[6] R. Erdefi *et al.*, "Combining depth image and skeleton data from Kinect for recognizing words in the sign system for Indonesian language (SIBI [Sistem Isyarat Bahasa Indonesia])," in *Advanced Computer Science and Information Systems (ICACSIS)*, 2013, DOI: 10.1109/ICACSIS.2013.6761606

[7] Microsoft, "Kinect hardware," Microsoft Developer Network, 2016. [Online]. Available: https://developer.microsoft.com/en-us/windows/kinect/hardware [Accessed: May 10, 2016]

eureca 2016 – Conference Paper
Paper Number 2EE04

Torque Angle Control for Scan Mirror Satellite Applications

Maitha Is'haq Yaquob Al-Sawafi[1], Aravind CV[2*], Charles R Sarimuthu[1], A Jagadeeswaran[2]
[1]School of Engineering, Taylor's University, Malaysia.
[2]Department of Electrical and Electronics, Sona College of Technology, Salem, India.
[*]*aravindcv@ieee.org*

Abstract
Several space mechanisms' positioning and motion control are established using brushless motors. The underlying reason of using the said motors is their strong construction, high power output to weight ratio and acceptable performance at low or high speed. Most commonly used applications are scan mirror, thrust vector control actuators, fuel valve control actuator, control moment gyroscopes and low thermal emission applications etc. For obtaining a system comprising of a low maintenance cost and optimized life, brushless motors are used instead of brushed motors. Besides these the brushless motors have many other advantages but the complexity of building up the power electronic commutation circuitry for driving the motor is inevitable. The strategy of replacing the brushed DC motors by brushless motors is adopted very often. The objective of this project is to tilt the scan mirror through an angle and evaluate the performance of proposed motor in comparison with existing motor. In this research, performance of the 2D models related to Limited Angle Brushless Torque (LABLT) motor with bread-loaf rotor magnet and radial rotor magnet was evaluated while comparing average torque and motor constant square density. From the selected proposed model, the average torque of 30.99 Nm and average magnetic flux of 0.34 Wb is higher as compared to the conventional model.

Keywords: Space, Scan Mirror, Limited Angle Brushless Torque Motor, Brushless Motor

1. Introduction

The positioning mechanism of the scan mirror application in the satellite system demands great fidelity and precision. Weight of the system is an important factor in the aerospace systems, therefore the weight of the application system is considered more important than the configuration. For obtaining a system comprising of a low maintenance cost and optimized life, brushless motors are used instead of brushed motors [1].

Besides these the brushless motors have many other advantages but the complexity of building up the power electronic commutation circuitry for driving the motor is inevitable. The strategy of replacing the brushed DC motors by brushless motors is adopted very often [2].

Competitive advantage of Permanent Magnet (PM) Brushless motors these days is due to their power electronics upgrade, high power density type PM, microelectronics upgrade and most importantly its cost effectiveness. These high fields PM machine works well in robotic, optical scanning for speed and position control. Furthermore, brushless motor has a competitive edge over DC commutator motor because of high torque to weight ratio, precise positioning and maintenance free operations [3].

Applications which requires small electrical signal to ignite limited mechanical rotation includes optical scanning, direct laser mirrors, thermal imaging etc. In scan mirror mechanism where angle resolution, position accuracy and controllability is used, brushless motors are preferred. The brushless direct current motor (BLDC) comprises of a permanent magnet rotor and an armature stator with electronic commutation circuitry fitted with a rotor position sensor. BLDC motor increases the complexity of the motor. Hence, the implementation of the BLDC is the most economical, and less maintenance cost demanding solution [4].

Not much research data and literature are available for the limited angle brushless torque motor (LABLT) and the ways of operating and controlling it. LABLT a rotatory electromagnetic actuator which analyzed to possess lesser weight, simple configuration and less cost consuming as compared to the other brushed and brushless DC motors [5]. The purpose of scan mechanism in the satellite is the rotation at positive and negative selectable scan positions. To meet the requirements of torque in the system, the software tool based on Finite Element Analysis is used for the optimized and proper designing and modeling of the LABLT motor. The obtained optimized results are then used to produce a frameless LABLT. Thus, motor is then constructed in JMAG software.

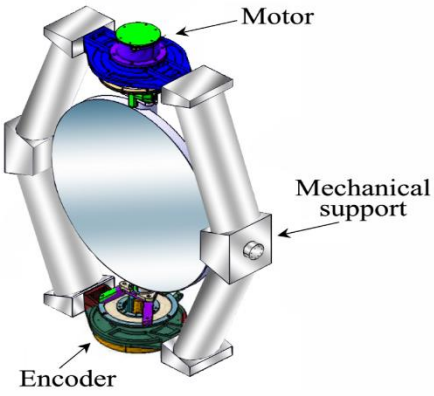


Figure 1. Scan Mirror Mechanism Model [6]

2. Design Concept

Frameless Limited Angle Brushless Torque (LABLT) is proposed for scan mirror satellite applications. LABLT motor is used based on the simplicity of configuration and lesser weight as required for space applications. As shown in Figure 1, this motor can be utilized to facilitate the scan mirror to tilt in two different angles (± θ) with constant torque. LABLT armature design has four poles and each winding is spread over degree 58 mechanical. In order to ensure ±θ degree uniformity in torque, four magnets are mounted on stainless steel ring.

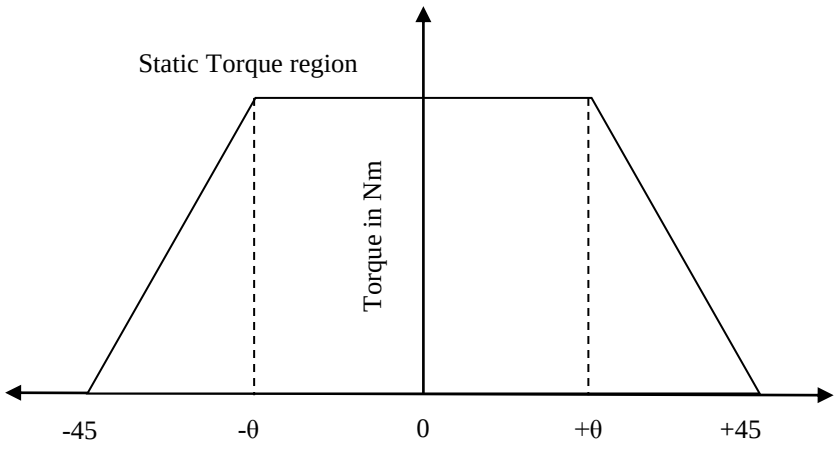
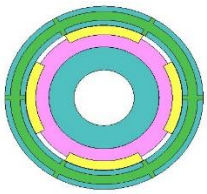
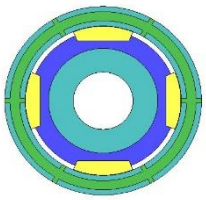
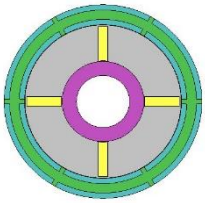
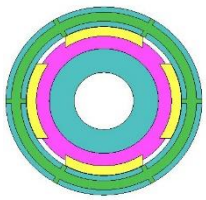
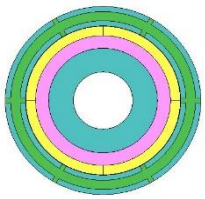
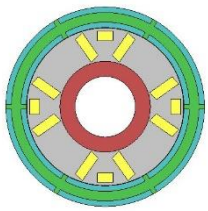


Figure 2. Torque Angle Characteristics

To get smooth and static torque angle characteristics as shown in Fig. 2, different type of permanent magnets are proposed and compared to the conventional machine. Table 1 shows the different configurations of permanent magnet brushless machine. Permanent magnet can be grouped into two different categories: surface PM and interior PM. Theses magnets are radially magnetized and mounted designs, hence no-load density is limited to magnet flux density. For interior PM, in order to concentrate the flux at the pole, larger air gap flux will be used. These large air gaps work in building a circumferential direction for opposite poles of magnets as compared to

surface magnets [7]. Therefore, different magnet orientation are constructed in JMAG® software to choose a suitable magnet for scan mirror space applications to compare with the existing machine. Table 1 shows different shapes of magnet rotor with comparison of average torque, average magnetic flux and Fast Fourier transform (FFT) of the magnetic flux. The higher the average torque the static the torque angle for scan mirror satellite applications [8].

Table 1. Configuration of Magnet Rotor

Model	Type of Magnet Rotor	Average Torque (Nm)	Average Magnetic Flux (Wb)	Fundamental Component of the flux
	Radial magnet rotor	16.42	0.33	0.35
	Bread-loaf magnet rotor	30.99	0.34	0.36
	Spoke magnet rotor	24.29	0.29	0.29
	Parallel magnet rotor	11.27	0.27	0.29
	Ring magnet rotor	32.75	0.18	0.16
	Delta magnet rotor	14.29	0.28	0.29

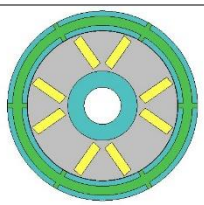
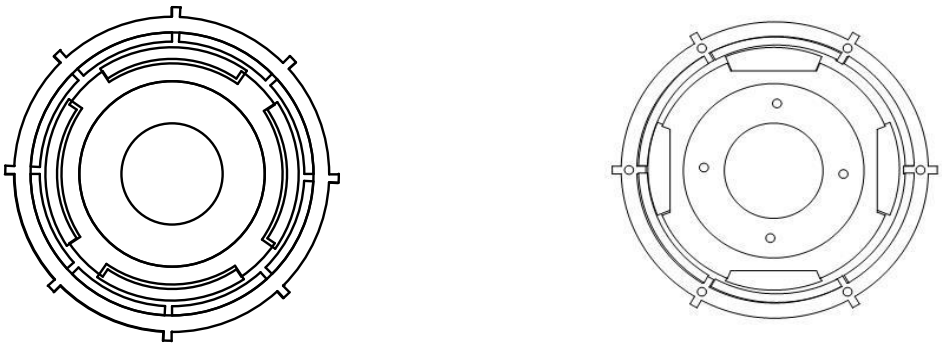
	V-pole magnet rotor	10.26	0.27	0.31

Figure 3(a) shows the conventional machine with radial magnet rotor magnet while Figure 3(b) shows the proposed motor with bread-loaf rotor magnet. The motors that are proposed for satellite applications are surface permanent magnet which is considered as high performance applications and results a smooth torque for the scan mirror to tilt in a critical angle. As the surface permanent magnet is commonly used in space applications by adopting fractional slot pitch windings it minimizes both ripple torque and cogging torque of the rotor magnet.



(a) Conventional Model (b) Proposed Model

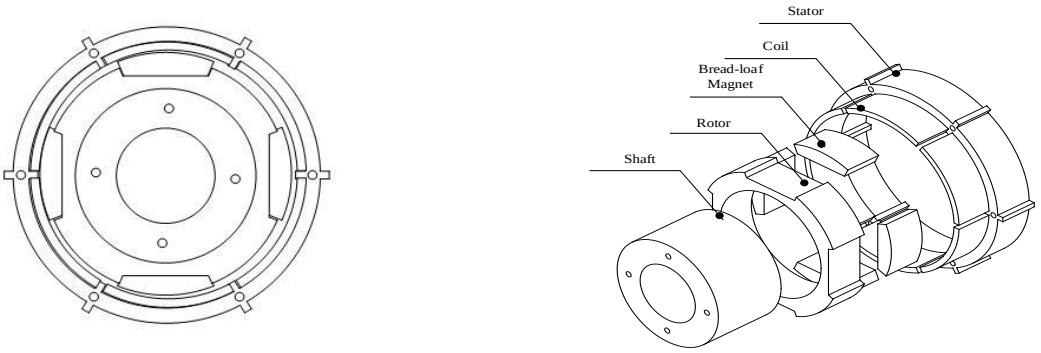
Figure 3. Conventional and the proposed model

To conclude, static torque performance can be improved by using LABLT machine by incorporating bread-loaf magnet to the radial side magnet conventional machine. Different type of magnet used in the machine can resolve the issue of torque pulsation factor. Moreover, the said reduction also increases torque performance and reduces the reluctance of contact flux linkage area. Increase in the number of permanent magnet of rotor poles results in higher torque [9]. Hence, it is inferred that introduction of bread-loaf rotor magnet machine has a smooth torque angle characteristic in comparison to conventional machines.

3. Proposed Design

Fig. 4(a) shows the 2D model constructed by using JMAG® and Fig. 4(b) shows the exploded view of the proposed model designed for scan mirror space applications. The machine has 3 phase armature winding, having four pole of bread-loaf magnet mounted on the surface of the rotor. The model with bread-loaf rotor magnet has more advantages than conventional radial rotor magnet as the design is more critical for scan mirror satellite applications. Since the torque angle characteristics requires a smooth and constant it's more reliable to use the proposed machine for space applications improvement [10]. Table 2 shows the parameter dimensions is used for

both proposed and existing model simulated in JMAG® software. As the proposed machine is designed to tilt the scan mirror into two different angles with no cogging torque. By using the JMAG® software both models are simulated with performance of transient magnetic study and magnetic circuit analysis through FEA and numerical tools.



(a) Proposed 2D Model (b) Proposed Exploded Model

Figure 4. Proposed structure

Table 2. Parameters of Proposed (bread-loaf) Model

Parameter	Value (in mm)
Rotor ring inner diameter	86
Magnet rotor outer diameter	115
Physical radial air gap	0.5
Armature coil inner diameter	116
Armature core inner diameter	124
Armature core outer diameter	138
Armature outer diameter	146

4. Finite Element Method

The overall performance is analyzed using torque and magnetic flux characteristic. The process of FEA method incorporates the original field problems domains. The domains are referred to as major domains which are further divided into different sub domains. Each sub domain considers the potential distribution which is calculated using numerical methods or polynomial solutions and determines the optimal criteria [11]. In order to ensure precise analysis of outcomes, transient magnetic study is necessary. Same methodology has been opted in designing of both conventional and proposed machine. In order to ensure numerical results, the torque characteristic and magnetic flux flow are plotted. The permanent magnet rotor of the machine generated with same size and different shapes.

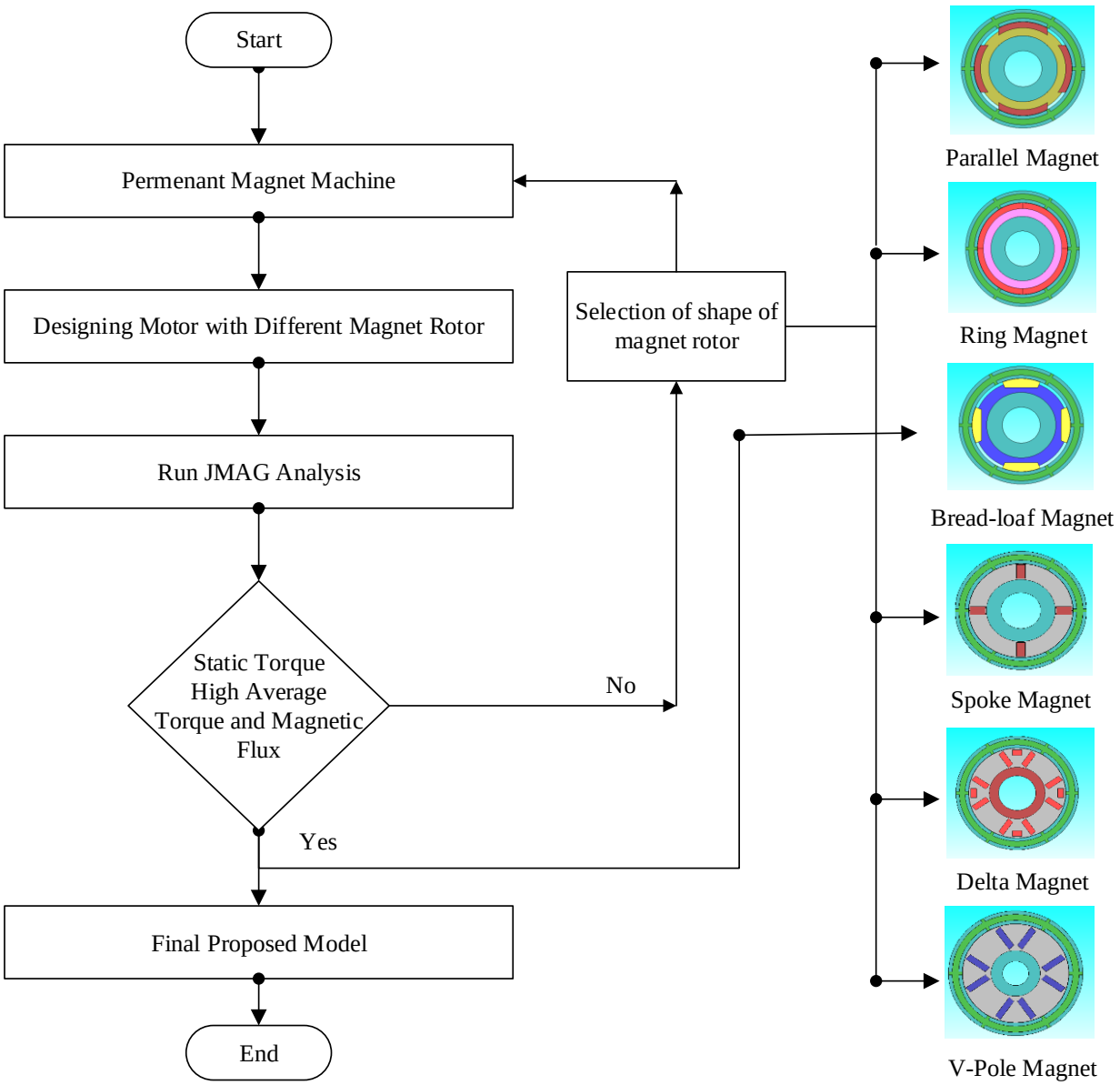


Figure 5. Selection Procedure

5. Parametric Consideration in Analyzing Machine design

There are several formulae used to analyze the results of the proposed machine constructed in JMAG® software. The formulas below determine the characteristics of the torque.

5.1 Frequency and Period of the Proposed Machine

In the proposed motor, the motor rotation through $1/N_r$ of revolution, the flux linkage of armature has one periodic cycle and thus, the frequency of back- emf induced in the armature coil N*r* times the mechanical rotational frequency. In general, the mechanical rotation frequency, f_m and the electrical frequency, f_e for the proposed three phase machine can expressed as in Equation 1 and end time, T is calculated using Equation 2.

$$f_e = N_r f_m \tag{1}$$

$$T = \frac{1}{f_e} \tag{2}$$

Where,
N_r = The number of rotor pole
f_e = The electrical frequency
f_m = The mechanical rotation frequency
T = End Time

5.2 FEC Flux Linkage at Maximum FEC Current Density, J_E

Equation (3) is important in order to determine the number of turn of the field excitation coil (FEC). First of all, the input current is assumed to be maximum in order to get an ideal number of turn that can withstand maximum current of DC coil and the coil slot area can be measured using the JMAG Designer. Equation (3) shows the FEC flux linkage formula.

$$A_E = \frac{J_E \alpha_E S_E}{N_E} \tag{3}$$

Where,

J_E = Coil current density
A_E = Input current FEC
α_E = FEC filling factor (set to 0.5)
N_E = Number of turns of FEC
S_E = Coil slot area (estimate the slot area from the drawing)

5.3 Parametric Consideration in Machine design

The formulas used to calculate the parameters are as follows:

$$K_t = \frac{T}{i} \tag{4}$$

Where T is the torque in newton meters and i represent the current in the coil in Amperes.

$$K_m = \frac{K_t}{\sqrt{P}} \tag{5}$$

$$P = I^2 R \tag{6}$$

Where K_t the torque constant and P is the resistive power loss in watts. The power is calculated using equations in the current in the coil in amperes whilst the R represents the resistance of the coil in ohms.

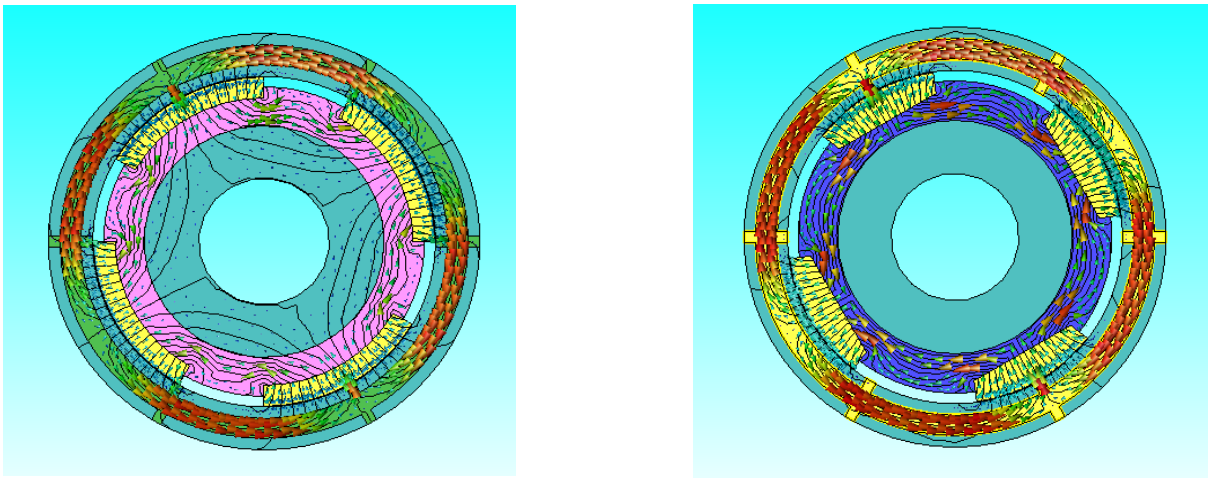
$$G = \frac{K_m{}^2}{V} \tag{7}$$

Where K_m is the motor constant and V represents the volume of the machine.

6. Results and Discussion

6.1 Magnetic Flux Density

Fig.6 shows the flux leakage of the proposed model is reduced as compared to the conventional model. Hence, the proposed machine is designed to enlarge the flux linkage generated in the air gap between bread-loaf magnet rotor and stator. Maximizing the linkage flux of the machine results a higher torque of the motor performance [10].



(a) Conventional Model (b) Proposed Model

Figure 6. Magnetic flux density

6.2 Motor Constant Square Density

In the table below the torque speed produced by two different types of magnet rotor bread-loaf and radial that is constructed in JMAG® software. To find the volume the cross sectional area is multiplied into the stack length of the model. The torque constant, motor constant and motor constant square density are calculated and shown in the Table 3 below for the conventional and proposed model. From the results calculated it shows that the bread-loaf magnet has a higher motor constant square density as compared to radial magnet rotor.

Table 3. Performance analysis

Parameter		Proposed Bread-loaf Magnet	Conventional Radial Magnet
I	$[A]$	5	5
V	$[mm^3]$	580156.9	572359.5
T_{avg}	$[Nm]$	0.0275	0.0248
K_t	$[Nm/A]$	0.0055	0.00496
K_m	$[Nm/A/W^{-(1/2)}]$	0.0055	0.00496
G	$[(Nm)^2/A^2/W^{-(1/2)}/mm^3]$	**5.214E-11**	4.298E-11

Fig.7 display the results of torque angle characteristics wherein the bread-loaf motor has a static torque speed characteristic that can run in both positive and negative regions.

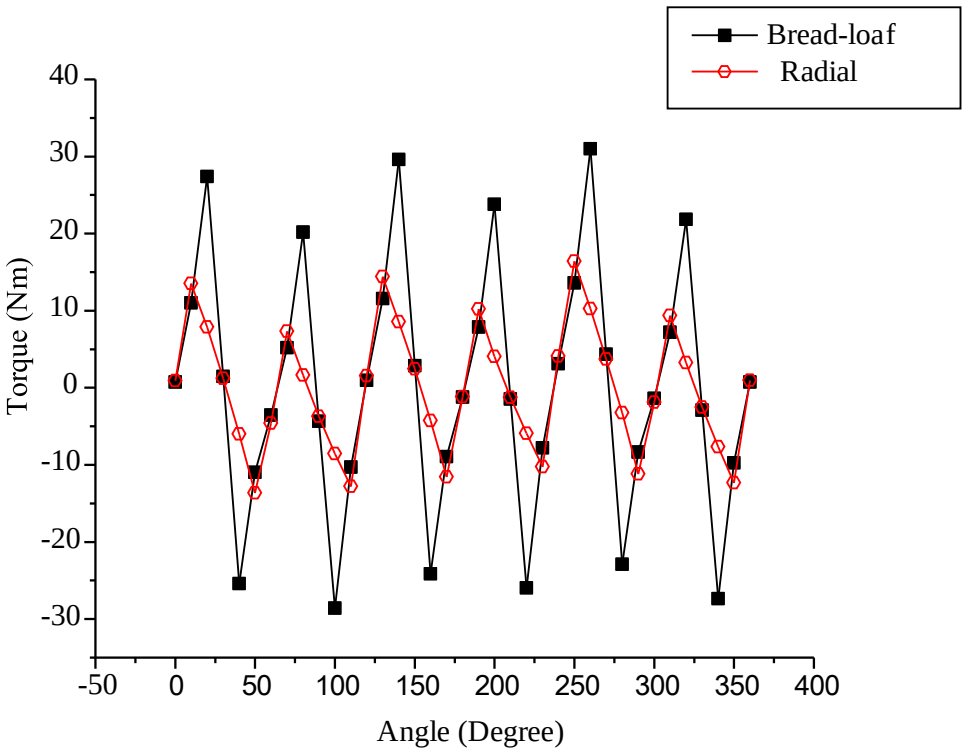


Figure 7. Torque characteristic comparison of conventional and proposed machine

7. Conclusion

The basic science behind scan mirror for satellite application is to get a stable torque which is achieved when the mirror is rotated in positive and negative region. The project was initiated after getting complete command on the software JMAG. The underlying reason of the research was to propose a new design of a motor for satellite space system. Software was introduced to initiate 2D model and analysis was conducted in order to have torque graph along with magnetic flux graph. The said parameters were evaluated using 7 different models. From the selected proposed model the average torque of 30.99 Nm and average magnetic flux of 0.34 Wb is higher as compared to the conventional model. Considering all the designs and topologies, they have identified that the bread loaf type topology has proved to have better performance which is quoted to be approximately higher than conventional model.

8. Reference

[1] W. Fei and P. Luk, “A New Technique of Cogging Torque Suppression in Direct-Drive Permanent-Magnet Brushless Machines,” IEEE Transactions on Industry Applications, vol. 46, no. 4, pp. 1332-1340, 2010.

[2] Y. Liu, Z. Zhu and D. Howe, “Direct Torque Control of Brushless DC Drives With Reduced Torque Ripple,” IEEE Transactions on Industry Applications, vol. 41, no. 2, pp. 599-608, 2005.

[3] B. Abdi, J. Milimonfared, J. Shokrollahi Moghani and A. Kashefi Kavani, "Simplified Design and Optimization of Slotless Synchronous PM Machine for Micro-Satellite Electro-Mechanical Batteries," Advances in Electrical and Computer Engineering, vol. 9, no. 3, pp. 84-88, 2009.

[4] Z. Zhu and D. Howe, "Analytical prediction of the cogging torque in radial-field permanent magnet brushless motors," IEEE Trans. Magn., vol. 28, no. 2, pp. 1371-1374, 1992.

[5] A. Jabbari, M. Shakeri and A. Gholamian, "Rotor Pole Shape Optimization of Permanent Magnet Brushless DC Motors Using the Reduced Basis Technique," Advances in Electrical and Computer Engineering, vol. 9, no. 2, pp. 75-81, 2009.

[6] A. Jagadeeshwaran, S. Vijayshankar, N. Kannan and C. V. Aravind, "Limited angle BLDC for scan mirror application in space satellite system," in IEEE Aerospace and Electronic Systems Magazine, vol. 31, no. 6, pp. 24-32, June 2016.
doi: 10.1109/MAES.2016.160015

[7] M.A. Rahman, "Advances in Interior Permanent Magnet (IPM) Motor Drives," in Conf. IEEE PES in Africa, Durban, South Africa, pp. 372-377, 2005.

[8] S. Morimoto, M. Sanada, and Y. Takeda, "Wide-Speed Operation of Interior Permanent Magnet Synchronous Motors with High-Performance Current Regulator," IEEE Trans. on Ind. Applicat., vol. 30, pp. 920-926, 1994.

[9] H. Toda, K. Senda and M. Ishida, "Effect of material properties on motor iron loss in PM brushless DC motor," IEEE Trans. Magn., vol. 41, no. 10, pp. 3937-3939, 2005.

[10] S. Morimoto, M. Sanada, and Y. Takeda, "Wide-Speed Operation of Interior Permanent Magnet Synchronous Motors with High-Performance Current Regulator," IEEE Trans. on Ind. Applicat., vol. 30, pp. 920-926, 1994.

[11] A. Kameari, "Local Force Calculation in 3D FEM with Edge Elements," Applied Electromagnetics in Materials, pp. 231-240, 1993.

eureca 2016 – Conference Paper
Paper Number 2EE05

A New Generator Topology for Wind Power Generation

Muhammad Sartaj Khan[1], Aravind CV[1,*], Charles R Sarimuthu[1], MD Shahrukh Adnan Khan[2]
[1]School of Engineering, Taylor's University, Malaysia.
[2]University of Asia Pacific,Bangladesh.
[*]*aravindcv@ieee.org*

Abstract
This paper illustrates the concept of electrical machine designed for wind turbine application. The energy consumption of the world is on a continuous rise due to increase in population as well as the advancement in technology which are responsible to provide a comfortable environment. Hence producing electrical power through renewable energy has been topic of research lately. Wind energy like solar energy is one of the renewable energy that is abundantly available at almost every part of the earth. Generators of various configurations are made to extract the electrical power from wind energy. The use of permanent magnet in generators has been on rise due to increased performances and cheaper cost factor. A topology for the operational conditions of such machine to increase the capability of wind turbine operation span under the low wind speed is also presented The power generating capability of such machine is influenced by the magnetic flux interactions in the air-gap. Recent studies in this domain, proposes use of dual magnetic circuit through a double stator or double rotor for various applications. As a reference wind generator developed using an outer rotor developed in our lab is taken and is re-modified with a dual magnetic circuit. To design a generator with capabilities of delivering electrical power output through connection with wind turbine, generators on the basis of slots-poles combination configuration were designed with interior permanent magnet implementation on rotor using numerical design tool. Through this software finite element analysis is applied on the models and analyzed based on the magnetic flux results. The model configuration of 12S-10P is selected as it provides an increase of 33% in magnetic flux flow. Furthermore, the machine is further modeled under two modes of half motoring and only generating operation to increase the capability of wind turbine operation under the low wind speed. The efficiency obtained when simulated under various low wind speed condition is an average of 75% under half motoring condition while when operated in completely generating mode under the optimum wind condition the efficiency lies in the region of 75%.

Keywords: Wind Energy, Double Stator, Generator Topology, Operating Capability, Low Wind Speed Span

1. Introduction

With the advancement of the society it is now generally accepted that combustion method for electromechanical conversion of energy such as burning of fossil fuels ends up contributing significant negative effect on the earth climate [1].

Several studies have been carried out to understand the whole phenomenon and it has been found out that the usage of bio-fuel is the primary source of carbon dioxide (CO_2) in the world, the emission of CO_2 contribution in world is approximately at 40% by the electricity generation sector as the highest among various contributors [2], hence the focus has shifted towards the development of energy harvesting procedure through the renewable resources such as solar, hydro, wind etc. Hence low-carbon electricity generation is becoming an essential objective of energy generation. This has resulted in the fastest growth of wind energy sector among other various forms of energy [3]. By 2020 European Union is aiming to supply 20% of its energy consumption demand through wind energy [4].A wind energy conversion system (WECS) works on the principles of kinetic energy. It can be viewed under aerodynamic, mechanical and electrical aspects; generator is the part which connects the mechanical part to electrical part [5].

A generator falls under the category of dynamic machine. Generally, in a generator a mechanical force comprising either of kinetic energy or potential energy is responsible for rotating the generator. The core components of a generator are the rotor which provides the required field through rotation and the stator which holds the armature windings on itself. The use of permanent magnets has been on rise in designing the electrical machines as they provide the ability of more precise speed control as well as better efficiency [6]. In a system, high amount of energy is lost due to the effects of power loss in copper wires, hence replacing the wires by permanent magnets results in increase in efficiency [7]. Furthermore, the advancement in magnet designing technologies and power electronics control field has also played a factor in the rise of permanent magnet usage in generation sector. Statistics have showed that since 2011 the use of permanent magnet generator has increased from 17% to 40%, indicating the radical increase as well as available market place for them [8].

Based on the wind speed characteristics of Malaysia recorded by Malaysian Metrological department, typical wind speed ranges from as low as $0ms^{-1}$ to $13ms^{-1}$ with a highest mean daily wind speed of 3.8 ms^{-1} recorded at Mersing, Johor [9-10], indicating the low force provided by the wind in Malaysia. Figure 1 shows the monthly wind speed trend for several cities in Malaysia throughout a year.

Technically it is not possible to have the wind turbine operate at high speed due to mechanical limitation such as tearing, however on the upper limit of the wind speed pitch control are responsible to maintain the working of wind turbine, in case of further increase of speed the wind turbine has to be shut down to prevent excessive wear and destruction.

Ideally for the wind turbine to start operating, around $3.5ms^{-1}$-$5ms^{-1}$ wind speed is required [11], however as indicated by the mean wind speed value for each month in Figure 1, most of the times the wind speed falls under the low side of the range and

can result in discontinuity in power generation. Hence for a generator which is to be used for wind turbine application in Malaysia, the most important factor to consider while designing is to have it provide an output of high torque and efficiency at low speed due to the fact that the wind speed is only capable of rotating the rotor at low speed most of the time [12]. Furthermore, by having a generator that is able to operate beneath the typical starting operating speed of 3m/s - 5m/s, the operating capability of the wind turbine power generation system can be increased and discontinuity could be decreased.

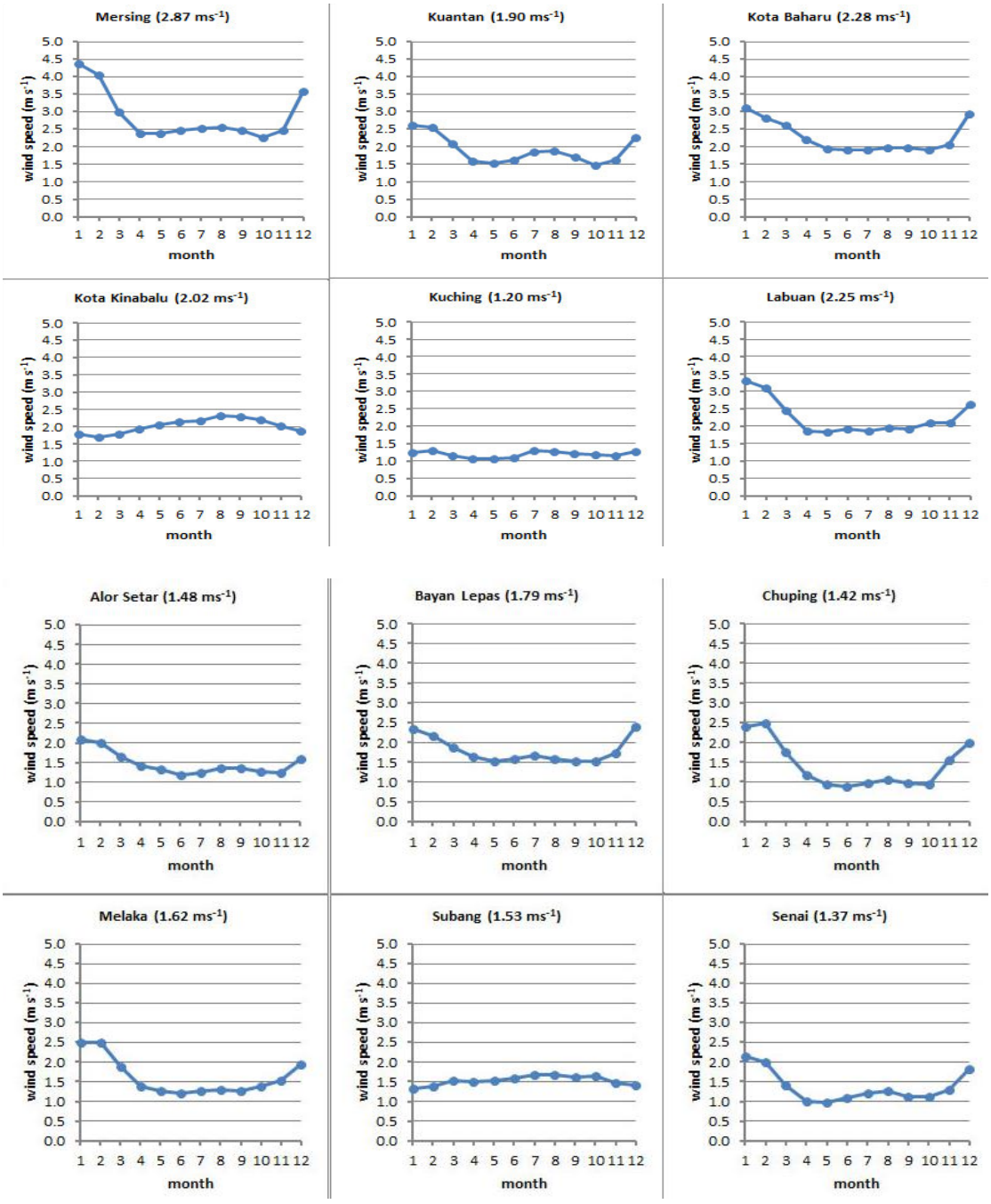


Figure 1 Monthly mean wind speed for cities in Malaysia, 1989-2008 [10].

2. Theoretical Framework

2.1 Design Concept

The continuous change in the wind speed poses the biggest factor in the discontinuity of the wind energy conversion smooth operating as well as low wind speed in Malaysia as shown in Figure 1. The wind can be divided into two categories i.e. increase in the speed and decrease in the speed. During the speed change in shape of increase or decrease to a certain extent, pitch control mechanism plays an important part in maintaining the speed of a turbine constant and hence also keeping the rpm of generator constant.

However, the pitch control is capable of performing the following act till a critical speed in both the upper and the lower limit of the speed. When the wind speed is very high, a shutdown is required due to mechanical constraints while when the speed is very low, the operation is also in need of cutting off due to variable low wind speed unable to move the generator in constant rpm. The following phenomenon is showed in Figure 2.

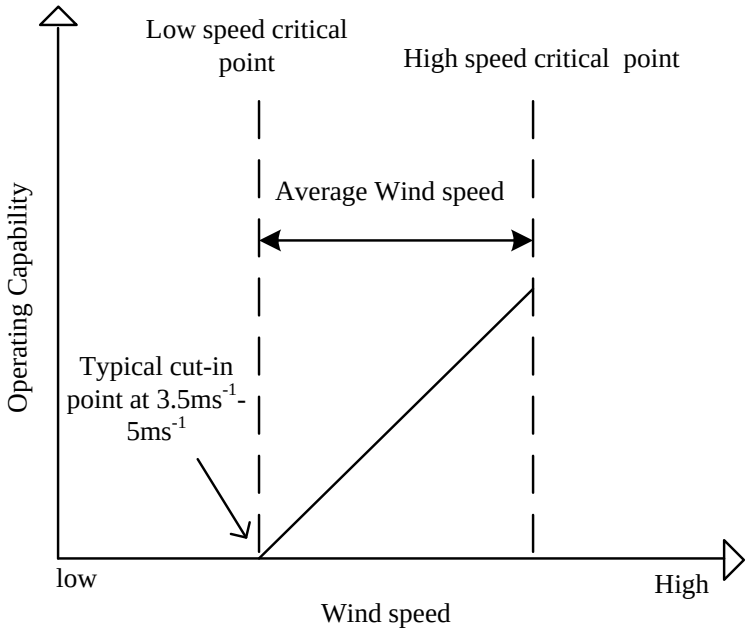


Figure 2 Typical wind turbine operating conditions

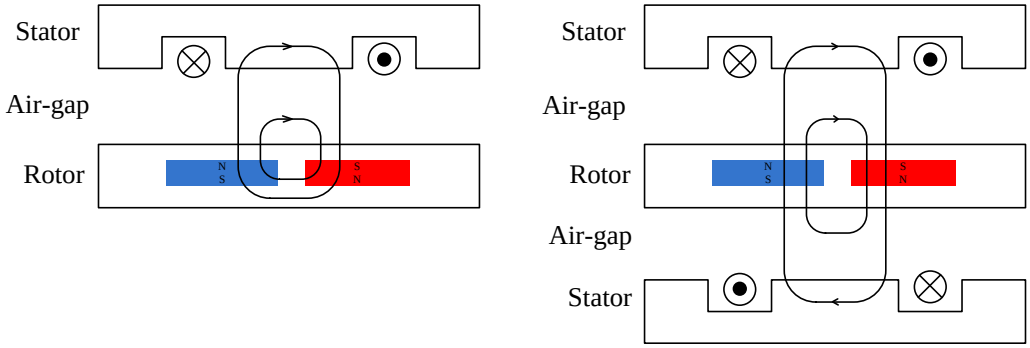
A typical wind generator operates on the principle of both motoring and generating. At first it operates as a motor in order to move the blades from static position into motion, the machine continues to act as a motor until the blades have enough momentum to match the force provided by the wind speed and is capable of rotating under wind speed and than switches to generation mode. For the optimization process in terms of increasing operating capability on lower wind speed, the designed model can be made to operate in two different modes as stated in Table 1.

Table 5 Modes of operation

Modes	Description
Half Motoring	In this mode, in order to move the wind turbine blades into

	motion when the wind speed is under the low critical, the machine will act as half motoring. The concept is to magnetize the half of the machine while supplying the current to reduce the power required to move the wind blade. With the increase in the efficiency, the mode will help in increasing the power generation capability under low wind operating conditions.
Generating	When the blade speed is under the ideal operating range or reached the critical cut in point and pitch control is able to maintain the constant rpm of the generator, the machine will switch intofull generating mode.

To achieve the mentioned objectives a basic model is selected based on a conventional single stator as shown in Figure 3(a). As a reference wind generator developed using an outer rotor developed in our lab is taken and is re-modified with a dual magnetic circuit. Dual circuit can be done using double rotor or double stator, however addition of the rotor induces less effectiveness as the generator would not be able to operate under low wind speed, and hence an outer stator is used in this research design application. This result into the addition of double coil windings and hence twice the magnetic flux as shown in the Figure 3(b) is feasible due to increase in the electrical loadings. Furthermore the modes of operation in both motoring and generating is capitalized with the use of two stator.



(a) Conventional model flux path (b) Proposed design flux path

Figure 3 Magnetic flux flows in conventional and proposed design

In a single stator single rotor machine magnetic flux density is given by Eq.1.

$$\text{Magnetic flux Density} = \frac{\pi n N i}{\pi d} \quad [1]$$

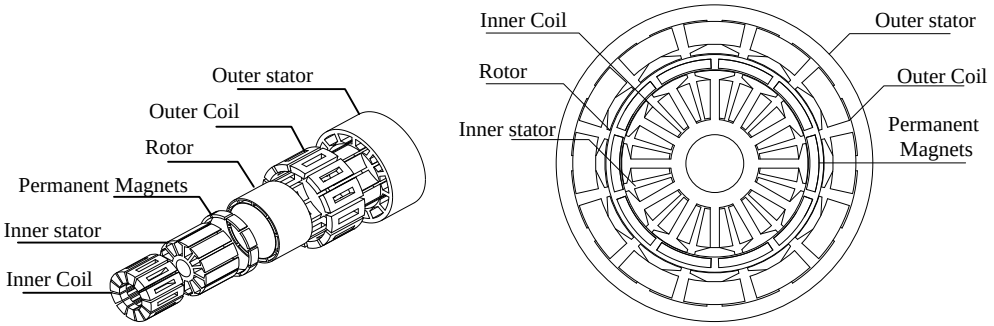
where n is number of stator, N is number of coil turns in stator winding, i is the current in Ampere and d is machine diameter

For multiple stator and single rotor the Eq. for magnetic flux density becomes as Eq.2

$$\text{Magnetic flux density} = \frac{2 N i}{\pi d} \quad [2]$$

2.2 Proposed Design

Based on the designed concept, the generator designed is shown in the Figure 4 (a) and 4(b).



(a) Exploded View (b) 12S-10P Front View

Figure 4 Proposed design

The parameters selected are based on the standard design mathematical equations as well as on commercially available generator designs to keep the commercial aspect in mind while designing [12]. The parameters of the designed generators are shown in Table 2. After doing the analysis based on finite element method with various configurations with a different slot poles combination, a configuration of 12Slots-10Poles is selected.

Table 2 Parameters of the designed machine

Parameter	Value
Stator pole arc length	13.24 mm
Outer Stator pole arc length	15.54 mm
Rotor diameter	30.75 mm
Air gap length	0.5 mm
Arc length of permanent magnet	18.69 mm
Number of magnets	10
Number of inner stator poles	12
Number of outer stator poles	12
Stack length	50 mm
Turns per phase in outer stator coil	55
Turns per phase in inner stator coil	36
Rated current at Phase A	5A
Rated current at Phase B	5A
Rated current at Phase C	5A

2.3 Finite Element Method

The process of machine characteristic evaluation is based on the concept of field distribution in the magnetic core. When analyzing a synchronous generator performance, the magnetic field is only known roughly. To calculate the performance, the Finite Element Method (FEM) is used. The traditional methods such as Analytical provides efficient evaluation results for the steady state operation, however in the transient operation stage of the machine, the results can be unreliable. The FEM is an

efficient tool for the analysis of machine when dealing with complicated geometries. The finite element method is a numerical method that is efficient in solving both linear and non-linear partial equations. The magnetic field distribution is solved by Maxwell's equation system [13]. To apply FEM a 2d model is first constructed followed by specifying the materials and conditions of torque and motions for different parts of the generator. The third step is to generate a mesh. A mesh basically breaks down the structure into small finite sections (elements) [14].

3.0 Methodology

3.1 Process Flow

The process flow has been divided into three stages i.e. designing of the base models, analysis of various slots-poles configurations with selection of preeminent model followed by optimization analysis stage to increase the operating capability.

The torque producing capability is affected immensely by slot pole combination of a machine [15], hence various structural slots-poles combinations were designed on the basis of dual stator magnetic flux flow using the slot-pole study formula given by Eq.3.

$$N_r = N_s(1 \pm \frac{k}{2q}) \tag{3}$$

where N_r is the number of poles, N_s is the number of slots, k is the natural number and q is the number of phases.

From the designed combinations (three of them shown in Figure 5), 12slots-10poles combination was selected through the procedure as shown in Figure 5. While designing the generators configuration all of the parameters including the volume of all designed models are kept same in order to compare them on the basis of generator square density. After the selection of the 12Slots-10Poles comibination, The procedure followed to calculate the efficiency carry out FEM analysis for the modes of operation through analysis is shown in Figure 6.

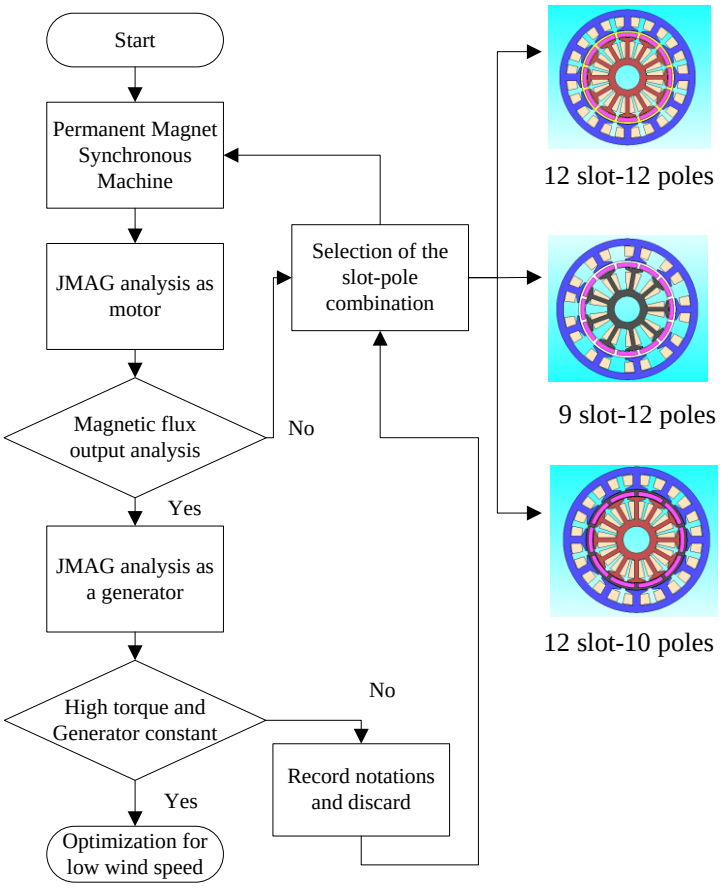


Figure 5 Model selection procedure

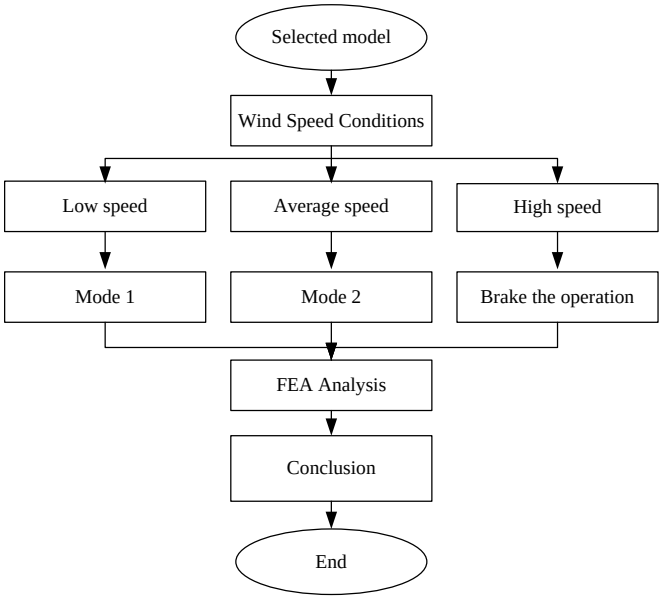


Figure 6 Modes of operation analysis procedure

3.2 Parameter Evaluation

To design a machine, is to have knowledge to model it considering cost, durability, compliance with the laid down specification and consumer requirement to provide an economic solution. Some factors that affect the performance of the machine are as follows:

Power constant can be calculated using by Eq. (4).

$$P_t = \frac{T\omega}{I} \tag{4}$$

where T is the torque in Nm and I is current in the coil in Ampere and ω is angular speed.

Generator constant is given by Eq. (5).

$$K_g = \frac{P_t}{I} \tag{5}$$

The core loss due to winding by Eq. (6).

$$P_{lc} = I^2R \tag{6}$$

where $P_{lc}$is the resistive power loss in watts.

The generator constant square density for the designed generator is as in Equation (7). The generator constant square density is used as a comparative analysis parameter. It helps in comparing generator capacity by comparing power density to the volume of the machine as a ratio.

$$G = \frac{P_m}{V} = \frac{K_g I^2 R_{lc}}{V} \tag{7}$$

where P_m is the generator constant and V represents the volume of the machine.
In order to calculate the efficiency of the machine under the different modes of operation, efficiency is given by Eq. (8)

$$\text{Efficiency}, \eta = \frac{P_{out}}{P_{out}+P_{lc}+P_i} \tag{8}$$

where P_{out} is output power, P_{lc} is copper loss and P_i is iron loss

4.0 Results and Discussion

4.1 Machine Characteristics

The result obtained through analysis of the selected model which is the configuration of 12S-10P gives the most smooth magnetic flux flow as shown in the Figure 7. The flux is divided evenly among the three phase of coil.

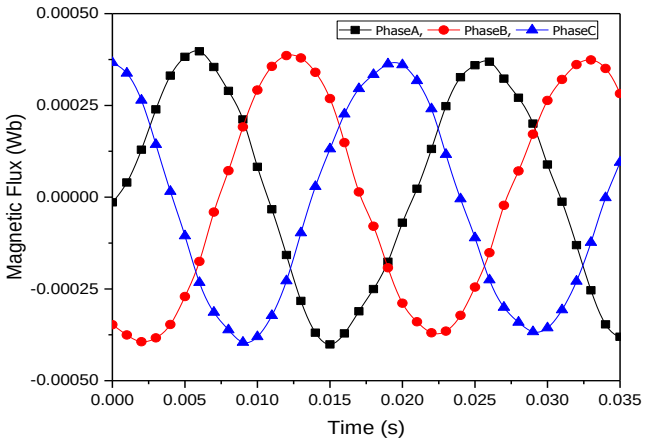


Figure 7 Flux for 12S-10P

Upon the selection of the machine, to analyze different angles of operation under the constant speed, the machine was simulated under different cases designed through case control by adjusting the angle starting from zero to 90 degree and the results are than recorded and plotted to analyze as shown in the Figure 8.

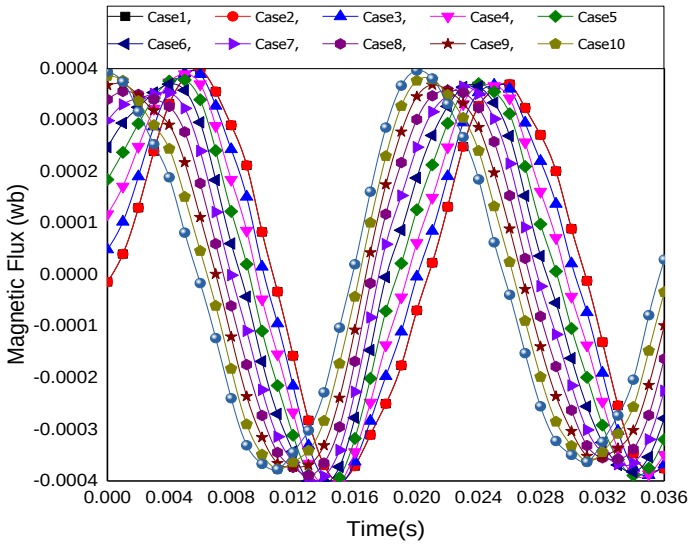


Figure 8 Comparison of magnetic flux obtained when operated at different phase angle.

Table 3 tabulates the data of the two best slots-poles configurations selected on the basis of smooth and evenly distributed magnetic flux output from the various slot-poles configurations simulated, to justify the selection of 12S-10P machine selection.

Table 3 Performance parameters

Parameter	12S-12P	12S-10P
I [A]	5	5
T_{avg} [Nm]	0.016	**0.031**
P_t [Nm/A]	0.0032	0.0062
K_g [Nm/A/W$^{-(1/2)}$]	0.002024	0.002024
G [(Nm)^2/A^2/W$^{-(1/2)}$/mm^3]	1.19274E-11	**4.47743E-11**

The generator constant as well as the average torque provided by the 12S-10P machine was greater than the other machine, indicates its suitability for wind turbine application.

4.2 Operating Characteristics at Various Modes of Operation

The designed machine has been operated under the two different modes, first as simultaneous motoring and generating under the wind speed lower than 3.5m/s and generating mode under the optimum operating wind speed of 3.5m/s to 6.5 m/s with an increment of 0.5m/s. The efficiency calculated is shown in the Table 4.

Table 4 Modes of operation comparative analysis

Mode 1	**Motoring & Generating**				
Speed (rpm)	403	537	672	806	941
Efficiency, η (%)	78.9	76.6	79.65	71.77	70.2
Mode 2	**Generating**				
Speed (rpm)	537	672	806	941	1075
Efficiency, η (%)	53.38	58.18	68.27	73.16	75.15
Speed (rpm)	1210	1344	1479	1613	1748
Efficiency, η (%)	75.21	75.24	75.26	75.21	75.16

From the comparative analysis it can be seen that at the lower speed (rpm) i.e 537, 672, 806 the efficiency is higher when operated under the Mode 1 operation when compared to being operated under mode 2 operation (generating), however when the wind speed reaches under the optimal speed range which is 941 rpm (3.5m/s), the mode 2 which is complete generation, provides a higher efficiency at 73.16% compared to mode 1 which operates at an efficiency of 70.19%.

An average of 75% efficiency is obtained when operated under the various wind speed conditions in the both modes. Based on the data collected, it can viewed that the operating range of wind turbine will be higher on the low wind speed range, hence the new generator topology will enable the wind turbine to operate before the typical cut-in speed range of 3.5ms^{-1} to 5ms^{-1} at an efficiency of around 75% and is shown in Figure 9 while relating to typical wind operating capability in Figure 2.

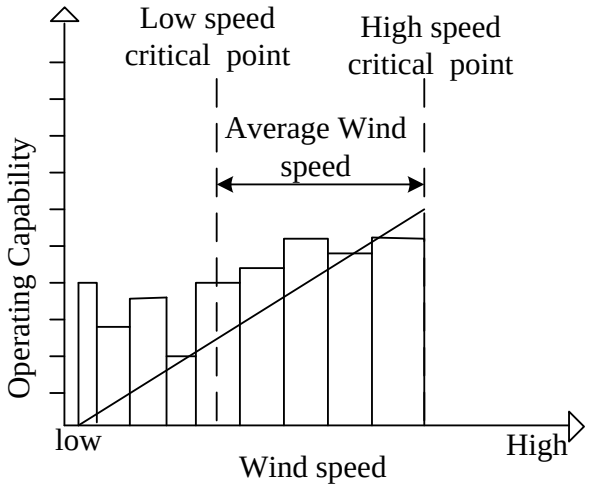


Figure 9 Designed Generator Operating Capability

5.0 Conclusions

From a conventional generator designed in Taylor's university [16], a double stator, single rotor 12S-10P machine has been designed on the basis of proposed concept and evaluated through FEA methods optimized to increase the capability of wind turbine operating range under low wind speed condition through the means of two different operating modes. The two different modes capitalize the presence of double stator configurations while delivering high efficiency in the region of 75% under each mode. Through the different stages of the study it has been also found that the design of the generator has high impact on wind energy conversion system efficiency, minor modifications can completely change the model operating structure. For the future work, having the model analyzed and evaluated while considering different heat conditions is suggested

References

[1] D. Spera, Wind turbine technology. New York, N.Y. (ASME, Three Park Avenue. New York, NY 10016): American Society of Mechanical Engineers, pp. 1-30, 2009.

[2] Altimania, M.R.M., Ofoli, A.R., Eltom, A.H. and Sisworahardjo, N., "Modelling of Doubly-Fed induction generators connected to distribution System based on eMEGASim® real-time digital simulator," pp. 13-27, 2014.

[3] O. Anaya-Lara, "Wind energy generation. Hoboken," NJ: John Wiley & Sons, pp 1-24, 2009.

[4] "Renewable energy - Energy - European Commission", Energy, 2016. [Online]. Available: https://ec.europa.eu/energy/en/topics/renewable-energy. [Accessed: 20 Oct- 2016].

[5] B. Guru, H. Hızıroğlu, J. Enríquez Brito and D. Díaz del Castillo, "Máquinas eléctricas y transformadores," Mexico d.f.: Oxford University Press, pp. 1-20, 2003.

[6] P. Plant and S. C. Wedum, "Rotor Design of Permanent Magnet Synchronous Machine for," NORGES Tek. Univ., no 1, pp. 3-7 July, 2015.

[7] M. Abbasian and A. H. Isfahani, "Optimal Design of a Direct-Drive Permanent Magnet Synchronous Generator for Small-Scale Wind Energy Conversion Systems," vol. 16, no. 4, pp. 379–385, 2011.

[8] C.-Y. Hsiao, S.-N. Yeh, and J.-C. Hwang, "Design of High Performance Permanent-Magnet Synchronous Wind Generators," Energies, vol. 7, no. 11, pp. 7105–7124, 2014.

[9] "General Climate Information - Malaysian Meteorological Department", Met.gov.my, 2016. [Online]. Available: http://www.met.gov.my/en/web/metmalaysia/education/climate/generalclimateinformation. [Accessed: 20- Oct- 2016].

[10] Christorpher The Boon Sung, "Possibility of electricity from wind energy in Malaysia: Some rough calculations, [Online] Avialable: http://www.christopherteh.com/blog/2010/11/wind-energy/ [Accessed: 20- Oct- 2016].

[11] "Irish Wind Energy Association - Wind Energy Technology", Iwea.com, 2016. [Online]. Available: http://www.iwea.com/technicalfaqs. [Accessed: 20- Oct- 2016].

[12] N. B. Misron, S. Rizuan, R. N. Firdaus, C. Aravind Vaithilingam, H. Wakiwaka, and M. Nirei, "Comparative evaluation on power-speed density of portable permanent magnet generators for agricultural application," Progress In Electromagnetics Research, Vol. 129, 345-363, 2012.

[13] Z. Kolondzovski and L. Petkovska, "Determination of a Synchronous Generator Characteristics via Finite Element Analysis," Serbian Journal of Electrical Engineering, vol. 2, no. 2, pp. 157–162, 2005.

[14] S. Mine, "Direct - drive permanent magnet synchronous generator design for hydrokinetic energy extraction," Master's Thesis, Missouri University of Science and Technology, pp. 22-34, 2013.

[15] C. Liu and K. T. Chau, "Electromagnetic Design and Analysis of Double Rotor Flux-Modulated Permanent Magnet Machines," Progress In Electromagnetics Research, vol. 131, no. 1, pp. 81–97, Sep. 2012.

[16] C. Aravind, Kamalinni, S. Tay, A. Jagadeeswaran and R. Firdaus, "Design analysis of MAGLEV-VAWT with modified magnetic circuit generator," Electrical Energy Systems (ICEES), 2014 IEEE 2nd International Conference on, Chennai, 2014, pp.82-86, 2014. doi: 10.1109/ICEES.2014.6924146

A new Brushless Motor for Electric Bike

Oh Wei Szin[1], Aravind CV[1,*], Charles R Sarimuthu[1], R Dhanasekaran[2]
[1]School of Engineering, Taylor's University, Malaysia.
[2]Syed Ammal Engineering College, Ramanathapuram, India.
[*]*aravindcv@ieee.org*

Abstract
The demand for vehicle has risen over the years due to the growing world population. With the harmful gases such as CO_2 emitted by ICE vehicle, better electrical Machine is needed to speed up the electrification of conventional transport vehicle as the issue of climate change is worsen every year. Although, there had been quiet few model of electric car available in the market, but the variety of transport such as bicycle or scooter is lacking behind. Electric bicycle and scooter possess high potential as greener personal transport due to their small size and energy consumption. Therefore, with this idea in mind, the objective of this paper is to bring impact to the transport industry by introducing machine with better flux density or motor square density through using the concept of different magnetic ratio. The proposed concept is to splitting a single magnet into two layer and with the inner layer in different ratio configuration. The idea for this concept is to utilize the repulsion between same polarity to converge the flux in the rotor to prevent flux leakage into the rotor. Thus producing machine with higher torque performance. Since conventional electric vehicle uses Brushless DC (BLDC) motor, the magnet splitting concept will be implemented into BLDC motor. This paper illustrates the process taken to design new BLDC machine using the proposed concept mentioned above. All the transient FEA simulation and 2D modelling is done using JMAG® Designer version 14.1. The chosen machine for research is a 12 slot 4 pole BLDC machine and three inner magnet split ratio such as 1:1, 1:2 and 1:3 is researched. The proposed model is the model with inner magnet ratio of 1 to 3. The reason for that configuration is ratio 1 to 3 produce the highest motor constant square density as compare to other two configurations with improvement of 29.32 % from the chosen conventional model.

Keywords: Permanent Magnet, Brushless, Machine, Electric Bicycle, Electric Vehicle.

1. Introduction

In the age of rising level of pollution and the worse effect of global warming, a cleaner, environmental friendly and efficient vehicle system is required. Alternatives had been continue researched by researcher and the solutions proposed are hydrogen car, hybrid electric car and electric car. Although each vehicle had different working principle but all of them focus on reducing carbon emission in transport vehicle [1, 2].

Bicycle had been the light weight transport option for human to travel in short distance. The power source for the system is mainly human pedaling which does not emit harmful gases to the environment, but due to relying on human pedal the range of this transport is limited. However, the range of the bicycle can be improved by adding an electric motor to the bicycle. Therefore, making this transport an attractive option for in city travel as compare to car and motorcycle [3].

The Electric bicycle (E-bike) consists of similar power system to Electric Vehicle (EV) which contains a Battery, Motor Controller and Electric Motor. However, the E-bike can be diverted into few different categories such as pedal assist, power-on-demand or both power-on-demand and pedal assist. But all of them uses electric machine as main source of propulsion. Figure 1 show the basic working concept of the electric vehicle such as E-bike [4].

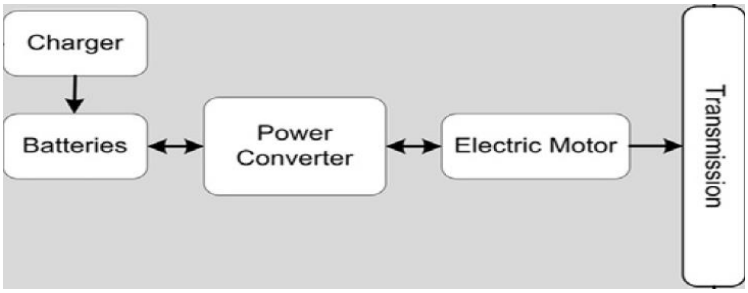


Figure 8: Working principle of the E-bike [5].

The common motor used in E-bike is the Brushless Direct Current (BLDC) motor. The motor consists of single rotor and single stator follow by magnet in the rotor [6, 7]. In this design, single layer magnet presents a direct leakage path for the flux to flow to the core of the rotor [8]. Therefore, the aim of this research is to experiment the effect of different double layer magnet configuration on the flux density of the machine. The concept of this research is to utilize the repulsion of magnet under same polarity to divert the flux and converge towards the opposite pole in the rotor. Different magnet ratio is experimented in this research. The torque and flux output is collected for evaluation of the motor torque density [9, 10].

The aim of this paper is to bring impact on reduction of CO_2 by introducing better electric machine for E-bike and further speed up the development of E-bike as substitute to car as personal transport. This achievable when the small electric machine that can deliver sufficient output power is available in the market. The scope of this research cover magnetic circuit study and Finite Element Analysis of the proposed concept model. The limitations of this research are only 2D model of the proposed structure is simulated and no thermal analysis conducted proposed model.

2 Concept work

E-bike is type of vehicle used to transport human or small cargo, which the load on the machine is similar or same as traction load. Hence traction load characteristics from car or hybrid car can be used as loading characteristics for the proposed machine. To normalize the graph a line is drawn to connect all the right side of each gear to obtain the characteristics required by of the motor which is shown in Figure 2 [11, 12]. The motor chosen for this application is BLDC motor due to the similar speed torque characteristics as shown in Figure 3. However, to further improve the machine with different inner magnet ratios are experimented. This different magnet ratios configuration allows the magnet of same polarity to create repulsion thus forcing the flux to converge more towards the opposite pole as compare to single magnet with same volume. The other effect of this configuration is obtaining machine with higher surface area per volume which provide better flux flow. With this concept, the flux leakage toward the rotor core is reduced and the torque performance of the machine is increased. The flux flow path of conventional and proposed machine is shown in Figure 4(a) and Figure 4(b).

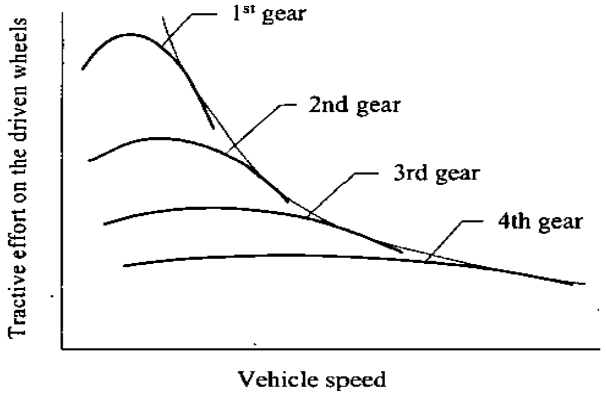


Figure 9: Tractive effort on the driven wheel against speed [12].

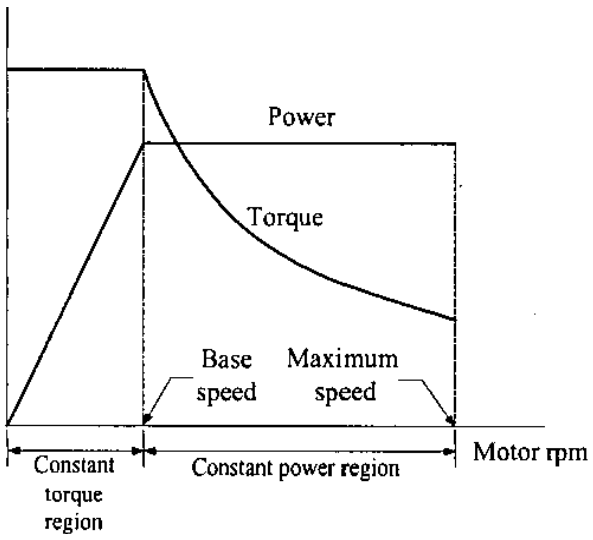
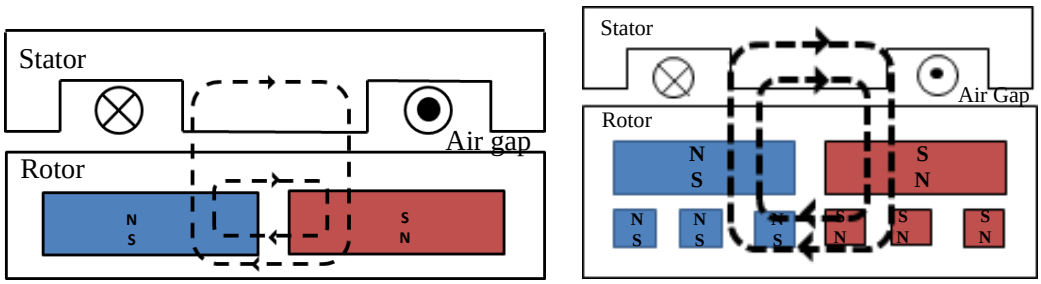


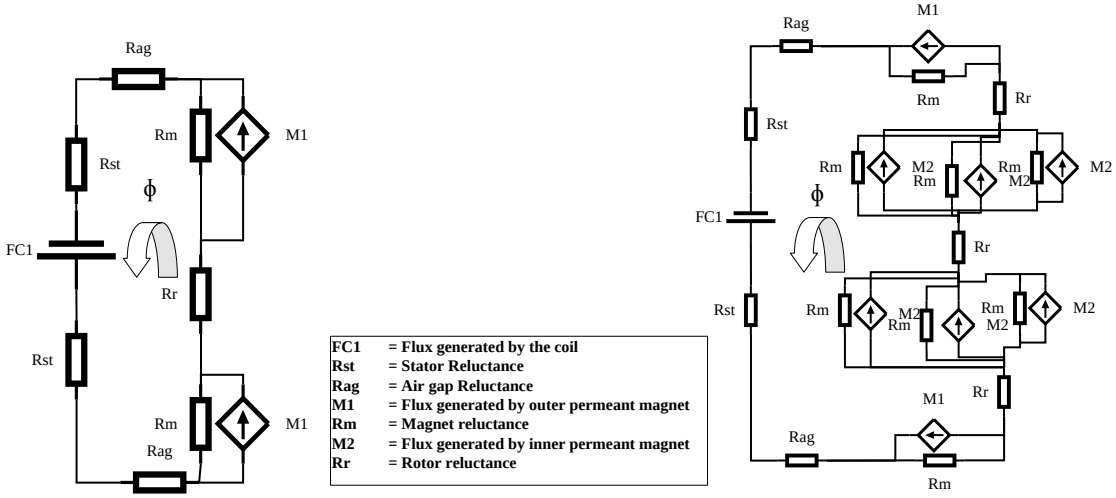
Figure 10: Speed torque graph of traction motor and tractive effort on the driven wheels [12].



(a) Flux path of conventional model **(b) Flux path of proposed model.**

Figure 11: Flux path of the conventional model and proposed model.

In magnetic circuit, all the structure in the machine such as stator, rotor and magnet are represented in terms of reluctance and voltage source. Stator is represented as a voltage source and reluctance connected in series connection. The rotor is presented as a reluctance and the magnet is presented as a current source and reluctance connected in parallel to each other. The connection of the reluctance components is connected according to the path of flux flow. The magnetic equivalent circuit of the conventional and proposed are shown in Figure 5. In this research, all the steps applied to conduct the research is summarized into a flow chart which shown in Figure 6. This flow chart includes the method of decision making and result verification. In the research all the 2D model and transient magnetic FEA analysis is conducted through using JMAG® Designer software.



(a) Magnetic circuit of the conventional model **(b) Magnetic circuit of the proposed model**

Figure 12 Magnetic circuit for both Conventional and Proposed Model

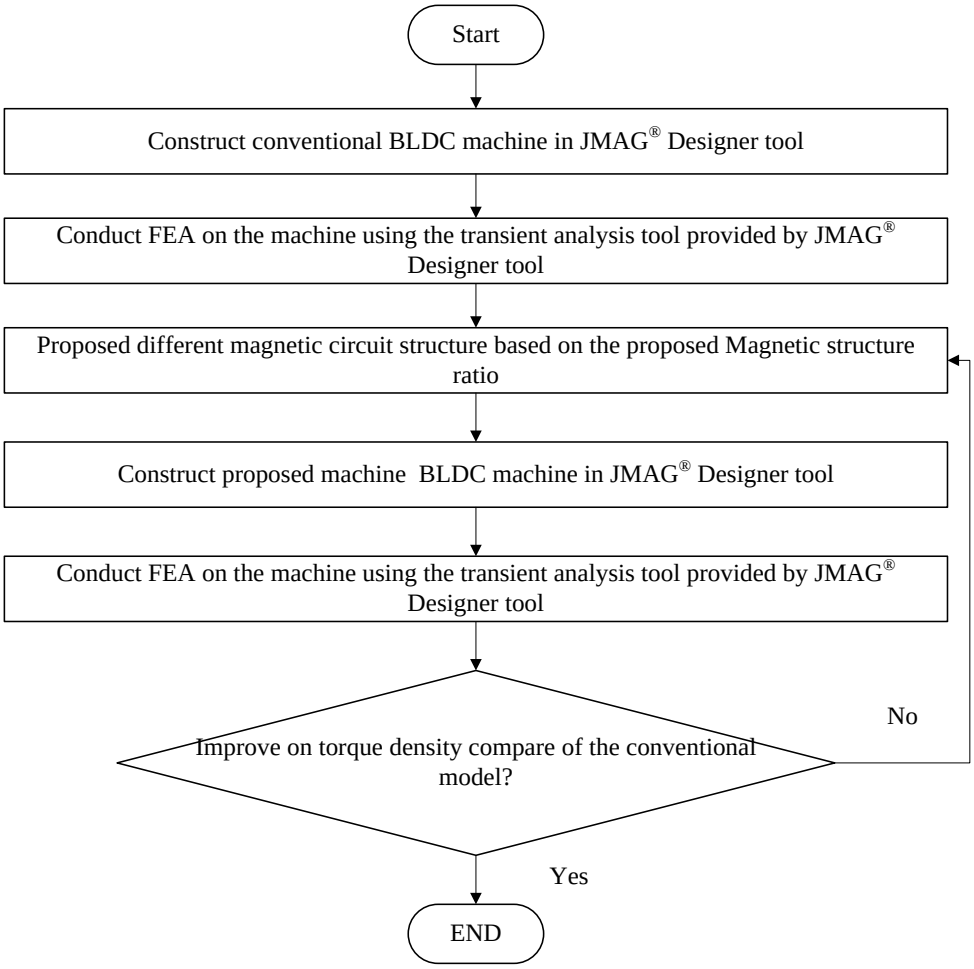
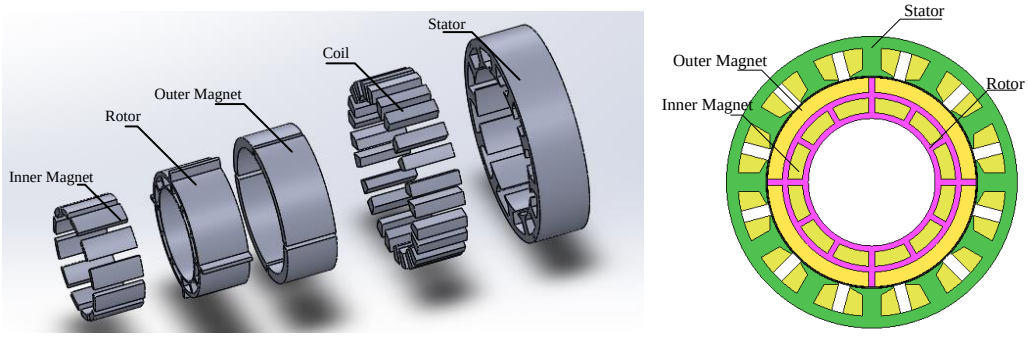


Figure 13 Flow chart of the model selection

3. Structural Layout

In this section the exploded view of the proposed Single Rotor Double Magnet Permanent Magnet (SRDMPM) machine for E-bike application is shown in Figure 7(a). The Figure 7(b) shows the front view of the SRDMPM machine, both stator and rotor is made up laminated steel. The winding in the of the coil is connected in star connection in 12 slots. 4 Surface mount magnet (SPM) is attached to the outer section of the rotor while 8 Internal Permanent magnet (IPM) is located in inner part of the rotor. Thus forming a 1:3 ratio of magnet structure in the rotor.



(a) Exploded view of the proposed machine (b) Front view of the proposed machine

Figure 14 Proposed structure with 1:3 magnet ratio

Table 6: Specification of the Proposed Model

Parameter	Value	Parameter	Value
Overall		Inner pole arc	86.3°
Diameter of the Machine	100mm	Outer radius of magnet	35.8mm
Stack Length	100mm	Inner radius of magnet	30.8mm
Rotor		**Stator**	
Outer radius	35.8mm	Number of Slots	12
Inner radius	21.8mm	Slot Arc	23.7°
Inner magnet		Outer radius	50mm
Number of poles	12	Inner radius	46mm
Outer pole arc	28.8°	Outer coil radius	46mm
Inner pole arc	26.3°	Inner coil radius	36mm
Outer radius of magnet	28mm	Tooth Width	6.6mm
Inner radius of magnet	23.8mm	Tooth radius	36.4mm
Outer magnet		Tooth thickness	1mm
Number of poles	4	Tooth slope	120°
Outer pole arc	86.8°		

4. Finite Element Analysis (FEA) Method

In terms of machine performance evaluation, the characteristics of magnetic flux and torque is evaluated to obtain the general performance of the machine. To obtain the flux and torque data Finite Element Analysis is conducted to calculate the output and behavior of the magnetic flux and torque. To reduce unwanted error, the material used for both machines are remained constant and kept the structure layout magnet as the variable in the simulation.

FEA split the machine model into many small mesh. The mesh is then calculated through using Maxwell's equation method [13]. To reduce the simulation time 2D model of the model is simulated with stack length instead of 3D model to reduce the simulation time. The procedure of conducting FEA analysis for the proposed model is shown in Figure 8. The flux flow in rotational angle 0°, 30°, 60°, 90°, 120° and 150° of the machine is shown in Figure 9 which show evenly distributed flux in both stator and rotor.

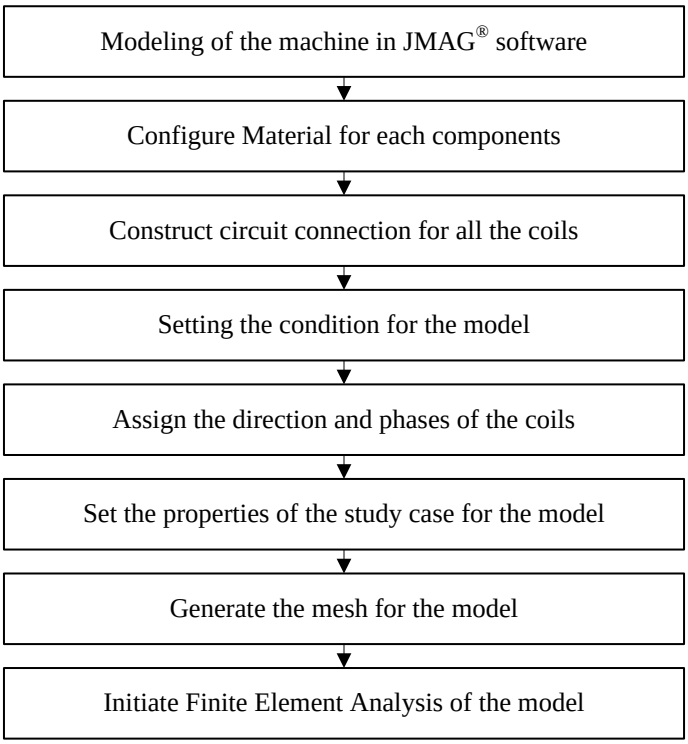


Figure 15:Flow chart of FEA process

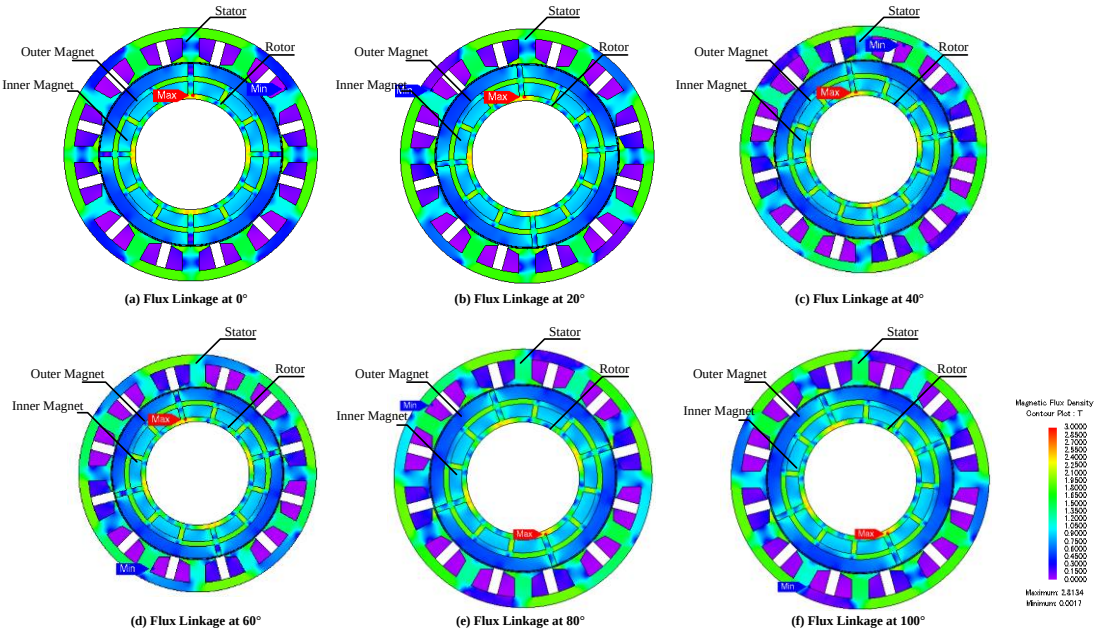


Figure 16: Density of flux in different angle

5. Quality of Measures

In machine design, the performance of any machine can be measure through evaluating the torque and magnetic flux performance of the machine. Motor constant square density is employed to evaluate the performance of both proposed and conventional model. The parameters used to determine the motor constant square density are the torque output and machine volume which are obtained through FEA analysis [13, 14].

Motor constant, $M_k = \frac{K_t}{\sqrt{2}IR}$ (1)

Where K_t s the torque constant in terms of Newton meter per ampere [Nm/A], I is the maximum current in the coil in terms of ampere [A] and R is the resistance in the coil located at the stator in terms of resistance [Ω].

Torque constant, $K_t = \frac{T_v}{I}$ (2)

T_v represented as the average torque of the machine Newton meter [Nm], and I is the maximum current in the coil in terms of ampere [A].

Motor constant square density, $G_m = \frac{M_k^2}{V}$ (3)

The M_k denote the motor constant or the average torque over the input power which symbolize the torque create per square root wattage [$Nm/A/W^{0.5}$]. V represent the volume of the motor in m^3. The unit for G_m is [$Nm^2/A^2/W/m^3$].

6. Result and discussions

In evaluating the machine, flux and torque performance of the machine is important. The flux flow of all 4 model is shown in Error! Reference source not found.**10. As shown in the** Error! Reference source not found.**10, model 1:3 has the highest flux amplitude which symbolize highest flux density in the machine structure. As for the pattern of the wave form, all model show pattern close to sinusoidal wave form which indicated the occurrence of minor harmonic. Figure 11 show the graph of torque compare of all four models. From the graph the conventional model has the highest peak torque value but in terms of cogging torque, model 1:3 show the lowest as compare to other model.**

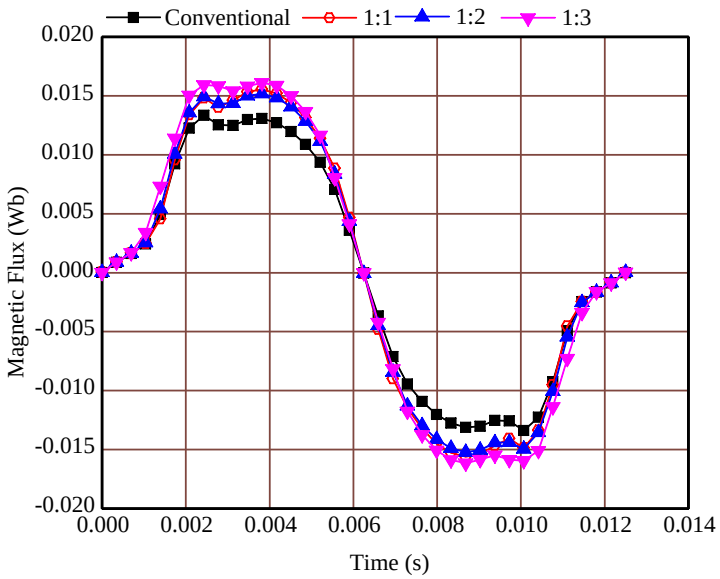


Figure 17 Three phase flux of the proposed machine

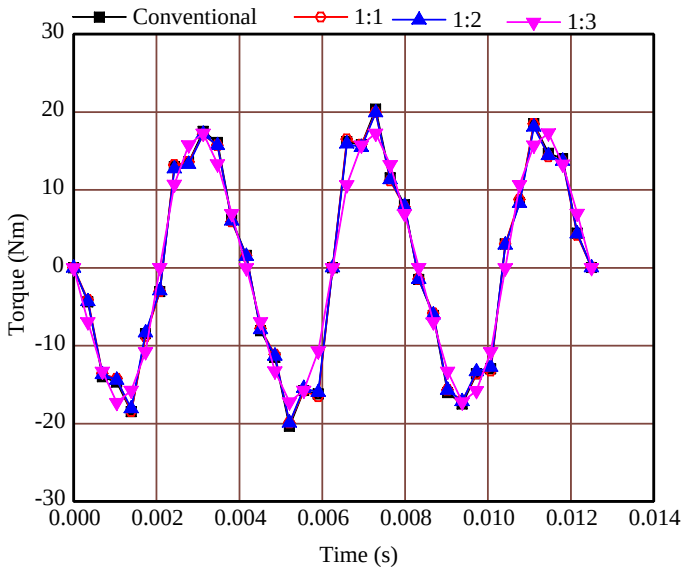


Figure 18 Torque compare of both conventional and proposed design

Figure 12 shows the speed torque characteristic of the machine. The speed torque graph of the developed machine is compared with the graph produced by ICE engine with gears. **Error! Reference source not found.**12 show the speed torque graph of all 4 machine models. As shown in the graph, the speed torque of all the machines are similar to the speed torque of the ICE engine. Therefore, the machine developed is suitable for traction application. Although model 1:3 does not have the highest torque but the model 1:3 has the lowest slope gradient compare to other mode which symbolize slowest power diminish as compare to other machines. In the comparison, model 1:1 show the highest efficiency as compare to others and model 1:3 show only 0.4% improvement in efficiency as compare to conventional model as observed from Table 2.

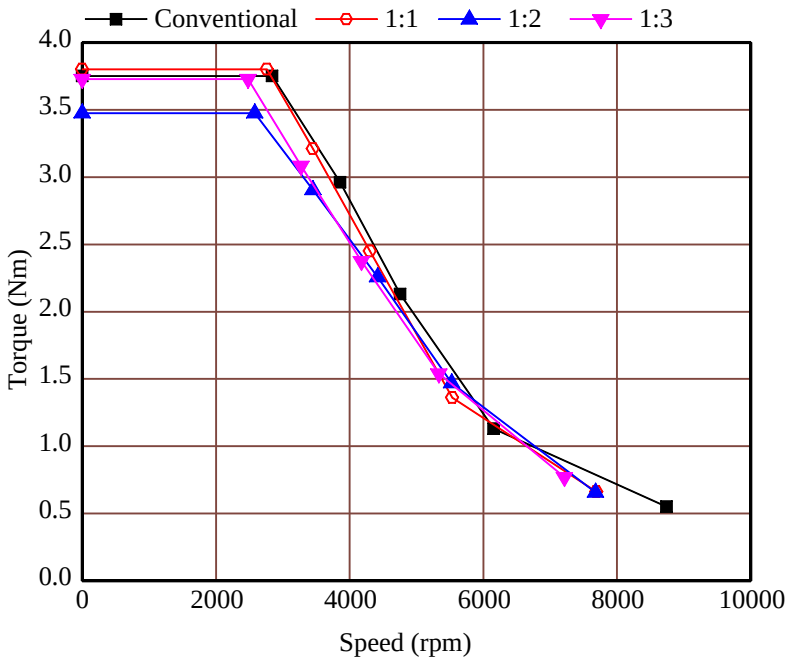


Figure 19 Speed torque graph of proposed machines

Table 2: Performance Characteristics of the Model

Parameter		Conventional model	Ratio 1:1	Ratio 1:2	Ratio 1:3
I^2R loss	**(W)**	25	25	25	25
Iron loss	**(W)**	37.67	38.01	37.19	36.12
Output power	**(W)**	90.36	102.05	91.73	87.92
Input power	**(W)**	153.017	165.07	153.92	149.04
Efficiency	**(%)**	70.10	72.41	70.67	70.38
Improvement	**(%)**	-	3.23	0.81	**0.40**

7. Conclusions

The concept work of this research is to obtain better flux diverge through splitting the magnet structure into different ratio and utilize the repulsion of the same magnet polarity to achieve higher flux converge. FEA is conducted to evaluate the proposed design and verification was done afterwards. The model with double layer magnet with 1:3 magnet ratio is proposed as the model has the highest improvement in motor square density of 29.32%. Although the efficiency of the model is the highest but the main focus in machine design is to obtain machine with highest motor constant square density.

References

[1] Z. Darabi and M. Ferdowsi, "Aggregated Impact of Plug-in Hybrid Electric Vehicles on Electricity Demand Profile," *IEEE Transactions on Sustainable Energy*, vol. 2, no. 4, pp. 501-508, 2011.

[2] Malaysian-German Chamber of Commerce and Industry, "1st Malaysian-German Sustainable Automotive Mobility Conference," in *Sustainable Mobility Conference*, Kuala Lumpur, 2011.

[3] W. Gruber, W. Bäck and W. Amrhein, "Design and implementation of a wheel hub motor for an electric scooter," in *2011 IEEE Vehicle Power and Propulsion Conference*, Chicago, IL, 2011.

[4] S. F. Tie and C. W. Tan, "A review of energy sources and energy management system in electric vehicles," *Renewable and Sustainable Energy Reviews,* vol. 20, pp. 82-102, 2013.

[5] J. Y. Yong, V. K. Ramachandaramurthy, K. M. Tan, and MithulananthanN., "A review on the state-of-the-art technologies of electric vehicle, its impacts and prospects," *Renewable and Sustainable Energy Reviews,* vol. 49, pp. 365-385, 2015.

[6] H. R. Cha, K. J. Shin and Y. J. Seo, "Design of outer rotor IPM type PMSM for 3 wheel electric vehicle," in *2011 International Conference on Electrical Machines and Systems*, Beijing, 2011.

[7] D. Fodorean, D. C. Popa, P. Minciunescu, C. Irimia and L. Szabó, "Study of a

high-speed motorization for electric vehicle based on PMSM, IM and VRSM," in *2014 International Conference on Electrical Machines (ICEM)*, Berlin, 2014.

[8] M. A. Rahman and M. A. Masrur, "Advances on IPM technology for hybrid electric vehicles," in *2009 IEEE Vehicle Power and Propulsion Conference*, Dearborn, MI, 2009.

[9] M. Cheng, W. Hua, J. Zhang and W. Zhao, "Overview of Stator-Permanent Magnet Brushless Machines," *IEEE Transactions on Industrial Electronics,* vol. 58, no. 11, pp. 50087-5101, 2011.

[10] W. Xu, J. Zhu, Y. Guo, S. Wang, Y. Wang and Z. Shi, "Survey on electrical machines in electrical vehicles," in *International Conference on Applied Superconductivity and Electromagnetic Devices*, Chengdu, 2009.

[11] C. L. Chu, M. C. Tsai and H. Y. Chen, "Torque control of brushless DC motors applied to electric vehicles," in *Electric Machines and Drives Conference, 2001. IEMDC 2001. IEEE International*, Cambridge, MA, 2001.

[12] M. Ehsani, Y. Gao and S. Gay, "Characterization of electric motor drives for traction applications," in *Industrial Electronics Society, 2003. IECON '03. The 29th Annual Conference of the IEEE*, 2003.

[13] A. C. V, M. Norhisam, I. Aris, M. H. Marhaban, D. Ahmad and M. Nirei, "Double-Rotor Switched Reluctance Machine (DRSRM): Fundamentals and magnetic circuit analysis," in *2011 IEEE Student Conference on Research and Development*, 2011.

[14] S. Niu, S. L. Ho and W. N. Fu, "A Novel Double-Stator Double Rotor Brushless Electrical Continuously Variable Transmission System," vol. 49, no. 7, 2013.

eureca 2016 – Conference Paper
Paper Number 2EE07

Design and Simulation of Power Protection Schemes for a Power Distribution System

Vincent Villamor Tan Soon Huat, Reynato Andal Gamboa*

[1]School of Engineering, Taylor's University, Malaysia.
[2]University of Asia Pacific,Bangladesh
ReynatoAndal.Gamboa@taylors.edu.my

Abstract
This paper documents the design and simulation of a power system protection network for a small segment of a power system distribution network used for the Final Year Project Thesis of the author. Only bolted symmetrical faults, i.e. zero impedance short-circuit on all three phases to ground, will be considered. The ETAP software will be used to perform the construction and simulation of the single-line diagram and also the load flow analysis, fault analysis and finally protection device coordination. Several settings for the relays have been tried out in order to find a tripping sequence that starts closest to the faulted end and moves closer to the power source. Those settings that have been determined to fulfil the subfield's main purpose will be used. From the experimentation done, the breakers have been successfully set so they trip in sequence at all fault points within the sub network worked on, although there are other tripping sequences that, while not ideal, do not disrupt upstream loads. Some of the findings of this research are the possibility of protective device miscoordination in the form of overlap, where a particular fault current causes both the load-end and the feeder breaker to trip, disrupting other loads on the same bus. Also, it is seen that the tripping time of coordinated breakers is dependent on the total impedance from the source to the fault, which then gives a different amount of fault current.

Keywords: power system protection, distribution protection, protection relay coordination, power systems protection coordination guidelines, time-current curves

1. Introduction

Power systems protection is practically a mandatory requirement in the many large power distribution systems used throughout the world. They mitigate the amount of damage caused to a system should an electrical fault, usually a short circuit, occur within the system. There are a few types of short-circuits that depend on what phases are shorted to each other and whether they're shorted to ground [1]. The most common short-circuit is the single-line-ground (SLG) fault [2].

Several types of protection devices exist where they measure an important parameter of the electrical system to detect faults. Current is most commonly measured, though other parameters such as voltage, real and reactive powers and even the impedance are measured to determine whether a fault is occurring. The relays can also be built in such a way that they are "directional", i.e. current or power flow in only one direction is considered [3].

Whenever electrical faults occur, damage usually occurs due to the large amount of energy dissipated in the fault arc [4]. Hence, protection devices usually have to act very quickly to clear the fault in order to limit the damage. Typically, the load end devices are the first ones to trip, usually isolating the faulty section and keeping the rest of the system unaffected [5].

However, in the event that the load-end protective device fails to trip, the protection devices upstream should also trip in the hopes of limiting the damage occurring. The trip times of these devices must be set so that they trip one after another in sequence towards the generating source. Setting the trip times wrongly, for example, overlapping them with the breaker after it, which is very easy to do via "mixing and matching" relay curves, or not accommodating inrush surges of equipment such as motors and transformers [6] can result in out-of-sequence and/or nuisance tripping, which then result in undue disruptions to other users of the power system [7]. Protection devices are said to trip more often due to incorrect settings rather than genuine faults [8].

Protective device coordination, also known as selective coordination, is used on critical loads where disruption could mean severe inconveniences and economic losses [9].

2. Methodology

For this research, the ETAP software will be used to construct and simulate a small feeder section of a much larger power system network. After that, load flow analysis will be performed to determine the suitability of components in the network. Specifications are adjusted as necessary to make sure they are feasible and then a fault analysis is run to determine the required fault current specifications of the circuit breakers. Then the current transformers and protective relays are added and linked to their associated circuit breakers and several "star views" which are time-

current graphs are created to initially adjust the curve, pickup and time dial settings of the relays so that they suit the operating curve of the device being protected.

A symmetrical bolted fault is placed at one of the busses and then the tripping sequence of the relays adjusted with the help of the fault current normalised time-current graphs created using the application. This is repeated for all busses within the system.

Symmetrical faults are used as they produce the highest fault current and are easier to calculate. (Only the positive sequence impedance is considered. Other short-circuit faults have their negative sequence and zero sequence impedances in series or parallel depending on the fault after the positive sequence impedance.) This is used to select a breaker capable of handling the fault current from manufacturer's tables. This high fault current is used to set the protective devices as protecting the system from bolted symmetrical faults also protects the system from other types of short-circuit faults.

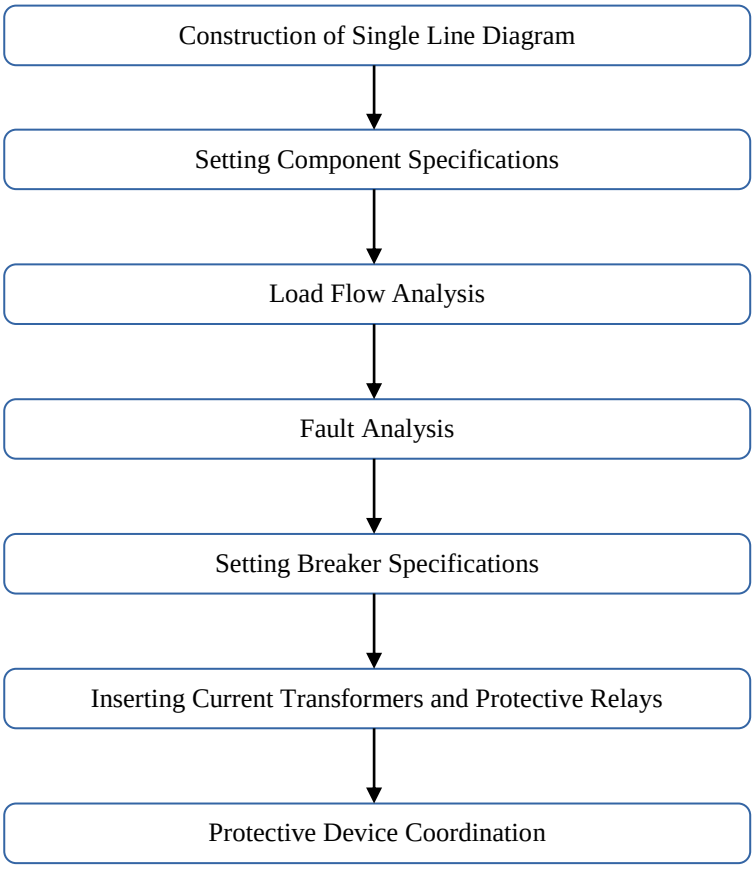


Figure 1: The flow of conducting protective device coordination.

2.1 Construction of Single-Line Diagram and Setting Component Specifications

A single-line diagram of the whole network to be simulated is constructed using the “Edit” mode of ETAP. Component specifications are also set at this stage to have some resemblance to what is used in the real-world. Lumping components together as one large device may be needed as ETAP does not allow a fault to be inserted close to components with a quantity greater than one. The single-line-diagram used in this case has been based upon another one from another research paper [10] and expanded with component specifications and loads are required.

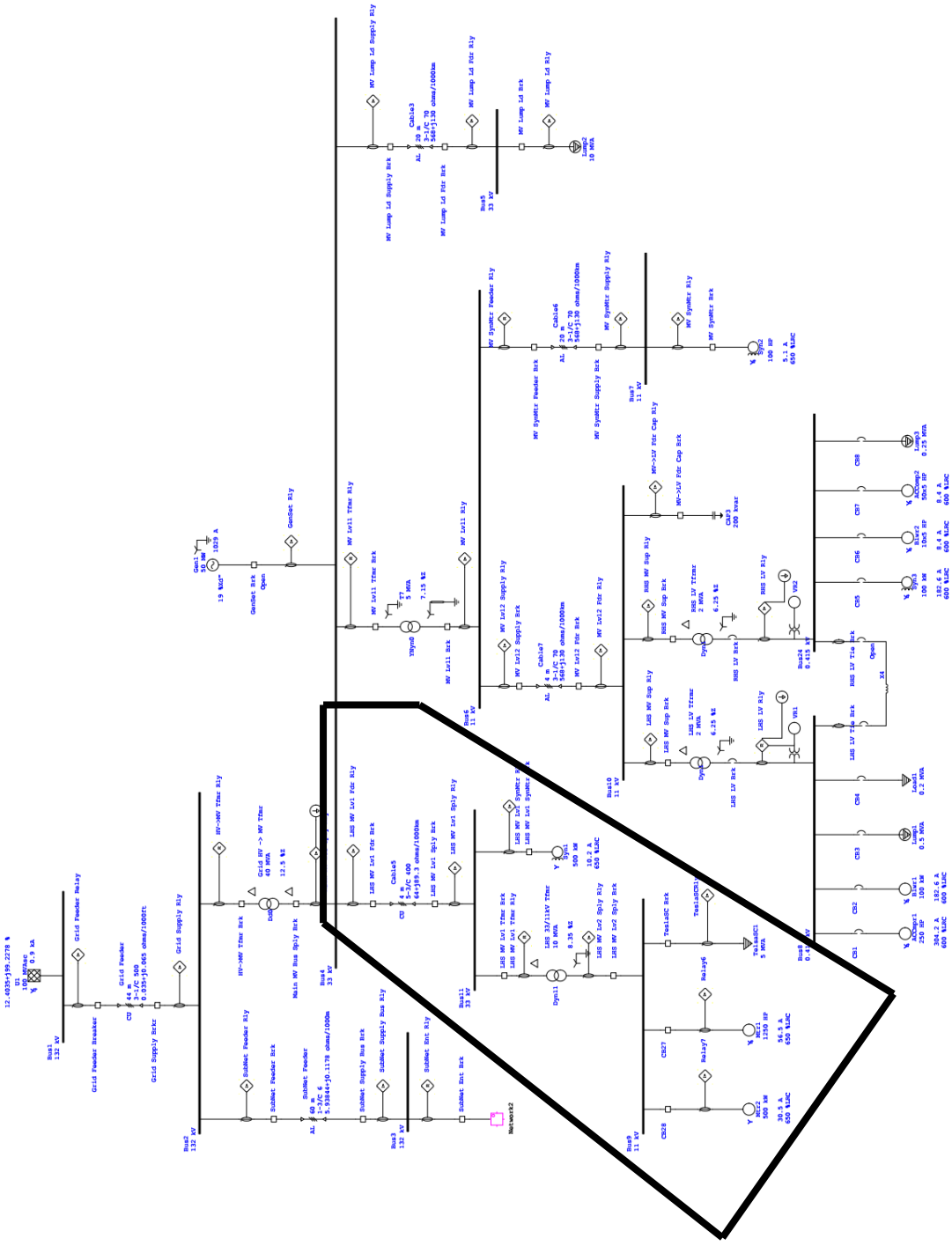


Figure 2: The large power system network from which a small part of the system (in the area marked by thick lines) has been selected to be worked on.

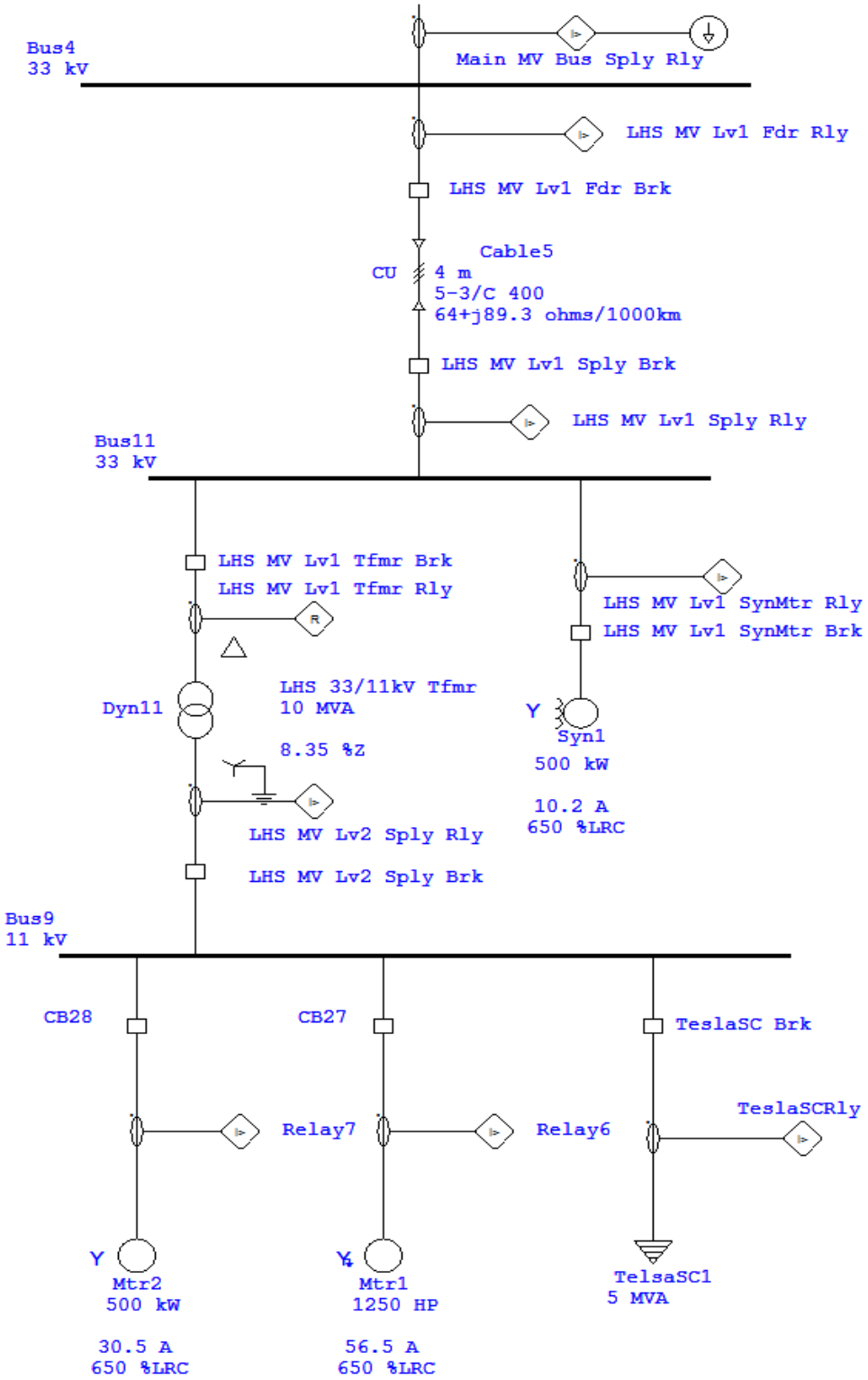


Figure 3: The part of the large power system network that will be used in this paper. Default impedance and X/R values are used in this case.

2.2 Load-Flow Analysis

Load-flow analysis is used to determine the nominal operating currents and voltages of the various components within the electrical system. This, along with the component ratings and specifications, determine if all the components in the system are operating normally, i.e. within operating specifications. Any abnormalities within the system are resolved by upgrading components or resizing loads to more reasonable values if component upgrades would result in unreasonable specifications being used.

For protection relays, this determines the specifications of the current transformers and also the minimum pickup current of the relay so it doesn't trip during normal operation.

2.3 Running Fault Analysis and Determining Circuit Breaker Specifications

Fault analysis is used to determine the maximum fault currents that will flow into the bus should it get faulted. This determines the required circuit breaker specifications so as to guarantee that the breaker will be able to safely interrupt the fault current when it occurs. In the course of using the ETAP program, it is found that the maximum fault current handled by the bus is used as the minimum rating required of the breakers.

2.4 Protective Device Coordination

This is the main part of this study. This involves finding the most optimum protective device settings so that they trip closest to the fault location first. Then, the other protection devices are adjusted so that they trip in the event the load-end device breaker fails to trip, taking in to account breaker operating times. This is a multistep process where due attention must be given to prevent setting the device incorrectly, which can result in nuisance tripping or worse, inadequate or even no protection should a fault occur.

ETAP implements what is called a "star view" in which components are selected and the "create star view" function invoked. This plots the selected device operating and damage curves on a time-current chart. Transformers and motors need to have some of their basic load characteristics like hot/cold stall time, acceleration time or inrush current provided so that their operating curves can be plotted on the time-current chart. The protection relays can then be initially set at this stage so that their curves are between their operating and damage curves, with being closer towards the operating curves preferable.

A bolted fault is then introduced into the system close to the load and ETAP will then flash the tripping sequence of the protective devices. Another "star view" is created with the fault in place to view a time-current graph with the protective device

curves normalised to the fault current. From there, the protective devices are adjusted as required, to ensure that the protective devices trip in sequence as a backup.

This is repeated several times for each load on the bus and then moving the fault closer towards the feeder bus, checking the relay coordination each time to make sure they trip in sequence. “Star Views” are created as necessary to check and adjust the relay coordination. The “Sequence Viewer” is also utilised to make sure no overlap exists where the next relay triggers before the breaker after it trips.

3. Results and Discussion

3.1 Relay Settings and Trip Times/Sequences

Table 1. Results of the Load Flow Analysis. The Load Flow Analysis results determine the CT ratio to be selected, which is the next highest rating available. This allows the relay’s tripping current to be set within the relay’s capability.

Load Currents			
Load	**Load Current (A)**	**CT Ratio**	**Relay Current (A)**
Mtr1	57	60:5	4.75
Mtr2	30.8	50:5	3.08
TeslaSC1	260	300:5	4.33
LHS 33/11kV Tfmr Secondary	342.7	400:5	4.28
LHS 33/11kV Tfmr Primary	114.2	150:5	3.81
Syn1	10.1	40:5	1.26
LHS MV Lvl1 Feeder	124.1	150:5	4.14

Table 2. Results of the Fault Analysis, giving the fault current contributions of each load to the bus being faulted. The total fault current of the bus is used to determine the fault rating of the breaker. The breaker’s fault rating must exceed the fault current values for the bus they are connected to in order to guarantee they will interrupt the fault current safely.

IEC 3-phase Device Duty Fault Analysis	
Load	Current (kA)
Mtr1	0.404
Mtr2	0.218
TeslaSC1	0
LHS 33/11kV Tfmr Secondary	3.7

Load Bus	**4.3**
LHS 33/11kV Tfmr Primary	0.19
Syn1	0.07
Feeder	2.57
Feeder Bus	**2.8**

Table 3. The settings of the protective relays that have been determined to allow the relays to operate in sequence whenever a fault occurs at any point in the power network.

Relay Settings				
Relay Protecting	**Relay Make & Model**	**Curve**	**Pickup (Pri. Current (A))**	**Time Dial**
Mtr1	ABB REG316*4	Normal Inverse	1.00 (60)	0.26
		Instantaneous	7.6 (456)	0.01
Mtr2	ABB REG316*4	Normal Inverse	0.7 (35)	0.22
		Instantaneous	5.0 (250)	0.01s
TeslaSC1	ABB Microshield (O/C)	IEC – Extremely Inverse	4.75 (285)	0.05
LHS 33/11kV Tfmr Secondary	ABB REB500	Extremely Inverse	0.9 (360)	16.85
LHS 33/11kV Tfmr Primary	ABB REB500	Extremely Inverse	0.84 (126)	32.87
Syn1	ABB REM543	IEEE – Long Time Inverse	0.35 (14)	7.7
		Instantaneous	1.79 (71.6)	0.05s
LHS MV Lvl1 Supply from Feeder	ABB REB500	Extremely Inverse	1.02 (153)	4.98
LHS MV Lvl1 Bus to Feeder	ABB REF541	Extremely Inverse	1.10 (165)	0.45

Table 4. The resulting tripping times of the protective devices for various faults placed in the 11kV section of the sub network. The bolded values are for the trip times that differ from those when a fault is placed at the bus bar.

Tripping times (milliseconds)					
Fault Location ->	**Mtr1**	**Mtr2**	**TeslaSC1**	**11kV Bus**	**Tfmr Sec.**
Mtr1	**40**	6720	6720	6720	6720
Mtr2	5935	**40**	5935	5935	5935
TeslaSC1	-	-	**65**	-	-
Tfmr Sec	191	191	191	191	**8531**
Tfmr Pri	392	392	392	392	392
Syn1	40247	40247	40247	40247	40247
Feeder Supply	797	797	797	797	797
Bus to Feeder	1037	1037	1037	1037	1037

Table 5. Tripping times for the 33 kV section of the sub network. Notice that only the trip time of the breaker whose fault current passes through is different compared to when the bus bar is faulted changes as the impedance from the supply towards the fault changes.

Tripping times (milliseconds)					
Fault Location ->	**Tfmr. Pri.**	**33kV bus**	**Syn1**	**Feeder Supply**	**Bus to Feeder**
Mtr1	7040	7040	7040	7040	7040
Mtr2	6230	6230	6230	6230	6230
TeslaSC1	-	-	-	-	-
Tfmr Sec	11163	11163	11163	11163	11163
Tfmr Pri	**121**	25728	25728	25728	25728
Syn1	21755	21755	**120**	21755	21755
Feeder Supply	385	385	385	**7199**	**7199**
Bus to Feeder	487	487	487	487	487

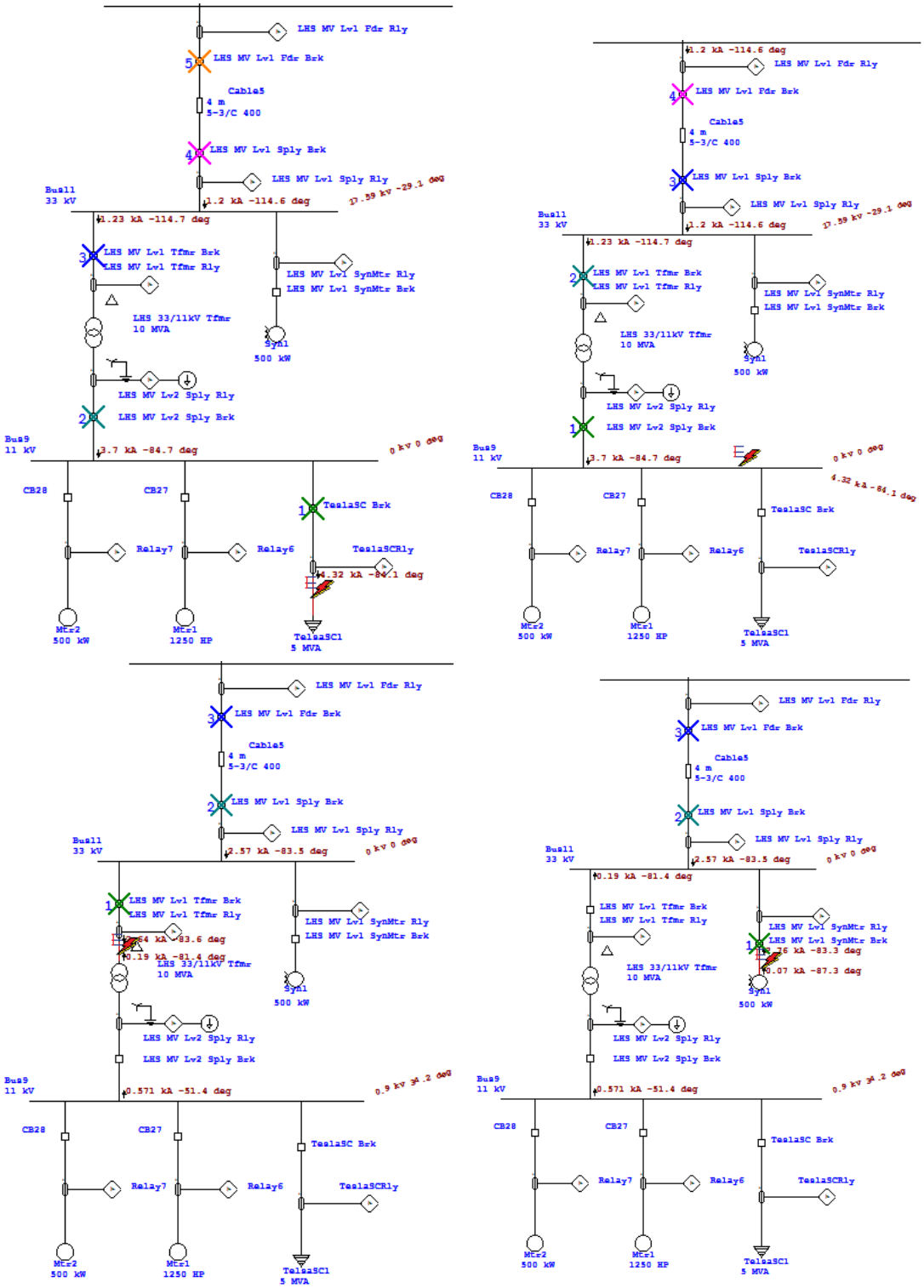


Figure 4: Four different fault locations showing the protective device's tripping sequences for faults located at different points in the sub network. This shows the ideal case where each protective device trips in sequence from the load fault.

Sequence-of-Operation Events - Output Report: Untitled

3-Phase (Symmetrical) fault on connector between CT3 & TelsaSC1. Adjacent bus: Bus9

Data Rev.: Base Config: Normal Date: 2016-11-28

Time (ms)	ID	If (k...	T1 (ms)	T2 (ms)	Condition
35.0	TeslaSCRly	4.323	35.0		Phase - OC1 - 51
65.0	TeslaSC Brk		30.0		Tripped by TeslaSCRly Phase - OC1 - 51
161	LHS MV Lv2 ...	3.702	161		Phase - OC1 - 51
191	LHS MV Lv2 ...		30.0		Tripped by LHS MV Lv2 Sply Rly Phase - OC1 - 51
346	LHS MV Lv1 ...	1.234	346		Phase - OC1 - 51
392	LHS MV Lv1 ...		46.0		Tripped by LHS MV Lv1 Tfmr Rly Phase - OC1 - 51
727	LHS MV Lv1 ...	1.201	727		Phase - OC1 - 51
797	LHS MV Lv1 ...		70.0		Tripped by LHS MV Lv1 Sply Rly Phase - OC1 - 51
5905	Relay7	0.218	5905		Phase - OC1 - 51
5935	CB28		30.0		Tripped by Relay7 Phase - OC1 - 51
6690	Relay6	0.404	6690		Phase - OC1 - 51
6720	CB27		30.0		Tripped by Relay6 Phase - OC1 - 51
40177	LHS MV Lv1 ...	0.033	40177		Phase - OC1 - 51
40247	LHS MV Lv1 ...		70.0		Tripped by LHS MV Lv1 SynMtr Rly Phase - OC1 - 51

Sequence-of-Operation Events - Output Report: Untitled

3-Phase (Symmetrical) fault on bus: Bus9

Data Rev.: Base Config: Normal Date: 2016-11-28

Time (ms)	ID	If (k...	T1 (ms)	T2 (ms)	Condition
161	LHS MV Lv2 ...	3.702	161		Phase - OC1 - 51
191	LHS MV Lv2 ...		30.0		Tripped by LHS MV Lv2 Sply Rly Phase - OC1 - 51
346	LHS MV Lv1 ...	1.234	346		Phase - OC1 - 51
392	LHS MV Lv1 ...		46.0		Tripped by LHS MV Lv1 Tfmr Rly Phase - OC1 - 51
727	LHS MV Lv1 ...	1.201	727		Phase - OC1 - 51
797	LHS MV Lv1 ...		70.0		Tripped by LHS MV Lv1 Sply Rly Phase - OC1 - 51
5905	Relay7	0.218	5905		Phase - OC1 - 51
5935	CB28		30.0		Tripped by Relay7 Phase - OC1 - 51
6690	Relay6	0.404	6690		Phase - OC1 - 51
6720	CB27		30.0		Tripped by Relay6 Phase - OC1 - 51
40177	LHS MV Lv1 ...	0.033	40177		Phase - OC1 - 51
40247	LHS MV Lv1 ...		70.0		Tripped by LHS MV Lv1 SynMtr Rly Phase - OC1 - 51

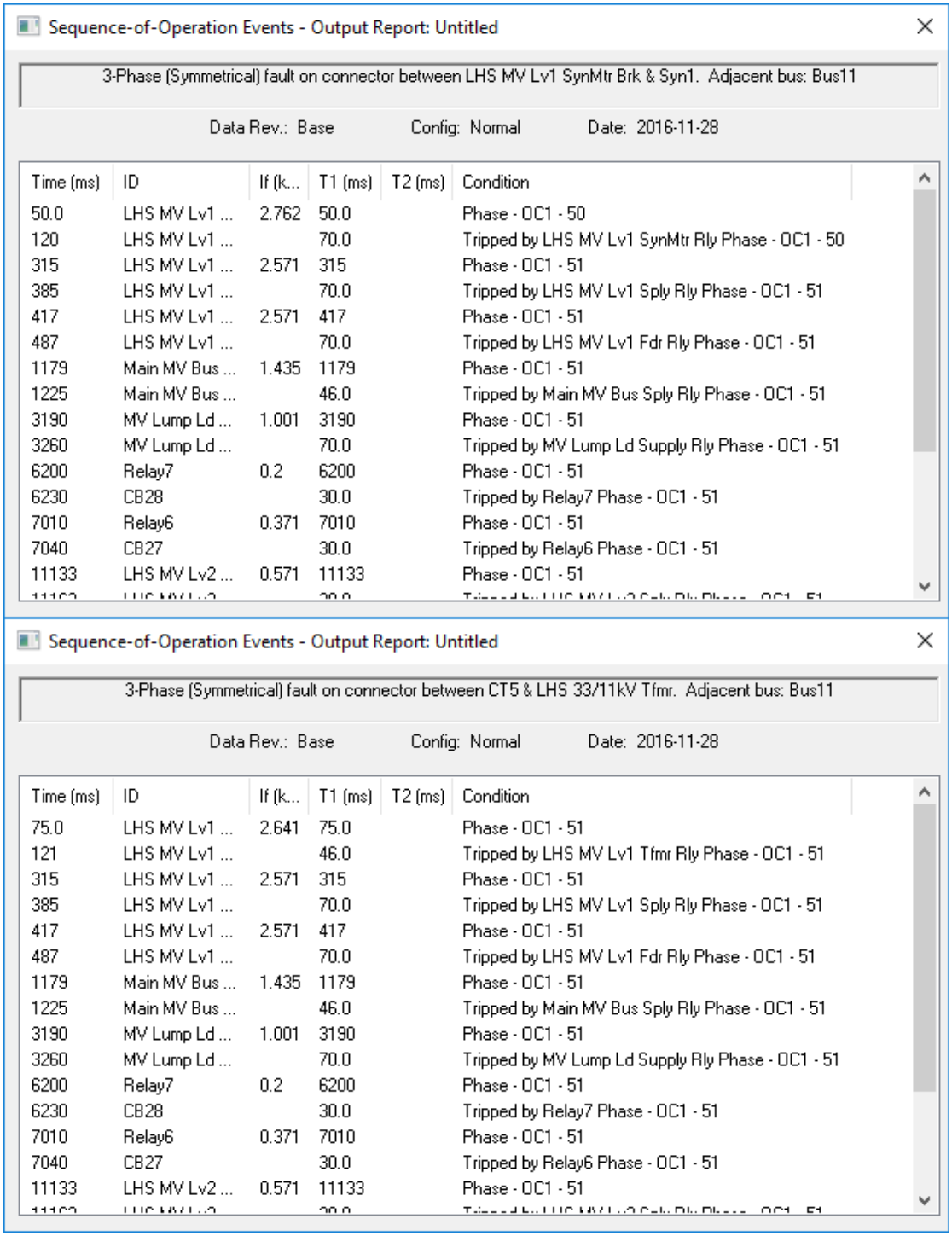


Figure 5: Viewing the sequence-of-operation report also shows the ideal case where there are also no "Tripped by…" conditions one after another, indicating overlap of operation times of the protective devices. (The protective device's trip time must also consider the downstream breaker's operating time too.)

3.2 Discussions

The above results show an ideal protective device operating sequence, where the protective device operates starting from the fault-end and progresses towards the supply as shown in the figures above.

Other trip sequences found during the course of experimentation are that the feeder or transformer primary breaker trips first before the receiving end breaker does. This has no effect on other consumers upstream and thus yields the same result of isolating a faulted zone. Through the use of different relay curves it may be possible to estimate the fault current by identifying which of these two breakers tripped due to the fault.

Undesired results are the most upstream breaker tripping first, or fault-end breakers tripping later than the supply-end breakers, showing a coordination problem, or the trigger times of two over current relays overlapping, where the next protective device begins to operate when the downstream breaker has not yet opened, and disrupting supply to the other loads.

In order to prevent this from happening, it is discovered that some practices are followed. For large motors, an instantaneous trip is used to safeguard against any currents greater than the start-up surge current of the motor while the time-overcurrent portion uses a Normal Inverse curve and pickup current slightly above the operating current to cover the portion where the motor has spun up to speed.

The protective devices also must have their operating times sufficiently spaced apart taking into account the breaker operating times. If the upstream protective device isn't sufficiently spaced enough, then it will operate before the downstream breaker has opened, causing both breakers to trip and bringing about supply disruptions.

4. Conclusion

The optimum protection relay settings for a feeder system have been determined with the help of ETAP. Various possible trip sequences can be obtained by using different types of relay curves along the supply line but the ideal trip sequences is one that begins from the fault-end and progresses towards the supply-end. The amount of experimenting done by the author to perform this research has increased the knowledge of the author in terms of the different practices followed to protect different types of loads and also the common complications and pitfalls of performing this job.

Acknowledgements

Many thanks to my supervisor Mr. Reynato Andal Gamboa for the assistance and guidance in performing this research. My gratitude also goes to ResearchGate for hosting research papers and B. Hussein, Suleiman Sharkh, and S. Hussein, for their

single-line diagram which I've based the single-line diagram for my power network on.

References

[1] J. Blackburn and T. Domin, *Protective relaying*. Third Edition. Boca Raton, FL: CRC Press, 2007

[2] Y. Paithankar and S. Bhide, *Fundamentals of power system protection*. New Delhi: PHI Learning, 2010.

[3] Ram, B. and Vishwakarma, D. (2011). *Power system protection and switchgear*. New Delhi: Tata McGraw Hill Education.

[4] P. Müller, Stefan Tenbohlen, Reinhard Maier, M. Anheuser, "Characteristics of Series and Parallel Low Current Arc Faults in the Time and Frequency Domain", in Electrical Contacts (HOLM), 2010 Proceedings of the 56th IEEE HOLM Conference, 2010.

[5] J. Blackburn and T. Domin, Protective relaying. Third Edition. Boca Raton, FL: CRC Press, 2007

[6] Seila Gruhonjic-Ferhatbegovic, Rinan Al-Tawil, "Application and settings inverse time relay characteristics for feeders overcurrent protection", in Electricity Distribution, 2005. CIRED 2005. 18th International Conference and Exhibition, 2005.

[7] Dinesh Birla, R.P. Maheshwari, Hari Om Gupta, "Time-Overcurrent Relay Coordination: A Review", in International Journal of Emerging Electric Power Systems 2(2), 2005.

[8] Y. Paithankar and S. Bhide, Fundamentals of power system protection. New Delhi: PHI Learning, 2010.

[9] *Breaker coordination: What you really need to know*. ABB [Online]. Available: http://www.tnbpowersolutions.com/sites/default/files/webfm/resources/upload/Cyberex%20Data%20Center/ABB%20Breakers%20and%20Panelboards/Breaker%20Coordination%20WP.pdf. [Accessed: 28- Nov- 2016]

[10] B. Hussain, S. Sharkh and S. Hussain, "*Impact studies of distributed generation on power quality and protection setup of an existing distribution network*", *SPEEDAM 2010*, 2010.

eureca 2016 – Conference Paper
Paper Number 2EE08

Effect of Integrating Derivative Control on SIPIC in Motor Speed Control

Jien Wong[1], Choon Lih Hoo[1*], Edwin Chin Yau Chung[1]

[1]*School of Engineering, Taylor's University, Malaysia*

[*]ChoonLih.Hoo@taylors.edu.my

Abstract

Proportional-Integral-Derivative (PID) controller is the most commonly used controller in control application due to its simplicity. PID controller is designed to perform in non-saturated control state. However, due to the plant input limitation, the control output may exceed the limiter which eventually deteriorates the system performance. The control will falls into saturated state and causes the system non-controllable. This deterioration of the performance is known as windup phenomenon, which causes large overshoot, long settling time, and sometimes even induces instability in the speed response. A number of anti-windup methods has been introduced to overcome the windup phenomenon such as Conditional Integration (1987), Tracking Back Calculation (2009), Integral State Prediction (2011), and Steady-State Integral Proportional-Integral Controller (SIPIC). In PID controller, it is difficult for non-overshoot and short settling time to coexist. This is due to the coupling of the tuning parameter k_p, k_d and k_i where k_p, k_i, and k_d represents proportional gain, integral gain and derivative gain respectively. With decoupling, a greater range of k_p, k_d and k_i can be applied to control the rising slope without disturbing the damping state. However, current PI anti-windup methods only took the tuning parameter k_p and k_i into account. This research aim to further study and explore on the effect of integrating derivative control, k_d on SIPIC in motor speed control. The decoupling effect with the derivative control will be observed for any changes. The speed control performance of the new controller will be simulated using SCILAB/ScicosLab software referring to parameter specification identified through system identification. This research shows a potential in contribution to knowledge by investigating the effect of incorporating derivative control in the control system.

Keywords: Motor Speed Control, Anti-windup, PI Controller, Steady-state Integral Proportional-Integral Controller, Decoupling

1. Introduction

Commonly used control algorithm among researchers in industrial application by far is Proportional-integral (PI) controller. PI controller able to eliminate errors or disturbance in a control system. However, due to the plant input limitation, when the control output exceeds the limiter which eventually deteriorates the system performance [1]. The control will falls into saturated state and causes the system non-controllable. This deterioration of the performance is known as windup phenomenon which subjected to large overshoot, prolonged settling time and sometimes even induces instability in the speed response [2, 3]. This will eventually cause physical degradation or damage to the system and soon leading to system malfunction [4].

In much newer research and development, a number of anti-windup methods has been introduced to resolve the windup phenomenon such as Conditional Integration (CI) (1987) [5], Tracking Back Calculation (TBC) (2009) [6], Integral State Prediction (ISP) (2011) [7], and Steady-State Integral Proportional-Integral Controller (SIPIC). Anti-windup control works in ensuring the control output to stay within the limit of the system input.

In PI controller, it is difficult for non-overshoot and short settling time to coexist as adding k_p and k_i value will increase the overshoot and settling time respectively [8]. This is due to the coupling of the tuning parameter k_p, k_d and k_i where k_p, k_i, and k_d represents proportional gain, integral gain and derivative gain respectively. Decoupling by means is the capability to separate the tuning parameter k_p, k_d and k_i into distinct pole in the dynamic equation model [8]. SIPIC has the capability to perform decoupling however, currently SIPIC only took the tuning parameter k_p and k_i into account and has shown results in better motor speed control performance as compared to the conventional anti-windup controllers [8].

In this paper, the effect of integrating derivative control, k_d on SIPIC in motor speed control will be studied and explored. The decoupling effect with the derivative control will be observed for any changes. The speed control performance of the new controller will be simulated using SCILAB/ScicosLab software referring to parameter specification identified through system identification.

This paper will continue with Section 2 that introduces the existing anti-windup controller schemes. Section 3 derives the equation for decoupling with integrating derivative control, k_d on SIPIC. Section 4 shows the setup for decoupling simulation and simulation of the anti-windup controller with derivative control. Simulation result will be discussed in Section 5 and followed by the conclusion of the research in Section 6.

1. Existing Anti-Windup Controller Schemes.

1.1 Anti-Windup Schemes comparison

Commonly used PI controller is famous for the speed control of variable-speed motor. PI controller has consequences of having system degradation when encounter with windup phenomenon that causes large overshoot, slow settling time, and sometimes even instability in speed response. A number of anti-windup methods has been introduced to resolve the windup phenomenon such as CI, TBC, and ISP. These

schemes have a similarity where the integral control switches during saturation and non-saturation [9]. These controller switches back to the conventional PI controller under non-saturation. All the anti-windup controller have their own integral control. Each of them are limited only to saturation state and switching at different states that will cause system degradation [9]. Table 1 below shows the advantages and disadvantages of the anti-windup controller mentioned above [9-10]. Table 2 shows the adaptive control for all the existing anti-windup controller which switches for the controller back to conventional PI controller under unsaturated state. The parameter e, u, v, k_a, q_{ss}, q, and w_i in Table 2 denotes the error signal, controller output, plant input, anti-windup gain, integral value at steady state, integral state and positive parameter of the low-pass filter for loading the initial value into the integrator respectively.

Table 7: Comparison of anti-windup schemes

Anti-windup	Advantage	Disadvantage
Conditional Integration (CI)	• Effective within saturation region • No overshoot	• Hard to select the gain required
Tracking Back Calculation (TBC)	• Wide range of gain selection • Improvement of overshoot than CI	• High gain will cause error • Possible risk of speed error
Integral State Prediction (ISP)	• Effective on both saturation and linear region • Prediction of steady state value to prevent unexpected integral state change	• Feedback is limited to happen only during linear region

Table 8: Integral control for existing anti-windup schemes and conventional PI scheme

Controller Scheme	Integral control under saturated state $u \neq v$	Integral control under unsaturated state $u = v$
Conventional PI controller	e	e
Conditional Integration (CI)	0	e
Tracking Back Calculation (TBC)	$e - k_a(u - v)$	e
Integral State Prediction (ISP)	$w_i(q_{ss} - q)$	e

1.2 Steady-State Integral Proportional Integral Controller (SIPIC)

SIPIC is another anti-windup PI method that has a separately built-in integral controller for variable-speed motor drive compared to CI [8]. Unlike CI method, SIPIC does not involve any switching of the integral control. Hence, SIPIC is free from any instability related with switching [11]. The research done in SIPIC has shown the possibility in decoupling which results in better motor speed control performance as compared to the conventional anti-windup controllers. According to Hoo et al. [12], SIPIC controlled system is stable regardless of k_p and k_i values.

2. Decoupling with Implementing Derivative Control, k_d.

In general the generic block diagram of a motor speed control is shown in Figure 1 where $V(s)$, $T_L(s)$, $P(s)$, and $\omega_r(s)$ denotes as controller output, external torque, system plant, and output speed respectively.

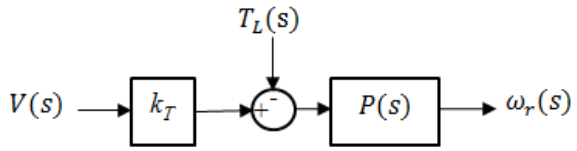


Figure 1: Block diagram for speed control [8]

The generality of the mathematical expressions will be denote as *a*, *b*, *c*, and *f* as the constant for the parameters of the plant. In a closed loop PID motor speed control, *e* is obtained from the difference between set reference, ω_r^* and ω_r as shown in equation (1) [8, 9, 11]. By referring to Figure 2, for $P(s) = \frac{f}{bs+a}$, the dynamic equation can be simplified as equation (2) with the aid from equation (1). The parameter k_T in equation (2) denotes torque constant.

$$e = \omega_r^* - \omega_r \tag{1}$$

$$vk_T = -\frac{b}{f}\dot{e} - \frac{a}{f}e + \frac{a}{f}\omega_r^* + T_L \tag{2}$$

PID controller can be described as equation (3) [8]. During steady state, the error signal will be zero meanwhile *q* will attain q_{ss}. Thus by substituting equation (3) into equation (2) will produce equation (4).

$$v = k_p e + k_i q + k_d \dot{e} \tag{3}$$

$$k_i k_T q_{ss} = T_L + \frac{a}{f}\omega_r^* \tag{4}$$

It can be seen that the last two terms on the right of equation (2) are related to equation (4). As a result, equation (1) can be converted into equation (5) when it is controlled by a PID controller using equation (3). Laplace transform equation (5) and upon rearranging the equation, equation (6) is obtained.

$$\left(\frac{b}{f} + k_d k_T\right)\dot{e} + \left(\frac{a}{f} + k_p k_T\right)e = k_i k_T (q_{ss} - q) \tag{5}$$

$$E(s) = \frac{e(0)\left(\frac{b}{f}+k_d k_T\right)+k_i k_T\left|\frac{a_{ss}}{s}-Q(s)\right|}{\left(\frac{b}{f}+k_d k_T\right)s+\frac{a}{f}+k_p k_T} \quad (6)$$

Considering **Theorem 5.2** in the research done by Hoo et al. [8], the integral component of SIPIC in S domain is represented as equation (7). Decoupling allows a greater range of k_p and k_d to manipulate the rising slope without much affecting the damping state, which indirectly allows the coexistence of non-overshoot and short settling time performance [8]. Since k_p and k_d always stay in the same pole, for simplicity, Hoo only taken k_p and k_i into consideration in equation (6) for SIPIC [8] and has shown the capability to separate the tuning parameter k_p and k_i into distinct poles [12]. In this paper, the parameter k_d will be included thus will be using equation (6) as it is. Substituting equation (7) into equation (6) results in equation (8).

$$Q(s) = \frac{q(0)-k_i\frac{a_{ss}}{s}}{s+k_i} \quad (7)$$

$$E(s) = \frac{e(0)\left(\frac{b}{f}+k_d k_T\right)+k_i k_T\left[\frac{a_{ss}}{s}-\frac{q(0)+k_i\frac{a_{ss}}{s}}{s+k_i}\right]}{\left(\frac{b}{f}+k_d k_T\right)s+\frac{a}{f}+k_p k_T} \quad (8)$$

Translated into the time domain, the error response of SIPIC+D is as described in equation (9). Noticed that k_p with k_d as a group and k_i tuning parameters are still separated in the error response expression. Thus it could be tuned to have no overshoot and still maintain a zero steady state error which will be illustrated in decoupling effect simulation in the next section.

$$e(t) = \left\{e(0) - \frac{k_i k_T(a_{ss}-q(0))}{\left(\frac{b}{f}+k_d k_T\right)\left(\frac{a+k_p k_T f}{b+k_d k_T f}-k_i\right)}\right\} e^{-\left(\frac{a+k_p k_T f}{b+k_d k_T f}\right)t} + \left\{\frac{k_i k_T(a_{ss}-q(0))}{\left(\frac{b}{f}+k_d k_T\right)\left(\frac{a+k_p k_T f}{b+k_d k_T f}-k_i\right)}\right\} e^{-k_i t} \quad (9)$$

3. Simulation for Decoupling Effect and Control Performance

In this research, there are two parts of the simulation. In the first simulation, is intended to demonstrate the tuning parameters decoupling mode of SIPIC+D in comparison to a normal PID controller. The second simulation is meant for performance testing between SIPIC+D and various controllers with derivative control.

3.1 Simulation for Decoupling Effect

For decoupling simulation, MATLAB R2016a/Simulink software was used. Simulations were structured as given in Figure 2 to investigate the effect of k_p, k_d and k_i on the system response. For simplicity the system plant is taken as $P(s) = \frac{1}{s+1}$ while other parameters are set to unity. The simulation was done for no load and load condition where load, $T_L = 5$. The parameter is set for $k_p = 1, 5, 10$, $k_i = 1, 5, 10$, and $k_d = 0.3, 0.6, 0.9$. The decoupling effect simulation will be simulated according to this set of parameter.

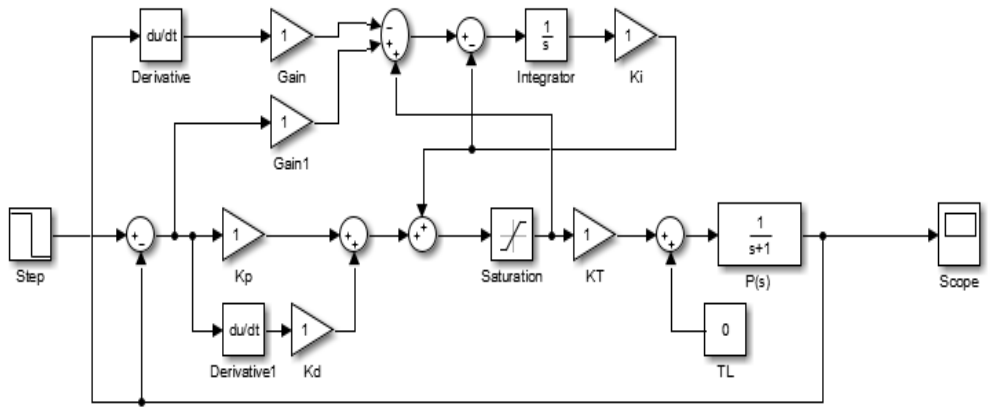


Figure 2: Structure for SIPIC+D in MATLAB R2016a/Simulink

3.2 Simulation for Control Performance

The work was simulated with Scilab/Scicoslab 4.4.1 for no load and loading conditions. The performance of SIPIC+D for speed control of a DC motor is compared against the conventional PI, conditional integration, tracking back calculation and integral state prediction schemes. All the anti-windup controller in this case is added with the derivative control. Figure 3 shows the structure for all the anti-windup scheme for hardware simulation. To ensure the reliability of the model built, system identification was performed using the System Ident feature in Scilab/Scicoslab 4.4.1.

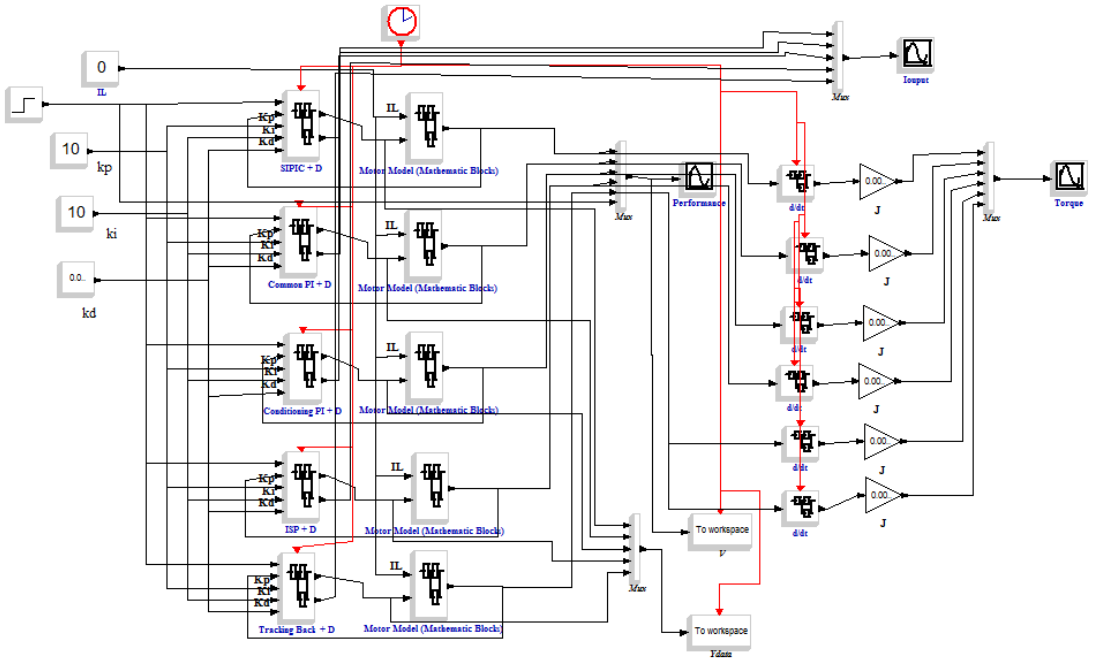


Figure 3: Structure for hardware simulation in Scilab/Scicoslab 4.4.1 software

The hardware simulation requires a setup of DC servo motor, motor encoder and host computer with Scilab/Scicoslab 4.4.1 software and real time kernel rtai installed under Linux. Table 3 shows the details of these setup components. The parameters for DC motor speed are tuned according to the values in Table 4 in order to obtain a stable performance. The simulation for control performance was done in

the speed of 50rad/s and 100rad/s. The simulation was done for no load and load of Aluminium plating with moment of inertia 2.83 x 10^{-5} kgm^2 on a range of tuning gain.

4. Simulation Results

4.1 Decoupling Effect

Figure 4 and Figure 5 show the result for the MATLAB simulation in investigating the decoupling effect for SIPIC+D under no load and loading condition. The response for common PID is not shown, however it will be discussed as listed in Table 5. The result shown in Figure 4 illustrates that increasing k_i will shorten the rise time and settling time for SIPIC+D as indicated in Table 5. The conventional PI controller with derivative control also reduces the rise time however increases the settling time with increasing k_i. Increasing k_p will also have the same effect. This result holds for no load condition regardless of any k_d value.

Table 3: Specification for DC servo motor

Characteristics	Values
Maximum supply voltage	40 Vdc
Maximum continuous torque	14 Ncm
Maximum peak torque	36 Ncm
Motor voltage constant	10.3 V at 1000 rpm
Motor torque constant	9.0 Ncm/A
Mechanical time constant	20 ms
Rotor inertia	0.214 kg cm
Terminal resistance	7.8 Ohms
Rated speed	1600 rpm
No load speed	2600 rpm @ 24 Vdc
Rated torque	12 Ncm
Peak torque	27 Ncm

Table 4: Parameter for DC motor speed test

Characteristics	Values
Viscous damping coefficient, B	2.12 x 10-4 kg m2/s
Inductance, L	0.005 H
Moment of inertia of motor, J	2.14 x 10-5 kg m2
Torque constant, kt	0.09 Nm/A
Back-emf constant, *km*	0.09 Nm/A
Efficiency, η	0.8
Resistance, R	7.8 Ω

The same performance can be observed even in loaded case as given in Figure 5. In Table 5, both SIPIC+D and conventional PID have faster rise time and shorter settling time at loading condition. However, the rise time and settling time will increase with increasing k_d. SIPIC+D does not have overshoot, which is not the case for conventional PID that contains undesirable high overshoot at high gain. Favourably, SIPIC+D has the capability to solve the issue commonly encountered in conventional PID.

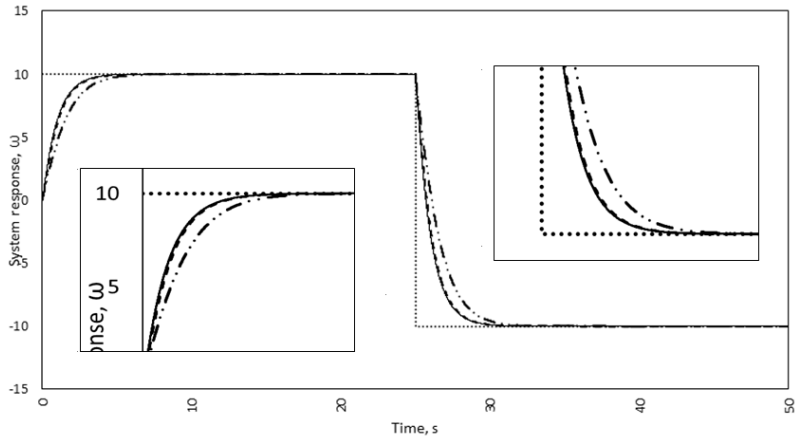


Figure 4: Decoupling simulation for SIPIC+D under no load condition for $k_i = 1$ (dash double dot), $k_i = 5$ (dash), $k_i = 10$ (solid) with both k_p and k_d are fixed at 1 and 0.9 respectively.

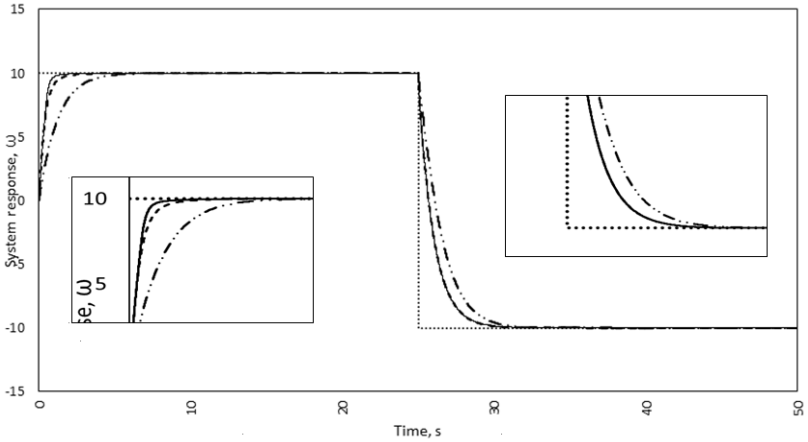


Figure 5: Decoupling simulation for SIPIC+D under load condition for $k_p = 1$ (dash double dot), $k_p = 5$ (dash), $k_p = 10$ (solid) with both k_i and k_d are fixed at 1 and 0.9 respectively.

From the result in Table 5, it is possible to conclude the effect of increasing the tuning gain for SIPIC+D in Table 6. The effect is different from the conventional PI tuning effort where increasing k_p and k_i will raise the overshooting and higher k_i should invite bigger settling time. This characteristic of SIPIC+D is seen to be attributed by its decoupling effect when changing the tuning gain. Consequently, this allows a wider range to tuning gain selection for different settling time or rise time requirement while maintaining low or no overshooting performance.

4.2 Control Performance

Figure 6 shows the simulated motor speed at 100 rad/s of SIPIC, conventional PI, conditional integral, tracking back calculation, and integral state prediction schemes with derivative control under no load condition. Conventional PID has the fastest integral speed as compare to other methods as indicated in Table 7 and Table 8. However, this drastic speed is responsible for the overshoot in its performance. The rise time and settling time for all the controller schemes decrease with increasing k_p and k_i values. SIPIC+D has no overshoot but has a shorter settling time as compared

to other anti-windup schemes with derivative control except for conventional PID at low k_p value. This is due to higher value of the integral gain that brought the system into saturation where the proportional component could not correct the error fast enough.

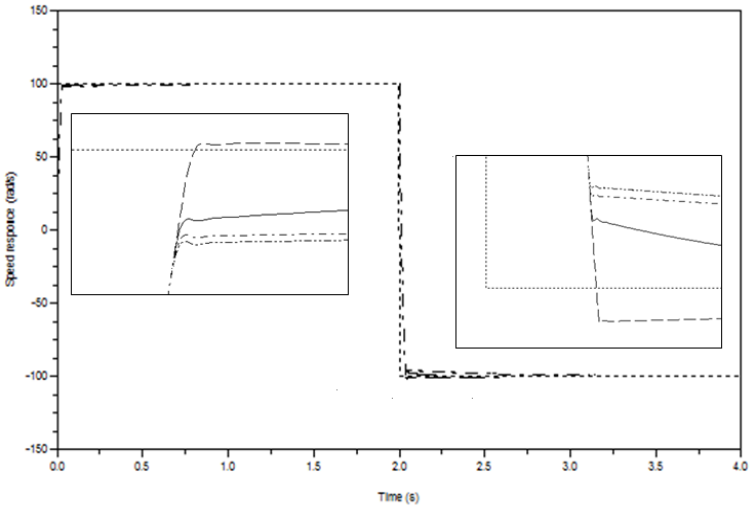


Figure 6: Comparison of speed control for SIPIC+D (Solid), conventional PID (dash), CI+D (big-dash dot), ISP+D (big-dash long-dash), and TBC+D (long-dash dot) under no load condition. Reference input (dot) (Speed = 100 rad/s, $k_p = 5, k_i = 10, k_d = 0.0006$)

Table 5: SIPIC+D and PID in decoupling simulation for no load and load condition

Case			No Load				Load			
			Rise time (s)		Settling time (s)		Rise time (s)		Settling time (s)	
k_p	k_i	k_d	SIPIC + D	PID	SIPIC + D	PID	SIPIC + D	PID	SIPIC + D	PID
1	1	0.3	2.448	2.14	3.301	2.73	1.997	1.247	2.748	3.841
1	1	0.6	2.71	2.166	3.636	2.685	2.298	1.478	3.124	5.062
1	1	0.9	2.98	2.224	3.992	5.564	2.6	1.601	3.513	5.857
1	5	0.3	1.514	0.868	2.079	4.43	1.479	0.594	2.017	3.713
1	5	0.6	1.606	0.89	2.521	4.879	1.801	0.645	2.462	4.191
1	5	0.9	2.15	0.914	2.966	5.283	2.125	0.701	2.909	4.621
1	10	0.3	1.452	0.848	2.005	5.05	1.443	0.553	1.978	4.105
1	10	0.6	1.777	0.851	2.453	5.486	1.77	0.564	2.426	4.521
1	10	0.9	2.104	0.857	2.902	5.866	2.097	0.579	2.875	5.928
5	1	0.3	0.992	1.2	1.516	4.54	0.712	0.678	1.058	0.984
5	1	0.6	1.066	1.301	1.61	4.446	0.796	0.753	1.177	1.096
5	1	0.9	1.146	1.4	1.709	4.3112	0.89	0.837	1.302	1.207
5	5	0.3	0.857	0.848	1.079	3.052	0.625	0.546	0.832	2.407
5	5	0.6	0.882	0.848	1.139	3.088	0.686	0.546	0.927	2.407
5	5	0.9	0.92	0.848	1.211	3.136	0.759	0.562	1.034	2.627
5	10	0.3	0.856	0.848	1.076	3.029	0.619	0.546	0.821	2.111
5	10	0.6	0.88	0.848	1.134	3.048	0.677	0.546	0.914	2.146
5	10	0.9	0.916	0.848	1.205	3.075	0.748	0.546	1.02	2.191
10	1	0.3	0.849	0.856	1.08	1.359	0.563	0.558	0.739	0.72
10	1	0.6	0.856	0.87	1.119	1.434	0.583	0.576	0.785	0.762
10	1	0.9	0.869	0.891	1.162	1.508	0.609	0.599	0.835	0.81
10	5	0.3	0.848	0.848	1.008	3.09	0.551	0.546	0.688	2.258
10	5	0.6	0.848	0.848	1.02	3.114	0.564	0.546	0.719	2.314
10	5	0.9	0.848	0.848	1.038	3.143	0.582	0.546	0.756	2.381

10	10	0.3	0.848	0.848	1.008	3.416	0.551	0.546	0.685	2.486
10	10	0.6	0.848	0.848	1.019	3.405	0.562	0.546	0.715	2.492
10	10	0.9	0.848	0.848	1.037	3.398	0.58	0.546	0.752	2.505

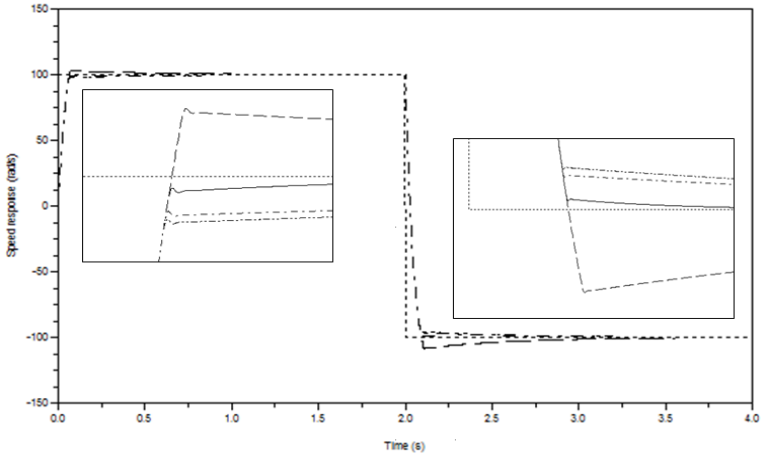


Figure 7: Comparison of speed control for SIPIC+D (Solid), conventional PID (dash), CI+D (big-dash dot), ISP+D (big-dash long-dash), and TBC+D (long-dash dot) under load condition. Reference input (dot) (Speed = 100 rad/s, $k_p = 5, k_i = 10, k_d = 0.0006$)

Table 6: Summary of tuning on the SIPIC+D performance

Case	Rise Time	Settling Time	Overshoot
Increase k_p	Decrease	Decrease	No change
Increase k_i	Decrease	Decrease	No change
Increase k_d	Increase	Increase	No change

The same observation is seen for the result in loading condition. This corresponds to their integral components that reach steady state slower than SIPIC+D. Take note that SIPIC+D drives the motor closest to the desired reference input value most of the time when compared to the other controller schemes. This is due to the fast attainment of steady state integral value in the system. However, there is limitation for SIPIC+D where it slowly exhibit minimum overshoot at higher k_p value. The CI+D and ISP+D do not suffer from any overshoot, however it took a longer settling time compared to SIPIC+D hence experience a slower error response. In comparison, SIPIC+D experiences minimum overshoot might be due to the noise at higher k_p value. This is regardless of the speed and the loading condition of the system. More different tuning parameter values will need to be tested in order to further refine the manifold factor that could specifically define the tuning limitation of SIPIC+D.

5. Conclusion

Integrating derivative control in SIPIC shows a potential in contributing to the society by serving as another choice of anti-windup controller for motor speed control. SIPIC+D could still be tuned to have no overshoot and still maintain a zero steady state error which shows the decoupling effect of the system. SIPIC+D shows a better result regardless of the loading condition compared to the other anti-windup controller schemes. However, there is limitation for SIPIC+D where it slowly exhibit minimum

overshoot at higher k_p value. Hence, in future work, more different tuning parameter will need to be tested to tackle the limitation of SIPIC+D.

Table 7: Performance at 50 rad/s under no load condition

K_p	K_i	K_d	Rise Time (s)					Settling Time (s)					Overshoot (%)				
			SIPIC + D	PID	CI + D	ISP + D	TBC + D	SIPIC + D	PID	CI + D	ISP + D	TBC + D	SIPIC + D	PID	CI + D	ISP + D	TBC + D
1	1	0.0003	0.019	0.019	0.022	0.022	0.016	0.931	0.988	1.038	1.038	1.018	0	0	0	0	0
1	1	0.0006	0.021	0.016	0.023	0.023	0.019	0.931	0.987	1.037	1.037	1.018	0	0	0	0	0
1	1	0.0009	0.023	0.018	0.024	0.024	0.021	0.93	0.985	1.031	1.031	1.018	0	0	0	0	0
1	5	0.0003	0.013	0.01	0.014	0.014	0.012	0.187	0.154	0.21	0.21	0.189	0	0	0	0	0
1	5	0.0006	0.015	0.011	0.016	0.016	0.013	0.187	0.152	0.208	0.208	0.189	0	0	0	0	0
1	5	0.0009	0.017	0.013	0.017	0.017	0.015	0.186	0.15	0.203	0.203	0.188	0	0	0	0	0
1	10	0.0003	0.012	0.009	0.013	0.013	0.01	0.094	0.038	0.106	0.106	0.084	0	0	0	0	0
1	10	0.0006	0.013	0.01	0.014	0.014	0.012	0.093	0.036	0.105	0.105	0.084	0	0	0	0	0
1	10	0.0009	0.015	0.011	0.015	0.015	0.013	0.009	0.033	0.099	0.099	0.083	0	0	0	0	0
5	1	0.0003	0.007	0.007	0.007	0.007	0.007	0.01	0.01	0.01	0.01	0.01	0	0	0	0	0
5	1	0.0006	0.007	0.007	0.007	0.007	0.007	0.01	0.01	0.01	0.01	0.01	0	0	0	0	0
5	1	0.0009	0.007	0.007	0.007	0.007	0.007	0.01	0.01	0.01	0.01	0.01	0	0	0	0	0
5	5	0.0003	0.007	0.007	0.007	0.007	0.007	0.01	0.01	0.01	0.01	0.01	0	0	0	0	0
5	5	0.0006	0.007	0.007	0.007	0.007	0.007	0.01	0.01	0.01	0.01	0.01	0	0	0	0	0
5	5	0.0009	0.007	0.007	0.007	0.007	0.007	0.01	0.01	0.01	0.01	0.01	0	0	0	0	0
5	10	0.0003	0.007	0.007	0.007	0.007	0.007	0.01	0.01	0.01	0.01	0.01	0	0	0	0	0
5	10	0.0006	0.007	0.007	0.007	0.007	0.007	0.01	0.01	0.01	0.01	0.01	0	0	0	0	0
5	10	0.0009	0.007	0.007	0.007	0.007	0.007	0.01	0.01	0.01	0.01	0.01	0	0	0	0	0
10	1	0.0003	0.007	0.007	0.007	0.007	0.007	0.01	0.01	0.01	0.01	0.01	0	0	0	0	0
10	1	0.0006	0.007	0.007	0.007	0.007	0.007	0.01	0.01	0.01	0.01	0.01	0	0	0	0	0
10	1	0.0009	0.007	0.007	0.007	0.007	0.007	0.01	0.01	0.01	0.01	0.01	0	0	0	0	0
10	5	0.0003	0.007	0.007	0.007	0.007	0.007	0.01	0.01	0.01	0.01	0.01	0	0	0	0	0
10	5	0.0006	0.007	0.007	0.007	0.007	0.007	0.01	0.01	0.01	0.01	0.01	0	0	0	0	0
10	5	0.0009	0.007	0.007	0.007	0.007	0.007	0.01	0.01	0.01	0.01	0.01	0	0	0	0	0
10	10	0.0003	0.007	0.007	0.007	0.007	0.007	0.01	0.01	0.01	0.01	0.01	0	0.17	0	0	0
10	10	0.0006	0.007	0.007	0.007	0.007	0.007	0.01	0.01	0.01	0.01	0.01	0	0	0	0	0
10	10	0.0009	0.007	0.007	0.007	0.007	0.007	0.01	0.01	0.01	0.01	0.01	0	0	0	0	0

Table 8: Performance at 100 rad/s for no load condition

K_p	K_i	K_d	Rise Time (s)					Settling Time (s)					Overshoot (%)				
			SIPIC + D	PID	CI + D	ISP + D	TBC + D	SIPIC + D	PID	CI + D	ISP + D	TBC + D	SIPIC + D	PID	CI + D	ISP + D	TBC + D
1	1	0.0003	0.027	0.023	0.037	0.037	0.026	0.709	0.689	0.81	0.808	0.777	0	0.00	0	0	0
1	1	0.0006	0.029	0.024	0.037	0.037	0.028	0.71	0.689	0.81	0.808	0.778	0	0.00	0	0	0
1	1	0.0009	0.03	0.025	0.038	0.038	0.03	0.71	0.689	0.81	0.808	0.778	0	0.00	0	0	0
1	5	0.0003	0.023	0.021	0.026	0.026	0.022	0.144	0.03	0.18	0.178	0.147	0	0.00	0	0	0
1	5	0.0006	0.024	0.021	0.028	0.028	0.023	0.144	0.032	0.18	0.178	0.147	0	0.00	0	0	0
1	5	0.0009	0.025	0.021	0.029	0.029	0.024	0.144	0.033	0.18	0.178	0.147	0	0.00	0	0	0
1	10	0.0003	0.022	0.021	0.025	0.025	0.021	0.073	0.026	0.1	0.099	0.067	0	0.67	0	0	0
1	10	0.0006	0.022	0.021	0.026	0.026	0.022	0.073	0.026	0.1	0.099	0.067	0	0.67	0	0	0
1	10	0.0009	0.023	0.021	0.027	0.027	0.022	0.073	0.027	0.1	0.099	0.067	0	0.68	0	0	0
5	1	0.0003	0.021	0.021	0.021	0.021	0.021	0.027	0.027	0.03	0.027	0.027	0	0.00	0	0	0
5	1	0.0006	0.021	0.021	0.021	0.021	0.021	0.027	0.027	0.03	0.027	0.027	0	0.00	0	0	0
5	1	0.0009	0.021	0.021	0.021	0.021	0.021	0.027	0.027	0.03	0.027	0.027	0	0.00	0	0	0
5	5	0.0003	0.021	0.021	0.021	0.021	0.021	0.027	0.027	0.03	0.027	0.027	0	0.00	0	0	0
5	5	0.0006	0.021	0.021	0.021	0.021	0.021	0.027	0.027	0.03	0.027	0.027	0	0.00	0	0	0
5	5	0.0009	0.021	0.021	0.021	0.021	0.021	0.027	0.027	0.03	0.027	0.027	0	0.00	0	0	0
5	10	0.0003	0.021	0.021	0.021	0.021	0.021	0.027	0.027	0.03	0.027	0.027	0	0.30	0	0	0
5	10	0.0006	0.021	0.021	0.021	0.021	0.021	0.027	0.027	0.03	0.027	0.027	0	0.16	0	0	0
5	10	0.0009	0.021	0.021	0.021	0.021	0.021	0.027	0.027	0.03	0.027	0.027	0	0.15	0	0	0
10	1	0.0003	0.021	0.021	0.021	0.021	0.021	0.027	0.027	0.03	0.027	0.027	0	0.00	0	0	0
10	1	0.0006	0.021	0.021	0.021	0.021	0.021	0.027	0.027	0.03	0.027	0.027	0	0.00	0	0	0
10	1	0.0009	0.021	0.021	0.021	0.021	0.021	0.027	0.027	0.03	0.027	0.027	0	0.00	0	0	0
10	5	0.0003	0.021	0.021	0.021	0.021	0.021	0.027	0.027	0.03	0.027	0.027	0	0.00	0	0	0
10	5	0.0006	0.021	0.021	0.021	0.021	0.021	0.027	0.027	0.03	0.027	0.027	0	0.00	0	0	0
10	5	0.0009	0.021	0.021	0.021	0.021	0.021	0.027	0.027	0.03	0.027	0.027	0	0.00	0	0	0
10	10	0.0003	0.021	0.021	0.021	0.021	0.021	0.027	0.027	0.03	0.027	0.027	0	0.14	0	0	0
10	10	0.0006	0.021	0.021	0.021	0.021	0.021	0.027	0.027	0.03	0.027	0.027	0	0.12	0	0	0
10	10	0.0009	0.021	0.021	0.021	0.021	0.021	0.027	0.027	0.03	0.027	0.027	0	0.11	0	0	0

Table 9: Performance for 50 rad/s for load condition

K_p	K_i	K_d	Rise Time (s)					Settling Time (s)					Overshoot (%)				
			SIPIC + D	PID	CI + D	ISP + D	TBC + D	SIPIC + D	PID	CI + D	ISP + D	TBC + D	SIPIC + D	PID	CI + D	ISP + D	TBC + D
1	1	0.0003	0.031	0.027	0.037	0.037	0.03	0.906	0.931	1.044	1.044	0.996	0	0	0	0	0
1	1	0.0006	0.033	0.029	0.039	0.039	0.033	0.906	0.93	1.039	1.039	0.996	0	0	0	0	0
1	1	0.0009	0.035	0.031	0.041	0.041	0.035	0.906	0.929	1.038	1.038	0.996	0	0	0	0	0
1	5	0.0003	0.024	0.021	0.029	0.029	0.024	0.159	0.061	0.215	0.215	0.163	0	0	0	0	0
1	5	0.0006	0.025	0.022	0.03	0.03	0.025	0.159	0.059	0.211	0.211	0.163	0	0	0	0	0
1	5	0.0009	0.027	0.023	0.031	0.031	0.026	0.159	0.057	0.209	0.209	0.162	0	0	0	0	0
1	10	0.0003	0.022	0.02	0.027	0.027	0.022	0.062	0.025	0.111	0.111	0.05	0	0.75	0	0	0
1	10	0.0006	0.023	0.02	0.027	0.027	0.022	0.061	0.026	0.106	0.106	0.049	0	0.82	0	0	0
1	10	0.0009	0.024	0.02	0.028	0.028	0.023	0.06	0.027	0.105	0.105	0.049	0	0.89	0	0	0
5	1	0.0003	0.019	0.019	0.019	0.019	0.019	0.023	0.023	0.023	0.023	0.023	0	0	0	0	0
5	1	0.0006	0.019	0.019	0.019	0.019	0.019	0.023	0.023	0.023	0.023	0.023	0	0	0	0	0
5	1	0.0009	0.019	0.019	0.019	0.019	0.019	0.023	0.023	0.023	0.023	0.023	0	0	0	0	0
5	5	0.0003	0.019	0.019	0.019	0.019	0.019	0.023	0.023	0.023	0.023	0.023	0	0.32	0	0	0
5	5	0.0006	0.019	0.019	0.019	0.019	0.019	0.023	0.023	0.023	0.023	0.023	0	0.02	0	0	0
5	5	0.0009	0.019	0.019	0.019	0.019	0.019	0.023	0.023	0.023	0.023	0.023	0	0	0	0	0
5	10	0.0003	0.019	0.019	0.019	0.019	0.019	0.023	0.023	0.023	0.023	0.023	0.18	1.35	0	0	0
5	10	0.0006	0.019	0.019	0.019	0.019	0.019	0.023	0.023	0.023	0.023	0.023	0	1	0	0	0
5	10	0.0009	0.019	0.019	0.019	0.019	0.019	0.023	0.023	0.023	0.023	0.023	0	0.73	0	0	0
10	1	0.0003	0.019	0.019	0.019	0.019	0.019	0.023	0.023	0.023	0.023	0.023	1.09	1.16	1.02	1.02	1.03
10	1	0.0006	0.019	0.019	0.019	0.019	0.019	0.023	0.023	0.023	0.023	0.023	0.88	0.95	0.81	0.81	0.82
10	1	0.0009	0.019	0.019	0.019	0.019	0.019	0.023	0.023	0.023	0.023	0.023	0.67	0.75	0.6	0.6	0.61
10	5	0.0003	0.019	0.019	0.019	0.019	0.019	0.023	0.023	0.023	0.023	0.023	1.31	1.63	1.01	1.01	1.04
10	5	0.0006	0.019	0.019	0.019	0.019	0.019	0.023	0.023	0.023	0.023	0.023	1.1	1.44	0.79	0.79	0.83
10	5	0.0009	0.019	0.019	0.019	0.019	0.019	0.023	0.023	0.023	0.023	0.023	0.91	1.26	0.58	0.58	0.62
10	10	0.0003	0.019	0.019	0.019	0.019	0.019	0.023	0.023	0.023	0.023	0.023	1.54	2.05	0.99	0.99	1.06
10	10	0.0006	0.019	0.019	0.019	0.019	0.019	0.023	0.023	0.023	0.023	0.023	1.36	1.93	0.78	0.78	0.86
10	10	0.0009	0.019	0.019	0.019	0.019	0.019	0.023	0.023	0.023	0.023	0.023	1.15	1.78	0.55	0.55	0.63

Table 10: Performance at 100 rad/s for load condition

K_p	K_i	K_d	Rise Time (s)					Settling Time (s)					Overshoot (%)				
			SIPIC + D	PID	CI + D	ISP + D	TBC + D	SIPIC + D	PID	CI + D	ISP + D	TBC + D	SIPIC + D	PID	CI + D	ISP + D	TBC + D
1	1	0.0003	0.054	0.05	0.067	0.067	0.054	0.685	0.547	0.836	0.836	0.763	0	0	0	0	0
1	1	0.0006	0.055	0.051	0.068	0.068	0.056	0.685	0.547	0.836	0.836	0.764	0	0	0	0	0
1	1	0.0009	0.056	0.051	0.07	0.07	0.057	0.685	0.547	0.836	0.836	0.764	0	0	0	0	0
1	5	0.0003	0.05	0.05	0.057	0.057	0.05	0.115	0.06	0.206	0.206	0.13	0	1.9	0	0	0
1	5	0.0006	0.05	0.05	0.058	0.058	0.05	0.115	0.06	0.206	0.206	0.13	0	1.89	0	0	0
1	5	0.0009	0.05	0.05	0.059	0.059	0.05	0.115	0.06	0.206	0.206	0.13	0	1.88	0	0	0
1	10	0.0003	0.05	0.05	0.055	0.055	0.05	0.062	0.195	0.127	0.127	0.063	0	12.55	0	0	0
1	10	0.0006	0.05	0.05	0.056	0.056	0.05	0.063	0.195	0.127	0.127	0.064	0	12.47	0	0	0
1	10	0.0009	0.05	0.05	0.056	0.056	0.05	0.063	0.195	0.127	0.127	0.065	0	12.41	0	0	0
5	1	0.0003	0.05	0.05	0.05	0.05	0.05	0.06	0.06	0.06	0.06	0.06	0	0	0	0	0
5	1	0.0006	0.05	0.05	0.05	0.05	0.05	0.06	0.06	0.06	0.06	0.06	0	0	0	0	0
5	1	0.0009	0.05	0.05	0.05	0.05	0.05	0.06	0.06	0.06	0.06	0.06	0	0	0	0	0
5	5	0.0003	0.05	0.05	0.05	0.05	0.05	0.06	0.06	0.06	0.06	0.06	0	0.69	0	0	0
5	5	0.0006	0.05	0.05	0.05	0.05	0.05	0.06	0.06	0.06	0.06	0.06	0	0.63	0	0	0
5	5	0.0009	0.05	0.05	0.05	0.05	0.05	0.06	0.06	0.06	0.06	0.06	0	0.57	0	0	0
5	10	0.0003	0.05	0.05	0.05	0.05	0.05	0.06	0.06	0.06	0.06	0.06	0	3.31	0	0	0
5	10	0.0006	0.05	0.05	0.05	0.05	0.05	0.06	0.06	0.06	0.06	0.06	0	3.25	0	0	0
5	10	0.0009	0.05	0.05	0.05	0.05	0.05	0.06	0.06	0.06	0.06	0.06	0	3.18	0	0	0
10	1	0.0003	0.05	0.05	0.05	0.05	0.05	0.06	0.06	0.06	0.06	0.06	0	0	0	0	0
10	1	0.0006	0.05	0.05	0.05	0.05	0.05	0.06	0.06	0.06	0.06	0.06	0	0	0	0	0
10	1	0.0009	0.05	0.05	0.05	0.05	0.05	0.06	0.06	0.06	0.06	0.06	0	0	0	0	0
10	5	0.0003	0.05	0.05	0.05	0.05	0.05	0.06	0.06	0.06	0.06	0.06	0	0.62	0	0	0
10	5	0.0006	0.05	0.05	0.05	0.05	0.05	0.06	0.06	0.06	0.06	0.06	0	0.56	0	0	0
10	5	0.0009	0.05	0.05	0.05	0.05	0.05	0.06	0.06	0.06	0.06	0.06	0	0.52	0	0	0
10	10	0.0003	0.05	0.05	0.05	0.05	0.05	0.06	0.06	0.06	0.06	0.06	0	1.91	0	0	0
10	10	0.0006	0.05	0.05	0.05	0.05	0.05	0.06	0.06	0.06	0.06	0.06	0	1.87	0	0	0
10	10	0.0009	0.05	0.05	0.05	0.05	0.05	0.06	0.06	0.06	0.06	0.06	0	1.82	0	0	0

References

[1] S. M. Gadoue, D. Giaouris and J. W. Finch, "Artificial intelligence-based speed control of DTC induction motor drives - a comparative study," *Electric Power Systems Research*, vol.79, no.1, pp.210-219, 2009.

[2] B. Bahrani, S. Kenzelmann, and A. Rufer, "Multivariable-PI-based dq current control of voltage source converters with superior axes decoupling capability," *IEEE Trans. Ind. Electron.*, vol. 58, no. 7, pp. 3016-3026, July 2011.

[3] R. J. Wai, J. D. Lee, and K. L. Chuang, "Real-time PID control strategy for Maglev transportation system via particle Swarm optimization," *IEEE Trans. Idn. Electron.*, vol. 58, no. 2, pp. 629-646, February 2016.

[4] K. Astrom and T. Hagglund, *PID Controllers: Theoty, Design, and Tuning*. Research Triangle Park, NC: ISA, 1995, pp. 59-92.

[5] N.J. Krikelis, "State Feedback Integral Control with Intelligent Integrator", *Int. J. Control*, vol.32, no.3, pp.465-473, 1980. [1] R. C. Dorf and R. H. Bishop, *Modern Control System*, Prentice Hall, 2001.

[6] H. B. Shin, "New Antiwindup PI Controller for Variable-Speed Motor Drives," *IEEE Trans. Ind. Electron*, vol.45, no.3, pp.445-450, 1998

[7] H. B. Shin and J. G. Park, "Anti-Windup PID Controller With Intergral State Predictor for Variable-Speed Motor Drives", *IEEE Transactions on Industrial Electronics*, vol.59, no.3, pp.1509-1516, 2012

[8] C. L. Hoo, Edwin. C. Y. Chung, S. M. Haris, and N.A.N. Mohamed, "The Generalization and decoupling mode of PI-based Control: Theoretical Approach," *ICIC Express Letters*, vol. 9, no. 7, pp. 1991-1996, July 2015.

[9] X.L. Li, J.G. Park, and H.B. Shin, "Comparison and Evaluation of Anti-Windup PI Controllers," *Journal of Power Electronics*, vol. 11, no. 1, January 2011

[10] J. G. Park, J. H. Chung and H. B. Shin, "Anti-Windup integral-proportional controller for variable-speed motor drives," *Journal of Power Electronics*, vol. 2, pp. 130-138, April 2002

[11] C. L. Hoo, Edwin. C. Y. Chung, S. M. Haris, and N.A.N. Mohamed, "Steady-State Integral Proportional Integral Controller for PI Motor Speed Controllers," *Journal of Power Electronic*, vol. 15, no. 1, pp. 177-189, January 2015

[12] C. L. Hoo, Edwin. C. Y. Chung, S. M. Haris, and N.A.N. Mohamed, "Steady-State Integral Proportional Integral Controller for PI Motor Speed Controllers: A Theoretical Approach," *ICIC Express Letters*, vol. 9, no. 6, pp. 1777-1782, June 2015.

eureca 2016 – Conference Paper
Paper Number 2ME01

Effect of the Inclination Angle of Front Window on the Drag of a Personal Vehicle

Khathman Abdul Sattar[1*], Abdulkareem Sh. Mahdi Al-Obaidi [2]

[1]*School of Engineering, Taylor's University, Malaysia*

[*]khathman@gmail.com

Abstract
The demand for non-renewable resources that are required to produce fuel is increasing day by day. The main factor contributing to this is the exponential increase in the number of vehicles used for personal means. This is an issue that requires immediate attention as the world's reserve of non-renewable energy sources are depleting at an alarming rate [1]. Hence the production of vehicles that are fuel-efficient is paramount. One of the methods to reduce the consumption of fuel is by reducing the drag force on the vehicle. The objective of the research is to obtain an optimum angle of inclination for which the drag experienced on the vehicle is minimum and hence reduce the fuel consumed. Data are collected from real vehicles and analysed in order to specify the range of inclination angles to be used in the analysis. In this paper, a numerical approach (namely, ANSYS) is used. Computational Fluid Dynamics (CFD) is then used to run the simulations in ANSYS. The data obtained from simulation is then verified by comparing with published data. A difference of 5% was obtained in the comparison of the result obtained from simulation and published data. The outcome of the research is to obtain a relationship between the drag coefficients of a vehicle as a function of the inclination angle of the front window at average cruising speed. This will be used to conclude by obtaining the optimum angle that produces minimum drag force on the vehicle. The obtained results conclude that the coefficient of drag is minimum at a specific angle of inclination. Any variation from this angle of inclination results in the increase of the coefficient of drag. Although ambitious, it can also be used to produce a novel and innovative mechanism to actively control the inclination angle of the front window corresponding to a certain speed in order to produce minimum drag on the vehicle.

Keywords: Inclination Angle, Front Window, Aerodynamic Drag, CFD.

1. Introduction

The world is changing and developing technologically at a rather fast speed rate. The three key points focused by the developing world in the progression of the work limit is by making it easier, safe and efficient. New and innovative studies are conducted in various aspects of life to reach a better and convenient approach. The means used as daily transportation is one of the fields that need to be concentrated on. This is because the usage of personal vehicles is increasingly frequent. Hence the fuel used for powering these vehicles consumes a relatively large amount of money. Approximately 34,600 USD is spent on fuel in the United States annually given that the amount of fuel consumed annually being 45,600 L [2]. According to Hsu and Davis [3] an estimation of 10,000 USD per year per vehicle can be saved by reducing the drag by 40%. As a result the main point to focus in the improvement of the current level of personal vehicles would be the fuel efficiency. The importance of this is further elevated due to the fact that the total reserve of the non-renewable energy resources in the world is depleting steadily [1].

In order to decrease the consumption of fuel by the vehicles, it is critical to understand the factors on which the efficiency of the vehicle depends. The amount of power produced by the engine against all the restrictive forces for the movement of the vehicles is closely related and depends on the efficiency of the vehicle. Among the opposing forces, the main component producing the highest contribution is the aerodynamic drag or the frictional force. This can be basically defined as the opposing force to the direction of the motion of the vehicle. Hence by reducing the drag force on the vehicle would increase the efficiency of the vehicle. The drag force experienced by the vehicle is different at different parts of the vehicle. It also depends on the size, shape, orientation and various other factors in relation to the vehicle [4]. Hucho et al. states that the coefficient of drag for a typical car is 0.35 today [5].

According to an analysis done by Selvaraju et al. [6], aerodynamics is defined as a branch of fluid dynamics, which deals with the study of the motion of air specifically in cases where it interacts with moving objects. Temperature, velocity, pressure and density are properties of a flow field that can be solved as a function of time and position. By defining a control volume around the flow field and the application of the equations for the conservation of momentum, mass and energy solves the properties. Friction drag, boundary layer and separation of flow field and pressure drag are the major factors that affect the flow field around the vehicle. It is crucial to understand these factors that affect the aerodynamic force before starting any analysis related to a vehicle used for personal means.

A study conducted by Hassan et al. [7] shows that approximately 50-60% of the total fuel consumed is in order to overcome the drag forces. The main component for the overall drag of the vehicle is highlighted to be the pressure difference between the front and the rear end of the vehicle. The difference in pressure leads to the separation of the airflow at the rear end of the vehicle creating a high suction area [6]. The analysis was done based on a numerical method by using Favre-averaged Navier-Stokes equation. It also concludes that the reduction of negative pressure at the rear end of the vehicle reduces the flow separation accordingly and the drag coefficient by 3.3%. The solution presented is the modification of the rear under-body that results in

the decrease of drag force by 22.13% and the redirection of the exhaust gases that reduce the drag force by 9.5%. Hence pressure drag is one of the main contributors to the overall drag experienced by the vehicle and more than half of the fuel energy is used to overcome this.

In another study conducted by Conan et al. [8], the varying relationship between the drag coefficients in relation to the change in the rear slant angle of the vehicle was examined. It has been found that 40% of the drag force is concentrated at the rear of the geometry [9]. The approach used is an experimental approach whereby a test model is used inside a wind tunnel and the nature of airflow around the vehicle is analyzed by using a combination of oil visualization and particle velocimetry. Wind tunnels generally produce highly accurate data quickly. The range of angle used for the variation of the rear slant angle is from 10° to 40°. The results indicate that the change in drag coefficient is increasing for small angles of 0° and 20° while the flow separation at 30° is no longer attached to the rear slant and this results in the constant drag coefficient.

Zheng et al. conducted an analysis on the effect of the front window angle of the automobile dynamic performance [10]. The study is conducted using a numerical approach whereby a 3-dimensional airflow around the vehicle is simulated with varying front window angles of 20°, 30° and 45. Computer software called FLOW3D is used for the simulation that applies the 2 turbulence models of Reynolds Stress transport Model (RSM) and k-epsilon (k−ε). The free space created around the vehicle is of 2-times the vehicles height and width for the downstream and 3-times the vehicles length for the upstream. The boundary conditions are no slip wall, inlet, outlet and the moving ground (movement is the same velocity as the wind). Fig. 1 shows the definition of the inclination angle used in the distribution of forces.

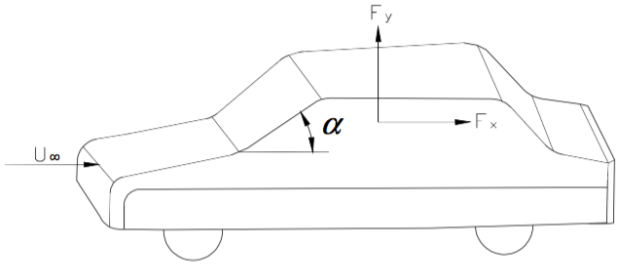


Figure 1. Coordinate of the vehicle (As per the analysis) [10]

The drag coefficient is defined using Eq. (1) as given below:

$$C_d = \frac{F_x}{\frac{1}{2}\rho v^2 \times A} \quad (1)$$

where A is the maximum cross-sectional area of the vehicle.

The results conclude that the drag coefficient, C_d was the highest for 20° and the lowest for 30°.

A number of studies show that the aerodynamic effect on the inclination angle of front window is one of the main design criteria to be focused on. This is due to the overall contribution by the inclination angle of front window to the overall drag [6]. The analysis done on the rear slant angle sparks the curiosity that the inclination angle of the front window also may have significant effect on the drag of the vehicle and further validated by the analysis done by Zheng et al. [10]. Although the requirements for the angle of the window to be selected are contradicting in the preliminary stages of design, it is clear that the inclination angle of the front window is not optimal from the aerodynamic point of view. The aim of the study is to obtain the optimal angle of inclination of the front window (defined as shown in Fig. 1) of a personal vehicle at average cruising speed of the vehicle. The results obtained numerically from the study would predict the drag of the front window at different inclination angles and speeds. The obtained results would be then analyzed and studied in order to find the optimum inclination angle of the front window corresponding to different speeds in order to give minimum overall drag of the vehicle. This expects to reduce the fuel consumption of the vehicle and increase the fuel efficiency.

2. Research Methodology

The research methodology consists of a numerical, 3-Dimensional (3D) simulation method in computer software called ANSYS Workbench. The software used Computational Fluid Dynamics (CFD) to run the simulation and the steps are summarized in a flow chart as shown in Fig. 2.

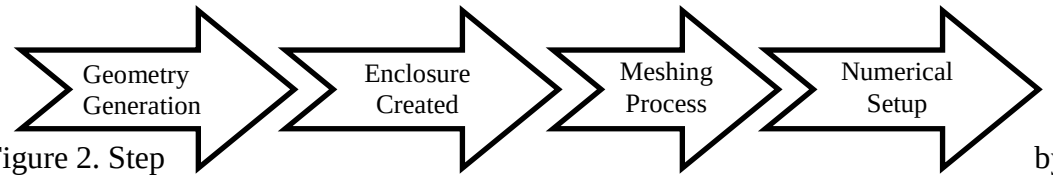


Figure 2. Step by step CFD process

2.1 Geometry Generation

In order to carry out the numerical simulation, the geometry of the car used for the simulation purpose is first generated in Solidworks. The car used for the analysis is the Myvi 2011 model. As the simulation is done in 3D, the model of the car is created in Solidworks using the function surface modeling. To increase the accuracy of the car model, blueprints of the car were obtained and then used to sketch the outline of the car. After that by using the function of surface modeling, the model of the car were generated and simplified as shown in Fig. 3.

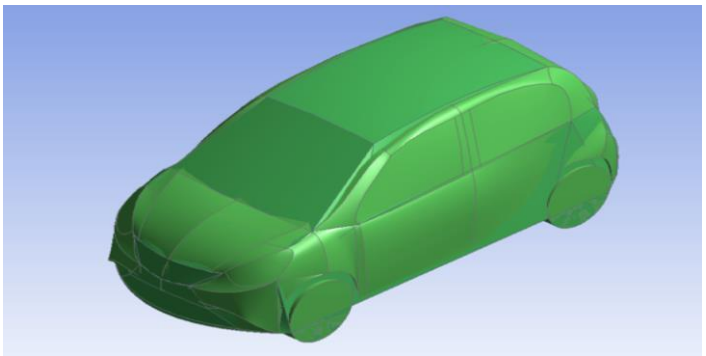


Figure 3. Simplified model of Myvi 2011

2.2 Enclosure Created

The finished model is then imported into ANSYS for the simulation process and opened in FLUENT design modeler. In order to create the area of space around the car for simulation, or otherwise known as the enclosure of the grid topology, a rectangular box is created enclosing the car. The dimensions of the box are as shown in Fig. 4. This is the space in which the flow of air will be simulated. Hence enough amount of space has to be left in front and behind of the car for the flow to continue without colliding a surface. The flow tends to be turbulent when the sufficient amount of space is not provided and this will affect the accuracy of the results. For the numerical simulation of the flow around a vehicle, 2 times the length of the car have to be provided in front of the car. However, more space (4 times the length of the vehicle) is provided behind as the flow separation happens behind and this is point of interest in continuing the simulation [11]. The height of the enclosure is 2 times the length of the car. This is considered an optimum size for the enclosure [12]. The size of the enclosure effects the simulation time; hence a bigger size of enclosure requires longer time for the simulation. The boundary conditions are inlet, outlet, symmetry and the car. Another box smaller than the enclosure is created, surrounding the car called the body of influence to increase the refinement of the mesh nearby the car in order to increase the accuracy of simulation. In addition to that, the whole enclosure is mirrored and split in half including the car and also the body of influence. The simulation will be done for half of the car in order to decrease the simulation time.

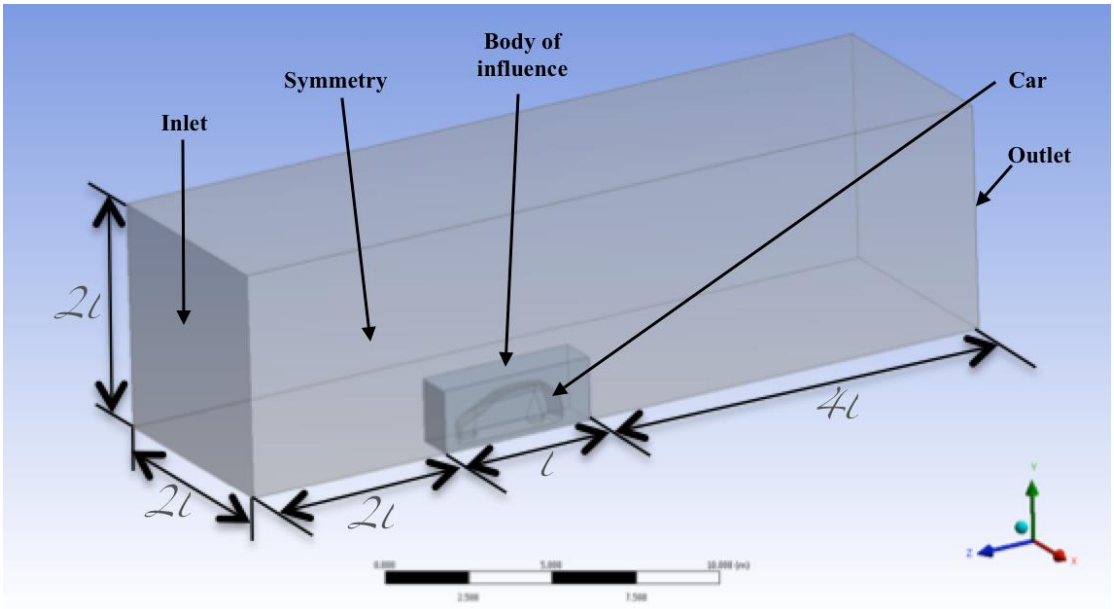


Figure 4. Enclosure for the simulation

2.3 Meshing Process

The accuracy of the results highly depends on the fineness of the mesh created. The mesh is done in different steps of body sizing and inflation to obtain the number of cells and a fine growth of cells. The first sizing is applied overall on the whole enclosure with the specification of 10 mm for the minimum size of the cells as shown

in Fig. 5. The second body sizing is applied to the smaller box created around the car, known as the body of influence, and for the car with the element size of 50 mm. The size of the elements was chosen based on the orthogonal quality of the mesh. When the minimum size of the orthogonal quality is below the value of 10 mm, the mesh is considered as a good mesh. However the element size can be specified to be smaller. Although the accuracy of the simulation increases, the time taken for simulation increases. Next inflation is applied to the bottom face of the enclosure and the car with the specification of the values given in Table 1. Inflation is used to generate thin cells adjacent to boundaries and to capture the wall boundary layers by resolving the viscous boundary layer in CFD and as shown in Fig. 6. A close of up of the mesh generated at the surface of the car is shown in Fig. 7.

Table 1 – Inflation specification

Dimensions		
Number of Layers	Growth Rate	First Layer Height
7	1.3	5 mm

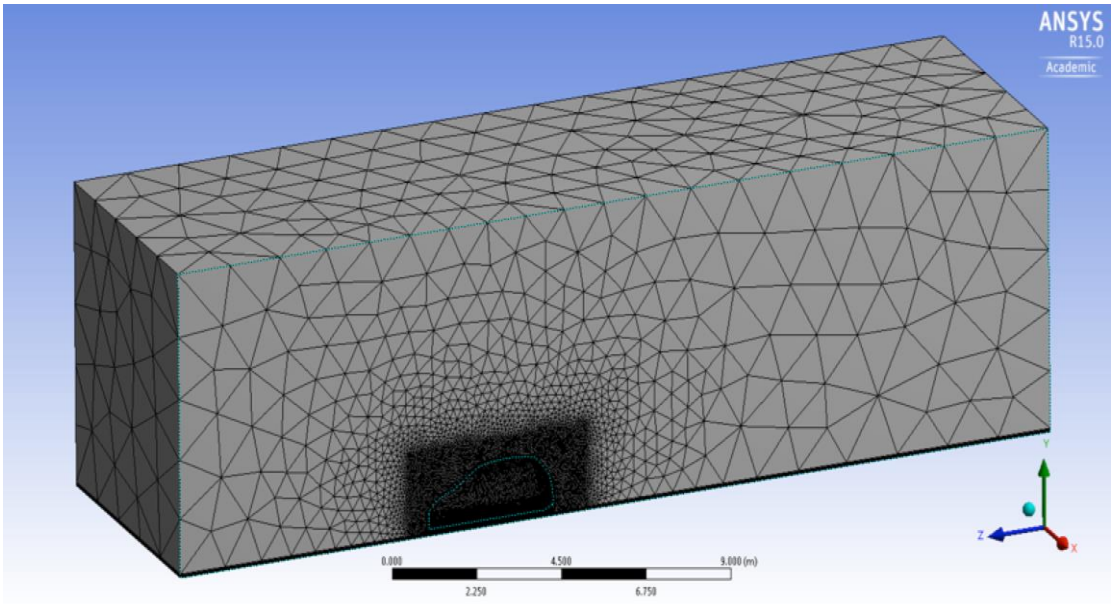


Figure 5. Mesh Generated

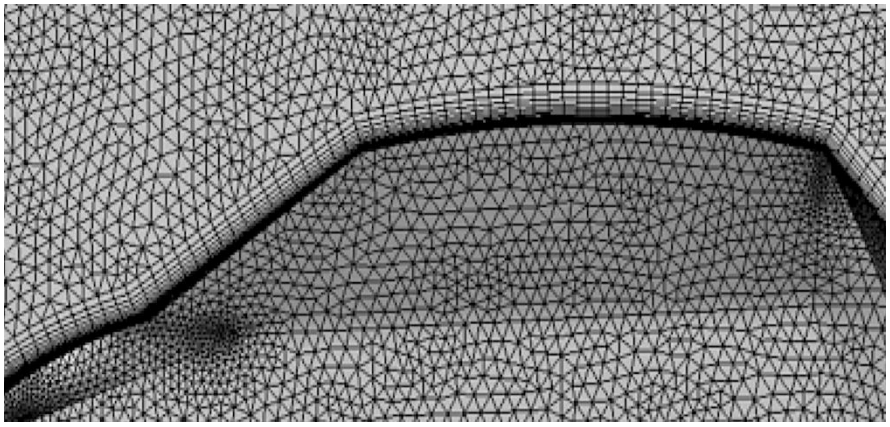


Figure 6. Close-up of inflation layers

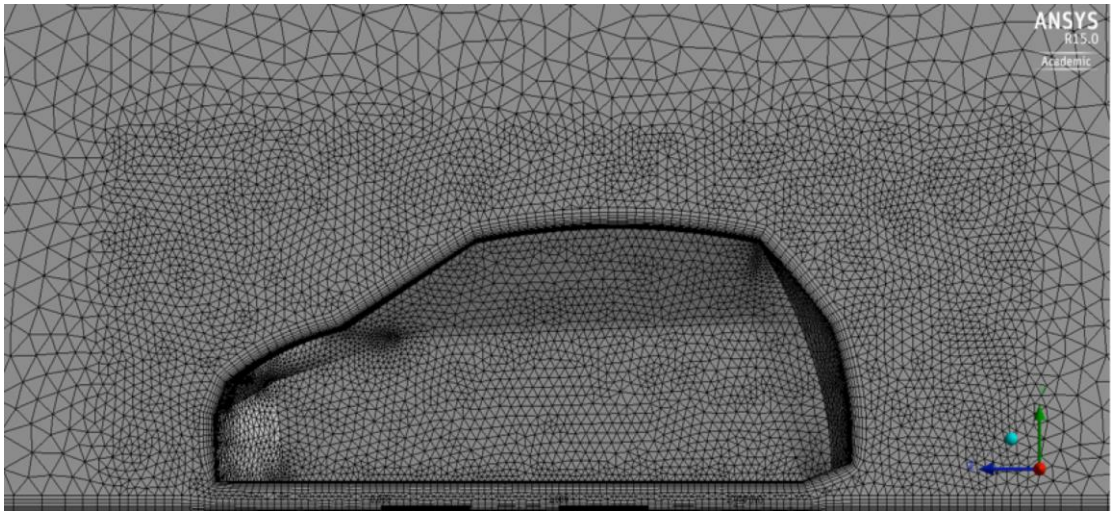


Figure 7. Close-up of the mesh

2.4 Numerical Setup

The flow is subsonic and is considered to be incompressible. Hence the simulation is run through out by the application of pressure based solver. Table 2 shows the properties of the fluid used for the simulation process.

Table 2 – Simulation Assumptions

Properties of Fluid		
Type of Fluid	Density (kg/m)	Viscosity (kg/ms)
Air	1.225	1.7894e-5

The model chosen for the study is the k-epsilon (k-ε) turbulence model as it is more suited for this analysis. As the flow is subsonic and deals with transonic and turbulent flow, literature validates that the k-ε model will obtain results without the compromising the accuracy of the simulation carried out [9, 10]. It also reduces the time taken for the simulation. The range of angles chosen for the analysis are 28°, 30°, 32°, 34° and 36°. The velocity of the airflow is input as 27.78 m/s (100 km/hr) as this is the general cruising speed maintained in vehicles used for personal transportation [13].

2.5 Range of Angles Selected

Statistical data were collected for different vehicles that are used commonly and the corresponding inclination angle as shown in Fig. 8. For the collection of data an application called ‘Angle Meter’ was downloaded to the mobile phone and used to measure the inclination angle. For the calibration of the application, known angles such as 45°, 90° and 180°, were measured first. This would aid in providing a range of inclination angles to be used for the analysis. As the data collected are taken from already existing vehicles that have been designed by taking into consideration of the aerodynamic effect, this reduces the range of angles to be considered in the analysis.

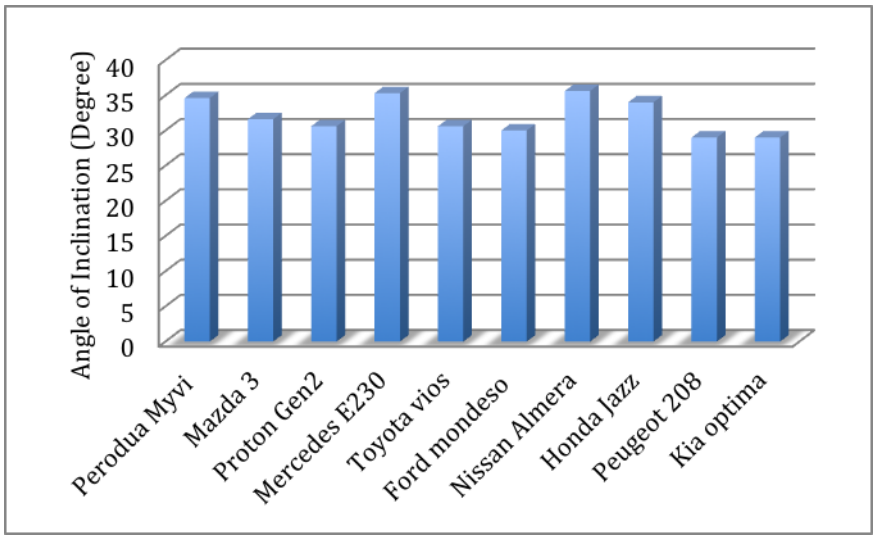


Figure 8. Angle of inclination of front window for different vehicles

3. Results and Discussion

3.1 Numerical Results

The results obtained from the simulations run in FLUENT ANSYS consist of different forces. However the only force presented in this study is the drag coefficient (C_d) as it is the force of interest. The range of angles used for the inclination angle of the front window is 28º, 30º, 32º, 34º and 36º. The obtained results from the simulation for coefficient of drag are then analyzed and compared with the literature available. The distribution of pressure is as shown in Fig. 9 and 10. It can be seen that the high-pressure region is in front of the car (in red) and the low-pressure region is behind the car (in blue). The results relating the angle of inclination and the coefficient of drag are as shown in Fig. 11.

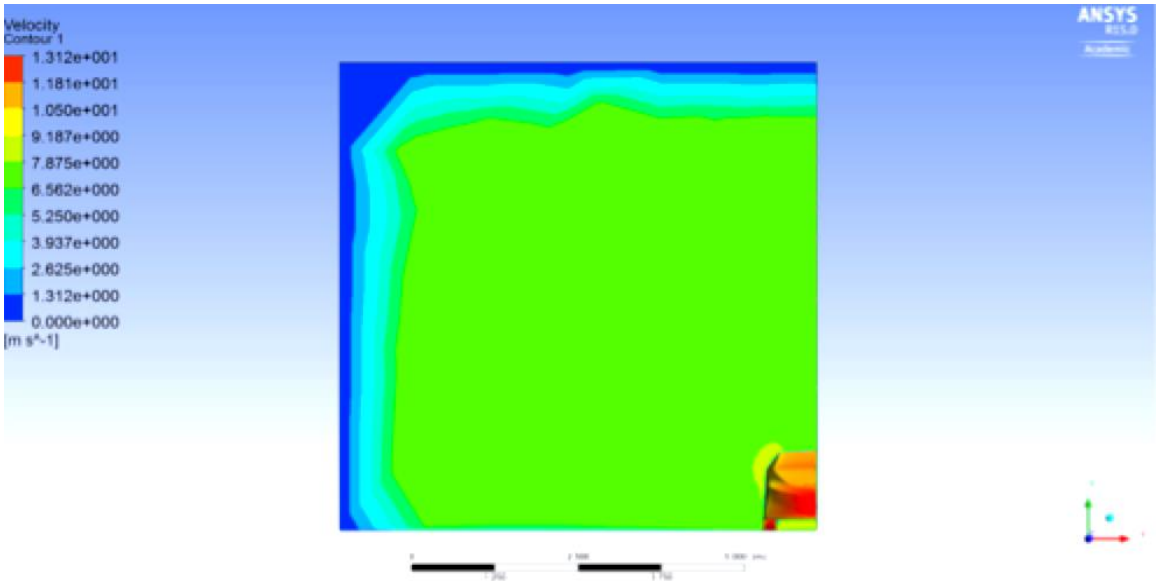


Figure 9. Pressure distribution (Front view)

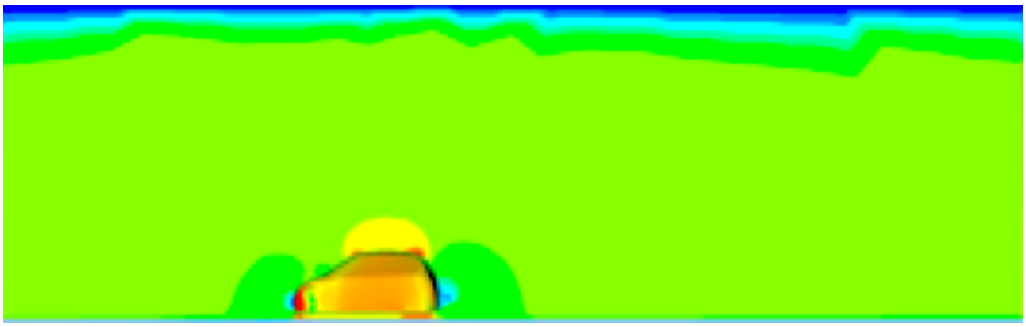


Figure 10. Pressure distribution (Side view)

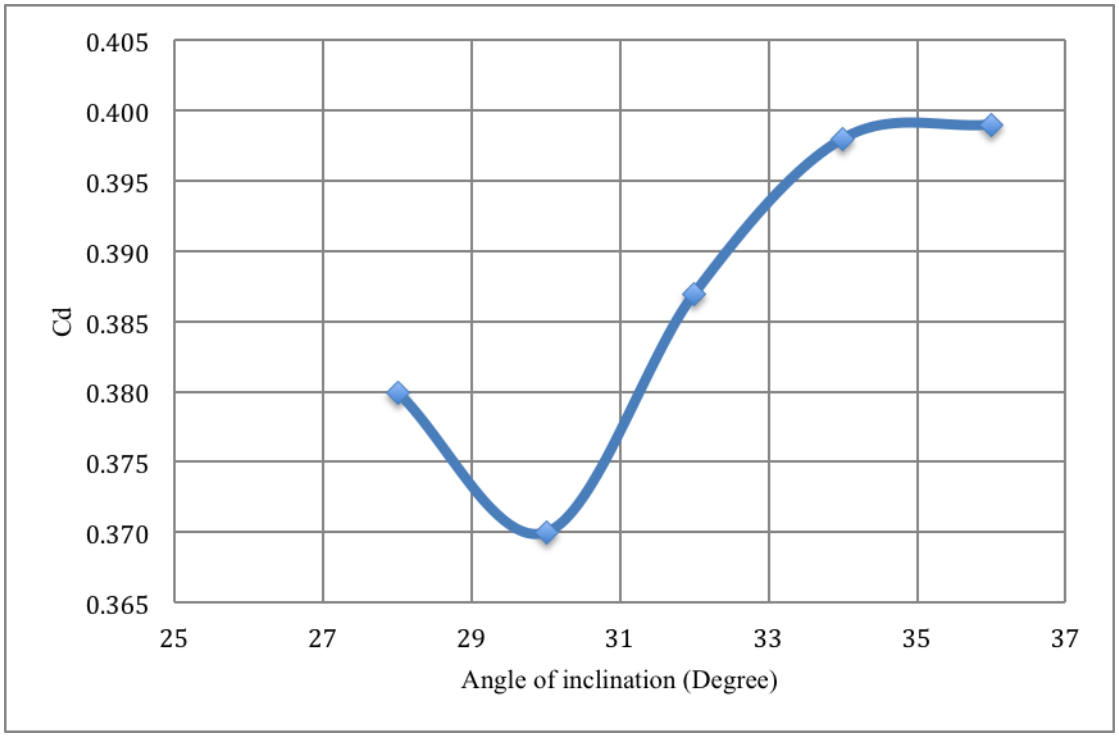


Figure 11. Drag Coefficient vs. Angle of Inclination

The obtained results resemble the available literature whereby the lowest value for the coefficient of drag is obtained for the 30^{o} inclination angle [10]. It is also observed that the coefficient of drag increases steadily up to 34^{o} and then becomes rather constant. Furthermore the decrease of angle to 28^{o} also raises the coefficient of drag in comparison to 30^{o} inclination angle. It was observed that the simulation of all the angles of inclination created a considerable separation in the flow. This results in the creation of strong vortices due to the separation, which in turn produces the negative force that contributes to the drag force. However the separation is the smallest at the 30^{o} angle of inclination and hence produces the minimum coefficient of drag. The results conclude that the optimum angle of inclination is for the 30^{o} angle. The value obtained for the optimum coefficient of drag is 0.37. This value is accepted, as the value obtained from literature is 0.35 [5]. The percentage error between the two values is 5.4%. This is considered to be an accurate result for the coefficient of drag and the obtained value from numerical simulation is verified.

7. Conclusions

To conclude based on the numerical simulation run and the available data from the literature converges that a specific angle of inclination produces a minimum value for the drag coefficient. Although a linear relationship between the angle of inclination of front window and the coefficient of drag was not obtained, it was observed that any change in that angle increases the value of drag coefficient. The results show that the minimum value of drag coefficient is obtained for 30 ^{o} angle of inclination.

Future recommendations for the analysis can include the angle of inclination of the bonnet in the simulations. This would provide a more in depth evaluation of the airflow around the car in relation to the varied angle of inclination. It also provides more combinations of simulations to be run in order to improve the accuracy of the results. Furthermore, the results obtained from numerical analysis can be validated from wind tunnel tests, which would be conducted under an experimental analysis. Hence aid in further understanding the factors that are related in reducing the coefficient of drag experienced by the car.

References

[1] A. Altaf, A. Omar and W. Asrar, "Passive drag reduction of square back road vehicles", Journal of Wind Engineering and Industrial Aerodynamics, vol. 134, pp. 30-43, 2014.

[2] Z. Mohamed-Kassim and A. Filippone, "Fuel savings on a heavy vehicle via aerodynamic drag reduction", Transportation Research Part D: Transport and Environment, vol. 15, no. 5, pp. 275-284, 2010.

[3] Hsu, F.-H., Davis, R. L. “Drag reduction of tractor-trailers using optimized add-on devices.” Journal. Fluids Engineering, 132(8), 084504. doi:10.1115/1.4001587.

[4] E. Miller, "Effects on the Boundary Layer Caused by Inclusion of Dimples at Varying Depths", Journal of Aircraft, vol. 49, no. 4, pp. 969-972, 2012.

[5] Hucho, W. H. and Sovran, G. (1993) Aerodynamics of road vehicles, Annual Review of Fluid Mechanics, Vol. 25(1), pp485-537.

[6] P.N.Selvaraju, K.M.Parammasivam, Shankar and G.Devaradjane, "Analysis of drag and lift performance in sedan car model using CFD", Journal of Chemical and Pharmaceutical Sciences, no. 7, pp. 429-435, 2015.

[7] S. Hassan, T. Islam, M. Ali and M. Islam, "Numerical Study on Aerodynamic Drag Reduction of Racing Cars", in 10th International Conference on Mechanical Engineering, ICME 2013, Bangladesh University of Engineering and Technology, 2013, pp. 308 – 313.

[8] B. Conan, J. Anthoine and P. Planquart, "Experimental aerodynamic study of a car-type bluff body", Exp Fluids (2011), vol. 50, no. 12731284, 2011.

[9] M. Nizam Sudin, M. Azman Abdullah, S. Anuar Shamsuddin, F. Redza Ramli and M. Mohd Tahir, "Review of Research on Vehicles Aerodynamic Drag Reduction Methods", International Journal of Mechanical & Mechatronics Engineering, vol. 14, no. 02, 2014.

[10] Z. Zheng, Z. Guan and A. Wang, "Effect of Front Window Angle on The Automobile Dynamic Performances", 2009.

[11] Cakir, Mustafa, "CFD study on aerodynamic e ects of a rear wing/spoiler on a passenger vehicle" (2012). Mechanical Engineering Masters Theses. Paper 1.

[12] Kumar, A., Singh, A., and Regin A, F., "Study on Effect of Ground Clearance on Performance of Aerodynamic Drag Reduction Devices for Passenger Vehicle Using CFD Simulations," SAE Technical Paper 2015-26-0197, 2015, doi:10.4271/2015-26- 0197.

[13] I. El-Shawarby, K. Ahn and H. Rakha, "Comparative field evaluation of vehicle cruise speed and acceleration level impacts on hot stabilized emissions", Transportation Research Part D: Transport and Environment, vol. 10, no. 1, pp. 13-30, 2005.

eureca 2016 – Conference Paper
Paper Number 2ME02

Vapor velocity effects on condensate inundation of integral-fin tubes

Ali Mbarak Ahmed[1], Satesh Namasivayam[2]*

alibarafoo@gmail.com
sateshnarayana.namasivayam@taylors.edu.my

The performance of a condenser plays an important role in power generation. That is why for the past five decades the factors influencing the efficiency of the condenser has been heavily researched. The effects of vapor velocity on condensate inundation is particularly a topic of interest, as it has been proven that vapor has high velocities shearing over inundated tubes thins the condensate film over it. As a result the heat transfer coefficient of the increases thus increasing the efficiency of the condenser. However different tube bundle geometry has proven to effects the vapor pressure though its rows of tubes, which in turn effects the vapor velocity through the tube bundle. This research aims to investigate experimentally the effects of vapor velocity on condensate inundation with different tube bundle geometries. The objective is to find a combination of vapor velocity and tube bundle geometry that will have an optimal overall heat transfer. A test rig will be designed based on the creative thinking process CDIO, and built using the resources of the university lab and an allocated budget of RM 500.With the completed test rig the experimental runs are conducted and the data required for analysis is collected. In the analysis of the data the experiment results will be compared to existing work to draw a conclusion. It is expected that with the widening the of the pitch of tube in the bundle the vapor pressure drop will decrease, allowing for deeper penetrations and higher shearing vapor velocities through the tube rows. This will translate to a higher overall heat transfer in the tube bundles. Today the world suffers from an energy crisis due to the finite unrenewable energy and pollution of the atmosphere as a result of burning fossil fuels. Any attempt to solve this problem will be of great contribution to the world. By increasing the efficiency of the condenser of a power generation plant, precious energy can be conserved and less would have to be burned.

Keywords

Vapor velocity, Tube bundle geometry, Integral fin-tubes, Vapor shear, Condensate inundation.

1.0 INTRODUCTION

The power generation plant is the heart and driving force of the modern civilization. According to online sources fossil fuel and nuclear power plants generates a total of 76.9% of the world's energy as of 2015[1], the rest of the power is generated by renewable sources. Until renewable energy sources displaces heat generation plants as the primary source of energy, research on increasing the efficiency of heat generation plants will be of great interest. In such heat power generation plant the steam generated by the burning of the fuel to turn turbines is condensed to water and is pumped back to the boiler to start the process again. The condensation of the steam takes place in the condenser, which is a heat exchanger that condenses vapors by cooling them. The vapor comes in contact with tubes that have a coolant flowing through them. The vapor gives up its latent heat to the coolant and condenses into liquid water. In power generation the coolant, generally is water, which has absorbed the latent heat of the vapor is sinked to a nearby lake or river. This is why most power generation plants are located near a renewable water source, such as rivers and lakes. According to the Ideal Rankine cycle depicted in Figure 1, the condenser sinks the heat out of the system. The efficiency of the whole system is greatly dependent on this stage (4-1). Increasing the efficiency of the condenser allows the temperature of the working fluid entering the boiler to be as low as possible, this will allow the boiler to transfer as much heat as possible to the working fluid thus making the cycle more energy efficient. One way to increase the efficiency of a condenser is to increase the pressure of the working fluid (steam) entering the condenser, this can be done by increasing the vapor velocity. However there are other ways to also increase the efficiency of a condenser.

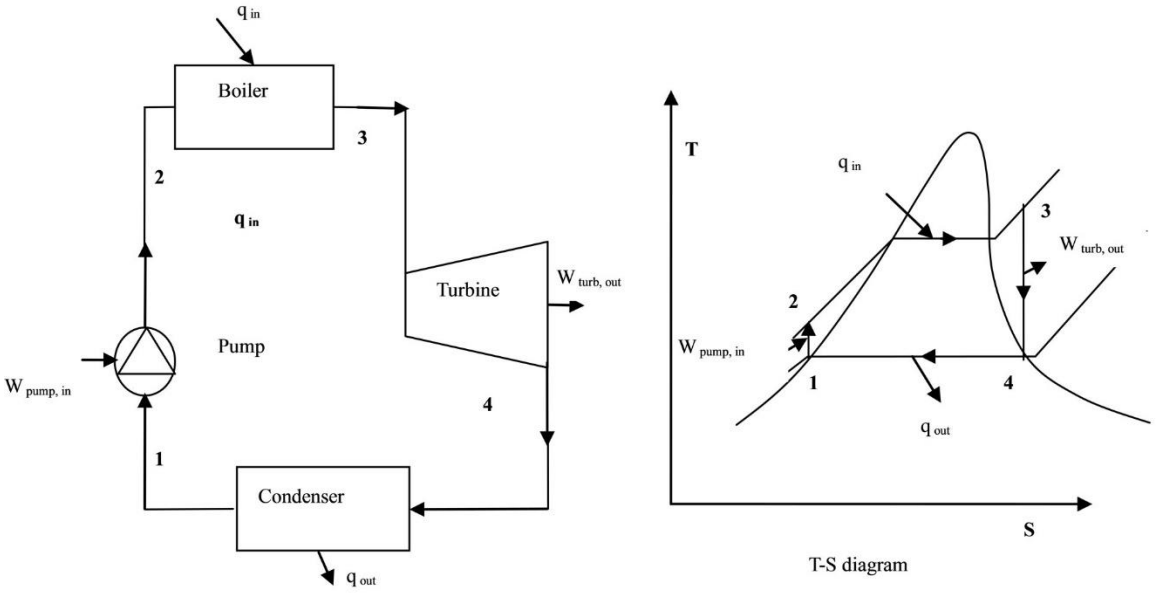


Figure 1: Ideal Rankine Cycle [2]

Many different tube surface geometries are available, with recent developments in the tube surface geometries the lead to enhanced heat transfer and a reduction in the size of the heat exchangers as a result of the increase efficiency of the newly developed tube

geometries. The simplest improvement to the basic smooth tube surface geometry is the integral finned tube, of which there are two general types, rectangular or trapezoidal in cross-section (see Figure 2). Integral fin tubes are manufactured by rolling helical fins onto the tube wall as in integrate the fins onto the tube (See Figure 3). Many investigations have been conducted with finned tubes as the focus or as a standard of comparison for other enhanced tubes. An investigation by Cheng et al [1] shows that finned tubes in a tube bundle have relatively high overall heat transfer at low vapor shearing velocities compared to four other enhanced tubes and a smooth tube. In fact even though the enhanced tube D (See Figure 4) outperform the 40fpi (fin per inch) finned tube at first but as the vapor velocity approaches 3 m/s tube D start to decline in performance whereas the finned tube is still on the rise. Many other investigations can testify for the high performance of the integral finned tube like R.L. Webb [3] and Cheng and Wang [4].

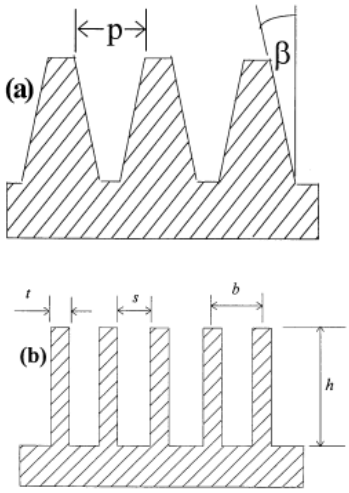


Figure 2: Integral finned tubes of two types a) trapezoidal and b) rectangular [12].

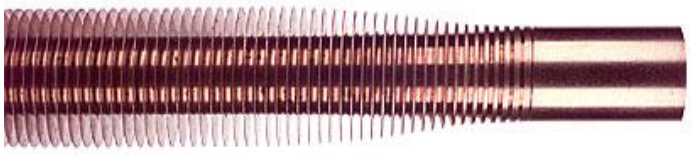


Figure 3: Integral fin tube from RayPak ASME [14].

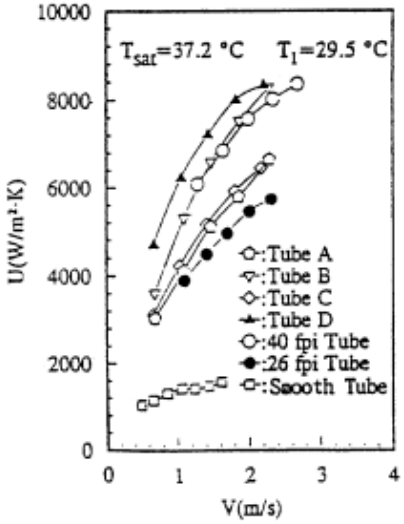


Figure 4: Overall heat transfer coefficient versus coolant velocity [2].

One of the Factors that greatly hinders the performance of condenser is the formation of condensate inundation on the tubes. Condensate inundation is when the condensate forms on a tube and drips down onto the tube below it forming a film of condensate that will pose a resistance to heat transfer this is depicted in Figure 5. An experimental investigation by J. Cunningham & M.Bahjernejad [5] has been done to find out the effects of condensate inundation and vapor velocity have been studied. The test runs have been carried out on three different bundles of roped tubes with different winding pitches the main experiment variables were cooling water velocity and logarithmic mean temperature difference. The results show that condensate inundation does actually reduce heat transfer in condensers. Also flooding of the lower tubes in the bundle have been observed, such results are supported by J.G Withers and K.H Young [6]. Flooding or condensate retention of the tubes is a phenomenon that occurs due to the effects of surface tension and it is influenced by tube surface geometry, Figure 6 depicts the a schematic of the geometry used by Rudy and Webb for their theoretical model.

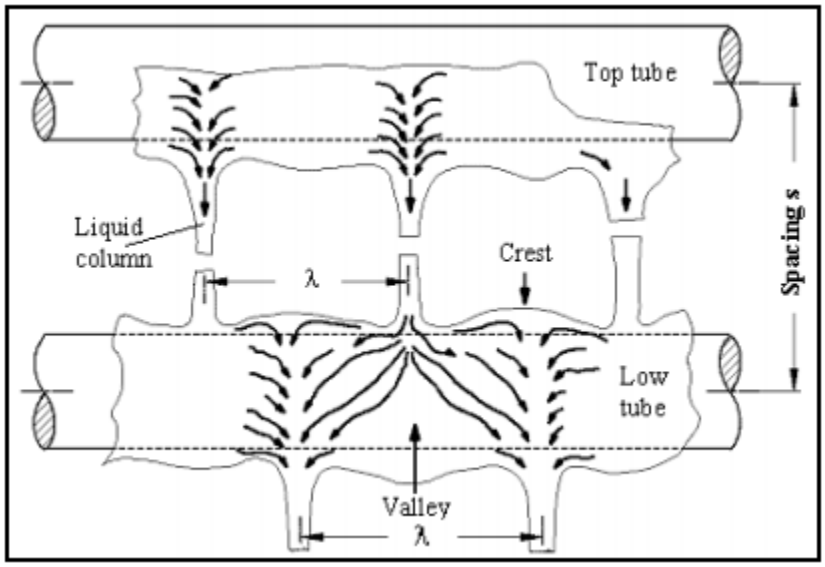


Figure 5: Condensate inundation of lower tube. [18]

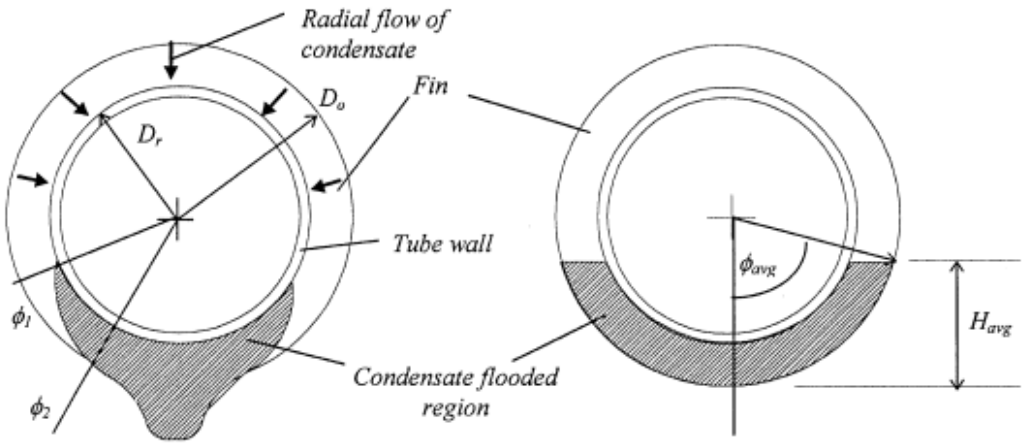


Figure 6: schematic of the geometry used by Rudy and Webb for their theoretical model. [15]

The velocity of the vapor entering a condenser has a great effect on the condensate inundation and condensate heat transfer. It is known that vapor velocity can cause a thinning of the condensate film, and as a result the HTC of the condenser will be reduce as more of the tube is exposed. An experimental study by Paul Jeffery Noftz [13] where he investigate the effects of vapor velocity and condensate inundation on heat transfer, proves this point. Many other investigations have been carried out on the effects of vapor velocity on condensate inundation. Rewerts et al. [7] condensed R-123 on integral fined tube bundles and other enhanced tubes and found that condensate inundation overpowered the effects of vapor shear up until a velocity of 4.6m/s. Moreover, at higher velocities vapor shear actually enhance the heat transfer coefficients for finned tubes. Such results are supported by Chu and McNaught [8].

In a condenser the tubes are arranged in bundles, these bundles may vary in their layout depending on the design of the condenser. Different tube bundle arrangement can have different effects on the condensate inundation and by extension the overall heat transfer of the condenser. The tube bundle maximizes the surface area for vapor to coolant interaction by packing as much tube as possible within a finite space that is the condenser shell or hull. Tube bundles come in two main types of geometries, this is depicted in Figure7.

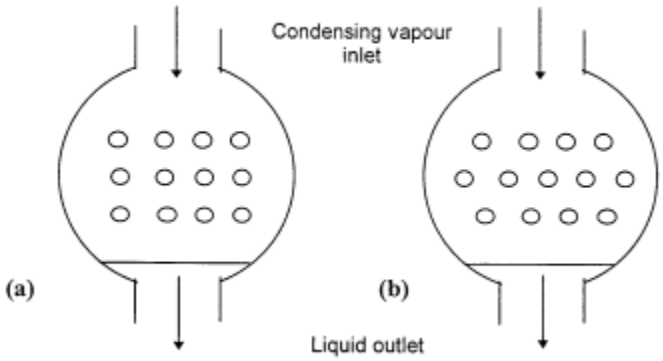


Figure 7: Schematic drawing of shell-and-tube condenser with vapor down flow. (a) In-line tube bundle (b) Staggered tube bundle [12].

The type of tube arrangement has a great impact on the pressure of the incoming vapor. In a Review paper by Brower et al [12] where he cites Honda et al. who studies the row by row film condensation of R-113 on in-line [9] and staggered [10] tube bundles. His studies revealed that the decrease in heat transfer coefficient (HTC) due to condensate inundation was less significant for staggered tube bundles as compared to in-line tube bundles.

Such investigations highlight the importance of vapor velocity and tube bundle geometry in the performance of a condenser. The question that begs to be asked is, what are the effects of vapor velocity on condensate inundation and how will the effects vary with different tube bundle geometries? Investigations have been conducted to answer these questions, such as the experimental research done by D.A McNeil, B.M Burnside, G.Cuthbertson [11]. However little is known about the combined effects of vapor velocity and a finned tube bundle geometry on condensate inundation.

The focus of this investigation are the two factors that greatly influence the condensate inundation and by extension the HTC of the tubes. The objectives of this research are:

1. To validate and verify the thinning and/or stripping effect that high vapor velocities have on the condensate film deposited on integral finned tubes formed by inundation of the condensate.
2. To experimentally investigate the effects of vapor velocity and varying tube bundle geometry on condensate inundation, and to analytically quantify the heat transfer of the integral fined tubes.

The surface tension of the tube surface geometry (TSG) causes the condensate to flood the bottom of the tube. This flooding or retention of the condensate at the lower part of the tube contributes contribute to the reduced HTCs of the fin tubes. Karkhu and Borovko [12] conducted and analytical calculation for a film condensation of steam and R-113 on a horizontal tube with trapezoidal fins. The investigation showed that the surface tension forces may increase the condensation rate by 50 to a 100 % over an equivalent smooth tube. They also found out that the surface tension of the fin tube contributes to this phenomenon of condensate retention or condensate flooding (see Figure 7). Rudy and Webb measured the flooding under static and dynamic conditions (no condensation and with condensation) of finned tubes with varying fin densities. Steam, r-11 and n-pentane were condensed on the tubes and the results showed that a considerable part of the fin tubes

was flooded with condensate. This part of the tube which was flooded seems to be greatly influenced by the TSG. The amount of condensate retention at the bottom of the tube is characterized by the flooding angle ϕf. This is measured from the top of the tube to the point where the space between the fins of the tube is filled with condensate (see Figure 8).

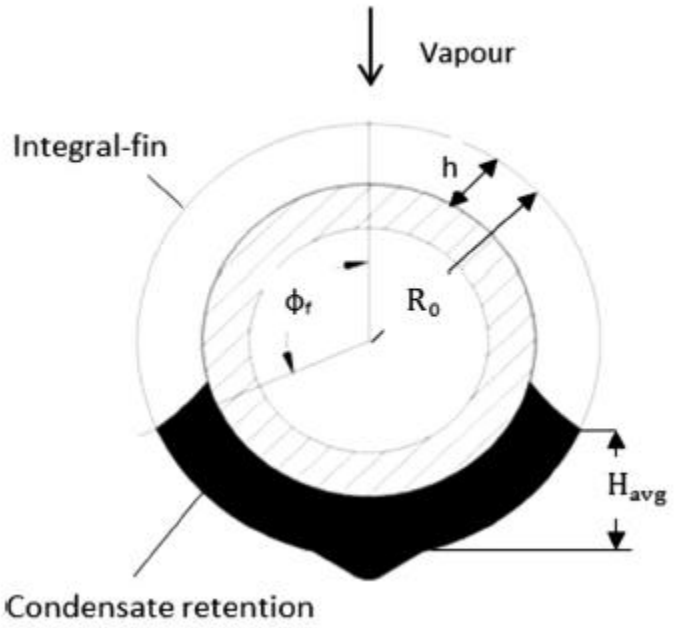


Figure 8: Schematic of condensate flooding on an integral fin tube. [13]

A journal by Briggs et al. [14] reported some experimental data for natural convection, condensation and heat transfer on a set of rectangular integral fin tubes made of brass, bronze, and copper using R-113. The HTC was found to be greatly dependent on the fin height. Another journal by Briggs et al. [15] also reports experimental data on three different integral fin tubes with fin spacing of 0.5 mm, 1.0 mm and 1.5 mm using steam and R-113 at atmospheric pressure and exposed them to a small range of vapor velocities the best performing tubes for the condensates of steam, ethylene glycol and R-113 are 1.5 mm, 1.0 mm and 0.5 mm respectively.

Honda et al [16] presented experimental data for the condensate flooding at low vapor velocities on integral- fin tubes using R-113 and methanol. Through this, they reported an analytical expression for predicting condensate flooding angle, $\emptyset_f$, on rectangular integral fin tubes given by the Equation 1):

$$\emptyset_f = cos^{-1}\left(\frac{2\sigma}{\rho_c g s R_0} - 1\right) \quad for\ s < 2h$$

Equation 1

Where, σ is the surface tension, ρ_c is the density of the condensate, β is the half angle at the fin tip (β = 0 for rectangular fin tubes), g is the gravitational constant, s is the fin spacing and R_o is the radius at the fin tip.

2.0 METHDOLOGY

To investigate the effects of vapor velocity across varying tube bundle geometries and to analytically derive the HTC associated with different flooding angles influenced by the combinations of the two factors, an experimental apparatus was built. The apparatus will allow for the observation of the flooding angle at different levels of vapor velocity, which is simulated by air, and varying tube bundle geometries. By measuring the flooding angle induced by the shearing vapor on the fin tubes the exposed area of the tube can calculated. It is then compared the theatrical model for flooding angle Equation 2 to see how the results generated match against established models of flooding angles. From this the heat transfer can be calculated using the Equation 3.

$$\emptyset_f = \cos^{-1}\left(\frac{2\sigma}{\rho_c g s R_0}(1-\Psi)-1\right) \quad for\ s < 2h$$

Equation 2: S.Namasivayam, Modification to Honda's flooding angle model to accommodate vapor velocity.[24]

$$Q = C_1\pi d_o t q_{tip} + \frac{\phi_f}{\pi}\left(C_2(1-f_f)\frac{\pi\left(d_o^{\,2}-d^2\right)}{2}q_{flank} + C_3(1-f_s)\pi b d q_{root}\right)$$

Equation 3: Heat flux Model of entire fin tubes by S.namasivayam.[24]

and the Heat transfet flux, can be compared to other investigations with actual heat transfer involved. Finally a graph of Q vs vapor velocity can be plotted for each of the tube bundle geometries an compare to published reaerched to verrify and validate the data obtained.

2.1 Apparatus

The apparatus was designed to simulate the conditions in a condenser. It had to simulate a complete inundation of the fin tube and a shearing vapor velocity. Similar apparatus had been used investigation of flooding angle in researches done by Claire L. Fitzgerald et al.[21] and Hafiz Muhammad Ali [22]. The general concept of the apparatus used in this research similar to that of Claire Fitzferald's and Hafiz Ali's. However the major difference is that their investigation was on single tubes whereas this investigation focuses on varying tube bundle. Which required the apparatus to be interchangeable between the two tube bundle geometries. Another major difference was the use of polylactic acid (PLA) 3D printed fin tubes as compared to the aluminum and copper tubes used by Claire and Ali. A picture of the apparatus is shown in Figure 9.

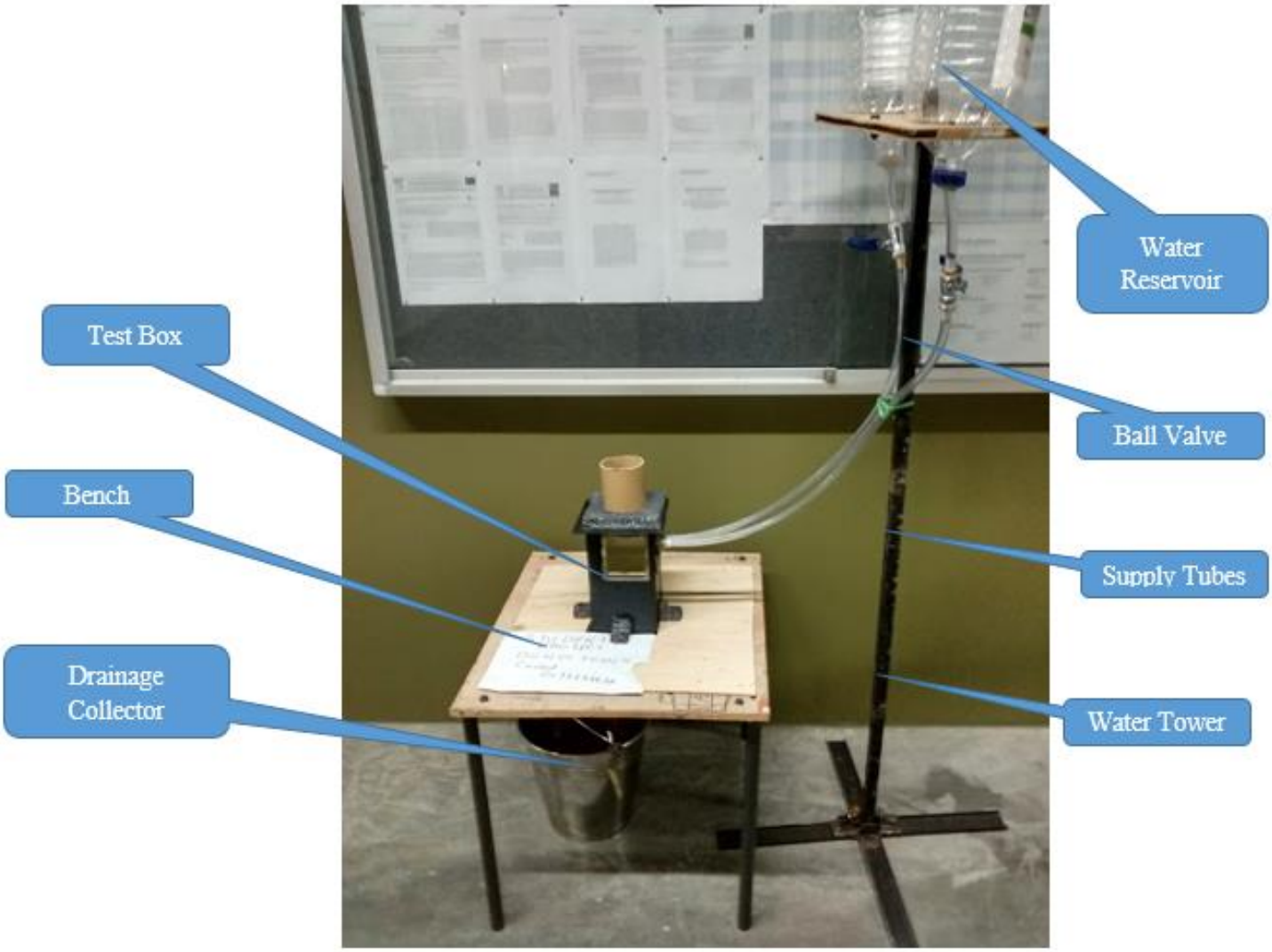


Figure 9: Picture of apparatus used.

Inundation was simulated by supplying water to the supply fin tubes, then and an air flow, generated by a 2000W hair dryer, which is made to simulate steam is blown across the inundated tubes and the flooding angle is observed. Table.1 summarizes the parameters of the experiment.

Tube Bundle Geometry	Wind Speed (m/s)	Inundation rates (l/min)
Staggered	0	1.5
	5.04	
	8.3	
In-line	0	1.5
	5.04	
	8.3	

Table 1: Experimental parameters.

The inundation rate was measured by taking note of how much water would be drained within a minute. The wind speed of a 2000W hair dryer was taken from the University of Guelph wind energy competition results [31]. Three tubes were used to represent a staggered tube bundle and two were used for the inline. An HD professional camera (Nikon D7000) was used to make a video recording of the six experimental runs. The video recording can then be properly analyzed to observe the flooding angle.

2.2 Procedure

The procedure of the entire experiment can be broken down into the following steps:

- The tubes are assembled into the test box according to the TBG being tested and the cover plate is placed over the tubes.
- The supply tubes are connected to the fin tubes (see Figure 10).
- The valves are checked to be close to avoid spillage.
- The water reservoir is filled with water and red food coloring is added and stirred.
- The hair dryer is placed on its housing.
- The camera is set up, focused on the observation window and the recording is started.
- The water valves are opened to allow a constant flow of 1.5l/min.
- The first recording is made with no air flow and is recorded for a minute.
- After the first minute, the air flow is set to 5.04 m/s and is recorded for a minute.
- Finally, the air flow is set to 8.4 m/s and is recorded for another minute.
- The remaining water is drained and the whole process is repeated with the second TBG.

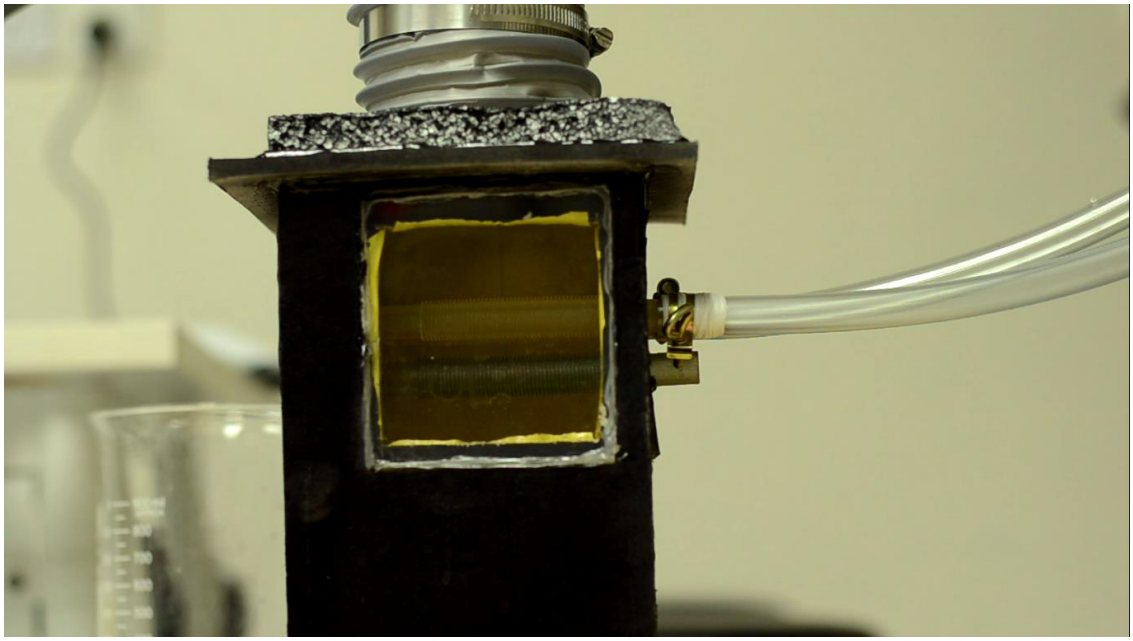


Figure 10: The water supply tubes connected to the fin tubes.

3.0 RESULT & DISCUSSION

In this chapter, the results of the experiment are presented and analyzed. The data collected from the experiment are photographs of the inundated tubes under three different levels of wind speed. Two different tube bundle geometries (TBGs) are tested and the difference between then are analyzed visually to observe the pattern of the condensate inundating the tubes and for flooding angle. However, No flooding angle has been observed, this is because the tube itself was translucent thus making it impossible to exactly determine where the flooding angle lies. The results of the flooding angle are inconclusive. However, the data analysis procedure will be explained in detail and examples of calculations and results will be explained.

3.1 VISUAL OBSERVATION

The experimental results for both the TBGs at three levels of wind speed are displayed below.

In-line tube bundle:

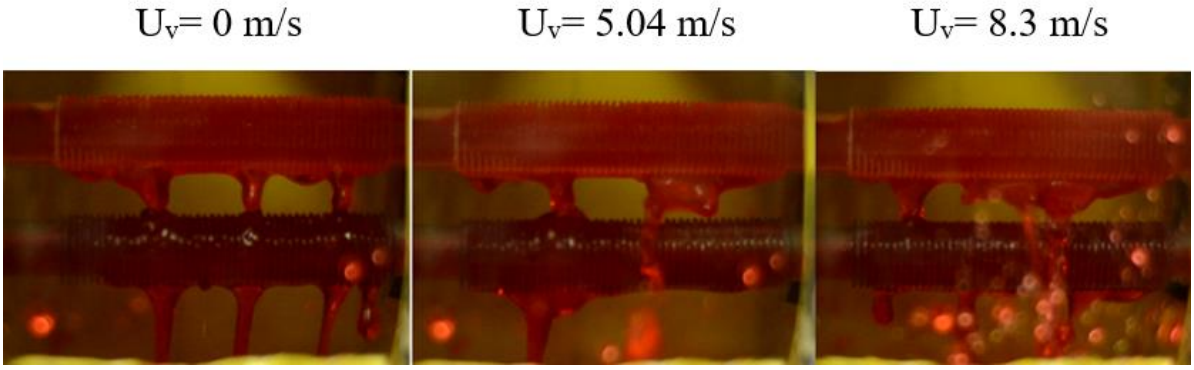


Figure 11: Experimental observations for in-line tube bundle.

Looking at the condensate flow pattern at Uv=0m/s a column dropwise film is formed, this is typical of mid-range inundation rate as seen in Figure 5. This result is a testimony to the successful operation of the apparatus. The condensate from the upper tube impinges on the lower tube thus inundating it completely. When the air flow is brought up to 5.04 m/s the columns of condensate are broken and begin to flicker. The condensate only impinges on parts of the tubes leaving other parts exposed to the air flow. In additions some of the condensate has been stripped off the tubes, this can be seen in both the images where the wind speed in ≠ 0 m/s as droplets of condensate scattering around. When the air flow is set at 8.3 m/s, a more aggressive behavior of the condensate columns are observed. In addition to the condensate column form at the second tube is also distorted unlike any of the other observations, this comes to show that increased vapor velocity hence increased pressure translates to increasing penetration power which confirms the results produced by Hassan [21].

Staggered tube bundle:

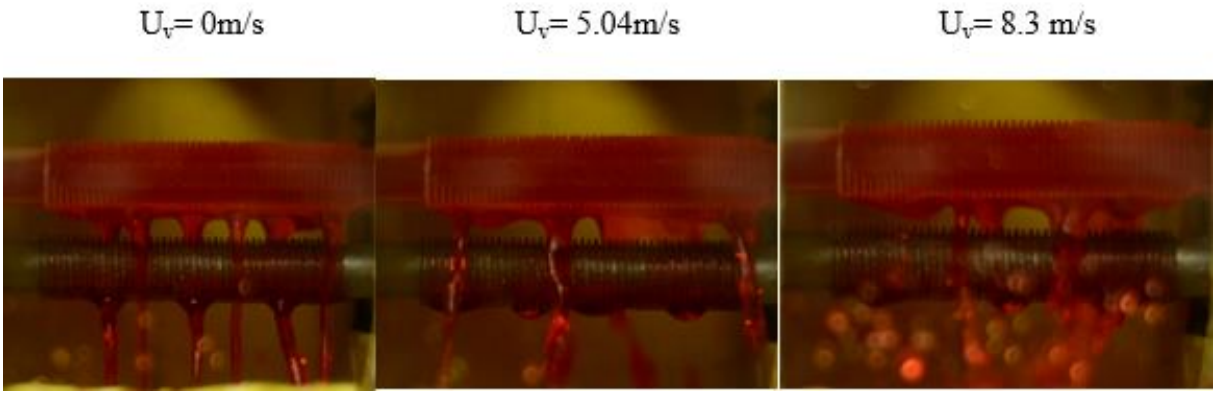


Figure12: Experimental observations for staggered tube bundle.

When the wind speed is set at 0 m/s the condensate columns are formed for both the tubes on the first row. Some of the condensate impinges onto the tube below but leaving most of the third tube in the second row exposed. This a confirmation for many investigations that states the superiority of the staggered tube arrangement over the in-line tube arrangement, some researchers worth noting are Paul Noftz [16] and Honda et al [20]. When the wind speed is increased to 5.04m/s the columns of condensate begin to flicker so much so that they actually misses the third tube in the second row only occasionally impinging upon it. This exposure translates to enhanced heat transfer on the third tube. When the wind speed is increased to 8.3 m/s the columns of condensate take a more random and aggressive pattern, however, no much difference had been observed as compared to the previous level of wind speed.

3.2 FLOODING ANGLE VALIDATION

From photographs of each of the tube bundles the observations of the flooding angle, ϕf, of the tube in the second row is recorded (see table 2).

	Staggered	In-line
	Flooding angle, ϕ_f,°	
U_v = 0 m/s	0	0
U_v = 5.04 m/s	8	5
U_v = 8.3 m/s	11	6

Table 2: Example of how the data would how been tabulated.

Symbol	Parameter	Set Value	Justification
T	Temperature of saturated liquid in Kelvin	25k	The temperature of the condensate on the tubes.
ρ_c	Density of condensate	1000kg/m^3	-
ρ_v	Density of vapor	0.804kg/m^3	-
s	Fin spacing	1mm	According to tube surface geometry design (see Table 2)
g	Gravitational constant	9.81m/s^2	-
d_o	Fin tip diameter	14.3	According to tube surface geometry design (see Table 2)
K	Empirical constant	0.105	
m	Empirical constant	0.379	

Table 1: Parameters involved in flooding angle calculations.

The results of the data would be crosschecked with S.Namasivayam's expression of flooding angle Equation 2

$$\emptyset_f = cos^{-1}\left(\frac{2\sigma}{\rho_c g s R_0}(1-\Psi)-1\right) \quad for\ s < 2h$$

Equation 2

Where,

$$\Psi = K\left(\frac{\rho_v U_v^2}{\rho_c g s}\right)^m$$

Equation 4

The surface tension, σ, is expressed as:

$$\sigma = \frac{\left(75.6 - 0.138\theta - 3\times10^{-4}\theta^2\right)}{1000}$$

Equation 5

Where θ = T – 273.15

The flooding angles are calculated for both Uv = 5.04 m/s and Uv = 8.03 m/s and the results are compared to the ones recorded in Table 10. Eq.2 is comparable to the majority of data within a deviation of ± 30%. If the results all within the ± 30% range then the observations made through this apparatus is comparable to the majority of the data available. Had there been any actual observations of flooding angle a graph of calculated flooding angle vs the experimentally observed flooding angle would have been made, this graph would show how far out or in is the experimental data from the ± 30% range (see Figure 13 for an example).

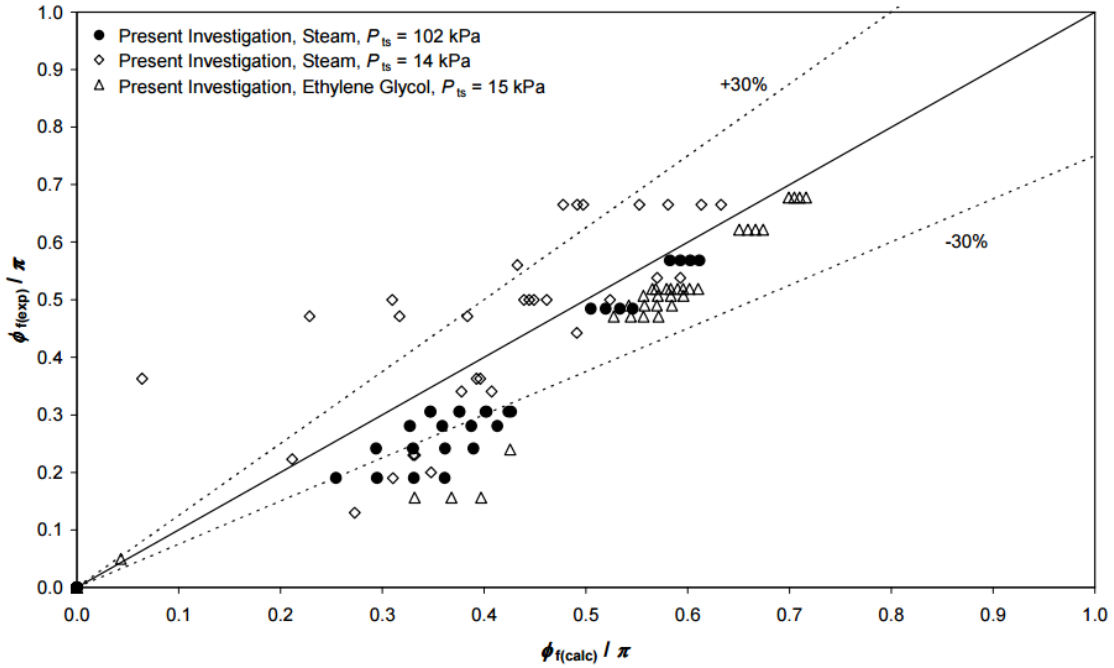


Figure 13: Calculated flooding angel vs experimental flooding angle with error bar at ±30%.

3.3 QUANTIFICATION OF HEAT TRANSFER

Quantifying the heat transfer of the tube will give an estimate of how much heat transfer occurs from the shearing vapor (simulated by wind flow) and the fin tube. The result of this calculation is be compared with existing experimental and theoretical data. This is done using the Equation 13 (see section 2.5 for background on the equations used). The flooding angles required in the calculation are the ones that are obtained from the flooding angle calculations from Equation 2 and the corresponding vapor velocity, Uv, is used.

Symbol	Parameter	Set Value	Justification
ΔT	Temperature of saturated liquid in Kelvin	25k	The temperature of the condensate on the tubes.
U_∞	Vapor velocity to infinity	= U_v m/s	Equal to the maximum vapor velocity, i.e. U_v
ρ	Density of condensate	1000kg/m^3	-
μ	Density of vapor	0.804kg/m^3	-
β		0	Flat fins have are perpendicular to the tube hence β *is 0.*
s	Fin spacing	1mm	According to tube surface geometry design (see Table 2)
h	Fin height	3.2mm	According to tube surface geometry design (see Table 2)
d_o	Fin tip diameter	14.3mm	According to tube surface geometry design (see Table 2)
d	Fin root diameter	12.7mm	According to tube surface geometry design (see Table 2)
k	Thermal conductivity	0.6791Wm^{-1}K^{-1}	Thermal conductivity of the saturated liquid.
C_1	Empirical constant	1	
C_2	Empirical constant	0.41	
C_3	Empirical constant	0.41	

Table 2: Parameters involved in heat transfer calculation.

Overall heat transfer of tube:

$$Q = C_1 \pi d_o t q_{tip} + \frac{\phi_f}{\pi}\left(C_2 (1 - f_f) \frac{\pi \left({d_o}^2 - d^2 \right)}{2} q_{flank} + C_3 (1 - f_s) \pi b d q_{root} \right)$$

Equation 3

Where,

Additional flooding at fin flank:

$$f_f = \frac{1 - \tan(\beta/2)}{1 + \tan(\beta/2)} \cdot \frac{2\sigma \cos(\beta) \tan(\phi_f/2)}{\rho g d h \phi_f}$$

Equation 6

Additional flooding at fin root:

$$f_s = \frac{1 - \tan(\beta/2)}{1 + \tan(\beta/2)} \cdot \frac{4\sigma \tan(\phi_f/2)}{\rho g d s \phi_f}$$

Equation 7

Heat flux at fin tip:

$$q_{tip} = \left[\frac{0.9^2 \rho k^2 \Delta T^2 \overline{U}_{tip}}{\mu d_o} \right]^{\frac{1}{2}}$$

Equation 8

$$\overline{U}_{tip} = U_\infty$$

Equation 9

Heat flux at fin root:

$$q_{root} = \left[\frac{\rho k^2 \Delta T^2 \beta(\phi_f) \overline{U}_{root}}{\mu d} \right]^{\frac{1}{2}}$$

Equation 10

$$\beta(\phi_f) = 1.4177+0.0172\phi_f -0.0477\phi_f^2$$

Equation 11

$$\overline{U}_{root} = U_\infty\left(1-\exp\left(-\left(\frac{s}{h}\right)\right)\right)$$

Equation 12

Heat flux at fin flank:

$$q_{flank} = \left[\frac{2\rho k^2 \Delta T^2 \overline{U}_{flank}}{\mu d_o \phi_f}\right]^{\frac{1}{2}}$$

Equation 13

$$\overline{U}_{flank} = \left(\overline{U}_{tip} + \overline{U}_{root}\right)/2$$

Equation 14

The OHT of the fin tubes is calculated for both the TBGs and a graph of Q vs Uv is made. These data points of the graph are analyzed to see whether it follows the typical flow shape of a Q vs Uv graph (see Figure 14). Typically the overall heat transfer of a fin tube increases as the vapor velocity does to this, of course, depends on several factors like condensate inundation rates and tube surface geometry. The graphs of each of the TBGs are compared with each other and an analysis is deducted.

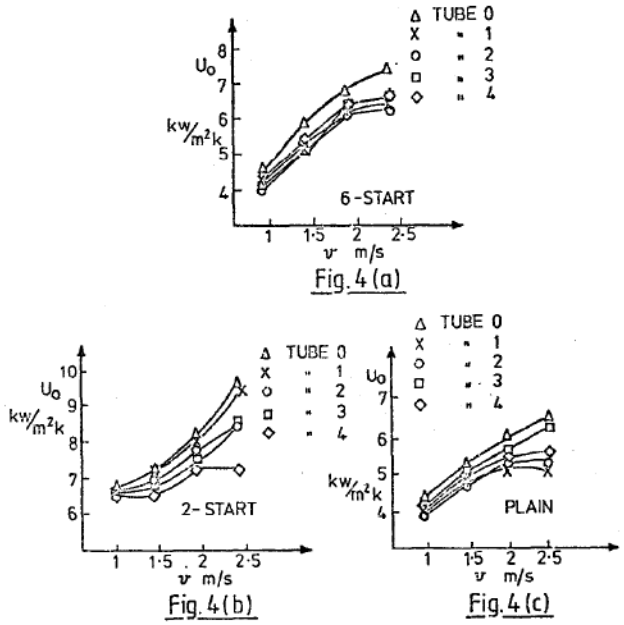


Figure 14: Example of Q vs Uv graphs J. Cunningham & M.Bahjernejad [11]

4.0 ANALYSIS & CORRECTIVE MEASURE

4.1 IMPLEMENTATION OF APPARATUS DESIGN

Before the apparatus was finalized it went through an iteration process where the design was changed several times to achieve the basic requirements mentioned is section 3.3.1.

The first design of the apparatus was designed to have a fully developed flow shear the tube bundle to avoid the interference of eddies current which could result in an irregular behavior of the condensate inundating the tubes. For this, a table fan was used to channel and air flow through a 3.31 m duct, which is the minimum length of the duct required to develop a full flow. A cone made from an acrylic sheet was used to reduce the flow from the 18in diameter fan to the 8in diameter duct. The issue faced was that the airflow that reaches test box was so small that no effect was observed on the inundated tubes, this is as a result of the pressure posed by the cone and the duct against the airflow generated by the fan. To attempt to fix this the length of the duct was reduced to only 40cm in hopes to reduce the pressure in the air flow channeling system. However, the air flow was still very weak and the conclusion was that most of the pressure was generated from the steep gradient of the cone.

The third attempt to resolve the issue required the design of the apparatus of to be changed. Instead of blowing the airflow to the test box the airflow was sucked through the test box. The fan placed directly under the test box blowing downwards and the reducer cone was set between them. The issue faced with the design what that instead of the air being sucked through the test box the air flow went in the opposite direction, the deduction made was that the fan created a negative pressure in the cone which caused the air to flow backward to achieve equilibrium.

Finally, the current design was adopted, where the cone was eliminated from the design and a 2000W hair dryer was used to produce the air flow.

4.2 ERROR ANALYSIS OF VISUAL OBSERVATIONS

The data extracted from the experiment is the observation of the flooding angle and observing the stripping of the condensate film off the tube. The stripping of the film has been observed with positive results sadly this is not the case for observing the flooding angle. This is as a result of the fin tube being translucent which makes it difficult to pinpoint flooding angle. Attempts were made to print the tube is solid colors using ABS and PLA 3D printers but the details of the fin was not able to be captured, only printing in SLA plastic could achieve this level of detail. However, SLA only comes in clear blue and white, a yellow background was kept to make a contrast in hopes to be able to have better observability but is did not help. The reason why the decision for 3D printing the tubes was made is because the cost of producing and importing a custom fin tube was too high to be an option. The entire apparatus was made as cheaply as possible and this came at the expense of its quality and the quality of results it produces. For this, the solution is to increase the budget of this project to allow for the construction of a quality apparatus.

Acknowledgment

First and foremost I need to thank Allah the opener of minds and hearts and the all-knowing One, for the blessing the blessing of being able to study and who made this project go with relative ease.

I would like to extend my respects and gratitude towards my mentor the project supervisor Dr.Satesh Namasivayam for his guidance and sharing his vast knowledge and experience on the topic.

I would also like to thank Yim Hoe Yen who has come to be a good friend of mine, for supporting me on this research. The late nights on campus and the meeting over a cup of coffee are memories that will forever be ingrained into my memory.

I would also like to thank Taylor's Engineering School for facilitating the resources that made this work possible.

Last but not least, I would love to thank my Mother (Muna Mahsen) who has always kept me in her prayers which words cannot describe who much I value. And my Father (Mbarak Ali) who has sacrificed his time, wealth and freedom to support me throughout my entire my academic life.

6.0 References

[1]"File:World electricity generation by source pie chart.svg - Wikimedia Commons", *Commons.wikimedia.org*, 2014. [Online]. Available: https://commons.wikimedia.org/wiki/File:World_electricity_generation_by_source_pie_chart.svg. [Accessed: 20- Oct- 2016].
[2]W. Cheng, C. Wang, Y. Hu and L. Huang, "Film condensation of HCFC-22 on horizontal enhanced tubes", International Communications in Heat and Mass Transfer, vol. 23, no. 1, pp. 79-90, 1996.
[3]R. Webb, "Enhancement of film condensation", International Communications in Heat and Mass Transfer, vol. 15, no. 4, pp. 475-507, 1988.
[4]"Condensation of R-134a on enhanced tubes", ASHRAE Trans, vol. 1002, pp. 809-817, 2016.
[5]J. Cunningham and M. Bahjernejad, "The effect of vapour shear and condensate drainage in condensers using roped tubes", Desalination, vol. 45, no. 1-3, pp. 135-142, 1983.
[6]J. Withers and E. Young, "Steam Condensing on Vertical Rows of Horizontal Corrugated and Plain Tubes. Application in Desalination of Water", Industrial & Engineering Chemistry Process Design and Development, vol. 10, no. 1, pp. 19-30, 1971.
[7]L. Rewerts, J. Huber and M. Pate, "The effect of R-123 condensate inundation and vapour shear on enhanced tube geometries,", 1996.
[8]C. Chu and J. McNaught, "Condensation on bundles of plain and low-finned tubes effects of shear and inundation,", 2016.
[9]H. Honda, B. Uchima, S. Nozu, E. Torigoe and S. Imai, "Film Condensation of R-113 on Staggered Bundles of Horizontal Finned Tubes", J. Heat Transfer, vol. 114, no. 2, p. 442, 1992.
[10]H. Honda, B. Uchima, S. Nozu, H. Nakata and E. Torigoe, "Film Condensation of R-113 on In-Line Bundles of Horizontal Finned Tubes", J. Heat Transfer, vol. 113, no. 2, p. 479, 1991.
[11]D. McNeil, B. Burnside and G. Cuthbertson, "A comparison between a small in-line and a staggered tube bank condensing steam filmwise at low-pressures", Experimental Thermal and Fluid Science, vol. 25, no. 3-4, pp. 113-123, 2001.
[12] V.A. Karkhu, V.P. Borovkov, Film condensation of vapour at finnely-finned horizontal tubes, Heat Transfer- Soviet Research 3 (2) (1971) 183-191.
[13]H. Ali and A. Ali, "Measurements and semi-empirical correlation for condensate retention on horizontal integral-fin tubes: Effect of vapour velocity", *Applied Thermal Engineering*, vol. 71, no. 1, pp. 24-33, 2014.
[14] A. Briggs, X.S. Huang, and J.W. Rose, An experimental investigation of condensation on integral-fin tubes: effect of fin thickness, height and thermal conductivity, in: Proceedings of the ASME National Heat Transfer Conference, vol. 308, 1995, pp. 21e29.
[15] A. Briggs, X.L. Wen, J.W. Rose, Accurate heat transfer measurements for condensation on horizontal integral-fin tubes, J. Heat Transfer 114 (3) (1992) 719-726.
[16] H. Honda, S. Nozu, K. Mitsumori, Augmentation of condensation on finned tubes by attaching a porous drainage plate, in: Proc. ASME-JSME Thermal Eng. Joint Conf., vol. 3, 1983, pp. 289–295.

[17]M. Browne and P. Bansal, "An overview of condensation heat transfer on horizontal tube bundles", Applied Thermal Engineering, vol. 19, no. 6, pp. 565-594, 1999.
[18]P. Nofz, Effect of condensate inundation and vapor velocity on heat transfer in condenser tube bundles, 1982.
[19]"Pool and Spa Heating Products", *66.254.69.183*, 2016. [Online]. Available: http://66.254.69.183/jumpPool.cfm?target=Raypakasme.htm. [Accessed: 20- Oct- 2016].
[20]R. Webb, T. Rudy and M. Kedzierski, "Prediction of the Condensation Coefficient on Horizontal Integral-Fin Tubes", *Journal of Heat Transfer*, vol. 107, no. 2, p. 369, 1985.
[21]C. Fitzgerald, A. Briggs, J. Rose and H. Wang, "Effect of vapour velocity on condensate retention between fins during condensation on low-finned tubes", *International Journal of Heat and Mass Transfer*, vol. 55, no. 4, pp. 1412-1418, 2012.
[22]H. Ali and A. Ali, "Measurements and semi-empirical correlation for condensate retention on horizontal integral-fin tubes: Effect of vapour velocity", *Applied Thermal Engineering*, vol. 71, no. 1, pp. 24-33, 2014.
[23]2016. [Online]. Available: http://www.wlv.com/wp-content/uploads/2014/06/databook3/data/db3ch7.pdf. [Accessed: 20- Oct- 2016].
[24]S. Namasivayam, "A Semi Empirical Model for Condensation on Integral-Fin Tubes at High Vapour Velocity", *CONDENSATION ON SINGLE HORIZONTAL INTEGRAL-FIN TUBES – EFFECT OF VAPOUR VELOCITY AND FIN GEOMETRY*, pp. 187-188, 2006.

eureca 2016 – Conference Paper
Paper Number 2ME03

Investigation of Heating Rate to optimize Mechanical Properties of Undoped Zirconia Ceramics

Alvin Diong Wern Xiong[1*], Sivakumar Sivanesan[2],
[1]*School of Engineering, Taylor's University, Malaysia*
[*]alvin_diong@hotmail.com

Abstract
Orthopaedic implant is an operation or surgery for the purpose of replacing missing joint, bone or support damaged bones. Zirconia ceramic is the material used for orthopaedic implant. It is known that zirconia ceramic have good mechanical properties such as high value hardness, elastic modulus, wear resistance and strength. However, zirconia ceramic has one weaknesses and that is it has poor fracture toughness. The poor fracture toughness of zirconia could also affect the friction and wear properties. The heating rate on zirconia ceramic has proven to influence the mechanical properties of zirconia ceramic. Therefore, it is the objective of this research to investigate how different heating rates influence mechanical properties of zirconia ceramic such as hardness, fracture toughness and Young's modulus in order to find the best and optimum value of heating rate. The process of this heating rate started by preparations of 3 mol% Y-TZP. After that, the prepared powder will be compacted into "green" bodies using cold isostatically pressed at 200 MPa. This will make the powder more uniformly packed in all direction, thus increases the density of the powder. The next step is powder consolidation where the samples will undergoes presureless sintering. 5 runs are performed here to get the average value. After that, there will be sample polishing where the sample were ground and then polished before measure the density, Vickers hardness and XRD evaluation. In order to determine the quantitative determination of tetragonal and monoclinic, X-Ray diffraction will be used. This is to make sure there are enough zirconia turning into tetragonal phase.. Young Modulus Determination will be find using commercial testing measurement and sonic resonance. Hardness testing will be done using Vickers hardness testing method. Finally, the testing of fracture toughness. It is expected there will be improvement on fracture toughness but also, it will not affect or compensate zirconia's other mechanical properties such as hardness, strength and elastic modulus. It is discovered that when heating rate decrease, the mechanical properties, hardness, density, fracture toughness and elasticity also increases.

Keyword: Zirconia, mechanical properties, density,sintering temperature

1. Introduction

In medical area, whenever someone lost his or her joint or bone, orthopaedic implant is needed to replace the missing joint, bone or support damaged bones. Material used to manufactured this orthopaedic implant is Yttria-Tetragonal Zirconia Polycrystals also known as Y-TZP. Beside in the field of medical, turbocharger rotors, diesel engine parts pump parts also uses Yttria-Tetragonal Zirconia. Zirconia ceramic is chosen due to their high value hardness, elastic modulus, strength and wear resistance.

However, a major issues with zirconia ceramic is that it has poor fracture toughness[1]. This fracture toughness also affects both the wear properties and friction of yttria tetragonal zirconia.[2] An example of fracture toughness failure occur during March 2002 where a 28 mm zirconia femoral head was implanted into a patient. As a result, the patient pain and the patient movement was limited. The patient went through radiograph and the radiograph result revealed that the head was fractured into many fragments. Figure below shows images of the fragments of the head.

Further research shows that there fracture up to 42% during the period 1999 where the year the transplant is first performed all the way until March 2003.[1]

Zirconia have three major phases during thermal cycling. They are tetragonal, monoclinic and cubic phase which zirconia experienced during the thermal cycling. Such transformation will affect the mechanical properties of zirconia.

Depending on how the heating rate or ramp rate is being manipulated, it will affect the mechanical properties of tetragonal zirconia ceramics. Different ramp rate influenced the mechanical properties of zirconia ceramic. To manipulate and optimize the toughening mechanism, zirconia transformation from tetragonal phase towards the monoclinic phase is observed as such transformation can affect fracture toughness. Beside fracture toughness, bulk density, hardness, strength and modulus elasticity will be tested as well to make sure the ramp rate does not give side effects which reduce zirconia other mechanical properties. Different sintering temperature, 1300,1350,1400 and 1450 will also be used to test how it affect the mechanical properties.

Applications of zirconia in biomedical can be found in THR ball heads. THR acetabular inlays, THR condyles, finger joints, spinal spacers, humeral epiphysis and hip endoprostheses.[2]

2. Methodology

This is to learn and gain knowledge about the project on what does Y-TZP ceramics does, what is it capable of and it's application. At the same time, through literature review, problem statement at hand is also address and learning why such research is performed is also understood here. Literature review also help form the scope, research questions and research objectives of the project. After all the literature review been done, then come the steps for experiment.

2.1 Powder Preparations

After learning about the background of Y-TZP, it's the initiation and construction powdering process. This stage is to imitate the powder characterization such as microstructure, temperature of sintering, size and others. No budget is needed

and powder is provided by the project supervisor. The 3Y-TZP, was manufactured by Kyoritsu Ltd, through hydrolysis method. It is then sprayed to become dry so that free flow is gain before press powder.

2.2 Preparation of Green Body

Next step is sintering green body and dope of iron oxide. This is to analysis the zirconia powders thermally during first stage. The sintering is carried out using 1300° C,1350 °C,1400°C and 1450 ° C with ramp rate 1.75°C /min, 2°C /min, 2.25° C/min and 2.5° C /min. Before sintering process, zirconia need to be put into green bodies first where it undergoes compaction. At first, it will experience manual pressing. After the manual pressing stage, it will go through cold isostatic pressing. Isostatic pressure compact the powder by applying pressure from many different directions using either gaseous or liquid around the compacted part. In cold isostatic pressing, the process will be done in room temperature. The advantage of cold isostatic pressing is that it is better uniformity and has more complex form. The main apparatus for this process is a flexible mold immersed in a pressurized liquid medium. Powder are inserted inside the glove's finger compartment. The glove is then put inside isostatic tank that is already been filled with fluid for pressing.

After that, it will undergo heating rate at 1.75°C /min, 2°C /min, 2.25° C/min and 2.5° C /min with sintering temperature 1300° C,1350 °C,1400°C and 1450 ° C.

2.3 Powder Consolidation

In ambient condition, the samples will then undergoes pressureles sintering. This is also done through standard rapid heating furnace at temperature ranging from 1200ºC to 1500ºC. With 10ºC/min as the ramp rate, plus the holding time of 2 hours were employed. There will be 5 runs per sample to get the average value.

2.4 X-Ray diffraction

This is followed by examination of the microstructure and physical of the sample using X-ray diffraction for measurement of grain size. X-ray diffraction will be used for the microstructural phase identification when it cools down to room temperature. It also allowed microstructure characterization such as crystallite sizes, dislocation densities and lattice distortions. One of the main objectives of this procedure is to ensure that the Y-TZP is still in tetragonal phase. During sintering or heating rate, Y-TZP could have transformed back into monoclinic or cubic during sintering. The radiation source for X-ray diffraction is Cu-K. The Scan speed is at 0.5°/min with 0.02 step scan. It works at 15mA and 35kV. It is important to make sure that the tetragonal phase is at 70% of the entire microstructure. If not, then powder preparation need to be done again. In order to determine the amount of tetragonal and monoclinic phase, the below equation, also known as Toraya's equation is used.[3]

$$V_m = \frac{1.311 X_m}{1 + 0.311 X_m} \qquad \text{(Equation 1)}$$

Vm = volume fraction of monoclinic zirconia
Xm=integrated intensity ratio

$$X_m = \frac{I(11\bar{1})_m + I(111)_m}{I(11\bar{1})_m + I(111)_m + I(111)_t}$$ (Equation 2)

I = peak intensity

To find the volume fraction of (t)-ZrO_2

$$V_t\% = 100\% - V_m\%$$ (Equation 3)

2.5 Mechanical Properties

Once checking the microstructure and grain size of the sample been done, it's time for testing the material properties which include the likes of fracture toughness, Young's modulus, hardness and flexural strength. The value is then recorded down and conclusion are made whether there are acceptable improvement on zirconia ceramic mechanical properties.

2.5.1 Density

To measure the density, water immersion technique based on Archimedes Principle was being used. For the immersion medium, distilled water will be used. By correlating its bulk the relative density can be determined. Equation below was used to determine the bulk density[4].

$$\rho = \frac{W_a}{W_a - W_w}\rho_w$$ (Equation 8)

Where;

ρ is the bulk density of the sample
W_a is the weight of the sample in air
W_w is the weight of the sample in water
ρ_w is the density of distilled water

2.5.2 Young Modulus Determination

Using commercial testing measurement and sonic resonance technique, the Young Modulus is determined. By monitoring the vibrational harmonics and evaluating it using a transducer, it can find the resonant frequency. The vibration is created in sample by tapping. Once the resonant frequency has been determined, it can then use to find the modulus elasticity using equation below.

$$E = 0.9465\left(\frac{mF^2}{b}\right)\left(\frac{L}{t}\right)^3 T$$ (Equation 4)

Where

E = Young's modulus

m = Mass of bar

b = Width of bar

L = Length of bar

t = Thickness of bar

F = Fundamental resonant frequency of the bar in flexural (Hz)

T = Correction factor for fundamental flexural mode to account for finite thickness of bar and Poisson's ratio of the material based on equation 5;

$$T = 1 + 6.585\,(1 + 0.0752\mu + 0.8109\,\mu^2)\left(\frac{t}{L}\right)^2 - 0.868\left(\frac{t}{L}\right)^4 - \frac{8.340(1+0.2023\mu+2.173\mu^2)\left(\frac{t}{L}\right)^4}{1+6.338(1+0.1408\mu+1.536\mu^2)\left(\frac{t}{L}\right)^2}$$

(Equation 5)

2.5.3 Hardness Determination

To determine the hardness, the Vickers hardness testing method was used. Load of 10 kg is applied slowly. Load is applied for 10 seconds. When the load is being removed, two impression diagonals, labeled as D1 and D2 which can be seen in figure below, were measured by using a filar micrometer which is attached in Vickers machine's microscope to the nearest 0.1 μm, then averaged. Using Hv = 1.854P/D^2, the hardness is calculated [5].

$$H_v = \frac{1.854P}{(D)^2}$$

(Equation 6)

P = Applied Load D is average diagonals = (D1+D2)/2

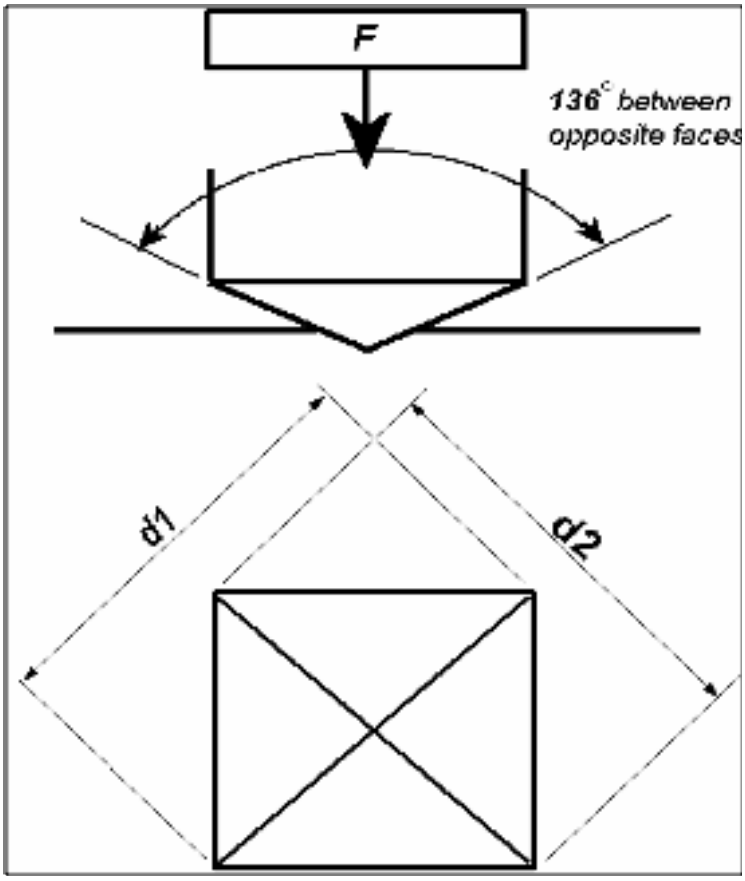


Figure 1:a) Vickers indenter (α= 136 ± 0.5° (b) Well formed indent.

2.5.4 Fracture Toughness

Once the hardness determination step been done, it is time to move on to the next step which is fracture toughness. Measure each of the lengths of the four cracks as shown in figure below. The fracture toughness, K_{IC} is determined using formula below.

Once each Vickers indentation have been go through, the length (L) of four cracks as can be seen in Fig. 5.3 was measured. Using equation 5.11 which is proposed by Niihara, fracture toughness, K_{IC} can be calculated.

$$\left(\frac{K_{Ic}\phi}{H_v a^{\frac{1}{2}}}\right)\left(\frac{H_v}{E\phi}\right)^{\frac{2}{5}} = 0.035\left(\frac{L}{a}\right)^{-\frac{1}{2}}$$

(Equation 7)

Where
K_{IC} = Fracture toughness
Hv = Vickers hardness
E = Young's modulus
α = Half length of the average diagonal
L = Average crack length = (L1+L2+L3+L4)/4
ϕ = Constraint factor

3.0 Results and Discussion

The results of experiment were tabulated as can be seen below. The first graph below, Figure 2 shows the relations between heating rate, sintering temperature and density. Sintering temperatures used are 1300°C, 1350°C, 1400°C and 1450°C. Different heating rate have been used with value of 1.75°C/min, 2°C/min, 2.25 °C/min and 2.5 °C/min. One noticeable common pattern is that as higher value of heating use increases, the densification of tetragonal ZrO_2 decreases. On the other hand, smaller value of heating rate created a bigger value of density. In addition, the increases of sintering temperature also improve the densification. Heating rate at 1.75°C/min at sintering temperature 1450°C created the highest value of fracture density at 98.7%.

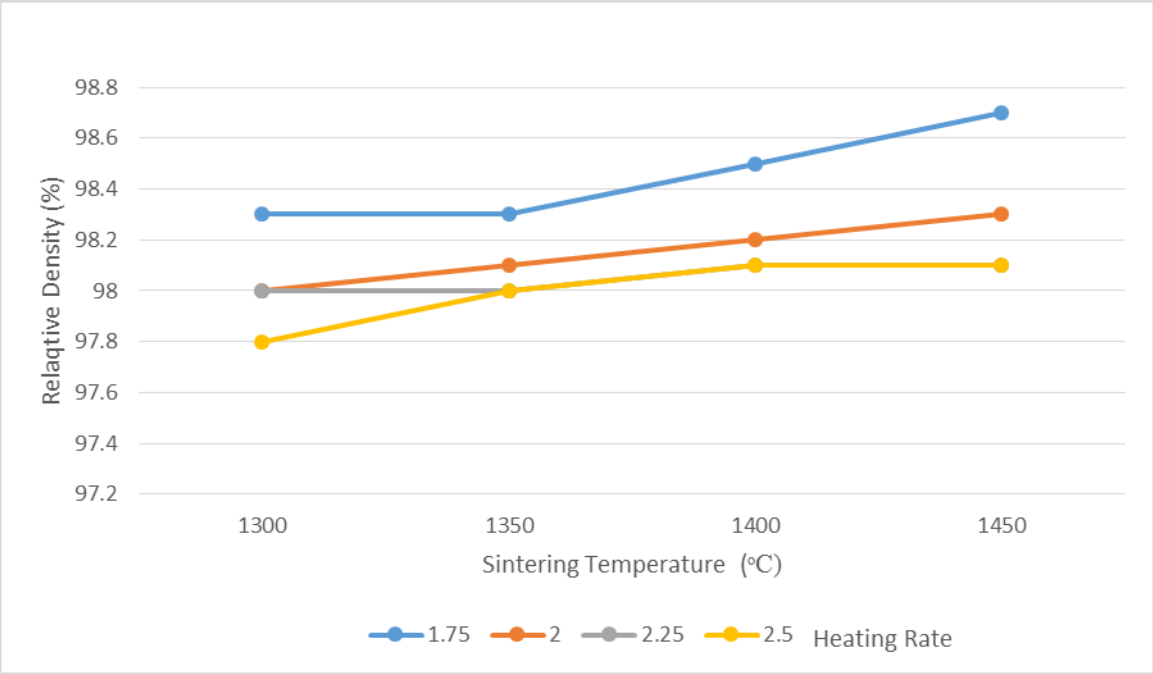


Figure 2: Relative Density at different Heating Rate and Sintering Temperature

Figure 3 shows how heating rate influence the fracture toughness of tetragonal ZrO_2 also with different sintering temperatures. As can be seen, heating rate with value 1.75°C/min at sintering 1450 °C created the highest value of fracture toughness which is at 14 MPa. Smaller heating rate cause higher fracture toughness value. The sintering temperature also influences the fracture toughness in direct proportional way. The reason for such result could be because lower heating rate took more time for heating to complete and absorb more energy compare to fast heating rate. This would mean lower heating rate cause more densification than fast heating rate and it is believed densification is direct proportional to fracture toughness.

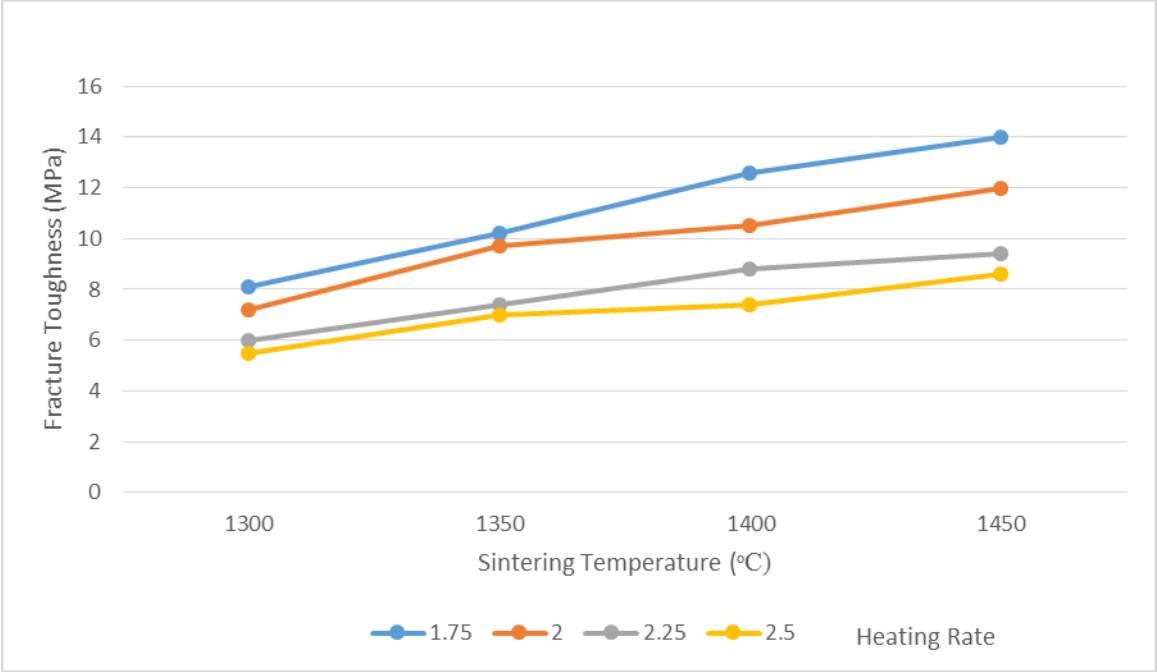


Figure 3: Fracture Toughness at different Heating Rate and Sintering Temperature

Figure 4 is how heating rate and sintering temperature affect the hardness value. For the heating rate influence on hardness, increase of heating rate decrease the value of hardness. Increase of sintering temperature increase the hardness. However, the range of hardness value is from 12 to 13 GPa. There are no huge changes in hardness value regardless of which heating rate of sintering temperature being used.

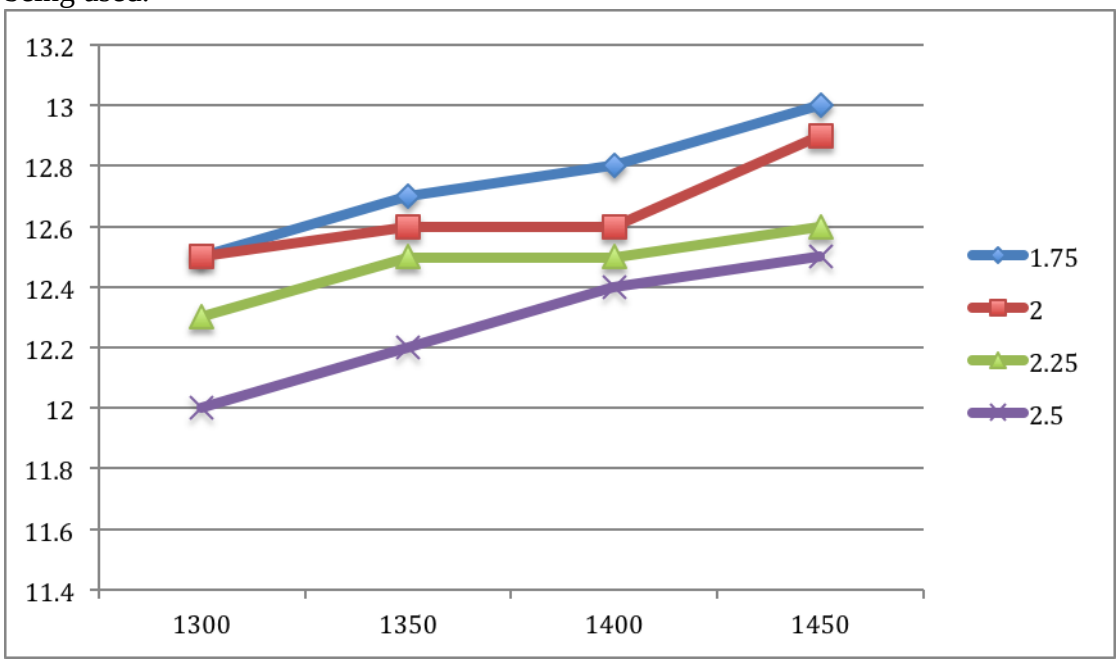


Figure 4: Hardness at different Heating Rate and Sintering Temperature

Young Modulus or elasticity of tetragonal ZrO_2 can be obtained in figure 5. Increase in heating rate decreases the elasticity while increase in sintering temperature increase the elasticity.

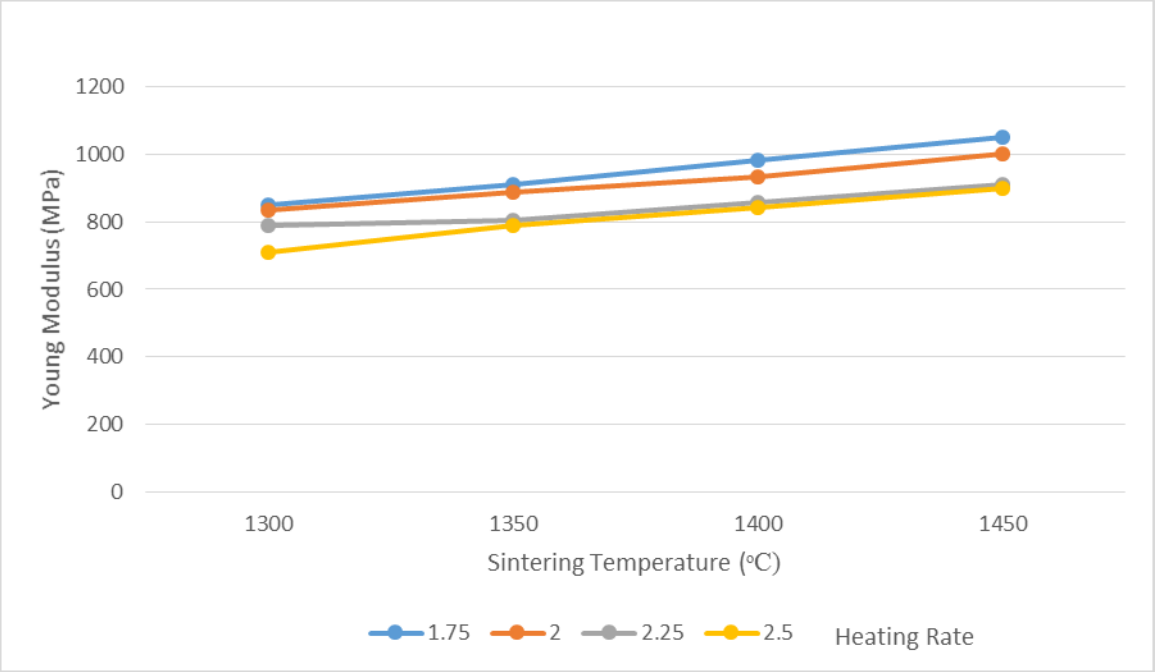


Figure 5: Elasticity at different Heating Rate and Sintering Temperature

4.0 Conclusion

To conclude this paper, there are two common pattern here. The first one is that using lower value of heating rate increases the density, fracture toughness,hardness and elasticity of the tetragonal zirconia ceramic. However, the increase of sintering temperature increases the value of density, fracture toughness, and elasticity. The increase in fracture toughness, hardness and elasticity could be because it is affected by increase of density which in turn is affected by the lower value heating rate. Finally, it is also concluded that heating rate at 1.75 °C/min with sintering temperature at 1450 °C is the best value to get the best value of densification,hardness, fracture toughness and Young's Modulus.

Acknowledgement

I would like to thank my supervisor, Mr Sivakumar for his guidance and advice in doing this project.

References

[1] Fracture of a Y-TZP ceramic femoral head ANALYSIS OF A FAULT G. Maccauro, C. Piconi,W. Burger,L. Pilloni,E. De Santis,F. Muratori, I. D. Learmonth

[2] Alumina and Zirconia Ceramic for Orthopaedic and Dental Devices, Giulio Maccauro, Pierfrancesco Rossi Iommetti,Luca Raffaelli and Paolo Francesco Manicone

[3] F. Zhang, K. Vanmeensel, M. Inokoshi, M. Batuk, J. Hadermann, B. Van Meerbeek, I. Naert, and J. Vleugels, "Critical influence of alumina content on the low temperature degradation of 2 – 3 mol % yttria-stabilized TZP for dental restorations," *J. Eur. Ceram. Soc.*, vol. 35, no. 2, pp. 741–750, 2015.

[4] K. Dadey, T. Janecek, and A. Klaus, "Dry-bulk Density: Its uses and determination," *Proc. Ocean Drill. Program, Sci. Results*, vol. 126, pp. 551–554, 1992.

[5] Z. Roell, "Vickers Hardness Test," *Indentec Hardness Test. Mach. Ltd.*, pp. 8–9.

eureca 2016 – Conference Paper
Paper Number 2ME04

Development of Piezoelectric based Fluid-Handling System for Microfluidic Applications

Brandon Hon Kah Jyun[1]*, Cheah Kean How[1]
[1] *Department of Mechanical Engineering,*
School of Engineering, Taylor's University, Malaysia

*Corresponding Author: brandonkahjyun.hon@sd.taylors.edu.my

Abstract
Microfluidics is the transportation of fluid in micrometer scale flow channels. A fluid-handling system was used to introduce sample fluid into or out of microfluidic channels. A common fluid-handling system is syringe pump but it is bulky, expensive and not portable. Micropump is a promising alternative to syringe pump where it is small in size with comparable fluid delivery capability. One type of micropump which operates using valveless pumping is called impedance pump. It operates based on impedance mismatch between two extremities of an elastic tube. Examples of impedance mismatch are sudden change in cross-sectional area or different material properties. Axisymmetric compression of elastic tube will produce bidirectional waves that reflect at rigid tube ends. Interaction between reflected waves causes changes in localized pressure, resulting in tube expansion and fluid suction at a unidirectional direction. One characteristic feature of impedance pump is fluid reversal which is dependent on voltage frequency. This research aims to integrate a commercialized piezoelectric actuator (microelectromechanical component) on a miniaturized impedance pump. Output performance of piezoelectric actuator (i.e. deflection, actuation force) was investigated using experimental and theoretical analysis. Piezoelectric actuator exhibits high performance at high voltage amplitude. Theory of Plates and Shells concerning partial loading on a sheet was utilized as design guideline in designing thickness and actuation area of polydimethylsiloxane (PDMS) elastic film. PDMS film is part of a novel stacked layer impedance pump and it is responsible for inducing wave propagation. Optimization of thickness and actuation area of elastic film was performed. Tradeoff exists between maximum film deflection and elastic limit of PDMS film. Two design parameters called elastic deflection ratio (EDR) and channel deflection ratio (CDR) were introduced in design of elastic film. This research proposed a design guideline for piezoelectric-actuated impedance pump. 5 design concepts were fabricated to illustrate successful downscale of impedance pump even though no net flow rate was observed.

Keywords: Piezoelectric, Impedance pump, Fluid-handling system, Valveless Pumping, Microfluidics.

1. Introduction

In microelectromechanical systems (MEMS), microfluidics is one of the first components to be fabricated in microscale using silicon technology [1]. Microfluidics is the transportation of fluid in flow channels of micrometer scale. It is related to the separation and detection of small volume of fluid (10^{-9} to 10^{-18} liters) with high resolution and sensitivity [2].

Microfluidics device, as shown in Figure 1, has an advantage of utilizing only a small sample volume for analysis which reduces total analysis time compared to macro-sized device [3]. In microfluidic applications, it has a size comparable with the volume of fluid to be pumped [4]. Therefore, it has a small footprint, relatively inexpensive and can be integrated with other miniature devices. In addition, microfluidic devices are reliable, consume lower power, portable, easy to fabricate and better dosage accuracy compared to macro-sized device [5]. Microfluidics device is widely used in applications such as electronics cooling [7-8], drug delivery [9], biomedical [10], and fuel cell technology [11-12].

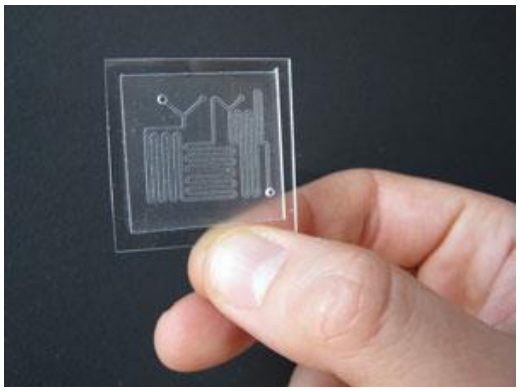
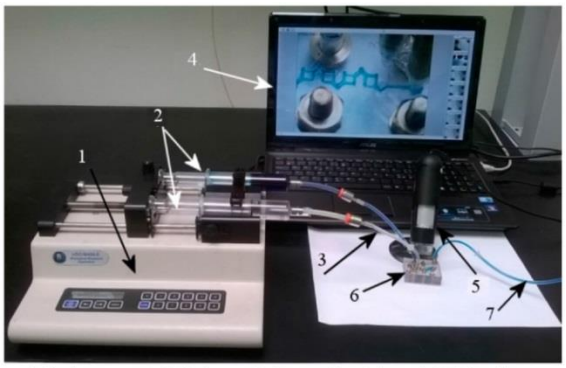


Figure 1. Microfluidic device [6].

The importance of a fluid-handling system in any microfluidic system is exemplified by the need of a method to introduce sample fluids into or out of the microfluidic device. Fluid-handling system should provide sufficient pumping force for transporting fluid in microchannels. An efficient fluid-handling system is able to produce constant volume flow rate under different pressure head.

One of the commercially available fluid-handling systems for microfluidics is syringe pump (Figure 2). It gradually administers small amount of fluid in a controlled manner. The pump is programmable and provides high accuracy and precision in fluid delivery [13-14]. However, its disadvantage is that it is bulky in size and not portable. Besides, it is costly and not disposable. Micropump is a promising alternative to syringe pump where it is small in size with comparable fluid delivery capability.



1. Syringe pump; 2. Syringes; 3. Connection tubes; 4. Notebook;
5. Microscope; 6. Y-Y mixer; 7. Output

Figure 2. Programmable syringe pump [15].

Impedance pump is a type of valveless micropump. A typical impedance pump has an assembly of an elastic tube connected to rigid fittings at both ends (Figure 3). It operates based on Liebau phenomenon, where axisymmetric compression of elastic region will produce a net flow rate. Bidirectional waves generated from tube compression will propagate and then reflect at tube ends due to impedance mismatch. The reflected waves will interact and cause changes in localized tube pressure, causing tube expansion and allowing volume suction thus producing flow rate.

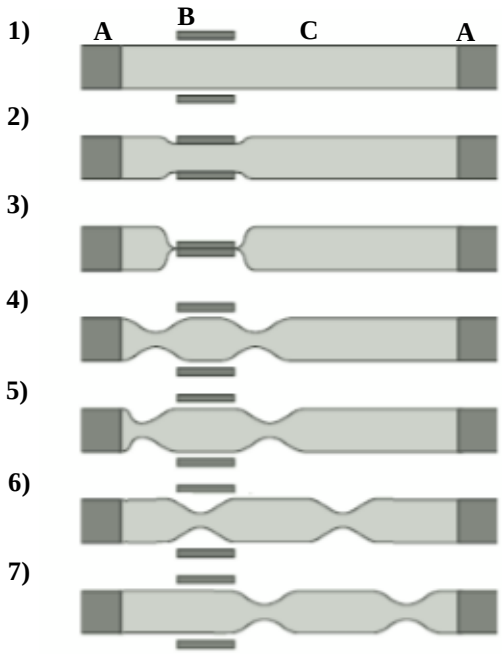


Figure 3. (From top to bottom) Changes in wave pattern due to axisymmetric tube compression. **A:** Rigid tube fittings. **B:** Pincher. **C:** Elastic tube. [16]

Impedance pump is similar to conventional valveless pump (Figure 4) which uses diffuser/nozzle feature in terms of ease of fabrication and low maintenance cost, but one characteristic feature of impedance pump is the ability to reverse flow

direction. The passive valves of fixed-geometry valveless pump pre-defined the flow direction, whereas the location of wave interactions along impedance pump can be altered by manipulating compression frequency, hence changing the location of volume suction and also flow direction.

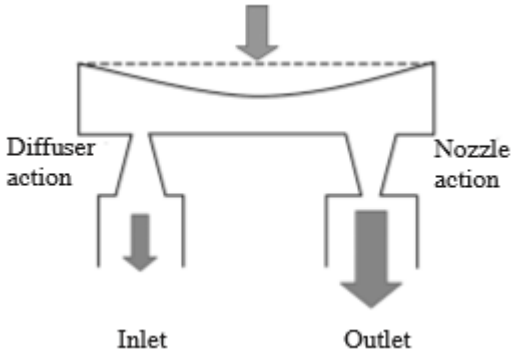


Figure 4. Diffuser/Nozzle Valve [17].

Hickerson *et al.* conducted a comprehensive experimental study on impedance pump where different parameters of the actuator (pincher frequency, pincher location and width, transmural pressure and loop resistance were investigated). It was concluded that axisymmetric compression of elastic tube will produce net flow [18]. Avrahami and Gharib illustrated the principle behind the importance of axisymmetric compression via visualization of constructive interaction of pressure waves and flow waves at different time intervals [19]. In addition, Jung and Peskin found that fluid flow in impedance pump is bidirectional and frequency-dependent using numerical simulations [20].

There is an opportunity to investigate the integration of an electromagnetic component called piezoelectric actuator on impedance pump. A piezoelectric actuator is a MEMS component which can convert mechanical energy to electrical energy and vice versa. There are limited studies about piezoelectric-actuated impedance pump. This research proposed a design guideline for development of piezoelectric-actuated impedance pump to address the research gap of lack of theoretical analysis on the design of piezoelectric-actuated impedance pump. Besides, key parameters affecting performance of impedance pump were proposed and tested in experimental stage.

Commercialized impedance pumps are normally in macroscale and not suitable for use in lab-on-a-chip applications. Miniaturization of impedance pump was investigated and developed. A new design concept known as stacked layer concept was proposed. It has advantages compared to the conventional elastic tube concept in terms of simplified layer patterns, higher structural rigidity and higher commercial value in terms of portability and ease of maintenance. Theoretical analysis based on Theory of Plates and Shells was utilized to assist in developing the design of impedance pump. Performance of impedance pump was experimentally tested.

2. Methodology

2.1. Data Acquisition on Performance of Piezoelectric Transducer

2.1.1 Materials

Piezoelectric actuators shown in Figure 5 (Murata Manufacturing) with different diameters and thicknesses were experimented using different operating frequencies and voltages. The two types of piezoelectric actuators that were selected have outer diameters of 20 mm and 27 mm (model 7BB-20-6L0 and 7BB-27-4L0 respectively).

Piezoelectric driver (DRV 2700 EVM, Texas Instruments) shown in Figure 3.7 was used to power piezoelectric actuator. Piezoelectric actuator was connected to the driver using two terminal differential output configuration shown in Figure 6. The piezoelectric driver has a maximum peak to peak voltage of 200V and maximum operating frequency of 500Hz. A graphical user interface provided by manufacturer was used to manipulate voltage and frequency output of the driver, shown in Figure 3.9. The displacement responses of piezoelectric actuators were used in theoretical analysis to determine force transmitted to PDMS film.

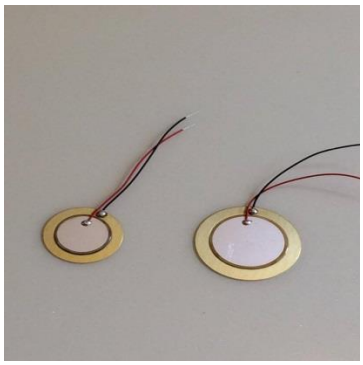


Figure 5. 20 mm (left) and 27 mm (right) piezoelectric actuators.

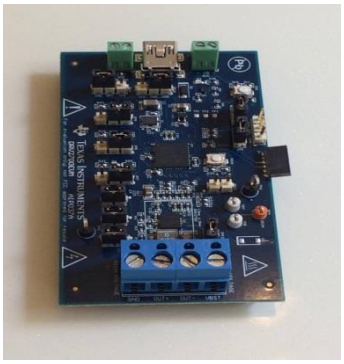


Figure 6. DRV 2700 EVM piezoelectric driver.

2.1.2 Experimental Setup

The experimental setup to analyze displacement response of piezoelectric actuator was shown in Figure 7. Mechanical stage and displacement sensor were utilized. Mechanical stage acts as fixed support for displacement sensor. Laser optical displacement sensor (HL-G103-S-J, Panasonic) with 0.5 μm resolution was mounted on the mechanical stage. Mechanical stage has three movable axis which eases researcher in adjusting sensor's position. Readings obtained from sensor were then transferred to computer via RS-422 cable.

Experimental setup to measure flow rate performance of piezoelectric impedance pump was shown in Figure 8. Silicone tubing on impedance pump which functions as inlet and outlet were connected to two reservoirs. Channel inside impedance pump was first filled with water by injecting fluid into silicone tubing using a syringe. This procedure helps to displace air trapped in pump channel. Next, both reservoirs were filled with equal volume of water to ensure there is no pressure head difference between reservoirs. Fluid inside each reservoir was made sure to be above tubing opening. Piezoelectric actuator was operated and water level in each reservoir was monitored.

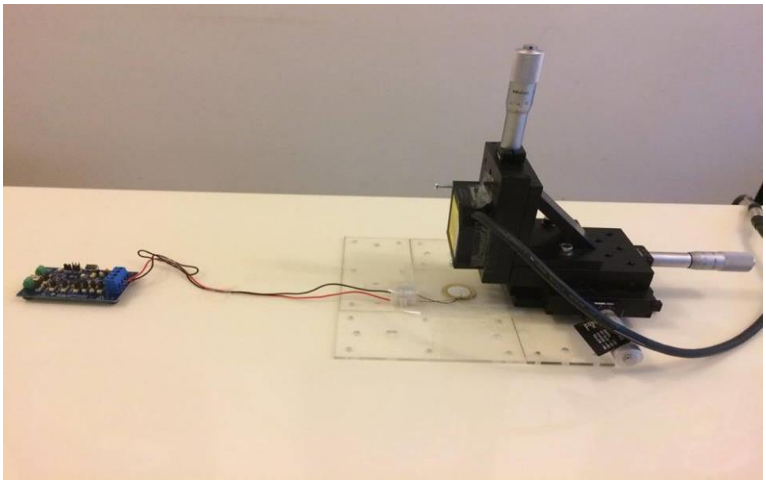


Figure 7. Experimental setup for data acquisition of piezoelectric actuator deflection.

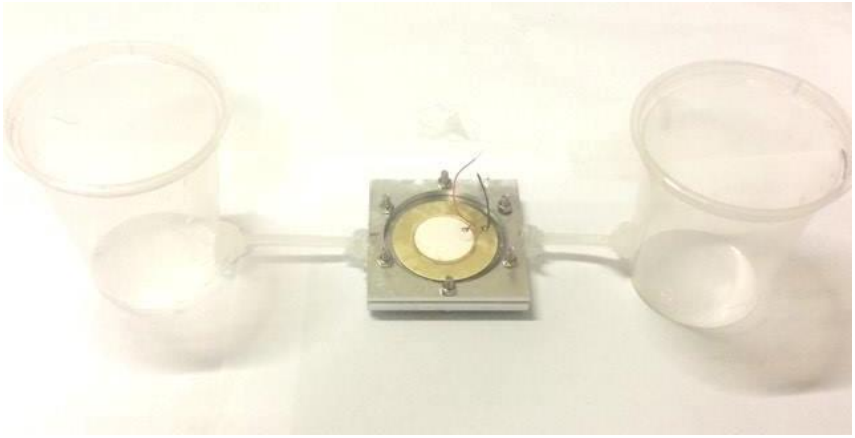


Figure 8. Experimental setup for analysis of impedance pump performance.

2.2 Theoretical Analysis on Equivalent Spring Constant and Force Generated by Piezoelectric Actuator

The main component of a piezoelectric actuator is piezoelectric material, which is integrated onto a brass plate. Piezoelectric material consists of an intermetallic inorganic compound which is lead zirconate titanate, commonly known as PZT. Piezoelectric actuator is well-known for exbiting piezoelectric effect. Direct piezoelectric effect is the generation of electricity when mechanical stress is applied on piezoelectric actuator. Inverse piezoelectric effect is the generation of mechanical deflection when electric field is applied on to piezoelectric actuator.

Piezoelectric actuator experiences deflection when there is a potential difference between the two electrodes on actuator. The two layers on piezoelectric actuator that is piezoelectric material and brass plate resembled two different electrodes. Piezoelectric actuator only deflects when there is a potential difference across the actuator. If there is no potential difference, the piezoelectric actuator will revert back to its original position. The ability to have reversible deformation is similar to elastic deformation of a spring. Hence, Hooke's Law concerning elastic force generated by an elastic spring can be applied to determine force generated by deflection of piezoelectric actuator.

Equivalent spring constant of the multi-layered piezoelectric actuator was analyzed. The piezoelectric actuator was modelled as an elastic spring where piezoelectric material (PZT) and brass base were two different spring configurations connected in series. Individual spring constants of PZT and brass base were calculated using Equation (1). The total spring constant of piezoelectric actuator was calculated using Equation (2). Hooke's Law illustrated in Equation (3) was then used to calculate force generated via deflection of piezoelectric actuator.

$$k = \frac{AE}{l} \tag{1}$$

$$k_T = \frac{1}{k_{PZT}} + \frac{1}{k_{copper}} \tag{2}$$

$$F = k_T \delta \tag{3}$$

Table 1. Parameters used in theoretical analysis of spring constant and force generated by piezoelectric actuator.

Symbol	Parameter	Unit
k_{PZT}	Spring constant of piezoelectric material	N m^{-1}
k_{brass}	Spring constant of brass plate	N m^{-1}
k_T	Equivalent spring constant of piezoelectric actuator	N m^{-1}
A	Surface area proportional to deflection axis	m^2
E	Modulus of elasticity	Pa
l	Layer thickness	M
F	Force generated by piezoelectric actuator	N
δ	Deflection of piezoelectric actuator	m

2.3 Theoretical Analysis on Force Transmission on PDMS Film

Theory of Plates and Shell [21] shown in Equation (4) concerning partial load on thin plates was utilized in the analysis. Maximum force output from piezoelectric actuator

was used in the calculation. Force transmitted from piezoelectric actuator to elastic layer was investigated. A PMMA block will act as the link between piezoelectric actuator and elastic layer. Length-to-width ratio of the PMMA block (actuation area) and thickness of PDMS film were optimized to obtain a suitable combination of parameters. A tradeoff was done between maximum performance output and its effect on the elastic limit of PDMS film.

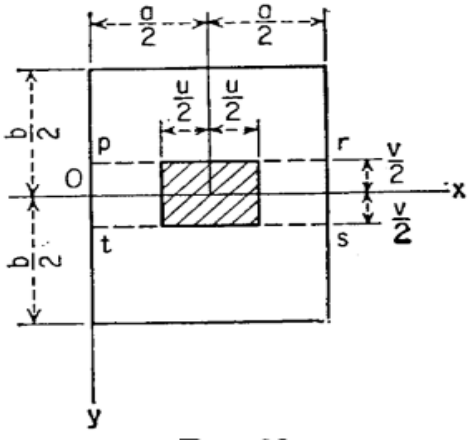


Figure 9. Schematic of partial loading on a sheet using Theory of Plates and Shells [21].

$$w = \frac{4qa^4}{D\pi^5}\sum_{m=1,3,5\ldots}^{\infty}\frac{(-1)^{(m-1)/2}}{m^5}\sin\frac{m\pi u}{2a}\left\{1-\frac{\cosh\frac{m\pi y}{a}}{\cosh\alpha_m}\left[\cosh(\alpha_m-2\gamma_m)+\gamma_m\sinh(\alpha_m-2\gamma_m)+\alpha_m\frac{\sinh 2\gamma_m}{2\cosh\alpha_m}\right]+\frac{\cosh(\alpha_m-2\gamma_m)}{2\cosh\alpha_m}\frac{m\pi y}{a}\sinh\frac{m\pi y}{a}\right\}\sin\frac{m\pi x}{a} \quad (4)$$

where: $\alpha_m = \frac{m\pi b}{2a}$; $\gamma_m = \frac{m\pi v}{4a}$

Table 2. Parameters used in theoretical analysis of spring constant and force generated by piezoelectric actuator.

Symbol	Parameter	Unit
k_{PZT}	Spring constant of piezoelectric material	N m^{-1}
k_{brass}	Spring constant of brass plate	N m^{-1}
k_T	Equivalent spring constant of piezoelectric actuator	N m^{-1}
A	Surface area proportional to deflection axis	m^2
E	Modulus of elasticity	Pa
l	Layer thickness	M
F	Force generated by piezoelectric actuator	N
δ	Deflection of piezoelectric actuator	m

3. Results and Discussions

3.1. Experimental Characterization of Piezoelectric Transducer

3.1.1 Analysis of Voltage Effect on Piezoelectric Actuator Deflection

Using the experimental setup in Figure 7, the deflection of piezoelectric actuator under different applied voltage was measured. Both 20 mm and 27 mm actuators were tested under two different support conditions (i.e. freely-oscillating edge and fixed edge) as shown in Figure 10. Graph of deflection against voltage for both actuators were plotted in Figure 11 and 12.

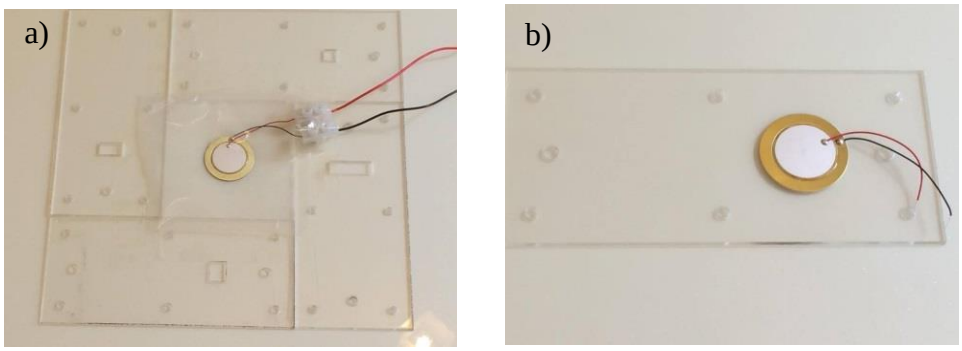


Figure 10: a) Freely-oscillating edge. b) Fixed edge.

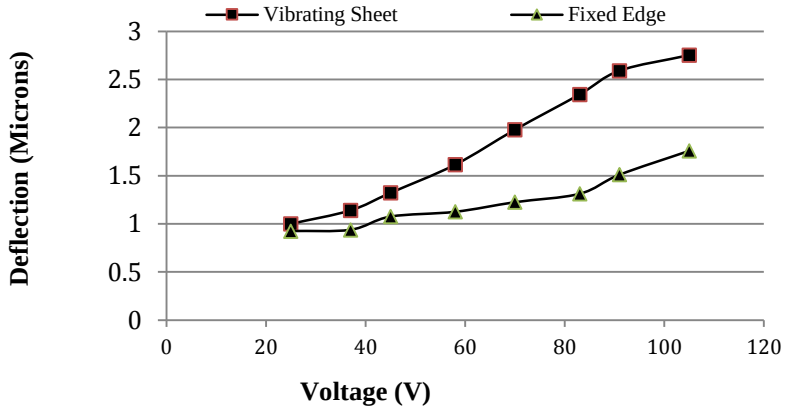


Figure 11. Graph of deflection against voltage for 20 mm piezoelectric actuator.

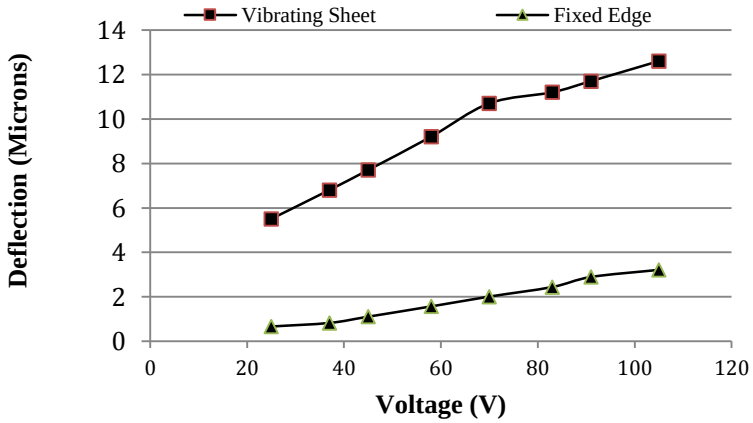


Figure 12. Graph of deflection against voltage for 27 mm piezoelectric actuator.

Deflection produced by both actuators increases linearly with voltage. Increase in applied voltage induced an increase in reverse piezoelectric effect, where piezoelectric crystal becomes more mechanically stressed thus producing higher deflection. In addition, piezoelectric actuator has higher deflection when its edges were allowed to oscillate freely on an elastic sheet. This integration allows the small deflection amplitude from actuator to be amplified, which is desirable for micropump design.

It was evaluated that actuator has a better performance when the diameter of the actuator increases. Actuator with large diameters will have higher radius of curvature, but there is a limitation to size of actuator as size is an important aspect in designing micropump. There will be a tradeoff between actuator size and its output performance. Based on Figure 10, the preference of using 27 mm actuator integrated on elastic sheet was justified by the significant increase in output deflection using this configuration.

3.1.2 Analysis of Force Generated via Actuator Deflection

Force generated by piezoelectric actuator was analyzed, which was then utilized in the design of elastic film subsequently. Equation (1) was used to determine spring constants of both components using its respective material properties tabulated in Table 3 and Table 4.

Table 3. Material properties of 20 mm piezoelectric actuator.

20 mm Piezoelectric Actuator		
Material Properties	PZT	Brass
Young Modulus (GPa)	63	125
Surface Area (mm^2)	128.67	31.16
Thickness (mm)	0.20	0.22
Spring Constant (N mm^{-1})	40.53×10^{6}	182.784×10^{6}
Total Spring Constant (N mm^{-1})	3.014×10^{-2}	

Table 4. Material properties of 27 mm piezoelectric actuator.

27 mm Piezoelectric Actuator		
Material Properties	PZT	Brass
Young Modulus (GPa)	63	125
Surface Area (mm^2)	260.16	572.56
Thickness (mm)	0.30	0.24
Spring Constant (N mm^{-1})	54.634×10^{6}	305.365×10^{6}
Total Spring Constant (N mm^{-1})	2.158×10^{-2}	

Equation (2) was then used to calculate the total spring constants of both actuators. **20 mm** and **27 mm** actuator has a **total spring constant of 3.014×10^{-2} N mm^{-1} and 2.158×10^{-2} N mm^{-1}** respectively. Using Equation (3), the force generated by different piezoelectric actuators was calculated. Deflection of both actuators obtained from freely-oscillating configuration was utilized in the calculations. Based on graph plotted in Figure 11, deflection of transducer also exhibits a linear increasing trend with force. *The **maximum force generated** was from **27 mm actuator which is 2.72×10^{-4} N** with **maximum peak deflection of 12.6 microns**.*

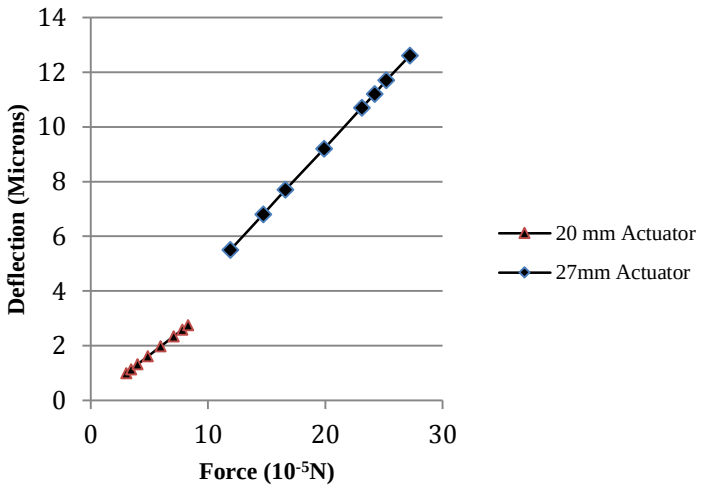


Figure 13. Graph of piezoelectric actuator deflection against force generated.

3.2. Design of PDMS Film

3.2.1 Optimization of Thickness and Actuation Area of PDMS Film

Optimization was done by determining the best combination of thickness and length-to-width ratio that provides the highest deflection. It was calculated that actuation area with length and width of 30 mm respectively provides the highest deflection compared to other sizes. Hence, it was then concluded that actuation area of 30 mm length and width will be selected.

Deflection using the chosen actuation area will then be compared among different elastic film thickness. It was shown that 0.5 mm and 1 mm elastic film experience deflection which exceeds layer thickness. On the other hand, 2 mm, 3 mm, and 4 mm elastic film have deflection which is approximately less than 20% of film thickness. It was identified that an elastic film within the range of thickness of 1mm to 2 mm will have optimum deflection, which will not be too little or too large. Further analysis was done on deflection of elastic film within the range of thickness of 1mm to 2 mm, but only using actuation area of 30 mm length and width. Data tabulated shown in Table 3.10. The ratio of PDMS deflection over PDMS thickness was introduced as elastic deflection ratio (EDR).

Table 5. Analysis of PDMS film with range of thickness between 1 mm to 2 mm using Equation 4.

PDMS Thickness (mm)	Deflection, w (mm)	Length, v (mm)	Width, u (mm)	Elastic Deflection Ratio
1	3.0000	30	30	3.000
1.1	1.4282	30	30	1.428
1.2	1.1001	30	30	0.917
1.3	0.8653	30	30	0.666

1.4	0.6928	30	30	0.495
1.5	0.5633	30	30	0.376
1.6	0.4641	30	30	0.291
1.7	0.3869	30	30	0.228
1.8	0.3260	30	30	0.181
1.9	0.2772	30	30	0.146
2	0.2376	30	30	0.119

Based on Table 5, PDMS thickness of 1 mm and 1.1 mm are not suitable to be used due to deflection that exceeds film thickness, thus exceeding elastic limit and at risk of tearing. Even though PDMS film of 1.2 mm thickness has the highest deflection which does not exceed film thickness, but its deflection exceeds suggested elastic limit of 80% (elastic deflection ratio of 0.8). Hence, it has a high probability of having permanent deformation upon deflection, which deteriorates pump performance. Therefore, elastic film of 1.3 mm film thickness was chosen. In conclusion, the suitable combination of **elastic film thickness** and **actuation area** is **1.3 mm and 30 mm x 30 mm** respectively.

3.3. Miniaturization of Impedance Pump

3.3.1 Miniaturized Impedance Pump

Experimental testing was done on miniaturized impedance pump shown in Figure 14. There is no movement of fluid in the fluid-filled channel even when piezoelectric actuator was operated. Vibration can be felt on the piezoelectric actuator accompanied by sound produced from high frequency vibration. The piezoelectric actuator was actuated at 105 peak voltage using a range of frequency from 1 to 500 Hz, at incremental of 1 Hz. It was suspected that one possible cause is the low PDMS deflection-to-channel depth ratio, where PDMS deflection has a maximum deflection of 0.86526 mm, while the channel depth is 3 mm. PDMS deflection-to-channel depth ratio was introduced as channel deflection ratio (CDR). The channel deflection ratio is 0.288.

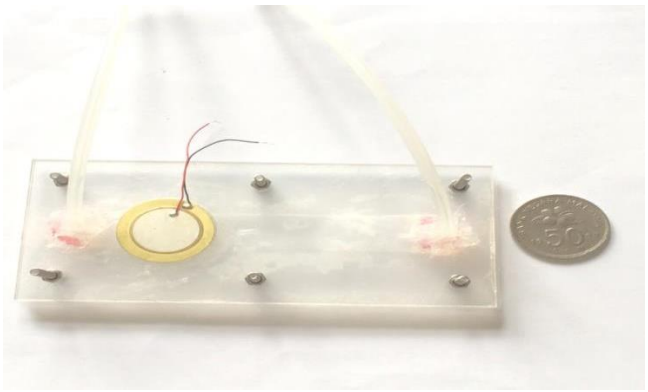


Figure 14. Miniaturized impedance pump (Design 1), coin as size scale comparison.

Channel depth was reduced to 1 mm. Design 2 (Figure 15) was experimented and it is not able to produce a flow rate. Even though the channel deflection ratio was significantly improved to 0.865, but there is a hypotheses channel width and length may affect impedance pumping effect. Hence, a micro impedance pump with reduced channel size scales was fabricated as shown in Design 4.

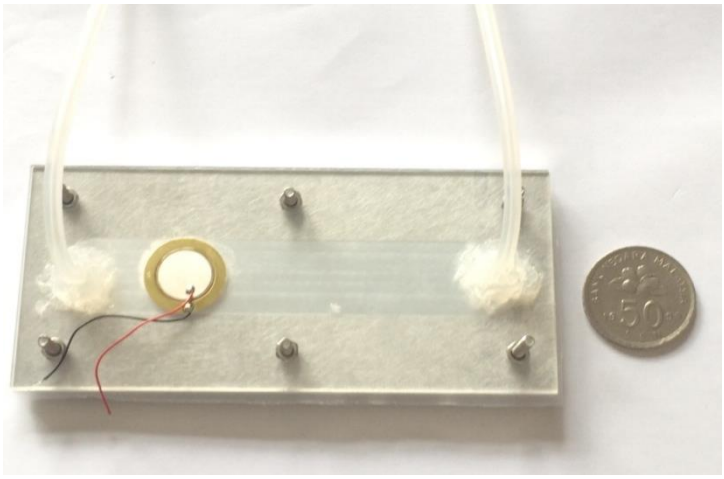


Figure 15. Design 2 prototype.

3.3.2 Micro Impedance Pump

The size of channel was reduced to a length of 30 mm and width of 3 mm. It has a thickness of 0.1 mm. Optimization was done on PDMS actuation area and film thickness since the size of elastic film has been reduced to 50 mm length and 50 mm width. Some of the optimum combinations of actuation area (length and width) and PDMS thickness were tabulated in Table 6. Elastic deflection ratio and channel deflection ratio of each combination were also analyzed.

Table 6: Analysis of PDMS thickness using Equation 4 with consideration of EDR and CDR.

PDMS Thickness (mm)	Width, u (mm)	Length, v (mm)	Deflection, w (mm)	Elastic Deflection Ratio	Channel Deflection Ratio
0.4	2	10	0.27879	0.697	0.558
0.4	2	15	0.30693	0.767	0.614
0.4	3	20	0.25672	0.642	0.513
0.5	3	10	0.21541	0.431	0.431
0.5	3	15	0.23872	0.477	0.477

Based on Table 6, it was shown that PDMS thickness of 0.4 mm and an actuation area with a 15 mm length and 2 mm width has the highest elastic deflection ratio and channel deflection ratio as compared to other combinations. Width of actuation area should be less than 3 mm as the width of the channel is 3 mm. An actuation area with width more than 3 mm may not be able to compress fluid in the channel.

Design 3 (Figure 16) was experimented and it was also concluded that there is no net flow rate and lacks impedance pumping effect. Design 1 to Design 3 relied on wave reflection at channel ends to produce impedance pumping effect, but it was unclear what the flaws in the design are.

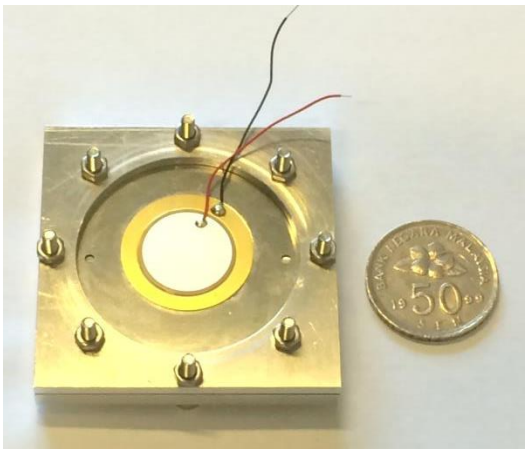


Figure 16. Design 3 prototype.

4. Conclusions

Experimental characterization of piezoelectric actuator illustrated that deflection of piezoelectric actuator has a linear increasing trend with operating voltage applied. This is due to the increase in mechanical stress of piezoelectric crystal as voltage applied increases, thus moving atoms in the crystal lattice will create deflection. This phenomenon is known as reverse piezoelectric effect.

Piezoelectric actuator is able to achieve higher deflection when its edges were allowed to oscillate freely as compared to having fixed edges. Maximum deflection occurs at the center of the transducer. Actuator with higher diameter has higher deflection due to its high radius of curvature. Using Hooke's Law, maximum force generated by 27 mm actuator was 2.72×10^{-4} N with maximum peak deflection of 12.6 microns.

The optimum combination of actuation area (length-to-width ratio) and thickness of PDMS film for miniaturized impedance pump is 30 mm length and width for actuation area and 1.3 mm PDMS thickness. This combination has the highest EDR and also CDR for a channel depth of 1 mm. On the other hand, the optimum combination of actuation area and PDMS thickness for micro impedance pump is 2 mm length and 15 mm width accompanied with 0.4 mm PDMS thickness for a channel depth of 0.5 mm.

Even though fabricated prototypes may not produce net flow rate, the successful illustration of downscaling process and development of a miniaturized impedance pump shows that impedance pump has high potential and commercial use in microfluidics in the future. The design guideline is a handy tool in developing stacked layer impedance pump which is novel. It may ease future researchers in replicating the same pump design for further research. Successful development of an operational piezoelectric-actuated stacked layer impedance pump in the future may impact the field of microfluidics.

References

[1]H. van Lintel, F. van De Pol and S. Bouwstra, "A piezoelectric micropump based on micromachining of silicon", *Sensors and Actuators*, vol. 15, no. 2, pp. 153-167, 1988.

[2]G. Whitesides, "The origins and the future of microfluidics", *Nature*, vol. 442, no. 7101, pp. 368-373, 2006.

[3]C. Baker, C. Duong, A. Grimley and M. Roper, "Recent advances in microfluidic detection systems", *Bioanalysis*, vol. 1, no. 5, pp. 967-975, 2009.

[4]D. Laser and J. Santiago, "A review of micropumps", *J. Micromech. Microeng.*, vol. 14, no. 6, pp. R35-R64, 2004.

[5]F. Abhari, H. Jaafar and N. Yunus, "A Comprehensive Study of Micropumps Technologies", *International Journal of Electrochemical Science*, vol. 7, pp. 9765-9780, 2012.

[6]*Didattica.polito.it*, 2016. [Online]. Available: https://goo.gl/rR4BF0 [Accessed: 23- Jun- 2016].

[7] L. Zhang, J.M. Koo, L. Jiang, M. Asheghi, K. Goodson, J. Santiago and T. Kenny, "Measurements and modeling of two-phase flow in microchannels with nearly constant heat flux boundary conditions", *Journal of Microelectromechanical Systems*, vol. 11, no. 1, pp. 12-19, 2002.

[8] L. Jiang, J. Mikkelsen, J.M. Koo, D. Huber, S.H Yao, L. Zhang, P. Zhou, J. Maveety, R. Prasher, J. Santiago, T. Kenny and K. Goodson, "Closed-loop electroosmotic microchannel cooling system for VLSI circuits", *IEEE Transactions on Components and Packaging Technologies*, vol. 25, no. 3, pp. 347-355, 2002.

[9]G. Liu, C. Shen, Z. Yang, X. Cai and H. Zhang, "A disposable piezoelectric micropump with high performance for closed-loop insulin therapy system", *Sensors and Actuators A: Physical*, vol. 163, no. 1, pp. 291-296, 2010.

[10]H. Ma, R. Chen and Y. Hsu, "Development of a piezoelectric-driven miniature pump for biomedical applications", *Sensors and Actuators A: Physical*, vol. 234, pp. 23-33, 2015.

[11]J. Park, M. Seo, Y. Ham, S. Yun and D. Kim, "A study on high-output piezoelectric micropumps for application in DMFC", *J Electroceram*, vol. 30, no. 1-2, pp. 102-107, 2012.

[12]S. Lee, Y. Kuan and M. Sung, "Diaphragm air–liquid micro pump applicable to the direct methanol fuel cell", *Journal of Power Sources*, vol. 238, pp. 290-295, 2013.

[13]T. Saleh, A. Abulkibash and A. Ibrahim, "Portable system of programmable syringe pump with potentiometer for determination of promethazine in pharmaceutical applications", *Saudi Pharmaceutical Journal*, vol. 20, no. 2, pp. 155-160, 2012.

[14]M. Appaji, G. Reddy, S. Arunkumar and M. Venkatesan, "An 8051 Microcontroller based Syringe Pump Control System for Surface Micromachining", *Procedia Materials Science*, vol. 5, pp. 1791-1800, 2014.

[15]*Mdpi.com*, 2016. [Online]. Available: https://goo.gl/zsJho2 [Accessed: 23- Jun- 2016].

[16] A.I. Hickerson. “An Experimental Analysis of the Characteristic Behaviors of an Impedance Pump”, PhD thesis, 2005.

[17]J. Johari, J. Yunas, A.A.Hamzah, B.Y. Majlis, "Piezoelectric micropump with nanoliter per minute flow for drug delivery systems ", *Sains Malaysiana* vol. 40, no. 3, pp. 275-281, 2011.
[18]A. Hickerson, D. Rinderknecht and M. Gharib, "Experimental study of the behavior of a valveless impedance pump", *Experiments in Fluids*, vol. 38, no. 4, pp. 534-540, 2005.
[19]I. Avrahami and M. Gharib, "Computational studies of resonance wave pumping in compliant tubes", *Journal of Fluid Mechanics*, vol. 608, 2008.
[20]E. Jung and C. Peskin, "Two-Dimensional Simulations of Valveless Pumping Using the Immersed Boundary Method", *SIAM Journal on Scientific Computing*, vol. 23, no. 1, pp. 19-45, 2001.
[21]S. Brodetsky, "Theory of Plates and Shells", *Nature*, vol. 148, no. 3760, pp. 606-606, 1941.

eureca 2016 – Conference Paper
Paper Number 2ME05

Reducing Train Track Vibration Using Anti-Vibration Slab Mat

Chan Jay Ren[1,*], A/P Dr. Mohammad Hosseini Fouladi[1], Ir. A/P Dr. Satesh[1], Prof. Miles Richard Tight[2], Dr. Sakdirat Kaewunruen[2]

[1]Department of Mechanical Engineering,
School of Engineering, Taylor's University, Malaysia
[2]Department of Civil Engineering, University of Birmingham, United Kingdom

*Corresponding Author: jayren.chan@sd.taylors.edu.my

Abstract
The purpose of this study is to discover the correlation between anti-vibration slab mat mechanical characteristics and vibration isolation performance. When the train accelerates on the track, the train movement and static load propagate together, thus transforming the static load to a dynamic load. The transformation is caused by imbalance in between the rail surface and wheel. Anti-vibration slab mat is located among the concrete layers of slab track. In order to acquire the optimum designation of slab mat, optimization process was conducted by utilizing elastic element which consists of excellent mechanical attributes. Numerical analysis was performed on a 3D model track-bridge structure, which was produced in SolidWorks by using the modal parameters acquired from literature review. Meshing using body sizing was performed. Next, the modal and harmonic response analysis were subjected to a suitable boundary condition setup. A frequency response graph of bridge acceleration was acquired from harmonic response analysis for different modal parameters of slab mat. In addition, a prelude outcome illustrated the efficiency of slab mat layer composed of synthetic rubber in minimizing vibration. To sum up the study, the mechanical attributions of anti-vibration slab mat, which is great damping ratio, less stiffness and expanded thickness are contributing factors to the minimization of bridge acceleration.

Keywords: Anti-vibration slab mat, Harmonic load, Train track vibration, High speed railway, Rubber

1. Introduction

Railway transportation is vital and provides an extensive connection within suburban and commercial zones, which is a huge benefit. The subway trains emit ground-borne vibrations, which is a huge problem as people and building structures are influenced by it [1]. Transportation systems produce sound and vibration due to the train track vibrations and these vibrations emitted travel to surrounding buildings through the tunnel construction and soils. Constant vibrations could cause damage and harm to the building material even though the vibrations are normally low [2]. In the surroundings areas of railway traffic, human will be affected by airborne noise and structural vibrations. They will experience discomfort which is caused by vibrations or noise produced by structural vibrations, called structural borne sound, that led the surface to radiate [3].

The wheel or rail interconnection point is the place where operational rail vibration emerges and propagates to the tunnel construction, ground and nearby infrastructures through the track support system. The vibrations induced by the trains operating in tunnels has a usual frequency that range from 4 Hz to thousands Hz [4]. The transmission of the weight of trains is from the wheel to rail which is then reallocated by the rail, track structure and ground and this is known as static load. As the train accelerates on the track, this force moves alongside with the train motion. The distinction at different parts of the train-track structure system, for example the non-uniform rail and wheel surface, and also the dissimilarities in the support structure underneath the rail will transform the static load to a dynamic load.

In order to segregate the supporting base from the train structure and decrease the conveyance of vibration from the train track, anti-vibration slab mat is usually situated and positioned between the concrete layers. The core function of anti-vibration slab mat is to suppress the vibrations emitted by the train, which is done by separating the soil from the buildings as the anti-vibration slab mat functions as a soft layer of foundation mat for buildings [2]. Because of the installation of an elastic slab mat beneath the slab, a low natural frequency is obtained by the system of the track and as for frequencies that is greater than the low track natural frequency, the reduction of force which produces the soil vibration is done [5]. By doing so, the track performance can be enhanced and issues generated from high speed train traffic can be solved.

In addition, there are two mechanical attributes that will influence the performance for vibration isolation of the anti-vibration slab mat. These are the damping coefficient followed by stiffness which relies on the mechanical attributes of the rubber elements utilized [1]. Hence, the anti-vibration slab mat should possess low stiffness and high damping coefficient for the purpose of enhancing the effectiveness for vibration reduction [6]. The most suitable material to be utilized for the slab mat is natural rubber, this is because it has a smaller ratio of dynamic to static stiffness, and can also sustain for a longer period. In addition to that, it shows insignificant indications of deterioration or transformation in the mechanical characteristics [7]. Mechanical energy dissipation and deformation capacity are examples of other characteristics that rely on the density, degree of thickness, sizes and type of compounds the mat is formed of. Generally, the thickness of the mats will range from

15 to 30 mm, and its horizontal dimensions are determined by the methods evolved in the construction period [8].

The purpose of this study is to overcome vibration problems by determining the ultimate designation of anti-vibration slab mat. The 3D model produced in SolidWorks was replicated to perform numerical analysis in ANSYS in order to examine the performance of slab mat vibration minimization. Furthermore, modal and harmonic responses were included in the ANSYS analysis. A calculation was done on the frequency response graphs which were affected by harmonic loading. Next, the outcomes acquired were in a graph format, which contains response quantity such as velocity, displacement or acceleration subjected to a prescribed range of frequency. To determine the ideal designation for an anti-vibration slab mat, a smaller degree of vibration response has to be acquired through manipulation of the modal parameters based on the results obtained.

2. Research Methodology

2.1 Design of Anti-Vibration Slab Mat

In the design process of anti-vibration slab mat, it involved the use of CAD software which was SolidWorks before importing the design for numerical analysis in ANSYS Workbench. The details of the design were discussed in the following section.

2.1.1 Geometrical modelling

Firstly, a computer aided design (CAD) software, SolidWorks was used to produce three dimensional (3D) track-bridge model as shown in Figure 1. This model was referred to the layout of slab track with slab mat layer and bridge sketch used by T. Xin and L. Gao [9] to interpret dynamic relations among high speed railway, running at 350 km/hr and the bridge. The model comprises of rail, rail pad, slab and bridge body. Located in between the concrete slab and bridge body was the anti-vibration slab mat. In addition, the model was originated from the mid-span area which was the prime span of the 48 m length bridge. Nevertheless, for the aim of reducing computing time and complexity in numerical simulation, merely train track of 1 m length was taken into account for the analysis. A half-track-bridge model of 1400 mm width was able to be simplified from a full track-bridge model as shown in Figure 2 and 3 due to the symmetrical property of geometry.

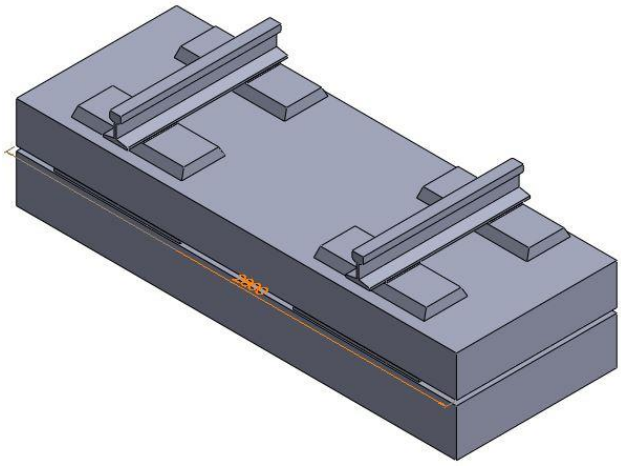


Figure 1: Isometric view of full track-bridge model.

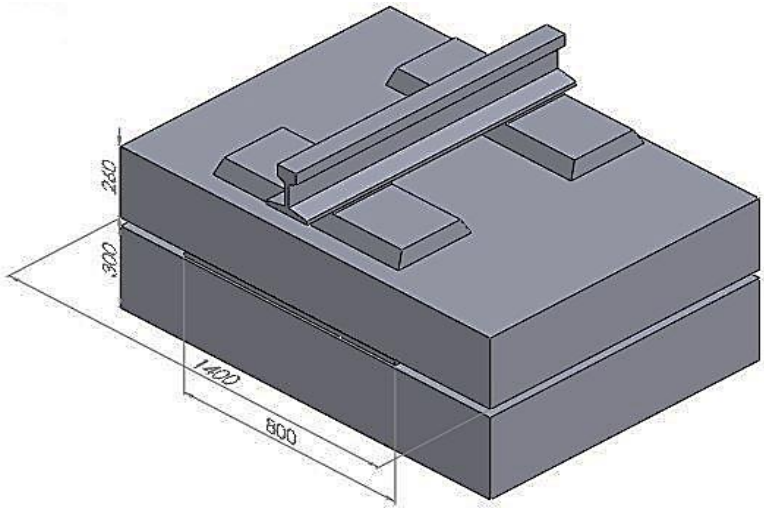


Figure 2: Isometric view of the half-track-bridge model in mm scale.

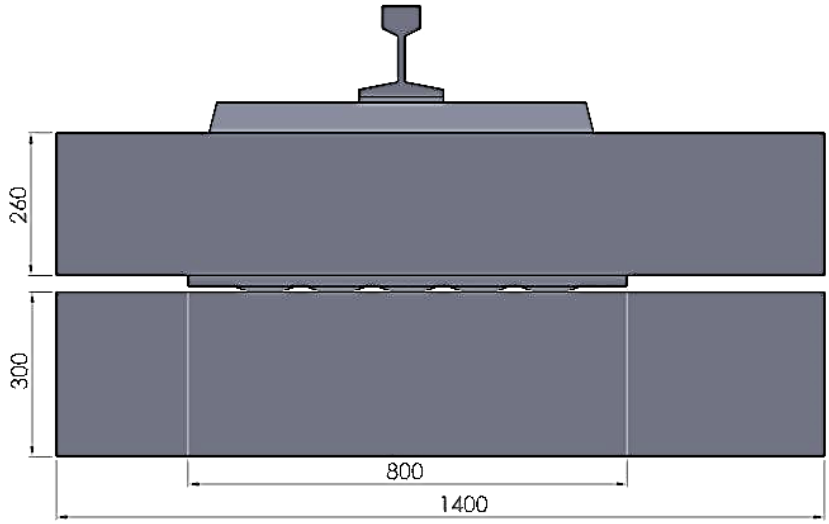


Figure 3: Front view of the half-track-bridge model in mm scale.

The thickness was set at 30 mm with 800 mm x 1020 mm area for the designation of anti-vibration slab mat. Based on Figure 4, the designation also consists of conical studs of 10 mm thickness on a mat surface. The material used to manufacture the conical studs was of synthetic rubber or natural rubber, which has a function similar to a spring with an ideal ratio of dynamic to static stiffness. Besides that, the assisting layer for the studs was constituted with the back of 20 mm thickness, whereas the composite materials serves as a damping and protective layer which was able to sustain slab track loads. Vibrations from railway were able to be minimized due to the excellent characteristics of rubber with the conical shape of the studs increasing the rubber's efficiency. The cone will disfigure into a hemisphere under pressure of load and the hemisphere shape was able to virtually reach uniform natural frequency for the range of loads. Conical studs has a compression set which is a measure of existing disfiguration, they were very tiny in that and thus, their dynamic efficiency was not affected in the long run.

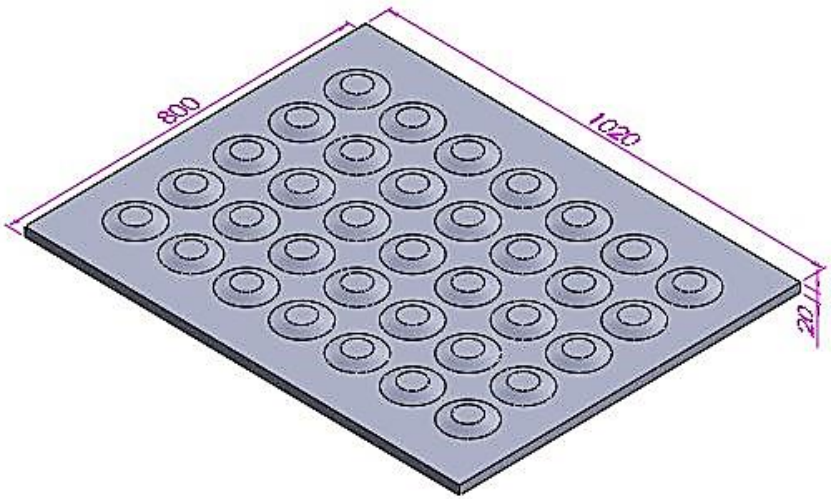


Figure 4: 3D model of anti-vibration slab mat in SolidWorks with units of mm.

2.2 Numerical Analysis

In numerical analysis, meshing was performed on the 3D half-track-bridge model before subjecting it to a boundary condition setting. The material properties were also mentioned and they were used to perform a two-step analysis which was modal analysis followed by harmonic response analysis. The settings of the analysis were also included in the section below.

2.2.1 Meshing

Body sizing was opted for the 3D model. In order to assure excellent standard of mesh, an evaluation was done on the element quality and skewness of the mesh. The ultimate ideal method for mesh is MultiZone method as it required less elements to discretize the model, it also contained the greatest element quality and minimum skewness. Hence, a greater accuracy of outcome and a rapid estimation can be achieved. Figure 5 showed the meshed model using MultiZone method.

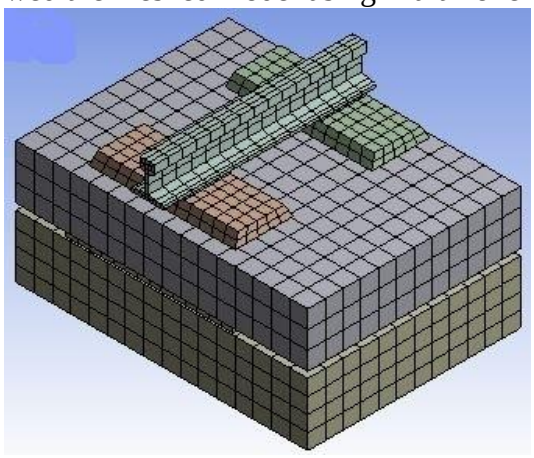


Figure 5: Meshing of 3D model using MultiZone method.

2.2.2 Setting of boundary conditions

After allocating the material properties for every component in ANSYS engineering data, as depicted in Table 2, the numerical analysis was set to Modal. The material properties of natural rubber and synthetic rubber were referred to the Material Data Book of Cambridge University Engineering Department [10]. The engineering data library in ANSYS also contains structural steel and concrete material properties. The ratio of Poisson's was 0.45 and 0.495 for synthetic rubber and natural rubber consecutively, based on [1]. A fixed support was set at the bridge body, which was the base of the model's lowest layer. Next, a variation of mode shapes and natural frequencies of model were produced and replicated.

Harmonic response analysis was conducted upon completion of the modal analysis. The high speed railway produces 119700 N of wheel-rail force which operates on the rail beam. Since the 3D model was modelled as half-track-bridge model, the vertical force applied on the rail beam surface was reduced to 59850 N. The boundary condition set for the analysis was shown in Figure 6.

Table 2: Material properties for all components in the 3D model [1, 10].

Components	Material	Density, ρ (kg/m^3)	Young's Modulus, E (GPa)	Poisson's Ratio, v
Rail	Structural Steel	7850	200	0.30
Rail Pad	Natural Rubber	920	0.0025	0.495
Slab	Concrete	2300	30	0.18
Slab Mat	Butyl Rubber	900	0.001	0.45
Bridge Body	Concrete	2300	30	0.18

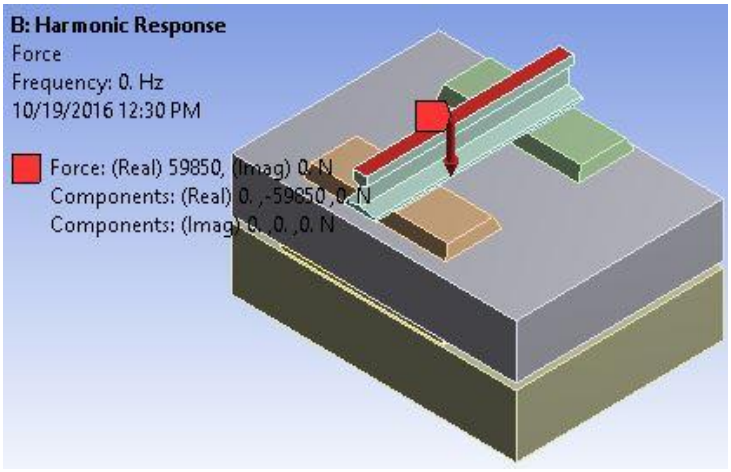


Figure 6: Boundary condition applied on the track-bridge model.

2.2.3 Modal analysis

Modal analysis is defined as the method to investigate the dynamic properties between the bridge and the track which is influenced by excitations of vibrations. Modal analysis can also be used to discover the mode shapes and natural frequencies of the composition. One of the advantages of utilizing ANSYS is the availability of precise visualization and simulation of the mode shapes, thus enable disfigurations of the track bridge model to be accurately detected.

ANSYS Workbench was used to determine frequency against graphical distinction of number of modes. The greatest number of modes was fixed at 10 for the analysis setting. Therefore, there will be 10 different mode shapes with their respective natural frequencies being generated.

2.2.4 Harmonic response analysis

The function of harmonic analysis is to discover the steady state response of a linear structure to loads which differs sinusoidally with time. Harmonic analysis does not include the transient vibrations which take place at the starting of stimulation. This has allows validation on the situations in which the designs are able to conquer problems such as resonance, fatigue and destructive consequences caused by forced vibrations.

The necessary input properties in harmonic analysis were density, Young's modulus and Poisson's ratio. Next, the analysis of harmonic response can be conducted as soon as the operation of modal analysis was done. The reason for this was that modal coordinates from the modal analysis were utilized. To enhance the efficiency of harmonic analysis, a harmonic solution with the Mode Superposition technique was used. The frequency consists of 10 intervals with a range of 0 - 200 Hz, this showed that simulation was able to resolve for 10 exciting frequencies of 20, 40, 60, 80, 100, 120, 140, 160, 180 and 200 Hz. A constant damping ratio of 1 % was set under the damping control of the analysis.

A graph of certain response quantity for example displacements and acceleration against frequency can be obtained through a standard harmonic analysis which is able to measure the structure response to cyclic loads over a range of frequency (sine sweep). Thus, this allows for "peak" responses to be determined from these graphs of response against frequency.

3. Results and Discussion

Modal and harmonic response analyses were performed in ANSYS Workbench to obtain frequency response graph for bridge acceleration. The simulations were repeated for different stiffness, damping ratio and thickness of slab mat. The results obtained were plotted into graphs in Excel to show the relationship between different parameters of slab mat and its vibration reducing effect.

3.1 Impact of Anti-Vibration Slab Mat in Reducing Vibration

To investigate the effect of minimizing vibrations, bridge acceleration was chosen as the indicator to show the changes caused by minimizing vibrations. 23.5 Hz was the frequency of excitation used in this study. Comparison and evaluation were performed for two conditions, slab track with slab mat layer, followed by slab mat without slab mat layer. Results in Figure 7 showed that the slab mat layer was able to reduce the bridge acceleration and maintained at a minimal acceleration close to 0.01 ms^{-2} as frequency increased. However, for slab track with no insertion of slab mat layer, the bridge acceleration kept increasing and reached a maximum value of approximately 4 ms^{-2}. Since the acceleration of the bridge is high, the vibration amplitude is greater as well. Therefore, to reduce vibrations transmission to surrounding infrastructures from the bridge, high speed railway must contain slab mat layer.

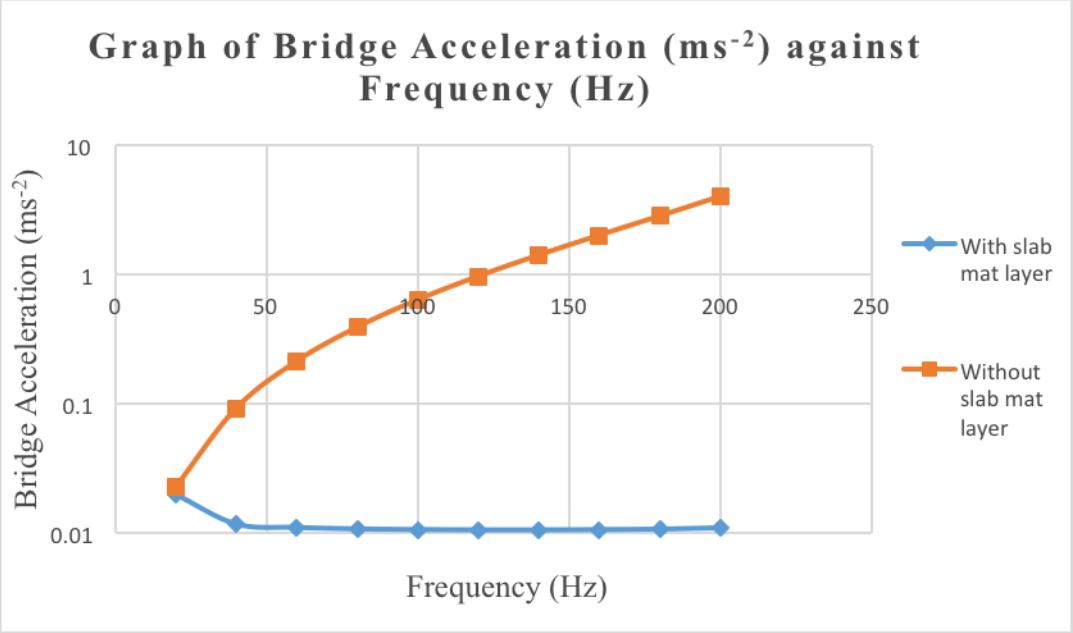


Figure 7: Bridge acceleration against frequency graph for slab track with and without slab mat layer.

3.2 Impact of Slab Mat Stiffness

The stiffness of elastic elements has a huge influence in minimizing vibrations produced by railway track. Synthetic rubber, acquired from worn tyres or recycled rubber was the elastic element utilized by the anti-vibration slab mat [1]. Besides that, butyl rubber with elastic modulus, E of 1.0 MPa acts as the elastomer. The stiffness of element varies accordingly to the elastic modulus based on the formula of $k = \frac{AE}{l}$. Neoprene, an elastomer with 0.7 MPa elastic modulus was used to examine dynamic response of a railway track by manipulating the slab mat stiffness from greater value to smaller value. The lower the elastic modulus, the lesser the stiffness.

According to Figure 8, a great reduction of accelerations on bridge was observed when the frequencies were less than 50 Hz. By using a neoprene slab mat, bridge acceleration can be minimized to 0.01 ms^{-2} at low frequency of 20 Hz. Conclusively, in comparison to butyl rubber slab mat, neoprene slab mat with a lower stiffness is greater in terms of efficiency. Furthermore, to effectively minimize the levels of vibration, lower stiffness mat is much preferable for it to cut down stresses acting on track and also force transmission from harmonic load.

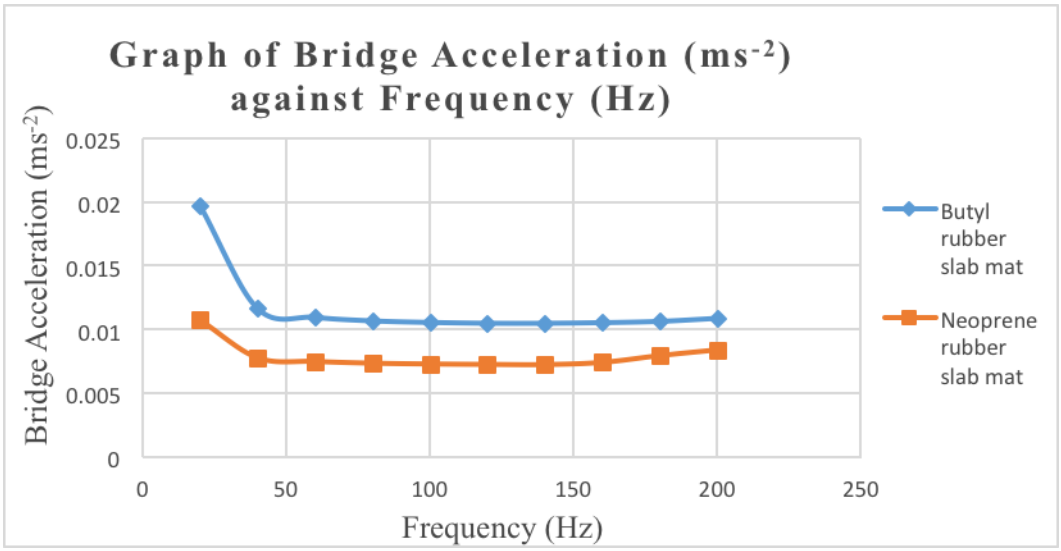


Figure 8: Bridge acceleration against frequency graph for slab track using two different types of material and stiffness for the slab mat layer.

3.3 Impact of Slab Mat Damping Ratio

The damping ratio of material utilized for slab mat is another important factor for minimizing vibration originated from train track. Mechanical energy is able to be converted to heat through damping. Thus, overall mechanical energy will reduce as it goes through material damping. Constant damping ratio was increased from 1 % up to 10 %.

Performance of butyl and neoprene slab mat were analyzed with greater damping ratio value and results were shown in Figure 9. It can be seen that as damping ratio for both butyl and neoprene increases, the acceleration of bridge reduces. The fall in the response for train vibration was not notable, probably because of the non-significant increase in damping ratio. Hence, to allow efficient absorption of vibration by slab mat and elimination of vibrational energy on the bridge, damping ratio has to be increased to a greater amount.

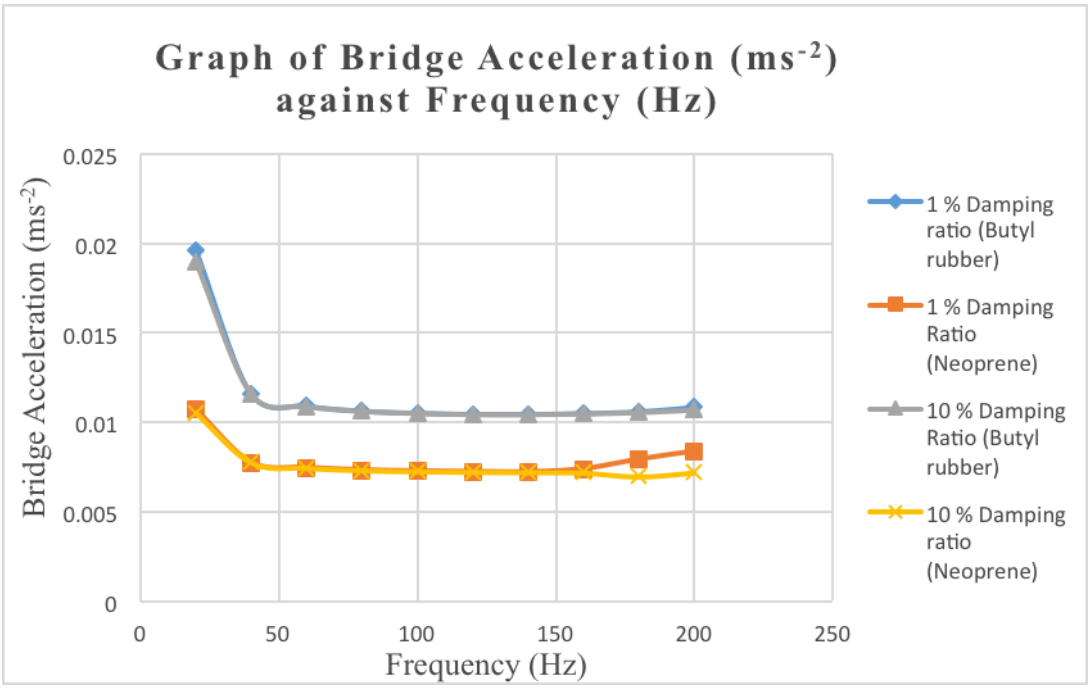


Figure 9: Bridge acceleration against frequency graph for slab track using two different types of material and damping ratio for the slab mat layer.

3.4 Impact of Slab Mat Thickness

The changes caused by minimizing vibration were able to be seen by manipulating the slab mat thickness from 25 mm to 35 mm, in which 30 mm was the starting thickness value of slab mat. An observation of performance reduction for butyl rubber and neoprene slab mat can be seen when bridge acceleration increases, this was due to the 5 mm decrement for thickness. Besides, when bridge acceleration decreases, butyl rubber and neoprene slab mat efficiency was enhanced, this was due to the increment of 5 mm on thickness of slab mat. Nevertheless, provided with similar thickness, neoprene slab mat has better vibration isolation characteristic when compared to butyl rubber mat. Based on Figure 10, vertical vibration transmitted from railway track was able to be minimized when slab mat thickness was increased. Hence, a slab mat with greater thickness is able to take in greater impact, dampen the vibration and also reduces the constant repetition vibration's impact which will ultimately cause damage to bridge structure.

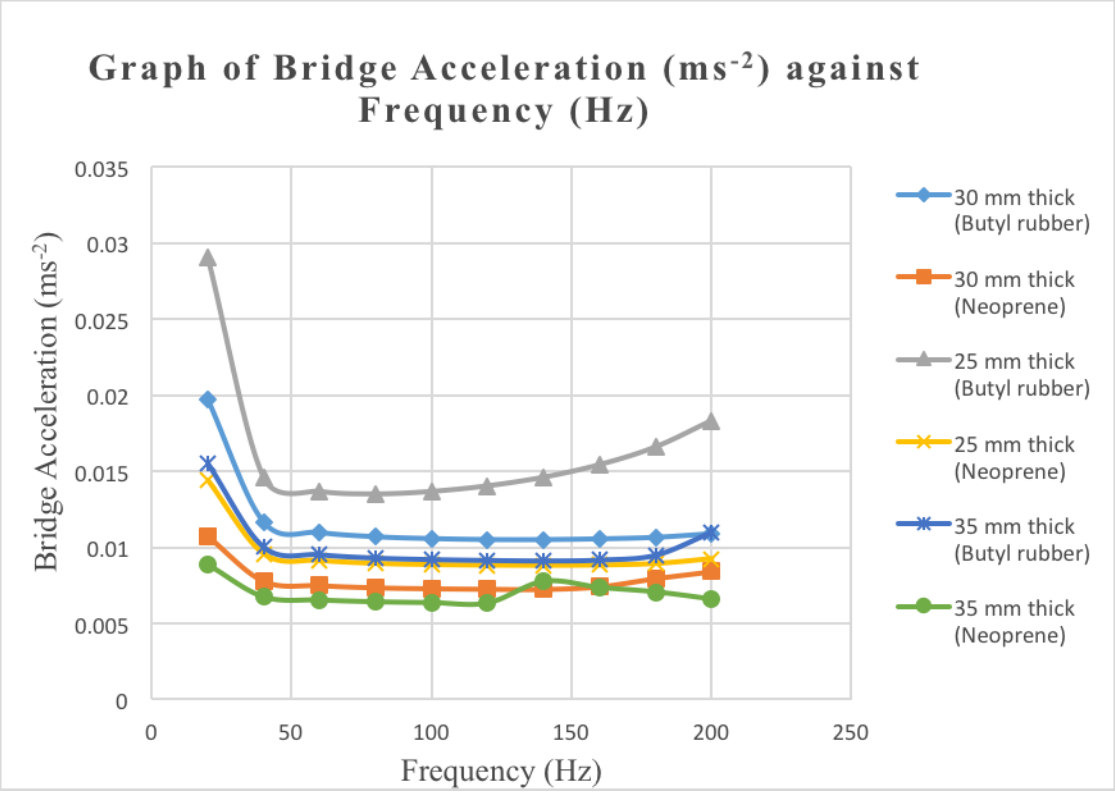


Figure 10: Bridge acceleration against frequency graph for slab track using two different types of material with varying thickness of slab mat layer.

4. Conclusion

In conclusion, the design of anti-vibration slab mat was produced in SolidWorks and simulated in ANSYS Workbench. Different modal parameters of slab mat such as material, stiffness, damping ratio and thickness were analyzed to demonstrate the effect of vibration reduction on the track-bridge model. Two types of analysis which were modal and harmonic response were required for the numerical simulation. To ensure higher efficiency of simulation and more accurate results, proper meshing was done using MultiZone method with body sizing due to its high element quality and low skewness values. Results were then obtained from the frequency response graphs of acceleration in harmonic analysis after completing modal analysis. From the results, the bridge acceleration was decreased when slab mat layer was applied in the track-bridge model due to its ability to absorb impact of harmonic load exerted along the train track.

In numerical simulation, the acceleration of bridge of the track-bridge model was analyzed with changing parameters of anti-vibration slab mat. Results showed that neoprene rubber with lower stiffness performs better than butyl rubber for the same damping ratio and thickness. Furthermore, when damping ratio and thickness of slab mat using neoprene rubber were increased from 1 % to 10 % and 30 mm to 35 mm respectively, the bridge acceleration decreases which shows a positive result in vibration reducing effect. Hence, optimization on the physical property of slab mat

using neoprene rubber should be carried out for further analysis. The results acquired will be analyzed using vibration nomograph to identify the acceptable vibration levels for human comfort.

References

[1] G. Montella, G. Mastroianni and G. Serino, "Experimental and numerical investigations on innovative floating-slab track including recycled rubber elements," *Proceedings of ISMA2012-USD2012*, Naples, Italy, 2012, pp. 2869-2880.

[2] R. Hildebrand, "Countermeasures against Railway Ground and Track Vibrations," Ph.D. dissertation, Department of Vehicle Engineering, Royal Institute of Technology, Stockholm, Sweden, 2001.

[3] M. Rantatalo and X. Tao, "Review of countermeasures and regulations for railway induced ground vibrations in tunnels," Lulea University of Technology and Lulea Railway Research Center JVTC, Rep., Feb. 2013.

[4] B. Hemsworth, "Reducing ground borne vibrations: state-of-the-art study," *Journal of Sound and Vibration*, vol. 231, no. 3, Academic Press (2000), pp. 703-709.

[5] G. De Roeck, G. Degrande, G. Lombaert and G. Muller, "The dynamic force transfer of slab tracks and floating slab tracks and the corresponding ground vibration," *Proceedings of the 8th International Conference on Structural Dynamics*, Leuven, Belgium, July 2011, pp. 820-827.

[6] C. Esveld, "Modern railway track," MRT-Productions, Netherlands, 2001.

[7] G.P. Wilson, "Rail system noise and vibration control," *Proceedings of ACOUSTICS 2004*, Gold Coast, Australia, November 3-5, 2004, pp. 1-9.

[8] M. Sol-Sanchez, F. Moreno-Navarro and M.C. Rubio-Gamez, "The use of elastic elements in railway tracks: A state of the art review," *Construction and Building Materials*, vol. 75, pp. 293-305, 2015.

[9] T. Xin and L. Gao, "Reducing slab track vibration into bridge using elastic materials in high speed railway," *Journal of Sound and Vibration*, vol. 330, pp. 2237-2248, 2011.

[10] Cambridge University Engineering Department, (2003). *Materials Data Book*.

eureca 2016 – Conference Paper
Paper Number 2ME06

Design and Analysis of Lunar Lander Bus Structure

Chew Hong Jun[1], Azadeh Ghadimi[1*], Izmir Yamin[2]
[1]*School of Engineering, Taylor's University, Malaysia*
[1]*Independence-X Aerospace Sdn. Bhd., Malaysia*

*Azadeh.Ghadimi@taylors.edu.my

Abstract
This project is a part of the Lunar Lander System offered by Independence-X Aerospace SDN. BHD. Official Team and a Finalist of the Google Lunar X-Prize, an international space race organized by Google since 2007. A structural system for an operational lunar lander is to be obtained to land on a specified site on the moon. The mission of the lander is to perform a soft landing on the Near Side of the moon surface and propel itself before landing for a second time at a specific distance. Besides, the lander itself will also be able to communicate with planet Earth. This project aims to design and optimize the bus structure support to keep the internal and external objects safe during the course of the mission. The model sketches are designed with SolidWorks 2014 and optimized by using ANSYS Workbench 15. Deformation, normal stress and shear stress of T-bars and square bars are compared to determine the better bar to be applied into the base plate support. Mass of the support is also optimized to ensure that the whole model is within a mass limit of 150kg. A hexagonal tripod concept bus structure containing a base plate is designed. The base plate is designed to be 6.35 mm thick and being supported with 38.1 mm width T-bars. Analysis is done to ensure that the supports and base plate will not fail due to bending and propulsion force. The analysis is expected to contribute in the development of the end product and perform accordingly, bringing the mission towards success.

Keywords: Lunar Lander, Bus Structure, Simulation, Design, SolidWorks

1. Introduction

Looking back at the evolution of means of transportation, man used to move from one place to another by foot. Soon after the innovation of wheels, different modes of land transportation start to emerge. Eventually, mankind begin to embrace their adventurous inner self and started sailing through water and flying in the sky [1]. Not long after where curiosity and advancement of technology brings human towards space exploration. Lunar exploration on the other hand has changed rather drastically since the beginning, from a mere observation or scouting mission to manned mission. The space attempts are summarized and shown in Table 1.

Table 1: Summarized Space Mission Attempts [2]

Timeline	Mission	Attempts
2 Jan 1959	Luna 1	Flyby
12 Sept 1959	Luna 2	Impact
4 Oct 1959	Luna 3	Probe
31 Jan 1966	Luna 9	Lander
31 Mar 1966	Luna 10	Orbiter
21 Dec 1968	Apollo 9	Crewed Orbiter
19 Jul 1969	Apollo 11	Crewed Landing
12 Sept 1970	Luna 16	Sample Return
10 Nov 1970	Luna 17	Rover

According to Table 1, lunar exploration first started since 1959 and is still ongoing till date. However, there are no new means of lunar explorations by far till date ever since the first rover mission on 1970. Since 2007, Google has organized an international space race, the Google Lunar X-Prize to incentivize space entrepreneurs to create a new era which is able to access to the moon and beyond [3]. This project is the part of Lunar Lander System offered by Independence-X Aerospace SDN. BHD. official team and a finalist of the Google Lunar X-Prize. A structural system for an operational lunar lander is to be obtained to perform soft landing on the Near Side of the moon surface. The lander will then propel itself again before landing for the second time 500 meters away. A bounty of $30 million will be rewarded to the successful teams from around the world who are able to land a privately funded rover onto the moon, travel 500 meters and transmit high definition video and images back to Earth. Sixteen teams from around the world are currently competing for the race, including team Independence-X from Malaysia.

The lunar lander comprises of three main components, the propulsion, landing mechanism and bus structure. The main components are separated into three main projects where this project is one of them. These three projects are running in parallel, providing simultaneous information for one another. The fuel and oxidizer used for the propulsion are Mono Methyl Hydrazine and Di-Nitrogen Tetroxide respectively. This combination of propellant is commonly used as the combination is extremely reactive and are hypergolic with each other [4].

The landing mechanism is tasked to absorb the landing impact of the lander, allowing it to perform soft landing on the lunar surface. As for the bus structure, it is responsible to provide attachment points for the landing mechanism, propellant tanks

and communication devices. The whole structure has to be sturdy to withstand forces applied due to propulsion as well as the landing impact. Most parts of the bus will be manufactured with aluminum alloy 6061-T6 due to the physical characteristics in which is commonly used in aircraft applications [5]. The ultimate tensile strength of 310 MPa is considerably strong relative to the low density for lower mass consideration applications.

Table 2: Property Table for Aluminum 6061-T6 [5],[6]

Physical Properties	**Metric Units**	**English Units**	**Comments**
Density	2.7 g/cm	0.0975 lb/in	AA: Typical
Mechanical Properties	**Metric Units**	**English Units**	**Comments**
Hardness, Brinell	95	95	AA; Typical; 500g load; 10 mm ball
Hardness, Knoop	120	120	Converted from Brinell Hardness Value
Hardness, Rockwell A	40	40	Converted from Brinell Hardness Value
Hardness, Rockwell B	60	60	Converted from Brinell Hardness Value
Hardness, Vickers	107	107	Converted from Brinell Hardness Value
Ultimate Tensile Strength	310 MPa	45000 psi	AA: Typical
Tensile Yield Strength	276 MPa	40000 psi	AA: Typical
Elongation at Break	12 %	12 %	AA: Typical; 1/16 in. (1.6 mm) Thickness
Elongation at Break	17 %	17 %	AA: Typical; 1/16 in. (12.7 mm) Thickness
Modulus of Elasticity	68.9 GPa	10000 ksi	AA: Typical; Average of tension and compression Compression modulus is about 2% greater than tensile modulus
Notched Tensile Strength	324 MPa	47000 psi	2.5 cm width x 0.16 cm thick side-notched specimen, K_t = 17
Ultimate Bearing Strength	607 MPa	88000 psi	Edge distance/pin diameter = 2.0
Bearing Yeild Strength	386 MPa	56000 psi	Edge distance/pin diameter = 2.0
Poisson's Ratio	0.33	0.33	Estimated from trends in similar Al alloys
Fatigue Strength	96.5 MPa	14000 psi	AA; 500,000,000 cycles completely reversed stress; RR Moore machine/specimen
Fracture Toughness	29 MPa-$m^{1/2}$	26.4 ksi-$in^{1/2}$	K_{IC}; TL orientation
Machinability	50 %	50 %	0-100 Scale of Aluminum Alloys
Shear Modulus	26 GPa	3770 ksi	Estimated from similar Al alloys
Shear Strength	207 MPa	30000 psi	AA; Typical
Electrical Properties	**Metric Units**	**English Units**	**Comments**
Electrical Resistivity	3.99e-006 ohm-cm	3.99e-006 ohm-cm	AA; Typical at 68ºF
Thermal Properties	**Metric Units**	**English Units**	**Comments**
CTE, linear 68ºF	23.6 µm/m-ºC	13.1 µin/in-ºF	AA; Typical; Average over 68-212 ºF range
CTE, linear 250ºF	25.2 µm/m-ºC	14 µin/in-ºF	Estimated from trends in similar Al alloys. 20-300 ºC
Specific Heat Capacity	0.896 J/g-ºC	0.214 BTU/lb-ºF	
Thermal Conductivity	167 W/m-K	116 BTU-in/hr-ft^2-ºF	AA; Typical at 77 ºF
Melting Point	582 – 652 ºC	1080 – 1205 ºF	AA; Typical range based on typical composition for wrought products ¼ inch thickness or greater; Eutetectic melting can be completely eliminated by homogenization
Solidus	582 ºC	1080 ºF	AA; Typical
Liquidus	652 ºC	1205 ºF	AA; Typical

Designs of each lunar exploration bus differ from mission to mission, catering to the mission objectives and limitations. There are certain differences and similarities in the designs of the past lunar modules. A collection of past designs of lunar modules for past missions has been done and being summarized in Table 3.

Table 3: Summary of Past Design Missions

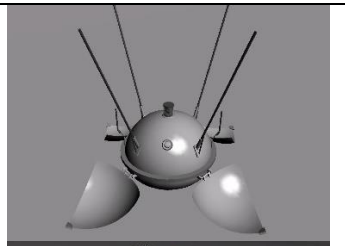
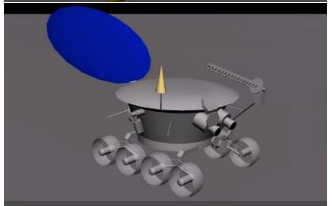
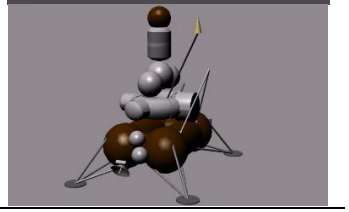
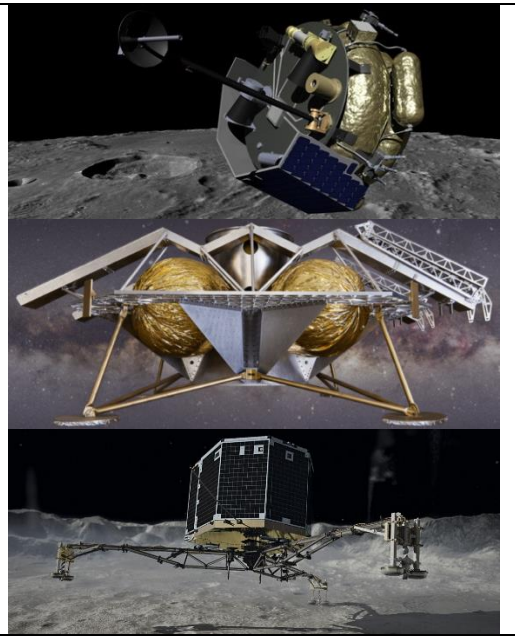
	Type of Lunar Module	Type of Lunar Mission	Day of Launch	Special Characteristic	Sample Image
Luna 9 [7],[8]	Lunar Lander	Surveillance	31 Jan 1966	Spherical with expanding petals and antenna	
Apollo 11 [9]	Lunar Lander	Crewed landing	19 Jul 1969	Comprises of two body, ascend and descend stages	
Lunakhod 1 [10]	Lunar Rover	Surveillance	19 Nov 1970	Provide tracks for rover to descent to lunar surface	
Luna 16 [11]	Lunar Lander	Sample Return	12 Sept 1970	Comprises of two body, ascend and descend stages	

Table 3 shows a summary of the past designs where each missions are unique from one another depending on the mission that is being carried out. Luna 9 and 13 were spherical, with expanding petals and antenna protruding while Apollo 11 module comprised of 2 body, ascent and descent stages for landing and return respectively. Besides, Lunakhod 1 & 2 models had tracks for rover to descent to the lunar surface. Nevertheless, some past designs were bigger than the other because it was a crewed mission where human comfort has to be taken into account.

Among the sixteen teams competing in the Google Lunar X-Prize, there are three teams that has already achieved the Landing Milestone, namely Moon Express, Astrobotic and Team Indus [3]. The teams are team Moon Express, team Astrobotic and team Indus. Similar to the past lunar module designs, the X-Prize competitor designs are being summarized in Table 4.

Table 4: Summary of X-Prize competitors

	Country of Origin	Type of Lunar Module	Achieved Milestones	Special Characteristics	Design Downside	Sample Image
MX-1, Moon Express [12]	United States	Lunar Lander	Landing, Imaging	Collapsible empty fuel tanks to act as impact cushion	Collapsed fuel tank only allow landing once	
Griffin, Astrobotic [13]	United States	Lunar Lander	Landing, Imaging, Mobility	Flexible mounting structure for variable mounting purposes	Overall big and heavy structure	
Philae, Indus [14]	India	Lunar Lander	Landing	Tripod design and small in size	Limited cargo capacity	

According to Table 4, the designs are extraordinary as compared to the past mission designs. Most designs are innovative and feasible for actual application.

Moon Express does not limit the design with the usual legged landing while innovatively utilizes their empty fuel tanks as cushion for landing. However, the collapsible landing concept could not be adopted into this project due to the mobility milestone reward. The industry requirement states to allow the lander to land once onto the lunar surface and then propel upwards to land the lander for the second time 500 meters apart. If the landing mechanism has collapsed during the first attempt, it will not be able to attempt for the second time.

As for the griffin lander, its flexible mounting structure enables it to mount a variety of appliances and mechanisms onto the lander. However, the mass of the structure has to be greatly reduced in order to comply with the mass limitation provided by team Independence-X. Despite that, the mounting concept could be adopted and modified to fit the requirement of this project.

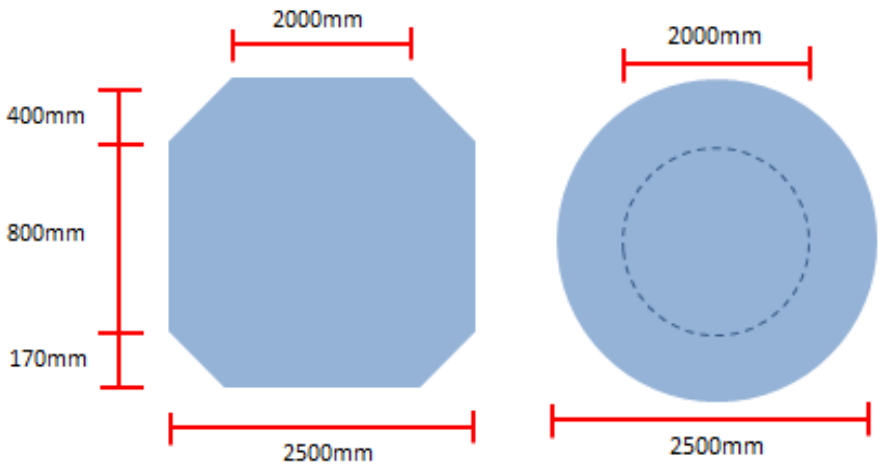
Philae on the other hand, adopting the same tripod design which this project is moving towards. These traits could be absorbed and modified into the current project in the bus structure design. The small body of the lander limits the load that could be carried along. Due to that reason, Philae could only achieve the Landing milestone.

The research gap of this project is to design a feasible bus structure specifically catered to the requirements of the space mission where it differs from the past lunar module and X-Prize competitor designs.

2. Research Methodology

2.1 Design of Lunar Lander Bus Structure

The generic concept of the lunar lander is set to be a tripod by the industrial partner and hence the basis of the design in this research. A general size limitation is provided by the industry due to the limitation of the allowed space in the supposed spacecraft that is going to launch the lander out of space. The space allocated is sketched and shown in Figure 1.



(a) (b)

Figure 1: Sketched space allocated (a) side view (b) top view

A series of designs are drafted to initiate the design phase. Basic shapes are being modified and refined progressively.

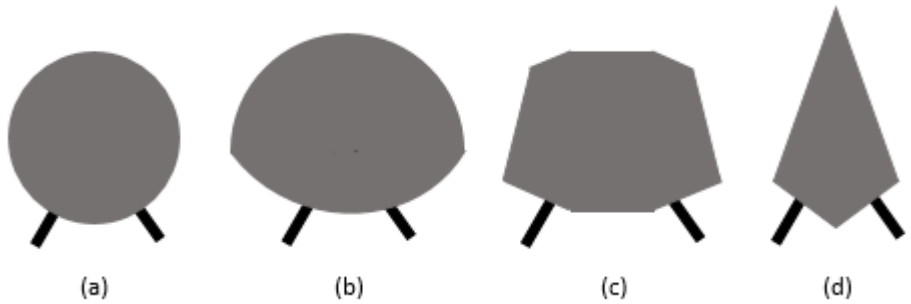
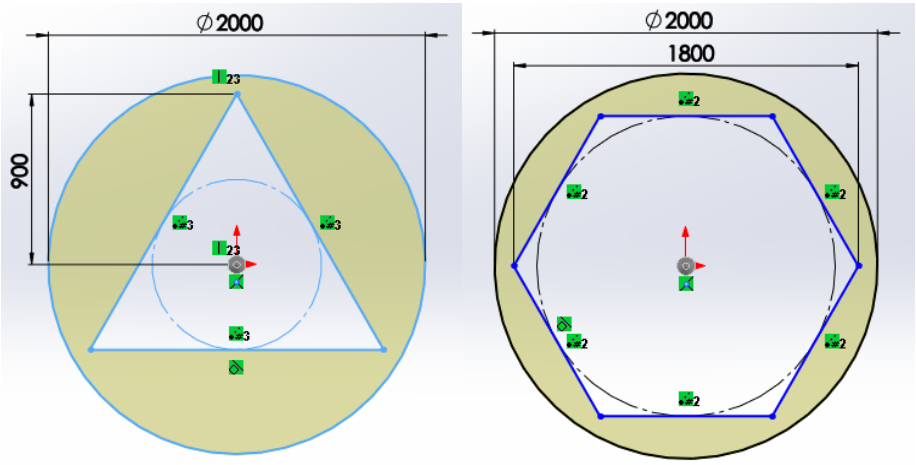


Figure 2: Sketched Design Variation (a) sphere (b) hemisphere (c) hexagonal (d) pyramid

Figure 2 shows the variation of the proposed sketched designs. The design starts with a basic round shape as shown in Figure 2(a), following the designs of Luna 9 and 13 which are spherical. Then, Figure 2(b) shows the circle is simplified into a hemisphere, being symmetrical at all sides as well as reducing the center of gravity and thus stabilizing the design due to the wider bottom area. The design is further simplified to flat surfaced hemisphere and then a pyramid shown in Figure 2(c) and 2(d). Manufacturability is put into consideration when sketching. Hence, flat surface is easier to be manufactured as compared to a curved surface as most metal comes in flat sheets.

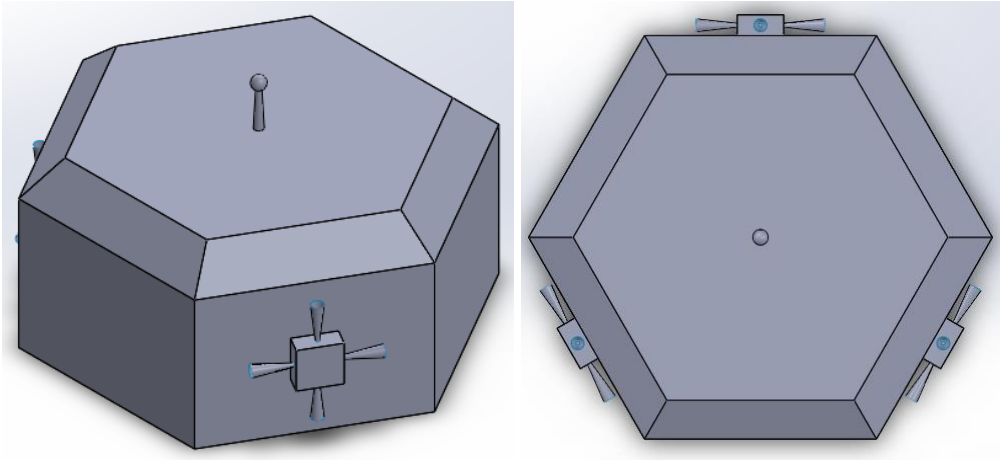


(a) (b)

Figure 3: Bus shape design comparison (a) triangle (b) hexagon

Since the lander will follow the tripod concept, there will be three legs supporting the structure during lading. Therefore, the basic shape for the lander is going to have a polygon with sides of multiple of three. The suggested shape is to be a triangle or hexagon with three and six sides respectively. As shown in Figure 3, a 2000 mm diameter circle is sketched and followed by a triangle or hexagon. The circle symbolizes the width limitation while the polygon symbolizes the outer geometry of the lander. The shaded region between the circle and the polygons are the unutilized area within the size limitation. In comparison, the triangle does not utilize as much of the area as compared to the hexagon. In fact, a circle instead of a polygon could be generated as the outer geometry in order to fully utilize the space. However,

manufacturability is brought into consideration and circular geometry is more complex to manufacture as compared to other polygons since most materials comes in flat sheets. Therefore, a hexagonal outer geometry is selected based on the above considerations.



(a) (b)

Figure 4: SolidWorks design (a) isometric view (b) top view

According to Figure 4, the design is given a height of 800 mm and being chamfered at the top edge. The chamfered face allows attachment of solar panels onto the lander, providing electrical supply to the lander. Four mini thrusters are attached perpendicular to one another at 3 faces of the sides to allow directional changes during flight. The three remaining sides will provide space for legs attachment. An antenna will be allowed to extend from the top surface, sending and receiving communication signals from Earth.

A base plate is installed in the housing which acts as the main support structure in the bus as shown in Figure 5. There are two 522 mm diameter and two 461 mm diameter holes available on the plate. It allows attachment of the propellant tanks, 461 mm diameter holes for oxidizer tanks and 522 mm diameter holes for fuel tanks. The dimensions of the propellant tanks are obtained from [15].

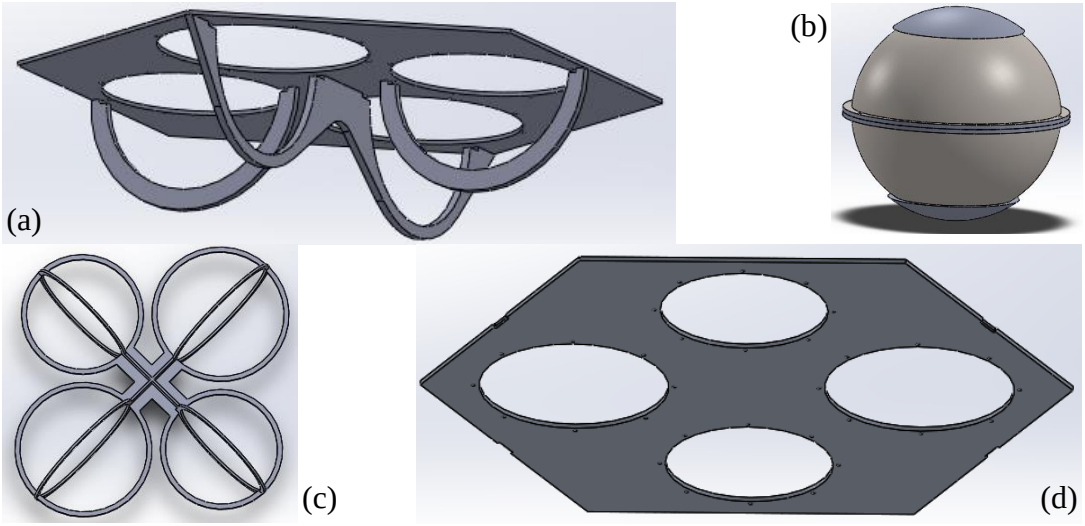
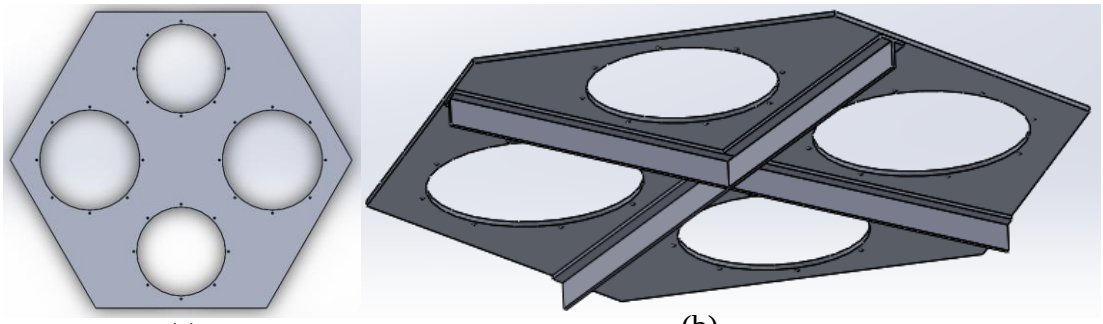


Figure 5: Base plate (a) tray (b) cup (c) hoop (d) plate

Figure 5(a) shows a plate with supports beneath the propellant tanks to hold the tank while Figure 5(b) shows two cups cupping the tanks together, one at the top, one at the bottom. Figure 5(c) shows hoops surrounding the propellant tanks, both vertically and horizontally while Figure 5(d) shows a basic plate holes. The comparison of the designs are shown in Table 5.

Table 5: Base plate design comparison

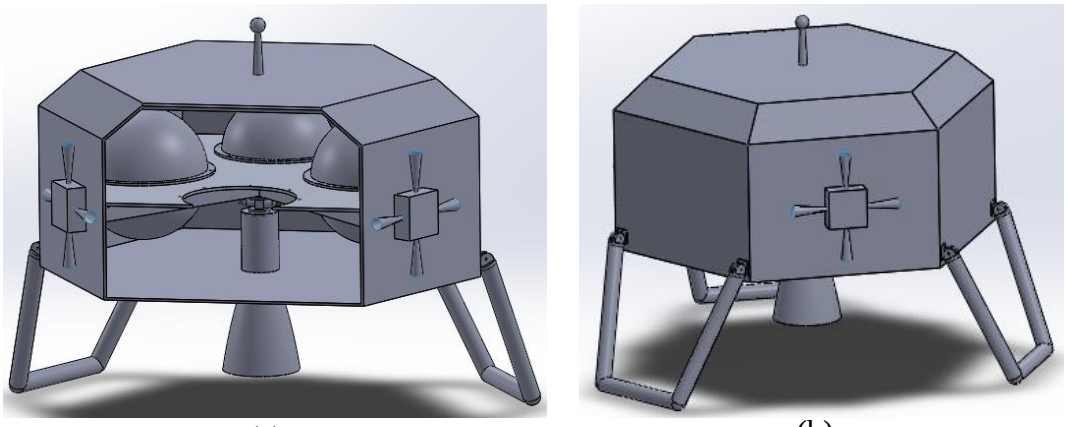
	Tray	Cup	Hoop	Plate
Advantages	Bottom supports absorb the weight of the propellant tanks	Reduce space occupancy and mass	Surrounding propellant from two directions, securing them in place	Simple and feasible. Provide room for more parts attachment if necessary.
Disadvantages	Heavier due to a larger volume	Require additional connection at the bottom and top to hold the cup	Hoop has to be thick or made of stronger material to avoid breaking	Require further support to prevent bending
Space Occupied	Most	Least	Average	Average



(a) (b)

Figure 6: Base plate (a) bottom view (b) angled view

As shown in Figure 6, plate design is selected due to the feasibility and practicality as compared to the other designs. In order to secure the propellant tanks onto the base plate, 10 mm holes are provided around the circular. Extra structural support is provided by securing T-bars beneath the hexagonal plate. L supports are bolted to the plate at the sides to allow the plate to be mounted onto the walls. Two sides of the L support will be brazed onto the wall.



(a) (b)

Figure 7: Bus structure assembly (a) sectioned view (b) isometric view

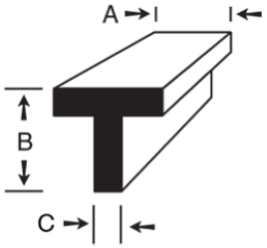
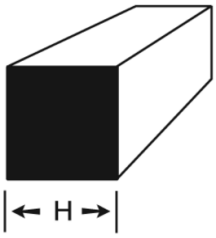
Figure 7 shows the sectioned view of the bus structure assembly. The hexagonal base plate is secured into the housing along with the propellant tanks attached. A propulsion engine is also mounted onto the bottom of the base while three landing legs are mounted to the sides of the housing. The dimensions of the propellant tank as well as the landing legs are obtained from [15] and [16] respectively.

2.2 Finite Element Analysis of Supports

2.2.1 Plate Support Selection

The hexagonal plate itself is not sufficient to support the mass of the propellant as well as the tanks. Hence, the support structures are attached onto the plate to increase the structural stability. T-bars and square bars are analyzed and compared to determine the differences in the bars in terms of structural support. Two bars with similar width are chosen and being attached onto the base plate of 19.05mm. The dimensions of the plate and bars are obtained online based on the dimensions that are being industrially manufactured and distributed. The dimensions are listed in inches which are being converted into millimeters. The dimensions of the two bars are shown in Table 6.

Table 6: Dimensions for T-bar [17] and square bar [18]

Aluminum 6061-T6	T-bar	Square bar
Guide		
Dimension (Inch)	3 x 3 x 0.375	3 x 3
Dimension (mm)	76.2 x 76.2 x 9.525	76.2 x 76.2

The bars are being modeled in SolidWorks 2014 and then being imported into ANSYS Workbench 15 Static Structural Analysis as shown in Figure 8. The boundary conditions applied onto the model are shown in Figure 8 and listed as follow:

- Fixed support on outer faces of the model
- Standard Earth Gravity at the center in –Y direction
- Point masses representing the propellant tanks and the respective propellant (Assuming the propellant tanks are fully filled with propellant)
- Force of 400 N at the center in +Y direction (Assuming the maximum thrust created by the propulsion engine is 400 N)

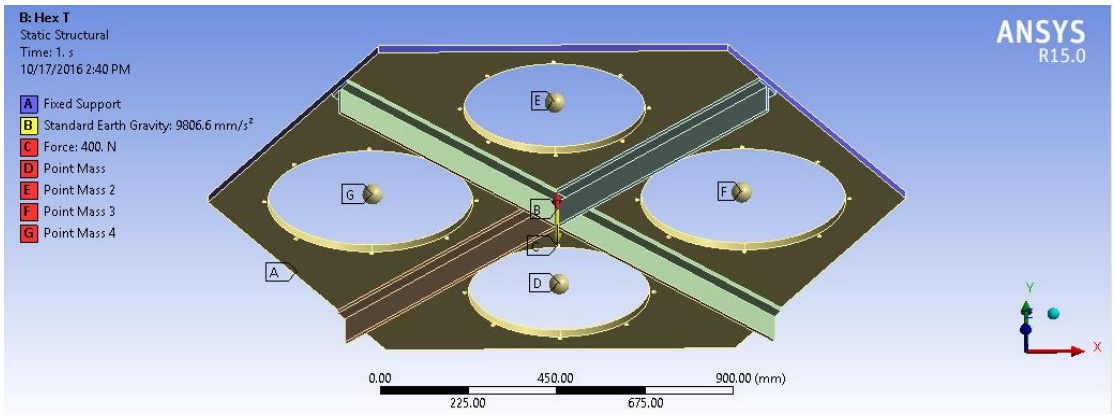


Figure 8: Boundary conditions applied

A general meshing is applied onto the model before refining. The whole model is then refined by modifying the element size to 10 mm, which is close to the thickness of the T-bar. The element size is reduced to 10 mm because a smaller mesh sizing could generate more elements and thus, a higher accuracy in the solution. The good quality of the mesh is determined by checking the skewness. The closer the skewness to zero, the better the quality of the meshing. A summary of the mesh is presented in Table 7 while the meshed models are shown in Figure 9.

Table 7: Meshing properties for support models

	T-bar	Square bar
Mesh Element	36097	51152
Skewness (Average)	0.13711	0.13976
Mesh type	Body Sizing	
Mesh size	10 mm	

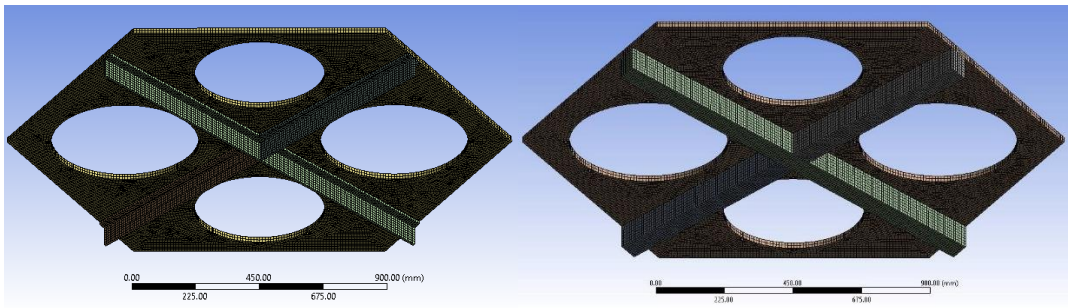


Figure 9: Meshing profile for both models

Contact conditions, “Bonded - solid to solid” is applied to the model where the different parts are in contact with each other. Material properties of aluminum 6061-T6 is inserted and applied to all of the parts in the model.

2.2.2 Mass Optimization

After the plate support selection process, the selected type of bar was used for mass optimization. Different combination of plates as well as bar thickness are analyzed and the total mass of the model was recorded. The boundary conditions used for this section was the same as section 2.2.1. However, the sizing of the elements varied according to the thickness of the bar and plate. The Total Deformation of the plate and bar was compared with the total mass of the model in order to identify the combination which contributes to the least mass while being structurally stable.

3.0 Results and Discussion

3.1 Plate Support Analysis

The meshed models are allowed to be calculated using ANSYS Workbench 15 with all the boundary conditions applied. The results to be obtained were total deformation, shear stress and normal stress. The mass of the bars are obtained by assigning the bars with the associated material and using the Mass Property function in SolidWorks 2014. The results are summarized and tabulated in Table 8.

Table 8: Plate support result

	Total Deformation (mm)	Maximum Shear Stress (MPa)	Maximum Normal Stress (MPa)	Bar Mass (g)
T-bar	0.053727	1.7967	1.4305	9848.27
Square bar	0.014778	0.3925	0.75667	18287.61

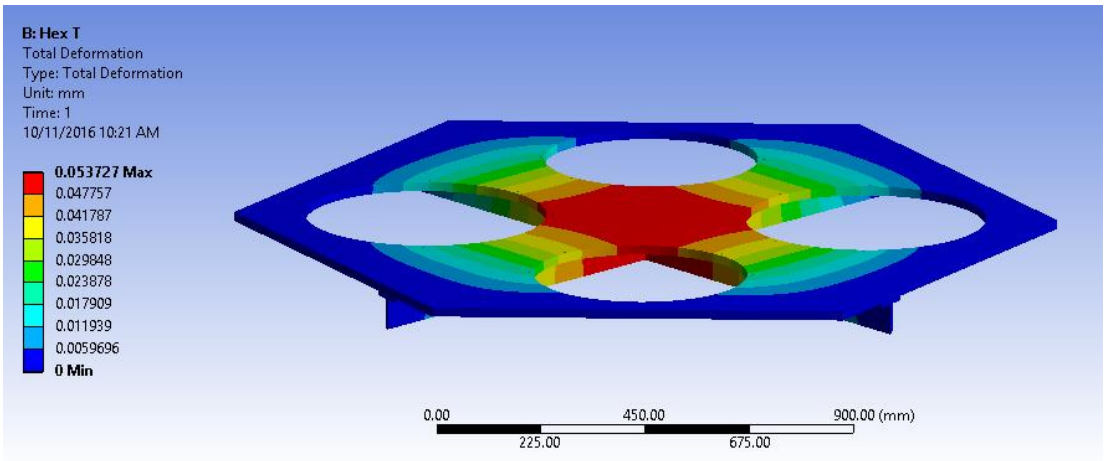


Figure 10: Total deformation (T-bar)

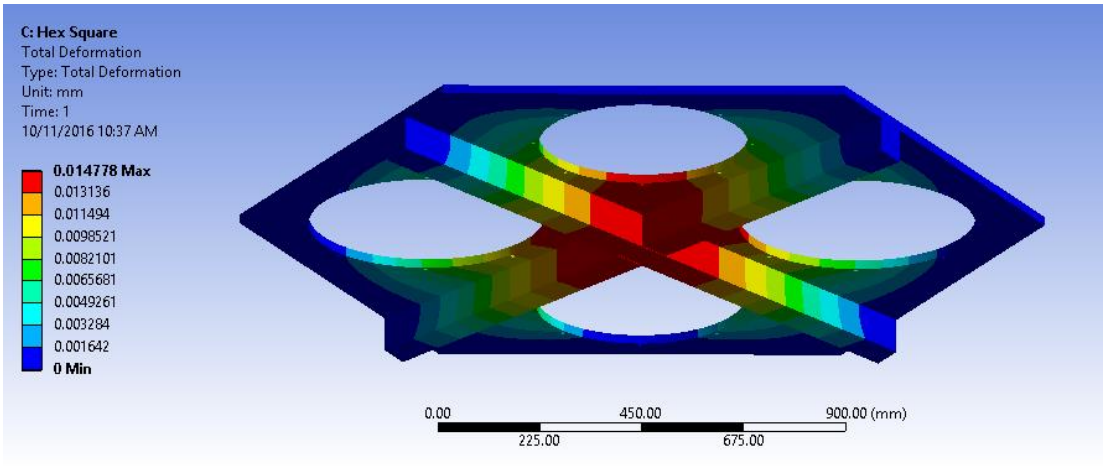


Figure 11: Total deformation (square bar)

As shown in Figure 10 and Figure 11, the total deformation of the two bars are concentrated at the center where the force is applied. The deformation of interest is only along the Y axis. This is because the forces are only applied along the Y axis. However, the deformation of the models are minimal, 0.054 mm for the T-bar and 0.015 mm for the square bar. This shows that the deformation are not significant and the structure is stable enough to withstand the mass of the propellant, propellant tanks as well as the maximum impulse from the propulsion engine.

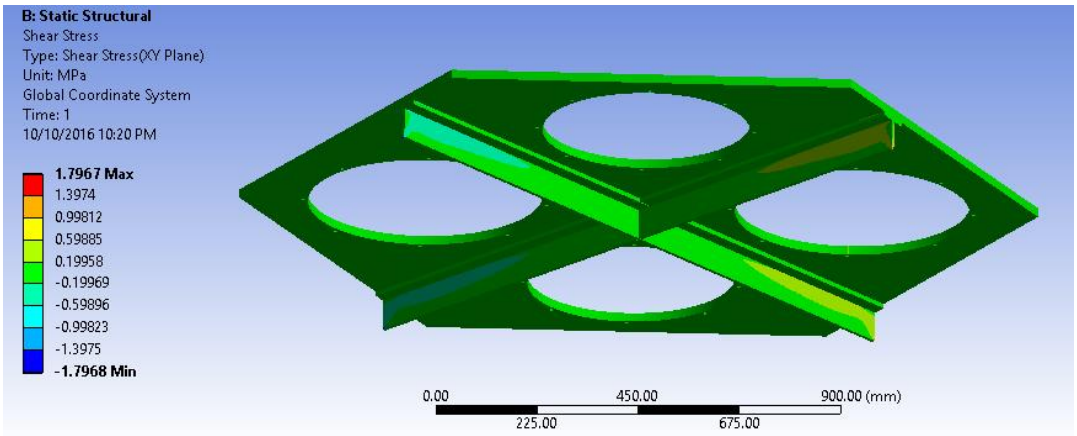


Figure 12: Shear stress (T-bar)

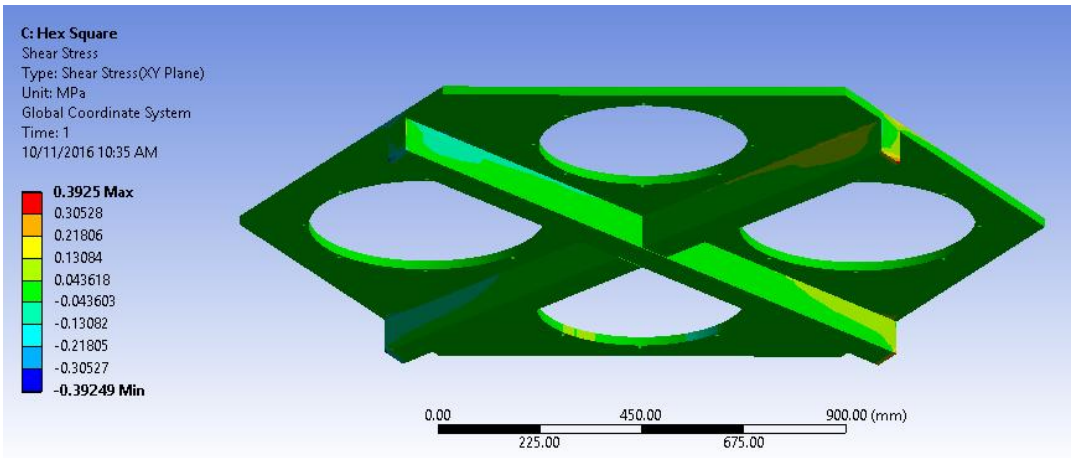


Figure 13: Shear stress (square bar)

Figure 12 and Figure 13 shows the shear stress of the two bars given the boundary conditions. Maximum shear stress only occurred at the very tip of the bars. However, when compared to the shear strength of the material obtained from Table 2 of 207 MPa, both shear strength shown in Figure 12 and 13 are relatively small. Hence, it could be concluded that both models will not fail due to shear.

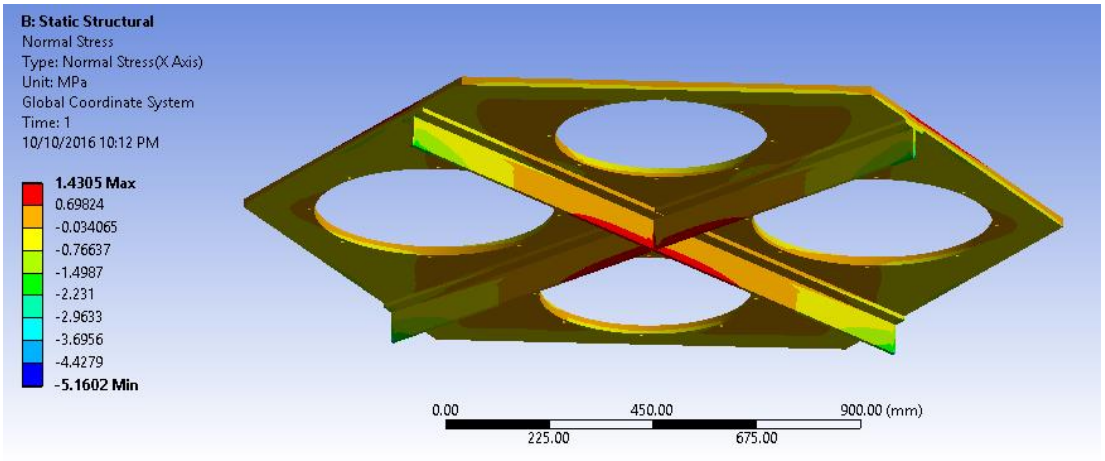


Figure 14: Normal stress (T-bar)

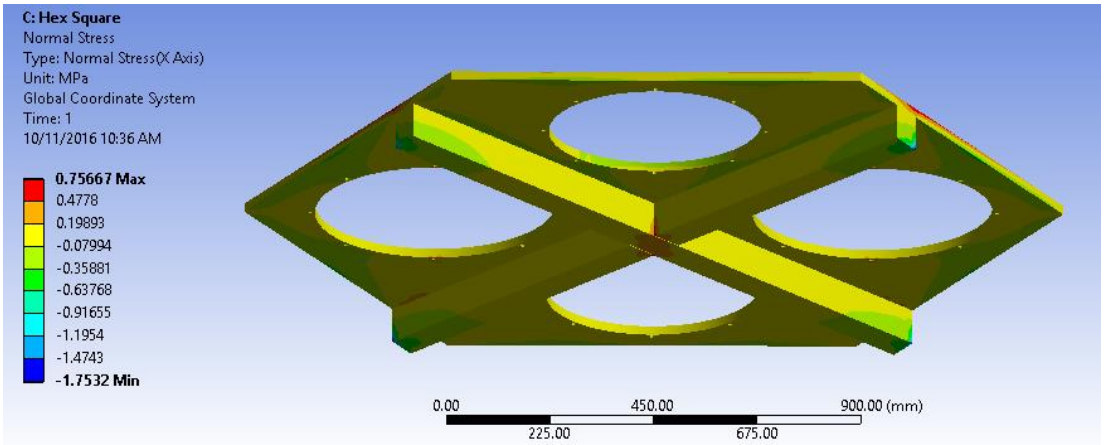


Figure 15: Normal stress (square bar)

Meanwhile, the normal stress acting onto the models were also analyzed as shown in Figure 14 and Figure 15. The maximum stress accumulates at the center as well as the edge of the models. However, similar to the shear stress, the stress applied onto both models were relatively small as compared to the tensile yield strength of the material of 276 MPa. Therefore, the models will not fail due to normal stress.

Based on the results obtained, both models are able to provide sufficient structural support without failing. However, the mass of the square bar is twice as high as the mass of the T-bar, given the similar length. Therefore, the T-bar is selected as the plate support since model mass is taken into consideration.

3.2 Mass Optimization

The list of different thickness and dimensions of the commercially manufactured and distributed aluminum 6061-T6 plates as well as T-bars are obtained and summarized in Table 9 and Table 10. The measurements are listed in inches

which are converted into millimeters by the author. The mass of the geometries are obtained using the Mass Property function in SolidWorks 2014.

Table 9: List of plate dimensions [19]

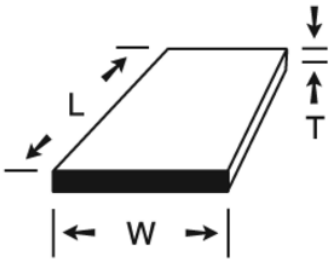
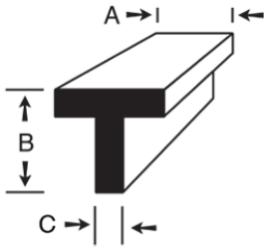
Plate **Guide:** 		
Thickness		Mass
inch	mm	kg
0.250	6.350	22.031
0.313	7.938	27.541
0.375	9.525	33.047
0.500	12.700	44.062
0.625	15.875	55.078
0.750	19.050	66.093
0.875	22.225	77.109
1.000	25.400	88.124
1.125	28.575	99.140
1.250	31.750	110.155
1.500	38.100	132.186

Table 10: List of T-bar dimensions [17]

T-Bar **Guide:** 			
Thickness (inch)			Mass
A	B	C	(kg)
1.500	1.500	0.250	3.846
2.000	2.000	0.250	5.220
3.000	3.000	0.375	9.848
4.000	4.000	0.375	13.242
Thickness (mm)			
38.100	38.100	6.350	
50.800	50.800	6.350	
76.200	76.200	9.525	
101.600	101.600	9.525	

Combination of different plate thicknesses as well as bar widths are made, modelled using SolidWorks 2014 and then imported into ANSYS Workbench 15 to determine the total deformation of the combinations. Table 11 shows the summary of the obtained results.

Table 11: Summary of combination results

Plate (T, mm)	T-bar (A, mm)	Max Deformation (mm)	Mass (kg)
6.35	38.1	0.704	25.877
	50.8	0.371	27.251
	76.2	0.095	31.879
7.938	38.1	0.591	31.387
	50.8	0.330	32.760
	7.62	0.104	37.389
9.525	38.1	0.504	36.893
	50.8	0.295	38.266
	7.62	0.104	42.895
12.7	38.1	0.360	47.908
	50.8	0.233	49.282
	76.2	0.140	53.910
19.05	76.2	0.054	75.941

According to Table 11, the highest maximum deformation results on the model is the combination between a 6.35 mm thick plate and a T-bar with 38.1 mm width of 0.704 mm. Comparing 0.704 mm with 0.054 mm from the model that was being referenced to in section 3.1, the difference in the deformation is relatively large, approximately 13 times the deformation. However, the maximum deformation is still less than 1 mm, which is still considerably low.

Meanwhile, the differences in the masses of the two models are big. The mass of the model is reduced by three times by reducing the thickness of the plate from 19.05 mm to 6.35 mm and the width of T-bar from 76.2 mm to 38.1 mm. Therefore, the combination of 6.35 mm plate and 38.1 mm T-bar is chosen to replace the initial combination since the maximum deformation is still low and two third of the mass could be reduced.

4.0 Conclusion

The base plate could withstand the masses of the propellant tanks and propellants with a total mass of 316 kg. The base plate could also withstand the impulsive force of maximum 400 N exerted from the propulsion engine. The combination of a 6.35 mm base plate and 38.1 mm width T-bar is sufficient to provide the necessary structural support to the model with a total mass of 25.88 kg. The housing of the bus structure was measured to be approximately 54 kg while the three landing legs are 30.9 kg in total. Therefore, the current accumulated dry mass is a total of 117.3 kg which is close to the proposed dry mass budget from the industry which is 150 kg.

Table 9: Mass breakdown

Parts	Mass per part (kg)	Number of parts	Total Mass (kg)
Fuel Tank	2.49	8	19.92
	65.00	2	130.00
Oxidizer Tank	2.20	8	17.60
Oxidizer	74.49	2	148.97
Housing	53.90	1	53.90
Base Plate Support	25.88	1	25.88
Landing Leg	10.30	3	30.90
Total			117.30

References

[1] J. H. Ausubel and C. Marchetti, "The Evolution of Transport," *Ind. Phys.*, vol. 2, pp. 20–24, 2001.
[2] I. A. Crawford and K. H. Joy, "Lunar Exploration: opening a window into the history and evolution of the inner Solar System," 11 Aug. 2014.
[3] A. Hall *et al*., "Google Lunar XPRIZE: New Space Entrepreneurs Go Back to the Moon – For Good," European Planetary Science Congr., UK, London, 8-13 Sept. 2013
[4] NASA, "Space Shuttle Propulsion Systems," Alabama, Huntsville, Pub 8-40381, 2002.
[5] Aalco Metals Ltd., "Aluminum Alloy Specifications," Surrey, Cobham, 2016.
[6] *Properties and selection: Nonferrous alloys and special-purpose materials*, vol. 2., ASM International Handbook Commitee, 1990.
[7] J. G. Davies *et al.*, "Observations of the Russian moon probe Lunar 9", *Nature*, vol. 209, 848-850, Feb. 1966.
[8] A. P. Vinogradov, *et al.*, "Study of the lunar surface by the Soviet Luna 9 and Luna 13 automatic stations", In -- Proc. of UN Conf. of the Expl. and Peaceful Uses of Outer Space, Vienna, Austria, UN, Paper 68-95769, New York, NY, 1969.
[9] P. R. Bell *et al*., "Apollo 11: Preliminary Science Report," 1969.
[10] "Luna-17", Soviet Report, 4, No. 10, Dec. 1970.
[11] "Luna 16 returns with lunar rock samples", Soviet Rept., 4, No. 8, Oct. 1970.
[12] B. Richard, "Moon Express, Pioneering the Lunar Frontier," 7 Mar. 2013.
[13] S. Taranovich, "Astrobotic technology: NASA's doorway to Mars exploration," 27 Jan. 2016.
[14] S. Ulamec and J. Biele, "From the Rosetta Lander Philae to an Asteroid Hopper: lander concepts for small bodies missions," Jan. 2006.
[15] L. Darren, "Design and Simulation of Propellant Tank for Lunar Landing System," M.S. thesis, Taylor's Univ., Malaysia, 2016.
[16] S. Raja, "Design and Analysis of Lunar Landing Structure," M.S. thesis, Taylor's Univ., Malaysia, 2016.
[17] Coast Aluminum and Architectural, "Aluminum Tee," 2016.
[18] Coast Aluminum and Architectural, "Aluminum Square Bar," 2016.
[19] Coast Aluminum and Architectural, "Aluminum Plate," 2016.

eureca 2016 – Conference Paper
Paper Number 2ME07

Investigation of Heat Treatment Effect on the As-Anodized TiO_2 Thin Film

Chia Jin Tong, Chou Pui May*
School of Engineering, Taylor's University, Malaysia
Puimay.chou@taylors.edu.my

Abstract
Titanium dioxide (TiO_2) has been studied intensively for use as a photocatalyst in water purification. The present study investigated the effect of annealing temperature on the photocatalytic activity of TiO_2. The change of crystalline structure of TiO_2 due to different annealing temperatures was investigated using X-ray Diffraction (XRD) analyses. The phase transition changed from amorphous phase to anatase-rutile phase and finally to mostly rutile phase with the increases of annealing temperature. It could be conclude that sample that annealed at 500°C had the best crystalline structure it has the most anatase phase among all the samples. The best crystalline structure lead to the best photocatalytic performance. Photocatalytic activities of the samples were compared for photodegradation of the Methyl Orange solution under the UV light illumination. The photocatalytic activity of the sample that anodized for 100 min and annealed for 500°C had the highest among all the samples. Furthermore, sample that anodized for 100 min and annealed at 300°C and 700°C had the lower photocatalytic activity as they had the lower absorption capacity and degradation rate. These results obtained indicate that anatase-rutile TiO_2 films are able to be used for the enhanced organic pollutants degradation.

Keywords: Titanium dioxide, electrochemical anodization, annealing temperature, X-ray spectrometer, X-Ray diffraction

1. Introduction

Clean water supply is essential in our daily life. It is one of the primary requirement to maintain ecological balance [1]. According to World Health Organization, more than 3.4 million people die per annum due to water pollution [2]. Persistent organic pollutants (POPs) are the main contributors to water pollution. POPs are organic compounds that resist to environment breakdown due to high lipids solubility and low waters solubility [2]. In this context, photocatalysis using semiconductor catalysts has become an advanced water treatment technique for water purification [2].

Photocatalysis technique has attracted great attention in the past decades because of its effectiveness in mineralizing and degrading persistent organic compounds. There are numerous photocatalysts such as titanium dioxide (TiO_2), tungsten oxide (WO_3), tin dioxide (SnO_2), zinc oxide (ZnO) and iron oxide ($Fe2O_3$) available for photocatalysis application. Among these photocatalysts, titanium dioxide (TiO_2) exhibits a relatively high efficiency and low cost [3]. Furthermore, TiO_2 is resistant to corrosion and chemical, biocompatible with specific ion intercalation properties [3]. TiO_2 is used widely in gas sensing, photocatalysis, photovoltaic cell, optoelectronics, electrochemical bio- sensing, and water splitting applications. In general, there are four type of TiO_2 nanostructures, namely nanowires, nanoporous, nanorods and nanotubes [4]. Nanostructured TiO_2 thin films can be prepared using electrochemical anodization, atomic layer deposition (ALD), sol-gel and hydrothermal methods. However, the most suitable method used to prepare TiO_2 thin film is electrochemical anodization. It is established that anodization time and annealing temperature play an important role in the nanostructure and crystalline structure of TiO_2 [5]. In addition, the photocatalytic activity and performance of TiO_2 is influenced by its nanostructure and crystalline structure [6]. Hence, the effects of anodization time and annealing temperature on the morphology and crystalline structure of TiO_2 were investigated in the present study.

The synthesis of TiO_2 film via electrochemical anodization was conducted at 100 min anodization time. The anodized TiO_2 were annealed at different annealing temperature i.e(300, 500, and 700°C) for an hour. The crystalline structures of the annealed TiO_2 thin films were characterized using X-Ray diffraction (XRD). The photocatalytic performance of TiO_2 thin films were evaluated by photocatalytic degradation of methyl orange (MO) solution under the UV light irradiation [7].

2. Methodology

In this research, nine pieces of titanium foils are used to produce titanium dioxide thin films. The TiO_2 films obtained by using electrochemical anodization method. There are some materials listed as below:

2.1 Materials

Titanium foils (99.5% purity, 1mm thickness), Ethanol, Acetone, Ethylene glycol, ammonium fluoride and Methyl orange aqueous solution were purchased from sigma-Aldrich Sdn, Bhd Malaysia.

2.2 Preparation of TiO_2 film

Commercial titanium foils were cut into pieces of 10 mm × 50 mm. Before the anodization take place, Ti foils were degreased by sonicating in ethanol, deionized water and acetone, respectively, for 10 minutes each before the electrochemical anodization [8]. The clean Ti foils were then dried in air. The electrochemical anodization is performed in a solution of 0.3g ammonium fluoride dissolved in 100ml ethylene glycol at an applied potential of 30 V which connected to a direct current (DC) power supply [9]. The anodization process was conducted at room temperature with 100 min anodization time, using two-electrode electrochemical cell at a constant potential (30 V) with carbon as cathode and Ti foil as anode as shown in Figure 2.1. The anodized samples were rinsed with deionized water, followed by drying at 60°C in an oven [8]. After drying, the anodized TiO_2 films were annealed at different annealing temperature (300, 500, and 700°C) for four hours.

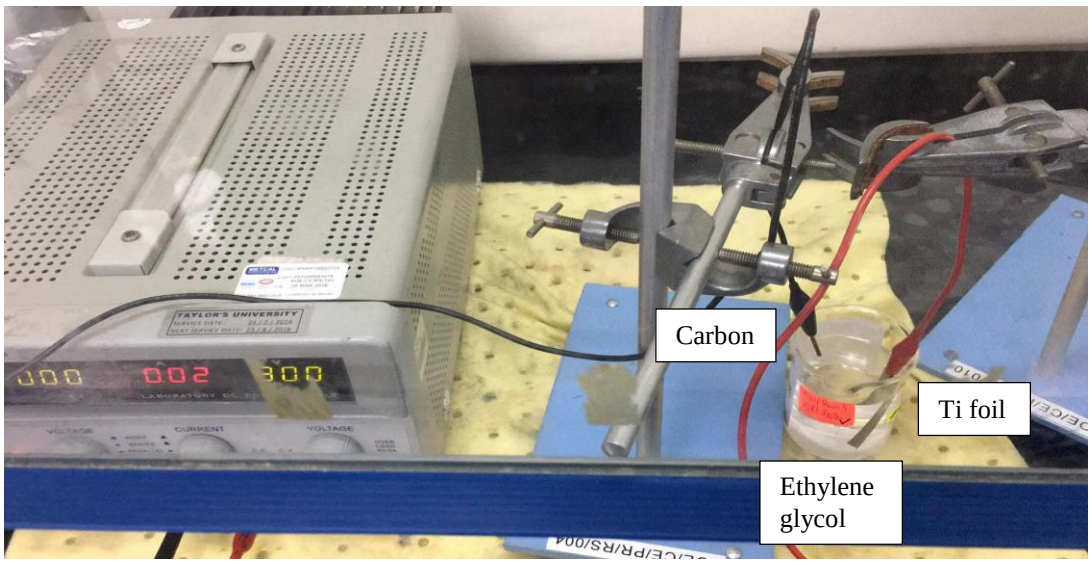


Figure 2.1. Setup of electrochemical anodization method.

2.3 Characterization

There are two characterizations to be used to get the morphology, crystalline structure and photocatalytic performance of the samples.

2.3.1 XRD

The crystalline structures of the annealed TiO_2 films were identified using D/MAX-RB-X-ray diffractometer (Japan, Rigaku) from Quantum Skynet Resources Sdn Bhd. Cu Kα radiation at a scan rate (2θ) of 0.05° s^{-1}, with an applied current of 30 mA and accelerating voltage of 40 kV were used [8].

2.3.3 UV-vis spectrometer

Photocatalytic performance of the TiO_2 samples were investigated via photodegradation of Methyl orange using UV-vis spectrometer (evolution 60S UV-visible spectrophotometer). Thin film sample of 10 mm × 30 mm were immersed into 50 ml solution of MO with a concentration of 10 ppm [10]. The sample were placed inside a dark room with the room temperature. After immersing the solution under UV light illumination (lab in Universiti Malaya) for 30 minutes, 5ml of MO was collected at every hour until seven hours illumination. The concentration of MO were measured using UV-vis spectrometer. The wavelength for MO was set at 465nm.

3. Results and Discussion

3.1 Crystalline Structure

Fig. 3.1 illustrates XRD diffractograms of the TiO_2 films annealed at different temperatures. XRD patterns indicate that the crystalline structure of TiO_2 is affected by annealing temperature. All three samples with different annealing temperature consisted a mixture of amorphous, anatase and rutile TiO_2 phases.

In this part of experiment, XRD analysis was used to investigate the effect of thermal treatment on the phase transition and crystallization of TiO_2 films. The result obtained clearly shows the crystal structure of TiO_2 is depend on the thermal treatment. Fig. 3.1a shows that the XRD diffractogram of the sample exhibited mostly Ti phase and anatase phase only, which indicates the amorphous nature of TiO_2. This indicates that the annealing temperature wasn't sufficient enough to transform the amorphous phase to crystalline phase. The Bragg reflection of Ti phase was detected at 2Θ values of 25°, 35°, 38°, 40°, 48°, 53°, 63°, 71° and 77° in the whole XRD diffractogrames, corresponding to (101), (010), (002), (011), (200), (012), (110), (013) and (112) crystal planes, respectively.

Fig. 3.1b shows that the XRD pattern of sample annealed at 500°C that promoted to the crystallization of anatase phase. This result shows that change of phase of amorphous and anatase TiO_2 films at a temperature between 300°C and 500°C. The obvious anatase peak were detected at 38°, corresponding to (002), crystal

planes for the anatase TiO_2 films. It has the higher peak of anatase and lower peak of Ti phase when comparing to XRD pattern of sample annealed at 300°C.

Fig. 3.1c shows that the further inceasing in annealing temperature to 700°C, the intensity of anatase phase decreased and the existence of rutile phase detected at 27°, 38° and 57° in the XRD patterns, corresponding to (110), (010) and (220) crystal planes, respectively. The results indicated the anatase phase mostly diminished and rutile as the major phase at fig. 3.1c.

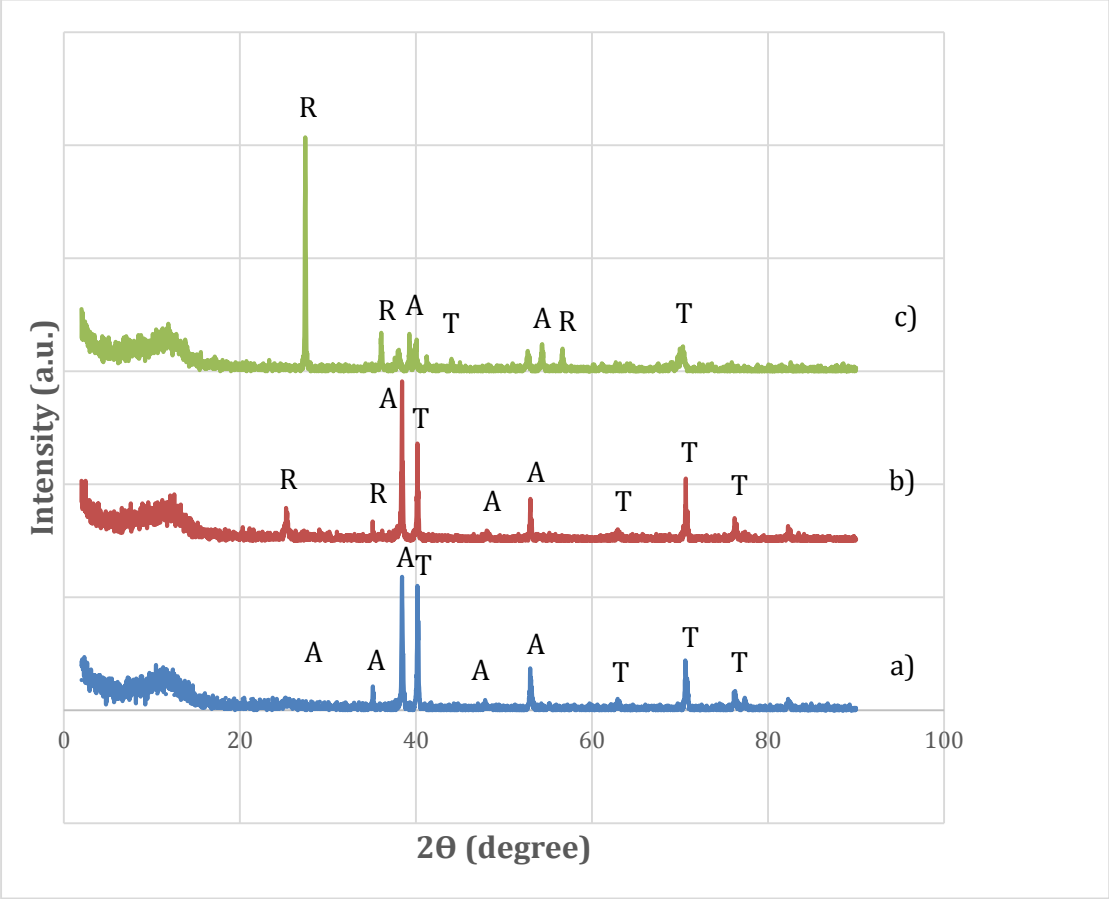


Figure 3.1. XRD diffractograms of the TiO_2 films annealed at different temperature, a) 300°C, b) 500°C, c) 700°C [A=Anatase; T=Titanium; R=Rutile].

As shown from fig. 3.1a and 3.1b, both of the XRD patterns are similar but the anatase phase increased and amorphous phase decreased for sample (500°C). This shows that the sample annealed at 500°C has the better anatase phase than sample annealed at 300°C. Fig. 3.1c illustrates that the only highest peak is the R(110) phase. This could be said that sample that annealed at 700 °C is more towards rutile phase. All of these can be concluded that sample annealed at 700°C has the most rutile phase where sample annealed at 500°C has mostly anatase phase and sample that annealed at 300°C is amorphous phase.

3.2 Photocatalytic activity

Fig. 3.2 presents the plot of absorbance against concentration of methyl orange. This graph is plotted as the reference for the photoegradation of MO under the UV

light illumination. Fig. 3.2 shows that the increases in concentration of methyl orange increase the absorbance. The equation that obtained from the graph is y= 0.082x + 0.0257. This equation is using as the reference to find the concentration of all the MO samples by substituting the absorbance of it into the equation.

Fig. 3.2 presents the concentration versus UV light irradiation time for the samples immersed in of 10ppm methyl orange. There are three samples immersed into methyl orange. Fig. 3.2 shows the shape indicate each and every of the characteristic for the three samples. Clearly, the sample with 100 min anodization time and 500°C annealing temperature has the highest absorption capacity and degradation rate. This can be seen from the graph where the concentration of the solution decreases the most within the 7 hours illumination time. The two MO samples have the similar absorption capacity and degradation rate. The reason could be due to the crystalline structure of the TiO_2 films. Hence, the sample anodized at 100 min and annealed at 300°C and sample anodized at 100 min and annealed at 700°C had lower photocatalytic activity. Furthermore, comparatively, the sample at 100 min anodization time and 500°C annealing temperature has the best photocatalytic activity. This may be due to the formantion of relatively optimum anatase crystalline phase crystallinity and fraction in the TiO_2.

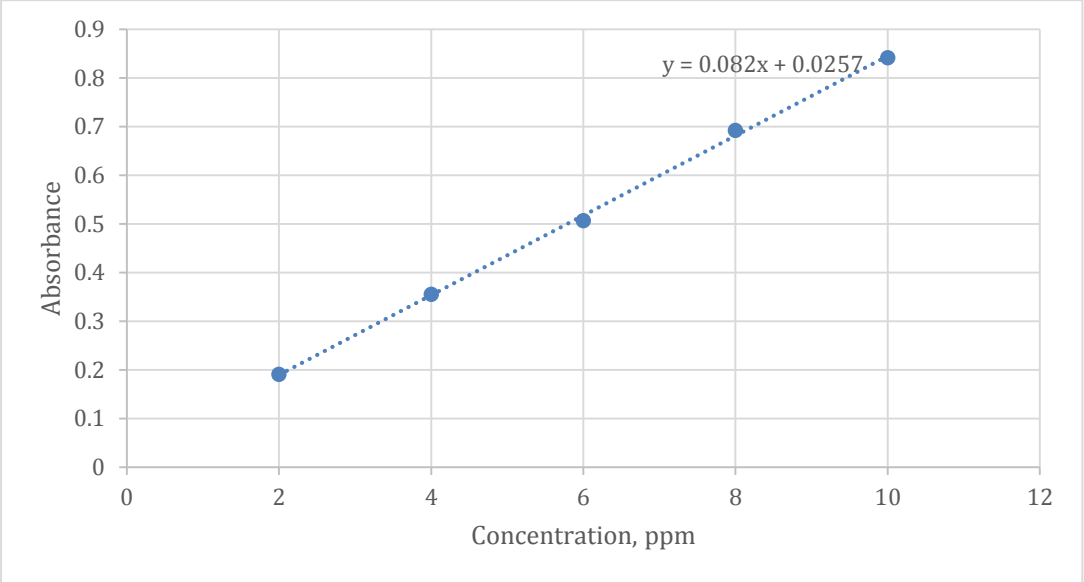


Figure 3.2. Plots of absorbance against the concentration of methyl orange.

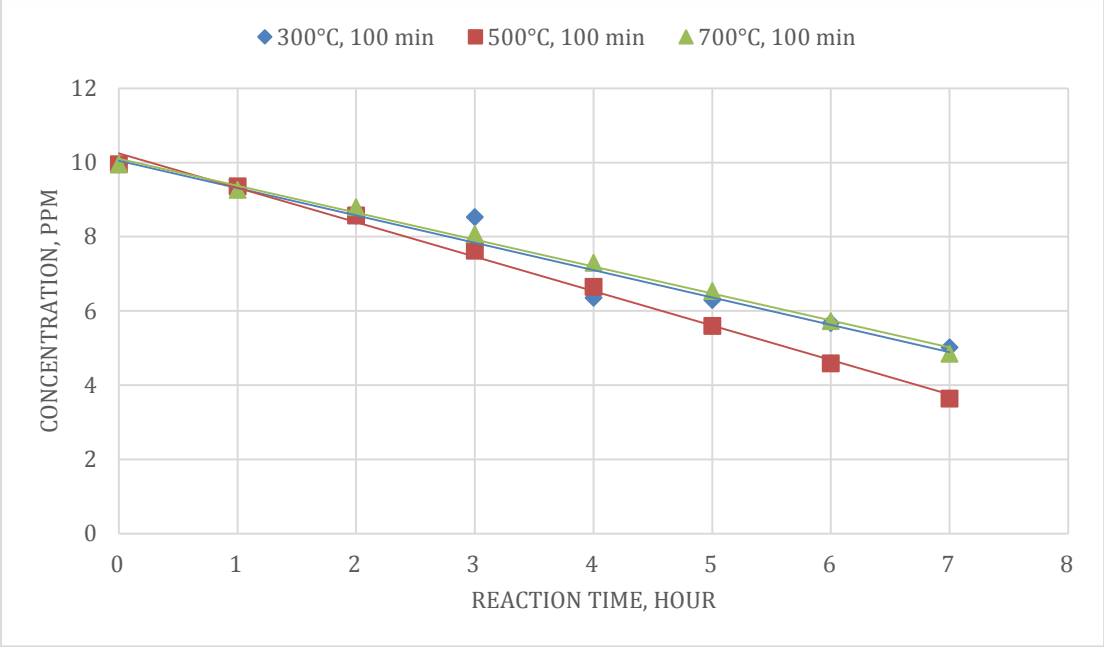


Figure 3.2. Plot of concentration versus UV irradiation time.

4. Conclusion

In summary, the mixture of anatase-rutile phase and amorphous phase of TiO_2 films were successfully prepared at different anodization time and annealing temperature by constant voltage of 30V when anodizing them. It was found that the phase transition of the samples were affected by the different anodization time and annealing temperature. The phase transition changed from amorphous phase to anatase-rutile phase and finally to mostly rutile phase with the increases of annealing temperature. Sample that annealed at temperature of 300°C had the mostly amorphous phase structure and sample that annealed at temperature of 500°C had mixture of anatase-rutile phase where sample annealed at 700°C had the rutile phase. It could be conclude that sample that annealed at 500°C had the best crystalline structure it has the most anatase phase among all the samples. The best crystalline structure lead to the best photocatalytic performance.

Photocatalytic activities of the samples were compared for photodegradation of the MO solution under the UV-vis light illumination. All the process parameters that influenced were performed and the photocatalytic activity of the sample that anodized for 100 min and annealed for 500°C had the highest among all the samples. The MO that sample immersed had degraded the most. Furthermore, sample that anodized for 100 min and annealed at 300°C and 700°C had the lower photocatalytic activity as they had the lower absorption capacity and degradation rate. These results obtained indicate that anatase-rutile TiO_2 films are able to be used for the enhanced organic pollutants degradation.

Acknowledgment

The authors would like to thank Dr. Chou Pui May for the supervisions and guidance throughout this research process. The authors would like to thank Dr. Steven Lai, Dr. Morris Lee and Ms. Tan Shiau Xuan from Nanotechnology and Catalyst Research Centre, for their advice and guidance. The authors would also like to thank Ms. Litness Palniandy for technical assistance.

References

[1] Y. Zhang, X. Xiong, Y. Han, X. Zhang, F. Shen, S. Deng, H. Xiao, X. Yang, G. Yang, and H. Peng, "Photoelectrocatalytic degradation of recalcitrant organic pollutants using TiO 2 film electrodes: An overview," *Chemosphere*, vol. 88, no. 2, pp. 145–154, 2012.

[2] N. Liu, X. Chen, J. Zhang, and J. W. Schwank, "A review on TiO2-based nanotubes synthesized via hydrothermal method: Formation mechanism, structure modification, and photocatalytic applications," *Catal. Today*, vol. 225, pp. 34–51, 2014.

[3] S. Pekárek, J. Mikeš, and J. Krýsa, "Comparative study of TiO2 and ZnO photocatalysts for the enhancement of ozone generation by surface dielectric barrier discharge in air," *Appl. Catal. A Gen.*, vol. 502, pp. 122–128, 2015.

[4] J. M. Macak, H. Tsuchiya, A. Ghicov, K. Yasuda, R. Hahn, S. Bauer, and P. Schmuki, "TiO2 nanotubes: Self-organized electrochemical formation, properties and applications," *Curr. Opin. Solid State Mater. Sci.*, vol. 11, no. 1–2, pp. 3–18, 2007.

[5] X. Yu, Y. Li, W. Wlodarski, S. Kandasamy, and K. Kalantar-zadeh, "Fabrication of nanostructured TiO2 by anodization: A comparison between electrolytes and substrates," *Sensors Actuators, B Chem.*, vol. 130, no. 1, pp. 25–31, 2008.

[6] H. Yang and C. Pan, "Diameter-controlled growth of TiO2 nanotube arrays by anodization and its photoelectric property," *J. Alloys Compd.*, vol. 492, no. 1–2, pp. 2009–2011, 2010.

[7] S. Sakthivel, B. Neppolian, M. V Shankar, B. Arabindoo, M. Palanichamy, and V. Murugesan, "Showes Zno Better Than Tio2," vol. 77, no. 3, pp. 65–82, 2003.

[8] J. Yu and B. Wang, "Effect of calcination temperature on morphology and photoelectrochemical properties of anodized titanium dioxide nanotube arrays," *Appl. Catal. B Environ.*, vol. 94, no. 3–4, pp. 295–302, 2010.

[9] G. K. Mor, O. K. Varghese, M. Paulose, K. Shankar, and C. A. Grimes, "A review on highly ordered, vertically oriented TiO2 nanotube arrays: Fabrication, material properties, and solar energy applications," *Sol. Energy Mater. Sol. Cells*, vol. 90, no. 14, pp. 2011–2075, 2006.

[10] L. Qin, Q. Chen, R. Lan, R. Jiang, X. Quan, B. Xu, F. Zhang, and Y. Jia, "Effect of Anodization Parameters on Morphology and Photocatalysis Properties of TiO2 Nanotube Arrays," *J. Mater. Sci. Technol.*, vol. 31, no. 10, pp. 1059–1064, 2015.

Development of Strain Rate Dependent Rubber Bushing Material Model for Impact FEA Application

Chiang Lin Chern[1*], Ch'ng Shiau Ying[1], Yap Kim Haw[2]

[1]*School of Engineering, Taylor's University, Malaysia*

[2]*Panasonic Appliances Air-Conditioning R&D Malaysia Sdn. Bhd.*

[*]Chianglinchern@sd.taylors.edu.my

Abstract

In this joint research study between Panasonic Appliances Air Conditioning R&D Malaysia and Taylor's University, the focus will be on developing a strain rate dependent material model that could predict the behavior of this hyperelastic RB between strain rate ranges from 0.01/s to 1/s. In this research study, Mooney-Rivlin material model equation were first studied. Stress response under tensile and compression were investigated by conducting experiments on the rubber specimens provided by Panasonic. The stress and stretch experimental data for 3 different strain rates obtained were used to solve for theoretical value by using Mooney-Rivlin equation. The material constants were identified from the output of theoretical data and were then used to formulate a relationship equation. The equation were then integrated into a script that is capable of receiving input and can be operated in open source SCILAB software in Panasonic. The theoretical results solved using Mooney-Rivlin equation has good correlation with the experimental value and have shown a close agreement with each other. The relationship formulas were also successfully integrated into SCILAB and capable of receiving strain rate input within the proposed range. The results produced by the user input capable script have also shown a good correlation and agreement to experimental results. In conclusion, all research objectives were achieved and successfully provide Panasonic a free platform to obtain stress strain behavior data of their rubber bushing.

Keywords: Strain rate dependent, Hyper-elastic materials, Rubber bushing, SCILAB

1.0 Introduction

Finite Element Analysis (FEA) and simulation application has been a very common practice in heavy industry such as aeronautical and automotive industries. The usage of FEA could allow time and cost reduction by conducting fewer tests on a newly designed prototype [1]. In Panasonic, the subject of interest in this research study will be the rubber bushing mount used to attach on the legs of an air-conditioner refrigerant compressor. These rubber bushings are responsible in preventing vibration failure, shock impact absorber and also as a medium for noise isolation [2].

As it holds such a significant role in failure prevention, it is extremely important for the company to ensure its reliability. However, due to incapability to sustain expensive software's license such as LS-DYNA® which would costs approximately 200 thousand ringgit annually, conventional drop test is typically conducted as a standard to identify the reliability of the rubber in a minimal cost. Although crash simulation can still be done in available cheaper FEA software, time were usually wasted in identifying material parameters as the material models available in the software are not strain rate sensitive [3]. Unlike MAT 181 hyperelastic material model available in LS-DYNA® which could allow operator to obtain the quasistatic response of a rubber directly by just inputting desired strain rate value [4].

A strain rate sensitive material model is necessary for a drop test simulation due to its complex dynamic phenomenon where a subject experiences variating stress coming from different directions and angles which makes it a dynamic and strain rate sensitive case [5]. Mooney Rivlin, Ogden and Neo-Hookean material models are few of the most used material models for numerical analysis of hyperelastic material as they are simple and could provide a reasonable accuracy. But in this study, Mooney-Rivlin (MR) will be the chosen material model for rubber bushing as it allows the simplest definition [6] for this case study due to time constraint and limited resources.

MR model which is widely used in most heavy industry nowadays was introduced by Melvin Mooney and Ronald Rivlin. This material model is constructed with the strain energy density functions that consist of 2 invariants of the left Cauchy-Green tensor B [7]. The energy function (1) is as follows:

$$W = C_1(\bar{I_1} - 3) + C_2(\bar{I_2} - 3) \quad (1)$$

Based on equation above, C_1 and C_2 are the material constants while I_1 and I_2 being the 2 invariants of the Cauchy-Green tensor value. Based on certain studies, it is well confirmed that the material constants can be identified by relating shear modulus G [8] as shown in the equation (2) below:

$$G = 2(C_1 + C_2) \quad (2)$$

Although MR is a simple material model and consist of its known limitation in certain cases, it could still be utilize in local values of strains up to about 200% [9].

This research study has been proposed by Panasonic with the objectives to manually produce a strain rate dependent material model for hyperelastic material with a strain rate

range of 0.01/s, 0.1/s and 1/s. The goal of this research will be to allow the reduction of cost from conducting drop tests and also to avoid expenses of purchasing expensive FEA software. Thus, all calculations and numerical script will be done in Scilab open-source software. Uniaxial tension and compression test on rubber specimens and actual rubber mounts will be conducted to obtain their material parameters for verification and validation purposes respectively.

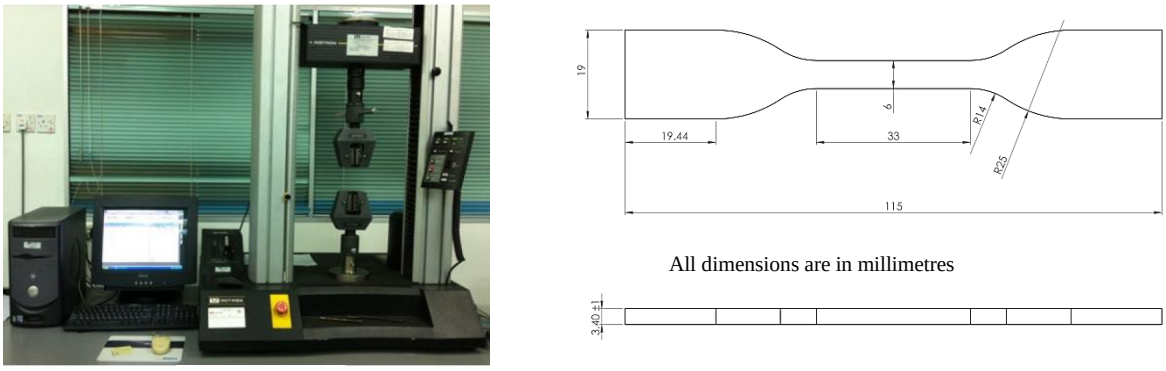
2.0 Research Methodology

2.1 Material Testing

In order to utilize the material model of hyperelastic material models, actual raw data is needed to obtain the material constant of the rubber. To obtain these constants and satisfy the input requirements of hyperelastic material, properties identification experiments are to be conducted which are the basic uniaxial tension and compression tests. Although these tests are carried out separately due to its specimen shape and depending on the strain rate required, their results are utilized as a set. This means that all the material use in the experiment must be the same despite of their structural shape. The rubber material used in this research study is provided by Panasonic while the supplier and material information remains classified based on company imposed policy.

2.1.1 Uniaxial Tensile Test

The specified strain rate tensile tests of rubber bushing were done by using Instron 3369 universal testing machine located in University of Malaya. The physical experimental setup is shown in Fig. 1(a). The experimental results were all captured by INSTRON® Console software which is installed in a pc which is provided along with the purchasing of the machine. The dimensions were designed based on the drawings given in the ASTM standard D412 which is shown in Fig. 1(b).



(a) **(b)**

Figure 1: (a) Experimental setup of INSTRON® 3369 and
(b) Dimensions and shape of test specimen

Due to low strain rate criteria in this research study, fracture point results are not necessary as it would take the specimen too long to achieve its fracture point. To mount the specimen onto the machine, the upper and lower part of the specimen is clamped by both the grips of the machine while maintaining a distance of considerably higher than the length of

the specimen between both grips for more accurate result. During the test, the upper grip will move up at the velocity set.

2.1.2 Uniaxial Compression Test

For uniaxial compression test, it was done by using Shimadzu tensile machine which is readily located in Panasonic Air conditioning appliances Shah Alam. The physical experimental setup can be seen in [Fig. 2(a)]. The experimental results were all captured by using TRAPEZIUM LITE X data collection software in a computer. The dimensions of the compression test specimen were designed and cut based on drawings provided in ASTM standard D695 which is shown in [Fig. 2(b)].

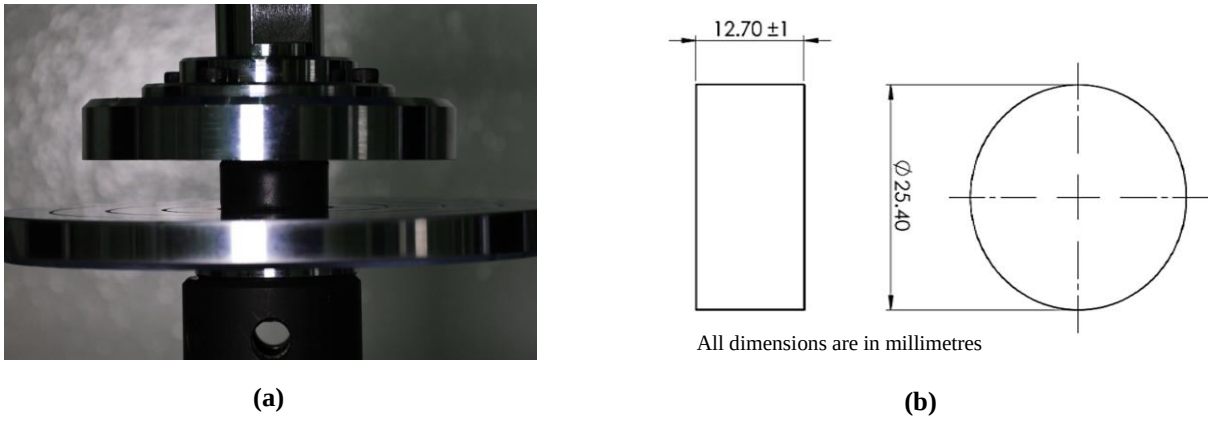


Figure 2: (a) Experimental setup of TRAPEXIUM LITE X and
(b) Dimensions and shape of test specimen

During the experiment, specimen was placed in between the upper and lower compression plate. For both tensile and compression tests, each specified strain rates were repeated 3 times such that to obtain a more accurate data while maintaining minimal error. Thus, there will be a total of 9 results for each tensile and compression experiment.

2.2 Experimental Results Analysis

The results collected for both tensile and compression test were converted into excel file format for data tabulation purposes. Based on the data from 3 experiment repetitions, the average data is obtained and plotted as shown in Figure 3 for tensile experiment data and Figure 4 for compression experiment data. Figure 5 shows the combined data.

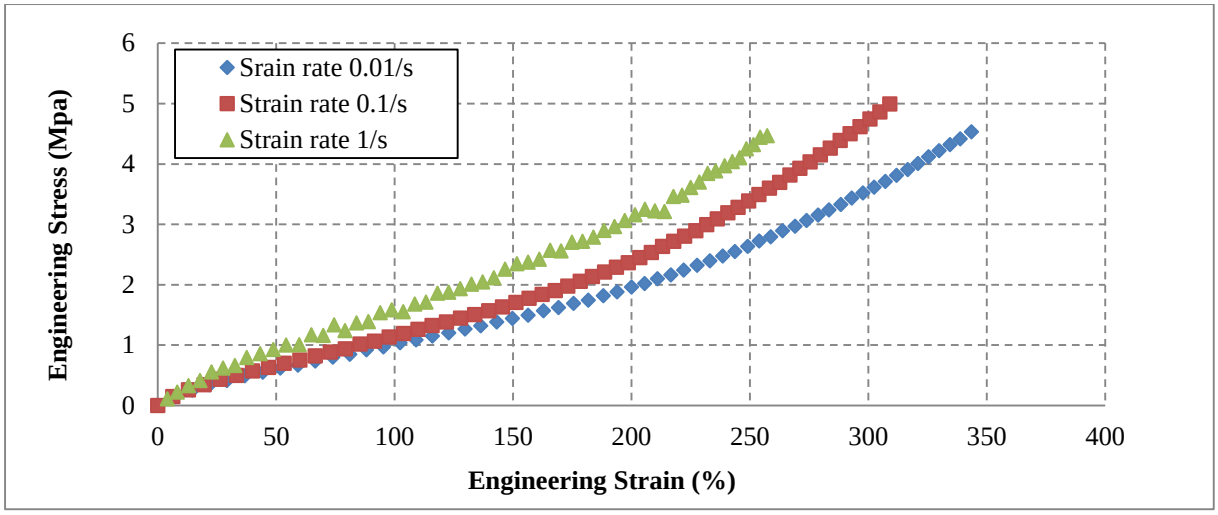


Figure 3: Tensile test experimental data

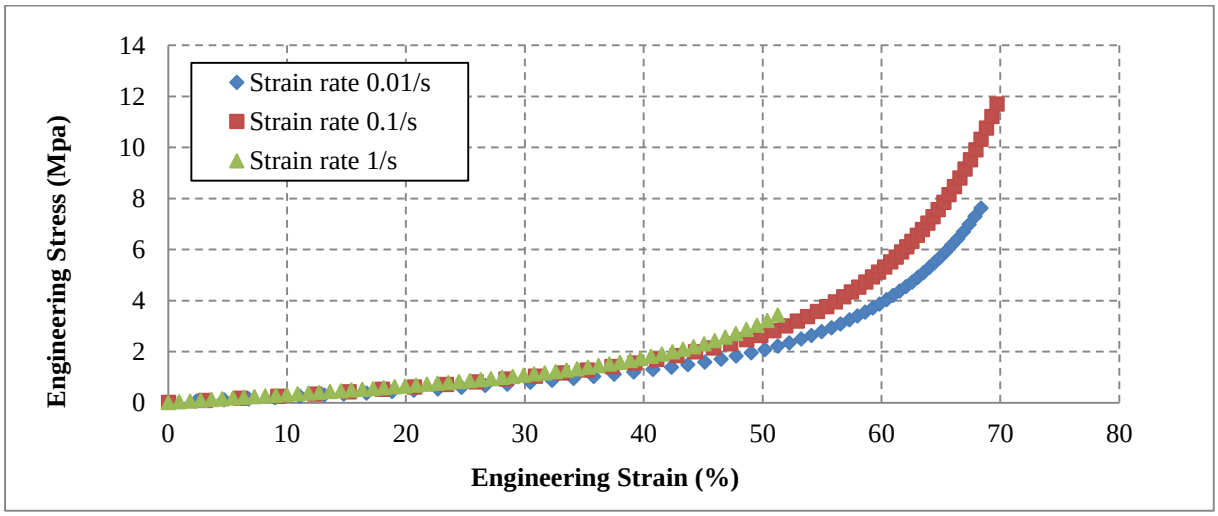


Figure 4: Compression test experimental data

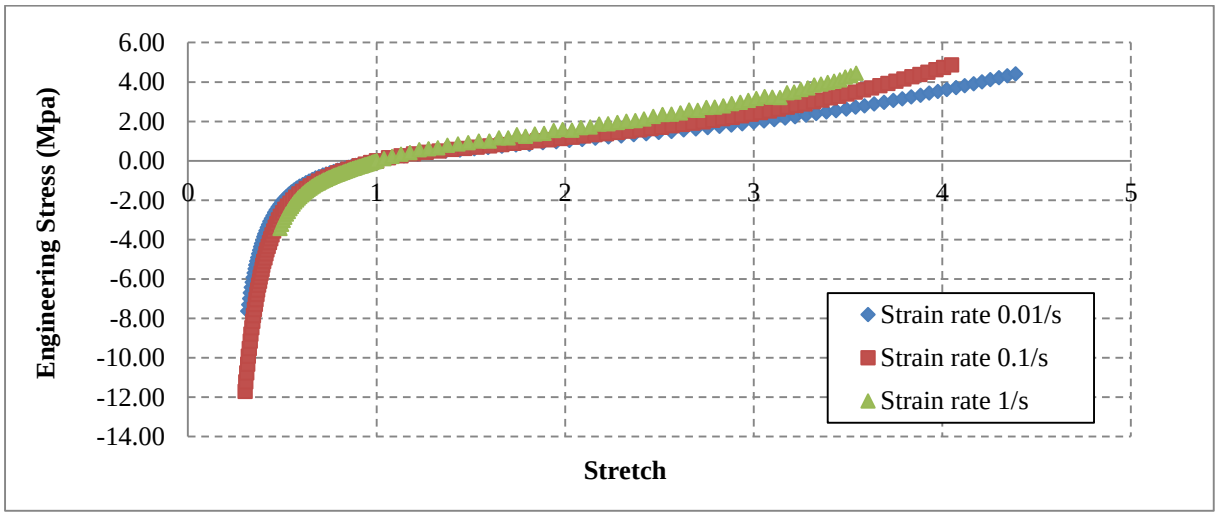


Figure 5: Combined experiment data

Based on results obtained from tensile test Figure 3 and compression test Figure 4, we can see that deviations are quite significant. From both experiments, we can conclude that the young modulus of natural rubber hyper-elastic material is rate dependent as there are variations of stress-strain relationship in different strain rate. In tensile test, we can see that natural rubber exhibits a linear elastic modulus for all 3 strain rates. In compression test, the data has shown an exponential relationship.

In order to obtain the combined data, the stress of compression data is shifted to the negative value by multiplying all data by -1 while strain in percentage is converted to stretch by dividing 100 and adding 1 to every strain value to satisfy the input of MR model. For tensile data, the strain value is also converted using by the same procedure done to compression data. The result of the combined data is shown in Figure 5. Thus giving us an overall view of the rubber from a 0.5 – 2.0 stretch ratio. Additionally, also allow MR to show its capability in both compression and tensile state.

2.3 Numerical Script

In this research study, all numerical work was done by using open source software SCILAB. By utilizing the stress strain data obtained from the experiments as base data, we can integrate the data with MR equation (1) to predict the stress strain behavior. The basic script flow works starts from receiving the readings of the experimental data in the form of stress and stretch. The data will then be first solved by using MR equation specified in the script. Initial value given at first will then be solved and error will be calculated to correct those estimated data by using curve fitting for non-linear regression case. By the end of the solution process, the material parameters C_{10} and C_{01} will be obtained.

3.0 Results and Discussion

3.1 Material constant

In order to obtain the generalized material equation and their parameters relationship, 3 pre-defined strain rates were inputted into the produced numerical script to obtain their material constants. The outputs are recorded in Table 1.

Table 1: MR model parameters for natural rubber

Reference Strain, /s rate/s	Mooney-Rivlin parameters, MPa	
	C_{10}	C_{01}
0.01	0.0211	0.3416
0.1	0.0021	0.4819
1	0.0573	0.3793

Fig 6 shows the output graph plotted by the produced MR script. It can be seen that at individual strain rate, MR model is capable of estimating the compressive state with quite a good agreement with the experimental data and deviate as strain rate increases. This illustrates the usability of MR model in predicting the stress strain behaviour of rubber material. As shown here, different material parameters are needed to predict the stress-strain behaviour for different strain rate. Thus, it is proven that a strain rate dependent material model is needed to simplify the procedures for predicting the behaviour of rubber at different strain rate.

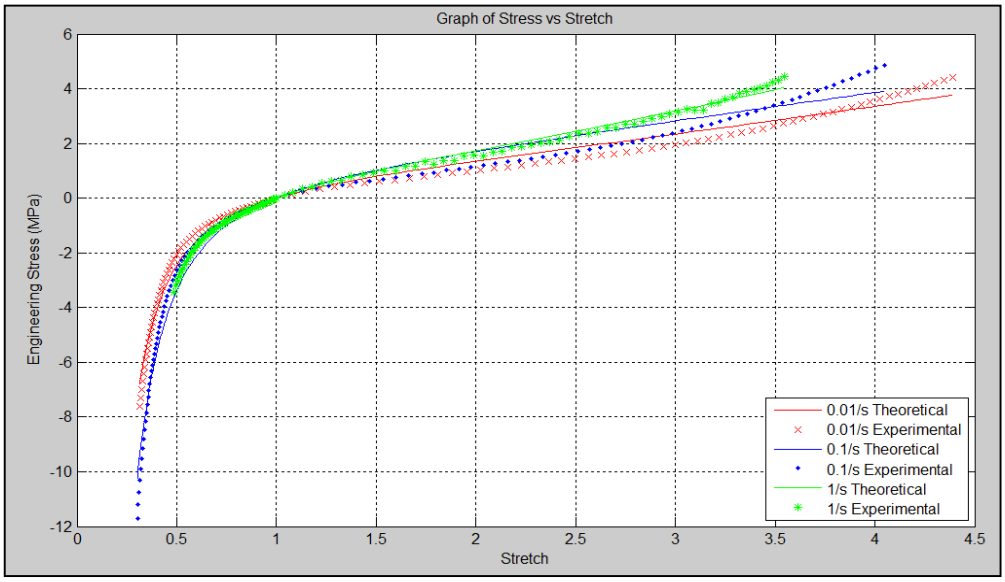
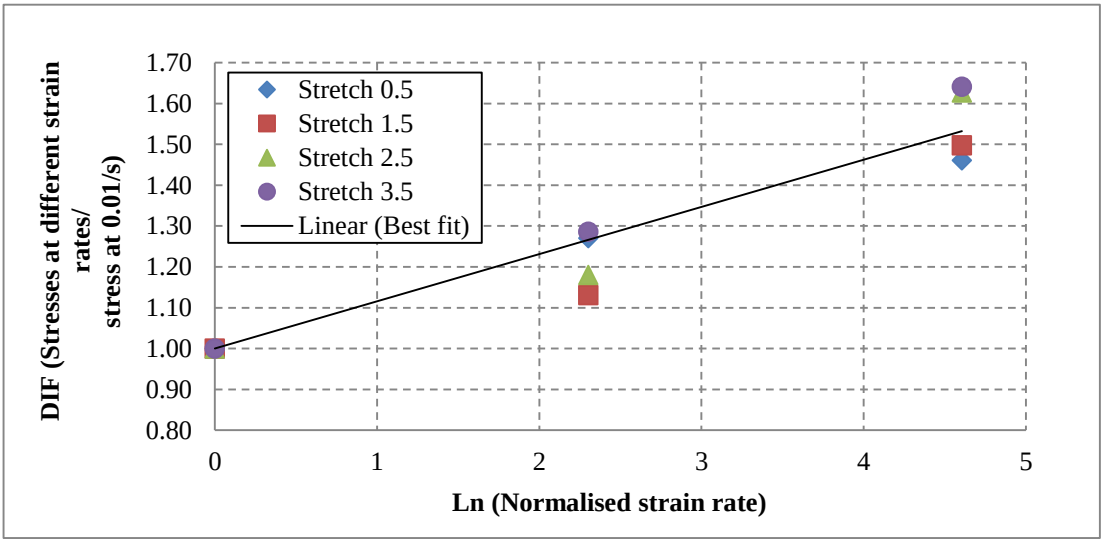


Figure 6: Graph of stress strain behavior with MR theoretical estimation

To quantify the increment of higher strain rate, usually the Dynamic increment factor (DIF) of the stress strain data is plotted. The DIF of a specific material parameters can be obtained by obtaining the ratio between the strain rate and the user defined strain rate which in this study will be lowest strain rate, 0.01/s. In order to produce a much clearer view, the strain rate is normalized. The DIF of the results is shown in Figure 7.



Based on Figure 7, it is clearly observed that stresses have a great increment with

Figure 7: DIF for Natural rubber

increasing strain. At each strain rates of 0.5, 1.5, 2.5 and 3.5, the DIF obtained for strain rate 0.1/s are 1.27, 1.13, 1.18 and 1.29 while for 1/s are 1.46, 1.50, 1.63 and 1.64. From these data obtained through calculating the DIF, it can be clearly observed that there is a significant increase of stress as strain increases. This justifies the significant of strain rate dependent model in a strain rate dynamic situation.

3.2 Generalized material parameters equation

By plotting a graph with the material parameter obtained from the MR script, we can acknowledge their relationship. The graph plotted is shown in Fig 8.

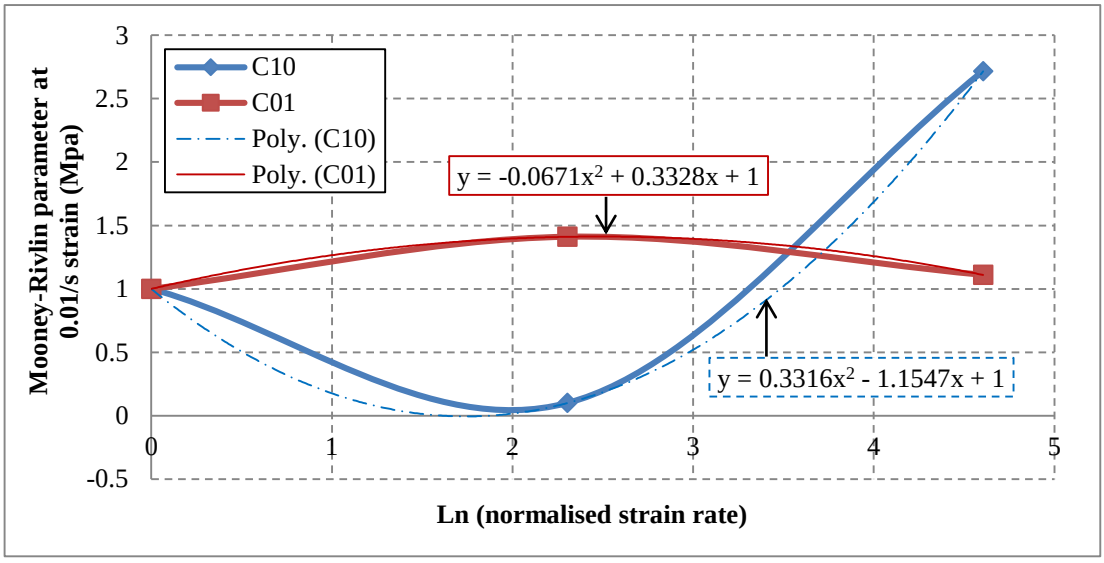


Figure 8: Combined relationship graph for C10 and C01

As 0.01/s strain rate is set as the base strain rate in this research study, the parameter scale shown in Figure 8 is in a ratio form against 0.01/s strain. By rearranging the equation obtained, the finalized proper equation is as follow:

$$C_{10} = C_{10(0.01/s)}\left[0.3316(ln\dot{\varepsilon})^2 - 1.1547(ln\dot{\varepsilon}) + 1\right] \quad (3)$$

$$C_{01} = C_{01(0.01/s)}\left[-0.0671(ln\dot{\varepsilon})^2 + 0.3328(ln\dot{\varepsilon}) + 1\right] \quad (4)$$

From equation (3) and (4), it can be seen that 0.01/s strain rate is made to be the base strain rate in this research study in order to generalize the material constant equation. Based on Fig. 8, it can be seen that C01 polynomial equation has very little deviation from the original line. However, for C10 polynomial equation, it can be seen that it has quite a large deviation from the experimental line but still falls under the acceptable range. This can be due to the number of strain rate given in the range for this research study.

3.3 Integration of Material Constant Relationship and SCILAB

By successfully formulating equation (3) and (4), integration between the equation and SCILAB must be done to produce a script that is capable of receiving strain rate input. The script flow is shown in Figure 9 below.

```
1  disp("--Strain rate range between 0.01/s to 1/s only--")
2  i = input("Please key in strain rate value = ")
3  e = i/0.01
4  GC10 = 0.0211
5  GC01 = 0.3416
6
7  C10 = GC10*((0.3316*(log(e))^2)-(1.1547*(log(e)))+1);
8  C01 = GC01*((-0.0671*(log(e))^2)+(0.3328*(log(e)))+1);
9
10 Stretch = 0.3:0.01:4.4;
11 pth = (2*C10+(2*C01./Stretch)).*(Stretch.^2-Stretch.^(-1));
12
13 disp ("C10 = ")
14 disp (C10)
15 disp ("C01 = ")
16 disp (C01)
```

Figure 9: User input capable material model script

Line 1 - 2

Line 1 display a message to notify user to only input strain rate ranged in between 0.01/s to 1/s only. Line 2 will prompt user to input desired strain rate and the value will be defined as subject of i.

Line 3 - 5

The inputted value will be divided by 0.01 as the equation in this script is generalized by 0.01/s as base strain rate value. The solved value will then be defined as subject of e. GC10 and GC01 is a pre-defined constant which has been discussed in section 4.3.

Line 7 – 8

Equation (8) and (9) which is formulated by the material constant relationship was written into the script.

Line 10 - 11

Line 10 limits the stretch value to minimum of 0.3 and maximum of 4.4 with an increment of 0.01. Line 11 is the Mooney-Rivlin equation which will calculate the stress value by taking in the solved strain value and repeat the process based on the increment within the limits.

Line 13 - 16

This section of code will display the material constant based of the user inputted strain rate value which is calculated by using equation (8) and (9) in SCILAB command window. By executing the script in SCILAB, the command window in SCILAB will display the message that request user to input a strain rate value. The command window is as shown in Figure 10.

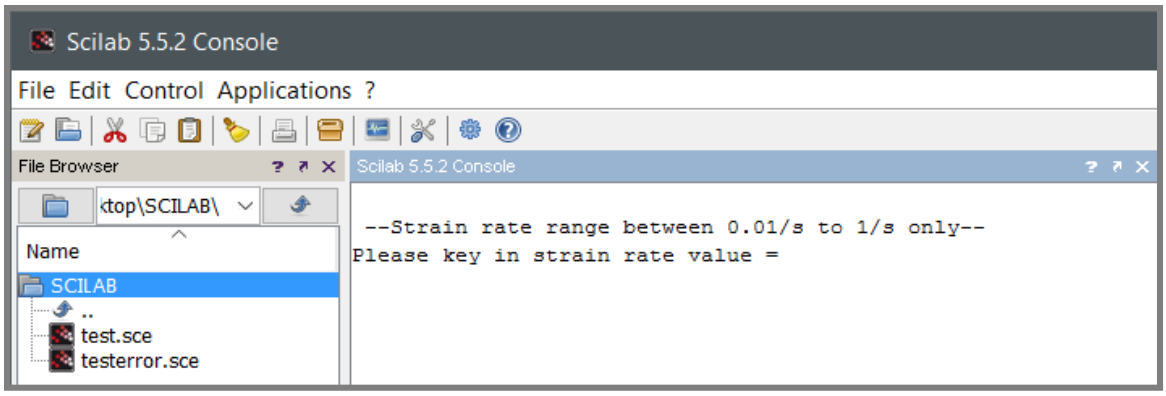


Figure 10: SCILAB Command window (Request)

By inputting a strain rate value, the results of C10 and C01 will be solved by the mathematical equation written in the script shown in Figure 9. The respond in the command window is shown in Figure 11.

Based on Figure 11, it can be seen that the material constant produced by input of 1/s strain rate is the same as the material constant obtained from the 1/s strain rate of theoretical material constant which is which can be seen in **Error! Reference source not found.** 4-1. This proves that the relationship equation formulation is correct and validated. By having this results validated and the script to be ready for Panasonic to utilize, graph output from this user input capable script were plotted along with the experimental results for validation. The results were shown in Figure 12 for 0.01/s, Figure 13 for 0.1/s, Figure 14 for 1/s and Figure 15 for compiled results.

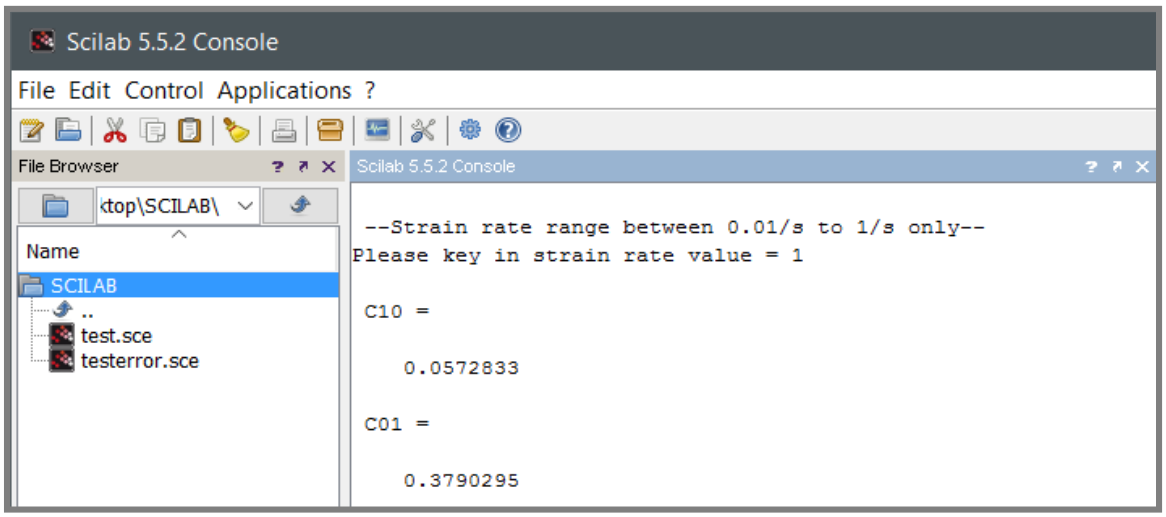


Figure 11: Material constant results from user input capable script

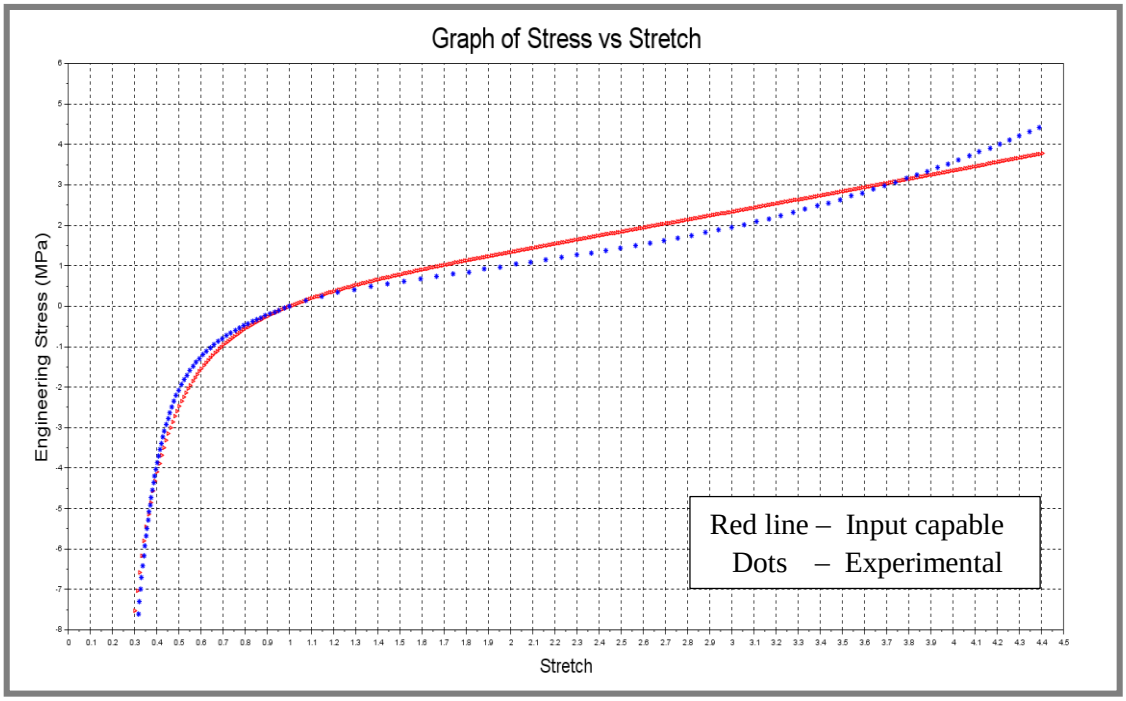


Figure 12: User input capable results with experimental curve (0.01/s)

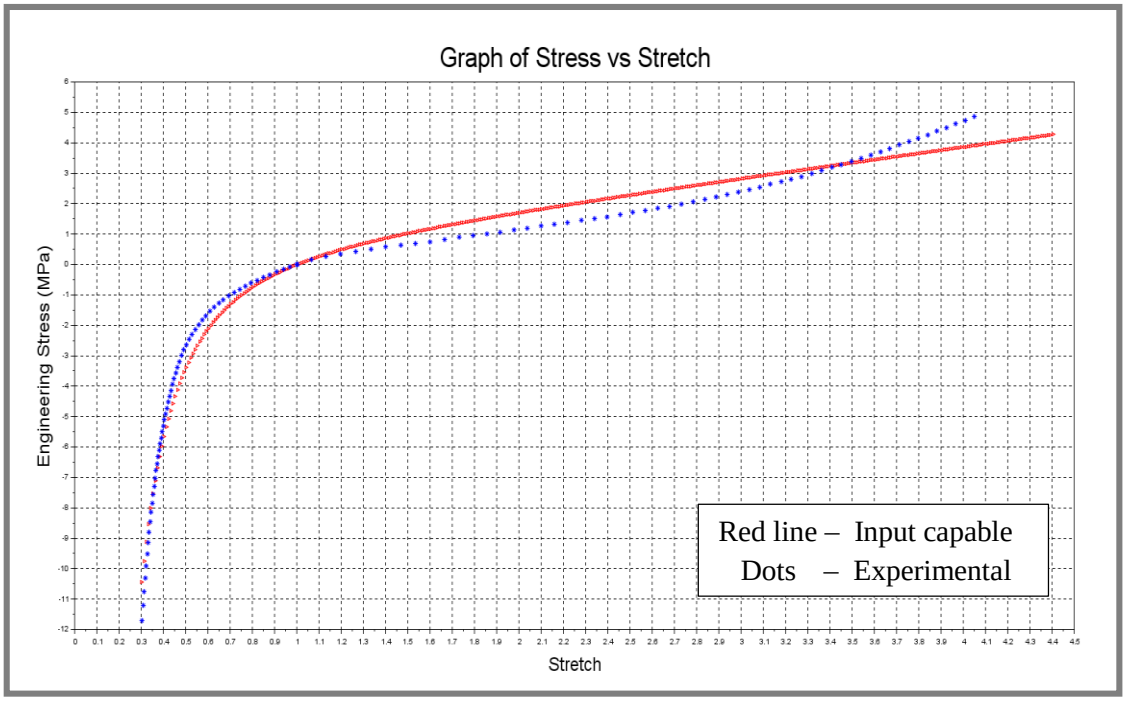


Figure 13: User input capable results with experimental curve (0.1/s)

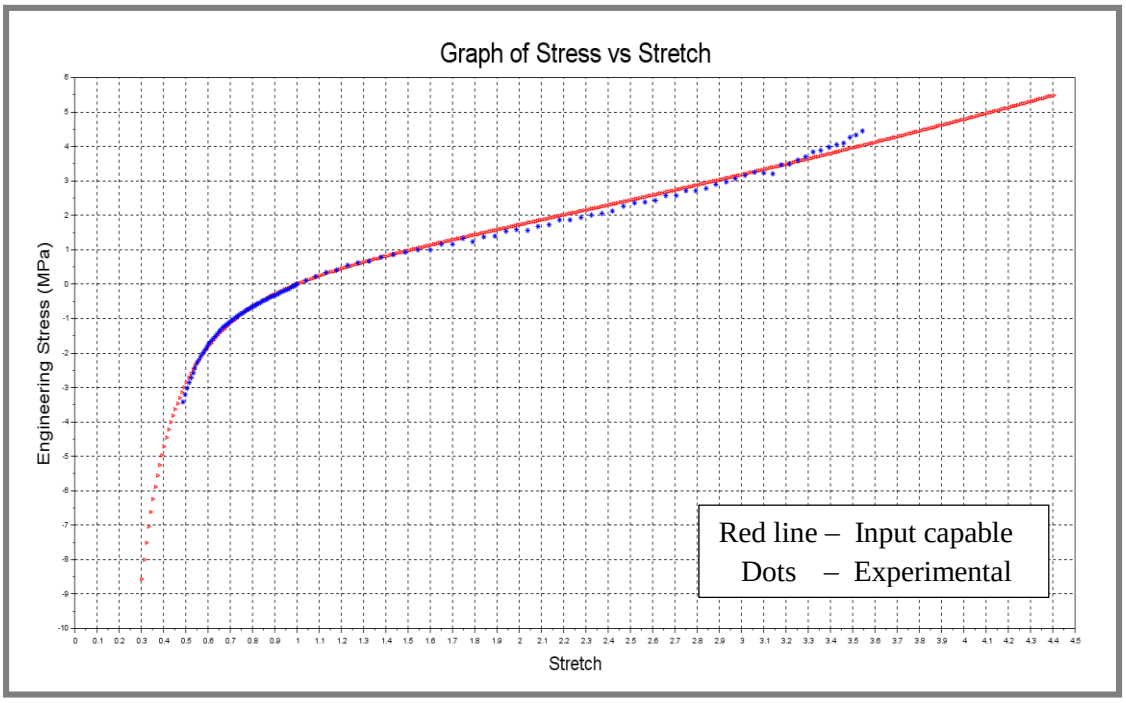


Figure 14: User input capable results with experimental curve (1/s)

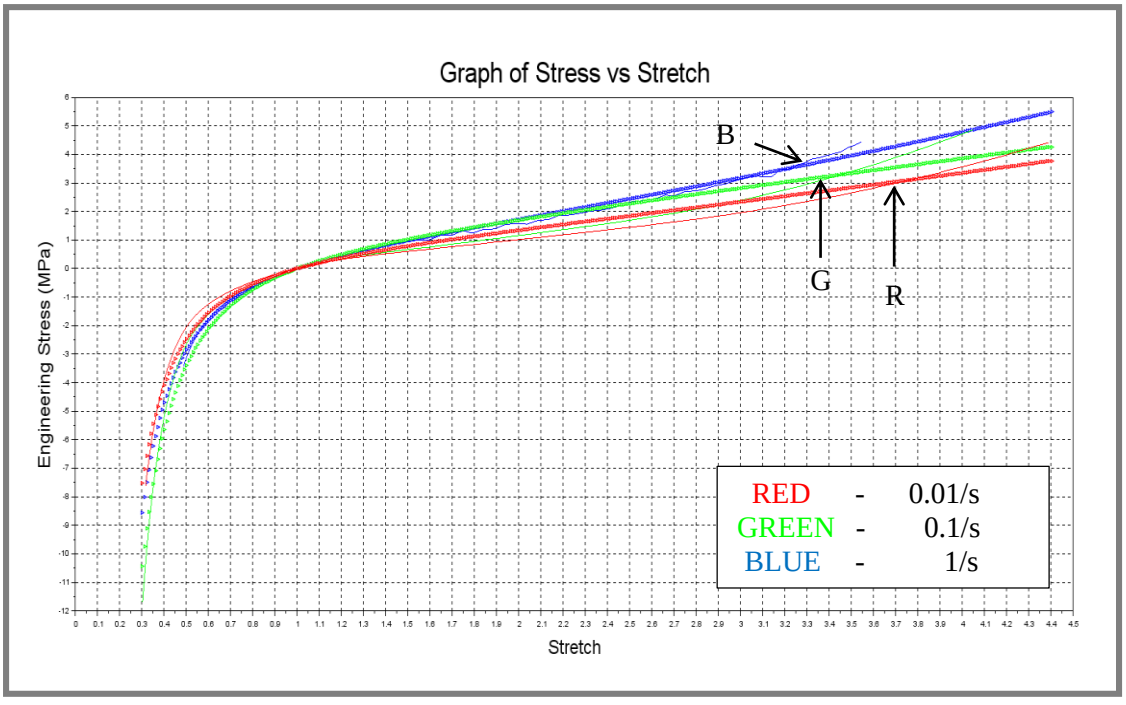


Figure 15: User input capable results with experimental curve (Compiled)

4.5 Summary and Limitations

Based on Figure 15, we can see that all 3 objective strain rates show a good correlation with its experimental data. This defines the usability and accurateness of the user input capable script. By having this correlation data, the script is ready to be used for input of any strain in between 0.01/s to 1/s. Although the script written is bound to the limitation of the strain rate range proposed for this project, but the output were proven to be fairly accurate and able to allow Panasonic to obtain stress strain behaviour of that particular rubber bushing material in a zero cost platform. As 2D and 3D analysis of this Hyperelastic material modelling will be a whole new research for this project, continuation will be carry out by new batch of interns from Panasonic industrial training course.

4.0 Conclusion

The dynamic tensile properties of a rubber material sample were investigated in this research study. Based on the experiment and analyses done by using the original MR model, it has shown that the unmodified MR model is highly capable in predicting the early stage deformation and stress strain behaviour of a hyperelastic material. Moreover, it has also proven that by manually obtaining the material constant that is derived for each strain rates, time would be wasted although there are only 3 strain rates proposed in this research study. The DIF results plotted in this report has also proven the significant of a strain affecting the behaviour of the rubber material. Thus, it is indicated that a strain rate dependent MR model is much more suitable and convenient for a dynamic situation.

In this research study, the generalized material equation itself is not sufficient to be integrated with the original MR model to make it strain rate sensitive. Thus, the strain energy density behaviour of the rubber material will be obtained later, so that the overall behaviour can be concluded and be written in the form of mathematical terms which could later be introduced into the conventional MR model.

References

[1] V. Jha, "Carbon black filler reinforcement of elastomers", *Unpublished doctoral dissertation*, University of London, Queen Mary, 2008.

[2] Z. L. Yu, "A Novel Semi-Empirical Dynamic Model of Rubber Bushing", *Automobile Technology*, pp. 6-11, Aug 2010.

[3] S. Park, M. Koka, K. Thomson and J. Robbins, "A FE Modeling and Validation of Vehicle Rubber Mount Preloading and Impact Response", *8th International LS-DYNA Users Conference*, Dearborn, pp. 5-23, 2004.

[4] P. Du Bois, "A simplified approach to the simulation of rubber-like materials under dynamic loading", *4th Eur. LS-DYNA Users Conf.*, pp. 31–46, 2003.

[5] M. Mooney, "A Theory of Large Elastic Deformation", *Journal of Applied Physics*, Vol. 11, pp. 582-592, 1940.

[6] D. Mohotti, "Strain rate dependent constitutive model for predicting the material behaviour of polyurea under high strain rate tensile loading", *Materials & Design*, vol. 53, pp. 830-837, 2014.

[7] Menderes, H. and Konter, A. W. A., "Advanced FE Analysis of Elastomeric Automobile Components under Realistic Loading Conditions", *Proceedings of the First European Conference on Constitutive Models for Rubber*, pp. 3-12, 1999.

[8] R. Ogden, "*Non-linear elastic deformations"*. Chichester: E. Horwood, 1984.

[9] R. S. Rivlin, “Large Elastic Deformations Isotropic Materials. IV. Further Developments of the General Theory”, *Philosophical Transactions of the Royal Society A*, Vol. 241, No. 835, pp. 379-397, 1948.

eureca 2016 – Conference Paper
Paper Number 2ME09

Numerical Modal Analysis of Mobius Shape Structure

Chong Chiang Hoong[1], A/P Dr. Hosseini[1], Ir A/P Dr. Satesh[1], Prof. Charalampos Baniotopoulos[2]

[1]*School of Engineering, Taylor's University, Malaysia*
[2]*University of Birmingham, UK*

[*]chianghoong.chong@sd.taylors.edu.my

Abstract
Mobius shape structure (MSS) is a three dimensional surface that is non-orientable. The surface of MSS consists of rotation that twisted at an angle of 180° at one end and joined together with another end. Vibration exists as a waste energy in the mechanical system and causes fatigue to mechanical structure and also people. MSS can be used as a vibration isolator in building foundation system. It is dissipated the energy away from resonance and reduce the vibration effect. The design parameters of a Mobius foundation are aspect ratio (length to width ratio), thickness, material stiffness and damping ratio. Finite Element Analysis (FEA) method is used to analyse how a MSS reacts to the real world forces and provide good vibration isolation. A MSS is able to have good vibration isolation by determining its optimum design parameters. Hex dominant meshing method is used to produce a good meshing of MSS and generate an accurate result in numerical modal analysis and harmonic response analysis. The aspect ratio of a Mobius support used in this research is 2.9 while its thickness is set as 10m. The damping ratio of the rubber is 0.01. Then, a Mobius foundation is compared with a foundation that without spring element which referred to a MSS. A Mobius foundation system has a total deformation of 0.085 mm. The maximum vibration displacement of a Mobius foundation is 0.135 mm at 1 Hz which is relatively small and caused no damage to the building structure. The acceleration of the building in vertical axis is determined as 0.005 m/s^2 at 1 Hz that is within human threshold of perception and the occupants feel comfortable inside the building. As a result, a Mobius foundation is concluded as a good vibration isolator because of its low structure deformation and less vibration effect to the people and building.

Keywords
Mobius Shape Structure, Vibration Isolator, Design Parameters, Finite Element Analysis.

1. Introduction

In the past few decades, the functionality and design of an object are the most important criterion to human. The design of object needs to be attractive and useful at the same time. Hence, Mobius Shape Structure (MSS) is one of the examples that can accomplish both of the criterions and also bring out a whole new design concept. It is a geometry structure that is non-orientable. The surface of the structure consists of rotation, translation or scaling properties. It will eventually join together from one end to another end [1].

Vibration is defined as the repetitive motion that can be measured and observed from a structure. It is a form of unwanted energy and eventually causes fatigue to the structure. There are two types of vibrations, which are free vibration and forced vibration. Free vibration is vibration system that sets off an initial force and let the object vibrates freely. Force vibration occurs when an external force or disturbance is applied to the vibration system. The external factor can be a periodic, steady-state input, transient input or a random input. For example, the rear view mirror of a car is vibrated due to high driving speed [2].

In mechanical term, vibration exists as an unwanted energy in the structures such as machines, buildings or vehicles. It exists in the form of sound or pressure wave. It causes fatigue that might damages the ear drum of human in excess. It also gives risk to the surrounding when it comes to worst consequence which is broken or spoil. The vibration effect is reduced by conducting vibration analysis and applying an effective vibration suppression method [2].

Vibration analysis can be done in two different approaches which are numerical analysis in MATLAB and numerical modal analysis in ANSYS Workbench. Numerical analysis in MATLAB is an analysis method that required the input of code for the vibration function to determine the amount of vibration displacement. Numerical modal analysis is a technique that required a 3D model from CAD software to perform the vibration analysis and it is chosen to determine the relationship between the structural properties of MSS and vibration behavior.

This project is studied because MSS can obtain better efficiency in term of less vibration and less energy loss. The design opens up more option to the designers and engineers if the vibration is able to be minimized by using MSS. It creates a more efficient mechanical system and less maintenance costs. It benefits the public by having a new design concept and has a longer lifespan.

The structural properties of MSS are identified and studied how it reacts when vibration takes place. The result is evaluated by using ANSYS which is an engineering software used for real life application simulation and analysis. This research could inspire other designers and engineers get to know more about Mobius shape structure. Then, this concept is able to apply in different field as much as possible. For engineering, the research required the study of mechanical vibration and its isolation method. In order to generate better efficiency, reducing the vibration can minimized the energy lost in the entire system.

This study is mainly aimed for identifying the relationship between damping coefficient and structural parameters of a Mobius shape structure. In ANSYS, the vibration analysis is carried out by modeling the building foundation system. Originally, a helical spring is used as the foundation system but now is replaced with Mobius foundation which can provide more vibration isolation to the building. Also, rubber pad is located in the middle of the Mobius foundation to increase the damping effect to the building structure. Hence, the vibration will reduce further. Besides, the structural properties of MSS also played an important role in reducing vibration effect. For examples, the aspect ratio of MSS is referred to the length and width ratio of MSS which is stated as 2π by Starostin [1]. However, Korhonen used an aspect ratio of 4 to build his MSS [3]. A best design of MSS is recommended after understanding the relationship between the structural properties and damping coefficient of a MSS that enhances vibration isolation.

The boundary of this project is focused on the numerical modal approach. After modeling out the design by using SOLIDWORKS, the structure will be analyzed in term of its structural properties and damping coefficient. ANSYS Workbench is used to conduct the testing whether a MSS can sustain the real world forces from the buildings and wind load. Finite element analysis (FEA) method is used for determining how a MSS react with vibration and real world forces.

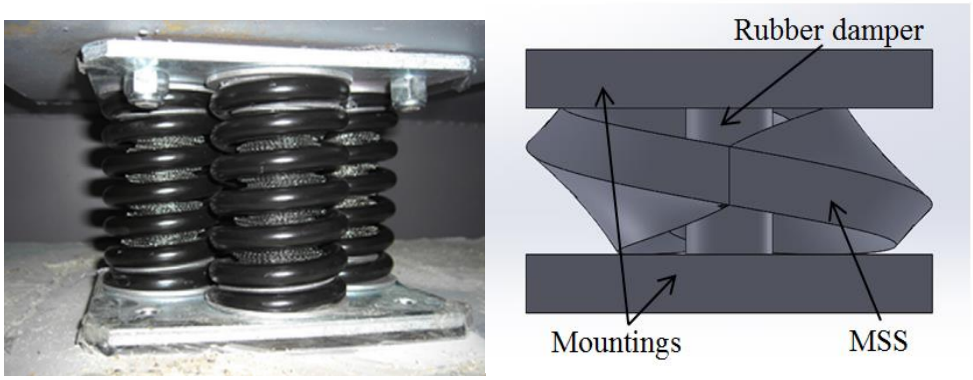
2. Methodology

A MSS design is modeled out in SOLIDWORKS. Then, MSS model is used to analyze and evaluate based on its deformation and vibration. ANSYS Workbench is used to analyze the MSS model and determine the best MSS design. The structural properties such as Young's modulus, thickness, aspect ratio (length to width ratio) and damping ratio are inputted into the model and undergo meshing. This project can be analyzed in two approaches which are numerical approach and numerical modal approach. Numerical approach is focused in modal analysis and harmonic response analysis that carried out in ANSYS while the numerical approach is calculated the solution in MATLAB.

2.1 Design Parameters of a Mobius Shape Structure

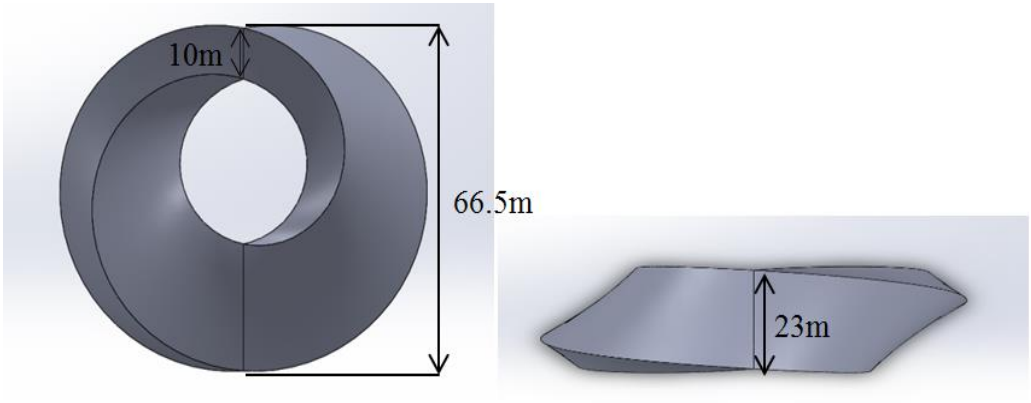
In the design stage, Mobius shape structure for the building foundation system is affected by a few structural properties such as aspect ratio (length to width ratio), Young's modulus, thickness (height) and damping coefficient. As the aspect ratio increases, the stiffness of the structure will also increase. Young's modulus is a mechanical property of elasticity of the material. It will increase the stiffness of structure as it increases. The damping coefficient is affecting the internal damping of the structure which can reduce the vibration effect. The elastic energy is directly proportional to the thickness of structure. It strengthen the structure and able to absorb higher external forces without deforming or bending. There are two types of foundation systems, which are spring foundation and Mobius foundation. The spring foundation and Mobius foundation system are shown in Figure 1 (a) and (b).

The aspect ratio of the MSS can be set within 6.28 [1]. Hence, the diameter of MSS is set as 66.5m and the width is set at 23m that has an aspect ratio of 2.9. The Young's modulus of the MSS is set as 200GPa. The damping coefficient of MSS foundation system is set as 0.03 [4]. The thickness of MSS is set as 10m. The MSS model is shown in Figure 2 (a) and (b) below.



(a) (b)

Figure 1: (a) Spring foundation system [4] and (b) Mobius foundation system.



(a) (b)

Figure 2: (a) Top view and (b) side view of MSS.

2.2 Numerical Analysis of a Mobius Shape Structure

2.2.1 3D Modelling of a MSS and File Exporting from SOLIDWORKS to ANSYS

The Mobius shape structure is modeled by using SOLIDWORKS. Firstly, a rectangle is drawn to represent the width and thickness of MSS. Then, a curve line is drawn in the middle of the rectangle to represent the diameter of the MSS. Next, sweep feature is used to generate out the twisting pattern of MSS and the twisting angle is set as 180°. After finish the MSS design, the file is saved as Parasolid (*.x_t) format so that it can export from SOLIDWORKS to ANSYS Workbench.

2.2.2 Inputting Material Data and Meshing

After the file is exported to ANSYS, the material data is needed to fill in from the engineering data sources. There are 2 types of material used in the MSS foundation system which are structural steel and rubber. The MSS and its mounting are made of structural steel while the rubber pad is made of small strain rubber that acted as a damper for the foundation system and located in the middle of the MSS.

Meshing is applied to the model to calculate the deformation rate when the external force is applied. It has a lot of 'nodes' that help to solve the governing equation using FEA method. A total of 4 bodies (two mountings, MSS and rubber pad) are meshed in hex dominant method and automatic method. Hex dominant method creates surface mesh with mapped face meshing and edge sizing for refinement of MSS. Automatic method is used and generated an accurate solution for simple model structures (mountings and rubber pad). It is not recommended to mesh with Multizone and tetrahedron method because the solution is not accurate as hex dominant method. The optimum element size for the foundation system is set at the range of 1-5m. It will generate a relatively good quality of mesh to the structure based on the skewness and element quality graph. A higher accuracy of result is generated when the element size is smaller. Foundation A is produced and compared with Mobius foundation. It is consisted of only damper element in the system while a Mobius foundation has both spring and damper elements. The role of foundation A is to determine the deformation without the support of spring element which is referred to the MSS. A 2 m meshing sizing data summary is applied in a Mobius foundation system and a foundation system without Mobius support. The Meshing statistics for both cases are shown in Table 1 below. The meshing models for both cases are shown in Figure 3 and 4.

Table 1: Meshing Statistics of a MSS foundation system

Properties	Statistic Results	
	Mobius Foundation	Foundation A (without Mobius support)
Mesh Nodes	95083	70217
Mesh Elements	20392	14753
Skewness (Average)	0.1214	0.0241
Element Quality (Average)	0.9046	0.9701

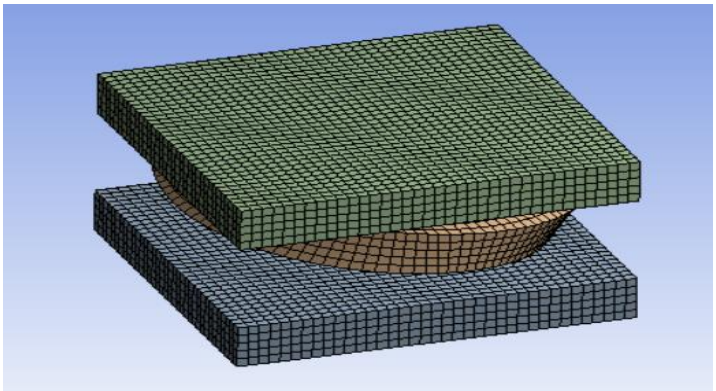


Figure 3: Meshed Mobius foundation system.

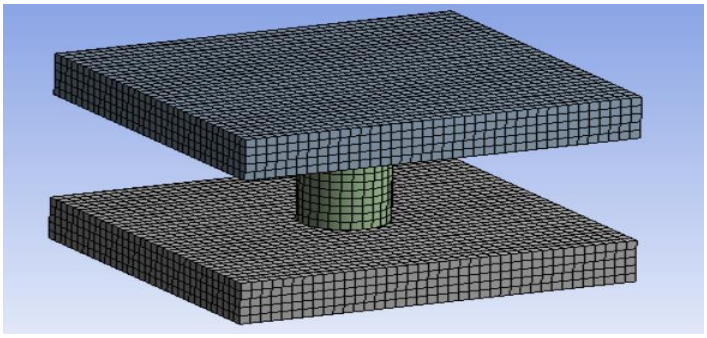


Figure 4: Meshed foundation A (without Mobius support).

Based the element quality in Table 1, foundation A have a better quality than Mobius foundation. There are more elements that are achieved to the maximum of 1 in Mobius foundation. It is due to the amount of perfect hexagonal elements are produced massively in the meshing process. However, Mobius foundation is generated some irregularities in the meshing because of the different shape of structures. These irregularities will affect the final solution of the dynamic analysis so it is needed to refine as much as possible.

From the skewness data, foundation A has a good skewness for the elements. Most of the element is close to 0 and this is because the elements have the equivalent shape by comparing with each other. Thus, it is generated a lower mean in automatic mesh comparing other meshing method.

2.2.3 Boundary Conditions

The boundary condition of this research project is limited in numerical analysis only. Hence, modal and harmonic response analyses are used to generate the numerical results. The result will show how the MSS reacts to a real world force and how much the vibration generates throughout the structure. The building structure that used in this case study is Taipei 101 and the real world force is coming from the weight of building, people, vehicles and wind force. The summation of real world forces is approximately 1.478×10^8N.

Moreover, the material properties of the Mobius foundation system are listed in Table 2 below. The parameter value of these properties will affect the stiffness of the structure and amount of vibration effect. The material used for the mounting and MSS are structural steel which is extracted from general materials under engineering data sources. The rubber pad is made of rubber and its properties are extracted from Mott [5].

Table 2: Material Properties of Mobius Foundation System.

	Density (kg m^{-3})	Young's Modulus (GPa)	Poisson's Ratio
Structural Steel	7850	200	0.3
Rubber	800	0.1	0.499

2.2.4 Modal Analysis

Modal analysis is a common method used to generate the vibration pattern of the structure. It is showed how the structure will vibrate naturally at a specific frequency. It also created the mode shape of the structure that would vibrate at each frequency. Hence, it is a most fundamental dynamic analysis to determine the possibility of deformation occurs.

There are a few benefits of doing modal analysis and one of them is that it is aided in solving solution for other dynamic analysis. It also avoided the resonant vibrations or to vibrate at a specified frequency which could damage the structure and causes harm to human comfort. Moreover, it also gave engineers a concept of how the structure will respond to different types of dynamic loads [6].

During this analysis process, the bottom surface of the mounting is selected as a fixed support that has a direct contact to the ground. Ten total deformation mode shapes are generated and showed different types of deformation patterns that might happen when load is applied to the foundation system.

2.2.4 Harmonic Response Analysis

Harmonic analysis is a technique to determine the steady state response of a structure when a harmonic load is acted on it. It is usually give out the harmonic displacement of the vibrated structure. Furthermore, acceleration, stress and strain also can be determined by using this analysis method to find out how the human comfort and structural fatigue behave at a specified harmonic load and frequency. It is used in designing supports, fixtures and rotating equipment such as engines, pumps and turbines.

It is important to complete this analysis because a good vibration isolator can be generated after detected the resonant response and avoid it if possible. For example, rubber pad is acted as a damper to further reduce the vibration effect. It is also to ensure that the MSS is able to withstand the harmonic load at a certain range of frequencies.

A real world force is added to the analysis setting and same fixed support is applied to the system. The frequency of the system is set from 0 to 10Hz because frequency of a building structure is quite low so that people will not feel much vibration in the building.

3. Results and Discussion

3.1 Total Deformation for a Mobius foundation and without Mobius shape structure foundation

The real world force is applied to the building in vertical axis and transmitted to the foundation system and the ground. The function of the foundation system is to reduce the vibration effect which causes uncomfortable to the people inside the building. In reality, there is spring foundation system that is used for isolating the

vibration. In order to further improve the vibration isolation, Mobius foundation system is introduced and applied for a skyscraper or high rise building such as Taipei 101.

The real world force is mainly referred to the weight force of vehicles, people, building and wind force. Taipei 101 is selected as the case study sample and investigates how good the vibration isolation method (Mobius foundation) to the building is. The building can accommodate at least 10000 people at one time [7]. The amount of car parking is 1200. For the wind speed, a worst case scenario is considered when a typhoon is hitting toward the building at 97 mph [8].

The force is applied on the top layer of the mounting from the building and deformation will occur to the foundation system. The total deformations for foundation system without Mobius and with Mobius are shown in Figure 5 and 6 below.

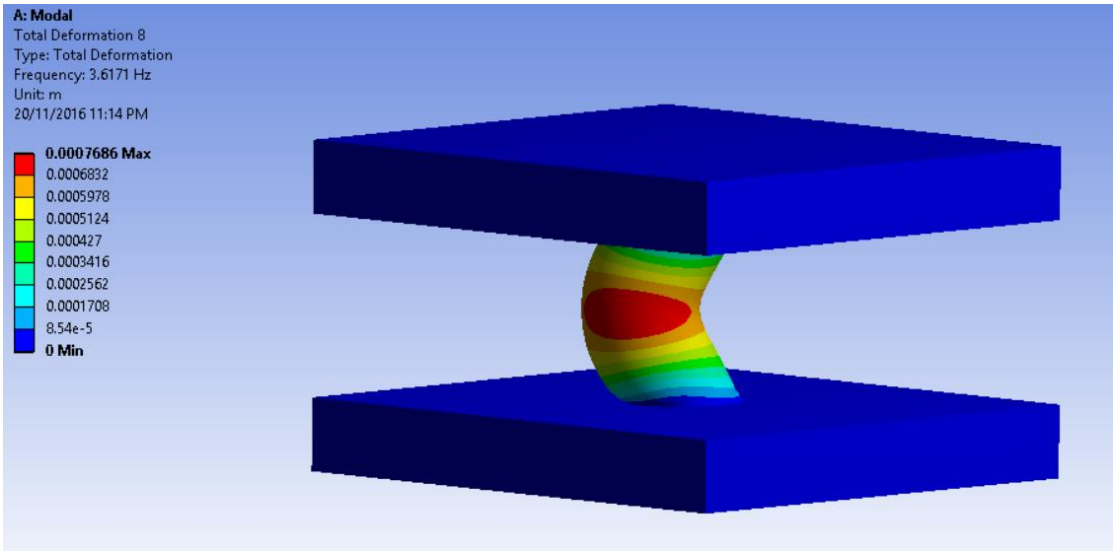


Figure 5: Total deformation for foundation A.

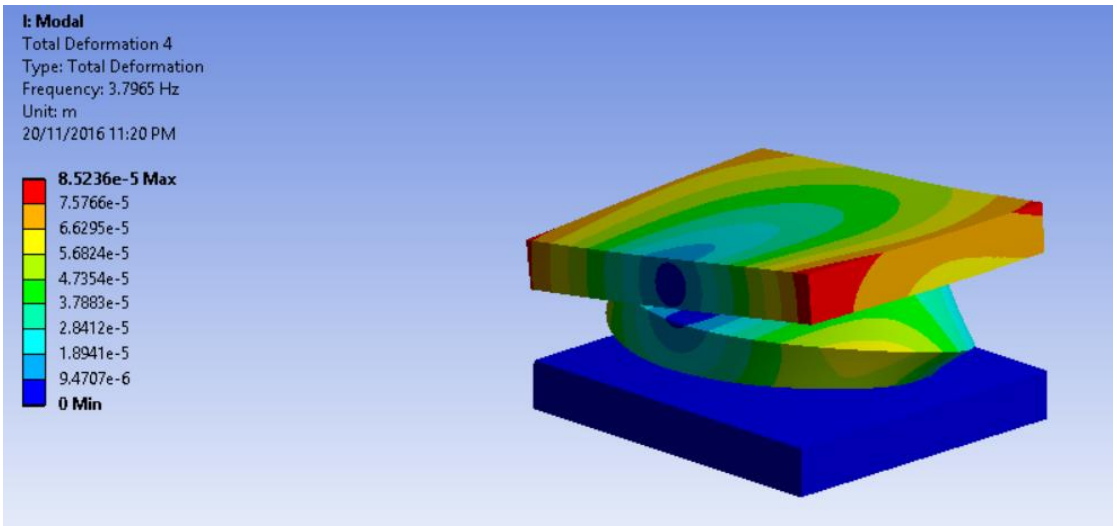


Figure 6: Total deformation for Mobius foundation.

Based on Figure 5 and 6 above, the maximum deformation for foundation A is 0.7686mm while the Mobius foundation is 0.0852mm. The overall deformation of Mobius foundation is lower because the force is distributed evenly from the mounting to MSS and rubber pad that involved 2 bodies. For foundation A, the force is distributed from the mounting to the rubber pad which is only involved 1 body. Thus, Mobius foundation that has both spring and damper elements is able to reduce more vibrate effect and share the pressure from the building forces compared to foundation A.

3.2 Vibration displacement in Y-axis

Vibration is exerted on both foundation systems after the harmonic force is applied. The amount of force will change by time. These changes are caused by the external factors such as wind speed or number of vehicle and people. Hence, it is a dynamic analysis because of the constant changing of force. This displacement analysis allows the designers and engineers to know that what frequency that need to be avoid so that less vibration on the building structure. Figure 7-8 shows that the displacement graphs for both foundations with the changing of frequency. The results will be further explained in section 3.4.

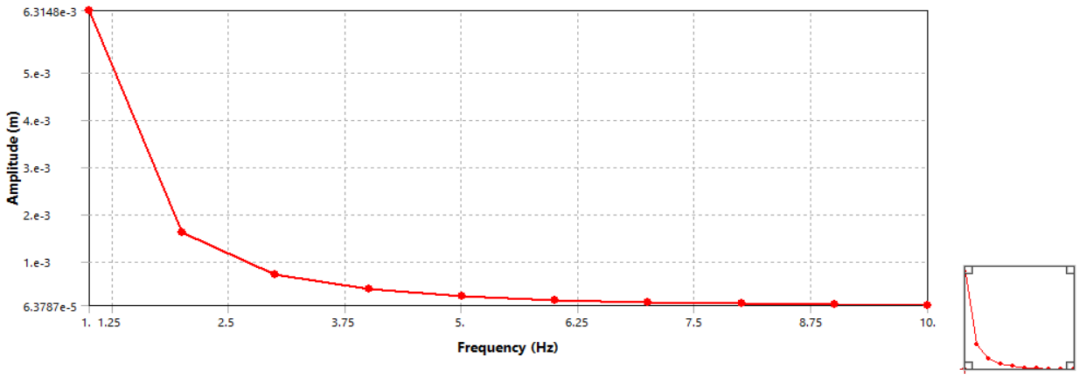


Figure 7: Displacement graph for foundation A.

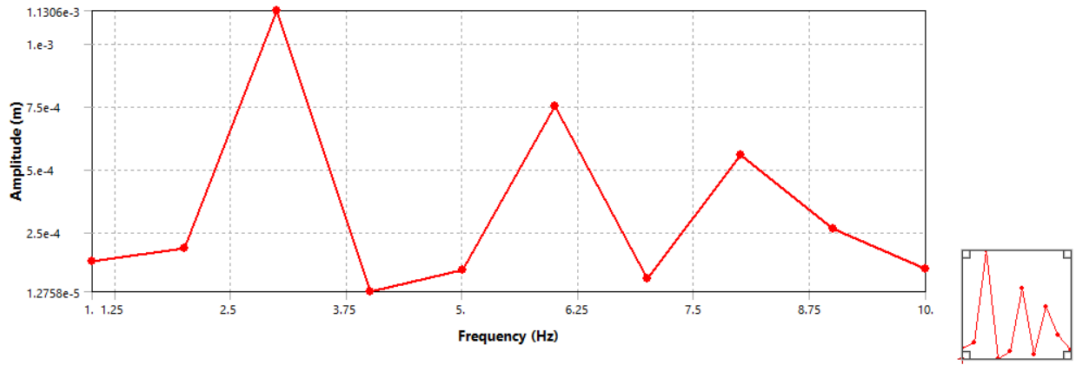


Figure 8: Displacement graph for Mobius foundation.

3.3 Acceleration in Y-axis

Acceleration is aimed to investigate the human comfort inside the building. It is recommended to have a low acceleration so that people will not feel a lot of vibration effect in the building. The acceleration graphs for both foundation systems are shown in Figure 9-10. The results will further explained in section 3.4.

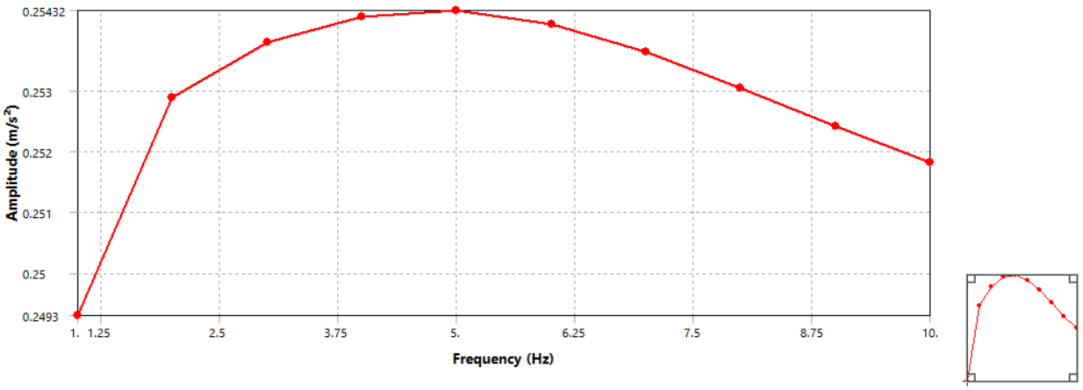


Figure 9: Acceleration graph for foundation A.

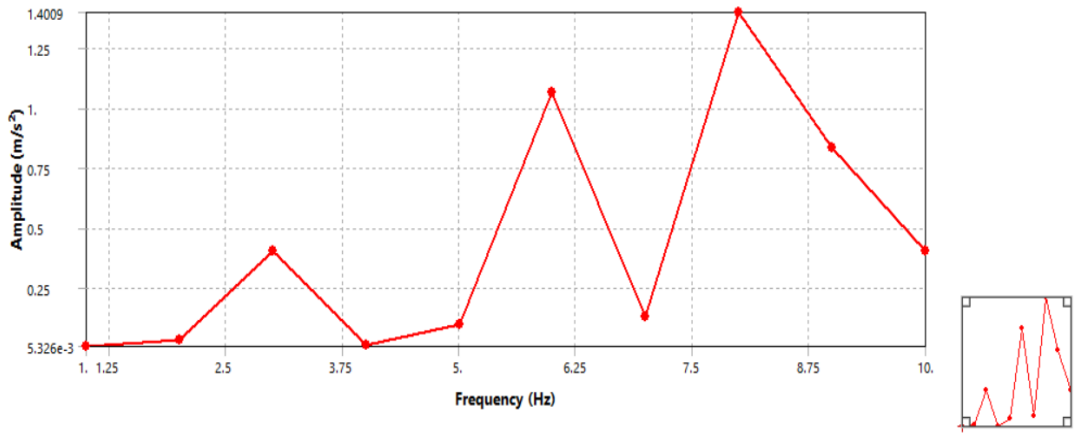


Figure 10: Acceleration graph for Mobius foundation.

3.4 Vibration Nomograph

The displacement of vibration moves in Y-axis is 6.3 mm at 1 Hz for foundation A while 0.135 mm for Mobius foundation. Based on the vibration nomograph in Figure 11, a displacement of 6.3 mm for foundation A is too much and unacceptable for a building because it will cause crack that leads to fatigue. Mobius foundation has a low displacement of 0.135 mm that is not causing any damage to the building. Hence, the vibration effect in Mobius foundation is lesser than foundation A.

Moreover, the maximum acceleration for foundation A is 0.2493 m/s^2 at 1 Hz while Mobius foundation has a maximum acceleration of 0.0053m/s^2 at 1 Hz. According to the vibration nomograph, Mobius foundation is under the threshold of perception for human. It means that people inside the building will feel comfortable because of the low acceleration and it can be further improved by adding better

damper. The acceleration for foundation A is too huge and it may cause a huge disturbance to the human comfort.

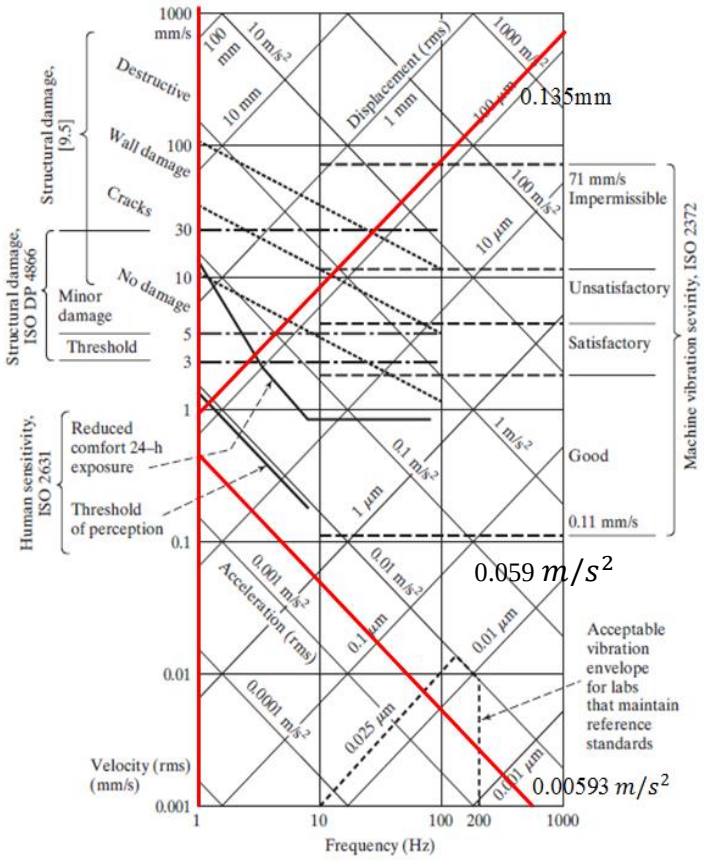


Figure 11: Vibration nomograph [9].

3.5 Aspect Ratio

Figure 12 below shows the graph of vibration displacement against frequency when different aspect ratio of MSS is used. The building foundation will vibrate in a harmonic motion which is in sinusoidal wave pattern and oppose the direction of vibration from the building. Thus, the building will not exert much vibration due to the vibration isolation from the Mobius structure and rubber pad. Mobius structure acted as a spring element in the foundation system and minimized the vibration.

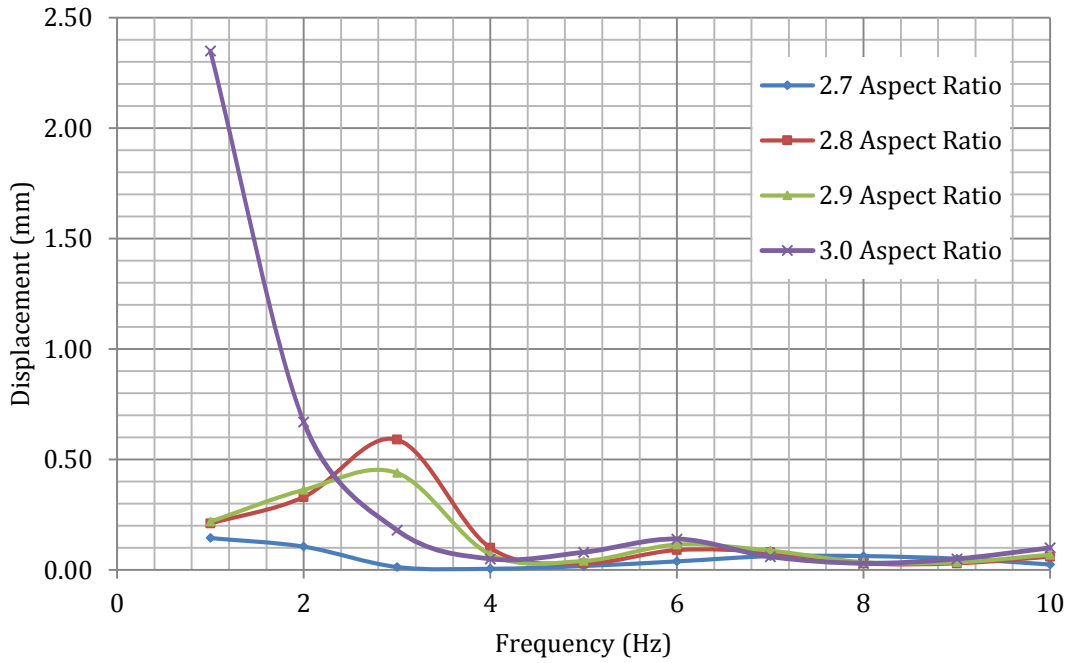


Figure 12: Graph of displacement against frequency with different aspect ratio.

The optimum aspect ratio for Mobius foundation is 2.9 or lesser. From the graph above, the highest vertical displacement for aspect ratio 2.9 is 0.44mm at frequency of 3 Hz. The frequency for reaching the maximum displacement in 2.9 aspect ratio is different from 3.0 aspect ratio because it vibrated at its natural frequency which has the highest chance to cause resonance and needed to be avoided. Hence, the aspect ratio is concluded to be less than 2.9 or equal to 2.9.

3.6 Damping Ratio of Rubber Pad

Figure 13 shows the graph of displacement against frequency when different damping ratio is used. Rubber pad that located in the middle of Mobius foundation is acted as a damper element and helped to reduce the vibration shock from the building. The damping ratio is inversely proportional to the vibration displacement. Thus, a damping ratio of 0.01 will have the highest vibration displacement while 0.9 damping ratio will have the least amount of vibration according to the graph below. Since the damping ratio of foundation system is hard to identify accurately, thus it is better to assume it as small as possible. If the damping ratio is applied to the foundation system and the displacement is exceeded 1mm, the Mobius foundation is considered as a failure because it went beyond the building structure vibration threshold in the vibration nomograph.

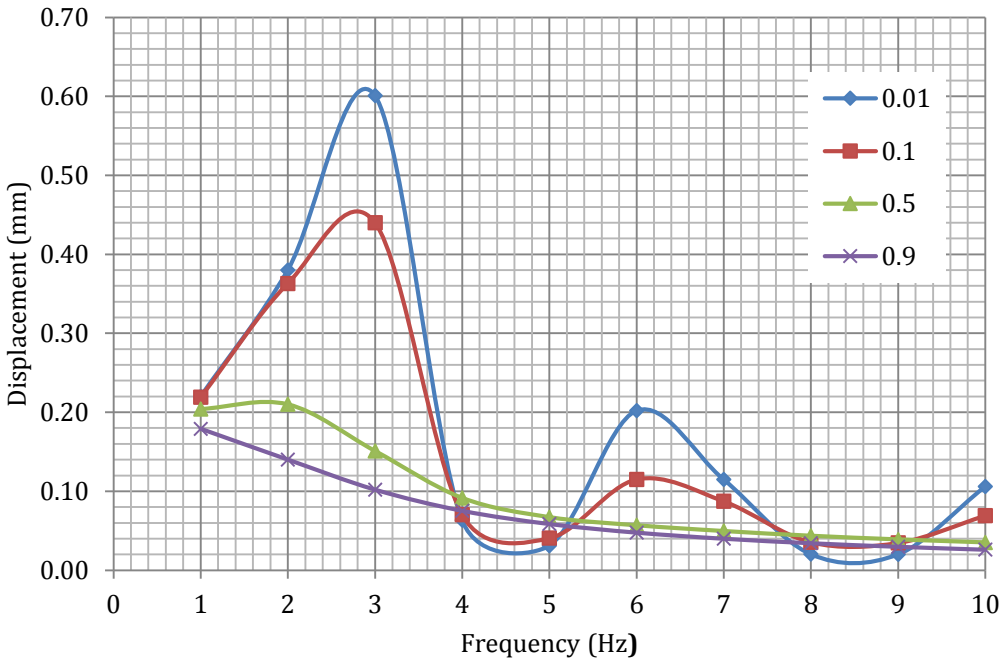


Figure 13: Graph of displacement against frequency with different damping ratio.

3.7 Thickness of MSS

Figure 14 shows the graph of displacement against frequency when different thickness of MSS is used. The increment of thickness of MSS will cause the vibration displacement to decrease. A thick MSS is able to absorb more vibration shock from the building without breaking its elastic limit. Hence, a 10m thick MSS is the most suitable for foundation system based on the graph below. It deformed the least compared to other thickness. A MSS with 5m thickness is too thin for a foundation because it is too fragile to absorb shock from the building. Hence, it has the highest displacement (2.6mm) among all the Mobius structures.

Although the 15m and 20m MSS have the greater value in term of thickness, however they are still exceeding the building structure threshold. As a result, they are losing the elasticity of the material and failed to return to its original shape after the deformation. They are able to withstand the vibration at the initial frequency, but once the frequency or time get higher and longer, it will not have the same performance as before.

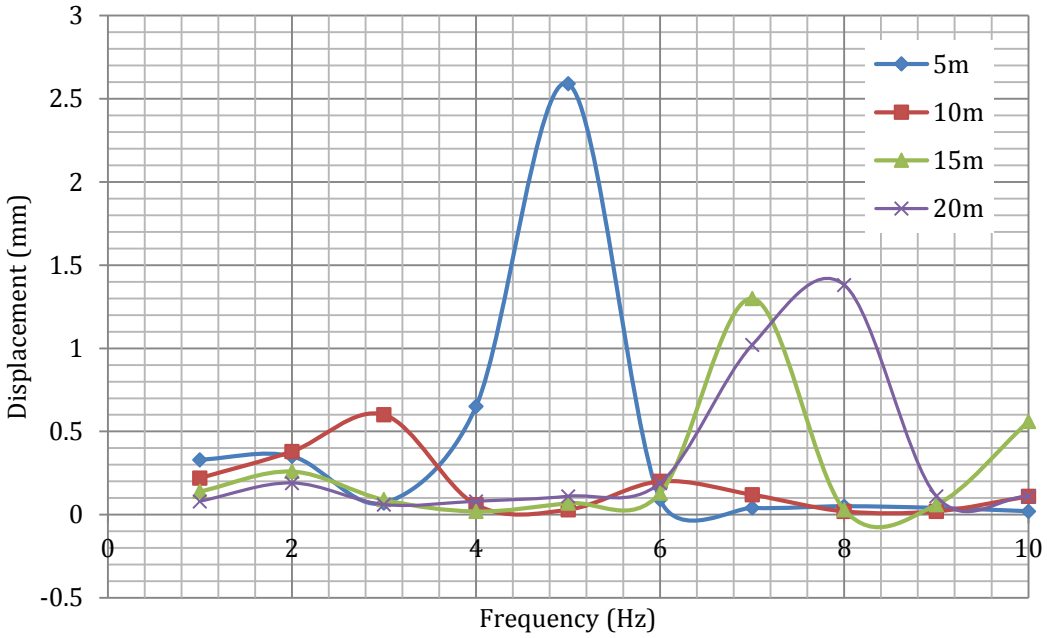


Figure 14: Graph of displacement against frequency with different thickness

3.8 Material Stiffness

Table 3 shows the different types of materials and its maximum vibration displacement. All materials have their own mechanical properties such as Young's modulus, Poisson ratio, ductility and tensile strength. Young's modulus and Poisson ratio are taken consideration for determining the material stiffness. The material stiffness increases as the Young's modulus. Higher stiffness material can resist the deformation of structure when an external force is applied. There are a few materials suggested in this numerical modal analysis which are structural steel, aluminum alloy, copper alloy, gray cast iron, stainless steel, titanium alloy, S15 carbon steel and Sandvik 20C steel. Each of the material is tested in term of its stiffness and determined the amount of deformation of MSS. Based on the Table 3 below, titanium alloy has the highest displacement among all the materials. Thus, it is the weakest material to absorb shock from the building and not suitable for a building foundation. The suitable materials for making a Mobius foundation are copper alloy, S15C carbon steel, structural steel and Sandvik 20C steel. Their vibration displacements are less than 1 mm and good in absorbing shock from the building.

Table 3: Type of materials and its maximum vibration displacement

Materials	Young's Modulus (GPa)	Poisson Ratio	Maximum Displacement (mm)
Structural Steel	200	0.3	0.79
S15C Carbon Steel	208	0.3	0.89
Sandvik 20C Steel	210	0.3	0.73
Aluminium Alloy	71	0.33	1.17
Copper Alloy	110	0.34	0.94
Gray Cast Iron	110	0.28	1.57
Stainless Steel	193	0.31	1.41
Titanium Alloy	96	0.36	1.72

3.9 Verification and Validation of Results

The verification for aspect ratio is comparing the numerical modal analysis result with literature review. The optimum aspect ratio is 2.9 from the simulation in ANSYS while Korhonen [3] said that Mobius should have an aspect ratio of 4 or more. Thus, this project is rejected the statement from Korhonen as the aspect ratio can be set below 4. However, it accepted the statement from Starostin [1] that the aspect ratio is set within 6.28.

Damping ratio is one of the structural parameter for Mobius foundation. The damping ratio in this project is set as 0.01 to determine the maximum vibration displacement. Based on the research from Ulgen [4], the damping ratio for his spring foundation system is 0.03 which is very close to the simulation result. It is verified that MSS also can be used as a building foundation instead of spring foundation and the vibration effect is reduced gradually with Mobius foundation.

The thickness of MSS is set as 10m in this project and it cannot be verified due to limitation of knowledge and resources. However, the effect of thickness is shown in Figure 14 and proved that it is also affecting the value vibration displacement. Last but not least, the material used for making a good Mobius foundation is Sandvik 20C steel. A normal spring foundation is usually made of carbon steel which is weaker than Sandvik 20C steel [4]. The damper element used in this project is a rubber pad which is same as the research from Ulgen. It has a higher damping capacity at high frequency compared to steel type isolators. Furthermore, the cost of Sandvik 20C steel is lower compared to other materials. According to the current market price, the cost for making a Mobius foundation is around RM 0.9 million while the market price of S15 carbon steel is around RM2.5 million. Plus, it is better to choose Sandvik 20C steel because the manufacturing factory is located at Singapore which has the benefit of time saving and less delivery cost.

Moreover, the result obtained from ANSYS is validated with the numerical result from MATLAB Simulink. The Simulink set up are shown in Figure 15, 16 (a) and (b) below. The Simulink result is given in Figure 17.



Figure 15: The block parameter used in MATLAB Simulink

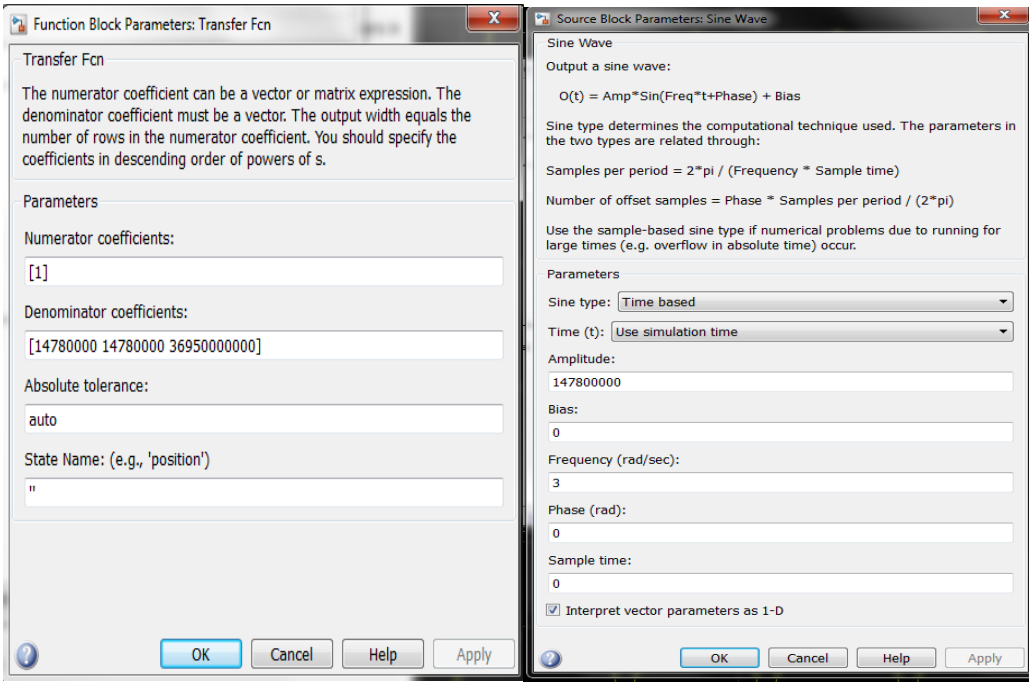


Figure 16: (a) Set up of transfer function and (b) Set up of sine wave for the system

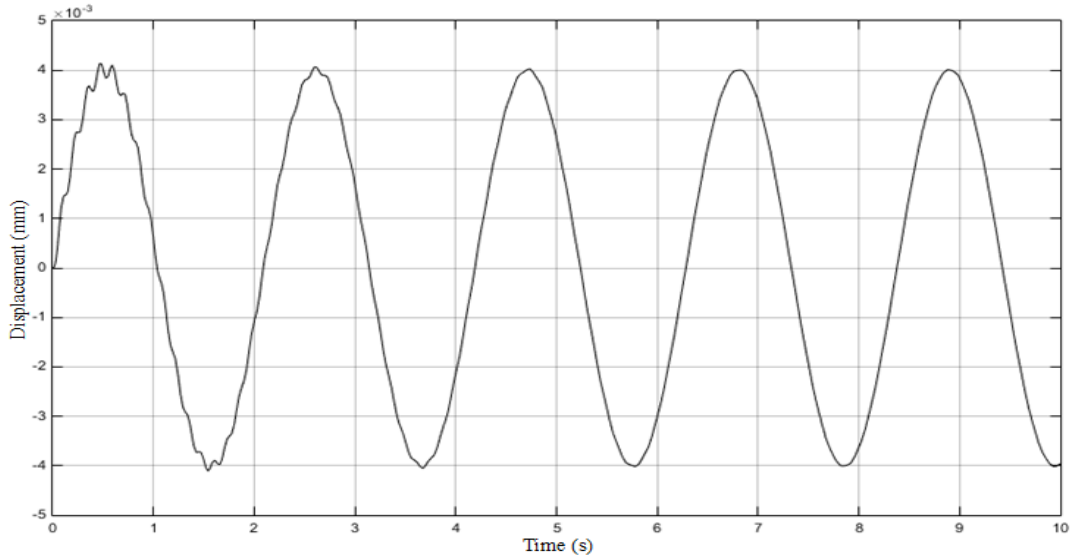


Figure 17: Graph of displacement against time (MATLAB Simulink method)

Based on graph above, the foundation system has a displacement of 4mm as the time goes on. It is unacceptable because it is exceeded the building threshold of perception and caused crack or wall damage to the building and its foundation according to the vibration nomograph. Hence, it is considered that this method is not accurate as numerical modal analysis in ANSYS due to some limitations. The reason that causing this inaccurate result is might be that MATLAB did not considered the overall model of Mobius foundation. It means that no mounting and rubber pad existed in the foundation system. Plus, the material stiffness is also not considered in MATLAB Simulink. In short, numerical modal analysis has higher accuracy and is recommended for this research project.

4. Conclusion

In conclusion, Mobius foundation is better than foundation A. The results reflect significant differences for both foundations in term of vibration displacement and acceleration. The amplitude of displacement and acceleration at 1 Hz for Mobius foundation is acceptable and within the human threshold of perception that the people inside the building feel comfortable since the vibration effect causes no damage to the building. This proves that Mobius foundation is a good vibration isolator and has a good market value. The total deformation of Mobius foundation is relatively small so it could have a longer lifespan.

SOLIDWORKS software is used to create the 3D model of the foundation system. The design parameter such as aspect ratio, thickness, damping ratio and material stiffness are manipulated to determine the optimum foundation design. FEA method is selected as the technique to simulate and solve the vibration equation of the system. The material properties and drag coefficient are inputted to the system so that the solution will be more accurate to real world application. The meshing method for MSS is hex dominant method in the analysis. It creates a better meshing of foundation after the refinements of edge sizing and face mapped mesh are made. Modal and harmonic analysis are used to determine the total deformation of the foundation system and the vibration effect to the buildings and people. The boundary conditions such as force, fixed support and damping ratio are inputted to the system. These values are used to simulate the system in a real world scenario so that the result is closer to the actual value and more accurate.

The relationship between the design parameters and the damping coefficient are determined to build out a good Mobius foundation that minimizes vibration effect from the building structures. The structural parameters that defined a good MSS are aspect ratio, thickness, damping ratio and material stiffness. From the numerical modal analysis, the optimum aspect ratio is determined as 2.9. Moreover, the thickness of MSS should set as 10m. Sandvik 20C steel is used to build the MSS which has a good elastic modulus to withstand the force from the building and wind load. All the results are validated with vibration nomograph and MATLAB Simulink. The vibration displacements for numerical modal analysis are within the building threshold (1mm) that is under safety region and no fatigues or cracks are occurred. The result from MATLAB Simulink is less accurate than ANSYS modal analysis due to some limitations. The errors are caused by the inconsideration of the whole foundation design model and also design parameters such as material stiffness. Thus, numerical modal analysis in ANSYS is recommended for this research project.

This research project is lacked of validation because there is no experimental value involved. Thus, the second recommendation is to conduct an experiment that compared Mobius and spring foundation in term of total deformation and vibration displacement. It is good to validate with a real life engineering application to prove that a Mobius foundation has better vibration isolation than a spring foundation. The experiment is scaled down into small sizing due to huge amount of cost involved and the big foundation model. The experiment set up is started from a force is applied on both Mobius and spring foundations by using vibration shaker. Then, accelerometer is set on both foundations to determine its vibration displacement. This main objective

of this experiment is to investigate the vibration isolation performance in both foundations. Hence, it is proposed as a future work by the student for this project.

References

[1] E.L. Starostin, "The Shape of a Mobius Strip". *Computation, Modelling and Theory*, 6, pp. 563-567, 2007.

[2] LDS Ltd, *"AN011 Basics of Structural Testing Analysis"*, LDS-Dactron, 2003.

[3] T. Korhonen and P. Koskinen, "Electronic structure trends of Mobius grapheme nanoribbons from minimal-cell simulations". *Computational Materials Science*, Vol. 81, pp. 264-268, Jan 2014.

[4] D. Ulgen, "Measurement of ground borne vibrations for foundation design and vibration isolation of a high-precision instrument". *Measurement*, Vol. 93, pp. 385-396, Nov 2016.

[5] P.H. Mott, "Limits to Poisson's ratio in isotropic materials". *Phys. Rev. B*, 132104, Oct 2009.

[6] ANSYS Inc., "*Shock & Vibration using ANSYS*", Kelly Morgan, 2015.

[7] The China Post, "Taipei 101 expects occupancy growth to slow on global recession", January 2009. [Online]. Available: http://www.chinapost.com.tw/taiwan/business/2009/01/23/193411/Taipei-101.htm [Accessed: Oct. 17, 2016].

[8] Dennis C.K. Poon, "Structural Design of Taipei 101, the World's Tallest Building". *Structural Engineering*, 2004.

[9] Singuresu S. Rao, *"Mechanical Vibrations"*, 5th Edition. Upper Saddle River: Prentice Hall, 2011.

eureca 2016 – Conference Paper
Paper Number 2ME10

Novel Electrospun Biocomposite Tissue Engineering Scaffold

Chong Eu Jin[1*], Yong Leng Chuan[2]

[1]*School of Engineering, Taylor's University, Malaysia*

*eujin.chong@sd.taylors.edu.my

Abstract

Tissue engineering is an interdisciplinary field of research to create tissue from the cell. The ultimate goal of tissue engineering serves to repair, restore damaged tissue or organ due to accident or disease. The material that helps the speed up the cell regeneration is called scaffold, it usually comes in a matrix-form that insert into the organ that is damaged. Tissue engineering scaffold is made out of biopolymer nanofiber as it is suitable to increase the *bioactivity* and decomposed to feed the cell after a 6 to 24 months. The main purpose of this research will be analyzing the crystallity of the polylactic acid and copolymer (polylactic acid and polycaprolactone) materials which is synthesis in lab. An additional material, bioceramic Hydroxyapatite (HA) will be mix with copolymer to form a nanocomposite material. Three polymers had been successfully synthesed and tested which are two cyclic type Poly (D-Lactic Acid) (PDLA), cyclic type Poly (L,-Lactic Acid) PLLA as well as blended copolymer of Poly-Caprolactone and Poly-Lactic Acid (PCL-PLA). Electrospinning process is executed to produce a homogeneous and uniform long fiber and for the fabrication of tissue engineering membrane from the synthesized materials. Parameters of electrospinning process will affect the physical property of the generate fibers, this project also aims to vary the solution and processing parameter of the electrospinning to determine a suitable setting. All four tissue engineering membranes fabricated is to be sent to scanning electron microscope (SEM) to analyze the morphological fiber structure such as the formation of beads, the diameter of the fiber as well as pores.

Keywords: Tissue Engineering Membrane, Scaffolds, Electrospinning, Biopolymers, Crystallinity.

1. Introduction

The field of tissue engineering and biomaterial have been rapidly improving since the past decades. Scientist, researchers, and engineers kept improving this medical field to provide a better remedy [1]. Tissue engineering studies the tissue system and produces temporary replaceable biopolymer that is designed to mimic the structure tissue system and also serve as interaction to the cell for regeneration.

This biomaterial is rather commonly referred as a scaffold. The scaffold can hold various kind of matrix shape bridging the damaged tissue to enable the cell attachment proliferation, delivering cell, allow diffusion nutrients and oxygen and improve the growth factor. The scaffold is made out of micro or nanofibrous biomaterial which is acceptable and suitable by the tissue system as it is biocompatible and biodegradable. Two most widely produced biopolymer types of fiber scaffolds are Poly (ε-caprolactone) (PCL) and Poly-lactic acid (PLA) [2].

The nanoscale fibrous scaffold can be fabricated by several methods like electrospinning, solvent casting, fiber bonding, phase separation and others. Electrospinning process is the most common approach to fabricate due to its relative simplicity [3] for studying and analzying. Solvent casting does not produce thin fiber instead it uses casting and evaparative method to build porous scaffold, varying the fibers properties will never be easy. While method has complicated method and also focusing on building scaffold. Electrospining does not instantly produce scaffold instead of jet of fibers is produced slowly from the syringe pump to the collector. The word electrospinning is a combination of two techniques which is electrospray and spinning process. High voltage power supply is being induced to nanocomposite solution in the syringe pump which leads to a jet of charging out from the tip of the cone traveling towards the rotating metal collector as depict on Figure 1-1 below [4-5].

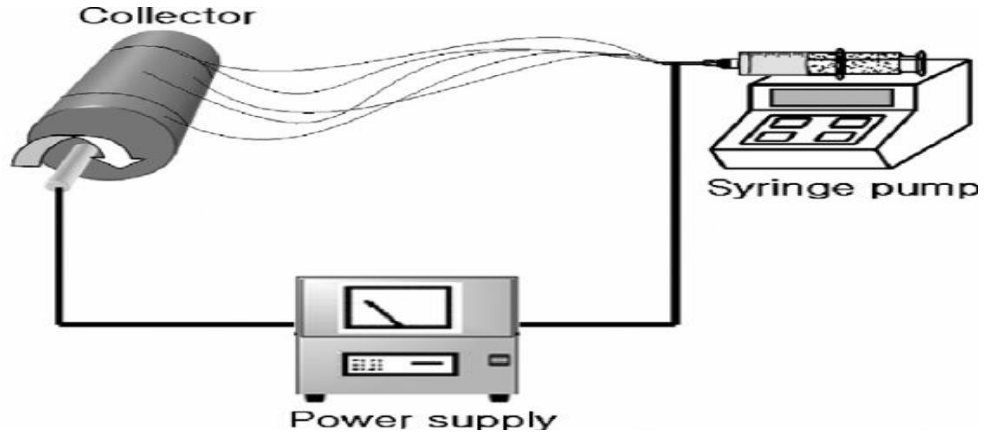


Figure 1. Electrospinning system

This project will carry out the electrospinning process to produce several fibers for studying purpose. Three different polymer and one bioceramic material will be used to fabricate the tissue engineer membrane and to be proceed with studying and comparing the physical characteristic as well as mechanical properties of each fiber. The project aims to generate a continuous and uniform structural. Hence, electrospinning parameter control is a crucial factor to this project as well. In one previous study done by Patrício shows that the copolymer, PCL/PLA scaffold was able to yield a compressive modulus strength of 146.5 ± 14 Mpa and maximum stress of 18.5 ± 1.3 Mpa [6].

For this research project, one of the polymer is a copolymer, PCL-PLA, blended around early January of 2016 in Shizuoka University. While the other two is novel polymer that had been synthesized by using the ring opening polymerization technique in Shizuoka University

early of 2016 January. The novel polymer is cyclic type Poly (D-Lactic Acid) and cyclic type Poly (L,-Lactic Acid).

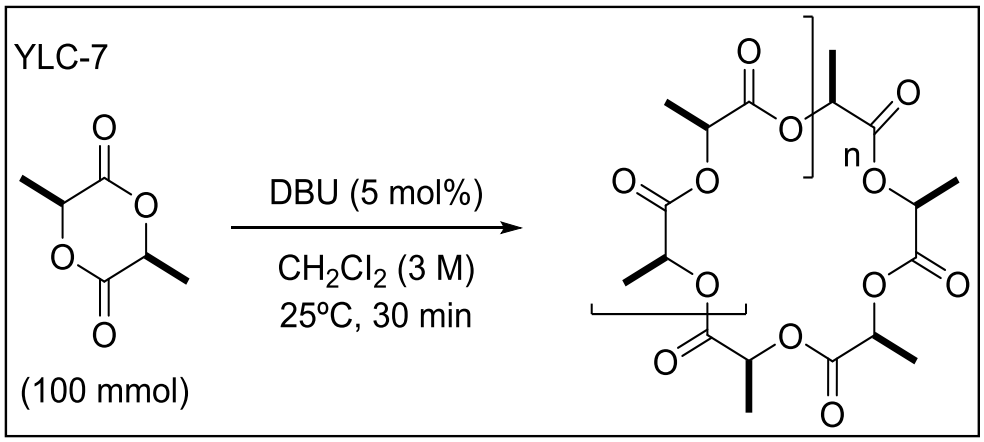


Figure 2. Cyclic type Poly (L,-Lactic Acid) monomer

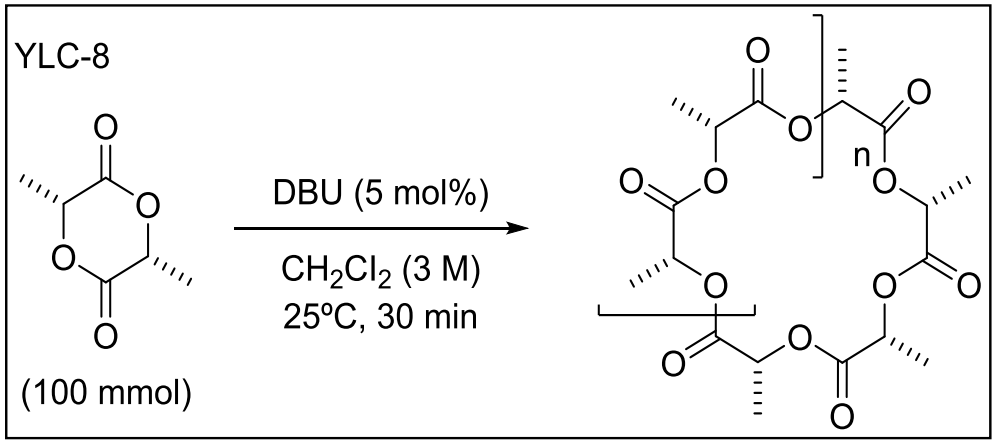


Figure 3. Cyclic type Poly (D,-Lactic Acid) monomer

2. Research Methodology

In Figure 3-7 below illustrate the flow chart of this project. This flow chart describe clearly on author project process.

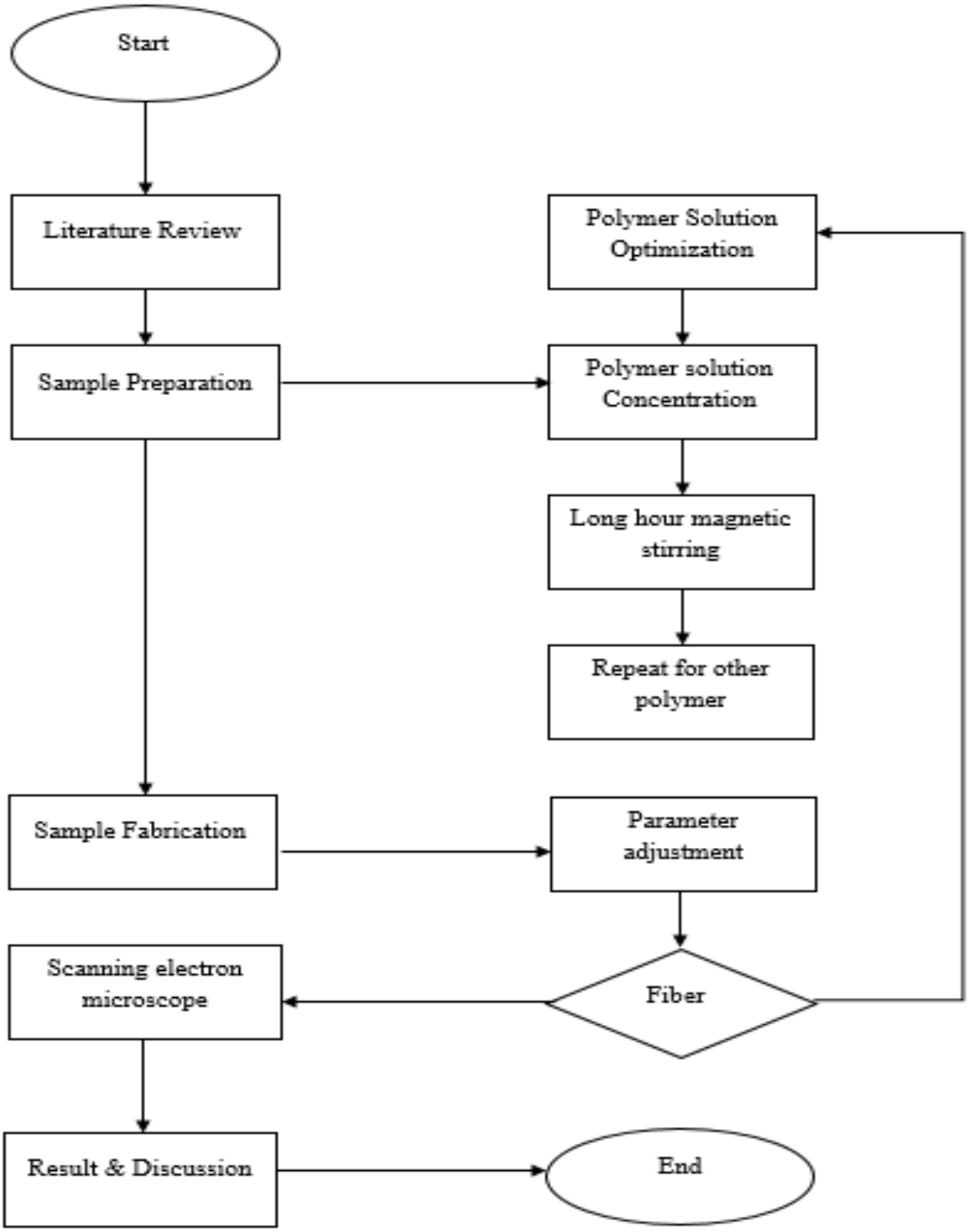


Figure 4. Research methodology flow chart

This project research is an experimented based project in which there are one blended copolymer, and two novel biomaterial which are being used in this project research. This experiment main research objective is to be able to produce a tissue membrane through an electrospun machine follow by determining each of the polymer fibers mechanical properties. Below Table 1 display few information about the novel cyclic polymer for this research project.

Table 1. Details of novel polymer

Novel polymer	Mn	Mw	PDI	Optical purity /%ee	Melting point (˚C)
Cyclic D type PLA	8400	16800	2.01	88.1	150
Cyclic L type PLA	3300	5500	1.67	71.6	N/A
PCL-PLA	22200	33400	1.5	94.4	150

1) 2.1 Sample Preparation

The sample preparation is about preparing the polymer solution for the electrospinning process. Polymer solution is produced by having a solute and solvent mix together and leave it for long stirring hour through magnetic stirrer. Since this is novel research project, there will be a lot of optimization on this sample preparation to attain an ideal case concentration which the polymer solution viscous flowing type. The concentration in preparing this polymer solution is calculated in unit of wv%, meaning that it concentration percentage is measure in weight (g) of polymer per 100 ml unit of solvent.

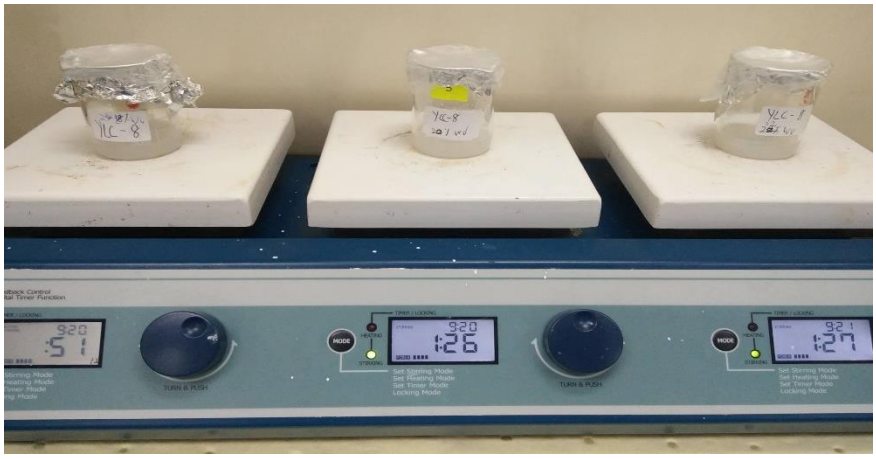


Figure 5. Polymer solution prepare through a magnetic stirrer process

The formula of calculating solution concentration percentage can be calculated with refer to Eq (1) below:

$$\text{Concentration percentage} = \frac{weight\ of\ solute\ (Polymer)}{Final\ mixture\ volume} \quad (1)$$

By rearranging Eq (1) expressing in the term of weight of solute:

$$\text{Weight of solute (polymer)} = \frac{Concentration\ Percentage}{Final\ mixture\ volume} \quad (2)$$

In the first attempt of this research project sample preparation, polymer solution concentration were set to be 10% wv. In a volume of 10ml set, each of all three polymer need the weight of 1g of solute to mix with a solvent, N,N-

Dimethylformamide (C_3H_7NO) in order to obtain a polymer solution concentration on 10% wv. These mixture undergo through a magnetic stir process for one hour duration. DMF was selected as a solvent due to its high dielectric constant and solubility [11]. A 20% wv concentration was prepared with one hour of stirring for observation.

2) 2.2 Electrospinning Mechanism

The electrospinning mechanism consist of few devices such as syringe pump, syringe, collector and power supply. There are a total of three process parameter can be vary during the fabrication. First is the distance between the syringe needle tip to the collector was 15cm - 25cm. Secondly, the syringe pump NE-1000 model with flow rate setting range from 0.7 – 1.5 ml/h. And last of all the voltage power supply has been varied around 15 -30 kV. The only parameter remained same throughout the entire experiment is the size of the needle of 21Gx40mm. Any form of fiber is deposited at the collector which wrap by an aluminum foil.

3) 2.3 Optimization

Polymer in this research played the most important role. An ideal of polymer solution should be flowing vicious liquid but not a gel-like [7]. All preparation is stir with a RPM of 200, due the solvent used is DMF which is flammable and hazard to health, the entire sample preparing process to be conducted in the fume hood with no direct heat apply. While the fabricating process has to execute vigilantly due to high voltage.

First Attempt

Table 2. First attempt of optimizing

Polymer	Concentration (wv%)	Distance between (cm)	Voltage (kV)	Flow Rate (ml/h)
PCL-PLA	10%	15 cm	22 kV	0.8 ml/h
Cyclic PLLA	10%	15 cm	22 kV	0.8 ml/h
Cyclic PDLA	10%	15 cm	22 kV	0.8 ml/h

Second Attempt

In the second Attempt, solvent Dichloromethane (DCM) was mixed with Dimethlyformamide with ratio of (30/70) to reduce the surface tension and decrease the volatility [8]. The stirring process took up a total of 15 hours with first day 6 hours follow by a break of 15 hours and continuing on second day 9 hours. The fabrication was executed third day.

Table 3. Second attempt of optimizing

Polymer	Concentration (wv%)	Distance between	Voltage (kV)	Flow Rate (ml/h)

		(cm)		
Cyclic PDLA	18%	15 cm	22 kV	1.25 ml/h
Cyclic PDLA	20%	15 cm	22 kV	1.3 ml/h
Cyclic PDLA	22%	20 cm	30 kV	1.7ml/h

Third Attempt
Solvent DCM was mixed with DMF with ratio of (30/70), summing up to volume of 7ml. The stirring process took up a total of 20 hours with first day 8 hours follow by a break of 15 hours and continuing on second day 8 hours, another break 15 hours of break and 3 hours on the third day, the fabrication was executed on the third day.

Table 4. Third attempt of optimizing

Polymer	Concentration (wv%)	Distance between (cm)	Voltage (kV)	Flow Rate (ml/h)
PCL-PLA	12%	20 cm	26 kV	1.1 ml/h
PCL-PLA	15%	20 cm	26 kV	0.8 ml/h
PCL-PLA	18%	20 cm	25 kV	1.2 ml/h

Fourth Attempt

Solvent DCM is mix with DMF with ratio of (75/35) inspired by Huan experiment data and result [8], summing up to volume of 5ml. The stirring process took up a total of 48 hours during the weekend. The fabrication was executed 4 hours after the stirring process. However, reducing solvent DMF will result in decreasing the viscosity and dielectric constant.

Table 5. Fourth attempt of optimizing

Polymer	Concentration (wv%)	Distance between (cm)	Voltage (kV)	Flow Rate (ml/h)
Cyclic PLLA	25%	25 cm	27 kV	0.8 ml/h
Cyclic PDLA	20%	25 cm	30 kV	1.1 ml/h
Cyclic PDLA	22%	25 cm	30 kV	1.1 ml/h
Cyclic PDLA + HA	20%	25 cm	25 kV	0.85 ml/h

4) 2.4 Morphology Study

The sample fabricated on a piece of aluminium foil is kept in a plastic casing to prevent any contamination form external. These morphology can be analyzed by

inserting into Scanning electron microscope (SEM). These sample specimen is initially cut in to small piece to be adhered on a metal stage. The sample surface is then scanned by using the electrostatic and electromagnetics force. The electron detector collect emerging electron from the upper surface specimen and project the zoom in image on the monitor screen. The SEM can magnify a sample specimen up to 100,000 times. However, specimen may burned if is zoom in too much depending on the material of the specimen due to voltage apply. Thus, this SEM process is ought to execute with carefully. The model of this SEM is ESEM (Environmental Scanning Electron Microscope) is named FEI Quanta 400F. High voltage of 10 kV is used.

3. Result & Discussion

3.1 Sample Preparation/Optimization

The first three attempt of sample preparation wasn't able to attain a viscous follow liquid instead all the polymer solution is following with very low viscosity. On top of that, after hours of stirring, the final polymer solution don't appear to be in colorless, translucent characteristic but a cloudy, milky solution. This could mean that the solute is not fully dissolved or other words not homogeneity mixed. This could be the reason of not having sufficient stirring time. On the 4^{th} attempt, the cyclic PDLA solution became a gel like as if the concentration is too thick.

3.2 Electrospinning

Throughout all the attempt, it has never been successful in achieving electrospinning but electrospraying droplet of solution on to the collector and that would be reason why the voltage set high and the distance between the tip and the collector is long to allow the solvent to be evaporate. In fact, the solution at the tip is not able to Taylor cone shape. Figure 6 shows the behavior of Taylor cone when voltage is low.

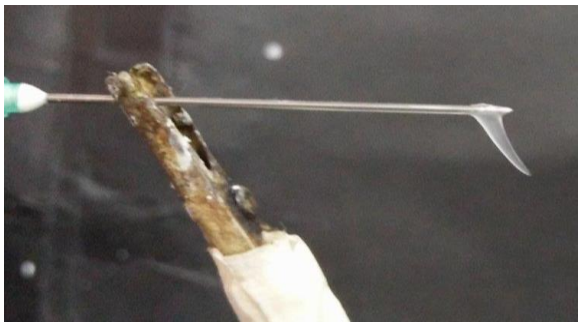


Figure 6. Unwanted Taylor cone

Besides that, Figure 7 illustrate a presentation of electrospraying and electrospinning [9] which explain solution concentration below the critical entanglement is reason of failure in obtaining fiber. In short, all attempt of preparing polymer solution fall under the electrospray beads region.

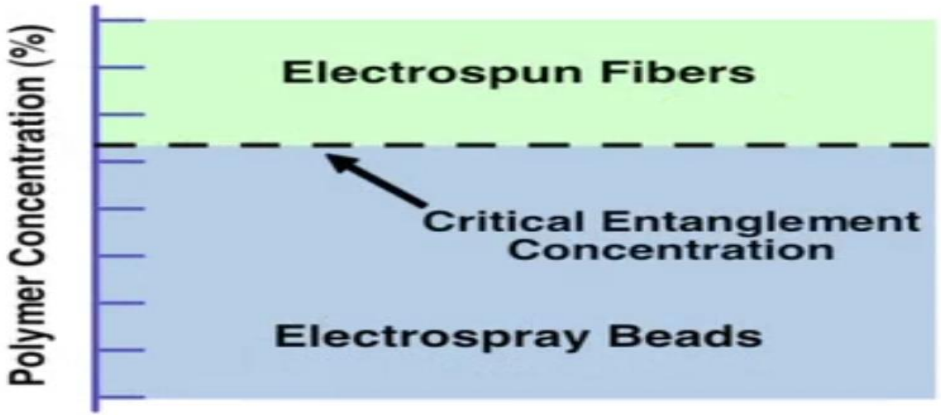
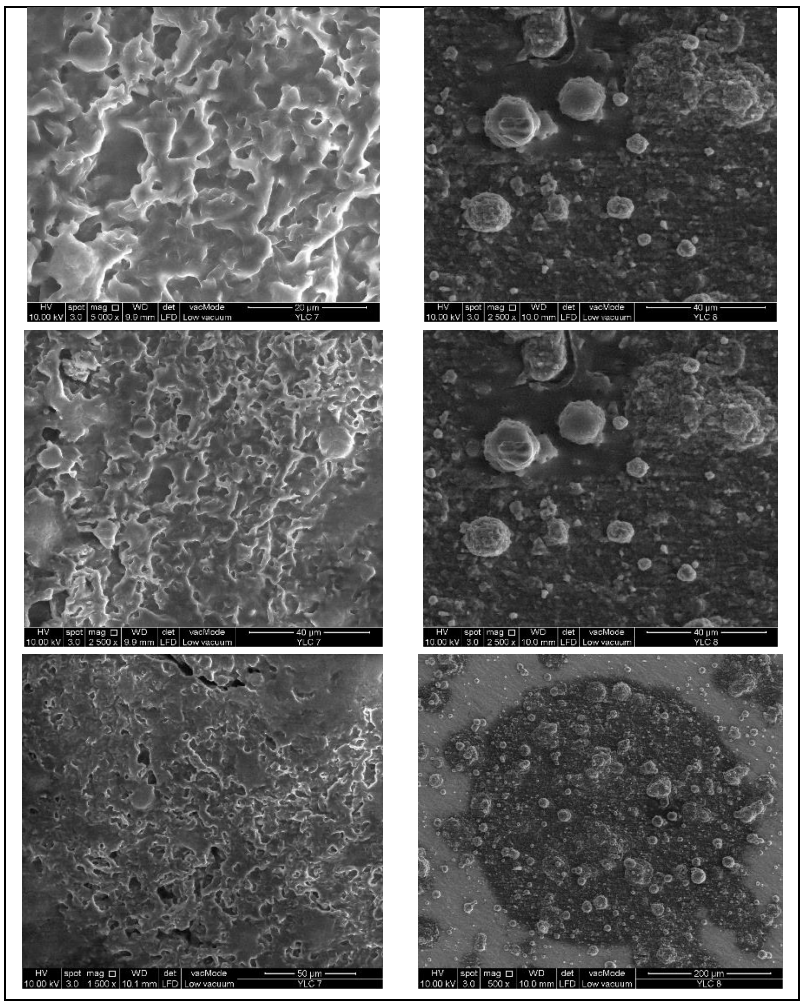


Figure 7. Presentation the boundary of critical entanglement concentration

3.3 Morphology Study

Morphology of the beads form on the collector can studied through the SEM. The FESEM machine analyze cyclic PLLA 25% wv and cyclic PDLA 22%wv. The SEM image produce by shows no characteristic of fiber formation instead droplet of solution and beads overlapping.



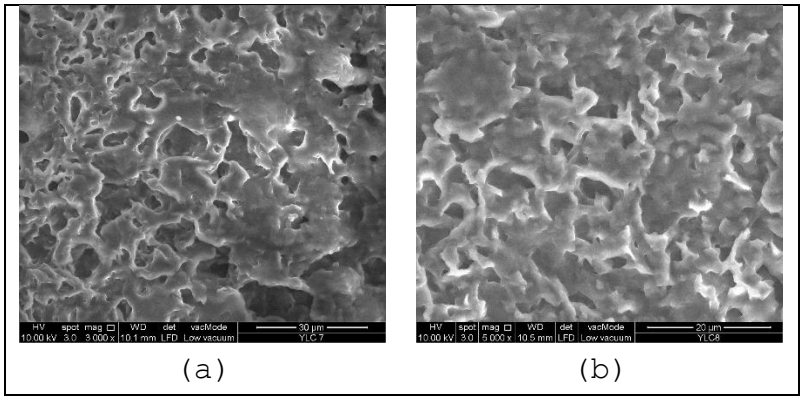


Figure 8. SEM image of (a) Cyclic PLLA (25%) and (b) Cyclic PDLA (22)

4.0 Conclusion

As a conclusion to this research, the optimization on polymer solution had not been optimize yet which result in no fiber deposited on the collector. More time is required to optimize all three polymer to find out the suitable parameter for electrospinning. It also believe that sample preparation technique prepared by the author may be not right.

ACKNOWLEDGEMENT

First and foremost, I would like to express my deepest gratitude to my family especially my parents for providing all any kind of support and strength throughout the entire research project to continue on with the project when this project planning is falling apart.

References

[1] R. Langer and D. Tirrell, "Designing materials for biology and medicine", Nature, vol. 428, no. 6982, pp. 487-492, 2004.

[2] L. Hench, "Third-Generation Biomedical Materials", Science, vol. 295, no. 5557, pp. 1014-1017, 2002.

[3] F. Melchels, M. Domingos, T. Klein, J. Malda, P. Bartolo and D. Hutmacher, "Additive manufacturing of tissues and organs", Progress in Polymer Science, vol. 37, no. 8, pp. 1079-1104, 2012.

[4] P. Bártolo, C. Chua, H. Almeida, S. Chou and A. Lim, "Biomanufacturing for tissue engineering: Present and future trends", Virtual and Physical Prototyping, vol. 4, no. 4, pp. 203-216, 2009.

[5] J. He, D. Li, Y. Liu, H. Gong and B. Lu, "Indirect fabrication of microstructured chitosan-gelatin scaffolds using rapid prototyping", Virtual and Physical Prototyping, vol. 3, no. 3, pp. 159-166, 2008.

[6] T. Patrício, A. Gloria and P. Bártolo, "PCL and PCL/PLA Scaffolds for Bone Tissue Regeneration", MAR, vol. 683, pp. 168-171, 2013.

[7] M. K. Leach, Z.-Q. Feng, S. J. Tuck, and J. M. Corey, "Electrospinning fundamentals: Optimizing solution and apparatus parameters," Journal of Visualized Experiments, no. 47, Jan. 2011.

[8] S. Huan et al., "Effect of experimental parameters on morphological, mechanical and hydrophobic properties of Electrospun polystyrene fibers," Materials, vol. 8, no. 5, pp. 2718–2734, May 2015.

[9] V. Orlovskii, V. Komlev and S. Barinov, “Hydroxyapatite and Hydroxyapatite-Based Ceramics ", Inorganic Materials, vol. 38, no. 10, pp. 973-984, 2002.

Design a Hybrid Rain Energy Harvesting System

Danesh Kumar, Douglas Tong Kum Tien

School of Engineering, Taylor's University, Malaysia.

Douglaskumtien.tong@taylors.edu.my

Abstract
Malaysia is a country in which it is blessed with an abundance of rainfall throughout the year that totals to an average of 7580 mm. Therefore, a study was done on the ways in which energy from rainfall can be harvested as it is an avenue to an alternative renewable source of energy. There exist two ways in which energy can be harvested from rainfall and this is by using a hydropower generator or a piezoelectric generator. Harvesting rain energy by modes of hydropower generator uses the potential energy (PE) of rain water stored in dams or reservoirs that is channelled to a control outlet into a turbine where it possesses kinetic energy (KE) to rotate the rotor. However by using piezoelectric generators, the force exerted by raindrops onto this membrane is converted directly to electrical discharges as it possesses kinetic energy before contact. Thus, focusing on rooftops of commercial buildings due to the abundance of space and heavy rainfall in the Kuala Lumpur region, an analytical evaluation was performed in which alterations were done to the head height, cross sectional area and mass flow rate to obtain the maximum energy output from 3 turbine types. Moreover, evaluation of piezoelectric generators such as polyvinylidene fluoride (PVDF), lead zirconate titanate (PZT) and poly (methyl methacrylate)/grapheme oxide (PMMA/GO) were done. Upon obtaining results, a 3D model of a hybrid rain energy harvesting system was drawn on Solidworks. As a conclusion the maximum energy output obtained is 14.83% of an average household electricity usage.

Keywords: Piezoelectric, Hydropower, Renewable Energy, Potential Energy, Kinetic Energy

1. Introduction

1.1 Background

In today's world, the demand for a constant major resource is electricity. Rising standard of living and development increases the power consumption in residential and industrial areas. Thus, to cater to growing power demands, extraction of power from non-conventional and renewable sources of energy is being focused on. [1]

Renewable energy is defined as energy that is collected from resources that are naturally replenished such as sunlight, wind, rain, and geothermal. Thus, focusing on Malaysia, it is a country that is blessed with an abundance of rainfall throughout the year which totals up to an average rainfall of 7580 mm. Peninsular Malaysia obtains an average rainfall of 2500 mm whereas East Malaysia obtains an average rainfall of 5080 mm [2]. Rainfall is measured as a unit of depth as an international standard in which it uses the units of length (mm, cm or inches) and refers to the net rainfall. This is used because of its simplicity to obtain volume. For every 1 mm of rainfall = 1 liter/m^2 or 0.001 m^3. [2] Therefore, the focus is done on harvesting rain energy in residential and industrial areas as high power demands are needed in these regions. Thus, taking an average building with roof area of 1500 m^2 and average of 240 mm of rainfall per month in that particular area, we get 360 m^3 or 360 000 liters of rain water monthly for harvesting. Figure 1.1 shows the average rainfall in (mm) for Kuala Lumpur, Malaysia.

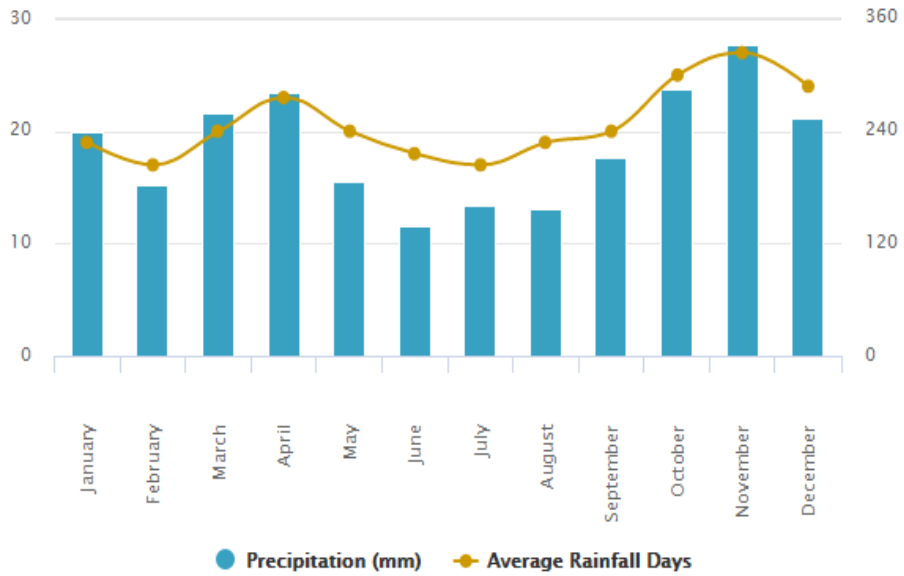


Figure 1.1. Average Rainfall in Kuala Lumpur [2]

With a substantial amount of rain water collected monthly, literature review was carried out to study ways in which energy can be harvested from it. Current studies show that the most common method of harvesting rain energy is by using a hydro-electric generator in which kinetic energy (KE) is converted to electrical energy by means of a turbine and generator. It is the most widely used form of renewable energy where rain water is stored in high raised containments/dams where it possesses

potential energy (PE) and is channeled through control outlets at high speed to the turbines that generates electrical energy. However, this method requires a high raised catchment area for rain fall to gain potential energy or used directly for its kinetic energy through a running river channel.

Besides using a hydro-electric generator, later studies have shown the possibility of harvesting rain energy using a piezoelectric generator. Piezoelectric materials that are subjected to a compressive or tensile stress generate an electric field across the material which creates a voltage difference resulting in current flow. [1] Polyvinylidene fluoride (PVDF), lead zirconate titanate (PZT) and poly (methyl methacrylate)/grapheme oxide (PMMA/GO) are types of piezoelectric material that are able to convert mechanical stress into electrical discharges. Mechanical stress in this case would be the force exerted by rain drops onto the piezoelectric plates during a drizzle, rain or downpour.

Upon understanding the fundamentals of rain energy harvesting, a design of a hybrid rain energy harvesting system will be produced upon conducting several analysis in the two main regions which are the hydropower generation and piezoelectric generation. As for hydropower generation, Bernoulli's equation will be used to apply the principle of conservation of energy shown in the equation below:

$$KE_1 + PE_1 = KE_2 + PE_2 \quad (1)$$

$$\frac{1}{2}mv_1^2 + mgh_1 = \frac{1}{2}mv_2^2 + mgh_2 \quad (2)$$

Where m is the mass of the accumulated rain water, g is gravitational acceleration, v is velocity of rain water and h is the head height. By altering the head height and cross sectional area of the nozzle, maximum power generation and duration of power output can be obtained. As for piezoelectric generation, alteration on plate sizes and materials was used to obtain the recoverable instantaneous power produced by 3 types of raindrop signifying drizzle, rain or downpour.

1.2 Project Objectives

This project involves research into design of a hybrid rain energy harvesting system which uses both potential and kinetic energy of rainfall. To achieve thus, the research is further divided into specific objectives as shown below:

1. To obtain maximum power output from small hydropower turbine by altering the head height and cross sectional area of nozzle.
2. To obtain maximum recoverable instantaneous power by altering size and material of piezoelectric plate.
3. To design a hybrid rain energy harvesting system using Solidworks.

2. Methodology

2.1 Analytical Evaluation of Head Height for Small Scale Hydropower Generator

Small scale hydropower generation can be broken down into 3 specific head length clearances which are low (<10 m), medium (10-50 m) and high (>50 m). Therefore with the limitation of having a standard commercial roof area of 1500 m², 360 000 liters of rain water can be accumulated monthly. Using this value, a calculation on velocity of rain water was performed using Bernoulli's equation of conservation of energy. Based on equation (1) and (2), the equation (5) below is formulated by assuming the initial condition of the stored fluid to have kinetic energy equivalent to 0.

$$mgh_1 = \frac{1}{2}mv_2{}^2 + mgh_2 \quad (3)$$

$$mg(h_1 - h_2) = \frac{1}{2}mv_2{}^2 \quad (4)$$

$$v_2 = \sqrt{2g(h_1 - h_2)} \quad (5)$$

These calculations were performed with 5 variations in head length based on the 3 main head length classifications which are 2 m, 4 m, 6 m, 8 m and 10 m for low head height, 10 m, 20 m, 30 m, 40 m and 50 m for medium head height and 50 m, 60 m, 70 m, 80 m and 90 m for high head height. The results were then tabulated.

2.2 Analytical Evaluation of Cross Sectional Are of Nozzle for Small Scale Hydropower Generator

Upon obtaining the velocity of rainwater for various head heights, calculations were performed to obtain mass flow rate of rain water through nozzles varying in sizes. The equations below are used to obtain mass flow rate of rain water.

$$A = \pi * r^2 \quad (6)$$

$$\dot{v} = v * A \quad (7)$$

$$\dot{m} = \dot{v} * \rho \quad (8)$$

$$\dot{m} = v * \rho * A\ in\ stream \quad (9)$$

Where A is the cross sectional area of the nozzle, r is the radius of the nozzle, v = velocity of rain water in nozzle, $\dot{v}$ is the volumetric flow rate, $\dot{m}$ is the mass flow rate and ρ is density of water = 1000 kg/m³. These calculations were performed with 4 variations in nozzle radius based on the 3 main head length classifications which are 0.02 m, 0.04 m, 0.06 m, 0.08 m for low, medium and high head. The results were then tabulated.

2.3 Analytical Evaluation of Power Output and Duration

Upon obtaining the mass flow rate of rain water at various head height and nozzle radius, power can be calculated by using the equation (4). In order to obtain the duration of power output, the inverse mass flow rate was multiplied by the amount of rain water accumulated as 1 liters of water = 1kg of water. Equation shown below:

$$t = \frac{1}{\dot{m}} * litres \tag{14}$$

Thus, to obtain total energy produced by the small scale hydro power generator, the power output is multiplied by the time. The equation below is used:

$$E = P * t \tag{15}$$

Where *t* is time in seconds, *E* is energy in kWh and *P* is power in watt.

2.4 Piezoelectric Generator Evaluation

For selection of piezoelectric material, a comparison on 3 main materials was done which are PVDF, PZT and PMMA/GO. The output power produced by various materials by various researches is tabulated in Table 2.1 below. Due to the higher level of understanding and knowledge needed for piezoelectric generators, simulation could not be performed thus reference to previous studies was done.

Table 2.1. Comparison of potential raindrop energy generation

6. Researches	7. Year	8. Piezoelectric Material	9. Vibration Source	10. Mechanism and Dimensions	11. Output
12. Guigon	13. 2008	14. PVDF	15. Impact by droplet 16. D: 5 mm 17. v: 5.7 m/s	18. Bridge 19. 100 mm x 3 mm x 0.25 mm	20. 12.5 mW
21. Sahaya Grinspan and Gnanamoorthy	22. 2010	23. PVDF	24. Impact by droplet 25. D: 3.57 mm 26. v: 2.96 m/s	27. Solid film 28. 35 mm x 80 mm x 5µm	29. 0.1 V
30. Ahmad and Jabbour	31. 2012	32. PZT	33. Impact by droplet 34. m: 0.23 g 35. v: 0.22 m/s	36. Cantilever 37. 8 mm x 20 mm x 0.58 mm	38. 0.8 V
39. Valentini	40. 2013	41. PMMA/ GO	42. Impact by droplet 43. m: 5 µg 44. h: 0.2 m	45. N/A	46. 6 nW
47. Viola	48. 2013	49. PVDF	50. Impact by droplet 51. D: 5 mm	52. Cantilever 53. (20 mm – 25 mm) x 20 mm x 0.58 mm	54. 4.5 µW
55. Lee	56. 2014	57. PVDF	58. 6 µL droplet actuated by acoustic wave	59. Cantilever 60. 73 mm x 15 mm x 0.2 mm	61. 72.2 µW

2.5 Design of Hybrid System

Upon comparison of results of velocity, mass flow rate, nozzle cross sectional area, power output and duration of power output, a 3D model of a hybrid rain energy harvesting system consisting of small hydropower generator and piezoelectric generator was performed on Solidworks. The design was broken down into 3 sections which are the top panels, storage tanks and turgo turbine.

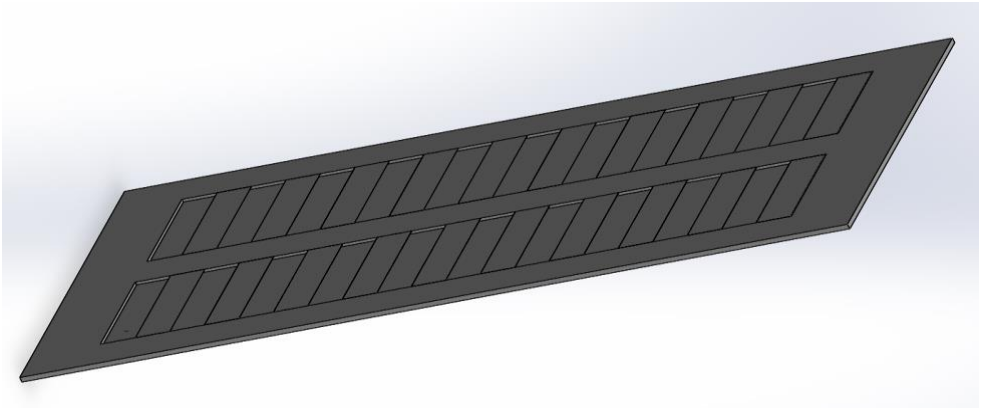


Figure 2.1. Solid view of top panel

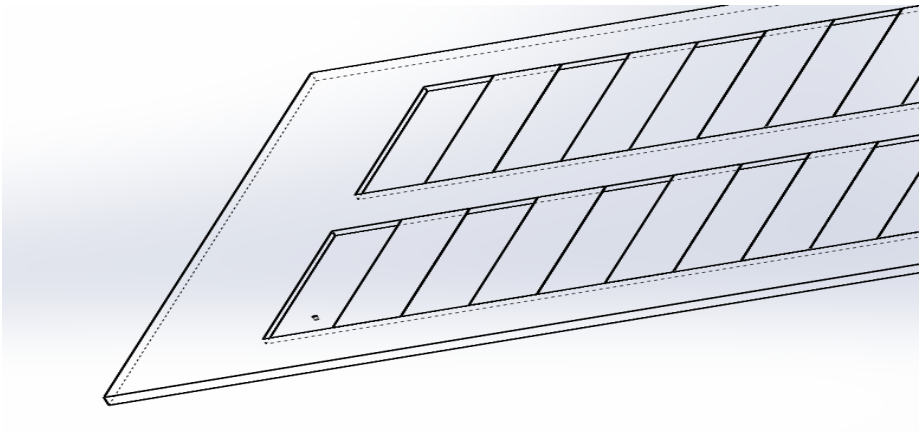


Figure 2.2. Wired-mesh view of top panel

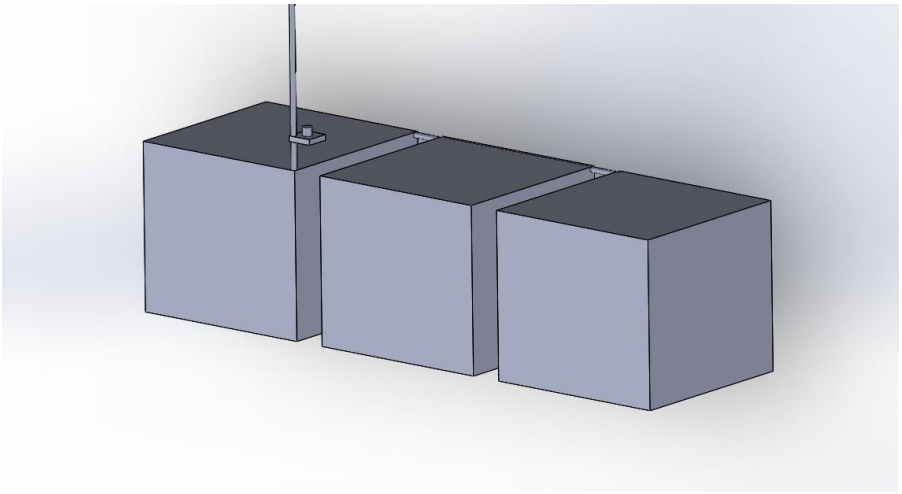


Figure 2.3. Storage tanks

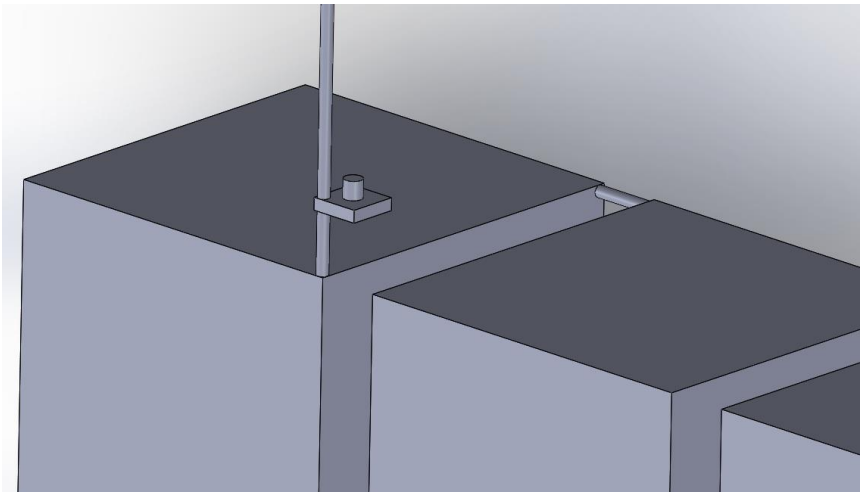


Figure 2.4. Turgo turbine

3. Results and Discussion

3.1 Duration of Power Output

Below are the results of power output and duration of power output given 3 classifications of head length and cross sectional area of 4 nozzle sizes. Also 3 graphs of output duration against power output were plotted for low, medium and high head classification.

Table 3.1. Power output and duration

Low (<10 m) (m)	Mass flow rate (kg/s)	Power, (W)	Time (hours)	Medium (10-50 m) (m)	Mass flow rate (kg/s)	Power, (W)	Time (hours)	High (>50 m) (m)	Mass flow rate (kg/s)	Power, (W)	Time (hours)
2	7.874	131.315	12.70	10	17.607	1468.160	5.68	50	39.370	16414.337	2.54
	31.489	525.142	3.18		70.413	5871.388	1.42		157.451	65645.258	0.64
	70.783	1180.448	1.41		158.279	13198.094	0.63		353.927	147561.015	0.28
	125.944	2100.368	0.79		281.625	23483.301	0.36		629.740	262554.350	0.16
4	11.136	371.430	8.98	20	24.900	4152.573	4.02	60	43.128	21577.370	2.32
	44.534	1485.387	2.25		99.580	16606.957	1.00		172.476	86291.468	0.58
	100.107	3338.969	0.99		223.842	37330.130	0.45		387.703	193971.688	0.26
	178.119	5940.981	0.56		398.280	66421.156	0.25		689.827	345127.346	0.14
6	13.638	682.323	7.33	30	30.496	7628.727	3.28	70	46.583	27190.264	2.15
	54.543	2728.841	1.83		121.960	30508.904	0.82		186.296	108740.044	0.54
	122.605	6134.051	0.82		274.149	68579.743	0.36		418.767	244432.204	0.24
	218.150	10914.263	0.46		487.792	122023.608	0.21		745.108	434915.814	0.13
8	15.748	1050.518	6.35	40	35.214	11745.278	2.84	80	49.800	33220.584	2.00
	62.978	4201.136	1.59		140.826	46971.104	0.71		199.160	132855.653	0.50
	141.566	9443.585	0.71		316.558	105584.755	0.32		447.683	298640.376	0.22
	251.888	16802.945	0.40		563.249	187866.072	0.18		796.560	531369.245	0.13
10	17.607	1468.160	5.68	50	39.370	16414.337	2.54	90	52.820	39639.561	1.89
	70.413	5871.388	1.42		157.451	65645.258	0.64		211.240	158528.227	0.47
	158.279	13198.094	0.63		353.927	147561.015	0.28		474.837	356348.549	0.21
	281.625	23483.301	0.36		629.740	262554.350	0.16		844.874	634048.366	0.12

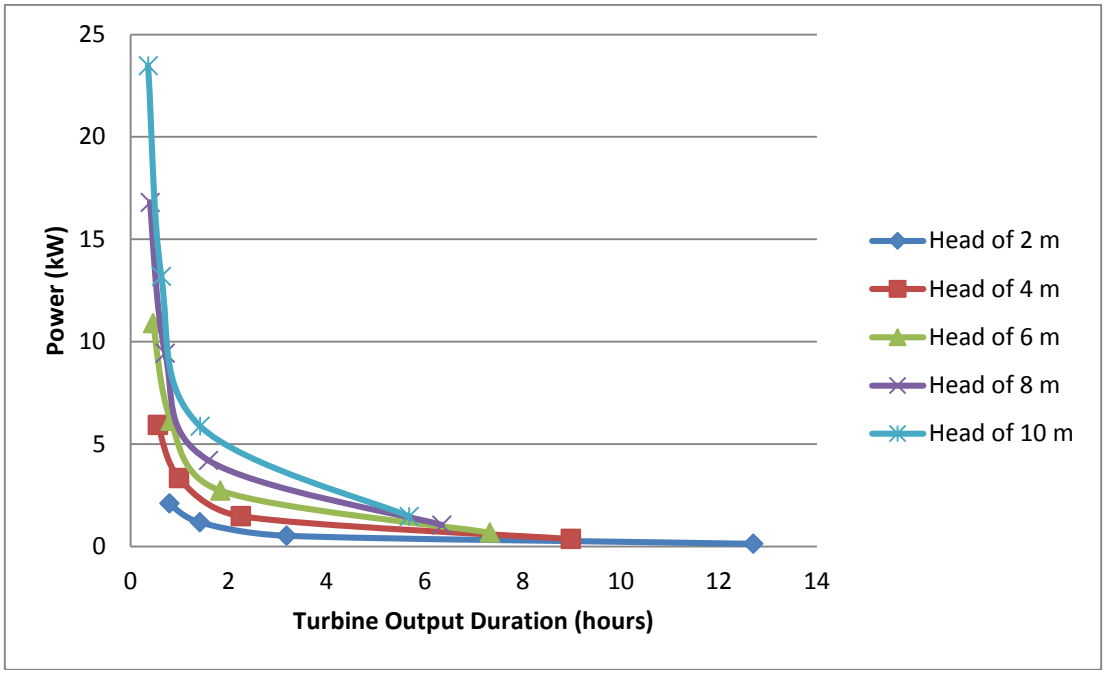


Figure 3.1. Graph of output duration against power output for low head turbine

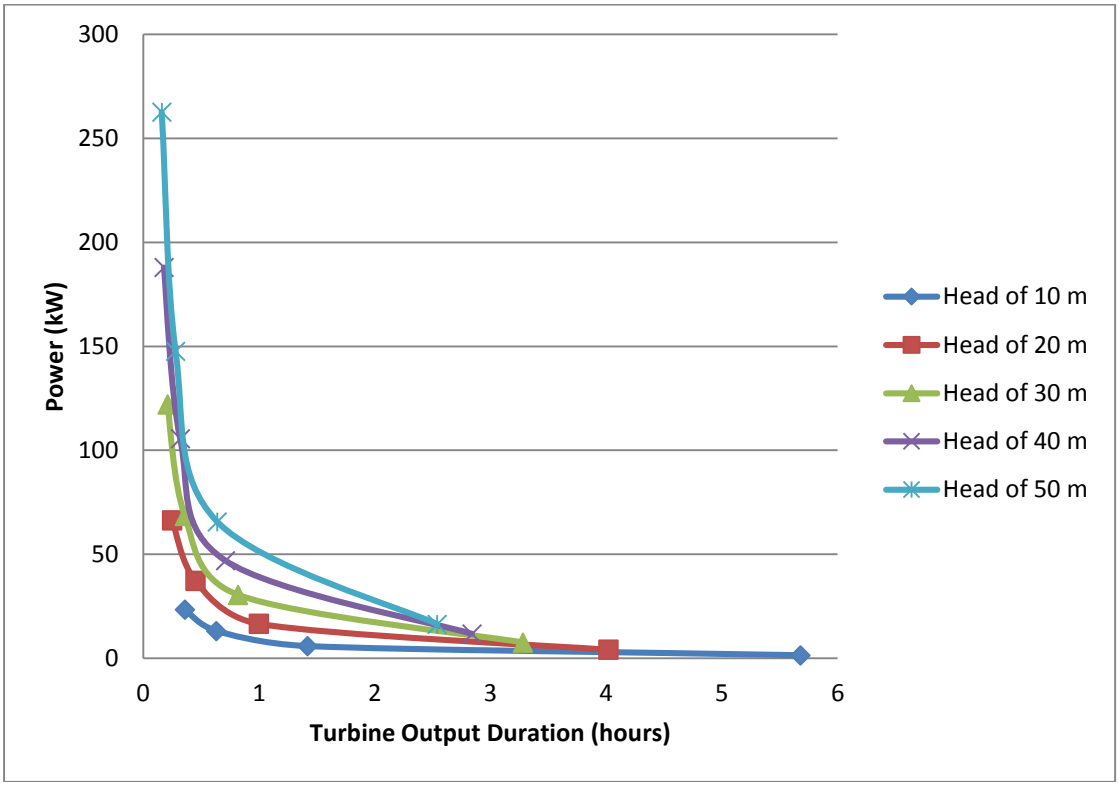


Figure 3.2. Graph of output duration against power output for medium head turbine

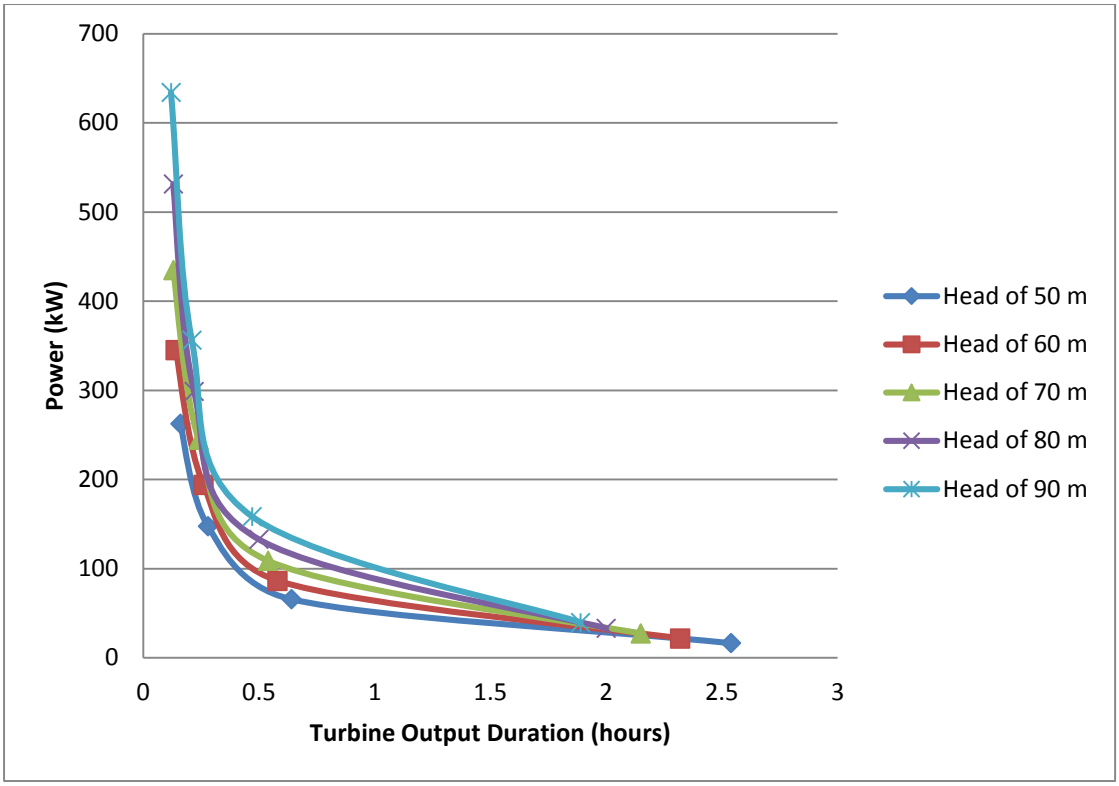


Figure 3.3. Graph of output duration against power output for high head turbine

Based on the Figures 3.1 to 3.3, it shows the duration and power output of all classifications from head length, cross sectional area and nozzle radius. The turbine with a head length of 2 m and a nozzle radius of 0.02 m has the lowest yet longest power output at 131.315 W for 12.7 hours whereas the turbine with a head length of 90 m and a nozzle radius of 0.08 m has the highest yet shortest power output at 634.048 kW for 0.12 hours.

3.2 Design of Hybrid Rain Energy Harvesting System

The energy output for piezoelectric harvesting and small hydropower harvesting are tabulated and a 3D model of the harvesting system was drawn on Solidworks.

Table 3.2. Energy output for small scale hydropower generation

Low (<10 m) (m)	Radius of Nozzle (m)	Energy (kWh)	Medium (10-50 m) (m)	Radius of Nozzle (m)	Energy (kWh)	High (>50 m) (m)	Radius of Nozzle (m)	Energy (kWh)
2	0.02	1.664	10	0.02	8.338	50	0.02	41.692
	0.04	1.670		0.04	8.337		0.04	42.013
	0.06	1.664		0.06	8.315		0.06	41.317
	0.08	1.659		0.08	8.454		0.08	42.009
4	0.02	3.332	20	0.02	16.695	60	0.02	50.059
	0.04	3.341		0.04	16.607		0.04	50.049
	0.06	3.306		0.06	16.799		0.06	50.433
	0.08	3.327		0.08	16.605		0.08	48.318
6	0.02	4.999	30	0.02	25.023	70	0.02	58.459
	0.04	4.994		0.04	25.017		0.04	58.720
	0.06	5.030		0.06	24.689		0.06	58.664
	0.08	5.020		0.08	25.625		0.08	56.539
8	0.02	6.674	40	0.02	33.356	80	0.02	66.442
	0.04	6.680		0.04	33.349		0.04	66.428
	0.06	6.705		0.06	33.787		0.06	65.701
	0.08	6.721		0.08	33.816		0.08	69.078
10	0.02	8.338	50	0.02	41.692	90	0.02	74.920
	0.04	8.337		0.04	42.013		0.04	74.508
	0.06	8.315		0.06	41.317		0.06	74.833
	0.08	8.454		0.08	42.009		0.08	76.086

Table 3.3. Energy output for PVDF generation

Types of drop	Recoverable Voltage	Recoverable electrical energy	Recoverable instantaneous power	Monthly Output with 20 000 plate
Rain: D: 1 mm V: 2.8 m/s	1.6 V	1.7 nJ	1.8 µW	0.36 W
Medium D: 2 mm V: 0.75 m/s	3 V	5 nJ	2.5µW	0.5 W
Downpour D: 5 mm V: 5.7 m/s	98 V	25 µJ	12.5 mW	2.5 kW

The results obtained in Table 3.2 shows that the most amount of energy produced is 76.086 kWh monthly from small scale hydropower generation using a Turgo turbine with the specification as follows:

Head length = 90 m
Nozzle radius = 0.08 m
Cross sectional area of nozzle = 0.020106 m²
Mass flow rate = 844.874 kg/s

The results obtained in Table 3.3 shows that the total amount of power produced monthly is 2500.86 W from using a PVDF piezoelectric generator as compared to PZT and PMMA/GO which are lower. Thus with these results, the design of a hybrid rain energy harvesting system was produced as shown in Figure 3.4 and 3.5 with the specifications shown in Table 4.3 below.

Table 4.3. Specifications

Components	Specifications	Quantity
Top frame	L: 60 m, W: 45 m, H: 0.5 m	1
Catchment area	L: 50 m, W: 15 m, H: 0.3 m	2
PVDF holder plate	L: 15 m, W: 2.5 m, H: 0.05 m	20
Piezoelectric PVDF plate	L: 100 m, W: 0.013 m, H: 0.025 mm	20 000
Nozzle	L: 90 m, Inner Diam: 0.16 m, Outer Diam: 0.19 m	1
Turgo turbine	L: 8 m, W: 8 m, H: 0.2 m	1
Storage tanks	L: 6 m, W: 6 m, H: 6 m	3



Figure 3.4. 3D model of hybrid rain energy harvesting system

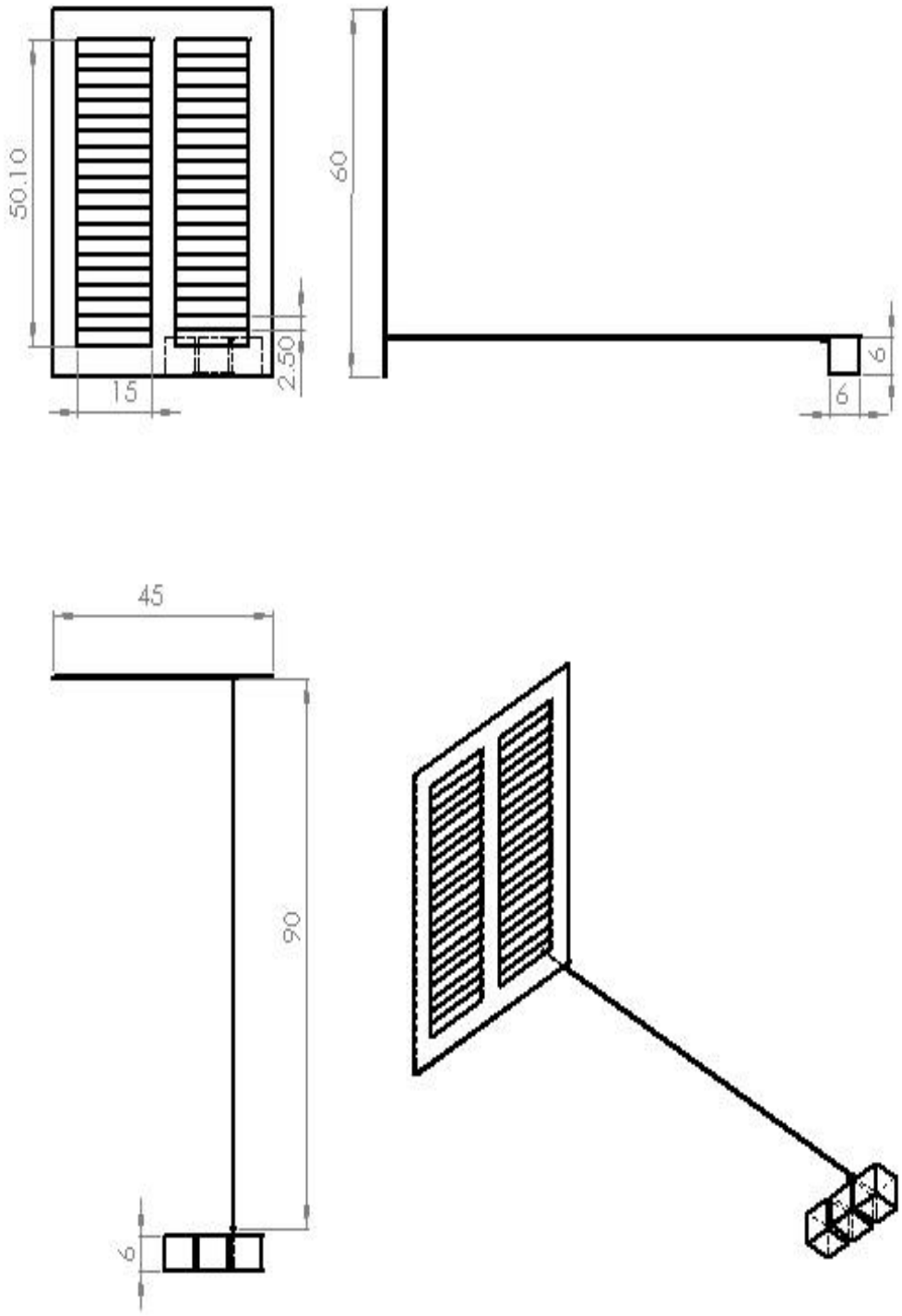


Figure 3.5. Drawing of 3D hybrid rain energy harvesting system

4. Future Work

Although the proposed objectives were met, there are still areas for improvement that can be done in the future. The current design is subjected to commercial buildings with a standard catchment area of 60 m by 45 m and a height of 100 m, therefore future work should consider exploiting residential rooftops as 76.086 kWh of electricity is 14.83% of an average household electricity usage (513 kWh a month). Moreover, research should be carried out to determine other piezoelectric materials that are able to generate higher power as compared to the PVDF generator and to build a prototype that can be tested.

5. Conclusion

This research project was carried out to assess the feasibility of harvesting rain energy through both potential and kinetic energy means. Thus, the parameters were limited to harvesting rain energy in commercial and residential areas in Malaysia based on an average rainfall of 240 mm a month in Kuala Lumpur. Focusing on rooftops of commercial buildings due to the abundance of space, there are 2 methods of harvesting rain energy which are the use of piezoelectric generators and the use of a small scale hydro power generator. Therefore, analysis evaluation were performed in which maximum power output from a small scale hydro power generator was done by altering the head height and cross sectional area of the nozzle leading to the turbine. The results show that the most amount of energy produced is 76.086 kWh a month with nozzle specifications of length 90 m (head height), radius of 0.08 m and a mass flow rate of 844.874 kg/s. In addition, evaluation were performed on 3 piezoelectric material which are PVDF, PZT and PMMA/GO in which PVDF produced the most amount of recoverable instantaneous power at 2.5 kW a month during a heavy downpour. Therefore, a 3D model of a hybrid rain energy harvesting system with their specifications were drawn on Solidworks to cater for commercial rooftops with an average roof dimension 60 m by 45 m and height of 100 m in Kuala Lumpur.

References

[1] Aashay Tinaikar, "Harvesting energy from rainfall", *International Journal of Renewable and Sustainable Energy*, vol.3, no.2, pp.130-132, June 2013

[2] Kementerian Sains, Teknologi dan Innovasi (MOSTI), "Purata Hujan Malaysia," *Jabatan Meteorologi Malaysia*, 2016. [Online]. Available: http://www.met.gov.my/ [accessed Oct 6th, 2016]

[2] Oliver Paish, "Small Hydro Power: Technology and Current Status", *Renewable & Sustainable energy Reviews*, vol.6, no.2, pp.537-556, February 2002

[3] Williams and Simpson, "Pico hydro – Reducing Technical Risk for Rural Electrification", *Renewable Energy*, vol.34, no.1, pp.1986-1991, January 2009

[4] Williamson, Stark, Booker, "Low Head Pico Hydro Turbine Selection using a Multi-criteria Analysis", *Renweable Energy*, vol.61, no.2, pp.43-50, July 2012

[5] Pietro Romano and Fabio Viola, "Harvesting Rainfall Energy by means of Piezoelectric Transducer", *International Journal of Renewable and Sustainable Energy*, vol.2, no.3, pp.1-7, June 2013

[6] Romain Guigon, Jean-Jacques Chaillout, Thomas Jager and Ghislain Despesse, "Harvesting Raindrop Energy: Experimental Study", *Smart Materials and Structures*, vol.17, pp.1-7, January 2008

[7] Romain Guigon, Jean-Jacques Chaillout, Thomas Jager and Ghislain Despesse, "Harvesting Raindrop Energy: Theory", *Smart Materials and Structures*, vol.17, pp.1-9, January 2008

[8] Chamil Perera and Sampath, "Harvesting of Kinetic Energy of the Raindrops", *International Journal of Mathematical, Computational, Physical, Electrical and Computer Engineering*, vol.8, no.2, pp.325-330, August 2014

eureca 2016 – Conference Paper
Paper Number 2ME12

Design and Simulation of propellant tank for a lunar landing system.

Darren Lee Jun Weng[1*], Azadeh Ghadimi[1*], Izmir Yamin[2]

[1]*School of Engineering, Taylor's University, Malaysia*
[2]*Independence-X Aerospace Sdn Bhd, Malaysia*

[*]Azadeh.Ghadimi@taylors.edu.my

Abstract
Propellant tanks had been widely used in the space industries to store propellants for propulsion purposes. A spherical propellant tank was designed to avoid fluid sloshing which would cause clogging in the tank itself. A 3D model of the spherical propellant tank made from titanium alloy, Ti-6Al-4V with bolts and nuts was designed using SolidWorks 2014 version and further analysed using ANSYS Workbench 15.0 via static structural analysis. The propellant tank's wall thickness was assumed as 0.01 meter whereby the calculated wall thickness was compared to previous Alliant Techsystems Inc. (ATK Space Systems) manufactured propellant tank's wall thickness based on the given mission parameters. In this regards, M10 x 12.9 bolts were used for the design due to its higher proof strength as compared to other bolt classes. The number of bolts required for the fuel and oxidizer tank were determined which were 10 and 14 bolts respectively. Static analysis is carried out in the propellant tanks by approaching two methods which focused on the propellant tank mounting parts and bolts respectively whereby this gives a more specific analysis for each part. Based on the static analysis, the total deformation of the propellant mounting parts were acceptable as no serious deformation were seen by applying the given operating conditions to the structure. However, the total deformation of the bolts were severely deform due to the high tensile force experienced by the bolt. Further improvements were recommended to analyse the bolted connection propellant tank for the future.

Keywords: Propellant Tanks, Lunar Lander, Moon Surface, Design, Simulation

1.0 Introduction

Mankind had been exploring the lunar surface for the past decades which revolutionized modern space technology to achieve even more extreme challenges for the future. One of the greatest mankind history was the successful landing attempt made by the American's Apollo 11 on July 20, 1969 which was led by astronaut Neil Armstrong whom was the first human to set foot on the lunar surface itself [1]. Since then, many space explorations agencies such as the National Aeronautics and Space Administration (NASA) had been continuously sending astronauts to the moon throughout the 20th century to pursue the knowledge of the lunar surface.

In regards to space applications, propellant tanks were used to store liquid propellants in the rocket engines for combustion purposes which leads to various space applications such as launching from Earth and landing on the lunar surface. The usage of green propellants had been increasing in the industry to conserve the Earth's environment. Some of the non-green propellants may harm environment in the long run during space launches and thus opt for green propellants which has the similar specific impulse as non-green propellants. This would lead to higher reaction and energy for combustion.

Ever since space missions in the 1960's, propellant tank research and development had grown vastly in the industry to provide more energy to the rockets. The most applied propellant tank shape for space missions would be a titanium alloy sphere propellant tank as it prevents fluid sloshing around the wall of the tank itself while the rocket or lunar lander travels in space. Fluid sloshing would pose a huge problem to a space mission as time increases. The fluid sloshed will build-up and freeze under the cold temperature of space and eventually clogged the propellant tank which unable the supply of propellants to the rocket engine thus causing major engine failure. Moreover, to prevent further blockage and non-smooth propellant flow from the tank's to the rocket, current propellant tanks are installed with a propellant management device (PMD) which allows only the propellants to be supplied to the rocket engine preventing further failures caused by small induced particles [2].

As the 21st century kicks in, many space enthusiast from up-rising space companies from various countries such as China, India, Japan and even Malaysia had the dream to explore the lunar surface itself just as NASA did decades ago. With that, Malaysia led by a notorious space company called Independence-X Space Sdn Bhd was then given the opportunity to launch an unmanned lunar landing system to the lunar surface by the end quarter of 2017 under the Google Lunar X-Prize (GLXP) competition. Malaysians then would have the opportunity to launch and explore the lunar surface in the coming future which then will revolutionize the space technology in Malaysia. Malaysia's objective for the GLXP would be landing the lunar lander on the moon, able to travel 500 meters and transmits high definitions pictures back to Earth.

The lunar landing system will be consisting of the bus structure, landing system and propellant tanks. The scope of the project would solely focus on the design and simulation of the propellant tank itself. This study aims to design and analyze the propellant tank using bolted connections based on the given operating conditions. The tank was designed using SolidWorks (2014 Edition) and the study on the stresses and deformations for structural analysis was done by using Analysis

System software 2015 Edition (ANSYS 15.0). Furthermore, the propellant tank's specifications were calculated based on the give parameters provided by Independence-X.

2.0. Research Methodology

2.1 Design of the propellant tanks

The lunar landing system will consist of 2 fuel and oxidizer tanks to store the propellants for the landing stage. Titanium alloy, Ti-6Al-4V is selected as the propellant tank's material due to its high strength and lightweight properties. The tank's wall thickness and number of bolts and nuts were to be calculated and determined based on the given operating conditions. Based on NASA review on space material's safety factor, the recommended safety factor is 1.5 for all space materials applications. [3]. In the present study, a safety factor value of 1.5 is considered for the propellant tank design and bolt's selection.

2.1.1 Propellant Tank's Wall thickness

For commonly used thin walled spherical vessels, the shell walls acts as membranes. There is no bending stress on the shell wall. The weight of the vessel can be neglected (common situation). Due to the shells axisymmetric of the vessel, the vessel is free to deform under pressure. Hence, only uniform normal stress or principal stresses called membrane stresses exist [4]

The allowable stress, σ_{all} for Ti-6Al-4V tank can be determine by:

$$\sigma_{all} = \frac{\sigma_{maximum}}{Safety\ Factor} \text{ [4]} \quad (1)$$

Stresses exerted on the face of small element of the wall must be equal. A section through the center of the shell is isolated for a hemisphere. The circumferential or tangential stress are:

$$\sigma = \frac{Pr}{2t} \text{ [4]} \quad (2)$$

Hence, the wall thickness can be determined by:

$$t = \frac{Pr}{2\sigma_{all}} \quad (3)$$

2.2 The type and number of bolts and nuts used

The bolt class of 5.8, 8.8 and 12.9 are compared to select the suitable bolt material for the research study. Moreover, the nominal diameter of the bolts which are M6, M8, M10 and M12 respectively are also compared to determine the suitable number of bolts needed for the tank.

2.2.1 The number of bolts and nuts required for each propellant tank based on the bolt materials

The maximum pressure which the Ti-6Al-4V propellant tanks could withstand can be calculated based on Eq. (4) below:

$$P_{tank,max} = P_{tank}(SF) \quad (4)$$

The $F_{fuel\ tank}$ and $F_{oxidizer\ tank}$ are both calculated using Eq. (5) below:

$$F_{tank} = P_{tank,max}\ A_{tank} \quad (5)$$

The safety factor of 1.5 is included into the $P_{bolt,maximum}$ to determine the $P_{bolt,allowable}$ on the tank as shown in Eq. (6)

$$P_{bolt,allowable} = \frac{P_{bolt,max}}{SF} \quad (6)$$

The bolt force, $F_{bolt,tensile}$ under tensile stress is calculated with Eq. (7):

$$F_{bolt,tensile} = P_{bolt\ allowable} A_{bolt} \quad (7)$$

By using the ratio of the maximum force exerted by the tanks with the maximum force the bolt can withstand before permanent deformation, the minimum number of bolts required for each propellant tanks can be approximate using Eq. (8):

$$n = \frac{F_{tanks}}{F_{bolts}} \quad (8)$$

2.3 Finite Element Analysis (FEA) on propellant tank's mounting parts.

2.3.1 Boundary Conditions and given specifications by Independence-X Aerospace

Table 1. Propellant Tank's Specifications

1) Parameters	2) Specifications
3) Fuel Propellant	4) Mono-methyl hydrazine (MMH)
5) Oxidizer Propellant	6) Nitrogen Tetroxide (MON3)
7) Fuel Tank Outer Diameter	8) 0.461 m
9) Oxidizer Tank Outer Diameter	10) 0.522 m
11) Operating Pressure	12) 500 kPa

Table 2. Ti-6Al-4V Parameters

13) TI-6Al-4V Properties	14) Parameters
15) Young's Modulus	16) 113.8 GPa
17) Density	18) 4.43 g/cc
19) Yield Tensile Strength	20) 880 MPa
21) Ultimate Tensile Strength	22) 950 MPa
23) Yield Compressive Strength	24) 970 MPa
25) Poisson Ratio	26) 0.342
27) Shear Strength	28) 550 MPa

2.3.2 Construction of 3D model

The 3D model of the spherical fuel and oxidizer tanks were constructed using SolidWorks 2014 Edition by constructing a hemispherical design at first with an outer diameter of 0.461 m and 0.522 m respectively. At the same time, a 0.03 meter flange from the outer diameter of both tanks were added to hold the bolts and nuts in place. By assuming the wall thickness of 0.01 meter, the inner diameter was then extruded cut to create a hollow spherical tank. The completed hemispherical propellant tank design was then copied for assembly. During the assembly, the two hemispherical tanks (top and bottom) for fuel and oxidizer tanks respectively. Bolts and nuts were then mated to the assembly to complete the finalized design.

2.3.3 Static Analysis

Two approaches were used to analyze the propellant tanks whereby the first approach was done by removing the bolts and nuts from the finalized design and just solely focused on the propellant tank's mounting part as shown in Figure 1. The second approach was focusing only on a single bolt and nut joint on the propellant tank's mounting part as shown in Figure 2. The finalized design then is imported to ANSYS 15.0. FEA workbench using static structural analysis is then selected to analyze the propellant tank's mounting parts.

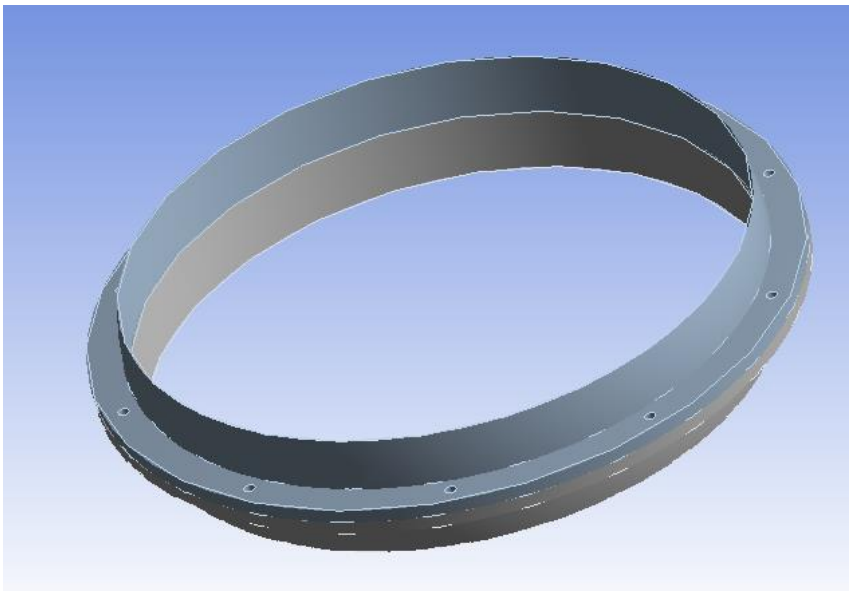


Figure 1. Propellant Tank Mounting Part.

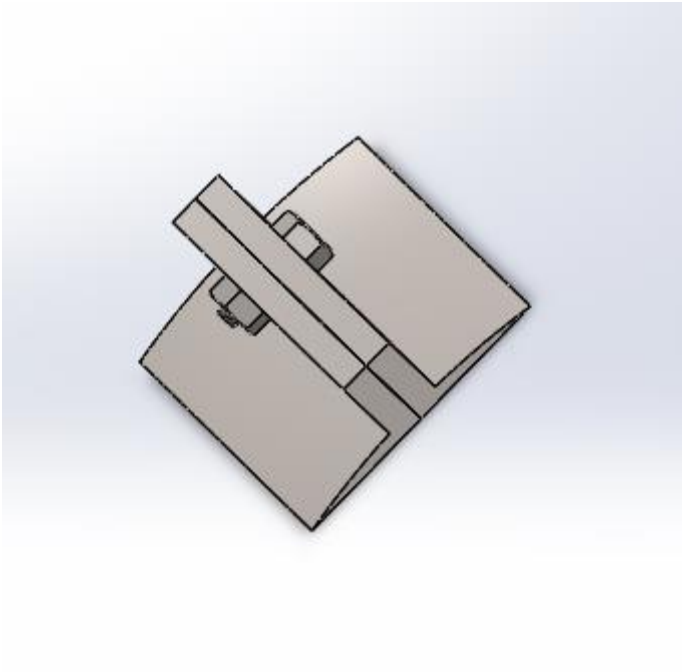


Figure 2. Propellant Tank section of bolt and nuts.

2.3.3.1 Meshing methods used for propellant tanks and bolts.

As shown in Figure 3 and 4, the meshing methods used for both propellant tank mounting part as well as bolt and nuts are using hex-dominant methods. The method utilized both tetrahedral and hex methods which improves the meshing quality to obtain a more accurate results for the project. Moreover, a solid bolt model was designed for the accuracy of the simulation results because it can predict the physical behavior of the structure [5].

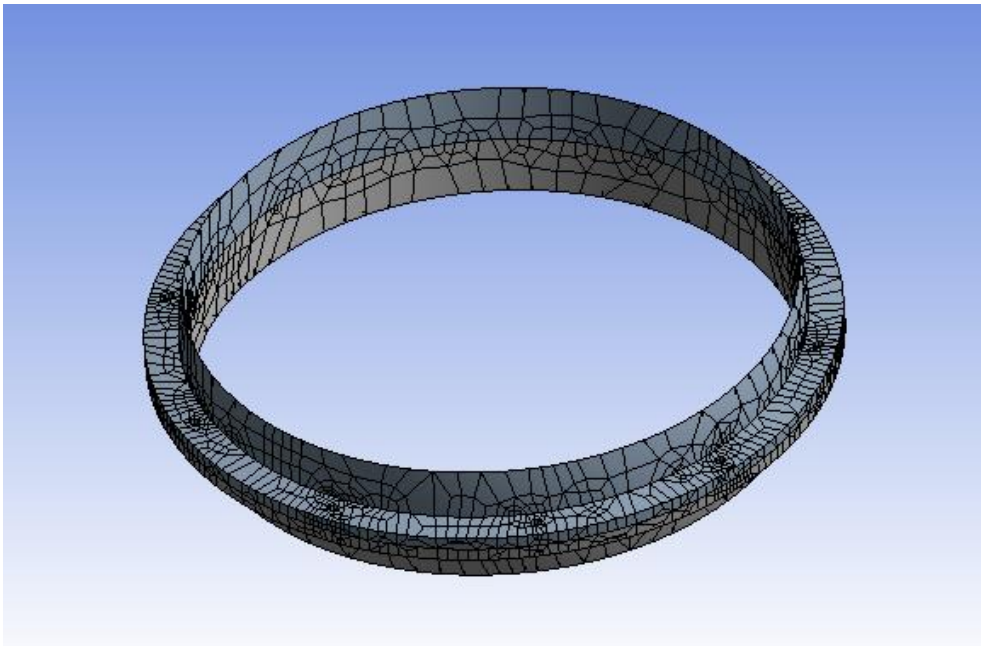


Figure 3. Hex-dominant meshing method on propellant mounting part.

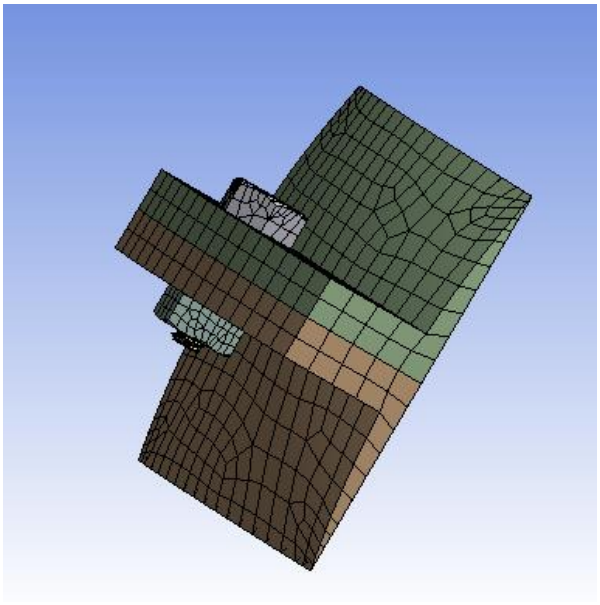


Figure 4. Hex-dominant for propellant tank bolt and nuts.

2.3.3.2 Setting boundary conditions

The boundary conditions of the project were set based on the given operating conditions and parameters provided in Table 1 and 2 respectively. As shown in Figure 18, a fixed support was applied onto the mounting part. The mounting part is to be fixed on an external surface of the lunar lander to hold the propellant tank intact. Since the given operating pressure of 500 000 Pa was given, an internal pressure is applied onto the mounting part internal surface. These procedures were then repeated for the propellant tank's bolt and nuts as shown in Figure 19. The tensile force of the bolt is then added onto the bolt structure to simulate and analyze the bolt deformation.

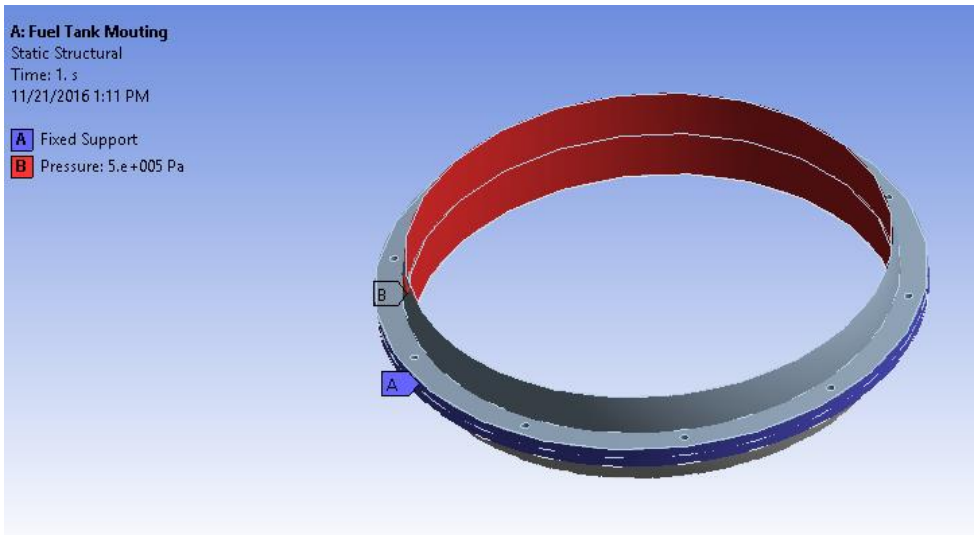


Figure 5. Boundary conditions applied for propellant tank mounting part.

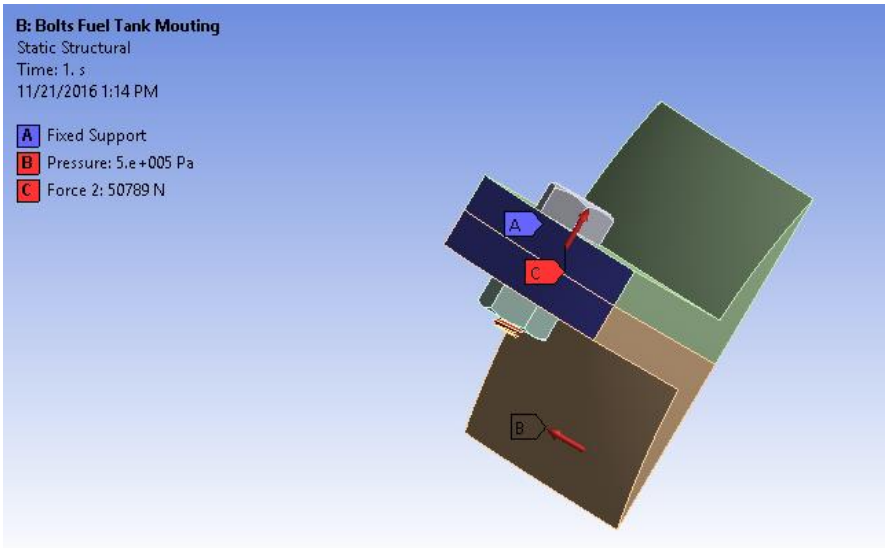


Figure 6. Boundary conditions applied for propellant tank bolts and nuts.

2.3.3.3 Static analysis solutions

In regards to the static analysis, the total deformation, equivalent elastic strain and equivalent stress is chosen to analyze the mounting part. Furthermore for the second approach which focused only on the bolts and nuts behavior, the total deformation and equivalent stresses is chosen.

3.0 Results and Discussions

3.1 Propellant Tank 3D Model

Based on previous space missions conducted for the past decades, the wide and most common ranged propellant tank design used was a spherical tank. The spherical tank was selected among different designs based on the literature [2]. Figure 3 below shows the constructed 3D model of the propellant tank.

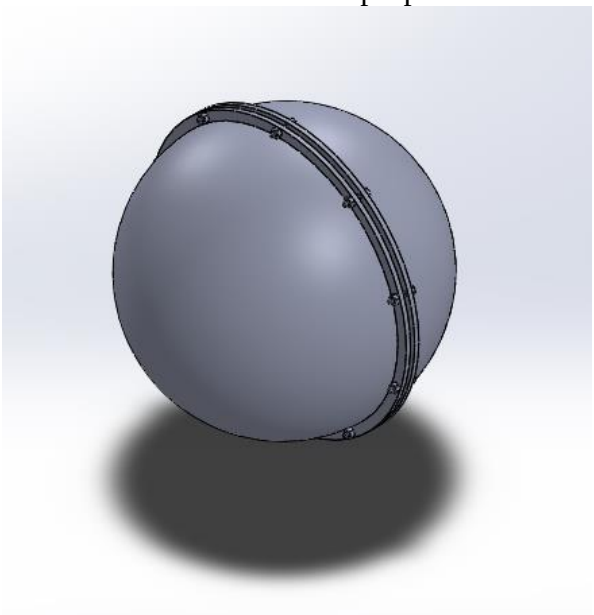


Figure 3. Propellant Tank 3D Model

3.1.1 The Propellant Tank Wall thickness used

As the propellant tank material used was Ti-6Al-4V, the wall thickness is calculated for the propellant tank from the equation (3) based on the parameters by Independence-X:

Table 3. Calculated wall thickness for fuel and oxidizer tanks.

29) Mission Propellant Tank Parameters	30) Outer Diameter 31) (m)	32) Calculated Wall Thickness, t 33) (m)
34) Mono methyl hydrazine, MMH 35) (Fuel Tank)	36) 0.461	37) 0.00008911
38) Nitrogen Tetroxide, MON3 39) (Oxidizer Tank)	40) 0.522	41) 0.00010090

Alliant Techsystems Inc. (ATK Space Systems) from the United States of America had been researching and developing various propellant tank solutions for various NASA or space programs for the past decades. As ATK had manufactured various types of propellant tanks, the technical papers for the closest propellant tank can be used to compare and obtain a reasonable wall thickness used by ATK. The technical reference values were inserted based on the current mission requirements to achieve a reasonable application as ATK System's propellant tanks were all manufactured in a large scale.

Table 4. Wall thickness of ATK System's products.

42) Author	43) Reference	44) Year	45) Technical paper wall thickness, t (m)	46) Difference for fuel tanks, (%)	47) Difference for oxidizer tanks, (%)
48) Walter T. Ham Gary H. Kawahara	49) [5]	50) 2000	51) 0.000110	52) 18.99	53) 8.27
54) Michael J. Debreceni T. K. Kuo	55) [7]	56) 2001	57) 0.000199	58) 54.97	59) 49.30
60) Walter H. Tam.	61) [8]	62) 20	63) 0.000104	64) 14.32	65) 2.98

Mark D. Drey		01			
66) Joe Benton Ian Ballinger	67) [2]	68) 2007	69) 0.000148	70) 39.79	71) 31.82

By comparing the calculated wall thickness for the designed propellant tanks in Table 3 with the applied ATK's designed propellant tank in Table 4 based on the current mission requirements, the calculated wall thickness can be approximated close with the ATK's wall thickness. Hence, the calculated wall thickness can be verified and be used for the further design and analysis by assuming the wall thickness to be 0.01 meters for each fuel and oxidizer tanks. The calculated wall thickness has a positive percentage difference which shows that the designed propellant tank can be assumed approximately close to the given wall thickness range hence the calculated wall thickness can be verified and validated to be used as the propellant tank's wall thickness.

3.2 Number of Bolts and Nuts required for each propellant tank

Bolts and nuts were used due to the limitation and weakness of welding onto a spherical propellant tank which had been brought up by [7] in previous missions. Moreover, highly skilled professional and skilled workers is needed to weld the two hemispherical tanks together but however it doesn't provide 100% leak prove. Although the usage of bolt and nuts were not to be 100% leak prove as well but however the usage can still be applied for the mission. Table 5 below shows the different types of bolt class and its material specifications which determined the number of bolts needed for both propellant tanks.

Table 5. Number of bolts for fuel and oxidizer tanks.

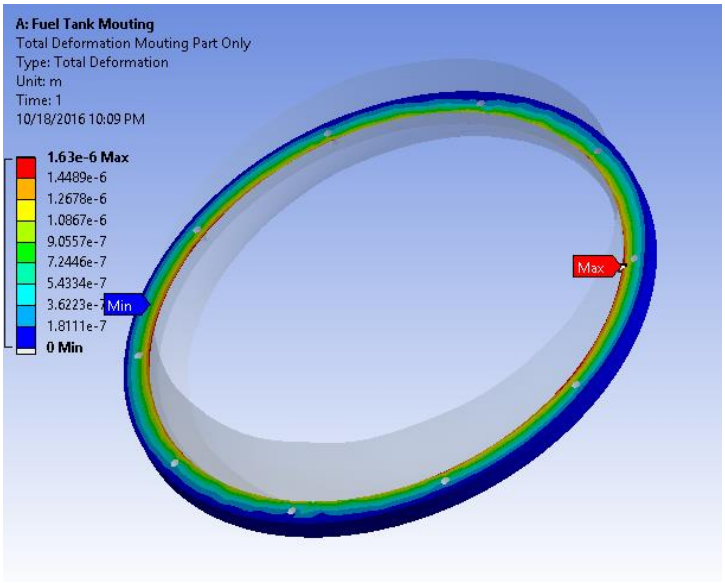
Bolt Class	Min Proof Load (MPa)	Allowable Bolt Pressure (MPa)	Nominal Diameter (m)	Number of Bolts for Fuel, n	Number of Bolts for Oxidizers, n	Diameter of Bolt Head (m)
5.8	380	253.33	0.006	70	90	0.010
	380	253.33	0.008	40	52	0.013
	380	253.33	0.01	26	34	0.017
	380	253.33	0.012	18	24	0.019
8.8	580	386.67	0.006	46	60	0.010
	580	386.67	0.008	26	34	0.013
	580	386.67	0.010	18	22	0.017
	580	386.67	0.012	12	16	0.019
12.9	970	646.67	0.006	28	36	0.010
	970	646.67	0.008	16	20	0.013
	970	646.67	0.010	10	14	0.017
	970	646.67	0.012	8	10	0.019

The bolt class 12.9 which is alloy steel was chosen for the propellant tank due to its higher allowable bolt pressure before permanently deforming. As the propellant tank would be travelling into space and lunar surface where by the environment would be more challenging, a higher allowable bolt pressure would provide extra safety precaution to prevent leakages to the propellant tank itself. Moreover, the ideal number of bolts for fuel and oxidizers to be used would be 10 bolts and 14 bolts respectively because too many bolts and nuts on the flanges would add extra weight to the propellant tank itself. Also, the bolt head diameter was sufficient to fit onto the 0.03 meter flange of the propellant tank. Hence, the selected bolts and nuts for both propellant tanks would be M10 X 12.9.

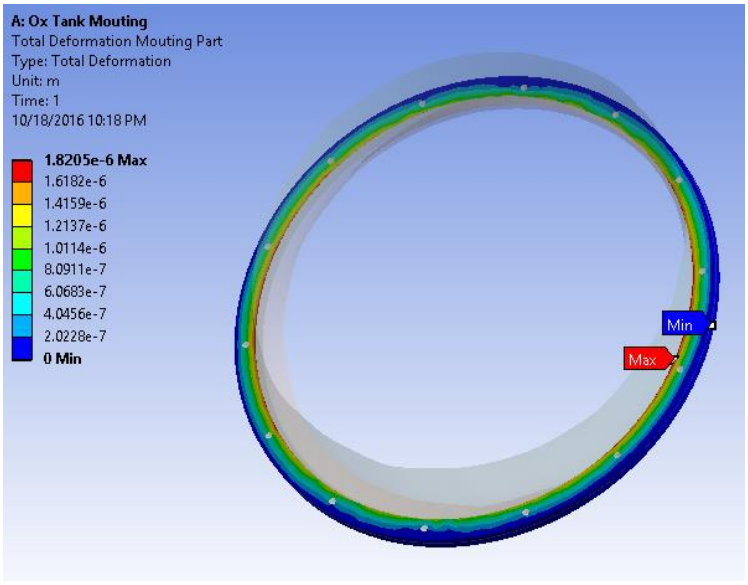
3.3 Stress and Deformations of Static Analysis of tank's mounting parts.

3.3.1 Static Analysis – Propellant Tank Mounting Parts

The total deformation of the propellant tank's mounting parts will determine if it will hold the structure under maximum operating conditions. Is it observed from the Figure 4 (a) and (b), the mounting part of the propellant tanks will deform with a maximum distance of 1.63 x 10^{-6} m and 1.8205 x 10^{-6} m respectively when the internal pressure of the tank is applied. Moreover, as the internal pressure uniformly distributed around the propellant tank, the mounting part will expand but however with the very small deformation the mounting part of the tank will able to support the structure itself.



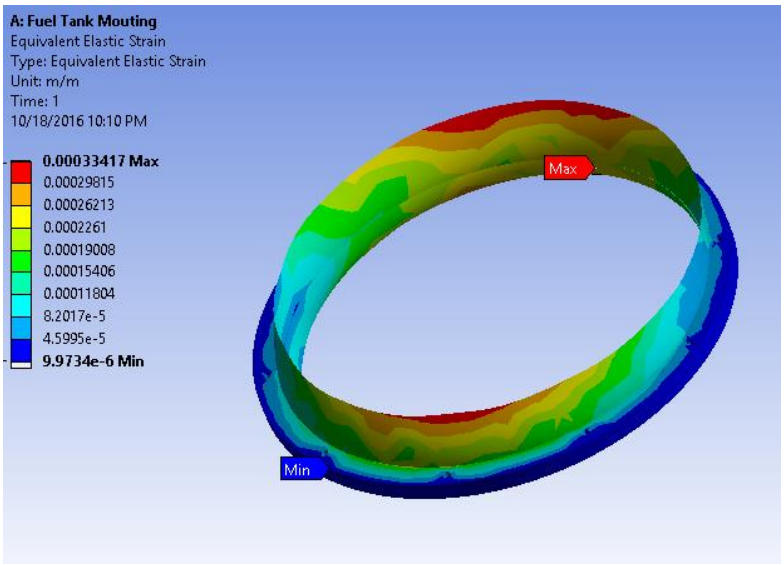
(a)



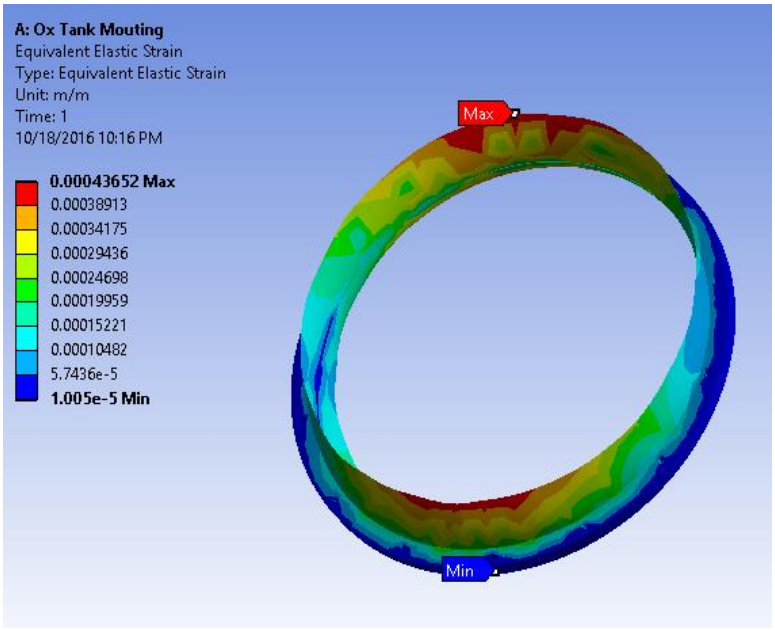
(b)

Figure 4: (a) Total deformation of fuel tank mounting part. (b) Total deformation of oxidizer tank mounting part.

Based on Figure 5 (a) and (b) respectively, the stress developed on the mounting part for both propellant tanks, the elastic strain of the mounting part was not at the maximum elastic strain region. Hence, the mounting part will not deform to the maximum region with the allowable stress used. The mounting part would be able to support the tank's structure under given operating conditions.



(a)

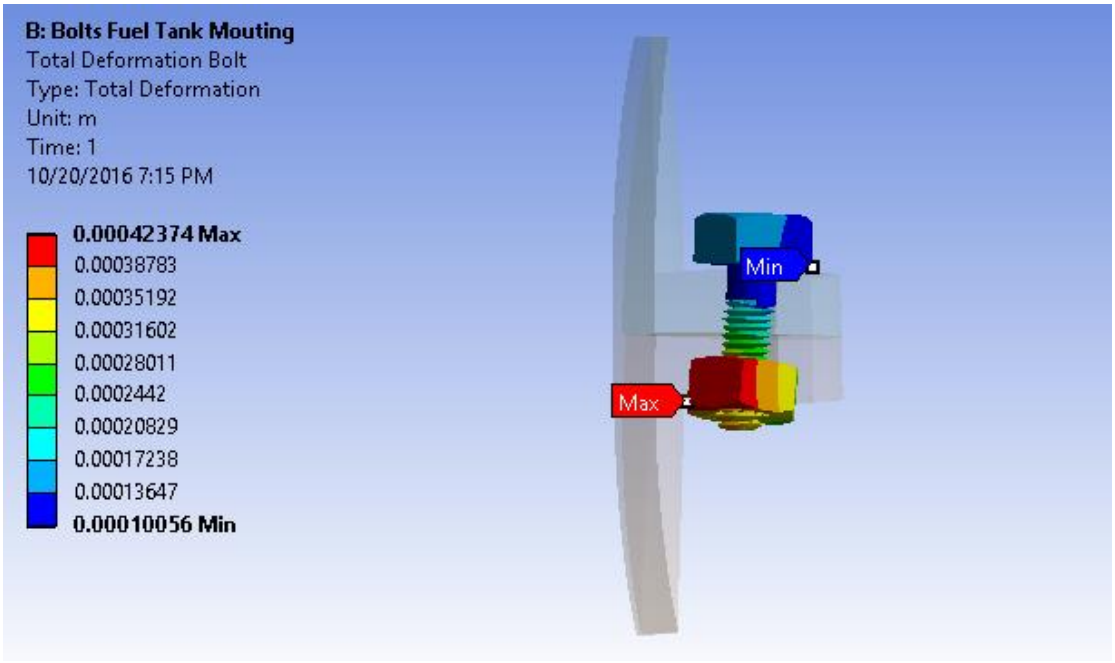


(b)

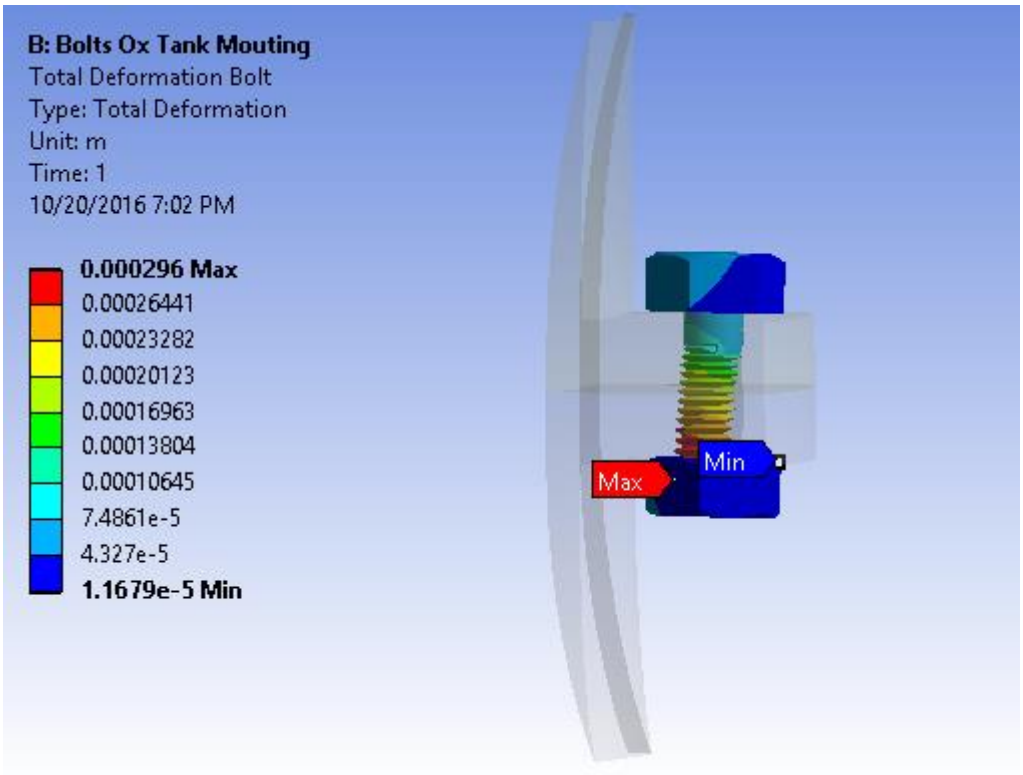
Figure 5: (a) Equivalent elastic strain of fuel tank. (b) Equivalent elastic strain of oxidizer tank.

3.3.2 Static Analysis – Propellant Tank Bolts and Nuts

The bolts and nuts used for each propellant tanks had to be analyzed to determine if it's able to support the mounting parts under operating conditions. The analyzation of a single bolt and nuts would be sufficient and the results can be assumed to be similar with other bolts and nuts because the total internal pressure of the propellant tank is uniformly distributed. Figure 6 (a) shows the bolt end deformed the most as the bolts experience high tensile force which caused it to bend towards the propellant tank wall. Furthermore, the nut also deforms deficiently towards the propellant tank wall and the mounting part due to the terrible deformation of the bolt end. This permanent deformation would affect the bolt's strength to hold the mounting parts together and cause potential leakages of propellants. With the maximum deformation by the bolt end, the propellant tank will also bend outwards which will affect the tank's structure. Figure 6 (b) shows that the bolt end deformed the most causing the oxidizer tank's structure to bend outwards. However, the nut doesn't deform much as it would able to hold the bolt end deformation.



(a)

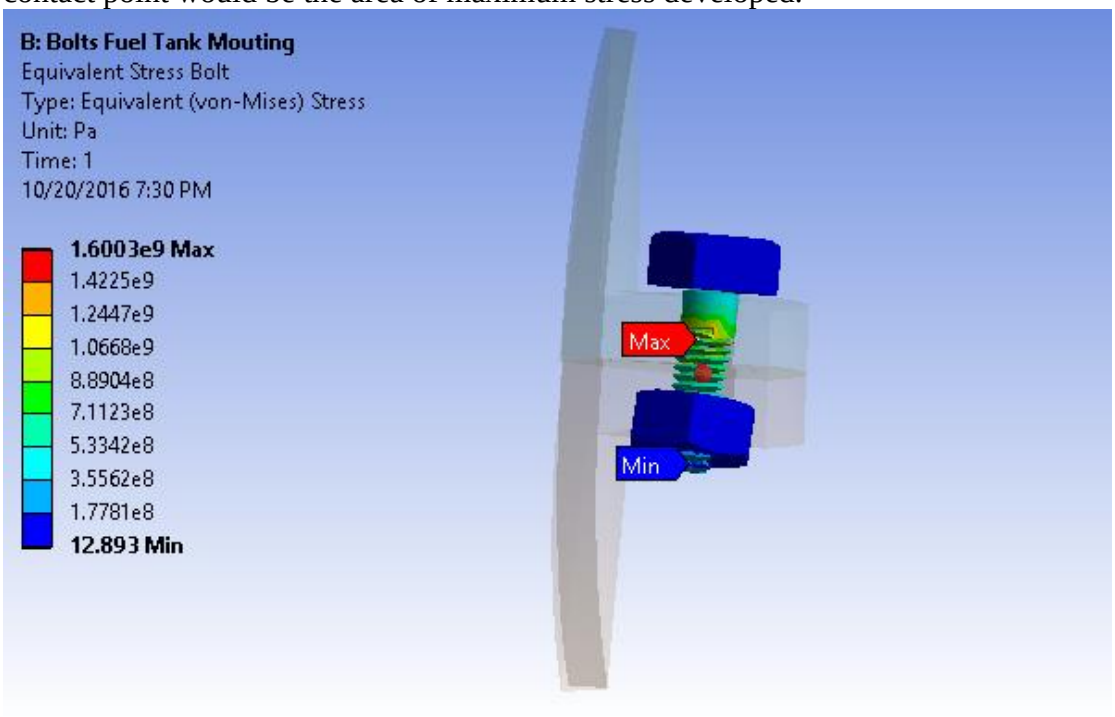


(b)

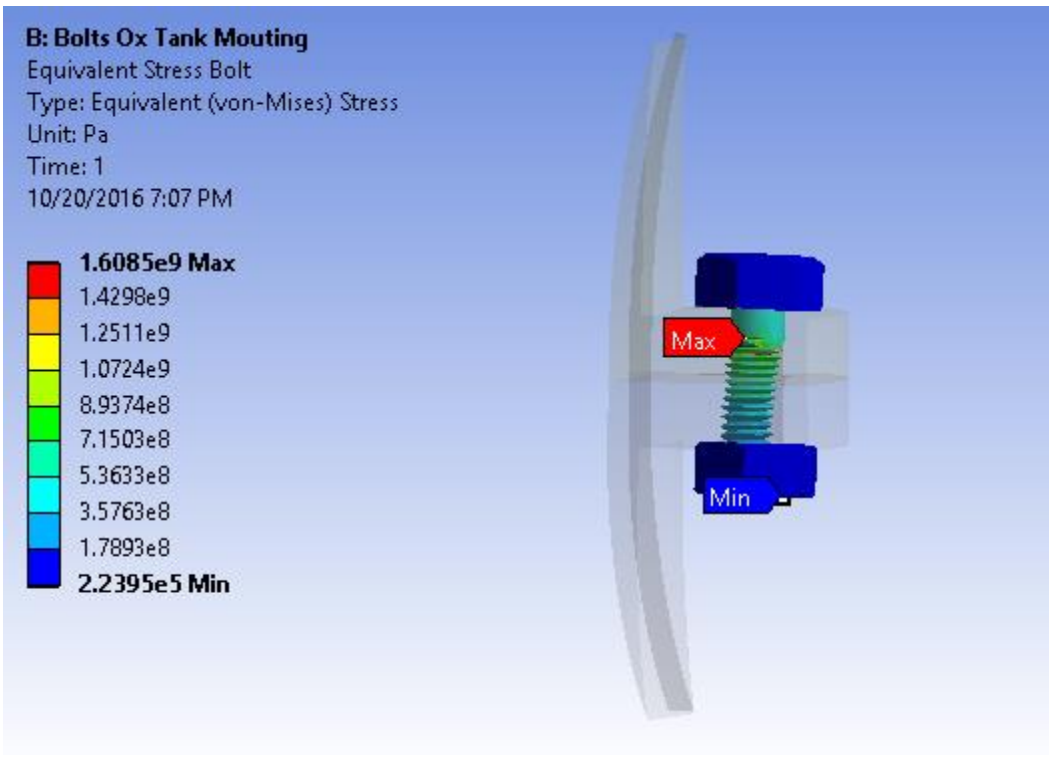
Figure 6: (a) Total deformation of fuel tank bolts. (b) Total deformation of oxidizer tank bolts.

The equivalent stress shown in Figure 7 (a) and (b) respectively shows the stress developed on the bolt itself as it deforms based on the bolt's tensile force and the tank's internal pressure. Both figures showed that the maximum equivalent stress developed onto the bolt itself would be approximately near the center of the bolt itself. This signifies that the bolt's leg experienced a higher stress contact compared to the

bolt's head during maximum deformation. If the bolt were to fracture, the critical contact point would be the area of maximum stress developed.



(a)



(b)

Figure 7: (a) Equivalent stress of fuel tank bolts. (b) Equivalent stress of oxidizer tank bolts.

Table [6]. Pre-Load stress of bolt class 12.9 of M10 nominal diameter [].

72) Bolt Class	73) Pre-load, [] (N)	74) Bolt tensile force (N)	75) Difference (%)
76) 12.9	77) 48 075	78) 50 789	79) 5.65

As shown in Table 6, the tensile force of the M10 x 12.9 bolts is higher than the pre-load force. Based on the total deformation results shown in Figure 7 (a) and (b), the bolts deforms severely under operating conditions which hence support the analytical values in Table 6.

4.0 Conclusion

A spherical propellant tank was used to avoid fluid sloshing which may clog the propellants and cause engine failure due to insufficient supply of propellants. Bolts and nuts were used in the propellant tank design compared to welded joints because welded joints had a weak parent material which would cause potential leakages. Furthermore, the wall thickness of the tank was calculated and determined to be 1 cm for both propellant tanks. It was determined that the calculated wall thickness was within the range with the manufactured ATK products under the similar operating condition. M10 X 12.9 bolts and nuts were to be used for the tanks due to its high proof strength. Hence, the number of bolts required for the fuel and oxidizer tanks were 10 and 14 bolts respectively. The static analysis were done on the propellant tank's mounting parts and bolts separately to determine the total deformation, equivalent strains and stresses respectively. Based on the given operating conditions, the ANSYS workbench simulation showed that the mounting part of the propellant tanks will deform minimally within an acceptable level. However, theoretically the bolt tensile force exceeded the pre-load stress of the bolt which resulted in a severe deformation as shown in the simulation. Thus, it is not recommended to use a bolted connection propellant tank due to the severe deformation of the bolts which will potentially cause leakages. One of the future work could be done is to decrease the safety factor used for the bolts or analyzing a double-lap bolted joint used in the aerospace industry [9].

Acknowledgements

The author would like to express his highest appreciation towards the project's industrial partner, Independence-X Sdn Bhd for their contribution and guidance with the research project.

References

[1] N. G. Society, "Moon Exploration, lunar exploration information, moon landing facts, news, photos -- national geographic," National Geographic, 2015.

[2] J. Benton, I. Bllinger, D. E. J. Jaekle, and M. F. Osborn, "Design and Manufacture of a Propellant Tank Assembly," AIAA, no. December 2004, p. 5559, 2007

[3] C. T. Modlin and J. J. Zipay, “for Aircraft & Spacecraft – History , Definition and Applications,” pp. 1–26, 2014.
[4] A. C. Ugural, Mechanics of materials. New York: McGraw-Hill Inc.,US, 1990.
[5] J. Kim, J.-C. Yoon, and B.-S. Kang, "Applied Mathematical Modelling," Finite element analysis and modeling of structure with bolted joints, Jul. 2006.
[6] W. H. Tam, G. H. Kawahara, and L. W. Larsson, “Design and manufacture of a propellant tank assembly,” no. January, 2000.
[7] W. H. Tam and M. D. Drey, “Design and manufacture of an oxdizer tank assembly,” 2001.
[8] M. Debreceni, D. Jaekle, and T. Kuo, “Development of a Titanium Propellant Tank,” 39th AIAA/ASME/SAE/ASEE Joint Propulsion Conference and Exhibit, 2003.
[9] R. H. Oskouei, M. Keikhosravy, and C. Soutis, "The Aeronautical Journal," A finite element stress analysis of aircraft bolted joints loaded in tension, vol. 114, no. 1156, Jun. 2010.

eureca 2016 – Conference Paper
Paper Number 2ME13

Poly-L-lactid Acid / Forsterite Hybrid Membrane for Bone Tissue Regeneration

Fadhli Hazim Abu Bakar, *Yong Leng Chuan*

School of Engineering, Taylor's University, Malaysia.
fadhli_abu@yahoo.com

Abstract

Poly-L-lactid acid (PLLA) / Forsterite (F) hybrid membranes were fabricated using a technique known as electrospinning, for the purpose of bone tissue recovery. PLLA is a well-known polymer and is widely used in fabricating tissue engineering scaffolds. The introduction of forsterite, which has a very high structural property is hoped to help strengthen the hybrid membrane produced. The aim is to produce nano scaled fibers that closely resembles the nano scale particles in the human bone and tissue. This research focuses on investigating the effects of molecular weight on electrospun material and also optimization of the electrospun PLLA/forsterite hybrid membrane. The study of the structural and morphological properties of the hybrid membrane was done by observing the Scanning Electron Microscope (SEM) and studying the diameter of the nanofibers. A mixture of dimethylformamide/dichloromethane was used as the solvent. Optimization helps determine the parameters of the electrospinning technique to obtain the best PLLA/forsterite hybrid material. Through optimization, smooth nanofibers were formed for PLLA sample with concentration 15% and solvent dimethylformamide (DMF) / dichloromethane (DCM) using supply voltage of 12kV, flow rate of 0.3 ml/h and distance from tip to collector of 15cm. It was observed that using a 15% concentration of PLLA with molecular weight 14.9754g shows smooth nanofibers being produced and has great promise towards tissue engineering research. The PLLA/forsterite blend also shows good results as the PLLA was seen to blend well with the forsterite nanoparticles. The size of the nanofibers produced also shows that the electrospun membrane has great structural properties.

*Keywords:*Electrospinning, Concentration, Optimization, Structural properties, Parameters.

1. Introduction

Bioengineering or biomedical engineering is a branch of engineering that combines the knowledge of engineering, biology and medicinal science into one and have endless possibilities. This discipline helps in improving the general health of humankind by integrating engineering concepts with biomedical ones and ultimately improves clinical practices, and this relates directly to the grand challenges faced by every engineer in improving health informatics and also providing better medicine. Engineers in this field mostly apply molecular biology to study and increases research done to create more advance biotechnology. Throughout the years, advancement in this field helps engineers develop tissue engineering, with the main goal to create artificial human tissue for patients that needs transplant. These artificial tissues are fabricated to achieve multiple purposes but they also must have high biocompatibility to avoid any complications to the patient's body. One of the main material used in producing artificial organs are actually composites of polymers or polyesters with ceramic materials. These composite materials or better known as hybrid membranes would be engineered to have the high biocompatibility of polymers combined with the high mechanical properties of ceramics [1].

Poly-L-lactid acid or PLLA is a bio-degradable polyester that is produced from renewable resources such as starch, corn starch and sugar cane. Basic Polylactide (PLA) is one of the highest consumed basic materials in producing bio-plastic, which are plastics produced from bio waste. PLA is produced by reacting 2 monomers, lactid acid and lactide and conducting ring-opening polymerization on the monomers. PLLA is produced using the same concept but uses L, L-lactide instead of normal lactide during polymerization [1]. PLLA has been used widely in the field of bioengineering due to its biocompatibility but the polymer itself is has very low mechanical properties. It has around 37% crystallinity, a melting point at around 173oC and a tensile modulus ranging from 2.7 GPa to 16 GPa.

A sample of pure forsterite is made of magnesium, oxygen and silicon with chemical formula Mg_2SiO_4 and has a molecular weight of 140.69 gm. Forsterite is known to have superior mechanical property due to their atomic structure and have a very high melting point that easily surpass human body temperature. Forterite has a very high fracture toughness and very similar to that of cortical bones and this makes them a good candidate to substitude bones [2]. In Vitro studies also proves that forsterite has good bioactivity and can help promote bone tissue proliferation and adhesion, but a sample with too high forsterite concentration can cause agglomeration of the polymer matrix and results in the depletion of the integral property of the composite.

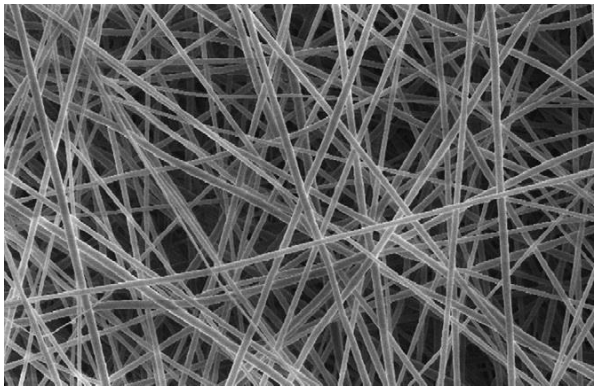


Figure 1. Scanning Electron Microscope (SEM) observation of electrospun nanoparticle [2]

The electrospinning system gives non-woven in the request of a couple of nanometers substantial surfaces, ease functionalization for different purposes and predominant mechanical properties. Moreover, the likelihood of vast preparations joined with the straightforwardness of the procedure makes this an extremely intriguing strategy for a wide range of utilizations. Biomedicine and bioengineering is a noteworthy application region that utilizes the many techniques of electrospinning strategy. Electrospinning set can be altered in various approaches to join the properties of materials with various morphological structures for these applications. Practical nanofibrous tissue engineering membrane created by electrospinning have extraordinary potential in numerous biomedical applications, for example, wound dressing, compound immobilization and medication delivery [3].

For a particular successful application, the substance, physical and organic properties of electrospun tissue engineering membrane ought to be conformed to coordinate nature by utilizing a mix of polymeric and ceramic structures and manufacture procedures in which electrospinning have become a tool of choice nowadays [3]. Electrospinning is a unique method where the electrostatic force is used to form micro- and nano-sized tubes from composite materials. Figure 2 shows the basic schematic of a typical electrospinning system. The syringe pump is used to force a polymer solution through the needle. The polymer solution passing through the needle is subjected to charges of certain polarity by the high voltage DC supply. A taylor cone is formed when the force created is sufficient to overcome the polymer's surface tension. A distorted fiber jet is then deposited and transferred to the collector [4].

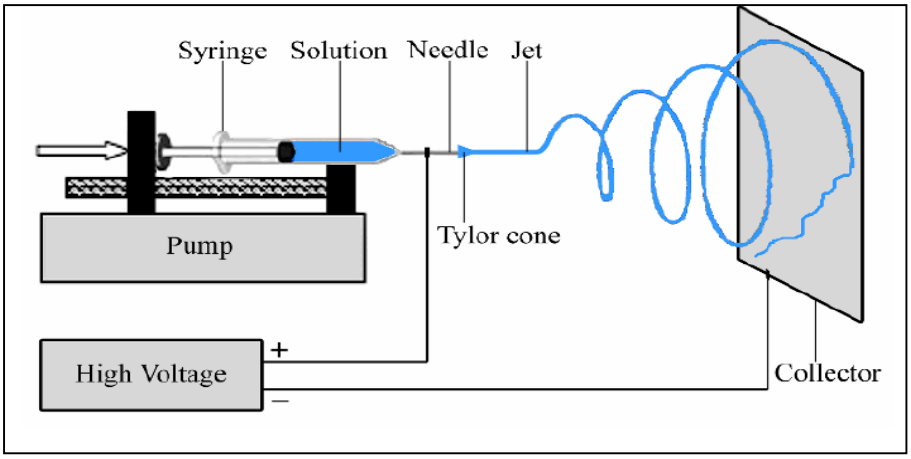


Figure 2. Illustration of horizontal electrospinning method **Error! Reference source not found.**

New innovative development in electrospinning processes, namely the two-component electrospinning and in-situ mixing electrospinning can help further enhance the property of the nanofibrous membrane. Post changes of electrospun films likewise give successful means to render the electrospun platforms with controlled anisotropy and porosity **Error! Reference source not found.**. This research is focused on fabricating tissue engineering membrane with electrospinning process with a composite material poly-L-lactic acid (PLLA)/forsterite, and the optimization of the hybrid membrane.

2. Methodology

In this research, a few samples of PLLA/Forsterite hybrid membranes are to be fabricated and the parameters need to be optimized to obtain the best results.

2.1 Properties of Electrospun Hybrid Membrane

Gang Sui *et al.*(2006), fabricated a poly-l-lactic acid/hydroxyapatite (HA) hybrid membrane using electrospinning and documented the process in their paper. They measured the Braunauer-Emmett-Teller specific surface area to investigate the structural properties and morphology of the specimen, while observing the SEM and TEM. Tensile test was also done to determine the mechanical properties. To investigate the biological performance of the membrane, the team carried out an *in vitro* degradation test. The results show that the PLLA/HA hybrid membrane not only has a higher tensile strength compared to PLLA on its own, but also shows stronger surface bonding [7]. Another promising result is that the PLLA/HA hybrid membrane promotes a far better re-growth of cell compared to pure PLLA. All though we will be focusing on the structural properties of the tissue engineering membrane, we also have to make sure that it still have good degrading rate as the composite material PLLA/HA and by running these type of test we can determine the biocompatibility. Figure 3 shows the observation of the electrospun membrane of PLLA and PLLA/ HA. It can be clearly seen that the introduction of HA gives a more complex structure to the membrane, thus giving the hybrid membrane a better mechanical property

2.2 Electrospinning

The dissolvable framework was worked to produce a spinnable PLLA/Forsterite dispersion. Then dimethylformamide (DMF) and PLLA particles were added to the suspension and the suspension was homogenized for 12 hours. Generally, the morphology of polymer nanofibers we aim to achieve is smooth and continuos nano-scaled fibers samples. These are impacted by different handling parameters, for example, the thickness, the connected voltage, the flow rate and the separation between tip of the syringe and the collector [7]. Therefore, these parameters are optimized and kept constant throughout the experiment.

The electrospinning machine consists of 3 main parts. The first part is the collector roller control. It consists of the collector drum that will roll as the nanoparticles are dispersed on it, and the speed controller that controls the speed which the drum will spin. A higher speed results in higher dispersion of the nanoparticles. Second part is the hydraulic pump. This pump is connected to a syringe and it controls the flow rate in which the mixture is dispersed. Lastly would be the power supply. It is connected directly to the needle of the syringe and provides the voltage needed to act on the polymer mixture. The PLLA/Forsterite solution was transferred into the 10 m/l syringe pump. The polymer solution is then forced out, passing through the needle that is subjected to charges of certain polarity by the high voltage DC supply. The voltage supply must be higher than the threshold frequency of the mixture. A taylor cone is formed when the force created is sufficient to overcome the polymer's surface tension. A distorted fiber jet is then deposited and transferred to the collector. The collector plate is grounded to generate an electrical field between them. The process is continued until a uniform distribution of the PLLA/Forsterite hybrid membrane was produced.

The membranes were then left to evaporate to remove the solvents. To achieve the best results, multiple preliminary samples were fabricated with varying parameters, namely the voltage of the power supply, flow rate and distance of needle from the collector and tested by SEM observation. The sample with the best SEM observation results was chosen and the parameters were kept constant throughout the experiment, with the exception of the concentration of the forsterite in the polymer mixture.

2.3 Structural properties and morphology

The auxiliary properties or the morphological properties of the membrane of PLLA/Forsterite include surface zone, pore volume and normal pore size. They will be examined by nitrogen adsorption-desorption isotherms utilizing surface area analyzer. Before measuring the properties, the specimen was degassed at 300^{o}c for 12 hours. The specific surface area was calculated by employing the Brunauer-Emmett-Teller (BET) approach, while using the adsorption-desorption profile to calculate the cumulative pore volume. The Joyner-Halenda method was then used to evaluate the average pore size. SEM observation was also taken to study the morphology of the hybrid membrane. This observation is used to determine the average diameter of the nanofibres.

3. Resullts and Discussion

3.1 Solvent

During early stages of fabrication, pure DMF was used as the main solvent to dissolve PLLA and PLLA/forsterite compound. However, extensive optimization could not produce any nanofibers and mainly resulted in electrospraying. Through study of literature and discussion with individuals more experienced in electrospinning, it was found that all though DMF has a very high electrical conductivity, it also have a very low evaporation rate. This causes the solvent not being able to polarize efficiently resulting in the formation of bead fibers with thick diameters as shown in figure 3.

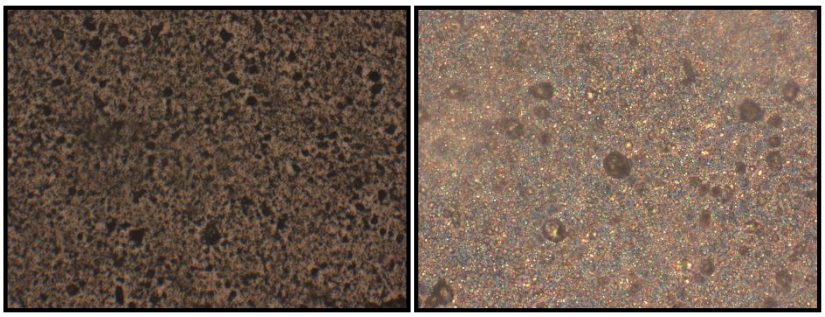


Figure 4 : Microscopic image of electrospun fibers using 100% DMF as solvent with (a) 10% concentration and (b) 15% concentration of PLLA.

To solve this problem, DCM was introduced to the mixture. DCM has a lower dielectric constant compared to DMF, but it has a higher evaporation rate. To determine the best ratio of DMF:DCM, several mixture were prepared with different ratios of DMF:DCM and were electrospun and observed under the microscope. Based on rough observation, a concentration ratio of 70% DCM and 30% DMF produced continuous nanofibers as shown in figure 5. This concentration ratio was then kept constant throughout the rest of the experiment.

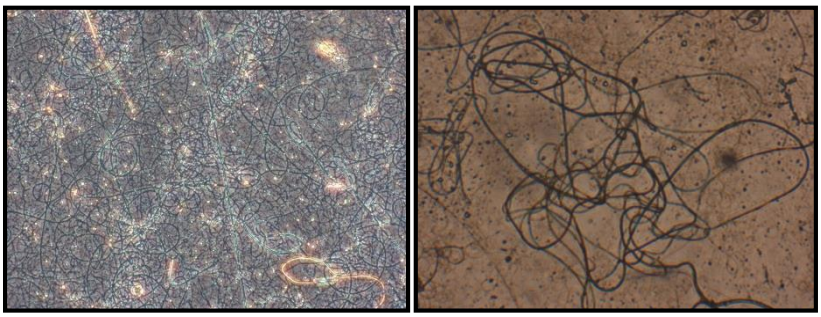


Figure 5 : Microscopic image of electrospun fiber using 70% DCM-30% DMF as a solvent with 15% concentration of PLLA.

3.2 Optimization of Parameters

To obtain the most accurate parameter of the electrospinning process, a check list table was done to shows all the range of parameters used during optimization of the electrospinning process. Though studying literature related to electrospinning of PLLA, a basic ground for the parameter were able to be obtained and were used in drawing up the checklist table. The experiment was repeated with different parameters and was checked of in the checklist indicating that the parameters are done. This process not only help in making sure that all available parameter were investigated, but also help in identifying the range of parameter that produce a good result. Table 1 shows an example of the checklist done using 15% concentration and a voltage of 5kV. A different checklist is used for every change in voltage and concentration. All of the equipment used that has contact with the mixture were first rinsed using ethanol as to avoid introducing contaminant to the mixture and possibly change the concentration and viscosity of the mixture.

Table 1 : Electrospinning parameter checklist at 15% PLLA concentration

PLLA concentration (m/v)	Voltage (kV)	Distance (cm)	Flow rate (ml/h)	
15%	5	10	0.1	0.6
			0.2	0.7
			0.3	0.8
			0.4	0.9
			0.5	1.0
		15	0.1	0.6
			0.2	0.7
			0.3	0.8
			0.4	0.9
			0.5	1.0

Optimization was done on all the different concentration of PLLA dissolved in pure DMF and DMF/DCM mixture. A cover slip was placed on the collector every time a parameter was changed and the fabricated membrane produced would be observed under a microscope to see the morphology. This was done to increase the

efficiency of the process. A lot of time was spent on optimization as even a slight change in the parameters could affect the morphology of the electrospun fibers. During optimization, it was observed that more electrospraying occur at higher voltage and flow rate rather than electrospinning. In electrospinning, the applied voltage needs to be higher than the threshold voltage of the mixture to produce a Taylor cone. However, using voltage and flow rate that is too high may cause the electrospun material to be ejected from the syringe too fast causing the solvent not being able to evaporate enough resulting in electrospraying. It was also observed that it was harder to produce a consistent Taylor cone at low concentration of polymer which in this case determined to be 5% concentration. At low concentration the mixture has lower viscosity and high surface tension causing electrospraying to occur. At 20% PLLA concentration the viscosity of the solution is too high and causing the solution to harden as it forms the Taylor cone. This makes it harder for the solution to be ejected. This hardening shows that agglomeration occurs at high viscosity. This is the result of the polymer chain in the mixture to overlap at a much higher rate without having enough energy to overcome the surface tension.

After performing the preliminary trials, the optimum parameters for the electrospinning process in this experiment were fixed as: voltage = 12kV, feed rate = 0.3ml/h, PLLA concentration = 15%, distance between syringe and collector = 15cm and inner diameter of syringe = 0.7mm. However, there are also parameters that have an effect on the electrospun material but very hard to control one of which is the humidity in the air. During experimentation, a breakdown in the air conditioning system in the electrospinning room causes the room to be hotter than before. Electrospinning process done after the breakdown shows that it was harder to reproduce the same results as before even with all the other parameters kept constant. The sample was placed in a sealed container as shown in figure 6 as to avoid any contamination to the nanofibers produced.



Figure 6: An electrospun sample placed in air tight case

3.3 SEM Images

The scanning electron microscope (SEM) image study was done in Nottingham University Malaysia Campus in Semenyih using their FESEM-EDX machine, model FEI Quanta 400F. As access to this machine was limited, only the best sample observed through normal microscope was brought over for SEM

observation. The sample was cut into 1cm x 1cm squares and placed on the plate as shown in figure 7.

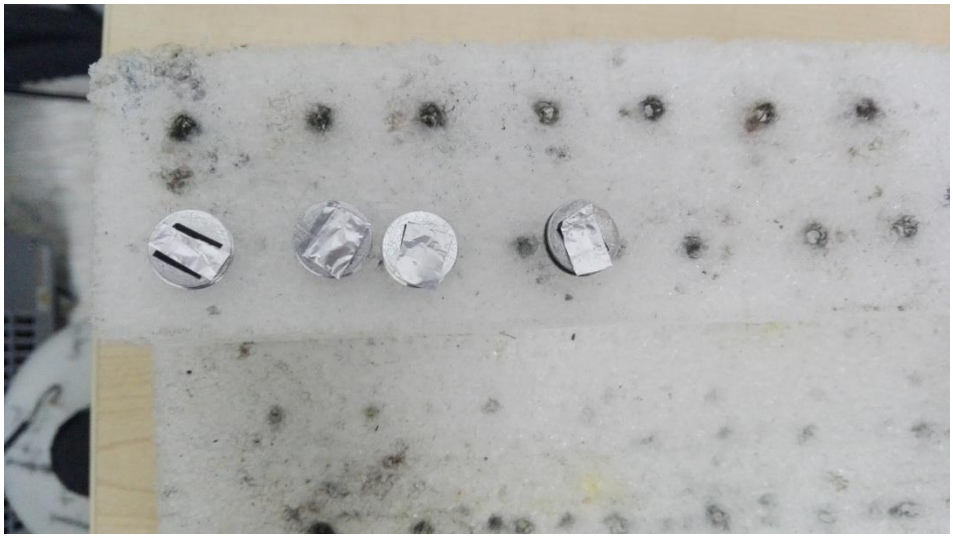


Figure 7 : Sample being prepared for SEM observation

The SEM image obtained was from three different samples using the same concentration of PLLA which is 15% dissolved in DCM/DMF mixture with ratio 70:30. The sample that produced the best SEM image was YLC-1. It was observed that the sample has proper 3D nanofibers. This shows that this sample can fabricate a good membrane not only with strong structural properties but also having good biocompatibility. The molecular weight plays an important role in formation of nanofibers. A lower molecular weight tends to form beads rather than fibers but going to high will promote the formation of micro-ribbons, both of which are not favorable. The SEM results shows that YLC-1 have the optimum molecular weight for 15% concentration. With higher molecular weight, a lower concentration might produce a better nanofiber. More beads formation was also observed in the YLC-2 sample. It can be observed that a 15% concentration of PLLA produced a smooth continuous nanofiber and is deemed the optimum concentration. Figure 8 and 9 shows SEM images of PLLA YLC-1 and YLC-2 respectively.

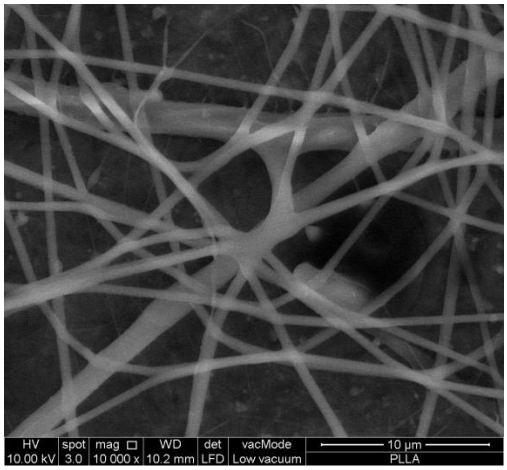


Figure 8 : PLLA (YLC-1) 15% concentration SEM image

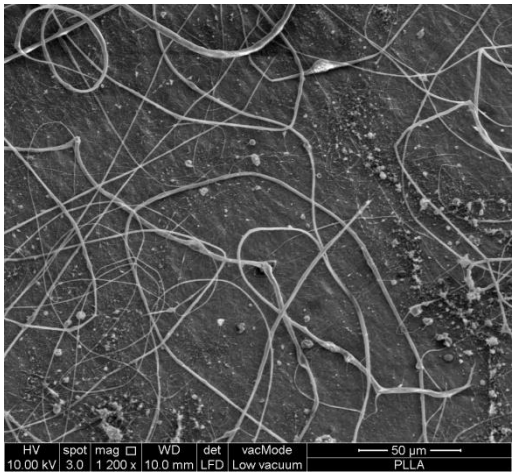


Figure 9 : PLLA (YLC-2) 15% concentration SEM image

The main focus of this experiment is to fabricate nanofibers as to mimic the real nano structure of the bone and tissue of the human body. Therefore the SEM image in figure 10 using a 20 µm scale shows the formation of much smaller nano-scaled fibers formed in the 15% YLC-1 sample. Unfortunately, no high magnification of the SEM image could be taken as the sample was sensitive to the electron bombardment due to sample limitations. When higher level of magnification was tried, the sample starts to deform. The magnification was reduced to avoid ruining the sample. The addition of DCM to the solution helps in increasing the evaporation rate for electrospinning but reduces the electrical conductivity of the sample, making it more sensitive to high energy electron.

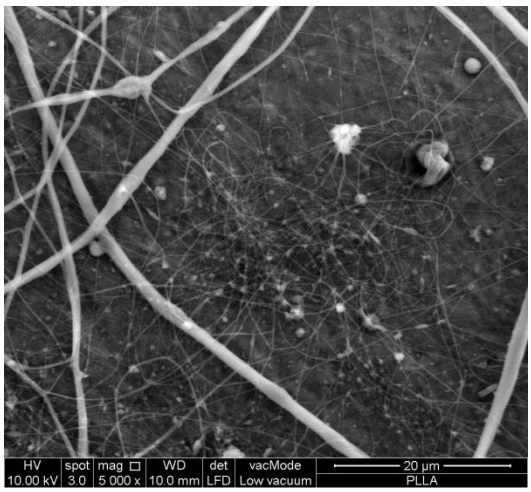


Figure 10 : Formation of nanofibers in the sample

Seeing the YLC-1 sample having the best morphology, forsterite was then added to a 15% concentration of YLC-1 to produce a PLLA/forsterite hybrid membrane The SEM image taken is shown in figure 11. The parameters were kept

constant as to produce the same optimum outcome. It was observed that no continuous nanofiber was able to be fabricated and a lot of beads formation was seen. The forsterite increases the viscosity of the mixture making it harder to eject continuous nanofibers. Non-continuous fibers were observed forming near clusters of particles of forsterite. The electrical field provided was not strong enough to overcome the high viscosity of the mixture causing non-continuous jet stream to form with the forsterite particle. Therefore it can be concluded that the mixture has excess intermolecular entanglement of polymer's molecular chain.

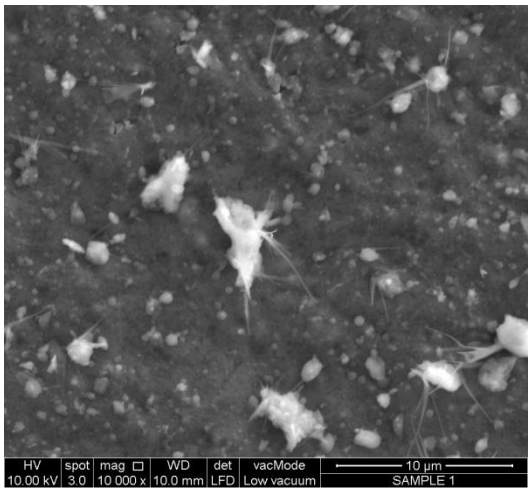


Figure 11 : PLLA 15% + Forsterite 5% concentration SEM image

3.4 Morphology Test

To study the morphology of the sample, the diameter of the nanofibers were obtained using the imageJ software of the FESEM machine. Figure 12 and 13 shows the SEM image with diameter of the nanofibers fabricated. Figure 13 shows the diameter of the smaller nanofibers observed. Low magnification was used so that the sample does not deform due to the bombardment of high energy electron. Table 2 shows the average diameter of the nanofibers formed in the samples.

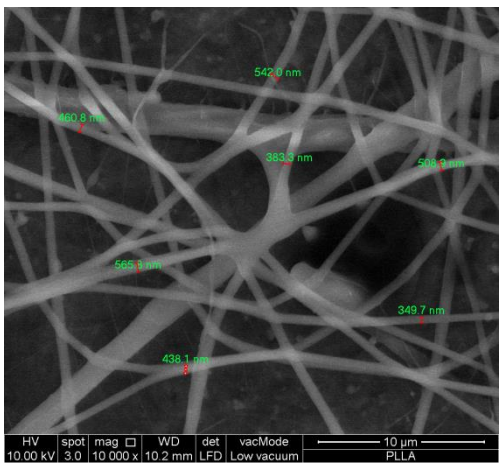


Figure 12 : Various diameter of electrospun nanofibers of YLC-1 sample

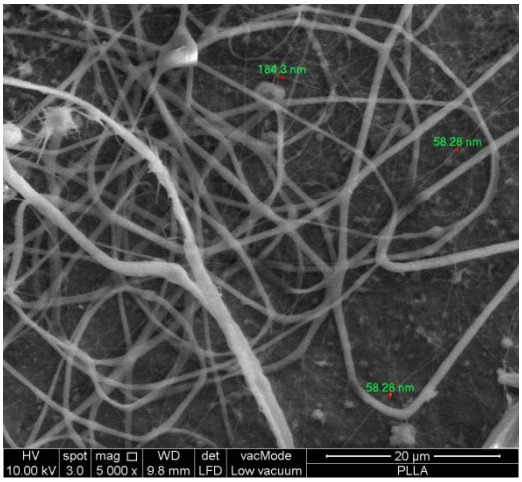


Figure 13 : Smaller diameter of nanofibers

Table 2 : Average diameter of nanofibers of the samples

Sample concentration	Average diameters of nanofibers (nm)
15% PLLA (YLC-1)	242.36
15% PLLA (YLC-2)	464.09
15% PLLA (YLC-1)/5% Forsterite	282.60

Using the EDX analysis, we can observe the chemical properties of the electrospun sample. Based on the data presented in figure 14, the high aluminum percentage is due to the aluminum foil used to collect the sample during electrospinning and can be ignored. We can observe that there is a significant hike in oxygen content in the sample. Oxidation may have occurred during storage of the samples. Limitations during this particular experiment might have lead to this problem arising. This particular problem could be avoided by performing the SEM and EDX analysis straight after the electrospinning process. There were no other contaminant in the sample thus proves that the concentration of the sample was accurate.

Spectrum processing :
Peak possibly omitted : 1.750 keV

Processing option : All elements analyzed (Normalised)
Number of iterations = 3

Standard :
C CaCO3 1-Jun-1999 12:00 AM
O SiO2 1-Jun-1999 12:00 AM
Al Al2O3 1-Jun-1999 12:00 AM

Element	Weight%	Atomic%
C K	40.24	55.58
O K	18.21	18.88
Al K	41.55	25.54
Totals	100.00	

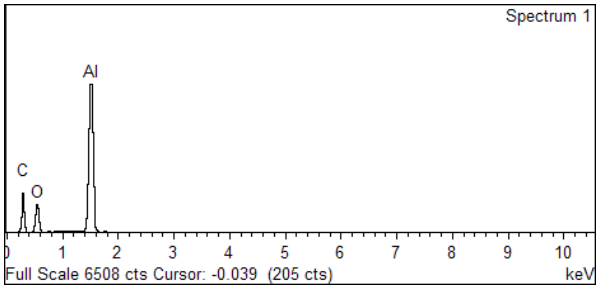


Figure 14 : EDX analysis of 15% PLLA (YLC-1) sample

The EDX analysis of the PLLA/forsterite sample shows the availability of silicon, Si and oxygen, O from the forsterite. This shows that this mixture blend well together and have a good potential to be studied further to study their biocompatibility and mechanical strength provided.

Processing option : All elements analyzed (Normalised)
Number of iterations = 4

Standard :
C CaCO3 1-Jun-1999 12:00 AM
O SiO2 1-Jun-1999 12:00 AM
Al Al2O3 1-Jun-1999 12:00 AM
Si SiO2 1-Jun-1999 12:00 AM
Fe Fe 1-Jun-1999 12:00 AM

Element	Weight%	Atomic%
C K	18.67	32.90
O K	6.50	8.59
Al K	73.71	57.81
Si K	0.71	0.54
Fe K	0.41	0.16
Totals	100.00	

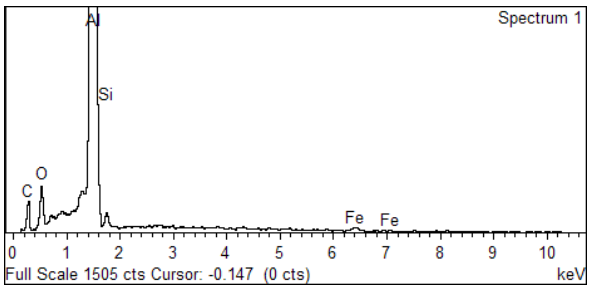


Figure 15 : EDX analysis of PLLA/forsterite sample

4 Conclusion

It can be concluded that electrospinning is a very delicate process. Electrospinning parameter plays an important role in determining the succession of electrospinning, and has a very small range for success for each parameter. Molecular weight was also proven to have an effect on the final product as YLC-1which has a lower molecular weight than YLC-2 produce smoother nanofibers with smaller average diameter. This makes the YLC-1 sample produced to have better structural property when fabricated with 15% concentration. Overall, a mixture of DMF and DCM was seen to be the best solvent for electrospinning of pure PLLA sample as it

has the high electrical conductivity of the DMF and also the high evaporation rate of the DCM solution. Fine continuous nanofibers were able to be produced for the PLLA sample but it was also difficult to obtain continuous bead free electrospun fibers for PLLA/forsterite mixture due to properties of the forsterite. It was determined that the high viscosity and surface tension that the forsterite provide to the mixture were the cause of not being able to obtain a good electrospun sample. SEM images and diameter study proved that these blends can produce nanofibers with good morphology.

Future Works

The PLLA/forsterite blend has very good potential and should be further researched on the best solvent to be used for electrospinning of these materials. Surface modification done on the forsterite sample could be the key to achieving the smooth nanofibers as it may be able to reduce the surface tension of the forsterite nano particle. Furthermore, the biocompatibility of can be further enhanced by performing cell culture on the samples.

References

[1] Pistner, H., Stallforth, H., Gutwald, R., & Muhling, J. (1994). Poly (L-lactide): A Long-term Degradation Study in vivo : Part II: Physico-mechanical Behavior of Implants. *Biomaterials,* Vol. 15, 439-450.

[2] Ramesh, S., Yaghoubi, A., Lee, K. Y., Christopher, K., Hamdi, M., & Hassan, M. (2013). Nanocrystalline Forsterite for Biomedical Applications: Synthesis, Microstructure & Mechanical Properties. *Journal of Mechanical Behavior of Biomedical Materials*, Vol. 25, 63-69.

[3] Liang, D., Hsiao, B. S., & Chu, B. (2007). Functional Electrospun Nanofibrous Scaffolds for Biomedical Application. *Advanced Drug Delivery Review, Vol. 59* , 1392-1412.

[4] TJ, S., & A., V. R. (2008). Electrospinning: Applications in Drug Delivery and Tissue Engineering. *Biomaterials, Vol 29* , 1989-2006.

[5] Haifeng Liu, X. D. (2013). Electrospinning of Nanofibers for Tissue Engineering Applications. *Journal of Nanomaterial* , 1-11.

[6] Kharaziha, M., Fathi, M., & Edris, H. (2013). Effects of Surface Modification on The Mechanical and Structural Properties of Nanofibrous Poly (ε-caprolactone)/Forsterite Scaffold for Tissue Engineering Applications. *Material Science and Engineering, C 33* , 4512-4519.

[7] Sui, G., Yang, X., Mei, F., Hu, X., Chen, G., Deng, X., et al. (2006). Poly-L-lactic acid/Hydroxyapatite Hybrid Membrane for Bone Tissue Regeneration. *Journal of Biomedical Materials Research Part A* , 445-454.

[8] Cohn, D., & Salomon, A. H. (2004). Designing Biodegradable Multiblock. *Biomaterials, Vol 26* , 2297-2305.

[9] Kim, H.-W., Lee, H.-H., & Knowles, J. C. (2006). Electrospinniing Biomedical Nanocomposite Fibers of Hydroxyapaite/poly(lactic acid) for Bone Regeneration. *Journal of Biomedical Materials Research Part A* , 643-649.

[10] Nampoothiri, K. M., Nair, N. R., & John, R. P. (2010). An Over of the Recent Developments in Polylactide (PLA) Research. 8493-8501.

[11] T., P., & M., D. (2013). Characteristion of PCL and PCL/PLA Scaffolds for Tissue Engineering. *Procedia* , 110-114.

[12] Fathi, M. H., Edris, H., Kharaziha, M., & al., e. (2015). PCL-forsterite nanocomposite fibrous membranes for controlled release of dexamethasone. *J Mater Sci: Mater Med* , 26-36.

[13] M., S. R., Hosseinpour, S., Ahsaie, M. G., & K., A. (2015). Smart Scaffolds in Bone Tissue Engineering: A Systematic Review of Literature. *World J Stem Cells*, 657-668.

[14] Mozafari, M., Gholipourmalek, M., Chauhan, N., Jalali, N., & Asgari, S. (2015). Synthesis and characterization of nanocrystalline forsterite coated poly(l-lactide-co-β-malic acid) scaffolds for bone tissue engineering applications. *Material Science and Engineering: C* , Vol 50, 117-123.

[15] Nam, B.-U., Min, K.-D., & Son, Y. (2015). Investigation of the nanostructure, thermal stability, and mechanical properties of polylactic acid/cellulose acetate butyrate/clay nanocomposites. *Materials Letters* , Vol. 150, 118-121.

eureca 2016 – Conference Paper
Paper Number 2ME14

Enhancement of Vibration for FSAE Race Car Driver

Farah Raman Danial*, Mohammad H. Fouladi

School of Engineering, Taylor's University, Malaysia
*farahraman.danial@gmail.com

Abstract
In the recent years of automotive development, car manufacturers have been improving Noise, Vibration and Harshness (NVH) in their vehicles. Ride comfort, drivability and stability are among vital factors in vehicle performances and customer satisfaction. Equally important are the Formula Student race cars which students design, built and race. The car usually runs on a motorcycle engine on a carbon steel spaceframe and is capable of reaching more than 200 km/hr whilst weighing less than 350 kg. Many researches were conducted to identify and reduce the vibration values on vehicles, however since FSAE Race Cars do not function the same way, it is important to test, measure and evaluate the vibration of the car. This paper presents the testing and analysing stage of the engine mounting points of the Taylor's Racing Team 2016 FSAE Race Car.

Keywords: Vibration, FSAE Race Car, Fast Fourier Transform, Power Spectral Density

1. Introduction

Vibration transmission to passengers can largely influence comfort, performance and health [1]. Vibration that is up to 12 Hz can affect all of the human organs while any values higher 12 Hz can have local effects [2]. In a vehicle, the internal combustion (IC) engine is the main source of vibration and should be reduced in order to improve the overall performance of the car and achieve passenger satisfaction. Hence, car manufacturers have been finding ways to achieve satisfactory performance through the development and optimization of Noise, Vibration and Harshness (NVH) by reducing the unbalanced forces and providing damping on the engine mounts [3].

Formula Student of Automotive Engineers (FSAE) is a student design competition whereby students are required to design, built and race a small scaled formula one race car which runs on a maximum of 600 cc engines. The Taylor's Racing Team FSAE 2016 race car, TR 16, runs on a Yamaha R6 600 cc engine on an American Iron and Steel Institute (AISI) 1010 Carbon Steel Spaceframe. As the engine is capable of revving up to 17,000 rpm, produce a 2G downforce and reaching to maximum speed of 225 km/hr, the vibration frequency on the driver and the chassis structure is extremely high. This is also due to the fact that the power to weight ratio is high as the weight of a typical FSAE car can range between 250 – 350 kg.



Figure 1: Taylor's Racing Team FSAE 2016 Race Car, TR16.

Various studies have been conducted in order to identify the amount of vibration on different types of vehicles. Paddan and Griffin [4] studied the vibration of more than 100 different types of vehicles and have emphasized that the measurement of vibration on a single vehicle could not be used to indicate the vibration of other vehicles of the same category. Among the vehicles being tested in the study are cars, dumper, lift truck, tractor and many more. In contrast, FSAE Race Cars are built with motorbike power transmission and car dynamics and while most vehicles engine are mounted on the front of the car, FSAE Race Car transmission is placed behind the driver. Hence, due to the configuration of the race car, more focus should be emphasized on the vibration of the car.

Due to the nature of the reciprocating and rotating members of the engine, the IC engines are the main source of vibration in vehicles. There are two dynamic forces

that are presence in an IC engine, the combustion force from mixing of fuel and air as well as the inertia force and torque from the piston, connecting rod and crankshaft [3]. As the piston moves from Bottom Dead Centre (BDC) to Top Dead Centre (TDC) to compress the air, the changes in a cylinder leads to a variation of inertial forces. These changes vary with respect to speed, fuel supply and combustion characteristics of the fuel [3]. The frequency of unbalanced forces depends on number of factors such as the number of cylinders, stroke number and engine speed. Typically, for a four-stroke, four-cylinder engine, the frequency can range between 20-200 Hz. This is the case for the Yamaha R6 engine that is configured in the TR16 car.

Vibration forces transmitted to the structure are proportional to the stiffness and damping of engine mounting. Therefore, an ideal engine mounts have stiffness and damping that is capable of dampening vibration for all frequency range [5]. If the stiffness of the engine mount is too low, transient response could occur which would lead to serious damage of the engine. Transient response develop because of shock excitation as a vehicle undergoes sudden acceleration and deceleration, braking or uneven road surface. To summarize, to dampen engine vibration at high frequency range, the engine mounts needs to be soft for both elastic stiffness and damping. On the other hand, to avoid engine bouncing at lower frequency range, an ideal engine mount should have harder stiffness and damping. This is known as frequency dependent engine mounting system [5]. This is depicted through the Figure 2 below:

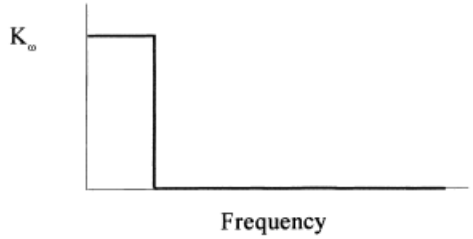


Figure 2: Dynamic stiffness of ideal mount [5]

One study conducted by India FSAE team members whereby the optimization of engine mounting system was performed through FEA analysis. In the study, frequency and loading response of the bracket were identified before the finalized design are being made [6]. Despite this, the forces applied during FEA analysis process, was just weight of the engine, disregarding the forces presence from the engine. The mode analysis that was performed in order to identify the frequency response for both design. The end results are then compared to the natural frequency of the engine to avoid resonance. However, the comparison of natural frequency is insufficient as it neglects to observe the vibration amplitude at the engine mount. Moreover, since this study was performed on different type of engine, the Suzuki GXSR 600cc, 4-cylinder engine on an engine mount fabricated from 6061 Aluminium, the information of this study is insufficient to improve vibration on FSAE race cars.

Conti and Bretl's presented a new way to analyze rigid body on its mounts. This was done by data acquired through an artificial excitation that was suspended to the

ground through mounts. This experiment was done to imitate the engine vibration on a car mount. Results of this study is capable of giving outputs of suitable rigid body mass and stiffness of the mounts [5]. However, the limitation of this vibration analysis was done based on an artificial excitation and was suspended. Complementary to this, the artificial excitation is not similar to the 4-cylinder engine of the Yamaha R6 and in the FSAE Race Car engine is mounted directly to a chassis.

A study conducted by Chung-Ha and Clifford G.Smith presented a simplified method to analyze the vibration amplitude of a 4-cylinder car engine when supported by viscoelastic mounts [6]. Pistons, crankshaft and connecting rods are modeled as rigid bodies whereas rubber mounts are modelled as spring and damping elements. In their study, they are able to manipulate variables such as the location, orientation and stiffness of the mount to reduce vibration in the engine design. Despite this, neither of this study are similar to the construction of a FSAE Race Car in terms of the type of engine and mounts.

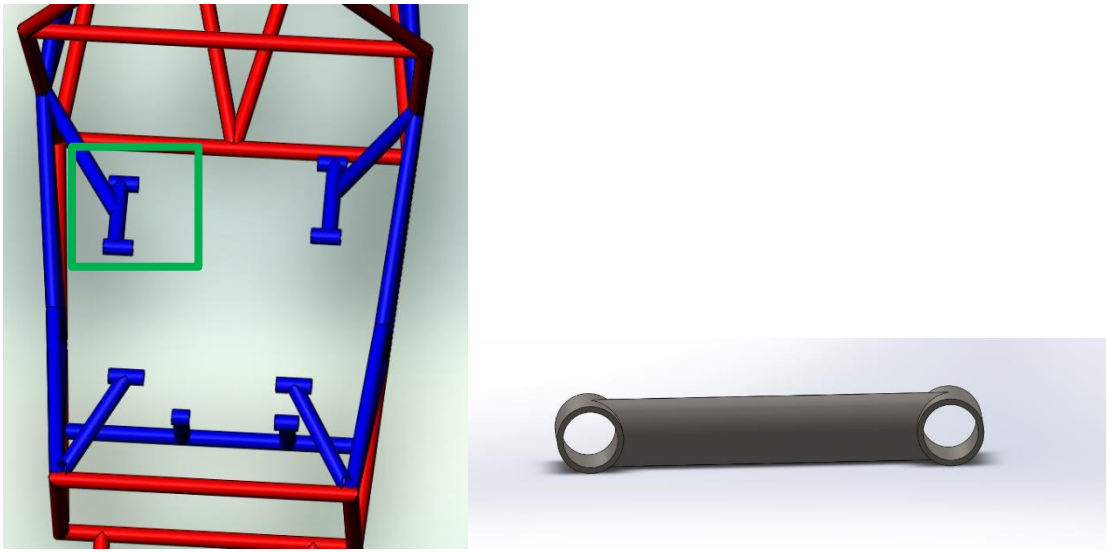
It has been known that engine vibration is the main cause of driver discomfort and can cause structural damage. Yet none of the studies presented are similar to the structure of the race car. Hence, the objective of this paper is to improve the overall vibration comfort of FSAE race car by improving the engine mounting system. This is done by identifying the vibration amplitude to frequency of the FSAE race car and comparing the results to Vibration Nomograph. From the results, multiple engine mounts will be modelled and modal and harmonic response analysis are conducted to identify the suitable engine mounts that can further reduce the amount of vibration paths to the chassis and driver.

2. Research Methodology

2.1 Design of Engine Mounts

The most basic function of an engine mounting system is to support the weight of the engine. On plan view, the engine should be located at the center of gravity, within the support base and the weight should be equally distributed to all mounting points [5]. Another major function of engine mounting system is to dampen the engine unbalanced force from transferring to the car structure. As there were no emphasized being made on the damping of engine vibration, the design of engine mount for the FSAE Race Car is only to achieve its primary function – to support the weight of the engine.

Figure 2 below shows the design of the engine mount on TR16. The design is done to mimic the placement of the Yamaha R6 engine on the bike as shown in Figure 3. This is to ensure that the engine weight is well distributed to the mounts and the engine center of gravity is within the support base.



(a) (b)

Figure 3(a): Finalized engine mount design (b) Top view of the engine mount on the TR16 chassis



Figure 4: Engine placement of the Yamaha R6 2006 model [8]

Once the design is finalized, the engine mounts are fabricated using the AISI 1010 Carbon Steel with an outside diameter of 26.9mm and thickness of 2.3mm. The supporting members are welded directly to the chassis using the metal inert gas (MIG) welding. Final result of the fabrication is shown below in Figure 4 below. Additional bracing support made out of steel thickness of 3mm is used in order to support the weight of the engine as shown in the green box in Figure 5.



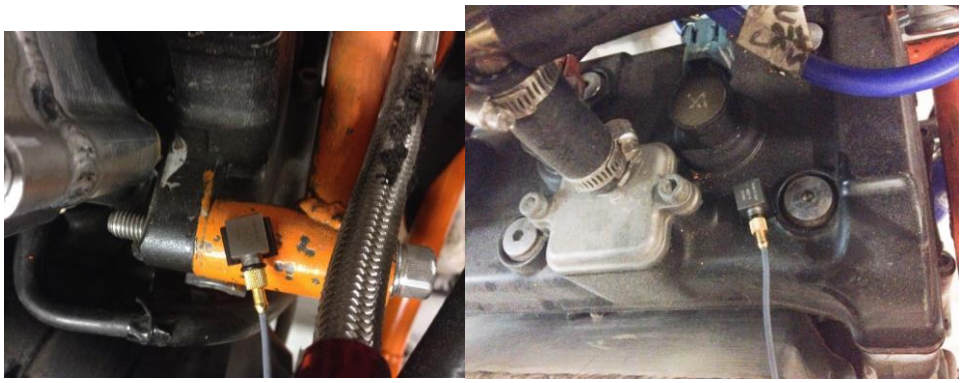
Figure 5: Finalized engine mounting on TR16

2.2 Experimental Analysis

2.2.1 Accelerometer Setup and Instrumentation

In this experiment, the vibration before and after mount was recorded. A portable Integrated Electronic Piezoelectric (IEPE) Brüel & Kjær type 4507 B accelerometer is utilized as the measurement device. In order to achieve accurate results, the transducer mounting is one of the most important factor. Bad mounting practice can lead to inaccurate results with a severely reduced usable frequency range [9]. The primary requirement is to attach the accelerometer as close as possible to the mechanical contact. Therefore, as recommended by [9], a little grease is applied on the mounting surface of the accelerometer and its mounted using a thin double adhesive tape. The usage of grease improves frequency response.

The accelerometer is mounted onto two different locations, the engine mounting that is connected to the chassis and on the engine cylinder head. This is to observe the amount of vibration that is reduced from the engine to the engine mounts. The placement of the accelerometer is shown in the figure 5 and the schematic test is shown in Figure 6. As the accelerometer sends time domain signals to the NI DAQ system, LabVIEW software are then used to convert the signals to frequency domain signals. This is done with the help of block diagram as shown in the figure 7 below.



(a) (b)

Figure 5(a) Placement of accelerometer on the engine cylinder head 5(b) Placement of accelerometer on the engine mount

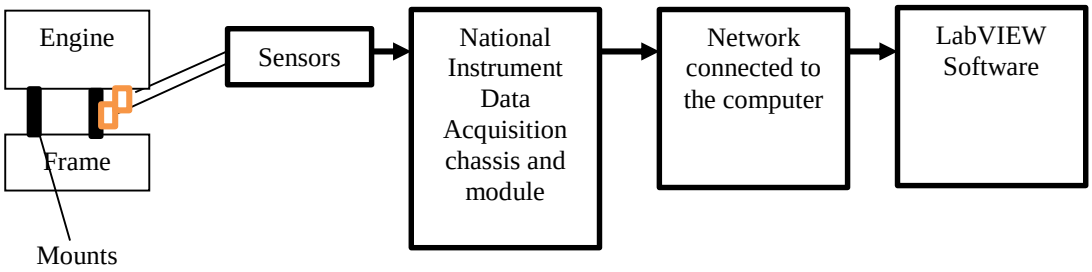


Figure 6 Schematic test of accelerometer placement connection to national instrument

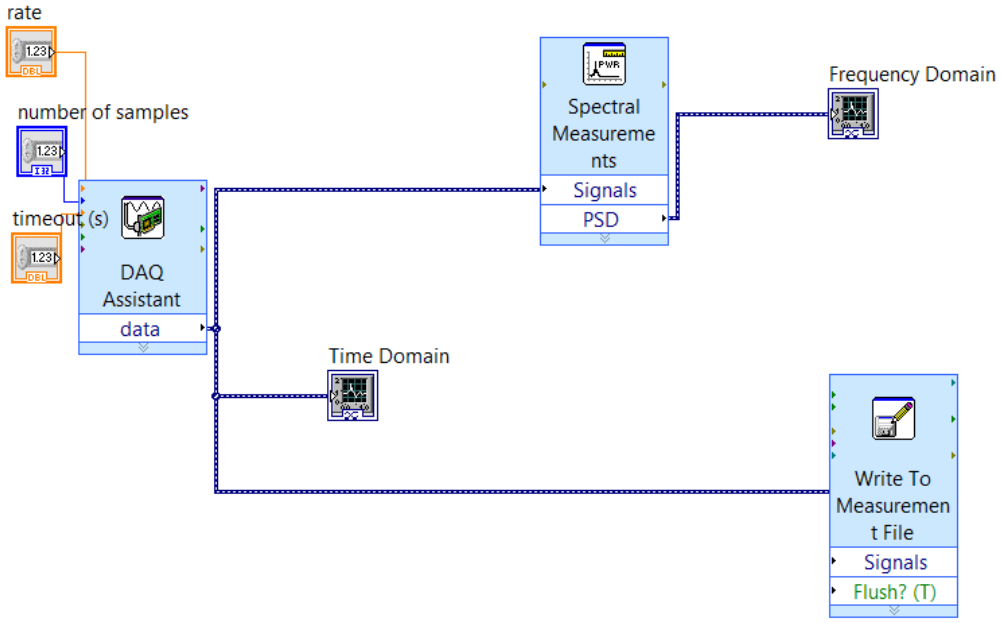


Figure 7 Block Diagram on LabVIEW

2.2.2 Data Acquisition and Analysis

Measurements are taken when the car is on idle, ranging between 4000-5000 rpm. The data was recorded over a period of 20 seconds, 2.5 kHz span and a sampling frequency of 5 kHz. For continuous signal, Hanning window with 50% overlap was implemented for Fast Fourier Transform (FFT) analysis. FFT analysis is used to analyze the vibration of the engine as it is capable of breaking down the original time-based waveform collected by the accelerometer into each magnitude, frequency and phase. FFT is also capable of identifying the fluctuating signal in a dynamic response [10]. Hence, this would be useful to identify any mechanical shocks that occurs on either placement of the accelerometer.

Another type of analysis that is performed is Power Spectral Density (PSD). PSD is capable of identifying random vibrations due to motion that occurs at different frequencies at the same time. PSD works by taking the frequency bin in FFT and multiply it to the complex conjugate resulting in real values of the amplitude [10]. Therefore, PSD is more useful than FFT for random vibration analysis as it is capable of normalizing the frequency bin width.

Once the vibration analysis is conducted, the results are then compared to the Vibration Nomograph. Acceptable values of vibration in responds to undamped single degree of freedom system are displayed on the vibration nomograph. The values are displayed in terms of displacement, velocity and acceleration amplitude against frequency of vibration [11]. The vibration acceptable levels are recognized by the International Standard of Organization (ISO). This is shown in the Figure 8 below.

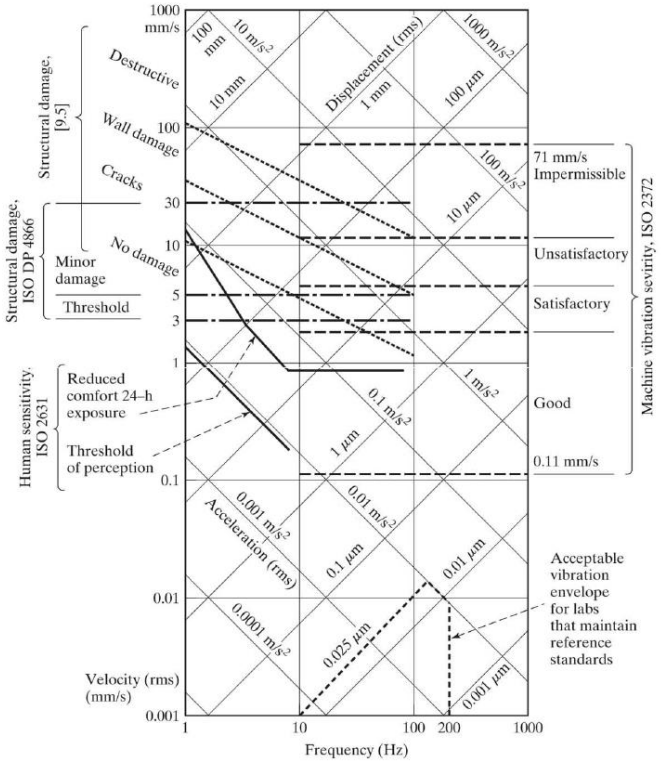


Figure 8: Vibration Nomograph [11]

2.3 Numerical Analysis

2.3.1 Geometric Modelling

Various mounting design are modelled and files are converted to Parasolid format is the first step to conducting FEA analysis. According to the FSAE 2016 Rules, the minimum requirement of an engine mount is to be made with dimensions of 26.9 mm external diameter and thickness of 1.65 mm. This baseline is used to model three designs and the characterization of the designs are tabulated in Table 1 below. The original TR16 design is shown in Figure 3(a) above whereas the other two designs are shown in Figure 9 and 10 below:

Table 1: Characterization of each engine mounting design

	Original TR16 Design	*Combination of steel and rubber*	*Elastomeric*
Characterization	Previous mounting design with 26.9 mm outer diameter and 2.3mm thickness made out of AISI 1010 Carbon Steel	Baseline of AISI 1010 Carbon Steel, outer diameter 26.9 mm and 2.3mm thickness with 2 mm EPDM 60 Durometer rubber and inner carbon steel layer of thickness 5mm with 10.7 mm hole for M12 bolt slot	Baseline of AISI 1010 Carbon Steel, outer diameter 26.9 mm and 2.3mm thickness with EPDM 60 Durometer rubber of 20.3 outer diameter and 5mm thickness.

EPDM (Ethylene Propylene Diene Terpolymer) 60 Durometer rubber is among the most common rubber used in commercial vehicles engine mounting system.

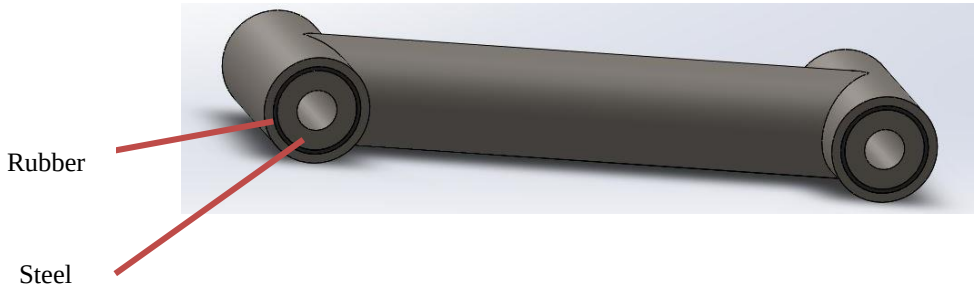


Figure 9 Combination of steel and rubber



Figure 10 Elastomeric Design

2.3.2 Modal Analysis

The next step in simulation process is to determine the natural frequencies and mode shapes of each design. This step is necessary to ensure that the natural frequencies of the design does not overlap with the natural frequency of the engine that could later lead to resonance. Modal analysis is conducted by inserting the

minimum and maximum frequency range which is between 0 to 2500 Hz. The number of nodes is set to 10 and the fixed support is set to the connecting bracing between the two holes. This is depicted in Figure 11 below.

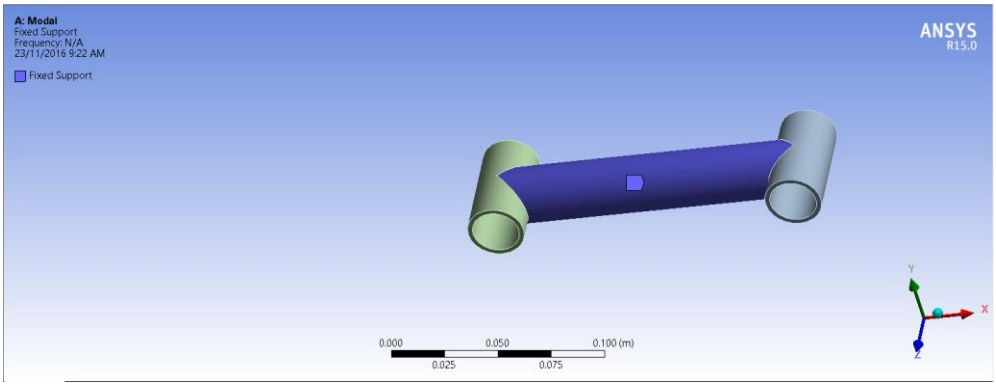


Figure 11 Fixed support for the engine mount

2.3.3 Harmonic Response Analysis

To understand the response of a structure under steady-state harmonic, harmonic analysis is conducted. This analysis take into account the loading at each frequency at a particular time. However, a few assumptions are made such as the mass, m, damping and stiffness coefficient c and k are made constant and the elastic material behavior is assumed as linear.

The total force acting on each mounting are included by calculating the total combustion force acting on a cylinder, using the equation below:

$$F = PA \tag{1}$$

Based on a study conducted by University of Auburn FSAE race team with the same engine, the peak cylinder pressure is 261 psi at 15% load and 3,000 rpm [13]. With a cylinder diameter of 26mm, the surface area is calculated using the following formula.

$$A = 2\pi rh + 2\pi r^2 \tag{2}$$

$$A = 2\pi\left(\frac{67}{2}\right)(42.5) + 2\pi\left(\frac{67}{2}\right) = 9.156\ m$$

Hence, total combustion force acting on once cylinder is:

$$F = PA$$

$$F = (265\ psi\ x\ 6894.76)(9.1567\ m) = 16.73\ x\ 10^6 N \tag{3}$$

Assumptions made for this analysis is each circular mount support 16.73 x 10^6 N of combustion force which is equal to the amount of force in 1 cylinder. This force is applied on the circular section where the M12 engine bolt is slotted in. This is shown in Figure 12 wherease the geometry placement of the frequency response is shown in Figure 13.

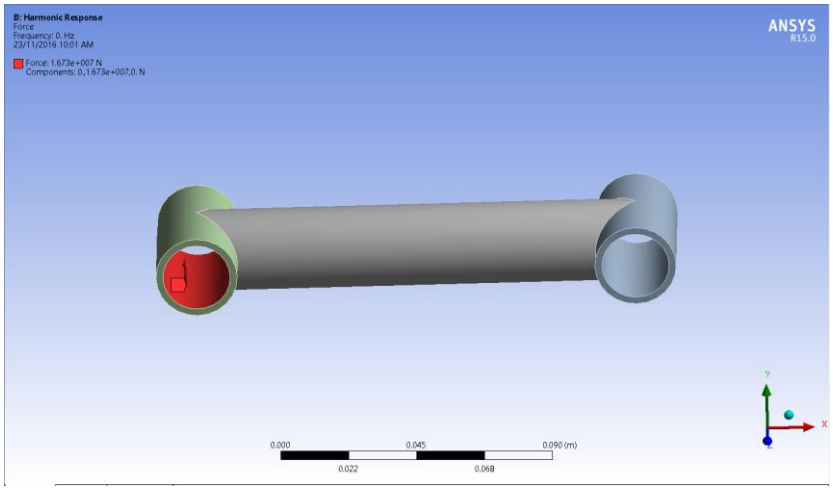


Figure 12: Force applied on the engine mount

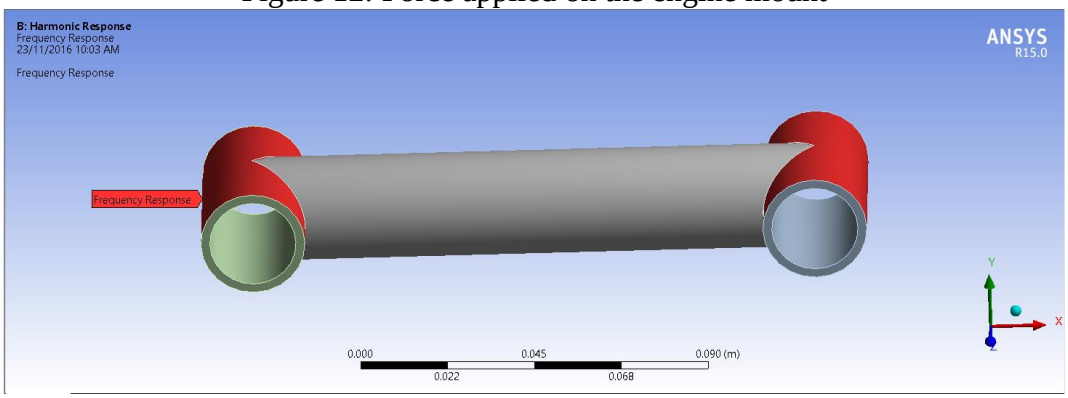


Figure 13: Frequency response of the engine mount

3. Results and Observations

3.1 Experimental Analysis

3.3.1 FFT Analysis for before and after engine mount

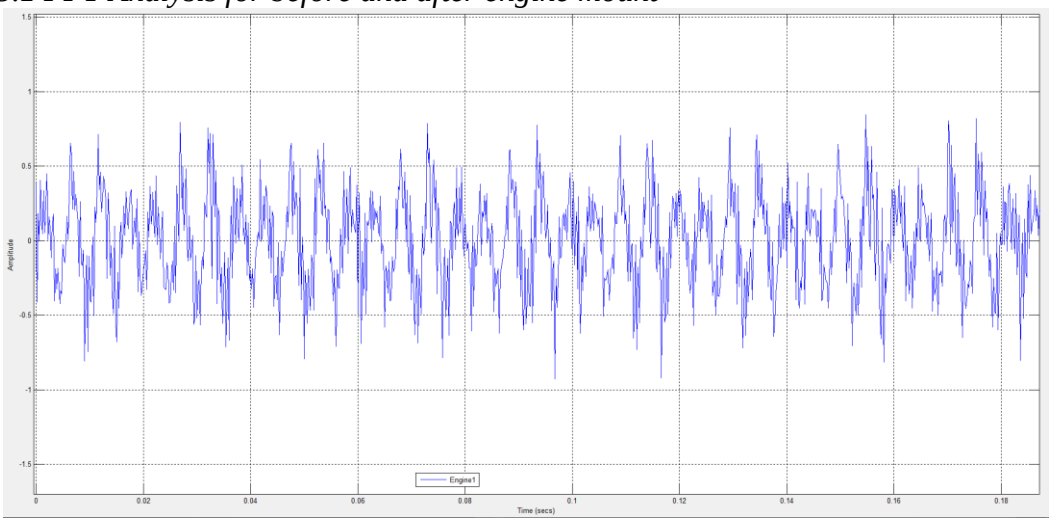


Figure 14: Signal Measurement at the engine cylinder head

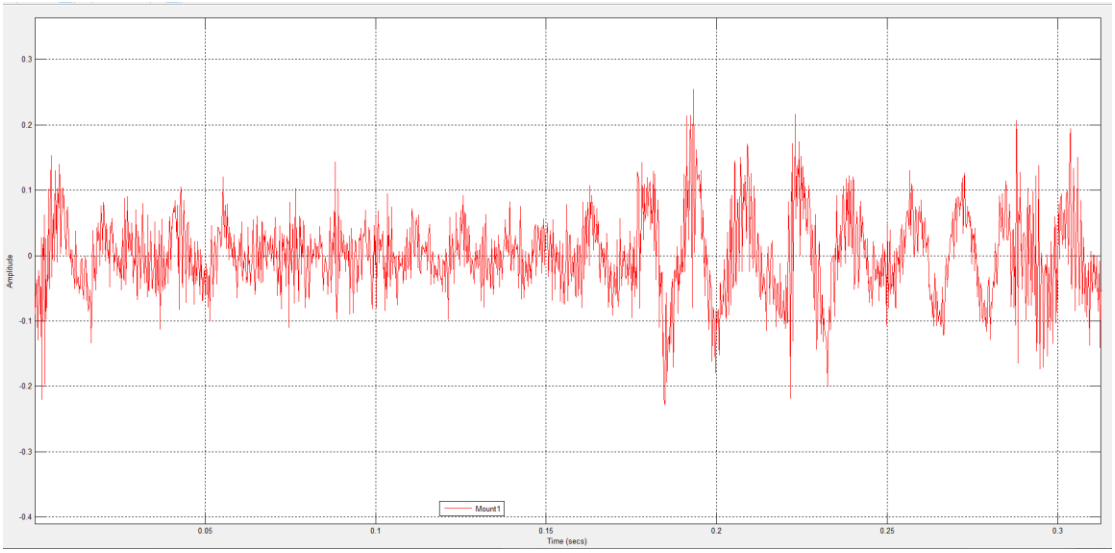


Figure 15: Signal Measurement at the engine mount

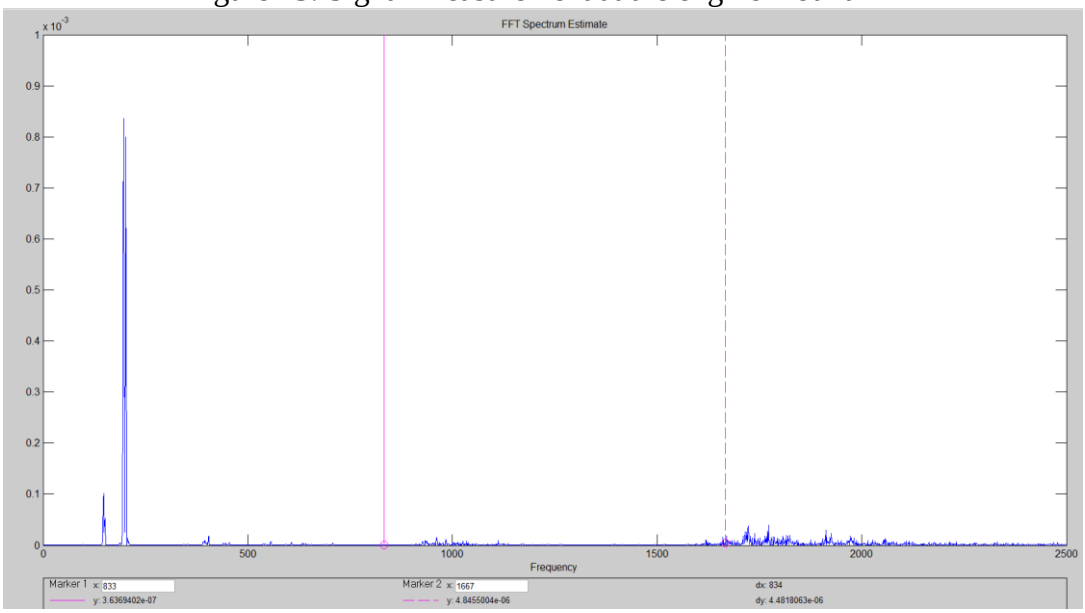


Figure 16: FFT Analysis at engine cylinder head

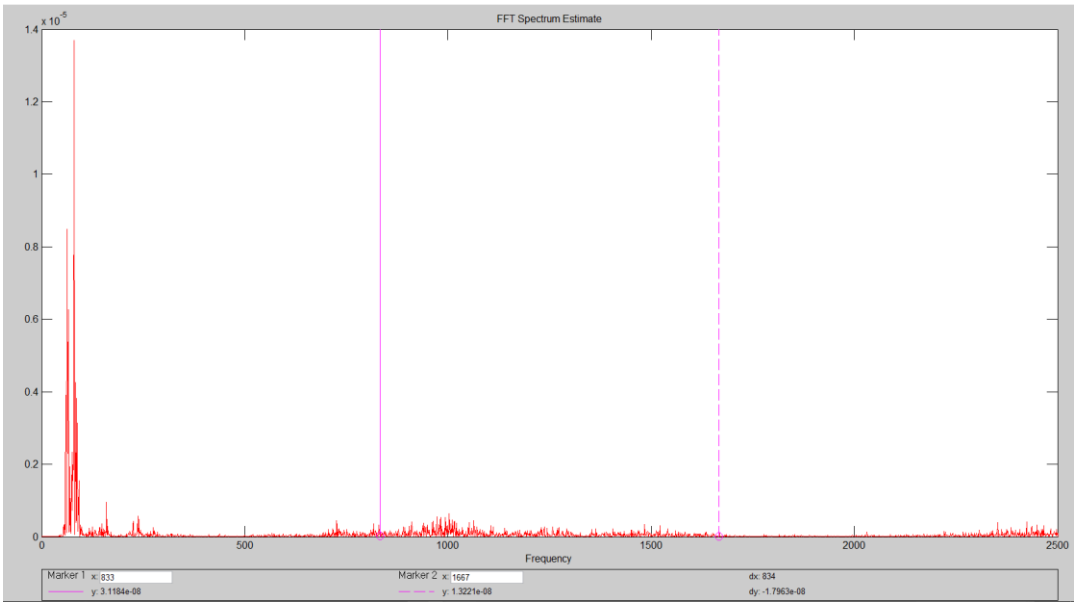


Figure 17: FFT Analysis at engine mount

Figure 14 and 15 demonstrates the results of signal measurement of acceleration against time for both engine cylinder head and engine mount whereas Figure 16 and 17 shows the FFT analysis for vibration measurement at the engine head and mount. Commonly, engine vibration results show harmonic or single sinusoidal response. However, results have shown that the signal measurement of the cylinder head shows a multi sinusoidal response. This is due to a combination of discrete frequency that is multiplied to the fundamental frequency. The cause of this combination is possibly due to unbalanced force that is coming from the crankshaft of piston which are causing high discrete frequency. On the other hand, the measurement on the engine mounts shows a lower multi sinusoidal force, moving at more random patterns. This is possibly due to the fact that some of the vibration has been transferred to other parts of the engine and mounting points.

FFT Analysis results for engine cylinder head shows that there might be a mechanical shock occurring at 200 Hz whereas the same shock is occurring at the engine mount at much earlier frequency. The amplitude where the shocks are happening are at very concerning values. Referring to the Vibration Nomograph in Figure 8, at a frequency of 200 Hz, the machine vibration severity at a level of unsatisfactory is at 10µm. The shock that is occurring at the engine head is at 1.4×10^{-3} and at engine mount is 1.4×10^{-5}, showing both values are at unsatisfactory level. The cause of the shock however has not been identified.

3.3.2 PSD Analysis for Before and After Engine Mount

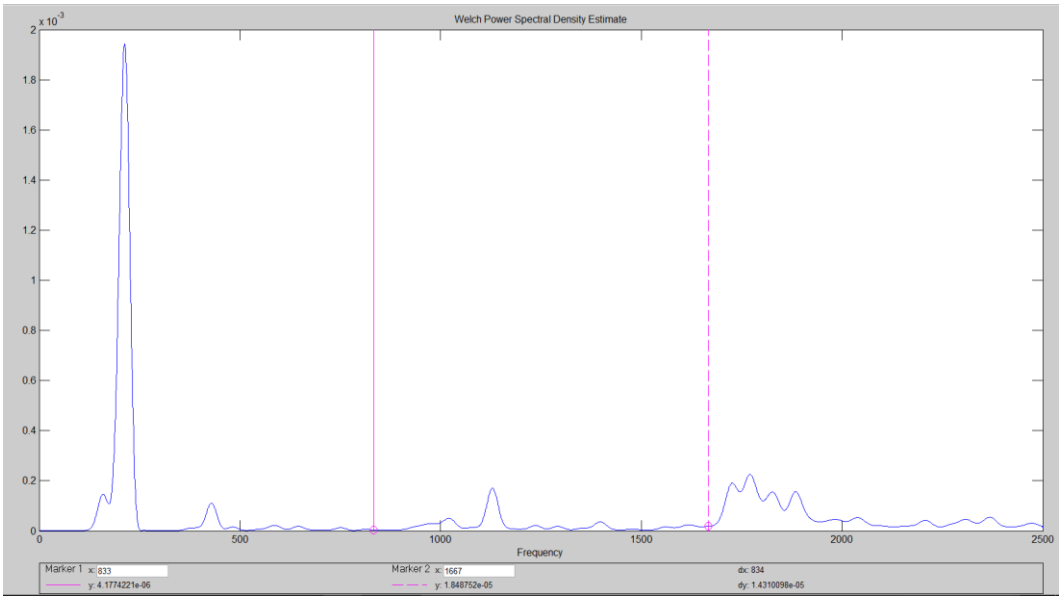


Figure 18: PSD Analysis at engine cylinder head

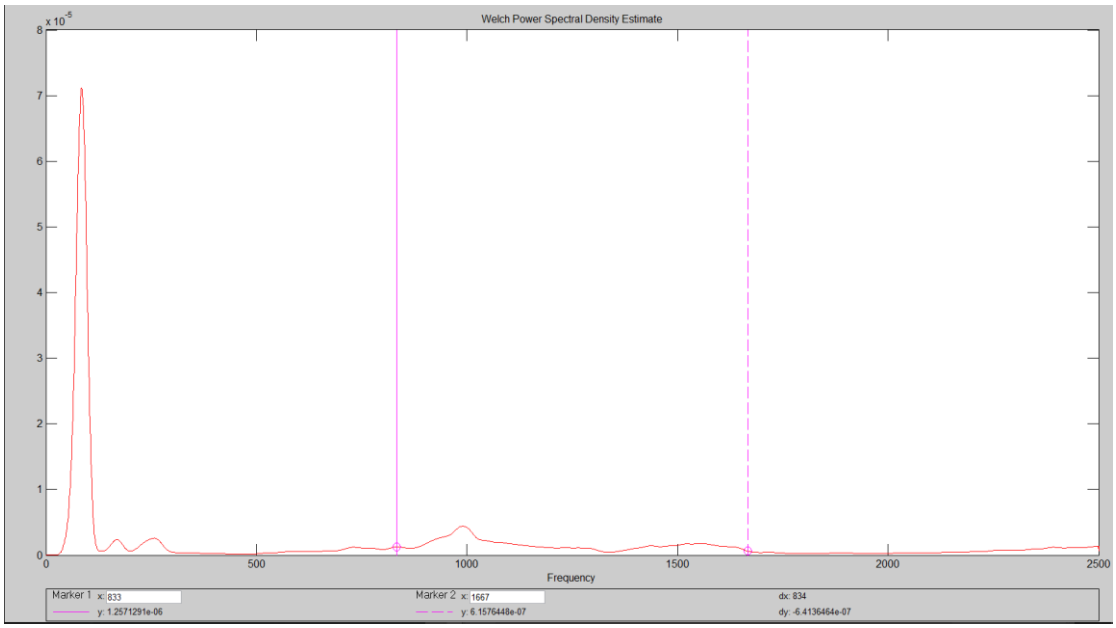


Figure 19: PSD Analysis at engine mount

The PSD analysis for both mounting points is corresponding to the same values as the FFT Analysis. There are shocks occurring at the same frequency level with the same amplitude. As measurements are taken when the car is on idle around 4000-5000 rpm, frequency at where the shocks are happening is at a very dangerous level for the structure of the car as well as the driver. This is a possibility that this value can increase as the car is running on different speed and riding conditions.

3.2 FEA Analysis

3.2.1 Natural Frequency

Modal analysis is conducted to identify the natural frequency at various mode shapes of the structure. The result of this analysis is tabulated in Table 2 below:

Table 2: Natural Frequency at each mode for 3 designs

Mode	Frequency (Hz)		
	Current TR 16 design	Combination of carbon steel and rubber design	Elastomeric design
1	8733.6	1549.5	2809.2
2	8756.6	1549.5	2809.3
3	9156.2	2043.9	3007.4
4	9176.7	2043.9	3007.4
5	13470	4402.7	3044.1
6	13474	4404	3044.2
7	15936	4571.9	3052.7
8	15948	4572.3	3052.8
9	20840	4676.4	3105
10	20845	4678.8	3105

Since natural frequency depends on the spring stiffness of a material of a structure, the current TR16 design have the highest natural frequency value as the spring stiffness of carbon steel is 203.403 x 10^3 N/m. On the other hand, the combination of rubber and carbon steel has the lowest natural frequency value as it considers the spring stiffness of both EPDM 60 Durometer rubber and carbon steel, causing the lowest overall stiffness coefficient. Notwithstanding, result have shown that the natural frequency of the engine mount ranges above the natural frequency of the engine, hence all 3 designs are safe to be used.

3.2.2 Harmonic Response Analysis

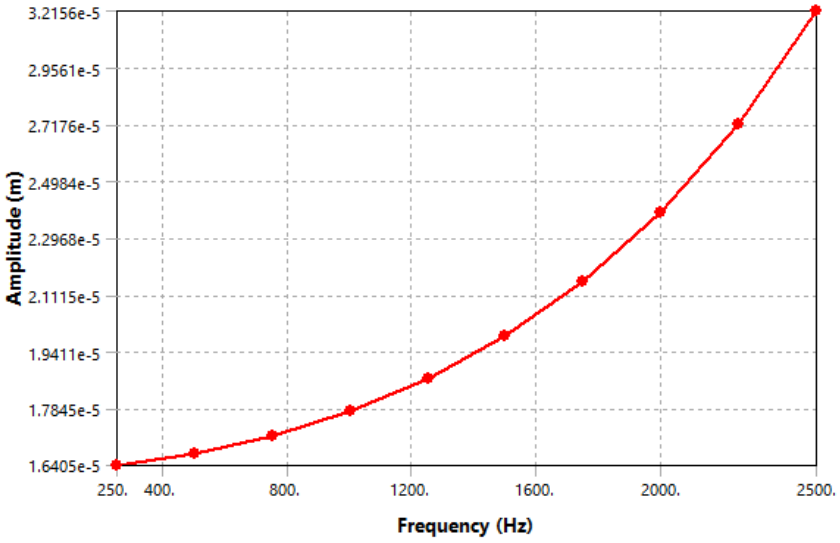


Figure 20: Harmonic Response Analysis for current TR16 engine mounting design

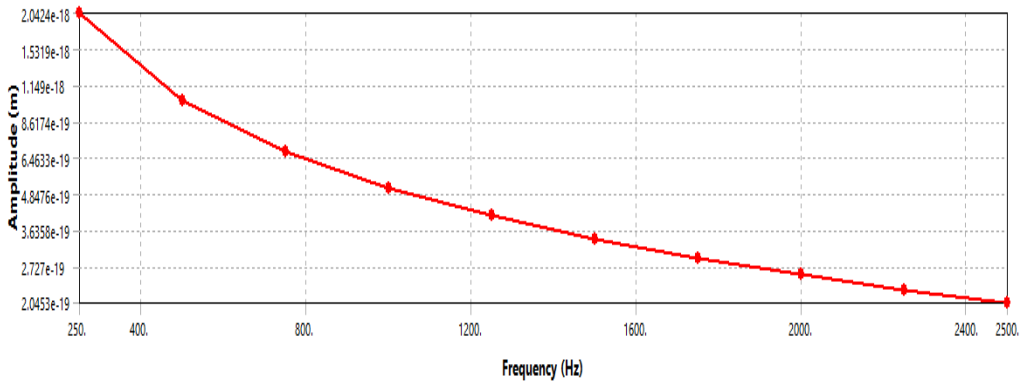


Figure 21 Harmonic Response Analysis for combination of carbon steel and rubber design

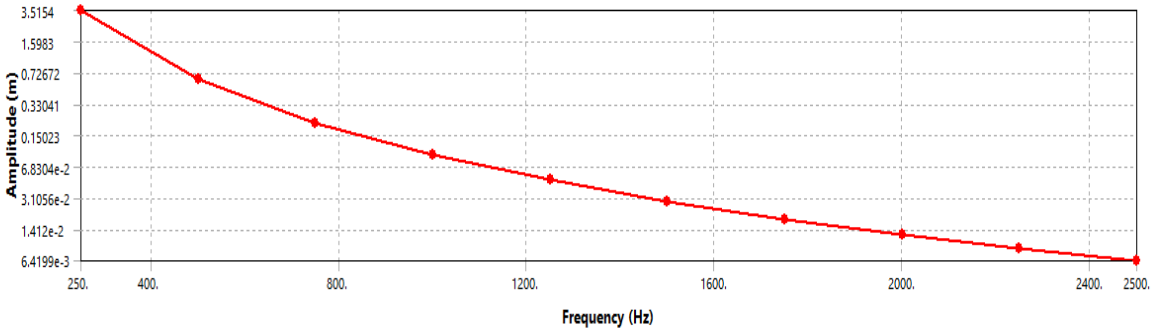


Figure 22 Harmonic Response Analysis for elastomeric design

Figure 20 to 22 above depicts the results of amplitude against frequency for each design based on the applied force calculated in Eq (3). It is summarized in Table 3 below:

Table 3: Results of amplitude against frequency for all 3 designs

Frequency (Hz)	Amplitude (m)		
	Current TR 16 design	Combination of carbon steel and rubber design	Elastomeric design
250	1.64E-05	2.04E-18	3.5154
500	1.67E-05	1.02E-18	0.61424
750	1.71E-05	6.82E-19	0.2073
1000	1.78E-05	5.11E-19	9.28E-02
1250	1.87E-05	4.09E-19	4.90E-02
1500	1.99E-05	3.41E-19	2.89E-02
1750	2.16E-05	2.92E-19	1.84E-02
2000	2.39E-05	2.56E-19	1.24E-02
2250	2.72E-05	2.27E-19	8.77E-03
2500	3.22E-05	2.05E-19	6.42E-03

From the summary above, the combination of carbon steel and rubber design shows amplitude ranging between $2.04x10^{-18}$ to 2.05×10^{-19}m. This results compared to the Vibration Nomograph shows the most significant improvement as compared to the other two designs. In addition, this design has shown that as frequency increases, the vibration amplitude increases indicating that the mounting system is capable of dampening vibration even at higher frequencies which is possibly due to the shock.

As for the current TR16 design, the vibration amplitude shows a lower value as compared to experimental analysis. This is possible due to the force applied only considers the combustion force of the engine excluding the inertial forces of the crankshaft. However, the result still shows that the vibration amplitude for the frequency range is still dangerous for the overall structure of the race car as well as the driver. On the other hand, the elastomeric design shows a surprising amplitude value as it is higher than the vibration amplitude of TR16. The cause for such results is due to the rubber has already deformed at high combustion force. Notwithstanding, a trend of decreasing vibration shows that the EPDM 60 Durometer is capable of dampening the vibration as frequency increase. This concludes that the combination design with EPDM 60 Durometer is suitable for the FSAE Race Car engine mounting system.

4. Conclusion

In conclusion, results have shown through signal measurements, FFT and PSD analysis that the current engine mounting point design is not suitable for the Yamaha R6 engine. The amplitude at lower frequency has shown that it is at an unsatisfactory level according to the Vibration Nomograph. As this measurement is taken at idle condition, this value is at a concerning level as the car is capable of revving up to 12,000 rpm at races for a long period of time. This result are also confirmed through the FEA analysis conducting, showing that as frequency increase, the vibration amplitude of the structure increases.

Two other designs are modelled where EPDM 60 Durometer is assembled in the minimum requirement of the engine mount. Result have shown that the combination design of carbon steel and rubber shows the most significant result with vibration amplitude as small as 2.05×10^{-19}m. Foundational to this, engine is the main source of vibration in a vehicle. It is crucial to test and measure the vibration caused by the engine and how it can affect the structure and ride comfort for the drivers. As FSAE Race Car is not similar to commercial vehicles, the awareness of Noise, Vibration and Harshness (NVH) amongst FSAE Competitors is important in order to build a safe car not just for the drivers but as well as the structural integrity.

References

[1] M. Griffin, Handbook of Human Vibration, San Diego: Academic Press Limited, 1990.

[2] Y. P. A. S. H. R. I. Hostens, "A study of vibration characteristics on a luxury wheelchair and a new prototype wheelchair," *Journal of Sound & Vibration*, vol. 266, pp. 443-452, 2003.

[3] K. P. T. Ramachandran, "Review on Internal Combustion Engine Vibrations and Mountings," *International Journal of Engineering Sciences & Emerging*

Technologies, vol. 3, no. 1, pp. 63-73, 2012.

[4] G. P. a. M. Griffin, "Evaluation of Whole Body Vibration and RIde Comfort in a Passenger Car," *International Journal of Acoustics and Vibration,* vol. 14, no. 1, pp. 143-149, 2009.

[5] N. G. N. R. V. D. Yunhe Yu, "Review of automotive vehicle engine mounting systems," *Mechanism and Machine Theory,* vol. 36, pp. 123-142, 2001.

[6] P. R. V. S. Jasvir Singh Dhillon, "Design of Engine Mount Bracket for a FSAE Car Using Finite Element Analysis," *International Journal of Engineering Reseach and Application,* vol. 4, no. 9, pp. 74-81, 2014.

[7] P. a. B. J. Conti, "Mount Stiffness and Inertia Properties from Modal Test Data," *ASME Journal of Vibration and Acoustics, Stress and Reliability in Design,* vol. 111, pp. 134-141, 1989.

[8] C. G. S. Chung-Ha Suh, "Dynamic Simulation of Engine-Mount Systems," *SAE International,* pp. 561-572, 1997.

[9] Brick7, "The Motorcycle Search Engine," Brick 7, South Africa, 2010.

[10] B. &. Kjær, "Vibration Transducers and Signal Conditioning," Brüel & Kjær Sound Vibration Measurement A/S, 1998.

[11] R. N. Bracewell, "The Fourier Transorm," *Scientific American,* pp. 86-95, 1989.

[12] S. S.Rao, Mechanical Vibration, Miami: Prentice Hall, 2011.

[13] J. T. Frederick, "Auburn University Electronic Theses and Dissertations," 29 March 2011. [Online]. Available: http://etd.auburn.edu/handle/10415/2488. [Accessed 20 November 2016].

[14] P. Nolan, "Farmingdale University," [Online]. Available: www.farmingdale.edu/faculty/peter-nolan/pdf/UPCh13.pdf. [Accessed 31 October 2016].

[15] S. International, "2016 Formula SAE Rules," SAE International, 2016.

eureca 2016 – Conference Paper
Paper Number 2ME15

Design Guideline of Critical Flanges for the Oleochemicals Industries Malaysia

Foo Kok Meng, Douglas Tong Kum Tien
School of Engineering, Taylor's University, Malaysia.
Douglaskumtien.tong@taylors.edu.my

Abstract
Design guideline of critical flanges for the oleochemicals industries Malaysia is a guideline for the proper selection of bolted and welded joints in order to run a leak free operation. This is necessary to avoid unplanned shutdowns, delayed of production, and process safety incident. An accurate design guideline from Joint Integrity Management System (JIMS) is highly critical in securing plant operation in terms of safety and cost. While there is a well-established Joint Integrity Management System (JIMS) for the petrochemical industry in Malaysia, there is none yet for the oleochemicals industry in Malaysia as reported by the senior manager of the largest oleochemicals company in Malaysia. Therefore, the purpose of this project is to identify the shortcomings in existing practices of joint integrity management in order to develop a new guideline which is applicable to the oleochemicals industry in Malaysia and which complies with American Society Mechanical Engineer (ASME) standards and the Department of Safety Health (DOSH) regulations. The objective of this project is to develop the most relevant set of design guidelines of Joint Integrity Management System for the oleochemicals industries under Malaysia conditions. The research of this project focuses on the oleochemical industry in Malaysia. It involved collecting data from one of the largest oleochemicals companies in Malaysia. Review of existing literature was conducted to identify the knowledge gaps in flanges leakage issues in the oleochemicals industry. From the result of this review, simulation of joints based on oleochemicals operating conditions were carried out to close the gaps. The simulation was verified and validated from quantitative and qualitative data collected from the oleochemical plant. Verified and validated results from the simulation were then compiled to develop the design guideline of critical flanges. This design guideline is intended to be shared with the entire oleochemicals industry in Malaysia and if adopted will be expected to make the industry more competitive through avoiding unnecessary costs associated with leakages, environmental pollution, and human safety.

Keywords: Oleochemicals, critical flanges, leak-free joints, Joint Integrity Management System.

1. Introduction

Malaysia is a country which has strong assets in palm oil and has become one of the largest producers of oleochemicals in the world though its palm oil. Oleochemicals are the products extracted from plants and animal fats. These substances undergo enzymatic reactions in well-equipped process plants to produce basic oleochemical substances such as fatty acid, methyl ester, fatty alcohols, and glycerol.

Oleochemicals process plants process organic compounds and their facilities operate using almost the same type of joints for pressure vessels as the petrochemical plants although petrochemical plants process non-organic compound such as crude oils including paraffinic, naphthenic, and asphaltic [1].

Joint Integrity Management System (JIMS) is mainly a practice of design, construction, operation and maintenance of joints, including bolted and welded joints, in order to run a leak free operation. This helps to avoid unplanned shutdowns, delayed of production, and process safety incidents. Design guideline of critical flanges is the most important component of JIMS and is extremely critical in securing plant operation in terms of safety and cost. There are various macro maintenance strategies, in particular for assets integrity management throughout their life cycle. However, to-date, micro management such as proper design selection tended to be neglected in some way. Any joint failure is potentially catastrophic in terms of cost and human life. For example, in the North Sea, a four-bolt hub joint connector failed to seal well and cause leakages leading to damage losses estimated at $30million USD. In addition, repair and replacement costs could go beyond $1 million USD even before taking into consideration the loss of production due to delayed start-up [2]. However, solutions for such issues such as online sealing measures are being developed. Although such sealing measures being developed, without the right selection of materials, these issues may not be completely mitigated.

Petrochemical plants have a standard design guideline selection of critical flanges, however, the oleochemicals industry still lacks such standards. The absence of such important guideline may result in preventable leakages. Leakages pose serious safety issues as it could cause fire or explosions that endanger human lives and production assets. Besides that, such losses require repair, which is a costly exercise in terms of man hours and loss of production [2].

Leakages are mainly caused by the design of pipes and fittings of the pressure vessels. One key area where leakage occurs is at the joints of the critical flanges. A critical flange is the flange of the joint connecting two sections of high-pressure pipelines originating from the pressure vessels. An example of one such flanged joint and the joint integrity management required for both the welded and bolted versions of the joint is shown in Figure 1.

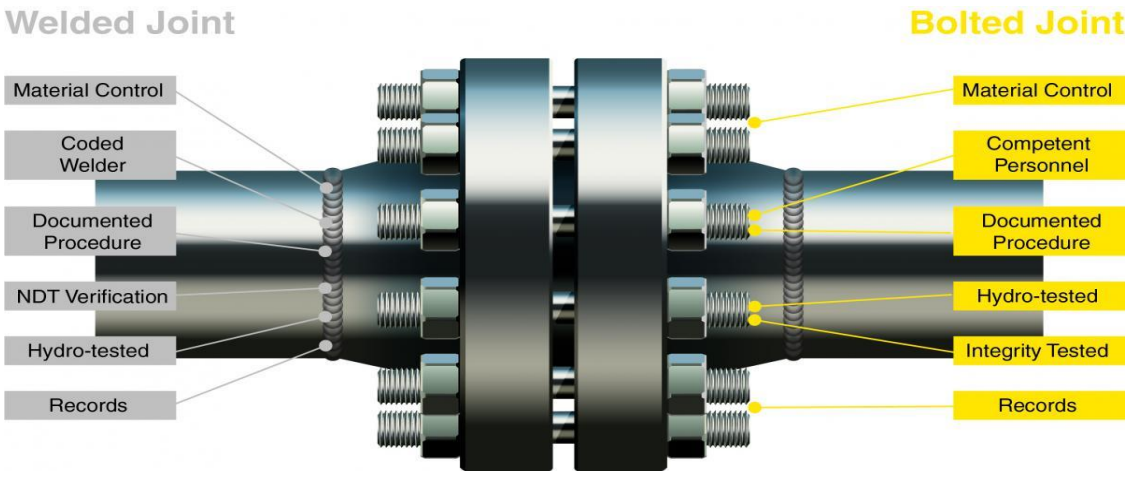


Figure 1: A critical flanged joint and its joint integrity management [2]

As reported by the senior manager of the largest oleochemicals company in Malaysia, proper design selection parameters still do not exist for the critical flanges for the oleochemicals industry, unlike the petrochemical, which has such standards. The senior plant manager also reported one of the leak incident occur on flanges due to poor bolt-up leads to plant turnaround which cause production losses over RM 5 million ringgit just to mitigate the issue. The presence of such standards in the petrochemical industry indicates its importance in safe and cost effective operations. Hence, the oleochemicals industry needs such standards also. This senior manager is also the industrial supervisor for this project and he identified the need for such a standard. However, due to company policies, the oleochemicals company details will not be reviewed. Although there will be restrictions in revealing the company name, the findings of this study conducted at this company is allowed to be shared with the public.

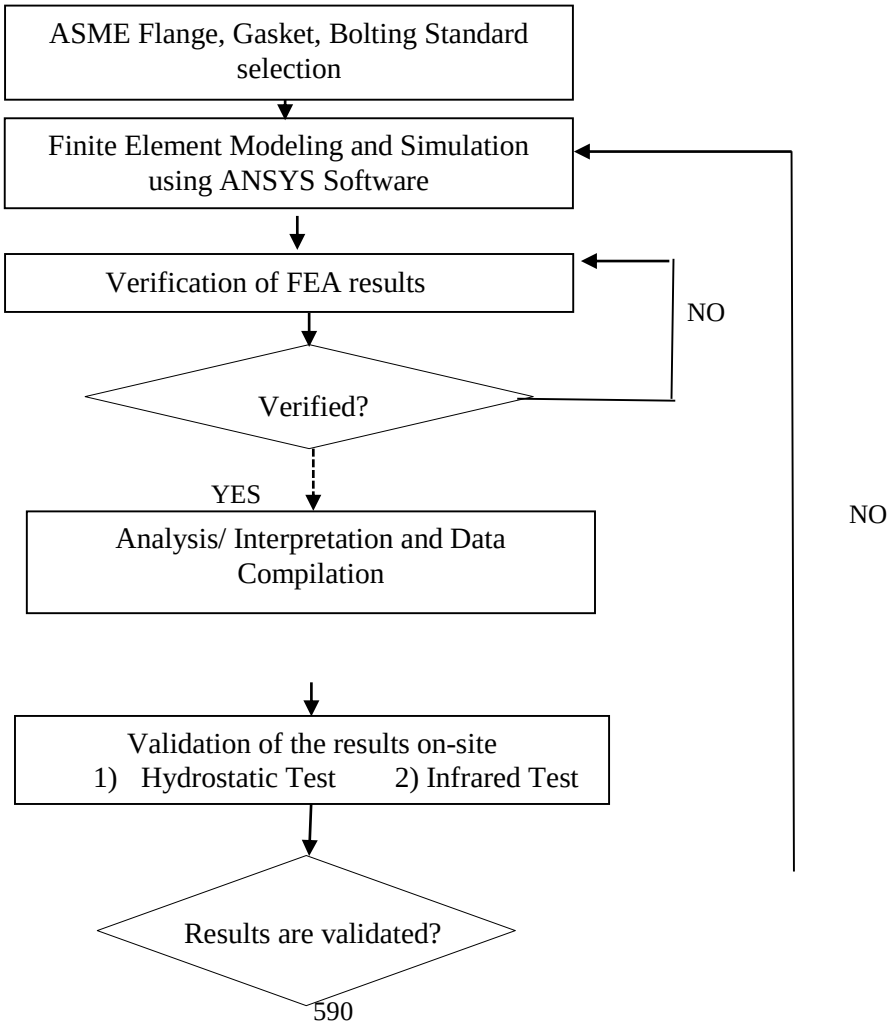
The existing guideline from petrochemical industries can serve as a reference to produce the guideline for the oleochemicals industry as both of these industries share the same concept of fitting pressure pipeline joints. However, a few modifications are required to adapt to the needs of the oleochemicals industry as the operating conditions are different. While oleochemicals plants process organic compounds, petrochemical plants process non-organic compounds. Adding on, oleochemical needs its own guideline which is difference from petrochemical guideline as it needs to be revised to suits oleochemical operating conditions. The JIMS will be completed in the authors thesis with construction procedure and operation and maintenance. However, the scope of the paper will be concentrating on the design guideline.

Large proportions of industrial emissions were from the by-products of combustion and products which are easily evaporated such as hydrocarbons and steam. These industrial emissions are mainly due to equipment leaks which are referred to as fugitive emissions. Sealing of joints plays a vital role to ensure zero or low emissions. Thus, right material selection and installation are required to enable good sealing performances.

Therefore, the purpose of this project is to identify the shortcomings in existing practices of design selection in order to develop a new guideline which is applicable to the oleochemicals industry in Malaysia and which complies with American Society Mechanical Engineer (ASME) standards and the Department of Safety Health (DOSH) regulations. The contribution of having a well-organized set of design guideline of critical flanges of Joint Integrity Management System will save the massive losses in terms of costs and possibly human life as described. In addition, it will also help to make the oleochemicals industry in Malaysia more competitive.

2. Methodology

Figure 1 shows the research methodology carried out to achieve a reliable standard of design guideline for the oleochemicals industries in Malaysia. There were three important phases carried out before the creation of the design guideline. Firstly, a research and compilation of data carried on the American Standard of Mechanical Engineers (ASME) of flanges, gaskets, and bolting standards. From the compiled data, one of the design parameters was chosen to undergo simulation to test out the reliability and accuracy of data. The chosen parameters for simulation were then used for the experimental test at the oleochemical site. Result considered validated when the experimental specimen able to work under permissible range set.



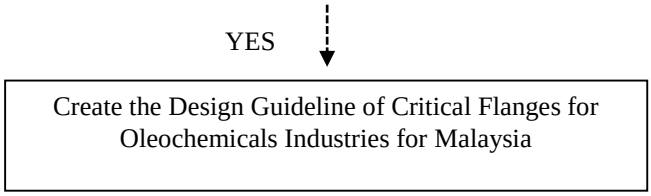


Figure 1: Research methodology creation for design guideline of critical flanges

2.1 ASME Flanges, Gaskets, Bolting Standard

American Society of Mechanical Engineers is a non-profit organization which concentrates on developing codes and standards related to art, science, and mechanical engineering. Nearly 600 codes and standards were released with compliances of safety, health, and quality of life as well as promoting innovation, trade, and competitiveness. Out of the 600 codes and standards available, the author had researched and selected the related codes and standards which match the current research project. The important components of critical flanges which were flanges, gaskets, and bolting standards data were collected. Data collected from the flanges standards, ASME B16.5 were the plate material, American Society for Testing and Materials (ASTM) code [9], and pressure rating of flange correspond to the operating conditions. Adding on, the author had done the same data collection for ASME 16.21 gasket standards and ASME B18.2.6 bolting standard. These data were then matched with the operating conditions of oleochemicals industries in Malaysia. As ASME is one of the world leading codes and standards developer, the results obtained by ASME was done by performing few test. For example, gasket test undergoes flexibility test (ASTM F147), tensile strength test (ASTM D4745, ASTM F152), sealability test (ASTM F2378) and finally maximum pressure test. Sample procedure of a gasket flexibility test is shown in Figure 2 [9].

i) Flexibility test (ASTM F147)
This test method measures the gasket flexibility and material flexibility factor. Firstly, the test specimen was cut into a “dog bone” shaped in both transverse and longitudinal orientations. It is then heated for 100 ℃ for an hour and left cooled to room temperature in a desiccator. The test specimen was then held firmly on the circular mandrel with a diameter ranging 4.8mm to 101.6mm. The specimen forced slowly to contact 180° of the full diameter starting from the largest diameter. It is then repeated with decreasing mandrel diameter until failure occurs and the mandrel diameter is recorded. By dividing the minimum diameter with the original thickness, the flexibility factor is achieved and the lower value will show the positive result [9].

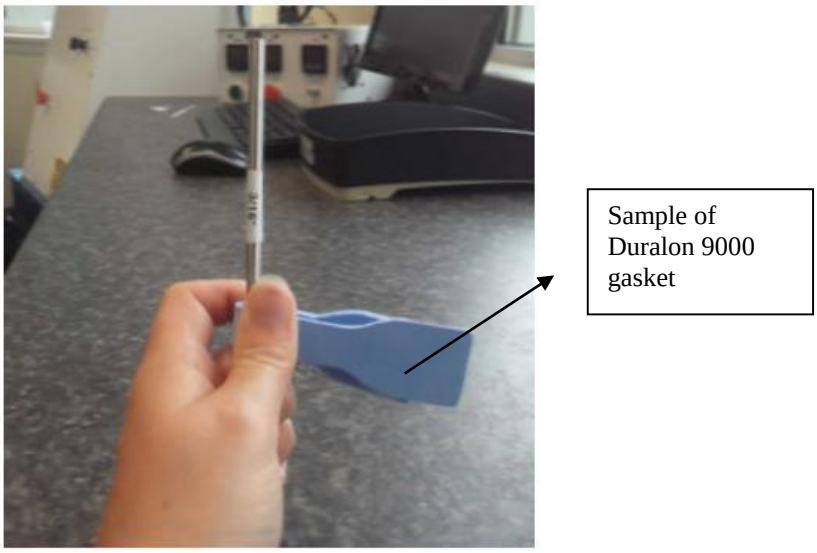


Figure 2: Duralon 9000 flexibility test

2.2 Finite Element Modeling and Simulation using ANSYS Software

As the compiled data were matched with the operating conditions of oleochemicals industries in Malaysia, the author had selected one of the design parameters of flange material, type of gasket and material, and bolting standards to perform simulation under the oleochemicals plant operating conditions to test out the reliability and accuracy of the ASME codes and standards. A 3D modeled is drawn in SolidWorks program and import into ANSYS 15.0 software. ANSYS was chosen as simulation software in this project which able to generate finite element analysis, structural analysis and computational fluid dynamics studies. Besides that, there are few software available can be used such as ADINA, LISA, and ABAQUS which able to perform same result. Firstly, engineering data was filled up with the specifications of material properties for each component of the critical flanges. In this case, the static structural analysis was chosen to analyze the mechanical behavior of the component. Figure 3 shows the sample of critical flanges after meshing which was used to perform the analysis. Design parameters and operating conditions were set based on Table 1.

Table 1: Design parameters and operating conditions set for simulation

Design Parameters / Materials	Operating Conditions
1) Flange = ANSI B16.5 Class 150 1.5" / Carbon Steel 2) Gasket = OD 90mm X ID 62mm X THK 3mm / Spiral Wound Gasket (Pure PTFE) 3) Bolt = 10mm / ASTM 193 B7 4) Nut = 10mm/ ASTM 194 2H	1) Pressure = 10bar (Normal to surface) 2) Temperature = 100 ℃ 3) Hydrostatic Pressure= -9.81m s^{-2} (y-direction)

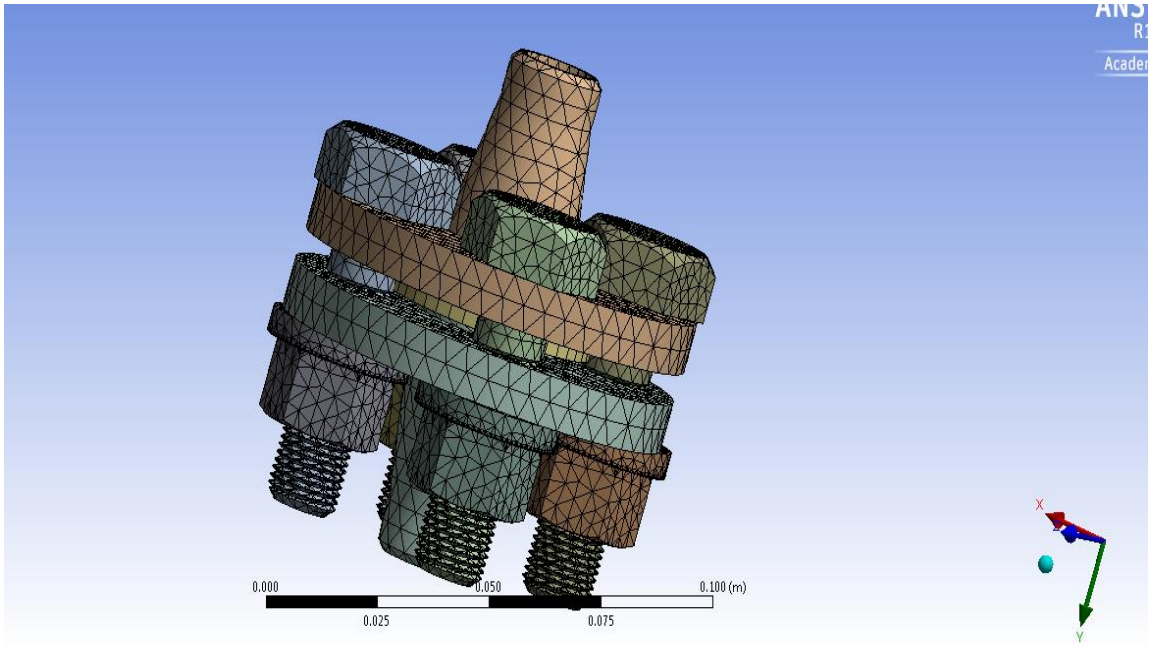


Figure 3: Sample of critical flanges after meshing

2.3 Validation of results on-site

The simulated results of the critical flanges component were then brought to one of the largest oleochemicals plants in Malaysia to undergo an on-site experimental test for validation purposes.

2.3.1 Hydrostatic Test

The hydrostatic test can be done in two ways such as pneumatic test and hydrostatic test whereby both test ways ensure safety, reliability, and leak tightness of pressure system. The hydrostatic test can be done by holding down each valve by means with appropriate test clamp. Pressurizes the system by raising the pressure gradually with water temperature less than 70°F. The test pressure is maintained for 10 minutes at the designated pressure and a thorough inspection for leakages was made. Figure 4 shows the hydrostatic test machine available in the oleochemicals plant workshop [3].



Figure 4: Hydrostatic test machine

2.3.2 Infrared Test

The infrared test is a non-destructive test designated by American Society for Nondestructive Test (ASNT) to determine the cracks of pressure vessels. Figure 5 shows the results of the infrared test on the flanges. The thermogram is a remote sensing tool which used on-site to scan the thermographic view of the pressure vessels and able to view the temperature patterns as red color indicates the high exposure of heat and gas test can be done in the area to detect any leakages occur [10].

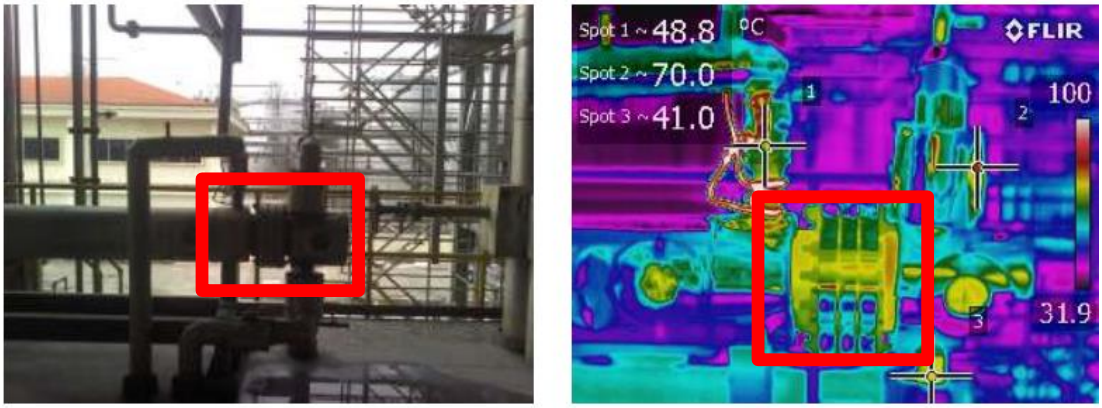


Figure 5: Infrared and thermal testing view

3. Results and Discussion

3.1 ANSYS Simulation Results

The compiled data from the ASME codes and standards were then chosen one of the design parameters undergo simulation as mention in the methodology. Table 2 shows the results achieved through the simulation conducted using ANSYS software.

3.1.1 Total Deformation

Total deformation shows area which experiences the deformation. The maximum deformation experience by the flange was 0.08mm (inlet) and minimum deformation of 0mm (outlet). The analysis of the flange deformation may not be accurate as the analysis was done based on clamping on both ends of the pipe flange. This allows the fluids to flow through the inlet and experiences high temperature and pressure which distort the actual situation. On actual situation, the medium continuously flows through the pipe flange where the pressure and temperature distribute evenly instead of concentration at the inlet. Therefore, analysis of results may not be accurate by just concentrating on the total deformation. Hence, it is best to consider the equivalent stress experienced by the flange and ensure it falls within the permissible allowable stress. Besides that, the bolt and nut show a fair allowable deformation of 0.05mm which falls within the permissible deformation (ASME B18.2.6) [4].

3.1.2 Equivalent Stress

Based on the flange material properties which was carbon steel, the ultimate yield strength of the material is 370MPa (ASME B16.5) and the simulation results of maximum allowable stress were 360MPa which falls within the permissible range. Thus, it is concluded that the flange is safe to use under leak free condition with the operating conditions set. This applies to the bolt and nuts too where the material used were alloy steel which falls in the permissible range of ultimate yield strength of material 415MPa [5].

3.1.3 Equivalent Strain

Strain analysis can be done calculating the young's modulus which is the elastic modulus whether it falls within the permissible range. Young's modulus equation is calculated by dividing the maximum stress (σ) and the maximum strain (ε) of the results achieved.

$$Young's\ Modulus\ E = \frac{\sigma}{\varepsilon}$$

$$E = \frac{360\ X\ 10^{6}\ Pa}{0.001806} = 1.99\ X\ 10^{11} = 199\ GPa$$

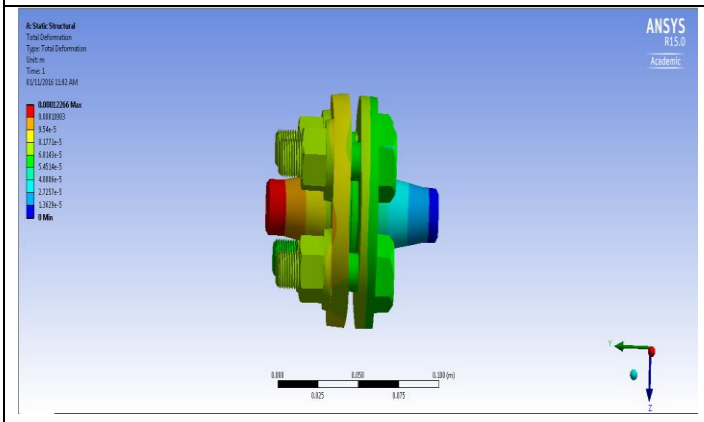
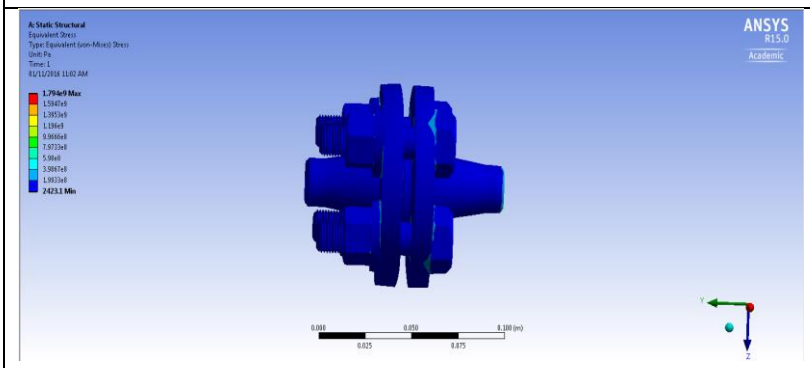
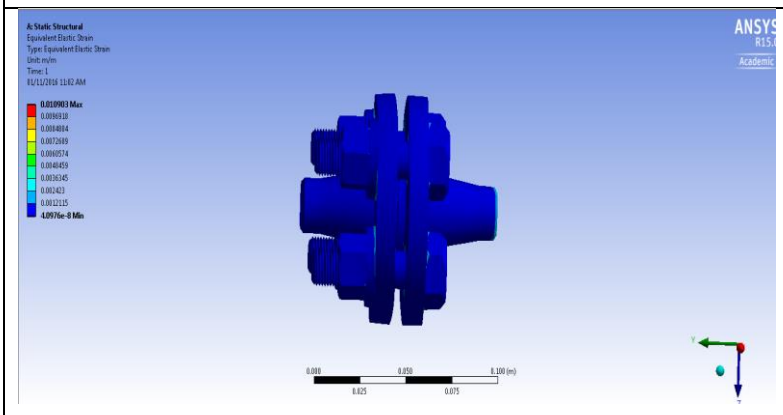
For critical flanges component of flange, bolt, and nut, the young's modulus calculated were 199GPa. The young's modulus of carbon steel material is 205 GPa [5] while for alloy steel is 210 GPa [4]. It is clearly proved that the results obtain falls within the permissible range and safe to operate.

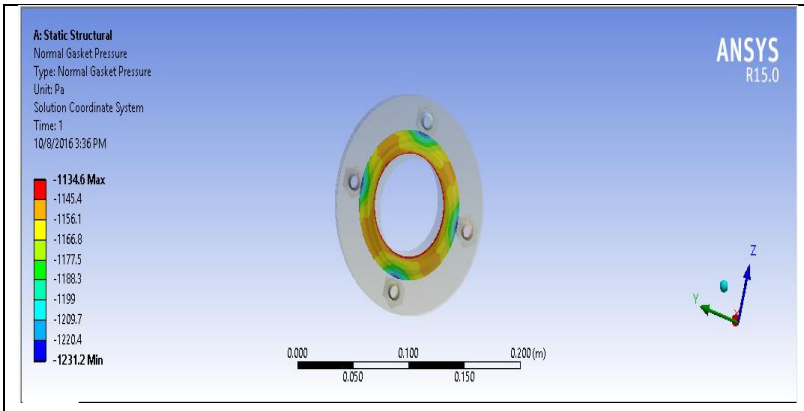
3.1.4 Normal Gasket Pressure

Analysis of gasket pressure is an important element as the gasket pressure experience affects the sealing capability of flanges. Thus, ensuring the gasket pressure stays within the permissible pressure range able to provide leak-free operation. In this simulation, the material properties of the gasket which is polytetrafluoroethylene PTFE has a maximum pressure of -0.0113bar and it is safe to operate as it stays within the permissible pressure range which is 20bar. However, the color scheme shows on the gasket indicates the critical point as operating temperature under

compression may affect the gasket mechanical behavior. The operating condition set was 100℃, and PTFE material has maximum operating temperature of 200℃. This clearly shows that the gasket is safe to be used but it signals on a new material consideration to perform for a longer period [6].

Table 2: ANSYS simulation results

Simulation figures	Type of Analysis
	Total Deformation: 1) Maximum deformation = 0.08mm 2) Minimum deformation= 0mm
	Equivalent Stress: 1) Maximum stress = 360 MPa 2) Minimum stress = 0.13 MPa
	Equivalent Strain: 1) Maximum strain = 0.001806 m/m 2) Minimum strain = 2.4678e-8 m/m

	Normal Gasket Pressure 1) Maximum pressure = -0.0113 bar 2) Minimum pressure = -0.0123 bar

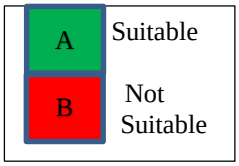
3.2 Design Guideline of Critical Flanges for Oleochemicals Industries in Malaysia

After completion of the simulation, the same design parameters were then brought to validation test on-site at one of the largest oleochemicals industries in Malaysia. There will be two test performed such as hydrostatic test and infrared test. The validated results will then be compiled and further develop into the design guideline of critical flanges component such as flanges, gaskets, bolts and nuts based on the operating conditions of oleochemicals industries.

3.2.1 Design Guideline of Flanges

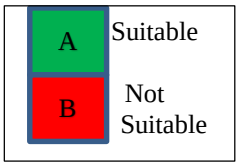
ASME B16.5 is the standard used for the flanges practices. It has seven primary pressure classes starting from 150, 300, 400, 600, 900, 1500 and 2500 [5]. The higher the number of classes, the higher pressure can handle by the flange as the construction of flange has more metal which enables better sealing capability under high pressure. Design guideline of different pressure classes, materials of flange were matched with oleochemicals operating conditions [5]. Table 3 and 4 shows the set of design guideline of 150lb and 300lb flanges matching with oleochemicals operating conditions. The alphabet ‘A’ represents the materials suits to use while alphabet ‘B’ represents flange materials is not safe to use under the operating conditions stated.

Table 3: Sample set of design guideline ASME 16.5 150lb flange



				Rating of Flange B16.5	150			
				ASTM Code	A515 Gr.70	A203 Gr.B/Gr.E	A515 Gr.65	A515.Gr.60
				Plates Material	Carbon-Silicon Steel	Nickel Steel	Carbon Steel	Carbon Steel
No.	Media	Operating Pressure (barG)	Operating Temperature (degC)	PH (Service Medium)				
1	Air	1 to 7	25 to 35	Neutral	A	A	A	A
2	Chilled Water	3 to 17	143.6 to 207.1	Neutral	B	B	B	B
3	Cooling Water	1 to 7	32 to 40	Neutral	A	A	A	A
4	Demin Water	1 to 7	<8	Neutral	A	A	A	A
5	Diathermic Oil	1 to 7	32 to 80	Neutral	A	A	A	A
6	Diesel	1 to 7	25 to 35	Neutral	A	A	A	A
7	Fatty Acid	0.025 to 15	80 to 150	Acidic	A	A	A	A
8	Fatty Alcohol	0.025 to 40	80 to 150	Neutral	B	B	B	B
9	Flue Gas	1	80 to 400	Neutral	A	A	A	A

Table 4: Sample set of design guideline ASME 16.5 300lb flange



				Rating of Flange B16.5	300			
				ASTM Code	A515 Gr.70	A203 Gr.B/Gr.E	A515 Gr.65	A515.Gr.60
				Plates Material	Carbon-Silicon Steel	Nickel Steel	Carbon Steel	Carbon Steel
No.	Media	Operating Pressure (barG)	Operating Temperature (degC)	PH (Service Medium)				
1	Air	1 to 7	25 to 35	Neutral	A	A	A	A
2	Chilled Water	3 to 17	143.6 to 207.1	Neutral	A	A	A	A
3	Cooling Water	1 to 7	32 to 40	Neutral	A	A	A	A
4	Demin Water	1 to 7	<8	Neutral	A	A	A	A
5	Diathermic Oil	1 to 7	32 to 80	Neutral	A	A	A	A
6	Diesel	1 to 7	25 to 35	Neutral	A	A	A	A
7	Fatty Acid	0.025 to 15	80 to 150	Acidic	A	A	A	A
8	Fatty Alcohol	0.025 to 40	80 to 150	Neutral	A	A	A	B

3.2.2 Gasket Design Guideline

A gasket is an element to retain a static seal between flanges which creates a complete barrier against the fluid which contained in joints. It is a mechanical element which helps to prevent potential leakage. There are three main types of gaskets such as the jointing sheets, fluoropolymer gasket, and semi-metallic gasket. All these gaskets were compiled and matched with oleochemicals operating conditions to determine which of them are safe to use and will ensure leak free operation. Table 5 shows a part of the results of gasket design guideline compiled with the aid of ASME B16.21 [6]. The alphabet ‘A’ represents the materials suits to use while alphabet ‘B’ represents gaskets materials is not safe to use under the operating conditions stated [7], [8].

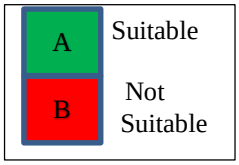
Table 5: Gasket design guideline

				Type of Gasket	Jointing Sheet		
A Suitable B Not Suitable				Material Construction	Glass Fibre with NBR	Aramid Fibre with NBR	Aramid & Glass Fibre with NBR
No.	Media	Operating Pressure (barG)	Operating Temperature (degC)	PH (Service Medium)			
1	Air	1 to 7	25 to 35	Neutral	A	A	A
2	Chilled Water	3 to 17	143.6 to 207.1	Neutral	A	B	B
3	Cooling Water	1 to 7	32 to 40	Neutral	A	A	A
4	Demin Water	1 to 7	<8	Neutral	A	A	A
5	Diathermic Oil	1 to 7	32 to 80	Neutral	A	A	A
6	Diesel	1 to 7	25 to 35	Neutral	A	A	A
7	Fatty Acid	0.025 to 15	80 to 150	Acidic	A	B	B
8	Fatty Alcohol	0.025 to 40	80 to 150	Neutral	B	B	B
9	Flue Gas	1	80 to 400	Neutral	B	B	B
10	Hot Water	1 to 7	Ambient to 150	Acidic	A	B	B
11	Hydrochloric Acid	1 to 7	Ambient to 70	Neutral	A	A	A

3.2.3 Bolts Design Guideline

Bolt and nuts are the final mechanical component enable connection of pipe flanges and gasket in a pressure vessel pipeline. There are three different strength of bolts, which separates into high strength followed by the intermediate strength and lastly the low strength. All of these bolts have their own material properties, which were matched with the oleochemicals service conditions. With the aid of bolting standards ASME B18.2.6 [4], Table 6 shows the compilation of a set of high strength bolts design guideline. The alphabet ‘A’ represents the materials suits to use while alphabet ‘B’ represents gaskets materials is not safe to use under the operating conditions stated.

Table 6: Bolts design guideline

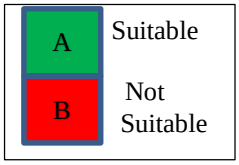


				Strength	High Strength			
				ASTM Code	A193	A193	A320	A354
				Material Properties	Alloy steel, AISI 4140/4142 quenched and tempered	Alloy Steel, CrMoVa	Alloy steel, AISI 4140/4142 quenched and tempered	Alloy steel, quenched and tempered
				Grade	B7	B16	L7	BC
No.	Media	Operating Pressure (barG)	Operating Temperature (degC)	PH (Service Medium)				
1	Air	1 to 7	25 to 35	Neutral	A	A	A	A
2	Chilled Water	3 to 17	143.6 to 207.1	Neutral	A	A	A	A
3	Cooling Water	1 to 7	32 to 40	Neutral	A	A	A	A
4	Demin Water	1 to 7	<8	Neutral	A	A	A	A
5	Diathermic Oil	1 to 7	32 to 80	Neutral	A	A	A	A
6	Diesel	1 to 7	25 to 35	Neutral	A	A	A	A
7	Fatty Alcohol	0.025 to 40	80 to 150	Neutral	B	A	B	A
8	Flue Gas	1	80 to 400	Neutral	A	A	A	A
9	Hot Water	1 to 7	Ambient to 150	Acidic	A	A	A	A
10	Hydrochloric Acid	1 to 7	Ambient to 70	Neutral	A	A	A	A

3.2.4 Nuts design guideline

A nut is a type of fastener with a threaded female hole which enables the mating of the bolt which has a threaded male to joint both two or more parts together. There 9 types of fasteners can be matched with the bolts and the recommended material used is ASTM 194 stated by ASME 18.2.6 [4]. These 9 types of fasteners were match with the oleochemicals operating conditions and compiled in Table 7.

Table 7: Nuts design guideline



				ASTM Code	A194	A194	A194	A194
				Material Properties	Carbon Steel heavy hex nuts	Quenched & tempered carbon steel heavy hex nuts	Quenched & tempered carbon steel heavy hex nuts, 100% hardness tested	Quenched & tempered carbon-molybdenum heavy hex nuts
				Grade	2	2H	2HM	4
No.	Media	Operating Pressure (barG)	Operating Temperature (degC)	PH (Service Medium)				
1	Air	1 to 7	25 to 35	Neutral	A	A	A	A
2	Chilled Water	3 to 17	143.6 to 207.1	Neutral	A	A	A	A
3	Cooling Water	1 to 7	32 to 40	Neutral	A	A	A	A
4	Demin Water	1 to 7	<8	Neutral	A	A	A	A
5	Diathermic Oil	1 to 7	32 to 80	Neutral	A	A	A	A
6	Diesel	1 to 7	25 to 35	Neutral	A	A	A	A
7	Fatty Alcohol	0.025 to 40	80 to 150	Neutral	A	A	A	A

3.3 Discussion of design guideline

The compiled data from Table 3 to Table 7 shows the design guideline of critical flanges in oleochemicals industries. The design guidelines enable the user to choose the right material for different operating conditions by just concentrating on the alphabet ‘A’ which indicates the material is safe to use and able to ensure leak free operation. The compilation of design guideline was done by integrating reliable sources and further revise in to oleochemical operating conditions hence formatting the table in as per ASME revision. Proper design selection is an essential aspect to be considered as fail in choosing right will lead to leakages due to inaccurate match of operating conditions with material. Thus, forcing the material to operate beyond its limit and fail eventually. Besides that, users able to save time by avoiding unnecessary tender request or feedback by the supplier on the right material selection. With the design guideline, users able to select the ideal materials and purchase without a doubt, avoiding wastage of cost by purchasing wrong materials. Furthermore, the creation of design guideline eases the workflows of the production

and maintenance team by having a proper reference to refer on if happens any downtime for spares change. This may help to avoid unnecessary downtime as interchangeability spares can be identified through the design guideline. The overall design guideline covers gaskets, flanges with pressure classes of 150, 300, 400, 900, 1500 and 2500, bolts and nuts. However, due to page limitation the sample of the guideline were attached on Figures 3,4,5,6 and 7 with complete matched and analyzed with 26 kinds of medium and operating conditions of oleochemicals which can be served as a guideline which done by verification and validation process.

4. Conclusion

In conclusion, design guideline selection which is one of the most important tools for JIMS and is develop in order to run a leak free operation. The proper material selection may prevent unnecessary wastage of cost thus providing a smooth operation plant process. Hence, with the aid of design guideline, users able to identify the wrong material selection that causes failure of critical flanges component. Besides that, if any doubt of design guideline, users able to perform verification by simulations on ANSYS software and validation test by hydrostatic or pneumatic test and finally thermal test. Design guideline of critical flanges which was done to provide a better reference for the further development of construction procedure and operation and maintenance system which includes in JIMS. The reason of adoption petrochemical industries guideline is due to oleochemical plants shares the same risk and hazard as petrochemical plants. Besides that, the oleochemical plant has the same operation process with the petrochemical plant as both operates high-pressure vessels pipeline. Adding on, as the current practices and standards are 100% applicable to oleochemical industry, it is rational to adopt it as it is a waste of resources to redo the standard. Therefore, the development of joint integrity management system (JIMS) shall be adopt and adapt the right applicable code of practice for actual field work to achieve leak free operation

5. References

[1] James, G. “Petrochemical processes”. *Unesco-Rolls*. September 2015.

[2] Ferguson, N. Best Practices of a joint integrity program. Inspectioneering journal. Volume 20, Issue 2. *Americas hydratight*. March/April 2014.

[3] Norton. C, C.E.T, Brent .A. “Understanding Standard Gasket Testing Metrics of Non-Metallic Gasket Materials”. Triangle Fluid Control Ltd. 10th September 2015.

[4] National Accelerator Laboratory, “Pressure Test Procedures”.Product 613,Rev 1790. *SLAC*. 9th December 2015.

[5] Infrared Training Center. “Infrared Testing”. World Class Infrared Training for Thermography Professionals. 2013

[6] The American Society of Mechanical Engineers. “Fasteners for Use in Structural Applications”. ASME B18.2.6. 16th June 2006.

[7] The American Society of Mechanical Engineers. “Pipe Flanges and Flanged Fittings”. ASME B16.5. 29th October 2004.

[8] The American Society of Mechanical Engineers. “Nonmetallic Flat Gaskets for Pipe Flanges”. ASME B16.21. 30th September 1992.

[9] Klinger Group. “Gasket Selection”. Product catalogue. *Industry Sealing Division. 2004*

[10] Nichias Group. “Handling Gasket. Tombo Brand Gasket. Nichias. 2003.

eureca 2016 – Conference Paper
Paper Number 2ME17

A Design and Simulation of Semi-Active Suspension System for Passenger Vehicle

Jasdeep Singh[1*], Mohd Farid Aladdin[2]
School of Engineering, Taylor's University, Malaysia
[*]jaz_jasdeep@yahoo.com

Abstract
A vehicle's suspension system plays two major roles, the first is to maintain constant contact of the wheels with the ground, and the second to isolate the occupants from vibrations resulting from uneven road surfaces such as bumps, humps and potholes. The most common suspension system that is used in passenger vehicles today is the passive suspension which is unable to provide any external energy to the system, hence the name passive. A passive suspension is made up of a spring and damper and suffers from the classic suspension tradeoff between comfort and performance, where designing the system to excel in one aspect will make it loose at the other. A fully active suspension couples the damper with an actuator where it is capable of varying its damping force, however this system is not commonly used in average passenger cars as they are heavy, expensive, complicated and hard to maintain. A semi-active suspension made up of a semi active damper such as a magneto-rheological (MR) damper that provides a much better solution where it requires little energy to alter its damping characteristics. There have been various different control methods to control a semi active suspension system, this paper studies the skyhook control and ground-hook control where the control is modeled with an imaginary damper linking the mass damper system to fixed imaginary points to obtain different control forces. The paper discusses the differences in performance between a passive and semi active suspension system using different control strategies. The paper also proposes a modified control strategy that is capable of improving both the comfort and handling performance.
Key Words: Semi active suspension, Magneto-rheological (MR) damper, Skyhook, Ground-hook, ¼ car suspension

1.0 Introduction

A vehicle's suspension system plays the vital role of ensuring there is constant contact and also traction between its tires and the road surface. The suspension system does this whilst enabling for passenger isolation from vibrations caused by road surfaces such as potholes, speed bumps and uneven road surfaces. However, it has been a tradeoff between this two primary functions of a vehicle's suspension system, known as the classic suspension compromise as shown in fig 1.1.

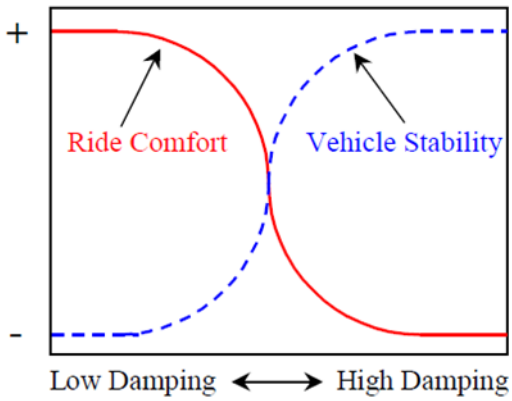


Figure 1.1 Suspension Compromise (adapted from Reference [1])

A classic suspension compromise is the compromise between a vehicles suspension performance and comfort. A vehicles performance is measured by its road holding capabilities, body roll during cornering, vehicles pitch and yaw during hard braking and acceleration and a qualitative measure that most drivers denote as the feel from the steering wheel. All of this is traditionally improved by running on a harder suspension set-up which then brings upon a quick drop it its comfort levels. A vehicle comfort level is quantitatively measured by its sprung mas acceleration and settling time after exposed to a bump or any other irregularities. A comfortable suspension is achieved with higher damping ratios and softer springs which allows for more vibration isolation for the vehicles occupants. However such setup usually results in a vehicle that has excessive body roll which reduces its performance levels.

Engineers have been actively working on reducing the tradeoff between a vehicles suspension performance and its comfort level by achieving a middle ground. This has resulted in leaps and bounds of improvement from the common suspension system also known as a passive suspension system. A passive suspension setup is made up of a spring and damper which are selected based on the design requirement of the vehicle [2]. For an example, a car designed for a more sporty drive will have a stiffer setup which will sacrifice comfort, where as an executive sedan on the other hand will be designed with passenger comfort in mind, hence its setup with be softer which will sacrifice on handling performance.

To eliminate this trade-off, there are two more types of suspension setups. First, we have a fully active suspension setup, which is the same as a passive suspension system with an addition of a force actuator to work in tandem with the spring and damper. The force actuators can be hydraulic [3], or air systems [4] that apply varying force based on the inputs of the system allowing for varying damping ratios of the entire suspension system.

However, a fully active system has yet to make its way into many production vehicles as it is expensive, hard to maintain, heavy and complex. Due to this, this suspension setup is only found in top marques such as the Mercedes S Class, with its Airmatic suspension system and Rolls Royce.

The second alternative to the classic passive suspension system is a semi-active suspension system. A semi-active suspension system is similar to a passive suspension system in the sense of being made up of two components of spring and damper. However the damper in a semi-active suspension system is capable of varying its damping ratio [5]. There are to different ways that this has been achieved.

The first, is by mechanically changing the orifices of the damper and the second is by using dampers containing fluids then are able to change their viscosity. One such fluid is a magneto-rheological (MR) fluid that is made up of ferromagnetic particles. These particles are effected by a magnetic field that is created around them which alters their arrangement in their carrier fluid. The change of the particle arrangements in turn changes their viscosity and the entire suspension system can be varied by controlling the magnetic field [6]. Fig 1.2 shows a

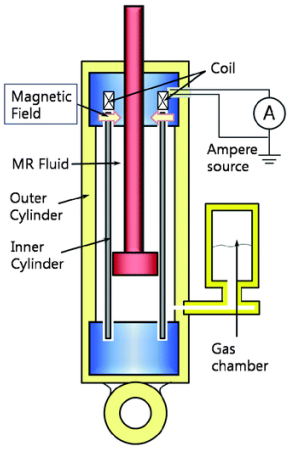


Figure 1.2 Cross section of a MR damper [7]

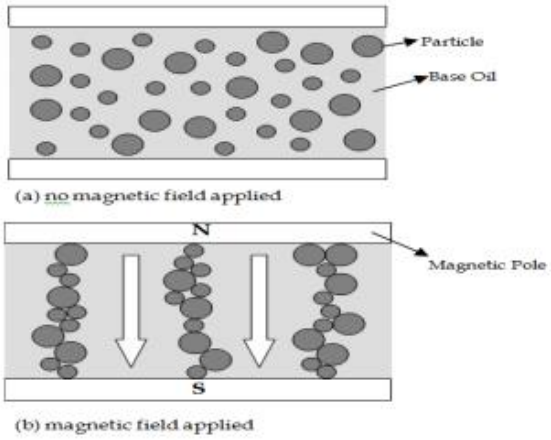


Figure 1.3 Difference in ferromagnetic particles when magnetic field is applied [7].

Just like a fully active suspension system, a semi-active suspension system too needs input from the suspension system in order to vary the damping applied. There are a couple of different control methods that have been studied upon such as the ground hook control, skyhook control and hybrid control. Previous studies have shown that skyhook control is an effective strategy when working with MR damper [8] where it is able to closely match the performance of a fully active suspension.

All of the studies mentioned above have primarily focused on analytical analysis and simulations. However, the parameters studied are limited with very few studies focusing on effect of control systems on tire loads, and the response of the resulting mass damper system at different frequency ranges. Previous studies have also focused on either improving comfort or increasing handling performance with very limited studies contributing to increasing the performance of the suspension

system in both this aspects. This research project intends to complement previous study by comparing passive and semi-active suspension system using two different control strategies and to propose a modified control strategy that is capable of increasing ride comfort and handling performance.

2.0 Research Methodology

The research is by first understanding the background of the project and establishing the research questions, objectives and the scope of the project. Literature review was carried out right after this where intensive reading of journals is carried out to aid with familiarity and increase basic understanding of the research paper. This step was vital and can't be ignored as it serves as the foundation of the entire research.

Next, the simulations was carried out using SIMULINK and MATLAB. The first simulation was carried out for a ¼ car passive suspension which is modeled of the free body diagram (FBD) as shown in fig 2.1

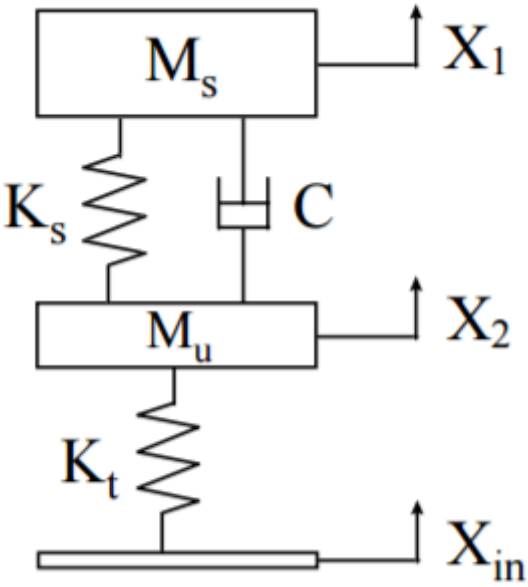


Figure 2.1. FBD of Passive Suspension System

$$M_s\ddot{X}_s = -C(\dot{X}_s - \dot{X}_u) - K_s(X_s - X_u) \quad \text{Eq (1)}$$

$$M_u\ddot{X}_u = C(\dot{X}_s - \dot{X}_u) + K_s(X_s - X_u) + K_t(X_{in} - X_u) \quad \text{Eq (2)}$$

From the FBD, equations (1) and (2) are obtained, which are used to come up with a Simulink block diagram as shown in fig 2.2.

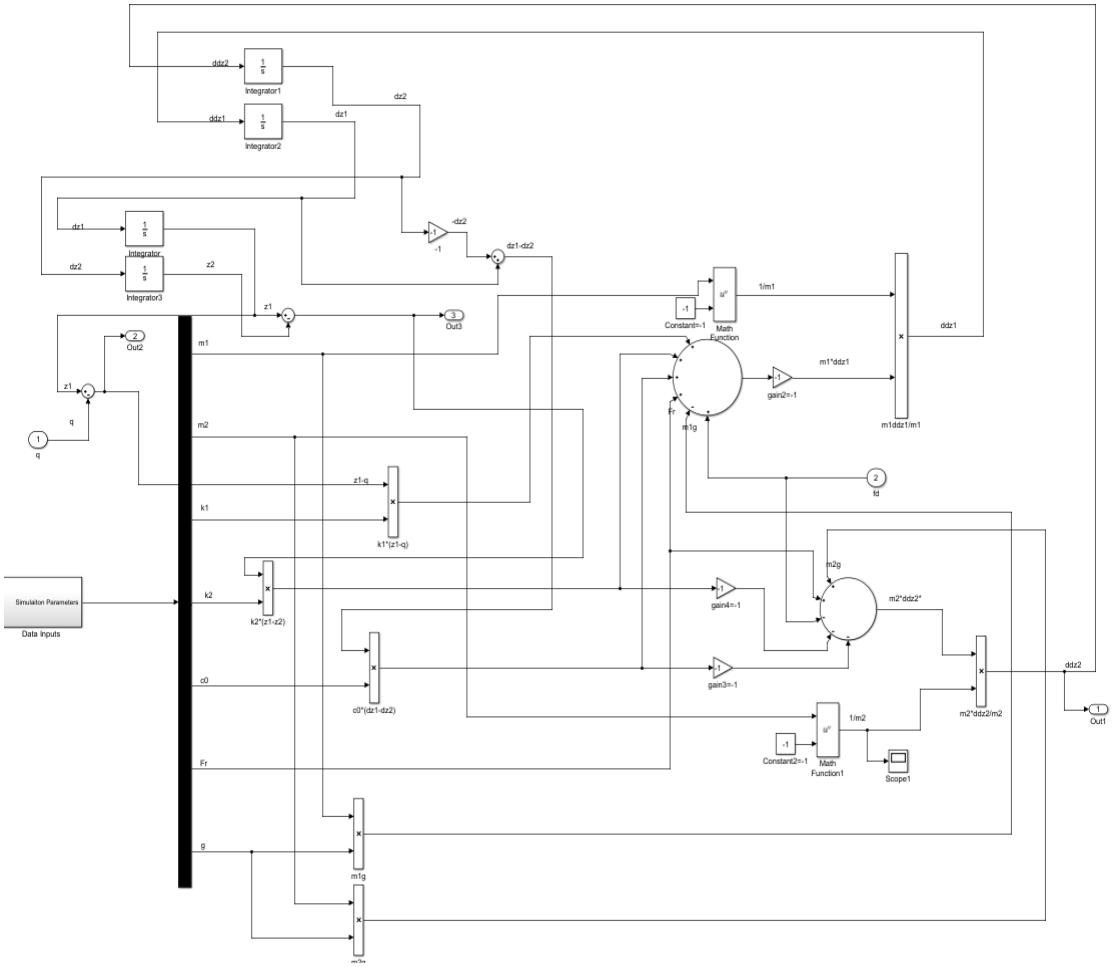


Figure 2.2. Simulink model of a ¼ car passive suspension

The only difference between a semi-active and passive suspension system is that it has a changing damping coefficient which is a result of the contol force provided by its control system. Hence the equation of motion has to include an additional parameter which is the control force. The resulting equation of motion is in equation (3) and (4)

$$M_s\ddot{X}_s = -C\left(\dot{X}_s - \dot{X}_u\right) - K_s(X_s - X_u) + F_{control} \quad \text{Eq (3)}$$

$$M_u\ddot{X}_u = C\left(\dot{X}_s - \dot{X}_u\right) + K_s(X_s - X_u) + K_t(X_{in} - X_u) - F_{control} \quad \text{Eq (4)}$$

A semi-active suspension receives a control force calculates based on the control logic used. The control logics are modeled using a S-function block builder. The first control logic implemented is the skyhook logic as shown below

$$\dot{X}_{12} = \dot{X}_1 - \dot{X}_2 \quad \text{Eq (5)}$$

If , $(\dot{X}_1\dot{X}_{12} > 0)$

$$F_{Control} = C_{sky}\dot{X}_1 \quad \text{Eq (6)}$$

Else

$F_{Control} = 0$

Where C_{sky} is a constant that is also referred to as a gain of the system. The next control strategy modeled was a ground-hook control which is modeled upon a fixed damper on a ground that is connected to the unsprung mass. Which is different to a skyhook that is modeled upon a fixed damper at an imaginary point in the sky, linked to the sprung mass. The ideal ground-hook damping logic is shown below

If , $(-\dot{X}_2\dot{X}_{12} > 0)$

$F_{Control} = C_{ground}\dot{X}_2$ Eq (8)

Else

$F_{Control} = 0$

Where Cground refers to the gain used for the control system.

The modified controller is modelled by using both skyhook and ground-hook control to eliminate the drawback of using each of the control system independently. The modified control logic is obtained by first slightly changing the original skyhook and groundhook control, and the ouputs are sent to the modifed control logic, as shown below.

For skyhook logic :

If , $(\dot{X}_1\dot{X}_{12} > 0)$

$Out_{sky} = \dot{X}_1$

Else

$Out_{sky} = 0$

For groundhook logic :

If , $(-\dot{X}_2\dot{X}_{12} > 0)$

$Out_{ground} = \dot{X}_2$

Else

$Out_{ground} = 0$

Modified skyhook logic :

$F_{Control} =$

$F_{Control} = C_{modified}\left(ZOut_{sky} + (1 - Z)Out_{ground}\right)$

Where $C_{modified}$ is a constant which is similar to that of the gains C-Sky and C-Ground, and Z is the relative ratio. For an example when Z = 1 the system will behave as a full skyhook control and when Z = 0 the system will behave as a full groundhook control. The modified skyhook logic is once again built using the s-function builder block in simulink which receives input from the other two logics as shown in Fig 2.7.

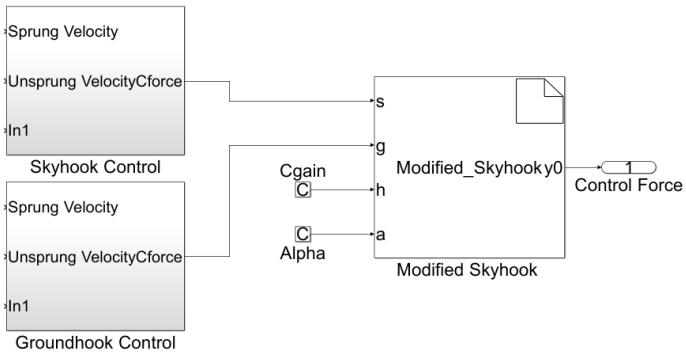


Figure 2.7 Modified Control Logic in Simulink

3.0 Result and Discussion

The first simulation is run with the modified skyhook control logic with a gain of 3000. A gain of 3000 is selected based on the previous simulations of ground-hook and skyhook control strategy where when a gain of 3000 is used the results were a better compromise between the advantages and the drawback that resulted in each of the control strategy. The next set of simulations were carried out to study the advantages and improvements of the modified skyhook control when compared to the traditional skyhook control, groundhook control and a passive suspension system.

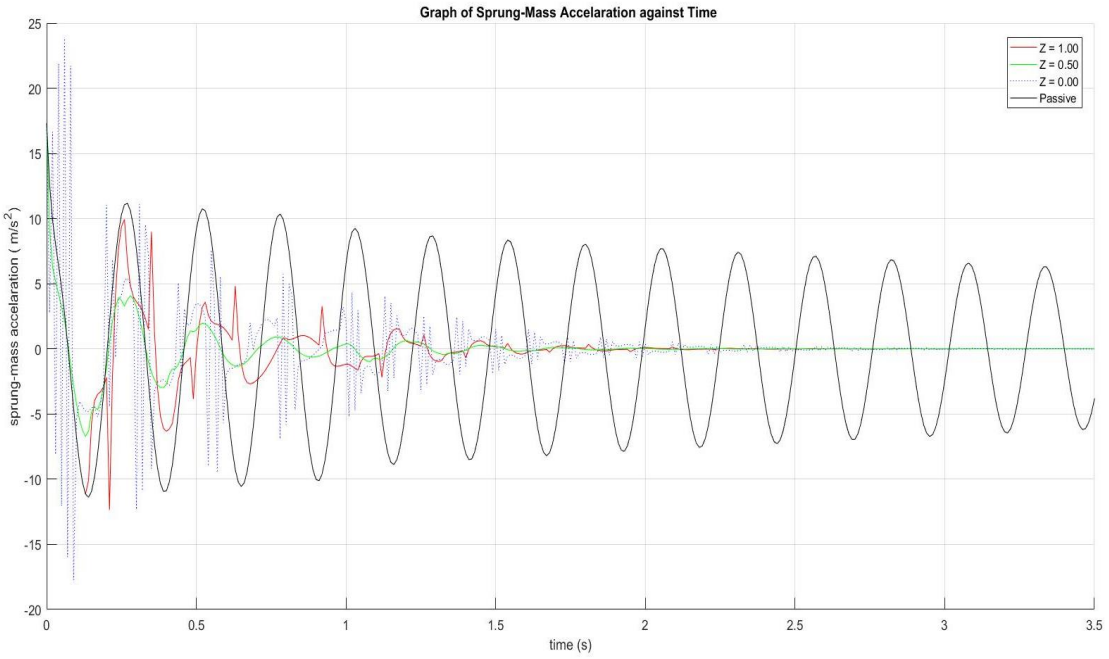


Figure 3.1 Sprung Mass Acceleration, Z= 1, 0.5, 0

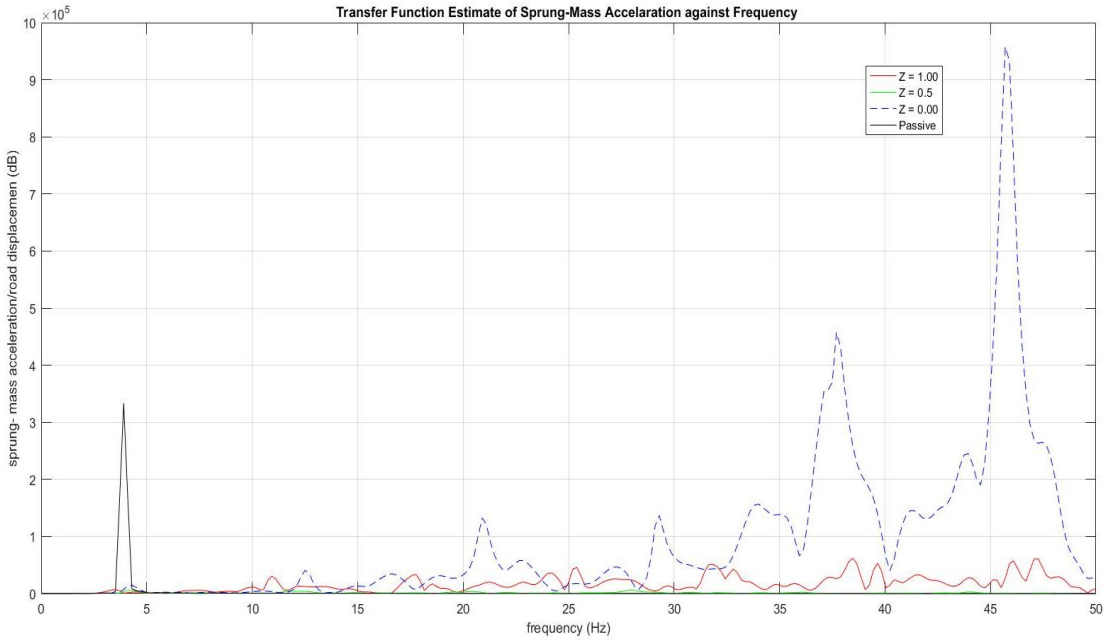


Figure 3.2 Transfer Function Estimate of Sprung Mass Acceleration Z= 1, 0.5, 0

The first evaluation was carried out based on the sprung-mass acceleration. It is to be noted that as discussed previously Z = 1.00 represent a full skyhook control strategy, Z = 0.00 a full groundhook control strategy whereas Z= 0.5 was the best Z value found and selected based on previous simulation. Based on fig 4.5 the improvement of the modified skyhook control is evident. Firstly it has no initial jerk of sprung mass acceleration as exhibited by the groundhook control. Next, it has also reduced the peaks in a single oscillation which can be seen by the smother curve produced by it. It is also noticed that its settling time is similar if not better than both the skyhook and groundhook control.

Using transfer function estimate in Matlab also allowed to predict the suspension system behavior at different frequency. The first transfer function estimate was used for the sprung mass acceleration. From fig 3.2 it is noticed that groundhook control stratergy managed to reduce the amplitude at resonance, however its acceleration increases substantially with higher frequency which shows that is unable to isolate the sprung-mass at higher frequencies. Skyhook control on the other performs much better at higher frequencies compared to groundhook whilst still successfully reducing the amplitude at resonance, however, the passive suspension system performs better at higher frequencies. The modified skyhook control not only managed to reduce the maximum amplitude at resonance but also performs well at the entire range of frequency tested.

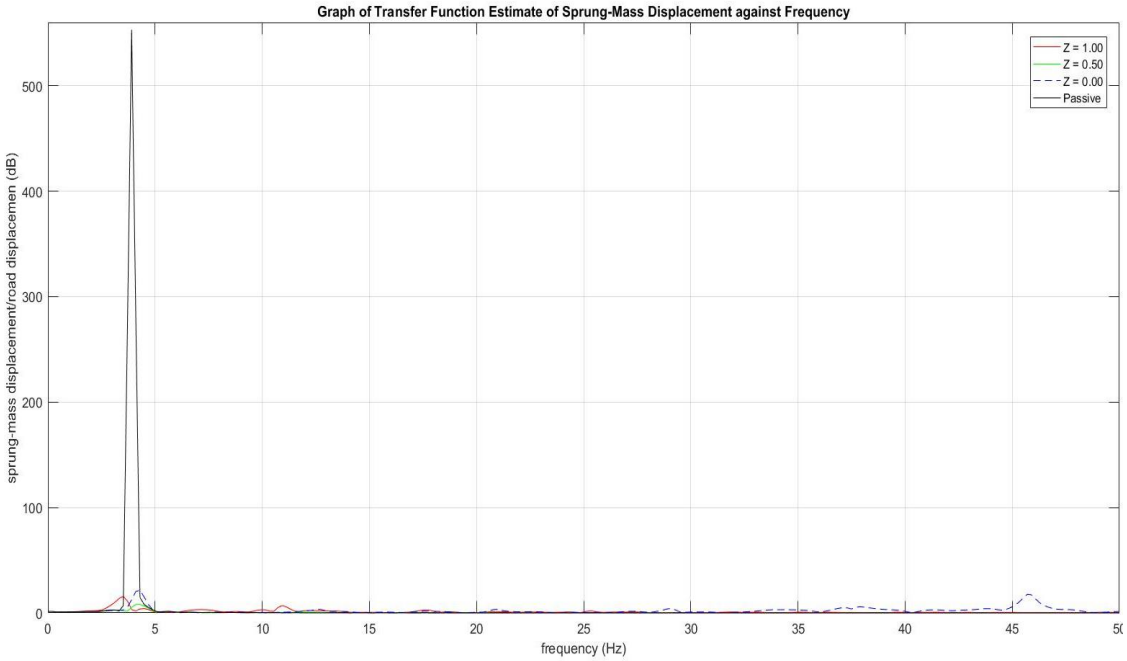


Figure 3.3 Transfer Function Estimate of Sprung Mass Displacement, Z= 1, 0.5, 0

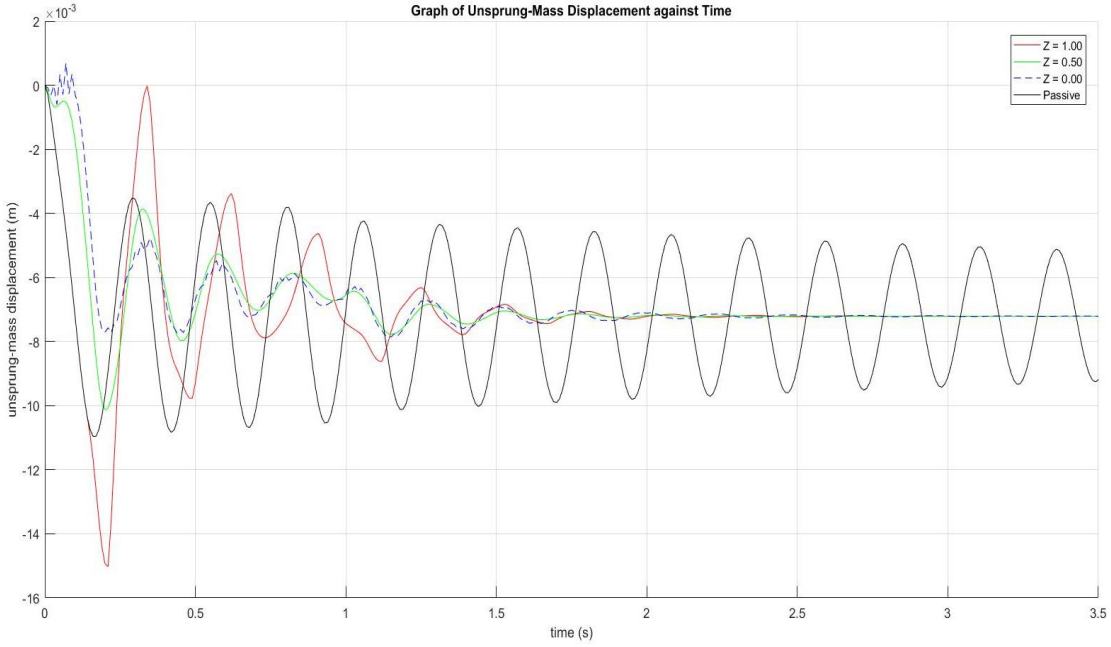


Figure 3.4 Unsprung Mass Displacement, Z = 1, 0.5, 0

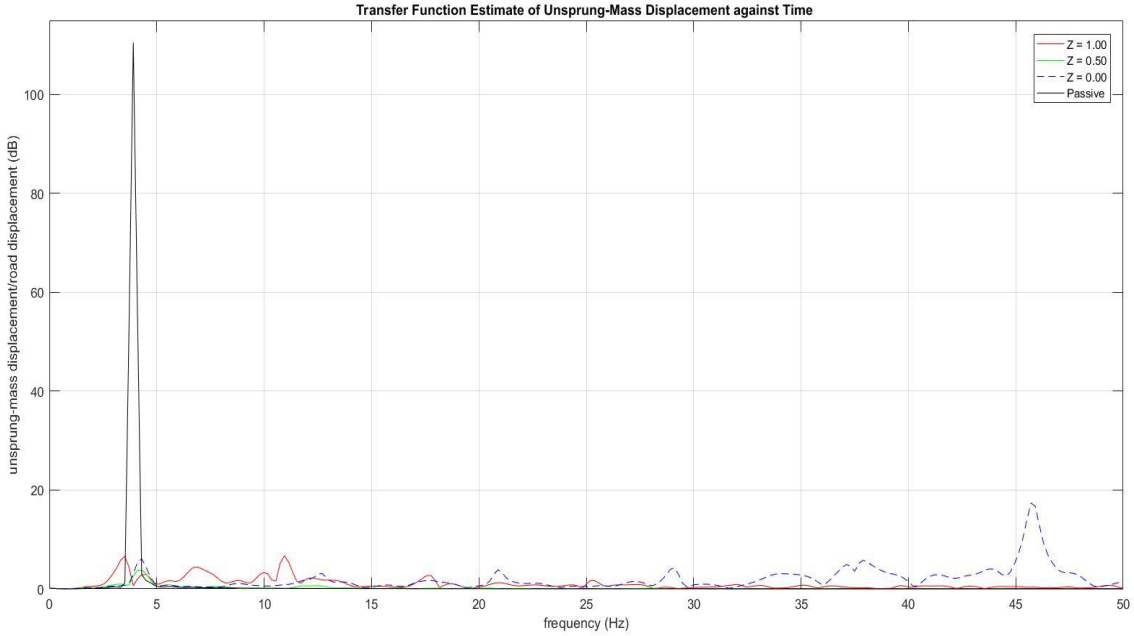


Figure 3.5 Transfer Function Estimate of Unsprung Mass Displacement, Z = 1, 0.5, 0

Fig 3.3 shows the estimated sprung mass displacement at different frequencies. Once again it is noticed that all three semi-active suspension setup reduce the resonance amplitude significantly. This can be contributed to two different aspects. The first, as resonance is dependent on the system damping, and semi-active suspension don't have a fixed damping coefficient hence the maximum amplitude is very low. Next, the simulation and control strategies were not modeled with a maximum control force, which allows the system to apply an equal but opposite force to reduce vibration. However in reality this is not possible as MR Damper have their maximum and minimum range of damping that it is capable of providing. Besides that, this graph also shows that a skyhook control shifts the resonance to the left and groundhook control shifts the resonance to the right of the passive suspension resonant frequency.

From fig 3.4, once again the modified skyhook control outperforms both groundhook control and skyhook control. This is said as it maximum amplitude is lower compared to skyhook control eliminating wheel hop whereas the initial spike in displacement that is noticed in the pure groundhook control is reduced. All of this is achieved with a smoother curve and similar settling time as skyhook and groundhook control.

Fig 3.5 shows the expected unsprung-mass displacement at different frequency. The same pattern is observed as fig 3.3, where the resonance amplitude is reduced substantially, which once again can be attributed to the factors discussed for fig 3.3. Once again, ground hook control relatively underperforms when compared to skyhook control at higher frequency. The modified skyhook control is not only able to reduce resonant amplitude but also perform well at higher frequency imitating the response of the passive suspension.

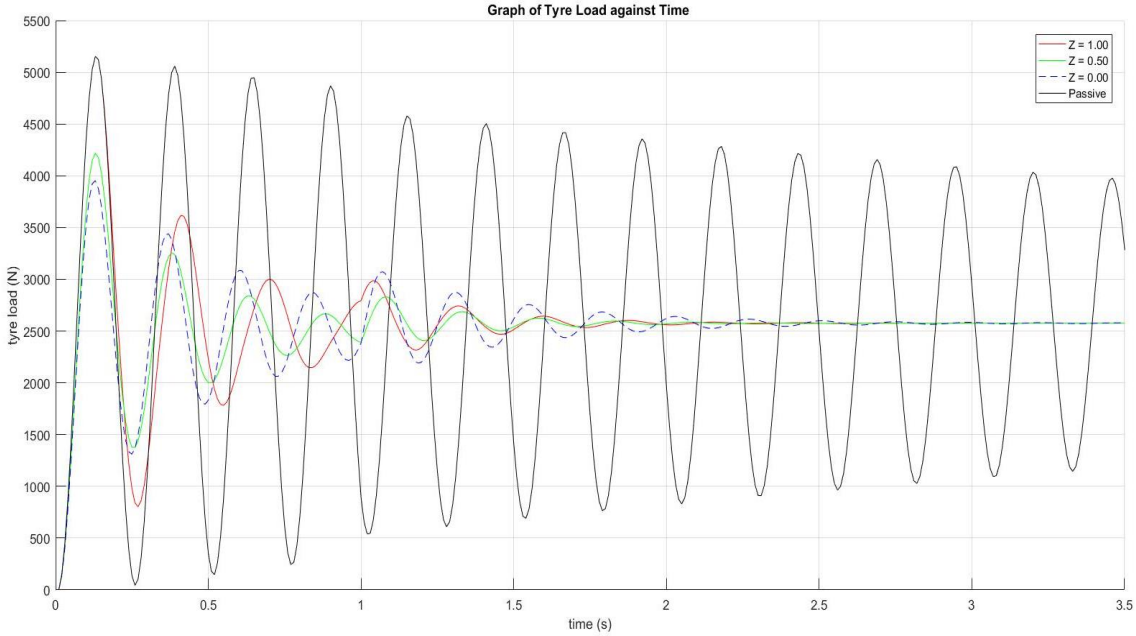


Figure 3.6 Tire Load, Z = 1, 0.5, 0

Fig 3.6 shows another aspect of the suspension system that is studied which are the tire loads. Tire loads can impact the handling performance of the car as very high forces can deform the tire which then effects its contact patch with the road. An alteration of the contact patch during hard cornering especially can change grip levels of the car during mid corner. Besides that, high tire loads can also become a safety issue as the tire may fail due to high forces on the side walls. All three of the semi-active suspension systems managed to reduce the tire loads with the modified skyhook control once again outperforming the skyhook and groundhook control strategies.

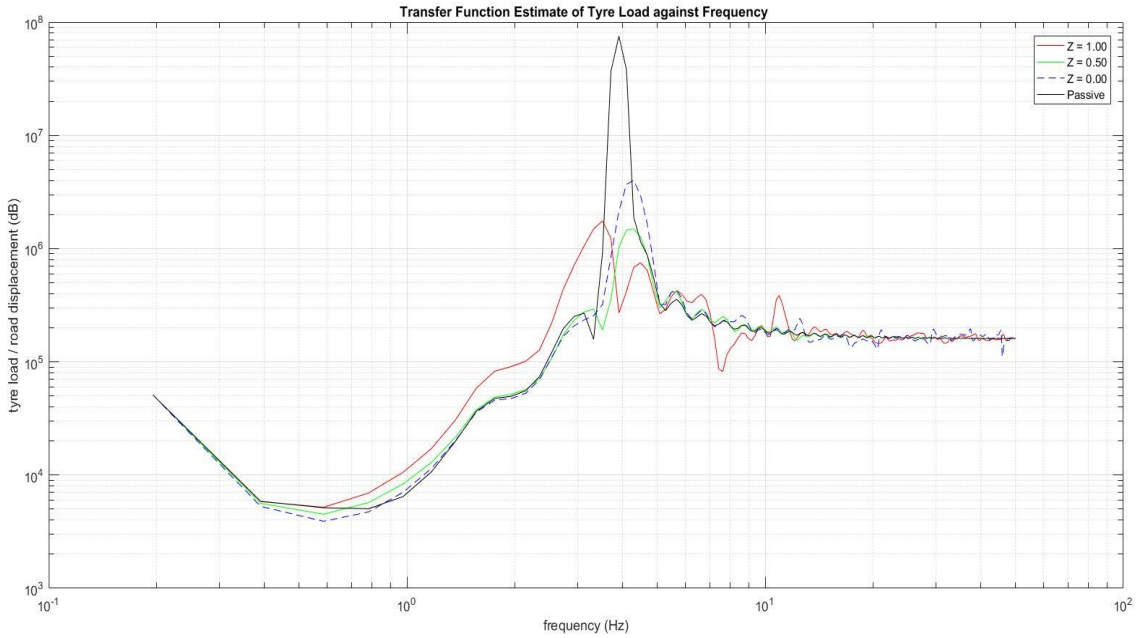


Figure 3.7 Transfer Function Estimate of Tire Load, Z = 1, 0.5, 0

Looking at the figure for the transfer function estimate of tire load, a similar pattern as previous graph is noticed where the resonant amplitude is reduced, skyhook

control moves the resonant frequency to the left, whereas the groundhook control moves the resonant frequency to the right of the passive suspension system resonant frequency. The modified skyhook control has the best performance as manages to reduce the resonant amplitude the most whilst still performing similarly to the passive suspension system at the entire range of frequency. It is also noticed that both the skyhook and groundhook control strategies have some irregular peaks at the higher frequency which can affect the grip level due to its sudden and unpredicted spikes which the modified skyhook control doesn't exhibit.

4.0 Conclusion

This research project has main objectives were to model a ¼ car passive and semi active suspension, compare the differences and to later on modify the control strategy to increase both the comfort of the vehicle and the suspension handling performance. Through the simulations carried out it is discovered that a semi-active suspension outperforms a passive suspension system. However the initial skyhook control strategy has a few drawback such as initial sprung-mass acceleration jerk and a higher unsprung-mass displacement when high C-Sky gains were used. To improve these drawbacks, an alternative control strategy, groundhook control strategy was studied and simulated where it managed to control the unsprung-mass displacement better but had a higher sprung-mass acceleration compared to skyhook control. Based on the simulations, the skyhook control strategy was more suited toward increasing comfort at the sacrifice of handling performance, whereas the groundhook control stratergy increases the handling performance at the sacrifice of comfort.

The modified skyhook control strategy combines both of the control logic into one and the best Z values were tested where Z = 0.5 was found to have best results both in increasing the comfort and the suspension handling performance. The modified skyhook control strategy was able to produce smoother curves for all simulations, eliminating initial jerks and rapid acceleration changes in the sprung-mass while also reducing the unsprung-mass displacement, eliminating the wheel hop phenomenon.

The next step for this research is to conduct lab testing of existing vehicle damper and springs to obtain more accurate parameters. Based on this a suitable MR dampers in the market can be determined allowing for its maximum and minimum damping to be determined. This will allow for more accurate simulations to be carried out as currently no maximum damping has been set for all the models. These testing will also allow for the thesis project to progress to the next level by converting the control forces feedback into the system as different magnitude of currents based on the specification of the MR dampers. This will take the entire research project one step closer as a proper control system based on an actual MR damper and a specific vehicle. Once this is done, the research project can also be progressed by modeling more degree of freedoms and taking into account camber angles and other parameters to further increase simulation accuracy and moving toward real life implementation and testing of the system.

References

[1] B. Gadhvi, V. Savsani and V. Patel, "Multi-Objective Optimization of Vehicle Passive Suspension System Using NSGA-II, SPEA2 and PESA-II", Procedia Technology, vol. 23, pp. 361-368, 2016.

[2] T. Xu, M. Liang, C. Li and S. Yang, "Design and analysis of a shock absorber with variable moment of inertia for passive vehicle suspensions", Journal of Sound and Vibration, vol. 355, pp. 66-85, 2015.

[3] M. Karkoub and M. Zribi, "Active/semi-active suspension control using magnetorheological actuators", International Journal of Systems Science, vol. 37, no. 1, pp. 35-44, 2006.

[4] Y. Ko, K. Park, I. Baek, G. Kim and J. Lee, "Study on Development of Virtual Components for Active Air Suspension System Based on HILS for Commercial Vehicle", Transactions of the Korean Society of Automotive Engineers, vol. 21, no. 2, pp. 26-36, 2013.

[5] Miller, L. R., "An Introduction to Semiactive Suspension Systems," Lord Library of Technical Articles, Document LL-1204, 1986.

[6] Lee, H. S., Choi, S. B., "Control and Response Characteristics of a Magneto-Rheological Fluid Damper for Passenger Vehicles," Journal of Intelligent Material Systems & Structures, Vol. 11, No. 1, p. 80-87, January 2000.

[7] M. Orečný, Š. Segľa, R. Huňady and Ž. Ferková, "Application of a Magneto-rheological Damper and a Dynamic Absorber for a Suspension of a Working Machine Seat", Procedia Engineering, vol. 96, pp. 338-344, 2014.

[8] L. Gopala Rao and S. Narayanan, "Sky-hook control of nonlinear quarter car model traversing rough road matching performance of LQR control", Journal of Sound and Vibration, vol. 323, no. 3-5, pp. 515-529, 2009.

eureca 2016 – Conference Paper
Paper Number 2ME17

Suppression of Vibration Transmission of Compressor Grommets

Justin Leong Chee Mun[1], *Mohammad Hosseini Fouladi*[1*], *Satesh Namasivayam*[2],
[1]*School of Engineering, Taylor's Univeristy, Malaysia*

**Hosseini@taylors.edu.my*

ABSTRACT

Unwanted vibrations can cause severe machinery and structural damage, this is shown in the nomograph under machine severity vibrations. The mechanical properties of a compressor grommet affects its vibration transmission. As this project is conducted under some limitations, the mechanical properties of the materials are sourced from online sources such as MATWEB. The designs featured in this project are accomplished using SolidWorks 2013. After analysing the new grommet design using ANSYS Workbench 15.0, it is found that a cone base grommet would be the best design, as it provided an improvement of 6.6% compared to the original grommet. Regarding the materials, after comparing the same design using 3 different materials, namely EPDM rubber, SBR, and neoprene rubber, EPDM rubber yield the best results under room temperature operations.

Keywords: Improved Grommet, Vibration Transmission, Grommet Design, Better Transmissibility Performance.

1. Introduction

Vibration is a form of oscillating motion whereby the object or system oscillates about its equilibrium point. [1] There are mainly two types of vibration, such is, forced vibration and free vibration. [2] Free vibrations occur when the object or system undergoes a temporary disturbance from its equilibrium point and is then unrestricted by any external force. [2] Inversely, forced vibrations occur when the oscillating system or object is dampened by an external forced intentionally. As such, the type of vibration I will be focusing in this research is forced vibration with an external damper (grommet) fixed underneath the compressor to dampen the vibrations transmitted to the shell casing.

In this research paper, I will be mainly looking at compressor grommets, to be specific, floor mounted grommets as shown in Figure 1 for the outdoor unit of a household air conditioning unit as shown in Figure 2 below. The vibrations caused by the outdoor unit can cause unwanted noise and also wear and tear to the compressor. As such, to reduce the vibration transmitted to the shell casing, grommets were invented. Such grommets have been made using, commonly neoprene (Polychloroprene) rubber, EPDM (Ethylene Propylene Diene Monomer) rubber, and also SBR (Styrene-Butadiene Rubber). [3]



Figure 1: Rubber compressor grommets. [4]



Figure 2: Image of outdoor compressor of household air conditioning unit. [5]

Improving the current grommets can help improve the dampening of vibrations transmitted to the casing of the compressor, this is important to prolong the lifespan of the compressor by reducing wear and tear caused by the long operation hours of the compressor. By prolonging the lifespan of the unit, the user will be able to reduce their worry of unexpected break downs while reducing maintenance cost. Aside from increasing the lifespan of the compressor, the reduction of vibration transmitted can reduce unwanted noise to the surroundings.

2. Research Methodology

2.1 Design of Grommet

The designing phase of the grommet begins with reviewing common shapes of grommets that are out in the market. This justifies the minor modifications to improve the grommet's design. Citing the initial design of the compressor grommet to the inventor Li et al [6], the design of the grommet is then modified to 3 different shapes. Figure 3 below shows the original design of the grommet.

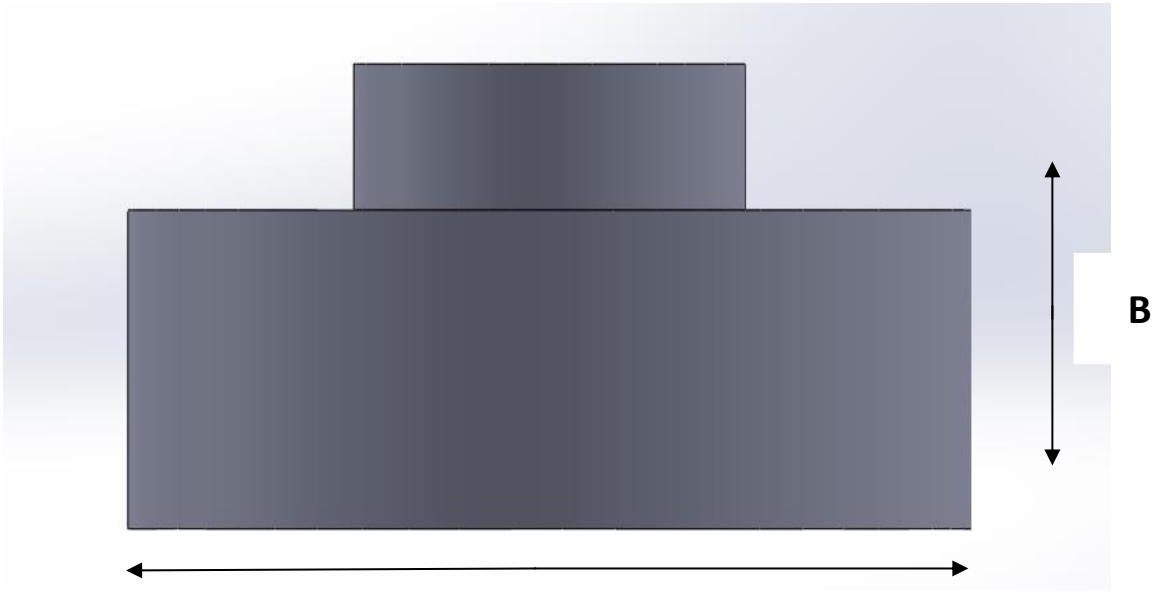


Figure 3: Initial grommet designed in SolidWorks

In Figure 4 below, the initial design is modified to save cost of materials while determining if the performance of the grommet remains the same. The inclination of the base proposes a cone base and will henceforth be called the cone base grommet.

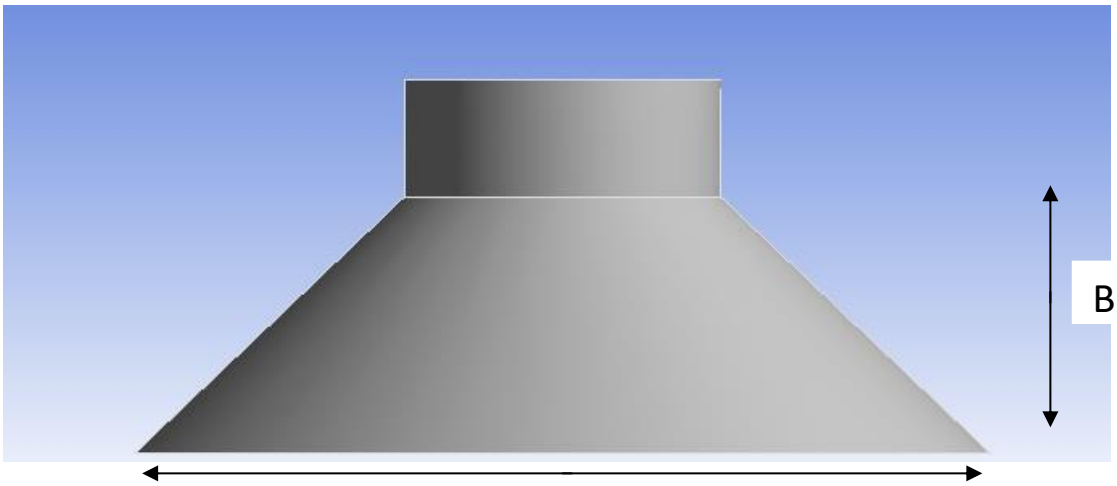


Figure 4: Cone base grommet designed in SolidWorks

Thirdly, the grommet is shown in Figure 5 below, which has been modified to be a trapezoidal shape when viewed from the side. This is just to experiment the possible new designs of the current grommet, to have a thicker overall height and thus possibly improving the grommet.

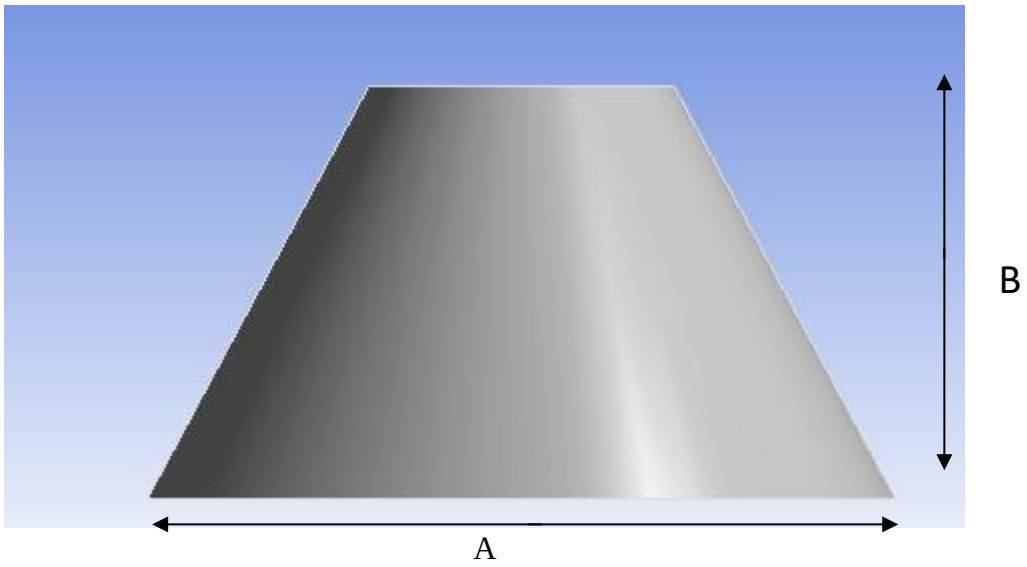


Figure 5: Trapezoidal grommet designed in SolidWorks

Lastly, in Figure 6 below, the original grommet has been modified to have a thicker base, this is to determine the performance of the vibration transmission of the grommet to the shell casing compared to the originally designed grommet. Although this incurs more cost to the manufacturer, the possible improvement in the vibration transmission value may provide its customers with better satisfaction.

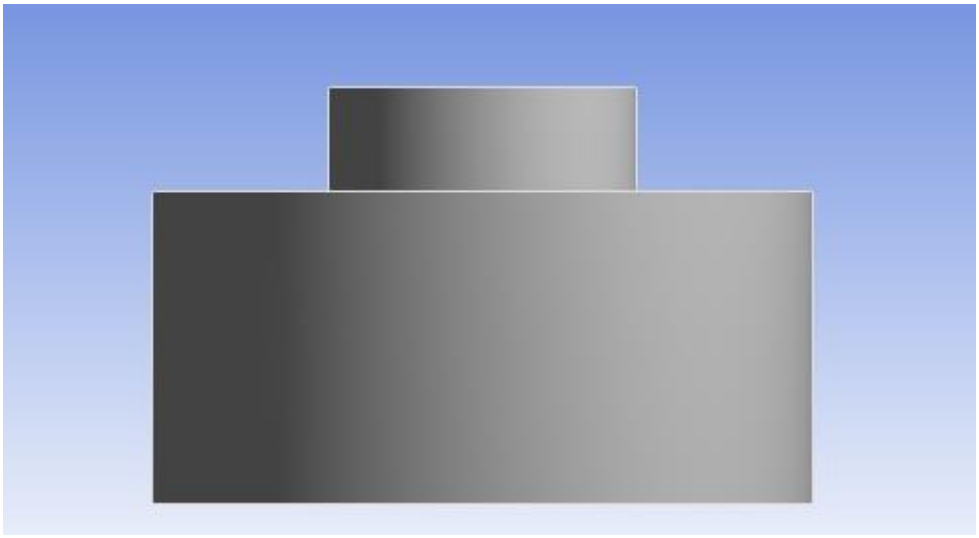


Figure 6: Thick base grommet designed in SolidWorks

For the ease of future manufacturing, displaying the dimensions of each grommet is crucial to the manufacturer, the Table 1 below clearly displays the dimensions of each grommet.

Table 1: Dimensions of Grommet

Type of Grommet	A (mm)	B (mm)
Original	31.8	12
Cone Base	31.8	12
Thick Base	31.8	15
Trapezoidal	31.8	17

2.2 Material

Looking at the characteristics of neoprene as a rubber material, it is shown in Table 2 that it has the lowest thermal conductivity value, this is important to note the difficulty in the rise of temperature of the material isn't high, and may cause unwanted issues. Compared to the other two selected materials, the young's modulus of neoprene isn't commendable, thus indicating that it deforms easily under tensile force. Although so, neoprene is widely used as a rubber material in manufacturing grommets due to its low cost and ease of availability. Aside from that, neoprene shows good resistance towards flame, abrasion, and also towards alcohol. This flexibility in characteristics are the main reasons it is so commonly used as a compressor grommet. [7] When taking SBR into consideration, this rubber exhibits good elongation at break and thermal conductivity values. Its thermal conductivity value proved to be the best among the 3 types of materials discussed. This is important, as having a high thermal conductivity value translates to lower fluctuations of temperature during operation. When compared to neoprene, although they both have the same operational temperature, having a higher thermal conductivity value allows SBR an advantage in this aspect. SBR performs very well under impact, abrasion and water resistance. This would allow SBR to be very useful in underwater situations. [7] EPDM rubber has the lowest elongation at break value, although this would seem to pose a threat when compared to the other two materials, it has a very high value of Young's Modulus, this allows the rubber to adhere to much more force before reaching its elongation at break value, and is considered highly when there are high amounts of force stretching the rubber. EPDM has a lower minimum range of operational temperature when compared to SBR and neoprene, although so, EPDM overcomes this negative characteristic by having a higher maximum value of operational temperature. This would permit it to operate under equipment with higher temperatures such as boilers. Aside from that, EPDM performs excellently under heat resistance, abrasion and water. As such, it is vital for the author to understand the pros and cons of each rubber, selecting wrongly would cause the grommet to be consistently underperforming. [7]

Table 2. Comparison of parameters of types of rubbers.

Type of rubber / Parameter	Thermal Conductivity (W/m.K)	Elongation at Break (%)	Young's Modulus (MPa)	Shear Modulus (MPa)	Density (kg m^-3)
Neoprene	0.19	450	1.25	4.17E+05	1250
SBR	0.2-0.25	700	11.89	3.97E+06	955
EPDM	0.2	400	17.4	5.81E+06	1100

3.0 Discussion and Results

3.1 Finite Element Analysis

The FEA will be conducted in ANSYS Workbench 15.0, although there are newer versions which offer more capability, the software provided by Taylor's University were not up to date. Before beginning the FEA, the material must be assigned to the model designed earlier through SolidWorks. The material used were not found within the educational license of ANSYS, plus, due to the lack of research licenses provided by Taylor's University, the materials to be tested were added into the library, and their mechanical properties were obtained through reliable sources. As smaller mesh sizes, would amount to a larger amount of meshing in the model, this would lead to an increase of time needed for the simulation to complete. Due to licensing issues faced by the educational license, the size of meshing could not be at the minimum, and thus be set at 0.001m. The relevance centre was set to be course to reduce the time needed to complete the simulation, as a finer relevance centre, paired with the minimum meshing size would not allow the computer to generate the simulation in a timely manner. Aside from that, the hex dominant mesh was chosen as it is the most accurate shape of mesh. Figure 7 below shows the model after the meshing is done.

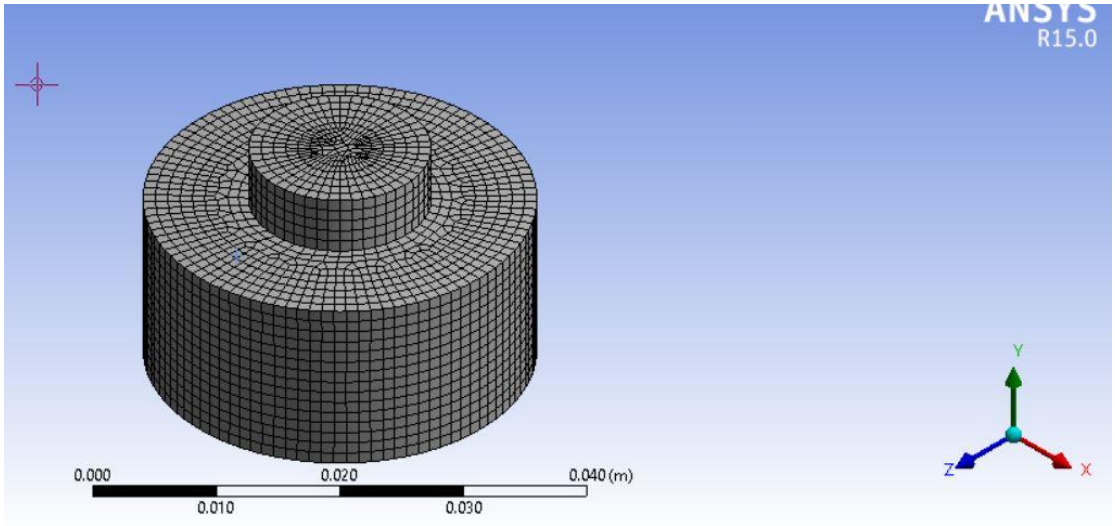


Figure 7: Model after meshing

3.1.1 Simulation on Neoprene Rubber

After obtaining the values of the mass of the outdoor unit of a household air-conditioner and the stable running frequency from Panasonic, the harmonic analysis simulation is conducted on the 4 different designs. The results are shown in the figures below.

Material	Neoprene			
Grommet Design	Original	Cone Base	Trapezoidal	Thick Base
Frequency	26	26	26	26
Static Deflection	0.00389	0.00372	0.00386	0.00376
Mass	15	15	15	15
Displacement of Base	0.000216	0.000207	0.000215	0.000209
Stiffness	37789.20308	39516.12903	38082.902	39095.74468
Natural Frequency	50.19243176	51.32649026	50.387103	51.05274702
Frequency Ratio	0.518006382	0.506561034	0.5160051	0.509277199
Displacement of Compressor	0.000295215	0.000278452	0.000293	0.00028219
Maximum Velocity	0.048233457	0.045494584	0.0478747	0.046105269

Figure 8: Results of Neoprene Rubber

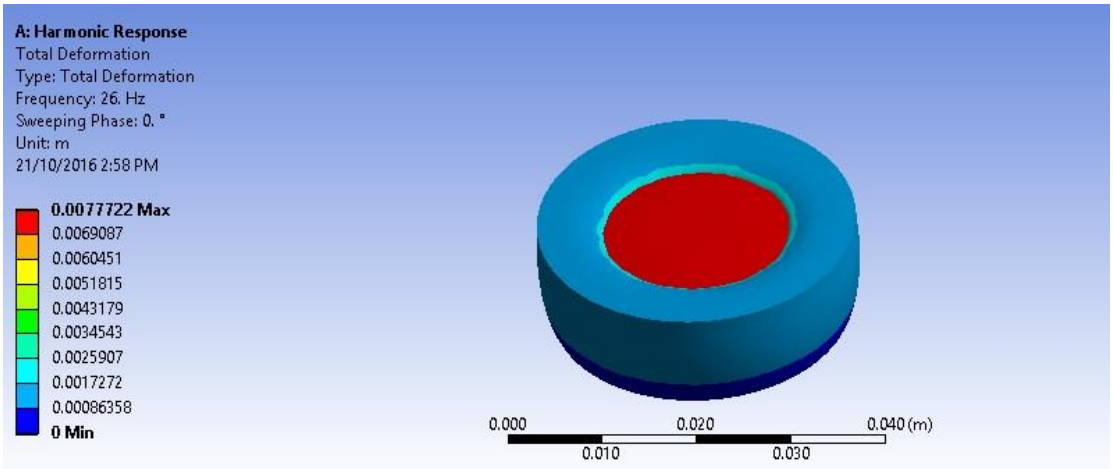


Figure 9: Displacement results on original grommet with neoprene rubber

From Figure 9, the maximum and minimum deflection that the grommet is undergoing is defined, the respective values for the maximum and minimum deflection are 0.00778 m and 0.000864 m. The value of 0 is not taken into account as the base of the grommet is considered a fixed point and will always yield a 0 value, thus to determine the amount of deflection the base is undergoing, the lowest reading above the 0 value is considered. After obtaining the said values, using Equation 1 to obtain the stiffness of the grommet. After solving Eq. (1), with the stiffness value *k*, utilizing Eq. (2) will yield the natural frequency of the grommet. After obtaining the natural frequency, ω_n, usage of Eq. (3) will yield the frequency ratio, *r*.

Getting the value of the frequency ratio is crucial to determine the displacement of compressor, X. Finding the displacement value of the compressor allows to finally obtain the Maximum velocity, v_{max} through Eq. (4) V_{max} is the most important attribute to compare the maximum allowable velocity and frequency in the nomograph to determine if the value is within satisfactory machine vibration severity, ISO 2372. Comparing the V_{max} value of neoprene with their individual designs show that the lowest V_{max} value would be the original grommet design at 48.23 mm/s. At this velocity and frequency, we can see in Figure 18 below that it is in the impermissible level of machine vibration severity. This is all due to the low value of Young's modulus, causing a severe static deflection level in the compressor grommet. This would lead on to lower the stiffness in the compressor, thus causing the V_{max} value to be severely high.

Equation to calculate stiffness:

$$k = \sqrt{\frac{W}{\delta_{st}}} \quad (1)$$

Equation to calculate natural frequency:

$$\omega_n = \sqrt{\frac{k}{m}} \quad (2)$$

Equation to calculate displacement of compressor:

$$X = \frac{Y}{1-r^2} \quad (3)$$

Equation to obtain V_{max}:

$$V_{max} = 2 * pi * \omega * X \quad (4)$$

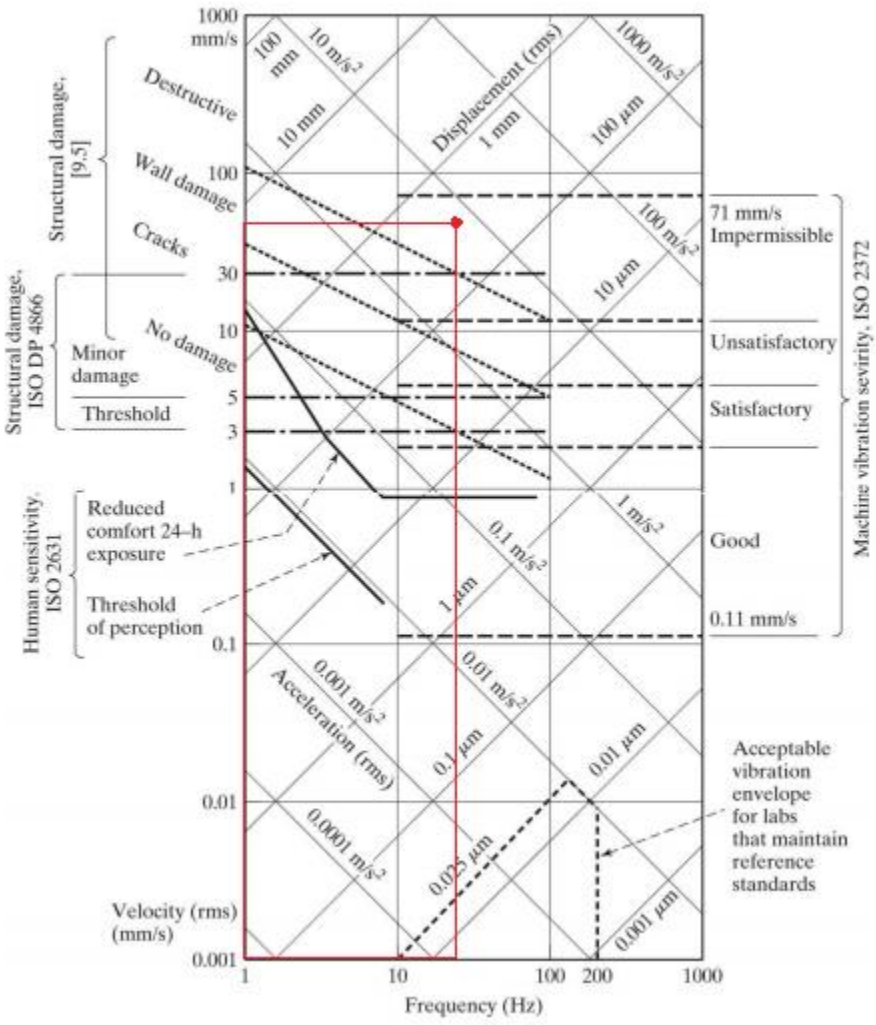


Figure 10: Nomograph of Neoprene with original grommet design.

3.1.2 Simulation on EPDM Rubber

Following the same steps taken to obtain the V_{max} for the neoprene rubber, the results for EPDM rubber on the 4 variations of design was obtained. Utilizing the 4 Equations above, the V_{max} of EPDM rubber that was found to be the lowest would be the cone base design as shown in Figure 11 below. The minimum and maximum values are shown in Figure 12 below. Whereas the correlation to the nomograph at V_{max} and frequency is shown in Figure 13.

Material	EPDM			
Grommet Design	Original	Cone Base	Trapezoidal	Thick Base
Frequency	26	26	26	26
Static Deflection	0.00028	0.00026	0.000277	0.00027
Mass	15	15	15	15
Displacement of Base	0.0000155	0.0000145	0.0000154	0.000015
Stiffness	525000	565384.6154	530685.92	544444.4
Natural Frequency	187.0828693	194.1450687	188.09323	190.5159
Frequency Ratio	0.138975846	0.133920476	0.1382293	0.136472
Displacement of Compressor	1.58053E-05	1.47648E-05	1.57E-05	1.53E-05
Maximum Velocity	0.002582328	0.002412332	0.0025651	0.002497

Figure 11: Results of EPDM rubber

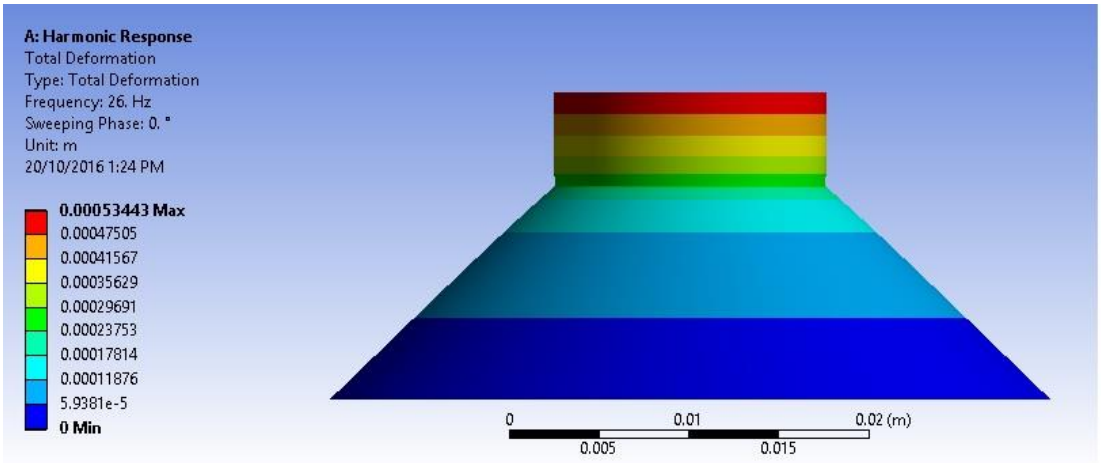


Figure 12: Displacement results on cone base grommet with EPDM rubber

Comparing the V_{max} values of the 4 designs of EPDM rubber, it is seen that the cone base design would yield the lowest maximum velocity of 2.412 mm/s. Compared to the 48.23 mm/s the neoprene rubber yield, the EPDM rubber shows an improvement of roughly 2000%. This is due to the high Young's Modulus value of the EPDM rubber, allowing it obtain much lower static deflection value, thus increasing its stiffness value to 565385 N/m. This stiffness value then translates to a higher natural frequency, thus yielding a much lower V_{max} value.

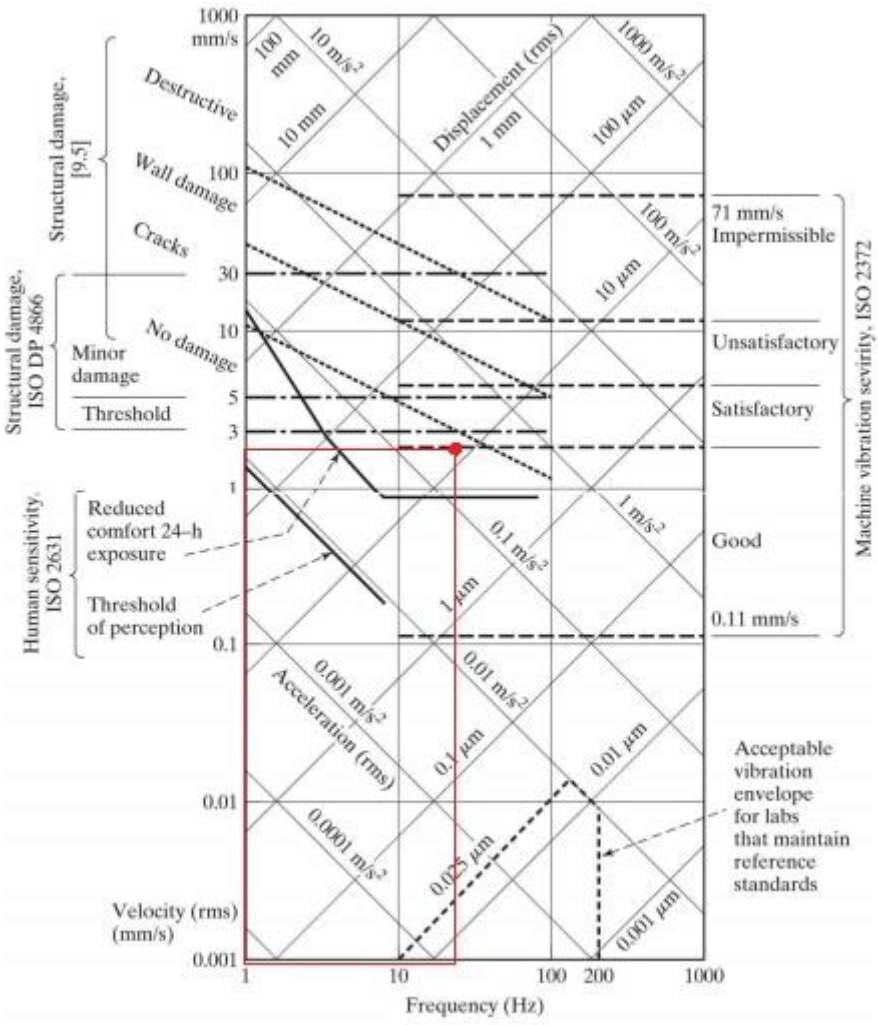


Figure 13: Nomograph of EPDM rubber with cone base design

From Figure 13 above, it is seen that the value of 2.412 mm/s at 26 Hz, was on the borderline of good and satisfactory to the machine vibration severity, ISO 2372. As the value was within the permissible stage, it is deemed as effective in reducing the vibrations from the compressor.

3.1.3 Simulation on SBR

Obtaining the results of V_{max}, k, ω_n, and X, through the same steps taken as the neoprene and EPDM rubber earlier, the results are shown in Figure 14 and 15 below. The results of SBR show that the lowest V_{max} value would be the cone base design at 3.644 mm/s. Comparing this to the neoprene and EPDM rubber value shows that EPDM rubber did indeed have a lower value. Although not as big of an improvement compared to the EPDM rubber's result, the SBR compared to the neoprene rubber still shows an improvement of over 1300%.

Material	SBR			
Grommet Design	Original	Cone Base	Trapezoidal	Thick Base
Frequency	26	26	26	26
Static Deflection	0.000408	0.000392	0.000405	0.00037
Mass	15	15	15	15
Displacement of Base	0.0000227	0.0000217	0.0000225	0.000022
Stiffness	360294.1176	375000	362962.96	397297.3
Natural Frequency	154.982605	158.113883	155.55556	162.7467
Frequency Ratio	0.167760763	0.164438438	0.1671429	0.159757
Displacement of Compressor	2.33574E-05	2.23031E-05	2.315E-05	2.26E-05
Maximum Velocity	0.003816219	0.003643966	0.0037818	0.003689

Figure 14: Results of SBR

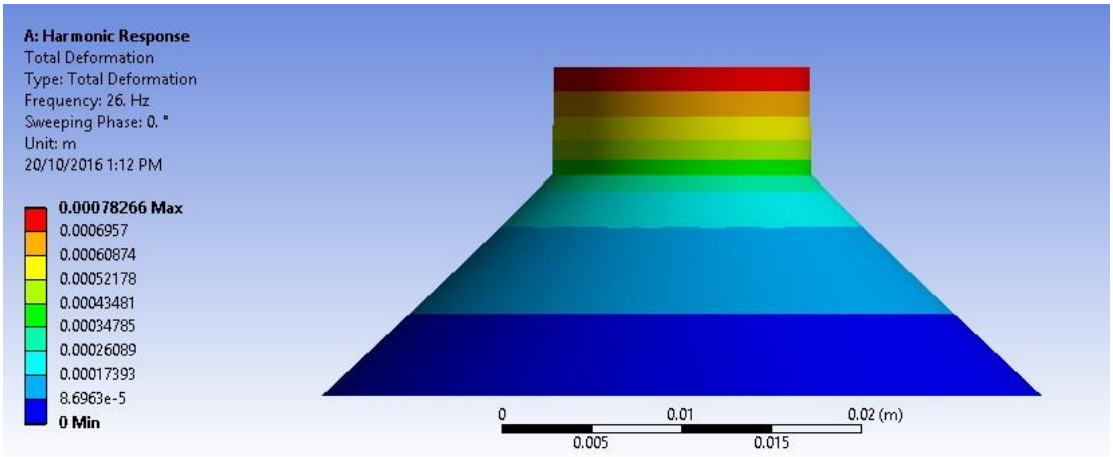


Figure 15: Displacement results on cone base grommet with SBR

Due to the higher Young's Modulus value compared to the neoprene rubber, this has enabled the SBR to have a lower maximum displacement value and thus providing a higher stiffness, k, this increase in stiffness proves to be significant in producing a lower ω_n and thus leading to the lower maximum velocity value compared to that of the neoprene rubber.

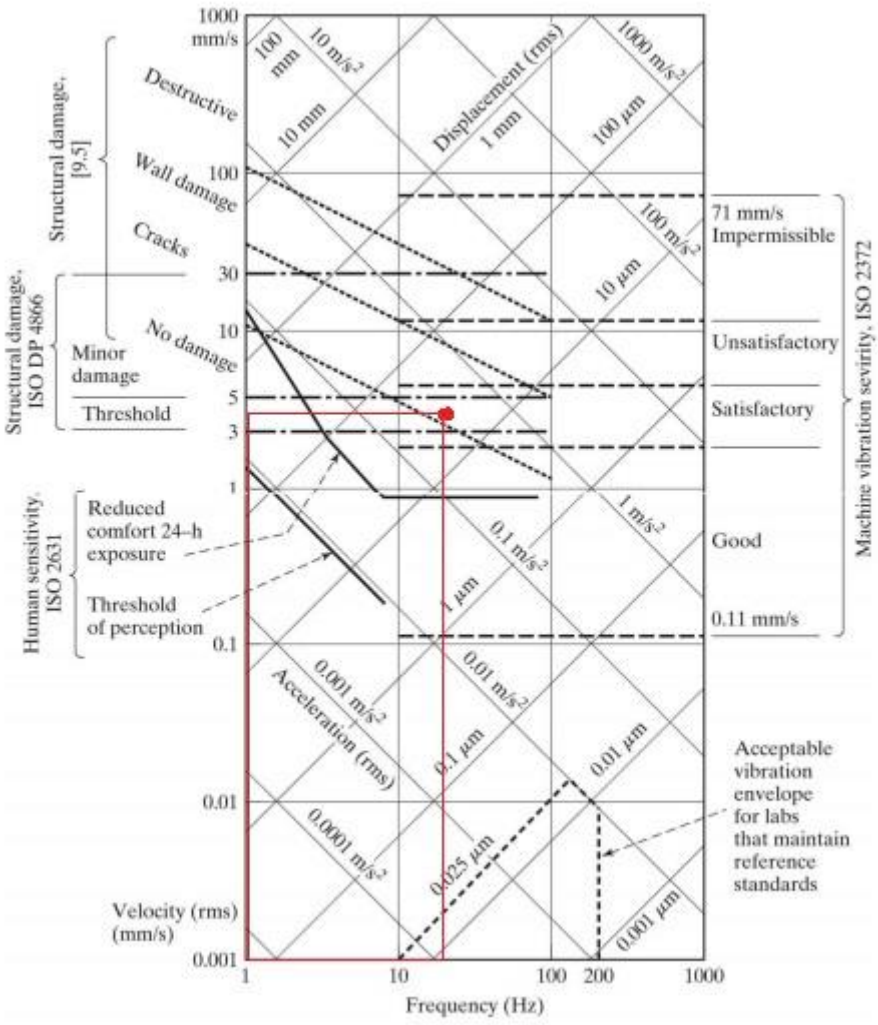


Figure 16: Nomograph of SBR with cone base design

As seen in Figure 16, the velocity of 3.64 mm/s coupled with the frequency of 26 Hz does not pose a significant problem to the machinery in terms of the machine vibration severity levels. It is still within the level of satisfactory, which signifies its improvement over neoprene rubber.

3.2 Comparing the Best Results

To compare the results of all the materials and designs of the grommet would be redundant, such, comparison of the best design for each material is chosen. For the clarification and ease of analysing, the best results for each of the material is shown in Figure 17. It is seen that the best material and design in terms of V_{max} would be EPDM rubber with the cone base design. Among the 3 chosen, aside from the V_{max}, the EPDM rubber with cone base also has the highest stiffness value at 565385 N/m compared to neoprene which only has a stiffness of 37789 N/m and the SBR which had a value of 375000 N/m. Through this figure, it can be seen that the higher the stiffness value of the grommet, the lower the maximum velocity the compressor would sustain. Since the stiffness value is derived from the static deflection, EPDM having the lowest static deflection value translates to a very high stiffness value and thus providing a very low maximum velocity. [8]

Material	Neoprene	SBR	EPDM
Grommet Design	Original	Cone Base	Cone Base
Frequency	26	26	26
Static Deflection	0.00389	0.000392	0.00026
Mass	15	15	15
Displacement of Base	0.000216	0.0000217	0.0000145
Stiffness	37789.20308	375000	565384.62
Natural Frequency	50.19243176	158.113883	194.14507
Frequency Ratio	0.518006382	0.164438438	0.1339205
Displacement of Compressor	0.000295215	2.23031E-05	1.476E-05
Maximum Velocity	0.048233457	0.003643966	0.0024123

Figure 17: Comparison of the best results of each material

4.0 Conclusion

In this project, investigations on the vibration transmission from the compressor was addressed and new design for the compressor grommet was created. The best material under room temperature is determined to be EPDM rubber, which has the lowest V_{max} value among all the materials. Aside from that, the new design of grommet proved to be an improvement from the original, with the V_{max} value dropping from 2.582 mm/s to 2.412 mm/s, the new design showed an overall improvement of 6.58%.

This value may not seem to be very large but its impact on machinery can be massive. The relationship between the mechanical properties and the vibration transmission was determined. The new design focuses on gradually spreading the impact rather than directly to the base of the grommet itself.

Reference

[1] S.S. Rao and R. Singiresu, *Mechanical Vibrations*, 6th ed. United States: Pearson Prentice Hall, 2016

[2] B. Balachandran and E. B. Magrab, *Vibrations*, 2nd ed. United States: Cengage Learning, 2009.

[3] Compressor Grommets. 2016. *Compressor Grommets.* [ONLINE] Available at: http://www.ejayrubber.com/compressor-grommets.html. [Accessed 18 October 2016]

[4] Rubber Products. 2016. *PartsBridge Associate, Inc. – Products – Rubber Products.* [ONLINE] Available at: http://www.partsbridgeassociate.com/rubber.htm. [Accessed 17 October 2016]

[5] Portfolio. 2016. *Ildar Sagdejev – Portfolio.* [ONLINE] Available at http://specious.foliohd.com/. [Accessed 20 October 2016]

[6] W. Li, *Compressor mounting*, 1st ed. 2002

[7] "Comparison of Elastomer Physical Properties", Primelineindustries.com, 2016. [Online]. Available: http://www.primelineindustries.com/elastomercompare.html. [Accessed: 13- Nov- 2016].

[8] A. T. Herfat, *Experimental Study of Vibration Transmissibility Using Characterization of Compressor Mounting Grommets, Dynamic Stiffnesses Part-II, Experimental Analysis and Measurements,* International Compressor Engineering Conference Paper. Paper 1569

eureca 2016 – Conference Paper
Paper Number 2ME18

Modelling and Analysis of Mountain Bike Rear Suspension System

Law Cheng Yee, Mohd. Farid Aladdin*
School of Engineering, Taylor's University, Malaysia
* MohdFarid.Aladdin@taylors.edu.my

Abstract
Different modes of transportation devices have seen increased usage lately, perhaps due to the emphasis and pressure from the environmentally conscious to reduce one's overall carbon footprint, or its relative cheaper cost compared to other forms of motor vehicles, or even for its simple fact that it is just easier to be able to traverse to one's destination without suffering major traffic congestions. The ease of access prompts the innovators to push out better designs in response to the rising demands, with better ergonomics and human designs that allow an easier access to the sport-turn hobby that everyone can enjoy. The end goal of this project is to access the data available out there on existing products that show promising signs in fitting the criteria set by the various conditions faced by the local (Malaysia) mountain bike enthusiasts, and would primarily focus on the riders' comfort in terms of the senses feedback experienced by the users. The project will attempt to answer questions on how each individual but different suspension designs would perform, and which one does it better. As well as how that performance translates to the unique terrain condition that is in Malaysia, and that a suspension design might have a better performance despite its overall stats. Lastly, how well would that suspension system cope with the local weather condition as well, being in a tropical country that is hot and humid all year round, with periodic monsoon season where the country experience a significant amount of rainfall. The project would rely on surveyed data on existing products, either from up-close real life study or data collected from online sources. The data can be tabulated digitally and have simulations performed on them to carry out kinematic analysis, followed up by kinetic analysis. The key outcome of this study is to determine the performance of the different suspension designs that can outperform others in conjunction with the unique conditions that the local environment poses. The power efficiency and the force response into the mountain bike frame would be considered heavily, with the end goal being that it falls under acceptable range with user's comfort being top priority.

Keywords: Mountain Bike, Rear Suspension, Analysis, Kinematic, Kinetic, CAD

1. Introduction

At this current era, one may come to a conclusion that a motor vehicle would be the pinnacle of human or general transportation method, where in some cases it signifies anything from status, wealth, even technological prowess, that such human invention of a mechanical workhouse trumps nature's design. However, one might also argue that, the dependence on alternative transportation has surged in the last decade or so, with the pressure to reduce carbon emissions from motor vehicles and the dependency on fossil fuel in general [1,2]. People have been shifting their attention back to lightweight alternative transportation methods such as bicycle or even electric bicycles, for multiple reasons. When it comes to comparing the alternatives to the norms, people have brought up efficiencies in such alternative methods.

Just like in a car or other motor vehicles, bicycles usually come equipped with a suspension system of various designs (except for rigid frame mountain bike). These differences in designs determine how each bicycles perform under certain conditions, with factors including the road condition [3], the rider, traffic conditions, and physical properties such as the material, dimensions, configurations and the stresses distribution during operation. While most might assume a proper suspension system is intended to absorb shocks appropriately during operation and that it prioritizes user's comfort as the end goal [3], however an improper vibrational stress distribution could potentially negatively affects the user's perception and in turn one's reaction time as well [4]. At times when on a busy road traffic, this poses risks to the user if their bikes aren't performing as intended, worse if the issues persist just because it is ill-suited for such conditions.

This research is intended to model and analyse the rear suspension system of a mountain bike. With each designs out there, there is some complicated engineering involved which found a compromise in terms of structural and vibrational stress that a bicycle frame would have to go through without yielding, while inducing minimal load onto its wheels during operation.

In particular, this research is putting its attention onto specifics on mountain bikes, whose operating conditions usually involves some more extreme circumstances [5], including but not limited to general terrain condition as well as the weather. Due to the nature of the activity, a mountain bike goes through a lot more extremes, and its intricate suspension system design is thought to be a suitable candidate to perform analysis on, as the general deviation in between the various designs and properties would be amplified under extreme circumstances. This makes the research more feasible and viable.

Instead of fabricating an entire set of suspension system, data and analysis for this project can be done through mathematical modelling and simulations, where kinematic and kinetic analysis can be carried out without incurring too much cost in terms of resources and time.

2. Methodology

In this phase of the research project, the rear suspension system would be the focus in the analysis. The mountain bikes are differentiated in terms of primarily its intended environment of use, varying in its unique designs and setup, which would impact its performance in a range of environment, including the terrain and weather condition. These performance outcomes will be taken into account, and tabulated against the different variables in between designs. Analysis made would be shown in the form of mechanical responses induced in the suspension system in the simulation, ran using ANSYS software, and compared against the mathematical modelling made in the previous phase of the project.

2.1. Choosing the Model

The mountain bike sport scene offers a handful of choices in terms of models available for users, each with different specifications and setup for different scenarios.

Often times the biggest differences relies on the suspension system design of the mountain bike, each specifically made to tackle different terrain and environment. Mountain bikes can be categorized in types regardless of its suspension system type in the following [8-10]:

- Cross-Country (XC)
- All-mountain (AM)
- Downhill (DH)
- Trials
- Trail riding

Cross-Country (XC) mountain bikes, as the name suggested, are built for conquering climbing tracks, often excelling in uphill action, and is considered a more extreme type of bikes compared with the rests. Endurance and efficiency is where these bikes aim to excel in, prioritizing in pedal performance to ensure that most of the pedal energy is transferred onto the back of the frame and the chain wheel. Usually very lightweight with a longer chainstay and wheel base length for more efficient climbing, the bikes usually ask just as much from the rider just like the rider would for its performance, with its climbing prowess and is capable of long distance travel, it can be ideal for experienced mountain bike enthusiasts who are looking to take part in a race or a challenging trail alike.

All-mountain bikes, or "Enduro", the race format it is named after, are usually more race-centric, designed to favors greatly in technical prowess in terms of gripping the right technique to earn scores in a skill-based competitions with obstacles and turns that involves multiple ascends and descends. As mentioned, mountain bikes in this category favored its performance in steep descent where most of the scores are timed and given in Enduro races. With long wheelbase and reach, low bottom bracket and slack head angle for those steep climbs and descents.

Downhill (DH), or Freeride bikes are distinct than the others mentioned above due to the fact that it is only meant to go downhill, and thus is not ideal for any sort of uphill pedaling action. It is built to take on steep descents, big drops and jumps that involve speed and airtime. Trails made for this category of biking usually start with a higher altitude where the top of the trail have to be traversed by other means such as hiking or shuttling as the bikes themselves are not made for that trip. These bikes have a stronger, tougher frame to take on the excessive forces from the multiple extreme descents. Equipped with a much lower head angle and a lower center of gravity, it compensates with its better performance in taking on steep terrain with sharp turns. Due to this, tires that are optimized for traction are usually favored in order to better find grip on the downhill trails, and are also strong enough to withstand the wear and tears associated with the risks of slashes and punctures from jagged rocks or foliage.

Lastly, the trail bikes are usually the most common ones, and would be the type of bikes that the public associate the term "mountain bikes" with. It caters to the more casual audience who are looking for mostly recreational mountain biking or is trying to break into the hobby as a beginner. The bikes in this category are not built based on any grounds or specifics which allow it to be a general all-rounder that most users new to the mountain biking scene can easily break into. Trail bikes usually come with "middle ground" stats, with a neutral head angle of around 67° and suspension that specializes in a balanced approach in strength and weight to suit a wide range of riding styles.

2.2. Specifications of the Bike

As mentioned above, aside from differentiating mountain bikes via its respective "types" or categories, the bike is usually sought after for its availability of flexible designs

2.2.1. Size and Dimension of the Bike

A mountain bike can be fully customized to suit a user's need and it plays a big role in providing ergonomic choices for the consumer to obtain a mountain bike that suits their body type.

The first impression necessary to judge a viability of a mountain bike is to make sure it suits the consumer's human factors. Asking any experienced rider about bike fit and one would conclude that all bikes ride and feel differently.

The factors involved would largely be dependent on the frame size of the suspension system:

- Effective top tube
- Head tube
- Handlebar stem
- Wheel base
- Seat tube
- Reach
- Stack

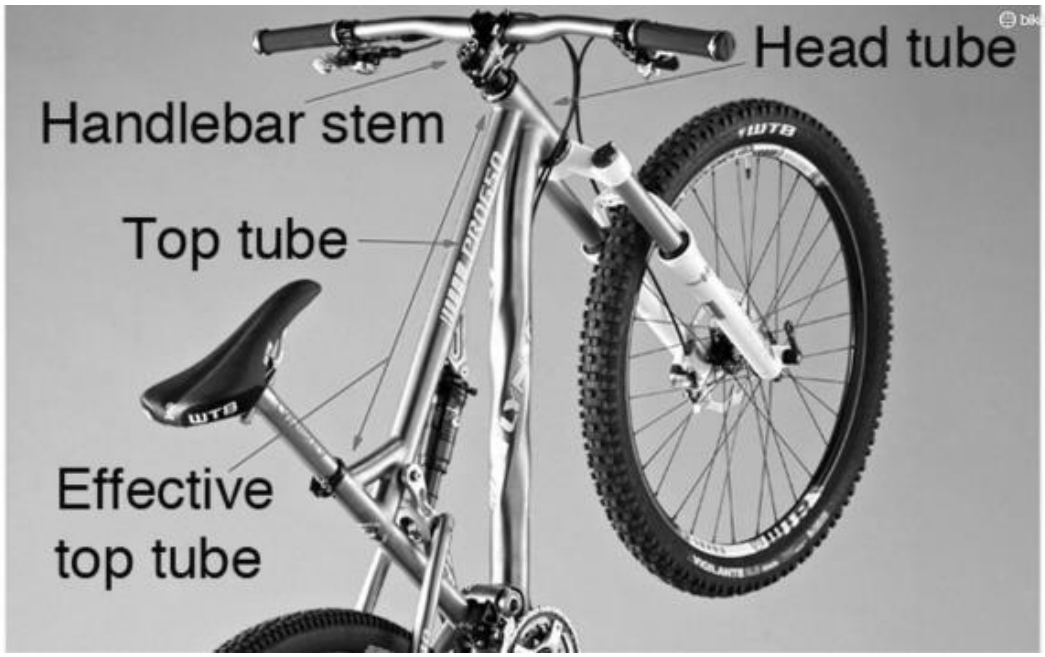


Figure 1. Aspects of the frontal bike frame, which dimensions can be used to determine user's choices

The effective top tube measures the length between the head tube and the rider seat. A horizontal line parallel to the ground, from the center of the head tube and intersects with the seat tube. It directly affects how "long" the mountain bike feels for the users, and can vary between sizes.

Head tube length measures the height of the frame from the bottom at the wheel arch up to the top at the handlebar stem, where the user's hands will be resting/gripping on. The height of which can determine another aspect of user fit as a mismatch in height can compromise the user's comfort and overall duration of use.

Using these criteria it can be used by the consumers to determine what specifications of the mountain bike will provide a suitable frame fit for them.

Table 1. Suitable frame size and its Effective Top Tube (ETT) in respective to rider's height

Rider Height		*Frame Size*	
Feet and Inches	*Centemetres*	*Effective Top Tube (cm)*	*Bike Size*
4'10" – 5'	148 – 152	47 – 48	XXS
5' – 5'3"	152 – 160	49 – 50	XS
5'3" – 5'6"	160 – 168	51 – 53	S
5'6" – 5'9"	168 – 175	54 – 55	M
5'9" – 6'	175 – 183	56 – 58	L
6' – 6'3"	183 - 191	58 – 60	XL
6'3" – 6'6"	191 – 198	61 – 63	XXL

2.2.2. Suspension Design of the Bike

The most crucial component in a mountain bike design falls under its suspension system, particularly the dimensions involved and the general build of the system, where the dimensions and angles of various joints and parts would help determine the performance of the mountain bike in conjunction with its rider's comfort.

As far as the types of mountain bikes are concerned, the suspension is another category on its own, and come in the following [8]:

- Rigid
- Hard tail
- Full suspension

A mountain bike with a rigid suspension simple means that the frame does not have any form of suspension, and comes with a rigid front fork and a fixed rear, and comes with its own advantages. A rigid frame with no suspension usually comes with a cheaper price tag, which can be a huge factor for some, the cheaper frame do not contain any moving parts which also means that it requires minimum maintenance. Having no suspension to help absorb the shocks and force responses, it is said that it is a good way to practice proper technique in learning how to correct existing mistakes that a biker would not have noticed due to a suspension system masking the mistakes [11].

A mountain bike with a hardtail suspension means that its frame comes only with a suspension on the front fork, but none on the rear of the bike, implying a "hardtail". Again this suspension system comes with a cheaper price tag compared to a full suspension frame, again with the lower maintenance cost and fewer moving parts. Hardtail suspension is said to favor cross-country bikers as it is more efficient

in transferring the power from the pedal strokes to the rear tire due to the lack of a rear suspension, making it ideal when a longer trail is involved.

A full suspension mountain bike sports a frame with a complete set of suspension system on both the front fork and the rear frame of the bike. A full suspension bike is generally ideal and is thus in common use as an all-rounder bike, due to its ability to absorb shock from both front and back, this in turn reduces the overall impact and moments felt by the rider, making the riding session more comfortable and enjoyable. On the other hand, due to its effectiveness in absorbing shocks, from the trail condition, it is just as effective in damping the force from the riders' pedal strokes, lowering the efficiency of the bike due to the loss in power transfer. Some rigs give the riders an option to "lockout" the rear suspension to provide a better efficiency by allowing better power transfer [9].

It cannot be denied that a lot more considerations went into deciding an ideal suspension system for any specific type of usage. A properly designed suspension system would help in absorbing and dispersing vibrational stress induced from the wheel as well as the pedalling action from the user. Energy loss may occur during excessive pedalling which causes overdamping in the suspension system, due to the nature of its design. This premature rear suspension activation induces a loss in efficiency in terms of resources and performances .With tests derived from the performances done test subjects, physiology of the individuals proved that with improper suspension system results in an oxygen uptake increase, yet with a negative result return, signifying an energy loss [4]. In that paper, it utilizes the kinematic equation dubbed the "Suspension Activation Ratio (SAR)", as a guideline to determine the performance of a particular suspension system, and is very dependent on the frame design, the suspension as well as the transmissions, in which the best case would be to have SAR be as close to zero as possible.

Though extensive, this project primarily focuses only on the suspension design itself, without regarding the notion that different terrain condition might impact the performance of the suspension system as well, which in turn affects the performance of the rider.

In another past research, rider's comfort is studied in conjunction with the suspension design applied in a mountain bike setup. Particularly on the vibrational stress induced from excessive stress in the frame during operation, which can impact the rider's performance on the road and can cause risks to any road users.

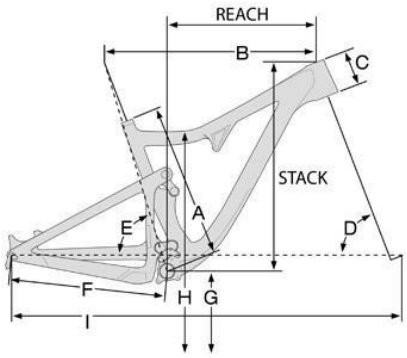
Through physical experimentation coupled with some simulation data, the team worked on this project to determine a compromise in terms of how a suspension system design would work best in a given situation. By altering the frame and rider's center of gravity, angles, vertical and horizontal distance, which in turns affects the moment of inertia, mass distribution and the overall center of gravity. Such variables can have some direct impact in terms of the stiffness and damper elements in the frame itself, which can determine what the rider would experience in terms of force feedbacks.

These results in two very polar designs based on the criteria and variables set. Experiments can then be carried for both the design and data be collected for

tabulation and analysis. One thing to note for this research paper is that they did multiple tests on different types of road conditions, such as the typical asphalt, brick stones, etc. [3]. This is part of the inspiration to introduce an additional research scope into our own project, where we try to simulate the suspension system in various environment and conditions, derived from the country Malaysia.

It however is still limited in certain aspects in a way that it only narrows its focus onto a particular suspension design. Out in the market, mountain bike is not restricted to just one suspension design, there is other patented design such as the High Single Pivot, Linkage Driven Single Pivot, FSR Link, Dave Weagle's (DW) Link, VPP (Virtual Pivot Point) Link, ABP (Active Braking Pivot)/Split Pivot, etc. [12]. Some of these aspects play well in different environment, which is the point of interest here for us, as we are trying to determine a suitable design for optimal performance suited to a specific environmental condition.

Still the past researches would serve as useful guidelines, as its experimental data would display a noticeable pattern regarding the configuration of a particular suspension design, depending on aspects such as rear axle height, suspension pivot height and position, chain pitch, crank length, etc. [4].



	S	M	L	XL
A Seat Tube Length (C-T)	40.64	44.45	48.26	52.07
B Top Tube Length	58.04	60.71	62.87	65.02
C Head Tube Length	10.16	10.16	11.94	14.99
D Head Tube Angle	67.50°	67.50°	67.50°	67.50°
E Seat Tube Angle	72.80°	72.80°	72.80°	72.80°
F Chain Stay Length	44.32	44.32	44.32	44.32
G Bottom Bracket Height	33.50	33.50	33.50	33.50
H Standover Height	72.49	73.61	74.40	76.30
I Wheelbase	111.00	113.51	115.49	118.01
Stack	60.73	60.78	62.46	65.30
Reach	38.35	40.92	42.32	43.54

Values in centimeters

Figure 2. Example of suspension system specifications and dimensions [13]

As established in this project, the focus would only be emphasized on the rear suspension system of the mountain bike, hence only full suspension bike will be considered, omitting bikes with rigid and hardtail suspension system. Hence with our project, part of the scope involving investigation on existing designs and brands to help understand why such designs are conceived in the first place, and test its viability with our own mathematical modelling in order to find out which one is best suited for our research. This would help save some cost and time as it will guide us in the proper path by having a firm idea of what kind of frame design would work best in our research project.



Figure 3. A single pivot suspension system [14]



Figure 4. A twin link four bar suspension system [14]



Figure 5. A floating drivetrain suspension system [14]



Figure 6. An active braking point (ABP) suspension system [14]



Figure 7. A standard four bar suspension system [14]



Figure 8. A faux bar suspension system [14]

2.3. CAD Modelling

The size chart tabulated from the selected model was used to construct a 3D model of the suspension system, omitting the wheels, handle bars, and chains to simplify the analysis process.

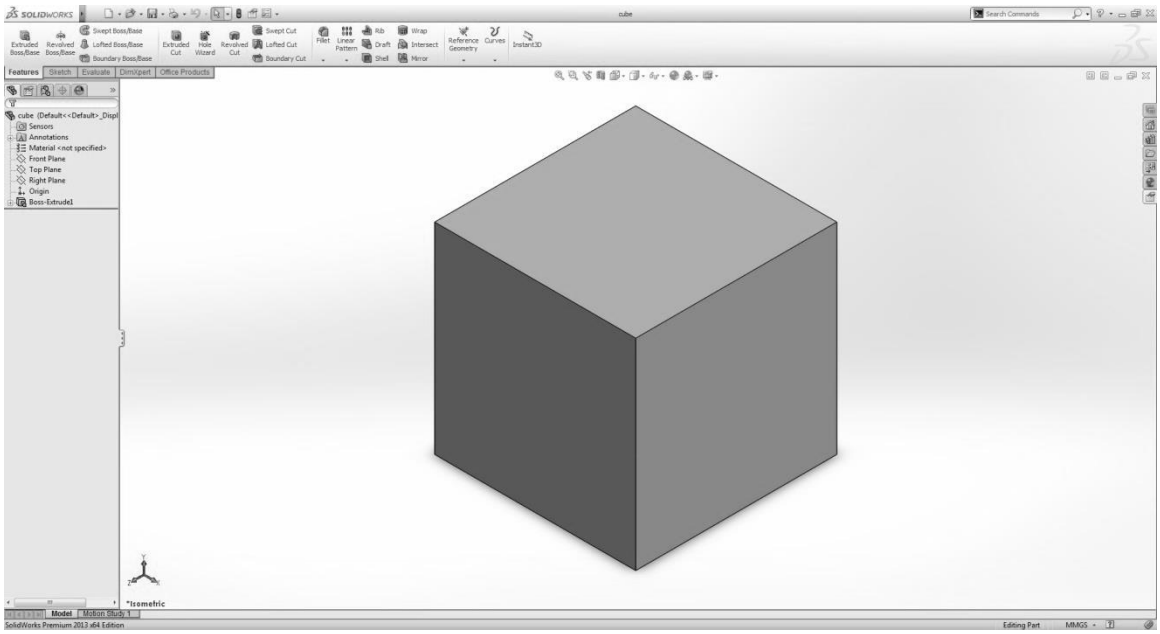


Figure 9. CAD 3D modelling in Solidworks software

The Solidworks software was used in order to construct a simplified 3D model of the selected suspension system design. Taking note of the dimensions specified as stated in the factory setting.

This step was pretty straight-forward, deconstructing the real life example into components and translating them into carious shapes and sizes according to the specification dimensions.

2.4. Kinetic Analysis

ANSYS software would be utilised in this project to conduct a series of simulations and analysis to determine how well the suspension system perform under various variables.

2.4.1. Types of meshing

Different types of meshings are available

i. Tetrahedrons

The tetrahedron meshing method is one of the simplest method and is usually setup in default by the software, this method breaks down the model geometries or surfaces into a series of tetrahedrons (triangles) with 3 vertices and 3 edges, making it an easier solution to mesh an object without too much hassle.

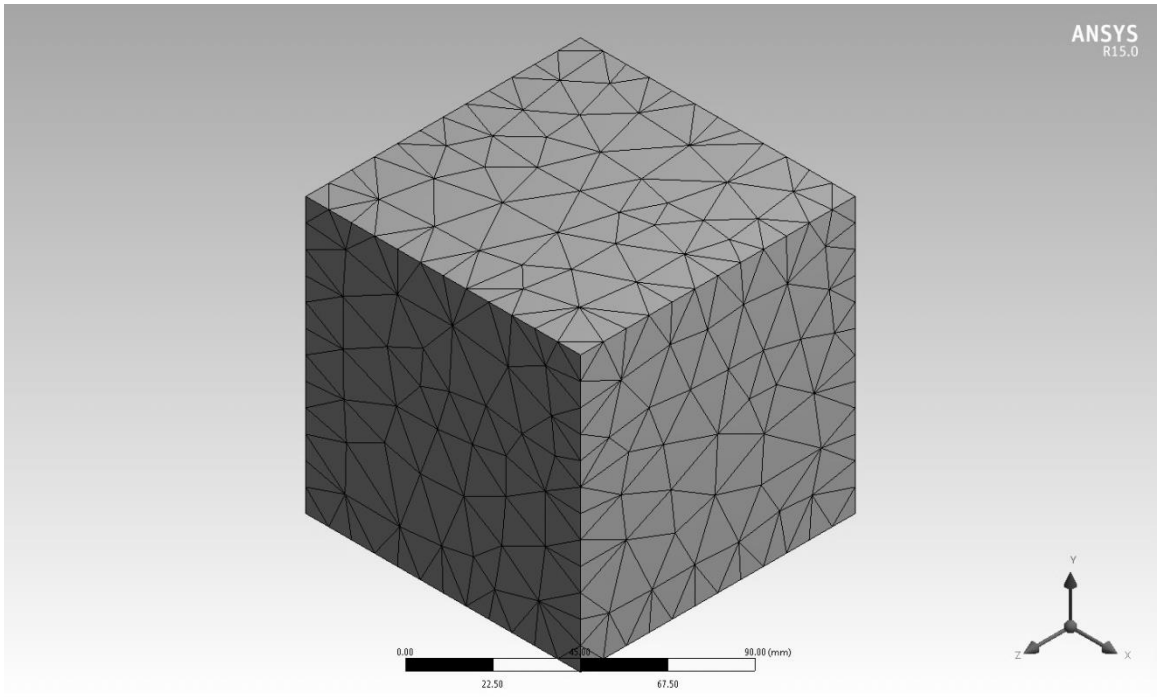


Figure 10. Example of tetrahedron meshing in ANSYS

ii. Hex dominant

This meshing method works best on regularly surfaces with flat areas. A model with clean geometry can benefit from this meshing method as it can be easily broken down into elements of parallelograms (squares or rectangles). Elements produced in this method are usually lower in count and numerical errors due to its alignment with the flow direction, which allows reduced run time in simulations and analysis.

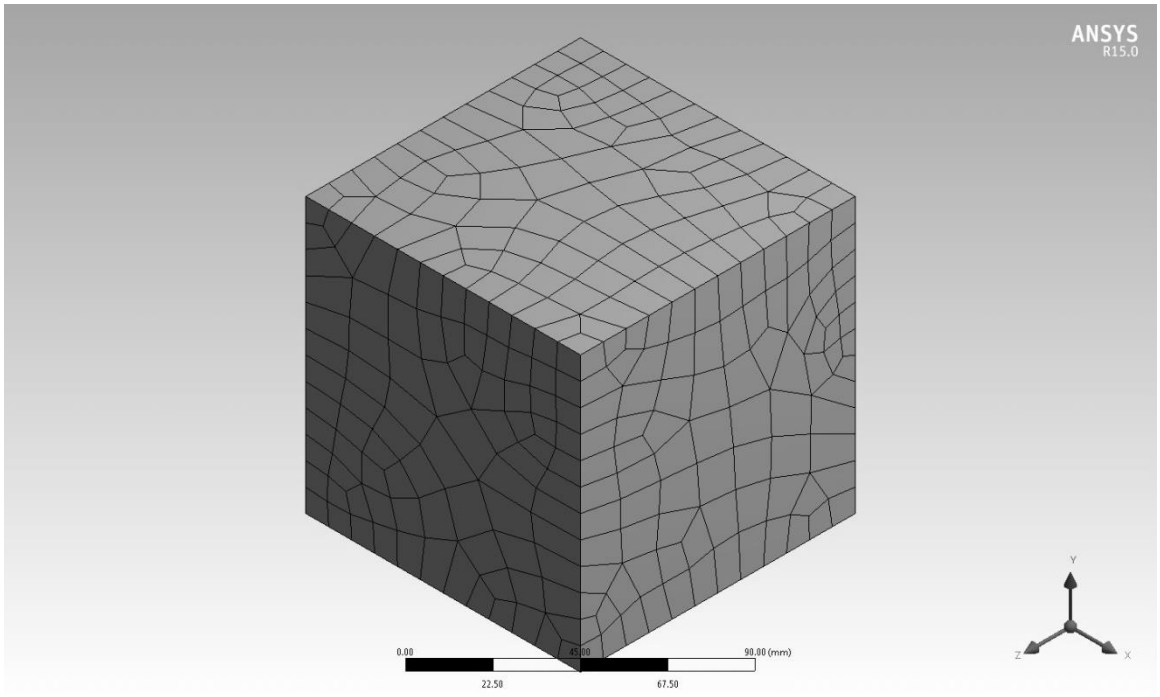


Figure 11. Example of hex dominant meshing in ANSYS

iii. Sweep meshing

This method allows the meshing to "sweep" through a geometry that allows the source and target geometry to be identified automatically as long as a direction is given. Elements are generated in hex and wedges. However this method is not suitable for multibody parts.

iv. Multizone meshing

This meshing method provides a lot of flexibility which allows analysis results to have a higher accuracy as the models are broken down into sizeable blocks and identified automatically. The user can specify which elements are preferred in between Hexa, Prism or a mix of both. However it comes with a cost of complications and extended run time.

2.3 Finite Element Modal Analysis

2.3.1 *Material Assignment*

The ANSYS software requires materials to be assigned to the geometry models before any simulation can be done. The ANSYS software has built in material library under the Engineering Data Sources. By assigning a material type to the assembly model, it allows the model to take on the physical properties of the assigned material, and this can be done to each individual part in the assembly model, wherever it may apply.

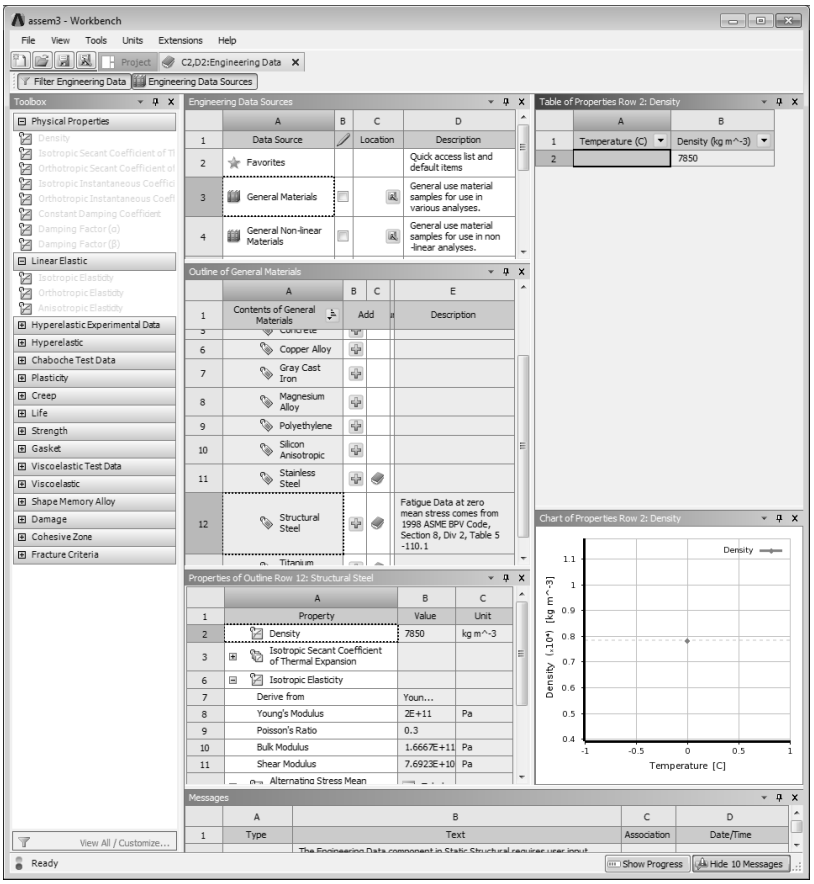


Figure 12. Material Library under Engineering Data on ANSYS software

However the material library is still limited to whatever is provided there, but the software has the option for the user to manually add on new materials as long as the user can define its properties, namely the density, Young's Modulus, Poisson's Ratio, Tensile Yield Strength and Tensile Ultimate Strength.

The materials to be studied here would be the Aluminium Alloy (Al6061), standard Carbon Fiber, Stainless Steel, and Titanium Alloy (Ti6Al4V).

Table 2. Materials and its physical properties to be assigned in the FEA method [14]

Material	*Density (kg/m^3)*	*Poisson's Ratio*	*Young's Modulus (MPa)*	*Tensile Yield Strength (MPa)*	*Tensile Ult. Strength (MPa)*
Aluminium Alloy (Al6061)	2770	0.33	68900	276	310
Carbon Fiber (Std CF)	1800	0.1	70000	N/A	600
Stainless Steel	7750	0.31	193000	207	586
Titanium Alloy (Ti6Al4V)	4430	0.36	114000	930	1070

2.3.2 Manual Contact Connection

Once the assembly model has complete meshing applied, the models have to be made sure that all connections are recognized by the ANSYS software. Usually this is done automatically and depending on the assembly model, the software can pick up any intersecting surfaces and geometries and assign a default contact region to any adjoining geometries. This helps prevent any free-floating components and parts which can then later clips into each other and compromise the FEA results.

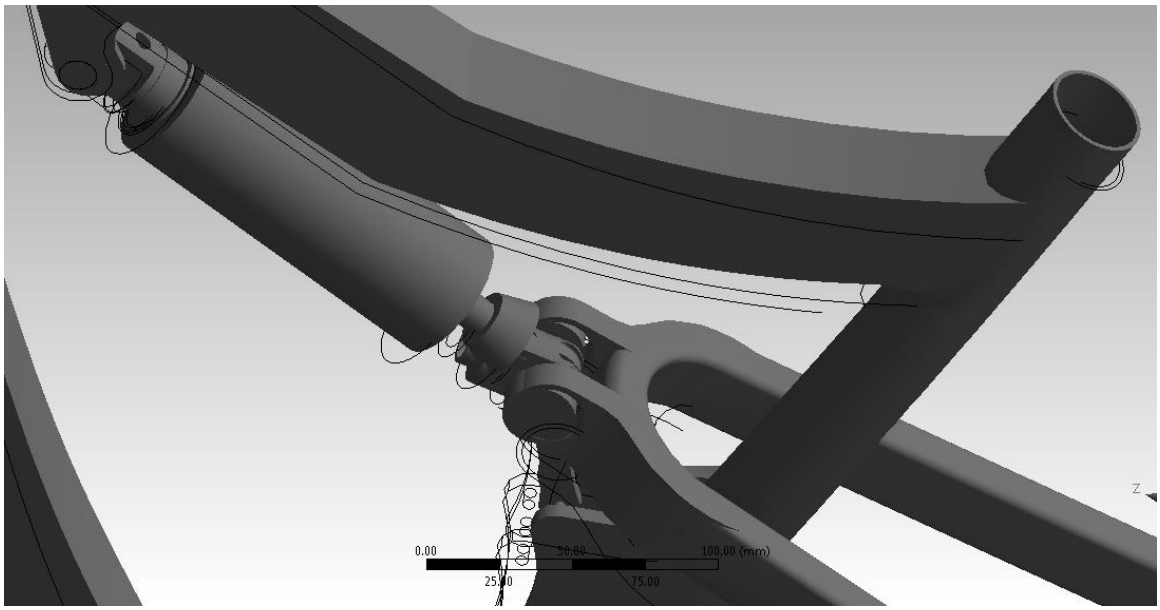


Figure 13. Components clipping into each other geometry during FEA simulation

In Figure 3-14 it shows that the clipping occurs in between the rear joint and the shock absorber, as despite the connection specified in the assembly model back in

SolidWorks. The clipping would have to be rectified otherwise the components would just phase through each other during the FEA process, producing inaccurate results.

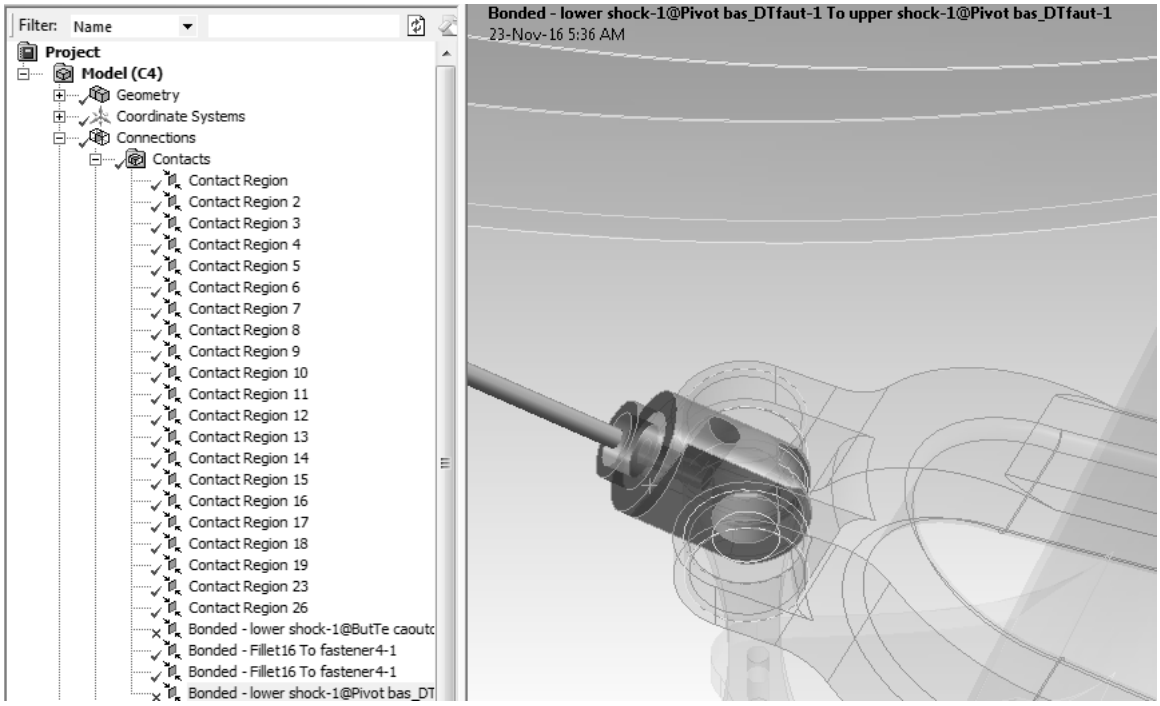


Figure 14. Assigning manual contact connection between components in the assembly model

By attaching the unbound parts together, it allows the ANSYS software to recognize the boundary conditions around the components and yield proper results during FEA process.

2.3.3 Response Parameter Setup

The aim of this research is to study the resulting displacement of the rear suspension system in clear, easy-to-read visuals.

The ANSYS software is set up to read the total and directional deformations occurred in the assembly model, thus it required some additional inputs such as the material assigned to the assembly mode, the total applied force, and the spring stiffness of the rear shock absorber.

Table 3. Parameters of the variables to be used in FEA process

Material	*Applied Force (N)*	*Spring Stiffness, k (lbs/in)*	*Spring Stiffness, k (N/m)*
Aluminium Alloy (Al6061)	1000	550	96320
Carbon Fiber (Std CF)	5000	650	113832
Stainless Steel	10000	750	131345
Titanium Alloy (Ti6Al4V)			

2.3.4 *Force Application and Support*

Before a force can be applied to an assembly model, it has to be bound to a point or else the resulting deformations will just shows up as simple translation as the models are not anchored. Thus a fixed support has to be added to geometry, preferably a spot where deformation is negliable and does not impact the overall results integrity.

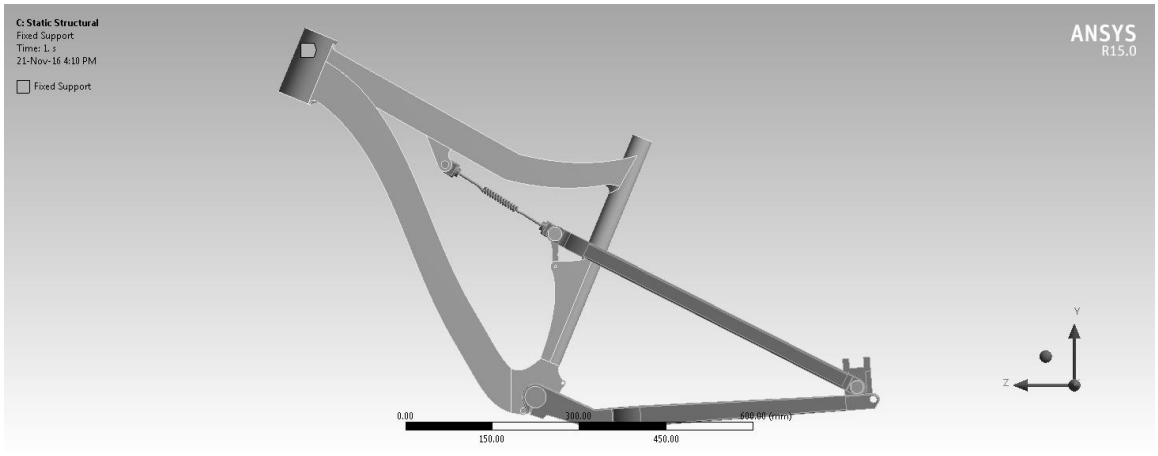


Figure 15. Fixed support applied onto the assembly model

The fixed support would have ANSYS recognize the highlighted geometry as immovable and stationary, despite the force acting on the assembly. The fixed support is applied to the front head tube because this research only focuses on the rear suspension system, and that the resulting deformation of the front suspension system and wheel are omitted from this study.

The force will be applied to a certain face of the assembly model, depending on the scenario, since this research project is to study the displacement of the rear suspension system resulting from vibration via the ground, it is logical to apply the force onto the bottom of the chain length bar.

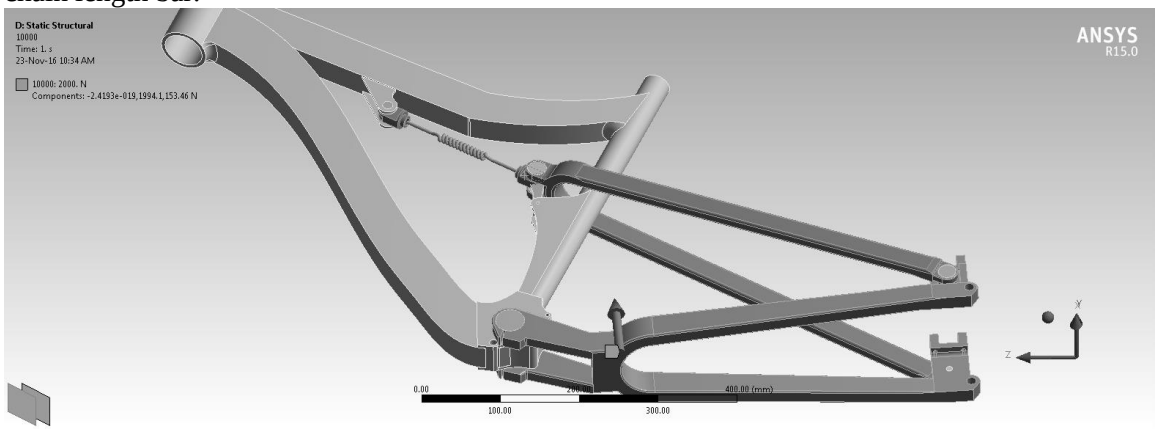


Figure 16. Force applied on the assembly model for FEA process

2.4 *Data Collection*

2.4.1 *Weight of the Suspension Frame*

Since the materials assigned to the assembly models each come with its own density value, this will directly impact the resulting weight of the rear suspension frame, assuming the volume of the assembly model stays constant throughout the study.

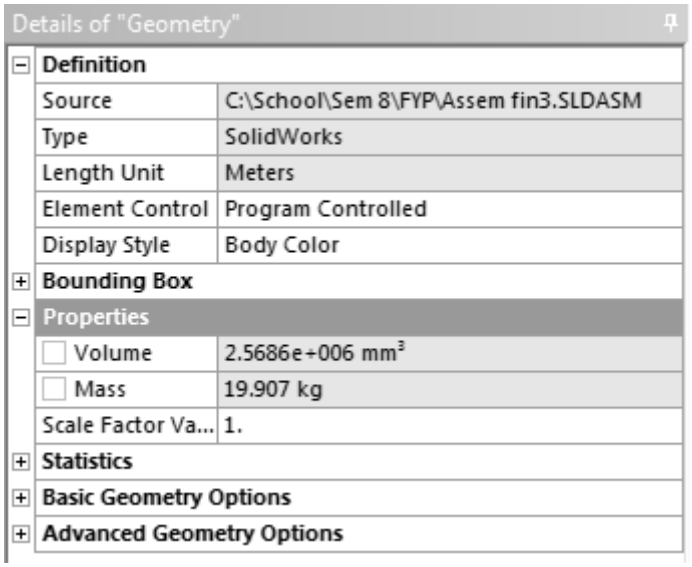


Figure 17. Weight of the assembly model in kg as shown on ANSYS software (stainless steel)

2.4.2 *Spring Stiffness of the Shock Absorber*

In order to test out the effect of spring stiffness onto the stress deformation occurred in the suspension frame, the shock absorber has to be changed in order to accommodate the specified spring stiffness as shown in Table 3-2. To modify the assembly model, specifically the rear shock absorber every time spring stiffness is changed is time consuming and not as efficient. Thus a more feasible method to carry out this FEA process is to replace the spring model with a simulated longitudinal spring contact connection that is available in the ANSYS software.

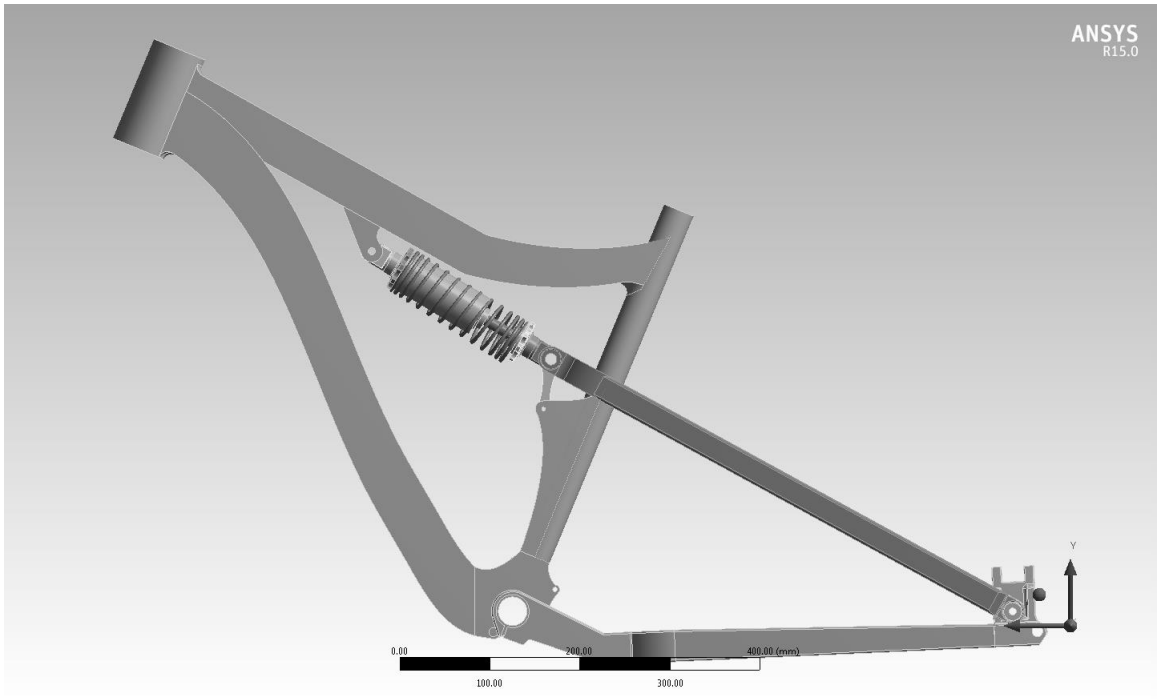


Figure 18. Assembly model with modelled rear shock absorber

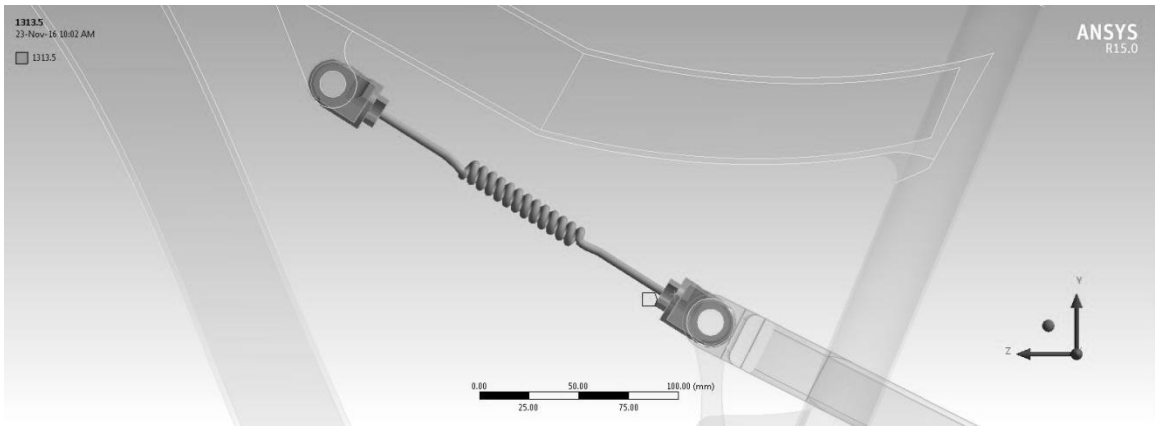


Figure 19. Assembly model with a longitudinal spring contact connection

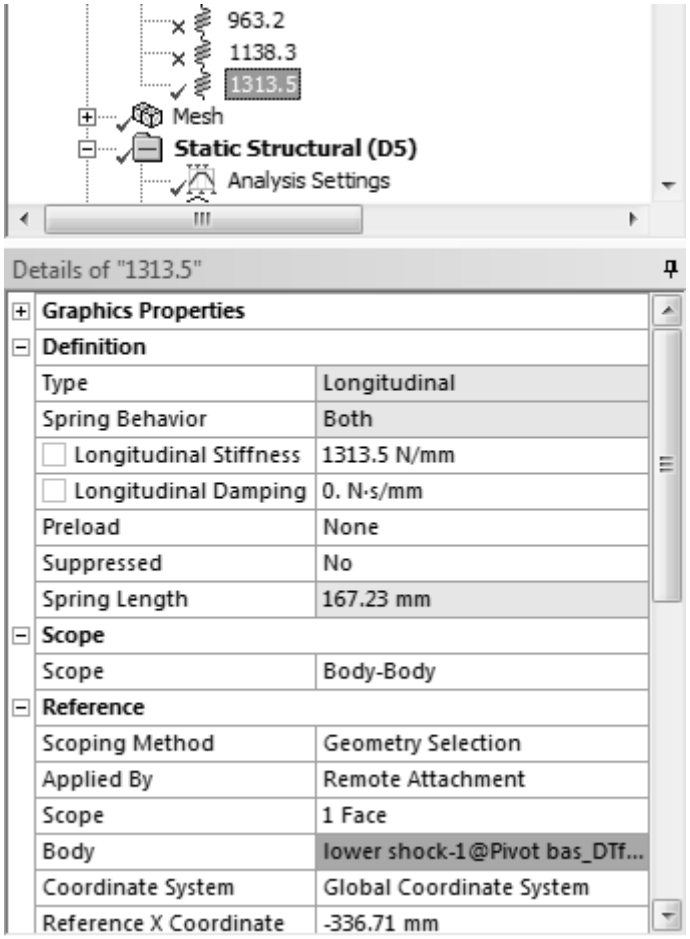


Figure 20. Setting up the spring stiffness and properties

This method allows the easy access to modify the spring stiffness without having to switch out different assembly models.

3. Results and Discussions

3.1. Mountain Bike Model Selection

For this project, much of the focus is put into the four bar system due to its exceptional performances and simplicity and its wide range of utilisations in various mountain bikes.

Specifically the twin link four bar design, for its more recent conception. This four bar variation composes of twin links that helps in isolating the rear end of the bike, improving the pedalling performances with its anti-squat curve which allows the users to pedal more efficiently by reducing the suspension travel, while not compromising the ability to absorbs external shocks and bumps during usage.



Figure 21. Pivot Mach 429 Trail XT/XTR Pro 1x [13]

The figure above features a trail-type mountain bike from Pivot, this bike features a carbon frame with DW-link suspension system. By default it comes equipped with a rear shock FOX Float DPS Kashima model.

3.2. Dimension and Specifications

Size	S	M	L	XL
Top Tube Length	58.04cm	60.71cm	62.87cm	65.02cm
Head Tube Angle	67.50°	67.50°	67.50°	67.50°
Head Tube Length	10.16cm	10.16cm	11.94cm	14.99cm
Seat Tube Angle	72.80°	72.80°	72.80°	72.80°
Seat Tube Length	40.64cm	44.45cm	48.26cm	52.07cm
Bottom Bracket Height	33.50cm	33.50cm	33.50cm	33.50cm
Chainstay Length	44.32cm	44.32cm	44.32cm	44.32cm
Wheelbase	111.00cm	113.51cm	115.49cm	118.01cm
Standover	72.49cm	73.61cm	74.40cm	76.30cm
Reach	38.35cm	40.92cm	42.32cm	43.54cm
Stack	60.73cm	60.78cm	62.46cm	65.30cm

Figure 22. Suspension design specifications [13]

The mountain bike would have to be simplified for this project. Essentially, the carbon frame is treated as a whole rigid body for its displacement is negligible and not as relevant to the study. The front shock's (or fork) performance is dependent on its fork length (130 mm from specifications) as well as the head tube angle (67.5°) (See figure 2.), and is most of the time rigid as well and its displacement is not relevant to our results.

From the official retailer site, the mountain bike itself weighs at 12.6 kg. This will be the reference mass for which we will be using for this study. However, the mass-spring system would also have its human rider taken into consideration. We've picked an average range of 50 to 70kg for this study. The rear shock however would be modeled into a simple spring component with the corresponding spring stiffness, k, and damping value, c.

The rear shock used in this bike model (Figure 1) is a FOX Float DPS Kashima, and according to the manufacturer, it comes in different models and is entirely dependent on the application of the bike and its operating condition. From its 3-Pos Lever (with adjustments) series, it is coded with a format of "A x B", where A defines its spring stiffness in lbs/in (eg. 5.5 = 550 lbs/in), and B defines the shock diameter (not relevant to study). The models chosen for this project are "5.5x1", "6x1.25" and "6.5x1.5".

For the damping value of the spring, the info related to this aspect is not readily available, however one assumption can be made is that the models must adhere to the industrial standard with relevance to the desired outcome and application. In the context of a passenger vehicle, a lower damping ratio in general returns a better rating in ride comfort due to its slower, more gentle excitation/displacement dissipation, while a higher damping ratio returns the suspension/frame to its equilibrium position in a faster, though more jerky, manner, allowing better body control and faster responses.

3.3. CAD 3D Modelling

The CAD 3D models were done using the SolidWorks software. The geometry of the mountain bike suspension system is broken down into several parts in references to its linkage bars for easier constructions.

- Top tube, down tube, seat tube
- Seat stay
- Chain stay
- Rear shock

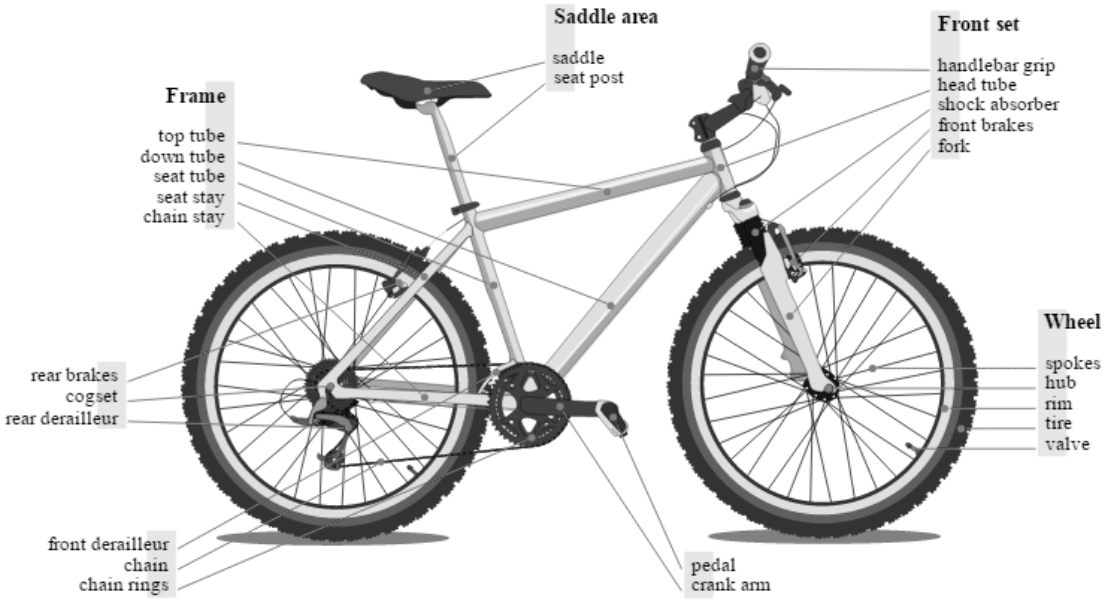


Figure 23. The anatomy of a mountain bike [13]

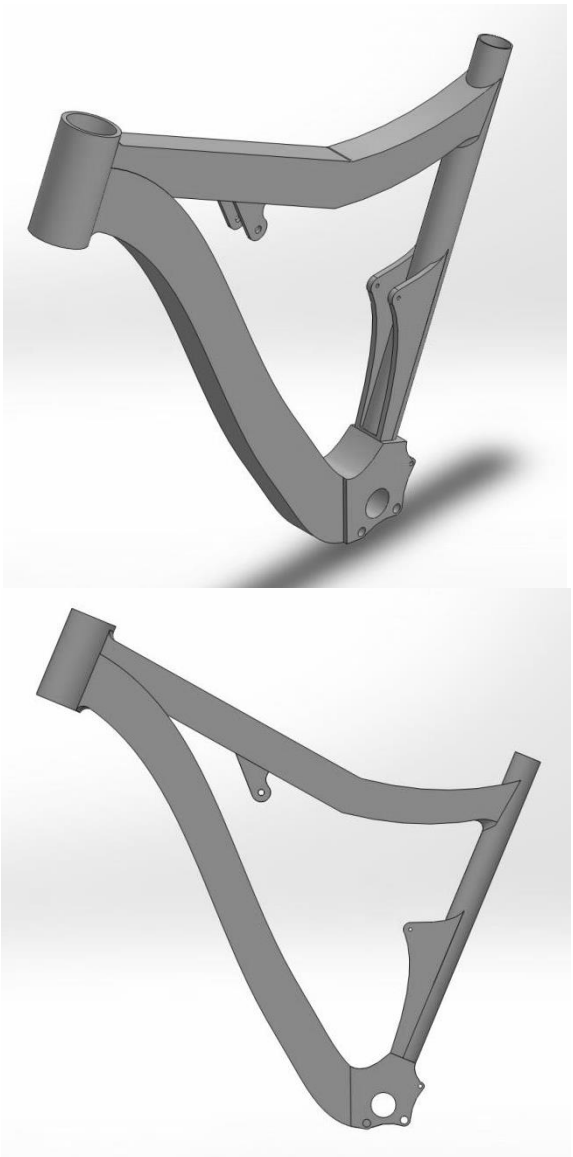
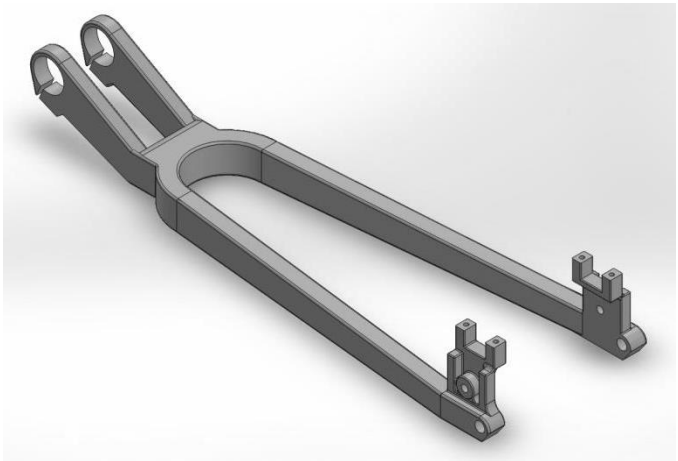


Figure 24. 3D models of top tube, down tube and seat tube



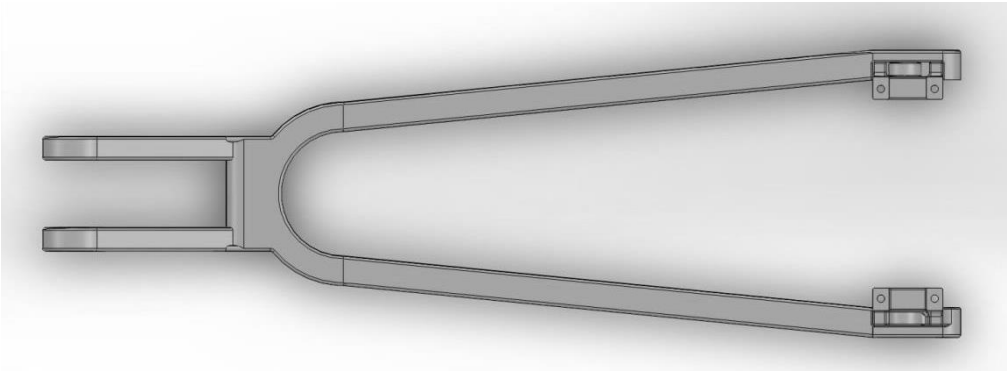


Figure 25. 3D model of seat stay



Figure 26. 3D model of chain stay

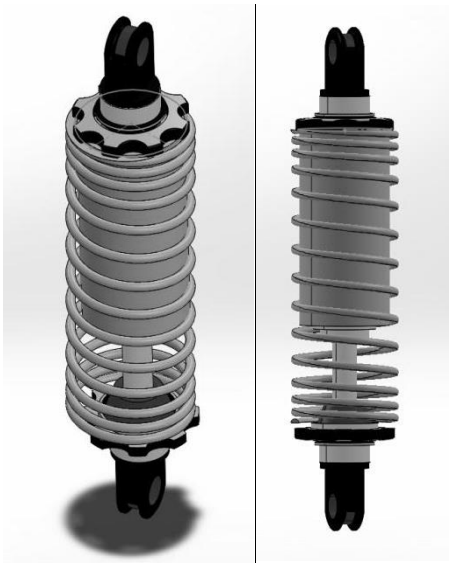


Figure 27. 3D model of rear shock

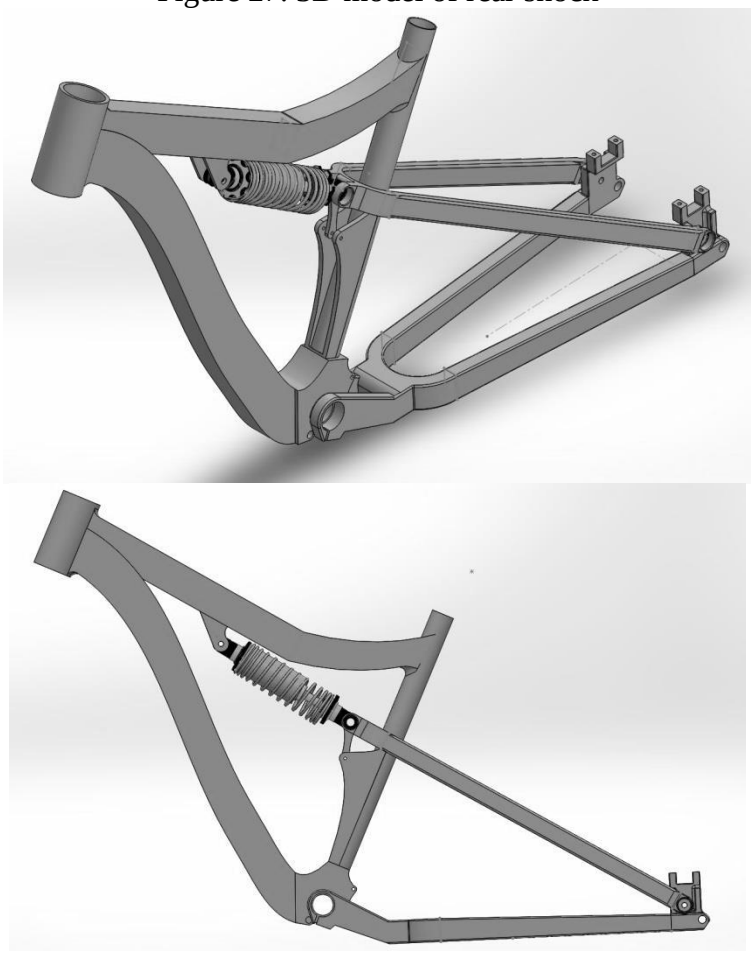


Figure 28. 3D model of the suspension spring assembly

3.4. Meshing

3.4.1. Default meshing (automatic)

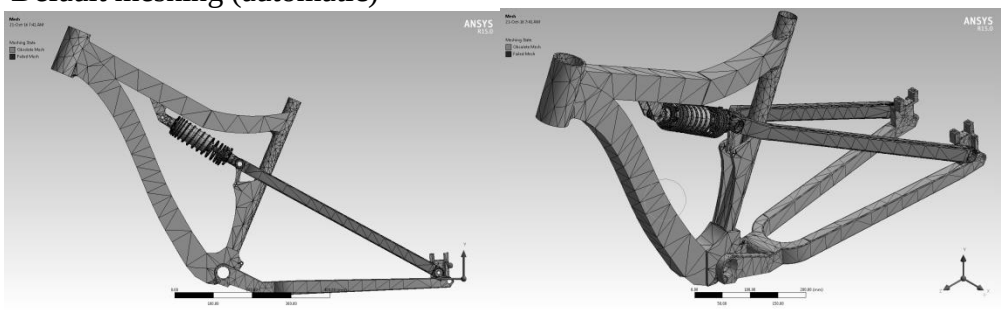


Figure 29. Assembly under default meshing

Node count: 55468

Element count: 25978

3.4.2. Default meshing (adjusted element size boundaries)

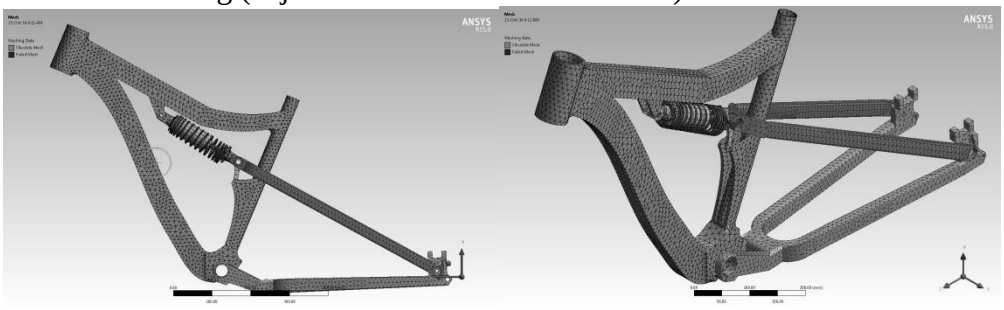


Figure 30. Assembly under default meshing with adjusted element size (large)

Node count: 62374

Element count: 30085

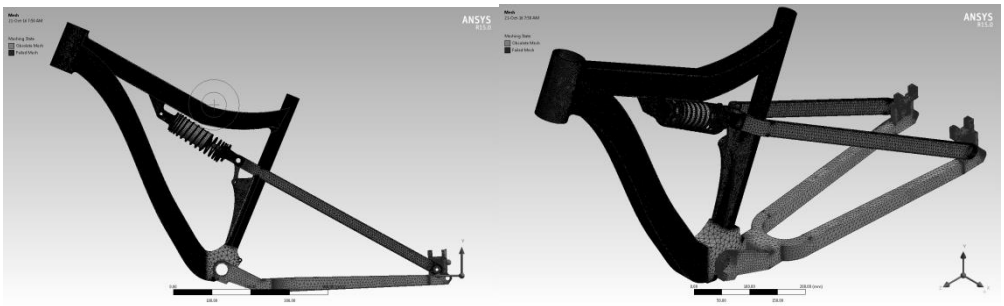


Figure 31. Assembly under default meshing with adjusted element size (small)

Node count: 6509800

Element count: 4157706 (excessive amount of elements, excessive run time)

3.4.3. Tetrahedron method

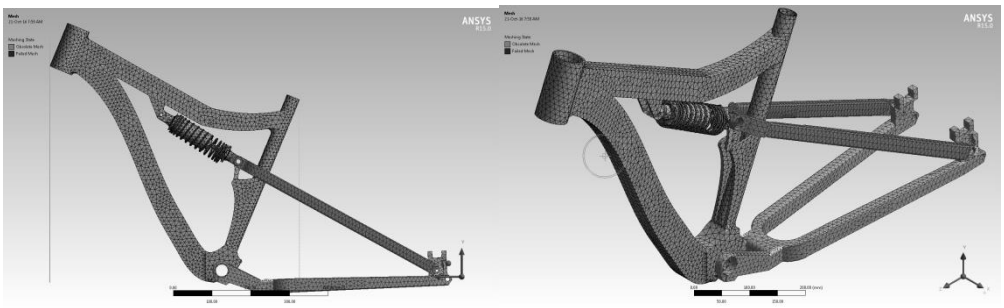


Figure 32. Assembly under default meshing with tetrahedron method

Node count: 63723

Element count: 31220

3.4.4. Hex dominant method

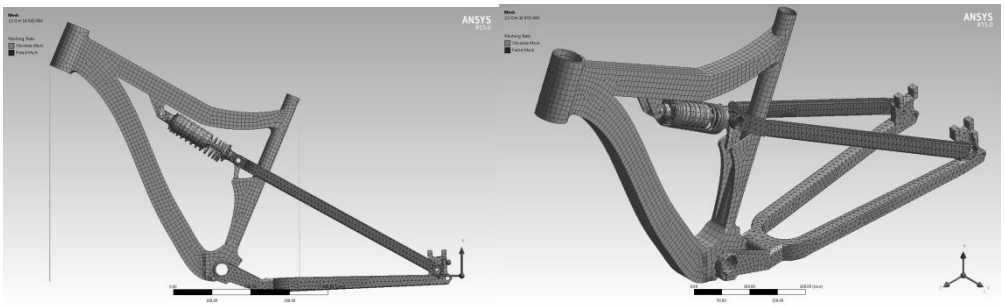


Figure 33. Assembly under default meshing with hex dominant method

Node count: 385085

Element count: 15219 (low element counts with excessive redundant nodes)

3.4.5. Sweep

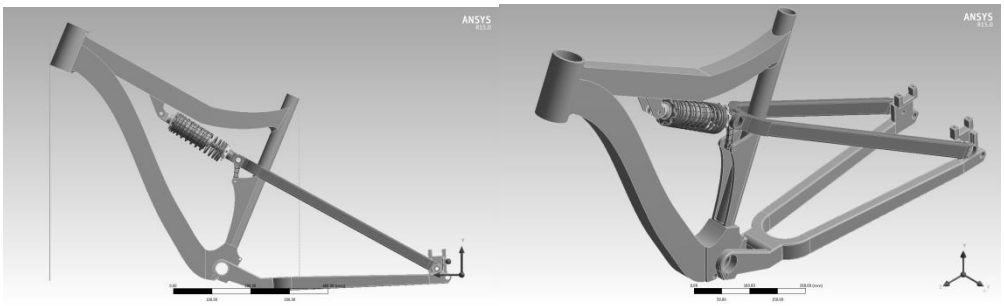


Figure 34. Assembly under default meshing with sweet method

Node count: 1374

Element count: 210 (Note: Critical failure in meshing, method not suitable)

3.4.6. Multizone

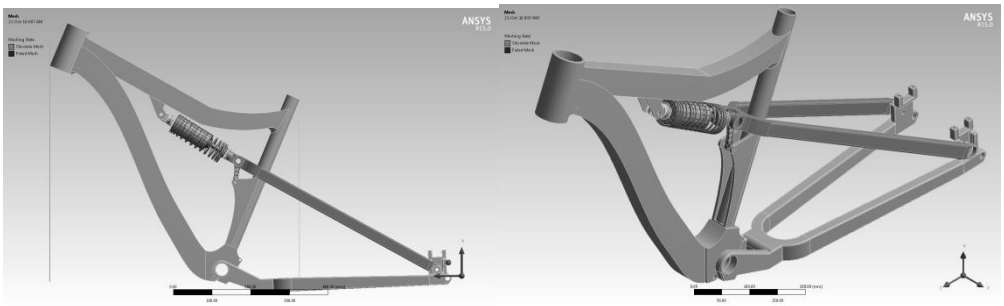


Figure 35. Assembly under default meshing with sweet method

Node count: 3860

Element count: 553 (Note: Critical failure in meshing, method not suitable)

Table 4. Tabulated data from different meshing methods, node and element count

Meshing method	*Node count*	*Element count*
Automatic	55468	25978
Automatic (adjusted, large)	62374	30085
Automatic (adjusted, small)	6509800	4157706
Tetrahedron	63723	31220
Hex dominant	385085	15219
Multizone	3860	553
Sweep	1374	210

A tetrahedron meshing method would be a more optimal choice for this project, providing a balance in between total element counts for accuracy, as well as a reasonable run time to simulate the results, as extensive effort and additional time are needed to evaluate the current results and to run continuous simulations in order to provide proper data to carry out the full kinetic analysis.

3.1 *Weight and Cost*

By applying the material assignment onto the assembly model, the weight of the assembly can be determined directly from the ANSYS software. Not only does this variable affect the FEA results, the resulting weight can also be correlated to a rough average cost in manufacturing a particular suspension frame in that material.

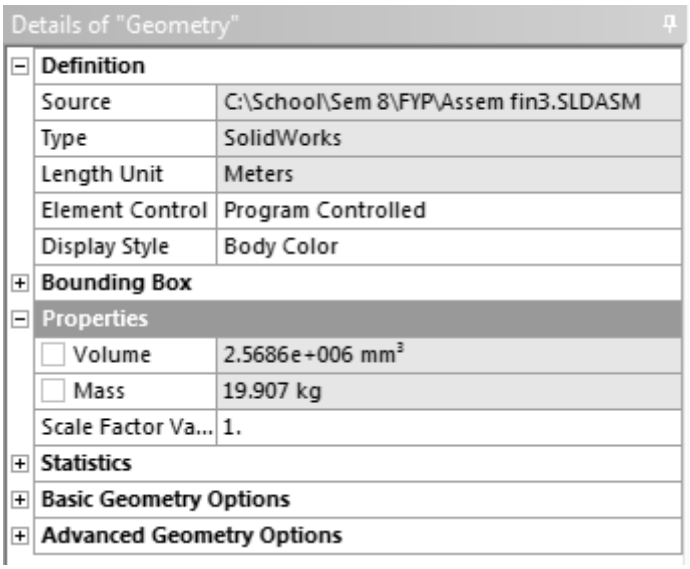


Figure 36. Weight of the assembly model after assigning a material type

Table 5. Weight of the rear suspension frame and its average metal cost

Material	*Weight (kg)*	*Cost (USD/kg)*	*Cost (USD)*
Aluminium Alloy (Al6061)	7.1151	2.1211 [15]	15.0918
Carbon Fiber (Std CF)	4.6236	140 [18]	647.304
Stainless Steel	19.907	1.8230 [16]	36.290
Titanium Alloy (Ti6Al4V)	11.379	16.8874 [17]	192.1617

3.2 *Displacement and Deformation*

Once the FEA is set up properly, the displacement and deformations in the suspension frames can be tabulated into numerical values, in terms of total deformation, directional deformation, as well as the displacement of the seat tube in Y-axis.

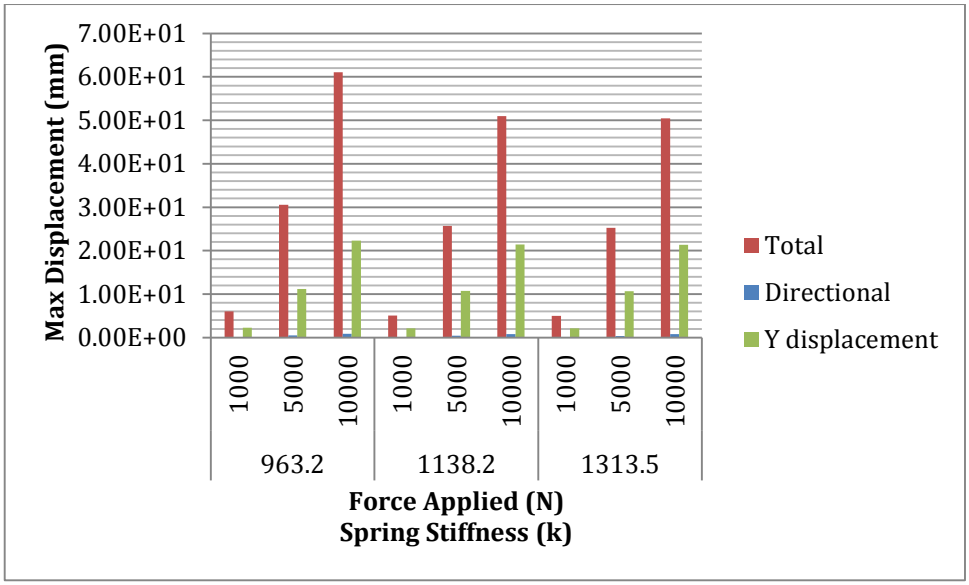


Figure 37. Displacement and deformation in an Aluminium frame

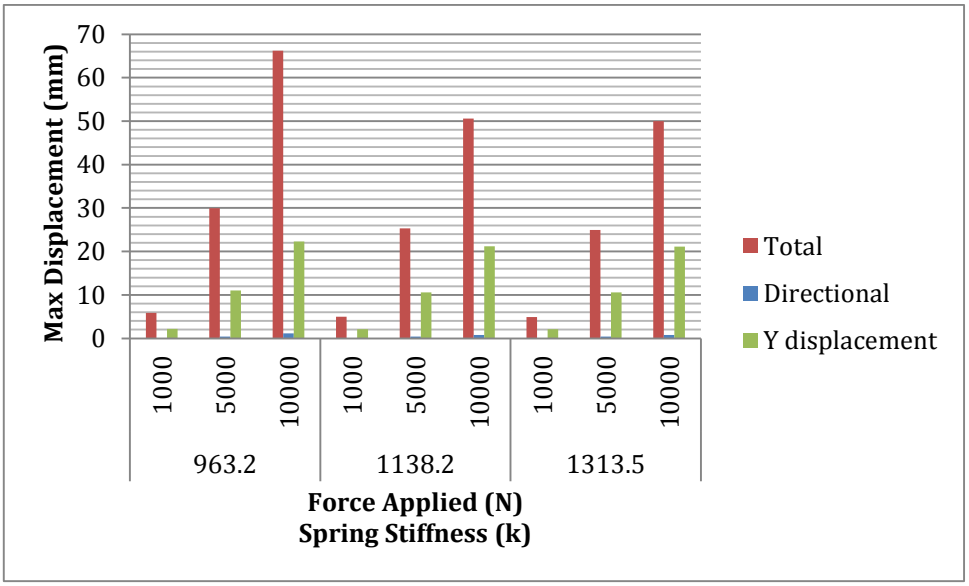


Figure 38. Displacement and deformation in a Carbon Fiber frame

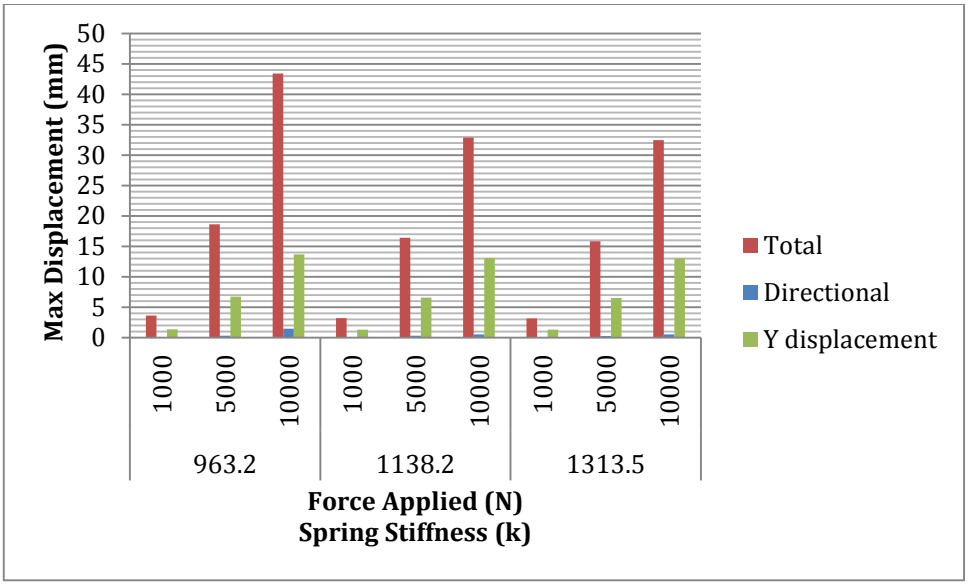


Figure 39. Displacement and deformation in a Titanium frame

3.3 Displacement and Deformation (Visual)

The ANSYS software has the option for the user to export screenshots and pictures of the simulation results.

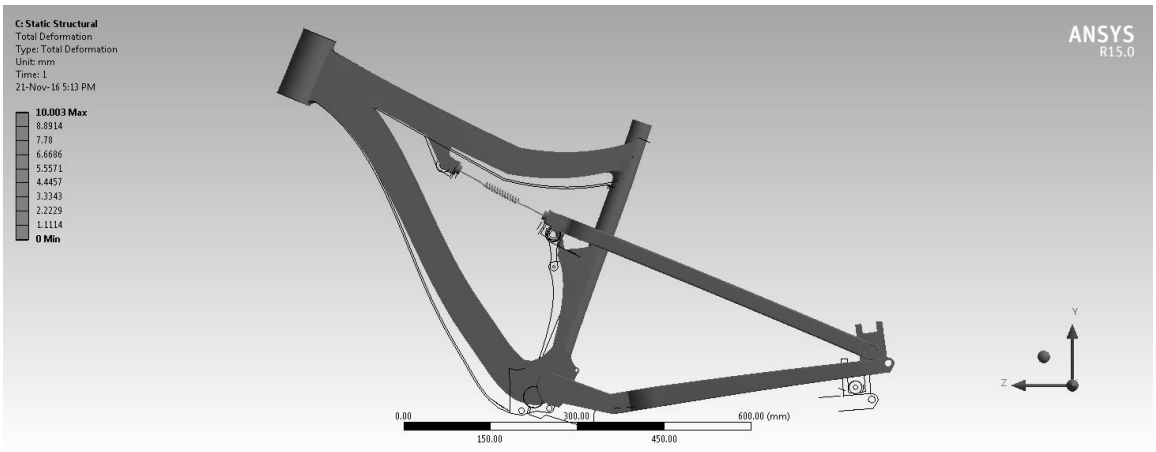


Figure 403 Maximum total displacement for Aluminium frame, k = 1313.5N/m, F=10k N

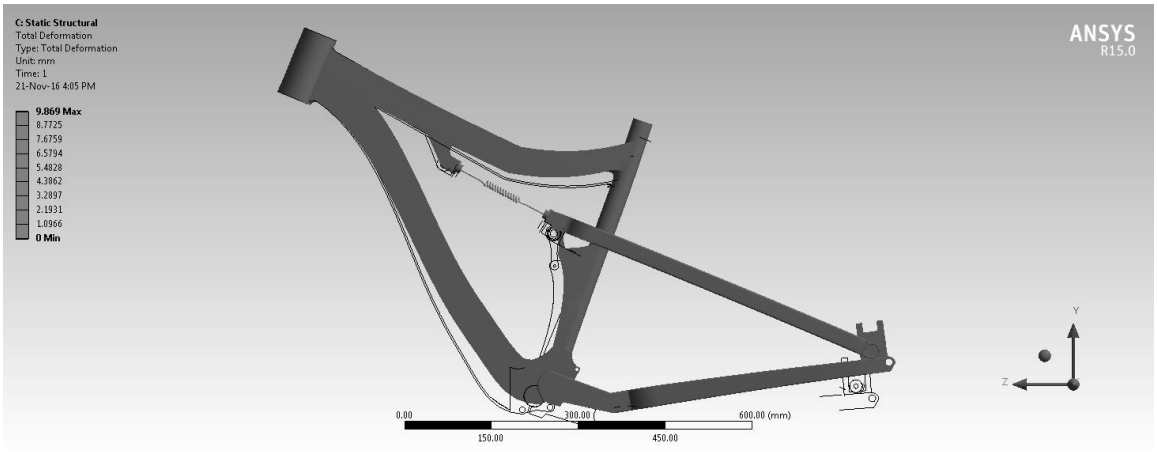


Figure 41. Maximum total displacement for Carbon Fiber frame, k=1313.5 N/m, F=10kN

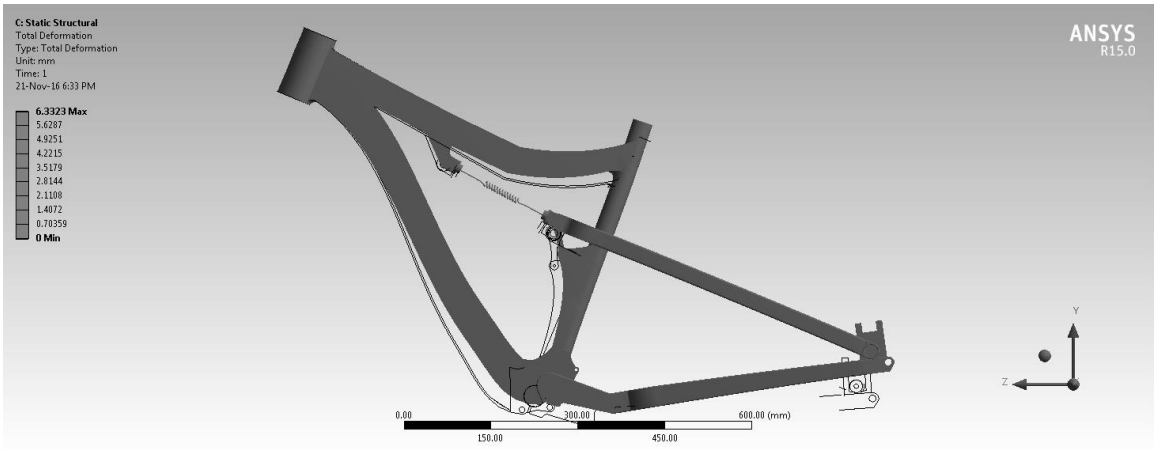


Figure 42. Maximum total displacement for Titanium frame, k = 1313.5 N/m, F = 10k N

4. Conclusion

This research project mainly focuses on the modelling and analysis of the rear suspension system of a selected mountain bike model, to determine how the rear suspension system would perform under various conditions and setup. By using the FEA method with the aid of the ANSYS and SolidWorks software, an assembly model of the rear suspension system can be constructed with reference to the dimension of the model in real life. The assembly model can then be exported into ANSYS to proceed with the FEA process, where materials can be assigned to the geometries, and take on the physical properties of said material, and then subjected to a static, predetermined force, applied from under the chain stay length of the suspension system. Alongside with the addition of a longitudinal spring contact connection, the component is given a set of spring stiffness variables.

From the results obtained from the FEA simulations, it is determined that the titanium frame exhibits the least deformation when subjected to the same condition mentioned. The material has a high yield strength value, pairing it with the spring stiffness provided by the model, hence it is expected to perform extremely well in absorbing and not buckle under the sudden force. However, it can be justified that aluminium, despite its poorer performance compared to the titanium and even carbon fiber, its cheaper price tag makes it more feasible for general hobbyist who doesn't have a huge budget.

References

[1] Li, T.Z., (2014). *Energy consumption and emission of pollutants from electric bicycles*. Trans Tech Publications Ltd, Kunming, China.

[2] Shu, S., (2014). *Modelling the reductions in carbon emissions resulting from public bicycles*. American Society of Civil Engineers (ASCE), Changsha, China.

[3] Matthias. W. and Falk. R. (2002). *A Multibody Model for the Simulation of Bicycle Suspension Systems*. Univ. Carl von Ossiestzky.

[4] Jody. E. M. (n.d). *Kinematic Analysis and Optimization of Bicycle Suspension*. Dept. Mech. Eng., Univ. Bath, UK.

[5] The American Journal of Orthopedics (2014). "Extreme sports provide thrills but also increased incidence of head and neck injuries" [Online]. Available: http://www.amjorthopedics.com/specialty-focus/trauma/article/extreme-sports-provide-thrills-but-also-increased-incidence-of-head-and-neck-injuries.html [Accessed: 12-Oct-2016]

[6] Ministry of Science, Technology and Innovation. (2016). Monthly Rainfall Review. Malaysian Meteorological Dept. (MetMalaysia)

[7] Michelle. L. A. (2014). *The Effects of Rain on Traffic Safely and Operations on Florida Freeways*. Dept. Computing, Eng. And Construction, Univ. North Florida, US

[8] ICEBIKE (2015). "The 5 Types of Mountain Bikes You Need to Know" [Online]. Available: http://www.icebike.org/the-5-types-of-mountain-bikes-you-need-to-know [Accessed: 12-Oct-2016]

[9] REI Co.op (n.d.). "Mountain Bikes: How to Choose" [Online]. Available: https://www.rei.com/learn/expert-advice/mountain-bike.html [Accessed: 12-Oct-2016]

[10] Evo. (n.d.). "How to Choose a Mountain Bike: Buyer's Guide & Bike Types" [Online]. Available: http://www.evo.com/how-to-choose-a-mountain-bike.aspx [Accessed: 13-Oct-2016]

[11]] Eric. N. (2015). "5 Reasons to Ride a Rigid Bike" [Online]. Cycle Science, JensonUSA. Available: https://blog.jensonusa.com/5-reasons-to-ride-a-rigid-bike/ [Accessed: 13-Oct-2016]

[12] Christian. W.(2013). “A beginner’s guide to mountain bike suspension design” [Online]. Available: http://www.bikeroar.com/tips/a-beginners-guide-to-mountain-bike-suspension-design [Accessed: 13-Oct-2016]

[13] PIVOT Cycles (n.d.). “Mach 429 Trail” [Online] Available: http://www.pivotcycles.com/bike/mach-429-trail/ [Accessed: 12-Oct-2016]

[14] Paul. H. and Andrew. D., (2010). “Buyer’s Guide to Mountain Bike Suspension, Part 2” [Online] Available: http://www.bikeradar.com/gear/article/buyers-guide-to-mountain-bike-suspension-part-2-28438/

[15] MetalPrices (n.d.) “Aluminium 6061 Extrusion Billet Spot Price” [Online] Available: https://www.metalprices.com/metal/aluminum/aluminum-6061-extrusion-billet-price [Accessed: 16-Nov-2016]

[16] MetalPrices (n.d.) “Stainless Steel 304 hot rolled coil 3mm Foshan domestic” [Online] Available: https://www.metalprices.com/metal/stainless-steel/stainless-steel-304-hot-rolled-coil-foshon [Accessed: 16-Nov-2016]

[17] MetalPrices (n.d.) “Titanium 6Al 4V Ingot FOB Rotterdam” [Online] Available: https://www.metalprices.com/metal/titanium/titanium-ingot-6al-4v-rotterdam [Accessed: 16-Nov-2016]

[18] Reuters (2014). “Cheaper carbon fibre will slash auto making costs-manufacturer.” [Online] Available: http://www.reuters.com/article/sgl-fibres-idUSL5N0MP2RP20140328 [Accessed: 16-Nov-2016]

eureca 2016 – Conference Paper
Paper Number 2ME19

Elimination of Noise in Conversion of CT Scan Images to FEA Model

Lew Tze Hao[1*], Cheah Kean How[2], Leong Wai Yie[3]

[1]*Department of Mechanical Engineering,*
School of Engineering, Taylor's University, Malaysia

[*]Corresponding Author: tzehao.lew@sd.taylors.edu.my

Abstract
An effort is made on how to eliminate noise when converting Computed Tomography (CT) scan images to finite element analysis (FEA) model. CT is able to provide accurate diagnostic images of the body in a painless and non-invasive manner. Unlike X-ray, CT scan provides detailed images of bones, soft tissues as well as blood vessels. In modern medical applications, CT imaging is able to provide a platform to further understand the human body, where needs of exploratory surgery and surgical biopsy are redundant. Presence of metal implants greatly affects the accuracy of CT imaging due to the metal artifacts generated on the images. Due to budget constraints, open-source software such as 3D Slicer, InVesalius and available software in the facility will be used to conduct this research as commercialized software are costly. Once the noise is eliminated, FEA model can then be used to accurately analyze the bone structures and to study on its mechanical properties. Segmentation method is used for this research to experiment on how to eliminate the metal artifacts in the images before generating FEA model. Segmentation is the selection of a region of interest while ignoring the other regions in the image and each slice of image will be stacked on top of one another accordingly, to generate a 3D model. 3D models obtained from both 3D Slicer and Invesalius are then imported into ANSYS in attempt to mesh the models. Computational time and quality of mesh is put into consideration. As a result, metal artifacts can be reduced in CT scan images and cheaper alternative methods to noise elimination can be determined. InVesalius and 3D Slicer were able to reduce noise and able to produce 3D FEA model.

Keywords: FEA, CT, Segmentation, Metal Implants, Mesh.

1. Introduction

Conventional X-ray imaging was widely used in the medical field. X-ray imaging utilizes low amount of ionizing radiation to project out a two-dimensional view of a body's internal structure. Essentially, it is casting a "shadow" to form an image of the internal structures. It is able to produce a good contrast between bones and soft tissues but it has poor separation between soft tissues. X-ray imaging is an inexpensive method to analyze a body's internal structure without the need of an operation. Without a three-dimensional image, it is difficult to distinguish the individual structures in the body as they overlap with one another. The invention of Computed Tomography (CT) has solved this issue.

CT is able to generate cross-sectional images of the desired area and to allow a much easier analyzing of the body. It is essentially an X-ray machine rotating around the body, capturing images slice-by-slice. In modern medical applications, CT is a non-invasive method that is able to provide diagnostic images of the body. Without CT imaging, it would be more challenging when it comes to analyzing and to studying the human body. CT can easily differentiate soft tissues while generating a patient's contour and this allows for accurate treatment planning. With the benefits it provides, it does come with risks as well. It utilizes radio waves in the form of ionizing radiation, a known human carcinogen, which may expose the patient to the risk of developing cancerous cells [1]. Nevertheless, CT imaging is still one of the fastest and most accurate tool in examining internal organs, especially the injuries due to trauma [2]. Diagnosing of osteoporosis could be performed with CT imaging because it is able to measure bone mineral density. CT scan images are obtained as "Digital Imaging and Communication in Medicine" (DICOM) file format. Each slice performed by the CT scanner will generate one DICOM file. The DICOM files can be arranged and displayed for further analysis.

More than 100 years ago, metal implants were already introduced to the medical field. Metal plate was first introduced by Lane for fixation of bone fracture back in 1895. In this modernized era, metal implants are commonly used. Metal implants have always been a go-to solution for patients with bone structural defects. However, in the early stages of development, metal implants often faced issues such as corrosion. At one point, stainless steel was introduced for biomedical applications. Since then, clinicians have been more interested to venture into the research of metal implants. Soon after, metal implants using alloys began to develop to cater to a wider range of clinical use. Currently, metal implants are widely used in many fields, such as cardiovascular (stents, artificial valves, pacemaker), orthopedic (bone fixation, artificial joints), and even dentistry (orthodontic wire, filling).

It is difficult to obtain an accurate analyzable image with CT when there are metal implants present in the patients. In CT imaging, the metal implant causes beam hardening and this reduces the effectiveness of X-ray beam. Beam hardening occurs when the X-ray beam is passing through a rather "hard" object. As it passes through the object, the beam hardens up, and because of that, its mean energy increases [3]. This is due to the fact that a higher amount of lower-energy photons is absorbed compared to higher energy photons, thus, more photons are detected when the X-ray beam has higher attenuation [4]. This will eventually cause artifacts or noise to be present in the images. Artifacts caused by the metal implants appear as a streaking

effect on the images. Streaking effects are basically dark and bright streaks adjacent to one another, which significantly reduces the diagnostic quality as shown in Figure 1. The top row illustrates CT images without beam hardening, while the bottom row of the figure illustrates the presence of beam hardening. Dark streaks are caused by X-ray beams with higher attenuation. This greatly affects the clinical applications of CT, especially for orthopedic, dentistry and spine imaging.

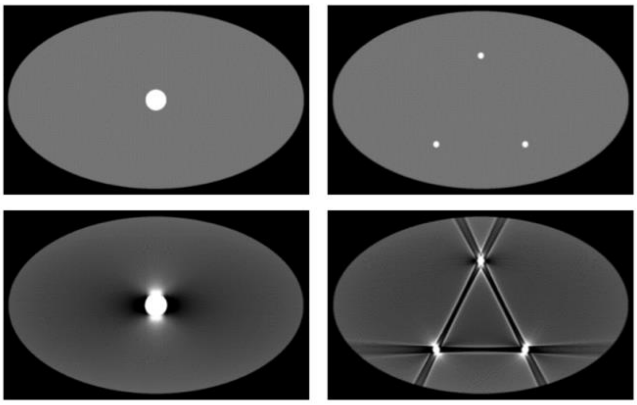


Figure 1: Simulated CT scan images. [4]

This limitation impairs visualization of the image as well as preclude the ability to produce an accurate Finite Element Analysis (FEA) model. FEA is a numerical method used to solve engineering and mathematical physics issues. It is mostly used for analysis of complicated structures which are difficult or expensive to be experimentally tested. FEA can also be used to determine mechanical properties of a structure and is very useful for biomechanical studies, particularly stress analysis. By generating FEA model from CT scan images, studies could be done to assess the bone strength and to analyze the stress acting on the implants and bone. For example, this could be used for osteoporosis patients and to assess fracture risks of the bones. With that information, proper implants could be designed and integrated to the bone, to minimize the stress acting on the bone structures. Therefore, metal artifact reduction (MAR) is very important when it comes to performing CT scan on patients with metal implants.

Open-source programs can be used to convert DICOM files into 3D model. It functions by stacking and layering each of the DICOM files on top of one another with a specific slice thickness. Once all the DICOM files are stacked, volume rendering can be done to generate a 3D model. However, based on previous work, limitations were present due to the high number of facets on the 3D model generated by the commercial software [5]. Even when the model can be imported into ANSYS, it will take an unnecessary long duration of time to apply the mesh elements as there are too many surfaces. The noises and metal artifacts caused by the metal implants do affect the meshing process as well. Although there are several methods in reducing and eliminating the noises or metal artifacts, there is no definite solution to this issue. However, the methods to be approached in this study is segmentation algorithms. Thresholding segmentation and manual segmentation are looked into for this study and results will be tabulated and evaluated.

2. Methodology

2.1 Acquisition and Analysis of DICOM files

CT images were received in the form of DICOM file format from a PhD scholar in Taylor's University School of Engineering. Data received is for a patient suffering from scoliosis, having undergone CT imaging pre-operation and post-operation. Surgery was done to correct the curved spinal cord and to prevent further increase in curvature. Metal implants, such as rods and screws were used in the operation. Post-operation images were selected to be the main focus for this study. Acquired DICOM files for pre-operation and post-operation were first viewed to better understand the effects of metal implants towards CT scan images. Brightness and contrast value were increased for post-operation images to obtain a clearer representation of the metal implants and the bone structures. Figure 2 shows the comparison between the I mages from pre-operation and post-operation. It can be seen that the metal implants in the post-operation images greatly affects the quality of the image.

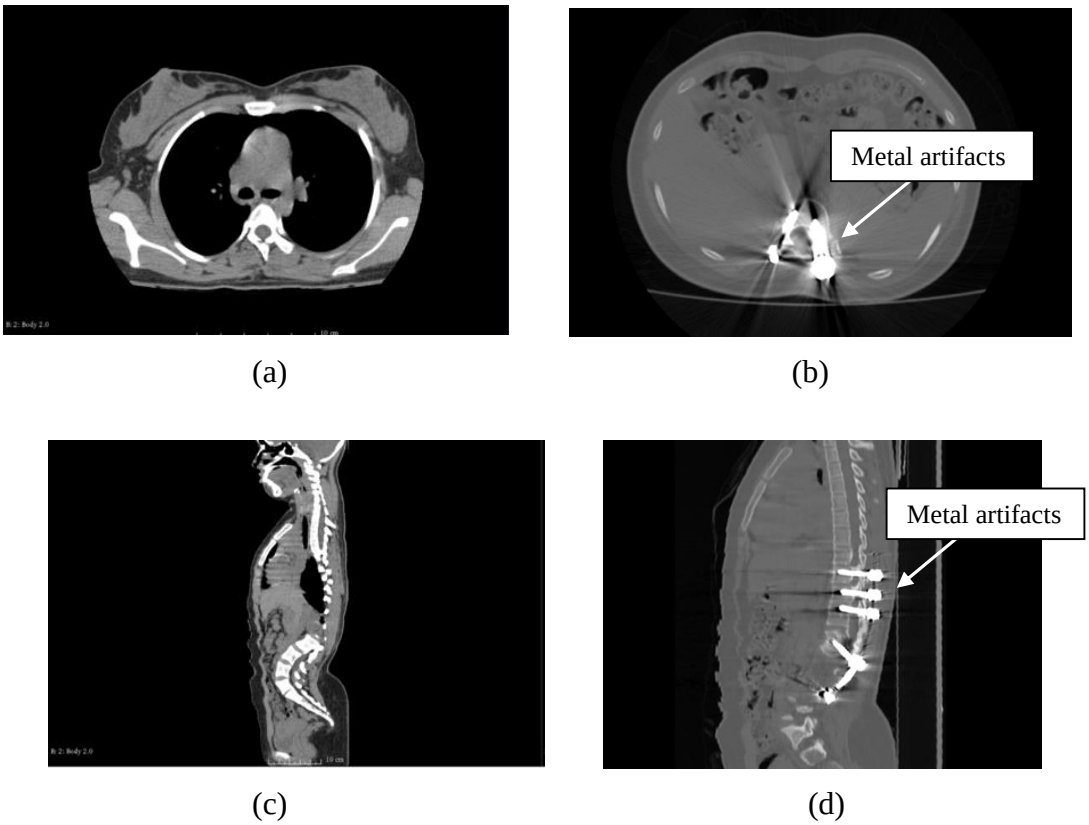


Figure 2: Axial view. (a) Pre-operation. (b) Post-operation; Sagittal view. (c) Pre-operation. (d) Post-operation.

2.2 Segmentation Technique

Segmentation is an image analyzing process where an object of interest is extracted from the background. In this study, bone at specific region of interest were separated from its surrounding in the CT scan images. The results from segmentation allow the generation of 3D bone model [6]. Thresholding-based techniques have been the main approach in image segmentation [7]. Previous work has successfully obtained an average optimal threshold for bone parameters [8]. However, partial volume effect shall be taken into consideration. Partial volume effect occurs when an image contains a mixture of two or more tissue types at the region of interest [9]. This is especially useful when eliminating metal artifacts from CT scan images. One vertebra was chosen as the region of interest in this study. There are two open source software available that are looked into, 3D Slicer and InVesalius. A comparison of the two software is provided in Table 1.

Table 1. Comparison of 3D Slicer and InVesalius

Name	License	Application Type	Standard	Operating System
3D Slicer	BSD	Visualization	DICOM	Windows/MacOS/Linux
InVesalius	GNU GPL	Visualization	DICOM	Windows/MacOS/Linux

2.2.1 Open Source Software – 3D Slicer

3D Slicer (available online at www.slicer.org) is a free open-source software application for medical image computing as well as visualization. Slicer has been developing into an integrated platform, which includes a number of powerful open-source projects and creating an open-source application for clinical researchers [10]. It has been applied in preclinical research applications and analysis of nonmedical images as well. As compared to commercial software, 3D Slicer provides a free research platform which does not require any specialized equipment. 3D Slicer visualization capabilities is able to support various imaging format, such as CT, positron emission tomography (PET), as well as magnetic resonance imaging (MRI).

Segmentation module is a tool used to separate individual sub regions in a set of data, which includes image-based segmentation. The “Editor” module is a tool which allows for manual and semiautomatic segmentation. Segmentation in 3D Slicer utilizes Hounsfield units (HU) as threshold values. Hounsfield units are standard units used for X-ray and CT density, at which air and water is at -1000 HU and 0 HU respectively [11]. It is widely used in CT imaging density calibration. Therefore, optimum threshold values to accurately segment bone regions were experimented. Hounsfield units for bone structures ranges from +400 to +1000 HU.

In the software’s segmentation module, “ThresholdEffect” allows manual setting of threshold value, a range of +400 to +1000 was set and the volume rendered is as shown in Figure 3.

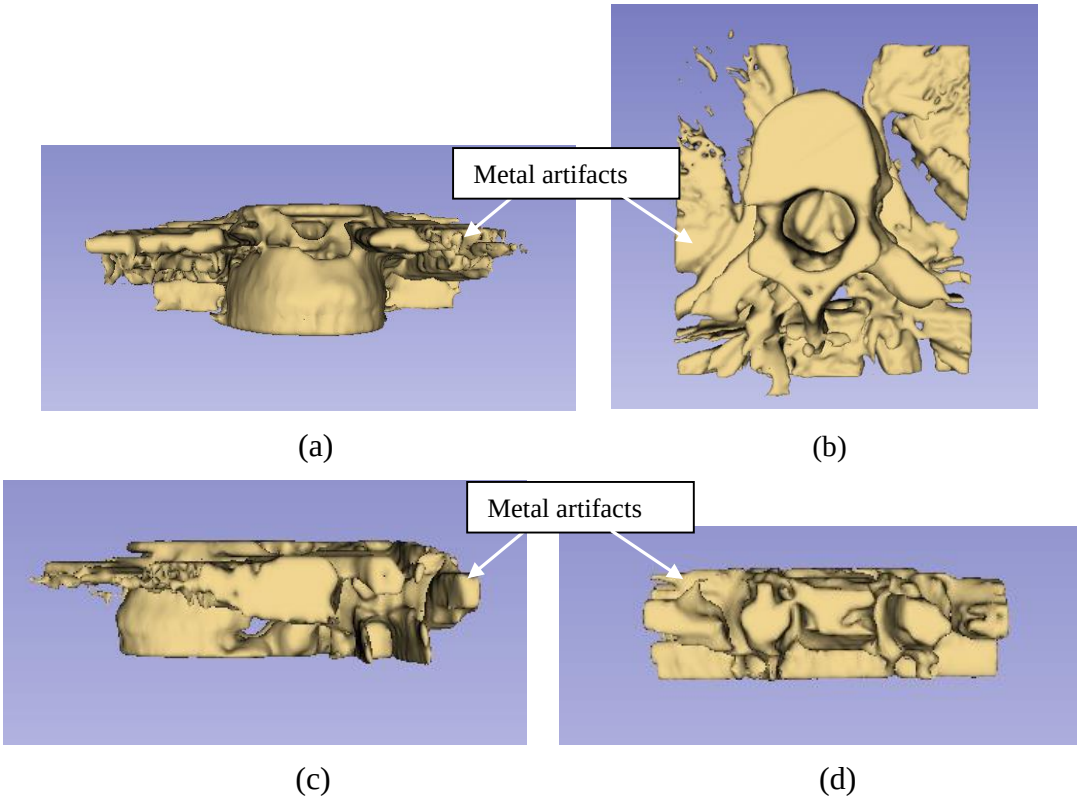


Figure 3: Manual threshold model. (a) Front view. (b) Top view. (c) Side view. (d) Rear view.

An "EraseLabel" function allows the manual removal of unnecessary segmentation and in this case, the segmentation of the metal artifacts and metal implants as shown in Figure 4.

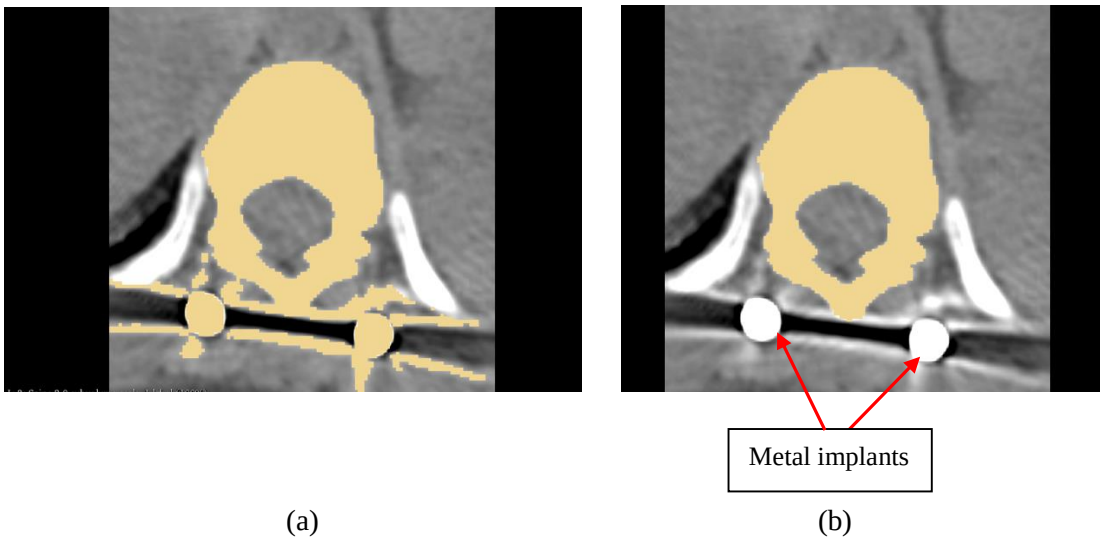


Figure 4: (a) Segmented metal artifacts. (b) Removal of unnecessary segmentation.

A function called “PaintEffect” allows manual segmentation by drawing on each of the CT scan slices. This is to allow a more accurate segmentation as the threshold range might not be able to segment all the bone regions. Once all the slices in the region of interest have been segmented, the slices are stacked upon one another to form the 3D model. Next, the stacked volume was then merged and built together with the initial model to generate a smooth surface for the 3D model.

2.2.2 Open Source Software – InVesalius

Manual segmentation, thresholding and watershed techniques are techniques available in InVesalius. In thresholding-based segmentation, users can select a range on the Hounsfield scale to apply a segmented layer on the images. One difference of InVesalius as compared to 3D Slicer is that the segmented layer has a slight transparency to it. It partially shows the original image at the background and this allows for an easier manual segmentation as shown in Figure 5. In InVesalius, thresholding-based technique is also referred to as “Mask”.

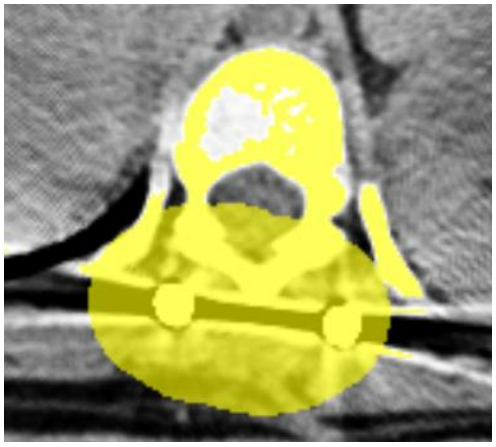


Figure 5: Slight transparency in the segmented area in showing the background image.

Once the layer was applied, manual removal of unwanted layer can be performed by using its “brush” tool. This can be used to remove layers applied during the thresholding technique. Regions that were not segmented out by the thresholding technique can be manually chosen with the “brush” tool as shown in Figure 6. Once the desired regions have been segmented in all the images, volume rendering can be done to produce a 3D model and exported out as a Stereolithography (STL) format.

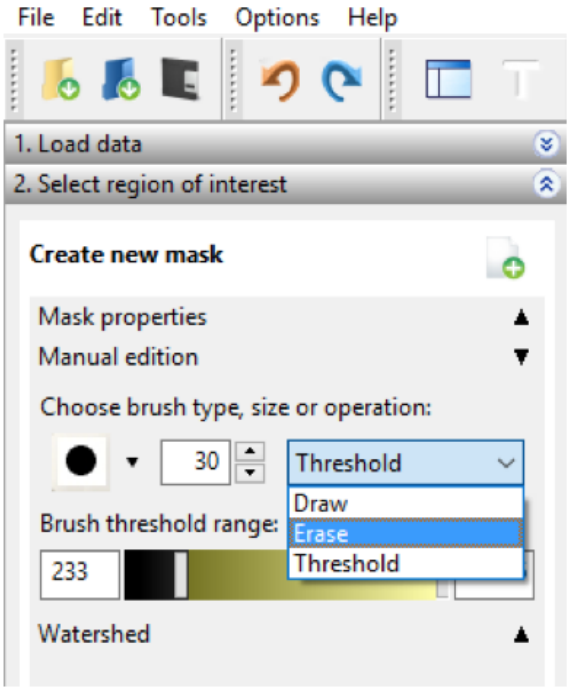


Figure 6: "Brush" tool for manual segmentation in InVesalius.

2.3 Meshing of 3D Model in ANSYS

3D rendered volumes were then exported to ANSYS in STL file format. Attempt was taken to mesh the 3D model. Smaller mesh element size would be preferred on critical points such as edges or corners of the 3D model. However, computational time will be placed into consideration as well. With smaller mesh element size, computational time was predicted to be longer as the number of elements would be increased. Quality of the mesh can be identified through the statistical data obtained in ANSYS. Meshing is considered good when the Skewness is closer to zero and the Orthogonal element quality is closer to unity. Good quality meshing allows for a more accurate analysis of the structure with minimal computational resources.

However, the rendered volume generated by 3D Slicer and InVesalius has a huge number of facets and this could greatly affect the computational time and most importantly, the quality of the mesh. Therefore, merging was done with both rendered volumes to reduce the number of facets on the 3D model. In Static Structural, the "Merge" function in DesignModeler is able to combine two or more surfaces into one single surface.

Once the total number of surface was reduced, meshing was carried out in Mechanical. Mesh control on body sizing was made on the models with merged surfaces. A body mesh sizing of 1.5mm was set equally for both the model from 3D Slicer and InVesalius. Smaller element size will be able to produce a better mesh, however, fine mesh does not equate to a good mesh. An optimum element size was chosen for the entire body but critical regions such as edges and corners have smaller element size. As for the unmerged models, a default mesh sizing was chosen for comparison. The meshing statistics of all four models were then compared to determine the mesh with the better quality.

3. Results and Discussion

3.1 Generation of 3D FEA Model and Reduction of Total Number of Faces

In order to produce a 3D FEA model of a vertebra, the CT scan images were processed to segment out desired region such as the bone geometry. One of the criteria in producing a good segmented model is to ensure that the segmented region forms a closed 3D volume. Manual segmentation can be used to ensure that each image is segmented to form a close 3D volume because thresholding segmentation may not fully segment out the region of interest. With the use of manual segmentation, the results will be affected by the procedures adopted by the user. Therefore, human errors will be one of the contributors to the results obtained. This has caused the 3D models between the two software to vary slightly in shape, due to the manual segmentation processes. However, both software was able to reduce the metal artifact noise present in the CT scan images. Figure 7 shows a rendered volume without the manual segmentation process taking place.

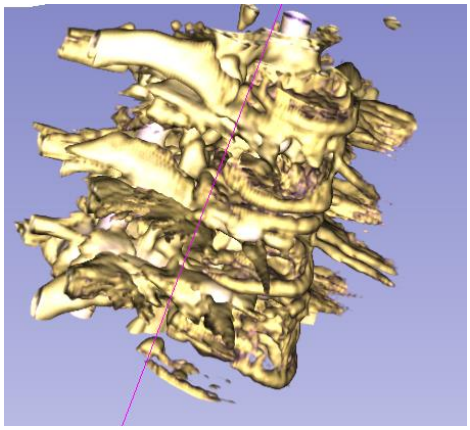
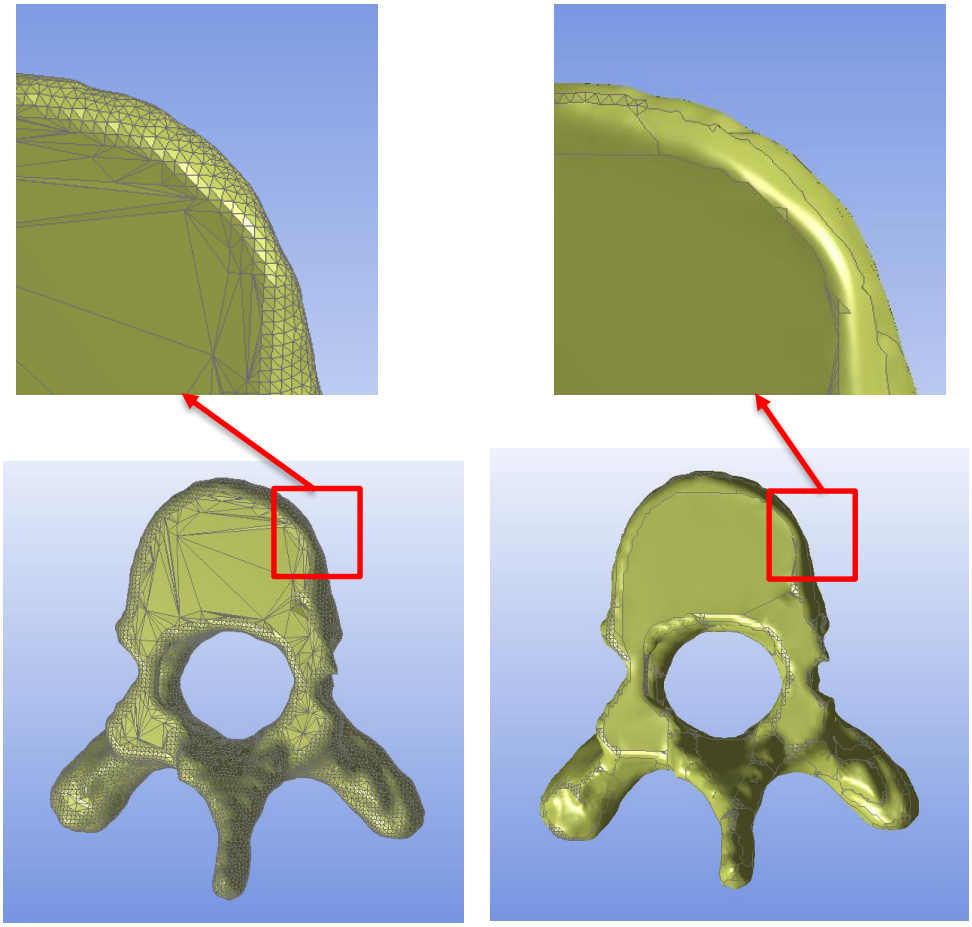


Figure 7: Rendered 3D model without manual segmentation.

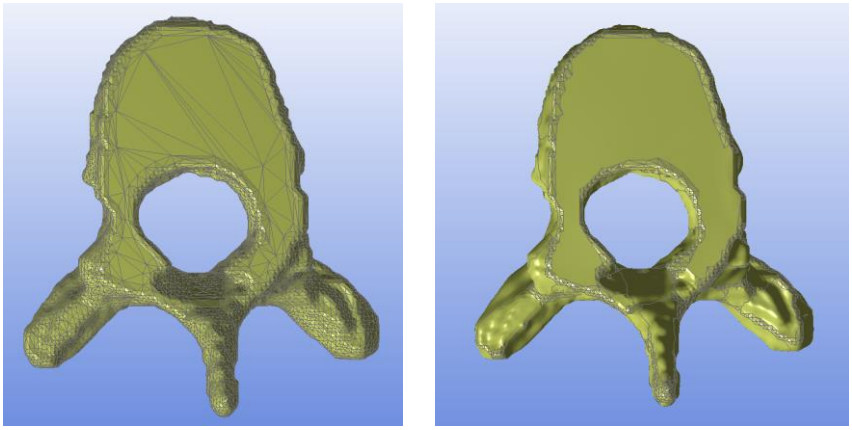
As for 3D Slicer and InVesalius, the rendered volume obtained after the segmentation process, can be exported out as Stereolithography (STL) file format. However, STL file format stores data of the 3D model as sets of triangles, which forms the outer layer of the model [12]. The sets of triangles share common sides and vertices and this converts the model into a closed surface, which results in producing a solid model. Therefore, the 3D models (in STL format) generated using 3D Slicer and InVesalius has a huge number of facets. Thus, a process to reduce the number of facets is necessary. With lesser facets, ANSYS will be able to generate a better quality mesh. “Merge” function in ANSYS was used to combine two or more adjacent faces into one single face. However, the merging process is a manual process as well and the results will be further subjected to human errors. Due to the uneven surfaces on both the models, merging of surfaces must be done by patches. The reduction in total number faces can be seen in Figure 8 and 9. The number of faces reduced is provided in Table 2. By combining adjacent faces together, this will allow the meshing process to be more effective. With lesser faces to work with, the computational time is reduced as well. The results from this merging process is considered good as it is able to greatly reduce the total number of faces for both 3D models. However, this merging process can be further improved and refined. One limitation to this

improvement is that some surfaces are too uneven for the merging process to take place. There is a maximum unevenness at which the faces are able to be merged. Therefore, in order to improve further on these models, the manual segmentation in the open-source software can be more refined to further reduce uneven surfaces. That allows for further reduction of the total number of faces.



(a) (b)

Figure 8: 3D Slicer model; (a) Unmerged faces. (b) Merged faces.



(a) (b)

Figure 9: InVesalius model; (a) Unmerged faces. (b) Merged faces.

Table 2. Reduction in total number of faces.

Software	Total number of faces	
	Unmerged	Merged
3D Slicer	18848	1812
InVesalius	15688	3374

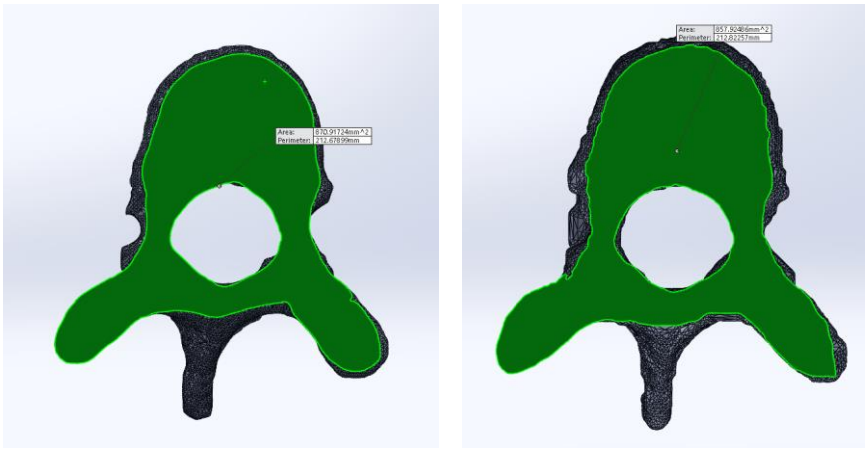
3.2 Surface Area Comparison (Error Analysis)

Measurement of the image's surface area using ImageJ was repeated for five times to obtain an average reading. Table 3 shows the five reading of the surface area together with the average value.

Table 3. Surface Area Measurement using ImageJ.

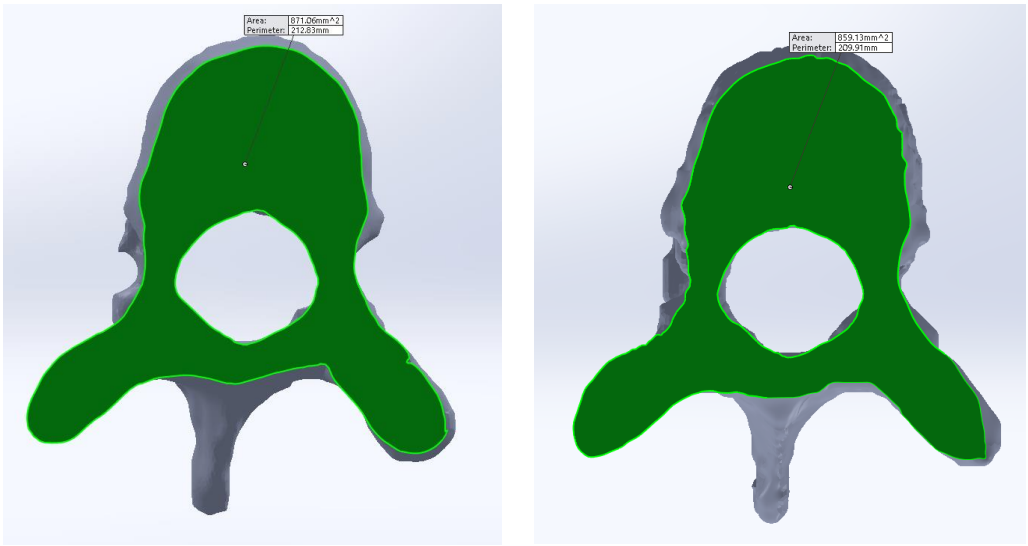
Measurement	Reading 1	Reading 2	Reading 3	Reading 4	Reading 5	**Average**
Surface Area (mm^2)	895.59	911.56	899.81	894.99	897.95	**899.98**

The value of 899.98 mm^2 was then used to compare with the cross-sectional surface area of the 3D models obtained using 3D Slicer and InVesalius. SolidWorks was used to obtain the cross-sectional surface area at 4 mm from the top surface, which equates to the fourth slice from the DICOM image. This allows for an accurate comparison of the change in cross-sectional surface area after all the processes had taken place. Figure 10 shows the cross-sectional surface area of 3D models obtained from 3D Slicer and InVesalius before surface merging in ANSYS and Figure 11 for post-merging 3D models.



(a) (b)

Figure 10: Cross-sectional surface area pre-merging; (a) 3D Slicer. (b) InVesalius.



(a) (b)

Figure 11: Cross-sectional surface area post-merging; (a) 3D Slicer. (b) InVesalius.

Both software could generate 3D models with cross-sectional areas close to the actual surface area of the vertebra. The actual surface area of the vertebra is measured at 899.98 mm^2. The cross-sectional surface areas of the 3D models for pre-merging and post-merging are tabulated into Table 4. Table 4 shows the variation of the experimental value from the actual value.

Table 4. Cross-sectional surface area comparison.

Software	Actual Surface Area (mm^2)	Pre-merging (mm^2)	Variation (%)	Post-merging (mm^2)	Variation (%)
3D Slicer	899.98	870.92	3.23	871.06	3.21

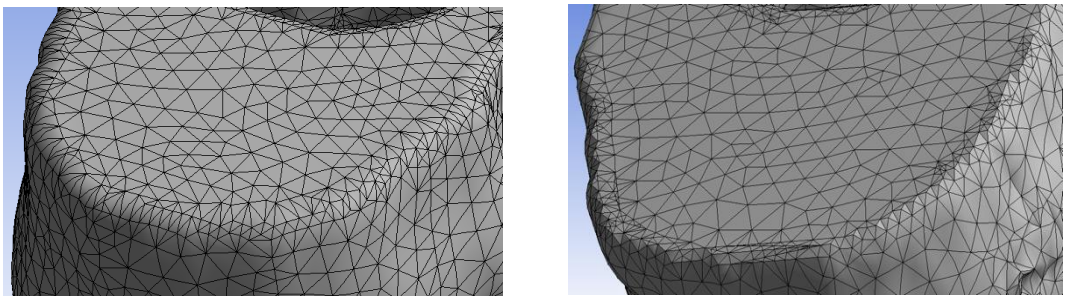
InVesalius	899.98	857.92	4.67	859.13	4.54

3D Slicer was able to generate a more accurate 3D model from the DICOM images as compared to InVesalius. The variation percentage of 3.23% is present due to human error as the segmentation process to eliminate the metal artifacts is a manual process. Therefore, the 3D model from the segmentation process may differ from an actual model. However, steps were taken to ensure that the segmented regions for both software are similar to compare. As for the "Merge" function in ANSYS, it could further refine the 3D model obtained from 3D Slicer. In both cases, the variation percentage varies slightly, therefore, it can be concluded that the merging process does not affect the surface area and the volume of the 3D model significantly.

3.3 Meshing of FEA Model

Generation of FEA model allows for the study of the bone's strength and stiffness. It can be used to compute the stress and strain experienced by the bone structure when an external loading is applied. This is especially useful to analyze the results of an operation on a Scoliosis patient. Based on previous studies on meshing of bone structures, the more commonly used method is the geometry based meshing [13]. Geometry based meshing emphasizes on the surface and volume representation of the bone's geometry. Quality of the mesh in this study is determined by two criteria; orthogonal quality and skewness. Low orthogonal quality and high skewness values are generally not acceptable as this indicates that the mesh generated is not recommended and further improvement steps can still be taken.

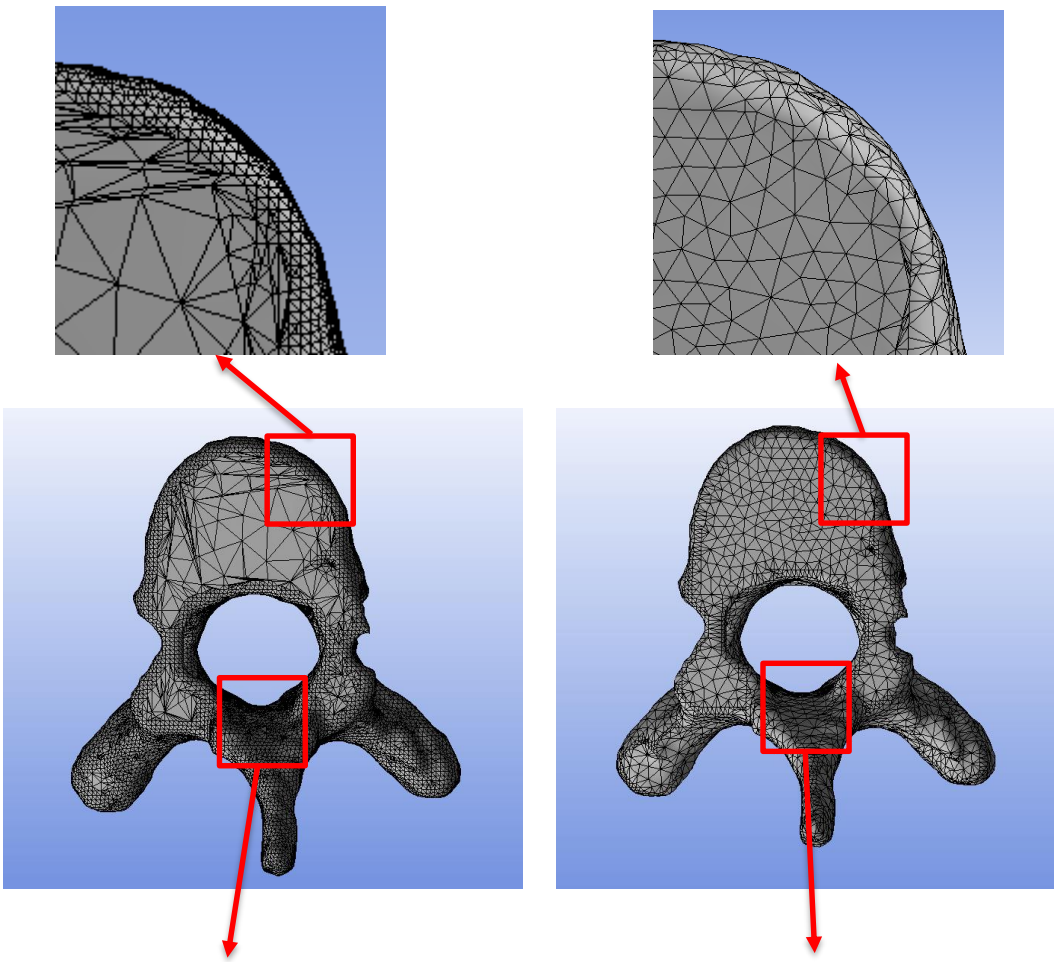
For critical regions on the geometry such as edges and corners, the element size of the mesh is made smaller to generate a better mesh as compared to having the same element size along the entire body. This allows for a more accurate finite element analysis of the bone structure. Figure 12 shows a close-up view of the mesh elements. Edges and critical regions of the 3D models are given a smaller mesh element size as this would generate a more accurate and acceptable mesh. With that, finite element analysis for mechanical strength and stresses experienced by the bone can be determined more accurately.

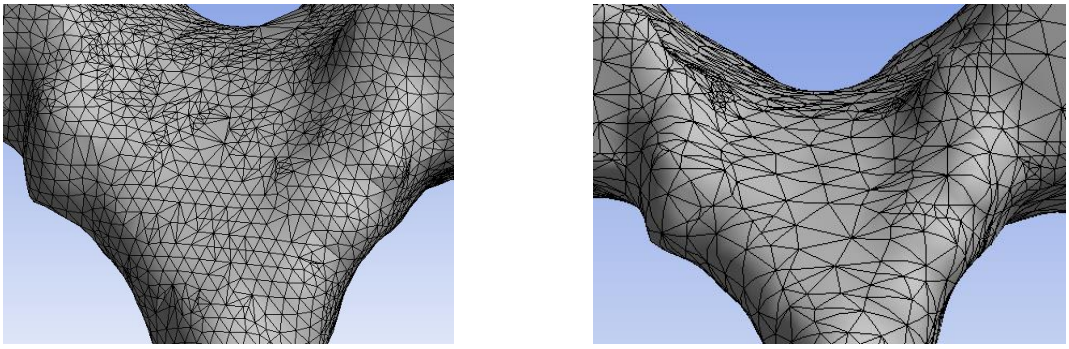


(a) (b)

Figure 12: Close up view of mesh elements. (a) 3D Slicer. (b) InVesalius.

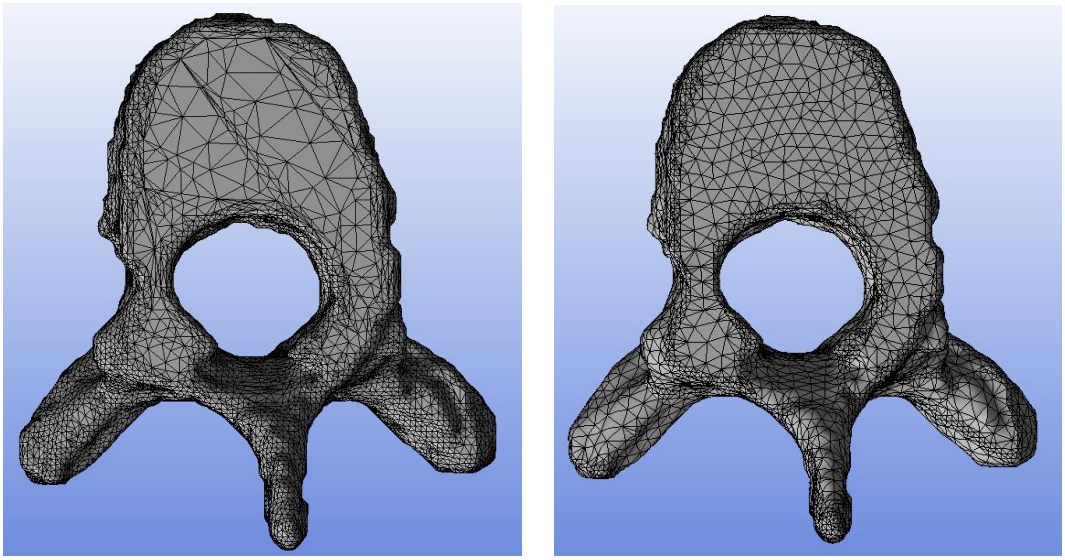
It can be seen that the models with merged faces produced a better mesh as compared to the models with unmerged faces. Smaller node count will not only produce good mesh, but also be able to utilize lesser computing resources. A good mesh is one that is able to resolve the physics that is being studied as well as have a reasonable quality such that a solution can be generated. For orthogonal quality, a value of 0.70 – 0.95 is considered as "Very Good" and 0.95 – 1.00 is considered as "Excellent". As for skewness, a value of 0.25 – 0.50 is considered as "Very Good" and 0 – 0.25 is considered "Excellent". With the merging process, both the orthogonal quality and skewness had improved from the unmerged models. Meshed models are shown in Figure 13 and 14. For merged faces, the mesh elements are arranged more uniformly and this would improve on the orthogonal quality as well as the skewness of the mesh. Meshes are generated on the faces of the model and if the model has uneven or irregular faces, the mesh element would not be consistent throughout the model. However, further improvements to the orthogonal quality and skewness can be considered. By using different mesh element type, such as Hex Dominant or MultiZone, the mesh can be further improved. Having a hybrid of prism and tetra mesh elements, whereby prisms are placed near-wall region and tetra in open faces. This would not only improve the mesh quality, but reduce computational time for finite element analysis as well. Given the statistical information of the mesh in Table 5, merged faces produced a better orthogonal quality and skewness as compared to unmerged faces.





(a) (b)

Figure 13: Mesh for 3D Slicer model; (a) Unmerged faces. (b) Merged faces.



(a) (b)

Figure 14: Mesh for InVesalius model; (a) Unmerged faces. (b) Merged faces.

Table 5. Comparison of Statistics

Software	Model Faces	Element Count	Node Count	Orthogonal Quality	Improve-ment (%)	Skewness	Improve-ment (%)
3D Slicer	Unmerged	87877	149701	0.6485	-	0.4958	-
	Merged	47511	73554	0.7766	19.75	0.3187	35.72
InVesalius	Unmerged	83858	143017	0.6453	-	0.4964	-
	Merged	62922	97883	0.7624	18.15	0.3339	32.74

4. Conclusion

In conclusion, this research aims to reduce and eliminate noise in conversion of CT scan images to 3D FEA model. Images acquired for a patient with scoliosis,

whom undergone surgery to insert metal implants. Metal implants act as a support for the backbone and to reduce the curvature of the backbone due to scoliosis. Images obtained are from pre-operation and post-operation. Segmentation technique is researched and performed to identify the more suitable method in eliminating noises caused by metal implants in CT scan images. Open source software can be used to reduce metal artifacts present in medical images. 3D Slicer and InVesalius were both able to reduce majority of the metal artifacts before generating a 3D model to be exported out in STL file format into ANSYS. InVesalius may be much more user-friendly as 3D Slicer has a slightly more complicated graphic user interface (GUI). Methods which require the minimal computational resources such as cost and time are considered. A single vertebra is chosen as the region of study and the results for the most suitable method is evaluated by the quality of the mesh on the 3D FEA model after the elimination of noise caused by metal artifacts. Merge function in ANSYS was used to improve the quality of mesh.

Acknowledgements

The author would like to thank Dr. Cheah Kean How for ongoing guidance during this study and Mr. Mohan for guidance and providing CT scan data. The author acknowledges the support from Taylor's University School of engineering.

References

[1] C. Schmidt, "CT Scans: Balancing Health Risks and Medical Benefits", *Environ Health Perspect*, vol. 120, no. 3, pp. a118-a121, 2012.

[2] S. Anderson and J. Soto, "Anorectal Trauma: The Use of Computed Tomography Scan in Diagnosis", *Seminars in Ultrasound, CT and MRI*, vol. 29, no. 6, pp. 472-482, 2008.

[3] J. Barrett and N. Keat, "Artifacts in CT: Recognition and Avoidance1", *RadioGraphics*, vol. 24, no. 6, pp. 1679-1691, 2004.

[4] F. Boas and D. Fleischmann, "CT artifacts: causes and reduction techniques", *Imaging in Medicine*, vol. 4, no. 2, pp. 229-240, 2012.

[5] M.A. Tyndyk, V. Barron, P.E. McHugh, D. O'Mahoney, "Generation of a finite element model of the thoracolumbar spine", *Acta Bioeng. Biomech*., 9 (2007), pp. 35–46

[6] J. Zhang, Y. Ge, S. Ong, C. Chui, S. Teoh and C. Yan, "Rapid surface registration of 3D volumes using a neural network approach", *Image and Vision Computing*, vol. 26, no. 2, pp. 201-210, 2008.

[7] D.L. Pham, C. Xu, J.L. Prince, "Current methods in medical image segmentation", *Annual Review of Biomedical Engineering 2*, pp. 315–337, 2000.

[8] T.N. Hangartner, "Thresholding technique for accurate analysis of density and geometry in QCT, pWCT and mCT images", *Journal of Musculoskeletal and Neuronal Interactions 7 (1)*, pp. 9–16, 2007.

[9] J. Dehmeshki, X. Ye, H. Amin, M. Abaei, X. Lin and S. Qanadli, "Volumetric Quantification of Atherosclerotic Plaque in CT Considering Partial Volume Effect", *IEEE Transactions on Medical Imaging*, vol. 26, no. 3, pp. 273-282, 2007.

[10] A. Fedorov, R. Beichel, J. Kalpathy-Cramer, J. Finet, J. Fillion-Robin, S. Pujol, C. Bauer, D. Jennings, F. Fennessy, M. Sonka, J. Buatti, S. Aylward, J. Miller, S. Pieper and R. Kikinis, "3D Slicer as an image computing platform for the Quantitative Imaging Network", *Magnetic Resonance Imaging*, vol. 30, no. 9, pp. 1323-1341, 2012.

[11] Shapurian T , Damoulis PD , Reiser GM , Griffin TJ , Rand WM . "Quantitative evaluation of bone density using the Hounsfield index", *Int J Oral Maxillofac Implants*, vol. 2, pp. 290–297, 2006.

[12] Janko D. Jovanović, Miomir Lj. Jovanović, "Finite Element Modeling of The Vertebra with Geometry and Material Properties Retrieved from CT-Scan Data", *Mechanical Engineering*, vol. 8, pp. 19-26, 2010.

[13] Wirthz D.C., Pandorf T., Portheine F., Radermacher K., Schiffers N., Presher A., Weichert D., Niethard F.U., "Con- cept and development of an orthotropic FE model of the proxi- mal femur", *Journal of Biomechanics*, 2003, 36, pp. 289–293.

eureca 2016 – Conference Paper
Paper Number 2ME20

Design and Analysis of a small Compressed Air Energy Storage System

Loh Yoon Hee, Douglas Tong Kum Tien*
School of Engineering, Taylor's University, Malaysia.
*douglaskumtien.tong@taylors.edu.my

Abstract
Energy supply is a pressing concern for the world as the main energy source, fossil fuel, is expected to completely run out within the next 41 years. To overcome this challenge, focus is increasingly given to renewable energy which offers better sustainability. Solar energy is an abundant source of renewable energy which is commonly harvested using solar panels. Solar panels are suitable to be installed on houses. Solar energy requires storage because energy generated is not used at the same time. It is usually stored in ion batteries but they are harmful to environment. Compressed air energy storage (CAES) is an environmentally friendly solution. The purpose of this study is to design a CAES system that is suitable for household with solar panels to store excess solar energy for later use so that minimal grid power is required. Another purpose of this paper is to determine the best design of CAES in term of efficiency and improve it by making changes in part. In this project, the calculation of the average daily household energy consumption and common use of solar panel energy generated daily will be made. The result will be used to scale the CAES system size. Then different type of compressor and heat recovery methods will be analyzed to find the best efficiencies. The highest efficiency compressor and heat recovery method will be integrated and further improvements will be made wherever possible. The performance of the designed system will be simulated using MATLAB and its efficiency compared against the average performance of current systems. If the result is satisfactory the project can be considered as completed. Otherwise the system will be redesigned until its performance is satisfactory. The outcome of the project is to have a suitable CAES system designed for individual household storage of solar energy. Therefore this research paper will provide a result of the specification for compressor and turbine in CAES system to sufficient supply energy to household and stay off grid from electricity utility company.

Keywords: Compressed Air, Energy Storage, Small scale, Renewable energy

1. Introduction

Fossil fuel will be run out within the next 41 years worldwide [1]. Therefore renewable energy is needed to overcome the issues. Engineers are improving the renewable energy system to make it more efficient and better sustainability. Renewable energy is a system to generate the energy from natural resources such as water, wind and sun [2]. Renewable energy technology also called as microgeneration or low-carbon technology. Renewable energy has been used in large scale or small scale for household.

Solar panel is a common source of renewable energy for households. In many countries, Feed-in tariffs has been use for household renewable energy system. Feed-in tariffs is a system where renewable energy generated by household will be sent back to the power plant. The energy sent back to power plant will be treated as selling with the same price of buying the energy. The purpose of Feed-in tariffs is prevent the house didn't have energy during night time as solar panels only generate energy during day time so Feed-in tariffs will prevent this happen by buying energy from renewable energy generator and continuously selling energy to household. [3]

However Feed-in tariffs can result in huge energy losses when the generated energy has to be send back to power plant. Based on online photovoltaic website's calculator, the losses of energy are 10.62% of energy for energy travel from house to power plant. For example, using solar panel peak performance voltage (415V), the voltage dropped 29.5V.

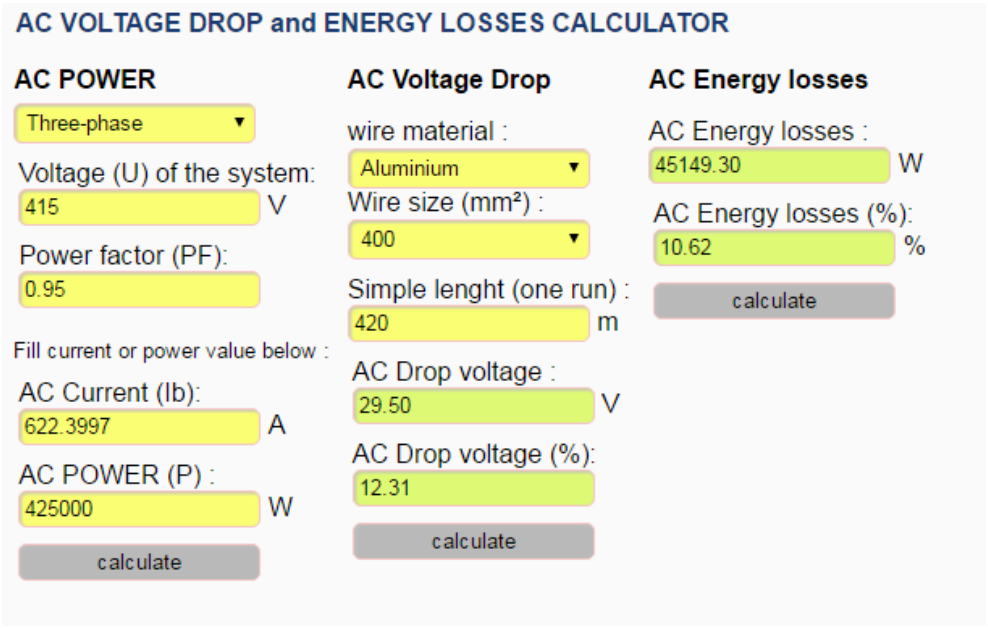


Figure 3: Energy losses Calculator. [13]

To overcome the energy losses caused by current travelling through the grid, one of the way is to store the renewable energy onsite in the house and use it when the solar panel is unable to generate energy when sunlight is unavailable.

Energy storage is the capture of *energy* produced at one time for use at a later time. Energy storage is a useful concept however it is still comparatively unexplored. [4]

There are several mechanical methods to store electric energy. The methods are pumped hydro system, flywheel and compressed air system. Pumped hydro energy storage system is store energy in the form of water in the upper reservoir. The water is pumped from a lower reservoir during the off peak period of energy usage. When peak period of energy usage, the energy is generated by releasing stored water at upper reservoir through turbines. However water pumped require a large space to store the hydro so it is not suitable to be install in house [5]. Flywheel energy storage system is convert the electric energy to kinetic energy. The kinetic energy will rotate a spinning mass (rotor), where the rotor will spin frictionless in a vacuum enclosure. The energy of flywheel only could supply a short-term backup power, therefore it is difficult to supply long term energy to houses [6]. Compressed Air energy storage system is use the excessive energy to compress air into sealed place and release it through turbine to generate energy when energy is needed. It require a space to store air and able to supply long term energy by depending on amount of air compressed [7].

Compressed Air Energy Storage (CAES) is one of the technique of storing energy in the form of air by using the potential energy of compressed air. When energy generator generated excessive energy, it will be used to run compressors to pump air into a storage cavern. The air will be release when electricity is needed. The air will be expanded through a gas turbine expander and energy will be generated by the turbine.

In this project, the study aim to design a small scale compressed air energy storage that is suitable for an individual household with solar renewable energy as power source and able to stay off grid from electric utility company. In order to design the CAES system, the compressor, heat exchanger and gas turbine are studied to determine which type are the most suitable.

The scope of project will be limited to Matlab simulation. The reason is because the lack of equipment in university and it is costly to do purchase the equipment for practically testing.

2.0 Research Methodology

2.1 Research

In Malaysia, the renewable energy commonly used by household user is solar energy. Data collected is based on the size of solar array which is suitable for household. Due to the privacy of solar user, the data are collected from a solar company named DICTROLIC SOLAR TECHNOLOGY [8]. The data show the energy generated by the household size solar array daily in a month.

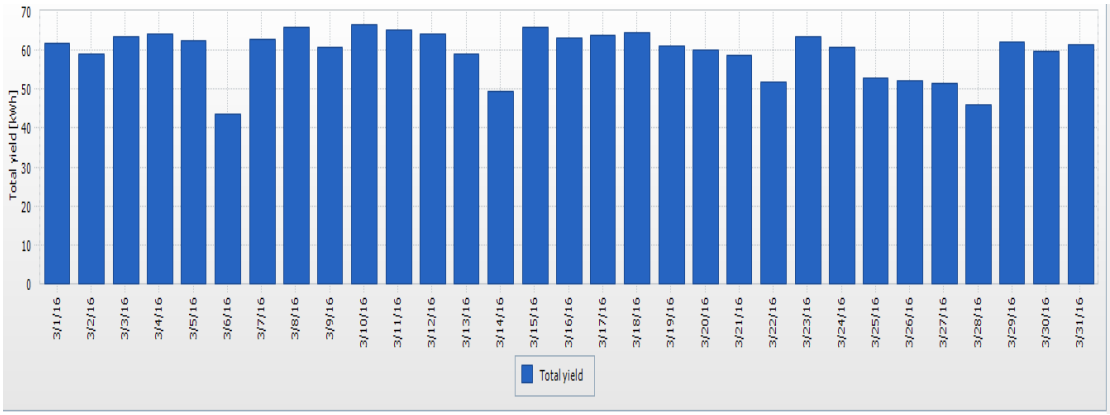


Figure 2: energy generated by 12kWh solar array, data collected from Ditrolic Solar Technology.

The minimum energy generated in a day is chosen to be use as the energy supply to the compressor motor. The minimum energy generated is 44kWh and the purpose of choosing it is to ensure the designed CAES system is able to supply the daily energy need with the lowest energy sources supply from solar panel. The maximum energy generated by solar panel is used to determine the size of air storage tank.

BERNAMA showed the average energy consumption of Malaysia household monthly which is 251kWh [9]. This value will be compared to the daily energy generated by the small CAES to determine the sufficient of energy supply the energy needs for household.

Compressed air energy system have 2 major components which are compressor and turbine. There are 4 type of compressor which are centrifugal, rotary screw, high speed and low speed reciprocating compressor. Each compressor has different efficiency and the efficiency is in range.

Table 1 : type of compressor and efficiency of it [10].

Type of Compressor	Efficiency, n
Centrifugal	0.70 – 0.85
Rotary screw	0.65 – 0.75
High speed Reciprocating	0.72 – 0.85
Low speed Reciprocating	0.75 – 0.90

For turbine, due to the short of information about gas turbine. The efficiency of gas turbine will be use is 60% which is 0.6 [11].

Beside compressor and turbine, heat recovery system is important to the system by improving the efficiency. Heat recovery absorb heat from compressed air after the compressor and store the heat energy in the heat recovery system. It will release the heat back to the air before the air is used to generated energy from the turbine. There are 3 type of heat recovery which are vertical flat panel, horizontal flat panel and cellular.

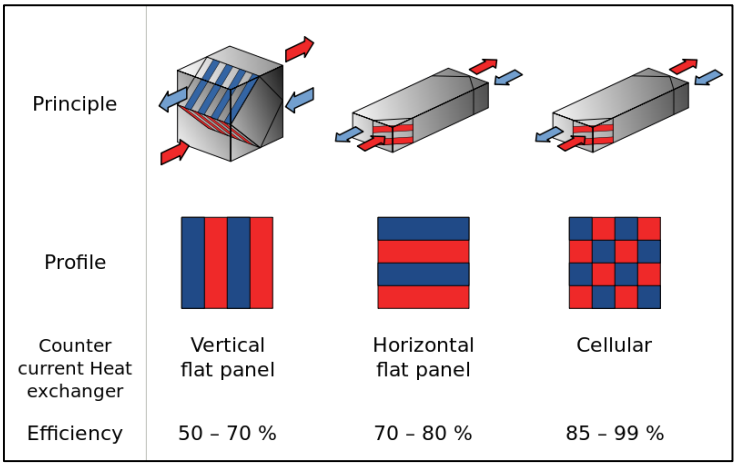


Figure 3: 3 types of counter flow heat recovery air-to-air system.

2.2 Calculation

2.2.1 Compressor

Compressor consumes energy that generated by solar panel. Compressor changes the pressure and temperature of air when it compressed. The enthalpy of the air will increase and the increased value will be used to determine the power of compressor. The compressor power input is depend on the energy generated by solar. Therefore the mass flow rate of air required by compressor will be calculated to determine the size of the compressor. The compressor power will multiply with the efficiency of compressor based on the type of compressor [10].
The formula to use for compressor is

$$P \; x \; \eta_c = m \; (\; h_2 - h_1)$$

Where,
P = Power input for compressor, kWh
η_c = Efficiency of compressor.
m = Mass flow rate of air. kg/h
h_2 = Enthalpy of air at compressor outlet.
h_1 = Enthalpy of air at compressor inlet.

2.2.2 Heat recovery

Heat recovery is use to recovery the heat from compressor and store it. The heat will be used to heat the air before the air enter into turbine. Temperature of air will affect the enthalpy of it. When the compressed air leave compressor, the temperature of it will be absorb by the air in heat recovery. The compressed air will enter to heat exchanges before enter to turbine for increase the temperature of the air. The higher temperature of air, the higher enthalpy of the air. When compressed air enthalpy increased, the power generated by turbine will increase. The temperature of recovery air will based on the efficiency of the type of compressor [12].

Heat recovery formula is

$$\eta_{he} = \left(\frac{T_{he} - T_1}{T_2 - T_1} \right)$$

Where
η_{he} = efficiency of temperature transfer
T_{he} = temperature of air in heat exchanger after heat exchanges
T_2 = temperature of compressed air before heat exchanges
T_1 = temperature of air in heat exchanger before heat exchanges

2.2.3 Turbine

In CAES system, turbine is used to generate energy to supply the energy needs of household. The amount of power generated will be based on the mass flow rate and the change of enthalpy before and after turbine [10].

Turbine formula is

$$P_t = m\ (\ h_4 - h_3)\ x\ \eta_t$$

Where
P_t = Power generated by turbine, kWh
m_t = mass flow rate for turbine
h_4 = enthalpy of air after turbine
h_3 = enthalpy of air before turbine

2.3 Simulation

Simulation used in this project is Matlab simulation. Matlab simulation is used to obtain the outcome of this project and compare it. Matlab simulation can only simulate formula and get result based on formula keyed in. However Matlab simulation is advantage on changing the input value. The minimum and maximum mass flow rate for compressor will be determine by Matlab simulation's graph.

For compressor, the 4 type of compressor's efficiency will key in to the Matlab and will generate 4 different graph. Each graph will provide the maximum and minimum mass flow rate for the compressor. The maximum and minimum mass flow rate will be used to determine the size of air storage tank and minimum air stored in a day. Different compressor will have different result of it. The minimum air stored in a day value will be used in simulation for turbine power output. Then the power output is in term of hour so it need to times with the total hour in a day to get the minimum total energy generated by turbine. The result will then compare to the average energy consumption by household to check the energy generated able to supply the energy needs for household.

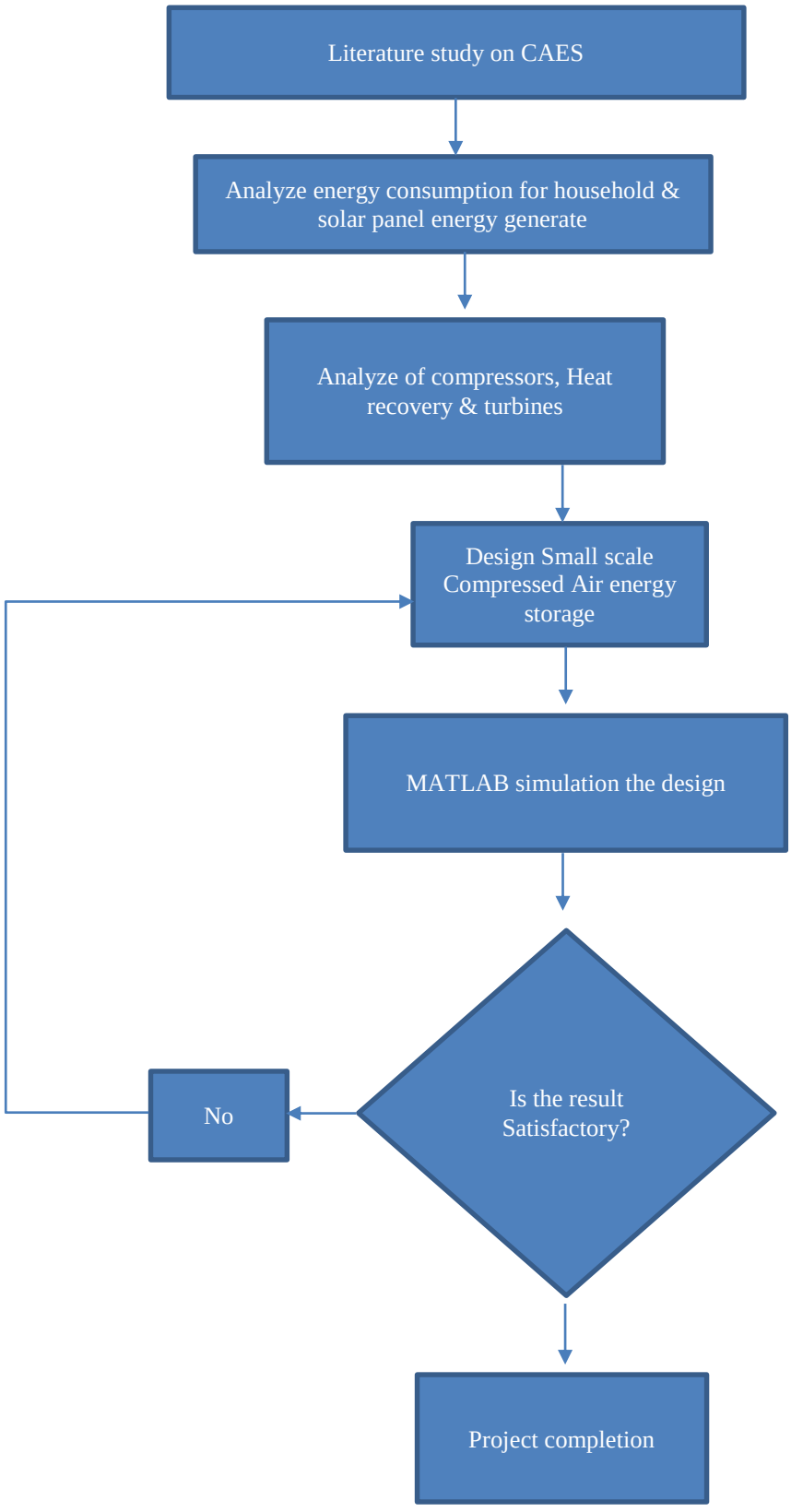


Figure 4: flow chart of the project.

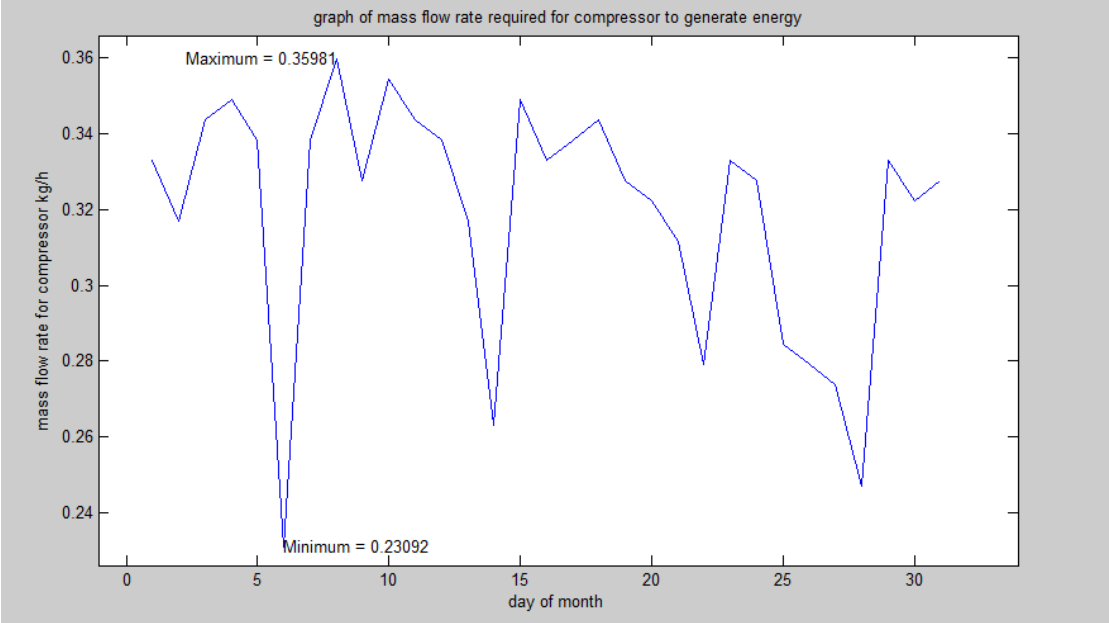
3.0 Results & Discussion

In this project, the enthalpy of air in each stage is needed to be determine for calculation purpose. Outdoor air or air before compressor temperature is fixed and the pressure of it is fixed too. By using the common compressor's pressure ratio 3.5, the temperature of air after compression can be found by using formula. The result of all stage temperature, pressure and enthalpy is shown in table below.

Stages	Temperature	Pressure	Enthalpy
T_1	**34**	**1**	**36.2702**
T_2	**53.5**	**3.5**	**55.473**
T_3	**50.5048**	**3.5**	**52.44**
T_4	**34**	**1**	**36.2702**

Table 2: Temperature, pressure and enthalpy of air in different stage.

By using Matlab simulation to determine the result for this project, the Matlab also able to determine the maximum and minimum mass flow rate of air for different compressor.



Graph 1: result of MATLAB simulation.

Beside of maximum and minimum mass flow rate of air, others result that generated are the total air stored in a day with 25% of safety factor, the minimum air stored by using the minimum mass flow rate and energy generated by turbine in hour or day. The air storage tank size will be generate by using the total air stored with 25% safety factor.

Table 3: result of 4 compressors generated by MATLAB simulation.

	Centrifugal	Rotary screw	High speed reciprocating	Low speed reciprocating
Min Mass flow rate (kg/h)	**0.2169**	**0.1959**	**0.2197**	**0.2309**
Max Mass flow rate (kg/h)	**0.3380**	**0.3053**	**0.3424**	**0.3598**
Total air stored (with safety factor of 25%) (kg)	**3.3800**	**3.0529**	**3.4237**	**3.5981**
Air tank size (m^3)	**2.61**	**2.36**	**2.65**	**2.78**
Minimum air stored (kg)	**1.7354**	**1.5675**	**1.7578**	**1.8474**
Power generated by turbine (kWh)	**0.7015**	**0.6337**	**0.7106**	**0.7468**
Power generated by turbine (kWh) per day	**16.8371**	**15.2077**	**17.0543**	**17.9233**

Average monthly power consumption of household in Malaysia is 251kWh. After divided to 31 days, the power consumption daily is 8.097kWh. Based on the results found, theoretically solar panels can help users' house off grid from electricity utility company. The solar array used in this project is 12kW size, and the result is oversized. Therefore this designed CAES might work on smaller solar array size and still able to make it off grid from electricity utility company.

4.0 Conclusion

In conclusion, the energy generated by solar panel is sufficient to be stored by small scale compressed air energy storage system that designed above. Different compressor has different efficiency therefore the mass flow of intake air has to set in the range calculated by Matlab. Since 4 type of compressors are sufficient to stored and supply the energy require by household, it show household with installed the correct amount of solar panel and the CAES system will be able to completely off grid from electricity utility company.

In this project, the value used is minimum energy generated by solar panel for that day. The assumption can be made is that day was a rainy day therefore the energy generated is lowest compare to other days. It shown that the size of air tank is possible to reduce if more data is collected and more factor are put in consideration. The mass flow rate calculated is based on the minimum energy generated which mean the air stored with minimum energy generated will be completely consumed in a day. However, the size of the tank is designed based on the most energy generated by solar panel in a day, which mean during the rainy day the CAES will not have any problem on shortage energy supply to the household.

The air storage tank will design according the type of compressor used. However, the air consumed daily is the lowest energy generated. Including a pressure gauge and pressure relief valve in the air storage tank as safety purpose when the air overly stored. So the pressure relief valve will releases the extra stored air out from air

storage tank. The extra stored air can be used in others purpose in the future, such as stop the compressor work and send the exceed energy generated by solar panel to electricity utility company.

References

[1] M. Pehnt , "Dynamic life cycle assessment (LCA) of renewable energy technologies." Renewable energy. Vol. 31, pp. 55-71, Jan 2006.

[2] M. Chandler. (2008, Jan. 1). *It's About Forty Years Until the Oil Runs Out* [Online]. Available: https://www.gsb.stanford.edu/insights/its-about-forty-years-until-oil-runs-out

[3] K. Y. Lau et al. "Grid-connected photovoltaic systems for Malaysian residential sector: Effects of component costs, feed-in tariffs, and carbon taxes." *Energy*. vol 102, pp. 65-82, May 2016.

[4] D. Connolly, "A Review of Energy Storage Technologies: For the integration of fluctuating renewable energy." unpublished.

[5] T.M. Letcher, "Chapter 2: Pumped Hydroelectric Storage," in Storing Energy: with Special Reference to Renewable Energy Sources, Netherlands, 2016, pp25-26.

[6] H.C. Liu, J.H. Jiang, "Flywheel energy storage—An upswing technology for energy susta-inability." Energy and buildings vol 39.5, pp. 599-604, May 2007.

[7] M. Ragheb, "COMPRESSED AIR ENERGY STORAGE," unpublished.

[8] http://www.ditrolic.com.my/

[9] I.Ali. "Cooling Appliances Uncool For Environment. Internet: http://www.bernama.com/bernama/v3/printable.php?id=676828, June. 29, 2012. [Sept. 8, 2016].

[10] J.M. Campbell, "Gas Conditioning and Processing, Volume 2: The Equipment Modules" , 9th Edition, 2nd Printing, Editors Hubbard, R. and Snow–McGregor, K., Campbell Petroleum Series, Norman, Oklahoma, 2014.

[11] V.Andiappan,R. R. Tan, K. B. Aviso, and D.K.S. Ng, "Synthesis and optimization of biomass-based tri-generation systems with reliability aspects," Energy, vol. 89, pp. 803-8181, Sep.2015.

[12] A. Kim. (1986, Jan)." Performance of an Air-to-Air Heat exchanger and an Exhaust Air Heat Recovery Heat pump." *Building Research Note.* [Online]. Available: http://web.mit.edu/parmstr/Public/NRCan/brn235.pdf [Sept.9,2016].

[13] "Electricity losses : voltage drop and energy losses free online calculator for AC and DC Power; electrical wire drop voltage quick calculation, cable energy losses, resistive heating, for three phase and single phase wiring", *Photovoltaic-software.com*, 2016. [Online]. Available: http://www.photovoltaic-software.com

eureca 2016 – Conference Paper
Paper Number 2ME21

Flywheel Energy Storage System

Muhammad Nur Redzuan bin Abadanjumi

School of Engineering, Taylor's University, Malaysia
muhammadnurredzuanabadanjumi02@sd.taylors.my

Abstract
The flywheel energy storage system is an initiative in searching another way of storing energy other than electrical battery. The energy stored is in the form of kinetic energy that will continuously rotate until the all the energy have either been transferred or loss to the surroundings. Three aspects that affect a flywheel storage capability are rotational velocity, strength of material and shape. To test this aspect, five case was generated using Solid work before being analysed further using ANSYS. The process during analysis involved the finding of the equivalence stress, maximum rotational velocity and finally the energy that could be stored in the geometry. In ANSYS simulation case 3 (annular disk) with solid filling have the highest energy storage capacity of 56.41MJ which clearly satisfy the energy usage per day in Malaysia (30MJ). However, to introduce a new design in which the flywheel radius could be change according to the power received by the electric motor case 6 geometry is selected (hollow shape). Even though the results garnered by this case unfavourable the geometry flexibility allowed the integration process to be implemented easily. By changing the radius, the structure can reduce the amount of torque needed to be exerted by motor during low sun intensity period while maintaining the desirable angular velocity.

Keywords: Flywheel Energy storage, kinetic energy, radius, simulation and torque.

1. Introduction

Depletion of non-renewable energy and the increase for energy demand causes researcher worldwide to sought alternative ways in which energy can be harvested. As time progressed many of these alternatives energy was discovered such as solar energy, wind powered turbine and many more. However, alternative energy sources are usually intermittent in nature and are affected by seasonal change and the region where it was installed [1]. To solve this problem a storage system is needed to store the harvested energy and also channeled it back whenever it is required. The most used storage system is the electrical storage system (chemical battery storage) which have the advantage of cheap initial investment and a well develop technology that could guaranteed it reliability [2]. The disadvantages of this storing techniques are chemical degradation which shorten it life span and chemical used may harm the environment. Table 1 below listed some of the alternative option in storing energy, in which this paper will covered the application of flywheel energy storage system in storing sufficient energy for the use of a household.

Table 1 – List of storing energy methods [3]

Technology		Typical Nominal Power	Discharge time	Respones Time	Efficiency	Lifetime
Pumped Hydroelectric Energy Storage		100-4000 MW	6-24 h	10s -3 min	65-85%	30-75 years
Compressed air energy storage		25-30000 MW	4- 24 h	3-15 min	50-85%	20-40 years
Battery	Flow Batteries	25 kW-10 MW	1-8 h	30 - 100 ms	65-85%	2-10 years
	Lithium Ion	10 kW - 10 MW	10 min - 1 h		85-90%	
	Lead Acid	50 kW - 30 MW	15 min – 4 h		70-80%	
	Sodium Sulphur	50 kW - 30 MW	1-8 h		75-90%	
Supercapacitors		10 kW - 1 MW	1s - 1min	5-10 ms	85-95%	40 years
Superconduction Magnetic energy storage		1 MW - 100 MW	1s - 1min	5-10 ms	85-95%	30-40 years
Flywheels		10 kW - 20 MW	1s - 1 h	5-10 ms	85-95%	20 years

Flywheel is a circular like device that have the capability of storing or discharge energy in the form of kinetic energy. A flywheel energy storage system generally has five components. First, the power input as this research focusses on storing renewable energy thus solar power are selected due to its availability in Malaysia all year long. Next, the motor use to rotate the flywheel to convert electrical energy to kinetic energy. Electrical motor is highly dependent to its power source thus it performance such as torque and speed will severely affect whenever there is any disruption at the power source. Next is the flywheel itself followed by the generator which convert the kinetic energy to electrical energy when it is required. Finally, the power output in which the electrical energy generated will be transferred to any electrical appliances.



Figure 1 – Flywheel energy storage general components.

There are three aspects that influence a flywheel energy storage system capability. First is the angular velocity as at a higher rotation speed more kinetic energy could be stored by the system. However, it will have a significant effect on determining the structural design especially the shaft and the bearing connection in order to reduce the energy loss due to friction. To deal with the loss of energy through friction, magnetic bearing was introduced into the design. Magnetic bearing (either passive or active) allowed the flywheel to levitate resulting in less energy loss at the shaft due to friction [4-8].

Second aspects will be the shape/ geometry of the flywheel as the amount of kinetic energy stored are linearly proportional to its polar moment of inertia. A body ability to resist any changes due to the change of angular acceleration is called the moment of inertia [1]. The third aspect is the material strength as at high rotation the amount of stress exerted onto the system will also increase thus a strong material is required [9]. The formula used to find the kinetic energy stored and stress on the system would further supports the aspects mention above.

Equation below shows two of the flywheel design aspect and how they are related to each other. Newer flywheel design usually emphasizes more on increasing the rotational speed and are generally lighter compared to old flywheel design. This preference was contributed by the amount of energy that could be stored as increasing it velocity will have a more significant affect rather than changing it polar moment of inertia.

$$E_k = \frac{1}{2}.I.\omega^2 \quad (1)$$

E_k is the amount of kinetic energy
ω is the angular velocity
I is the moment of inertia for the object

Hoop stress should be taken into consideration in the design as it is important to determine the amount of energy that could be stored safely before the structure collapsed or break [9,10(12)].

$$\sigma_t = \rho r^2 \omega^2 \quad (2)$$

σ_t is tensile stress
p is the density of the object
r is the radius
ω is the angular velocity

Current produce by a solar panel is highly dependent on the solar intensity for the day. Resulted in the electrical supply to the motor to be varied, this in turn will affect it torque capability. A DC motor torque is affected by armature current supplied into it refer to equation 3. T_g is the electromagnetic torque and to obtain the mechanical torque, the value for T_g have to be subtracted with the mechanical losses. While an AC motor torque value is affected by rotor current, flux for producing emf and its power factor refer to equation 4. To address the issues above a flywheel with a design that

could change its own torque value by changing its own radius was proposed and study. The design should also have the capability to stores energy for the use of a household in Malaysia.

$$T_g = k_a \phi I_a \quad (3)$$

$$k_a = \frac{P.Z}{2\pi.A}$$

Φ = Flux from poles
I_a = Armature current
k_a = Constant for a machine

$$T_{ac} \propto I_2 cos\Theta_2 \quad (4)$$

T_{ac}= torque produced by the induction motor
I_2 = rotor current.
Θ_2 = power factor

The research will simulate different geometry in which to determine the energy storage capacity using Ansys. The objectives of this research are as listed:

1. To conceive and design a small scale flywheel energy storage system comparable to electrical batteries for a household use.

2. To assess the reliability and performance of this flywheel energy storage system using simulation.

2. Methodology

For this research in order to obtain a flywheel design that complied with the household demand several step have to be followed through. First identify the amount of energy used by a household in Malaysia per day and targeted household appliances that will be supplied. Ansys analysis is then conducted to find the appropriate geometry which could withhold the amount of energy without shattering or break. Incorporate the change of motor torque due to power supply availability (intensity) into the finalized design.

2.1 Power usage for Malaysia households.

Malaysian household use a total of 251 kWh per month. As mentioned earlier the power input for the system will be supplied from the solar panel as solar energy is easily accessible in Malaysia. Below are the steps to find the amount of energy needed to be stored in the flywheel energy storage system.

1. Determine the household energy consumption in Malaysia (251 kWh per month).

2. Find the AC rating as household appliance use alternating current.

   Use the formula –

   $$AC\ rating = \frac{Avg\ kWh\ per\ month/30days}{Hour\ of\ sunshine\ per\ day} \quad (5)$$

3. DC rating (or the current produce by generator) could be determine using the AC rating formula

   Use the formula –

   $$DC\ rating = \frac{AC\ rating}{derate\ factor\ (values\ varies\ from\ 0.8\ to\ 0.85)} \quad (6)$$

4. DC rating will provide the power generated by the solar panel generator in terms of kilowatt. To convert it into joules the generated power will have to be multiplied by 24 hours and assuming the energy loss from conversion of electrical to mechanical energy is negligible. The final answer gave the amount of kinetic energy required to be stored by the flywheel.

   $$E_k = DC\ rating\ x\ 24\ hours \quad (7)$$

2.1.1 Power usage for household appliances

Categorizing household appliances according to its power consumption is an essential step since the collective amount of energy could be stored within the flywheel is finite and limited. Table 2 below is a list of household appliances alongside their respective power consumption. From their power consumption we could determine to which appliance should the stored energy be used for.

Table 2. House hold appliances and their power consumption

Appliance	Watts	Appliance	Watts
Central Air Conditioner NA	5,000	Electric blanket	200
Electric Clothes Dryer NA	3,400	Shaver	15
Oven	3,000	Waterpik	100
Hair Dryer	1,538	Well Pump (1/3-1 HP)	480-1200
Dishwasher	1200-1500	Laptop	60-250
Coffee Machine	1,500	Plasma TV	339
Microwave	1,500	LCD TV	213
Popcorn Popper	1,400	25" color TV	150
Toaster oven	1,200	19" color TV	70
Hot Plate	1200	12" black and white TV	20
Iron	1,100	Stereo	10-30
Toaster	1,100	Satellite dish	30
Microwave	500-1500	Radiotelephone - Receive	5
Room Air Conditioner NA	1,100	Radiotelephone - Transmit	40-150
Vacuum Cleaner	500	**Lights**	
Water heater	479	100 watt incandescent bulb	100
Sink Waste Disposal	450	25 watt compact fluor. bulb	28
Espresso Machine	360	50 watt DC incandescent	50
Dehumidifier	350	40 watt DC halogen	40
Blender	300	20 watt DC compact fluor.	22
Humidifier	300-1000	CFL Bulb (60-watt equivalent)	18
Video Game Player	195	CFL Bulb (40-watt equivalent)	11
Standard TV	188	CFL Bulb (75-watt equivalent)	20
LCD Monitor	80-150	CFL Bulb (100-watt equivalent)	30
Desktop Computer (Standard home/business)	80-120	**Heaters*** **	
Desktop Computer (Gaming)	400-1000+		
Laptop Computer	40-120		
Portable Fan	100	Engine Block Heater NA	150-1000
Ceiling Fan	100	Portable Heater NA	1500
Can Opener	100	Waterbed Heater NA	400
Curling Iron	90	Stock Tank Heater NA	100
Stereo	60	Furnace Blower	300-1000
Cable Box	20	Clothes Dryer - Gas Heated	300-400
Clock Radio	7	Well Pump (1/3-1HP)	480-1200

Appliance	Watts
Hedge trimmer	450
Weed eater	500
1/4" drill	250
1/2" drill	750
1" drill	1000
9" disc sander	1200
3" belt sander	1000
12" chain saw	1100
14" band saw	1100
7-1/4" circular saw	900
8-1/4" circular saw	1400
Refrigerator/ Freezer**	
20 cu. ft. (AC)	1411 watt-hours/day*
16 cu. ft. (AC)	1200 watt-hours /day*
Freezer	
15 cu. ft. (Upright)	1240 watt-hours /day*
15 cu. ft. (Chest)	1080 watt-hours /day*
Cell Phone - recharge	2-4 watts
MP3 Player - recharge	.25-.40 watts

2.2 Flywheel geometry generation using Solidworks

Five different geometry were selected to be used and the model for each cases are developed using Solid works. Each model has the same radius for its rim and also the shaft. Material used to make a flywheel can be either from a composite or isotropic material as for this research the material selected to be used for the model is AISI 1006 Steel (cold drawn). Composite material is often difficult to obtain and the price for it will make it unsuitable with the budget given. The second it was chosen because the data regarding its properties are readily available. The properties for the material are listed in the table 3. Lastly, Taylor's University mechanical workshop have the all the equipment necessary to modify steel based material such as welding equipment and plasma cutter.

Table 3. Material properties for 1006 Steel (cold drawn)

Properties	Value	unit
Modulus of elasticity	205	GPa
Density (ρ)	7.872	g/cm
Poisson's ratio	0.29	-
Yield stress (σ_y)	290	Mpa

Figure 2,3,4,5 and 6 below shows all the geometry use in this study. For the cases three (1 to 3) of it is a full solid geometry while case 4 and 5 is a hollow geometry.

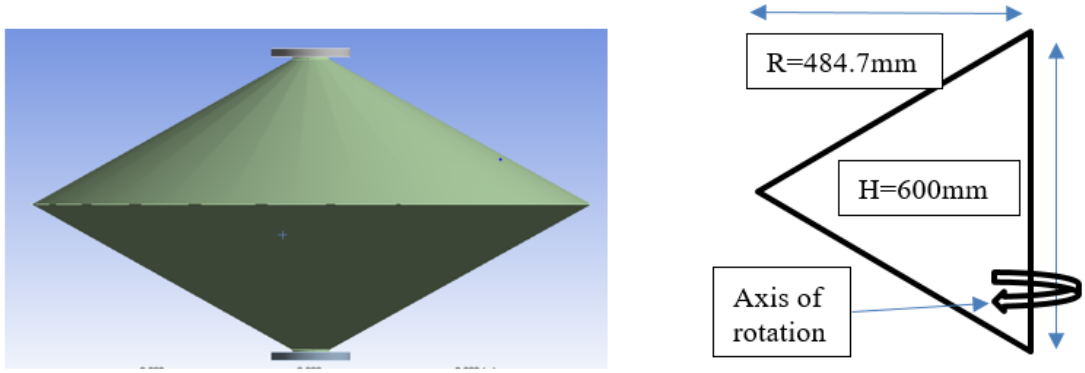


Figure 2. Case 1 flywheel geometry (2D and 3D view)

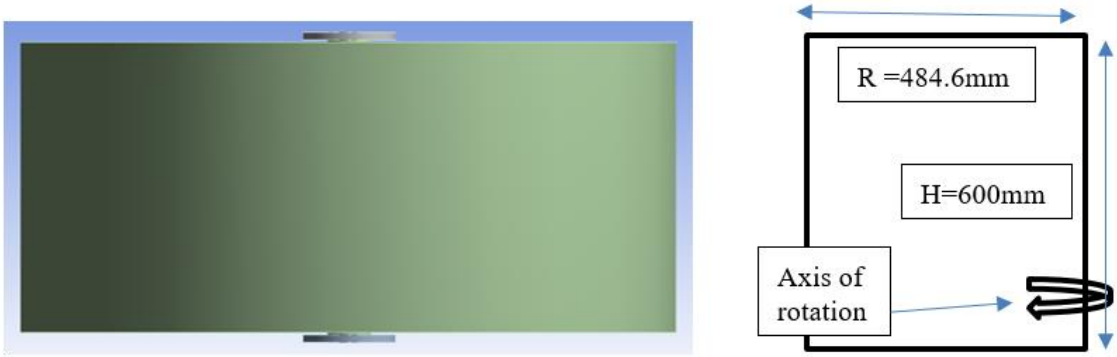


Figure 3. Case 2 flywheel geometry (2D and 3D view)

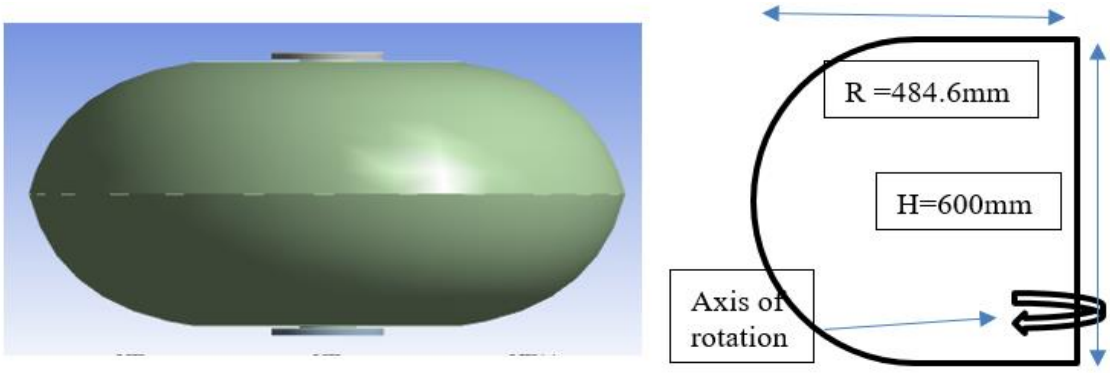


Figure 4. Case 3 flywheel geometry (2D and 3D view)

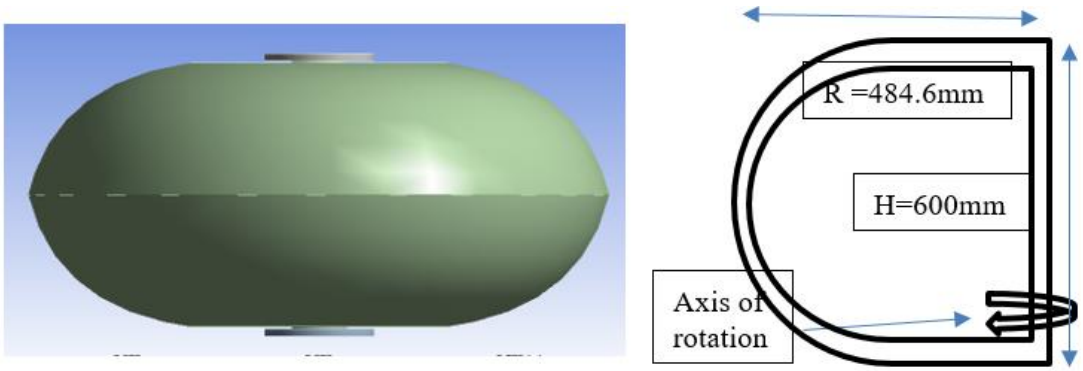


Figure 5. Case 4 hollow flywheel geometry (2D and 3D view)

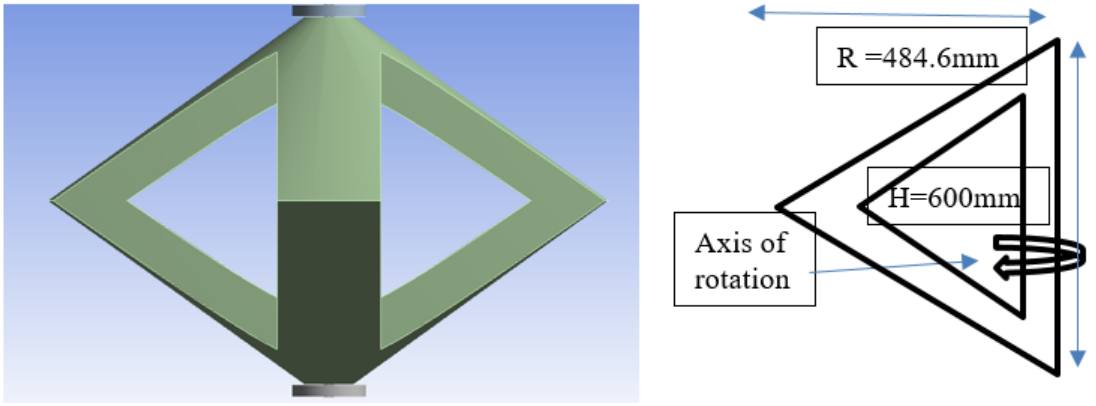


Figure 6. Case 5 hollow flywheel geometry (2D and 3D view)

2.3 Ansys Analysis

After the model for all the cases were generated in Solidworks it was then analyzed using ANSYS. The cases are analyzed to gain the amount of kinetic energy that could be stored, rotational speed, stress distribution and region in which the deformation occur. Three steps were done for each case iteration first modal analysis, secondly transient structure analysis and finally rigid dynamic analysis.

2.3.1 Modal analysis.

Modal analysis is useful in finding the way in which the structure should fail by inputting all the the connection for each part of the structure and how they interact with each other.

2.3.2 Transient structure analysis.

Transient structure analysis is used since the body of the structure could be set into flexible in which stress analysis could be done. Transient analysis requires an input in term of action (movement) that are experience by the structure. For this study, rotation was inputted as the action that occurred and the value magnitude is in rad/s or rotation velocity. From the simulation we could obtain the equivalent stress that could be compared with the material yield strength. The change in rotation velocity will increase the maximum equivalent stress and vice versa.

2.3.3 Rigid body analysis.

Rigid body analysis uses a different setting for its body structure in which it must be set-up to rigid. In this analysis the amount of kinetic energy that a structure could store can be found. After defining all the connection between each component the next step should be to define the action (rotational motion). The magnitude (rotation velocity) for this action could be retrieved from the transient simulation data.

2.4 Introduction of a New Flywheel Design.

Solar energy intensity differs according to time and climate, which in turns affected the power that could be harvested. Thus the motor that were used to rotate the flywheel will have a decrease in torque capability since it receives less current from the solar panel. However, this could be solved if the flywheel design itself incorporate the change of radius mechanism as that would affect the torque needed to spin the flywheel. Two formulas below will further support this argument.

Equation 5 shows the relation between power, torque and angular velocity. Thus if the power is constant both angular velocity and torque will have an inversely proportional relationship.

$$Power = Torque\ x\ Angular\ velocity \tag{8}$$

In equation 6 on the other hand show that radius of an object plays an important roles in reducing the moment of inertia for a shape.

$$I = m\ x\ r^2 \tag{9}$$

I is moment of inertia

m is the mass of the object

r is radius of the object.

In tandem with the all the geometry that was studied in the previous section, this concept was introduced to the selected geometry. The geometry chosen may not be the one which could withhold the most kinetic energy but it should also be feasible enough to have a movement that allowed the change of radius. Thus case 5 geometry was chosen and the final design did have modification in term of inserting hinges to the rim to allow movement and spring mechanism that help in the changing of radius process.

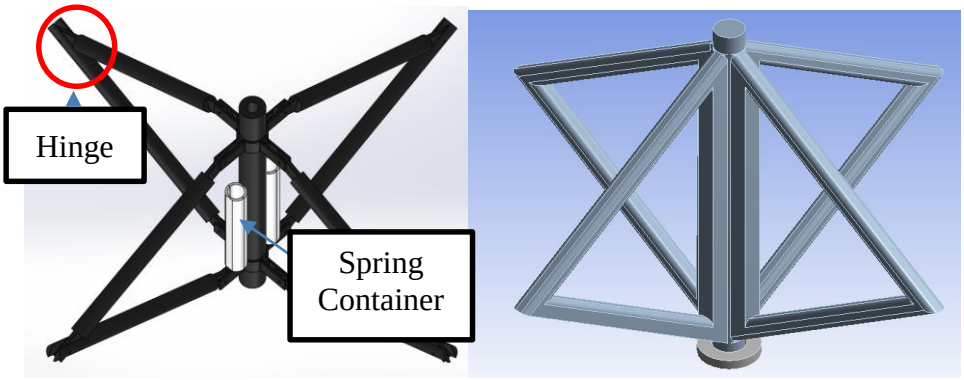


Figure 7. The Solidwork model(left) and the simplified model for ANSYS (right)

3. Results and discussion.

3.1 Power usage for a household.

Malaysian household 8.36 Kwh worth of power every day, however by using equation 1 to 5 it is found that the amount of energy that need to be stored based on the amount of solar energy that may be generated per day is 2.61 Kwh or in term of joules it will be 9.36 MJ. The value is calculated using the assumption that Malaysia receive a total of 4 hours of intense solar energy. Storing 9.36 MJ worth of energy will cause the flywheel energy storage system to be heavy (refers to table 5).

3.1.1 Segregation of household appliances.

To store an exact amount of energy that were used by a household in Malaysia will be very difficult. The solution for the problem is to prioritize low power consumption appliances as the receiver of the energy from the storage system. As a low power rating appliances would be able to operate for hours with the energy stored. For example, if we take geometry 5 (refer to table 6) the amount of energy it could store is around 1.38MJ which is equivalent of lighting up of a 25-watt compact fluorescence for 17 hours in comparison to an air conditioner with a power rating of 1100watts that could only be powered up for around 20.38 minutes with the same amount of energy contained.

Table 5 - household appliances with low power rating

Appliances	Power rating(watts)	Appliances	Power rating (watts)
Portable fan	100	25-watt compact fluorescence bulb	28
Ceiling fan	100	50-watt DC incandescent bulb	50
Can opener	100	40-watt DC halogen	40
Curling iron	90	20-watt DC compact	22

		fluorescence	
Stereo	60	CFL Bulb (60-watt equivalent)	11
Cable box	20	CFL bulb (40 watts equivalent)	20
Clock radio	7	CFL bulb (100-watt equivalent)	30
Cell Phone -recharge	2-4	MP3 player- recharge	25-40

3.2 Flywheel geometry and analysis.

Five case study and one new design were made to further analyzed the effect of geometry on the structure integrity and the maximum amount of energy it could store. The finding was then summarized in table 5.

Table 6 – The results obtained from the ANSYS simulation.

Items	case 1	case 2	case3	case4	case 5	case 6 (T)
max rotational speed (rpm)	4698	496	5634	3447	2865	3146
Mass (kg)	1406.33	3933.57	2913.83	960.52	417.09	67.84
Kinetic energy (MJ)	14.19	0.73	56.41	9.34	1.38	0.16
Max. equivalent stress (Mpa)	290	290	290	290	290	290
E/mass (kJ/kg)	10.09	0.19	19.36	9.72	3.31	2.36
E/mass (W-h/kg)	2.81	0.05	5.38	2.59	0.92	0.65

From the table case 3 could withhold the most amount of kinetic energy and this could be attributed to its very high rotational speed and the shape good stress distribution. The good stress distribution allowed the flywheel to increase it rotation velocity without the material yielding, the value comparable to a material yield strength is the equivalence stress. As 1006 steel cold drawn are considered a ductile material thus von Mises yield criterion (equivalence stress) which is a plasticity theory is very suitable to be compared with.

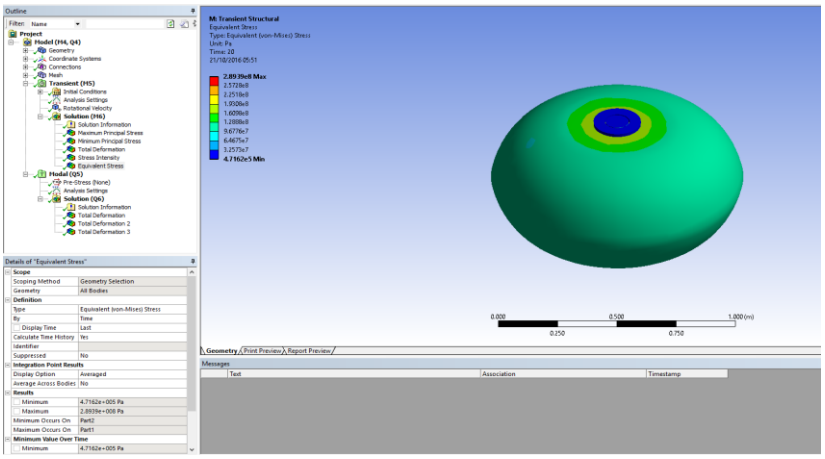


Figure 8 – Shows the equivalence stress distribution throughout case 3 geometry.

Case 2 which has the lowest rotation speed are caused by the structured to fail whenever the speed is increases. The part that failed whenever the simulation is done is where the shaft and the rim is connected (figure 9). The contour shows that as the rim spin the stress accumulated at area in which the rotation force is applied causing it to deform under a high velocity or being exposed to the same stress for a long period of time.

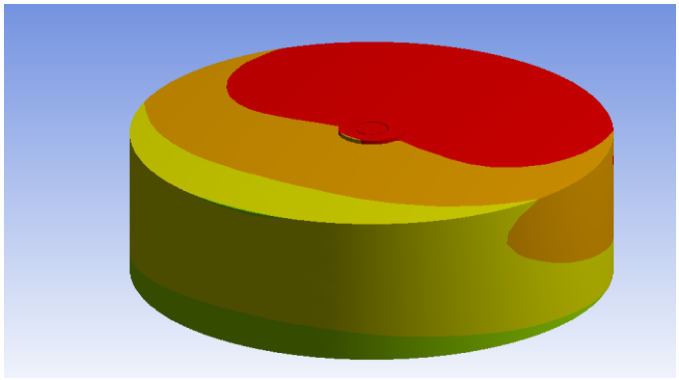


Figure 9. case 2 total deformation contour.

Case 5 uses a hollow structure in which case 4 and 6 (new design) also have the same structure. The reason why this structure was used is to test the theory of strength to weight ratio to the product deformation rate. For this case 4 have the smallest inner to outer diameter, followed by case 6 and case 5. However, all three cases do not manage to store more energy than a solid model which is case 3.

Case 6 is incorporated with a new feature in which it could change it owns radius depending on the torque able to be given by the motor. The point in which the hinge is situated is lowered down by 35mm. That resulted in the increases of radius from the 484.6mm to 504.65mm. From equation 5 and 6 as the radius increase the torque will be affected which in returns increases the need of power if the angular velocity wanted to be kept the same. A motor (DC or AC) have their own torque capability value which can be calculated using formula 3 and 4. The motor is highly dependent on the armature current (DC) and rotor current (AC). Since solar intensity and availability is directly proportional towards it current production it will cause the

motor to have varied torque capability depending on the solar conditions for that particular day.

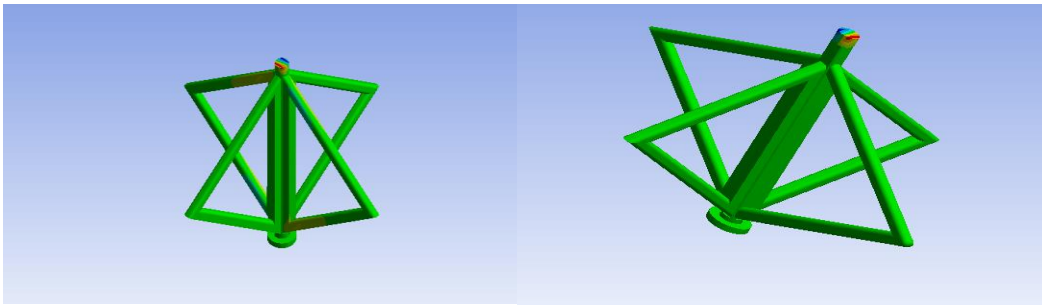


Figure 10. to design in which the right has a bigger radius rather than the flywheel in the left.

7. Conclusions

Flywheel energy storage system could store energy in the form of kinetic energy and there are three aspects that effect the amount of energy it could store. Five different geometry are simulate using ANSYS to garner the understanding in which form does a flywheel energy storage system could store energy optimally. The concept of changing the radius of the flywheel was also introduced as a way to compensate with the ever changing sun intensity that will results in varying degree of power supplied to the motor.

The simulation results for all the six cases shows that if we take into consideration regarding the amount of energy needed to be store to satisfied Malaysian household which is around 9.36 MJ. Only case 1, 3 and 4 geometries is fit for that intended purposes as it could store up energy up to 14.19 MJ, 56.41MJ and 9.34MJ respectively. On the contrary the solid geometry will cause the overall structure to be heavy and since during the simulation the friction at the shaft and bearing are considered to be zero. The inclusion of it may cause the value calculated earlier to be lowered down due to frictional loss and bearing (mechanical bearing only) speed limitation. However, for all three cases it has a solid structure that would prove difficult to implement the change of radius design thus geometry 5 is chosen as the base for the new design. For case 6 (new design), if the design also added up weightage into the system the amount of energy it could store may rise significantly.

References

[1]S. Bankston and C. Mo, "Geometry Modification of Flywheels and its Effect on Energy Storage", *Energy Research Journal*, vol. 6, no. 2, pp. 54-63, 2015.

[2] *Renewables and Electricity Storage roadmap for Remap 2030,* International Renewable Energy Agency, Abu Dhabi, UAE, 2015, pp. 26.

[3] S.Samineni, “Modelling and Analysis of a Flywheel Energy Storage System for Voltage Sag Correction” M.S thesis, Dept. Elect.Eng, Idaho Univ., Idaho, U.S.A, 2003.

[4] Jae-Seok Choi and Jeonghoon Yoo, "Design of a Halbach Magnet Array Based on Optimization Techniques", *IEEE Trans. Magn.*, vol. 44, no. 10, pp. 2361-2366, 2008.

[5] LaunchPoint Tecnologies, "Third generation flywheels for high power electricity storage", Launchpoint Tecnologies, Inc, Goleta, California, 2006.

[6]J. Liu, Z. Ren, S. Wu and Y. Tang, "Theoretical Vibration Analysis on 600 Wh Energy Storage Flywheel Rotor—Active Magnetic Bearing System", *International Journal of Rotating Machinery*, vol. 2013, pp. 1-11, 2013.

[7]R. de Andrade, G. Sotelo, A. Ferreira, L. Rolim, J. da Silva Neto, R. Stephan, W. Suemitsu and R.Nicolsky, "Flywheel Energy Storage System Description and Tests", *IEEE Trans. Appl. Supercond.*, vol. 17, no. 2, pp. 2154-2157, 2007.

[8] A. Canziz, A. Campbell and T. Coombs, "An Evershed Type Superconducting Flywheel Bearing", *Physica C*, vol. 390, no.1, pp. 305-310, 2003.

[9] M.Mathew, “Design of flywheel for improved energy storage using computer aided analysis” Degree dissertation, Dept. Mech. Eng., National Institute of Technology, Rourkela, 2009.

eureca 2016 – Conference Paper
Paper Number 2ME22

A Study of Tower Cranes for Construction Site Applications

Rubinder Singh Bhattal[1*], Edwin Chung Chin Yau[2], Lim Chin Hong[3]
[1-3]*School of Engineering, Taylor's University, Malaysia*

[*]rubinder15@gmail.com

Abstract
There are many types of cranes that are used in the construction industry and one common type would be the tower crane. Tower cranes are needed at construction sites to lift materials desired to complete the structure and accessories of a building. Having a tower crane at a construction site would mean that there should be many safety precautions taken to avoid any damages but often than not, failure on a tower crane do occur. Studying these failures could help in conceiving a solution to avoid such failures in the future and by improving on the current design, it may also aid in that direction. From studying the failures of tower cranes, majority of the failures are due to strong winds and is the main cause of structural failure. This study focuses on the horizontal jib of a tower crane and a 3D model of the horizontal jib is modeled using the SolidWorks software and is then used in the ANSYS software for simulation analysis. Constant resultant force at different angles is applied to determine the critical angles for maximum total deformation and maximum stress on the horizontal jib. The results from the analysis show that the critical angle for maximum total deformation is at an angle of 65^0 as it is in the direction of the triangles of the horizontal jib. Also, the critical angle for maximum stress is at an angle of 25^0 because it is perpendicular to the triangles of the horizontal jib. As a conclusion, the part of the model which has the highest stress is the part most likely to fail and reinforcement on that part would seek to lower the stress value which in return would reduce the failure rate and this would be the future work of this research project.

Keywords: Construction, Tower Cranes, Analysis, Horizontal Jib, Wind Loading

1.0 Introduction

Tower cranes have been around ever since high rise buildings have been developed and have played an important role in lifting the materials needed to complete the structure of the building and also the components in the building. Tower cranes are one type of the many types of cranes and are widely used in the construction industry. In 1949, Hans Liebherr [1] made it possible for tower cranes to move in the horizontal direction and this innovation has been extremely beneficial at that era as tower cranes at that time could only carry loads in the vertical directions and construction workers had to manually unload them there on. His invention had also led tower cranes to be transported easily and could be assembled at the construction site [2].

The tower crane that is studied is the hammerhead tower crane as it is more common at construction sites. This tower crane consists of a mast section and the jib section. The mast section is held vertically by concrete foundation at the ground and has a slewing unit together with an operator cab at the top section. The jib section consists of two parts with the mast section between them. The shorter horizontal jib has concrete counterweights for stability and motors to run the cable for the trolley. The longer horizontal jib has a trolley which moves horizontally along the jib and serves in lifting and unloading the materials. The two jib sections are held firmly by cables that are attached to the tower of the mast section.

The information needed for this study is the failure of a tower crane which is important to aid in the direction of reducing the failure rate of a tower crane. An analysis was done by Nenad et al. [3] to find the reasons of failure of a tower crane which collapsed in a hydropower dam. The tower crane is a hammerhead tower crane and the damages endured led to the removal of the tower crane from the working site. The research done by the author led to a conclusion of four main reasons [4] whereby a tower crane would collapse. The four reasons could be fault in the design, fault in the manufacturing process, wrongly operated, and lastly environmental impacts. The main reason of failure of the tower crane was by the failure of a gusset plate. A 3D model of the gusset plate was done followed by analysis through linear Finite Element Method and experiment on the chemical and mechanical properties of the plate. The results obtained from the analysis and experiment lead to a conclusion that the failure was due to a few reasons which are the gusset plate was not correctly designed and fabricated, the welding done was inappropriate and lastly the stresses endured when the tower crane was operating was higher that it should have been.

Another incident analysis was done by Paul Swuste [5] when an incident was classified as “a normal accident” when the tower crane collapsed. A CE mark was present on the collapsed tower crane which means that is was certified by a body responsible to certify the tower crane in the European continent. Once this certification is given, there will be no other tests or detections of fatigue done on the tower crane. Upon carrying out the analysis on the tower crane’s design, the author concluded that the failure had occurred due to the flexibility of the mast and horizontal jib. The result shows that the values obtained by analysis were much greater than the values given by the design engineers of the manufacturers.

From the two analyses above, it is difficult to know precisely the main reason of the failure of a tower crane so collective failures of tower cranes was done in a report from the Health and Safety Executive (HSE) [6]. This report consists of tower crane incidents from 1999 till 2009. The number of cases reported from those 11 years is 85 cases. The lowest number of cases was in 2001 and the highest number of cases was in 2007. As this study is concern with the horizontal jib only, the cause of failures was separated into two parts which are the horizontal jib and other parts of the tower crane. The other parts of the tower crane consist of components such as the mast section, foundation on the ground, slewing unit and others. The horizontal jib accounts for 27 of the 85 cases (32%) while the other parts account for the remaining 58 cases which were mainly failures in the main mast during erection and dismantling. Failures in the main mast during erection and dismantling are mostly human errors and not structural. Accordingly, the jib is the one component in the tower crane that has the highest concentration of structural failure. The breakdown of the cause of failures can be seen in Table 1 for the horizontal jib and Table 2 for the other parts of the tower crane.

Table 1. Causes of failure for the horizontal jib [6].

Cause of Failure	Number of cases	Percentage (%)
Cable snapped	1	3.7
Overload	1	3.7
Collided	1	3.7
Earthquake	1	3.7
Weld failure	1	3.7
Faulty	2	7.4
Slowing ring spin	2	7.4
Motor brake jammed	2	7.4
Bolt failure	2	7.4
Strong winds	5	18.5
Unknown	9	33.3

Table 2. Causes of failure for other parts of the tower crane [6].

Causes of failure	Number of cases	Percentage (%)
Turn incorrect moment	1	1.7
Earthquake	1	1.7
Bolts over tightened	1	1.7
Shorter mast section	1	1.7
Brake failed	1	1.7
Cable snapped	2	3.4
Overload	2	3.4
Failed hydraulic cylinder	3	5.2
Structure gave way	3	5.2
Foundation failed	3	5.2
Bolts untightened	3	5.2
Extreme weather	5	8.6
Unknown	32	60.3

From Table 1, it is clear that the main cause of failure on the horizontal jib is due to strong winds and looking at Table 2, similarly extreme weather is the main cause of failure for the other parts of the tower crane. This is seen when the unknown

causes are discarded as it does not give any information. From the data collected, the analysis done on the horizontal jib would simulate the wind loadings that the jib would experience in actual situations. The simulation results would show the behavior of the horizontal jib which could then be studied and possibly improved the results to yield a model that could withstand a greater wind loading. The objectives of this research are as follow:

1. Identify the component of the tower crane which has the highest concentration of structural failure.
2. To perform 3D simulation analysis on the identified component as a means to identify the root cause of these structural failures.
3. To propose an improve alternative to the current horizontal jib design that has the potential to reduce the failure rate.

2.0 Methodology

2.1 Design of 3D Horizontal Jib Model

The 3D model of the horizontal jib section is done based on the 280 EC-H16 Litronic tower crane manufactured by Liebherr [7]. This is done to get the dimensions of the model which are given in the datasheet provided by Liebherr. The SolidWorks software is used to draw the 3D section model of this tower crane. The horizontal jib section consists of three parts which are the base, middle triangles and top support. The base has a measurement of 6.4m x 1.5m x 0.08m in a rectangular form. The center of the base has a slant which connects two edges of the base with a thickness of 0.08m as well.

For the middle triangles, the shape of the triangles is in the form of a rod with a diameter of 0.08m and is attached to the inside edge of the base at one end and the other end at the bottom surface of the top support. Next, the top surface also has a rectangular shape and has the dimensions of 6.4m x 0.16m x 0.1m. The midpoint of the top support is located 1.8m from the top surface of the base. Fig. 1 shows the 3D model of the horizontal jib section.

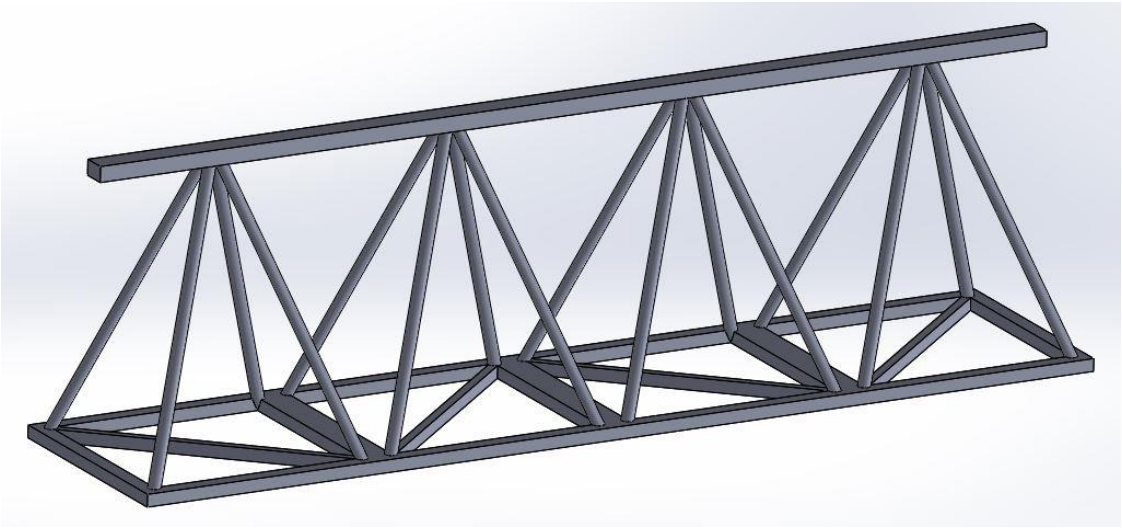


Figure 1. 3D model of the horizontal jib section.

The full model is based on the shortest jib length that the manufacturer has which is about 40m. The full model consists of three parts which are the section model which is mirrored a total of six times, the jib head section and the connection of the cable section. As for the jib head section, it has the same base dimensions as the section model base dimensions. For the middle triangles, two triangles are converged in an upright position to the top support and the other two triangles are also converged to the top support at an angle. All four triangles are with a diameter of 0.08m. The top support of the jib head section has the dimensions similar to that of the section jib except for the length, which is equal to the diameter of two middle triangles which would be 0.16m. Fig. 2 shows the jib head section.



Figure 2. Jib head section.

Moving on to the connection of the cable support, to simplify the analysis, a cylindrical shape is placed at the top surface of the top section of the horizontal jib. It is placed 28m of length of the 40m horizontal jib as seen in the datasheet by Liebherr [7]. The cylindrical shape has a diameter of 0.10m and a thickness of 0.02m. Fig. 3 shows the simplified connection of the cable support. The assembly is done by mirroring the section model by six times and then importing the jib head section into the geometry. The surfaces where the section model and jib head section touches are highlighted in the relation tab. Adding the relation would bring the surfaces together and make the two sections into one body. The next step is to add the connection of the cable support by drawing a circle on the top surface of the top support. The midpoint of the circle is at a length of 28m from the start of the jib. The circle is of 0.10m diameter and it is then extruded by a thickness of 0.02m. Assembling all three of these sections would give a full horizontal jib model which is shown in Fig. 4.

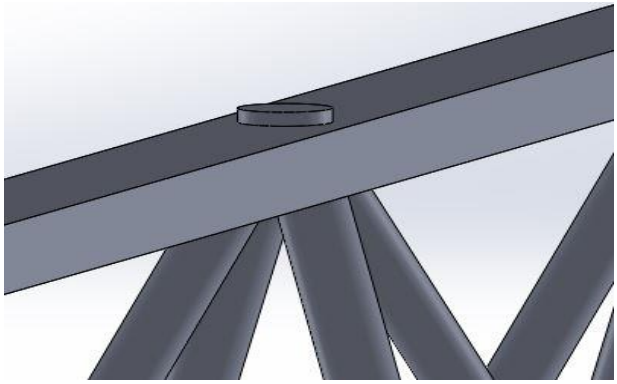


Figure 3. Simplified connection of the cable support.

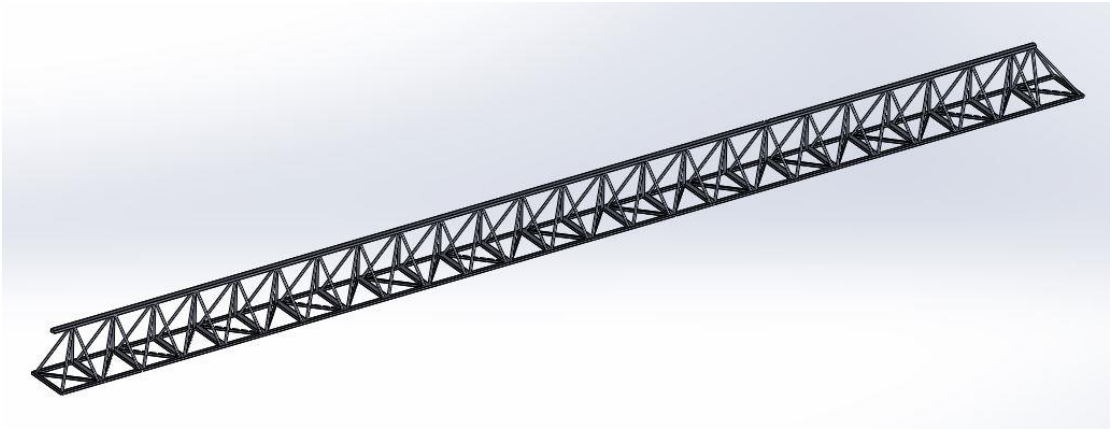


Figure 4. Full model horizontal jib.

2.2 Simulation Analysis of 3D Horizontal Jib Model

2.2.1 Engineering Data

The software used for analysis is ANSYS Workbench. Static Structural is chosen in the Analysis System tab and is placed in the Project Schematic section. The engineering data is then edited to choose the material that the model is made of. The material that makes a tower crane is steel and so the structural steel material is chosen. The material properties such as the mass density, Young's Modulus and Poisson's Ratio are all readily available in the selection of the material. The material properties are shown in Table 3. Moving on, the full model assembled in SolidWorks is then imported in the Geometry section.

Table 3. Material properties of structural steel.

Properties	Values
Mass Density	7850 kg/m^3
Young's Modulus	200 GPa
Poisson's Ratio	0.3
Tensile Yield Strength	250 MPa
Compression Yield Strength	250 MPa

2.2.2 Meshing

The meshing of the model is done by editing the Model section. A new tab would open and under the mesh section where an Automatic Method was selected. The mesh from this is then generated to obtain the Element Quality and Skewness. The element sizing by default is set to 100mm and refinement of the model is done by lowering the element sizing to produce an overall better quality of the mesh. The element sizing is changed to 70mm and 50mm to refine the mesh. As seen from the Table 4, as the element sizing deceases, the element quality increases and the skewness decreases. This shows that the meshing done has an overall good quality.

Table 4. Meshing properties of the horizontal jib.

Properties	Element Sizing (mm)		
	100	70	50
Nodes	128698	244783	455270
Elements	53770	114753	234625
Element Quality	0.7418	0.8150	0.8499
Skewness	0.4558	0.3450	0.2385

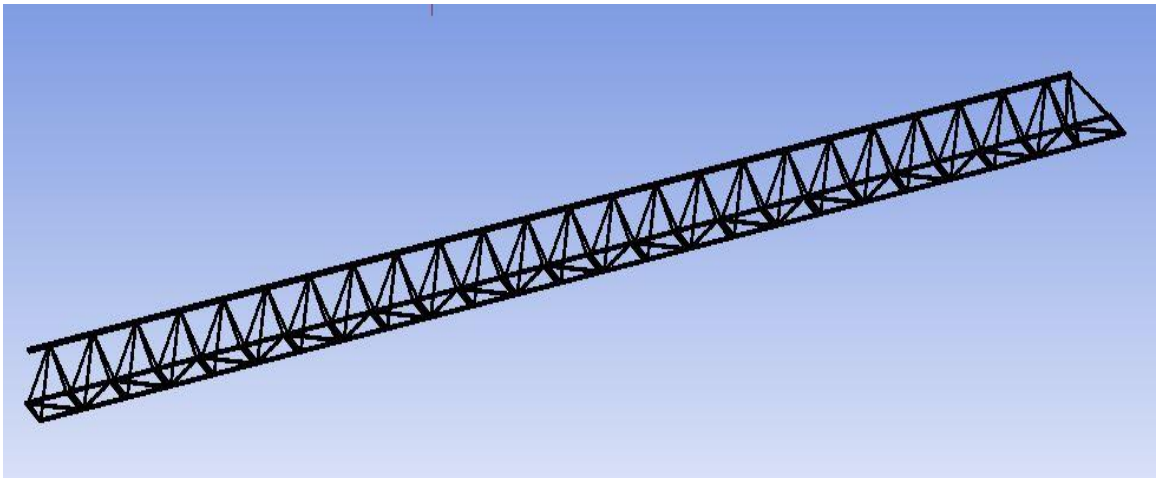


Figure 5. Meshing of horizontal jib.

2.2.3 Boundary Conditions

The boundary conditions are important to pin point the areas on the model that the forces are to be applied and also the areas on the model that has support. The first step is to assign the supports on the full model. The fixed support is placed on the side surface of the base. Next, an elastic support is added to the connection of the cable part. The value for this is gathered from the material properties of the cable. Since the unit for the elastic support in AWB is in N/mm^3, and the unit for stiffness from the material properties of the cable is N/mm^2, the stiffness is divided by the length of the cable. The length of the cable is known from the datasheet given by Liebherr [7].

As for the forces acting on the horizontal jib, one is the standard earth gravity, and the other one is the resultant lateral force. For the standard earth gravity, the entire model is subjected to it and thus it is applied to the entire horizontal jib. The forces added to the horizontal jib are in the x-axis and y-axis direction to attain the resultant force. The initial resultant force was calculated at an angle of 45^0 which would mean that the x-axis force and y-axis force would be identical. At that angle, the resultant force is added until it exceeds the tensile yield stress of the material which is set as structural steel mentioned in the earlier section. Then the resultant force is kept constant but applied in angles from 0^0 to 90^0 with 5^0 increments for each simulation to determine the critical angle at which the horizontal jib would have the highest total deformation and stress. Fig. 6 shows the boundary conditions for this analysis.

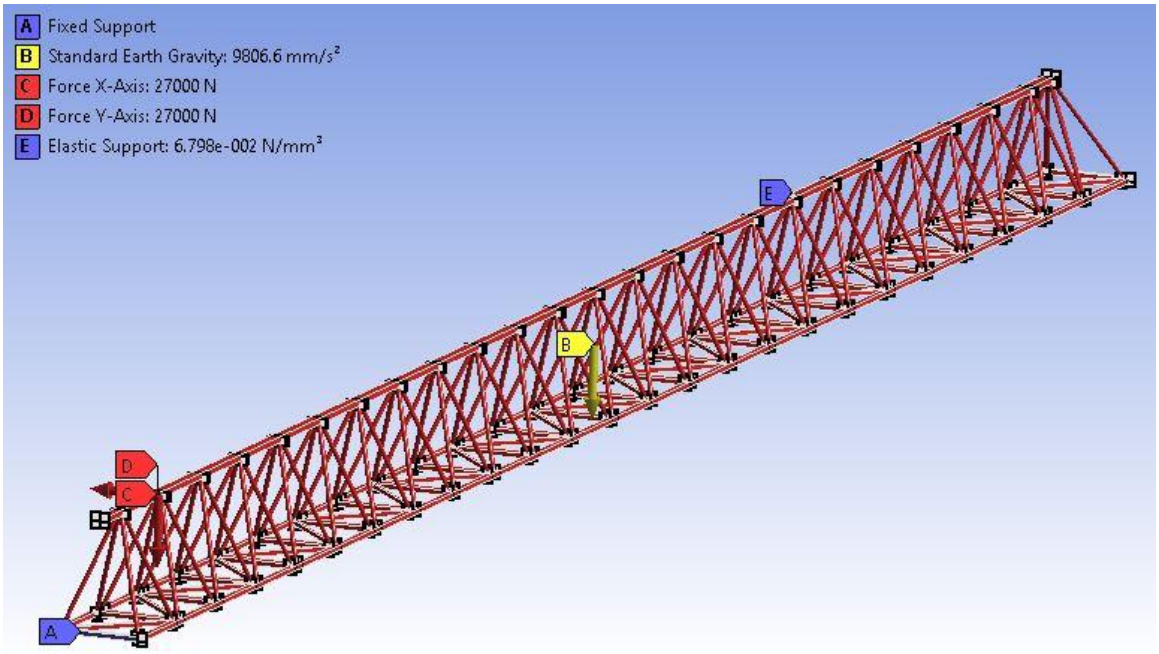


Figure 6. Boundary conditions of horizontal jib.

2.2.4 Simulation Analysis

The cable holding the horizontal jib is simplified by using a cylindrical shape on the top surface of the top support on the horizontal jib. Since there is no cable, the top surface of the cylindrical shape is chosen for the elastic support. The value for the elastic support is gathered from the material stiffness of an Extra Improved Plow Steel (EIPS) grade cable which is commonly used for the derricking cable for the tower crane. The EIPS grade cable has a stiffness of 1960 N/mm^2 and this value is divided with the length of the cable from the Liebherr datasheet to get the value for the elastic support as the boundary conditions of the simulation analysis. The resultant force is only in the lateral direction of the horizontal jib which is on the x-axis and y-axis. The angle for the resultant force is 0^0 at the x-axis and 90^0 at the y-axis. The resultant force is kept constant and is applied at different angles on the horizontal jib to know the critical angles. The values of the x-axis forces and y-axis forces are calculated using the formulas below.

$$F_X = F_R \cos\theta \quad (2.1)$$

$$F_Y = F_R \sin\theta \quad (2.2)$$

$$F_R = \sqrt{{F_X}^2 + {F_Y}^2} \quad (2.3)$$

3.0 Results and Discussion

The simulation would give closure to whether the angle at which the resultant lateral force applied would have an impact on the total deformation and the stress. Running the simulation with no forces added would yield some deformation and stress to be in the initial form. The total deformation and the maximum stress from the simulation are found to be 416.34 mm and 184.32 MPa respectively. This is

acceptable as the horizontal jib would experience some initial deformation and stress as it has a mass and also the standard earth gravity. The angles would be in the range of 0^0 to 90^0 with an increment of 5^0. Angle at 0^0 would mean at the resultant force will be in the direction of the x-axis and angle at 90^0, the resultant force would be in the direction of the y-axis. Directions of the forces are shown in Fig. 7.

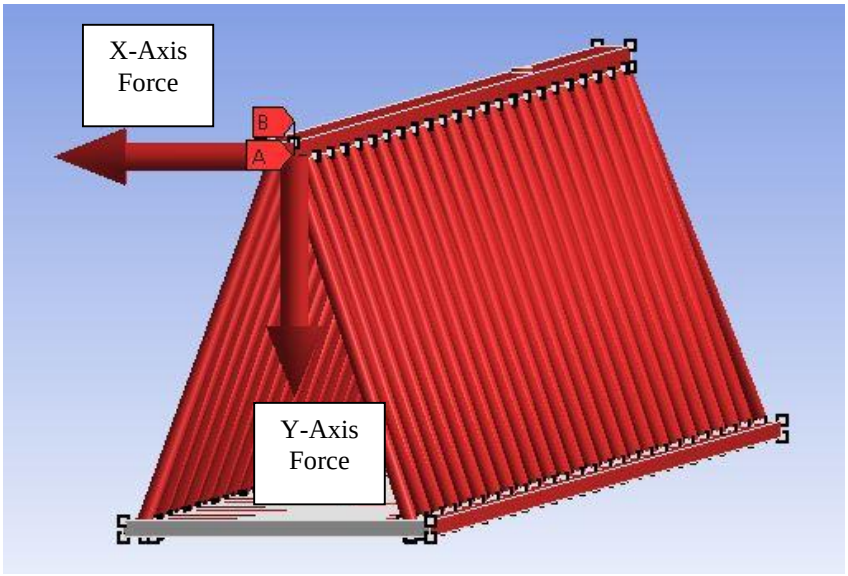


Figure 7. Direction of forces in the x-axis and y-axis.

With that, the estimation of the resultant force is done at an angle of 45^0, which would give an equal amount of force in the x-axis and the y-axis. The material's tensile and compressive yield stress is of a value of 250 MPa. Using the ANSYS Workbench software, the horizontal jib is placed with an equal x-axis force and y-axis force until it just exceeds the tensile and compressive stress of the material. From the simulation, the amount of force needed for the horizontal jib to just exceed the tensile and compressive yield stress would be a force of 27 kN in the x-axis and y-axis. The maximum stress endured by the horizontal jib is a value of 250.3 MPa which exceeds the tensile and compressive yield stress of the material.

The calculation of the resultant force is done using the formula from Eq. (2.3) and it is found to be 38.183 kN. With this resultant force, it would be kept constant and the variables would be the forces acting on the horizontal jib in the x-axis and the y-axis. The values for the forces in the x-axis and y-axis at different angles are calculated using Eq. (2.1) and Eq. (2.2) respectively. Table 5 is the results from the calculations using the equations.

Table 5. Forces in the x-axis and y-axis at different angles.

Angle (θ)	X-Axis Force (N)	Y-Axis Force (N)
0	38183.77	0
5	38038.47	3327.93
10	37603.67	6630.54
15	36882.69	9882.69
20	35881.00	13059.62

25	34606.24	16137.16
30	33068.11	19091.88
35	31278.31	21901.31
40	29250.46	24544.05
45	27000.00	27000.00
50	24544.05	29250.46
55	21901.31	31278.31
60	19091.88	33068.11
65	16137.16	34606.24
70	13059.62	35881.00
75	9882.69	36882.69
80	6630.54	37603.67
85	3327.93	38038.47
90	0	38183.767

3.1 Total Deformation at Different Angle

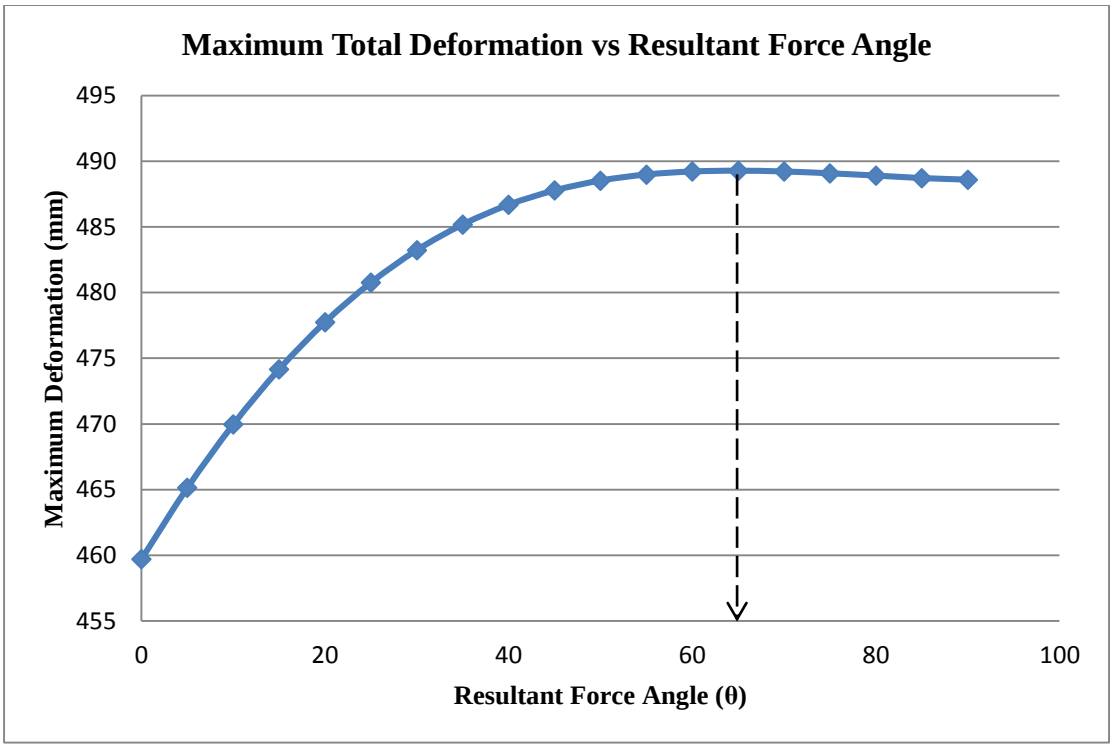


Figure 8. Graph of maximum total deformation versus the resultant force angle.

The total deformation of the simulation is plotted in the graph above for the ease of analysis in Fig. 8. From Fig. 8, it is observed that as the resultant force angle increases, there is an increase in the maximum total deformation up to 65^0 and then it drops slightly till it reaches 90^0. The highest deformation is achieved when the angle of the resultant force is at an angle of 65^0 and the lowest at 0^0. This shows that the critical angle for the highest total deformation is when then resultant force is at an angle of 65^0. Fig. 9 and Fig. 10 shows the position of the highest concentration of total deformation.

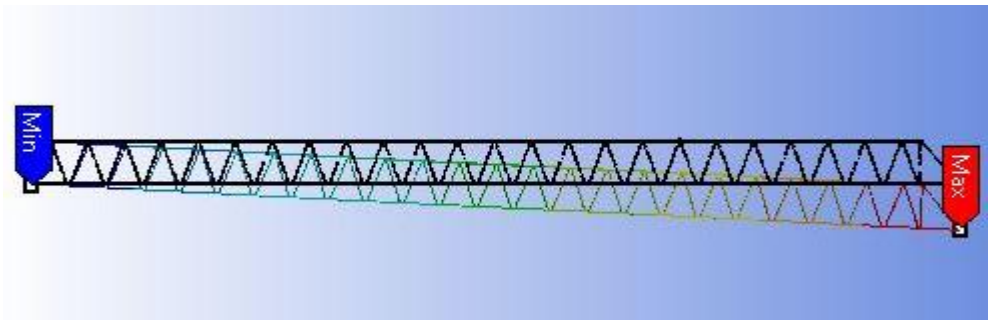


Figure 9. Side view of deformation of horizontal jib at 65^0.

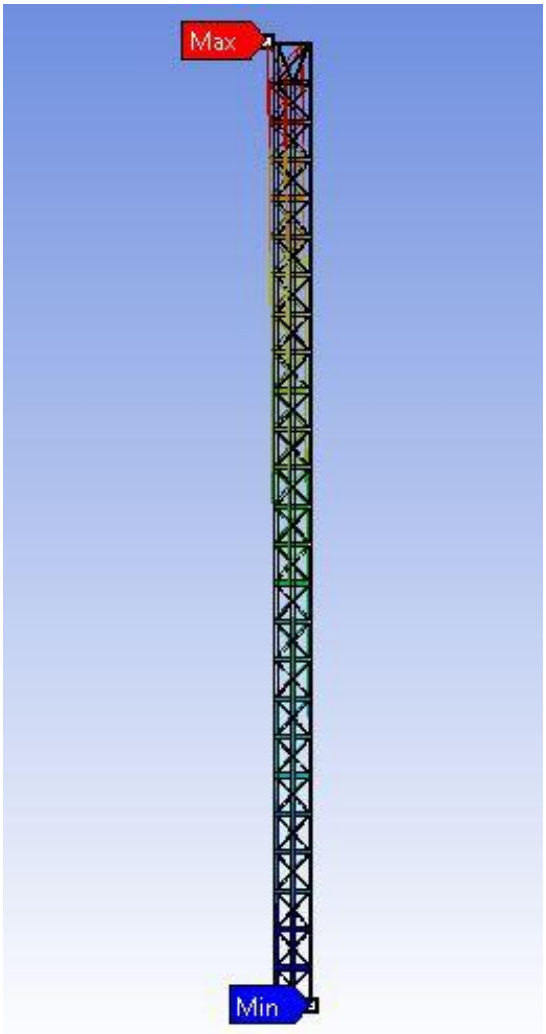


Figure 10. Top view of deformation of horizontal jib at 65^0.

From the figure above, it can be seen that the highest deformation is at the jib head section and the minimum deformation is at the fixed end of the horizontal jib. Since the jib head is at the end of the horizontal jib, the weight of the entire structure is in its direction because of the critical angle which is almost equal to the angle between the triangles. This can be seen in the Fig. 11.

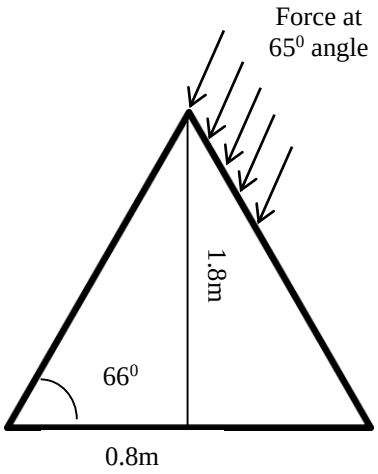


Figure 11. Angle of horizontal jib triangles.

3.2 Stresses at Different Angle



Figure 12. Graph of maximum stress versus the resultant force angle.

The data is plotted in Fig. 12 to perform analysis. As seen in Fig. 12, as the angle of resultant force increases up to 25^0, the maximum stress on the horizontal jib increases. Beyond 25^0, as the angle of the resultant force increases, the maximum stress on the horizontal jib decreases. The maximum stress the horizontal jib endures is when the angle of the resultant force is 25^0 and the minimum stress is at 90^0. Form this observation, it can be said that the critical angle for maximum stress on the horizontal jib is when the resultant for is at an angle of 25^0. When the resultant force is applied at an angle of 25^0, the triangle at which the force is acting on is disabled

causing all the weight of the structure to concentrate on the other middle triangle as well as the base. This causes it to supply additional pressure to that point which causes the stress around that area to be the highest.

Fig. 13 and Fig. 14 shows the area of the highest maximum stress. Looking at Fig. 14, the area with the highest concentration of stress is the area at the top surface of the base section which is closer to the fixed support. The area with the least stress it the area of the top support. This is because the resultant force at the angle of 25^0 is directly perpendicular to the middle triangle which is at an angle of 66^0. Summing up these two forces would be 91^0 which is roughly 90^0. This would mean that the actual critical angle for the highest maximum stress would be around 24^0 to 25^0.

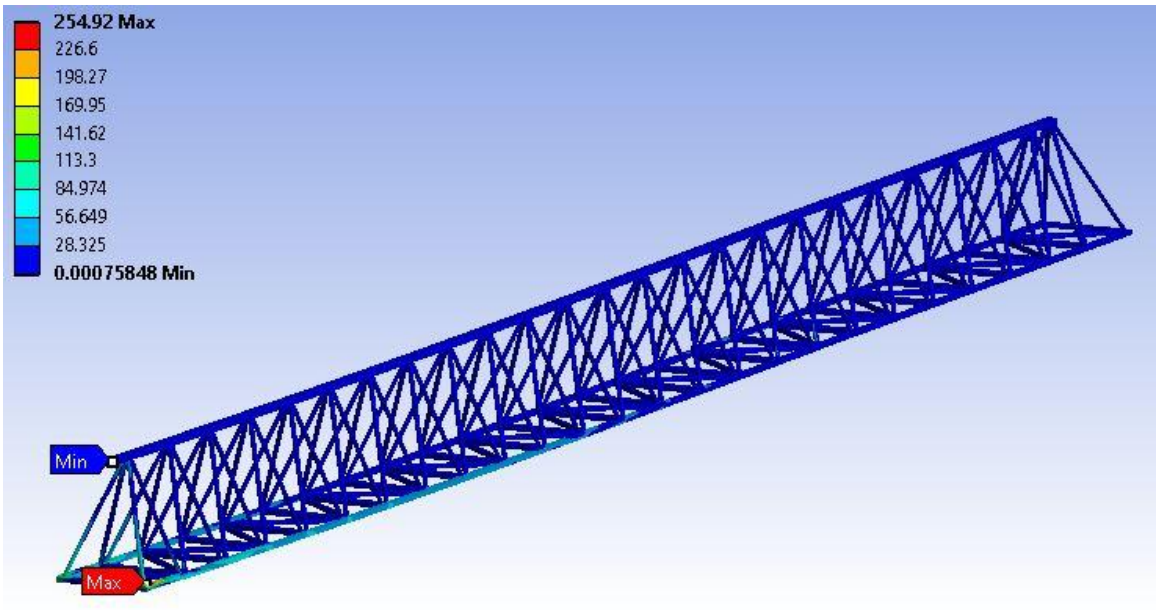


Figure 13. Stress of horizontal jib at 25^0.

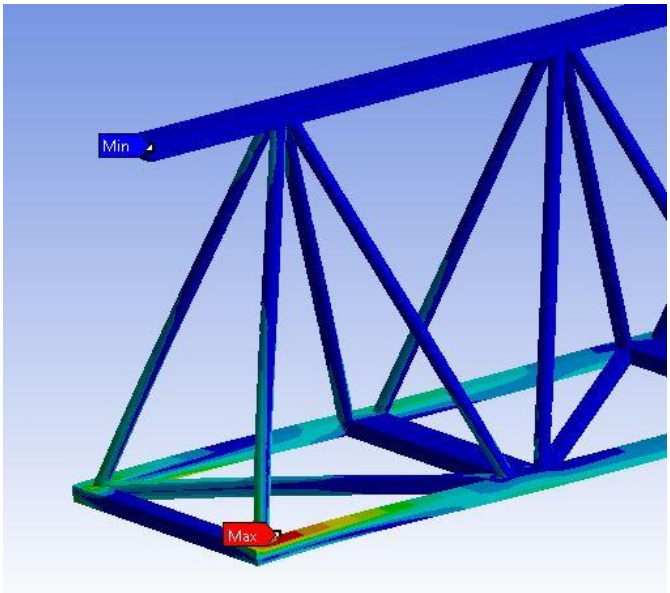


Figure 14. Stress area of horizontal jib at 25^0.

4.0 Conclusion

The model of the horizontal jib is done using SolidWorks software and it follows the dimensions of the 280 EC-H16 Litronic tower crane manufactured by Liebherr. The simulation analysis done from the ANSYS software is to determine the critical angle at which the horizontal jib would endure the maximum stress and also the highest total deformation. As for the deformation, the critical angle is found to be when the resultant force is at an angle of 65^0. Calculating the angle of the triangle, it is found to be at an angle of 66^0 which is very close to the critical angle for the highest total deformation. As for the stress, the critical angle is found to be when the resultant force is at an angle of 25^0. Looking at the middle triangles on the horizontal jib, 25^0 would closely resemble a perpendicular resultant force angle acting on the horizontal jib. As a conclusion, the critical angle for the highest total deformation is at an angle of 65^0 and the critical angle for the maximum stress is at an angle of 25^0.
With that said, the part of the model which has the highest stress is the part most likely to fail and reinforcement on that part would seek to lower the stress value which in return would reduce the failure rate of tower cranes and this would be the future work for this research project.

References

[1] M. Newberry, "1949: Tower cranes," History of Innovation, 1949. [Online]. Available: https://aehistory.wordpress.com/1949/10/04/1949-tower-cranes/. Accessed: Oct. 1, 2016.
[2] "1949-1960," 2011. [Online]. Available: http://www.liebherr.com/en/deu/about-liebherr/history/1949-1960.html. Accessed: Oct. 1, 2016.
[3] N. D. Zrnic, S. M. Bosnjak, V. M. Gasic, M. A. Arsic, and Z. D. Petkovic, "Failure analysis of the tower crane Counterjib," Procedia Engineering, vol. 10, pp. 2238–2243, 2011.
[4] C. R. Gagg, "Failure of components and products by 'engineered-in' defects: Case studies," Engineering Failure Analysis, vol. 12, no. 6, pp. 1000–1026, Dec. 2005.
[5] P. Swuste, "A 'normal accident' with a tower crane? An accident analysis conducted by the Dutch safety board," Safety Science, vol. 57, pp. 276–282, Aug. 2013.
[6] Richard Isherwood, http://www.hse.gov.uk/construction/safetytopics/cranes.htm, 2010. [Online]. Available: http://www.hse.gov.uk/research/rrpdf/rr820.pdf. Accessed: Oct. 1, 2016.
[7] Liebherr, "280 EC-H 16 Litronic," in https://www.liebherr.com/en/deu/products/construction-machines/tower-cranes/top-slewing-cranes/high-top-ec-h/details/72354.html, 2016. [Online]. Available: https://www.liebherr.com/external/products/products-assets/249212/liebherr-280ec-h-16-litronic-datasheet.pdf. Accessed: Oct. 4, 2016.

eureca 2016 – Conference Paper
Paper Number 2ME23

Numerical Analysis of Parallel Flow Field Design for Polymer Electrolyte Membrane Fuel Cell and Operation for Effective Water Removal

Sanjan Peter Balan[1*], Mohd Hardie Hidayat b. Mohyi[1]

[1]*Taylors University, No.1 Jalan Taylor's, 47500 Subang Jaya, Selangor DE, Malaysia*

[*]Sanjan7888@gmail.com

Abstract
The world is starting to demand an alternative energy source that does not impact the environment and provides the same amount of energy that is currently being used today. Alternative fuel converters like fuel cells are the next step, however more research is needed to be able to produce the same amount of power needed. Proton Electrolyte Membrane fuel cell (PEMFC) is becoming popular due to good power to size ratio, nevertheless there are challenges that must be tackled to meet energy consumptions. The issue that most PEMFCs face is water flooding that would occur in the system that would disrupt the operation. There are many factors that contribute to this issue however the main factor would be the flow channels at the cathode that distribute air to the system and removes water from the fuel cell. A one dimensional model was constructed to determine the mass flowrates in each flow channel of a parallel flow field and compare with the water generated from the PEMFC. The results show that 25cm channel length compared to the 5cm length has significant impact on the water removal capabilities of the parallel flow field. Furthermore, the first 5 flow channels closest to the inlet has higher water removal compared to flow channels after them. This is shown in the decay of the graph curve for the mass flowrates in the flow channels. Comparison between the water generation and flow channel mass flowrate indicate that parallel flow field channels are not effective in removing the water.

Keywords: PEM fuel cell, water generation, mass flowrate, parallel flow channels, current density, PEMFC

1. Introduction

World energy consumption ties to the use of non-renewable sources for power generation that leads to the increase of carbon emissions. This has led to the lack of development of technology that utilizes renewable energy. Thus the development and application of fuel cells that has been around for more than 150 years [1], has not significantly progressed as compared to non-renewable technologies. However the recent demand over the past few years for renewable energy sources has boosted technology development of fuel cells. Many countries have started to recognize the importance of shifting towards renewable energies and have started to make policies that would advance this development; Examples of events like the UN climate summit in Paris [2] are leading this change for both developed and developing countries. This has led to advances in the use of renewable sources which in 2014 contributed to half of the world's new power generation capacity [2]. The demand and investment into renewable technologies have spurred the fuel cell industry to produce more powerful and efficient power generating fuel cells. Fuel cell research has led to interesting knowledge, concepts, and applications that were not feasible in the past.

The fuel cell under research is the Polymer Electrolyte Membrane Fuel Cell (PEMFC). The reasons that fuel cells are becoming popular for renewable energy conversion devices is as follows [3]:

- Potential for high operating efficiency
- Highly scalable design
- Weight to power ratio is good allowing for portable system
- Produces no pollutants
- Has low maintenance due to no moving parts
- Does not need to be recharged, just supplied with fuel and power is produced
- Many types of fuel sources and methods to supply fuel to fuel cell

There are a few drawbacks like costly parts for the fuel cell, fuel reformation technology is costly, heavy and needs power to run as well as hydrogen fuel is necessary and other fuels would degrade the catalyst and cause electrolyte poisoning [3].

The basis of PEMFC is the chemical reaction known as an electrochemical conversion which is actually a reversed electrolysis reaction [4]. This reaction occurs in a closed system comprising of four parts; anode, cathode, electrolyte and the external circuit [3]. In Figure 1 below, the fuel cell reaction for the PEMFC is shown to occur in three parts; the first part being the oxidization of hydrogen into protons and electrons at the anode; the second part is the reduction of oxygen at the cathode and the final part is the combination of the oxidized hydrogen and reduced oxygen to

produce water at the cathode. During this process, the electrons from the anode are passed through an external circuit and brought back to cathode to combine the hydrogen protons and oxygen ions giving the by-product water. The electrolyte acts as a barrier to all except the hydrogen protons passing from the anode to the cathode. These reactions for PEMFC are shown below [3, 4]:

$$Anode: 2H_2 \rightarrow 4H^+ + 4e^-$$

$$Cathode: O_2 + 4e^- + 4H^+ \rightarrow 2H_2O$$

PEM fuel cells is a direct combination of hydrogen and oxygen to produce electricity while the other fuel cells utilize not only H_2 but also CO, CH_4, CH_3OH and other fuels to achieve the necessary reactions to produce electricity [4]. PEM fuel cells also produce the highest cell voltage of 1.1V; the only fuel cell that have similar results is PAFC [4]. The only difference between PEMFC and PAFC is the electrolyte that is utilized. This makes PEMFCs a promising fuel cell to further develop and eventually mass-produce this fuel cell.

As shown previously, the PEM fuel cell reactions requires the combination of pure hydrogen and oxygen in air to produce electricity. This would result in a water byproduct from this reaction. The management of this byproduct to ensure smooth PEMFC operation is essential to be able to produce the highest power density. The operating temperature of PEMFCs is from 50-100^{o}C with electrical efficiency of 53-58% and system output of 1-250KW [4]. Configuration of the PEM fuel cell is as follows; two bipolar plates, two gas diffusion layers, two catalysts (anode and cathode) and the proton electrolyte membrane in the middle. These components are sandwiched together to form a closed system for the reactions needed to produce electricity. Below is the figure for the configuration of the PEM fuel cell:

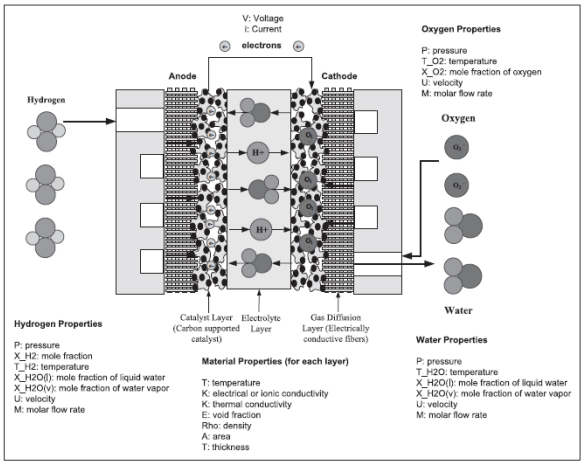


Fig 1: PEMFC with property considerations for mathematical model [3]

The above figure displays the structure of the PEMFC and chemical reactions that would occur; however for the reactions to occur smoothly: precise control of flow rates of reactants, temperature control and effective water removal are necessary to keep the PEM fuel cell working efficiently. This project focuses on the removal of the by-product, water from the bipolar plate that employs parallel flow field. Parallel flow fields is the gas channel etched into the bipolar plate that not only feeds reactants into the system but also removes water from the system. Below is a figure of a parallel flow field design:

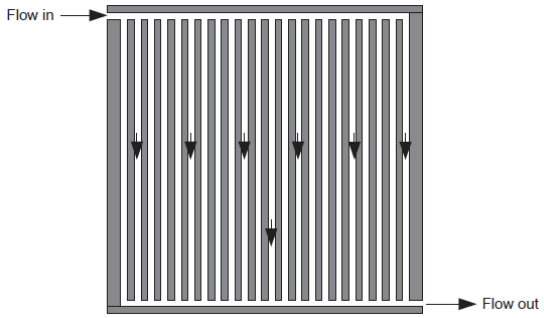


Fig 2: Parallel Flow field design [3]

As mentioned, the focus of this project is effective water removal using parallel flow field design. Water management is important as the PEMFC would degrade rapidly without water and water flooding would occur if there is no proper water removal system [3]. This project objective is fulfilled by mathematically modeling the water removal of the fuel cell that utilizes a parallel flow field using MatLab. This is done to minimize the cost of manufacturing fuel cells for testing and to produce a model that could predict whether the flow field design is capable of effective water removal.

2. Methodology

For this research, the most essential step is research into existing models especially for PEMFCs with parallel flow fields. The steps are as follows:

1. Research into current mathematical models
2. Mathematical model assumptions
3. Mathematical model construction and validation

The research into the subject matter has shown that most of the models are based on the overall voltage produced from the fuel cell or the chemical equations to determine the electrochemical reaction efficiency based on material of the fuel cell, the operating conditions and flow field designs; most flow field designs based on serpentine or a variation of it due to is effectiveness in fuel cells. There has been

research into the water removal for flow field designs but not significant research into the parallel flow field water removal capabilities.

2.1 Mathematical Model Assumptions

The common assumptions made for the mathematical model are as follows [3]:

- Ideal gas properties
- Isotropic and homogenous electrolyte, electrode, and bipolar material structures
- Negligible ohmic potential drop in components
- Mass and energy transport is modeled from macroperspective using volume-averaged conservation equations
- Electrodes and PEM is considered hydrated to perform efficiently

This assumptions will help assist in creating the first model of the PEM fuel cell and later iterations can be made to better fit the experimental data that is taken from other journal experiments.

2.2 Mathematical Model Construction and Validation

Mathematical model construction and validation work hand in hand in order to produce a one dimensional model of the PEM fuel cell capable of predicting water removal that occurs in the flow channels. The model will be comparing the water generation that occurs from the electrochemical reaction and the mass flow rate that the parallel flow field is capable of removing from the PEM fuel cell system.

The first step would be accumulating the necessary experimental data on parallel flow field experiments. Most journals present their data in terms of voltage vs cell density graphs. Therefore extracting this information gives the water generation capability of the PEM fuel cell which would be compared to the mass flowrate in the flow channels. This data is taken from two journal papers that have researched on different aspects of the fuel cell but have utilized the parallel flow field design in their experiments. This will be listed as experiment 1 and 2 as shown below in Table 1.

Next is utilizing an equation that could determine the water mass production rate in the fuel cell as shown [5]:

$$\dot{m}_{H_2O} = \frac{M_{H_2O} P_t}{n_e F V_c N_c} \quad (1)$$

where $M_{H_2O} = 18.01528 \times 10^{-3}\ kg/mol$
$F = Faraday\ constant = 96485\ C\ mol^{-1}$
$V_c = cell\ voltage$
$N_c = number\ of\ cells\ in\ a\ stack$

$n_e = number\ of\ electrons\ per\ molecule\ of\ reactant\ transferred = 2$

$P_t = total\ power\ of\ a\ fuel\ stack = V_c I N_c$

For this one dimensional model, the assumption is that all of the water generated flows to the cathode side of the PEM fuel cell. The reality of the situation is that there will be a portion of water content that would remain in the system. This happens due to back flow diffusion and friction, furthermore without a hydrated PEM fuel cell; the fuel cell will degrade rapidly [3, 5].

The next part is to determine the mass flow rate that would occur in the parallel flow channels. This can be determined by assessing the pressure drop that would occur in the parallel flow channel as well as the volumetric flowrate of the oxygen reactant. The volumetric flowrate and the pressure difference would act as a driving force for water removal. Pressure difference is different for each channel in the parallel flow channel, therefore the change in pressure must be calculated for each channel. The calculation for each channel is done through Matlab using the following equation [3, 5]:

$$\Delta P = f\frac{L}{D_H}\rho\frac{\bar{\nabla}^2}{2} + \sum K_L \rho\frac{\bar{\nabla}^2}{2} \qquad (2)$$

Where $f = friction\ factor$

$L = channel\ length$

$\rho = density$

$\bar{\nabla} = velocity\ in\ flow\ channel$

$D_H = hydraulic\ diameter\ of\ flow\ channel$

Volumetric flowrate equation at the stack entrance would display the flowrate of the incoming reactant. The inlet volumetric flowrate would impact the mass flowrate of the parallel flow field. The equation is as follows [3, 5]:

$$Q_{stack} = \frac{I}{4F}\left(\frac{S_{O2}}{r_{O2}}\right)\frac{RT_{in}}{P_{in} - \varphi P_{sat(Tin)}}N_{cell} \qquad (3)$$

Where $Q_{stack} = volumetric\ flow\ rate$

$F = Faraday\ constant = 96485\ C\ mol^{-1}$

$S_{O2} = oxygen\ stoichiometric\ ratio$

$r_{O2} = oxygen\ content\ in\ air$

$R = universal\ gas\ constant$

$T_{in} = stack\ inlet\ temperature$

$P_{in} = pressure\ at\ stack\ inlet$

$P_{sat} = saturation\ pressure\ at\ the\ given\ inlet\ temperature$

$\varphi = relative\ humidity$

$N_{cell} = number\ of\ cells\ in\ the\ stack$

All relevant information from the experimental data will be utilized to determine the mass flow rates and then a comparison is made between them. The experimental data is taken from two journals that have the experimental apparatus to conduct the parallel flow PEM fuel cell experiment. The experimental data would be classified under experiment 1 and 2 due to the different operation conditions. The experiments conducted from the journals are as follows:

Table 1: Experiment conditions for experiment 1 & 2

Experiment 1 [7, 6]	Experiment 2 [8]
Channel dimensions: Width = 1.2mm Depth = 1mm Rib length = 1mm	Channel dimensions: Width = 1mm Depth = 1mm Rib length = 1mm
Stoichiometry of air: $\alpha_{air} = 2, 3\ \&\ 6$	Stoichiometry of air: $\alpha_{air} = 3$
Number of channels:23	Number of channels:10
Active area: 25cm^2	Active area: 10.92cm^2, 31.92cm^2 and 52.92cm^2
Inlet pressure: 101325 Pa	Inlet pressure: 101325 Pa
Inlet temperature: 328K	Inlet temperature: 353K

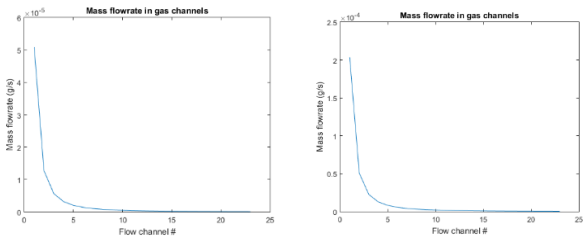
3. Results and Discussion

The data from the experimental conditions as shown in Table 1 and polarization curve were used to determine the mass flow rate of the fuel cell and of the parallel flow channel. Table 2 below is a portion of the calculated data for the mass flowrate in the flow channels:

Table 2: Calculated mass flow rates in flow channels from experiment 1 & 2

Experiment 1 Mass flow rate through each channel ($\alpha_{air} = 2$, current density 0.25) Columns 1 to 23 (unit g/s)									
6.428 x10^{-3}	1.607 x10^{-3}	7.142 x10^{-4}	4.016 x10^{-4}	2.574 x10^{-4}	1.786 x10^{-4}	1.313 x10^{-4}	1.004 x10^{-4}	7.951 x10^{-5}	6.401 x10^{-5}
5.323 x10^{-5}	4.447 x10^{-5}	3.773 x10^{-5}	3.302 x10^{-5}	2.829 x10^{-5}	2.493 x10^{-5}	2.224 x10^{-5}	1.954 x10^{-5}	1.752 x10^{-5}	1.617 x10^{-5}
1.482 x10^{-5}	1.348 x10^{-5}	1.213 x10^{-5}							
Experiment 1 Mass flow rate through each channel ($\alpha_{air} = 2$, current density 0.5) Columns 1 to 23 (unit g/s)									
6.989 x10^{-3}	1.747 x10^{-3}	7.766 x10^{-4}	4.377 x10^{-4}	2.802 x10^{-4}	1.941 x10^{-4}	1.429 x10^{-4}	1.098 x10^{-4}	8.608 x10^{-5}	6.959 x10^{-5}
5.861 x10^{-5}	4.945 x10^{-5}	4.213 x10^{-5}	3.479 x10^{-5}	3.114 x10^{-5}	2.747 x10^{-5}	2.381 x10^{-5}	2.198 x10^{-5}	2.015 x10^{-5}	1.832 x10^{-5}
1.648 x10^{-5}	1.465 x10^{-5}	1.282 x10^{-5}							
Experiment 2 Mass flow rate through each channel ($\alpha_{air} = 3$, current density 0.25) Columns 1 to 10 (unit g/s)									
2.954 x10^{-3}	7.381 x10^{-4}	3.278 x10^{-4}	1.849 x10^{-4}	1.1905 x10^{-4}	8.242 x10^{-5}	6.044 x10^{-5}	4.578 x10^{-5}	3.663 x10^{-5}	2.931 x10^{-5}
Experiment 2 Mass flow rate through each channel ($\alpha_{air} = 3$, current density 0.5) Columns 1 to 10 (unit g/s)									
0.0118	2.954 x10^{-3}	1.313 x10^{-3}	7.381 x10^{-4}	4.725 x10^{-4}	3.278 x10^{-4}	2.418 x10^{-4}	1.849 x10^{-4}	1.465 x10^{-4}	1.1905 x10^{-4}

As shown from Table 2, the mass flow rate for each channel decreases the further away it is from the inlet, thereby reducing its effectiveness to transport the reactant to the system as well as the water accumulation. This is properly shown in the graphs below for both experiment 1 and 2:



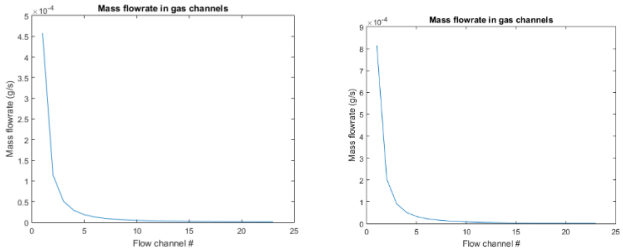


Fig 3: Experiment 1; α =2 at current density of 0.25, 0.5, 0.75 & 1 from left to right, top to bottom

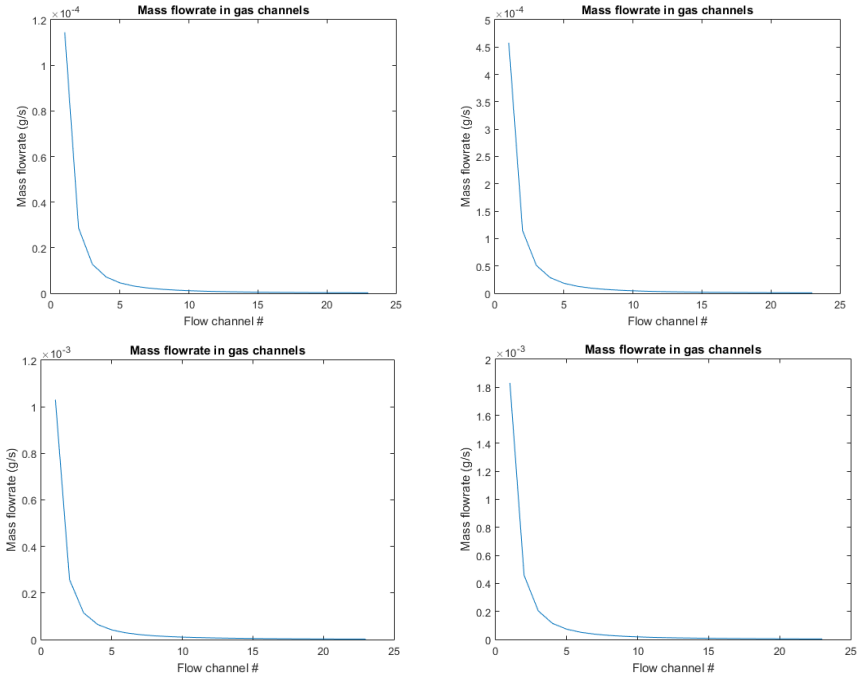


Fig 4: Experiment 1; α =3 at current density of 0.25, 0.5, 0.75 & 1 from left to right, top to bottom

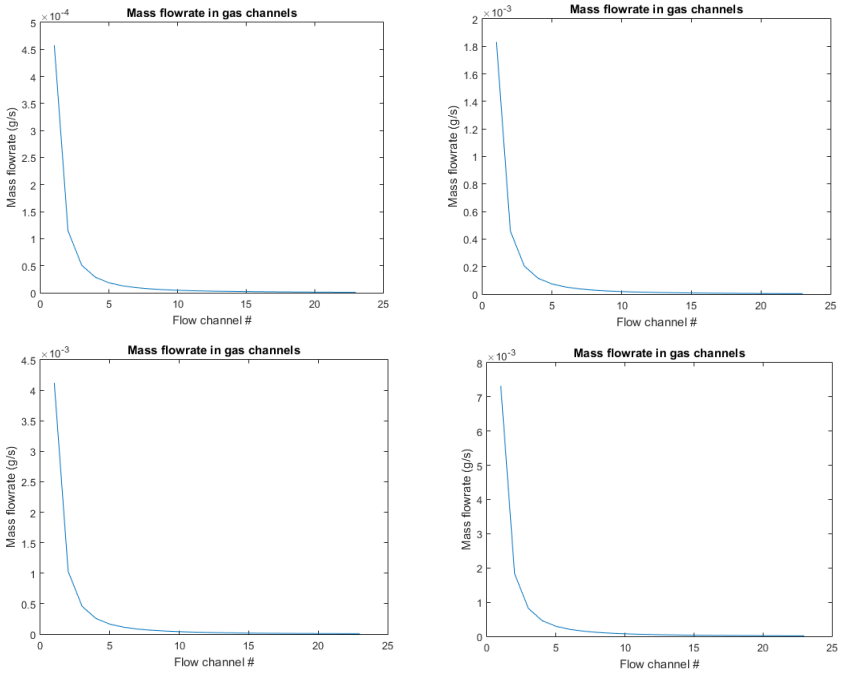


Fig 5: Experiment 1; α =6 at current density of 0.25, 0.5, 0.75 & 1 from left to right, top to bottom

Figures 1-5 show the mass flowrate of the parallel flow channels for experiment 1. The data shows that the flow channels from 1 to 5 have the largest mass flowrate as compared to the flow channels from 6 to 23. The decay rate of the graphs from channels 1 to 23 indicate that the flow channels further away from the inlet entrance suffer from lower mass flowrate. This would definitely impact the effectiveness of the parallel flow channels to remove water. Furthermore, from the data; the most optimal stoichiometry is 6 as compared to 2 and 3. However the different stoichiometry that have been used does not impact mass flowrate of in the gas channels by much as the decay rate in graphs are similar for the different operating conditions. Additionally the water generated from the PEMFC for experiment 1 at current density 0.25, 0.5, 0.75 and 1 are 5.83e-4 g/s, 0.0012 g/s, 0.0017 g/s and 0.0023 g/s respectively. The water generated shown is the water mass flowrate throughout the PEMFC across the all the flow channels. From this, it can be observed that water removal in the parallel flow channels is occurring but not as effective as to completely remove the water generated. As seen in table 2 for the stoichiometry of 2 at 0.25 current density; the gas channels 1-3 can remove the water generated. However after 3, the ability to remove the water is diminished; this results in a buildup of water in the system and eventual water flooding to occur. This is due to the non-uniform distribution that occurs in the PEM fuel cells that utilize parallel flow channels [9].

For experiment 2, the figures below are the mass flowrates in graphical form according to the different channel lengths used and the stoichiometry of 3:

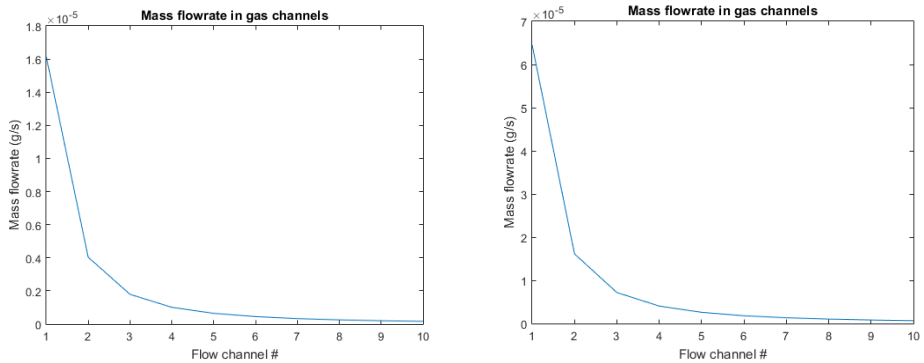


Fig 6: Experiment 2; current density of 0.25, 0.5 for channel length of 5cm from left

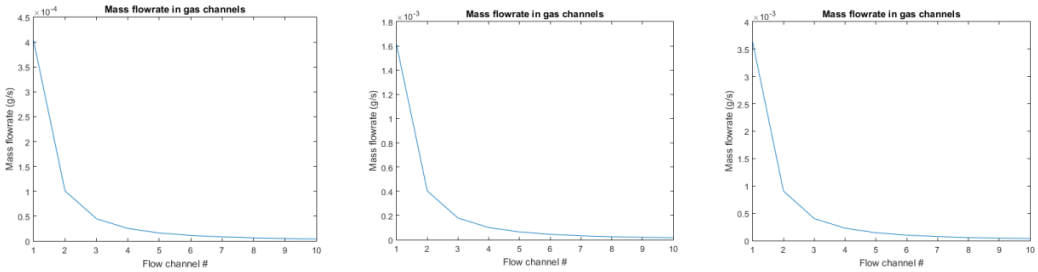


Fig 7: Experiment 2; current density of 0.25, 0.5 & 0.75 for channel length of 15cm from left to right

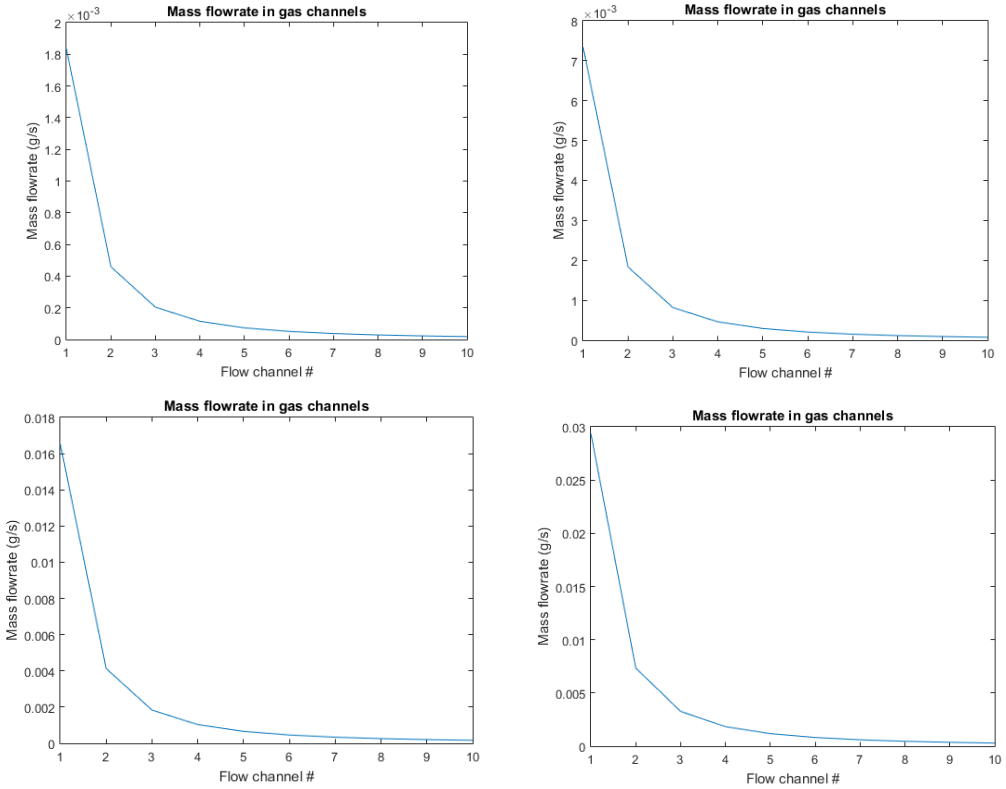


Fig 7: Experiment 2; current density of 0.25, 0.5, 0.75 & 1 for channel length of 25cm from left to right, top to bottom

Figures 5-7 show similarities to the data of experiment 1. However the difference of active areas prove to change the mass flowrate in the parallel flow channels. The PEMFC with channel length of 25cm has a superior mass flowrate as compared to 5cm and 15cm channel length. This means that the mass flowrate in the flow channels are affected by the channel length of the flow channels; unfortunately, this is not conclusive as experiments 1 and 2 operate at different temperatures and different flow channel dimensions, making it possible for the temperature and the dimensions to play a role in mass flowrate in the flow channels. However, the channel length does play a significant role in the mass flowrate for the flow channels from 1-5. It is higher compared to the other data from experiment 2 as well as experiment 1. This makes parallel flow field design more effective in water removal; however the change in channel length does not seem to affect the mass flowrate of the flow

channels after channel 5; the decay rate of the graph is similar to experiment 1. The water generated from the PEMFC for experiment 2 is shown below in Table 3:

Table 3: Calculated water generated mass flow rates for experiment 2 at different current densities

Channel Length	Water generated mass flowrate (g/s) at current densities (i/cm^2)			
α = 3	0.25	0.5	0.75	1
5cm	2.55e-4	5.09e-4		
15cm	7.44e-4	0.0015	0.0022	
25cm	0.0012	0.0025	0.0037	0.0049

After comparison, the most effective parallel gas flow channel is the flow field with channel length of 25cm. It is capable of removing water from the system more effectively compared to channels length of 5cm and 15cm. However, the major issue is still the mass flowrate in the flow channels further away from the inlet; the reduced capability to remove water from the PEMFC affects the overall water removal performance. This shows that the placement of the inlet is also crucial to the effectiveness of water removal in parallel flow field designs.

4. Conclusion

This one dimensional model does display a rudimentary view of the parallel flow channel and its capability to remove water. Mass flow rates shows a simple view of the water removal from the PEM fuel cell system; however the model does not take into account the heat generated and the diffusivity between air and water that would occur in the cathode area. However from this model, I can assert that the parallel flow field design is not effective in water removal. It is possible to improve the water removal performance of the parallel flow field by changing the channel length and considering the placement of multiple inlets. Furthermore in the future, a controlled experiment for different channel lengths, different stoichiometries and more inlets is necessary to confirm whether the parallel flow fields are capable of effective water removal. However the basic parallel flow field is not capable of it. Additionally, refinement of the model is needed to include the heat generated as well as diffusivity of air and water.

Acknowledgements

Many thanks and much gratitude towards Dr Mohd Hardie Hidayat Mohyi for the guidance and supervision during the research process. I would also like to thank Mr Wandeh Elwon, a fellow researcher on a similar topic for the help and guidance he

has provided. Additionally I would like to thank my lecturer, Dr Reynato Gamboa for his guidance for FYP 2 as well as my fellow researchers for the support and advice.

References

[1] Smithsonian Institution, "Fuel cells: Discovering the science," in Collecting the History of Fuel Cells, 2004. [Online]. Available: http://americanhistory.si.edu/fuelcells/origins/origins.htm.

[2] (2015). World Energy Outlook Executive Summary. Paris: International Energy Agency

[3] C. Spiegel. (2008). PEM fuel cell modeling and simulation using Matlab. London: Academic Press.

[4] S. Mekhilef, R. Saidur, and A. Safari. (2012). Comparative study of different fuel cell technologies. *Renewable and Sustainable Energy Reviews, vol. 16, no. 1,* (pp. 981–989).

[5] S. T. Revankar and P. Majumdar. (2010). *Fuel cells: Principles, design, and analysis*. Boca Raton, FL: CRC Press.

[6] S. Litster, C. R. Buie, T. Fabian, J. K. Eaton, and J. G. Santiago. (2007). Active water management for PEM fuel cells. *Journal of The Electrochemical Society, vol. 154, no. 10,* p. B1049.

[7] D. G. Strickland, S. Litster, and J. G. Santiago. (2007).Current distribution in polymer electrolyte membrane fuel cell with active water management. *Journal of Power Sources, vol. 174, no. 1,* (pp. 272–281).

[8] J. Bachman, M. Charvet, A. Santamaria, H.-Y. Tang, J. W. Park, and R. Walker. (2012). Experimental investigation of the effect of channel length on performance and water accumulation in a PEMFC parallel flow field. *International Journal of Hydrogen Energy, vol. 37, no. 22,* (pp. 17172–17179).

[9] H. Li et al. (2008). A review of water flooding issues in the proton exchange membrane fuel cell. *Journal of Power Sources, vol. 178, no. 1,* (pp. 103–117).

eureca 2016 – Conference Paper
Paper Number 2ME24

Effect of Preloads on the Mechanical Properties of Under Sleeper Pads (USPs)

Selvindaraj Anandarajah*, Dr. Ch'ng Shiau Ying
[1]*School of Engineering, Taylor's University, Malaysia*
*selvindaraj16@gmail.com

Abstract
The under sleeper pads also known as USPs has a great involvement in improvement of resilience in railway tracks. Ground vibrations and damaging of the ballast can be prevented by the use of USP. It also helps to abate the stiffness of the track at turnouts and crossings. The USPs are normally made of an elastic material like polyurethane and it is positioned at the base of the sleeper between the sleeper and the ballast. Recent studies proves that, the performance of the USPs will be affected by several elements. In particular, we are especially interested in the effect of pre-loads as various simulations and testing done previously did not include this effect. Hence, this effect will be addressed in this research. Thus, this leads to the objectives of the research which is to investigate the effect of preloads on mechanical properties of under sleeper pads and also to evaluate the mechanical properties of USPs using various methods. In order to determine this, dynamic simulation was done as part of the research using ANSYS Workbench software. The simulation was started with modal analysis then continued with harmonic response analysis in order to obtain the solution. The total deformation, phase response as well as the amplitude response of the USPs under at different stiffness and applied force was obtained from the simulation. All in all, it was concluded that the amplitude response increases with the stiffness of the USPs whereas the force is directly proportional to the amplitude response.

Keywords: Under Sleeper Pad, Preloads, Rail Pad, Rubber, and Dynamic Simulation

1. Introduction

The first reinforced concrete sleeper was introduced by Joseph Monier who is a French Gardener back in 1877. In 1896, the concrete sleepers were used by the Reading Company in America on a main line railway. Great progress was attained during the World War II which is mainly due to the reduction in timber due to other use. The European railways studied and carried out various researches and came up with the modern pre-stressed concrete sleeper. The pre-stressed concrete had advanced after the World War II in terms of design, quality and production which caused the increase in the usage of concrete railway sleepers. At turnouts and bends, the degradation of the ballast of a ballast track with concrete sleeper is much quicker than other parts of the track. In order to overcome this issue, rail pads or better known as under sleeper pads (USPs) were introduced to manage this issue [1].

Under sleeper pads (USPs) is a type of flexible pad attached at the base of a concrete sleeper to create resiliency between the ballast and the sleepers. It is normally placed in between the concrete sleeper and the ballast as in Fig 1. The thickness of the USPs are normally in the range of 10 mm to 20 mm and it is manufactures of polyurethane with a specific stiffness. The arrangement is such that the material on the outer side protects the material inside from any sort of damage [2]. Ground vibrations and also damaging of the ballast will be reduced by using the USPs as it helps to isolate the vibration of the concrete sleeper. Other than that, track stiffness at turnouts, crossings as well level crossings can be reduced with the use of USPs. This is so that the ballast and formation are uncoupled from the wheel or rail interaction which results in the reduction of the ground vibration affecting surrounding buildings and structures. A much better distribution of load will be achieved by using the USPs as the contact pressure and also smaller variation of the support stiffness along the track will be reduced [3].

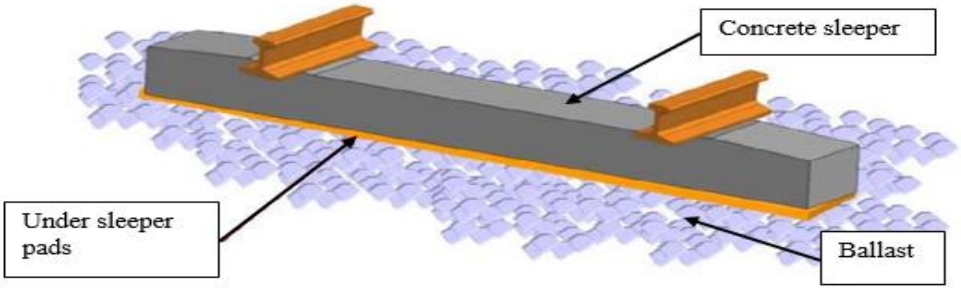


Figure 1. The under sleeper pad together with the ballast and concrete sleeper. [3]

The USPs will experience deformation due to the force acting on it. The force basically comes from weight of trains as well as from the weight of the concrete sleeper and the railway. This will result not only in the deformation of the USP but also will cause a change in the mechanical properties of the USPs. Despite having a great performance throughout the years, the USPs still have an issue that is not being addressed. The current USPs have not been tested by including the effect caused by

the preload. The preloads here is referred as the weight of the concrete sleeper and as well as the railway. This is because the USPs experiences a slight deformation due to this two weights even before experiencing the force caused by the train. Most experiments and test run on the USPs were done based on just the force caused by train without even including the preloads. Simulations will be carried out in this research to study the effect of preloading on the mechanical properties of the sleeper pads. Before starting the research, work done by others was reviewed to aid and have a better understanding regarding the issue.

Carrascal *et al*. tested rail pads to study the degradation experienced by it. Fatigue test was carried to test the pads at various temperatures, humidity and loads. By doing so, the changes in dynamic properties of the rail pads over time could be determined. At the end, it was seen that the major source of degradation is due to humidity and the dynamic stiffness decreases as the temperature increases [4]. Guigou-Carter *et al.* carried out test to deduce the dynamic stiffness of the rail pads and sleeper pads. Combination of vertical and horizontal pre-loads were used and applied in the test. Besides, an analytic model for the track system was developed and the damping of each component was modelled as hysteretic damping for this model. At the end, it was concluded that the frequency and the dynamic stiffness of the pad is inversely proportional to the load/force [5].

Maes *et al.* used loss factor to determine the stiffness values and also the damping values of rail pads. Test was carried out using the direct method with variable pre-loads and three different materials in a certain frequency range. Pre-loads of different values were used to test the rail pads. The dynamic stiffness and also the lost factor was calculated based on the ISO 10846 guidelines. It was concluded that, the dynamic stiffness of the rail pads increases when the frequency and preload increases [6]. According to the German DB-TL 918.071 standard, Lapčík *et al*. tested rail pads to deduce the dynamic stiffness of the rail pads. The pads were tested in the frequency range of 10 to 100 Hz with varying static pre-loads of 75, 15 and 25 kN. At the end, it was seen that the dynamic stiffness increases with frequency and static preload [7].

The static and as well the dynamic stiffness of a rail pad was tested by Thompson *et al.* From the results obtained, the static load-deflection and load-stiffness curve was constructed. The curve indicates that the load is directly proportional stiffness and deflection. A gradual increase in the static stiffness was seen as the loads increased to 25 kN. The range of preloads used were I the range of 20 kN to 80 kN. Besides, it was also seen that the dynamic stiffness is frequency dependent [8].

The aim of this research is to investigate the effect of preload on mechanical properties of under sleeper pads (USPs), to evaluate the mechanical properties of under sleeper pads (USPs) using various methods and lastly to carry out simulation using simulation software. In this research all the possible effects of the preloads on the mechanical properties of the USPs will be identified. There will be no creation of a prototype in this research as it is not part of the scope. The project solely depends on research, analysis and simulation. Due to lack in facilities and also budget constraints, the actual experimental test cannot be conducted. Therefore, simulation using ANSYS

Workbench was done to achieve these objectives as this would aid in the study of how would a certain force or condition will affect the mechanical properties of the USPs.

2.4 Research Methodology

2.5 Design and sketching of the Sleeper

The 3D model of the the sleeper together with the under sleeper pad (USPs) was drawn using the Design Modeler. The 3D model of the concrete sleeper as well as the USPs was drawn exactly as the actual dimension obtained from the journals. First the simple rectangle which is the sleeper of dimension 2.6 m in length and a width of 0.15 m. Then another rectangle which is the USPs is drawn right below of dimension 2.6 m in leghth and width of 0.02 m. After that the two track fasteners of equal dimensions were drawn at the top of the sleeper. The extrude function is used next as the entire sketched is extruded by 0.25 m which is the thickness of the entire design. The bonded function was used to attach the bodies together. This function will enable the entire structure to stick together and act like one structure. This function is important so that there will be no interuptions during the dynamic simulation part. The reason behind having separate bodies is because each body has different propertiesa nd engineering data. Therefore, it is better to create one different bodies and attached then using the bonded function. The model drawn using the Design Modeler is as shown below:

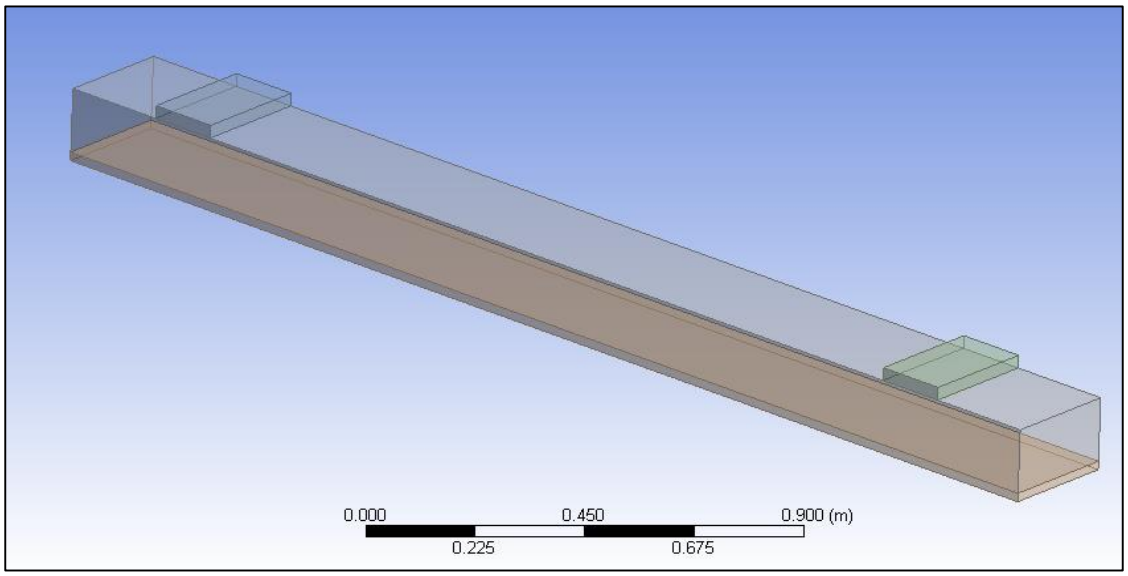


Figure 2. The design of the concrete sleeper together with under sleeper pad.

2.6 Modal Analysis

The first step of carrying out the dynamic simulation, modal analysis is to be done. It is a technique used to determine the vibration characteristics of the structure and also acts as the prerequisite for the harmonic response analysis carried out later on. By carrying out the modal analysis, the natural frequencies at what frequencies the structure would tend to naturally vibrate mode shapes and also in what shape the

structure would tend to vibrate at each frequency will be known. The advantage of carrying out this analysis is so that it allows the design to avoid the resonant vibration, shown how the design will respond to different type of dynamic loads and lastly helps to calculate solution controls for the next step of the analysis.

The first step in modal analysis is to key in the engineering data for all the materials that will be used in the analysis. The material selected will be stainless steel for the track fasteners, concrete for the sleeper and lastly polyurethane for the under sleeper pad. Once that is done, Mechanical is launched followed by the meshing of the design. Since the entire design does not have any sort of curve shape, the standard multizone mesh of element size 0.02 m is selected. After that, the fixed supports is selected. For this design, the fixed supports are at the bottom of the design as well as the top of the track fasteners. The bottom of the under sleeper pad is selected as a fixed support because that's where the USP will be placed on the ballast. The other fixed support is at the top where it will be fixed to the train track. Once all that is completed, the solution can be generated. From the modal analysis, how the structure will deform based on the natural frequency is known. The example of the solution obtained from modal analysis and total deformation at one of the frequency is shown below:

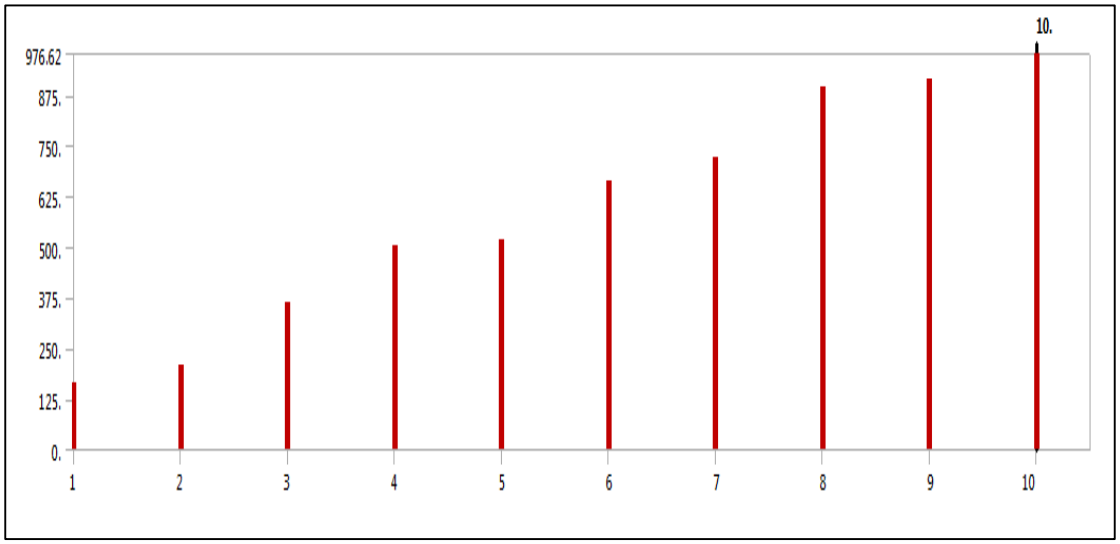


Figure 3. The solution obtained from Modal Analysis.

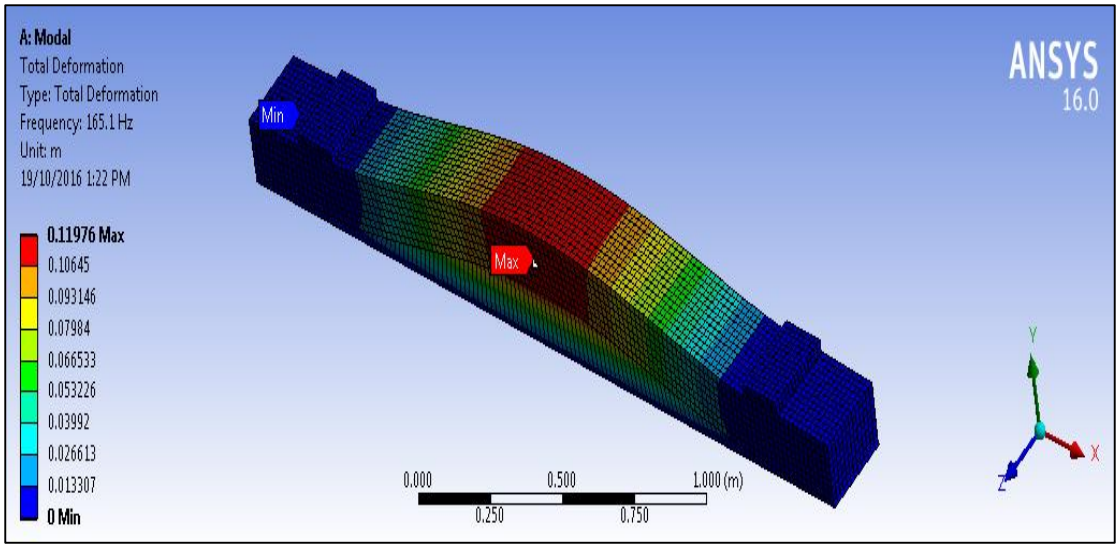


Figure 4. The total deformation at the first natural frequency.

2.7 Harmonic Response Analysis

Harmonic response analysis is the next step of the dynamic analysis. It is a technique to determine the steady state response of a structure due to the harmonic loads of known frequency. The example of harmonic loads are force, pressures, and impossed displacements of known magnitude and frequency. This harmonic loads acts as the input of the analysis and the loads can be single as well as multiple loads. At the end of the harmonic analysis, the displacement at each DOF is obtained.

The first step of harmonic analysis is to set the initial conditions of the analysis. For this case, the initial condition is the force acting in the Y-axis at the top of the design. The force is actually comes from the weight of a fully loaded train itself which is 10787315 N acting downward. Once that is done, the analysis can be continued by inserting the total deformation, frequency response as well as the phase response. Then the solution is obtained. The analysis is focussed mainly on the USP itself. The stiffness of the USP is varied from 0.6 MPa to 1.4 MPa to find out how does the stiffness effect the USP. Other than that, the force was also varried to see how does the force effect the output. The forces were varried and the solutions were obtained for each of stiffness. Example of the soultion obtained from the analysis is shown below:

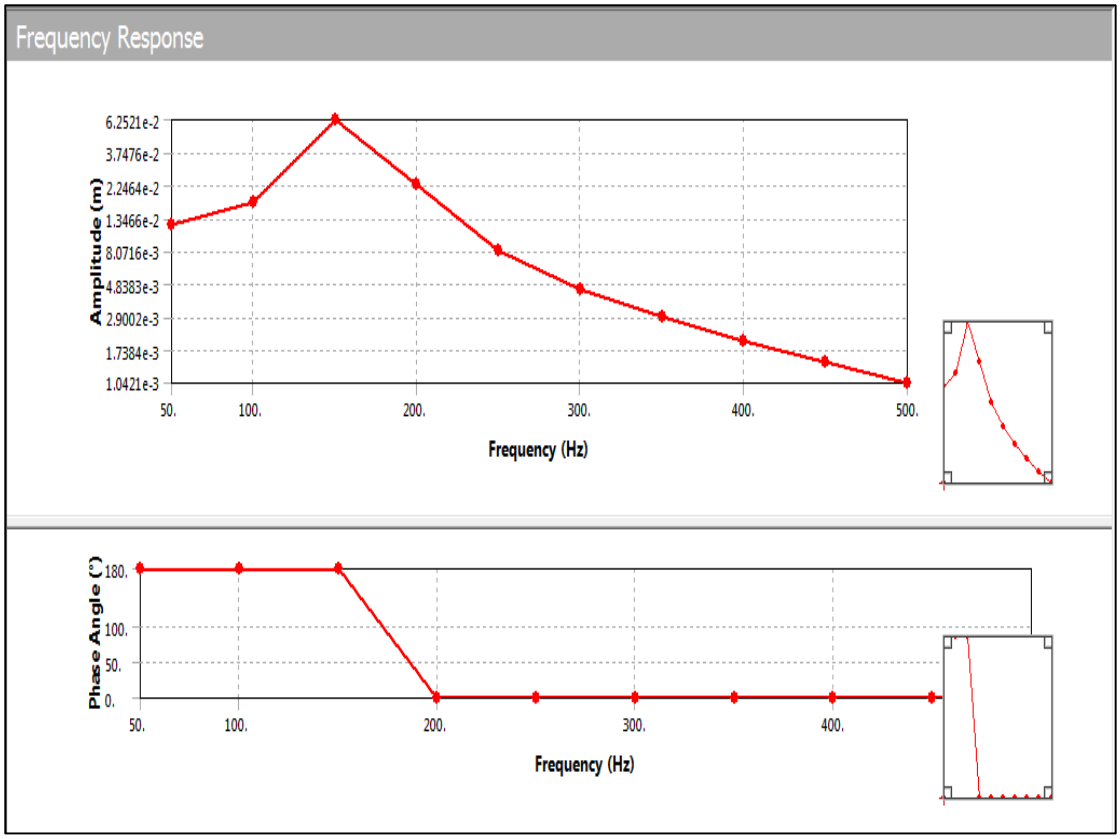


Figure 5. The frequency response solution obtained from Harmonic Response Analysis.

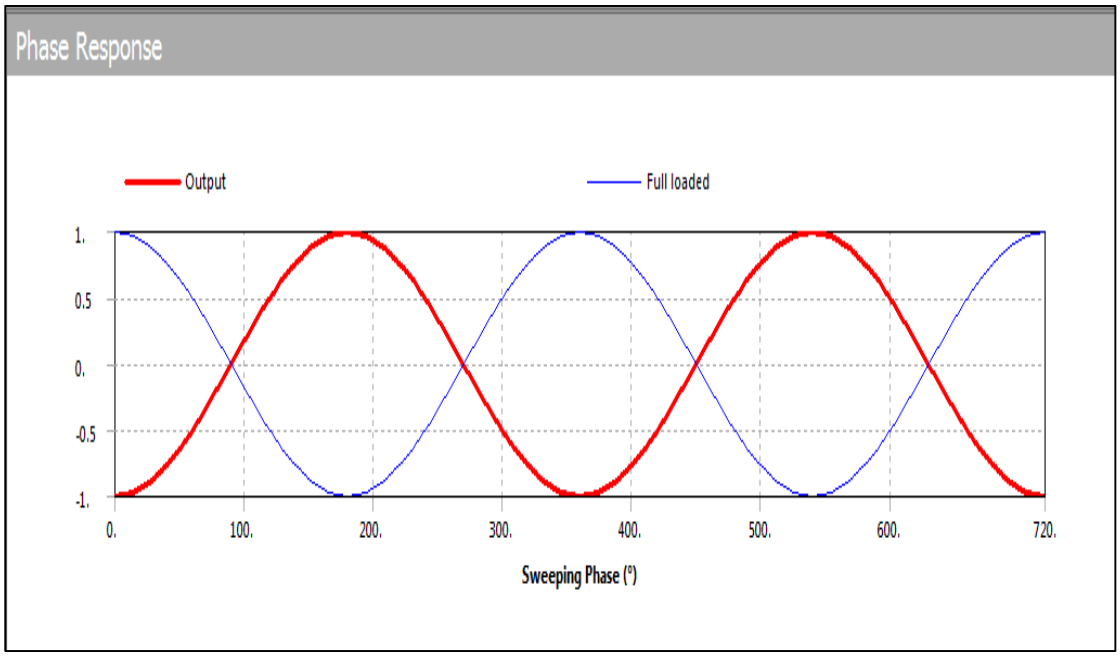


Figure 6. The phase response solution obtained from Harmonic Response Analysis.

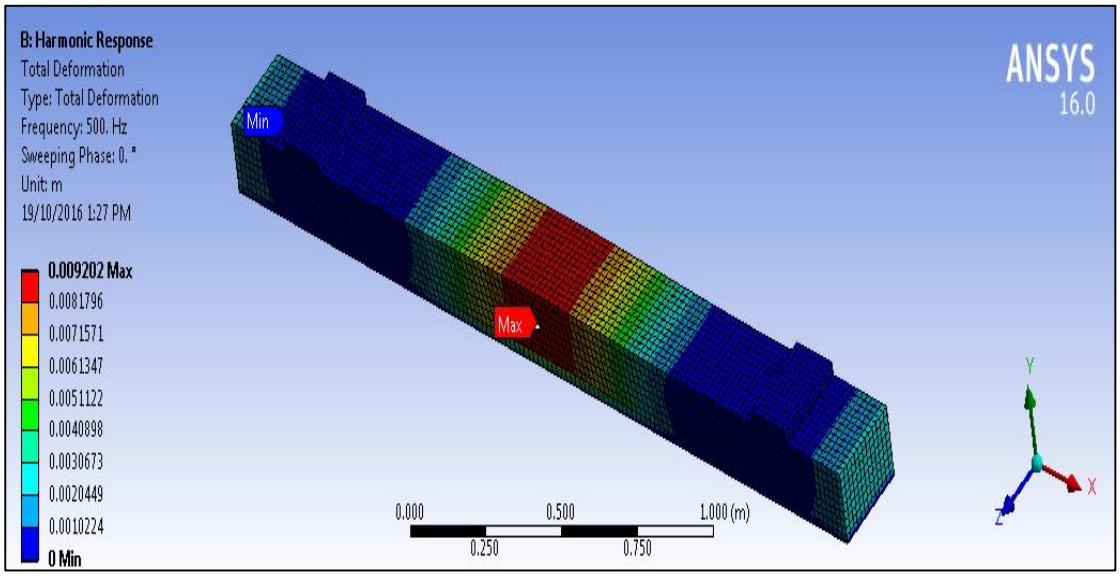


Figure 7. The total deformation solution obtained from Harmonic Response Analysis.

2.8 Data analysis and conclusion

The data from the dynamic simulation will be analyzed and observed to pick out the key information that would aid in the research. These results are compared for different stiffness to study how stiffness effects the performance of the USPs. Other than that, another relationship was also derived which is between force and amplitude. After completing the analysis, a conclusion was drawn to answer the objective.

5.0 Results & Discussion

The simulation was done for different stiffness of under sleeper pads (USPs). The stiffness selected is 0.6 MPa, 0.8 MPa, 1.0 MPa, 1.2 MPa and also 1.4 MPa. By varying the stiffness, the relationship between the stiffness, force and deformation of the USPs will be derived. Although the stiffness is varied, the Poisson's ratio is maintained. The engineering data was obtained from the journals. The solution was obtained for total deformation, phase response and also for frequency response.

3.1 Total Deformation

The total deformation gives information about where in particular in the structure where the highest and lowest deformation will occur. The total deformation was done twice in the analysis, one is for the full structure as shown in Fig 6 and the other just for the USP. As the aim here is to study the effect of the USP therefore focus was shifted to just the deformation of the USP. The total deformation solution obtained is show below:

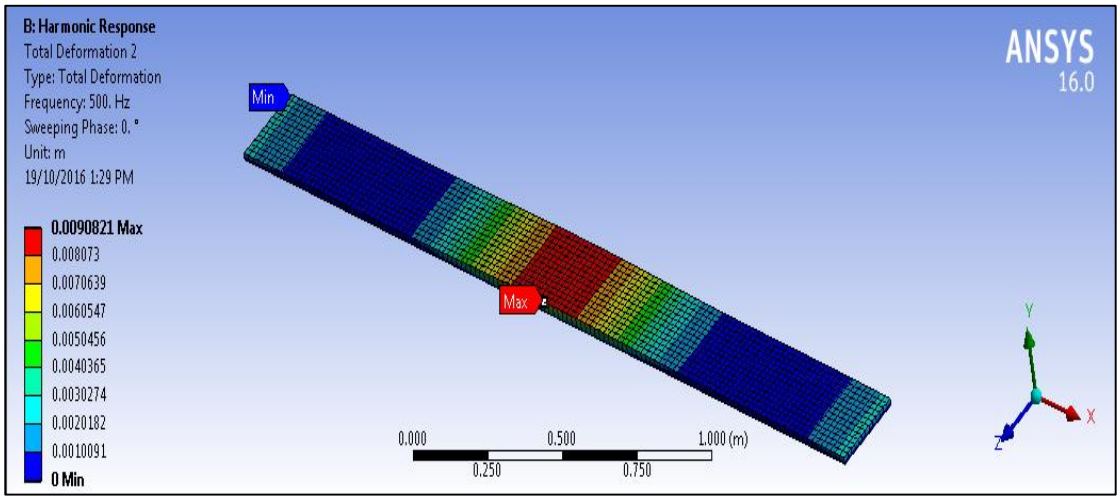


Figure 8. The total deformation of the USP.

From the Figure above, it was seen that at the center is where the USP experiences the greatest deformation. The total deformation was observed for all the different stiffness and it was seen that the maximum deformation occurs in the same area but having different values. The greater the stiffness is, the higher the maximum deformation of the USP.

3.2 Phase Response

The Phase Response plots that show how much a response lags behind the applied loads over a phase period. For this case, the phase response graph above shows the results of how the output lags at different force. Based on the results for stiffness of 1.0 MPa, the output and the force are exactly opposite. The results for the other stiffness are exactly the same pattern just that the values differ. The 1.0 MPa is shown as it is the common stiffness used for USPs. The graph below shows the phase response for stiffness of 1.0 MPa and also the combined stiffness.

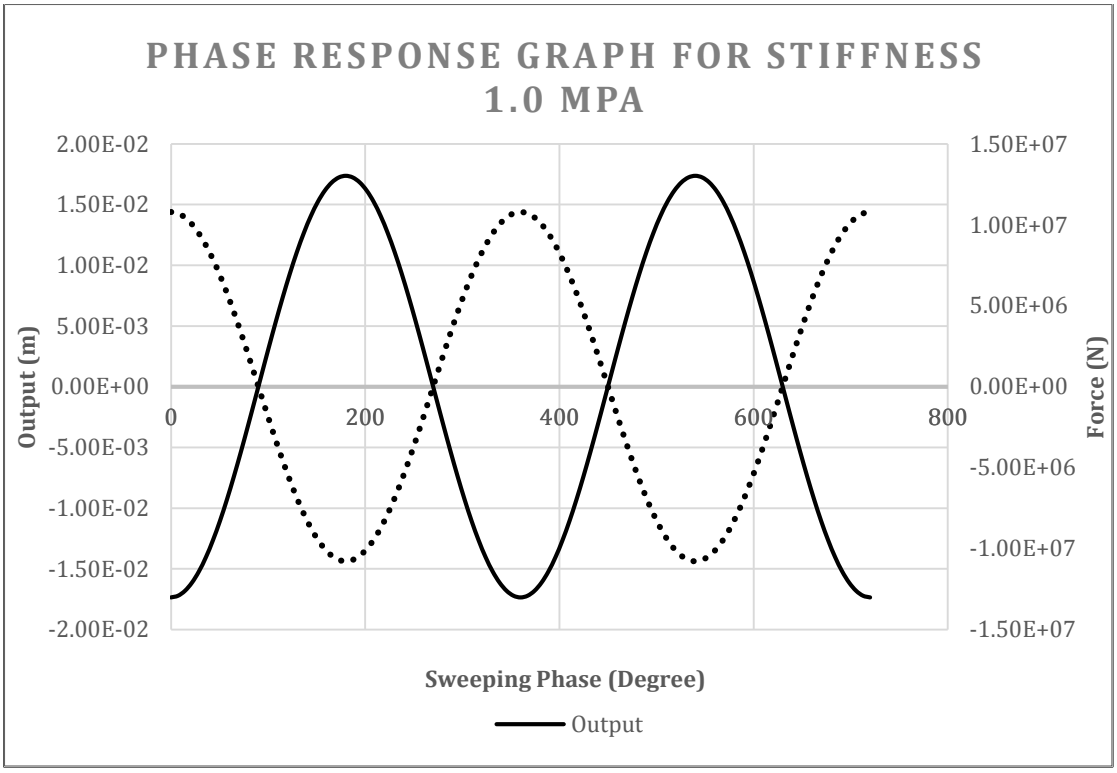


Figure 9. The phase response for stiffness of 1.0 MPa.

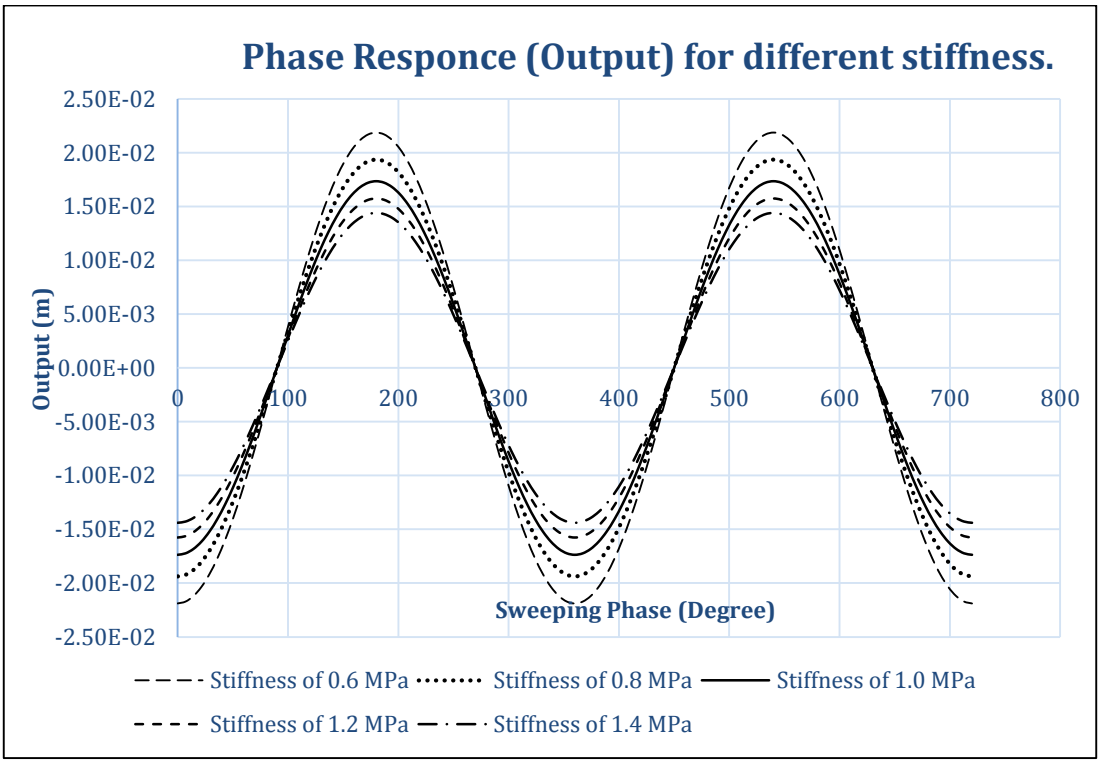


Figure 10. The phase response (output) for different stiffness.

Figure 10 shows the output section of the phase response for the all the different stiffness. From here it is observed that, when the stiffness is lowest, a highest

amplitude response (output) is obtained. The same pattern is maintained throughout the entire sweeping phase from 0° to 720°.

3.3 Amplitude Response

Amplitude Response graph that display how the amplitude varies with different stiffness at a certain frequency is obtained from the frequency response graph. A portion of the frequency response graph is picked and observed. The graph shows basically what the amplitude of the vibration when the stiffness is varied at the frequency of 150 Hz. Different forces were also used to compare the amplitude response obtained. The initial force used was 10787315 N which is the weight of the full loaded train. In order to derive the relationship between force, stiffness and also amplitude, the force was the manipulated. The forces used are 8433719 N (unloaded), 9610517 N (partially loaded) and 9934136 N (3-quarter loaded). From here, it can be seen how does the structure or design responds when the stiffness as well as the force is varied when frequency is maintained. The response obtained for all the different stiffness is as shown below:

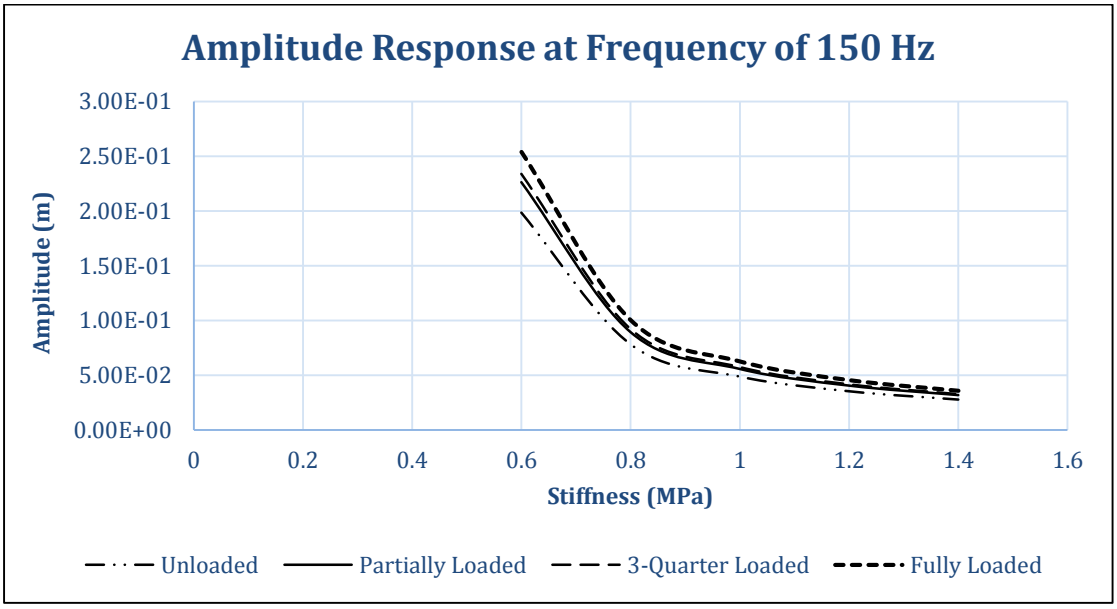


Figure 11. The amplitude response at different stiffness.

From the amplitude response graph above it can be seen that the amplitude response for all the different stiffness of USP are not the same. The relationship between the stiffness of the under sleeper pads and the amplitude is derived. It can be seen that, when the stiffness increases, the amplitude decreases at the same frequency. Based on this, it was concluded that the results obtained does support the theory of the stiffness being inversely proportional to amplitude response. Besides that, another relationship was also derived which is between force and amplitude. Based on the graph plotted, as the amplitude response increases as the force (load) increases at the same stiffness. Therefore, it is safe to say that the force is directly proportional to the amplitude.

6.0 Conclusion

All in all, how stiffness and force effects the USP was derived. ANSYS Workbench software was used to carry out the dynamic analysis on 3D model of the concrete sleeper together with the USP drawn using the Design Modeler software. Two-step method was used for the dynamic analysis, starting with modal analysis and followed by the harmonic analysis. Modal analysis helps determine the vibration characteristics of the structure and also acts as the prerequisite for the harmonic analysis. As part of the modal analysis, meshing of the 3D model was done and the standard mesh was choosen due to the design on the 3D model. The solutions obtained from the modal analysis was then linked to the harmonic analysis to carry out the dyamanic analysis.

As part of the analysis, the solution was obtained for total deformation, phase response and also for amplitude response. The analysis was carried out for different stiffness of USP as well various applied forces. It was seen that when the stiffness of USP is incresed, the lesser the deformation the USP experiences. Lesser deformation will result less wear of the USP. Besides, it was also seen that the as the stiffness increases, the amplititude response decreases. Threfore, it can be said that the stiffness is inversely proportional to the deformation and amplitude response. Other than that, it was also noticed that when the force applied is increased, the deformation experienced by the USP is much greater. The same concept applies to the amplitude response as well. The amplitude response increses as the force applied increased. Therefore, when a fully loaded train travels on the railway, the USP will experience a much greater deformation. This is mainly due to a larger applied force acts on the USP. Thus, its best to use a much stiffer USP as the lifespan can be increased.

References

[1] A. Remennikov and S. Kaewunruen, "A review of loading conditions for railway track structures due to train and track vertical interaction", Structural Control and Health Monitoring, vol. 15, no. 2, pp. 207-234, 2008

[2] A. Johansson, J. Nielsen, R. Bolmsvik, A. Karlström and R. Lundén, "Under sleeper pads—Influence on dynamic train–track interaction", Wear, vol. 265, no. 9-10, pp. 1479-1487, 2008.

[3] S. Nimbalkar, B. Indraratna, S. Dash and D. Christie, "Improved Performance of Railway Ballast under Impact Loads Using Shock Mats", *J. Geotech. Geoenviron. Eng.*, vol. 138, no. 3, pp. 281-294, 2012.

[4] I. Carrascal, J. Casado, J. Polanco and F. Gutiérrez-Solana, "Dynamic behaviour of railway fastening setting pads", Engineering Failure Analysis, vol. 14, no. 2, pp. 364-373, 2007.

[5] C. Guigou-Carter, M. Villot, B. Guillerme and C. Petit, "Analytical and experimental study of sleeper SAT S 312 in slab track Sateba system", Journal of Sound and Vibration, vol. 293, no. 3-5, pp. 878-887, 2006.

[6] J. Maes and H. Sol, "A double tuned rail damper—increased damping at the two first pinned–pinned frequencies", Journal of Sound and Vibration, vol. 267, no. 3, pp. 721-737, 2003.

[7] L. Lapčík, P. Augustin, A. Píštěk and L. Bujnoch, "Measurement of the dynamic stiffness of recycled rubber based railway track mats according to the

DB-TL 918.071 standard", Applied Acoustics, vol. 62, no. 9, pp. 1123-1128, 2001.

[8] T. Wu and D. Thompson, "The Effect of Local Preload on The Foundation Stiffness and Vertical Vibration of Railway Track", Journal of Sound and Vibration, vol. 219, no. 5, pp. 881-904, 1999.

eureca 2016 – Conference Paper
Paper Number 2ME25

Design & Analysis of Lunar Landing Structure

Sivaneshwaran Raja[1], Azadeh Ghadimi[1], Izmir Yamin[2]*
[1]School of Engineering, Taylors University, Malaysia
[2]Independence-X Aerospace Sdn. Bhd., Malaysia

[*]Azadeh.Ghadimi@taylors.edu.my

ABSTRACT

The project was offered by Independence-X Aerospace Sdn. Bhd. who is one of the 16 finalist teams that are participating in the Google Lunar X-Prize competition. The objective of this mission is to land a privately funded lander on the moon and cover a distance of 500 meters by transmit images and high definition videos back to earth. The aim of this project is to develop a landing structure that is capable of withstanding the impact during landing while stabilizing the bus structure. The results of the analysis would give a better understanding on the behavior of the landing structure as well as determine if it's able to perform its task accordingly which would ensure the success of the mission. Furthermore, the mass of the lander has to be taken into account as the dry mass should not exceed 150kg. SolidWorks 2014 and ANSYS Workbench 15.0 has been used for design and simulation of the model in order to obtain the shear stress and the deformation. The maximum shear stress of the landing strut connector and the plate joint was found to be 2.6398E5 Pa and 1.4713E6 Pa. As for the deflection of the landing structure (outer layer), the cross-sectional view of the landing strut and the plate joint are 0.00082156 m, 1.3269E-5 m and 6.121E-6 m. The landing structure angle is 22.2º and the force of the landing impact that occurs on the strut is 589.1 N.

Keywords: Simulation, lunar lander, structural design, lunar module, deformation

1. Introduction

Lunar lander which is also known as lunar module is able to fly unmanned or manned on a space objectives to gather scientific data which benefits the humanity, improve present technologies and make path for future technologies [1]. Fast forward to the 21st century, we now have a competition called Google Lunar X-Prize where 16 countries compete with each other to be the first team to transmit high definition images and videos back to Earth successfully [2]. This project was given by Independence-X Aerospace, where the competition was created by Google Lunar X Prize with a total prize pool for this competition is $30 million. The main aim of this mission is to create an affordable transportation to moon and encourage younger generations to take part in future aerospace programs.

The first successful unmanned mission was the Soviet Union's Lunar 17 [3] followed by Apollo 15. This were all possible due to the astounding number of man-hours that were put into the research, testing's, simulations, manufacturing and further improvements. By participating in this competition, it encourages the younger generations to participate in space related programs which enhances their understanding of technologies and the space. According to Pham, Zhao and Goo [4] design and analysis of a lunar lander is very important because it shows how it affects the landing system. The landing structure is used to absorb the impact energy, stability and safety of the lander. Another important part is to protect the devices inside the lander.

The entire lunar lander has been split into 3 different interrelated projects where this landing structure represents one of them. The other components are the bus structure and propellant tank. At this study, the landing impact of the structure, design and simulations of the landing structure as well as tilting and stability have been studied. Figure 1 shows the unconventional design of the landing strut which is assembled to the bus structure.

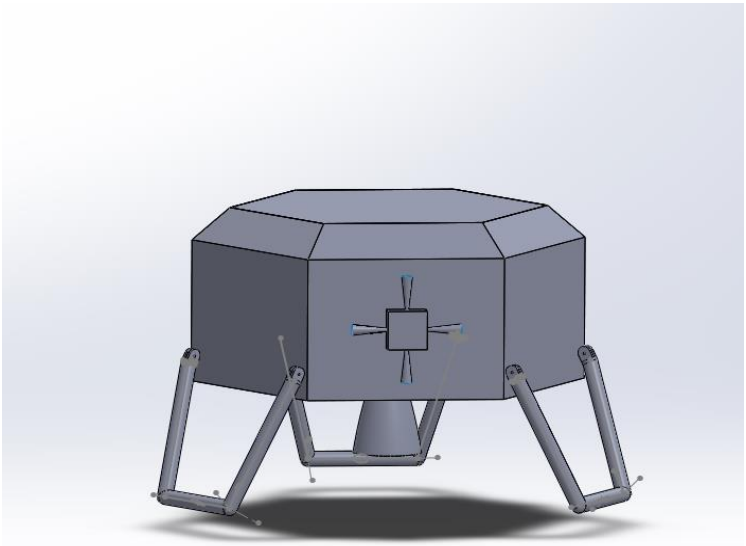


Figure 1: Lunar lander [5]

1.1 Project Objectives

There are two objectives that has to be met by the end of the project. These are as follows:

1. To find out the design which includes the length, angle, and the material that will be used
2. To design and analyze the landing structure by SolidWorks and SpaceClaim

2.0 Research Methodology

2.1 Materials

The material that is being used for the lunar lander is aluminum alloy T6-6061 after comparing with titanium Ti-6Al-4V (Grade 5) and AISI Type 304 stainless steel. Table 1-3 shows the mechanical properties of the materials. Aluminum alloy was chosen, because the material is not only cheaper compared to stainless steel and titanium but it also weighs less compared to them. For stainless steel the price range around $1500-3000/kg, titanium is around $100/kg and aluminum is around $50/kg. Although, stainless steel and titanium are stronger compared to aluminum, they are harder to work with in terms of bending, welding and manufacturing. Hence, titanium was chosen amongst them. By choosing aluminum, the requirement of the lander mass to be within 150 kg and a budget of RM 10 000 can be achieved.

Table 1: Mechanical properties of aluminum alloy T6-6061 [6]

Physical Properties	Metric	English
Density	2.7 g/cm	0.0975 lb/in
Mechanical Properties		
Hardness, Brinell	95	95
Hardness, Knoop	120	120
Hardness, Rockwell A	40	40
Hardness, Rockwell B	60	60
Hardness, Vickers	107	107
Ultimate Tensile Strength	310 MPa	45000 psi
Tensile Yield Strength	276 MPa	40000 psi
Modulus of Elasticity	68.9 GPa	10000 ksi
Notched Tensile Strength	324 MPa	47000 psi
Ultimate Bearing Strength	607 MPa	88000 psi
Bearing Yield Strength	386 MPa	56000 psi
Poisson's Ratio	0.33	0.33
Fatigue Strength	96.5 MPa	14000 psi
Fracture Toughness	29 MPa-m^1/2	26.4 ksi-in^1/2
Machinability	50%	50%
Shear Modulus	26 GPa	3770 ksi
Shear Strength	207 MPa	30000 psi

Table 2: Mechanical properties of AISI Type 304 stainless steel [7]

Physical Properties	Metric	English
Density	8 g/cc	0.289 lb/in^3
Mechanical Proeprties		
Hardness, Brinell	123	123
Hardness, Knoop	138	138
Hardness, Rockwell B	70	70
Hardness, Vickers	129	129
Tensile Strength, Ultimate	505 MPa	73200 psi
Tensile Strength, Yield	215 MPa	31200 psi
Elongation at Break	70%	70%
Modulus of Elasticity	193 - 200 GPa	28000 – 29000 ksi
Poisson's Ratio	0.29	0.29
Charpy Impact	325 J	240 ft-lb
Shear Modulus	86 Gpa	12500 ksi

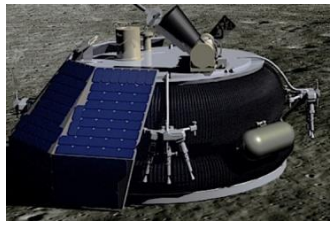
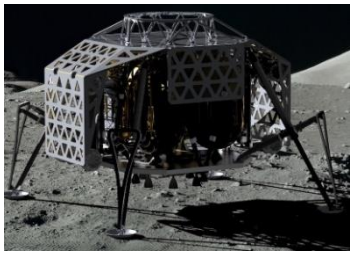
Table 3: Mechanical properties of titanium Ti-6Al-4V (Grade 5) [8]

Physical Properties	Metric	English
Density	4.43 g/cc	0.16 lb/in^3
Mechanical Properties		
Hardness, Brinell	334	334
Hardness, Knoop	363	363
Hardness, Rockwell C	36	36
Hardness, Vickers	349	349
Tensile Strength, Ultimate	950 Mpa	138000 psi
Tensile Strength, Yield	880 Mpa	128000 psi
Elongation at Break	14%	14%
Reduction of Area	36%	36%
Modulus of Elasticity	11308 Gpa	16500 ksi
Compressive Yield Strength	970 Mpa	141000 psi
Notched Tensile Strength	1450 Mpa	210000 psi
Ultimte Bearing Strength	1860 Mpa	270000 psi
Bearing Yield Strength	1480 Mpa	215000 psi
Poisson's Ratio	0.342	0.0342
Charpy Impact	17 J	12.5 gt-lb
Fatigue Srength	240 Mpa	34800 psi
Fatigue Srength	510 Mpa	74000 psi
Fracture Toughness	75 Mpa-m^1/2	68.3 ksi-in^1/2
Shear Modulus	44 Gpa	6380 ksi
Shear Strength	550 Mpa	79800 psi

2.1 Design of Landing Structure

There are many types of landing system which consist of 3-4 legs. The number of legs depends on the shape of the bus structure whether it may be hexagon, octagon, decagon or other shapes that is suitable to the parameters set by the industry or the designer. However, for this lunar module, it was decided that the bus structure would be in the shape of hexagon it would consist of 3 legs. Table 4 describes the chosen number of legs based on other competitor's results.

Table 4: Summary of landing gears of Lunar X-Prize competitors [9]

	Moon Express	Astrobotics	Team Indus	Part Time Scientist
Country of Origin	United States	United States	India	Germany
Type of Lunar Module	Lunar Lander	Lunar Lander	Lunar Lander	Lunar Lander
Achieved Milestone	Landing & Imaging	Landing, Imaging & Mobility	Landing	Landing, Imaging & Mobility
Special Characteristics	Collapsible empty fuel tank to act as impact cushion	Flexible mounting structure	Tripod design & small in size	Flexible landing gear, able to carry heavy loads
Landing Gear Downside	Only allows landing once	Static landing gear, exceeds the given parameter	Heavy bus structure & requires springs and dampers	Heavy bus structure & requires springs and dampers
Pictures				

According to the parameters that was given by the industry, the dry mass had to be within 150 kg, wet mass is within 350 kg and the dimensions should not exceed 2.5 m in diameter and 1.37 m in height. Other than that, the landing gear would not be using any damper or spring in the landing gear thus reducing the cost, material used and the weight of the structure. Due to this, a conventional landing gear could not have been used because by having a landing pad, it would require the landing gears to have springs and dampers to absorb the impact upon landing. Since no springs and dampers should be used, a new landing structure without a foot pad was designed by the author which is shown in Figure 2. Figure 3 shows the dimension which are was used as one of the parameters that were given by the industries. The design of the lander should not exceed 2.5 m in diameter and 1.37 m in height.

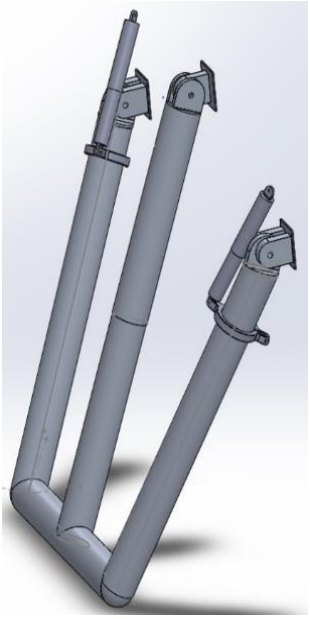


Figure 2: New landing structure

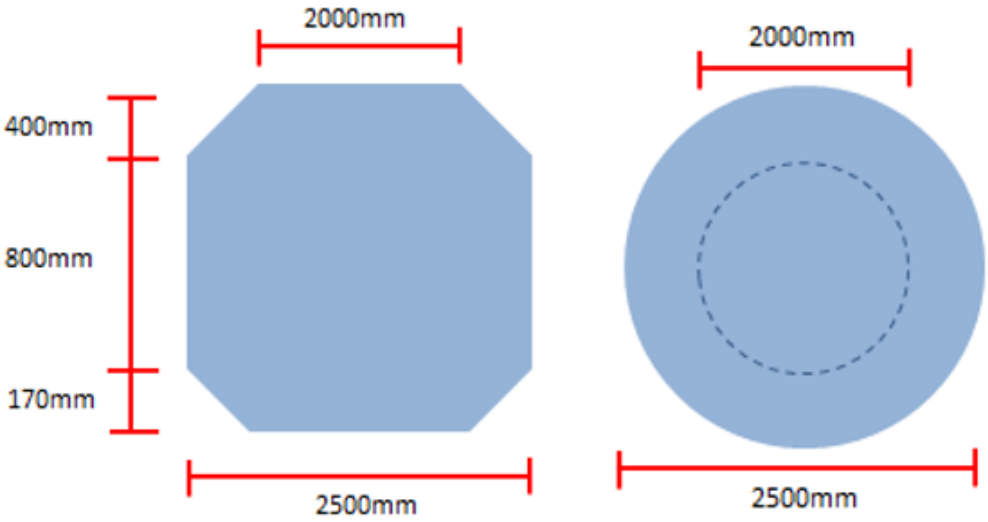


Figure 3: Dimensions that were given by industry

3.0 Results and Discussion

3.1Analysis and Calculation of the Landing Strut

The first step in designing the lander is figuring out the landing system specifications such as the length, height, angle of the landing strut and the force that is going to be applied on the strut. Since the specifications were not given expect for the diameter of the landing strut, multiple assumptions had to be made and compared to past landing strut results. Figure 4 shows the static calculations and free body diagram of the lunar lander from the front view and Figure 5 shows the side view of the landing strut. By solving the equations derived from the free body diagram, the angle, the length, the height and the force of the landing strut were achieved which are shown in Table 5 and 6.

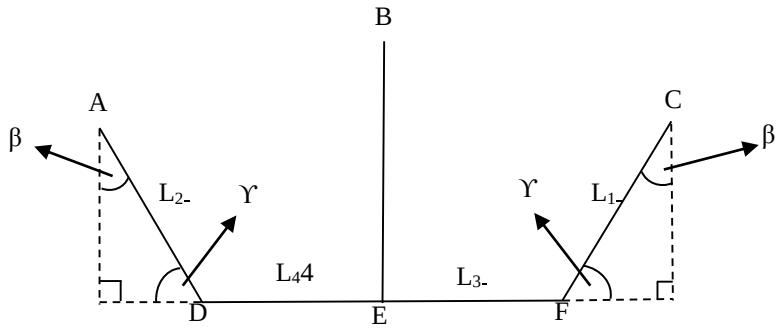


Figure 4: Free body diagram of the lander from the front view

The calculation of the angles and the length was derived from the following equations;

$L_1 = [(\text{Height of CF})^2 + (\text{Length of CF})^2]^{1/2}$ (1)

$\text{Cos } \beta = (\text{height of CF} / c)$ (2)

$\Upsilon = 180 - 90 - \beta$ (3)

By applying the assumed height and length of the landing strut, the tabulated data in Table 5 was achieved. The determining factor in assuming the height and the angle of the landing strut was that the landing gear had to folded which is one of the requirements from the industry. By taking that into consideration, the height of the bus structure, the length of the rocket engine and a tolerance 20 cm which is a requirement from the industry between the rocket engine and the landing surface was computed. Since the middle strut is higher than the secondary struts, the middle strut was designed to slide in and out just like a piston, to ensure that the same height throughout the landing gear can be accomplished.

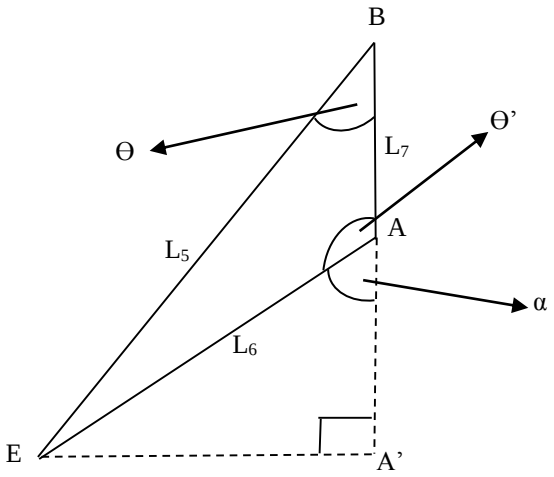


Figure 5: Free body diagram of the lander from the side view.

	Gravity (m/s^2)	Mass (kg)	Length A (mm)	Height B (mm)	Length A to C (mm)	Length C to F (mm)	L_4 to L_3 (mm)	L_1 (mm)	Beta (β)	Gamma (ϒ)
Front View	9.81	350	614	814	780	150	480	632.1	13.7	76.3
			584	784	760			603.0	14.4	75.6
			554	754	740			573.9	15.2	74.8
			524	724	720			545.0	16.0	74.0
			494	694	700			516.3	16.9	73.1
			464	664	680			487.6	17.9	72.1
			434	634	660			459.2	19.1	70.9
			404	604	640			430.9	20.4	69.6
			344	544	620			375.3	23.6	66.4
			314	514	600			348.0	25.5	64.5

The calculation of the angles and the length was derived from the following equations;

$$\text{Tan } \alpha = (\text{Length of EA'} / \text{Height of A'A}) \quad (4)$$

$$L_6 = [(\text{Height of A'A})^2 + (\text{Length of E A'})^2]^{1/2} \quad (5)$$

$$\Theta' = 180 - \alpha \quad (6)$$

$$L_5 = [(L_6)^2 + (L_7)^2 - (2*b*c*\cos(\Theta'))]^{1/2} \quad (7)$$

$$\text{Sine } \Theta = (\text{length of EA'} / L_5) \quad (8)$$

From equation 4-8, a tabulated data was created in Table 6 by assuming the lengths and heights of the landing strut. A graph was also plotted which is shown in Figure 7, where it shows the variation of angles vs the height of the strut. The trend line form Figure 7 shows that as the height of the strut is increased, the angle increases as well. From this we can conclude that the major factor that decides the angle of the strut is the height. By increasing the height, the angle is also increased. But the angle must not be too small as well, as by having a smaller angle might tilt the lander during landing as its too vertical.

Table 6: Side View Calculation of the Landing Strut

	Gravity (m/s^2)	Mass (kg)	Length A' to E (mm)	Height A to B (mm)	Height A' to B (mm)	Height A' to A	b (mm)	a (mm)	Theta (Θ')	Alpha (α)	Theta (Θ)
Side View	9.81	350	250	200	814	614	662.9	851.5	157.8	22.2	17.1
			240	190	784	594	640.7	668.2	158.0	22.0	21.0
			230	180	754	574	618.4	644.0	158.2	21.8	20.9
			220	170	724	554	596.1	619.9	158.3	21.7	20.8
			210	160	694	534	573.8	595.7	158.5	21.5	20.6
			200	150	664	514	551.5	571.6	158.7	21.3	20.5
			190	140	634	494	529.3	547.5	159.0	21.0	20.3
			180	130	604	474	507.0	523.4	159.2	20.8	20.1
			170	120	544	454	484.8	499.4	159.5	20.5	19.9
			160	110	514	434	462.6	475.5	159.8	20.2	19.7

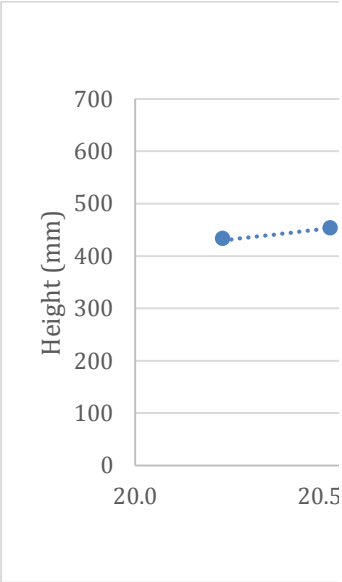


Figure 7: Height vs. Alpha

According to Banks and Cameron [9], the minimum required angle has to be 16.7° and the maximum angle is 47°. This minimum angle ensures that there will be no tilt unless the leg is being angled too vertically where the forces will be focused on a single point in the. It was then decided that the angle that would be used for the strut is 22.2°. This was chosen by taking the height of the strut into account. Therefore, the ideal height of the structure was found out to be 814 mm. The next step was determining the forces acting on each strut. There are 3 struts in a leg which are named as middle strut and secondary struts. Since the middle strut is acting as a zero-force member shown in Figure 8, there will be no force acting on that strut except for stability purposes. The force is then distributed amongst the secondary strut which is shown in Figure 9.

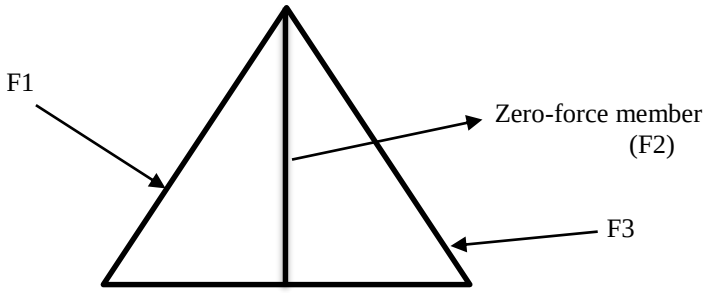


Figure 8: Example of a zero- force member

The calculation of the forces was derived from the following equations;

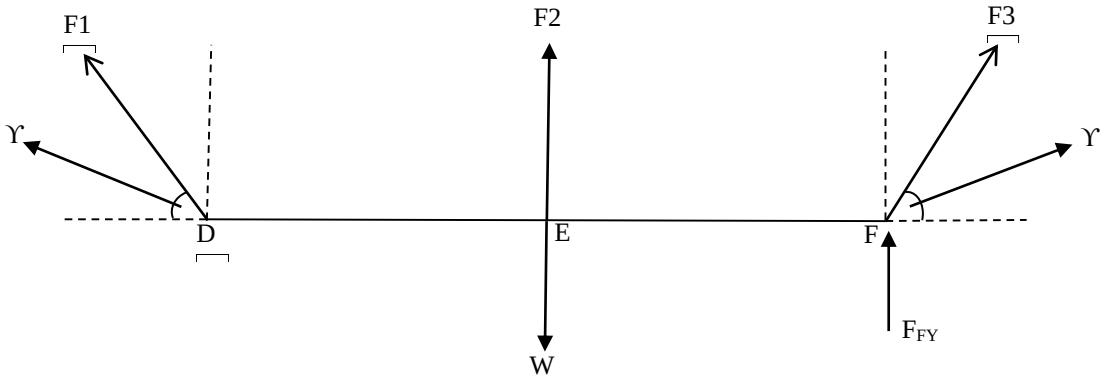


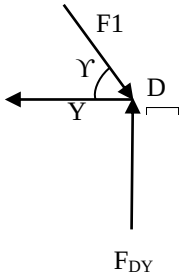
Figure 9: Force components acting on the landing struts

$F1 = F3$ (9)

$\sum M_D = 0$; -W*(length of DF/2) + (length of DF)*$F_{FY} = 0$ (10)

$\sum F_Y = 0$; $F_{DY} + F_{FY} - W = 0$ (11)

Point D



$$\sum Fy = 0; (W/2) - F1*\sin(\Upsilon) = 0 \quad (12)$$

$$\sum Fx = 0; F1*\cos(\Upsilon) - Y = 0 \quad (13)$$

By solving equations 10-13, F1 was found to be 589N. The data was tabulated in Table 7, where it shows the forces that are acting on F1 and F3. The finalized angles, heights and forces that was used to do the simulation using ANSYS is underlined on Table 5 to 7.

Table 7: Forces acting on the secondary struts

Weight (N)/leg	Force of DY (N)	Force of FY (N)	F1	F2	F3
1144.5	572.25	572.25	589.1	0	589.1
			590.8		590.8
			592.9		592.9
			595.2		595.2
			598.0		598.0
			601.4		601.4
			605.5		605.5
			610.4		610.4
			624.3		624.3
			634.2		634.2

3.2 Finite Element Analysis

In this research, a 0.01m meshing size was used to achieve the maximum achievable results. The material that was used for the landing gear is Aluminum Alloy 6061-T6 as this material can withstand greater temperature and is lighter compared to titanium alloy or stainless steel.

Figure 10, shows the total deformation acting on the landing strut. It can be seen that the total deformation is acting on the base of the landing strut. Therefore, the deformation will be focused on the contacting strut and according to the value generated by ANSYS, there was a minimal non-significant deformation which is not contributing to any form of serious damage or collapse of the landing strut. The maximum deflection was found out to be 0.00082156 m.

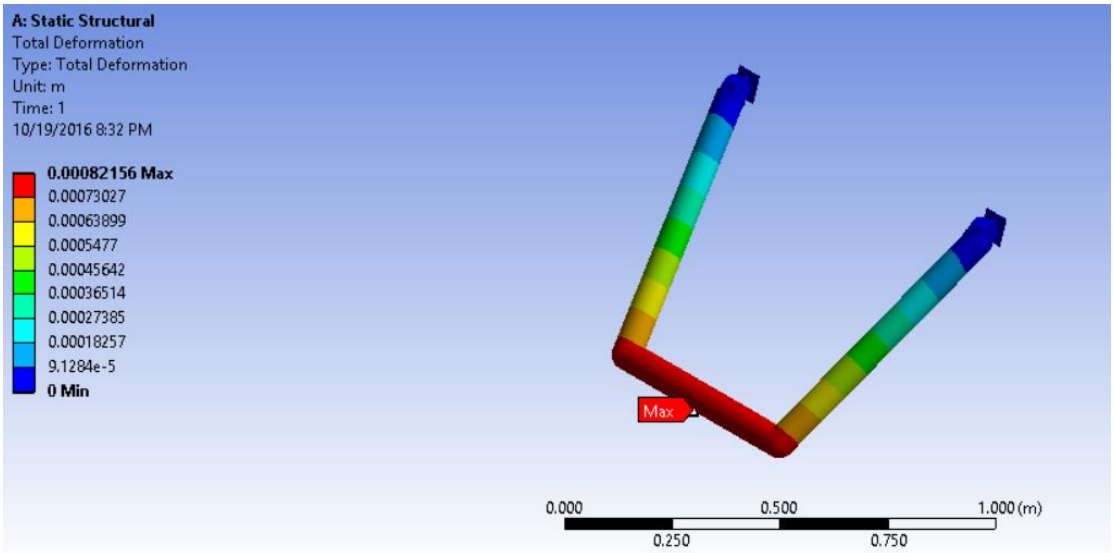


Figure 10: Total deformation of the landing strut

Figure 11 shows the total deformation that occurred during impact on the landing strut joint which is the connection of the landing strut to the bus structure. From the result that was obtained, the maximum deflection is 6.121E-6 m which is very minimal to have an impact on the landing strut. The maximum deflection is at the edge of the joint because that is where the force acts during the landing.

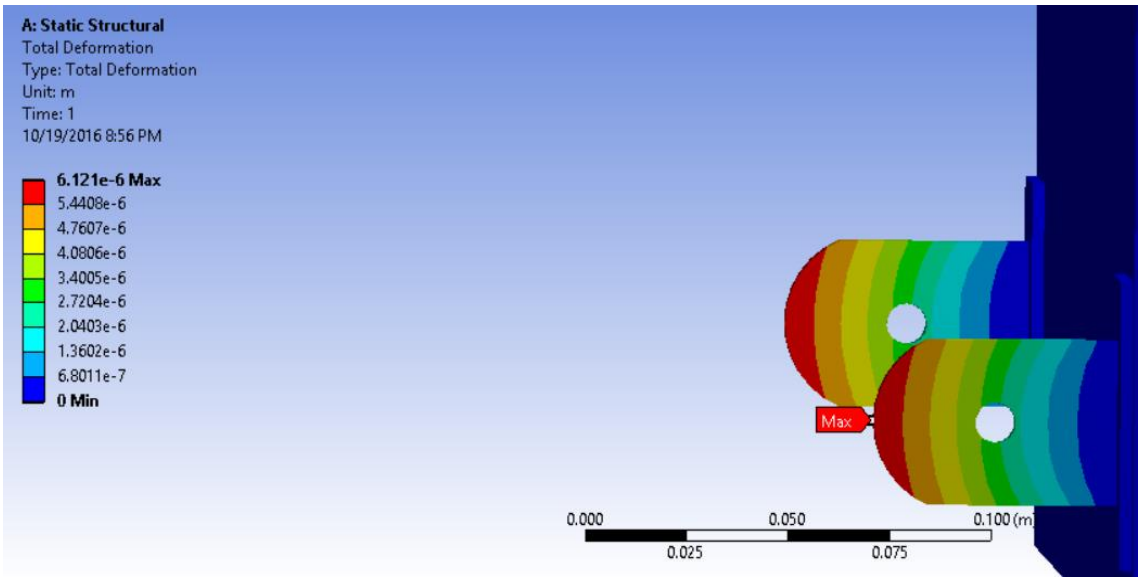


Figure 11: Total deformation of the plate joint

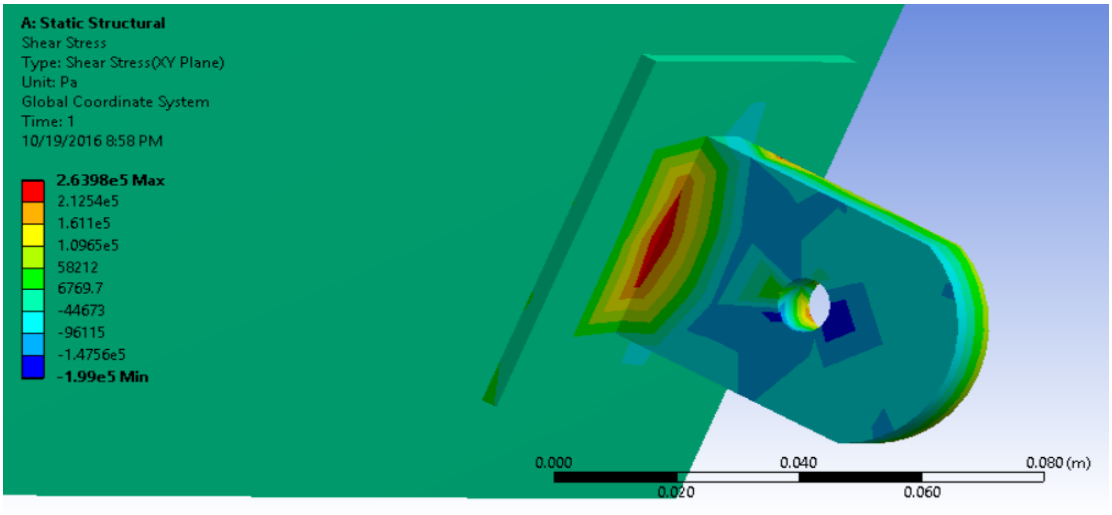


Figure 12: Shear stress of the plate joint

As for the shear stress shown in Figure 12, the max stress occurs in the plate joint. This is because during landing, shear occurs when there is a connection between two different parts. In this case, it is between the landing strut and the joint where they are connected and during landing the shear would try to break the connection. But by comparing with the shear strength of the material, it was found that the max shear stress which is 2.6398E5 Pa is smaller compared to the shear strength of the material which is 207 MPa. This ensures that the joint will not fail due to shear.

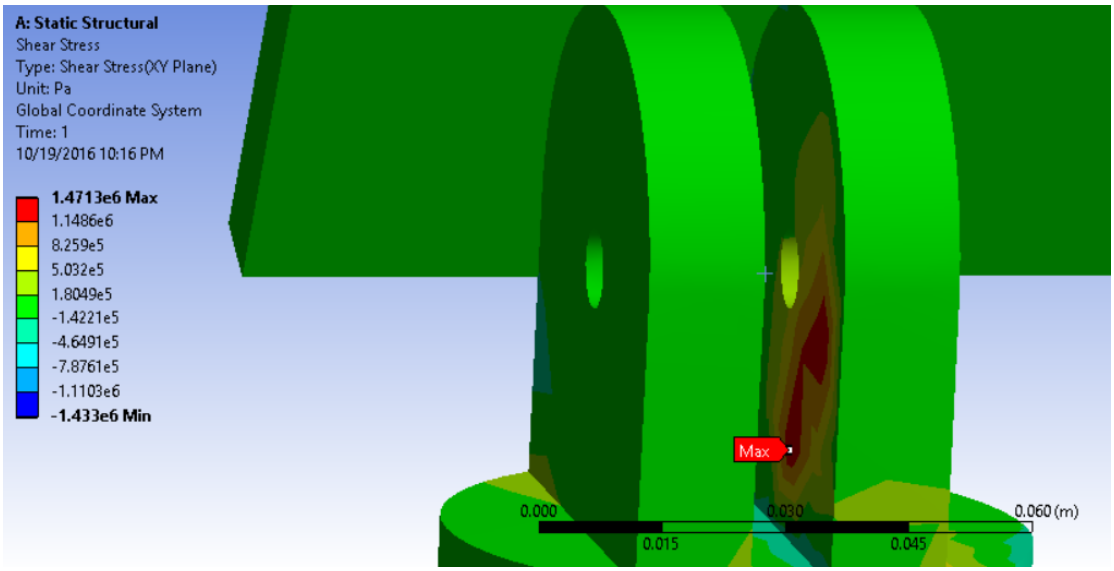


Figure 13: Shear stress on the landing strut connector

The same observation is found in Figure 13, where the shear stress occurs on the landing strut connector which is 1.4713E6 Pa. When the lander lands on the lunar surface, there is an opposite reaction which in this case is the force. The force is applied on the strut where it might break the strut which will results in mission failure but from Table 1, the shear strength of the material indicates that the material strength is greater than the shear stress. Therefore, the material will no break from shearing.

Figure 14 shows the total deformation that the landing strut goes through from a cross-sectional view. By having a cross-sectional view, more information can be gathered on the effect of the material due to the landing impact. The difference between Figure 10 and Figure 14, is that Figure 10 shows the deformation that's acting outer layer of the landing strut but Figure 14 shows more in depth

of the deformation that occurs inside the landing strut. The maximum deflection which is 1.3269E-5 m, is not significant enough to damage or destroy the landing strut.

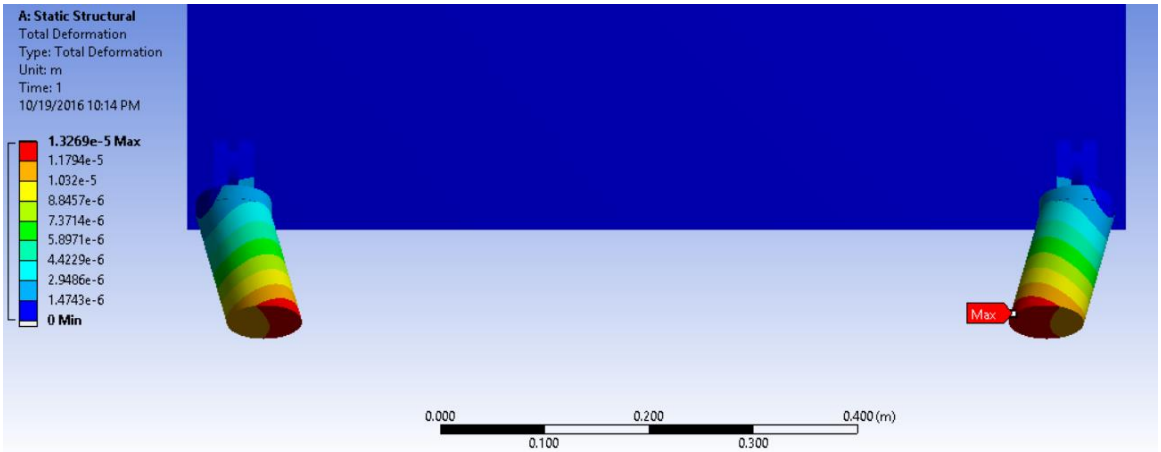


Figure 14: Total deformation of the landing strut (cross-sectional view)

4.0 Conclusion

In conclusion, the landing gear angle was found out to be 22.2º where it is in between the maximum and the minimum angle required to achieve stability. The force that's acting on the strut during impact was calculated to be 589.1 N where the forces are the same on the both the struts as they are symmetrical. From the ANSYS results, it can be concluded that the landing gear will not fail by deformation or by shearing due to the mechanical properties of the material. The maximum shear stress of the landing strut connector and the plate joint is 2.6398E5 Pa and 1.4713E6 Pa. Furthermore, the maximum deflection of the landing structure (outer layer), cross-sectional view of the landing strut and the plate joint are 0.00082156 m, 1.3269E-5 m and 6.121E-6 m.

Reference

[1] Jakobsen, H. 2012. What would we do without the moon?,*sciencenordic*.

[2] Foundation, X. 2016. Overview, Google Lunar XPRIZE. [Online]. Available: http://lunar.xprize.org/about/overview. Accessed: October 17

[3] Zak, A. 2016. Russia's unmanned missions toward the moon. [Online]. Available: http://www.russianspaceweb.com/spacecraft_planetary_lunar.html.Accessed: October. 17

[4] Pham, V. L., Zhao, J., Goo, N. S. (2013). Landing Stability Simulation of a 1/6 Lunar Module with Aluminum Honeycomb Dampers. *International Journal of Aeronautical and Space Sciences*, 14(4), 356-368.

[5] Jun, C. H. (2016). *Design and Simulation of Lunar Lander Bus Structure*. Taylor's University

[6] ASM International Handbook Commitee, Properties and selection: Nonferrous alloys and special-purpose materials, vol. 2. 1990.

[7] Inox E., Stainless Steel: Tables of Technical Properties, vol. 5, 2010.

[8] ASM Material Data Sheet Close Analogs, Properties and selection: Titanium Ti-6Al-4V, pp1-2, 2015

[9] Banks, B. and Cameron, I. (2009). *Lunar Landing Gear*. Queen's University.

eureca 2016 – Conference Paper
Paper Number 2ME26

Effect of Size and Shape of Side Mirrors on the Drag of a Personal Vehicle

Stephanie Lai Shen Ai*, Abdulkareem Sh. Mahdi Al-Obaidi, Lim Chin Hong

Department of Mechanical Engineering,
School of Engineering, Taylor's University, Malaysia.

*Corresponding Author: stephanieshenai.lai@sd.taylors.edu.my

Abstract

This study aims to evaluate the effect of size and shape of side mirrors on the drag force of a personal vehicle. In running conditions of a vehicle, the side mirror contributes to the increase of drag, hence increasing the fuel consumption. However, the side mirror only contributes to the drag when velocity is greater than 60 km/h. This study was carried out on a locally manufactured vehicle, the Perodua Myvi and its side mirrors. The average drag coefficients of a Perodua Myvi and its standard mirror were calculated as 0.354 and 0.175, respectively. The side mirror comprises of 3% of the total frontal area of the Perodua Myvi. The removal of standard side mirrors reduces the total drag coefficient of the vehicle by 4.9%. Three parameters of side mirrors were investigated using Computational Fluid Dynamic simulation. The meshing and solution methods were verified with published papers. The study was conducted at subsonic speeds with Mach number less than 0.1. The simulation was performed at a range of velocities between 80 km/h (22.22 m/s) to 120 km/h (33.33 m/s). The results obtained from the simulation were validated with published results and show at low subsonic speeds, the drag coefficient of the car is almost constant. A shorter side mirror mount would decrease the drag coefficient of the side mirror by 1-5%. In addition, a smaller side mirror produces a lower drag coefficient of the side mirror by 14-43%. Finally, increasing the radius of housing curvature would decrease the drag coefficient of the side mirror.

Keywords: Side mirror, Perodua Myvi, Drag coefficient, Subsonic, Computational Fluid Dynamic

1. Introduction

Side mirrors can be commonly found mounted onto the exterior of vehicles. The side mirror functions as a visual aid to view the parameters of the car. Otten [1] conducted a survey and found the average frontal area of a pair of side mirrors consists of 2-3% of the overall frontal area. In running conditions of the vehicle, the side mirror contributes to the drag of the vehicle. The side mirror only contributes to the drag when the velocity is greater than 60 km/h [2].

Aerodynamic drag is the force opposing the forward motion of a moving vehicle. Viscous force is the main contributor to drag at lower velocities. Therefore, skin friction drag is the main source of aerodynamic drag in a vehicle at low velocities [3]. However, pressure drag is a main source of drag at cruising speeds. Pressure drag is present when a shape changes abruptly. Pressure drag at the front of a vehicle is found to be higher than the rear [4]. Aerodynamic drag can be reduced by streamlining of the body as it is highly dependent on an object's shape. Magazoni, et al. [5] found that the upper body of a vehicle experiences 45% of aerodynamic drag force. One of the components found in the upper body that contributes to drag is the side mirror. Turbulent wake is formed at the rear of the side mirror due to its shape. The total drag produced by side mirrors is 2-7% of the total drag of a vehicle [6]. Complex aerodynamic characteristics such as drag coefficient can be calculated using Eq. (1) in which F_D can be obtained through experiments.

$$F_D = \frac{1}{2} C_D \rho A V^2 \tag{1}$$

where, F_D is the drag force, C_D is the drag coefficient, ρ is the density of air, A is the frontal area, and V is the velocity of the object.

Olsson [6] numerically studied the drag coefficient of a simplified Mercedes-Benz A-class with no interior components or engine compartments. The author analyzes the optimization of the side mirrors that adheres to the law and regulations of European Union Law. Vibration noise factors were excluded from this study. Olsson studied ten different cases, which such as including the car with mirror, without mirror, using a reference mirror, different housing curvatures and varying gaps. The CFD simulation was conducted using PowerCASE software. The simulation results were validated with wind tunnel experiment. The CFD simulation shows a 13% percentage error as compared to wind tunnel results. The study concluded that modified side mirror produces an up wash effect in the rear front, which results in a reduction of drag. Olsson also found that a combination of two different modifications that individually reduces the drag can together produce a worse drag.

Batchelder [7] conducted research with a Smart Fortwo on the different components which enhances the aerodynamic shape of the vehicle. The author studied side mirrors, stock style wheels, door handle, antenna and wheel well covers. The car was meshed using TGrid and imported into FLUENT to conduct the simulation. The removal of the side mirror reduces the drag coefficient by 4.8%.

Buscariolo and Roshilho [8] considered the applications of side mirror removal and the implementation of outside rear-view cameras using CFD simulation. The research conducted focused on the drag coefficient in respect to the frontal areas

of a car. Four cases were studied including car with mirror, without mirror, and two concepts of outside rear view camera housing. The turbulence model used was k-ε to establish pressure, wake profile and drag coefficient. The removal of side mirror, and two implementation of camera installation reduces the drag coefficient by 1% and 0.4% respectively.

Ramdan and Lim [9] conducted a research to determine the fuel economy of a Perodua Myvi within the city and on highways. MATLAB backward-facing discretized simulation was used to solve the fuel consumption of the vehicle. Experiments were physically conducted to compare with the results obtained numerically. The simulation shows an average error percentage of 13% as compared to the experiments conducted. The results obviously showed that the highway routes produce a better fuel economy as it travels constantly at a cruising speed. Similarly, Alam and Mahmood [10] analyzed the effect of side view mirror on fuel efficiency. Two types of mirror geometry were considered, a 13-cm diameter flat back and hemispherical back mirror. The drag coefficient was solved analytically travelling at an average speed of 60 km/h and 120 km/h. The hemispherical back mirror produces a lower fuel consumption which saves 7.33 and 29.3 liters of petrol a year respectively.

The present paper aims to determine the effect of size and shape of side mirrors on the drag of a personal vehicle. First, the study will consider how the size and shape of side mirrors affect the drag by comprehending the fundamental background of fluid mechanics and aerodynamic by analyzing numerically. Mirror optimization is carried out to determine the best shape and size of a side mirror that produces a minimum drag. The design process of the side mirror should adhere to the legal demands of Malaysia. The research parameters are governed by the scope of study. A clean simplified side mirror, without interior or exterior components, was studied. Only personal vehicles such as sedans, hatchback are considered. The drag coefficient is solved numerically using CFD application. Lastly, the design of a side mirror must abide with the legal demands and regulations of Malaysia, taken from section 11 (2) of [11], which states that the dimensions of the main exterior rear-view mirrors for Classes II and III. A personal vehicle falls under the category M1 (carriage of passengers no more than eight seats) of Class III (small main side mirror).

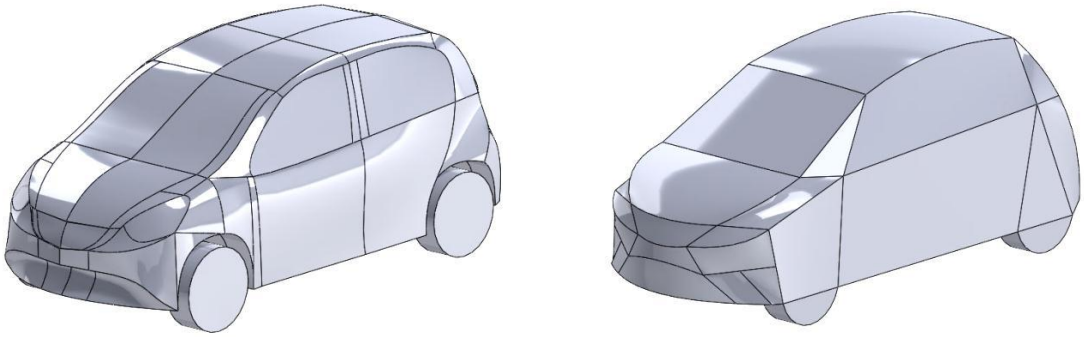
2. Research Methodology

This section discusses the method in conducting this research. The discussion contains justification of each task and the configurations used for this study.

2.1 3-D Geometry Modelling

Based on the scope derived for this study, a personal vehicle was chosen from a locally manufactured car, the Perodua Myvi. The second generation of Perodua Myvi 1.3 EZi was released in 2012. This model was chosen as the test model for this research due to its relevance in studying a localized vehicle. The car was constructed by surface modelling using SolidWorks as shown in Fig. 1(a). The vehicle and side mirror were separately modelled. The vehicle without side mirror was modelled with ground clearance, length, width and height of 0.218 m, 3.576 m, 1.605 m and 1.31 m, respectively. However, due to the complexity of shape and limitation of time, a

simplified model was produced by outlining the general shape of the existing test model as shown in Fig. 1(b). The simplified model was modelled with ground clearance, length, width, height of 0.207 m, 3.558 m, 1.507 m and 1.487 m, respectively.



(a) (b)

Figure 1. Myvi Configuration (a) Modelled (b) Simplified

The frontal area for the original and simplified model measures to be 2.06 m^2 and 1.97 m^2 respectively. The frontal area of the simplified model has an average percentage error of 4.4% compared to the first model.

The dimensions of the side mirror were measured with a physical model. The side mirror was modelled with SolidWorks as shown in Fig. 2. The frontal area of two modelled side mirrors is measured to be 3% of the total frontal area of the simplified car. This value is verified with the survey conducted by Otten [2]. As this research studies the effect of size and shape of side mirror to drag, three different designs were modified from the standard side mirror. The designs will be further discussed under results and calculations.

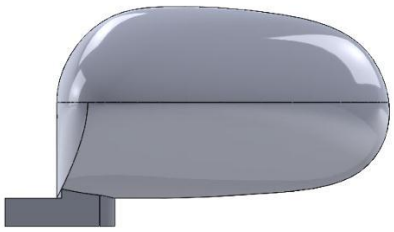


Figure 2. Standard Side Mirror

2.2 Numerical Method

2.2.1 Geometry Modelling

To simulate wind tunnel conditions of a stationary car with fluid flow, an enclosed domain was created. The enclosed domain is defined by a half-body model. The model is assumed to be symmetric with a steady flow. Therefore, a large enclosed domain is produced to create an undisturbed inlet and outlet flow. To obtain accurate results, the recommended dimensions of an enclosed domain should be 30 times of the car's length, L. However, with the limitation of time, the dimension units of the enclosed domain were taken from the studies of [4, 12]. The dimensions were standardized with L. The inlet and outlet distance are at a distance of 2L and 4L as

shown in Fig. 3. A body of influence was created to direct the focus to the vehicle. The body of influence was placed at a distance of 0.5 m, 2 m and 1.25 m from the front, rear and side of the car respectively. The enclosed domain and body of influenced was placed slightly above the x-axis, intersecting the tires of the model. This is to ensure there is no fluid passing the tires to simulate real running conditions.

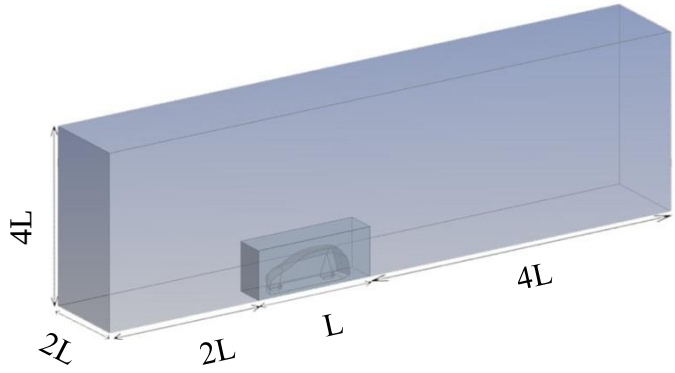


Figure 3. 3-D Enclosed Domain

In addition, an enclosed domain was done similarly for the side mirror with specific dimensions as in Fig. 4. The side mirror is suspended 2 m from the ground.

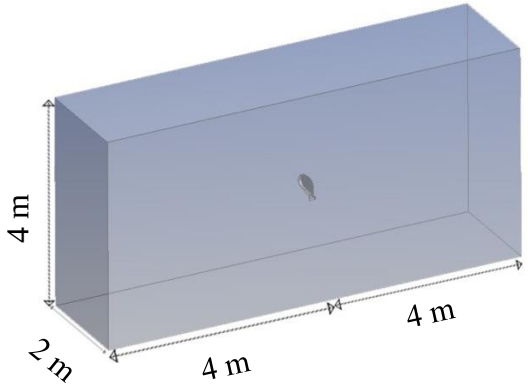


Figure 4. 3-D Enclosed Domain

2.2.2 Meshing Method

Meshing is an important factor in producing accurate results. An exercise was conducted prior to this study with NACA 4415 at Reynolds number $3 \times 10^6$for 0° angle of attack. This exercise was done to validate the meshing method used in studying the drag coefficient. The results were verified with a NACA report [13] and obtained an error percentage of 19%.

Tetrahedral mesh was used due to its proximity and curvature of the vehicle. The global mesh size settings had a coarse relevance center which produces an appropriate mesh that creates finer mesh around the curvatures of vehicle's body and produces large mesh sizes further away from the body. The default mesh was improved to capture the flow around the vehicle. This study uses a combination of meshing method from [4, 12, 14]. Firstly, face sizing was applied to the faces of the vehicle to refine the mesh of the faces of the vehicle. The number of elements in the

vehicle increases as the size of each element decreases as compare to the default mesh. Secondly, two inflation layers were added. The first inflation layer was around the vehicle to capture the boundary effects of flow around the vehicle. The second inflation layer on the wind tunnel floor. This would reduce numerical diffusion and provide good analysis of flows near the floor and the vehicle [15]. Both inflation have a first layer thickness of 0.005 m with a seven layers at a growth rate of 1.3. Lastly, body sizing was applied on the body of influence as a local refinement. The majority of elements are found around the vehicle and wake region as shown in Fig. 5.

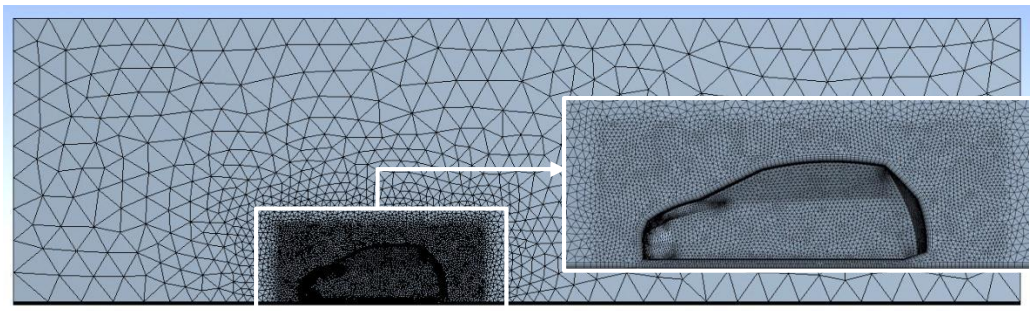


Figure 5. Final Mesh Generation

Similarly, the standard side mirror uses the same global mesh size setting as the vehicle. The inflation was generated on the mirror with a growth rate of 1.2. The edge sizing was applied to the edges of the mount. Fig. 6 shows the details of mesh on the side mirror.

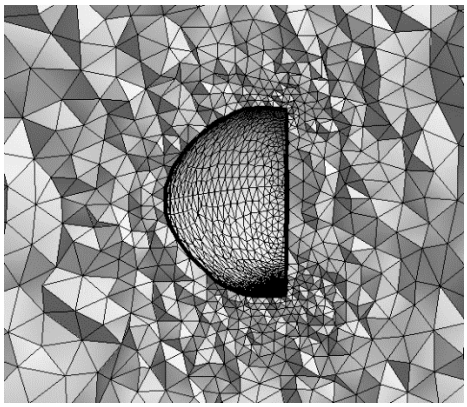


Figure 6. Mirror Name Selections

2.2.3 Numerical Setup

Navier-Stokes equation was used together with k-ε turbulence model to solve the airflow. Navier-Strokes equations consists of governing equations such as continuity equation Eq. (2) and momentum equations Eq. (3-5).

$$\frac{\partial \rho}{\partial t} + \nabla \cdot (\rho V) = 0 \tag{2}$$

$$\frac{\partial \rho u}{\partial t} + \nabla \cdot \rho u V = -\frac{\partial P}{\partial x} + \nabla \cdot (\mu \nabla u) + S_{m,x} \tag{3}$$

$$\frac{\partial \rho v}{\partial t} + \nabla \cdot \rho v V = -\frac{\partial P}{\partial y} + \nabla \cdot (\mu \nabla v) + S_{m,y} \quad (4)$$

$$\frac{\partial \rho w}{\partial t} + \nabla \cdot \rho w V = -\frac{\partial P}{\partial z} + \nabla \cdot (\mu \nabla w) + S_{m,z} \quad (5)$$

where *u*, *v* and *z* is the component of velocity vector in *x*, *y* and *z*-components. ρ is the air density, *P* is static pressure and $S_{m,x}, S_{m,y}$ and $S_{m,z}$ are source terms for *x*, *y* and *z*-components.

The flow is considered as incompressible as the Mach number is less than 0.3. The material of the fluid is set to air with its default values of density and viscosity. The k-ε turbulence model was selected with standard wall treatment to follow the conditions of a wind tunnel. The turbulence model was selected based on the setup by Magazoni, et al. and Buscariolo and Rosilho [5, 8] Besides that, k-ε turbulence model is a suitable model due to the ground clearance which emulates an internal flow. Whereas, the Spalart Allmaras turbulence model was selected for the side mirror as it is suspended on air and attached to the walls. The body of the vehicle, side mirror and floor of wind tunnel were set to no slip wall condition. The symmetry was set as a symmetry plane. The inlet specified the velocities ranging from 80 km/h to 120 km/h, with intervals of 10 km/h. However, the velocity input in FLUENT is in m/s. The output boundary condition uses an outlet pressure of 0 Pa. Pressure far field was not selected due to the intersection between the wheels and wind tunnel floor, which prevents the selection of pressure far field. The simulations were conducted at varying speeds for the following cases.

1. Vehicle without mirror.
2. Isolated standard side mirror.
3. Three different designs of an isolated side mirror.

2.2.4 Study Cases

Table 1 represents the different designs of side mirror studied in this research. A range was given to each parameter to determine an optimum design that produces minimum drag coefficient. The parameters were set by non-dimensional ranges starting from 70% up to 130%, with 10% increment. Abbreviations are used to identify the design as Height of Foot (HF), Scale Factor (SF) and Radius of Housing Curvature (RC) is equivalent to the standard mirror.

Table 1. Parameters of Case Study

Parameters	Range of Application
Height of Foot (HF)	0.7 HF ≤ HF ≤ 1.3 HF
Scale Factor (SF)	0.7 SF ≤ SF ≤ 1.3 SF
Radius of Housing Curvature (RC)	0.7 RC ≤ RC ≤ 1.3 RC

Height of Foot

The first parameter, height of foot represents the height and thickness of the side mirror's mount. Six different heights were simulated at various speeds. Other components of the side mirror were kept constant. Figure 7 represents three ranges of

different heights of foot. The range 0.7 HF ⩽ HF ⩽ 1.3 HF ranges from 140 mm to 260 mm respectively.



0.9 HF 0.8 HF 0.7 HF

Figure 7. Height of Foot

Scale Factor

The second parameter changes the scale of the side mirror only, as the dimensions of the mount remains constant. This is to study the effect of size on the drag of a side mirror. Figure 8 shows three ranges of different scale factors. The range 0.7 SF ⩽ SF ⩽ 1.3 SF ranges from 164.50 mm to 305.50 mm respectively.

.

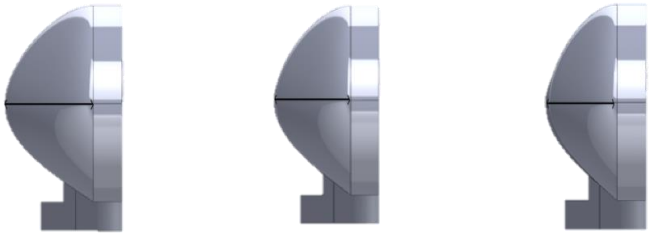


0.9 SF 0.8 SF 0.7 SF

Figure 8. Scale Factor

Radius of Housing Curvature

The last parameter considered is the curvature of the housing. The radius of housing curvature was adjusted as shown in Fig. 9. Six different housing curvatures were simulated. The frontal area of the mirror housing was kept constant. The range 0.7 RC ⩽ RC ⩽ 1.3 RC ranges from 69.35 mm to 107.68 respectively.



0.9 RC 0.8 RC 0.7 RC

Figure 9. Radius of Housing Curvature

2.2.5 Assumption

Few assumptions were established at the beginning of this research are stated below.

1. The effect of the ground is not considered.
2. The computational domain is to replicate the set up of a wind tunnel.
3. The car configuration is approximately due to the complexity of the shape which requires more time.
4. The side mirror is perpendicular to the airflow. Inclination angle is not considered.

2.2.6 Calculation of Side Mirror

The subtraction of drag coefficient of a vehicle with mirror and without mirror equals to the drag coefficient of an isolated side mirror. However, this study simulates an isolated mirror separated from the vehicle. Therefore, a ratio must be used to calculate the the drag coefficient of a side mirror in respect to the whole vehicle in Eq. (6).

$$C_{D(mirror)} = C_{D(value\ obtained\ from\ CFD)} \frac{A_{Two\ mirrors}}{S_{ref}} \quad (6)$$

where $C_{D(mirror)}$ is the drag coefficient of mirror, $C_{D(value\ obtained\ from\ CFD)}$ is the drag coefficient solved by ANSYS FLUENT, $A_{Two\ mirrors}$ is the frontal area of each side mirror, and S_{ref} is the frontal area of the vehicle without mirrors. The frontal areas for both mirrors and vehicle are measured using SolidWorks.

3. Results and Discussion

3.1 Car

The relation between drag coefficient and velocity of the car is shown in Fig. 10. It can be observed that the highest contributor to drag coefficient is from pressure drag. Fig. 10 displays a constant drag coefficient through different velocities. This was validated as drag coefficient is constant at low Reynolds number [3]. The drag coefficient of a Perodua Myvi is said to be between 0.32 - 0.35 [9, 16, 17]. However, these values are not verified as the official provider does not state the drag coefficient of this model.

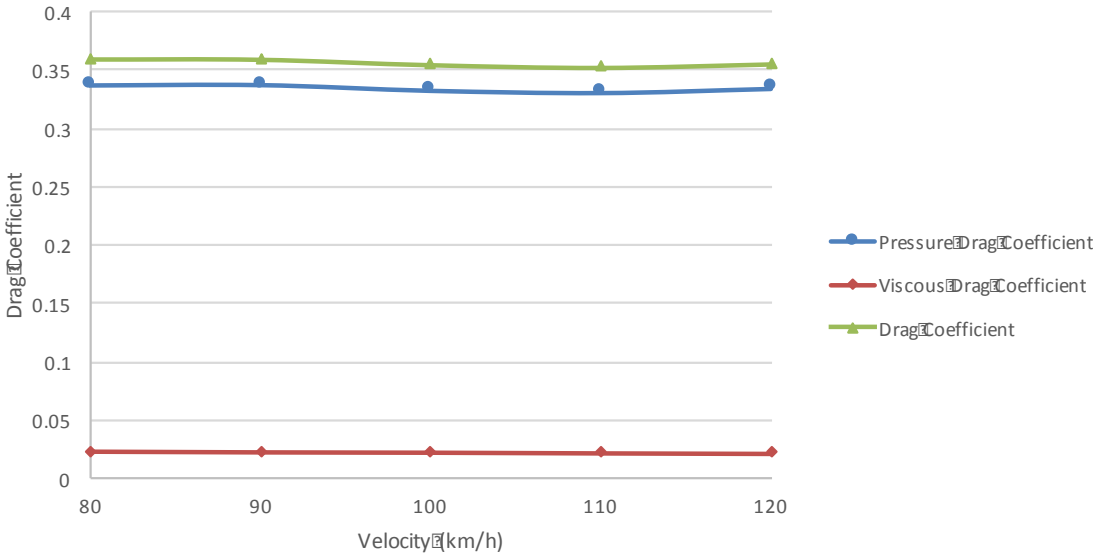


Figure 10. Drag Coefficient vs. Velocity

Figure 11 exhibits the pressure distribution of a car running at 100 km/h. The pressure is highest at the front of the vehicle. The pressure behind the vehicle is lower than the front. Simultaneously, velocity is lowest at the front of the vehicle due to stagnation point as shown in Fig. 12. The boundary layer was created over the vehicle with an inflation mesh. The wake can be found when air exits the rear of the vehicle.

Figure 13 displays the pressure distribution of the vehicle. The fluid compresses at the front of the vehicle, resulting in high pressure and a downward force. Simultaneously, air is travelling along the side of the vehicle at atmospheric pressure, forming a lower pressure than the front.



Figure 11. Pressure Distribution over Symmetric Plane

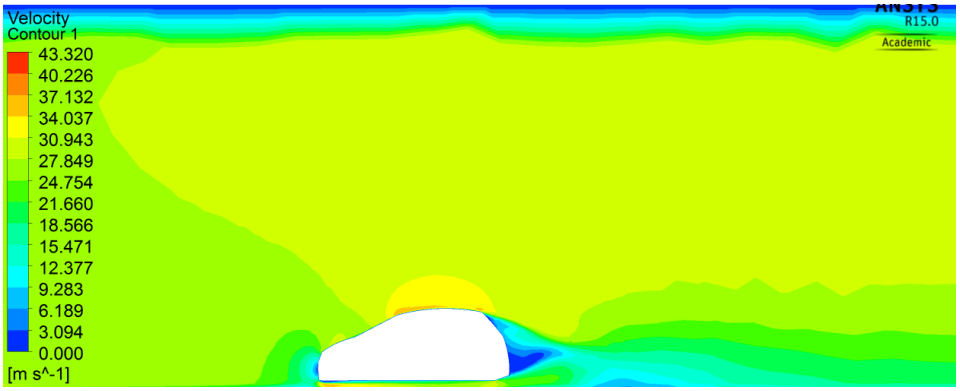


Figure 12. Velocity Distribution over Symmetric Plane

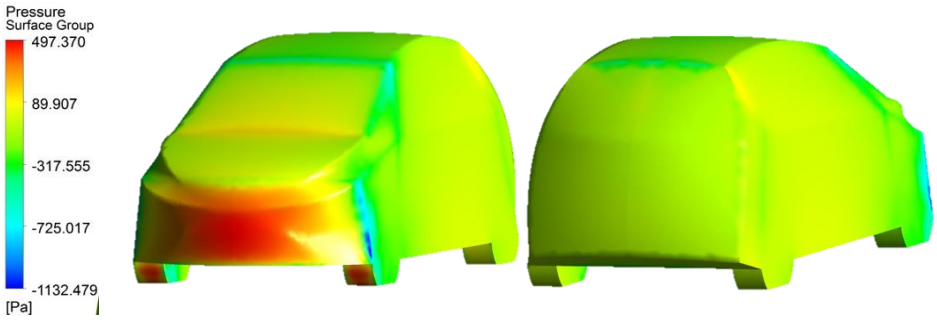


Figure 13. Pressure Distribution over the Vehicle

3.2 Side Mirror

3.2.1 Standard Mirror

Figures 14 and 15 represent the pressure contour and velocity vector profile of a standard side mirror at 100 km/h. The standard mirror shows high pressure when the flow reaches the front surface of the side mirror, this reduces the airflow speed and reducing the boundary flow separation. The standard mirror contributes to approximately 4.9% of drag reduction to the whole vehicle.

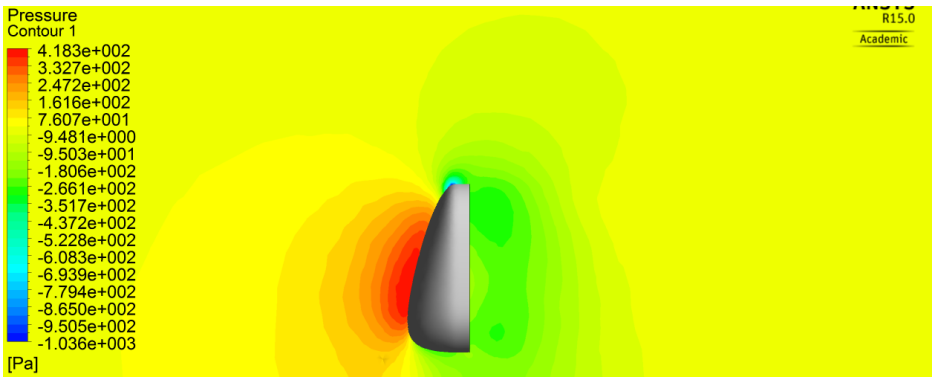


Figure 14. Pressure Contours over the Side Mirror from Top View

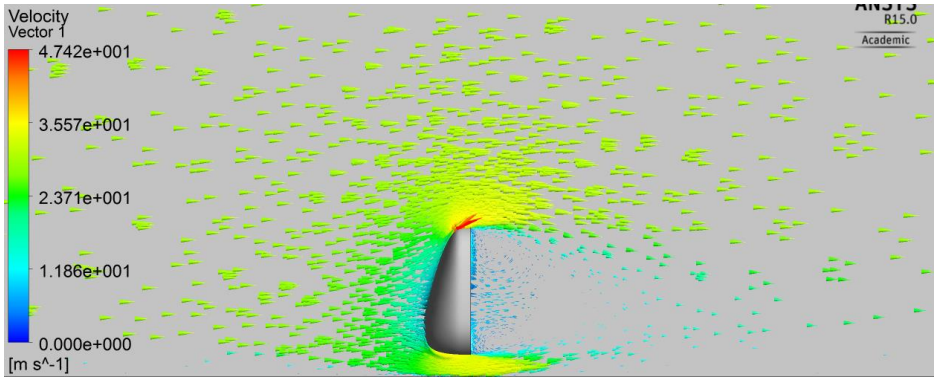


Figure 15. Velocity Vector over the Side Mirror from Top View

3.2.2 Height of Foot

Figure 16 shows the results obtained for the parameter height of foot at different velocities. Based on Fig. 16, a similar trend is observed for all ranges. The drag coefficient increase when height of the mount increases. The flow separation between the wall of a wind tunnel and the side mirror slightly affects the total drag coefficient of a side mirror. However, the reduction of thickness has no significant in the reduction of drag coefficient. Reducing the thickness might affect the stability of the side mirror and may produce vibration.

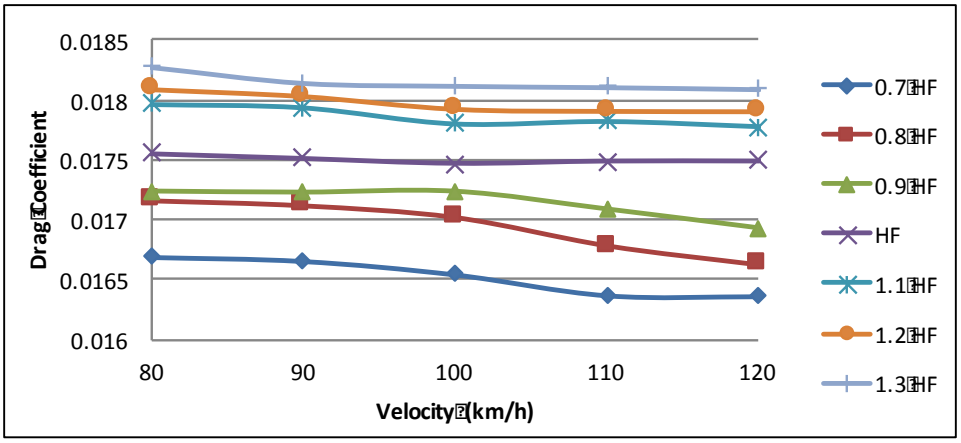


Figure 16. Drag Comparison between Different Height of Foot and Velocity

3.2.3 Scale Factor

Figure 17 illustrates the results from varying the scale factor of the side mirror at different velocities. Fig. 17 clearly shows a consistent trend through all the ranges. Drag coefficient decreases with a smaller scaled side mirror. Eq. (1) clearly shows that the dependency of drag coefficient to the frontal area. Therefore, a smaller area would result in a lower drag. This parameter shows a larger contribution to the reduction of drag coefficient than the height of foot parameter.

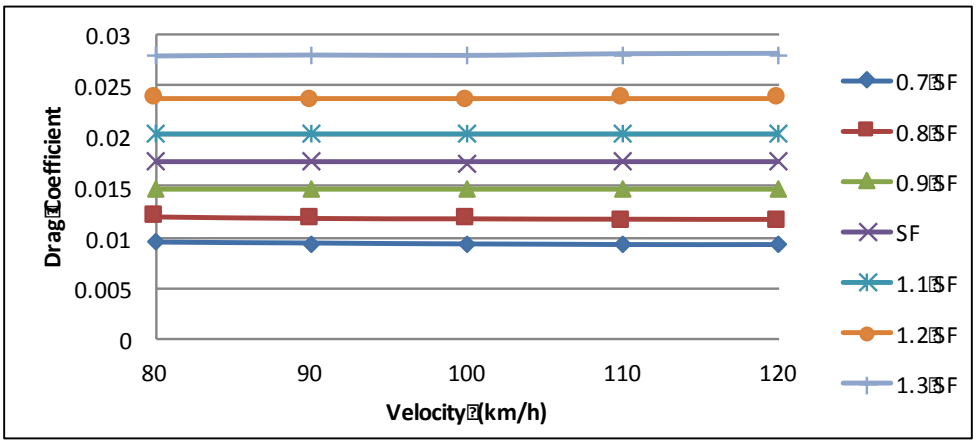


Figure 17. Drag Comparison between Different Scale Factors and Velocity

3.2.4 Radius of Housing Curvature

Figure 18 exhibits the results from different housing curvatures based on the standard mirror. A similar trend is observed, however the affect of drag to this parameter is the reverse of Figs. 16 and 17. A flatter housing is produced when the radius of housing curvature decreases, thus the drag coefficient increases. There is no major significance in the reduction of drag coefficient. However, the ranges in Fig. 18 have exceeded the results for standard side mirror. This result occurred as all these parameters shares the same frontal area as the standard side mirror.

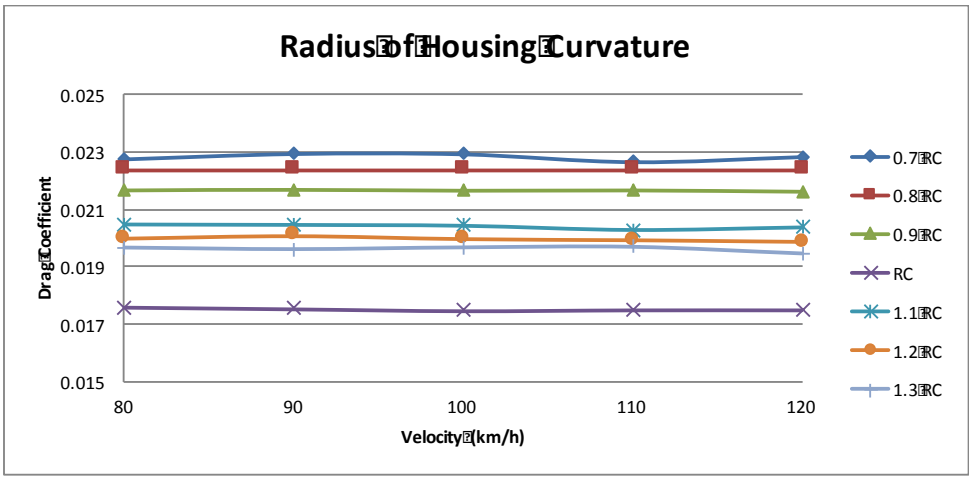


Figure 18. Drag Comparison between Different Radius of Housing Curvature and Velocity

4. Conclusions

The effect of size and shape of side mirror to drag of a personal vehicle was studied numerically. The frontal area of both side mirrors consist of 3% of the total frontal area of the vehicle. The standard mirror reduces 4.9% the drag coefficient of a Perodua Myvi. Three different parameters were considered to study the drag effect. The effect of these parameters is summarized as follows.

- The decrease of height and thickness of the mount reduces the drag coefficient of the side mirror.

- The decrease of volume of the side mirror reduces the drag coefficient of the side mirror.
- The increase of radius of housing curvature reduces the drag coefficient of the side mirror.
- The drag coefficient is approximately constant at low subsonic speeds.
- The size and shape of side mirror have effect on the vehicle's drag.

Acknowledgement

Throughout this whole research process, various guidance, supervision and assistance was offered. Much gratitude and appreciation to Shahrooz Eftekhari, Wesley Otten and Abdul Sattar Khathman as research partners.

Nomenclatures

A	Frontal area, m^2
$A_{Two\ mirrors}$	Frontal area of two side mirrors, m^2
C_D	Drag coefficient
$C_{D(mirror)}$	Drag coefficient of side mirror
F_D	Drag force, N
L	Length of car, m
S_{ref}	Frontal area of car, m^2
V	Velocity of fluid flow, m/s
ρ	Density, kg/m^3

Abbreviations

CFD	Computational Fluid Dynamic
HF	Height of foot
NACA	National Advisory Committee for Aeronautics
RC	Radius of housing curvature
SF	Scale factor

References

1. Otten, W. (2016). *Aerodynamic analysis of a personal vehicle side mirror.* Final Year Project, Interim Report, Taylor's University, Malaysia. (Private Communication).

2. Barnard, R.H. (2009). *Road vehicle aerodynamic design*. St Albans, United Kingdom: Mechaero Publishing.

3. Anderson, J.D. (2010). *Fundamentals of aerodynamics.* Avenue of Americas, New York: McGraw-Hill.

4. Birwa, K.S.; Rathi, N.; Gupta, R. (2013). Aerodynamic analysis of Audi A4 Sedan using CFD. *Journal of the Instituition of Engineering (India), 94*(2), 105-111.

5. Magazoni, F.C.; Maruyama, F.K.; Buscariolo, F.F.; Alves, J.C.L.; Volpe, L.J.D. (2015). Aerodynamic shape improvement for driver side view mirror of hatchback vehicle using adjoint optimization method. *SAE Technical Paper Series,* 36-0156.

6. Olsson, M. (2011). *Designing and optimizing side view mirrors.* Master's thesis, Chalmer University of Technology, Sweden.

7. Batchelder, J.H. (2009). *A CFD investigation of potential aerodynamic enhancements to a microcar class vehicle.* Master's thesis, Rensselaer Polytechnic Institute, USA.

8. Buscariolo, F.F., Rosilho, V. (2013). Comparative CFD study of outside rearview mirror removal and outside rearview cameras proposals on a current production car. *SAE Technical Paper Series,* 36-0298.

9. Ramdan, M. I., Lim, C.P. (2015). Fuel economy comparison of perodua myvi passenger vehicle on Malaysia city and highway drive cycles. *Journal of Scientific Research and Development, 2*(13), 76-82.

10. Alam, S., Mahmood, S.M. (2014). Study of side view mirrors design on the fuel consumption of a car. *Global Sri-Tech, 6*(4), 224-227.

11. Economic Commission for Europe of the United *Nations* (2013). *Uniform provisions concerning the approval of devices for indirect vision and of motor vehicles with regard to the installation of these devices.* Addendum 45: Regulation 46.

12. Damjanovic, D.; Kozak, D.; Zivic, M.; Ivandic, Z.; Baskaric T. (2010). CFD analysis of concept car in order to improve aerodynamics. *Keynote Address at International Scientific and Expert Conference TEAM,* Kecskemet.

13. Abbott, I.H.; Doenhoff, A.E.V.; Stivers, L.S.J. (1945). *Summary of Airfoil Data. Report No. 824.*

14. Cakir, M. (2012). *CFD study on aerodynamic effects of a rear wing/spoiler on a passenger vehicle.* Master's thesis, Santa Clara University, USA.

15. Lanfrit, M. (2005). *Best practice guidelines for handling automotive external aerodynamics with FLUENT.* Fluent Deutschland GmbH, Germany.

16. Zal, P. (2012). *2012 Perodua Myvi 1.3 EZi (model for Asia) specifications and performance data review.* Retrieved on 17 Oct from: http://www.automobile-catalog.com/car/2012/1224230/perodua_myvi_1_3_ezi.html

17. One Shift (2012). *Perodua Myvi EZI (A).* Retrieved on 17 Oct from: http://www.oneshift.com/new_cars/car-specs.php?pid=2090

eureca 2016 – Conference Paper
Paper Number 2ME27

Modelling and Optimization of Eco-Friendly Cardboard Furniture Stool

Tang Sheng Jiang, Ch'ng Shiau Ying
School of Engineering, Taylor's University, Malaysia
ShiauYing.Chng@taylors.edu.my

ABSTRACT
In this paper, the major issue of waste generation problem is being analyzed and it was found out that the corrugated cardboard occupied the most in the landfills. To provide a solution to minimize the landfills, an innovative idea is suggested of turning the cardboard into functional eco-furniture which is 100 percent bio-degradable to the surroundings. It is able to optimize the life-span of corrugated cardboard before sending them to landfill. In order to create functional eco-furniture, the internal design structure of corrugated cardboard may affect its strength which is the research question of this project. The objective is to model and analyze the design of the stool meanwhile minimizing the cost production by maximizing the strength and stiffness of the stool using SolidWorks and ANSYS. From the studies, the unique corrugated has different material strength when the force applied in different directions. In this project, an initial design A and improved design B were both undergoes simulation to determine the structural strength and material cost. The design B has improved 13.31% of structural strength as well as saved up the material cost by 6.43% compare to design A. Therefore, design B is chosen instead after the improvement were completed. Lastly, this project is able to reduce the problem of the landfill if most of the cardboard is used to reproduce into furniture made of the cardboard which may become a great sustainability for the environment.

Keywords: Corrugated Cardboard, Compression Test, Eco-Furniture, Simulation

1. Introduction

Waste generation is becoming a world issue for everyone, it can be heard from the news, social network or radio about how polluted the world has become. We as the human have continuously generated the solid waste which caused the major pollution to the environment such as water pollution and increasing of landfill. In Malaysia, waste generated is increasing rapidly due to the industrialization and urbanization that polluted the environment.

A study was done regarding to the generation of Malaysia Solid Waste (MSW) in the past 10 years and found out it has increased more than 91% [1]. It is estimated that the Malaysia has generated 0.81 kg/capita/day of solid waste which equivalent to 5.475 million ton in 2001 alone [2]. A shocking report was found out that the solid waste generated in Penang has the highest rate which is 7.34 million tons in 2006 that is able to fill up 42 buildings [3]. Therefore, it is very terrifying if no action or solution is provided to reduce and solve the issue.

Besides, the solid waste can be broken down into few categories such as plastics, woods, paper, metal, cardboard and so on. However, the highest percentage among the wastes generated is the paper and cardboard which occupied almost 40%. In order to reduce the waste, the paper and cardboard is the way to tackle on since it has the highest percentage among others. Instead of directly recycling the cardboard, an innovation way was suggested to solve and reduce the waste generated by re-producing eco-furniture.

There is always a value for everything, which including the waste generated by the human if we fully utilized them. Most of the cardboard and packaging material has very minimum lifespan as the users will throw them into trash after removing the goods. In such case, the amount of cardboard found in the landfill is higher comparing to others. In addition, it is such as waste to throw away the cardboard packaging especially with good and clean condition where it still has the value to turn it into a new product such as eco-furniture. Some of the eco-furniture are invented by a guy called Zach Rotholz where he used triple layers of corrugated cardboard to create furniture and started his own company by just selling these innovative products. Recently, there was another creation done by LEXUS Car Company where the model of the car is completely made out of just corrugated cardboard [4]. Both of these evidence show a great opportunity of creating products made out of cardboard with different type of application.

It is possible to turn the cardboard material into functional furniture that allows the people to actually use it for real life application. However, in order to create such furniture from the cardboard, it must fulfill some safety criteria such as the ability to support human weights up to a certain kilogram. From previous works done by the researchers, they have found that the factors affect the strength of cardboard include the height and angle of the flute, number of flute, bond length, direction against the flute and the material properties of the cardboard [5,6]. Besides, the researchers have done experimental and simulation to validate the final result. Most of the experiment is tensile testing where else the simulation is using ANSYS software [6]. However, a compression testing will be performed instead of tensile test to identify the stiffness in different axis where the force is being applied.

In this project, the relationship of the internal structure of the cardboard arrangement and the strength will be studied through simulation software and experiment. Also, software such as ANSYS will be used to verify the strength of the furniture cardboard. The objectives of this project are to model and analyses the design stool. At the end of the experiment, the result will be validated with ANSYS software too.

2. Research Methodology

2.1 Preparation of specimens

Preparation of the sample specimen was done before conducting the experiment. There were 4 set of sample preparation to investigate the properties of the cardboard material when the force is applied in different directions. Compression testing is carried out for 10 samples for each direction. The dimension of the cardboard is cut and design as figure 1. Figure 2 shows the dimension of 4 different directions when the force is being applied.

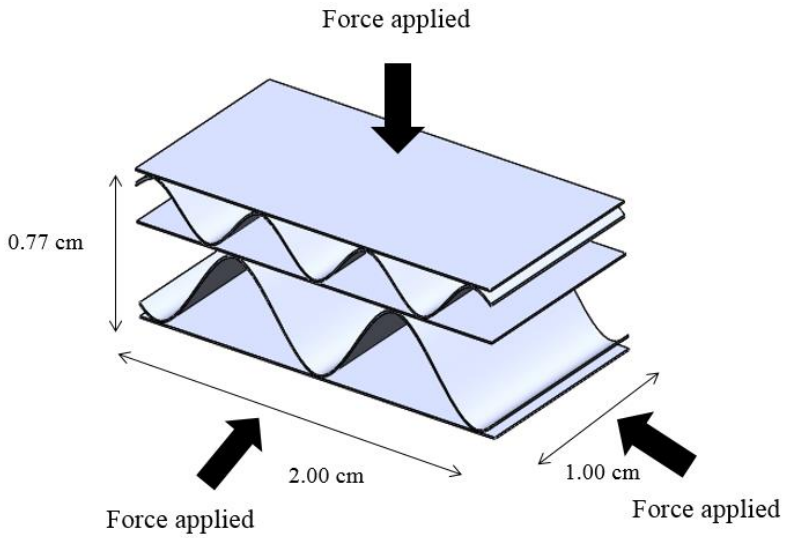


Figure 1. Dimension of the specimen with force applied in different directions

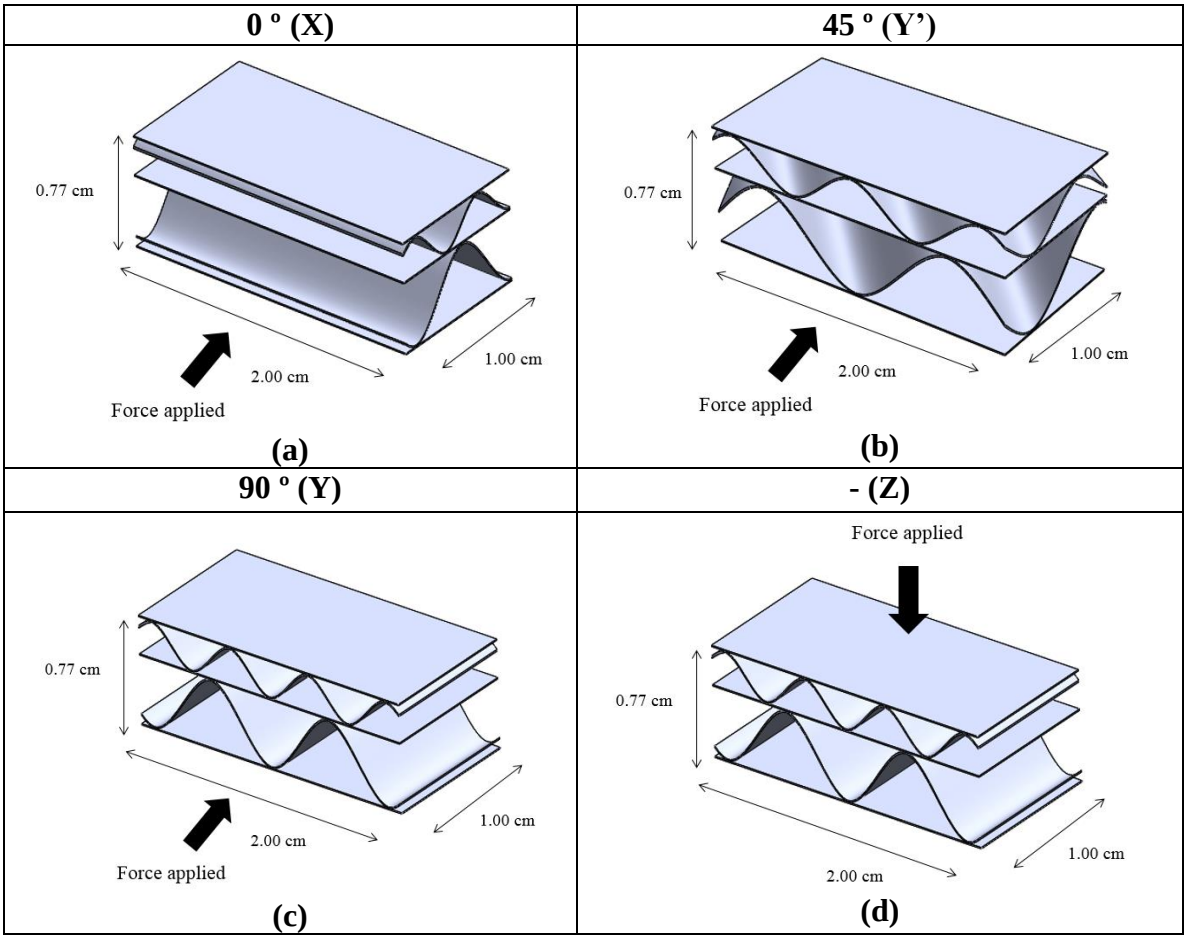


Figure 2. Force acting in different direction (a) 0°(X-direction), (b) 45°(Y'-direction), (c) 90°(Y-direction), (d) – (Z-direction)

2.2 Experimental Testing

In experimental testing, compression test is used to determine the mechanical properties of the sample corrugated cardboard. The main objective of conducting this testing is to obtain the Young's Modulus of the sample in different directions when the load is being applied. A compression INSTRON 5960 Dual Column Tabletop machine is used to conduct the experiment in University Melaya, Malaysia. Before conducting the experiment, calibration such as reseting the previous data and using the correct compression dual plates were set up. The machine is calibrated so that the accuracy of the result is maintained.

The sample specimens were then inserted carefully in the middle of the compression plate and the compression machine is set to compress 50% of the original length.To obtain the Young's Modulus of the sample properties, a graph of Stress against Strain is plotted and the gradient is the indication of Young's Modulus. These result then will be used to analyse the structural strength by comparison of the Young's Modulus.

2.3 SolidWorks Modelling

SolidWorks is used to create the model of the stool. It is very effective to convert the design into the software before undergoes simulation. However, the progress of drawing cardboard in the software must have minimal error especially the flute structure before comparing to the practical result. After completion of the modeling, the design will be imported to Finite Element Analysis to undergo stress simulation to determine the strength of the cardboard when a load is applied.

2.4 Finite Element Analysis Modelling

Finite Element Analysis (FEA) software is used to analyze the design and produce expected result in simulation. Some properties of the material such as Young's Modulus and Poison ratio must be filled in correctly in simulation because they can greatly affected the final result.With 4 difference axis x, y, y' and z, the Young's Modulus will be difference corresponding to the force applied.

2.4.1 Simplification of modelling

In order to further simplify the complicated structure of the corrugated cardboard, an alternative way was introduced by the researcher which is using the homogenization approach [7]. The original 3D structure in this experiment is able to simplify into a simple solid form in figure 3 to obtain a similar result. Hence, this will help to reduce the time with heavy numerical dimensioning studies for other cases.

By using the homogenization approach with correct mechanical properties, the user can simulate different kind of design with minimum effort. This is very suitable for this project because the objective is to create a stool under simulation to analyze the structure in order to maximize the strength with minimum material used. Furthermore, the tedious steps of creating the sandwich structure parts are avoided before assembly and turn into simple homogenous material instead. However, a validation process is also being conducted to ensure the result obtained from the experiment is similar to the simulation. Therefore, there main advantages of simulating mechanical behavior of corrugated cardboard are:

- Reduce development cost with lesser experiments.
- A faster development phase where the mechanical properties and information is obtained in early stage.
- Having the potential to analyze and test with different design made by corrugated cardboard.
- Able to detect and study about the weakness point of the design and improve it.

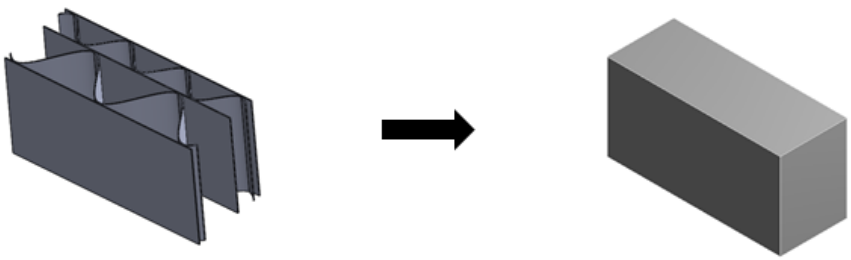


Figure 3. Homogenization approach applied to the specimen

2.4.2 Modelling of actual stool

An initial design A and improved design B were being constructed to investigate and undergoes simulation testing in ANSYS. Both design were constructed and assembled into a solid form through SolidWorks before transferring to ANSYS simulation in figure 4 and 5. Different material properties have applied in different type of textures in figure 6 and 7 in 2 designs. The reason of applying different parts of material properties is to model the structure as close as the product in real application. Also, the arrangement of the component structure is constructed to provide higher strength when load is being applied. Therefore, the simulation results will be discussed under result and discussion section.

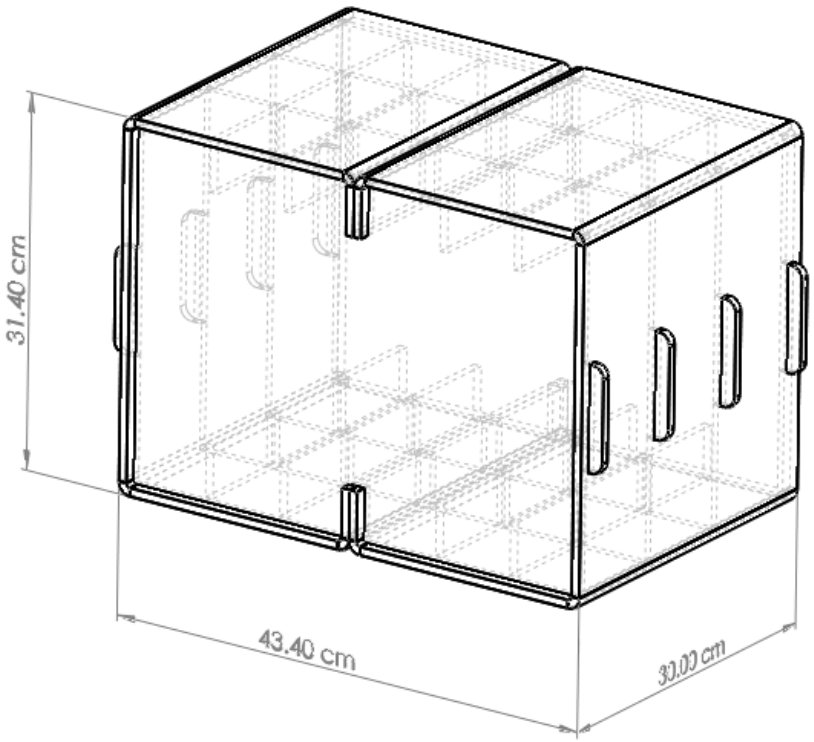


Figure 4. Dimension of actual Design A

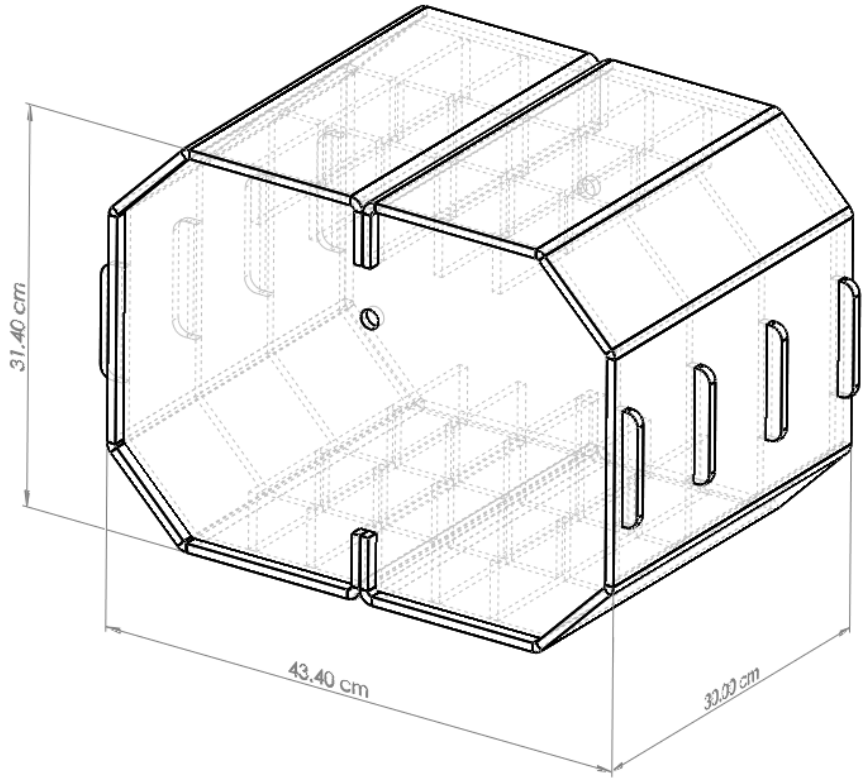


Figure 5. Dimension of actual Design B

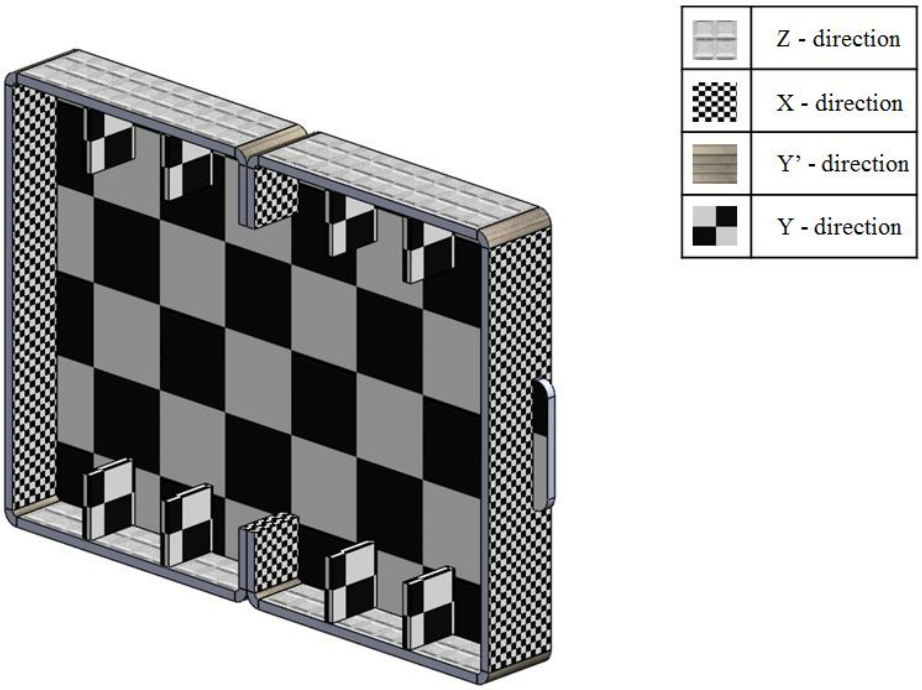


Figure 6. Material properties plane selection in cross-sectional view (Design A)

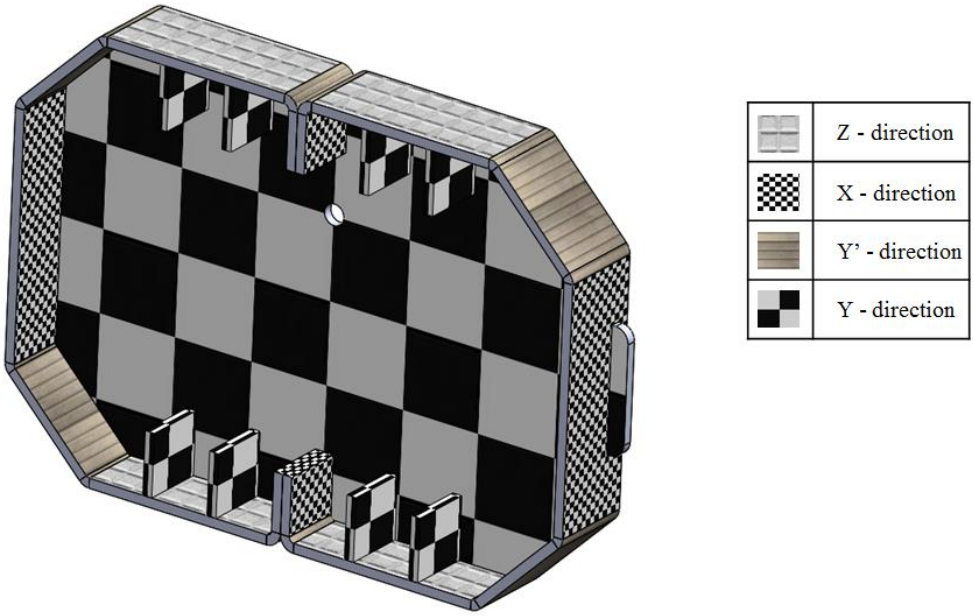


Figure 7. Material properties plane selection in cross-sectional view (Design B)

3. Results and Discussion

3.1 Result Analysis of Compression Testing

Based on the concept, the stiffness which also call the Young's modulus (E) can be determined by using the formula (1) of Hooke's Law:

$$E = \frac{\sigma(\varepsilon)}{\varepsilon} = \frac{F\ /\ Ao}{\Delta L\ /\ Lo} = \frac{FLo}{Ao\Delta L} \quad (1)$$

where

E is the Young's modulus (modulus of elasticity)
F is the force exerted on an object under tensionl;
Ao is the actual cross-sectional area though which the force is applied;
ΔL is the amount by which the length of the object changes;
Lo is the original length of the object

The Young's Modulus (E) can be obtained from the graph of compression stress against compression strain by calculating the gradient. The data and information were recorded and tabulated into table form. Based on the value of Young's Modulus, it is able shows the relationship between difference direction of force applied and the stiffness of the cardboard.

During the experiment, 10 samples of each direction were used to determine the material strength properties and the compression strain is set to 50% of its original length. Based on the results, the graph tends to have linear elasticity pattern in the first 10% and slowly lead to non-linear elasticity. Hence, the simulation will be limited to the first 10% deformation where the material behaves linearly. Therefore, only the

first 10% compression strain data will be selected to calculate the Young's Modulus of the specimens due to its linearity.

From figure 8, the highest Young's modulus of the corrugated cardboard is when the force is directly applied against the flute in 90˚ follows by 45˚ and 0˚. This might due to the unique flute pattern that provides a larger surface area that able to transmit the force straight to the bottom of the body that creates a higher reaction force without failure. From the observation, as the angle of flute decreases, the material strength decreases when the load is applied. However, the specimen in Z direction is being conducted to determine its Young's modulus regardless of the flute angle. Therefore, table 1 is tabulated to show the mechanical properties of the corrugated cardboard from highest to lowest in term of different directions accordingly. The poison ratio of the cardboard properties is set as constant 0.01 [7].

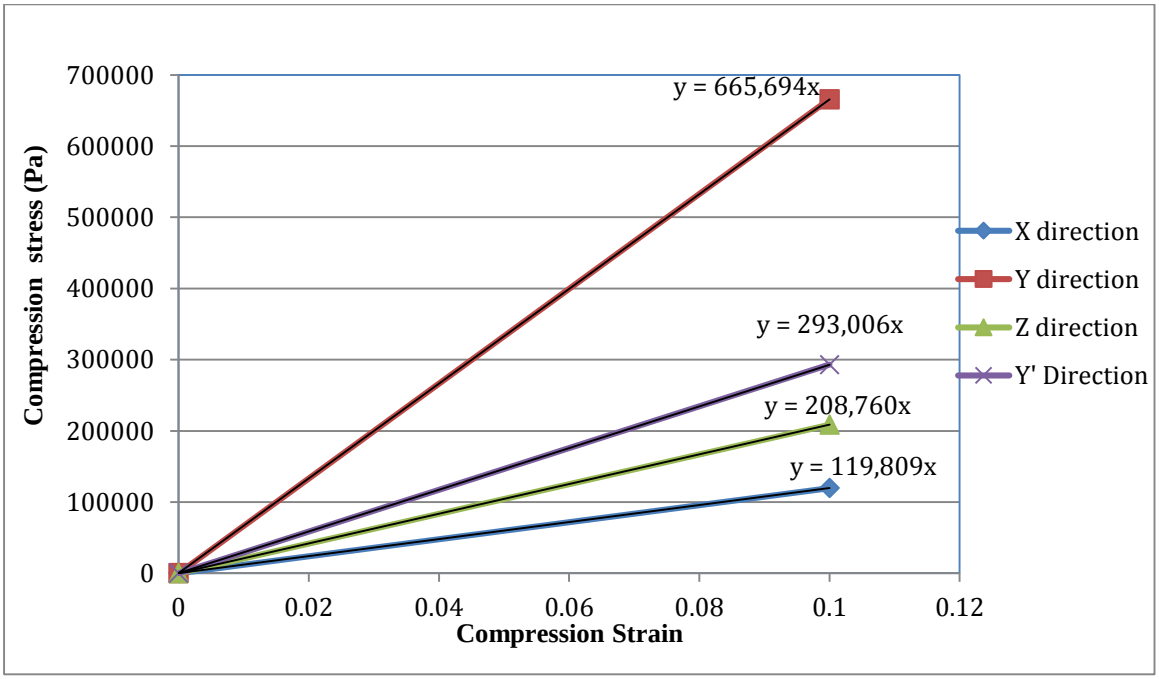


Figure 8. Compression Stress against Compression Strain

Table 1. Experimental result for different directions

Direction	Angle of flute (º)	Young Modulus (Pa)	Poisson's ratio	Strength (Highest to lowest)
X	0	119,809	0.01	Y > Y' > Z > X
Y'	45	293,007		
Y	90	665,694		
Z	-	208,760		

3.2 Validation between simulation result and experimental result

In term of validation result, the simulation outcomes should have the similar Young's modulus as the experimental result. By understanding the concept and formula for Young's modulus, the data retrieved from the simulation can be calculated with formula and compare to the experimental result. This step is

extremely important to ensure the data key into the ANSYS software is accurate and precise because it would affect the final result as the design gets more complicated. Since the data retrieved from the experimental result is 10% compression strain, the simulation is set to have a similar 10% displacement with fix support at the bottom surface of the block.

Moreover, the percentage error is used to determine the error percentage of different sample compare to its actual result. The percentage error should be as minimum as possible to produce result with higher accuracy. Based on the percentage error, the result is acceptable as the error is below 10% compare to its original data. Hence, the properties material result in different directions were calculated and tabulated into table form.

From table 2, it shows that highest Young's Modulus which is Y direction has the highest strength compare to the other directions. However, the deformation and normal strain for all directions are the same because the system is set to 10% compression to its original length. Therefore, the samples were compressed up to 10% during the simulation.

Table 2. Summary result of validation

	Displacement			
Direction	**Young modulus (Pa)**	**Normal Stress (Pa)**	**Normal Strain**	**Percentage error (%)**
Y	665,694	300,410	0.45107	0.0451
Y'	293,006	132,230	0.45107	0.0483
X	119,809	54,067	0.45107	0.0458
Z	208,760	94,208	0.45107	0.0453

3.3 Simulation of actual stool

By using the ANSYS software, the actual stool product is being simulated to analyze the overall structural strength. Static structural simulation is being selected, with key in material properties of cardboard in different directions.

In order to design a functional stool that can support average human weight, it is challenging to produce especially by using the soft corrugated cardboard material. Therefore, understanding the structural strength is the key to optimize the overall quality to withstand a higher load. Hence, most of the arrangement of the cardboard is placed in Y-direction due to its highest Young's modulus value that provides a greater strength.

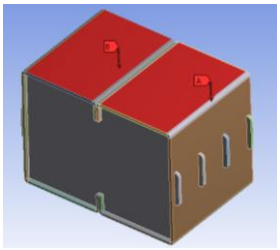
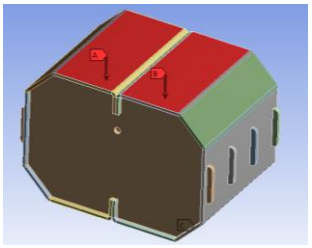
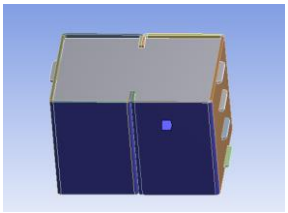
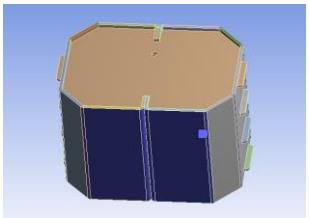
During the simulation, the direction of the force is acting on top surface of the design stool where it indicates the actual scenario when a person weight is applied. For instance, an average body mass (kg) of adult is approximately 800N is used to simulate the result [8]. However, the load is assumed to distribute evenly on top of the stool to analyze the strength of the overall stool. Hence, the expected result of total deformation might be different from the actual product.

In design A, the stool is designed in a square box form and the total deformation is 0.17739 compare to design B which is 0.15378. This is due to the larger surface area that more force acting evenly that leads to a larger deformation. As in contra, design structure B is produced by reducing the top surface area to prevent a higher deformation. It has restrained the contact surface of human sitting position but strengthen the design structure by 13.31%.

Since the total volume of initial design A is cut down from 7600.5cm^3 to 7112.0cm^3, it has reduces the material used by 6.43%. In term of manufacturing wise, it has saved up the material cost and also the time to produce the product with laser cutter. Hence, design B is more economical viable compare to design A.

On the other hand, there are pros and cons in both designs such as stronger material, bigger comfort sitting area. As to achieve the main objective of this project which is to optimize the strength of the cardboard stool, design B is chosen due to its higher structural strength. Also, the overall appearance of design B is much more aesthetic compare to design A which given higher potential to commercialize. It is very difficult to improve a design without increasing the material used while maintaining its structural strength. Therefore, the improvement of the design B is still on going to minimize the material used as much as possible while optimizing its structural strength. A summarize table is tabulated in table 3.

Table 3. Comparison between Design A and B

	A	B
Direction of force applied		
Boundary Condition (Fix Support)		
Total Deformation	0.17739	0.15378
Total Volume	7600.5cm^3	7112.0cm^3
Advantages	• Larger sitting surface area • Larger space for storage	• Higher supporting strength • Require less materials • Less cost and time consuming

		• Aesthetic • Light and portable
Disadvantages	• Lower supporting strength • Require more materials • More cost and time consuming • Less aesthetic	• Smaller sitting surface area • Lesser space for storage
Optimization of strength and material	$\boldsymbol{Structural\ Strength\ (deformation)} = \frac{(0.17739 - 0.15378)}{0.17739} x\ 100$ $= 13.31\%$	
	$\boldsymbol{Material\ saved\ (volume)} = \frac{(7600.5 - 7112.0)}{7600.5}\ x\ 100$ $= 6.43\%$	

4. Conclusions

Both experimental and simulation were conducted to achieve the main objectives of this project which are to model and analyses the design stool using SolidWorks Modelling and finite element analysis and also to optimize the cost and strength of the stool by reducing the number of cardboard used. For the first objective, the sample block models were being constructed as well as the actual stool design by using SolidWorks and transfer to finite element analysis undergoes simulation. Besides, validation between the experimental data and simulation was completed to ensure the accuracy of result before proceeding to complicated design.

Furthermore, an initial design A is created to determine the overall structural strength to withstand human body weights using simulation. The real life scenario parameters such as amount of force and fix ground were inserted into the programme as simulation. However, limitations such as total force acting on top surface of stool is evenly distributed in simulation which is different in life application. Moreover, the design A is further improved with design B that decreases the total deformation, volume that strengthen the overall structure. In design B, the structural strength has improved with and efficiency of 13.31% whereas the total material saved efficiency is 6.43% compare to the original design. Some of the advantages and disadvantages were mentioned to compare both designs such as bigger surface area for sitting position and so on.

On other hand, there is limited resources literature reviews that can be referred with this project due to its unique project outcomes. Based on previous research, most of the researcher has done simulation to figure out the material properties of the corrugated cardboard but not the application. Moreover, the grammage of the corrugated cardboard is different and subjective to the production of the company. Another limitation of this project is the design A and B can be only compared within the simulation but not physical experiment because the compression plate has limited

space to fit in the design with actual scale. Hence, this project is an innovative way to turn the recycle corrugated cardboard into something that contain value and reduce the landfill at the same time optimizing the life-span of the cardboard. Improvement of the design B will be on going to further optimize the structural strength as well to reduce the material used.

References

[1]A. Periathamby, F. Hamid and K. Khidzir, "Evolution of solid waste management in Malaysia: impacts and implications of the solid waste bill, 2007", *J Mater Cycles Waste Manag*, vol. 11, no. 2, pp. 96-103, 2009.

[2]U. Ngoc and H. Schnitzer, "Sustainable solutions for solid waste management in Southeast Asian countries", *Waste Management*, vol. 29, no. 6, pp. 1982-1995, 2009.

[3]M. Saeed, M. Hassan and M. Mujeebu, "Assessment of municipal solid waste generation and recyclable materials potential in Kuala Lumpur, Malaysia", *Waste Management*, vol. 29, no. 7, pp. 2209-2213, 2009.

[4] MailOnline, "Lexus creates working full size vehicle made of cardboard", Mark Prigg, Oct 5, 2015 [Online].Available:http://www.dailymail.co.uk/sciencetech/article-3261232/Just-don-t-drive-home-rain-Lexus-creates-working-size-vehicle-CARDBOARD-worker-s-origami-skills.html

[5] Z. Zhang, T. Qiu, R. Song and Y. Sun, "Nonlinear Finite Element Analysis of the Fluted Corrugated Sheet in the Corrugated Cardboard", *Advances in Materials Science and Engineering*, vol. 2014, pp. 1-8, 2014.

[6] Z. Aboura, N. Talbi, S. Allaoui and M. Benzeggagh, "Elastic behavior of corrugated cardboard: experiments and modeling", *Composite Structures*, vol. 63, no. 1, pp. 53-62, 2004.

[7] Z. Aboura, M. Benzeggagh and S. Allaoui, "Contribution to the modelling of the corrugated cardboard behaviour", *Corrugated cardboard behavior*, vol. 10, p. 2, 2011.

[8] S. Walpole, D. Prieto-Merino, P. Edwards, J. Cleland, G. Stevens and I. Roberts, "The weight of nations: an estimation of adult human biomass", *BMC Public Health*, vol. 12, no. 1, p. 439, 2012.

eureca 2016 – Conference Paper
Paper Number 2ME28

Mechanical Properties and Intervertebral Pressure of Post-operative Scoliosis of Human Vertebrae

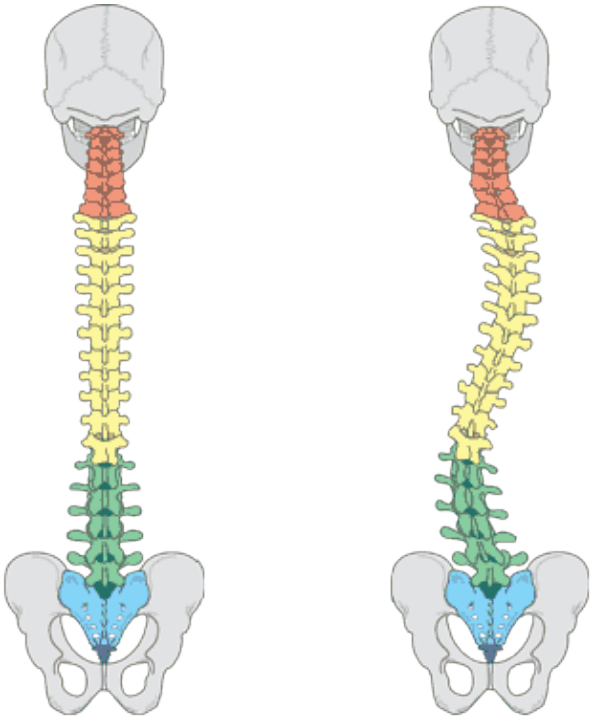
Tham Chuan Jun*, Leong Wai Yie, Jeffrey Chin Kong Leong
Department of Mechanical Engineering,
School of Engineering, Taylor's University, Malaysia.
*chuanjun.tham02@sd.taylors.edu.my

Abstract
Pre-operative and post-operative patients offer different kind of treatments that providing them better functionary in locomotion and posture. However, medical practitioners are suffering from being unable to comprehend the mechanical properties and intervertebral pressure of the spine after operation of scoliotic human vertebrae due to implantation of the Harrington rod on vertebral column. To further investigate the current limitation, noise reduction has been applied to the Computer Tomography (CT) images to remove metallic artifacts noise so that mechanical properties and intervertebral pressure can be analyzed through Finite Element Analysis (FEA) in ANSYS simulation software. The objective of the project is to investigate the mechanical properties and intervertebral pressure of the post-operative scoliotic human vertebrae. The mechanical properties and intervertebral pressure of human vertebrae is comparing with pre-operative and post-operative scoliotic human vertebrae. For research methodology, the Digital Imaging Communications in Medicine (DICOM) of patient suffered from human vertebrae scoliotic was obtained from CT scan, and then the image files were converted to suitable 3D file format known as STL for simulation by FEA. The noises that were found in the post-operative patient after implantation of metallic artefacts Harrington's rod in the spine has been eliminated by applying the 3D segmentation method in Blender software. The overall lumbar region model has imported to ANSYS workbench to conduct simulation on region of interest (lumbar region) and produce FEA outcome with proper meshing. Boundary condition such as pressures (0.7 kg/cm2, 1.4 kg/cm2, and 2.1 kg/cm2) and fixed support (bottom of vertebra) were inserted before conducting simulation. The related information such as stress, strain, and total deformation of the lumbar were identified, critical and weakest points were analyzed during the simulation. Under 0.7 kg/cm2 of pressure, the maximum stress is 0.005696MPa, maximum strain is 7.417e-8 (mm/mm) and total deformation is 0.008032mm. The results attained such as mechanical properties and intervertebral pressure has been analyzed and compared with the previous theoretical study. The outcomes of the project are the noises generated by the metallic artifacts were eliminated by using 3D segmentation method. Analysis on region of interest had conducted with using FEA by simulation. The mechanical properties and intervertebral pressure of post-operative scoliosis patient were investigated.

Keywords: Human Vertebrae, Scoliosis, Noise Reduction, Segmentation, Finite Element Analysis.

1. Introduction

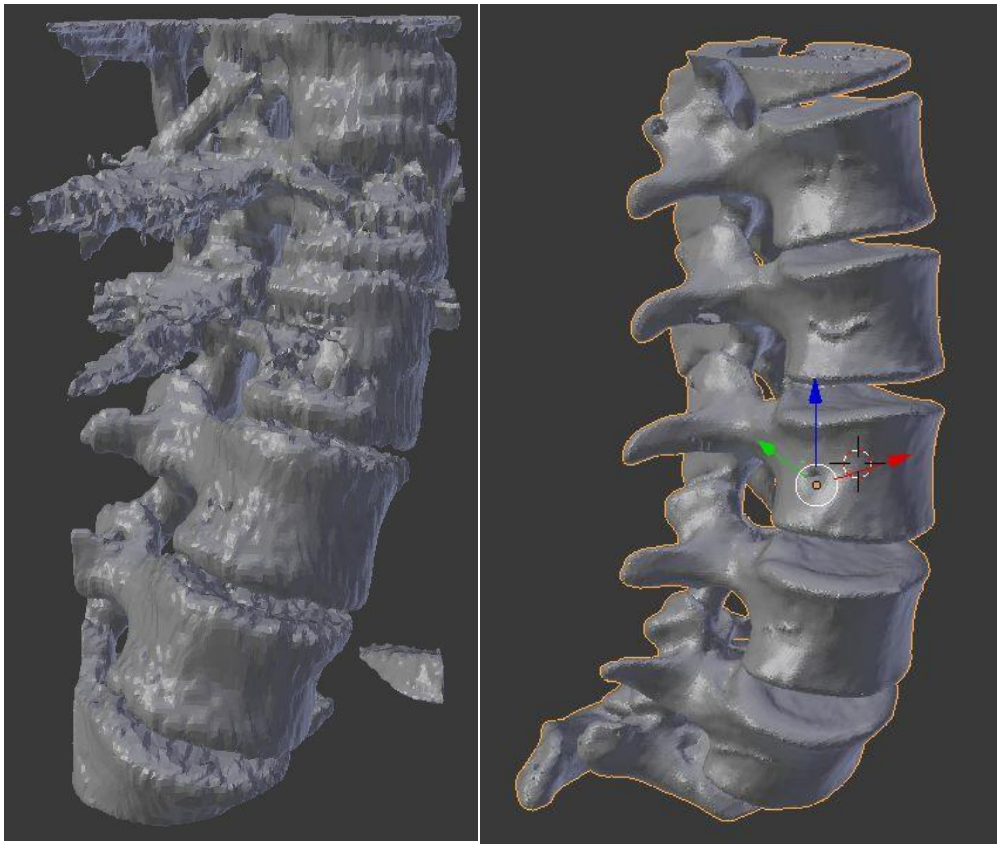
Scoliosis defines inclination curvature of the human spine, normally in straight vertical line [1]. There are number of reasons that causes scoliotic human vertebrae such as congenital scoliosis that caused by abnormalities bone present since birth, neuromuscular scoliosis that caused by abnormal muscle and nerves, and many more. Individual that experiencing degenerative scoliosis of human spine is progressively building pain due to instability of spine and greater extremity pain due to compression of nerves around the spine [2]. By comparing to non-scoliosis patients, patients that experiencing scoliosis will experience a lot of pain when there is a pressure from external or internal applied. Due to the improper posture of the spine, patients with scoliosis are unable to perform many extreme movements such as sports [3]. Figure 1 shows the dissimilarity between normal and impaired scoliosis vertebrae column.



(a) Normal (b) Impaired

Figure 1. Normal vertebral column and impaired scoliosis vertebral column [4].

Image Noise defines the formation of unusual variation of contrast or color in the images, usually the acts of external signal noise. Due to post-operative patient has implanted metallic artifacts (Harrington implant) in the human spine as treatment of scoliosis, the images produced in the CT (computed tomography) scan are distorted due to the metallic artifacts. In order to investigate the mechanical properties and intervertebral pressure of post-operative patient, noise cancelling must be conducted to remove the unwanted variation on the images. 3D segmentation method by using BLENDER software is introduced to conduct noise cancelling. Figure 2 shows the lumbar region before and after conducted 3D segmentation noise cancelling.



(a) Lumbar before noise cancelling. (b) Lumbar after noise cancelling.

Figure 2. Lumbar region before and after conducted 3D segmentation noise cancelling.

The objective of carrying out this research project is to improve medical practitioner comprehension of mechanical properties and intervertebral pressure of the post-operative scoliotic human vertebrae by using Finite Element Analysis (FEA), on ANSYS Workbench simulation software to investigate the elements. The current issue of practitioners are suffering is from being unable to correctly comprehend the mechanical properties and intervertebral pressure of the spine after operation of scoliotic human vertebrae due to the distortion created from the metallic artifacts noise. This will lead to inaccurate of diagnostics due to lack of proper data projected.

In this research project, the region of interested is lumbar curve. This research project will determine the mechanical properties and intervertebral pressure of the post-operative scoliotic human vertebrae, mainly focused on lumbar curve. The scope of study will be limited to 3D modeling and simulation. The reason for this is due short of resources needed in order to test designs in the current period. Since post-operative images are distorted due to metallic artifacts noise, the practitioner does not have a proper equipment of such precision to evaluate the data.

Since this project has related implantation of metallic rod (Harrington rod implant) as the treatment of scoliosis patient, LEXTON Industrial Supplies from Malaysia had stayed connection with this project on the research of types of noise created from the metallic artifacts. LEXTON Industrial Supplies is an authorized supplier of the world renowned a top quality industrial mechanical components such as pneumatic components and prosthesis component for medical field. LEXTON Industrial Supplies planned to ameliorate the material properties of the current design

of Harrington rod, so that it reduces noise created in the CT scan images. Figure 3 illustrated the company logo.



Figure 3. Company logo of LEXTON Industrial Supplies.

Upon completion of this project, the mechanical properties and intervertebral pressure of post-operative scoliosis of human vertebrae will be contributed to medical and engineering body. The intervertebral pressure in post-operative will be helpful in determining the areas of deterioration. It is essential to understanding the mechanical properties and intervertebral pressure of post-operative scoliosis patient, which allows practitioner to provide better treatment after operation.

2. Research Methodology

2.1 Creation of 3D Model

The 3D model design was created by using few software such as InVesalius, 3D Slicer and Blender. First, after obtaining the DICOM file samples from Mr. Mohan, the DICOM files are imported into InVesalius to construct 3D model. In InVesalius, each of the DICOM image files indicates like a vertebral column ‘slices’. The vertebral column ‘slices’ are reconstructed by stacking all of the images to combine into 3D model and can be inspected in 4 perspectives such as Axial (Top), Sagittal (Side), Coronal (Front) and Volume (3D View) [5] as shown in figure 4. The 3D model constructed in InVesalius will be exported in STL format for simulation and FEA purposes.

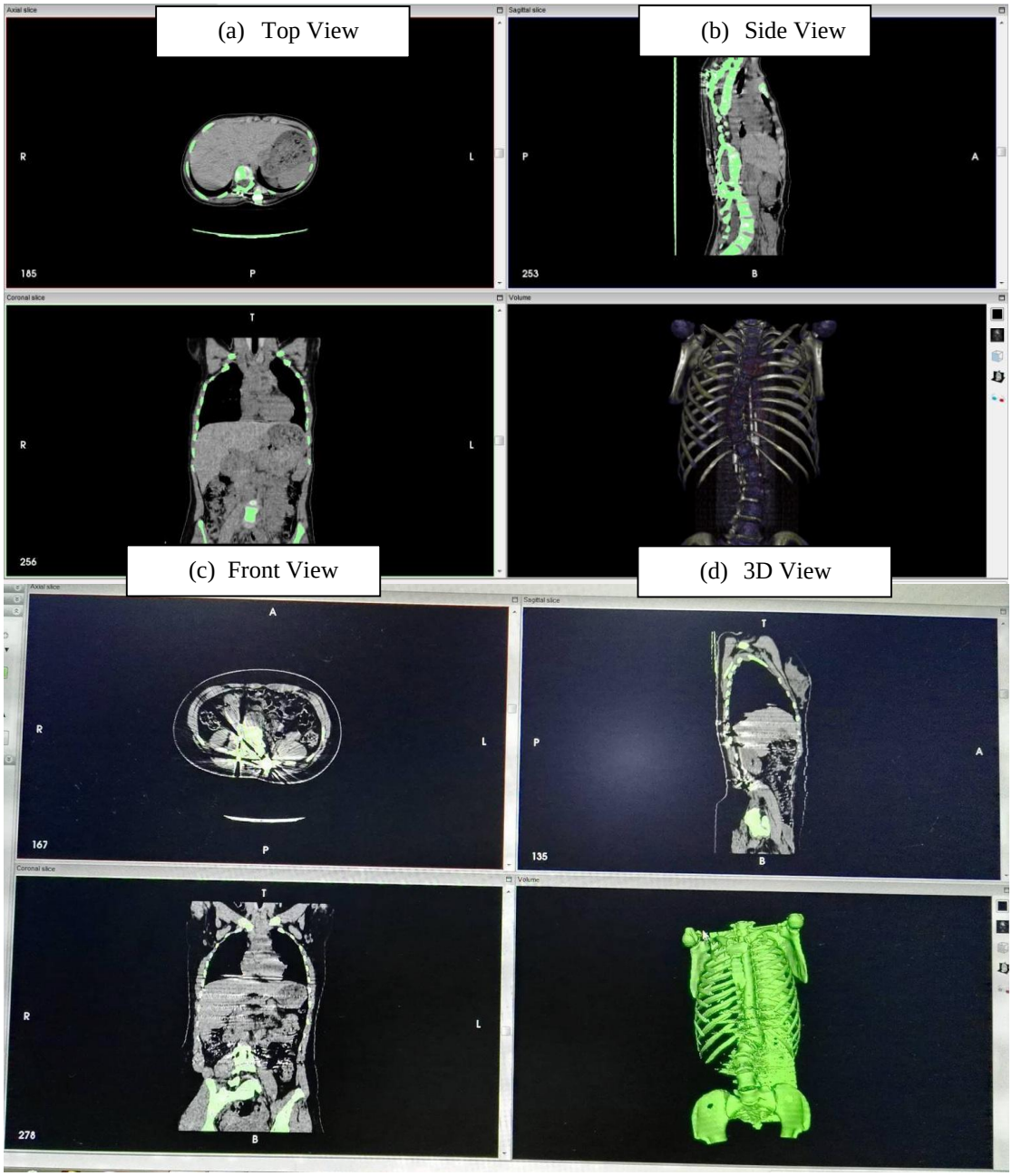


Figure 4. Overall view of post-operative scoliotic of human vertebrae in InVesalius software (a) Top view, (b) Side view, (c) Front view, (d) 3D view.

In addition, 3D slicer was used to conduct segmentation of the human vertebrae. Since the research region of interest is Lumbar region, hence, lumbar was extracted from the human vertebrae by using 3D slicers. Volume rendering feature was used to crop out the region of interest (lumbar) and exported out as 3D model format (STL format). Figure 5 illustrated volume rendering process in 3D slicer.

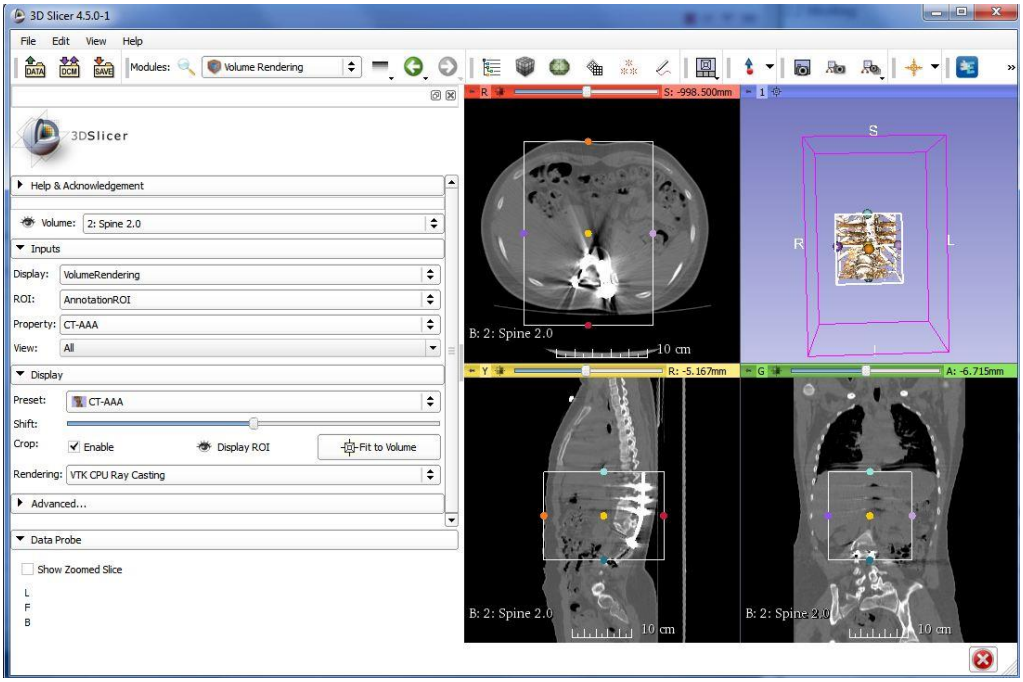


Figure 5. Volume rendering process in 3D Slicer.

2.2 3D Segmentation Noise Cancelling

Furthermore, Blender was introduced to conduct noise cancelling in the lumbar region. Based on figure 2, it illustrated the before and after noise cancelling treatment in the software. 3D model segmentation defines a process of dividing the model into desired parts. In order to apply into this project, 3D model segmentation was used to divide the unwanted variation (spiky distortion) that formed at lumbar region and remove it. Figure 6 shows the unwanted variation ready to be removed.

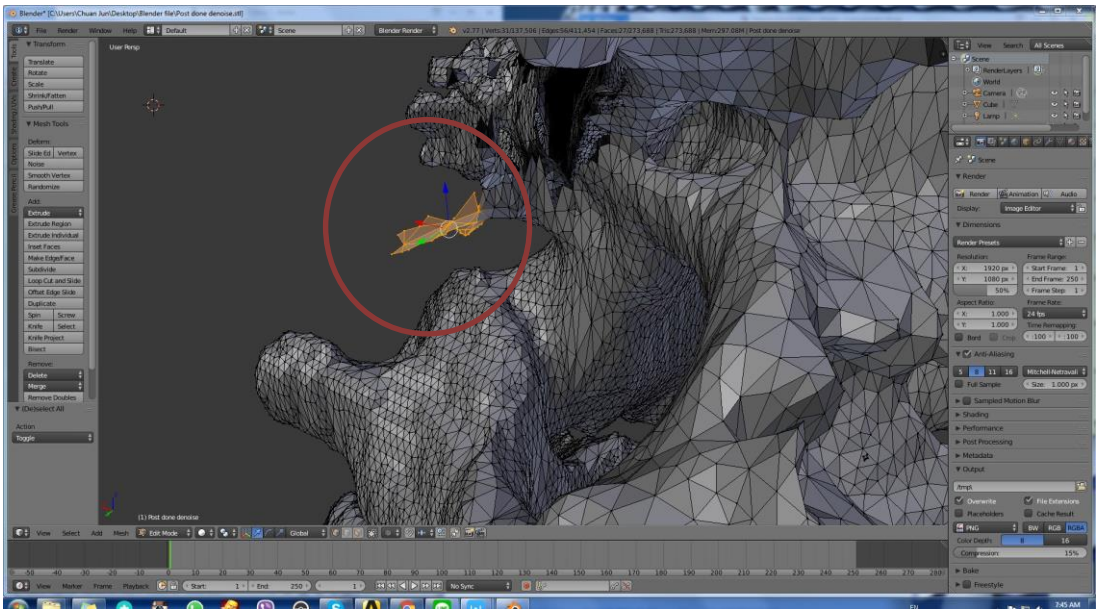
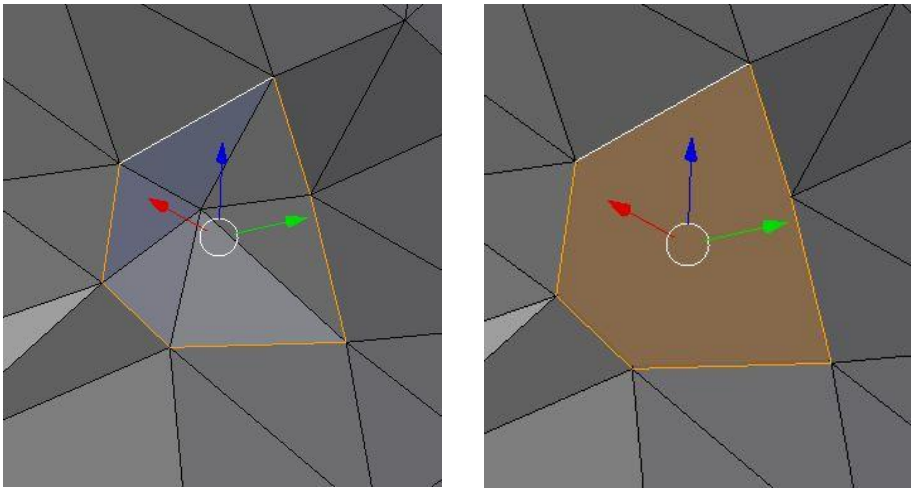


Figure 6. 3D model segmentation on the unwanted variation (circled).

After removing the noise from the lumbar region, holes and pits were appeared on the surface of lumbar. In order to conduct treatment, the holes and pits were recovered by using joining and facing feature in Blender. Pre-operative lumbar

was used to trace back the original shape of lumbar while doing recovering. Figure 7 shows the before and after applied joining and facing feature on a pit.



(a) Before treatment. (b) After treatment.

Figure 7. Before and after treatment of pits on the surface of lumbar.

In order to reduce the processing time, a single vertebra L2 was extracted out to conduct proper model editing and simulation. Remesh was applied into the model to reduce the amount of mesh surface on the contour. Great amount of mesh surface will requires longer processing time during simulation. Remesh was carefully applied to the model to avoid distortion or destruction happens. Figure 8 shows the remesh function in Blender.

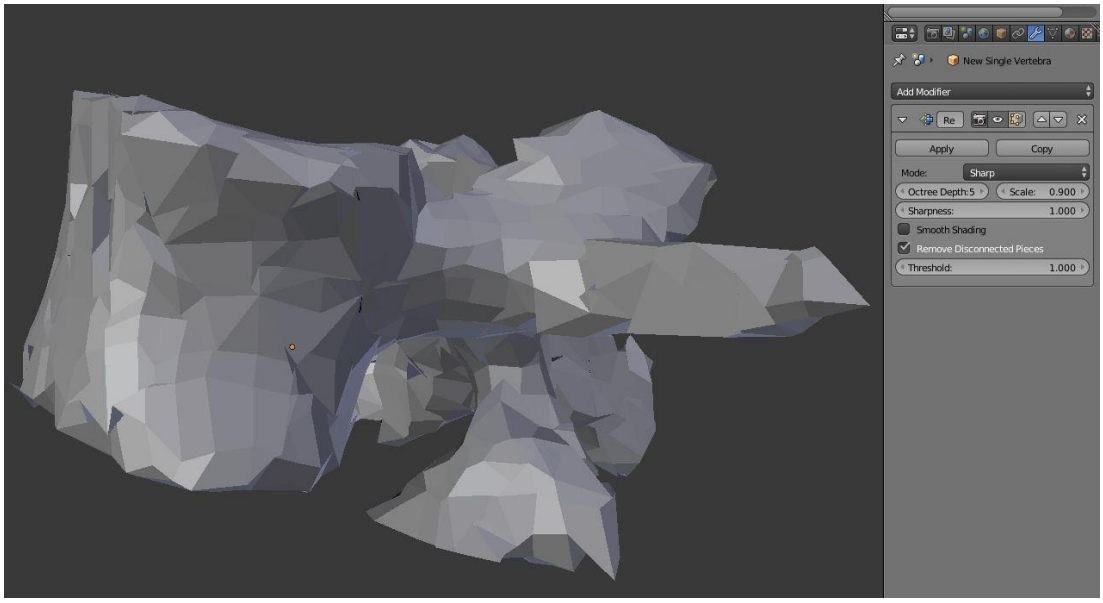


Figure 8. Remesh modifier on single vertebra.

2.3 Numerical Analysis

After completed on editing model in Blender, the model has imported into ANSYS Workbench to conduct FEA simulation. Before the simulation started, there were few components preset as initial condition such as system option and material

information. Static Structural Analysis was chosen as the simulation system. Material properties of bone has inserted into the system as shown in Figure 9. Figure 10 shows the flowchart of the simulation process for better visualization purpose of this project.

Properties of Outline Row 3: Bone

	A	B	C	D	E
1	Property	Value	Unit		
2	Density	7850	kg m^-3		
3	Isotropic Secant Coefficient of Thermal Expansion				
4	Coefficient of Thermal Expansion	1.2E-05	C^-1		
5	Reference Temperature	22	C		
6	Isotropic Elasticity				
7	Derive from	Young's Mod...			
8	Young's Modulus	2E+11	Pa		
9	Poisson's Ratio	0.3			
10	Bulk Modulus	1.6667E+11	Pa		
11	Shear Modulus	7.6923E+10	Pa		
12	Alternating Stress Mean Stress	Tabular			
16	Strain-Life Parameters				
17	Display Curve Type	Strain-Life			
18	Strength Coefficient	9.2E+08	Pa		
19	Strength Exponent	-0.106			
20	Ductility Coefficient	0.213			
21	Ductility Exponent	-0.47			
22	Cyclic Strength Coefficient	1E+09	Pa		
23	Cyclic Strain Hardening Exponent	0.2			
24	Tensile Yield Strength	2.5E+08	Pa		
25	Compressive Yield Strength	2.5E+08	Pa		
26	Tensile Ultimate Strength	4.6E+08	Pa		
27	Compressive Ultimate Strength	0	Pa		

Figure 9. Material properties of Bone.

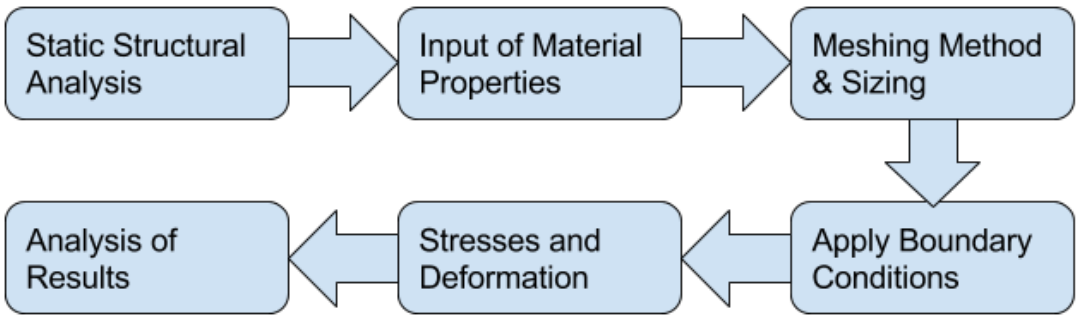


Figure 10. Flowchart of simulation in ANSYS Workbench software.

2.3.1 Construction of 3D FEA Model

The model was shown in the simulation platform and preset thickness of 5mm. Next, overall model was selected as simulation geometry. Stiffness behavior had switched to rigid with temperature condition of 35° Celsius. By using the node merge tool, the overall model edges had improved into better precision joint.

2.3.2 Meshing

The model was meshed by preset the meshing method and sizing. For meshing method, quadrilateral dominant method was used with mesh type of quadrilateral and triangle. For mesh sizing, 0.05m and 0.07m were fixed as element size. Both of the

mesh size had determined based on the convergence analysis of mesh at the end of simulation. The amount of mesh element is more than 100000, this reflected to have higher accuracy in calculation. Skewness value was checked to ensure the good quality of the meshing result. Skewness value that approaching to zero will be chosen as default mesh sizing. Table 1 shows the relevant meshing information such as meshing method and statistic.

Table 1. Meshing Information.

Meshing Method	Quadrilateral Dominant	
Sizing	0.05m	0.07m
Mesh Element	208526	183531
Element Quality (Average)	0.8847	0.8615
Skewness (Average)	0.1171	0.1351

2.3.3 Boundary Condition

After preset the contacts condition, a force assumption of 0.7 kg/cm^2 was used and applied on the top of the L2 lumbar as boundary condition set in FEA. The initial force value was assumed to be approximately 1kg of weight required support by the L2 lumbar. Time scale of the stresses and deformation analysis were set to 5 seconds, at a program-controlled time step.

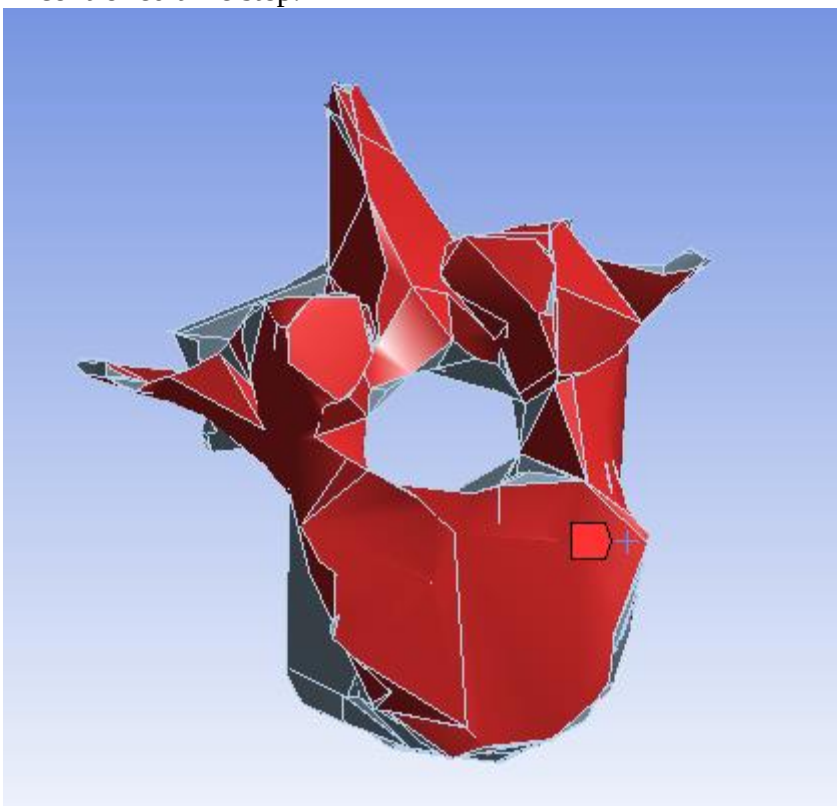


Figure 11. Boundary condition set on the top of L2 lumbar.

3. Result and Discussion

3.1 3D Model Segmentation in Noise Cancelling

For noise cancelling, most of the noises attached in the model were removed by using 3D Model segmentation. In order to complete noise cancelling in Blender software,

few features were used to generate the result as shown in figure 12, such as remesh, merging, joining, smoothing, and remove doubles. Remesh scale was set to 0.2, it is because to reduce the meshing surface to 20% of the amount (from 280 000 to 56 000). Next, joining was used to repair the distorted region caused by the noise. During repairing, the model was tracing the pre-operative L2 lumber to ensure the actual shape of the vertebrae. In addition, merging was used to combine the surfaces together in order to further reduce the amount of meshing (from 56 000 to 3 000). Furthermore, smoothing was applied to the model contour for better visualization and reduced the processing time in FEA by simulation. Lastly, remove doubles was applied on the 3D model to reduce the flaws and deficiency appeared on the model, so that the results generated in the simulation will be more accurate and precise. Figure 12 shows the completed model in Blender software before export to ANSYS workbench software.

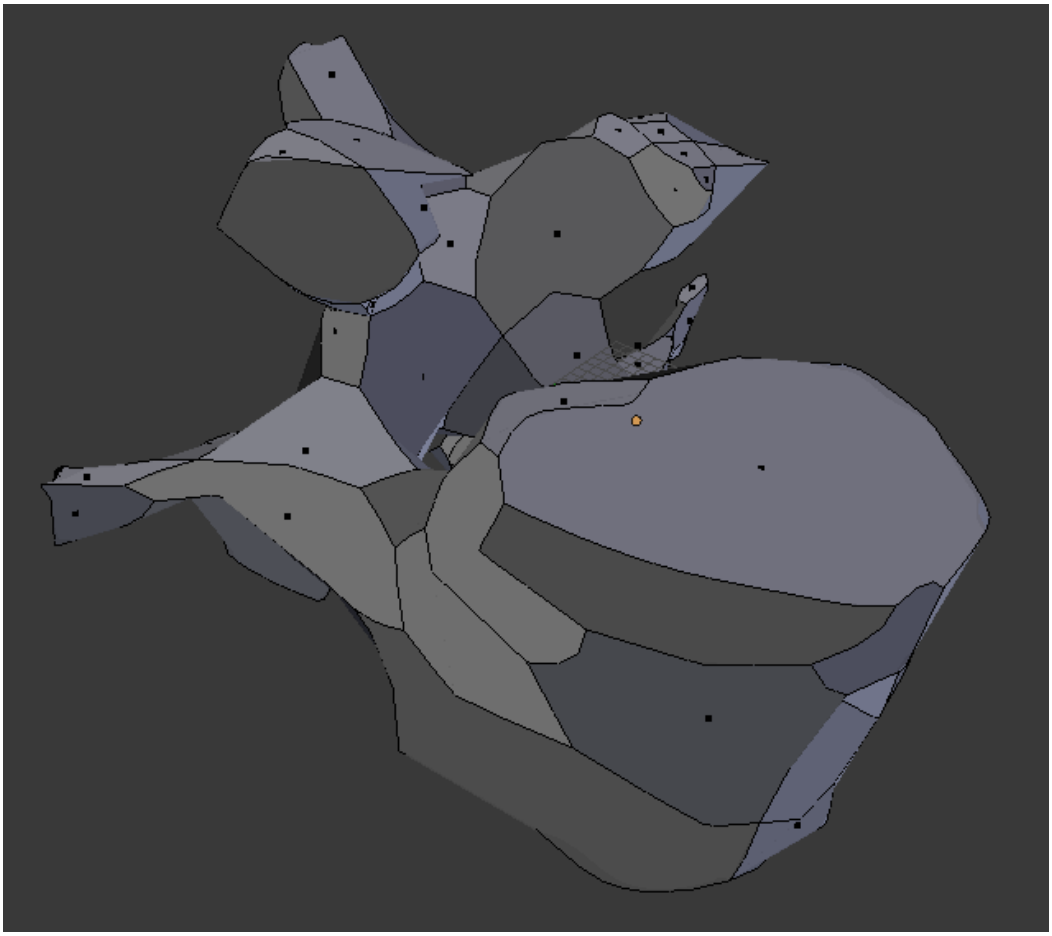


Figure 12. Completed model in Blender software.

3.2 Simulation of the L2 lumbar

The simulation has carried out in 3 pressures assumptions such as 0.7 kg/cm^2, 1.4 kg/cm^2, and 2.1 kg/cm^2 are respected to the original value, double of it, and triple of it. The reason of choosing 0.7 kg/cm^2 as original value is due to the previous research shows that the average of vertebral body has 0.7 kg/cm^2 of pressure acting [35]. The various in pressures helps to determine the condition of lumbar in most of the situation from idle to extreme. 3 simulation options were chosen such as total deformation, stress and strain. Figure 13 shows the total deformation of L2 lumbar when being exerted 0.7 kg/cm^2 of pressure. Table 2. shows the summary of results in each of the pressure assumptions.

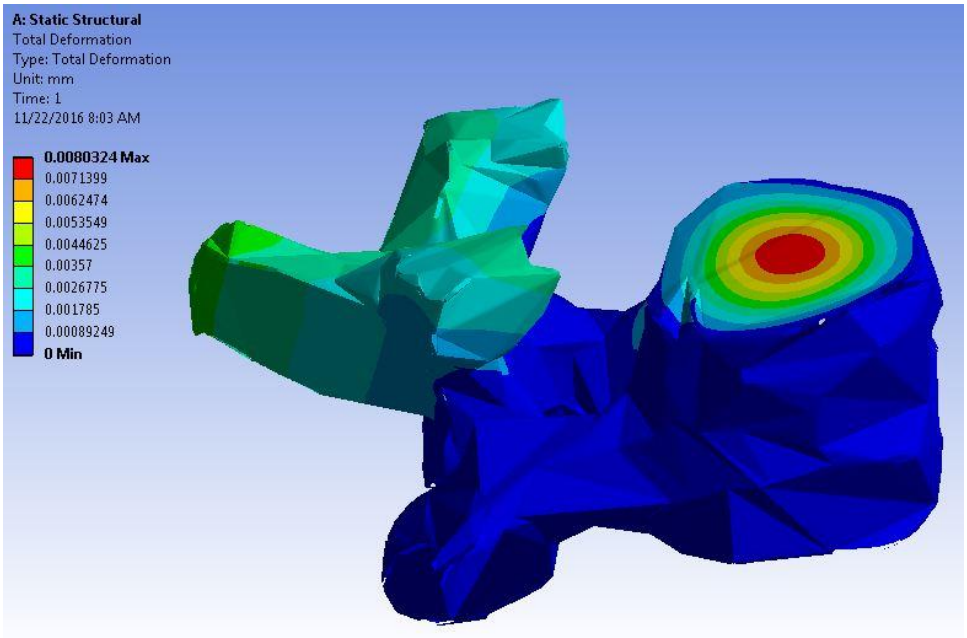


Figure 13. Total Deformation of L2 lumbar.

Table 10. Summary of results in each of the pressure assumptions.

Aspects	Maximum value under 0.7kg/cm^2	Maximum value under 1.4kg/cm^2	Maximum value under 2.1kg/cm^2
Stress (MPa)	0.005696	0.01139	0.01709
Strain (mm/mm)	7.417e-8	1.4834e-7	2.2251e-7
Total deformation (mm)	0.008032	0.01607	0.02410

4. Conclusion

After compiling all post-operative DICOM images files from the patient, the 3D model of the spine with scoliosis problem has been discovered. Next, region of interest has selected by using 3D slicers software by manually removing the unwanted region. Noise acts as an obstruction for the project due to the metallic artifacts creates noise on the model structural. Noise reduction has been done on the model structural by using Blender image segmentation method and proper editor. The modified model has exported out as STL file format and imported into ANSYS to undergo simulation and determine the mechanical properties and intervertebral pressure of the post-operative of human vertebrae. The material properties such as density, young's modulus and yield strength have be inserted into the model in simulation in post-operative scoliosis model. Meshing was done by proper preset information such as meshing type and size. Meshing quality was justified by high average element quality of 0.8847 and low average skewness value of 0.1171. Boundary condition such as pressures (0.7 kg/cm2, 1.4 kg/cm2, and 2.1 kg/cm2) and fixed support (bottom of vertebra) were inserted before conduct simulation. The related information such as stress, strain, and total deformation of the lumbar were identified, critical and weakest points were analyzed during the simulation. Under 0.7 kg/cm2 of pressure, the maximum stress is 0.005696MPa, maximum strain is 7.417e-8 (mm/mm) and total

deformation is 0.008032mm. The mechanical properties and intervertebral pressure for post-operative model have been compared with theoretical study and determined the area that needs to be improved.

In future, the effects on the spine after motion or modification can be easily determined in simulations that help the practitioner to obtain better understanding on the patient. From the intervertebral disc pressure, practitioner is able to determine where are the possible areas that lead to imbalance of spine and bone degeneration that resulting in scoliosis and neuromuscular pain. Practitioner is able to apply proper medication or physiological treatment on the affected patient, which is accurately apply diagnosis against the main problem. Patients that affected by scoliosis will tend to have better treatment and able to rehabilitate on a healthy lifestyle.

References

[1] D. T. Derrer, "Scoliosis," *WebMD*, May. 23, 2014. [Online]. Available: http://www.webmd.com/osteoarthritis/guide/arthritis-scoliosis. [Accessed: October. 10, 2016].

[2] J. D. Lewin, "Are you suffering from degenerative Scoliosis?," *The Center for Spinal Disorders*, Jan. 3, 2015. [Online]. Available: http://www.njspinaldisorders.com/suffering-degenerative-scoliosis/. [Accessed: October. 10, 2016].

[3] Y. Abe, M. Ito, K. Abumi, and H. Sudo, "Scoliosis corrective force estimation from the implanted rod deformation using 3D-FEM analysis," *BioMed Central*, vol. 10, no. 2, pp. 10-22, 2015. [Online]. Available: BioMed Central, http://scoliosisjournal.biomedcentral.com/articles/10.1186/1748-7161-10-S2-S2. [Accessed: October. 10, 2016].

[4] The Luklinski' Spine Care, "Structural Defects - Scoliosis," *The Luklinski' Spine Care*, May. 8, 2014. [Online]. Available: http://www.theluklinskispineclinic.com/backrack/en/conditions/scoliosis. [Accessed: October. 10, 2016].

[5] T. F. de Moraes, P. H. J. Amorim and F. S. Azevedo, "InVesalius An open source imaging application," *Computational Vision and Medical Image*, vol. 1. no. 1, pp . 28-31, January 2012.

[6] K. Sairyo, V. K. Goel, A. Masuda and S.Vishnubhotla, "Three dimensional finite element analysis of the pediatric lumbar spine. Part II: biomechanical change as the initiating factor for pediatric isthmic spondylolisthesis at the growth plate," *Finite Element Analysis in Medical*, vol. 1, no. 1, pp. 10-15, August 2010.

eureca 2016 – Conference Paper
Paper Number 2ME29

Analysis of Segmented Parallel Flow Field Design for Polymer Electrolyte Membrane Fuel Cell and Operation for Effective Water Removal

Wandeh Elwon, Mohd. Hardie Hidayat Mohyi
ewandeh@yahoo.com
School of Engineering, Taylor's University, Malaysia

Abstract

This research was studied to investigate the sufficiency of segmented parallel flow field design for PEMFC for water removal. Polymer Electrolyte Membrane Fuel Cell is a modern technology with a huge potential to replace the usage of fossil fuels for power generation that apply the basic concept of electrolysis. Electrolysis of water is a process that spit up water ($\boldsymbol{H_2O}$) into hydrogen gas ($\boldsymbol{H_2}$) and oxygen gas ($\boldsymbol{O_2}$) by using electric current that pass through water. In any fuel cell, the design of flow field is the main criteria that affect the performance of a fuel cell. The water removal rate is effected by changing the flow field design of PEMFC. This research selected two PEMFC flow field design for analysis in MATLAB software. The two design that are selected in this research are parallel segmented single inlet and single outlet design and the other one is dual inlet and single outlet design. The analysis are done using MATLAB software with a set of equation. The equation are tested numerically to determine it accuracy before being use in MATLABB software for simulation. This analysis are done to investigate the sufficiency of water removal rate for both design based on the current density and power density drawn from each design. These result are then validated with a data from a journal. The dimension and the active area are made similar for both design. This is to allow comparison to be made between the two design.

Keywords: PEM fuel cell, Segmented flow channel design, Effective PEM fuel cell water removal

1. Introduction

During early 2000, Proton Exchange Membrane (PEM) fuel cell are tested for its ability to provide nighttime power for solar-powered Helios long duration aircraft made by Aerovironment. The main objective is to run unpiloted aircraft that could fly continuously day and night for six months. On June 1998, Proton Exchange Membrane (PEM) fuel cell began to powering home in New York which could supply electric power up to five kilowatt. Basic fuel cell has a negatively charged anode and positively charged cathode. At the anode, hydrogen (H_2) is oxidized and the proton are transported via the electrolyte membrane to the cathode. At the cathode, oxygen (o_2) is reduced. Electron that are produced at the anode early on are carried to the cathode over the external circuit provided[1]. The hydrogen and oxygen used to alter the electrolysis process are then removed as a byproduct of water. Below is a simple reaction equation (1), (2) and (3).

$2H_2 + O_2 \rightarrow 2H_2O$ (1)

$2H_2 \rightarrow 4H^+ + 4e^-$ (2)

$O_2 + 4H^+ + 4e^- \rightarrow 2H_2O$ (3)

The main advantages of fuel cell is the ability to generate energy with minimum pollution during the entire process compared to fossil fuels. It is a promising technology for future generation as it emits lower pollution gases and at the same time operates with high efficiency. There are several types of fuel cell namely [2]:

- Alkali Fuel cell
- Molten Carbonate fuel cell
- Phosphoric acid fuel cell
- Proton Exchange Membrane (PEM) fuel cell
- Solid Oxide fuel cells

Researches from all levels has spent their time and efforts in order to maximize the PEM fuel cell performance and at the same time maintains it sustainability. Numerous researches had been done for the past years, however most of the researched focus on the different design of flow channel. By only spend most of their time and effort on the design process, the lack of data and analysis had led to the selection of the project which will provides future researches more data collection for comparison purposes. Based on the research question generated, "Does segmented parallel flow field design for Proton Exchange Membrane (PEM) fuel cell sufficient for water removal", the author conducted researches which will lead to the analysis of segmented flow field channel for Proton Exchange Membrane (PEM) fuel cell.

Based on the researched question generated earlier, the main objective for this project are:

1. To investigate the sufficiency of parallel segmented flow field design for Proton Exchange Membrane (PEM) fuel cell design to remove water.
2. To maintain the idle humidity of Proton Exchange Membrane (PEM) fuel cell to maximize its performance.

2. Methodology

In this research, a set of equation to relate the pressure drop and velocity of segmented parallel flow with one inlet one outlet and two inlet one outlet flow channel PEMFC configuration with the current density and power density produced. Both analytical and numerical method using MATLAB were apply to get the final result which are then presented in graph form of power density againts current density which are then further analyse for the sufficiency of the flow channel for water removal.

2.1 Computational Model

The equation was prepared based on the literature review gathered earlier during the early stage of this project. This paper utilize the usage of commercial MATLAB computational domain in order to predict the behavior of PEMFC.

A. Kinetic energy, KE

$$\mathrm{KE} = {}^{1}/_{2}\, \mathrm{m}v^{2} \qquad (4)$$

Where, *m* is the mass of electron [2] and *v* is the flow velocity of reactant in flow channel [4].

B. Fuel cell voltage, V

$$V = \frac{ke}{q_e} \qquad (5)$$

Where, q_e is the electron charge q_e = 1.6 x 10^{-19}[ ].
Fuel cell current, I

$$I = \frac{V}{R} \qquad (6)$$

Where, R is the electrical resistivity of Nafion membrane 115 [4].

Table 1. Geometrical Parameter

	Design A	Design B
Active volume (mm^3)	2663.57	2898.35
Bipolar plate dimension	170mm x 75mm x 2mm	170mm x 75mm x 2mm
Flow field layout	Parallel segmented 1 inlet 1 outlet	Parallel segmented 2 inlet 1 outlet

3. Result and Discussion

3.1 Simulation Validation

To validate the MATLAB computational model, a journal by K. I Sainan, R. Atan, W .A. N. W. Mohamed [6] is referred to allowing the result of this simulation to be compared. Based on the parameter of operation and the data in this project, the final result of current density is 2.5% percentage of error. Therefore the computational model developed is reasonable and acceptable due to some assumption made in the set of equation.

3.2 Result

Fiq. 1 shows the simulation of power density against current for design A. At current density of 2.04 A/cm^2 the maximum power density for design A is $0.7W/cm^2$. Fiq. 2 shows the simulation of power density against current for design B. At current density of 1.95 A/cm^2 the maximum power density for design B is 0.64 W/cm^2. Based on the result collected above shows that the current density is higher for design A due to the higher velocity of reactant entering the flow channel at the inlet. The current density produce throughout the operation for design A shows a significant decrease in the middle part of the flow channel as the velocity of reactant decreased. Design B show a lower maximum current density compared to design A due to the slower velocity of reactant entering the flow channel since it has 2 inlet. The current density produced throughout the entire operation for design B show a better improvement compared to design A due to the velocity of reactant at the middle of the flow channel are almost distributed evenly without any significant drop since it has 2 inlet.

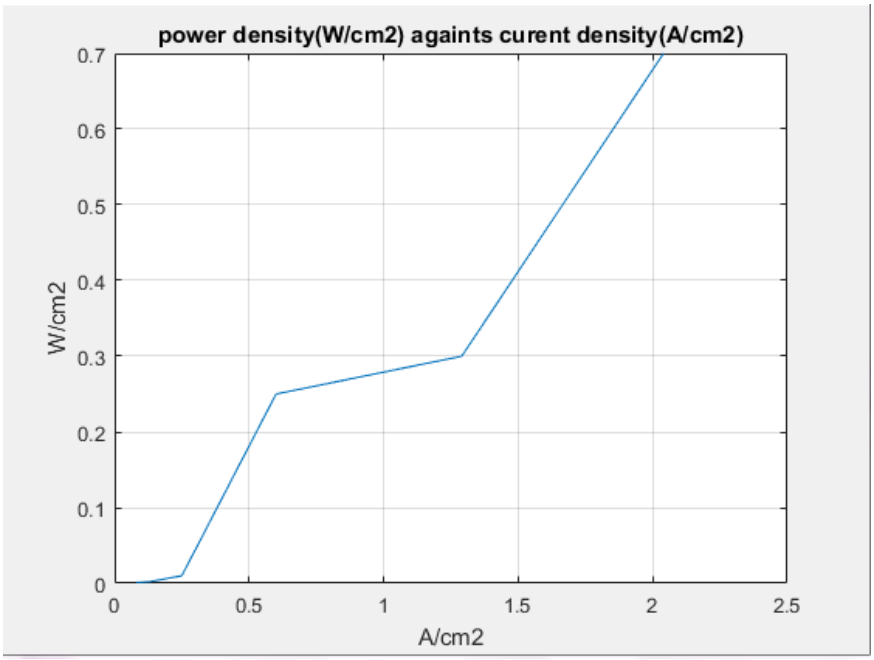


Figure 1. power density against current density for design A

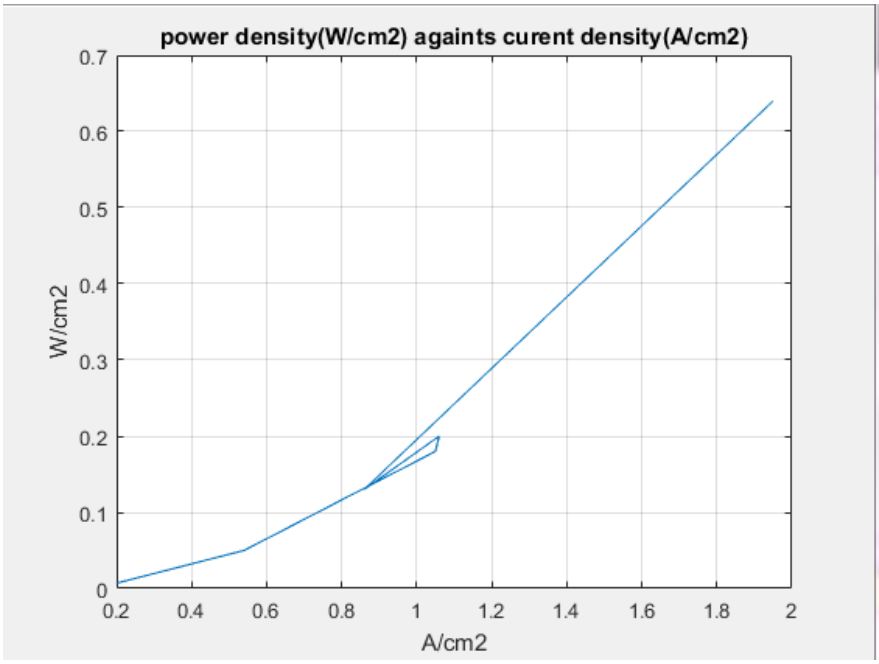


Figure 2. power density against current density for design B

4. Conclusion

In this study, two segmented parallel flow field channel were analysed. From the analysis shows that the distribution of velocity in design B which is slightly lower with no sudden drop of velocity in the middle part of the flow channel than design A allow more chemical reaction between the reactant to occur []. Higher current density drawn indicate that the current produce per unit area inside the flow channel is at the optimum level. Since PEM Fuel cell produce water as a by-product resulted from the chemical reaction, it is crucial for it to maintain water level at the optimum level to prevent from membrane dehydration to occur []. Higher current density indicate the electron produced flow through the external circuit rather than conducted by the water produce inside the flow channel that may lead to short circuit and reduce the density of electron flow via the external circuit.

Acknowledgment

Gratitude and thanks to Mr. Mohd Hardie Hidayat Bin Mohyi and research partner, Sanjan Peter Balan for the guidance and supervision throughout this research process.

Reference

[1] American History, “Collecting Fuel Cell History,” *American History*, June 15, 2014.[Online].Available:http://americanhistory.si.edu/fuelcells/origins/origins

[2] Sang Moon Kim, Yun Sik Kang, chiyeong Ahn, Segeun Jang, Minhyoung Kim, Yun-Eun Sung, Sung Jong Yoo, Mansoo Choi, “Prism-patterned Nafion membrane for enhanced water transport in polymer lectrolyte membrane fuel cell,” **Journal of Power Source**, vol 317,pp.10-24, March.2016.

[3] C.C Thompson, “Charge and mass of the electron. An introductory experiment,”

Journal of Chemical Education, vol 50 (6), pp 435, 1973.

[4] J. Larminie, and A Dicks, fuel cell system explained, Second Edition. West Sussex,UK: John Wiley & Sons Ltd, 2003

[5] C. Moisés Bautista-Rodríguez, Araceli Rosas-Paleta, J. Antonio Rivera-Márquez, Omar Solorza-Feria, "Study of Electrical Resistance on the Surface of Nafion 115® Membrane Used as Electrolyte in PEMFC Technology," **International Journal of Electrochemical Science,** vol 4, pp 45-59, March 2009.

[6] K.I Sainan, R. Atan, and W.A.N W. Mohamed "analysis of PEM fuel cell flow field design and operation for effective water removal," **Alternative Energy Research centre (AERC**), Universiti Teknologi MARA (UiTM),April,2015.

[7] Colleen Spiegel, **PEM Fuecl Cell Modeling and Simulation using MATLAB**, 84 Theobald's Road, London WC1X *RR, United Kingdom: Elseviar Inc, 2008.

[8] Mengbo Ji and Zidong Wei, "A review of water management in Polymer Electrolyte Membrane Fuel Cells," **Journal Energies**, vol 2. pp 1057-1106, Nov, 2009.

[9] Colleen Spiegel, *PEM Fuel Cell Modelling and Simulation using MATLAB***.** 84. Theobald's Road, London WCIX 8RR, United Kingdom: Elsevier Inc, 2008.

[10] I. Sabir, J. Park, and X.Li, "A flow channel design procedure for PEM fuel cells with effective water removal," Journal of Power Sources, vol. 163, pp. 933-942, 2007.

eureca 2016 – Conference Paper
Paper Number 2ME30

Aerodynamic Analysis of Personal Vehicle Side Mirror

Wesley Allen Otten[1*], Abdulkareem Sh. Mahdi Al-Obaidi [1]

[1]*School of Engineering, Taylor's University, Malaysia*

[*] Abdulkareem.Mahdi@taylors.edu.my

Abstract
Side mirrors are important parts of a vehicle to aid the driver in order to view behind and the side of the vehicle to assess traffic conditions. However, side mirrors contribute to increase aerodynamic drag of the vehicle due to the increased frontal area. The objective of this study is to calculate the aerodynamic drag of side mirrors using numerical methods. Statistical data is gathered regarding the dimensions of side mirrors from different vehicles. This data is used to find the averages such as the size of the mirrors compared to the car, the side mirrors angle and the streamline factor of the side mirror. A 2011 Perodua Myvi is used for CFD simulation with and without side mirrors. By comparing the two configurations, the effect of the side mirrors on the total drag coefficient of the car can be studied. Results from this study are that side mirrors contribute between 2-5% increase to the total drag of a car. This study also aims to analyse the impact of the drag in terms of fuel consumption and cost. Current calculations for the Myvi find that removing the side mirrors can save a maximum of RM 96 a year at 100 km/h.

Keywords: Automobiles, Side Mirrors, Drag, Fuel Consumption, CFD

1. Introduction

Improving vehicle aerodynamics is a steady innovation for automakers to improve and create more efficient vehicles. Over the years, cars have become more streamlined with lesser exposed operational components. Side mirrors are obvious protrusions on the car body that cannot be simply removed for many reasons. Drag is a force that opposes the movement of object through the air. Its factors are velocity, area, air density and drag coefficient. The flow separation caused by the side mirror creates a pressure difference which causes pressure drag. The high pressure of the flow creates a force towards the low pressure region to the flat mirror behind the side mirror housing. The increased frontal area of the side mirror is the main contributor to the drag force. Side mirrors also increases the wetted area which increases viscous friction. Eq. (1) and Eq. (2) are used to calculate drag force.

$$F_D = \frac{1}{2} V^2 A \rho C_D \tag{1}$$

$$C_D = C_p + C_f \tag{2}$$

where C_D is drag coefficient, C_p is pressure drag coefficient and C_f is skin friction drag coefficient.

In a study by Shah and Mahmood [1], the objective was to examine the impact due to aerodynamic drag of side mirrors to fuel consumption. By doing analytical calculations using basic shapes, the focus of the analysis was towards the mirror face. The author compared between a flat back and a hemispherical back mirror. The test was conducted at wind speeds of 60 – 120 km/h. The results reveal a reduction of fuel consumed for the hemispherical back mirror which is 17 litres/year less than the flat back mirror at 120 km/h. This study was focused on the rear face of the side mirror where the drag was due to the turbulent flow of the side mirror after the front face. The results reveal a reduction of fuel consumed for the hemispherical back mirror which is 29.3 litres/year less than the flat back mirror at 120 km/h. This study was focused on the rear face of the side mirror where the pressure drag was due to the flow of the side mirror after the front face.

$$\dot{m}_{fuel} \cdot H_{v,fuel} = P_{engine} = \frac{F_D v}{\eta} \tag{3}$$

where $\dot{m}_{fuel}$ is the flow rate of fuel consumed, $H_{v,fuel}$ is the calorific value of fuel, P_{engine} is engine power required, F_D is drag force, v is velocity and η is engine efficiency. This formula will be used to quantify the fuel used to overcome the side mirror drag.

Studies from University Malaysia Pahang have conducted simulations to find the aerodynamic drag of side mirrors [2] and the effects of aerodynamic pressure towards the mirror surface [3]. Three designs were tested at speeds of 60, 90 and 120 km/h. Results show that the coefficient of drag for all cases was around 0.4 to 0.6 specific to its reference area which is the frontal area facing the wind. Another study found that the yaw should be considered accounting for increased drag coefficient [4]. Therefore, yaw angle is added for statistical data gathering. Filipe and Vinicius [5] conducted a similar study to compare a production car's aerodynamic drag with and without mirrors. The authors also went further to include a suggested camera replacement for the side mirrors and also compare the drag coefficients between the three configurations. The setup was using a k-ε turbulence model with 0.6% turbulence intensity. The CFD simulation was conducted at 100 km/h with full underbody geometry with a rolling road and wheels. This was to simulate closely to real operating conditions. The results in the study show a drop by 1% for the drag coefficient and a 2.3% reduction in frontal area without the side mirror.

A study by Olsson [6] was also done with a focus on multiple factors of the side mirror that affect aerodynamic drag. Simulations were conducted on the side mirrors for a first generation 2000 Mercedes-Benz A-Class. CFD results shows that side mirrors contribute a drag coefficient of 0.012. Flow conditions were at 50 m/s with a turbulence intensity of 0.01%.

This paper aims to study the difference between a vehicle with and without mirrors using numerical methods. Statistical data will be gathered in order to establish the average characteristics of side mirrors. The simulation will be done using ANSYS FLUENT. Analysis is done to quantify to effect of side mirrors in terms of fuel used to overcome the side mirrors drag. Based on previous literature, expected drag coefficient due to side mirrors is around 0.012 and that drag coefficient of side mirrors to cars is about 5%. A 2011 Perodua Myvi shown in Figure 1 was chosen due to being commonly owned by many motorists. The expected drag coefficient of the car is around 0.32 based on Ramdan and Chee's findings [7].



Figure 1. 2011 Perodua Myvi. *Image by Wikipedia Commons.*

2. Research Methodology

The paper contains two main sections, statistical data gathering and numerical simulation.

2.1 Statistical Data Gathering

Data was gathered using technical drawings to statistically analyze the different shapes and sizes mirrors have. This data is categorized into three general measurable aspects.

2.1.1 Side Mirror Area Percentage

A primary factor of aerodynamic drag is due to frontal area perpendicular to the wind direction. The area can be found by using scaled technical drawings and comparing with known vehicle specifications to find the area of the side mirror. Side mirror area percentage is defined as the frontal area of both side mirrors over total frontal area of the vehicle. As a larger reference area will displace more fluid in motion, it will have a higher drag force. The side mirror area is as shown for example in Figure 2. By recording in percentage, the influence of side mirrors can be quantified in terms of the reference area.

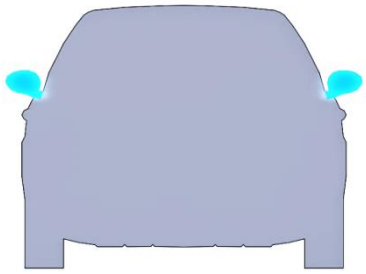


Figure 2. Example of Side Mirror Area Percentage

2.1.2 Yaw Angle

The yaw angle on the mirror is defined as the angle in which the side mirror is towards the wind from the body of the car as shown in Figure 3. A higher angle will indicate more exposed frontal area. As the frontal curvature of the side mirror housing is uneven, the angle will be taken based on the mirror plane which is where boundary separation occurs.

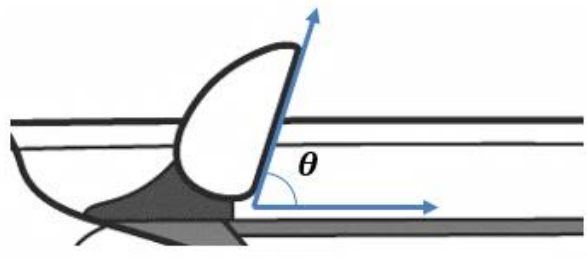


Figure 3. Example of Side Mirror Yaw Angle (Top View)

2.1.3 Thickness to Chord Ratio

To quantify the streamlined aspect of the side mirror housing, the side mirror's thickness and chord length is recorded. It will be used to calculate thickness to chord ratio which can give into perspective how streamlined the side mirror housing is to upcoming wind. An example of thickness and chord is shown in Figure 4.

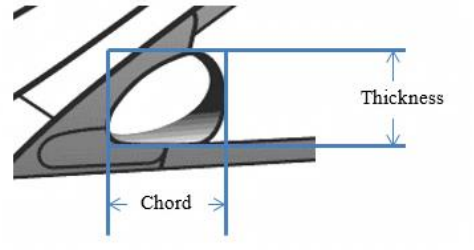


Figure 4. Example of Side Mirror Thickness and Chord

2.2 Numerical Method

2.2.1 Geometry Modelling

The original modelled Myvi had openings in the wheel well. Due to constraints with hardware and time, a simplified model is used to avoid meshing tight openings. Results of the side mirrors are not directly affected by the turbulence generated by the wheel. Figure 5 shows the models differences. The dimensions of the models are similar with the actual car.

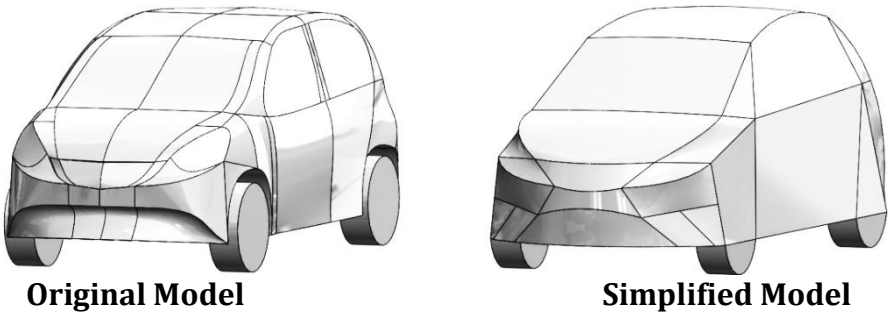


Figure 5. Car Geometry for Simulation

The side mirror is also modelled accurately with actual dimensions. Small cavities are removed and the mirror face is flat. The mirror will be attached to the simplified model during simulation. Figure 6 shows the side mirror.



Figure 6. Side Mirror for Simulation

2.2.2 Meshing Method

The computational domain of the simulation is based on the major length of the vehicle. Figure 7 shows the discretization of lengths which is based on Damjanović et al. (2011) [8]. Adequate spacing is provided to provide uniform flow before and after the car model to have an undisturbed flow. A symmetry based simulation is used due to limited hardware and time.

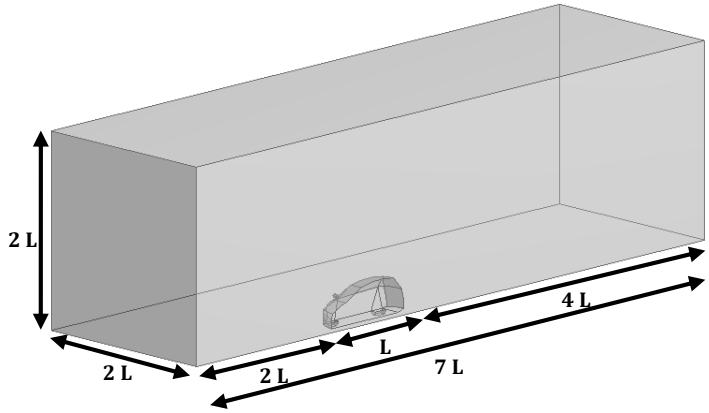


Figure 7, Discretization of Computational Domain

A fine mesh is necessary in order to have a converging simulation. Smaller elements are placed closer towards the car and side mirror in order to capture the boundary layer. A majority of the elements are prism wedges (Wed6) due to their flexibility and high orthogonal quality. Figure 8 shows the bias of the mesh towards the car and Figure is a close up of the mesh on the car. Table 1 shows the meshing characteristics used with Table 2 showing the meshing statistics after generating.

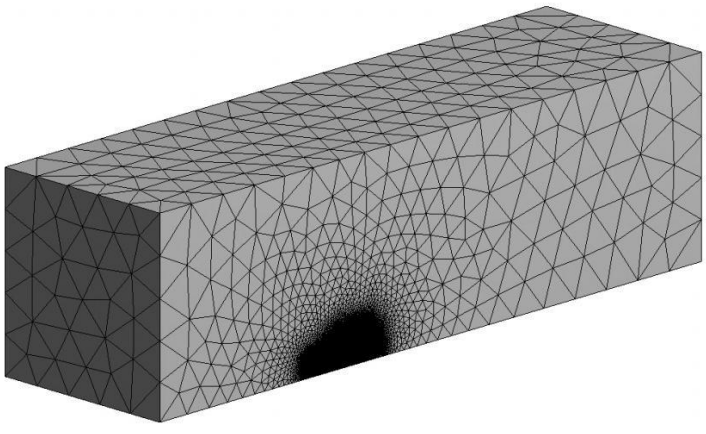


Figure 8, Generated Mesh for Fluid Simulation

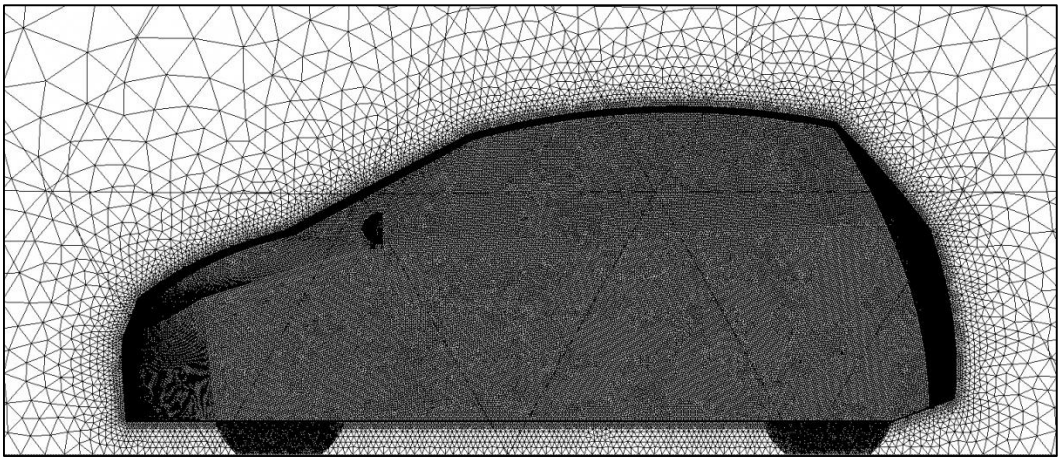


Figure 9. Mesh Elements around Simplified Model

Table 1. Characteristics of Mesh Sizing

Global Mesh Size	
Curvature Normal Angle	12^o
Number Cells Across Gap	5
Minimum Size	1e-2 m
Maximum Face Size	1.5 m
Maximum Size	1.5 m
Face Sizing	
Geometry Selection	All Car Faces
Element Size	1e-2 m
Behavior	Soft
Inflation	
Geometry Selection	All Car Faces
First Layer Height	1e-4 m
Maximum Layers	14
Growth Rate	1.2
Inflation Algorithm	Pre

Table 2. Meshing Quality Statistics

Nodes	2094644
Elements	5772518
Aspect Ratio	
Minimum	1.15
Maximum	351.21
Average	23.77
Skewness	
Minimum	1.7e-8
Maximum	0.88
Average	0.15
Orthogonal Quality	
Minimum	3.42e-2
Maximum	0.99
Average	0.91

2.2.3 Numerical Setup

The simulation is set using a pressure based solver. A symmetry plane is made on the car since the flow is similar on each side. Results are taken once the continuity residuals converge at 1E-6. The car in the simulation setup is placed similarly like a wind tunnel setup. The surrounding walls are boundaries since a using pressure far field will result in the solution crashing. The full setup of parameters is shown in Table 3.

Table 3. Simulation Setup

Input Parameters	
Turbulence Model	k-ε
Inlet Velocity	27.78 m/s (100 km/h)
Turbulence Intensity	0.01%
Output Pressure	Atmosphere
Air Density	1.225 kg/m^3
Air Viscosity	1.7894×10^{-5} kg/m·s
Boundary Walls	No Slip Conditions

3. Results and Discussion

3.1 Statistical Results

From the data gathered, the scatter plot of side mirror area percentage shown in Figure 10 show a maximum percentage of 3%. From these samples, the average sizes of mirrors exist between 1.5% to 3%. Based on this, a selection of cars at for 3% is the 2005 Alfa Romeo 159 for future work. However, the technical drawings have poor resolution and closest model is the 2010 Alfa Romeo Giullieta with 2%.

In this sample, yaw angle as shown in Figure 11 for cars are around 60º to 75º. A lower angle is desirable as it is similar to angle of attack of aerofoils. A lower angle of attack will have less drag. The value at 85º is much greater than the rest of the samples therefore it is considered an outlier. Mirrors do not go below 60º due to specific safety regulations involving the ability to view behind the vehicle.

The thickness to chord ratio shown in Figure 12 indicates the streamlined aspect of the side mirrors. In this case, a lower number is desirable as the flow separation is less. Any values above 1 indicate a large area that displaces the air therefore causing more drag. Two outliers exist in this data which is caused by parallax error in which the yaw angle is directly towards the camera. Values of thickness to chord ratio exist between 0.6 to 1.

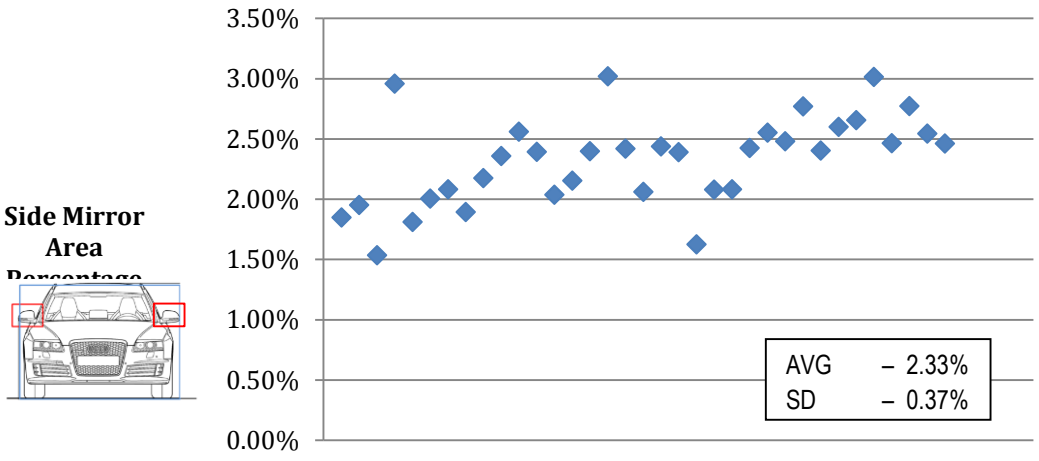


Figure 10. Scatter Graph of Side Mirror Area Percentage

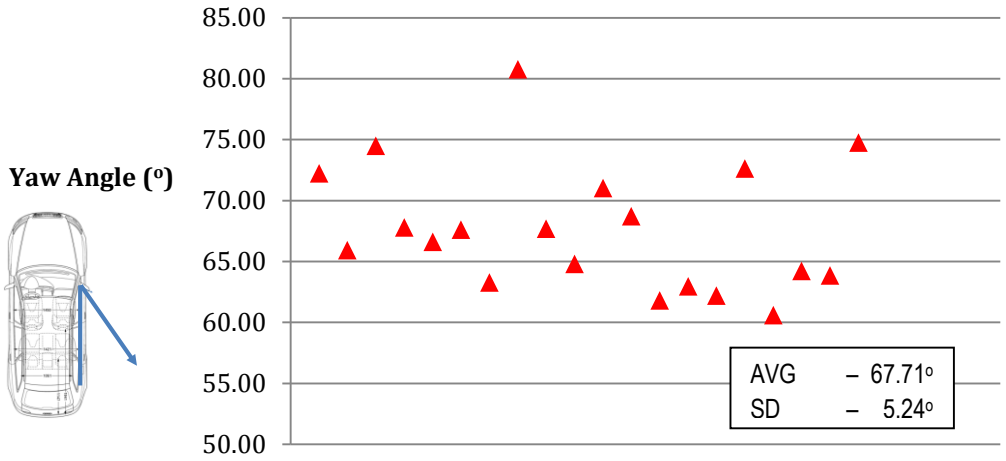


Figure 11. Scatter Graph of Side Mirror Yaw Angle

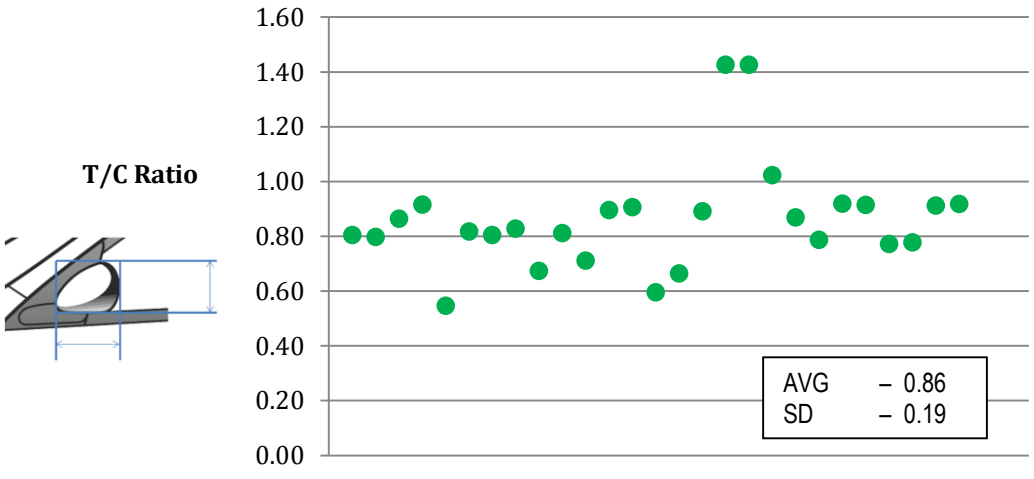


Figure 12. Scatter Graph of Side Mirror Thickness to Chord Ratio

3.2 Numerical Results

The results obtained from the ANSYS FLUENT simulation are forces acting on the car faces. The forces are comprised of lift force and drag force. The main focus of this paper is drag forces which is divided into pressure forces and viscous forces. These forces are calculated with the reference area, which is the frontal area perpendicular to the incoming wind, to give the total drag coefficient. The results are shown in Table 4.

Table 4. Simulation Results

	Drag Coefficient Value
Car with Mirror	0.3759
Car without Mirror	0.3587
Percentage Difference	4.5%

Based on Ramdan and Chee's findings [7], the Perodua Myvi is reported to have 0.32 drag coefficient. The value found in this work is validated with a 17% error which is acceptable since drag is difficult to simulate compared with lift. The viscous boundaries require a much smaller mesh sizing to gain accurate results. The 4.5% drag coefficient difference is validated based on Batchelder's (2009) [9] investigation which is around 4.8%.

The main contributing force of drag is pressure drag which is expected. The air approaching the car surfaces will have a reduced velocity. This will increase the pressure and the pressure difference will create a force. This is shown in the pressure distribution as presented in Figure 13 and Figure 14. The pressure distribution on the side mirror is shown in Figure 15.

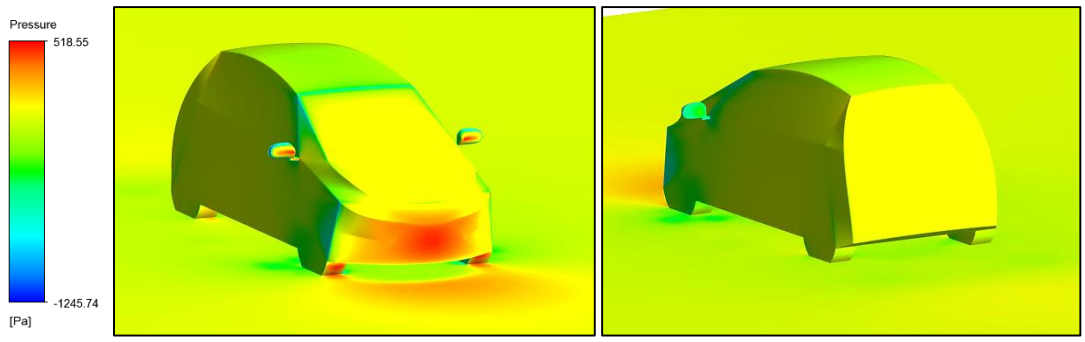


Figure 13. Pressure Distribution Contours on Car and Road Surfaces

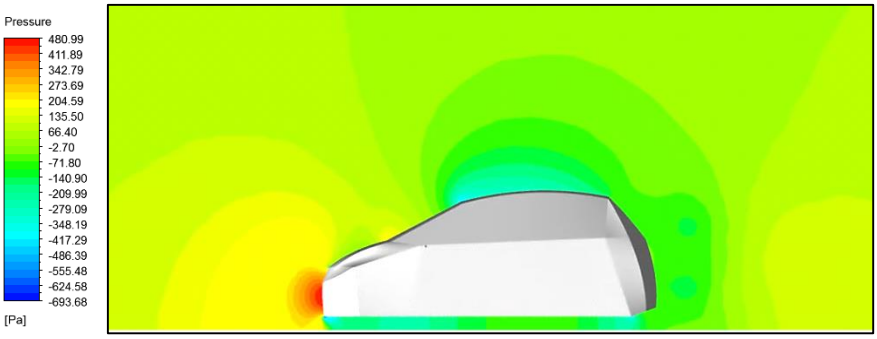


Figure 14. Pressure Distribution Contours in Fluid around Car (Side Plane)

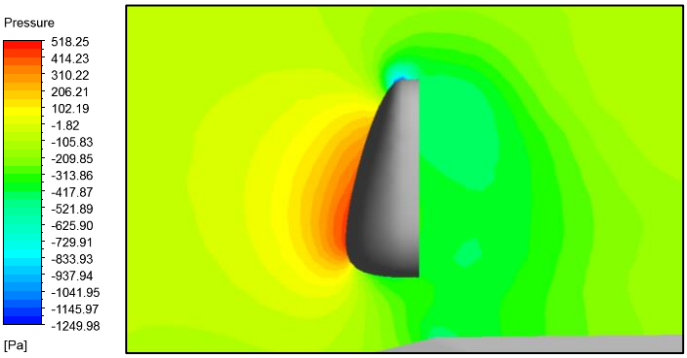


Figure 15. Pressure Distribution Contour in Fluid around Side Mirror (Top Plane)

Although not the contributing factor with the drag coefficient, the viscous skin drag coefficient is lower than the pressure drag coefficient. However, the velocity of the flow is affected by the viscosity towards the car surface which impacts the pressure. The velocity streamlines of the car and mirror are shown in Figure 16 and Figure 17.

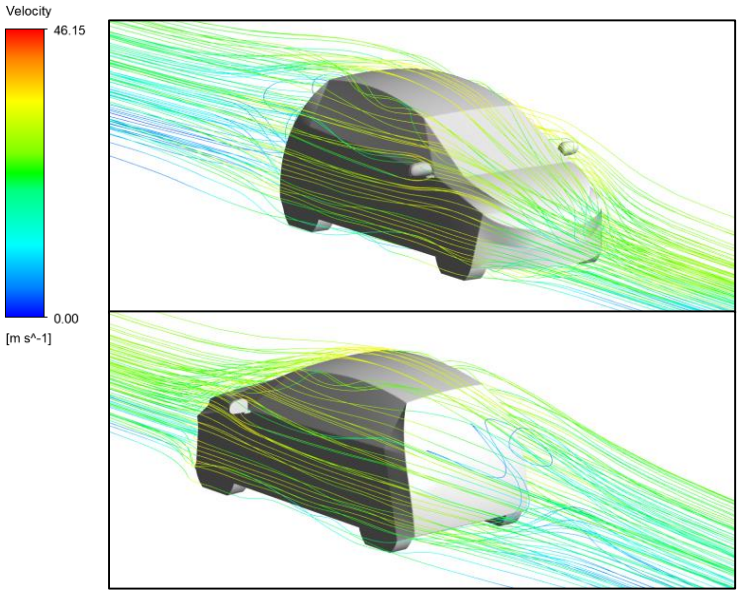


Figure 16. Velocity Streamline around Car

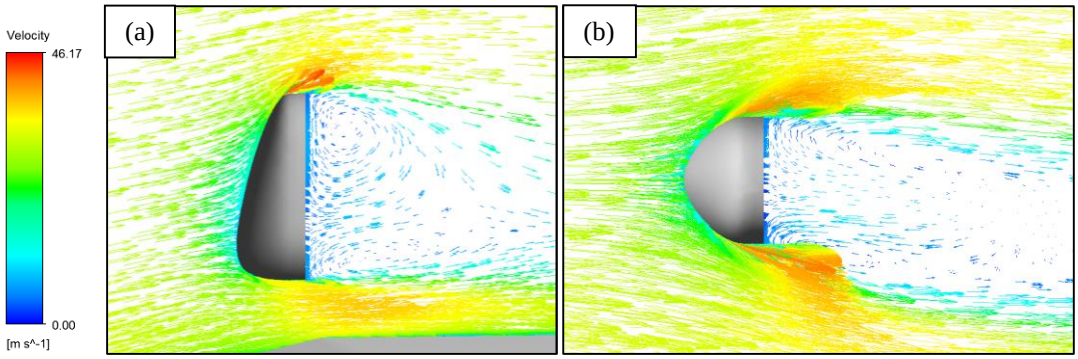


Figure 17. Velocity Vectors around Side Mirror (a) Top View (b) Side View

Based on the values obtained, calculations on fuel used can be done using Eq. (3). By assuming a 47300 kJ/kg heat value of fuel, engine efficiency at 30% and the frontal area of both side mirrors is 0.06 m^3, Table 5 shows the fuel saved using different average velocities. At time of writing, fuel cost for RON95 is RM 1.95. It should be noted that this does not take into account actual distance travelled. The table below is based on full usage of the car throughout the month. Car usage is dependent on the user therefore; to create a more relevant figure, multiply the values with the percentage of use.

Table 5. Potential Fuel Save Calculations

Fuel Saved by Removing Side Mirrors Based on Average Velocity		
Average Velocity (km/h)	Fuel Saved / Year	Money Saved / Year
20	0.39 L	RM 0.77
40	3.15 L	RM 6.15
60	10.64 L	RM 20.74
80	25.21 L	RM 49.16
100	49.24 L	RM 96.02

4. Conclusion

It is well known that decreasing the frontal area would decrease drag force. In this study, it is found that the side mirrors have a 5.8% influence of total drag. The removal of the side mirrors would help reduce fuel consumption however, the savings towards the consumer is very low therefore it is not viable from an economic standpoint. Likewise, side mirrors are important in ensuring driver safety by providing surrounding awareness around the vehicle. In conclusion, side mirrors can be replaced to advance vehicle efficiency however the savings are low and the safety concerns surrounding it should be looked into.

References

[1] Shah, A. and Mahmood, S.M. (2014). Study of Side View Mirror Design on the Fuel Consumption of a Car, *Global Sci-Tech*, 6(4), (pp. 224-227).

[2] Murukesavan, P. (2012). *Computational Fluid Flow Analysis of a Side Mirror for a Passenger Car*. Kuantan, Pahang: University Pahang Malaysia, Faculty of Mechanical Engineering.

[3] Murukesavan, P., Mu'tasim, M., Sahat, I. (2013). *Computational Analysis of an Effect of Aerodynamic Pressure on the Side View Mirror Geometry*. Paper presented at the International Conference on Mechanical Engineering Research, Kuantan, Pahang: University Pahang Malaysia.

[4] Mat, N. R., Nasir, A., and Razak, S. (2015). *The Effect of Diffuser Angle on Modified Generic Side View Mirror*. Presented in the Preoceedings of Mechanical Engineering Research Day 2015, (pp. 39-40).

[5] Buscariolo, F., Rosilho, V. (2013). Comparative CFD Study of Outside

Rearview Mirror Removal and Outside Rearview Cameras Proposals on a Current Production Car, *SAE Technical Paper Series*, no. 36.

[6] Olsson, M. (2011). *Designing and Optimizing Side-View Mirrors*. Master's Thesis, Göteborg, Sweden: Chalmers University of Technology, Division of Vehicle Engineering and Autonomous Systems.

[7] Ramdan, M., Chee, P. (2015). Fuel economy comparison of Perodua Myvi passenger vehicle on Malaysian city and highway drive cycles. *Journal of Scientific Research and Development*, 2(13), (pp.76-82).

[8] Damjanović, D., Kozak, D., Živić, M., Ivandić, Ž. and Baškarić, T. (2011). CFD analysis of concept car in order to improve aerodynamics. *Járműipari innováció*, 1(2), (pp.108-115).

[9] Batchelder, J.H. (2009). *A CFD investigation of potential aerodynamic enchancements to a microcar class vehicle*. Master's Thesis, Rensselaer Polytechnic Institute, USA.

eureca 2016 – Conference Paper
Paper Number 2ME31

Design and Fabrication of Multi-Position Test Rig Seat for Whole-Body Vibrations

Wong Chuen Yeong[1*], Mohd Farid bin Aladdin[1]

[1]*School of Engineering, Taylor's University, Malaysia*

*Chuenyeong.wong@sd.taylors.edu.my

Abstract

Whole Body Vibrations (WBV) is a phenomena which involves the extensive study of the response of an object when it is being subjected to a vibrational force.In order to replicate the WBV phenomena in vehicles, most researchers re-create an environment whereby a subject will be placed in a chair. A vibrational source from the base will provide the excitation to the subject sitting on the chair. However, different scope of WBV requires different experimental test rig, which limits the number of WBV experiments that can be conducted. Therefore, this research is intended to answer the research question on the methods to design and fabricate a test rig which can be used as a universal WBV test rig. For this research, the methodologies can be broken down into three main parts which include, design, analysis and fabrication. The first section is to draw the Computer Aided Design (CAD) model of the test rig based on literature review of various chair designs. Secondly, Finite Element Analysis (FEA), specifically Harmonic Reponse Analysis will be conducted to determine the response of the chair subjected to a vibrational load (acceleration) in the X, Y and Z-axis on specific points/ bodies of the chair respectively. The fabrication stage will be completed to replicate the 3D model into real life and scaled prototype model of the test rig. The results have been concluded that the acceleration frequency relationship is linearly proportional, the greater the frequency the greater the acceleration response of the points on the chair. Besides that, specific points of vibration response measurement shows different maximum acceleration amplitude, with greatest discomfort at 80 Hz at the X axis for backrest, points 3 and 4 with X axis is on the Seat pan, armrests, points 1, points 2 and headrest while Vertical Supports for Y-axis will experience greatest discomfort.

Keywords: Whole Body Vibration, Harmonic Response, Test Rig

1. Introduction

Whole-Body Vibration (WBV) is a phenomena whereby studies were done to determine the response of the body of the subject when it is exposed to vibrating source [1]. Vibrational sources are so common they can be essentially found in every aspect of environment which range from using a pneumatic jackhammer in construction sites to vibrational effects from driving. According to studies done by Meloni [1], though long term exposure to vibrations would not contribute to major significant health issues, nevertheless a person will definitely feel a sense of discomfort [1]. Therefore, it is important to determine the response of the person being subjected to vibration in the long term exposure. Understanding of this knowledge is important to enable better design of structures and mechanism to improve comfort level and to reduce the discomfort felt by the user when being subjected to WBV. For this research, the scope was narrowed down specifically to determine the how the passengers and drivers perceived comfort in vehicles when they're being subjected to WBV [1-9].

The International Organization for Standardization for vibration evaluation has identified the six different types of vibrational forces and the range of frequency a human can detect and identified. The 6 types of vibrational forces include 3 translational vibration and 3 rotational vibration (X-Roll, Y-Pitch, Z-Yaw) in the X,Y and Z axis according to the basic-centric axis provided [1] as shown in Fig. 1 below.

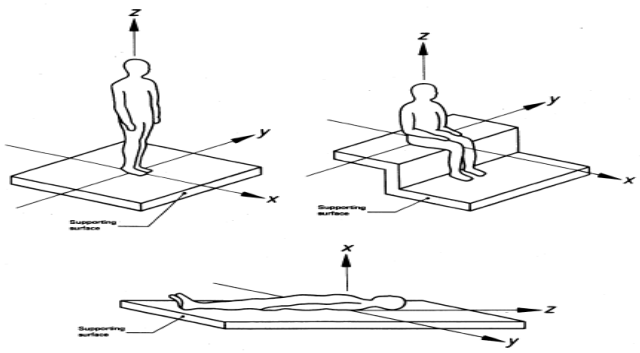


Figure 1: Basicentric axis relative to gravitational field [1]

In the studies conducted to determine the perception of passengers comfort in vehicles when subjected to WBV, it has been identified the following which includes Hand-Arm transmitted vibration [1,9], Fore-aft vibration [2,3] Horizontal [3,8] and Vertical vibration [1,3-5, 7-9]. Hand transmitted vibration deals with the vibrational forces acting on the hands of the driver holding the steering wheel due to the interactions from the engines and the tyres with the surface of the road [9]. This information is important for the driver to access the state of the car running on different surfaces from the vibrational feedback through the hands. Fore-aft vibration is the study of the vibrational forces acting in the X-direction of the basic-centric axis [3]. Similarly, Horizontal and Vertical vibration deals with the study of WBV in the Z and Y axis respectively.

In the field of WBV particularly the study of passengers perception of comfort in vehicles, there are two methods that can be conducted to determine the response to vibration which includes field testing through obtaining the vibrational frequency and magnitude inside a real vehicle's seat [9], or replicating it inside the lab with artificial vibrational simulation [1]. In order to investigate the response of the passengers subjected to WBV, the researchers usually re-create the environment through the usage of a test rig seat, placed on a platform. A vibrational source (electro-dynamic shaker) will provide the harmonic load necessary to simulate the test rig, as if the passengers is actually sitting inside the vehicle, subjected to vibration from the road, engine and other interactions with the car. Figure 2 below shows an example of a test rig, which is a rigid chair used by Bellmann [1] to investigate the comfort response of the human when being subjected to vertical vibration.



Figure 2: Vibration Floor Test Rig [1]

However, different scopes of WBVstudies demand different setup of the test rig, provided that other factors such as human subjects, conditions and the usage of various types of vibrational sources of magnitude and frequency to obtain the most optimum analytical results and discussion are kept constant. Since the main focus of this research is the test rig, therefore the following objectives of the research are as follows;

1. To design and fabricate a multi-position test rig seat which can be used as a universal test seat for the various Whole Body Vibration studies.
2. To investigate the Harmonic Response of the test rig seat when it is being subjected to vibrational forces and how it is affected by the design of the test rig.

2. Methodology

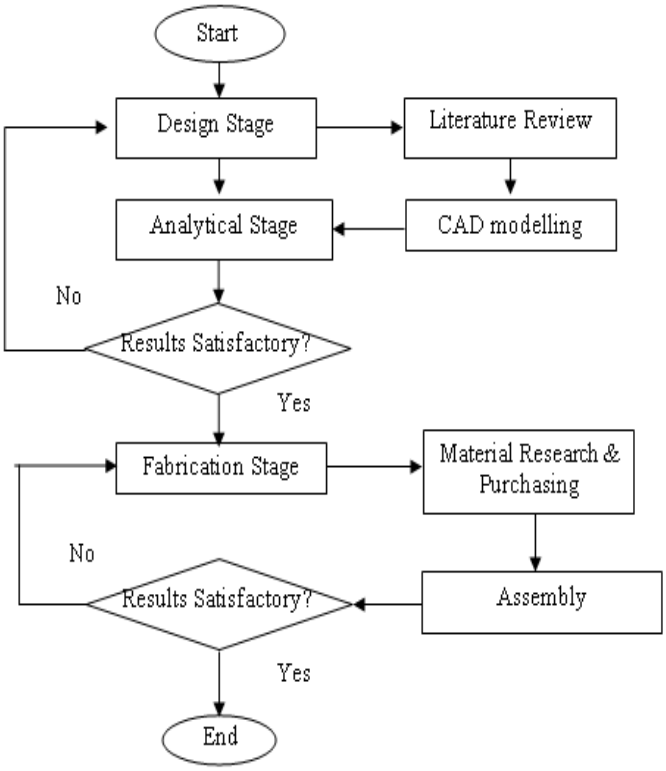


Figure 3: Research Methodology Flowchart

2.1 Design Stage

The design stage can be divided into two main stages, which were literature review and CAD modelling of the test rig using SOLIDWORKS® 2015.

2.1.1 Literature Review

The first section of the design stage is conducting necessary literature review, which will be divided into two phases. The first phase involves the comparison of different types of test rig seats which either have been fabricated/ brought throughout the WBV studies. This stage is crucial to determine what are the parameters required for the chair which includes armrest, headrest, legs and etc. Some of the chairs that were reviewed will be used as reference for the CAD model design. An example is the CAD model of the backrest frame as shown were also used as the reference for the test rig seat design [14]. Second phase involved determining the suitable anthropometric data for the whole population of Malaysia in order to design and fabricate a chair which fits to a 5^{th} to 95^{th} percentile of population. Table 1 shows the results of the selected anthropometric data picked from the study of D. Mohammad et.al [10].

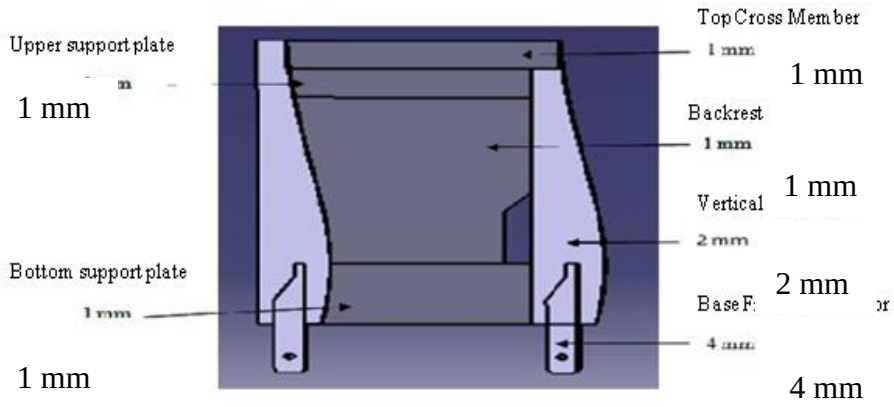


Figure 4: Seat Base Frame [14]

Table 1: Selected Anthropometric Data of Malaysians 2010 [10]

No	Anthropometric Dimensions(mm)	Mean	SD	5th Percentile	95th Percentile
1	Sitting Height	792.86	76.7	667.12	918.59
2	Popliteal Height	424.8	42.68	354.38	495.21
3	Sitting Shoulder Height	515.84	62.66	412.45	619.23
4	Hips Breadth	378.34	70.98	261.22	495.45
5	Length of buttocks to popliteal	448.6	48.93	367.87	529.33
6	Interscye Breadth	354.69	50.84	270.75	438.53
7	Elbow Height	224.66	56.82	130.91	318.41
8	Shoulder Breadth	438.97	55.88	346.77	531.17
9	Forearm Hand length	522.59	37.53	398.75	460.67

2.1.2 CAD Modelling

Based on the reference seat base frame and reference backrest frame taken, coupled with the selected anthropometric data as shown above, the 3D CAD drawing of the chair can proceed. The 3D CAD model will first be drawn with a rough sketch using pencil and translated to a real life model based on the criteria's chosen above. Table 1 results were just used as reference and the final dimensions of the chair will be dictated by chosen requirements, whether to fit the chair to the 5^{th}, 95^{th} or to accommodate between 5^{th} to 95^{th} percentile of Malaysian population.

2.2 Analytical Stage

In ANSYS workbench, the test rig seat will undergo two different types of dynamic analysis mainly (a) Modal analysis and (b) Harmonic response analysis. A modal analysis will be performed to determine the range of natural frequencies and mode shapes results for the experimenter to work with. This knowledge is important to plan future WBV experiments outside and away from these natural frequencies

range to avoid resonance, which long term exposure can cause structural damage to the test rig and/or human subjects comfort, health and safety. Also, a harmonic response analysis will be conducted whereby the test rig seat will be subjected to a vertical vibrational force in the Z-axis with a range of acceleration magnitude, (0.1) root mean square (r.m.s) acceleration value, which is the value of acceleration used for referenced according to ISO 2631 comfort standards.

Also, the frequencies of the acceleration force will be varied between 5-80Hz, which is the range of optimum frequency used for the study of comfort perception due to WBV as recommended by ISO 2631-1/2. The harmonic response analysis is used to determine the amplitude of acceleration in the X, Y and Z axis of the seat top surface and its corresponding frequencies being investigated. The data will be tabulated and a graph of acceleration against frequency be plotted. In this research, the main scope that is investigated is the perception of comfort/ human sensitivity according to ISO 2631.

2.3 Fabrication Stage

Fabrication stage involves a combination of Material Research and Purchasing, Fabrication and finally assembly of the individual components. The following subsection presents the overall view of the sub-process that occurs in the fabrication stages as a whole.

2.3.1 Material Research and Purchasing

In this stage, it is important to access the suitability of materials which can be used to fabricate the test rig seat. There are many consideration of the type of materials ranging from metal, wood, plastic and etc. The factors that dictate the type of materials will be evaluated according to the density and Young's Modulus (Stiffness) according to the Michael Ashby chart as shown in Fig. 6. Cost and weight were also considered whereby the maximum mass of the test rig was placed at 10kg and below for convenience of transportation purposes. The cost of fabrication was kept to RM500 and below.

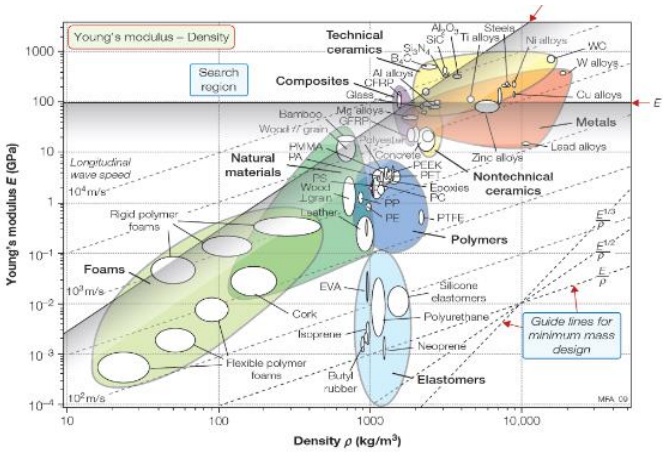


Figure 5: Michael Ashby Chart [12]

2.3.2 Fabrication

In fabrication stage, all of the parts/ components will be drawn, cut and bend (If necessary) to form the parts exactly which were drawn in the 3D modelling

software. The material that was primarily chosen for the fabrication after thorough consideration of the cost, weight and the Young's Modulus as shown above is Aluminum alloy 5052-H32.In the assembly stages, all of the parts and components that were fabricated, cut, formed, bend, and milled will be assembled according to the final CAD assembly. Necessary joining techniques were employed such using bolts and nuts to secure the parts or to use Metal Inert Gas Welding (MIG) welding technique to weld two aluminum parts together to form a secure part.

3. Results and Discussion

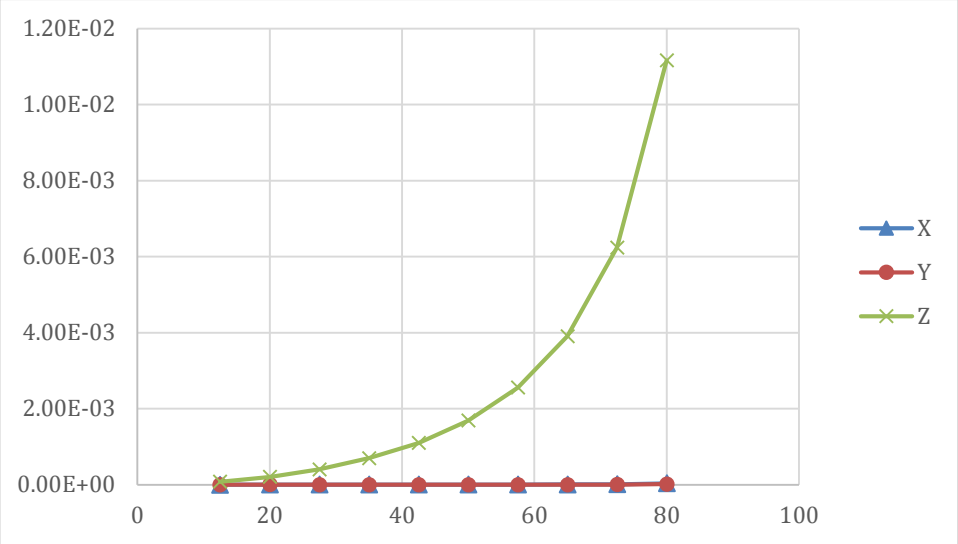


Figure 6: Frequency Response Graph for Seat Pan

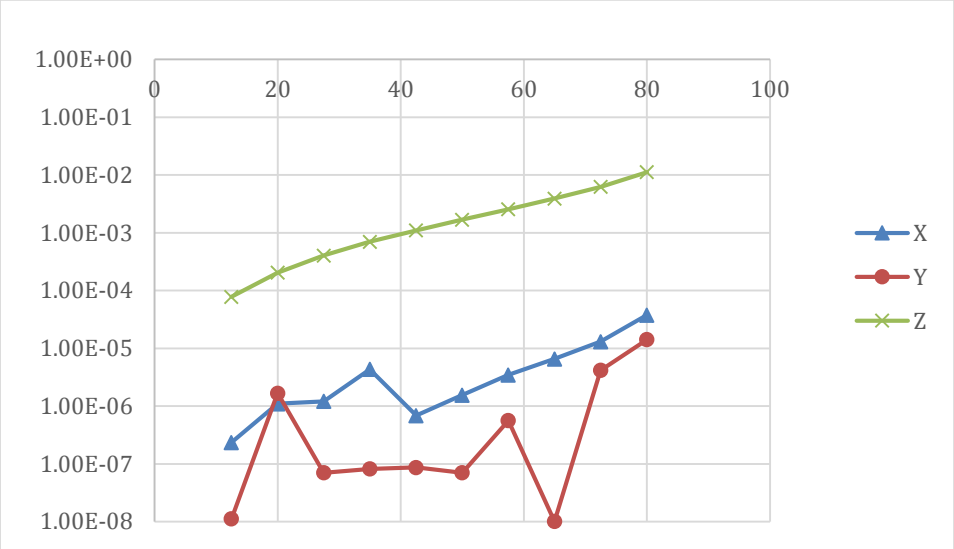


Figure 7: Logarithmic Frequency Response Graph

Table 2: Modal analysis and natural frequency tabulation

Mode	Minimum Deformation(m)	Maximum Deformation(m)	Frequency [Hz]
1st	0.19673	1.7706	15.309
2nd	0.25122	2.2609	18.783
3rd	0.25055	2.2549	18.845
4th	0.15502	1.3952	37.266
5th	0.20953	1.8858	63.692
6th	0.14795	1.3315	84.242
7th	0.28737	2.5863	89.424
8th	0.28595	2.5736	90.00
9th	0.15414	1.3873	93.538
10th	0.2057	1.8513	112.02

Table 3: Harmonic Response Tabulation in the X, Y and Z axis

No.	Frequency [Hz]	Amplitude [m/s²]		
		X	Y	Z
1	12.5	2.35E-06	1.12E-07	7.76E-04
2	20	1.10E-05	1.68E-05	2.04E-03
3	27.5	1.21E-05	7.01E-07	4.03E-03
4	35	4.32E-05	8.19E-07	6.97E-03
5	42.5	6.84E-06	8.68E-07	1.10E-02
6	50	1.54E-05	7.01E-07	1.69E-02
7	57.5	3.46E-05	5.60E-06	2.55E-02
8	65	6.56E-05	1.01E-07	3.91E-02
9	72.5	1.30E-04	4.17E-05	6.24E-02
10	80	3.77E-04	1.41E-04	0.1116

3.2 Discussion of Results

Throughout the analytical experiment which was conducted in ANSYS workbench R15, certain assumptions and boundary conditions were made. These boundary conditions are important for the solver in Workbench to calculate and solve for the frequency response against the amplitude of acceleration as shown in Table 3 above. The assumptions include placing a fixed support at the legs to simulate the real life test whereby the test rig seat will be bolted to the surface of the electro-dynamic shaker. Due to the limitation of the experiment, whereby the electro-dynamic shaker available in UPM cannot sustain heavy loads, the human subject factor sitting on the test rig will be excluded and the analysis will be conducted just on the chair itself.

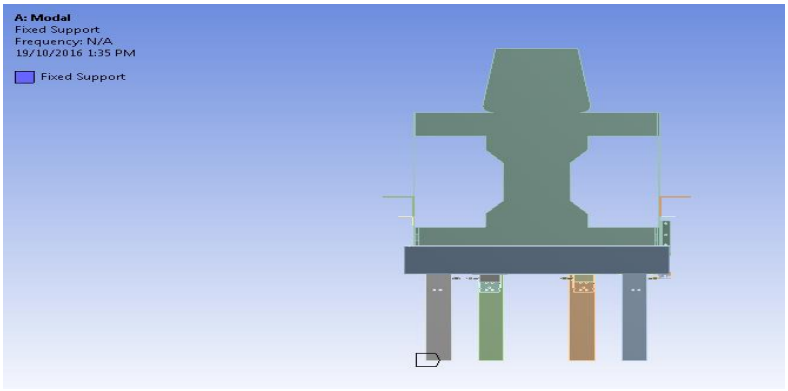


Figure 10: Boundary and Initial Conditions

3.2.1 Modal Analysis Results

Table 2 shows the frequency modal analysis for determining the natural frequency of the test rig seat. It is seen that when the number of solution intervals was set to 10 in ANSYS workbench, the solver was able compute a natural frequency with a range between 15.31 Hz to 112.02 Hz. This information is useful as it gives a limitation to the researchers, a range of frequencies to avoid in the experiments which resonance can occur. Resonance will occur if the frequency of the excitation matches with any of the chair's natural frequency, therefore producing double the amplitude of displacement on the chair, which makes the person sitting on it uncomfortable. Besides that, resonance also weakens structural integrity of the chair when exposed under long duration of vibration.

3.2.2 Frequency Response of Seat Pan

For this research, the graph of frequency response (acceleration amplitude) against corresponding frequencies were plotted as shown in Figure 6. It is seen that from both the tabulated results and graph, that the relationship is linear for both acceleration and frequency. The greater the frequency of the excitation, the greater the acceleration amplitude. This is true for the X, Y and Z axis. Because the acceleration amplitude is too big relative to the response in the Y and Z axis, the lines of graph in Y and Z axis looks like a straight line, but if the graphs were separately plotted, the difference will be noticeable.

Also, the greatest acceleration amplitude seems to occur at 80Hz, in the Z axis with an amplitude of 0.1116 m/s^{-2}, while the lowest acceleration amplitude of 1.41 x $10^{-4} m/s^{-2}$ occurs in the Y axis. With an excitation magnitude of 0.1 m/s^{-2} in the Z vertical axis, it seems that the chair has a transmissibility of more than 1.0 because the output acceleration is greater than the input. This makes sense because in the simulation, there is no damping materials/factors that would be added to the test rig to dampen the vibration. Adding a damper in the simulation as well as real life testing will affect the final results as reduced vibration will affect the perception of comfort of a human sitting on the test rig, therefore damping should be avoided at all cost.

3.2.3 Logarithmic Frequency Response

When a logarithmic acceleration amplitude against the frequency of the seat pan was plotted, it is seen that the difference in response is more obvious in the X, Y and Z axis. The gradient of the graph is much higher in the Z axis, followed by Y and

X axis. This indicates that the person sitting on the test rig will experienced the highest discomfort in the Z axis, and the least discomfort feeling in the Y axis. However, this linear relationship between acceleration and frequency seems to be true after a frequency of 20Hz when the graphs of X and Y axis were compared. Before 20Hz, the acceleration frequency increases linearly with frequency for the X axis, but peak at Y axis with frequency of 20Hz. Above 20Hz, the acceleration amplitude in the Y axis decreases and increases linearly, but the acceleration amplitude is always lower than the X axis results.

This can indicate that the seat will experienced strongest lateral vibration response in the Y axis at frequency of 20Hz. A possible explanation of the phenomena is that around this frequency, the seat pan experiences a slight resonance in the Y axis, therefore explaining why the amplitude at the Y axis is greater. But since the gradient of graph is greater in the Z axis, therefore the person sitting on the test rig will experience vertical vibration first, then accompany by smaller, less discomfort brought upon by the Y axis response at 20 Hz. Therefore, plotting logarithmic frequency response according to the ISO 2631 guidelines is useful as it shows a better linear relationship between acceleration and frequency.

4. Conclusion

In conclusion, the analytical experiment data that was obtained has shown that the greater the frequency of the excitation source, the greater the acceleration amplitude experienced. Similarly, the acceleration amplitude is in phase with the direction of the excitation. For this experiment, the greatest acceleration amplitude occurs at frequency of 80 Hz and lowest at 5 Hz, regardless of acceleration value. However, because the experiment is only concerned with the response of the chair under vertical vibration at the moment, the greatest amplitude of acceleration is achieved at the Z-axis, with amplitude of 0.1116 m/s^{-2} and the lowest at the Y-axis of 1.41×10^{-4} m/s^{-2}. Therefore, if the experiment was repeated with the direction changed to X and Y axis respectively, it is expected that the acceleration value will be the greatest in the direction of excitation.

Acknowledgement

I want to thank my supervisor, Mohd Farid bin Aladdin, my parents, Mr. Ahmad, Mr. Alif, Ms. Habbibah, Ms. Aimi and Mr. Reynato Andal Gamboa for their guidance, patience and supervisions throughout this project. Without them, I would have not been able to complete this project in time and safely by myself.

References

[1] M.A.Bellman, “Perception of Whole-Body Vibrations: From basic experiments to effects of seat and steering-wheel vibrations on the passengers comfort inside vechicles,”Ph.D.dissertation, Dept.Phy.,Oldenburg Univ.,Oldenburg,Nl,2002.

[2] J.DeShaw, “Effect of head-neck posture on human discomfort during whole body vibration,”M.S.thesis.Dept.BME.,Iowa Univ.,Iowa City,IA,2010

[3] M.Lo and M.J.Griffin., "Effect of fore-and-aft, lateral and vertical whole body vibration on typing,"Southampton ISVR. Inst., Southampton Univ., Southampton, ENG, Tech.Rep.327, Apr.2009

[4] E.Parizet, J.Brocard and B.Piquet, " Influence of noise and vibration to comfort in diesel engine cars running at idle"., Acta Acustica with united Acustica, Hirzel Verlag,2004, 90,pp.987-983. <hal-00849428>

[5] E.Parizet, M.Amari and V.Roussarie, "Contribution of noise and vertical vibration to comfort in diesel engine cars running at idle".,EuroRegio 2010, 2010, Ljublana, Slovenia. pp.1, 2010. <hal-00993903>

[6] J.Smith, N.Mansfield and D. Gyi., " Long-term discomfort evaluation: Comparison of reported discomfort between a concept elevated driving posture and a conventional driving posture "in *6th International Conference on Applied Human Factors and Ergonomics (AHFE 2015) and the Affiliated Conferences, AHFE 2015*., Las Vegas,NV, 2015, pp.2387-2394

[7] I.Singh, S.P.Nigam and V,H Saran., "Effect of backrest inclination on sitting subjects exposed to WBV"in *3rd International Conference on Innovations in Automation and Mechatronics Engineering ICIAME 2016*., Vallabh Vidyanagar, GJ,2016, pp.76-83

[8] Y.Huang, "Human response to combined noise and vibration,"Ph.D.dissertation, Fac.Eng.Env., Southampton Univ., Southampton, ENG,2012.

[9]M. Morioka and M.J.Griffin, "Equivalent comfort contours for vertical vibration in steering wheels: Effect of vibration magnitude, grip force and hand position, "*Applied Ergonomics*", vol.no 56, no. 40, pp. 817-825, September 2007.

[10] D.Mohammad et al., "Development of A Malaysian Anthropometric Database," in *World Engineering Congress 2010, Conference on Manufacturing Technology and Management*., Kuching., SWK, 2010

[11] D.Mohammad et al., "Comfortable Drivers Car Seat Dimensions Based on Malaysian Anthropometric Data", vol.45, no.1, pp.106-113, Feb. 2016.

[12] M.F.Ashby, "Chapter 5- Material Selections- The Basic," in *Materials Selection in Mechanical Design*, 4th ed. Oxford, UK: Butterworth-Heinemann, 2010, ch.5,pp. 97-124

[13] Shrikant. B(2010). Chapter 7: Vibration Diagnosis and Control, *Mechanical Vibration Theory and Practices* (pp. 235-289). New Delhi, India: Pearson.

[14] A.Chelikani, "Simulation of a Backrest Moment Test for An Automotive Front Seat Using Non-Linear Contact Finite Element Analysis," M.S.thesis, Dept. Mech.Eng., Clemson.Univ., Clemson.,S.C, 2007.

eureca 2016 – Conference Paper
Paper Number 2ME32

To Investigate the Natural Ventilation of a House Using Solar Chimney via CFD

Yap Lih Ter[1], Lim Chin Hong[*]
[1]School of Engineering, Taylors University, Malaysia

[*]ChinHong.Lim@taylors.edu.my

Abstract
This research presents study and design of solar thermal chimney system under tropical weather. CFD (Computational Fluid Dynamics) software Fluent is utilized to generate the flow in the system. The simulation run is based on the architectural part of solar chimney which includes various chimney length, cavity width, and inclination angle. In this report, real sized room of width 4m and height 4m is drawn in 2 dimensional for simulation. The chimney is heated with 500K while the inlet and outlet are set to be atmospheric pressure. Ventilation flow rate effects and pattern are obtained from the proposed parameters. Cavity width of 0.4meter with inclination angle of 15° 30° 45, 60° is simulated. This is repeated with different cavity width of 0.6m and 0.8m and 1m. Based on the simulation result, highest mass flow rate obtained from the experiment will then be experimented with different stack height of 1m, 3m. Results of mass flow rate could be obtained through the simulation of the proposed parameters. Three criteria will be discussed and simulated whereby 2 criteria will be fixed as constant and one criterion will be manipulated. As for the first simulation whereby various cavity width such as 0.4m, 0.6m 0.8m and 1m will be simulated with the constant value of inclination angle 30° and chimney length of 2m. It shows that cavity width of 0.8 m will generate the highest mass flow rate which is 0.472kg/s will be the determinant value for the cavity width for the next simulation. Second simulation whereby various inclination angle such as 15° 30° 45, 60° will be simulated with the constant value of cavity width of 0.8m and chimney length of 2m. It shows that inclination angle of 30° will generate the highest mass flow rate which is 0.472kg/s. Based on the highest mass flow rate obtained from cavity width of 0.8m and inclination angle of 30°, this value will be set constant for the simulation of variation chimney length of 1m and 3m. Based on the simulation result, the highest mass flow rate obtained are 0.983kg/s for chimney length 3m.

Keywords: CFD, passive cooling, natural ventilation, solar chimney.

1. Introduction

In tropical weather, usage of energy from mechanical devices such as fan and air-conditioning are unavoidable to maintain comfort. Energy obtained primarily from fossil fuels such as coal, oil and natural gas are estimated to face depletion in the coming 50 years due to the rapid growth of population of nearly 9 billion people. Hence, shortage of energy is to be foreseen due to high energy demand from the increase of populations. Due to environmental effects that are associated with the usage of fossil fuels and depletion of fossil fuels, renewable energy such as sun and wind energy are widely studied.

Global warming has been one of the major issues arising from the usage of air-conditioning which emits gases that contributes to the greenhouse effect. In a house, HVAC which stands off heating, ventilation and air conditioning are the main energy consumption. Hence, solar heating and cooling tools which utilize sun energy which is renewable has attracted many studying as sun energy is free. In a typical building, it takes up to approximately 35.3% of energy usage for maintaining the comfort during summer or heating during winter. [1] Cooling and heating of a building are the main component of energy consumption and hence, controlling the temperature and humidity are unavoidable to maintain the comfort and interior air quality. This can be seen based on the air conditioning usage during summer in United Kingdom and Shanghai it shows a staggering value of 50% and 40% energy usage. [2] Besides that, radiation of sun plays an important role in both cooling and heating system. This can explained as for heating, sun ray collected would be stored and used to maintain the heat in the building likewise for cooling system, it will create natural ventilation due to temperature difference whereby hot air will exit through the chimney and causes cold air to be drawn inside.

1.1 Basic Principle of Solar Chimney

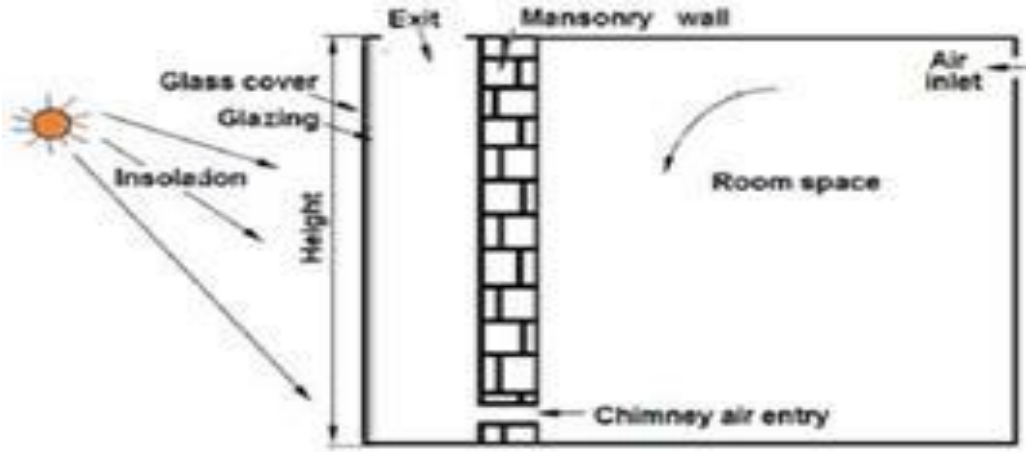


Figure 1: Solar Chimney Operation [4]

Solar chimney basically used for cooling by the means of ventilation. Solar chimney operates using air movement by conversion of thermal energy into kinetic energy. This will create buoyancy effect as the inlet and outlet will have a change in

air density which would be the driving force whereby hot air will exit from the chimney and cold air being drawn inside which could be seen in figure 1. In addition, solar chimney could also be utilized for heating as fan will be stored at the top to blow the hot air generated into the house. There are numerous factors that should be taken into account for the designing of solar chimney which includes solar intensity, stack height, width and depth of cavity, materials, inclination angle and others. For this paper, external factors such as materials and intensity of sun are set as constant.

The research question and objective of this research are as follow:

- How does length of chimney, inclination angle of solar chimney and solar chimney cavity depth influence the solar chimney natural ventilation
- Propose solar thermal chimney design that has best ventilation rate in terms of highest mass flow rate. This is due to mass flow rate indicates the air being drawn out from the chimney.

2. Methodology

In this research, steps are that taken to complete the simulation comprises of geometry description, simulation method, assumption and boundary and lastly results.

2.1 Geometry Description

This section presents the geometry of the model of real room sized of width 4 meter and height 4m drawn in 2 dimensional as shown in figure 2 below. This is based on the literature review. At the lower portion of room there is a gap for the entering of air. This air is then heated in the chimney due to the heating of chimney which was set constant to be 500 Kelvin. This causes the air to have a density difference and hence hot air rises out through the chimney and cold air being drawn from the gap at the lower portion of the room.

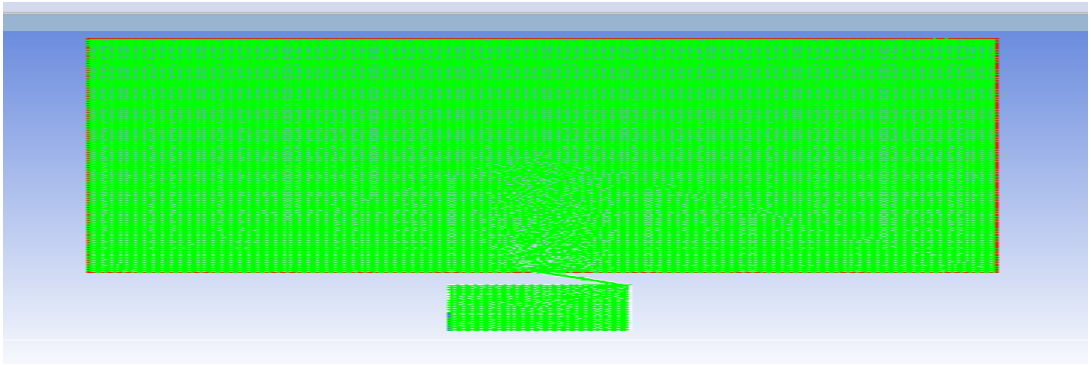


Figure 2: 2-dimensional room drawing

2.2 Simulation Method

CFD tools which is Ansys (Fluent) software was utilized for numerical simulations. Ansys Fluent solver engine is utilized for the calculation of fluid flow and thermal and deliver fast and robust calculation. Ventilation flow rate has been

studied for the following parameters of solar chimney to obtain the mass flow rate from the inlet which is the lower portion of the room.

- Solar chimney with cavity width of 0.4 m, 0.6m, 0.8m, and 1m with constant inclination angle of 30° and chimney length of 2m
- Solar chimney with inclination angle of 15°, 45°, 60° with constant cavity width of 0.8m and chimney length of 2m
- Solar chimney with chimney length of 1m, 2m, and 3m with constant inclination angle of 30° and chimney cavity width of 0.8m

2.3 Assumptions and Boundary

Assumptions that are made to run the simulation includes:

a) Steady state condition for the system,
b) The working air behave as ideal gas,
c) Frictionless and no leakage from the solar chimney inlet and outlet.

Boundary conditions that are made to run the simulation includes:

a) Ideal gas (Density of gas changes with temperature)
b) Pressure at the inlet (1atm) and 300 K
c) Pressure at the outlet (1atm) and 300 K
d) Heating of Chimney with a constant value of 500 K

3. Results and Discussion

3.1 Manipulation of cavity width

To determine the ventilation of solar chimney, one of the most important factors is cavity width. This is due to cavity width influences natural ventilation efficiency via movement of air and turbulence inside the room and solar chimney. In this study, mass flow rate from the inlet of the room is the vital parameter that defines ventilation capability. This is because mass flow rate indicates air being drawn in and sucked out from the room via chimney. In this experiment, cavity width is manipulated with the incorporation of constant chimney length of 2m and inclination angle of 30°. The parameters stated to be constant which is chimney length of 2m and inclination angle 30° is just a starting point whereby it will be altered in the next cases simulations. The result obtained from the simulation via CFD Fluent which is mass flow rate of each experiment is shown below in figure 1.

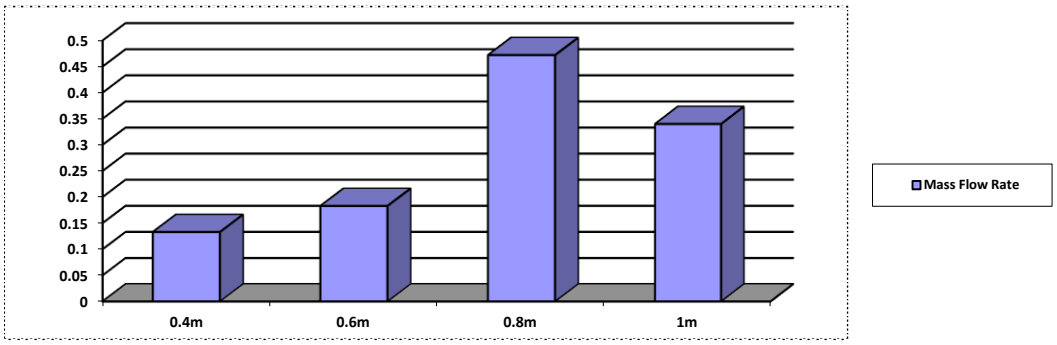


Figure 3: Mass flow rate of different cavity width

Based on the graph shown above, it can be seen that the higher cavity width will have a higher mass flow rate. Cavity width of 0.4m will yield a mass flow rate of 0.133kg/s whereby cavity width of 0.6m will yield a mass flow rate of 0.183kg/s and 0.8m will yield a mass flow rate of 0.472kg/s and lastly 1m will yield a mass flow rate of 0.339kg/s. This shows that increasing cavity width will increase in the mass flow rate. These mass flow rates are obtained through the inlet of the room via simulation. As it can be seen cavity width of 0.8 m will yield the highest mass flow rate due to the low pressure lost whereby 0.4m will yield the lowest mass flow rate due to high pressure lost. As the outlet is based on pressure configuration, Pressure lost is the difference in pressure between 2 points which is the inlet and chimney width. Low pressure lost will enhance ventilation rate due to pressure difference is the main contribution for stronger driven force to the stack effect ventilation. As the inlet and outlet are pressure configuration of 1 atm, low pressure lost indicates a higher pressure difference between the inlet and outlet whereby higher pressure lost indicates a lower pressure difference. This can be seen on the mass flow rates that are obtained and it signifies the validity of the mass flow rate obtained. However, at 1m cavity width the mass flow rate can be seen dropping due higher area of recirculation of air based on the velocity vector as compared to 0.8m cavity width. The large cavity width has the tendency to recirculate air more and hence reducing in the mass flow rate. Recirculation of air will minimize the air from being drawn out from the chimney. Hence, the optimum cavity width that can be concluded from these simulations is 0.8m based on the proposed parameters.

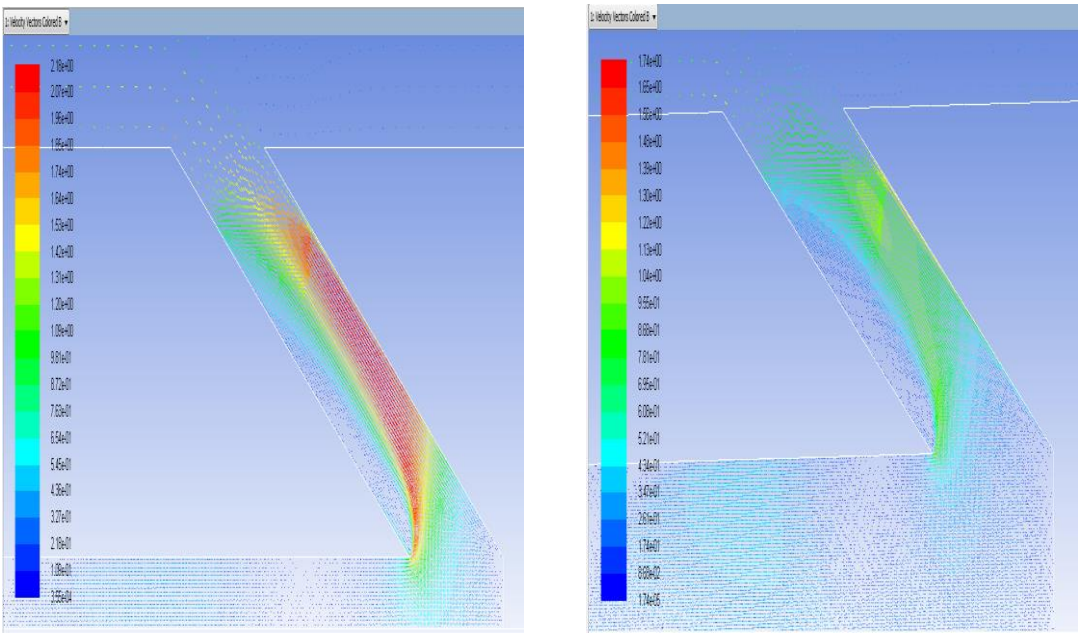


Figure 4: Comparison of velocity vector of cavity width of 0.8m and 1m

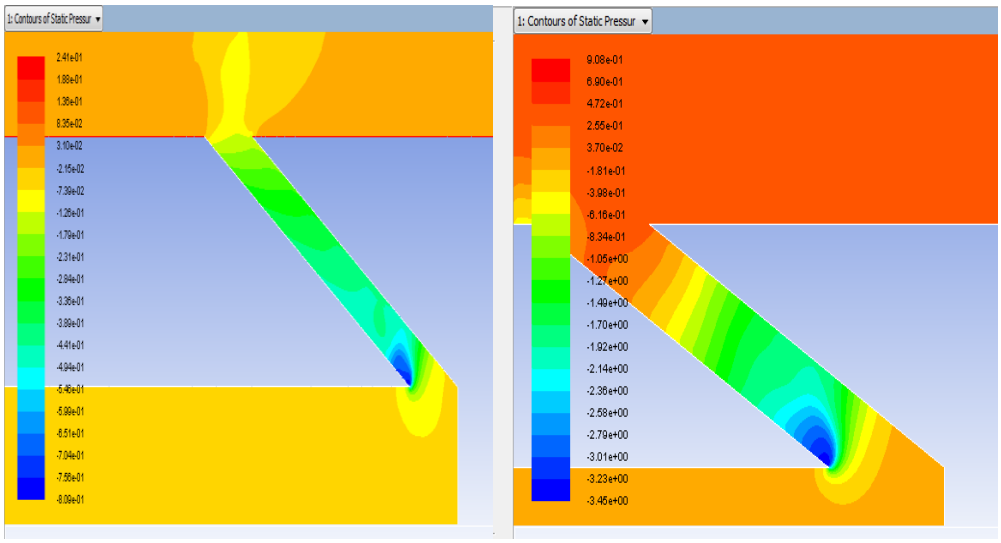


Figure 5: Comparison of pressure contour of cavity width of 0.4m and 0.8m.

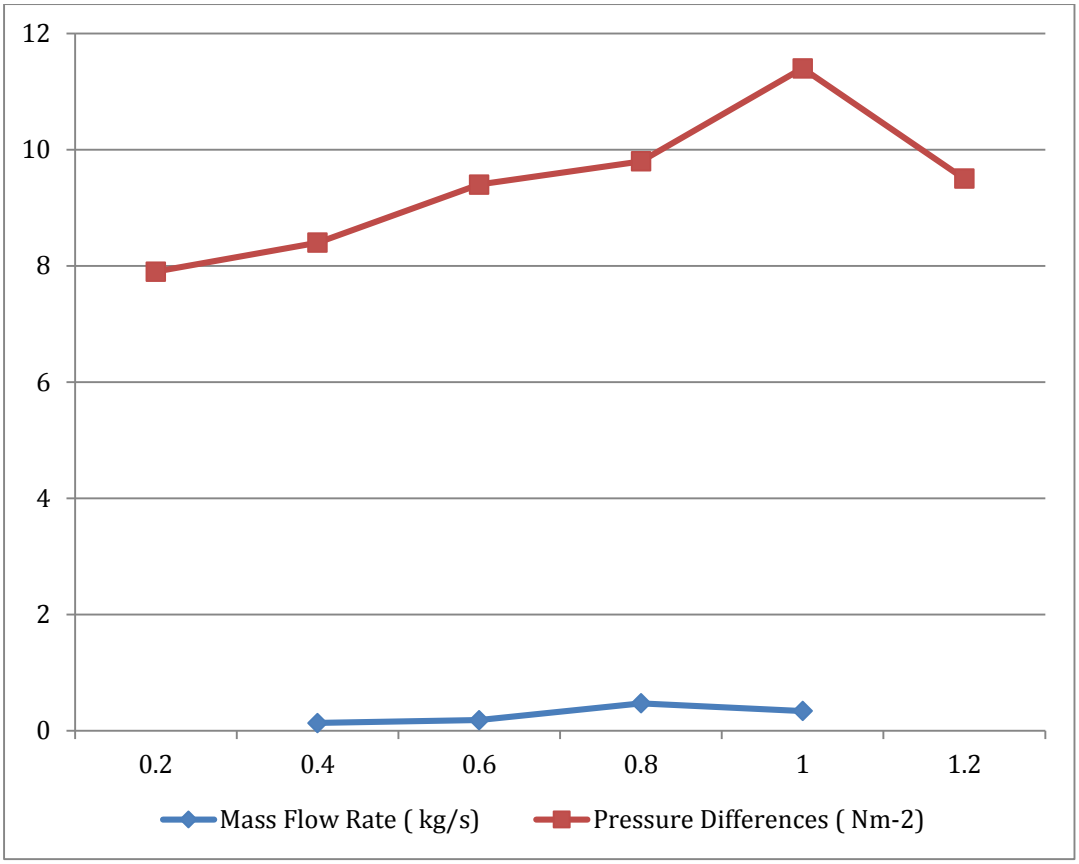


Figure 6: Comparison of mass flow rate and pressure differences

Based on the literature review the only result that was presented are in the term of pressure differences. The result from the literature review cannot be compared directly to the result from the simulation due to different criteria. However, mass flow rate and pressure differences determine the ventilation rate that happens in the chimney. Hence although the value cannot be compared theoretically, the trend of the line graph can be compared. As can be seen from the figure above, the mass flow rate and pressure difference have the same pattern whereby it increases to a certain point and then diverges back. Hence, it can be said that it validates the literature review result.

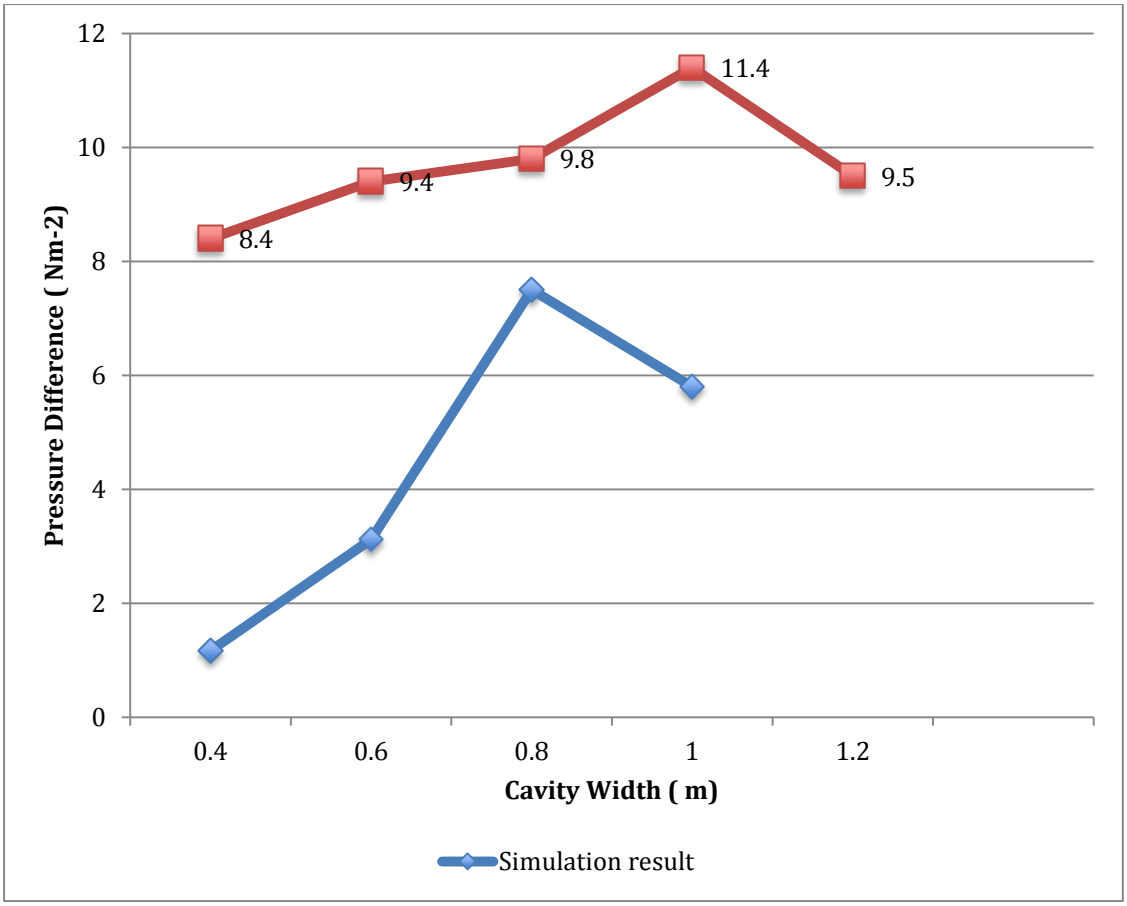


Figure 7: Comparison of pressure differences between simulated result and literature review

Based on the figure above, the pressure difference of the simulation result and the literature review shows a different reading. The higher line graph shows a higher value as compared to the simulated value. This is due to the different parameters that are used for the simulation as compared to the literature review. For instance, the sizes of the geometry, values that are used are not well defined in the literature review. This will affect the results that are simulated. However, it can be seen that the trend of the pressure difference graph is the same whereby the trend of the line graph is the same whereby it increases with the increase of the cavity width and diverges once the optimum cavity width is exceeded.

3.2 Manipulation of Inclination angle

In this area of study, inclination angle is manipulated with the incorporation of constant chimney cavity width of 0.8m and stack height of 2m. Cavity width of 0.8m is selected due to simulations that have been done earlier whereby it gives the highest mass flow rate. Hence, with the 2 parameters that are set constant, simulations are done on angle of 15°, 45° and 60°. Angle of inclination is mainly dependent on the solar irradiance whereby which angle will capture the most sun energy to gives highest thermal energy so that more air will be sucked out from the chimney. Mass flow rate of each angle is then tabulated in the figure 5 shown below.

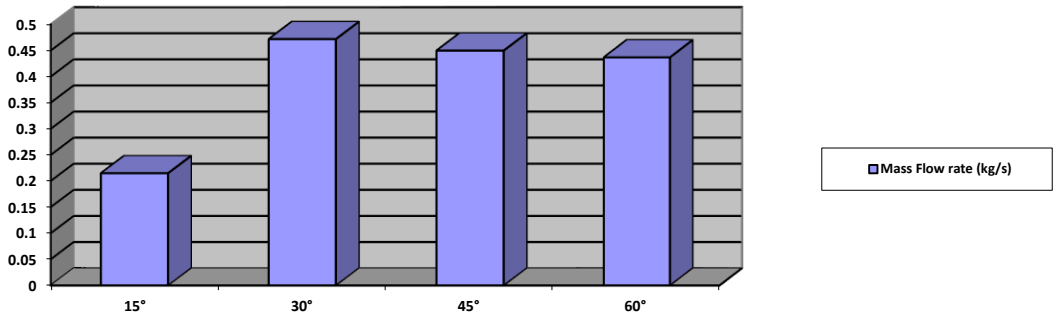


Figure 8: Mass flow rate of different Inclination Angle

As can be seen from the figure above, angle of 15° will yield the lowest mass flow rate which is 0.215kg/s, follow by angle of 30° yield the highest mass flow rate which is 0.472kg/s, follow by angle of 45° yield mass flow rate which is 0.450kg/s and lastly angle of 30° yield the mass flow rate which is 0.437kg/s. This result does not coincide with literature review whereby highest mass flow rate obtained should be at the angle of 45° as at this angle highest solar radiance will be captured. Besides that, the simulation steps that are done by literature review is that they alter the sun intensity which is sun irradiance whereas as for the simulations that are done by the students the chimney is heated and set to be a constant 500K for all angle. When the angle is too small for instance 15°, pressure lost is high due to bending which causes the low mass flow rate. This can also be indicated by sudden flow contraction at the chimney base due to high flow resistance which causes high pressure lost. As the angle is inclined at 30°, the flow inside the chimney will have lesser restriction whereby pressure lost will be low and hence a higher mass flow rate. Based on the pressure contour of 15°, it can be seen that the highest outlet chimney pressure are in the range of 0.518 pa whereas the pressure contour of 30°, it can be seen that the highest outlet pressure of chimney are in the range of 0.690 pa. This shows that the pressure outlet of inclination angle of 30° as compared to the pressure of the outlet of inclination angle of 15° is higher whereby lower pressure is lost inside the chimney.

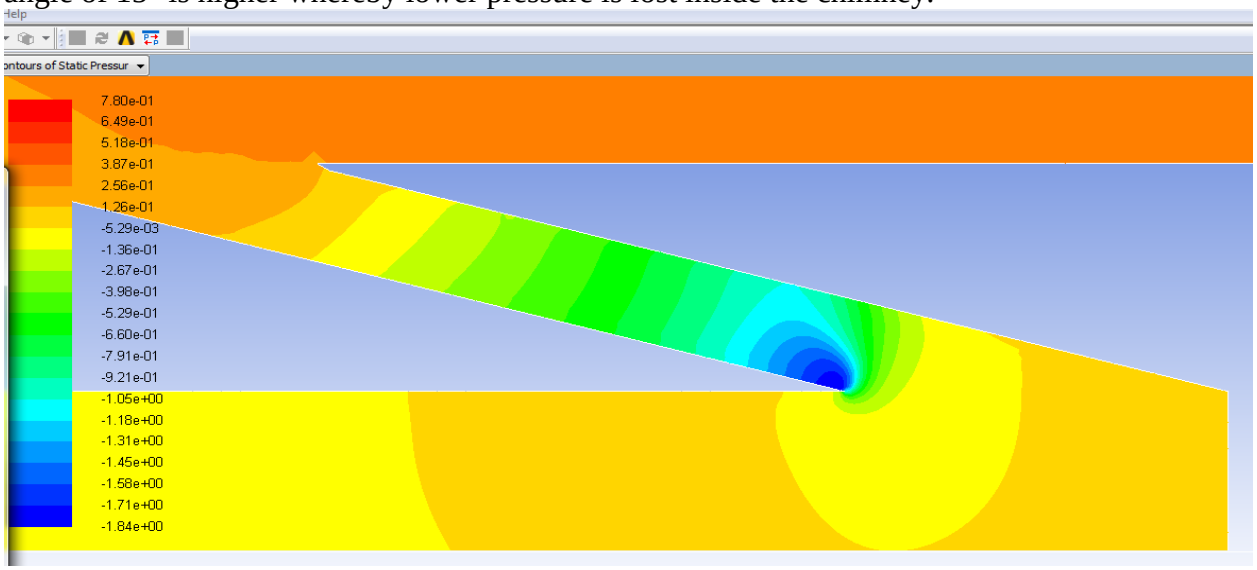


Figure 9: Pressure contour of inclination angle of 15°

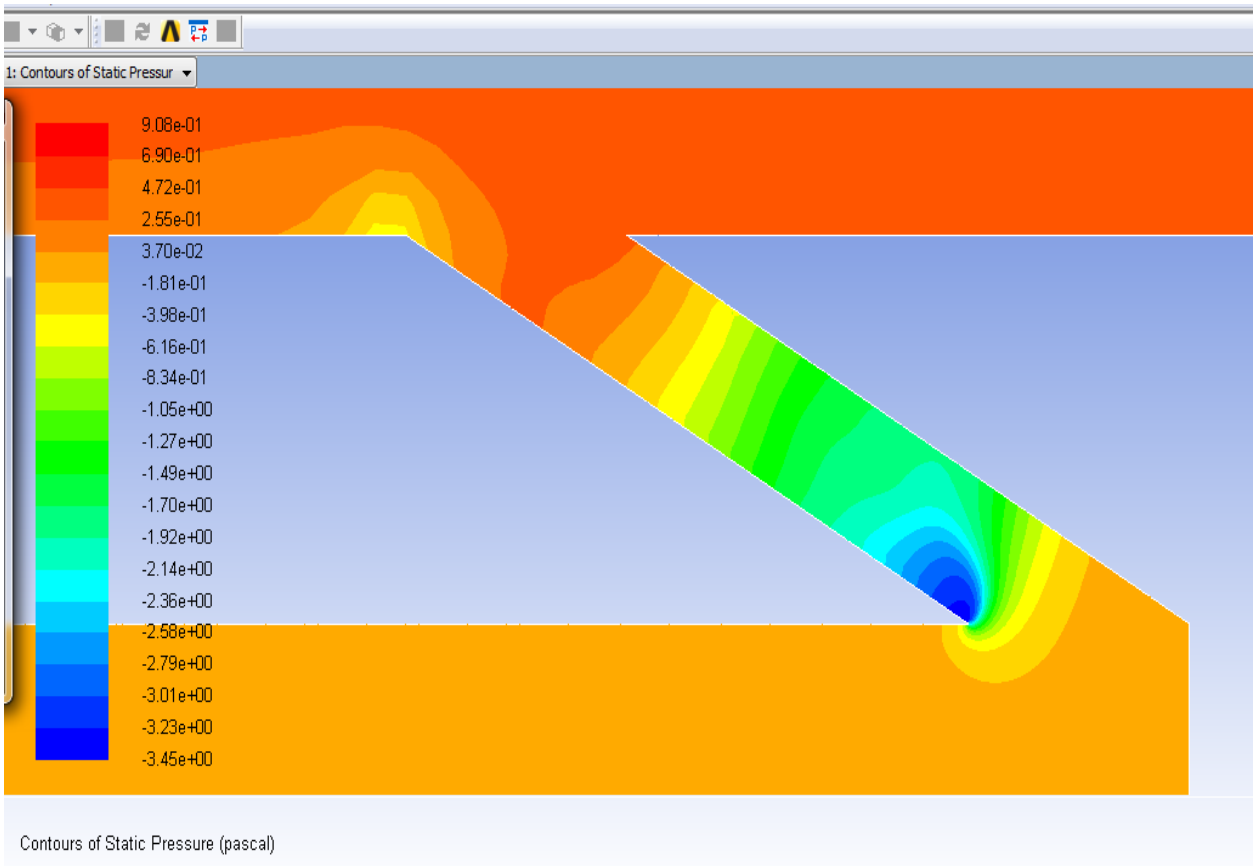


Figure 10: Pressure contour of inclination angle of 30°

3.3 Manipulation of Chimney Length

In this area of study, stack length is manipulated with the incorporation of constant chimney cavity width of 0.8m and angle of 30°. Parameters such as cavity width of 0.8m and angle of inclination of 30° is selected due to simulations that have been done earlier whereby it gives the highest mass flow rate. Hence, with the 2 parameters that are set constant, simulations are done on stack length of 1m and 3m.

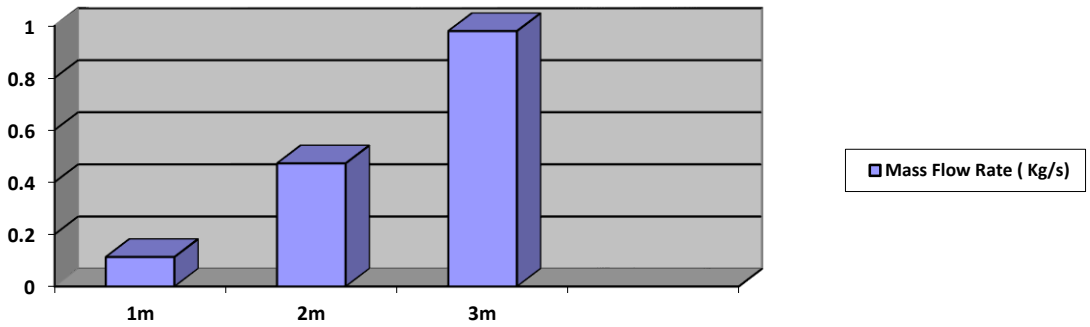


Figure 11: Mass flow rate with different chimney length

Based on the figure shown above, it can be seen that higher chimney length will have a higher mass flow rate. This can be seen as chimney length of 1m will yield mass flow rate of 0.113kg/s, follow by stack length of 2m will yield mass flow rate of

0.472kg/s and lastly stack length of 3 m will yield mass flow rate of 0.987kg/s This can be explained due to higher chimney length will have a higher surface area whereby more sun ray will be absorbed and hence higher temperature difference between the outlet and the inlet of the chimney. It can be said that higher stack length will accounts in the higher mass flow rate due to higher stack effect. However there are a drawback of higher stack length whereby it will incur a higher cost for the construction and material of the stack length.

4. Conclusion

In conclusion, many factors contributes to the rate of natural ventilation that happens in solar chimney. It includes wind velocity, sun intensity, inlet, cavity width, inclination angle, and chimney length. As for this project only the architechtural features are taken into account of the natural ventilation while setting the other external factors such as wind velocity and sun intensity to be constant. Based on the numerical simulation and results, it can be said that increasing the cavity width will increase the mass flow rate. The mass flow rate increases with increase of cavity width until it reaches an optimum value of 0.8m and decreases back. This is due to backflow of air occurs when the cavity width exceeded the optimum cavity with which makes the mass flow rate to decrease. As for inclination angle, the angle obtained to have the highest mass flow eate in this report is 30° as opposed by the literature review of inclination angle of 45°. This is whereby sun intensity is set constant whereby chimney is heated into a 500K instead of using a different sun intensity as opposed by the literature review. At this angle of 45°, it is said to have captured the most sun intensity which is sun irradiance. Lastly, an increase in chimney height will increase the mass flow rate due to higher surface area whereby more sun ray will be absorbed and hence higher temperature difference between the outlet and the inlet of the chimney. However, higher chimney height will incur in a higher cost. To summarize, based on the simulations that have been, for this cases whereby velocity inlet of 0.4m/s and chimney of 500K in a 4m width and 4m height 2 dimensional room. The cavity width of 0.8m, inclination angle of 30° and chimney height of 3m will have the highest mass flow rate of 0.988kg/s

Acknowledgment

I would like to take this opportunity to express my gratitude and thanks to Dr. Lim Chin Hong for the supervision and patient guidance throughout the whole research.

References

[1] Kalkan, N., Dagtekin. I. (2015) CFD Analysis of Passive Cooling Building Using Solar Chimney System. *World Academy of Science, Engineering and Technology*, Vol:9, No:10

[2] Ahmad, S., Badshah, S., & Chochun, G. (2014) Modelling and Simulation of Natural Ventilation of Building Using Solar Chimney. *World Applied Science*. 32, 741-746

[3] Nugroho, A. M. (2007). *Solar chimney geometry for stack ventilation in Malaysia terrace house.* Doctoral Degree. Universiti Teknologi Malaysia

[4] P.O.Fanger(1970). *Thermal comfort: Analysis and applications in Environmental Engineering* New York, McGraw-Hill Book Company

[5] Chen, Z. D., Bandopadhayay, P., Halldorsson, J., Byrjalsen, C., Heiselberg, P. & LI, Y. (2013). An experiment investigation of a solar chimney model with uniform wall heat flux. *Building and Environment*, 38, 893-906

[6] Sadafi, N., Salleh, E., Haw, L. C. & Jaafar, Z. (2011). Evaluating thermal effects of internal courtyard computational simulation. *Energy and Buildings*, 43, 887-893.

[7] Zhai, X. Q., Dai, Y. J. & Wang, R. Z. (2005). Experimental investigation on air heating and natural ventilation of solar air collector. *Energy and Buildings*, 37,373-381

[8] Hassanein, S. A., & Abdel-Fadeel, W. A., (2012) Improvement Of Natural Ventilation In Building Using Multi Solar Chimney At Different Directions. *Engineering Sciences* Vol.40 No 6 pp. 1661-1667

[9] Chungloo. S., Limmeechokchai. B., (2006) A Numerical Study of Natural Ventilation in Buildings Utilized Solar Chimney and Cool Ceiling. *Sustainable Energy and Environment*

eureca 2016 – Conference Paper
Paper Number 2ME33

The Development of a Semi-Empirical Model for Forced-Convection Condensation Heat-Transfer on Integral-Fin Tubes

Hoe-Yen, Yim[1], Namasivayam Satesh[*]

[1]*School of Engineering, Taylor's University, Malaysia*

[*]*SateshNarayana.Namasivayam@taylors.edu.my*

Abstract

This paper presents the development of a semi-empirical heat-transfer model for forced-convective condensation on an integral-fin tube that provides predictions applicable to practical ranges of vapour velocities, tube geometries and fluid properties. Development includes the incorporation of a new semi-empirical model to predict flooding angle, new constants, and a proposed modification to the heat-transfer model. The empirical constants in the heat-transfer expression is found by determining the closest correlation between the heat-transfer predictions by the model with a wide range of experimental data using the method of least squares. To determine empirical constants, computer-aided statistical analysis is employed to correlate model predictions with more than 800 experimental data points obtained using various tube geometries and fluid properties over a practical range of vapour velocity. The model, with the new constants, prior to and after modification, provides a correlation with experimental data with a standard deviation 16.06%.

Keywords*: Forced-convection condensation, vapour velocity, fin-tube, heat-transfer, semi-empirical model*

1. Introduction

Condensation on horizontal integral-fin tubes has been researched upon extensively to improve the efficiency of industrial steam condensers.

Numerous investigations have been done towards heat-transfer of laminar, filmwise condensation of pure vapours on solid surfaces. These solid surfaces include tubes and plates oriented in various positions, and may be enhanced, typically by modifying its geometry to provide additional surface area, to improve vapour-side heat-transfer. Heat-transfer coefficients for plates and tubes oriented horizontally or vertically can be predicted accurately for free-convection condensation with various empirical and theoretical models. Integral-fin tubes are a widely used in condensers as it is established to improve vapour-side heat-transfer [1].

Given the common usage of integral-fin tubes, a huge amount of theoretical and experimental work has been done to study quiescent vapour condensation on integral-fin tubes. Between the fins at the bottom of the tube, flooding (condensate retention) forms a barrier to heat-transfer, reducing the surface area available for heat transfer. Above the flooding, the condensate film is thinned by surface tension, thus enhancing the local heat-transfer. Theoretical models have been developed by Honda et al. [2] and Briggs & Rose [3] to predict vapour side heat-transfer for condensation on fin tubes. These two theoretical models took into account the effects of surface tension and gravity, providing excellent agreement to experimental data.

However, the velocity of steam entering the condenser is typically high in power plants. At sufficiently high velocity, vapour shear has proven to enhance heat-transfer [4]. Experimental investigations suggests that vapour shear during condensation on integral-fin tubes enhances condensation heat-transfer[4], [5]. Both free-convection and forced-convection condensation investigations are included. Noteworthy, experimental investigations prior to 1983 use different methods to obtain the vapour-side heat-transfer coefficient, arbitrary choices of tube geometry and inaccurate measurements in coolant temperature rise, thus difficult to draw accurate conclusions. In terms of obtaining experimental heat-transfer coefficient, Briggs [6] detailed an analysis on the methods used to evaluate vapour-side heat-transfer coefficient, including the method of Wilson [7], the "modified" Wilson plot, the coolant-side subtraction method and the direct tube wall temperature measurement. More recently, Fernandez-Seara et al. [8] presented a review of the Wilson plot method and its modifications to determine convection coefficients in heat exchange devices.

However, due to the complexity of the heat-transfer process in forced-convection condensation, mathematical models developed have yet able to produce appropriate predictions on the effects of vapour velocity during condensation on integral-fin tubes. A semi-empirical mathematical model will aid engineers in the development of condensers.

The gap lies in a model that combines the effects of vapour velocity together with other parameters affecting heat-transfer during forced-convection condensation. Cavallini et al. [9] developed a model that includes effects of vapour velocity, surface tension and gravity. However, Cavallini's model only agrees with experimental data of refrigerants as test fluid, as found by Namasivayam & Briggs [10].

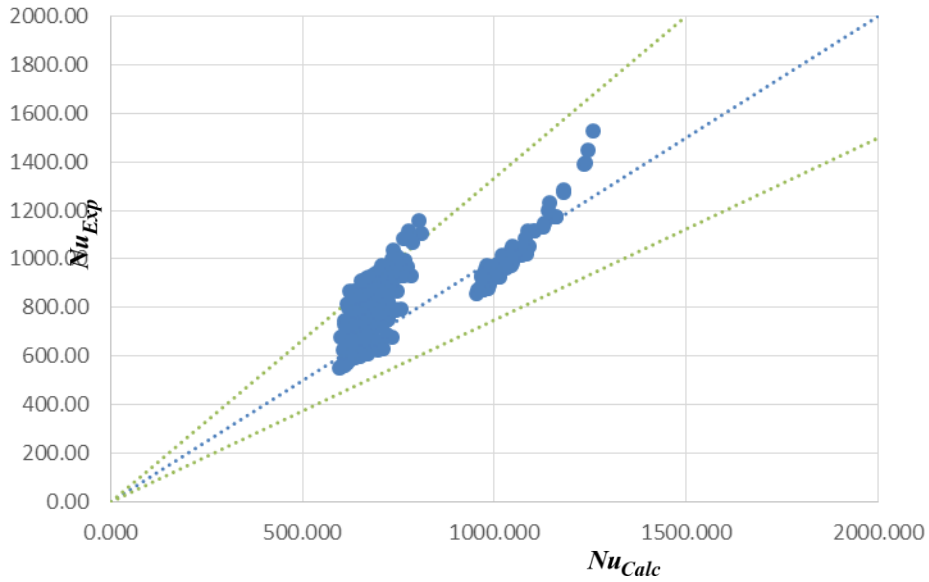
Namasivayam & Briggs [11] developed an empirical model for pure forced-convection condensation, neglecting gravity and surface tension, producing a correlation with a margin of 21%. The model, which covers forced-convection on fin tubes covering practical ranges vapour velocities, tube geometries and fluid properties, has to be further developed.
Also presented in this paper is an analysis of the semi-empirical model developed by Ali & Ali [12] to predict condensate retention for forced-convective condensation. The predictions of the model is compared to the experimental data given by Namasivayam & Briggs [4], [5], [13], [14].
Present work is aimed at increasing the accuracy and preciseness of the semi-empirical model provided by Namasivayam & Briggs [11] for forced-convection condensation heat-transfer on integral-fin tubes by,

1. Analyzing and incorporating the newly developed semi-empirical model for condensate retention to improve the prediction of heat-transfer.
2. Improving the empirical constants within the heat-transfer model for forced-convection condensation through computer-aided statistical analysis.
3. Modifying the expression within the heat-transfer model for forced-convection condensation.

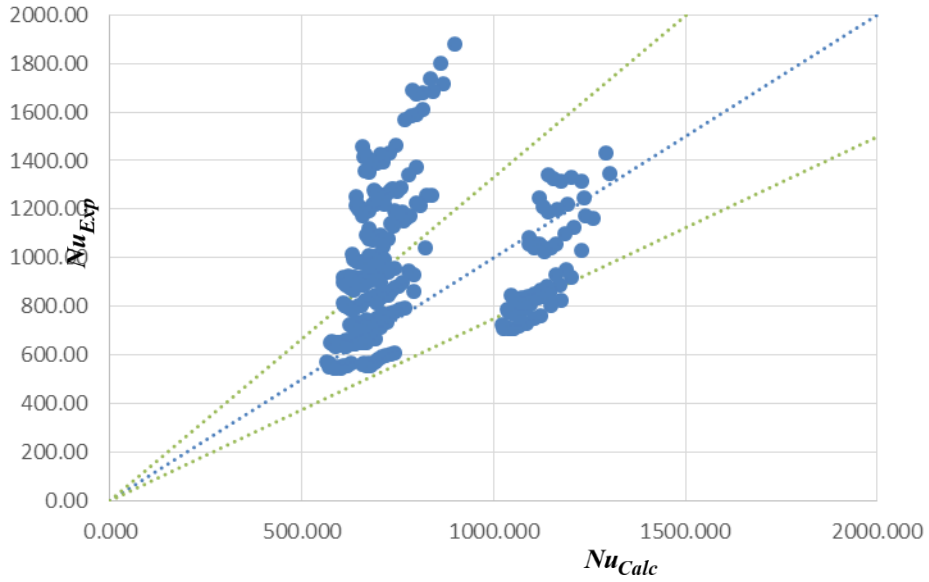
2. Theoretical Framework and Methodology

2.1 Condensation at High Vapour Velocities

This paper presents the semi-empirical model for forced-convection condensation heat-transfer on integral-fin tubes developed by Namasivayam & Briggs [11]. The model incorporates the forced-convective model developed by Shekriladze & Gomelauri [15] for horizontal tubes and vertical flat plats by deriving suitable expressions for each part of the integral-fin tube, i.e. fin-tip, fin-flank and fin-root. The model was developed with the intention of predicting heat-transfer purely for forced-convective condensation, thus the effects of surface tension is not fully considered in this model [11]. The surface tension effects that cause flooding between the fins and the effects of condensate thinning due to gravity is neglected, therefore the model is only applicable to condensation at high vapour velocities, in which the effects of vapour shear overpowers that of surface tension. This gives an opening for future work, since the incorporation of these effects extends the applicability of the model to lower vapour velocities.
Prior to present work, it is meaningful to compare the model of Rose [16] for free-convective condensation and the model of Namasivayam & Briggs [11] for forced-convective condensation. Figure 1a and 1b compares the prediction of the model of Rose [16] to the experimental data given by Namasivayam & Briggs [4], [5], [13], [14]. Unsurprisingly, the model underestimates most of the data points due to the negligence of the heat-transfer enhancement caused by vapour shear. For the model provided by Namasivayam & Briggs [11], 2 sets of pre-existing empirical constants presented in the author's thesis and published conference paper. Figure 2a, 2b, 3a and 3b compares the prediction using the model of Namasivayam & Briggs [11] to the same set of data.

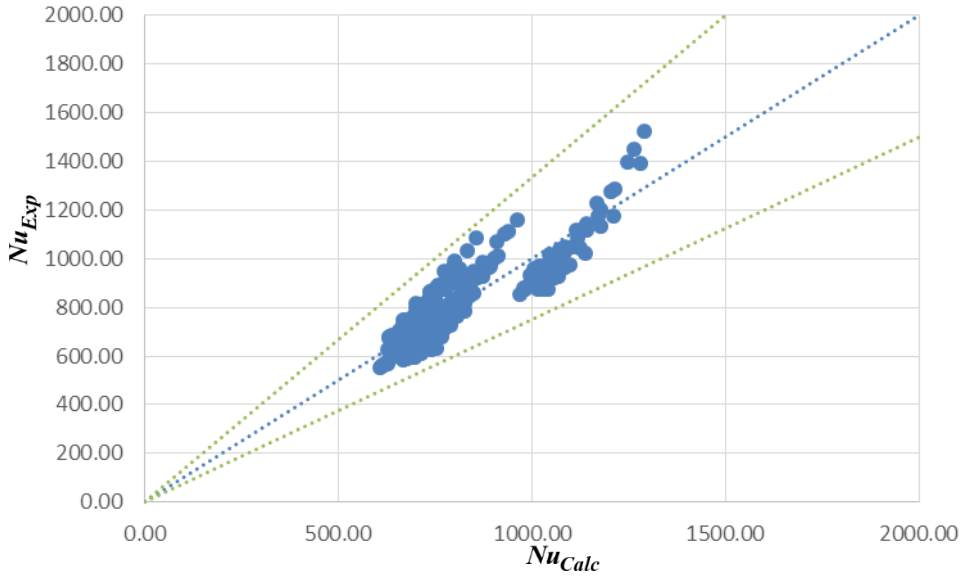


a. Steam at Atmospheric Pressure

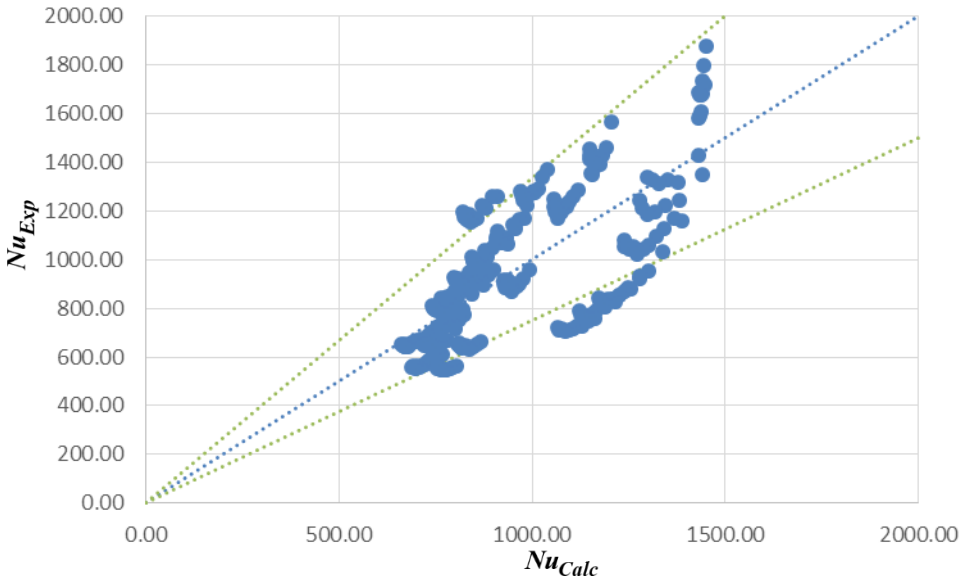


b. Steam at low pressure (14kPa)

Figure 1: Comparison of the model of Rose [16] with Experimental Data [4], [5], [13], [14]

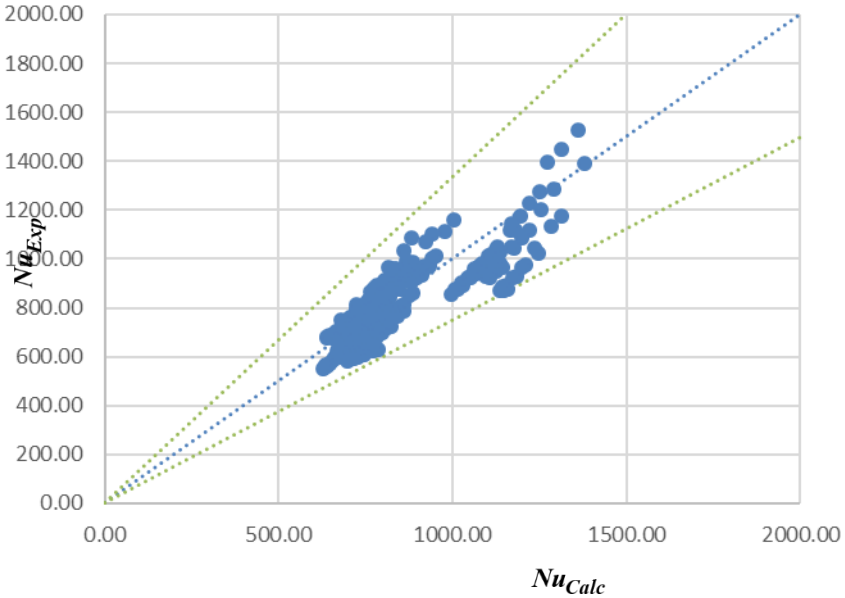


a. Steam at Atmospheric Pressure

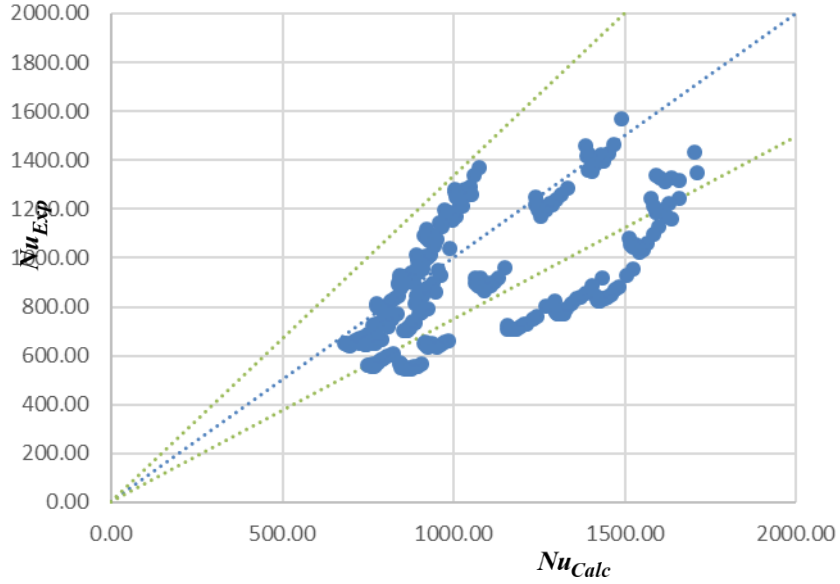


b. Steam at Low Pressure (14kPa)

Figure 2: Comparison of the model of Namasivayam & Briggs [11] with Experimental Data [4], [5], [13], [14], using constants C_1, C_2 and C3 of 1, 0.41 and 0.41 respectively



a. Steam at Atmospheric Pressure



b. Steam at Low Pressure (14kPa)

Figure 3: Comparison of the model of Namasivayam & Briggs [11] with Experimental Data [4], [5], [13], [14], using constants C_1, C_2 and C3 of 2.6, 0.7 and 1 respectively

2.2 Optimization Methodology

One of the main challenges in determining empirical constants lies in the obscurity of the effects of each constant within expressions given by various authors – there are simply too many combinations possible. It is also difficult to determine effective ranges of empirical constants. In order to overcome the challenge, a programme is written using Visual Basic for Applications to test each of the constants of each expression by brute force (see Figure 4 for programme flowchart).

Each constant of each expression is tested using a wide range of numbers that are generated randomly by the computer. The randomness of each set of constants being input in the expression is crucial to ensure the accurate incorporation of error within the regression model. Multiple iterations of the same programme process is done with 'tightened' ranges for each constant in order to improve the accuracy of the final set of constants for the given expression.

Two different methods can be used to determine the final set of constants. Not seen in the flowchart, the user of the programme can technically sort the data and find the constants that produce the best correlation (by finding the lowest sum of least squares). However, this method is not repeatable for larger sets of data and may require an increased number of iterations. The second method is to run a regression analysis on the data generated, in this case using the Data Analysis function within Excel.

From the output of the regression data, the user can determine several information crucial to improving the model. Using the F-test, the 'fit-to-data' for each coefficient can be determined. Failure of the F-test may suggest that a certain constant within a model does not affect the prediction of the model significantly. Another important information would be the coefficients generated by the regression model, which may determine, (i) the relationship between constants (ii) the significance of the constants in the prediction.

Limitations of this method would be the linearity of the regression function within the Data Analysis function of Excel. Through observation of the graphs produced, a non-linear relationship is found between constants and predictions. This is overcome by running the regression multiple times to determine a best fitting regression. The ranges of constants are also tweaked to improve the data output, and is done by (i) determining ranges of constants within good fitting data and (ii) rough estimation through the observation of the graphs.

A total of 1.2 million sets of constants were tested for the 2 models tested in this study.

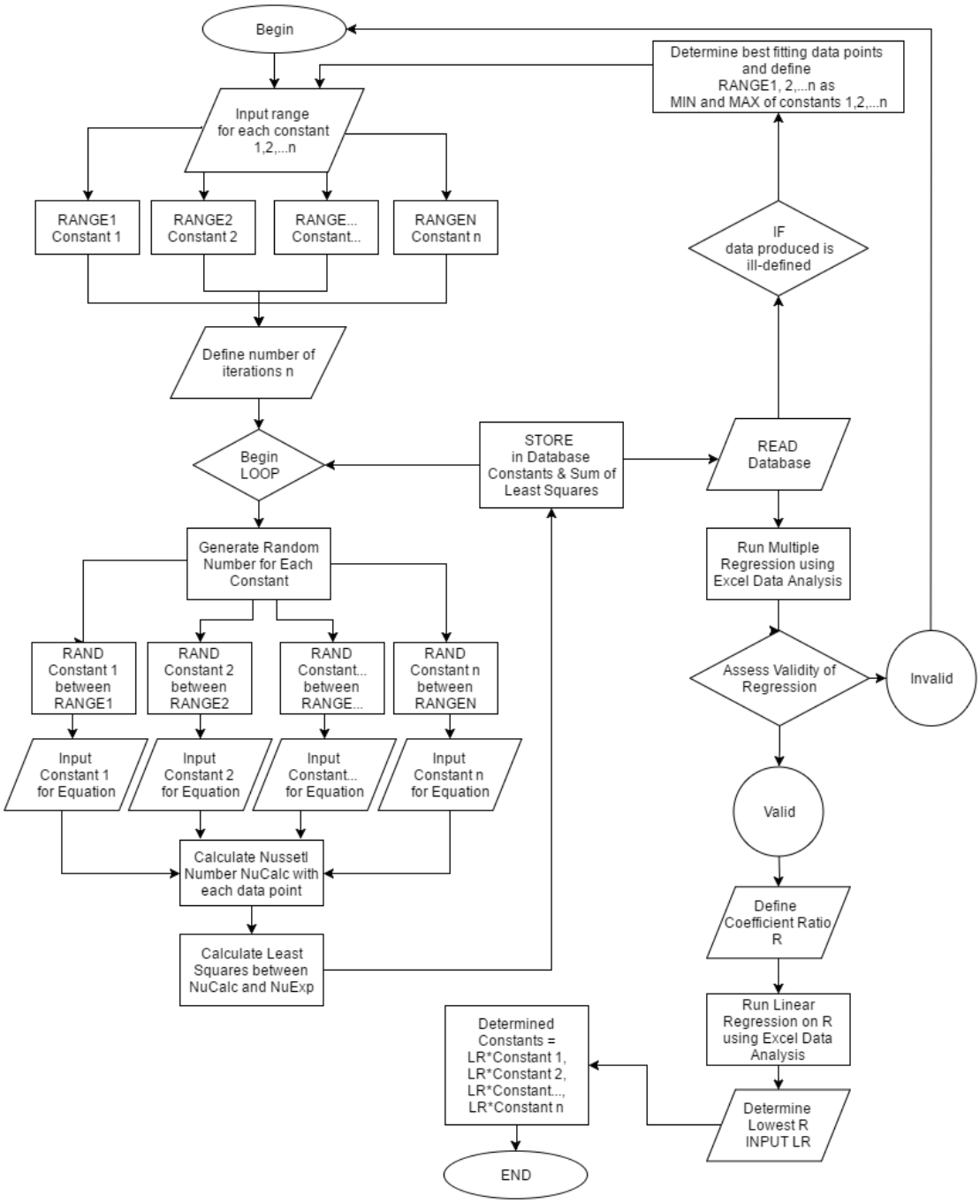


Figure 4: Visual Basic Application Programme Flowchart

3. Results and Discussion

3.2 Condensate Retention Prediction

1) 3.2.1 Condensate Retention for Quiescent Vapour Condensation

Capillary action forces vapour condensate to collect at interfin spaces, causing the condensate film to be thicker than that of the fin tips and fin flanks, thus increasing heat-transfer resistance at the interfin spaces. Surface tension also causes 'condensate retention' or 'condensate flooding'. To characterize condensate flooding, the flooding angle (flooding angle, ϕ_f, is the angle where condensate flooding occurs measured from the top of the tube). Honda et al. [17] performed analysis of condensate flooding and produced the equation below for trapezoidal shaped fins.

$$\emptyset_f = \cos^{-1}\left[\frac{4\sigma\cos\beta}{\rho g b d_o} - 1\right] \quad (1a)$$

where,

$$b < \frac{2h\cos\beta}{1-\sin\beta} \quad (1b)$$

For rectangular shaped fins, Equation 1a reduces to,

$$\emptyset_f = \cos^{-1}\left[\frac{4\sigma}{\rho g b d_o} - 1\right] \quad (1c)$$

where,

$$b < 2h \quad (1d)$$

Equation (1) agrees with experimental observations [17]–[20] for a good range of variables. However, experimental data given by Namasivayam & Briggs [4], [5], [13], [14] and Fitzgerald et al. [21] has shown that Equation (1) is unable to appropriately predict condensation retention angles at high vapour velocities.

2) 3.2.2 Condensate retention for Forced-Convective Condensation

In order to account for vapour shear altering the condensate retention, the following expression was proposed by Namasivayam & Briggs [11].

$$\emptyset_f = \cos^{-1}\left[\frac{4\sigma(1-\psi)}{\rho g b d_o} - 1\right] \quad (2a)$$

where,

$$\psi = K\left[\frac{\rho_v {U_\infty}^2}{\rho g s}\right]^m \quad (2b)$$

K and m are empirical constants determined by the authors through observation of the condensate retention, and were found to be 0.105 and 0.379 respectively. Noteworthy, Ψ approaches 0 as U_v approaches 0 m/s, therefore reducing equation (2) to equation (1). Applied only to experimental data of higher vapour velocities given by Namasivayam & Briggs [4], [5], [13], [14], equation (2) predicts condensate retention to within 30%. Equation (2) is applied unaltered to the present work, given the fact that the semi-empirical model proposed by Ali & Ali [12] is unable to predict flooding angle appropriately to produce more accurate prediction (see section 3.1.3). Granted the lack of experimental evidence of vapour velocity affecting condensate flooding at the fin-roots, and given the significantly smaller vapour velocity at the fin-root, the expression for additional flooding at fin-roots given by Masuda & Rose [22], which is extended by Rose [16] for trapezoidal cross-section fins, is given as below.

$$f_f = \left[\frac{1-\tan\left(\frac{\beta}{2}\right)}{1+\tan\left(\frac{\beta}{2}\right)}\right]\left[\frac{2\sigma}{\rho g d h}\right]\left[\frac{\tan\left(\frac{\emptyset_f}{2}\right)}{\emptyset_f}\right] \quad (3a)$$

$$f_s = \left[\frac{1-\tan\left(\frac{\beta}{2}\right)}{1+\tan\left(\frac{\beta}{2}\right)}\right]\left[\frac{4\sigma}{\rho g d s}\right]\left[\frac{\tan\left(\frac{\emptyset_f}{2}\right)}{\emptyset_f}\right] \quad (3b)$$

3) 3.2.3 Analysis of the semi-empirical model developed by Ali & Ali [12]

Recently, Ali & Ali [12] presented a study based on simulated forced-convection condensation of water, ethylene glycol and R-141b) on horizontal integral-fin tubes to accurately predict condensate flooding. 8 tubes of varying dimensions, but of fixed fin-root diameter and internal diameter were used. To simulate the condensation, fluid is flowed with a constant flowrate through small drilled holes in between the fins. The flowrate of the test fluid is adjusted to a minimum to produce a smooth film. Air of velocity between 0 and 19 m/s is flowed downwards across the tubes to simulate vapour-velocity. Flooding angle was found to be strongly correlated to the vapour Reynold's number. The flooding angle increases in tandem with the vapour Reynold's number for fluids which have a higher surface tension to density ratio (e.g. steam), whereas flooding angle behaves the opposite for fluids with lower surface tension to density ratio (e.g. low surface tension refrigerants). The authors developed a semi-empirical model that includes the effects of vapour velocity for the retention angle. The model predicts most of experimental data to within ±15% for water and ethylene glycol, and to within ±5% for refrigerants. The expression for flooding angle given by Ali & Ali [12] is as follows,

$$\emptyset_f = \cos^{-1}\left[\frac{2}{d_o}\left(A \times s \times \left(\frac{\sigma}{v^2 s \rho_c}\right)^a \times \left(\frac{sg}{v^2}\right)^b \times \left(\frac{\rho_a}{\rho_c}\right)^c\right) - 1\right] \quad (4)$$

where,

A, a, b and c are the semi-empirical constants found using the least squares method. With the set of constants provided by Ali & Ali [12], the condensate retention is compared with the experimental data at hand. The model is unable to determine most of the flooding angle, especially at lower vapour velocities. Given the erroneous predictions, a new set of constants is determined using the optimization technique in Section 2.2. The best fitting constants were found to be as Table 1, and are able to determine the experimental data given by Namasivayam & Briggs [4], [5], [13], [14] within a standard deviation of 16.9%, which is close to the reported correlation of a standard deviation of 17.46% in the study of Ali & Ali [12].

Table 1: Empirical Constants for the Model of Ali & Ali [12].

A	**a**	**b**	**c**
0.000991508	1.803925314	-1.390025266	-1.19788611

Incorporating the flooding angle predicted using the model given by Ali & Ali [12], the prediction of the heat-transfer model given by Namasivayam & Briggs [11] is found to be within 28.2%.

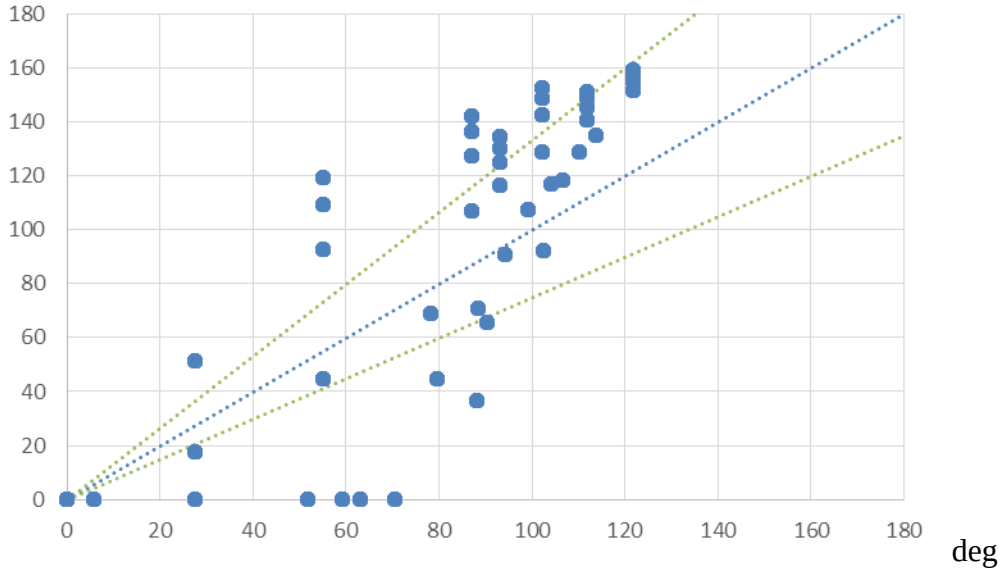


Figure 5: Comparison of the model of Ali & Ali [23] with Experimental Data given by Namasivayam & Briggs [4], [5], [13], [14]

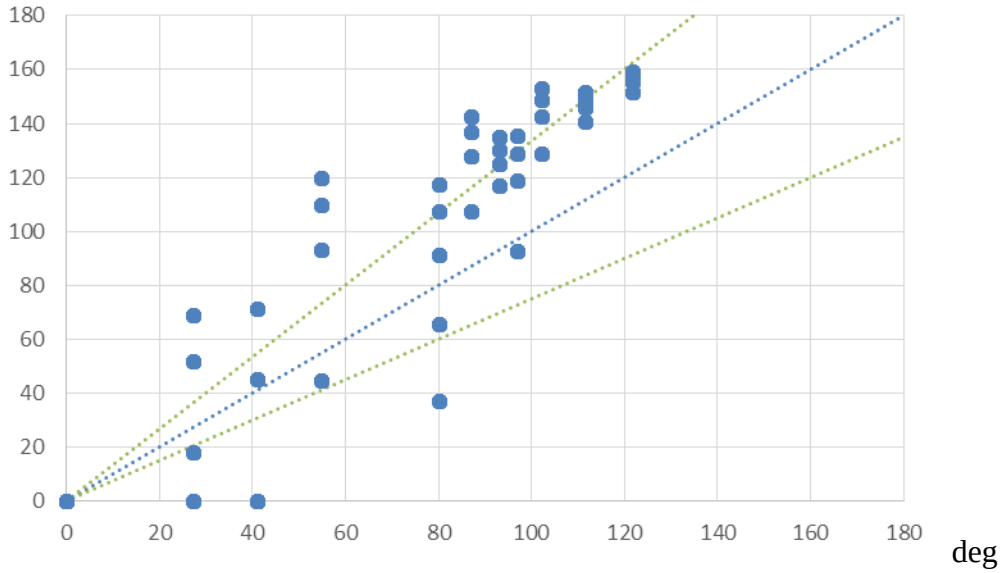


Figure 6: Comparison of Ali & Ali [23] model with Predictions of Equation (1)

As seen in figures above, the model of Ali & Ali [23] does not predict the flooding angle to within 25% to both the experimental data used in this study and the predictions of the well-established flooding angle prediction model of given by Honda et al. [24].

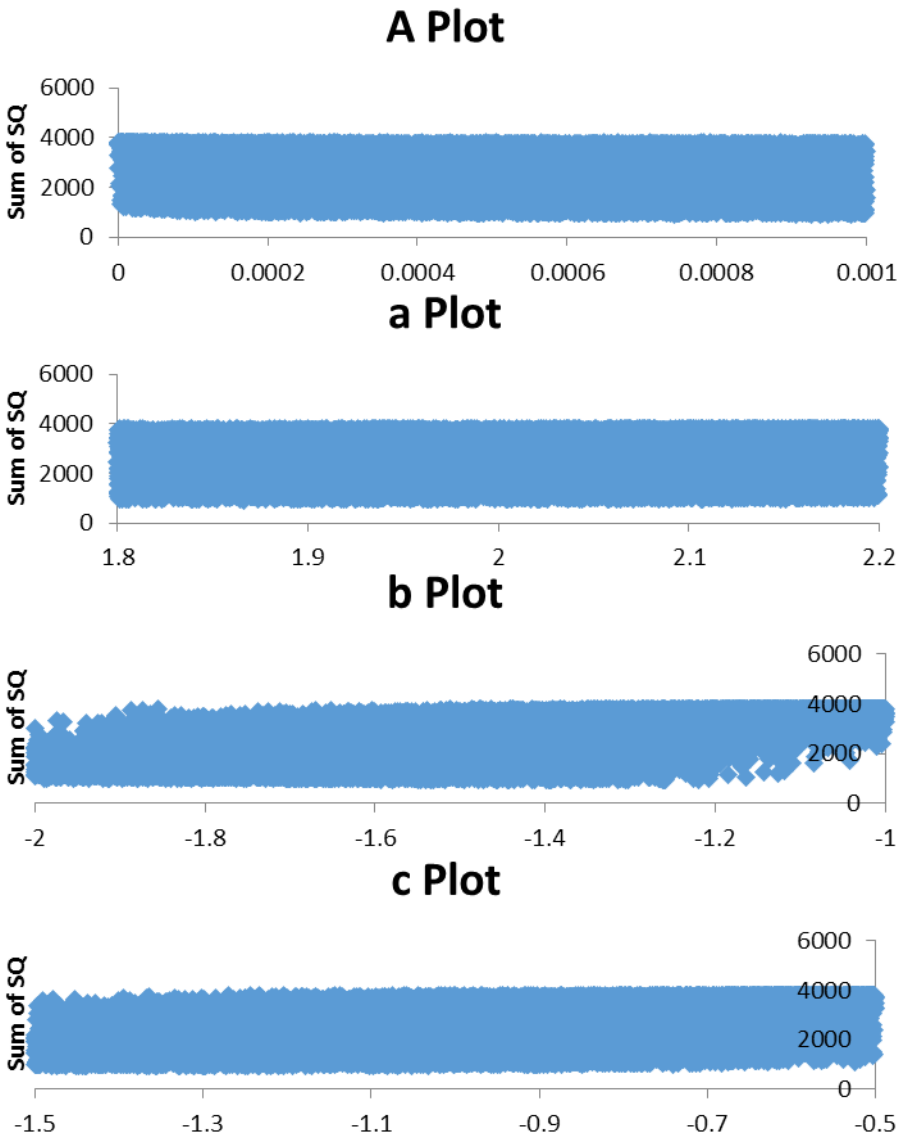


Figure 7: Plots of Data Generated for the Model of Ali & Ali [12]

From the data generated through the optimization process, plots of the sum of squares versus the empirical constants are made (Figure 7). The constants does not seem to produce any discernible relationship, or may have Omitted Variable Bias (OVB). The model has to be re-optimized for each different set of experimental data. We can conclude:
New constants have to be generated in order to be used with the experimental data available to the author
With new constants, the model does not produce better predictions the flooding angle model provided by Namasivayam & Briggs [11].

3.3 Heat-Transfer Model

4) 3.3.1 Heat-Transfer at Fin-Tip

The model of Shekriladze & Gomelauri [15] for heat-transfer condensation on a smooth horizontal tube gives

$$Nu = 0.9(Re_{tp})^{\frac{1}{2}} \quad (5a)$$

where Re_{tp}, the two phase Reynolds number, depends on the fin-tip diameter. Equation (5a) is rearranged to give heat-transfer at fin-tip

$$q_{tip} = \left[\frac{0.9^2 \rho k^2 \Delta T^2 \bar{U}_{tip}}{\mu d_o}\right]^{\frac{1}{2}} \quad (5b)$$

where $\bar{U}_{tip} = \bar{U}_{\infty}$

5) 3.3.1 Heat-Transfer at Fin-Root

Only a portion of the interfin surfaces above the flooding is considered. The method of Shekriladze and Gomelauri [15] gives

$$Nu = \frac{(Re_{tp})^{\frac{1}{2}}}{\emptyset_f} \int_0^{\emptyset_f} (1 + \cos \emptyset)^{1/2} \, d\emptyset \quad (6a)$$

where Re_{tp} depends on the fin-root diameter. Equation (6a) is rearranged to give heat-transfer at fin-root

$$q_{tip} = \left[\frac{\rho k^2 \Delta T^2 \beta(\phi_f) \bar{U}_{root}}{\mu d}\right]^{\frac{1}{2}} \quad (6b)$$

where,

$$\beta(\phi_f) = \frac{1}{\emptyset_f} \int_0^{\emptyset_f} (1 + \cos \emptyset)^{1/2} \, d\emptyset \quad (6c)$$

…and is approximately the following expression

$$\beta(\phi_f) = 1.4177 + 0.0172\phi_f - 0.0477{\phi_f}^2 \quad (6d)$$

As the effects of vapour velocity between the tips is difficult to estimate, several authors, namely Briggs & Sabaratnam [25] suggests that the vapour velour at the root is intuitively smaller. An approximation of the vapour velocity at the root is given

$$\bar{U}_{root} = \bar{U}_{\infty} \left[1 - \exp[-\left(\frac{s}{h}\right)]\right] \quad (7)$$

The equation (7) gives the characteristics of $\bar{U}_{root} \rightarrow \bar{U}_{\infty}$ for large ratios of s/h, and $\bar{U}_{root} \rightarrow 0$ for small ratios of s/h

6) 3.3.3 Heat-Transfer at Fin-Flank

The heat-transfer at the fin-flank is approximated as a vertical flat plate with a length of ($\varphi_f\ d_o/2$) because gravity is neglected. Thus, Shekriladze and Gomelauri [15] rearranges to

$$q_{flank} = \left[\frac{2\rho k^2 \Delta T^2 \bar{U}_{flank}}{\mu d_o \phi_f}\right]^{\frac{1}{2}} \quad (8)$$

The vapour velocity at the flank is approximated as

$$\bar{U}_{flank} = (\bar{U}_{tip} + \bar{U}_{root})/2 \quad (9)$$

7) 3.3.4 Overall Heat-Transfer Expression

Combining the relevant heat fluxes for the various sections of the tube, and provision of condensate retention correction, the overall expression for heat-transfer is given below

$$Q = C_1 \pi d_o t q_{tip} + \frac{\phi_f}{\pi}\left[C_2\left(1 - f_f\right)\frac{\pi({d_o}^2 + d^2}{2} q_{flank} + C_3(1 - f_s)\pi b d q_{root}\right] \quad (10)$$

where C_1, C_2 and C_3 are empirical constant to be determined from obtaining the best correlation between calculated Nusselt Number with the experimental Nusselt Number. The Nusselt Number is calculated using the following expression

$$Nu = \frac{q_d d}{\Delta T k} = \frac{Q}{\pi(s+t)\Delta T k} \quad (11)$$

8) 3.3.5 Combining Free and Forced-Convection

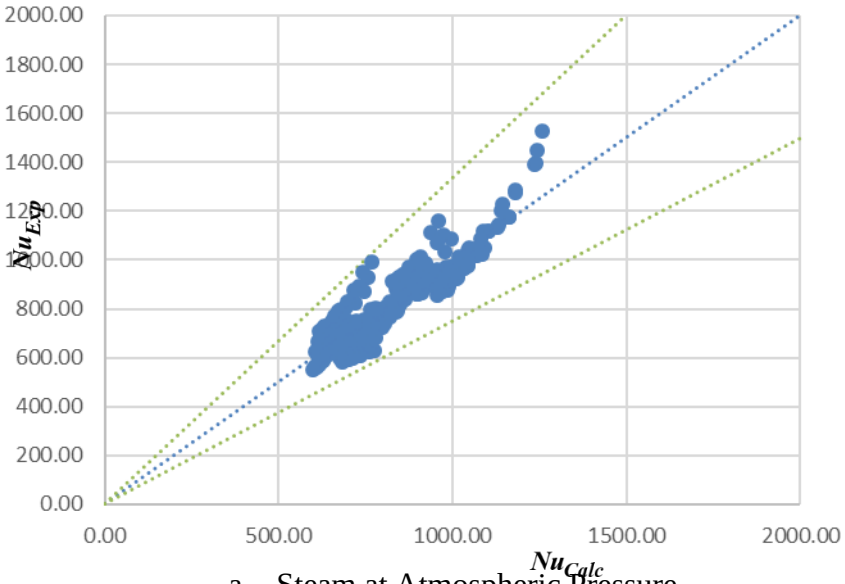
With the Nusselt's number calculated for forced-convection condensation, the overall Nusselt number can be calculated using the following asymptotic expression.

$$Nu_{calc} = \left({Nu_{g\sigma}}^n + {Nu_u}^n\right)^{\frac{1}{n}} \quad (12)$$

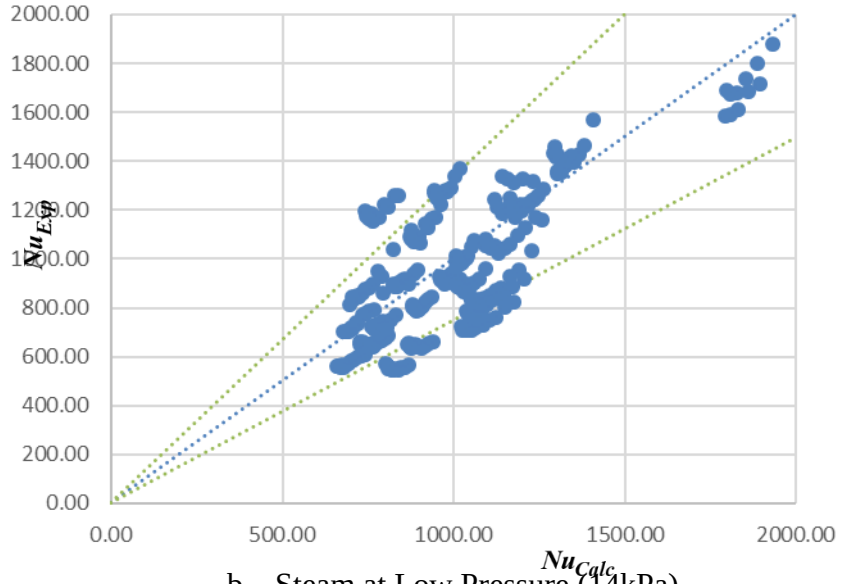
In the equation above, $Nu_{g\sigma}$ is the Nusselt number calculated using the model of Rose [16] for free-convection condensation and Nu_u is the Nusselt number calculated using the model for forced-convection condensation used in this study. The value of n used for this study is 2, as it provides the behavior that is required for the asymptotic model, where the model tends towards the free-convective condensation model of Rose [16] during low vapour velocities, whilst tending towards the forced-convective condensation model developed in this study during higher vapour velocities.

9) 3.3.6 Optimization of Empirical Constants

The optimization method given in Section 2.2 was used to determine the constants that provide the best fit, and is tabulated in table 2 along with the results using previous given constants and after the proposed modification of the expression. It was found that C1, C2 and C3 are 0.288, 1.015 and 3.333, respectively. The standard deviation between the prediction and the experimental data for this study is 16.08%. The results suggest that the Nusselt's Number is not affected at the fin-tip at higher vapour velocities. This is possible as the exposure of the fin-tip surface is not significantly affected by the vapour velocity.



a. Steam at Atmospheric Pressure



b. Steam at Low Pressure (14kPa)

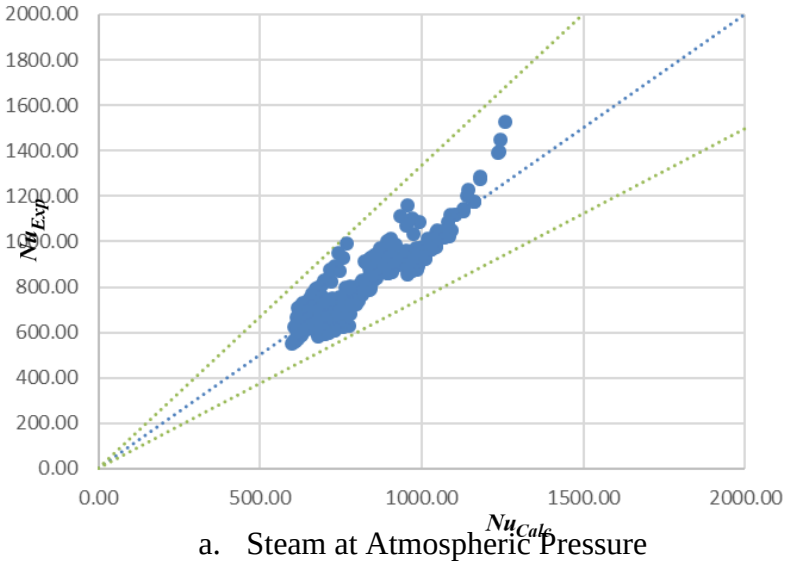
Figure 8: Comparison of the model of Namasivayam & Briggs [11] with Experimental Data [4], [5], [13], [14], using constants C_1, C_2 and C3 of 0.288, 1.015 and 3.333 respectively

10) 3.3.7 Modifying the Heat-Transfer Expression

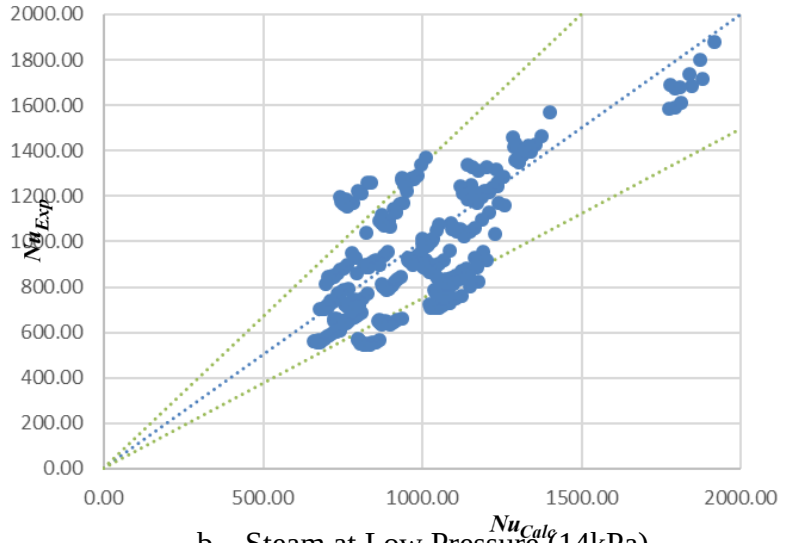
An analysis of the multiple regression reveals that constant C_1 gives limited perceivable correlation with the prediction produced – a change in C_1 is only compensated by the adjustment of C_2 and C_3. Dropping constant C_1, similar standard deviation can be found (16.06%) and reduces the 'noise' to the correlation of C_2 and C_3 with the prediction. Thus, we propose C1, C2, and C3 as 0, 1.057 and 3.374 respectively.

$$Q = \frac{\phi_f}{\pi}\left[C_2(1-f_f)\frac{\pi({d_o}^2+d^2}{2}q_{flank} + C_3(1-f_s)\pi b d q_{root}\right] \quad (13)$$

However, it is not worthy that this new correlation may not be suitable for a wider range of experimental data, where the Nusselt's number is hugely affected at the fin-tip.



a. Steam at Atmospheric Pressure



b. Steam at Low Pressure (14kPa)

Figure 9: Comparison of the model of Namasivayam & Briggs [11] with Experimental Data [4], [5], [13], [14], using constants C_1, C_2 and C3 of 0, 1.057 and 3.374 respectively.

4. Concluding Remarks

The semi-empirical condensate retention model developed by Ali & Ali [23] is critically analyzed for its application. Better constants (see Table 2) are presented for the semi-empirical heat-transfer model for forced-convection condensation on integral-fin tubes. The heat-transfer model is also proposed to be modified to improve accuracy and precision. The models are correlated to experimental data of over 800 data points, for steam with a wide range of vapour velocities, on 15 tube geometries. The standard deviation with for both the existing model, and the modified model was 16.1% using relevant constants as seen in table below.

Table 2: Summary of Results

Study	C1	C2	C3	Steam %	Low Pressure Steam	Steam SD%
1	1	0.41	0.41	9.531%	23.445%	17.896%
2	2.7	0.7	1	10.461%	27.126%	20.558%
Present (3)	0.288	1.015	3.333	8.554%	21.041%	16.085%
Modified (4)	-	1.057	3.374	8.542%	21.047%	16.061%

NOMENCLATURE

b	Fin root spacing
C_1, C_2, C_3	Constants in Equation (10)
d	Diameter of plain tube or fin-root diameter of finned tube
d_o	Fin-tip diameter of finned tube
f_f	Proportion of fin flank above flooding angle covered by retained condensate
f_s	Proportion of fin root above flooding angle covered by retained condensate
g	Specific force of gravity
h	Fin height
K	Constant in Equation (2b)
k	Thermal conductivity
m	Constant in Equation (2b)
Nu	Vapour-side Nusselt number, $q_d\, d/\Delta T k$
Q	Heat transfer rate
q	Heat flux
q_d	Heat flux based on area of smooth tube, diameter d
Re_{tp}	"Two-phase" Reynolds number
s	Fin tip spacing
t	Fin thickness
$\bar{U}$	Effective vapour velocity
$\bar{U}_\infty$	Free stream vapour velocity

Greek Symbols

β	Function defined by Equation (6c)
ΔT	Vapour-side temperature difference (vapour temperature minus mean outside wall temperature at fin root)
θ	Fin-tip half angle
μ	Viscosity
σ	Surface tension of condensate
ρ	Density
φ	Angle measured from top of tube
φ_f	Flooding angle (position at which fin space becomes fully flooded with condensate) measured from top of tube
ψ	Dimensionless quantity defined by Equation (2b)

Subscripts

none	Condensate
Calc	Theoretical
flank	Pertaining to fin flank
root	Pertaining to fin root
tip	Pertaining to fin tip
v	vapour

REFERENCES

[1] M. B. Pate, “Recent Developments in Condensers and Condensation for Refrigerants and Air-Conditioning Applications.,” in *2nd International Symposium University of Bath*, 1990, pp. 1–27.

[2] H. Honda, S. Nozu, and B. Uchima, “A Generalized Prediction Method for Heat Transfer During Film Condensation on a Horizontal Low-Finned Tube,” in *2nd ASME-JSME Thermal Engineering Joint Conference*, 1987, pp. 4, 385–392.

[3] A. Briggs and J. W. Rose, “Models for Condensation Heat Transfer on Low Finned Tubes,” in *2nd Baltic Heat Transfer Conference*, 1995.

[4] S. Namasivayam and A. Briggs, “Effect of Vapor Velocity on Condensation of Low-Pressure Steam on Integral-Fin Tubes,” *J. Heat Transfer*, vol. 129, no. 11, p. 1486, 2007.

[5] S. Namasivayam and A. Briggs, “Effect of Vapour Velocity on Condensation of Atmospheric Pressure Steam on Integral-Fin Tubes,” *Appl. Therm. Eng.*, vol. 24, no. 8–9, pp. 1353–1364, 2004.

[6] A. Briggs, “Forced-Convection Condensation on Horizontal Finned Tubes,” University of London, 1991.

[7] E. E. Wilson, “A Basis for Rational Design of Heat Transfer Apparatus,” *Trans. ASME. J. Heat Transf.*, vol. 37, pp. 47–82, 1915.

[8] J. Fernández-Seara *et al.*, “A general review of the Wilson plot method and its modifications to determine convection coefficients in heat exchange devices,” *Appl. Therm. Eng.*, vol. 27, no. 17–18, pp. 2745–2757, Dec. 2007.

[9] A. Cavallini, L. Doretti, G. A. Longo, and L. Rossetto, “A New Model for Forced-Convection Condensation on Integral-Fin Tubes,” *J. Heat Transfer*, vol. 118, no. 3, p. 689, 1996.

[10] S. Namasivayam and A. Briggs, “Forced-Convection Condenstaion of Ethylene Glycol on Integral-Fin Tubes,” in *IMECE04*, 2004, pp. 1–7.

[11] S. Namasivayam and A. Briggs, “An empirical correlation for forced-convection condensation on integral-fin tubes,” in *9th U.K. National Heat Transfer Conference*, 2005.

[12] H. M. Ali and A. Ali, “Measurements and semi-empirical correlation for condensate retention on horizontal integral-fin tubes: Effect of vapour velocity,” *Appl. Therm. Eng.*, vol. 71, no. 1, pp. 24–33, Oct. 2014.

[13] S. Namasivayam and A. Briggs, “Forced-Convection Condensation of Steam on Integral-Fin Tubes,” in *8th U.K. National Heat Transfer Conference*, 2003.

[14] S. Namasivayam and A. Briggs, “Condensation of Atmospheric Pressure Steam on Integral-Fin Tubes - Effect of Fin Height and Vapour Velocity,” in *13th International Heat Transfer Conference*.

[15] I. G. Shekriladze and V. I. Gomelauri, “Theoretical study of laminar film condensation of flowing vapour,” *Int. J. Heat Mass Transf.*, vol. 9, pp. 581–591, 1966.

[16] J. W. Rose, “An approximate equation for the vapour-side heat-transfer coefficient for condensation on low-finned tubes,” *Int. J. Heat Mass Transf.*, vol. 37, no. 5, pp. 865–875, 1994.

[17] H. Honda, S. Nozu, and K. Mitsumori, “Augmentation of condensation on finned tubes by attaching a porous drainage plate,” in *ASME-JSME Thermal Engineering Joint Conference*, 1983, pp. 3, 289–295.

[18] T. M. Rudy and R. L. Webb, “An Analytical Model to Predict Condensate Retention on Horizontal Integral-Fin Tubes,” *J. Heat Transfer*, vol. 107, no. May 1985, p. 361, 1985.

[19] K. K. Yau, J. R. Cooper, and J. W. Rose, “Horizontal Plain and Low-Finned Condenser Tubes-Effect of Fin Spacing and Drainage Strips on Heat Transfer and Condensate Retention,” *Trans. ASME. J. Heat Transf.*, vol. 108, no. November 1986, pp. 946–950, 1986.

[20] A. Briggs, “Liquid Retention Measurements on Three Dimensional Pin-Fin Tubes,” in *Proceedings of the 2nd International Exergy, Energy and Environmental Symposium*, 2005.

[21] C. L. Fitzgerald, A. Briggs, J. W. Rose, and H. S. Wang, “Effect of vapour velocity on condensate retention between fins during condensation on low-finned tubes,” *Int. J. Heat Mass Transf.*, vol. 55, no. 4, pp. 1412–1418, 2012.

[22] H. Masuda and J. W. Rose, “An Experimental Study of Condensation of Refrigerant-113 on Low Integral-Fin Tubes,” in *International Symposium on Heat Transfer*, 1985, p. 2, Paper No. 32.

[23] H. M. Ali and A. Briggs, “A semi-empirical model for free-convection condensation on horizontal pin-fin tubes,” *Int. J. Heat Mass Transf.*, vol. 81, pp. 157–166, 2015.

[24] H. Honda, S. Nozu, and Y. Takeda, “A Theoretical Model of Film Condensation in a Bundle of

Horizontal Low Finned Tubes," *J. Heat Transfer*, vol. 111, no. 2, p. 525, 1989.
[25] A. Briggs and S. Sabaratnam, "Condensation From Pure Steam and Steam–Air Mixtures on Integral-Fin Tubes in a Bank," *J. Heat Transf.*, vol. 127(6), 2004.

eureca 2016 – Conference Paper
Paper Number CE_UG001

Biosorption of Bromocresol Green from Aqueous Solutions Using Orange Peel

Kanaga Luckshimi[1], Nazlina Binti Zulbadli[2*], Voon-Loong Wong [3]

[1]*Faculty of Engineering and the Built Environment, SEGi University, Kota Damansara, 47810 Petaling Jaya, Selangor, Malaysia*

[*]corresponding author: nazlina@segi.edu.my

Abstract
In past, there are various treatment in removal of dye from textile industrial effluents has been conducted. Use of low-cost and environmentally friendly sorbents have been studied as an ideal alternative to the current costly methods of removing dye from wastewater. In the present study, the equilibrium behaviour of *Citrus Sinensis* peel was investigated by performing batch adsorption experiments using Bromocresol Green as an adsorbate. The effects of initial dye concentration varied from 40 mg/L to 140 mg/L, adsorbent dosage (0.5 g to 2 g) and type of biomass have been studied to evaluate biosorption capacity, respectively. The batch biosorption capacity is directly proportional to initial dye concentration. A maximum removal of 95% was adsorbed in the 100 mg/L of dye solution for an adsorbent dosage of 1 g. Langmuir and Freundlich isotherms were used to model the adsorption equilibrium data, whereas pseudo-first order and pseudo-second order models were used to correlate the kinetic data of the adsorption process. It was found that Freundlich adsorption isotherm fitted well (R^2 = 0.9637), indicating that heterogeneous adsorbent surface. Kinetic studies show that the sorption process follows pseudo-second-order rate and indicating the chemisorption process which describe dye sorption on nano-porous adsorbent. Based on the results, cellulose based agro-waste such as orange peel is an alternative low cost adsorbent and gaining prominence as a method for the removal of dye from textile effluent. In conclusion, this study has a profound impact in the effectively control water pollution as well improve water quality and reduce the orange peel waste pollution.

Keywords: Adsorption Isotherm, Bromocresol Green, Batch Sorption, Wastewater, *Citrus Sinensis*.

1. Introduction

Environmental pollutions are the most contemporary problems and water pollution considers as the most hazardous threats. Supplying freshwater becoming a question on the global level (Allegre et al., 2006). By comparing the volumes of discharged and the effluent composition, textile industries is graded as one of the most polluting agents producing wastewater. Every year, 100 billion gallons of water used by textile industries during dyeing and finishing processes (Christie, 2007). Huge number of chemicals especially dyes added into dyebath during the dyeing stage. During this process dyes associated with chemicals and other contaminants eliminated from the textiles are leading textile wastewater pollution. Some literature studies show that there are in excess of 100,000 commercially available dyes with a production of $7x10^5$ tons of dyes produced annually out of 10-15% discharged to the environment (Hai, Yamamoto and Fukushi, 2007).

Textile industry dyes can be classified as acid basic dyes, azoic, disperse, direct, mordant, reactive, sulfur and vat dyes (Mishra and Tripathy, 1993). A reactive dye, named as Bromocresol Green (BCG) was used in present study. Reactive dyes are predominately comprising azo compounds have different reactive groups including nuclei metal, vinyl sulfone and cholorotriazine. Generally, reactive dyes are covalently bind to textile fibers and hardly removed by conventional method compare from different kinds of dyes (Horton, 2009). Once the reactive dyes released into receiving water bodies, toxic amines are produced through cleavage reduction of azo linkages causing human health to severe risks of waterborne diseases. Furthermore, the human body's immune system could not break down the dyes and caused gastrointestinal symptoms such as vomiting, diarrhea and nausea (Sigmaaldrich.com, 2016). The discharge of colored wastewater into the river or natural stream prevent sunrays penetration into water and hinder photochemical activities. This result raises of chemical oxygen demand (COD) and gives negative impact on the aquatic environment because of insufficient oxygen in water (Mittal and Gupta, 2006). In addition, textile wastewater contains reactive dyes causing carcinogenic and mutagenic for aquatic life (Slokar and Majcen Le Marechal, 1998). Thus, various effective methods of treating dye contaminated wastewater are very significance to maintain purity of water and saving aquatic environment.

Conventional methods for removal dye containing wastewater includes combination of physical and chemical process such as color irradiation, coagulation, flocculation, floatation, filtration ozonation, oxidation, reverse osmosis and sedimentation (Iqbal,2008). Most of these methods are ineffective and have drawback due to limitation in application when dealing with water-soluble reactive dyes and acid dyes which are in brightly colored. Dyes being stable when exposed to various chemicals, sunrays, biological degradation and oxidizing agents (Namasivayam *et al*., 1997). Adsorption is one of the method proved as an effective process for dye removal in wastewater (Sharma et al., 2010). Primarily, activated carbon is most popular and commonly used adsorbent for the treatment of dye contaminated wastewater because of its larger surface area, surface reactivity and adsorption capacity is high and microporous structures (Bharathi *et al*., 2013). Yet, the major drawbacks of the commercially available activated carbon are expensive and has high cost for renewable while being exhausted (Waranusantigul *et al*., 2003).

Biosorption is an alternative method replacing adsorption process which utilize agricultural waste and extensive use of microorganism in dead, pretreated and immobilized forms. Biosorption is a process whereby some molecules bind and concentrate selected molecules from aqueous solutions (Aksu and Tezer, 2005). Biosorption has proven to be very effective method for removal of dye in textile wastewater. The advantages of this process are eco-friendly, inexpensive, high efficiency in terms of binding sites its provide wide range for dye molecules (Ahalya and Ramachandra, 2003). Therefore, many researches has been studied this method for the removal of various dyes from contaminated wastewater.

Keeping this point of view, many researches has been conducted on the development of effective, economical and despite easily available types of adsorbent, especially from the waste materials. Table 1 illustrates the different research studies on the type of biosorbents on dye removal.

Table 1. A comparison of different biomass for the adsorption of dyes.

Type of Biosorbents	**Removal of Dyes**	**Researchers**
Garlic peel	Methylene Blue	Hameed *et al*., 2009
Almond shell	Direct Red 80	Doulati Ardejani *et al*., 2008
Wood	Astrazone Blue	Poots *et al*., 1978
Straw	Methylene Blue	Kannan *et al*., 2001
Syzgium cumini leaves	Crystal violet	Mehmood *et al*., 2015
Tamarind fruit shell	Congo Red	Reddy *et al*., 2006
Saw Dust	Methylene Blue	Zou *et al*., 2013
Coir pith	Congo Red	Namasivayam *et al*., 2001
Duckweed	Methylene Blue	Waranusantigul *et al*., 2003
Agaricus bisporus	Reactive Blue 49	Akar *et al*., 2009
Sunflower seed	Methyl violet	Hameed, 2008
Banana peel	Violet 54	Kumar *et al*., 2010
Papaya leaf stem	Malachite green	Raj *et al*.,2014
Cotton	Basic blue 9	Bouzida *et al*., 2002
Rice husk charcoal	Congo Red	Janveja *et al*., 2008

From this pioneering work, orange peel is known as one of the common agricultural waste that can be obtained from orange juice production. In general, orange peels *(Citrus Sinensis and Citrus Reticulata)* used as raw material for manufacturing cattle feed, burning which can contribute to the emission of global warming gases thus is not an efficient method (Lapuerta *et al*., 2008). Besides, the peels do not have any commercial value in the market it's being dumped as waste everywhere around the world and it's causes eye sore. Therefore, utilization of orange peels plays major role to protect the environment. This will prevent further disposal of orange peels as a waste and also reduces the waste generation which lead to a sustainable development for better future preservation. Orange peels composed of cellulose, chlorophyll pigments, hemicellulose, pectin and other low molecular weight of hydrocarbons (Liang *et al*., 2010). Besides, all these components consist of different functional groups such as hydroxyl and carboxyl groups enable an interaction with the chromophores of BCG dye from aqueous solutions (Arami *et al*., 2005). Considering all this issues, this research has been studied to convert these

agro-waste into useful products by investigating its viability as biosorbent for dye removal. As seen from previous research, for removal of BCG molecules from effluent were studied using different adsorbent such as *Ziziphus nummularia* (Shokrollahi *et al*., 2011) and cadmium hydroxide nanowire (Ghaedi *et al*., 2012). In present research, the feasibility of using orange peels as biosorbent were carried out for the removal of Bromocresol Green (BCG) colorant.

1. 2. Materials and methods

2.1 Biosorbent preparation

The orange peels *(Citrus Sinensis, Citrus Reticulata),* are used as an adsorbent in this study were collected from the local fruit juice stalls. The collected orange peels were washed with tapped water to get rid of the surface adhered dirt, soluble components such as colouring agents, resins, reducing sugar and tannins. Then, the peels were cut into small pieces to facilitate the grinding process and dried in a hot air oven at temperature of 50^{o}C for 24 hours. The dried and powdered orange peels were sieved in 50 mesh ASTM standard size to obtain similar particle size of 300 μm. Next, the powdered biomass were sealed in a plastic bag and persevered in a refrigerator at temperature (4^{o}C) to avoid any degradation.

2.2 Adsorbate preparation

Bromocresol Green (BCG) (Synertec Enterprise) with 400ppm concentration, pH and used as the main adsorbate in this research. BCG stock solution were prepared in a 100 mL volumetric flask by dissolving accurately weighed dye in distilled water with a concentration of 400 mg/L.

2.3 Calibration curve

A calibration curve was plotted using six samples of different concentration of BCG dye solutions ranging from 10 to 100 mg/L that were obtained by diluting the stock solution using distilled water. The maximum absorbance wavelength of this dye solutions is (λ= 600 nm) and the absorbance values for each concentration were determined by UV/VIS spectrophotometer (Shimadzu, Model UV 1601, Japan) which operates visible range on absorbance mode.

2.4 Batch adsorption experiment

Batch biosorption experiments were performed using 250 mL conical flask, each containing 1 g of dried biomass in 100 mL of BCG solution with concentration of 100 mg/L, unless otherwise stated. This mixture was stirred in an orbital shaker at constant agitation speed of 200 rpm at room temperature (28^{o}C±4^{o}C). The dye concentration from the flasks were measured spectrophotometrically, once the samples were withdrawn at pre-determined time intervals (24 hours interval). Before the dye absorbance values were measured at maximum wavelength, the samples were centrifuged at 6000 rpm for 15 minutes. After centrifugation, the supernatant solution from the vials were carefully extracted using pipette to determine the corresponding absorbance values using the UV-Vis spectrophotometer.

In this research, to analyze the dye adsorption, Langmuir and Freundlich's equilibrium isotherm models were studied. Effect of initial concentration was studied by adjusting the BCG dye concentration. Research on the effect of each parameter were studied while other parameters values were fixed. All experiments were done in triplicates and the average value considered for analysis of percentage uptake and sorption capacity using Equation 1.

$$q = \frac{(Ci-Ce)V}{M} \quad (1)$$

where q is the amount of BCG adsorbed per unit weight of biomass at any time (mg/g), Ci and Ce are initial and equilibrium dye concentration in a sample (mg/L), V the dye solution volume (L) and M is the amount of adsorbent (g).

3. Results and Discussion

3.1 Effects of Initial Dye Concentration

Figure 1 shows effect of initial BCG concentration on sorption capacity of the *Citrus Sinensis* peels. As the initial dye concentration was increased from 40 to 140 mg/L, the sorption capacity of the peels increased from 3.68 mg/g to13.13 mg/g as shown in Figure 1. Besides the sorption capacity of the adsorbent is directly proportional to the initial dye concentration.

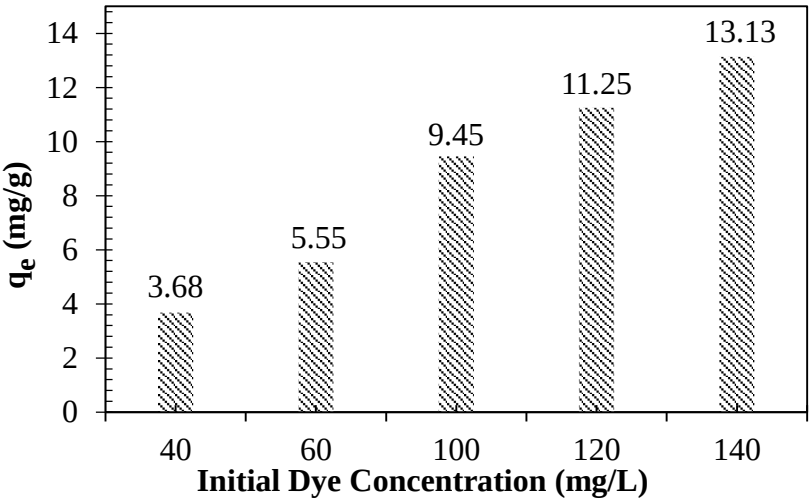


Figure 1: Adsorption capacity (q_e, mg/g) of *Citrus Sinensis* in solution with different concentrations (mg/L) of BCG *(V =100 ml; M =1.0g).*

As seen in Figure 1, the interaction between the adsorbent and dye concentration plays a significance role as the concentration of dye increased. Increase in interaction between the concentration of dyes provides a driving force that required to overcome the resistance of adsorbent in separation of dye amount that has transferred from the aqueous phase to the surface of the adsorbent (Suyamboo, 2012). Collisions between dyes and biosorbent increases with increasing initial concentration of the dye; thus, improves the adsorption capacity. Similar findings as reported by (Yedduo-mezenner, 2010) as dye amount gradually increases resulting higher concentration gradient subsequently there's an increment in adsorption capacity of biosorbent.

3.2 Effects of Adsorbent Dosage

In order to study the relationship between adsorbent dosage and performance of dye removal the quantity of orange peels was varied from 0.5 g to 2 g for removal of BCG Figure 2 illustrates equilibrium uptake capacity depressed with increasing of adsorbent dosage, from 15.83 mg/g at 0.5 g of adsorbent to 4.78 mg/g at 2 g of adsorbent. Biosorbent dose is a significance parameter to be considered for effective sorption from aqueous solutions. The resulting effect can be explained with the increase in vacant sorption sites of dye molecules adsorbed with proportion of adsorbent dosage (dye concentration standardized to 100 mg/L) subsequent to increase in the amount of adsorbent dosage. Similar results have been stated by a researcher (Suyamboo, 2012). The reason for this behavior can be attributed to a larger surface area and great vacant number adsorption site which facilitates more dye adsorption (Gong *et al*., 2005).

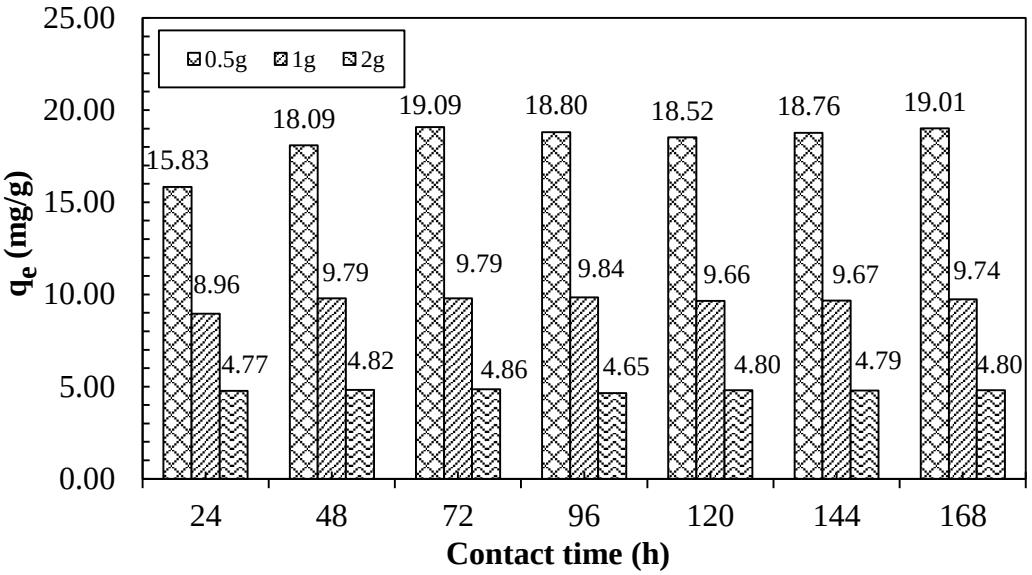


Figure 2: Adsorption capacity ($q_{e,}$ mg/g) of Citrus Sinensis at equilibrium in solution with different dosage (g) of BCG *(V=100 ml).*

3.3 Effects of the Adsorption Capacity on Different Species of Orange Peel Biosorbents

Figure 3 shows comparison of adsorption capacity for different species of orange peel. It was observed that *Citrus Reticulata* possesses relatively high adsorption capacity in comparison with of *Citrus Sinensis*. The result reveal that the reactive dye ions were found effectively adsorbed by *Citrus Reticulata*. Follow up studies, *Citrus Sinensis* species were selected for removal of BCG dye.

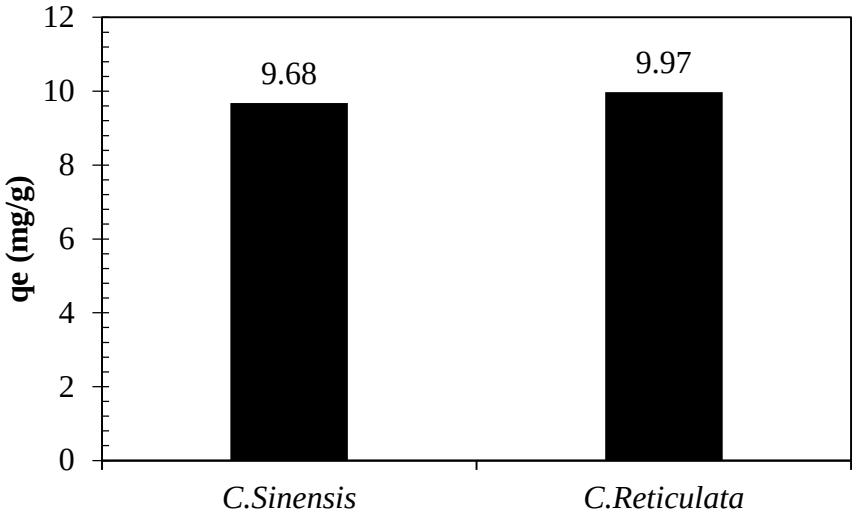


Figure 3: Adsorption capacity (q_e, mg/g) of Citrus Sinensis and Citrus Reticulata in removal of BCG *(V=100 ml; M=1.0g).*

From the comparative results, it's shows that *Citrus Sinensis* peel, *Citus Reticulata* peel made up of more cellulosic fiber, unique pores structure and with the existence of alcohols and carbonyl groups hydrogen bonding and efficient electrostatic interactions provides greater platform for adsorption process (Mehmood et al., 2015). Besides, different functional groups such as carboxylic, ester and ether groups greater tendency to interact efficiently with acidic group of dye including reactive dyes as well (Rehman and Nisar et al., 2014). Therefore, the variation in percentage uptake phenomena attributed by a strong chemical reaction between the functional groups of citrus peels and BCG dye (Chitra *et al.*, 1996).

3.4 Biosorption Isotherm

The adsorption isotherm data were analyze using the adsorption model, known as Langmuir and Freundlich. Langmuir adsorption model is based on the assumption that the maximum adsorption with corresponds to the saturation monolayer of solute molecules to the surface of the adsorbent. The Freundlich isotherm is extensively used to provide coverage of expression on the surface heterogeneity and the exponential distribution of active sites (Crini *et al*., 2007).

Langmuir equation:

$$\frac{1}{q_e} = \frac{1}{q_{max}} + \left(\frac{1}{b_{q_{max}}}\right)\left(\frac{1}{C_e}\right) \quad (2)$$

where q_e is the amount of BCG adsorbed at equilibrium (mg/g), q_{max} is maximum monolayer adsorption capacity (mg/g), C_e is the equilibrium BCG concentration in sample (mg/g) and b is Langmuir constant (L/mg). The plot of $1/q_e$ versus $1/C_e$ for the adsorption of BCG shows a liner curve of slope of $1/b_{q_{max}}$ and intercept of $1/q_{max}$.

Freundlich equation:

$$\log q_e = \log K_f + \left(\frac{1}{n}\right) log C_e \quad (3)$$

where K_f is Freundlich constant related to the distribution coefficient ((mg/g) (L/mg)$^{1}/_{n}$ is the Freundlich exponent. The values of $log\ K_f$ and 1/n can be obtained from the slope and intercept of the plot of $\log q_e$ versus $logC_e$.

The Langmuir and Freundlich isotherm parameters for the adsorption of BCG dyes studies as shown in Table 2. From Table 2, the Langmuir constants obtained was negative values indicates these models is not appropriate to describe the adsorption process. As seen in Table 2, a very high regression correlation coefficient was obtained from Freundlich adsorption isotherm. Therefore, sorption of BCG more favorable to Fruendlich isotherm model while Langmuir isotherm model was unfavorable to this research.

Table 2. Langmuir and Fruendlich constant for BCG adsorption.

Isotherm	**Parameters**		
Langmuir	B (L/mg)	q_{max}	R^2
	-0.05	-18.69	0.95
Freundlich	K_f (mg/g)(L/mg)$^{1/n}$	1/n	R^2
	0.8346	0.7669	0.96

3.5 Kinetics Modelling

Adsorption kinetics data are processed in terms of order rate to understand mechanism of adsorption (Ahmad et al., 2007). In this research, two kinetic models were proposed pseudo-first-order model, pseudo-second-order model to analyze adsorption data at different initial BCG concentration.

Pseudo-first-order rate expression:

$$\log(q_{e-}q_t) = \log q_e - \frac{k_f}{2.303} t \quad (4)$$

Pseudo-second-order rate expression:

$$\frac{t}{q} = \frac{1}{k_s q_{e^2}} + \frac{1}{q_{et}} \quad (5)$$

where q_t is the amount of BCG uptake at time t (mg/g), k_f is the rate constant pseudo-first-order (1/h), k_s is the pseudo-second-order rate constant (g/mg h) t is the contact time (h) and $k_s q_{e^2}$ is the initial sorption rate, h (mg/g h). By plotting both kinetics models, $\log(q_{e-}q_t)$ versus time t (pseudo-first-order) and t/q_t versus time t

(pseudo-second-order) the slope and intercepts of the graphsk_f, k_s and equilibrium dye concentration q_e on adsorbent were obtained.

As seen from Figure 4 and Figure 5, the most favorable kinetics models depend on the higher coefficient values of R^2 adsorption data presented by pseudo-second-order kinetics. This supports the validity of the basic assumptions of the pseudo-second order that chemisorption is significance in adsorption (Yedduo-mezenner, 2010).

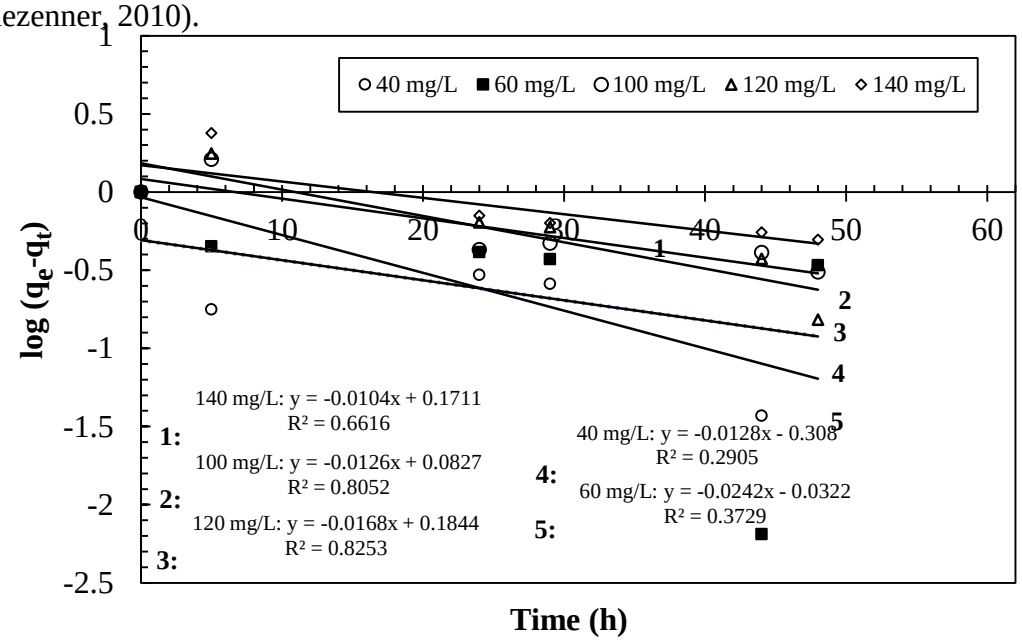


Figure 4: Pseudo first-order sorption kinetics plots (*log* q_e-q_t versus *time, h*) of BCG biosorption on *Citrus Sinensis* peels. The trend line appears to indicate the performance of curve fitting with the value of R-squared.

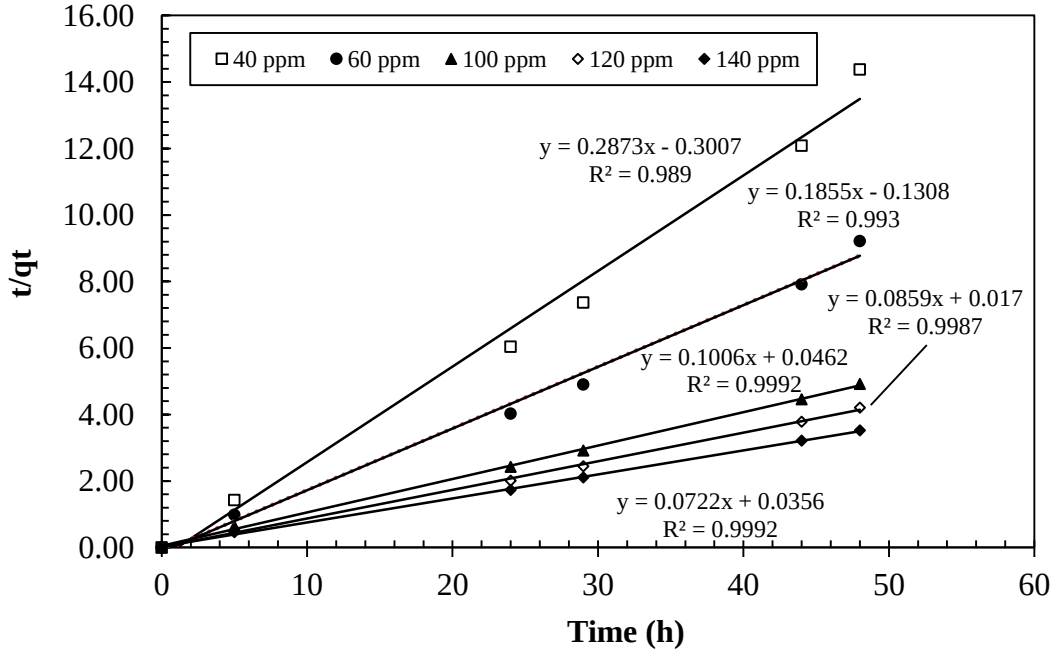


Figure 5: Pseudo- Second Order sorption kinetics plots (*log* q_e-q_t versus *time, h*) of BCG biosorption on *Citrus Sinensis* peels. The trend line appears to indicate the performance of curve fitting with the value of R-squared.

The theoretical model obtained from BCG adsorption by *Citrus Sinensis* were used to compare the experimental values and were plotted in Figure 6. As seen from the graphs, the experimental adsorption capacities, q_t values were almost similar to the experimental data for the BCG sorption system.

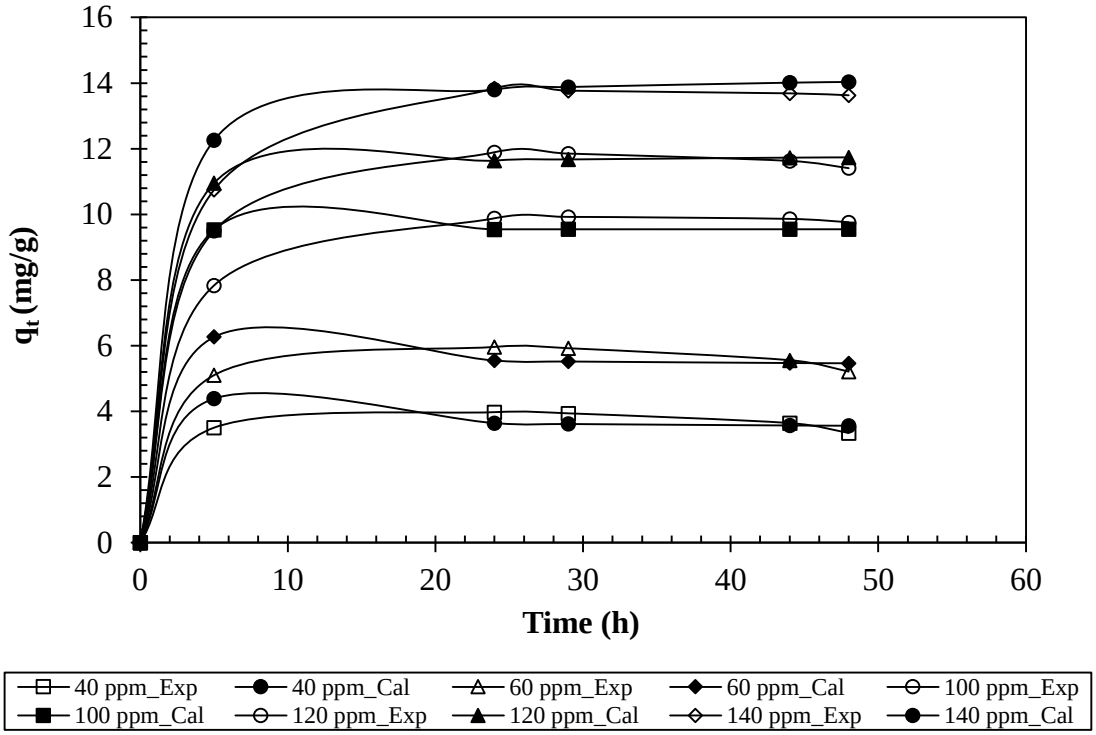


Figure 6: Comparison of experimental data and kinetics model (pseudo second-order) for BCG biosorption (V=100 ml).

1. Conclusion

The study shows that orange peels is more effective adsorbents for removal of Bromocresol Green (BCG) from aqueous solutions. The batch experiment studies show that sorption is highly dependent on various parameters such as the effect of initial dye concentration, type and dosage of the biosorbents. The experimental data were best correlated by Freundlich isotherm. The sorption kinetics of BCG onto *Citrus Sinensis* peels is well described by pseudo-second-order kinetic with high regression coefficient of 0.99. The findings indicated that in an adsorption process chemisorption and effective electrostatic interaction is very significance. In conclusion orange peels is a good selection, abundantly available, inexpensive adsorbent and does not require any pretreatment step for the removal of dye and colorant from wastewater effluent, especially for the removal of reactive dye (BCG). As for future work, analyze the feasibility of orange peels as biosorbent for various dyes and study the performance of orange peel biomass for dye removal at industries level are the recommendations that can be taken into consideration.

5. References

Ahalya, N., Ramachandra, T.V. and Kanamadi, R.D, (2003). Biosorption of heavy metals. *Res. J. Chem. Environ*, 7(4), pp.71-79.

Ahmad, A.A., Hameed, B.H., & Aziz, N. (2007). Adsorption of direct dye on palm ash: kinetic and equilibrium modelling. *Journal of Hazardous Material,* 141, 70-76.

Aksu, Z. and Tezer, S, (2005). Biosorption of reactive dyes on the green alga Chlorella vulgaris. Process Biochemistry, 40(3), pp.1347-1361.

Arami, M., Limaee, N., Mahmoodi, N. and Tabrizi, N. (2005). Removal of dyes from colored textile wastewater by orange peel adsorbent: Equilibrium and kinetic studies. *Journal of Colloid and Interface Science*, 288(2), pp.371-376.

Ardejani, F.D., Badii, K., Limaee, N.Y., Shafaei, S.Z. and Mirhabibi, A.R., 2008. Adsorption of Direct Red 80 dye from aqueous solution onto almond shells: Effect of pH, initial concentration and shell type. *Journal of Hazardous Materials*, 151(2), pp.730-737.

Bharathi, K.S. and Ramesh, S.T, (2013). Removal of dyes using agricultural waste as low-cost adsorbents: a review. *Applied Water Science*, 3(4), pp.773-790.

Bouzaida, I. and Rammah, M.B., 2002. Adsorption of acid dyes on treated cotton in a continuous system. *Materials Science and Engineering*: C, 21(1), pp.151-155.

Christie, R.M. (2001). Colour Chemistry (p.124-135). *Royal Society of Chemistry Cambridge, UK.*

Crini, G., Peindy, H., Gimbert, F. and Robert, C. (2007). Removal of C.I. Basic Green 4 (Malachite Green) from aqueous solutions by adsorption using cyclodextrin-based adsorbent: Kinetic and equilibrium studies. Separation and Purification Technology, 53(1), pp.97-110.

Ghaedi, M., Khajesharifi, H., Hemmati Yadkuri, A., Roosta, M., Sahraei, R. and Daneshfar, A. (2012). Cadmium hydroxide nanowire loaded on activated carbon as efficient adsorbent for removal of Bromocresol Green. *Spectrochimica Acta Part A: Molecular and Biomolecular Spectroscopy*, 86, pp.62-68.

Gong, R., Ding, Y., Li, M., Yang, H. Liu, C., & Sun, Y. (2005). Utilization of powdered peanut hull as biosorbent for removal of anionic dyes from aqueous solution. Dyes and Pigments, 64, 187–192.

Hai, F., Yamamoto, K. and Fukushi, K. (2007). Hybrid Treatment Systems for Dye Wastewater. *Critical Reviews in Environmental Science and Technology*, 37(4), pp.315-377.

Hameed, B.H. and Ahmad, A.A., 2009. Batch adsorption of methylene blue from aqueous solution by garlic peel, an agricultural waste biomass. *Journal of Hazardous Materials*, 164(2), pp.870-875.

Horton, A.M. (2009). Novel Reactive Dyes Based on Pyrimidine and Quinoxaline.

Iqbal, M. (2008). Textile Dyes (p.62-87). *Rehbar Publishers Karachi*.

Kannan, N. and Sundaram, M.M., 2001. Kinetics and mechanism of removal of methylene blue by adsorption on various carbons—a comparative study. Dyes and pigments, 51(1), pp.25-40.

Kumar, G.V., Ramalingam, P., Kim, M.J., Yoo, C.K. and Kumar, M.D., 2010. Removal of acid dye (violet 54) and adsorption kinetics model of using musa spp. waste: A low-cost natural sorbent material. Korean Journal of Chemical Engineering, 27(5), pp.1469-1475.

Lapuerta, M, Hernández, J, Pazo, A. and López, J. (2008). Gasification and co-gasification of biomass wastes: Effect of the biomass origin and the gasifier operating conditions. *Fuel Processing Technology*, 89(9), pp.828-837.

Liang, S., Guo, X., Feng, N. and Tian, Q. (2010). Isotherms, kinetics and thermodynamic studies of adsorption of Cu2+ from aqueous solutions by Mg2+/K+ type orange peel adsorbents. *Journal of Hazardous Materials*, 174(1-3), pp.756-762.

Mehmood, A., Bano, S., Fahim, A., Parveen, R. and Khurshid, S., 2015. Efficient removal of crystal violet and eosin B from aqueous solution using Syzygium cumini leaves: A comparative study of acidic and basic dyes on a single adsorbent. Korean Journal of Chemical Engineering, 32(5), pp.882-895.

Mishra G, Tripathy M (1993) A critical review of the treatment for decolourization of textile effluent. *Colourage,* 40:35-38.

Mittal, A.K. and Gupta, S.K., 1996. Biosorption of cationic dyes by dead macro fungus Fomitopsis carnea: batch studies. *Water science and technology*, 34(10), pp.81-87.

Namasivayam, C. and Arasi, D.J.S.E., (1997). Removal of congo red from wastewater by adsorption onto waste red mud. *Chemosphere*, 34(2), pp.401-417.

Pearce, C. I., Lloyd, L. R, & Guthrie, J. T. (2003). Dyes pigment. *Journal of Industrial Microbiology and Biotechnology*, 58, 179-196.

Poots, V.J.P., McKay, G. and Healy, J.J., 1978. Removal of basic dye from effluent using wood as an adsorbent. Journal (Water Pollution Control Federation), pp.926-935.

Raj, R.M. and Asaithambi, M., 2014. Microwave Assisted Chemical Activation of Papaya Leaf Stem Activated Carbon for the Removal of Dyes from Aqueous Solution. *J. Environ. Nanotechnolgy*, 3(4), pp.91-95.

Reddy, M.S., 2006. Removal of direct dye from aqueous solutions with an adsorbent made from tamarind fruit shell, an agricultural solid waste. *Journal of Scientific and Industrial Research*, 65(5), p.443.

Sharma, P., Kaur, R., Baskar, C. and Chung, W. (2010). Removal of methylene blue from aqueous waste using rice husk and rice husk ash. *Desalination*, 259(1-3), pp.249-257.

Shokrollahi, A., Alizadeh, A., Malekhosseini, Z. and Ranjbar, M. (2011). Removal of Bromocresol Green from Aqueous Solution via Adsorption on Ziziphus nummularia as a New, Natural, and Low-Cost Adsorbent: Kinetic and Thermodynamic Study of Removal Process. *Journal of Chemical & Engineering Data*, 56(10), pp.3738-3746.

Sigmaaldrich.com. (2016). Bromocresol Green ACS reagent, Dye content 95 % | Sigma-Aldrich. [online] Available at http://www.sigmaaldrich.com/catalog/product/sial/114359?lang=en&region=MY [Accessed 20 Jul. 2016].

Slokar, Y. and Majcen Le Marechal, A. (1998). Methods of decoloration of textile wastewaters. *Dyes and Pigments*, 37(4), pp.335-356.

Suyamboo, B. (2012). Equilibrium, Thermodynamic and Kinetic Studies on Adsorption of a Basic Dye by Citrullus Lanatus Rind. *Iranica Journal of Energy & Environment*, 3(1), pp.23-34.

Waranusantigul, P., Pokethitiyook, P., Kruatrachue, M. and Upatham, E. (2003). Kinetics of basic dye (methylene blue) biosorption by giant duckweed (Spirodela polyrrhiza). *Environmental Pollution*, 125(3), pp.385-392.

Yeddou-Mezenner, N. (2010). Kinetics and mechanism of dye biosorption onto on untreated antibiotic waste. *Desalination*, doi:10.1016/j.desal.2010.06.023.

Zou, W., Bai, H., Gao, S. and Li, K., 2013. Characterization of modified sawdust, kinetic and equilibrium study about methylene blue adsorption in batch mode. *Korean Journal of Chemical Engineering*, 30(1), pp.111-122.

eureca 2016 – Conference Paper
Paper Number CE_PG01

Corrosion Study on Carbon Cold Rolled Steel with Pulsed Laser Ablation in Liquid

Sze Ney Chan[1*], Rashmi Gangasa Walvekar[1], Wai Yin Wong[2], Abdul Amir H. Kadhum[2]

[1] Taylor's University Lakeside Campus, Jalan Taylor's, Subang Jaya, 47500, Selangor, Malaysia;
[2]Fuel Cell Institute, University Kebangsaan Malaysia, Bangi, 43600, Selangor, Malaysia

szeney@gmail.com

Abstract
In the chase of enhanced performance and characteristics of metals in terms of surface properties and corrosion behavior, one of the solutions is to introduce pulsed laser ablation in liquid (PLAL) method for metal surface modification. Although many methods have been developed with the intent of preventing corrosion from occurring, most methods either requires chemicals, maintenance or high installation cost that are less environmental friendly. PLAL is seen to be a viable approach that enables one to modify the surface microstructure which is safe and economical as no poisonous or hazardous gases will be produced during the process. This study aims to investigate the effect of PLAL on the corrosion behavior and surface properties of laser ablated ASTM 1008 carbon cold rolled steel using fiber laser source. The laser ablated targets are characterised through scanning electron microscope (SEM) coupled with EDX, X-ray diffraction and electrochemical corrosion. From the observation of SEM and XRD, there are less corroded pits spotted on the laser-treated sample owing to the possibility of formation of magnetite upon subjection to laser treatment that acts as barrier against corrosion as well as formation of carbides that improve hardness and resistivity. In addition, corrosion study showed a lower corrosion rate of 21.82 mpy on laser-treated sample, as compared to that of the as-received sample (25.91 mpy). Electrochemical impedance spectroscopy also showed a value of 85.1% of inhibition efficiency on the laser-treated sample with respect to the as-received sample indicating the effectiveness of liquid pulsed laser ablation on inhibiting corrosion via surface modification.

Keywords: Surface modification; fiber laser; corrosion behavior, PLAL

1. Introduction

In recent years, manufacturing of metallic materials for commercial applications has grown significantly interest among the researchers. Metallic materials such as iron and aluminum have drawn attention especially in the field of electrical, medical therapy, industrial equipment as well as structural engineering. This is given that the metallic materials have high structural strength per unit mass, high thermal and electrical conductivity, high reflectivity and high resistance to shear or deform. However, there are certain properties that restrict the widespread application of metals in the structural uses such as inadequate strength and low resistivity to heat and corrosion. Meanwhile, fatigue, corrosion and wear failure of material are common phenomenon, implied that the materials are vulnerable to the environment and subsequently losing its original function.

Without any denies carbon steels are the essential classes of metals. From low end applications such as kitchenware, structural beams, and furniture to vehicles, the utilisation of stainless steels and carbon steels are necessary. Carbon steels are widely used throughout the world due to its good strength, desired ductility, ease of fabrication, availability, weldability and cost. Meanwhile, carbon steels, in particularly, the low carbon steel is also appeared to be imperfect since it is not strong for its weight, rust easily and cannot be made better by heat treatment. Despite of these drawbacks, carbon steel is still widely used as the most economical materials of construction under different conditions.

Corrosion is the deterioration of materials through chemical interaction with the environment where it also applied to the degradation of plastics, concrete and wood, although it is more commonly referred to metal. Electrochemical corrosion of metals occurs when electrons from atoms at the surface of metal are transferred to a suitable electron acceptor, water are present as medium for ions transport at the same time [1]. Corrosion affects the performance of process equipment and pipelines which results in the injuries to people, structural failure, product loss, environmental pollution as well as contamination leakage [2]. Corrosion is also a main economic issue where the World Corrosion Organization (WCO) appraises that the cost of corrosion worldwide is about $US 2.4 trillion annually which is 3% of the world's Gross Domestic Product (GDP) [3]. Apart from that, there are a total of 2313 hydrocarbon released cases reported from the offshore facilities in the duration of nine and half years according to the "Offshore Hydrocarbon Release Statistics and Analysis" report 2002-2003, Hazardous Installations Directorate (HID) Statistics Report [4]. This invisible corrosion damage leads to unpleasant accidents from benign effects to severe financial or even loss of life. It has been reported that 25% of all the safety accidents are due to corrosion, wear and degradation issues in the oil and gas industry [5].

There are many methods by using organic, inorganic coatings or surface modification to extend the working life and corrosion resistance of metals under aggressive condition. In order to improve the corrosion resistance, advanced technologies such as alloying, ion implantation, electron beam and laser beam are able to synthesis a surface modified layer that can delay corrosion [6]. As a matter of fact, alloying element such as Mo, Cr and Ni to enhance corrosion resistance of the stainless steels are cost consuming. In a contrary, surface modification of metal using

laser-induced applications is an improved technology that could alter parts of metal to receive different composition and microstructure with better properties. There are few types of laser-induced techniques such as laser surface melting, laser cladding and laser alloying [7]. For instance, Yue et al. [8] modify surface of Ti-6Al-4V alloy using excimer laser to improve corrosion behavior for dental applications. They revealed that the corrosion resistance in the alloys has increase for 7 times compared to the original. Meanwhile, Shadangi et al. [9] concluded that hardness of interstitial free steel increased when the pulse energy of the laser shock peening increases.

Pulsed laser ablation in liquid (PLAL) has become the novel technique for removing first atoms or molecules from the solid surface in a liquid environment due to the result of laser pulse [10]. Generally, PLAL is effective in covering intricate geometry and rather easy in modifying the surface composition with high speed, low processing time and easy operation [11]. Apart from that, water enable to cool the workpiece more effectively than gases given that water has extraordinary high heat capacity [20]. Hence, this technique could be able to induce surface properties by enhancing corrosion resistance, mechanical properties and biocompatibility of the uniform microstructures [11]. PLAL is relatively simple where there is no byproduct with the final product, thus no purification after synthesis is needed which is considered as being environmental friendly due to its "green techniques". With the ease in controlling laser parameters and being cost efficient, PLAL is thought to be an attractive technique in enhancing corrosion resistance via the modification of surface structure.

This research mainly emphasizes on the influence of "green technique", pulsed laser ablation in liquid (PLAL) method using fiber laser on ASTM 1008 carbon cold rolled steel in order to determine the corrosion behavior of this laser treated metal. The working environment of laser processing (air, water or vacuum) can be improved by introducing water as liquid environment since water is able to gain better results to deposition of debris and also cooled down the material. The metal targets are prepared by washing, polishing and cleaning to avoid rust formation and to ensure even surface obtained. Sample characterisation takes place to determine the effect of different sample surface modification with respect to surface morphology by using Scanning Electron Microscope (SEM). In order to determine the corrosion behavior of metal targets after the PLAL technique, electrochemical corrosion testing is conducted to determine the corrosion inhibition efficiency. The implemented approach in the corrosion studies are open circuit potential (OCP), electrochemical impedance spectroscopy (EIS) techniques and potentiodynamic polarization (PDP) in order to correlate the relationship on the metal surface modification with its localised corrosion resistance. This research is mainly focused on the corrosion behaviour and surface properties of laser-treated and as-received carbon cold rolled steel with a major objectives to investigate effect of PLAL on the modification of corrosion behavior & surface properties of ablated carbon cold rolled steel.

2. Materials and methods

2.1 Materials

Solid plate of ASTM 1008 carbon cold rolled steel with dimension of 2 x 0.7 cm with thickness of 1.2 mm are used as metal targets throughout the study. The composition

of the (wt.%) of each metals used are tabulated as shown in Table 1. 99% purity of sodium chloride for electrochemical corrosion testing are obtained from Chem Soln. Ethyl alcohol (C_2H_5OH) with 95% of purity and acetone (CH_3COCH_3) which were used as sample cleaning purposes were obtained from R&M Chemicals. In addition, 180 ml of ALS alumina suspension with size particle, 0.05 µm is purchased for metal polishing purpose.

- Table 1. Nominal chemical composition of metal used in the study (wt.%)

Types Of Metal	*C*	*Mn*	*P*	*S*	*Fe*
ASTM 1008 carbon cold rolled steel	0.15	0.60	0.10	0.05	99.1

2.3 Sample Preparation

In order to ensure sample's surface is even and smooth, mechanical polishing with SiC abrasive paper (grain size 500–2000) were performed to produce unvarying and smooth surface finish, free from mold contaminants. Subsequently, the sample targets were fine polished with 0.05 µm alumina suspension in accordance to ASTM standard E3-11[12]. Metal targets were ultrasonically clean with acetone and ethanol using Crest 5 Gallon Heated Ultrasonic Cleaner (4HT-1014-6, Crest Ultrasonics Corp.) for 20 minutes at the temperature of 50°C sequentially and air dried before storing. The cleaned and dry specimens were measured and weighed again to determine the weight lost. The samples were clean with ethanol and deionised water before performing laser irradiation.

2.4 Experimental Set Up

Laser ablation was conducted using a pulsed mode Ytterbrium-doped fiber laser (YLP-1-100-20-20-HC, IPG Photonics) with a maximum output power of 21 W. The laser beam output characteristics as follows: a wavelength, λ = 1064 nm, a pulse width ~ 100 ns. Vertical configuration was utilised for PLAL experiments to direct and focus the laser beam on the metal targets. The metal target were attached to a perspex block at the bottom of 800 ml of beaker glass vessel filled with ultrapure water up to 5 mm over the upper surface of the metal targets. At the same time, the vessel was fixed on an x-y motion stage (micro-positioner) for experimental displacement. Laser pulsed ablation was carried out in water with 4 different parameters which issues on the metal target surface, i.e. overlapping percentage, scanning speed, power of laser irradiation and number of laser pulses. Typically, 50 µm impact diameter was used to treat 6 x 4 cm rectangular metal targets. After laser ablation experiment, the metal targets were wiped with a clean paper and air dried. The obtained laser ablated metal targets were stored tightly in a sealed polyethylene zipper bags contained silica gels to avoid moisture. On the other hand, the liquid medium produced during the experimental work will be disposed as scheduled waste. The laser treatment conditions are shown in Table 2.

- Table 2. Laser processing parameters

Overlap rate, %	*Scanning speed, mm/s*	*Power of laser irradiation, %*	*Number of laser pulses*
60	2000	20	100000

2.5 Sample Characterization

1) 2.5.1 Electrochemical Corrosion Testing

Corrosion behavior of the samples was evaluated based on potentiodynamic polarization in 3.5 wt% NaCl, solution at 25°C using potentiostat (Gamry Instrument Potentiostat/Galvanostat/ZRA model Ref. 600). The conventional three electrode system is used for the corrosion testing with the working, counter and the reference electrodes that are consists of test samples metal, graphite electrode and saturated calomel electrode (SCE), respectively. The working electrode, i.e., the samples are slightly polished with 0.05 µm alumina suspension then ultrasonically degreased with acetone and ethanol for 10 minutes, sequentially prior any electrochemical corrosion testing based on the ASTM G1-03 [13]. The surface of the laser-treated and as-received samples are mounted into the corrosion cell setup with an exposed area of 1.0 cm^2, which is polished prior the test. The working electrode to be tested were subjected to exposure to the solution to stabilise the open circuit potential (OCP) for 1 hour indicated as corrosion tendency in solutions. Followed by electrochemical impedance spectroscopy (EIS) study at the measured over a frequency range of 10 kHz to 0.01 Hz, with a signal amplitude perturbation of 10 mV. Potentiodynamic polarization (PDP) measurement was carried out after OCP measurement from -200 to 200 mV (SCE) at a scan rate of 0.5 mV/s, in order to assure the former potential to achieve stable value before the test. The electrochemical measurement was initiated about 1 hour after the working electrode is exposed to the solution and measurement was performed until it reached the steady state potential. The values of E_{corr} and corrosion current density (i_{corr}) was calculated from the intersection of the cathodic and anodic Tafel curves extrapolated from the cathodic and anodic polarization curves. To ensure the accuracy of the experimental results, three different scans were performed to characterise each surface treatment to define an average value of the breakdown potential.

2) 2.5.2 Scanning Electron Microscope (SEM)

The surface morphologies on the received and laser metal targets surface were observed using Field Emission Scanning Electron (FESEM) equipped with Energy Dispersive Spectrometer (EDS) (FEI Model, Quanta 400F) with current beam of 1.1 nA. The EDS was employed simultaneously to analyse the elements content or chemical composition of the metal surface after PLAL experiment. The samples were scanned under magnification of 120 times to 20 k times with electron beam voltage of 10 kV. The metal samples were ultrasonically clean with ethanol in order to remove the oxide layer form during PLAL process before examined using FESEM and EDS.

3) 2.5.3 X-Ray Diffraction (XRD) test

The crystallographic structure and phase purity of the metal target on the received and laser-treated metal targets surface were investigated using high-angle X-ray diffractometer (Bruker/D8 Advance) in 2θ range from 20° to 90° equipped with Ni-

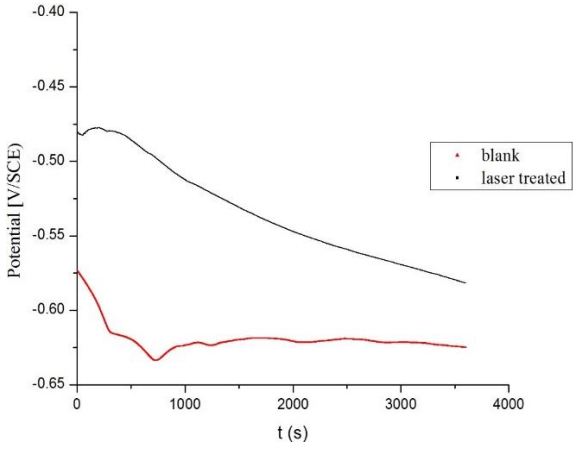
filtered Cu Kα radiation at room temperature with an accelerating voltage of 40kV and current of 40 mA. In order to obtain the accurate information about the oxides formed on the carbon cold rolled steel surface, the grazing incidence technique was adopted (small angle).

3. Results and Discussion

3.1 Electrochemical measurement

4) 3.1.1 Open circuit potential (OCP)

The open circuit potentials (OCP) is the free corrosion potential of experimental samples, indicating thermodynamically tendency of material to electrochemical oxidation in the solutions and it offers a benchmark for corrosion behavior of targets. After a certain period of immersion, it stabilise around steady value. In order to gather electrochemical impedance spectroscopy (EIS) data, the OCP must be allowed to reach a steady state. Figure 1 represent the OCP with time in in 3.5 wt.% NaCl solution at 25℃ for 1 hours, for the carbon cold rolled steel samples before and after laser treatment. From the observation of the curves as shown in Figure 1, variations in the time evolution of OCP values determined in both samples was observed. The duration needed to reach steady state was noted as half an hour. It was noticed that the OCP of as-received carbon cold rolled steel undergo cathodic fall at the beginning between 300-700 seconds from -0.573 V to -0.634 V; followed by slight fluctuation at the potential throughout 20 minutes. This cathodic fall indicated that oxide formed on the metal surface are getting weak due to removal of the thin surface oxides formed in air [14]. The instability of potential of as-received sample fell in the range between -0.573 V to -0.634 V. However, the potential may varied with time since changes in the nature surface of electrode such as formation of passive layer or oxidation may take place [15]. It is noticed that the OCP exhibited on the laser-treated sample reach a stationary OCP value 0.0958V more positive than the as-received sample.



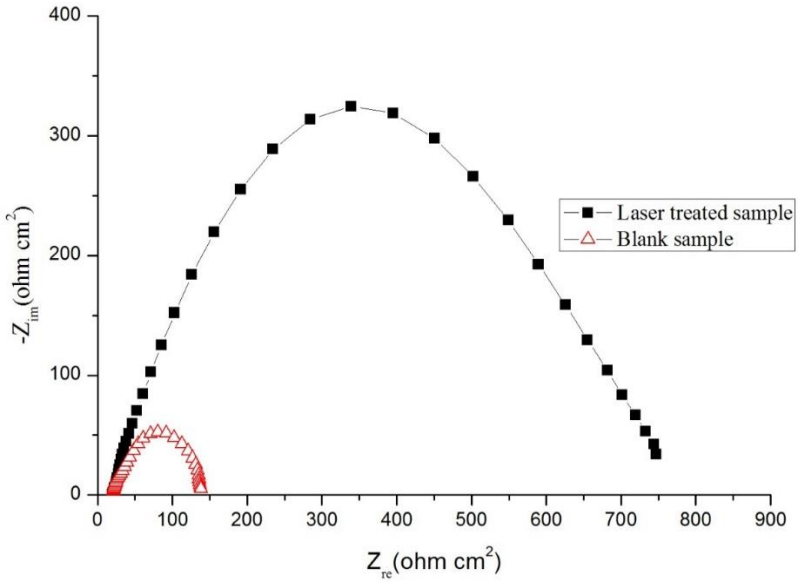
- Figure 1. OCP-time curves of as-received and laser-treated sample in 3.5 wt.% NaCl solution.

It was noted that laser-treated sample illustrated a slight rise in the corrosion potential from -0.483V at 44 seconds to -0.477V at 198 seconds but its tendency changes showing a withdrawal at the end of the sample period. This demonstrates that the corrosion rate with time increases for both samples. The potential rise represents film

growth on the surface of sample in the solution. From Figure 1, it can be concluded that the corrosion resistance with respect to time of laser-treated carbon cold rolled steel shown to be higher than the as-received/untreated carbon cold rolled steel attribute to the reason that the laser-treated sample exhibited the highest resistance to corrosion and demonstrate good oxidation behaviour. In other word, laser-treated sample revealed an enhancement the corrosion resistance of carbon cold rolled steel and also surface modification on the surface remarkably improved the corrosion resistance with respect to time.

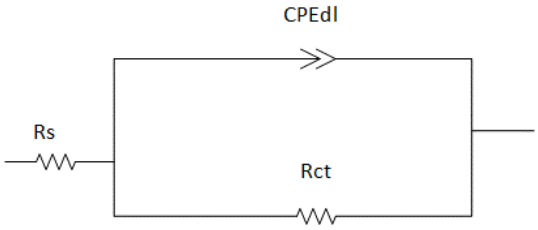
5) 3.1.2 Electrochemical Impedance Spectroscopy (EIS)

In order to further verify the corrosion resistance of the laser-treated and as-received carbon cold rolled steel, impedance measurement of the EIS is presented in the Nyquist plot of samples immersed in 3.5 wt.% solutions as shown in Figure 2. The Nyquist plot of the samples showed capacitive loop. The capacitive loop is also associated to the charge transfer of the corrosion process in the oxide film covering electrode surface [16]. It can be observed from Nyquist plot that the diameter of depressed semi-circle (R_{ct}) increased when the sample is treated with laser. Besides, it is also noted that diameter of Nyquist plot can determine the film inhibition as well as resistance of diffuse layer and resistance of corrosion product formed on the metal surface [17, 18].



- Figure 2. Nyquist plots of the EIS responses of laser-treated and as-received samples in 3.5 wt.%NaCl solution.

The equivalent circuit model used to fit the experimental results of laser-treated and as-received samples is shown in Figure 3. The components in the equivalent circuit include: a solution resistance, R_s, a constant phase element, CPE_{dl} and a charge transfer resistance, R_{ct}. The corroding surface carbon cold rolled steel in 3.5 wt.% NaCl solution is expected to be inhomogeneous due to its roughness after laser treatment; hence, the capacitance is required through a constant phase element (CPE) [19].



• Figure 3. Equivalent circuit model used to fit the impedance data for laser-treated and as-received carbon cold rolled steel.

The equivalent circuit component values are obtained and tabulated in Table 3. In order to validate the polarisation result, the inhibition efficiency (IE%) in 3.5w.% NaCl solution under study are calculated from the relevant electrochemical impedance data according to Eq.

$$IE\% = \frac{Rct - R^{\circ}ct}{Rct} \times 100$$

Where R_{ct} and R°_{ct} are the charge-transfer resistance with respect to laser-treated and as-received sample, respectively obtained from the curve fitting.

Double-layer capacitance (C_{dl}) values can be obtained using the following equation:

$$C_{dl} = \frac{1}{2\pi f_{max} R_{ct}}$$

Where f_{max} is the frequency values at which the imaginary component of the impedance is greatest.

The magnitude of R_{ct} increased while the value of double layer capacitance (C_{dl}) decreased which result to an increase in the inhibition efficiency. This increase in R_{ct} value observed on the laser-treated sample signifies that a great amount surface coverage due to the metal surface resistivity without altering the corrosion mechanism was present. Meanwhile, C_{dl} decreases for laser-treated sample implies a decrease in the local dielectric constant or an increase in the thickness of the electrical double layer; representing that there is a formation of protective layer on the metal as a results of PLAL treatment [20].

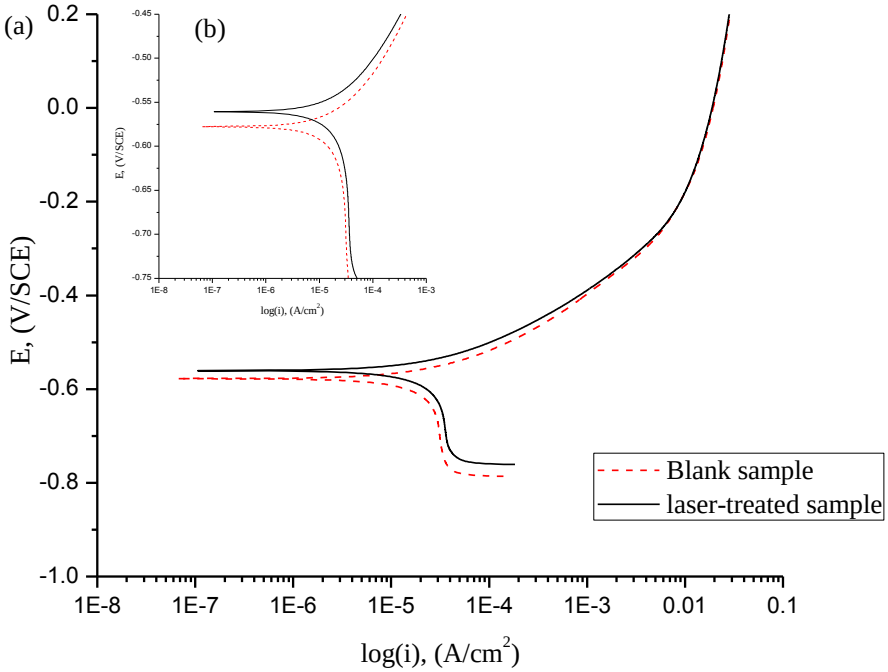
• Table 3. Electrochemical impedance parameters and inhibition efficiency of carbon cold rolled steel in 3.5 wt.% NaCl at 25°C.

Sample	R_s (Ωcm^2)	R_{ct} (Ωcm^2)	f_{max} (Hz)	C_{dl} (μFcm^{-2})	Goodness of Fit	IE%
Laser-treated	21.04	593.4	36.41	7.3663	8.72E-03	85.10617
As-received	19.53	88.38	32.32	55.718	1.04E-03	-

6) 3.1.3 Potentiodynamic polarization (PDP) measurement

Figure 4 shows the results from potentiodynamic polarization (PDP) of laser-treated and as-received sample in 3.5 wt.% NaCl solution at 25°C. The magnified Tafel

regions of the polarization curves are shown. In order to determine the corrosion mechanisms of carbon cold rolled steel, samples were immersed in the electrolyte at the OCP value for 20 minutes. The relevant corrosion potential (E_{corr}) and corrosion current density (i_{corr}) calculated using Tafel extrapolation method were tabulated in Table 4.



- Figure 4. (a) Polarisation curve of the carbon cold rolled steel samples immersed in 3.5 wt.% NaCl solution with blank and laser-treated sample; (b) magnified Tafel region of the polarization curve shown in (a).

The as-received sample demonstrated a typical polarization curve of an active material. However, the laser-treated sample improved its corrosion behavior compared to the as-received sample. After applying cathodic polarization, the laser-treated sample exhibited a shift in E_{corr} towards noble direction and the value of I_{corr} decreased conversely. From the curve, it was indicated that the corrosion resistance of laser-treated sample is relatively higher compared to as-received sample, revealed that there is existence of protective film on the surface of the laser-treated sample.

- Table 4. The results of potentiodynamic corrosion test in 3.5 wt.% NaCl solution.

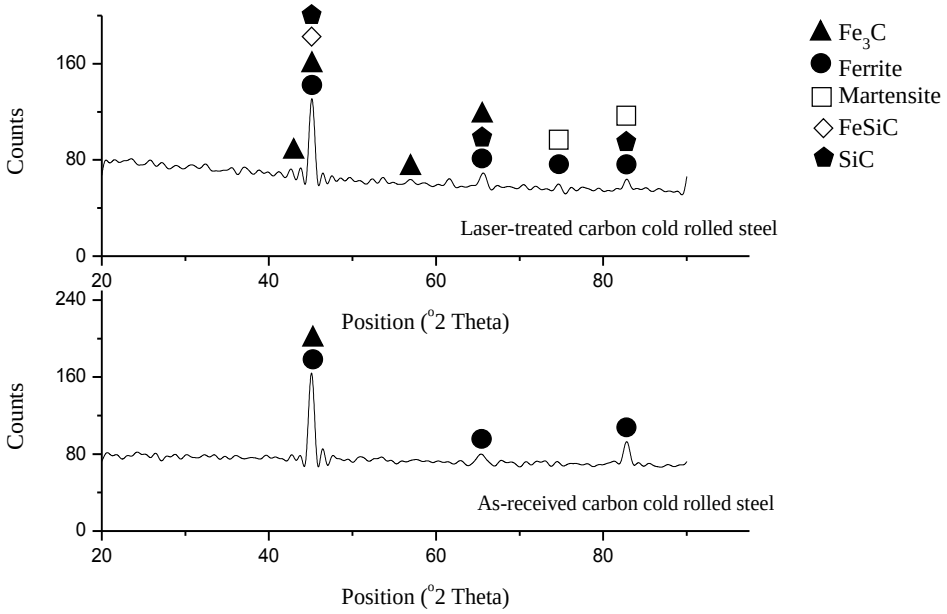
Sample	E_{corr} (mV)	I_{corr} (μA/cm^2)	Corrosion rate (mpy)
As-received	-578.0	57.30	25.91
Laser-treated	-560.0	48.30	21.82

The corrosion current densities of laser-treated and as-received samples were 48.30 μA/cm^2 and 57.03 μA/cm^2, respectively. It is noted that corrosion resistance is directly proportional to corrosion potential, E_{corr} but inversely proportional to corrosion current density, I_{corr}. From Table 4, it can be observed that E_{corr} shift to more positive values and i_{corr} is greatly decreasing after being laser-treated. This implies that there is considerable enhancement of carbon cold rolled steel surface

condition after PLAL. According to study [6], there are presence of oxides and fine grains form which lead to different corrosion properties. These compact oxide layer can act as protective barrier to protect the carbon cold rolled steel against corrosion phenomena. For the laser-treated sample that treated at 60% overlap rate, the passive current density is reduced by more than one order of magnitude indicating higher corrosion resistance it exhibited. The corrosion potential shift to more noble value involved a larger passive range which indicate additional heat treatment as a result of overlapping laser spot that influence microstructure and chemical composition of the metal surface [21]. Besides, it is clear from Table 4 that the laser-treated carbon steel exhibited a more noble corrosion potential and about 18mV higher than as-received sample, displayed that the laser-treated sample effectively enhanced the corrosion resistance of carbon cold rolled steel. From Table 4 revealed that PLAL technique has remarkably reduced the corrosion rate to 15.7% as compared to as-received carbon cold rolled steel in a 3.5 wt.% NaCl solution.

3.2 X-Ray Diffraction (XRD) Test

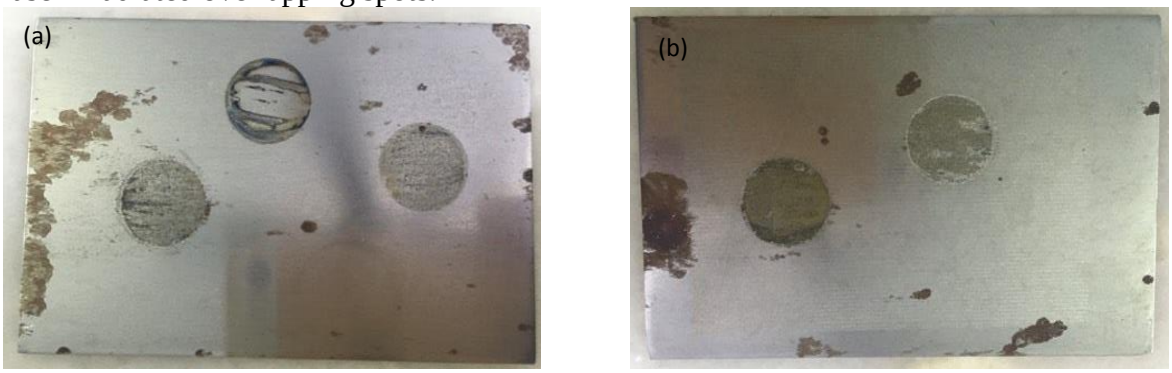
Figure 5 shows X-ray diffraction (XRD) profiles of the as-received sample and PLAL treated sample. After PLAL treatment, there are noticeable alteration occur in phase composition on the metal surface. From Figure 5(b), it can be observed that high peak of ferrite occur at 49° and other low peak of ferrite occur twice at 65.3° and 83.1°, respectively. Besides of the ferrite peaks from the samples, the laser treated sample comprise some additional diffraction peaks. This revealed that presence of different forms of iron carbides in the as-received as well as laser treated sample. It is also noted that presence of cementite (Fe_3C), martensite, FeSiC and silicon carbide (SiC) element as shown in Figure 5(a) denoted that FeSiC, SiC and along with martensite are accountable to enhance the hardness of the steel [22]. The appearance of Si as detected in EDX (Figure 8(b)) was possibly due to that Si exists as the impurities in carbon cold rolled steel. Upon laser ablation, Si may react with carbon in the steel chemically to form carbide that was later uncovered on the metal surface. In addition, the presence of martensite that usually formed due to rapid cooling effect known as annealing which offer harder and resistant steel [19]. Furthermore, the amount and intensity of ferrite peak decreases when it is treated with laser, indicating that increment of surface roughness of metal after PLAL treatment [22]. It is obvious that the Bragg diffraction peak of the laser-treated sample is seem to be fairly broader than the as-received sample due to the grain refinement and increase in the atomic level lattice strain in the laser-treated sample [9].



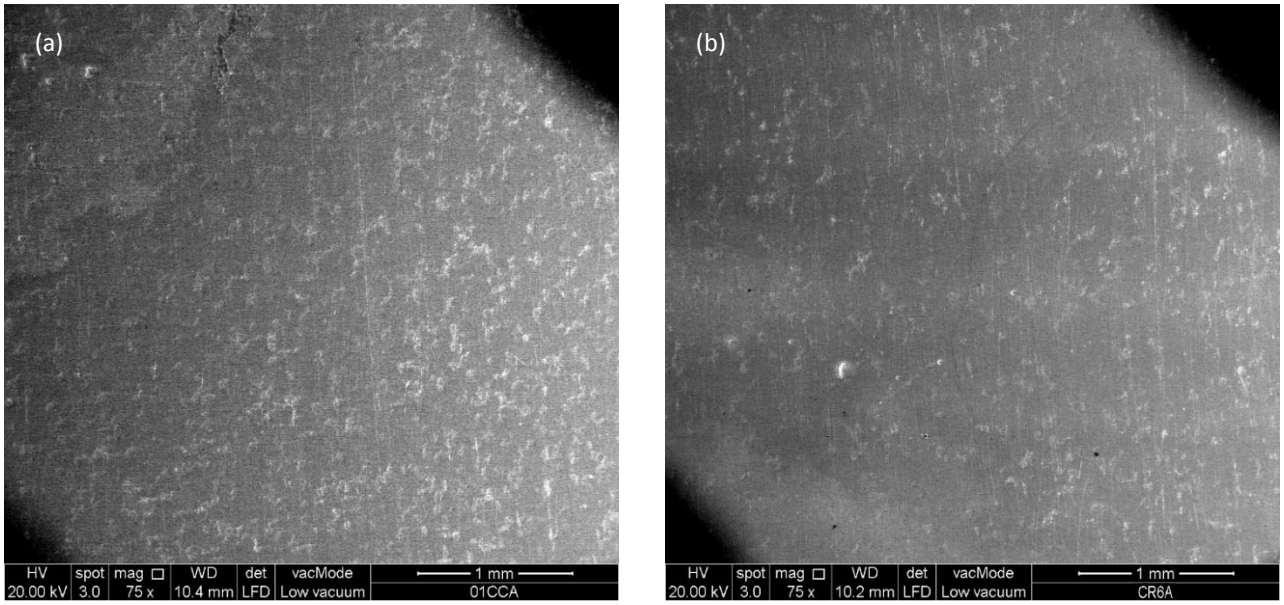
- Figure 5. X-ray diffraction profiles of (a) laser-treated carbon cold rolled steel and (b) as received

3.3 Surface morphology and microstructure

SEM analysis allows the inspection on the nature of specimens that has endured corrosion during the electrochemical corrosion analysis as well as received sample. This analysis is essential to further validate, support and discuss the corroded behavior exhibited by stainless steel and carbon cold rolled steel in electrochemical corrosion analysis. Figure 6 shows the captured image of metal plate after undergo electrochemical measurement (corrosion process). Figure 7 shows the surface morphologies of sample before and after treated with laser. Laser-treated surface composes of regular laser scanning tracks as shown in Figure 7(b), which are mainly shaped by overlapping of laser irradiated spots. This is due to laser beam that irradiate the metal surface via repetitive pulse of high frequency (100kHz) which results to laser irradiated overlapping spots.

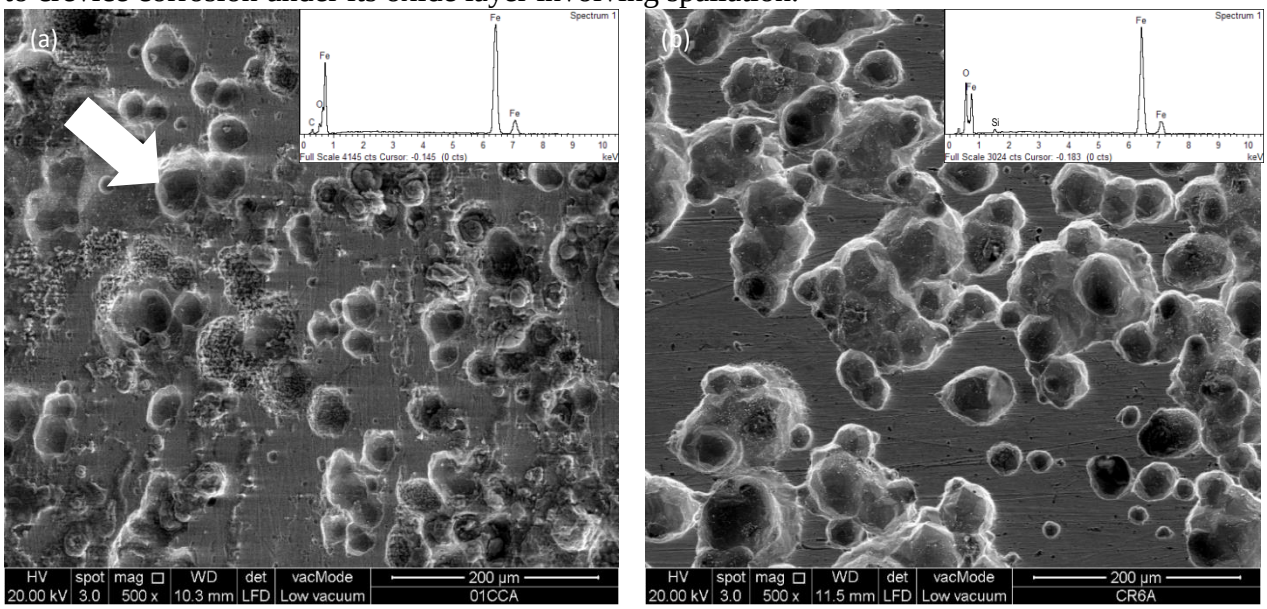


- Figure 6. Image of metal plate (a) as-received sample; (b) laser-treated sample with corroded spot.



- Figure 7. Surface observation by SEM of as-received sample and laser-treated samples. (a) carbon cold rolled steel as-received; (b) laser treated with 60% overlap rate sample

As shown in Figure 7 surface observations by SEM of the both samples shown that the oxide layer of the laser-treated sample with 60% overlap rate is homogeneous are beneficial to prevent Cl^- (from NaCl solution) whereas the surface of the as-received sample exhibit a lot of small and scattered voids on the surface. In a contrary, laser treated surface is free from voids and crack networks which represent that thermal stress is slightly lower compared to as-received sample . Therefore, it can be understand that electrolyte can be able to penetrate into the oxide layer which led to crevice corrosion under its oxide layer involving spallation.



- Figure 8. Corroded surface of the (a) as-received sample; (b) laser-treated sample with relevant EDX result respectively.

Apparently, severe corrosive attack where a dense layer of corrosion products are seen for the as-received sample exposed to NaCl. It is observed that the grain in the laser-treated sample surface as indicated with white arrow in Figure 8 where the grains after corrosion are larger and more uniform in size as compared to the as-received sample where appearance of grain is irregular as a result of severe corrosion attack. In addition, the corrosion pits on the laser-treated sample are slightly lesser and uniform compared to as-received sample.

EDX analysis in Figure 8 showed that there was a significant increment in oxide content on the laser treated sample after corrosion in comparison to the untreated sample. Although it was well noted that the oxide layer formed on the carbon steel has a positive correlation with the degree of corrosion, yet, it was shown differently in our results. In this study PLAL treatment was shown to result in significant improvement on corrosion resistance despite large amount of oxide formed on laser treated sample after corrosion as mentioned. Hence, it is suspected that PLAL treatment was able to produce a homogeneous iron oxide on the surface which is identified as magnetite (Fe_3O_4). Magnetite is commonly known as protective metal oxide film that acts as barrier against corrosion which passivate iron and retard further corrosion due to its low solubility in the moist condition (solubility in aqueous environment is a measure of stability)[23, 24]. Hence, it is possible that appearance of larger grains of laser treated sample are magnetite that are able to inhibit corrosion on the surface.

In summary, this study has shown that the laser treatment has successfully improved the corrosion resistance of carbon cold rolled steel without the need of coating or addition of inhibitor. Through physicochemical and electrochemical analysis, it is likely that this improvement is attributed to two possible reasons: (1) the effect of chemical reaction occur on the metal surface that resulted in the carbide formation that hardened the metal surface, and (2) the formation of magnetite that passivate the corrosion on the metal surface.

4.0 Conclusion

In the present investigation, PLAL technique seems to be able to enhance the corrosion resistance and surface microstructure properties of ASTM 1008 carbon cold rolled steel. Some important conclusion can be made that where fiber laser impacts effectively which lead to considerably enhancement on electrochemical resistance and change of corrosion pits morphology of carbon cold rolled steel. Corrosion resistance of carbon cold rolled steel was enhanced with a shift of potential up to 18 mV higher than as-received sample as well as EIS also showed a value of 85.1% of inhibition efficiency on the laser-treated sample with respect to the as-received sample. This relatively reflects the effectiveness of liquid pulsed laser ablation on inhibiting corrosion via surface modification where uniform microstructure are shown. This phenomenon may attributed to the surface layer with compressive residual stress and refine grain induced by fiber laser source. From the observation, laser-treated surface has enhanced the corrosion resistance of carbon cold rolled steel due to formation of carbide results to surface hardening and composition of oxide that acts as passivating film. Therefore, elaboration of pulse laser ablated in liquid water (PLAL) with the metal surface arise an uprising alternative with its improved hardness as well as

corrosion behavior for application as basic elements (metal element) in the major areas such as building construction, transportation, manufacturing, biomaterial and so on.

References

[1] N. D. H. University, "Corrosion," N. D. H. University, Ed., ed: National Dong Hwa University, p. 38.

[2] J. Bhandari, F. Khan, R. Abbassi, V. Garaniya, and R. Ojeda, "Modelling of pitting corrosion in marine and offshore steel structures – A technical review," *Journal of Loss Prevention in the Process Industries,* vol. 37, pp. 39-62, 2015.

[3] J. A. M. V. D. W. J.C. Velázquez, Enrique Hernández, Héctor Herrera Hernández, "Statistical Modelling of Pitting Corrosion: Extrapolation of the Maximum Pit Depth-Growth," *International Journal of Electrochemical Science of Advanced Materials,* 2014.

[4] H. S. Executive, "HSE Offshore: Offshore Hydrocarbon Releases Statistics, 2002," 2003.

[5] M. B. Kermani and A. Morshed, "Carbon Dioxide Corrosion in Oil and Gas Production—A Compendium," *Corrosion,* vol. 59, pp. 659-683, 2003.

[6] C. Y. Cui, X. G. Cui, Y. K. Zhang, Q. Zhao, J. Z. Lu, J. D. Hu, *et al.*, "Microstructure and corrosion behavior of the AISI 304 stainless steel after Nd:YAG pulsed laser surface melting," *Surface and Coatings Technology,* vol. 206, pp. 1146-1154, 2011.

[7] R. C. o. A. Condea, R. Vilarb, J. de Damborenea, "Corrosion behaviour of steels after laser surface melting," 2000.

[8] T. M. Yue, J. K. Yu, Z. Mei, and H. C. Man, "Excimer laser surface treatment of Ti–6Al–4V alloy for corrosion resistance enhancement," *Materials Letters,* vol. 52, pp. 206-212, 1// 2002.

[9] Y. Shadangi, K. Chattopadhyay, S. B. Rai, and V. Singh, "Effect of LASER shock peening on microstructure, mechanical properties and corrosion behavior of interstitial free steel," *Surface and Coatings Technology,* vol. 280, pp. 216-224, 2015.

[10] I. Carrasco-García, Vadillo, José M., Javier Laserna, J., "Visualization of surface transformations during laser ablation of solids by femtosecond pump–probe time-resolved microscopy," *Spectrochimica Acta Part B: Atomic Spectroscopy,* vol. 113, pp. 30-36, 2015.

[11] M. T. Mohammed, Z. A. Khan, and A. N. Siddiquee, "Surface Modifications of Titanium Materials for developing Corrosion Behavior in Human Body Environment: A Review," *Procedia Materials Science,* vol. 6, pp. 1610-1618, 2014.

[12] A. International, "ASTM Standards Related to Corrosion Testing of Metals ", ed, 2013.

[13] A. G, *ASTM G1 - 03(2011) Standard Practice for Preparing, Cleaning, and Evaluating Corrosion Test Specimens*. West Conshohocken, PA: ASTM International, 2011.

[14] Y. Ait Albrimi, A. Ait Addi, J. Douch, R. M. Souto, and M. Hamdani, "Inhibition of the pitting corrosion of 304 stainless steel in 0.5M hydrochloric acid solution by heptamolybdate ions," *Corrosion Science,* vol. 90, pp. 522-528, 2015.

[15] Y. S. Jiménez, M. T. Gil, M. T. Guerra, L. S. Baltes, and J. C. M. Rosca, "Interpretation of open circuit potential of two titanium alloys for a long time immersion in physiological fluid," *Bulletin of the Transilvania University of Brasov, Series I: Eng;2009*, vol. Vol. 2, p. p197, 2009.

[16] A. A. El Maghraby, "Corrosion Inhibition of Aluminum in Hydrochloric Acid Solution Using Potassium Iodate Inhibitor," *The Open Corrosion Journal*, vol. 2, 2009/7/03 2009.

[17] M. Özcan, İ. Dehri, and M. Erbil, "Organic sulphur-containing compounds as corrosion inhibitors for mild steel in acidic media: correlation between inhibition efficiency and chemical structure," *Applied Surface Science*, vol. 236, pp. 155-164, 9/15/ 2004.

[18] A. Döner and G. Kardaş, "N-Aminorhodanine as an effective corrosion inhibitor for mild steel in 0.5 M H2SO4," *Corrosion Science*, vol. 53, pp. 4223-4232, 12// 2011.

[19] J. R. J. Marcuci, E. C. d. Souza, C. C. Camilo, P. L. Di Lorenzo, and J. M. D. d. A. Rollo, "Corrosion and microstructural characterization of martensitic stainless steels submitted to industrial thermal processes for use in surgical tools," *Revista Brasileira de Engenharia Biomédica*, vol. 30, pp. 257-264, 2014.

[20] M. Benabdellah, A. Tounsi, K. F. Khaled, and B. Hammouti, "Thermodynamic, chemical and electrochemical investigations of 2-mercapto benzimidazole as corrosion inhibitor for mild steel in hydrochloric acid solutions," *Arabian Journal of Chemistry*, vol. 4, pp. 17-24, 1// 2011.

[21] W. Pacquentin, N. Caron, and R. Oltra, "Nanosecond laser surface modification of AISI 304L stainless steel: Influence the beam overlap on pitting corrosion resistance," *Applied Surface Science*, vol. 288, pp. 34-39, 2014.

[22] S. Sarkar, M. Gopinath, S. S. Chakraborty, B. Syed, and A. K. Nath, "Analysis of temperature and surface hardening of low carbon thin steel sheets using Yb-fiber laser," *Surface and Coatings Technology*, vol. 302, pp. 344-358, 9/25/ 2016.

[23] K.-S. Jung and K.-W. Sung, "Magnetite: Electrochemical Properties And Its Role On Flow Accelerated Corrosion," ed: Nova Science Publishers», Daejeon, 2010.

[24] H.-P. Hermansson, *The stability of magnetite and its significance as a passivating film in the repository environment*: Statens kärnkraftinspektion, 2004.

eureca 2016 – Conference Paper
Paper Number CE_PG02

A Novel Approach in Using Membrane Reactors for Enzymatic Hydrolysis of Cellulose

Thao Thy Nguyen Huynh[1], Rajesh Nithyanandan[1*], Chien Hwa Chong[1], Duduku Krishnaiah[2]

[1]*School of Engineering, Taylor's University, Malaysia*
[2]*Faculty of Engineering, University Malaysia Sabah, Malaysia*

[*]Rajesh.Rajasekaran@taylors.edu.my

Abstract
Enzymatic hydrolysis is known to be the key step in the production of bioethanol fuel from cellulose based feedstock. The incorporation of ultrafiltration membrane in the reactors, known as membrane reactors has been effectively solved some issues which are the limiting factors of the batch reactor such as product inhibition and enzyme recovery. In this research, the modified membrane reactor which was introduced in the previous work was further investigated by looking its operation, process optimisation and potential of reusing enzymes. It is found that the low concentration of glucose at the permeate of the ultrafiltration membrane was due to the over-dilution of buffer when continuous product removal was practised as reported in the literature. Instead, intermittent product removal at 50% volume is more favoured to result in a higher glucose concentration profile and save cost as well as time for pumping. Operation of the modified membrane reactor is independent of the cellulose concentration since variation of it have an insignificant effect on the production of glucose. A regression model developed by response surface methodology - Box Behnken design is well-fitted to represent the relationship of three factors (cellulose concentration, enzyme to substrate (E/S) ratio and product removal). As a result, it is found that the E/S ratio and the interaction between cellulose concentration and degree of product removal are the most significant factors for hydrolysis conducted in the membrane reactor. To maximise the glucose concentration, optimal conditions for the membrane reactor are 10% cellulose concentration, 6% E/S ratio and 50% volume for product removal. With an effective retain of enzymes by the ultrafiltration membrane for the reusing purpose, the process is highly able to extend for longer period of time to continue hydrolysing fresh pretreated cellulose with an insignificant reduction in the glucose concentration.

Keywords: Membrane reactors, Ultrafiltration, Inhibition, Glucose removal, Hydrolysis of cellulose.

1. Introduction

In the recent years, the world has slowly recognised the 'high price' to pay for industrialisation, continuous advancement in technology and urbanisation is the exchange of depletion of natural resources and environmental pollution. Without sacrificing the need of the future generation, this is when sustainable development becomes of paramount importance; not only to embrace but to consider how to incorporate it in every development sector of the global organisations and countries. One of three crucial pillars in sustainable development is the environmental stewardship which involves affordable and clean energy with responsible consumption and production [1].

In the search for a new source of energy, the criteria of being renewable and alternative should be the priorities to consider the fore front. Bioenergy, especially cellulosed-based bioethanol is a very potential alternate to replace fossil fuel, as it is carbon-neutral, and more favourable than the first generation ethanol production from corn and sugar. Agricultural and forestry residues such as palm empty fruit bunches, corncob, sugar bagasse, rice/wheat straw and chip wood having a high cellulose content (30%-50%) is able to reutilise for conversion from sugar to bioethanol fuel [2].

The production of bioethanol from cellulose consists of four main processes, i.e. pretreatment, hydrolysis, fermentation and purification as shown in Fig. 1. Enzymatic hydrolysis is the key step which is responsible for an efficient conversion of pretreated cellulose to fermentable hydrolysate which is rich in glucose for the subsequent fermentation and purification to obtain bioethanol [3, 4].

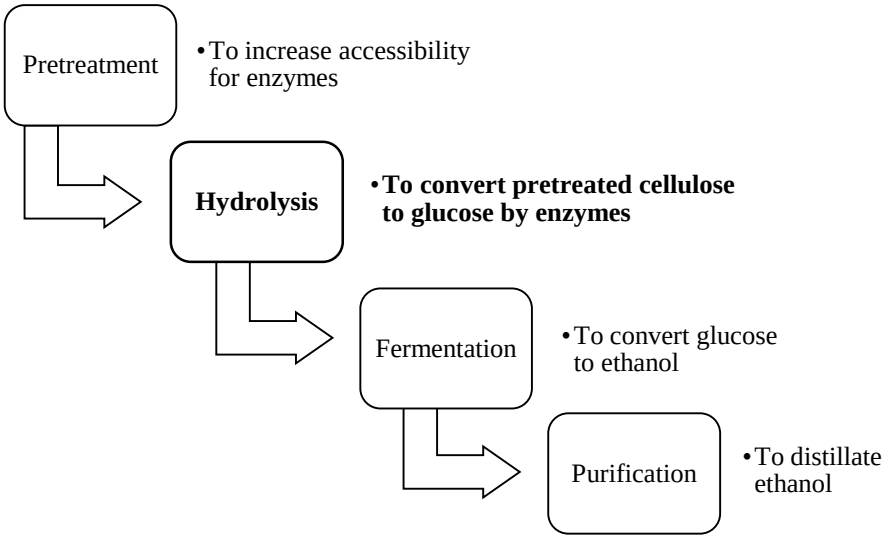


Figure 9. Bioethanol process from cellulose feedstock.

The enzymatic hydrolysis of cellulose is a complex reaction system, which involves an interfacial heterogeneity of solid cellulose substrate, cellulase enzyme adsorption, inhibition of glucose and cellobiose on enzymes [5, 6]. However, the use of reactors in the batch mode or batch reactors has been practising conventionally. Therefore, it results in severe product inhibition and high enzyme cost which are known as the major challenges making the process far from being economically and technologically feasible. As the glucose accumulates inside the batch reactors during

hydrolysis, it becomes an inhibitor on enzymes and rapidly retards the reaction [7]. Simultaneously the consumption of cellulase enzymes contributes significantly 20% of the total cost of the entire ethanol process and 50% of the hydrolysis process, while these enzymes are able to be recycled and reused for a longer period of time [8, 9]. To overcome these challenges, research in enzymatic hydrolysis has been working on different approaches from simultaneous saccharification and fermentation (SSF), developing new enzymes with higher tolerance for glucose inhibitor to improvement in pretreatment step [10]. Among all, integrating a membrane separation in the hydrolysis reactors is proved to be the promising approach as a process intensification which has attracted an increasing interest in research these days with a large numbers of publications from 35 to 200 over the last ten years [3].

The membrane integration approach with two configurations of membrane reactors, i.e. external loop and submerged membranes, has effectively solved two main issues. Ultrafiltration used in the membrane reactors allows an effective removal of glucose from the reactor to the permeate, hence minimises product inhibition. While enzymes are rejected by the membrane and retained inside the reactor for continuing hydrolysis of cellulose. However, for membrane reactors to be more applicable in hydrolysis it requires research to further look at other aspects which are still the limiting factors. They are low concentrations of glucose at the permeate, occurrence of membrane fouling, and enzyme recovery limited at the liquid phase [7, 11].

In our previous work, a new configuration of the submerged membrane reactor was proposed for testing. The study was able to obtain some preliminary results showing to be suitable for carrying enzymatic hydrolysis to minimise product inhibition and recover enzymes in the liquid phase [12]. In this present work, the modified membrane reactor was further explored by looking into its operations at different product removal modes, variation in cellulose concentrations, process optimisation, and potential of reusing the enzymes for hydrolysis of fresh cellulose.

1. Aim

To further investigate the technical feasibility of the proposed configuration of the submerged. membrane reactor applied in the enzymatic hydrolysis process.

2. Methodology

2.1. Materials

Cellulase enzymes (Cellic CTec2) was provided by Novozymes (China) Investment Co. Ltd as free samples. The enzymes are a complex blending of aggressive cellulases, with high level of β-glucosidase [13]. Citrate buffer pH 5.0 was prepared by using citric acid purchased from Bendosen (M=210.14 g/mol, assay: 99.0%), and sodium citrate purchased from Systerm (dehydrate, M=294.10 g/mol, assay: >99.0-100.5%). The other chemicals such as sodium hydroxide used for pretreatment, sulfuric acid, glucose and cellobiose used in the experiments were at standard grade.

Microcrystalline cellulose is in power form, purchased from Sigma Aldrich (Code:435236). Prior to enzymatic hydrolysis, cellulose was pretreated with sodium

hydroxide (NaOH) 0.5M solution in a boiling water batch for three hours to make it more susceptible for the adsorption of enzymes [10, 12, 14]. Concentrations of cellulose in pretreatment were 10%, 15% and 20% (w/v). Cellulose after pretreatment was washed three time with distilled water to drain out the residual NaOH, preserved in distilled water at room temperature and ready to be used for hydrolysis.

Ultrafiltration disk membranes are made of polyethersulfone (PES), with molecular weight cut off 10 kDa, diameter 25 mm, from Satorius Stedim Biotech GmbH, Germany.

A small, porous and sealed bag/infuser made of fibre was used to contained cellulose and immersed in the membrane reactor.

2.2. Experimental design of the modified membrane reactor

The modified submerged membrane reactor proposed in this work is shown in Fig.2. In this set-up, the enzymatic hydrolysis of cellulose was carried out simultaneously with glucose removal and enzyme recovery. A 500 ml beaker placed on a thermo-magnetic stirrer was used as a reactor tank. The solid and liquid phases inside the reactor were separated by the sealed bag/infuser as a phase separation. Specifically, the solid phase is pretreated cellulose contained inside the sealed bag immersing in the liquid phase which is a mixture of enzymes and citrate buffer. As the hydrolysis reaction was being carried out, glucose was released from cellulose and infused via the sealed bag into the liquid hydrolysate. A filtration device as represented in Fig. 3 consisted of an ultrafiltration membrane attached to a nozzle which was secured by a ring and submerged in the reactor. A tubing connection between the filtration device to a glucose storage container via a peristaltic pump to remove glucose solution from the reactor. Due to the removal of glucose from the reactor, a supplement of citrate buffer to the reactor was needed in order to maintain a constant volume for the reaction in the system.

The arrangement of the sealed bag and the ultrafiltration device both immersing in the membrane reactor is the novelty in this research in term of creating a new configuration for the submerged membrane reactor used for hydrolysis of cellulose. In other research work, fouling due to the deposition of solid cellulose on the surface of the membrane caused an interruption during ultrafiltration taking place where a complete mixing of cellulose, enzymes and buffer was applied, and hence, affected hydrolysis process [6, 15, 16]. This issue of fouling occurred in both the submerged membrane reactor (membrane located inside the reactor) and external loop membrane reactor (membrane located outside the reactor as a separated unit) [11]. In this new configuration of the submerged membrane reactor, the immersed sealed bag containing cellulose would help to prevent membrane fouling without affecting the access of enzyme to cellulose substrate. The liquid phase which was rich in glucose infusing from cellulose in the sealed was removed easily by the ultrafiltration membrane without allowing enzymes to pass through, thus enzymes were retained inside reactor.

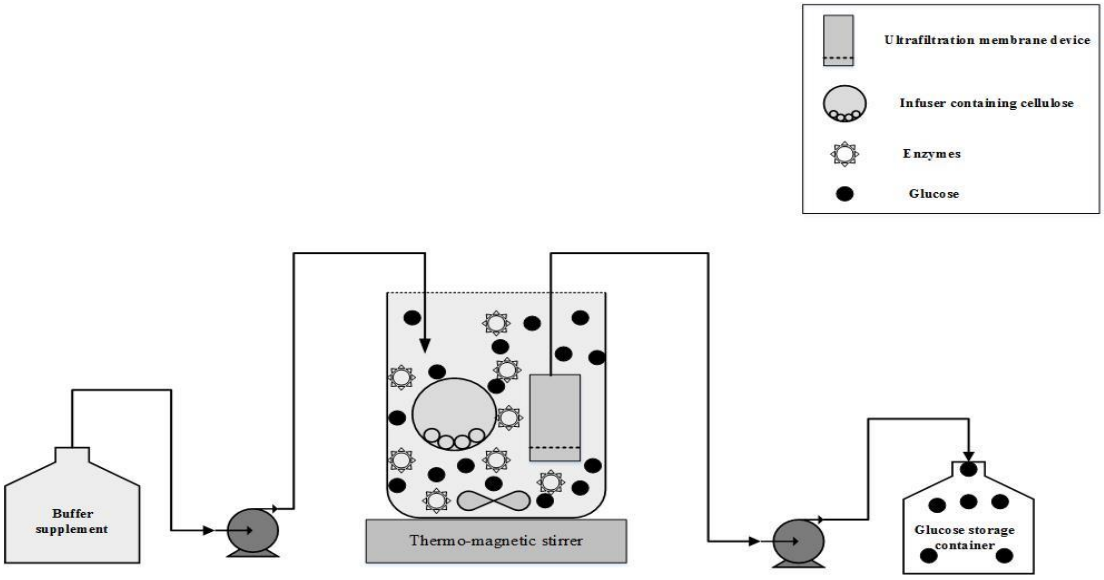


Figure 10. A schematic of the modified membrane reactor [12].

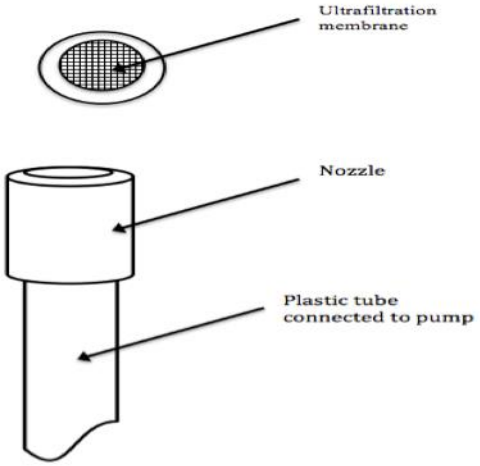


Figure 11. A representation for the ultrafiltration membrane device [12].

In this work, a number of experiments were designed to further test this modified submerged membrane reactor on its performance in enzymatic hydrolysis of cellulose. First, operation of the membrane reactor was tested with different modes of product removal and variation in cellulose concentrations. Secondly, the process was optimised to maximise the glucose concentration with three factors (cellulose concentration, enzyme to substrate ratio, and volume removal). Lastly hydrolysis conducted at the optimal conditions was continued to hydrolyse fresh pretreated cellulose by reusing enzyme. All experiments were conducted in duplicate.

2.3. Analytics

High performance liquid chromatography (HPLC) analysis is used to quantify the glucose and cellobiose concentrations. Condition for HPLC analysis is Agilent (Model: 1220 Infinity) with Hi-Plex H column for glucose and cellobiose, mobile phase: 0.005 M sulphuric acid, isocratic gradient, flow rate 0.7 ml/min, injection volume 20 μm, temperature 60 ºC, pressure 4.6 MPa, and refractive index detector,

retention times of 10-15 minutes according to the instruction of Agilent and method of Lozano et al. [17]. Two calibration graphs were constructed for glucose and cellobiose with the R^2 values of 0.99819 and 0.99905 respectively.

The rate of hydrolysis reaction is the rate of change of the glucose concentration measured by HPLC analysis as shown in Eq. (1).

$$\frac{dG}{dt} = \frac{\Delta G}{\Delta t} \quad \text{.....(1)}$$

Where, G is the concentration of glucose (mg/ml) and t is hydrolysis time (minute).

Some statistical analysis such as independent T-test and analysis of variance (ANOVA) were applied for testing the significant difference by using IBM SPSS Statistics 20 software.

Design Expert DX 7 software was used for developing a regression model in the process optimisation to represent the relationship between factors (independent variables) and the response (dependent variables).

3. Results and discussion

The proposed membrane reactor was further investigated to evaluate its technical feasibility in applying for enzymatic hydrolysis of cellulose. Results obtained from experiments were presented by dividing into four sections including operation of the modified membrane reactor in term of product removal modes and variation in cellulose concentrations; process optimisation; and potential reuse of enzymes.

3.1. Different modes of product removal

Although being a product released from enzymatic hydrolysis of cellulose, glucose is a strong inhibitor on the enzymes, and causes to retard the reaction [4, 7]. Therefore, the presence of glucose in the reactor is not desired and removal of glucose by ultrafiltration membrane is necessary to minimise product inhibition. However, the degree or amount of glucose removed from the reactor should be quantified because it can affect conversion of cellulose in hydrolysis, glucose concentration at permeate and product inhibition.

Based on the reaction volume studied in this work (400 ml), three modes of product removal were tested, i.e. continuous and intermittent removal at 50% and 100% volume by starting ultrafiltration after 3 to 4 hour hydrolysis in batch mode. Glucose concentration profiles during the enzymatic hydrolysis are presented in Figs. 4 and 5. The intermittent removal results in dramatically higher glucose concentrations during hydrolysis than that in continuous removal mode. At both retentate (Fig. 4) and permeate (Fig. 5), the concentration of glucose increases initially to approximately 3 g/l and then decreases gradually to below 1 g/l under continuous product removal. In contrast, the intermittent removal modes produce glucose profiles in a periodic pattern which concentration increases, reaches a peak, then reduces sharply during the short time for ultrafiltration and then refilling of fresh buffer to compensate the volume

removed and increases again at the retentate of the membrane. The highest glucose concentration obtained from hydrolysis in the membrane reactor with intermittent removal is around 6 g/l which is double for that obtained in continuous removal.

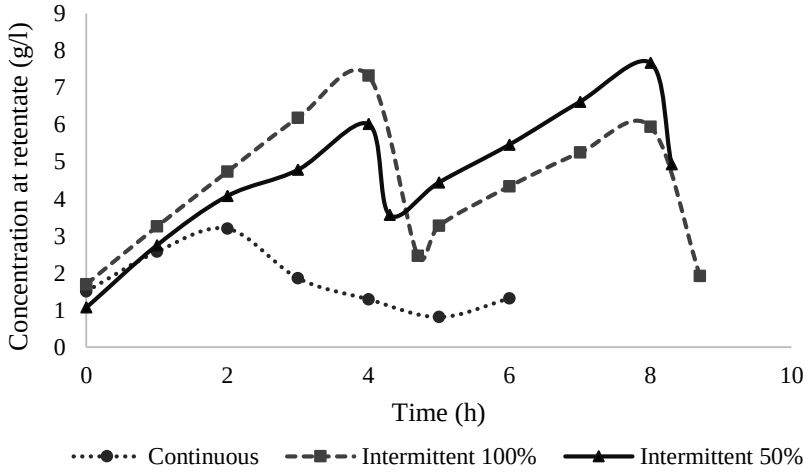


Figure 12. Glucose profile at retentate at different modes of product removal.

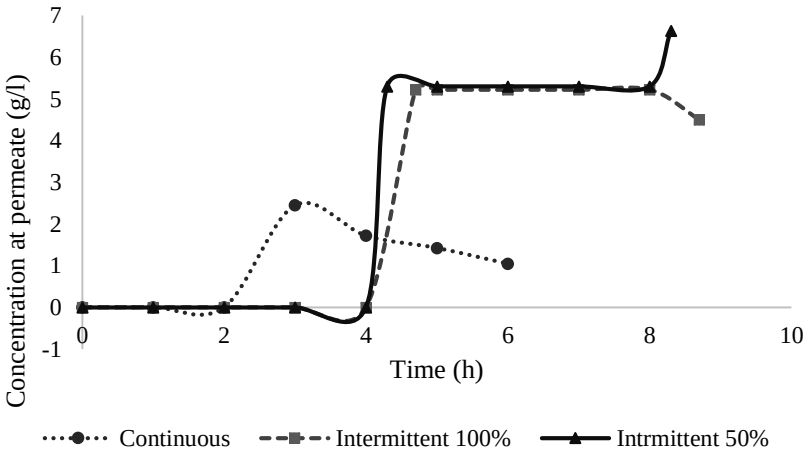


Figure 13. Glucose profile at permeate at different modes of product removal.

In order to test for a significant difference in glucose concentrations obtained in hydrolysis conducted in three different modes of product removal, one way ANOVA (analysis of variance) was used for testing. Based on the results with 95% confident level p=0.004 and F=6.942, there is a statistically significant difference in the released glucose from hydrolysis under continuous, intermittent product removal. Further testing using independent sample T-test to compare between continuous and intermittent 100% product removal, the glucose concentration in intermittent 100% product removal is significantly higher than that in continuous mode as the p=0.028 less than 0.05, and F=5.890.

The very low and continuous decrease in glucose concentration in continuous removal mode can be due to over-dilution by the supplement of buffer to the membrane reactor. By referring back to Fig. 2 for the diagram of the membrane

reactor, to maintain the constant volume (400ml) for the reaction, continuous removal of liquid containing glucose inside the reactor had to carry simultaneously with the supplement of fresh citrate buffer since ultrafiltration started. This continuous addition of buffer caused unnecessary dilution of glucose obtained at the permeate of the membrane. This issue was also recognised as the limitation of the membrane reactors in some review work recently [7, 8] and other research work [6, 15–17]. This is because of the operation of the membrane reactor at continuous product removal mode.

In comparison within intermittent product removal, from Figs. 4 and 5 it can be seen that the profiles of intermittent 50% are just slightly different than that in 100% intermittent. The final glucose concentrations at permeate are 6.63 g/l for intermittent 50% and 4.5 g/l for intermittent 100%. Since there is only a slight difference in the obtained glucose concentrations, the intermittent 50% volume removal is more preferred than that of 100% because it can save cost, and time for pumping during ultrafiltration period. In addition, it is proved by statistical analysis using independent T-test that intermittent 50% product removal is insignificantly higher than that in intermittent 100% product removal with p value of 0.679 (greater than 0.05) and F =0.177.

3.2. Variation in concentrations of cellulose substrate

Concentrations of cellulose as a substrate in hydrolysis was varied from 10% to 20% (w/v) to study its effect on the release of glucose obtained the permeate of ultrafiltration. The time to start ultrafiltration for hydrolysis at 10% and 20% cellulose concentrations was after 4 and 2 hours respectively. This is due to an observation from hydrolysis in batch reactors showing that the higher concentration of cellulose was used in hydrolysis, the faster in time the rate of glucose formation started to decrease. Therefore, ultrafiltration needed to start earlier for the hydrolysis at 20% cellulose concentration than that at 10% cellulose concentration. After 8 hour hydrolysis with intermittent 50% volume product removal, the concentration of glucose obtained in both cases are quite closed to each other at approximately 5.3 g/l as shown in Fig. 6. Variation in cellulose concentrations from 10% to 20% has an insignificant effect on the hydrolysis of cellulose conducted the membrane reactor.

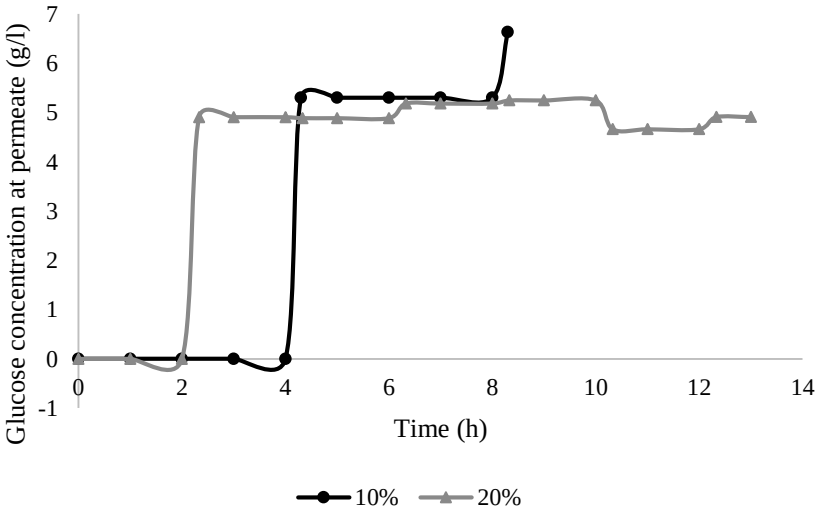


Figure 14. Variation in cellulose concentrations.

One-way ANOVA was used to test if the variation in cellulose concentrations has a significant effect on the release of glucose. With 95% confident level, the statistical result (F=1.089, p =0.305) shows that when conducting hydrolysis in the membrane reactor, the factor cellulose concentration has no significant effect on the glucose

3.3. Process optimisation

The enzymatic hydrolysis conducted in the membrane reactor were optimised by Response Surface Methodology (RSM)-Box Behnken Design with three center points, using the software Design Expert DX7. The purpose for this process optimisation were first to develop a regression model for hydrolysis specifically conducted in the modified membrane reactor, secondly to find the optimal conditions in this system to maximise the glucose concentration. A design summary of the RSM is presented in Table 5. There are three factors and one response for the optimisation study, i.e. cellulose concentration, enzyme to substrate (E/S) ratio, and product removal and glucose concentration.

Table 5. Design summary of RSM.

Factor name	Unit	Low actual	High actual	Mean	Std. Dev.
A-Cellulose concentration	%	10	20	15	3.651
B-Enzyme to substrate ratio (E/S)	%	3	6	4.5	1.095
C-Product removal	%	50	100	75	18.257
Response: Glucose concentration Unit: mg/ml or g/l Number of runs: 15 Analysis: Polynomial					

A regression model was developed using analysis of variance (ANOVA) for response surface reduced quadratic model. From the ANOVA result presented in Table 6, the model is significant with F = 4.610 and the p value of 0.0231. It implies that there is only 2.31%, this model could occur due to chance or noise. In addition, two factors, i.e. B-enzyme to substrate (E/S) ratio and AC-interaction of cellulose concentration with volume removal (highlighted in Table 6) are found to be the most significant factors as their p values are less than 0.05. In term of testing for the lack of fit, with F and corresponding p values of 0.5658 and 0.7608, the data is well-fitted with an insignificant lack of fit.

The model developed to study the relationships of three factors (cellulose concentration, E/S ratio and volume removal) is represented in the Eq. (2) and the model graph in Fig. 7. The obtained R-square value is R^2 = 0.7192 which is interpreted that this model is able to explain nearly 72% of the variation of the response data.

$$G = 24.68 - 2.07\,A + 0.68\,B - 0.20\,C + 0.01\,AC + 0.04\,A^2 \quad \text{.....(2)}$$

Where, G: glucose concentration (g/l or mg/ml); A: cellulose concentration (% w/v); B: enzyme to substrate (cellulose) ratio (%w/w); C: product removal (% vol.)

Table 6. Analysis of variance (ANOVA).

Source	Sum of Squares	df	Mean Square	F Value	p-value Prob > F	
Model	23.24864	5	4.649727	4.610047	0.0231	significant
A-Cellulose cont.	0.407112	1	0.407112	0.403637	0.5410	
B-E/S ratio	8.245109	1	8.245109	8.174746	0.0188	significant
C-Volume removal	1.899765	1	1.899765	1.883553	0.2032	
AC	8.812734	1	8.812734	8.737528	0.0161	significant
A^2	3.883916	1	3.883916	3.850771	0.0813	
Residual	9.077466	9	1.008607			
Lack of Fit	6.031973	7	0.86171	0.565892	0.7608	not significant
Pure Error	3.045493	2	1.522746			
Cor Total	32.3261	14				

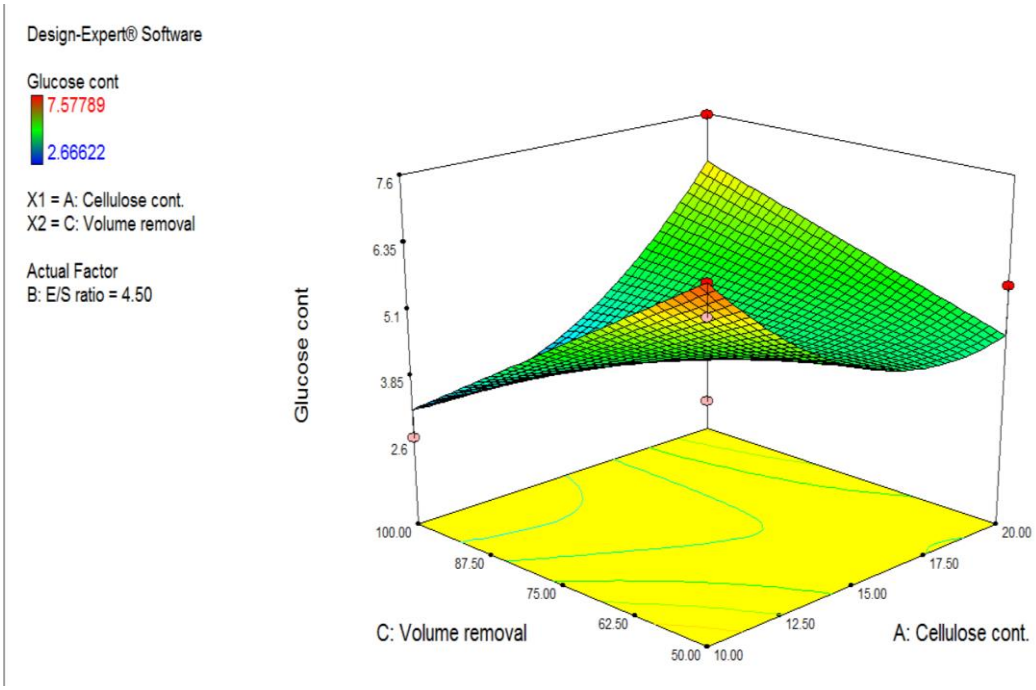


Figure 15. Model graph.

Factor A-Cellulose concentration which has earlier studied not to have a strong effect on the production of glucose in section 4.2 is for the second time confirmed to be an insignificant factor affecting glucose concentration with a high p value of 0.541 greater than 5% (table 1). Surprisingly the interaction of factor A-cellulose concentration with factor B-product removal has a strong effect on the glucose concentration (p value = 0.0161 and less than 5%). A 3D surface in Fig. 7 expresses this interaction relationship of factors A and C. As can be seen in Fig. 7, it is noticed high concentrations of glucose at above 7 g/l were obtained at either two conditions for the modified membrane reactor, i.e. 1. Operation at 50% product removal (volume removal) and 10% cellulose concentration or 2. Operation at 100% product removal and 20% cellulose concentration. In other words, for the modified

membrane reactor conducted for enzymatic hydrolysis, operation at an increased cellulose concentration would correspondingly require an increase in the intermittent volume removal of the product or vice versa. Hence, a further investigation in the interaction between the volume removal of glucose and cellulose concentration is suggested for quantification or degree of product removal in hydrolysis.

3.4. Reuse of enzymes

From the process optimisation, the response surface quadratic model was used to maximise the response (glucose concentration) at a predicted value of 7.95 g/l with 95% confident interval. The optimal conditions for three factors are 10.07% cellulose concentration, 6% E/S ratio and 50.06% volume removal.

In this section, hydrolysis was conducted in the membrane reactor at the optimal condition for the first eight hours (1h to 8h). After that, hydrolysis reaction was extended by replacing the solid cellulose with the fresh pretreated cellulose substrate. But enzymes which remained in the liquid phase were reused to continue hydrolysis for another eight hours (8h to 16h). The concentration profiles at permeate and retentate are shown in Figs. 8 and 9. The experimental value of glucose concentration at 8h obtained from hydrolysis in the optimal conditions is 6.67 g/l

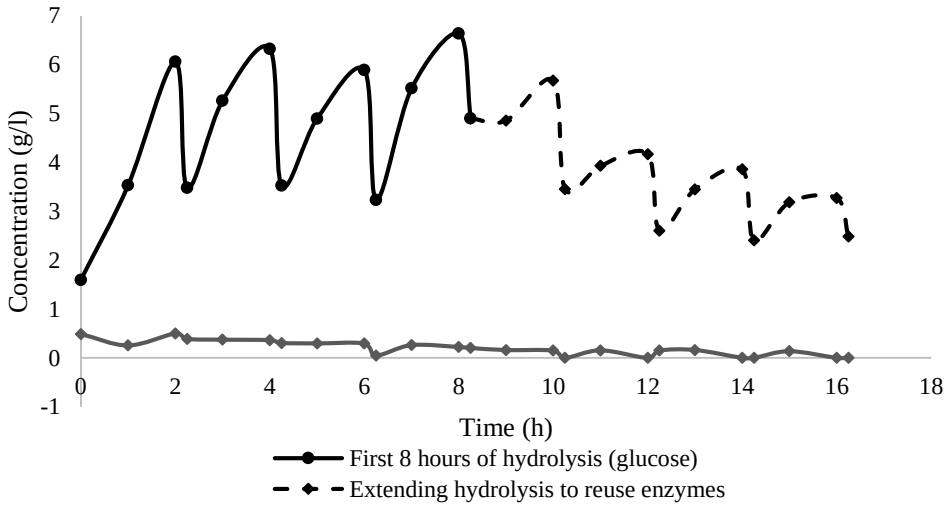


Figure 16. Profile at retentate in hydrolysis reusing enzymes.

In the extended hydrolysis from 8h to 16 h, the concentrations of glucose at retentate in overall are lower than that in the first 8 hours (Fig. 8). It implied that the conversion of cellulose to glucose decreased when enzymes were reused to hydrolyse fresh pretreated cellulose. However, at the permeate of the ultrafiltration (Fig. 9) glucose concentrations during 16h hydrolysis was able to maintain slightly below 7 g/l with no significant reduction. In comparison of the concentration of glucose between hydrolysis in the first 8 hours and the extended period reusing enzyme, the independent T-test reveals that there is no statistically significant difference as p value obtained is 0.081 and F=3.314. Thus, it is confirmed in this test that the ultrafiltration membrane was very effective to retain enzymes inside the reactor and these enzymes are highly able to reutilise to extend hydrolysis of fresh pretreated cellulose.

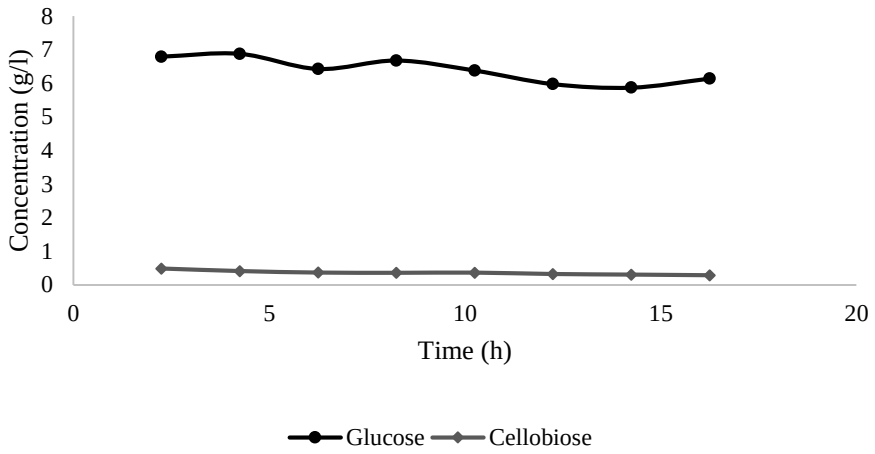


Figure 17. Profile at permeate in hydrolysis reusing enzymes.

Cellobiose which is an intermediate product of conversion from cellulose to glucose, has very low concentrations of less than 0.5 g/l during the entire 16h hydrolysis (Figs. 8 and 9). It is understood that the enzyme Cellic CTec2 and its amount used for hydrolysis was suitable and sufficient for a quick conversion of cellobiose to glucose.

4. Conclusions and recommendations

The present study has successfully conducted for further investigation on the modified submerged membrane reactor with a new configuration applied for the enzymatic hydrolysis of cellulose. In term of operation of the modified submerged membrane reactor, intermittent removal of 50% reactor volume is more advantageous than that of 100% and continuous product removal modes because it can save the cost as well as the time for pumping and avoid the over-dilution of glucose stream in the permeate. The variation of cellulose substrate concentration is not a significant factor to affect the conversion of cellulose to glucose when using the membrane reactor for hydrolysis. In addition, a reduced quadratic model developed by response surface methodology is significant to represent the relationship between three factors, in which enzyme to substrate ratio and interaction of cellulose concentration with volume removal were found to be the significant factors that affect the release of glucose from cellulose in hydrolysis. The optimal conditions to maximise the glucose concentration are 10% cellulose concentration, 6% enzyme to substrate ratio, and product removal at 50% volume. The ultrafiltration membrane used in this modified membrane reactor is very effectively to retain and reuse enzymes for extending hydrolysis with fresh pretreated cellulose without affecting the conversion of cellulose. Thus, it can be concluded that the modified membrane reactor is highly applicable to use for hydrolysis of cellulose to produce glucose as an alternative solution for the batch reactor.

Acknowledgement

We are thankful for the enzyme Cellic CTec2 as free samples provided by Novozymes (China) Investment Co. Ltd. who shows a great interest in this research project. Meanwhile, Taylor's University School of Engineering has facilitated the

research for materials and equipment together with training from very helpful laboratory technicians. Without them, this study would not be completed.

References

[1] United Nations (2015). Resolution adopted by the General Assemply on 25 September 2015. [Online]. Available: https://sustainabledevelopment.un.org/sdgs.

[2] Van Dyk, J. S. and Pletschke, B. I. (2012). A review of lignocellulose bioconversion using enzymatic hydrolysis and synergistic cooperation between enzymes-Factors affecting enzymes, conversion and synergy, *Biotechnological Advances*, 3(6), 1458–1480.

[3] Abels, C., Carstensen, F. and Wessling, M. (2013). Membrane processes in biorefinery applications. *Journal of Membrane Sciences*, 444, 285–317.

[4] Andrić, P., Meyer, A. S., Jensen, P. A. and Dam-Johansen, K. (2010). Reactor design for minimizing product inhibition during enzymatic lignocellulose hydrolysis: I. Significance and mechanism of cellobiose and glucose inhibition on cellulolytic enzymes. *Biotechnological Advances*, 28(3), 308–324.

[5] Belafi-Bako, K., Koutinas, A., Nemestthy, N., Gubicza, L. and Webb, C.(2006). Continuous enzymatic cellulose hydrolysis in a tubular membrane bioreactor. *Enzyme Microbial Technology*, 38(1–2), 155–161.

[6] Gan, Q., Allen, S. J. and Taylor, G. (2002). Design and operation of an integrated membrane reactor for enzymatic cellulose hydrolysis, *Biochemical Engineering Journal*, 12(3), 223–229.

[7] Andric, P., Meyer, A. S, Jensen, P. A. and Dam-Johansen, K. (2010). Reactor design for minimizing product inhibition during enzymatic lignocellulose hydrolysis. II. Quantification of inhibition and suitability of membrane reactors. *Biotechnological Advances*, 28(3), 407–425.

[8] Tu, M., Chandra, R., and Saddler, J. N.(2007). Evaluating the distribution of cellulases and the recycling of free cellulases during the ydrolysis of lignocellulosic substrate. *Biotechnological Progresses*, 23(2), 398–406.

[9] Knutsen, J. and Davis, R. (2002). Combined sedimentation and filtration process for cellulase recovery during hydrolysis of lignocellulosic biomass, *Applied Biochemical Biotechnology*, 98(1), 1161–1172.

[10] Draphcho, M., Nghiem, P. and Walker, H. (2008). *Biofuels Engineering Process Technology*. USA: McGraw-Hill.

[11] NguyenHuynh, T.T., R. Nithyanandam, C. H. Chong, and D. Krishnaiah, "A REVIEW ON USING MEMBRANE REACTORS IN ENZYMATIC HYDROLYSIS OF CELLULOSE," *J. Eng. Sci. Technol.*, pp. 1–24.

[12] T. Nguyenhuynh and Nithyanandam, R. (2016).Fractionation of hydrolysed microcrystalline cellulose by ultrafiltration membrane. *Journal of Engineering Science and Technology*, 11(1), 136-148.

[13] Novozymes (2010). Cellic® CTec2 and HTec2 - Enzymes for hydrolysis of lignocellulosic materials.

[14] Joshi, B., Bhatt, M., Sharma, D., Joshi, J., Malla, R. and Sreerama, L.(2011). Lignocellulosic ethanol production: current practices and recent developments. *Biotechnological Advances*, 6(8), 172–182.

[15] Malmali, M., Stickel, J. and Wickramasinghe, S. R. (2015). Investigation of a submerged membrane reactor for continuous biomass hydrolysis. *Food Bioproduct Processing*, 96, 189–197.

[16] Abels, C., Thimm, K., Wulfhorst, H., Spiess, A. C. and Wessling, M. (2013). Membrane-based recovery of glucose from enzymatic hydrolysis of ionic liquid pretreated cellulose. *Bioresource Technology*, 149, 58–64.

[17] Lozano, P., Bernal, B., Jara, A. G., and Belleville, M. P.(2014). Enzymatic membrane reactor for full saccharification of ionic liquid-pretreated microcrystalline cellulose. *Bioresource Technology*, 151,159–165.

[18] Al-Zuhair, S., Al-Hosany, M., Zooba, Y., Al-Hammadi, A. and Al-Kaabi, S. (2013). Development of a membrane bioreactor for enzymatic hydrolysis of cellulose, *Renewable Energy*, 56, 85–89.

eureca 2016 – Conference Paper
Paper Number CE_PG03

Thermogravimetric Analysis of Alkali Treated and Untreated Oil Palm Mesocarp Fibre for biochar production

Nida Jafri[1*], Veena A. Doshi[1], Wai Yin Wong[2], Kean How Cheah[1]

[1] *Discipline of Chemical Engineering, School of Engineering, Taylor's University Malaysia, No.1 Jalan Taylors, 47500, Subang Jaya, Selangor Darul Ehsan, Malaysia*

[2] *Fuel Cell Institute, University Kebangsaan Malaysia, Bangi, 43600, Selangor, Malaysia*

**nidajafri7@gmail.com*

Abstract
The purpose of this paper is to study the characteristics of alkali treated and untreated oil palm mesocarp fibre (OPMF) for biochar production via pyrolysis technology. The study investigates on the comparison of thermal stability between alkali treated and untreated OPMF in pyrolytic environment by using thermogravimetric analyzer (TGA). It also focusses on the thermal degradation of lignin present in the OPMF biochar. A clear understanding about the thermal degradation mechanism of OPMF is thus required for the design and operation of an efficient fuel cell system. The OPMF samples were treated with three different NaOH concentrations to study the effect of thermal degradation and the decomposition of lignin before being subjected to pyrolysis at 600°C. It was found that 0.5M NaOH treated biochar had the highest thermal stability among all the tested biochars. The pretreatment method thus proves to be important in determining the thermal properties of OPMF. The experimental values were used for curve fitting in MATLAB for all the biochar samples and the results showed that the Gaussian model was the best fit to the experimental values carrying a R^2 value close to 1 with a minimum root mean square (RMSE) error.

Keywords: Oil palm mesocarp fibre (OPMF); Alkali treatment; Pyrolysis; Biochar; Thermogravimetric analysis (TGA)

1. Introduction

Biomass is a complex biogenic product consisting of organic and inorganic components and represents a renewable and sustainable alternative to fossil fuels. The conversion of biomass is a carbon-neutral process as it releases the same amount of CO_2 during combustion as previously taken up during growth. Biomass used as energy feedstock is environment friendly because it recycles the carbon in the environment and does not add CO_2 in atmosphere. In the past 10 years, there has been renewed interest, world-wide, in biomass as an energy source.

Biomass is composed mainly of three organic compounds: cellulose, hemicellulose and lignin. Cellulose is the structural component of the primary cell wall of all green vegetable matter- it is a high molecular weight linear polymer that has anhydrous glucose as the basic repeating unit. Cellulose provides the basic strength to the biomass and makes up to about 40%-50% of the weight of dry woods. Hemicellulose makes up for about 20% to 35% of the mass of dry woods, the harder the wood, the higher the hemicellulose content. Lignin is a complex chemical compound and is an essential part of the secondary cell wall of plants. It is an amorphous cross linked-resin and makes up for about 15% to 30% of the mass of hardwoods. Different biomass materials vary in their relative amounts of cellulose, hemicellulose and lignin. Lignin component in the biomass is supposed to be the main contributor to the carbon contained in the biomass and its composition has been shown to influence the final char weight [1, 2, 3, 4].

Thus choosing the biomass with a high lignin content becomes significantly important. The lignin content in oil palm mesocarp fibre is reported to be quite high in the range of about 28%. Another reason for choosing oil palm waste is because of its abundant availability in Malaysia covering a total of 5.230 million hectare representing 79% of the total area (6.6 million ha) designated for agriculture and 15% of overall Malaysian territory [5].

Biochar is made from range of biomasses that have different chemical and physical properties. It is the solid product which is formed in a moderately high temperature in an inert atmosphere through the process of pyrolysis. The process thermally decomposes the carbohydrate structure of biomass into carbonaceous solid residue (biochar), and condensable and non-condensable vapors of various molecular weight compounds. It is a value-added product, which can be used for many purposes. It is highly carbonaceous and hence contains a high energy content, comparable to high rank coals. In addition, the heterogeneous reaction of solid carbon with oxygen is slower than homogeneous oxidation, which is relatively safe and easy to control. For this reason, the primary use has been as fuel (charcoal) for heat production and electricity generation [6]. Oil palm mesocarp fibre (OPMF) is a renewable biomass and supplies fuel in the form of solid biochar through thermochemical conversion which is capable of generating electrical energy through a fuel cell system.

Unfortunately, raw biomass can’t be used directly in its raw form because of its inherent properties such as poor grindability, high moisture content and low energy density [7]. Poor grindability of biomass can be attributed to its fibrous structure

which significantly increases energy consumption and forms a challenge during fuel preparation. The high moisture content lowers the maximum combustion temperature and consequently could reduce the thermal efficiency and increase pollutant emissions [7]. Thus, to overcome these drawbacks, a pretreatment process is necessary prior to combustion. The effect of pretreatment steps plays a vital role for improving the characteristics of the biochar. Chemical pretreatment could detach the components of the lignocellulosic biomass, strip the biomass chains and increase the accessible surface area during pyrolysis [8]. Chemical treatment for biochar conversion is activated at a lower temperature and there is less carbon burning in the process. The chemically treated biochar has been reported to have a higher thermal stability along with good conductivity in a fuel cell which is attributed to the removal of significant amount of minerals, such as potassium, phosphorus and sodium from the biochar [9]. Dilute-NaOH pretreatment of lignocellulosic biomass has been found to cause swelling, leading to an increase in internal surface area and disruption of the lignin structure [10]. Silverstein et al. [11] reported that 2% NaOH (0.5M) in 90 min at 121°C was the best pretreatment condition, which resulted in 65% of delignification. Thus this particular pretreatment method was employed in this study.

Slow pyrolysis is an ideal technology to produce biochar, which involves thermal decomposition in an inert atmosphere at a slow heating rate (10 °C/min) (Mohan et al., 2006). Pyrolysis converts solid fuels, such as coal and biomass, into char (solid), vapours of condensable hydrocarbons (called ‘oil’ for use after condensation) and non-condensable gases (e.g., CO, CO_2, H_2 and CH_4). Biochar, or char originating from biomass, is typically 20–40 wt. % of dry lignocellulosic biomass. However, the yield and characteristics of the pyrolysis products are strongly influenced by the operating conditions (e.g., temperature, heating rate, pressure, purge gas and particle size) and the properties of the feedstock. Therefore, the operating conditions of the pyrolysis process can be adjusted to meet the product requirements, however the actual process needs to be carefully designed and performed. Compared to fast pyrolysis, slow pyrolysis is ideal for biochar production, since it increases the yield of biochar. It can be performed at various scales by a simple heating process without specific requirements for particle size reduction. Feed stocks with high lignin content produce the highest bio-char yields when pyrolyzed at moderate temperatures (approx. 600 °C). In addition, the ratios of volatile matter, fixed carbon, ash content and moisture are also indicators of pyrolysis product yields [2].

However, there exists a gap since there are no comparisons done on mesocarp fibre for alkali treatment using NaOH as the agent. Hence the objective of this study is to produce an alkali treated pyrolyzed biochar which is thermally stable and compare it with the non- treated pyrolyzed biochar.

2. Methodology

2.1 Sample Preparation

Raw oil palm mesocarp fibre biomass was acquired from the Seri Ulu Langat Palm Oil Mill Sdn. Bhd located in Dengkil, Selangor. The biomass was first sun dried after which it was dried in an electric oven at 105^{o}C for 24 hours to remove unbound moisture. The oven-dried biomass was then milled and sieved to obtain uniformed sized particles in the size range of 0.5mm. The samples were stored in a desiccator to keep it moisture free until use.

2.2 Alkali Treatment

20g of dried mesocarp fibre was impregnated with three different NaOH concentrations of 0.1M, 0.5M and 1M at a temperature of 121°C for 90 minutes on a magnetic stirrer. The stirring speed was constant at 150rpm to ensure the solution reacts with the biomass evenly. After the reaction was over, the samples were washed with distilled water and tested in a pH meter to a neutral pH.

2.3 Pyrolysis Treatment

For pyrolysis run, a horizontal split tube furnace was used which was operated at 600°C for 1 hour. The sample was heated to 600^{o}C with a holding time of 30 minutes at a heating rate of 10 ^{o}C /min. Nitrogen gas was used for purging at a constant rate of 1 l/min to eliminate oxygen in the furnace while pyrolysis is ongoing.

2.4 Proximate Analysis

Proximate analysis was conducted according ASTM E 897-88 to investigate the ash content of samples after chemical pretreatment and after pyrolysis. Samples are weighed at 1.0g and dried at 105^{o}C for 1 hour to remove bound moisture. After which, samples are put into a muffle furnace at 750^{o}C for 1 hour at a heating rate of 10^{o}C/min.

2.5 Thermogravimetric Analysis (TGA)

TGA was carried out in the presence of nitrogen (N_2) at a flow rate of 20 ml/min. 5mg of the pyrolyzed OPMF samples were tested at a final temperature of 1000°C. The sample was first heated to 850°C with a fixed flow rate of N_2 and then the gas was switched to oxygen with a flow rate of 20 ml/min for the char oxidation process to take place. After which the run was done upto the maximum temperature of 1000°C.

3. Results and discussion

3.1 ***Proximate Analysis***

The proximate analysis of palm oil wastes was carried out in TGA (TA 2050, USA) and the carbon, hydrogen, nitrogen and sulfur contents were determined on an EA3000 Elemental Analyzer (Italy). The results are listed in Table 3.1 The ash content has reduced to almost half its value owing to the subjected treatment with the increase in the total carbon content which is a significant change.

Table 3.1 Proximate and Ultimate Analysis of OPMF (wt %)

Ash Content	C	H	N	S	Ash
Raw OPMF	51.50	6.60	1.50	0.30	8.30
OPMF Biochar	73.07	1.385	6.769	0.049	4.27

C- carbon; H- hydrogen; N- nitogen; S- sulphur

3.2 Thermogravimetric analysis of alkali treated and untreated biochar

All experimental results are plotted as a function of temperature, as shown in the figures below. Figure. 1 shows the individual TGA curves for NaOH treated biochar and untreated biochar samples and Figure 2 shows the combined plot for the all the treated and the untreated biochar samples.

TGA curve displays weight loss as a function of temperature in a controlled atmosphere, whereby DTG curve emphasizes the zone of reaction where various reaction steps are taking place over the entire temperature range. The TGA phases of OPMF can be divided into three phases which are drying and evaporation of light components (phase I), devolatilization of hemicellulose and cellulose (phase II) and decomposition of lignin (phase III). Phase I occurs at temperature below 150°C, phase II starts from 150°C to 450°C and finally phase III is achieved at temperatures above 450°C as shown in Figure 1.

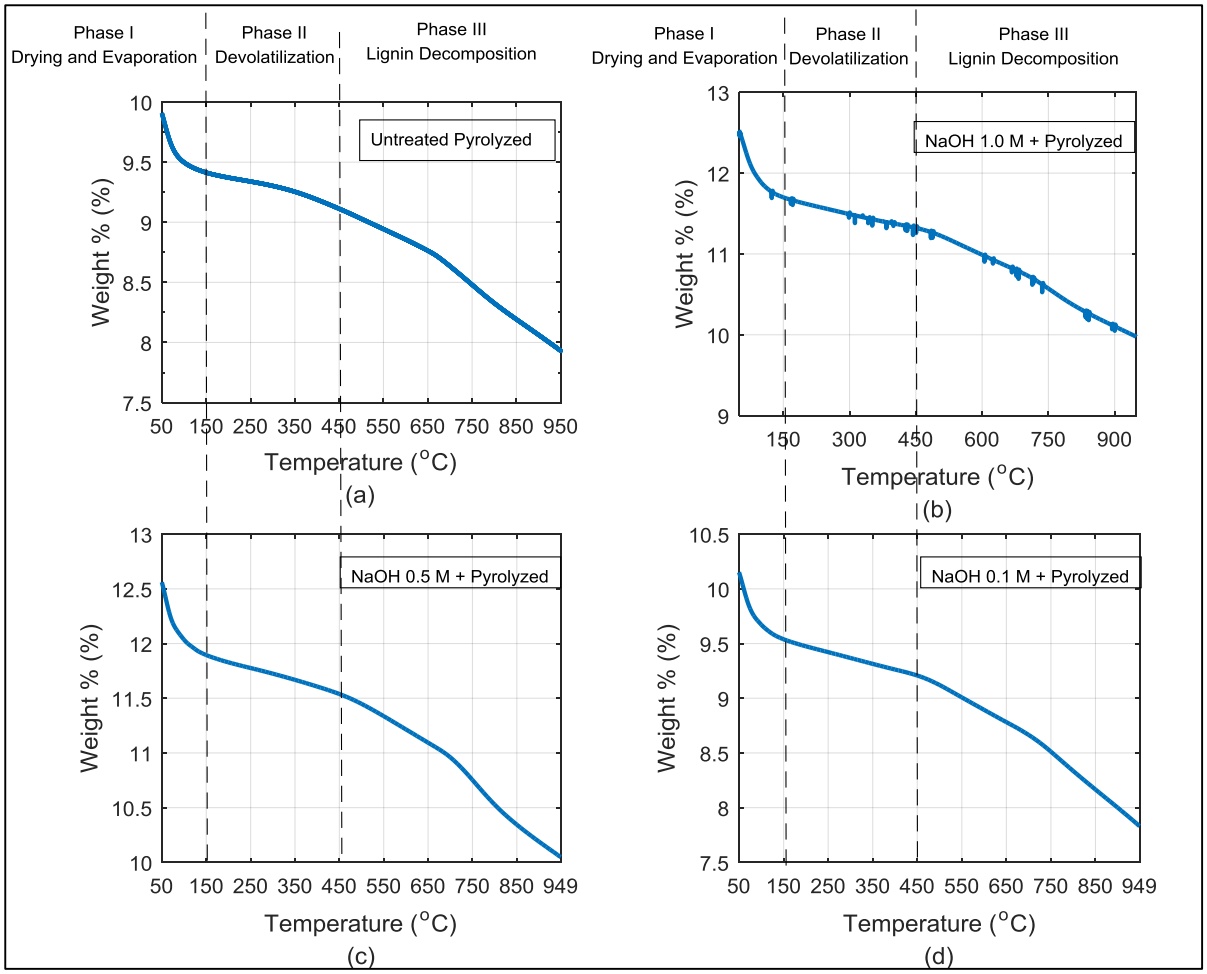


Figure 1. Plot of TGA for (a) Untreated pyrolyzed biochar (b) 1.0M NaOH treated pyrolyzed (c) 0.5M NaOH treated pyrolyzed and (d) 0.1M NaOH treated pyrolyzed biochar

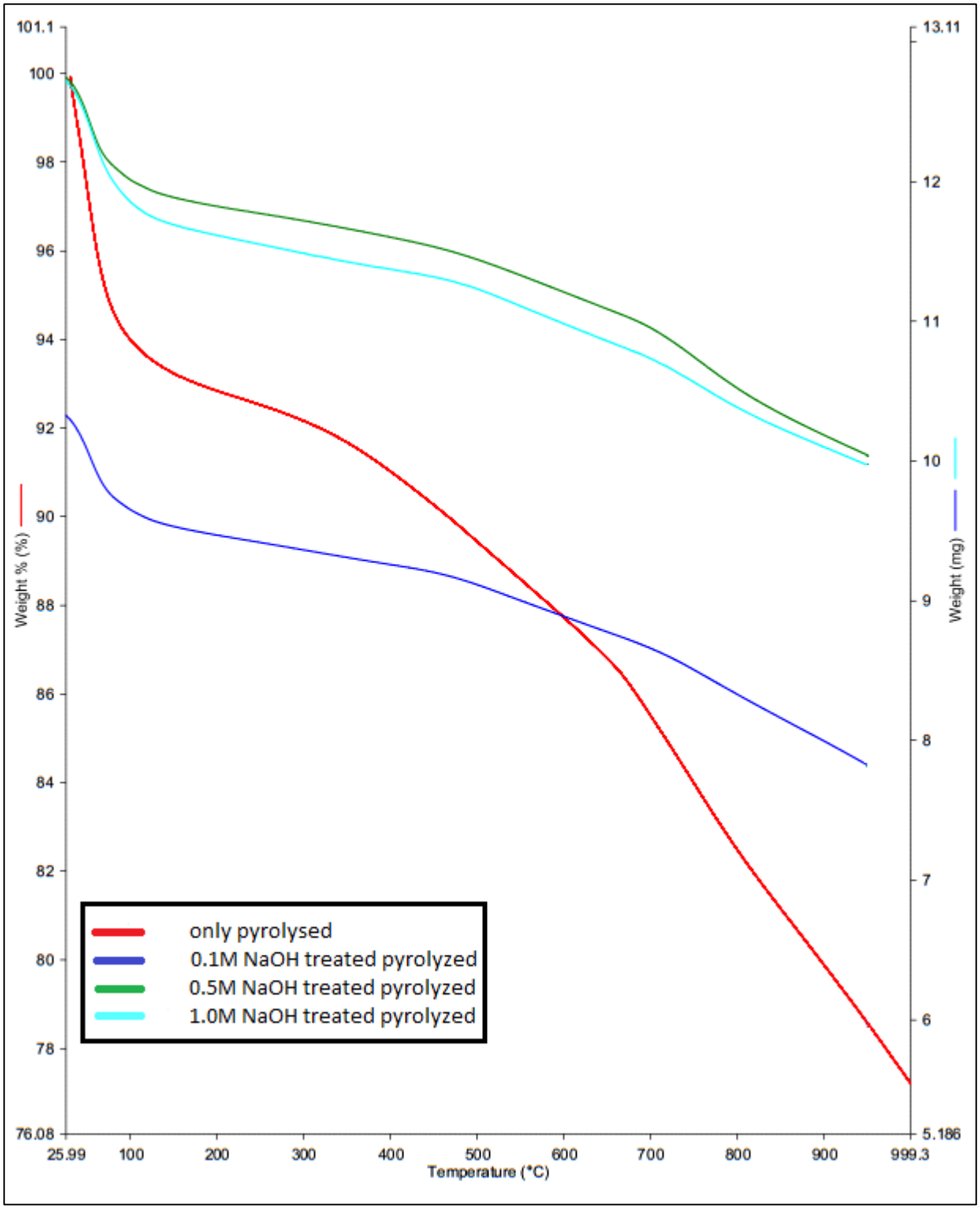


Figure 2. Plot of TGA for NaOH treated pyrolyzed and non- treated pyrolyzed biochar

TGA analysis was carried out to study thermal stability and decomposition/ degradation of biochars. When heating temperature was implemented between 30 and 100 °C, the mass of all the biochars only decreased slightly (due to water loss) and then became stable until at least 200 °C. No phase change was found on all the

biochars at 100–200 °C, indicating decomposition did not occur at this temperature range.

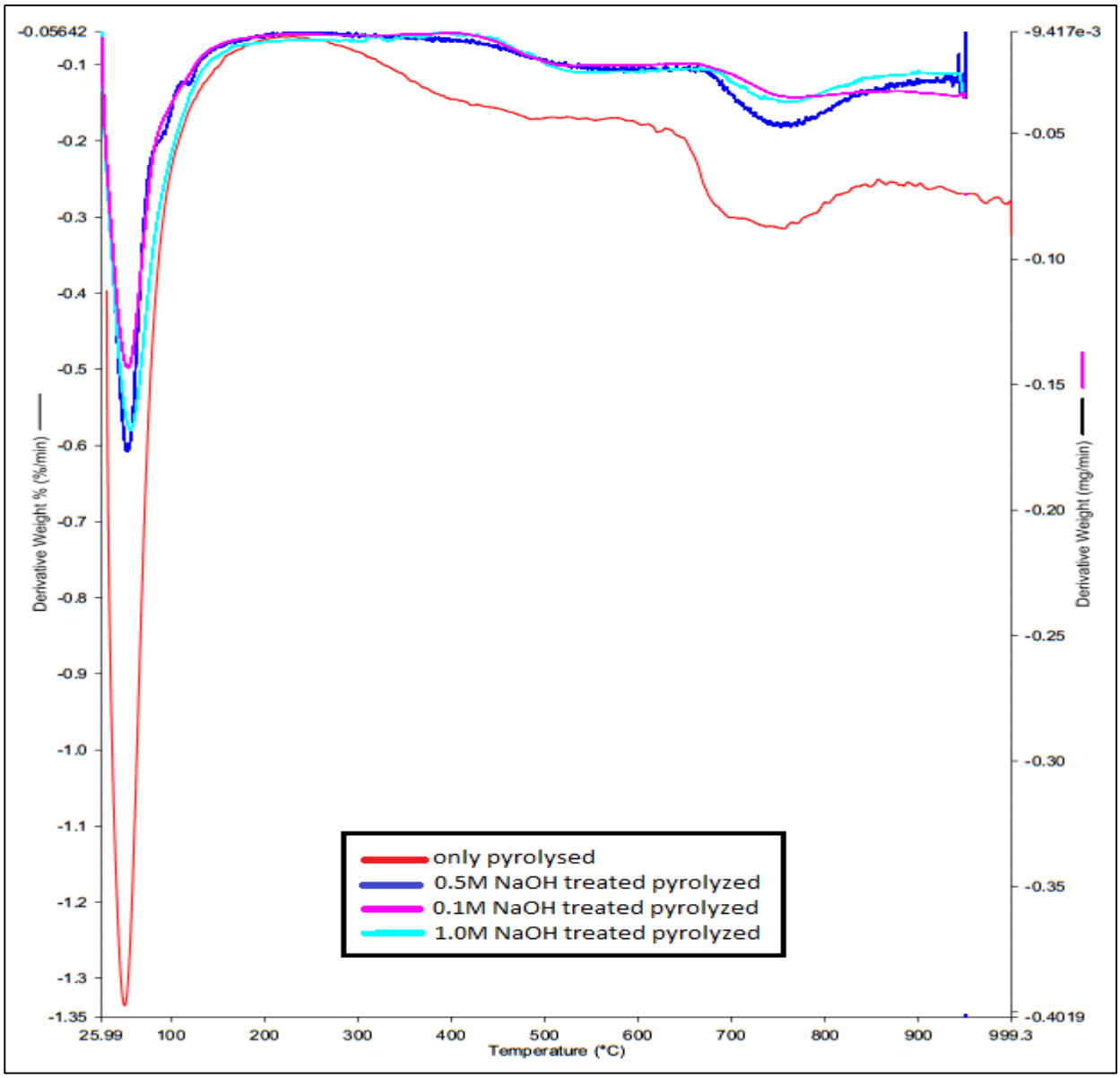


Figure 3. Plot of DTG for NaOH treated and untreated biochar

Figure 3 shows derivative thermogravimetric (DTG) curve for the NaOH treated and untreated biochar samples. Generally, two separate peaks can be identified for heat treatment of biomass in an inert atmosphere. The first one is assigned to the thermal decomposition of hemi-cellulose and the second one is for cellulose and lignin decomposition. Normally, the second peak covers longer temperature range. Thermal degradation data indicates weight loss and the first derivative (DTG) indicates the corresponding rate of weight loss. Lignin molecular structure is composed of mostly aromatic rings having various branching, these chemical bonds lead to a wide range of degradation temperature from 100 to 1200 ◦C as expressed by Yang et al. [12]. The degradation of the lignin component takes place around 180–350

◦C and is attributed to the degradation of components of carbohydrates in the lignin samples, which are converted to volatile gases such as CO, CO_2, and CH_4. The final stage of degradation occurs over a wide range of temperatures above 350 ◦C. Within this stage, degraded volatile products derived from lignin including phenolics, alcohols, aldehyde acids along with the formation of gaseous products are removed.

3.3 Curve fitting using MATLAB

The experimental data points of temperature against weight drop (%) for untreated biochar and NaOH treated biochar were plotted in MATLAB through curve fitting to get the best fit. The results indicated that Gaussian model was a good fit for the experimental results as shown in Figure 4. The generated model is in a form of an equation which is shown below as eq. (1) & eq. (2) for untreated biochar and NaOH treated biochar, respectively. The equations can be used to find out the weight drop of the biochar at any given value of temperature by substituting in the values of temperature given by x in the equations (1) & (2). The respective R^2 values of untreated biochar and NaOH treated biochar are close to the value of 1 and the respective root mean square error (RMSE) values are obtained as minimum. This demonstrates that the Gaussian model is fit for these experimental values and could be used to generate results effectively. The R-square values for untreated biochar are found to be slightly higher than the alkali treated biochar. Although, the R-square values found for alkali treated biochar are found to be satisfactory, there needs to be more experimental done to be able to improve these values. Further experimental work and its analysis will reveal more factors that influence the overall dynamics of the alkali pretreatment method. In short, the current curve fitting has been used to create the best fit model which will be used later for further investigations into the treatment processes. This model will be enhanced by including other important factors like degree of graphitization, surface area and functional groups analysis that affect the process greatly.

Untreated

$$f(x) = a_1 * \exp((-((x - b_1)/c_1)^2)$$

(1)

Coefficients (with 95% confidence bounds):

a_1 = 9.719 (9.703, 9.735)
b_1 = -225.5 (-242.3, -208.7)
c_1 = 2628 (2598, 2658)

Goodness of fit:
R-square: 0.9785
RMSE: 0.07934

NaOH treated (average of all the 3 concentrations)

$$f(x) = a * \exp(-((x-b)/c)^2$$
(2)

a = 11.2687
b= 2.1233
c=1983
Goodness of fit:

R-square: 0.8567
RMSE: 0.3138

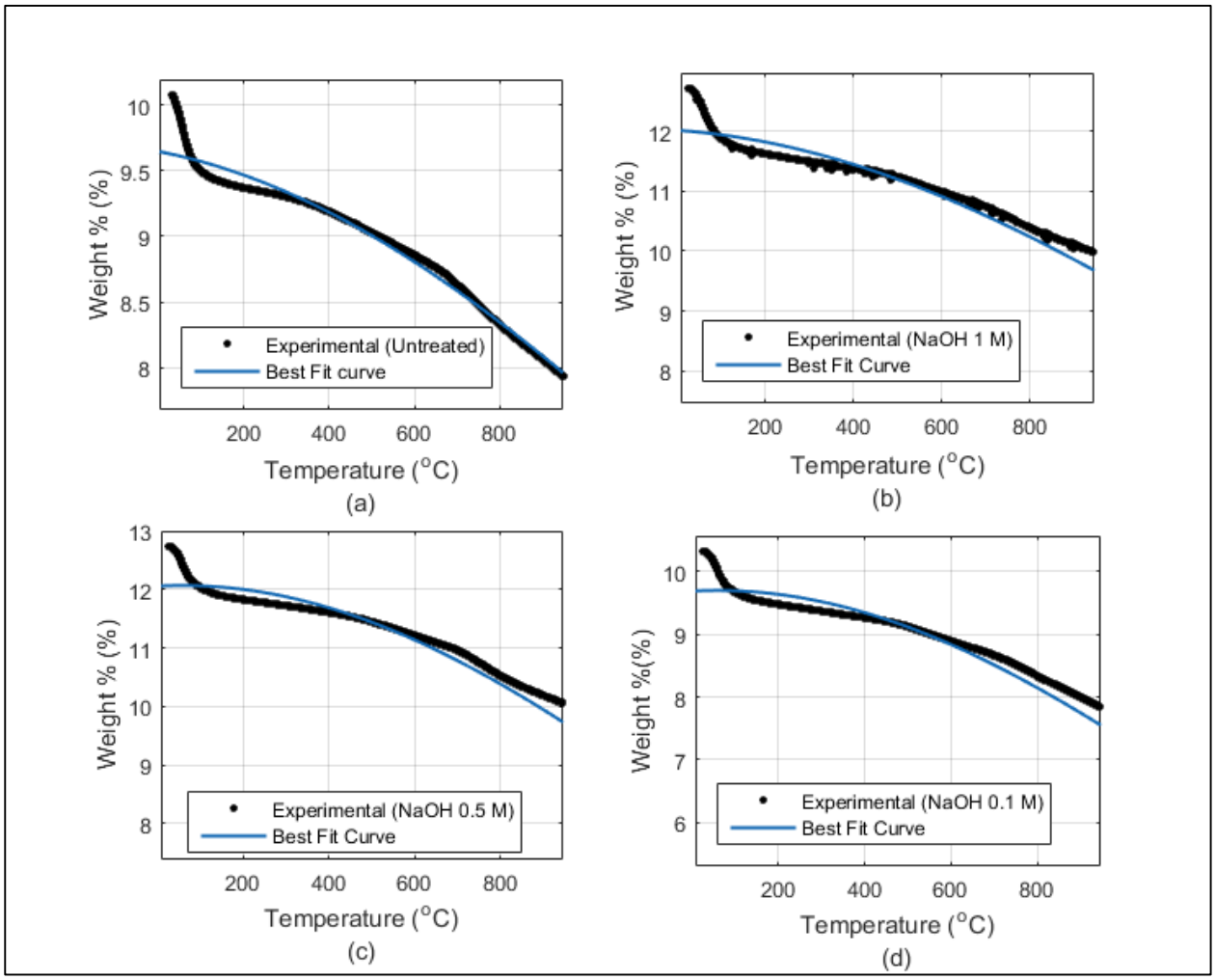


Figure 4. Curve fitting plots for (a) Untreated pyrolyzed biochar (b) 1.0M NaOH treated pyrolyzed (c) 0.5M NaOH treated pyrolyzed and (d) 0.1M NaOH treated pyrolyzed biochar

4. Conclusion

Pretreatment of OPMF was performed using NaOH as the alkali and pyrolysis was employed as the thermal treatment for the production of biochar. The TGA analysis showed that the 0.5M NaOH treated biochar was the most thermally stable among all the tested biochars. This results shows that the pretreatment step has a positive implication on the thermal properties of biochar. This is one of the important

characteristics of biochar to be used a fuel source in a fuel cell. The TGA analysis also showed the thermal degradation of the hemicellulose, cellulose and the lignin components of the cell wall of OPMF. The graphs showed the degradation effect occurring on the respective temperature ranges of all the three cell wall components. The degradation of lignin is vital as it the component which is responsible for the formation of char and thus for the level of carbon in the biochar. The curve fitting results generated Gaussian model which was the closest fit to the experimental values and will be used to determine the weight loss of the biochar at various operating temperatures.

References

1. Asadieraghi, M. and Daud, W.W. (2014). Characterization of lignocellulosic biomass thermal degradation and physiochemical structure: Effects of demineralization by diverse acid solutions. *Energy Conversion and Management*, 82:71-82.
2. Luo, L., Xu, C., Chen, Z., and Zhang, S. (2015). Properties of biomass-derived biochars: Combined effects of operating conditions and biomass types. *Bioresource Technology*, 192:83–89.
3. Loo, V and Koppejan, (2002). *Handbook of biomass combustion and co-firing*. Twente University Press.
4. McKendry, P. (2002). Energy production from biomass (part 1): overview of biomass. *Bioresource Technol*., 83:37–46.
5. Basiron, Y. and Chan, K.W. (2004). The oil palm and its sustainability. *J. Oil Palm Res*., 16, 1-10.
6. Enders, A., Hanley, K., Whitman, T., Joseph, S., Lehmann, J. (2012). Characterization of biochars to evaluate recalcitrance and agronomic performance. *Bioresource Technology*, 114, 644–653.
7. Khan, A. A, Jong, W., Jansens, P. J., Spliethoff, H. (2009). Biomass combustion in fluidized bed boilers: potential problems and remedies. *Fuel Process Technol.*, 90:21–50.
8. Sun, R., Tomkinson, J., Bolton, J. (1999). Effects of precipitation pH on the physico-chemical properties of the lignins isolated from the black liquor of oil palm empty fruit bunch fibre pulping. *Polymer Degradation and Stability*, 63:195-200.
9. Muniandy, L., Adam, F., Mohamed, A. R. and Ng, E.P. (2014). The synthesis and characterization of high purity mixed microporous/mesoporous activated carbon from rice husk using chemical activation with NaOH and KOH. *Microporous Mesoporous Mater.*, 197:316–323.
10. Cao, W., Sun, C., Liu, R., Yin, R. and Wu, X. (2012). Comparison of the effects of five pretreatment methods on enhancing the enzymatic digestibility and ethanol production from sweet sorghum bagasse, *Bioresource Technology*.
11. Silverstein, R. A., Chen, Y., Sharma-Shivappa, R. R., Boyette, M. D. and Osborne, J. (2007). A comparison of chemical pretreatment methods for improving saccharification of cotton stalks. *Bioresource Technology*, 98, No. 16, 3000-3011.
12. Yang, H., Yan, R., Chen, H., Lee, D.H., Zheg, C. (2007). Characteristics of hemicellulose, cellulose, and lignin pyrolysis. *Fuel*, 86:1781–8.

eureca 2016 – Conference Paper
Paper Number CE_PG04

Refractive Index, Viscosity and Thermal Conductivity of Bio-Mineral Oils

Mohamed Osama[1], Rashmi G. Walvekar[1*], Gupta TCSM[2], Wong W. Yin[3]

[1]Department of Chemical Engineering, Taylor's University Lakeside Campus, Malaysia. [2]Research and Development, Apar Industries, Mumbai, India

[3]Fuel Cell Institute, Universiti Kebangsaan Malaysia, 43600 UKM Bangi, Selangor,Malaysia.

[*]Corresponding Author E-mail: rashmigangasa.walvekar@taylors.edu.my

Abstract

Lubricants in metal machining operations play an essential role in controlling the quality of the final product. Different approaches have been researched to improve the performance of metalworking fluids. The use of vegetable oils and fatty acid methyl esters such as palm oil methyl ester (POME) has been studied and has been shown to improve the machining operation parameters. These two types of lubricants have environmental and lubricating advantages over conventional mineral oil based lubricants. Characterization of the properties of metalworking fluids helps to identify the composition of the base fluid, predict the coefficient of friction and film thickness, and assess the ability of heat removal of a fluid of interest. In this study, the refractive index, dynamic viscosity and thermal conductivity were measured and analyzed for naphthenic base oil, groundnut oil, blend of 1:1 ratio by weight of naphthenic-groundnut oil and POME formulated samples of the aforementioned. POME was added at volume fractions of 0.03, 0.05 and 0.07. The refractive index was measured at a fixed temperature. Meanwhile, the dynamic viscosity and thermal conductivity were measured at different temperatures. Results show that the refractive index of all the tested samples can be predicted accurately using the Arago-Bilot relation. The dynamic viscosity was found to decrease with temperature and POME content, and increase with groundnut oil content. The results indicate that groundnut oil can provide thicker film than mineral oil. If the film thickness is desired to be reduced by a certain fraction, then the use of POME as an additive can reduce the viscosity. The behavior of the dynamic viscosity as a function of temperature was modeled using different equations. The Power Law Model and the Andrade equation were shown to fit the experimental data with the least standard error of estimate. Analysis of the thermal conductivity shows that groundnut oil has a higher thermal conductivity when it is compared to the naphthenic based mineral oil. This shows that groundnut oil is more capable of removing the heat generated during machining than the naphthenic base oil. In contrast, POME content and temperature did not show strong influence on thermal conductivity.

Keywords: Metalworking, Naphthenic Base, Groundnut Oil, POME, Refractive Index, Thermal Conductivity, Viscosity.

1. Introduction

Since antiquity, the making of things has been an essential feature of human civilization. Nowadays, the making of things is known as manufacturing. In an economic sense, manufacturing is the act of transforming the material by changing its shape or properties into an item of a greater value. Metalworking process is a shaping operation that can be viewed as a part of both deformation and material removal processes [1, 2]. Cutting is an example of a material removal process, meanwhile drawing is an example of metal forming process. In both modes, lubrication plays an important role. For instance, in metal forming operations lubricants control the flow of the material, friction and the final surface quality of the product to be formed [3]. Generally, all the metal forming operations involve high pressures, temperature, friction and wear. On the other hand, the cutting operation involves the brining of two solids; a tool and workpiece into contact in order to create a new shape. The process involves elevated temperatures, high pressure, considerable friction and tool wear. The function of the lubricant in cutting is to control these parameters through lubrication, cooling and protection against corrosion to increase the efficiency and productivity. [1]. Lubricants or fluids that are applied in metalworking operations are known as metalworking fluids (MWFs). Two general types of MWFs are generally applied which are labeled as either lubricants or coolants. The former is more effective in low speed operations. In contrast, coolants are more effective at high speed operations in which high heat and temperatures are problems. The lubricants type is usually oil-type fluids, meanwhile coolants are usually water based [2].

The majority of modern lubricants are mostly petroleum based, also known as mineral oils. The principle attribute of mineral oils fractions is their low cost [4]. Mineral oils can be classified according to their chemical forms into paraffinic, naphthenic or aromatic. Among these naphthenic type has average properties among the two extremes, paraffinic and aromatic. On one hand, naphthenic structures have higher densities and viscosities than paraffins. Furthermore, they are advantageous in terms of their melting points as when they are compared to paraffinic structures [5]. This means that they do not contribute to wax. Furthermore, paraffinic oils are costlier as they need more refining stages [6]. However, naphthenic structures have an inferior viscosity-temperature and oxidative stability behavior as when they are compared to paraffinic structures. Nevertheless, naphthenic structures have an excellent solvency affiliation for additives as when they are compared to paraffinic [5]. On the top of this, naphthenic base oils are more preferred in metal forming operations [1].

Due to the growing concern of the technology impacts on the environment, the demand for biodegradable lubricants has increased [7]. Mineral oils based lubricants are not always in harmony with the environment, hence disposal of them poses a problem [1]. In fact, it has been reported that more than 50% of the sold lubricants in the world pollute the environment through spillage, evaporation and total-loss lubrication. Vegetable oils are regarded as environmentally friendly. This is since they are renewable, highly biodegradable, harmless to aquatic systems and noncumulative to the environment. Generally, when it comes to thermal and oxidative stabilities, vegetable oils are deficient to mineral oils, chemically modified vegetable oils and most synthetic lubricants. Along with this, vegetable oils suffer from poor low-temperature properties [7]. Fortunately, vegetable oils have a number of advantages in addition to biodegradability. These include, highly good lubricity, excellent viscosity-

temperature relationship, nontoxicity, environmental safety, low volatility and non-carcinogenicity. The good lubricity as a characteristic of vegetable oil allows it to be used as a friction-reducing additive [1]. Groundnut oil as a MWF showed superior performance in two different studies. Ojolo et al. [8], investigated the effects of four straight biological oils on the cutting force during cylindrical turning. The biological oils that were tested are groundnut, coconut, palm kernel and shear butter oils. In the study, groundnut oil exhibited the highest reduction of the cutting force. In another study, Lawal et al. [9], studied the performance of a commercial cutting fluid which was compared with groundnut, palm and palm kernel oils. The temperature was used to evaluate the performance of the cutting fluids. It was found that the groundnut oil performed as the best coolant at all the experimented speeds.

Vegetable oils although have many advantages, suffer from a number of disadvantages which are related to their oxidative stability and low-temperature properties. Therefore, prior to applying them, correcting vegetable oils properties must be considered. One way to correct the properties of vegetable oils is through chemical modification of their structures. Transesterification is a chemical modification process which is widely used to produce alternatives to vegetable oils such as biodiesels [10]. The process uses an alcohol such as methanol or ethanol to break the molecule of the raw vegetable oils into their methyl or ethyl esters with a byproduct of glycerol [11]. The palm oil industry contributes considerably to the industrialization of Malaysia, as well as it holds significant lead in the global market. In order that the palm oil industry grows and remains competitive in the global marks, palm oil product diversification must be taken into consideration. One of the forms of palm oil product diversification is POME. It is produced by the transesterification of the palm oil [12]. Dayou et al. [13], reported that the presence of POME in amounts as low as 5 vol.%, resulted in a lower steady state friction coefficient. Furthermore, the occurrence of fracture and cracking were delayed during the milling operation.

A number of properties are important for lubricants. The refractive index (RI) is quite unique to oil composition and therefore it can be used to characterize basestoke. Viscosity plays a crucial role in lubrication. The film thickness that is generated by the oil is proportional to the viscosity. Thus, the more viscous the oil is, the thicker the generated film is. Thicker films might give better separation between the two surfaces, however viscous oils requires more power to be sheared. This in turn leads to more power losses and more heat is generated. This could lead to the failure of the components due to the temperature rise [14]. The thermal conductivity (TC) is another important property which can determine the ability of the fluid to remove heat and cool the system components. In the present paper, different blends of base fluids are prepared using naphthenic base oil, groundnut oil and POME at different proportions. The properties measured for each sample are RI, dynamic viscosity and TC.

2. Experimental Method

2.1 Sample Preparation

The naphthenic oil was supplied from Nynas and the POME was supplied from Excel Vite. The groundnut oil was purchased from Waitrose. Pure naphthenic and groundnut oils are mixed with POME at volume percentages of 3%, 5% and 7%.

Along with this, one blend of naphthenic and groundnut oils is prepared by mixing an equal proportion by weight of each. Similarly, POME was mixed with the blend sample at the same volumetric percentages. (Table 1) shows the labels and the compositions for all the samples prepared.

Table 1. Base Fluids Composition

Label	Mineral Oil (wt.%)	Vegetable Oil (wt.%)	POME (vol.%)
ML	100	0	0
PML1			3
PML2			5
PML3			7
BML	50	50	0
PBML1			3
PBML2			5
PBML3			7
BL	100	0	0
PBL1			3
PBL2			5
PBL3			7

2.2 Refractive Index

The RI was measured for each sample using digital Abbe Refractometer DR-A1 at a temperature of roughly 24 ℃. The RI was measured three times to obtain an average value.

2.3 Dynamic Viscosity

The dynamic viscosity was measured using Haake Mars Rheometer. The viscosity was measured at temperatures of 24 ℃, 40 ℃ and 100 ℃. For each temperature, the viscosity was measured at two different shear rates which are 10 s^{-1} and 500 s^{-1}. The average viscosity between these two shear rates is used for further analysis.

2.4 Thermal Conductivity

The TC was measured using thermal property analyzer KD2 Pro. The TC was measured at temperatures of 25 ℃, 40 ℃, 55 ℃ and 70 ℃. Three values of TC are recorded for each temperature to obtain an average value. Only readings which have an error value below 0.7% are accepted.

3. Results and Discussion

3.1 Analysis of Refractive Index

RI is very useful in characterization of basestocks of fluids that have equal molecular mass. The property measures the ratio of the velocity of light in air to that in the fluid medium. Knowledge of RI along with viscosity and specific gravity is very useful in hydrocarbon identification. The RI is proportional to the molecular weight of the oil [15]. (Table 2) shows the RI of pure naphthenic base oil, groundnut oil and POME.

Table 2. Refractive Index Results of Pure Fluids

Fluid	RI
Naphthenic	1.4911
Groundnut	1.4675
POME	1.4461

As it can be seen from (Table 2), the naphthenic base oil has the highest RI, followed by groundnut oil and then POME. The results could indicate as well that the naphthenic base has the highest molecular weight while POME has the lowest molecular weight. A blend of these oils is expected to have RI that is between the values of the pure components. This has been shown to be true by measuring the RIs of the blend and formulated base fluids. (Fig. 1) and (Fig. 2) show the RI as a function of groundnut oil weight percentage and as a function of POME volume percentage, respectively. It can be seen from (Fig. 1) that the RI decreases as the amount of groundnut oil added is increased. Similarly, it can be seen from (Fig. 2) that for each POME formulated sample group, the RI decreases as the amount of POME added is increased. The RI was found to be predicted with high accuracy using the simple Arago-Bilot relation [16]:

$$\boldsymbol{RI_m = vol_1\, RI_1 + vol_2\, RI_2} \quad (1)$$

Where RI_m is the refractive index of a mixture and vol is the volume fraction. This model was extended to account for three components.

$$\boldsymbol{RI_m = vol_1\, RI_1 + vol_2\, RI_2 + vol_3\, RI_3} \quad (2)$$

The formula was further manipulated to come up with a formula where the RI is presented as a function of POME vol.% and groundnut wt.%.

$$RI_m = \frac{vol_{pome}\%}{100}\left(RI_{pome} - \frac{\left(\frac{wt_{vo}\%}{100-wt_{vo}\%}\frac{\rho_{mo}}{\rho_{vo}}RI_{vo}+RI_{mo}\right)}{\left(\frac{wt_{vo}\%}{100-wt_{vo}\%}\frac{\rho_{mo}}{\rho_{vo}}+1\right)}\right) + \frac{\left(\frac{wt_{vo}\%}{100-wt_{vo}\%}\frac{\rho_{mo}}{\rho_{vo}}RI_{vo}+RI_{mo}\right)}{\left(\frac{wt_{vo}\%}{100-wt_{vo}\%}\frac{\rho_{mo}}{\rho_{vo}}+1\right)} \quad (3)$$

Where $wt_{vo}\%$ is the weight percentage of the vegetable oil, $vol_{pome}\%$ is volumetric percentage of POME and ρ is the density. The above model was able to predict the experimental data with very small errors. The subscripts *mo* and *vo* stand for mineral and vegetable oils, respectively. The coefficient of determination of the model was found to be very high, $R^2 = 0.99$. (Fig 3) shows a three-dimensional plot of the RI as a function of POME volumetric percentage and groundnut oil weight percentage. The response surface in (Fig 3) shows that the RI decreases as the amount of groundnut oil and POME are increased. The model derived can be used to estimate the composition of the samples tested by knowing the RI value and at least the amount of one component.

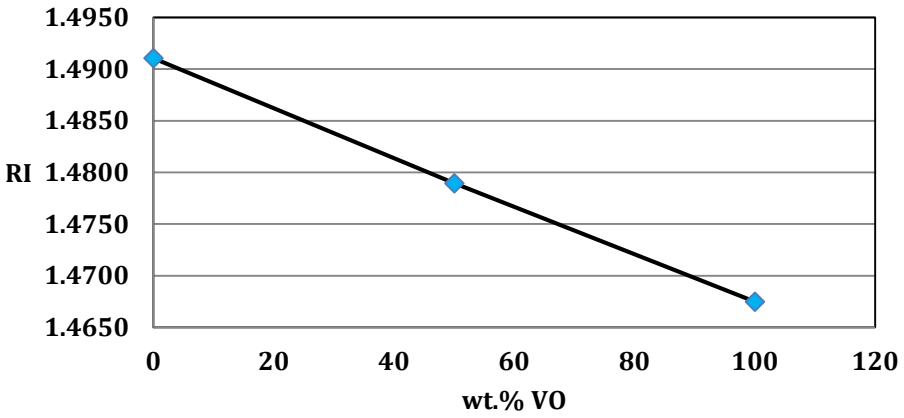


Figure 1. RIs of POME-free Additive Samples

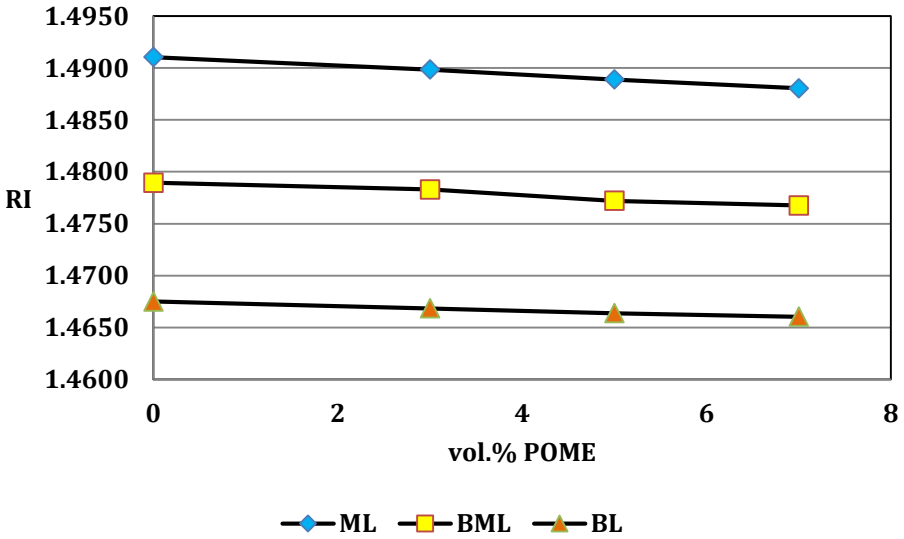


Figure 2. RIs of POME Formulated Samples

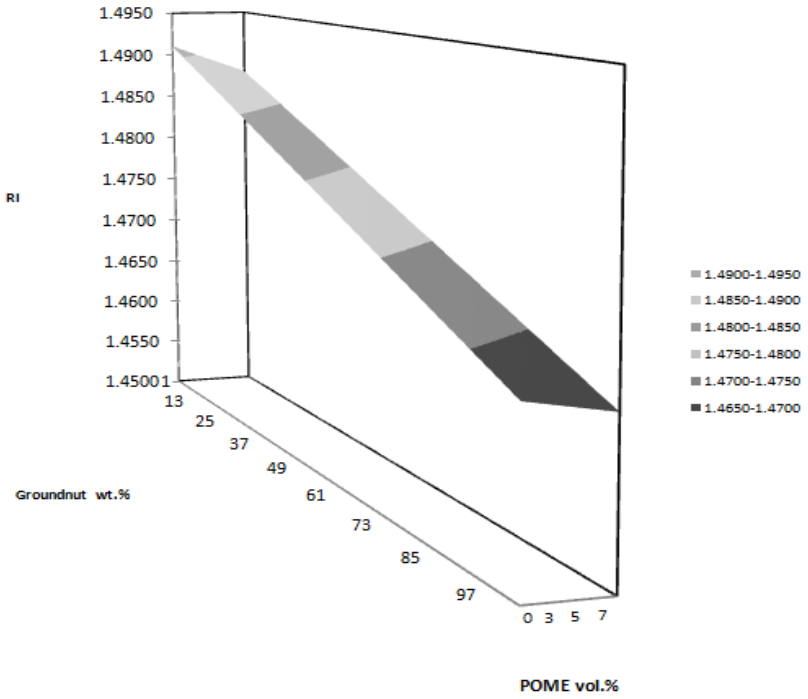


Figure 3. Response Surface of RI

3.2 Analysis of Dynamic Viscosity

Generally, it is an established fact that temperature has a strong influence on viscosity. Generally, the viscosity of a fluid decreases with the increase of temperature [17]. Measurements of the viscosities of the test samples confirm this fact. Viscosity represents the interaction of molecular forces. At higher temperatures, molecules slide over each other which make the fluid less viscous. (Fig. 4) shows the viscosities of ML, BL and BML samples as a function of groundnut oil weight percentage. It can be seen from (Fig. 4) that the viscosity increases with increasing the fraction of groundnut oil. Furthermore, the 100 ℃ curve has the lowest viscosities. On the other hand, the 24 ℃ curve has the highest viscosities. This shows that the viscosity decreases with increasing temperature.

(Fig. 5), (Fig. 6) and (Fig. 7) show the viscosities of the POME formulated samples at a temperature of 24 ℃, 40 ℃ and 100 ℃, respectively. It can be seen from (Fig. 5), (Fig. 6) and (Fig. 7) that viscosity decreases with increasing POME volume fraction. It can be seen as well that the vertical distance between ML and BML curves is shorter than that between BML and BL. This shows that the rate of viscosity increase with respect to groundnut oil content increases at higher values of groundnut oil weight fractions. The results show that the thickness of the generated film for all the sample groups can be reduced by addition of POME. In contrast, addition of groundnut oil can increase the film thickness. In metal machining, two modes of lubrications are experienced which are the boundary (extreme pressure) or the hydrodynamic which is also known as full-film. The film thickness is a function of the variable $\frac{ZN}{P}$ where Z is the dynamic viscosity, N is the relative speed of the moving surfaces and P is the load applied [18]. The desired viscosity for a certain application depends on the speed and the applied load.

Different models were applied to assess how well existing models predict dynamic viscosity as a function temperature. The models used in this paper are shown in (Table 3). In (Table 3), T is the absolute temperature and μ is the dynamic viscosity. The variables k, n, a, b, A and B are constants. The reference temperature to be used in the PLM model is $T_{Ref} = 273.15$ K. The Andrade equation in (Table 3) is re-expression of the Arrhenius equation. The standard error of estimate (SEE) was calculated for each model with respect to each prepared sample. The SEE values are shown in (Table 4). The SEE values represent the average distance for which the measured or observed values are away from the prediction line. The lower the SEE value is, the closer the actual values to the fitted line are.

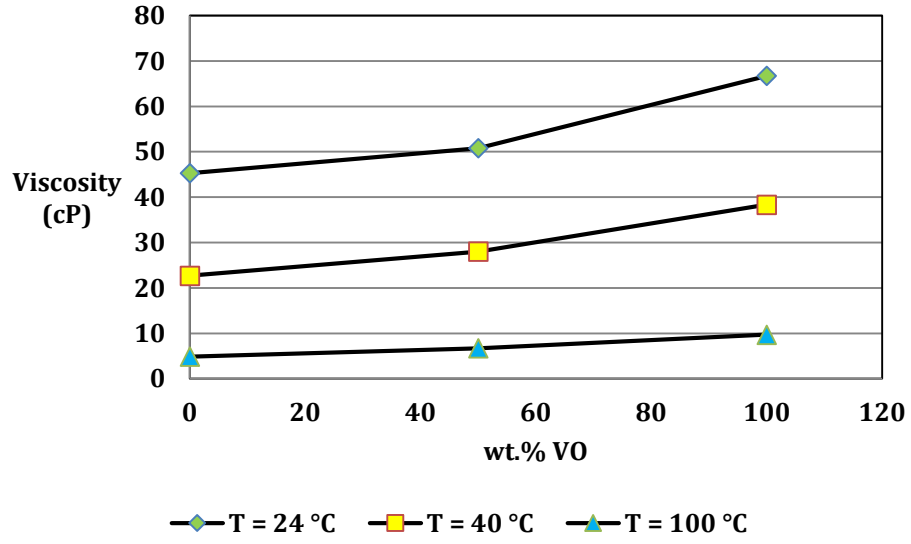


Figure 4. Viscosities of POME-free Additive Samples

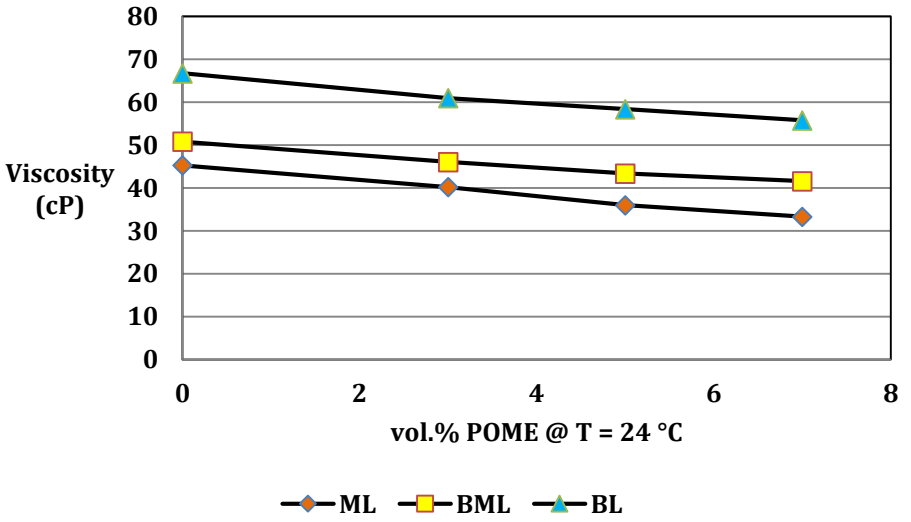


Figure 5. Viscosity of POME Formulated Samples at $T = 24$ ℃

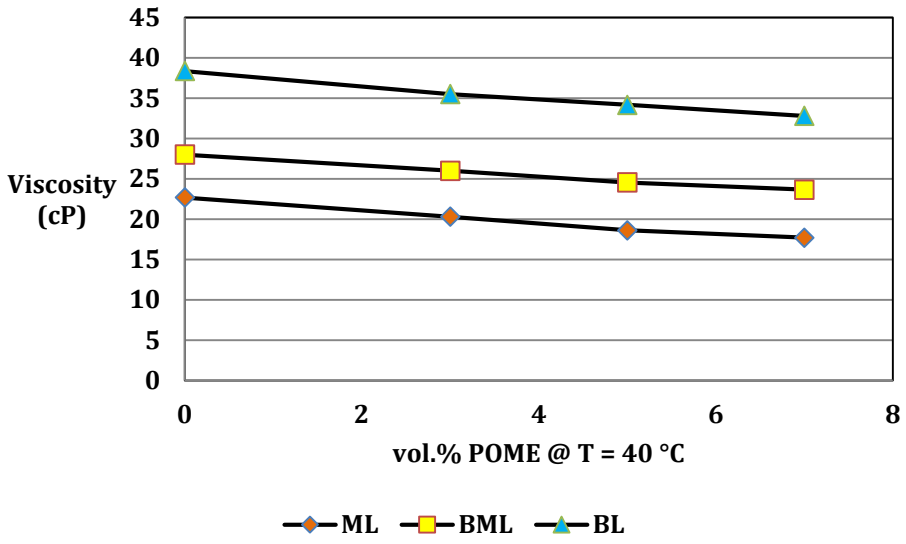


Figure 6. Viscosity of POME Formulated Samples at $T = 40$ ℃

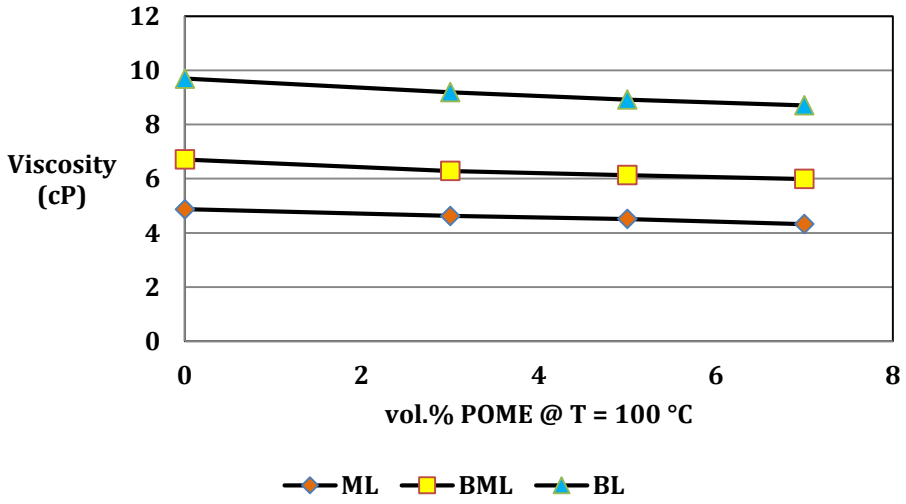


Figure 7. Viscosity of POME Formulated Samples at $T = 100$ ℃

Table 3. Viscosity-Temperature Dependency Equations

Model	Expression	
Power Law Model (PLM) [17]	$\mu = k\,(T - T_{Ref})^n$	(4)
Modified William Landel-Ferry (mod-WLF) [17]	$\mu = e^{\frac{a\,T}{b+T}}$	(5)
Reynolds [14]	$\mu = b\,e^{-a\,T}$	(6)
Andrade [19]	$\mu = Ae^{\frac{B}{T}}$	(7)
		(8)

Power Function	$\mu = k\,T^{n}$

Table 4. SEE Values for Viscosity-Temperature Models

Sample	PLM	mod-WLF	Reynolds	Andarde	Power Function
ML	1.469	8.322	3.158	1.912	8.191
PBML1	1.121	6.880	2.911	1.806	5.223
PBML2	0.937	5.572	2.566	1.601	3.695
PBML3	1.025	5.521	2.135	1.302	4.107
ML Ave	1.138	6.574	2.693	1.655	5.304
BML	2.074	6.164	3.009	1.476	9.540
PBML1	2.076	6.046	2.315	1.114	2.144
PBML2	1.826	5.378	2.220	1.130	3.366
PBML3	1.735	5.129	2.204	2.916	6.177
BML Ave	1.928	5.679	2.437	1.659	5.307
BL	2.938	5.970	3.293	1.568	5.805
PBL1	2.691	5.421	2.852	1.367	2.970
PBL2	2.605	5.284	2.829	1.264	1.933
PBL3	2.428	4.902	2.663	1.231	3.968
BL Ave	2.666	5.394	2.909	1.358	3.669

Based on (Table 4), it can be noted that PLM and Andrade models describe the viscosity-temperature dependency better than other models. The ML group samples are better described by the PLM model, meanwhile the BML group and BL group samples are better described on average by the Andrade equation. (Table 5) shows the constants of the PLM and Andrade equation for all samples considered in this paper.

Table 5. Constants of PLM and Andrade Model

Sample	PLM		Andrade Model	
	k	n	A	B
ML	7.09×10^{3}	-1.576	9.20×10^{-4}	3.19×10^{3}

PML1	5.34×10^3	-1.527	11.5×10^{-3}	3.09×10^3
PML2	3.93×10^3	-1.466	15.6×10^{-3}	2.96×10^3
PML3	3.41×10^3	-1.443	16.8×10^{-3}	2.92×10^3
BML2	5.12×10^3	-1.435	27.01×10^{-3}	2.91×10^3
PBML1	4.37×10^3	-1.414	28.18×10^{-3}	2.87×10^3
PBML2	3.77×10^3	-1.388	31.79×10^{-3}	2.82×10^3
PBML3	3.47×10^3	-1.375	30.51×10^{-3}	2.79×10^3
BL	5.48×10^3	-1.369	55.49×10^{-3}	2.78×10^3
PBL1	4.61×10^3	-1.343	60.70×10^{-3}	2.73×10^3
PBL2	4.29×10^3	-1.334	61.78×10^{-3}	2.71×10^3
PBL3	3.90×10^3	-1.319	65.72×10^{-3}	2.68×10^3

3.3 Analysis of Thermal Conductivity

Thermal conductivity is an important parameter that is related to the capability of heat removal of the fluid of interest. (Fig. 8) shows the TC of free-POME samples as a function of temperature. It can be seen from (Fig. 8) that increasing groundnut oil proportion leads to higher thermal conductivities. With respect to temperature, the variation does not seem to be of a greater influence. The TC curve for all the samples increases as the temperature increases and achieves a maximum point at around $40\ ℃ - 55\ ℃$. Then, TC drops at higher temperatures. The BL and ML samples have smoother curve when they are compared to the BML group. This could be due to the blending effect. Similarly, POME formulated samples did not show strong correlation with temperature. The results indicate POME does not show strong effect on TC when it is added at very small amounts. Due to this the average TC at different temperatures for the POME formulated samples are used for further analysis. (Fig. 9) shows the average TC as a function of POME volume percentage for different samples group.

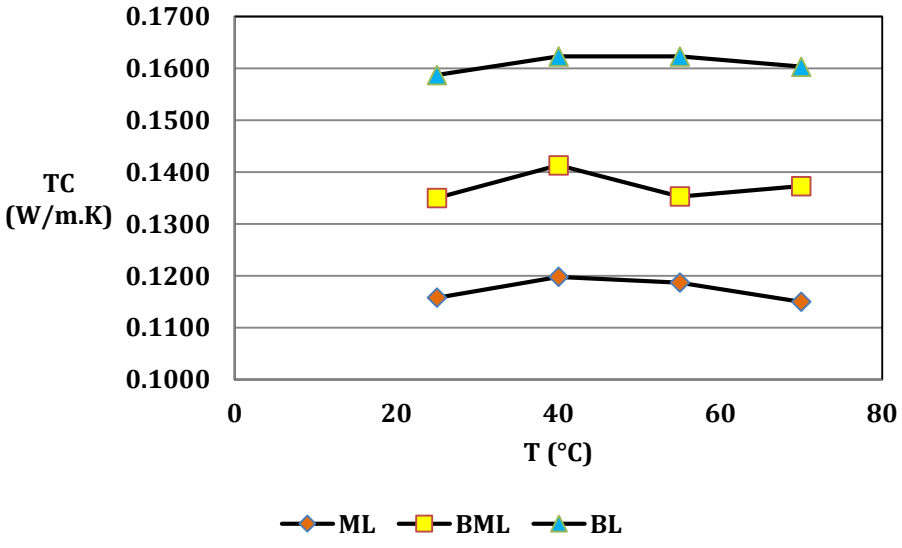


Figure 8. TCs of POME-free Samples

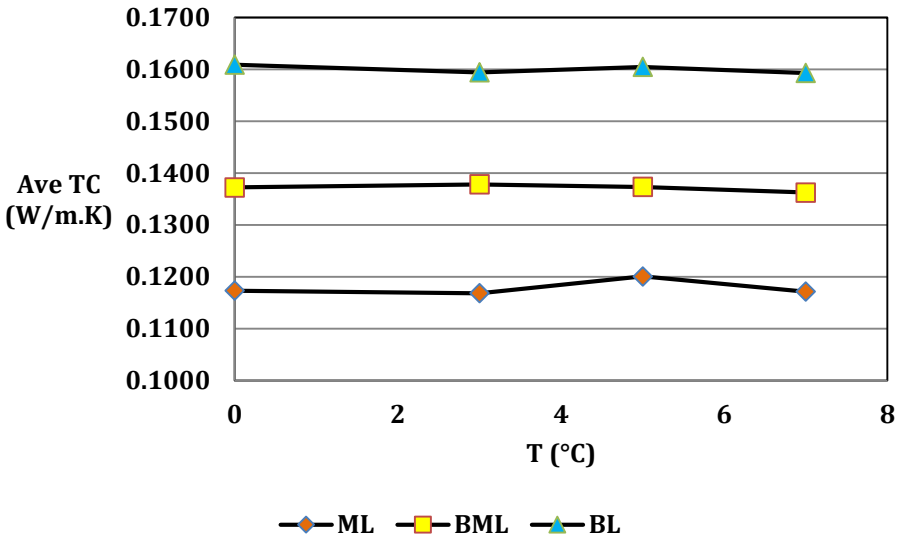


Figure 9. Average TCs of POME Formulated Samples

It can be seen from (Fig. 9), the effect of POME is not consistent and rather random. For the ML group, the 5 vol.% obtains the highest enhancement of TC. The BML group shows that the enhancement of TC decreases as the vol.% of POME is increased. The BL group generally shows negative enhancement, however the least negative enhancement is achieved at 5 vol.% of POME. In order to analyze the variance statistically, the F-test is performed for each sample group separately. The test is based on two-factorial design where the parameters of interest are the temperature and volume precentage of POME. (Table 6) shows the F-test results. The test is performed based on $\alpha = 0.01$ level of significance.

Table 6. Analysis of Variance of TC

Sample Group	Source of Variation	Degrees of Freedom	F-value
ML	POME	3	14.8
	Temperature	3	9.9
	Interaction	9	5.4
	Error	32	
BML	POME	3	9.2
	Temperature	3	88.8
	Interaction	9	11.8
	Error	32	
BL	POME	3	1.4
	Temperature	3	4.8
	Interaction	9	2.3
	Error	32	

Based on the F-table, $F_{3,32,0.01} = 4.47$ and $F_{9,32,0.01} = 3.03$. If the F-computed value is larger than the values obtained from the F-table, then the effect of the particular source of variation is significant. From (Table 6), it can be deduced that the effects of POME, temperature and interaction are significant for ML and BML group samples. However, for the BL group samples, temperature is the only significant effect.

4. Conclusion

In this study, the RI, dynamic viscosity and TC were measured for pure naphthenic oil, pure groundnut oil and a blend of both. POME was added to each sample at 3 volume fractions. The results show that the RI is the highest for the mineral oil and the lowest of POME. For the POME-free samples, the RI decreases as the amount of the vegetable oil is increased. For the POME formulated samples, the RI decreases as the amount of POME added is increased. It was found that RI for the samples tested can be modeled with relatively high accuracy using the Arago-Bilot relation. The results of the dynamic viscosity show that viscosity increases with increasing the vegetable oil content and decreases with increasing the POME content. The viscosity for all the samples decreases with increasing the temperature. It was found that Andrade and PLM models fit the experimental data with relatively low SEE values.

Analysis of the TC shows that the TC increases as the amount of groundnut oil used is increased. This shows that groundnut as a vegetable oil will have a better performance as a MWF in terms of heat removal than the mineral oil. Nevertheless, the changes of TC due to changes of temperature and addition of POME were small. Indeed, Analysis of variance showed that POME effect is not significant for the groundnut samples group. Although very small, the temperature and POME effects were found to be significant for both mineral oil and blend samples group. The 5 vol.% of POME achieves the highest enhancement of TC on average for the mineral oil group, meanwhile 3 vol.% of POME resulted in the highest enhancement of TC for the blend samples group. In contrast, the addition of POME resulted in reduction of TC for the groundnut samples group.

In future research, measurements of the density are to be done in order to compute the viscosity index. Analysis of oxidation stability and vapor loss are to be conducted as well. Tribological test and relevant cutting application are of high importance. These tests are to be conducted and be correlated with the measured properties of each sample. If the tribological and cutting tests correlate very well with the measured properties, one can hope that models can be derived in order to allow selection of cutting fluid for certain application without the need of reliance on trial and error test approach.

Acknowledgement

The study was supported by ExcelVite Sdn Bhd by providing POME and by Nynas Pte Ltd which provided Naphthenic base Oil.

References

[1] S. Q. A. Rizvi, *Comprehensive Review of Lubricant Chemistry, Technology, Selection, and Design*, 2009.

[2] M. P. Groover, *FUNDAMENTALS OF MODERN MANUFACTURING Materials, Processes, and Systems*, Fourth Edition. United States of America, JOHN WILEY & SONS, INC., 2010.

[3] E. V. D. Heide and D. J. Schipper, "Friction and Wear in Lubricated Sheet Metal Forming Processes" in *Handbook of Lubrication and Tribology*, 2006.

[4] E. E. Klause and E. J. Tewksbury, "LIQUID LUBRICANTS" in *CRC HANDBOOK of LUBRICATION (Theory and Practice of Tribology)*, vol. II, 1983, pp. 229-54.

[5] R. J. Prince, "Base Oils from Petroleum" in *Chemistry and Technology of Lubricants*, Netherlands, 2010, pp. 3-33.

[6] G. W. Stachowiak and A. W. Batchelor, "3 - Lubricants and Their Composition" in *Engineering Tribology (Third Edition)*, 2006, pp. 51-101.

[7] M. P. Joseph, R. R. Leslie and Z. E. Sevim, "Natural Oils as Lubricants" in *Synthetics, Mineral Oils, and Bio-Based Lubricants*, 2013, pp. 375-84.

[8] S. J. Ojolo, M. O. H. Amuda, O. Y. Ogunmola and C. U. Ononiwu, "Experimental determination of the effect of some straight biological oils on cutting force during cylindrical turning", *Matéria (Rio de Janeiro)*, vol. 13, pp. 650-63, 2008.

[9] S. A. LAWAL, M. S. ABOLARIN, B. I. UGHEOKE and E. O. ONCHE, "Performance Evaluation of Cutting Fluids Developed from Fixed Oils", *Leonardo Electronic Journal of Practices and Technologies*, 2007.

[10] K. Khalid and K. Khalid, "Transesterification of Palm Oil for the Production of Biodiesel", *American Journal of Applied Sciences*, vol. 8, pp. 804-9, 2011.

[11] Z. E. Sevim, A. Atanu and K. S. Brajendra, "Chemically Functionalized Vegetable Oils" in *Synthetics, Mineral Oils, and Bio-Based Lubricants*, 2005.

[12] W. L. Y. Hsien, "Utilization of Vegetable Oil as Bio-lubricant and Additive" in *Towards Green Lubrication in Machining* Singapore, 2015, pp. 7-17.

[13] S. Dayou, W. Y. H. Liew, M. A. B. Ismail and J. Dayou, "EVLUATION OF PALM OIL METHYL ESTER AS LUBRICANT ADDITIVE USING MILLING AND FOUR-BALL TESTS", *International Journal of Mechanical and Materials Engineering*, vol. 6, pp. 374-9, 2011.

[14] G. W. Stachowiak and A. W. Batchelor, "2 - Physical Properties of Lubricants" in *Engineering Tribology (Third Edition)*, 2006, pp. 11-50.

[15] A. T. Larry and M. T. Allison, "Lubricant Properties and Test Methods" in *Lubrication and Maintenance of Industrial Machinery*, 2008.

[16] S. O. Isehunwa, E. B. Olaniseba, O. O. Ajiboye and S. A. Akintola, "Estimation of the refractive indices of some binary mixtures", *African Journal of Pure and Applied Chemistry*, vol. 9, pp. 58-64, 2015.

[17] O. O. Fasina and Z. Colley, "Viscosity and Specific Heat of Vegetable Oils as a Function of Temperature: 35°C to 180°C", *International Journal of Food Properties*, vol. 11, pp. 738-46, 2008.

[18] G. B. Richard and L. B. William, "Metalworking Fluids" in *Synthetics, Mineral Oils, and Bio-Based Lubricants*, 2005.

[19] B. Esteban, J. R. Riba, G. Baquero, A. Rius and R. Puig, "Temperature dependence of density and viscosity of vegetable oils", *Biomass and Bioenergy*, vol. 42, pp. 164-71, 2012.

eureca 2016 – Conference Paper
Paper Number CE_PG05

Thermophysical Properties of Glycerol and Polyethylene Glycol 600 based Deep Eutectic Solvents (DESs)

Amarpreet Singh[1], Rashmi Walvekar[1*], Kaveh Shahbaz[2], Wong Wai Yin[3], Khalid Siddiqui[4]

[1] *Taylor's University, Jalan Taylor's, Subang Jaya, 47500 Selangor, Malaysia*
[2]*University of Auckland, Auckland 1010, New Zealand*
[3]*Fuel Cell Institute, Universiti Kebangsaan Malaysia, 43600 UKM Bangi, Selangor, Malaysia.*
[4]*University of Nottingham, 43500 Semenyih, Selangor,Malaysia*

[*]rashmigangasa.walvekar@taylors.edu.my

Abstract
In this study, the DESs are based on glycerol and polyethylene glycol 600 (PEG) as hydrogen bond donor and common salt of choline chloride (ChCl). The glycerol based DESs were formed with ratio of 1:2, 1:3, 1:4 and 1:5 whereas three-component DESs of ChCl, PEG and glycerol were synthesized with ratio 1:3:2, 1:4:2 and 1:5:2. The DESs were subjected to Karl Fishcer, thermal conductivity, viscosity and density testing. The moisture content in DESs were identified through Karl Fishcer testing was found to be lower than 1% which is desired when synthesizing DES. The thermal conductivity of glycerol based DESs decreases with respect to pure HBD whereas for PEG based DESs shows positive enhancement of thermal conductivity. Similarly, the viscosity of glycerol DESs decreases with increasing temperature and PEG DESs increases in comparison to pure HBDs. All the DES samples have linear decrease across a temperature range with highest density achieved at 1.2155 g/cm^3 with temperature of 25℃ for molar ratio of ChCl to glycerol of 1:4 (DES 4). In general, the DESs can be considered as a tailor made solvent by changing the type of salt and HBDs combination as well as the molar ratio to suit any specific application.

Keywords: Deep Eutectic Solvent, Ionic Liquid, Glycerol, Polyethylene Glycol, Viscosity.

1. Introduction

Ionic Liquid (IL) is relatively new type of chemical that has been discovered for different application and has promising potential for other implication which is rapidly being explored. Currently, ILs have been applied in food science, separation, nanomaterial processing and may other industries. ILs are a type of liquid salt that consist of ions and ions pair which have relatively low melting points. IL compounds have asymmetrical cations and anions structure that allows ILs to have low melting point. The type of anions and cations determine the physical and chemical properties of IL. The common type of cations are imidazolium, ammonium, and pyridinium whereas anions are PF_6, BF_4, and others [1].

There might be plenty of advantages of using ILs but unfortunately there are some disadvantages. In the usage of anions such as PF_6 and BF_4 imidazolium salts can lead to reaction with water which results in formation of hydrogen fluoride. The unwanted formation can greatly affect the surroundings [2]. Some ILs showed severe corrosiveness towards copper metal strips when tested at elevated temperatures [3]. The decomposition of IL with the existence of air and moisture results in corrosion. The occurrence of corrosion on the lubricating surface will reduce the lifespan of the equipment causing failure and increased cost due to replacement of the specific part.

These disadvantages are overcome by the discovery of Deep Eutectic Solvents (DESs). DES is a type of mixture formed by two or more components which have similar properties as IL but is different in composition and structure. The physical properties of DESs and ILs are similar but the chemical properties are different. The difference allows wider potential application of DES in different areas compared to IL. DES is formed with a quaternary ammonium salt and hydrogen bond donor which has charge delocalization in the form hydrogen bonding. The hydrogen bond is formed between halide ion and HBD having lower melting point compared to the individual component [4]. The HBD can be amide, acid, alcohol and other suitable compound that is capable of forming hydrogen bond. DES is produced by simple mixing process which is relatively cheap in order to obtain a eutectic mixture [5]. This process is even cheaper than the production of ILs which makes it more feasible to replace ILs with DES.

DES has lower melting point than the individual component due to formation of complex anion that decreases the lattice energy[6]. The components are prepared by mixing and heating to produce the required DES. The melting point or freezing point of the DES is achieved by eutectic composition of the mixture of the two component. Eutectic point is achieved by varying the molar ratio of the salt and HBD.

In Abbot, Ahmed, Harris & Ryder (2014), four types of DESs were synthesised. The DESs used ChCl [$(CH_3)_3$-N^+-CH_2-OH Cl^-] as salt and four different HBD which were urea (1:2), ethylene glycol (1:2), glycerol (1:2) and oxalic acid (1:1). DESs together with imidazolium based ILs were tested for the corrosive nature towards metals. All the DES have extremely low freezing point except for urea based DES. This DES has the tendency to decompose at high temperature and form ammonia whereas oxalic acid based DES has high corrosiveness towards mild steel. Thus, ChCl and glycerol showed promising properties with low corrosivity and good viscosity profile. Similarly, all the DESs were tested with different type of metals

such as Iron (Fe), Aluminium (Al) and Nickel (Ni) together with water to observe the corrosive nature of ChCl based DES. The outcome showed low corrosion of DESs towards these metals except for oxalic acid based DES. The least corrosion was observed for glycerol based DES. [7].

Polyethylene glycol (PEG) is a form of polymer that consist of ethylene glycol monomers that has formula of $HO\text{-}(CH_2CH_2OH)_n\text{-}H$ and widely used in synthetic based lubricant. PEG is non-toxic and is classified according to the molecular weight of the compound [8]. When the molecular weight increases, the melting point of the compound increases. Besides that, the viscosity is known to increase with increasing molecular weight. Therefore, the formation of PEG based DES would be a new innovation and the physical properties can be investigated. The formation of glycerol and PEG based DES will allow to investigate the resultant thermophysical properties with respect to the individual HBDs whether DES formation has positive effect or negative effect on thermophysical properties.

2. Experimental

2.1 Materials

Choline Chloride (ChCL) $[HOC_2H_4N(CH_3)_3Cl]$ was purchased from Merck with purity 99% is used as the common salt for both the DESs. The industrial glycerol $[C_3H_8O_3]$ with purity of 97% was purchased together with polyethylene glycol 600 (PEG) $HO\text{-}(CH_2CH_2OH)_n\text{-}H$ of R&M chemicals from Wataka Trading. PEG 600 was selected because PEG 600 exist in liquid form at room temperature and further increasing the molecular weight will result in semi-solid compound that will not be suitable as HBD.

2.2 Preparation of DES

Glycerol based DESs were formed with four different molar ratio whereas the PEG based DESs were formed with three different molar ratios as shown in Table 1. The DESs were formed by mixing the components based on the molar ratio and stirred at 300 rpm at 120°C until a colourless liquid is formed. The molar ratio for glycerol based DESs were found from literature study whereas the inability of PEG to form two component DESs lead to three component DESs which were successfully synthesized.

Table 1. The molar ratios of salt to HBDs with their abbreviation.

Salt	HBD		Molar Ratio	Abbreviation
ChCl	Glycerol		1:2	DES 1
			1:3	DES 2
			1:4	DES 3
			1:5	DES 4
	PEG 600	Glycerol	1:3:2	DES 5
			1:4:2	DES 6

	1:5:2	DES 7

2.3 Physical Properties measurement

In order to measure the moisture content of DESs, Mettler Toledo Karl Fishcer was used. The thermal conductivity was measured as a function of temperature by using the KD2 Pro Deacgon Device with uncertainty of ± 5% and jacketed circulating water bath. The thermal conductivity was measured at 25°C, 40°C, 60°C, 80°C and 100°C. The viscosity was measure using Harkee Mars III Rheometer with spindle plate size of P35 Ti L and lower plate TMP 35. The viscosity was measured at 25°C, 40°C and 100°C with shear rate of 10 s^{-1} and 500 s^{-1}. The viscosity was obtained by taking the average viscosity of the two different shear rate at a specific temperature. The density was measured by using the Anton Par DMA 4500 M at temperature of 25°C, 40°C and 90°C. The viscosity was measured at temperature of 100°C which was selected due to limitation of the equipment and as the highest temperature to observe the behavior of DES at extreme temperature whereas the heating element of DMA 4500 M limits the temperature to 90°C to prevent any damage to the U-tube thus the DESs were measured at that particular temperatures.

3. Results and Discussion

3.1 Moisture Content

The process of mixing the DES component might lead to absorbance of moisture from the surroundings. Thus the Karl Fishcer titration determines the moisture content of the sample. The moisture content of glycerol and PEG based DESs are shown in Table 2 from which the moisture content was found to be lesser than 1% for all the samples. The least moisture was in DES 6 at 0.48% whereas the highest content was found in DES 1. Lower content of moisture is desired for DES for this research in order to achieve high resultant purity of the solvent. The existents of high moisture content can lead to alteration of physical properties where density, surface tension and viscosity decreases whereas thermal conductivity increases. However, there are some researcher focusses on the influence of DES-water mixture such as metal electrodeposition [9].

Table 2. The Percentage of water content in DESs

Sample	Percentage of Water (%)		
	1	2	Average
DES 1	0.79	0.66	0.73
DES 2	0.71	0.54	0.63
DES 3	0.77	0.54	0.66
DES 4	0.45	0.54	0.50
DES 5	0.61	0.62	0.62
DES 6	0.51	0.44	0.48
DES 7	0.44	0.56	0.50

3.2 Thermal Conductivity

Thermal conductivity is an important physical properties where amount of heat passes through a certain material is expressed. From Fig 1, it can be seen that increasing the ratio of HBD and increasing sample temperature results in thermal conductivity to be increased. Pure glycerol has relatively high thermal conductivity and the DESs derivative exhibit similar pattern. DES 1 has the lowest thermal conductivity followed by DES 2 while DES 3 has the highest conductivity whereas DES 4 has slightly lower conductivity than DES 3. The difference in thermal conductivity is closely related to the molar ratio of the DES. Glycerol is known for high thermal conductivity but when hydrogen bond is formed with salt the conductivity is reduced due to nature of the ChCl.

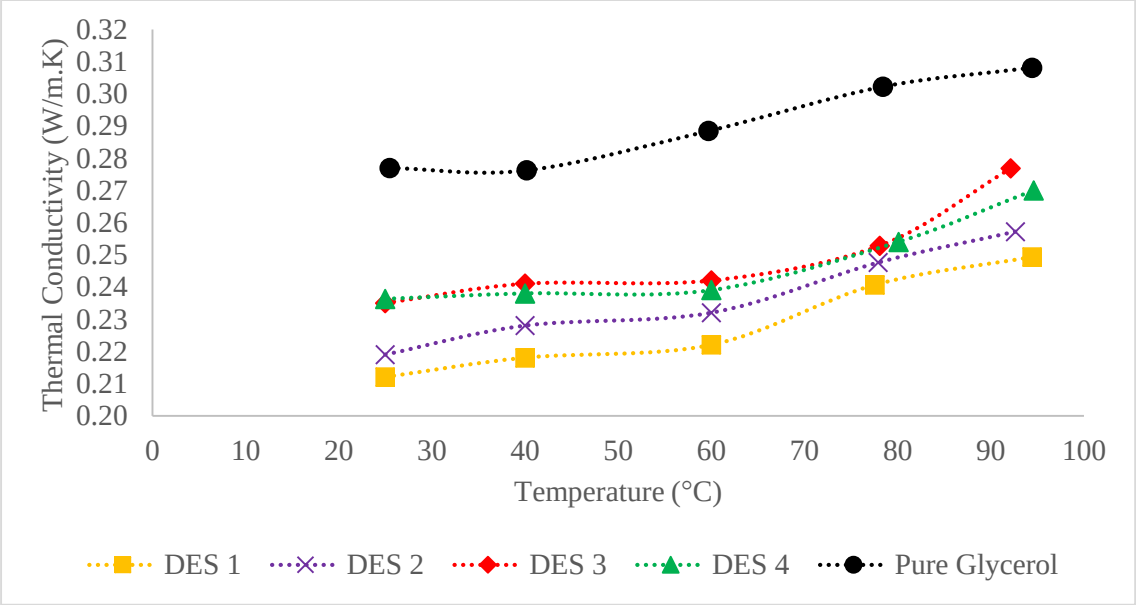


Figure 1. Thermal Conductivity of pure glycerol HBD and glycerol based DESs.

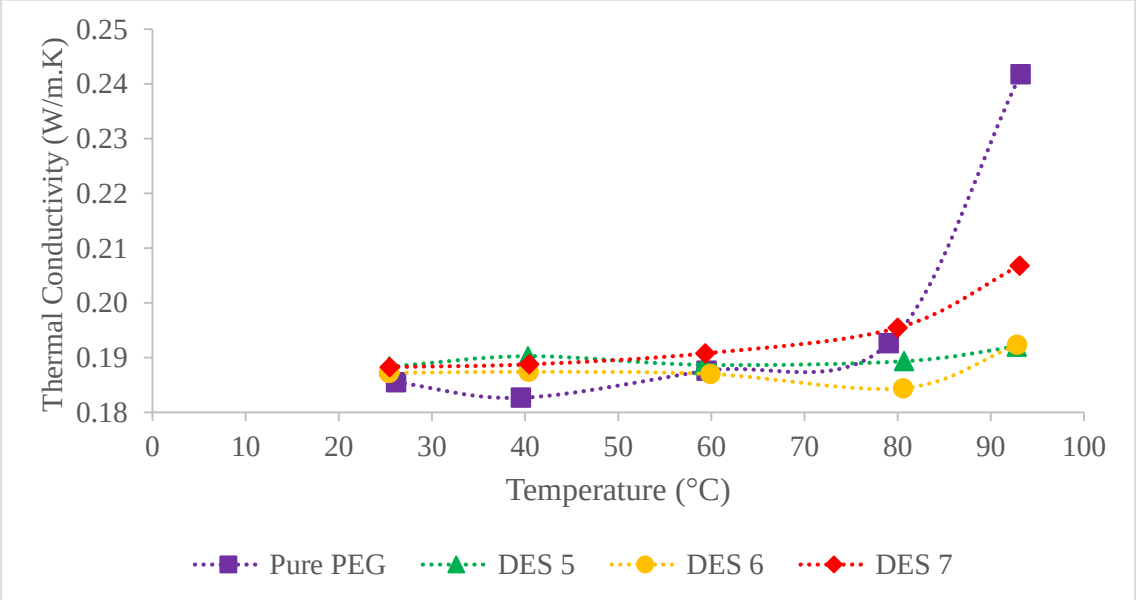


Figure 2. Thermal Conductivity of pure PEG HBD and PEG based DESs.

On the other hand, it is noted from Fig. 2 that PEG and the PEG based DESs are not significantly affect the thermal conductivity. The thermal conductivity of the DES 5, 6 and 7 was found to higher compare to pure PEG at lower temperatures but only at elevated temperature of 94°C PEG exhibit extremely high conductivity. The DESs show higher conductivity due to the addition of glycerol as the DESs formed with three different component compared to DES 1, DES 2, DES 3 and DES 4. Unfortunately, the DESs exhibit lower increment of conductivity at higher temperature in comparison with PEG HBD. The limitation that was encountered was to achieve temperature of 100°C with the water bath. Even though the water bath was set 100°C and the experiment was conducted in a fume hood, there was some heat lost and the jacket was only able to achieve temperature of 94°C.

3.3 Viscosity

Viscosity is a vital parameter that can studied. The viscosity generally decreases as the temperature increases that Fig 3 and Fig 4 show similar behavior. Glycerol has very high viscosity (0.7058 Pa.s) at room temperature and rapid decreases as the temperature increase. The DESs exhibit lower viscosity values compared to pure HBD and has a very small difference at temperature of 100°C. The lowest viscosity was obtained by DES 1 (0.2002 Pa.s) at 25°C followed by DES 3 (0.2440 Pa.s), DES 2 (0.2607 Pa.s), and DES 4 (0.3038 Pa.s). The variation of viscosity at 100°C is small with lowest being DES 3 (0.01271 Pa.s) then DES 1 (0.01339 Pa.s), DES 2 (0.01363 Pa.s), and finally DES 4 (0.01386 Pa.s).

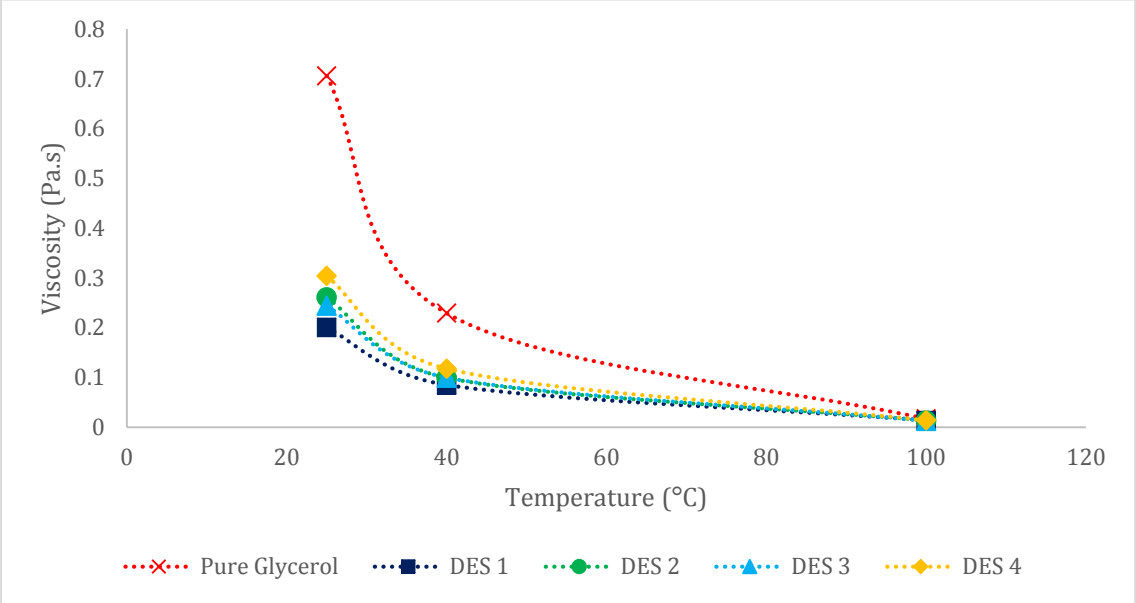


Figure 3. Viscosity of pure glycerol HBD and glycerol based DESs at 25°C, 40°C and 100°C.

From Fig.4, it is noted that viscosity of PEG is lower than PEG based DESs. At 25°C viscosity of PEG is 0.1282 Pa.s while increases with DES 7 (0.1686 Pa.s), DES 6 (0.1823 Pa.s) and DES 5 (0.1962 Pa.s). An opposite pattern is observed for PEG based DESs compared to the glycerol based DES. From the viscosity

information of DES, the suitable application with respect to an optimum molar ratio can be identified and selected. For certain application, high viscosity is not a desired factor thus DES synthesis is able to alter the viscosity for the application [10].

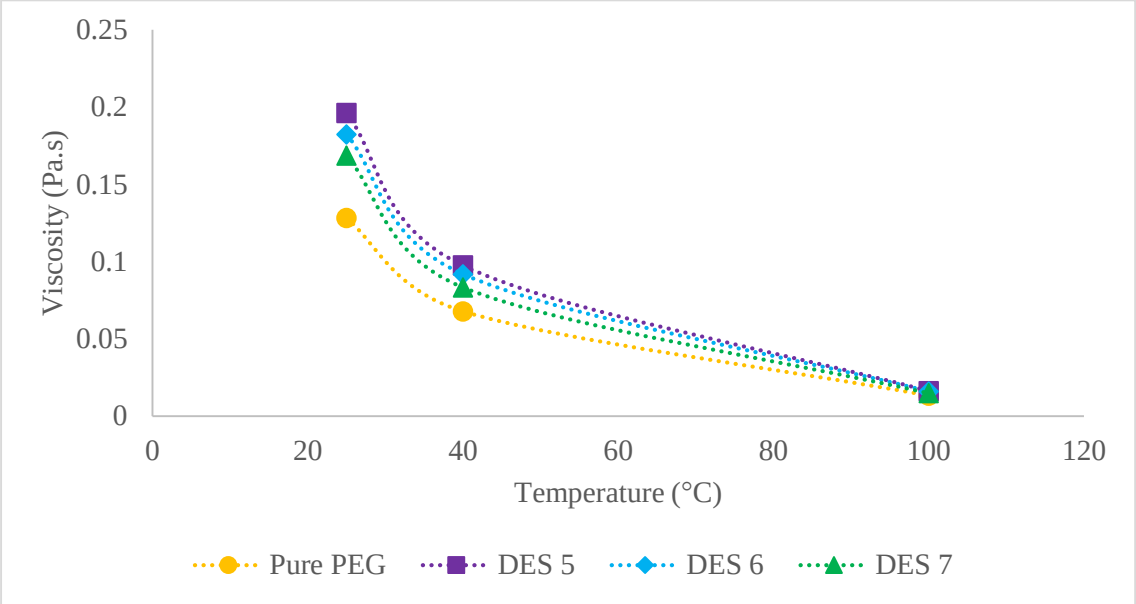


Figure 4. Viscosity of pure PEG HBD and PEG based DESs at 25°C, 40°C and 100°C.

3.4 Density

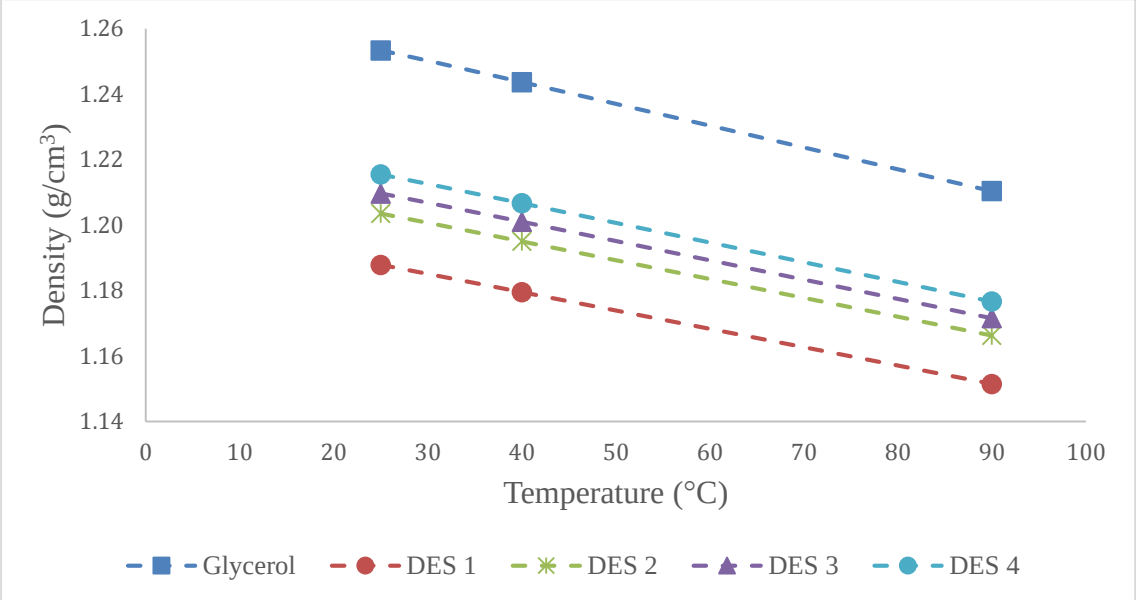


Figure 5. Density of pure glycerol HBD and glycerol based DESs at 25°C, 40°C and 90°C.

Density of the DESs depends on the type of the HBD and salt. It is noted from Fig.4 that DES 1 has the lowest density and DES 4 has the highest density when comparing all the glycerol based DESs. Pure glycerol has the highest density with 1.2534 g/cm^3 at 25°C. Thus, as the amount of glycerol HBD increases in DES with

the molar, the higher the density obtained. From Fig. 5, the lowest density was shown by pure PEG with all the DES having higher density. The highest density at 25°C was measured for DES 6 with 1.1350 g/cm^3. The lowest density was DES 7 with 1.1318 g/cm^3 is higher compared to alkylimidazolium dialkyl phosphates ILs which are PEE (1.125 g/cm^3), PBE (1.038 g/cm^3), and POE (1.016 g/cm^3) [11].

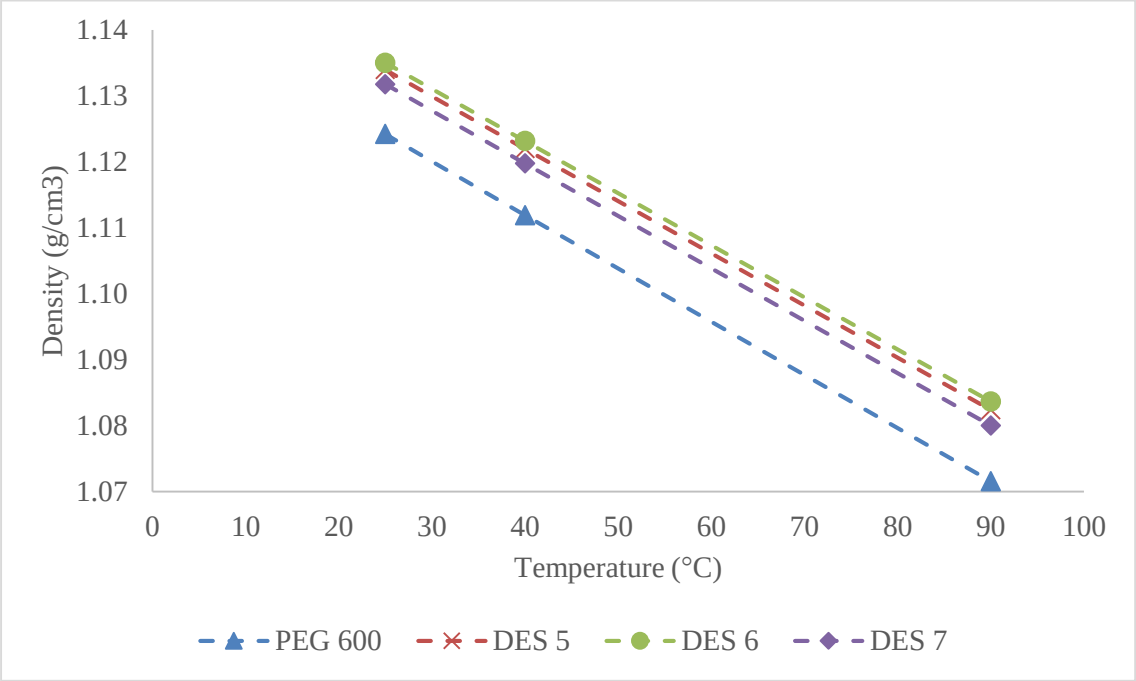


Figure 6. Density of pure PEG HBD and PEG based DESs at 25°C, 40°C and 90°C.

4. Conclusion

The glycerol and PEG based DESs were successfully synthesized from ChCl with different molar ratios. The thermophysical properties were investigated showed that the properties of DESs can be altered by changing the HBDs and varying molar ratios. For glycerol based DES, the thermal conductivity, viscosity and density decreases compared to pure glycerol. On the other hand, all this properties showed increased when tested with PEG based DES. Thus, the term of designer solvent suits DES as the properties can be altered and has the potential for wide range of application compared to IL due to environmental friendly nature. The process of synthesis of DES is much simpler hence the cost of production is low.

References

[1] Y. Dai, J. Van Spronsen, G. J. Witkamp, R. Verpoorte, and Y. H. Choi (2013). Ionic liquids and deep eutectic solvents in natural products research: Mixtures of solids as extraction solvents. *Journal of Natural Products.*, *76(11)*, 2162–2173.

[2] K. S. Torimoto T, Tsuda T, Okazaki K (2010). New Frontiers in Materials Science Opened by Ionic Liquids. *Advance Material*, *22(11)*, 1196–1221.

[3] N. Dörr, I. Gebeshuber, D. Holzer, H. D. Wanzenböck, a Ecker, a Pauschitz,

and F. Franek (2010). Evaluation of Ionic Liquids as Lubricants. *Journal of. Microengineering Nanoelectron., 1(1),* 29–34.

[4] E. L. Smith, A. P. Abbott, and K. S. Ryder (2014). Deep Eutectic Solvents (DESs) and Their Applications (2014). *Chemical Reviews, 114(21),* 11060–1108.

[5] A. Abo-Hamad, M. Hayyan, M. A. AlSaadi, and M. A. Hashim (2015). Potential applications of deep eutectic solvents in nanotechnology. *Chemical Engineering Journal, 273*, 551–567.

[6] A. P. Abbott, G. Capper, D. L. Davies, R. K. Rasheed, and V. Tambyrajah (2003). Novel solvent properties of choline chloride/urea mixtures.*Chemical Communications (Cambridge), 1,* 70–71 .

[7] A. P. Abbott, E. I. Ahmed, R. C. Harris, and K. S. Ryder (2014). Evaluating water miscible deep eutectic solvents (DESs) and ionic liquids as potential lubricants. *Green Chemistry, 16(9),* 4156.

[8] M. Kobayashi, T. Koide, and S.-H. Hyon (2014). Tribological characteristics of polyethylene glycol (PEG) as a lubricant for wear resistance of ultra-high-molecular-weight polyethylene (UHMWPE) in artificial knee joint. *Journal of Mechanical Behaviour of Biomedicals Materials, 38,* 33–8.

[9] Protsenko, V., Kityk, A., Shaiderov, D. and Danilov, F. (2015). Effect of water content on physicochemical properties and electrochemical behavior of ionic liquids containing choline chloride , ethylene glycol and hydrated nickel chloride. *Journal of Molecular Liquids. 212*, 716-722.

[10] A. Hayyan, F. S. Mjalli, I. M. AlNashef, Y. M. Al-Wahaibi, T. Al-Wahaibi, and M. A. Hashim (2013). Glucose-based deep eutectic solvents: Physical properties. *Journal of Molecular Liquids*, *178,* 137–141.

[11] L. Yong-ming, P. Wei, L. Shuqin, C. Jian, W. Ruigang, and L. Jianqiang (2002). Mechanical properties and microstructure of a Si 3 N 4 / Ti 3 SiC 2 multilayer composite. *Ceramics International, 28(2),* 223–226.

eureca 2016 – Conference Paper
Paper Number EE_PG01

Hybrid Visible Light Communication Power Optimization for Indoor Environment

Ching Han Tan,* Florence Chiao Mei Choong, Yan Dan Lin
School of Engineering, Taylor's University, Malaysia
tanch28@gmail.com

Abstract

Traditional way of handling more traffic is by having higher cell density, higher spectral efficiency and carrier aggregation. Many network optimization has been put in place to overcome this high growth in data traffic demand. However, the network electricity consumption also increase tremendously. Therefore, it is hard to keep up the pace without consuming more energy. Hence, higher energy efficient network must be introduced to overcome this issue. Hence, hybrid visible light communication (VLC) with proven energy efficiency that rides on solid-state light emitting diode lighting infrastructure will potentially become a natural solution paradigm. Hybrid VLC has the advantages of high data rates, higher bandwidth, un-licence requirement, lower cost and more energy efficient. This paper focuses on recent breakthrough and advancement in hybrid visible light communication especially for indoor applications. Two indoor lighting topologies were studied in detail in order to determine their power optimization performances. The power optimization through linear programming methods were used to simulate and compare the performance of square and ring topology design. Based on the average SNR vs FOV graphs, after optimization, square topology showed better performance as compared to ring topology. In addition, the number of users versus received power and channel assignment's performance is also better for square topology. The findings show the feasibility of hybrid VLC for indoor application and is a cost effective alternative to radio frequency (RF).

Keywords: RF, VLC, HVLC

1. INTRODUCTION

Nowadays mobile communication has reached a critical congestion stage. By 2017, from the recent Cisco's report, data traffic will go beyond ten-fold the data traffic of 2012 [1]. Traditional way of handling more traffic is by higher cell density, higher spectral efficiency and carrier aggregation. Many network optimization has been put in place to overcome this high growth in data traffic demand. However, the network electricity consumption also increase tremendously. Therefore, it is hard to keep up the pace without consuming more energy. Hence, higher energy efficient network must be introduced as soon as possible [2]. Therefore, this paper aims to introduce a more efficient technique for overcoming this capacity congestion in radio-frequency spectrum.

A visible light communication (VLC) system is expected to deliver higher capacity and faster speed with lower cost and energy efficient to the mobile users when compared to radio frequency (RF). The popularity of Light-emitting-diodes (LEDs) in today's households and offices infrastructure is making mobile communication readily available. This is especially true for indoor environment. With the ever increasing installation of fibre optic telecommunication networks, high speed and more efficient information highway is already co-exist in our daily life [3]. However, these high data rates and higher speed information highway are still insufficient for the 'last-mile' of wireless communication due to limited RF bandwidth.

2.0 HYBRID VISIBLE LIGHT COMMUNICATION SYSTEM

This paper is to explore the potential of hybrid visible light communication (HVLC) to fill the gaps of near depletion radio frequency band currently in-used widely in our daily life. Hybrid VLC provides ease of interchangeability in wireless communication, low cost and abundant access points (APs) also along with LEDs lighting installations. The key challenge is the handover issues between wireless Fidelity (Wi-Fi) and Visible light communication (VLC) or Light Fidelity (Li-Fi). The wide spread use of wireless fidelity (Wi-Fi) and mobile devices will ensure new technology with higher bandwidth and capacity will co-exist with established RF communication.

The main reason to adopt the hybrid VLC is to combine the advantage of the current RF network mobility advantage and the security and high security bandwidth of VLC in the downlink. Another main issue is the blue light symptoms which may affect certain group of human user with eye disorderly problem. The biggest concern of eye safety is photo-retinitis [4]. Photo-retinitis is a photo-chemical damage to the retina. It is caused by over exposure to violet and blue lights which is also called blue light hazard. This risk is primarily caused by LEDs. White LEDs may not emit blue lights with the same colour temperature. White lights used in general lightings may not harmful to retina for healthy adults. Special care must be provided to infants or adults with eye disease. Optical radiation affects skin and eyes. This energy passed through thermal reactions or photochemical processes. Too much radiation could damage tissue thus affecting sensory reaction of human's perception. LEDs used for lighting do not emit IR or UV, hence is safe under international safety standards which provide harmonized optical radiation safe limits, proper measurement techniques, exposure hazards and a risk classification system including:

(i) ANSI/IEC RP27: Recommended Practice for Photo-biological Safety for Lamps and Lamp Systems
(ii) CIE S009-2002: Photo-biological Safety of Lamps and Lamp Systems
(iii) IEC/EN 62471: Photo-biological Safety of Lamps and Luminaires. Supporting guidance is provided in IEC/TR 62471-2 (2009) and IEC/TR 62778 (2012)

Services providing continuous streaming and constant cloud connectivity are particularly required in today's indoor environment. Optic fibre technology can increase transmission along the network delivery path. However, the limited capacity of wireless fidelity (Wi-Fi) will severely constraint transmission rates in indoor environment. The use of VLC hotspots nowadays can be enhanced with the HVLC with very high data rate throughput. The ability to visually see the hotspots and move toward them is an advantage.

In a typical hybrid visible light communication system, two independent hardware and software systems co-exist. VLC has opened up new wireless bandwidth that is owned by the lighting. It is attractive due to the low cost overlay of reusable lighting backbone infra-structure. Hence, this solution will be best overall network for the users. RF communications has the complexity of electronic processing, whereas VLC uses low cost digital electronics with complex heterogeneous semiconductor. This future solution aims to resolve these limitation with associated channel bandwidth.

3.0 LITERATURE REVIEWS OF HYBRID VLC

There are various reviews in Visible light communications [21,22,23,24,25]. A visible light communication (VLC) system is utilizing the electro-magnetic spectrum from 400nm to 790 nm wavelength. The optical source of transmitter converts the electrical signal to a visible light signal. It is so fast that even our eyes do not detect the changes in modulated signals. The receiver or detector will then convert the light signals into electrical current. Common materials such as solid state LEDs are used for communication as well as for illuminations. On the other hand, photodiodes (PDs) are used as detectors.

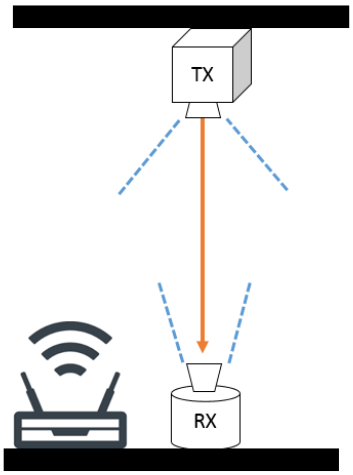
The main challenge in designing VLC systems is to achieve high transmission rate that arises from the free space loss (FSL), inter-symbol interference (ISI) due to multi-path dispersion, ambient and background noise. This configuration of link design will degrade the induced signal. Traditionally, four lighting configurations are defined for indoor VLC applications [5]. There are differentiated by line of sight (LOS) and the degree of directionality as well as the field of view of detectors. There are as shown in Fig. 1(i) to 1(iv). The first is the Line-of-Sight Directed link. It uses directional transmitter and receiver. It must be aimed so that a link can be established. The second is the Line-of-Sight non-directed link. It employs wide angle transmitter and receiver. In this case, there is no need for pointing between transmitter and receiver. The third case is the non-Line-of-Sight directed (NLOS) scenario. NLOS link rely on the light reflection from the ceiling or other diffusively reflecting surface. The fourth case is the non-directed- non-LOS link design. This is often referred to as a diffuse link. It has the greatest robustness and ease-of-use. Those Line-of-Sight (LOS) cases provided uninterrupted path between transmitters and receivers. It minimizes

multipath distortion and maximizes power efficiency. The NLOS enables transmissions between transmitter and receivers over partitions or passers-by barriers.

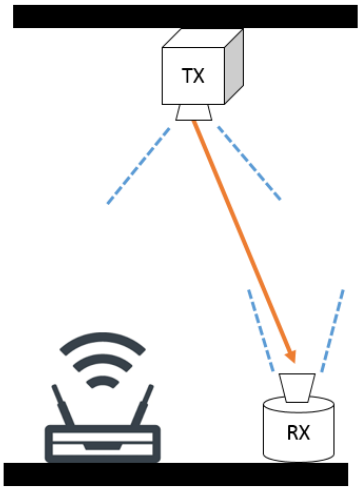
Generally, for LOS communication link, there is a direct path of un-obstructive as well as spatial alignment amongst the radiation pattern between the transmitter and the detection pattern of the receiver. Whereas, the NLOS communication link, has directed and diffuse or non-directed NLOS. In NLOS, the signal will arrive at the receiver after one or many bounces off the ceiling, walls or objects in the room. They are differentiated from their transmitter's directivity. In directed NLOS, there is a narrow radiation characteristic from transmitter. The projecting light from another spot on the ceiling will serves as a new transmitter. The light will relay to the receiver characterised from reflection. The single reflection will result in stronger light intensity. In non-directed NLOS, there is a wide radiation. The characteristic will be irradiation from a large part of the reflecting surface. The radiated light will reach receiver after single or multiple reflections from the surface.

White LEDs (WLED) are used for VLC and illuminations, i.e. trichromatic and blue-chip LEDs. Tanaka et al., investigated trichromatic LEDs. Simulated results of 400 Mb/s data rate are recorded. Whereas a data rates of 500 Mb/s or above are reported for blue-chip LEDs VLC system [6]. Two VLC standards, JEITA CP-1221 and 1222 are issued by Japan Electronics and Information Technology Industries Association (JEITA) in 2007 [7]. In March 2009, a standard for VLC local area network (LAN) is being generated by the Infrared Communication system association (ICSA) [8]. It is based on full duplex wavelength-division multiplexing (WDM). In 2009, new physical and medium access control (MAC) layers based on a clean-slate methodology is proposed for IEEE 802.15.7. In 2010, IEEE 802.15.7 standard established [9].

(i) Line of Sight



(ii) Line of Sight: Non-directed



(iii) Non-Line-Of-Sight: Directed

(iv) By diffusion link

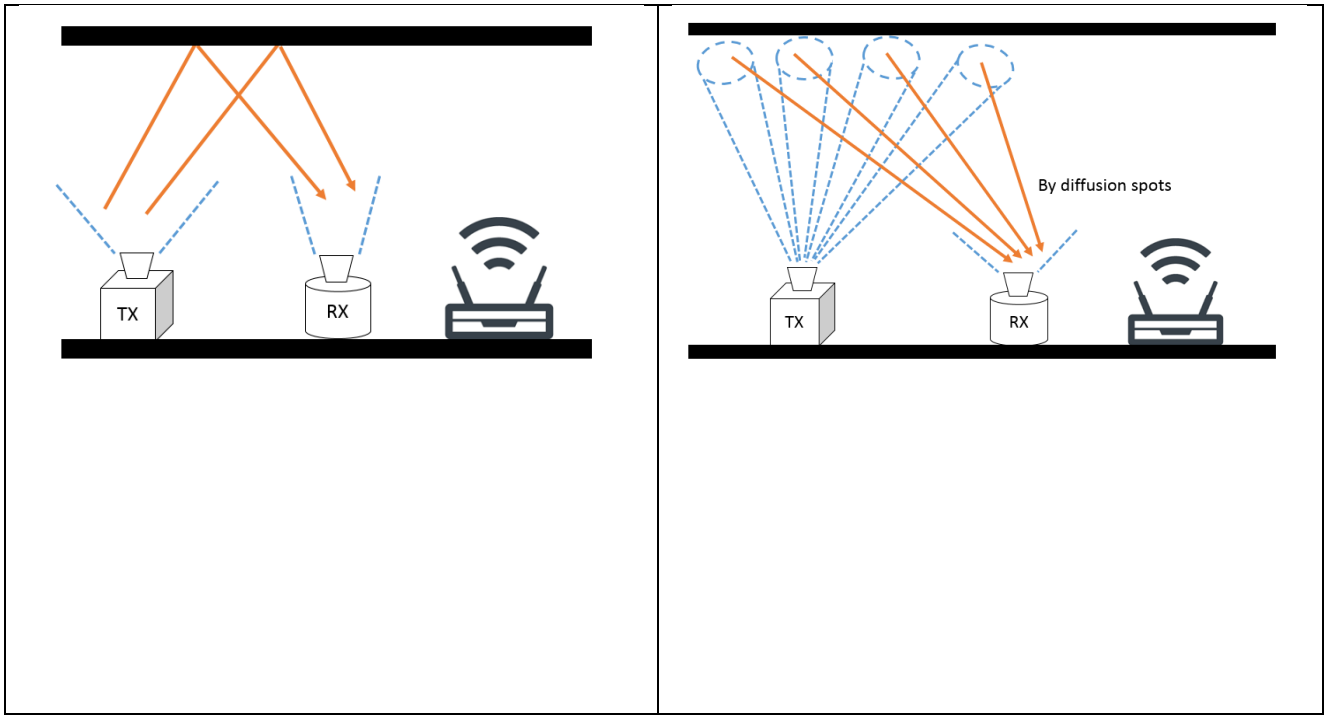


Fig.1(i)-(iv) VLC configuration with LOS and degree of directionality between transmitter and receiver [5].

Deploying femto-cells architecture is inefficient with backhaul challenge and exorbitant maintenance cost. Power line communication (PLC) is used to interlink different WLED units. Diversification of lighting infra-structure will make a dominant LOS module of small path loss with bandwidth of at least 88 MHz [10]. But this connection is subjected to rotation and movement of the detectors. Therefore handover and link reuse algorithm schemes are needed. VLC does not necessary need to be in full intensity [10]. However, in order to achieve a high signal-to-noise ratio (SNR) of >60 dB for the whole room space, luminous level must meet the minimum standards. Once the minimum SNR for stated Bit-error-rate (BER) is attained, dimming can be considered [25,26,27,28,29,30].

4.0 PROPOSED INDOOR HVLC SYSTEM

Fig.2 shows the proposed block diagram of a hybrid VLC (HVLC) system prototype. A typical HVLC system consists of a light source in free space and a Photo-diode detector. The light source modulates the input signal and passes through LEDs into the free space. Light is focused onto the detector through a lens system. An optical filter will reject optical noise in between. The resulting photocurrent will be amplified through signal processing circuitry. LEDs with relaxed safety regulation, high reliability and low cost, is an ideal light source. Photodiodes (PDs) is low cost, operation with low-bias voltage and wide temperature tolerance. Intensity modulation with direct detection (IM/DD) provides low cost and simple optical carrier modulation and demodulation. The instantaneous power of the optical carrier modulated the desired waveform. The received instantaneous power is proportional to the detector current. It detects only the intensity of the optical waveform.

There are two techniques for digital carrier modulation (i) On-off keying (OOK) and (ii) pulse-position modulation (PPM) [11]. OOK can be implemented with

simple hardware with good performance. In PPM, an optical pulse is conveyed in one out of S slots per symbol time. The bit combination transmitted by the symbol indicates the occupied slot position. PPM provides higher power efficiency but expands the signal bandwidth. At receiver end, PPM imposes more complexity than OOK.

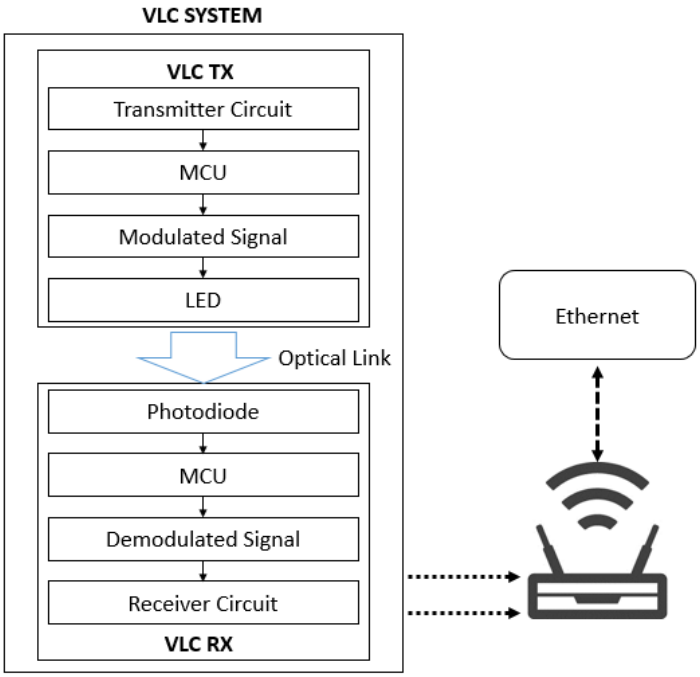


Fig.2: The proposed HVLC system architecture

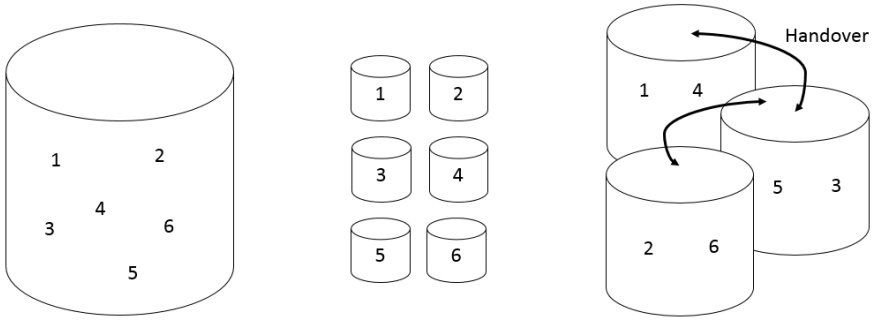
Japan Nakagawa laboratories implemented a full-duplex VLC system using carrier sense multiple access with collision detection (CSMA/CA). The uplink is using infra-red as a point-to-multipoint bidirectional case study. The OMEGA project (European Community Home Gigabit Access) provides wireless connectivity with PLC as backbone in home. This is a technology-independent MAC layer that control its network and services to any number of access points. It allows the service to follow the user from one access point to another [12].

Hou *et al.* in 2003 proposed a modified polling protocol with blockage sensing that assigns channels with channel state information. Hence, this will avoid blockage in user transmissions. The channel is reassigned to ensure system effectiveness and user's quality of service (QoS) [13].

5.0 MULTIPLE ACCESS VLC MIMO

Multiple access are performed in the physical layer to allow several users to access simultaneously to the available network services. Single cell topology using single VLC access point (VAP) per room and a cellular topology with spatial reuse using multiple VOPs for indoor coverage as shown in Fig.3. In a single cell topology per user, each user has a dedicated VAP. This topology is practical when the existing reading lamp on top of each seat in airplane, bus or train are used in VLC. A single cell per room topology can then be utilized in moderate size rooms or offices. A

cellular topology provides coverage in a big conference hall. Multiple-input-multiple-output (MIMO) techniques achieves high data rate for indoor VLC systems [14].



(a) (b) (c)

Figure 3: Different topologies for indoor coverage (a)per room (b) per user (c)Multiple

Parallel single-input-single-output (SISO) can be implemented for VLC MIMO system. In this system, different data streams is sent simultaneously using transmitter array individually illuminated by a light source detector in the receiver array with accurate alignment of transmitter and receiver. On top of that, the beam-width from the detector enables interference to be assumed through appropriate settings of the array structures [15].

T.H.Do et al. [16] stated that VLC system with optimal link quality and power usage is hard to design. This is solved by adopting a multi-objective optimization scheme. In this paper, the parameters with optimal results of maximum link quality and minimum power used are obtained within illumination and other constraints. An inter-carrier interference suppression algorithm is employed to enhance SNR of the VLC system. Also, SNR also affected by LED position and direction. SNR is higher when LED half angle power is smaller. Lower energy consumption and better configuration will give a higher SNR. Small angle of FOV allows better SNR as inter-state-interference (ISI) is decreased.

C.C.Lee et al. in 2013 [17] illustrated a hybrid VLC system achieving a power consumption of 68% and a reduction in cost by 3% when compared to fluorescent lights with RF technology. While LEDs with RF technology can reduced power consumption by 49% and achieved device cost saving as high as 47%, hybrid VLC has paved the way for greater cost saving and energy efficiency.

X. Bao et al. described a Hybrid VLC-OFDMA network model is linked to the server via wired connections. Analytical and simulation results showed large improvements in the capacity performance of the hybrid, when compared to OFDMA system [18].

N.Rajagopal et al. stated that the use of VLC in smart-phone camera and LED light has gain recognition for indoor localization applications. This paper provided adaptive duty cycling as a scheme for mixing camera communication with higher speed data. The camera communication with more extreme duty cycles increased the data speed with reduced performance. A wakeup circuit to support aggressive duty

cycling of low power embedded devices such as wireless sensors has also been shown [19].

This research study used a proprietary code developed to achieve a Hybrid VLC smart home system with unique security features through a novel vertical hangover methodology.

6.0 Research Methodology Through Linear Programming Optimization

The author et al. in 2016 [20] has demonstrated that there is a variation of power optimization between different topologies of lighting arrangements through linear programming technique..

The mobile users are assumed to have random locations and the locations are randomly generated by MATLAB. The Power Optimization (PO) should be multi-objective and multiple-variables as defined by equation (1):

$$SNR(u,n) = \frac{\left(SP_t(G_{LOS}(ui,nj)\right)^2}{\left(SP_t \sum_{a\neq i}\sum_{b\neq j}(G_{LOS}(ua,nb)\right)^2} \quad (1)$$

where P_t is the optical power emitted from light source, and S is the responsibility of photodiode. The received power at a particular user is the power which belong to a particular light sources and particular channel. Interference comes from the sum of the received power which do not belong to serving light source and serving channel $(a \neq i)$ and $(b \neq j)$. It is obvious that the PO has to minimize $(SP_t \sum_{a\neq i}\sum_{b\neq j}(G_{LOS}(ua,nb))^2$ and also the $SP_t\ (G_{LOS\ (ui,\ nj)})^2$.

Fig.4 shows the square and ring LED array topologies under test. Fig.5 shows 90 random users generated in the room having the same size for square and ring configurations respectively. It is seen that the square topology can accommodate more users than ring topology [20]. Fig.6 is the optimization process flow chart using linear programming methodology.

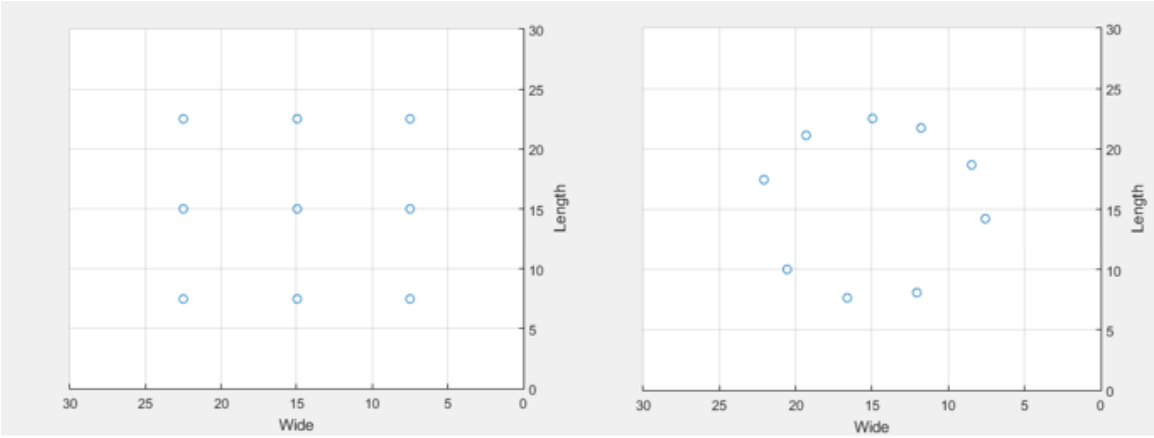


Fig.4: Square and Ring LED array topologies under test

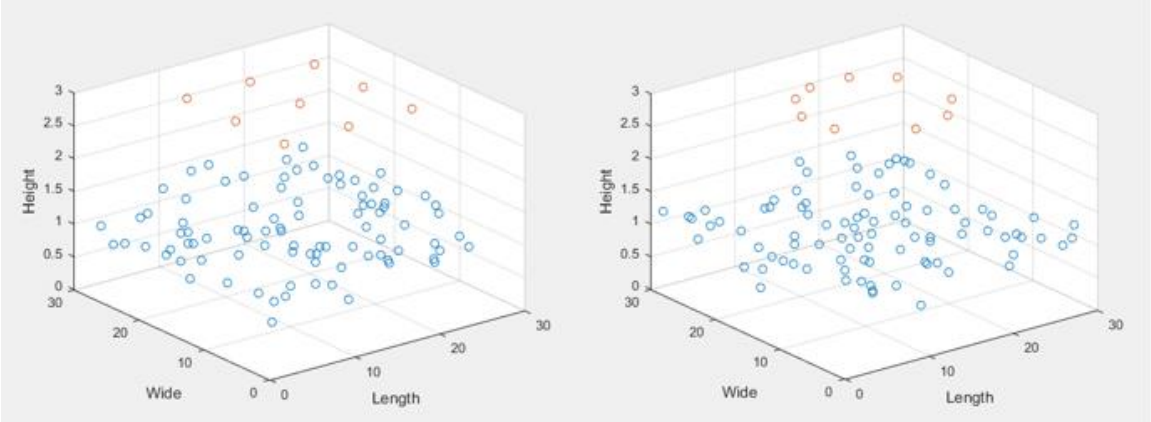
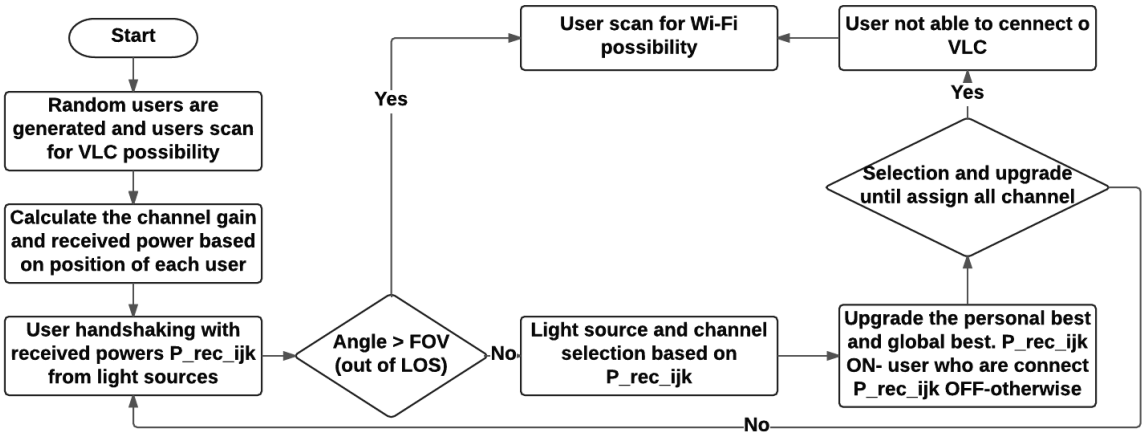


Fig.5 shows 90 random users generated in the room having the same size for square and ring configurations respectively.



optimization, the signal to interference ratio is higher. Square topology provide higher signal to noise ratio compared to ring topology. It can be seen that the square topology is 6.67% to 46.67% better performance after optimization in terms of the average SNR versus FOV graphs. Therefore, the placement of light source affect the VLC performance.

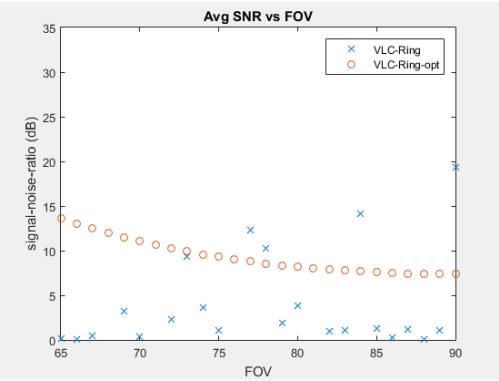


Fig.7 (i): Average SNR vs FOV before optimization (square and ring)

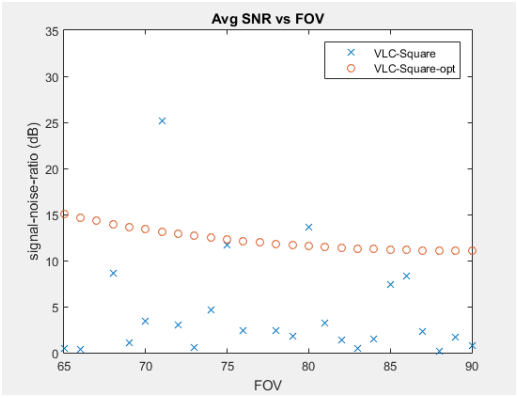


Fig 7 (ii): Average SNR vs FOV after optimization (square and ring)

In Fig. 8, square topology showed more coverage in terms of received power for square topology than ring topology. The number of users versus received power for square topology showed 5.4% to 20% better performance than that of ring topology.

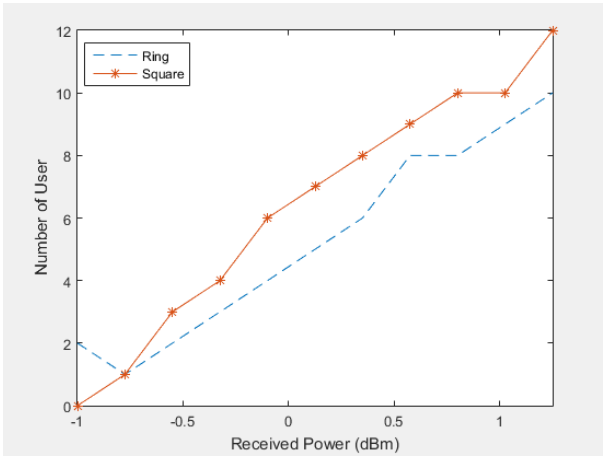


Fig. 8: Graph of no. of users vs Received Power for Square and Ring topologies respectively.

In addition, Fig.9 showed a new simulation of channel assignment performance results for the square and ring configurations respectively. Square topology showed a better and more stable coverage performance.

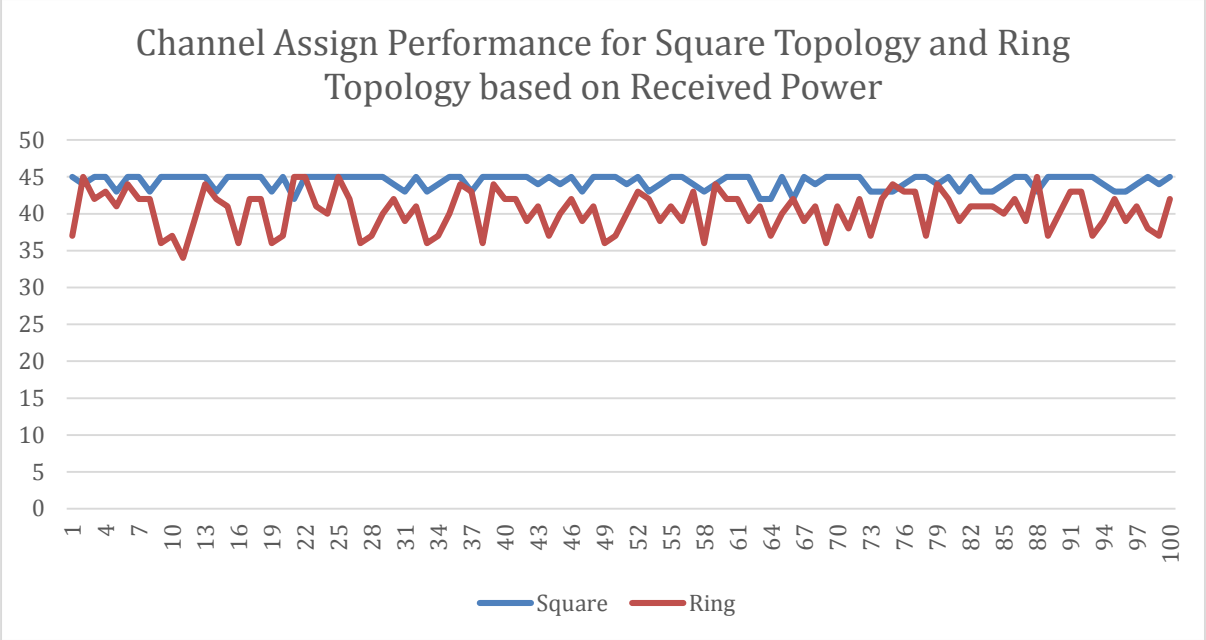


Fig.9: Channel assignment performance on received power

8.0 CONCLUSION

In conclusion, this paper showed how hybrid VLC can complement RF in a cost effective way. The power optimization through linear programming methods can be used to simulate and compare square and ring topology scenarios performances. From average SNR vs FOV graphs, after optimization, square topology showed better performance than that of ring topology. Moreover, the number of users versus received power and channel assignment's performance for square topology is better when compared to that of ring topology.

ACKNOWLEDGEMENTS

This work is supported by Daikin Electronic Devices Malaysia and Taylor's University Malaysia.

REFERENCES:

[1] Cisco Visual Networking Index. "Forecast and Methodology, 2010-2015". San Jose, CA, June 1, 2011.

[2] Ratheesh R. and Vetrivelan P., "Power optimization Techniques for Next Generation Wireless Networks", IJET, Mar 2016

[3] A.Selvarajan, S Kar, T.Srinivas, "Optical Fiber Communication:Principles and systems", McGraw-Hill, 2002

[4] BS EN 62471:2008, "Photo-biological Safety of Lamps and Lamp Systems", BSI British standards, Sept. 2008

[5] H. Elgala, R. Mesleh and H. Haas, "Indoor Optical Wireless Communication: Potential and State-of-the-Art", IEEE Comm. Mag., vol. 49, no. 9, pp. 56–62, Sep. 2011

[6]J. Vucic, C.Kotte, S. Nerrer, K.D. Langer, and J.W. Walewski, "513Mbit/s Visible Light Communication Link Based on DMT-Modulation of a White LED", Journal of Lightwave Tech., vol. 28. No. 24, pp. 3512-3518, Dec. 2010.

[7] Visible Light Communications Consortium (VLCC), Feb. 2007. retrieved from http://www.vlcc.net.

[8] J. Kahn, and J. R. Barry, "Wireless Infrafed Communications", IEEE, 1997.

[9] W.Guo, Q.Li; H. Yu and J.Liu, "A parallel Transmission MAC Protocol in Hybrid VLC-RF Network", Engg and Tech., 2015.
[10] S Shao, Adb.K.and Issa Khalil, "Joint Link Scheduling and Brightness Control for Greening VLC-based Indoor Access Network", IEEE, 2015
[11] M. S. Islim and H. Haas, "Modulation Techniques for LiFi", ZTE Communication, Vol 14no. 2, Apr. 2016.

[12] Komine, Toshihiko, and Masao Nakagawa. "Fundamental analysis for visible-light communication system using LED lights." Consumer Electronics, IEEE Transactions on 50.1, pp100-107, 2004.
[13] S.Rajbhandari, H.Chun, G.Faulkner, K.Cameron, Dominic O'Brien, " High Speed Integrated VLC system: Device constraints and Design Considerations", IEEE, 2015.

[14] J. Hou and D. O'Brien, "Vertical handover decision making algorithm using fuzzy logic for the integrated Radio and OW system.",IEEE Trans Wireless Commun., Vol 5, no.1, pp 176-185, 2006.
[15] J. Chen, Y. Hong, X. You, H. Zheng, and C. Yu, "Conceptual Design of Multi-user Visible Light Communication Systems Over Indoor Lighting Infrastructure",IEEE, 2014
[16] T.H. Do and M. Yoo, "Optimization for link quality and power consumption of visible light communication system", Photonic Network comm. Issue 3, pp 99-105, 2014
[17] C.C. Lee, C. S. Tan, H. Y. Wong, M. Yahya, "Performance evaluation of Hybrid VLC Design using device cost over data throughput criterion", SPIE Conference on Ultrafast Imaging and Spectroscopy, 2013.
[18] M. B. Rahaim, A.M.Vegni, and T.Little, "A Hybrid Radio Frequency and Broadcast Visible Light Communication System", IEEE, 2011.
[19] N.Rajagopal, P.Lazik and A.Rowe, "Hybrid Visible Light Communication for cameras and low-Power Embedded devices", Carnegie Mellon University, 2015.
[20] C.H.Tan, C.M.Choong, Y.C.Teo, Y.D.Lin and K.C.Ho, "Power Optimization in Hyrbid VLC for Indoor Application", PIERS conf., Aug. 2016
[21] Herald Haas, "High-speed wireless networking using visible light", SPIE, 2010.
[22] D. O'Brien, "Visible light communications: achieving high data rates", ERC, 2011.
[23] H. L. Minh, Z. Ghassemlooy, D. O'Brien, G. Faulkner, "Indoor Gigabit Optical Wireless Communications: Challenges and Possibilities", ICTON pp. 1-6, 2010.
[24] S. Dimitrov and H. Herald, "Principles of LED Light Communications Towards Networked Li-Fi", Cambridge University Press, 2015.
[25] Y. Wang, J. Shi, C.Yang, and N. Chi, " Integrated 10Gb/s multi-level Multiband passive optical network and 500 Mb/s Indoor Visible light communication system based on Nyguist single carrier frequency domain equalization modulation", Optic letters,2014.
[26] V.V.Veeravalli and O.E. Kelly, "A locally optimal handover algorithm for cellular communications", IEEE Trans, 1997.
[27] H.Maturino-Lozoya. D. Munoz-Rodriguez, and H,Tawfik, "Pattern recognition techniques in handoff and service area determination", IEEE conf., 1994
[28] A. Hatami, P.Krishnamurthy, K.Pahlavan, J.Makela, M.Ylianttila, R.Pichna, and J. talvitie, "Fuzzy logic, neural networks and other algorithms for handoff in wireless networks" Proc ICSC, 1999.
[29] D. Munoz-Rodriguez, and K.W. Cattermole, "Handoff Procedure for fuzzy defined radio cells", IEEE VH conf., 1987.

[30] Q.Zhang, C.Guo, Z.Guo and W.Zhu," Efficient mobility management for verticle handoff between WWAN and WLAN", IEEE Comm. Mag., 2003
[31] G.P.Pollini, "Trends in handover design", IEEE Commun. Mag., 1996.

Noise Filtering and Feature Extraction Process for ECG Signal Processing

Chow Shee Onn[1,*], Leong Wai Yie[2]
[1]*School of Engineering, Taylor's University, Malaysia*
[2]*School of Engineering, Taylor's University, Malaysia*

[*]chowshee@yahoo.com

ABSTRACT
In this paper, feature extraction will be studied with the purpose of extracting a particular syndrome associated with a heart signal. There are many different types of signals generated from the organs of a human body. One of those signals is ECG (Electrocardiography) signal which is generated from the heart of a human body. Another type of signal EEG (Electroencephalography) is generated from the brain. Most of the human organs can generate signal that can be detected using electrodes. The heart syndromes to be studied with ECG (Electrocardiography) is poor blood supply to the heart and cardiac arrest. Sometimes there are abnormalities in the human hearts. All these abnormalities are shown in the signal which can be detected using electrodes. Most of those signals generated containing noises and other interferences. All of those noises and interferences have to be filtered off in order to find out the abnormalities in the hearts. Special filter needed to be designed to filter off those unwanted noises. Mathematical algorithm can be used to generate Expectation Value which, in conjunction with Wiener Filter and improved wavelet (Wi-Wave), are used to design the filter. The filter can be designed using a variety of algorithms that can remove noises in the signals. All of these are carried out for the purpose of extracting features from the human heart, investigating the pattern of the signals and looking for the best algorithm to remove noises. Mathematical algorithm will be applied on the original signal to remove the unwanted interference. Further refinement is to be carried out on the algorithm so as to remove more interferences from the original signal.
Keywords : filter, algorithm, signals, ECG, Wi-Wave.

1. Introduction

The analysis and identification of the shape of ECG signal is important for the diagnosis of cardiac disorders. This project is to study the problem of identifying the features associated with the signals from the heart. The ECG signal pattern shows the amplitudes and relative intervals of the different waves (P, QRS and T wave). Automatic ECG feature extraction methods are important as manual beat-by-beat measurement of ECG points is not practical in clinical practice [1].

QT interval is one of the most important ECG features. The prolonged time-interval for QT means malign cardiac arrhythmias and can lead to sudden cardiac death. Study had shown that certain drug can prolong the QT interval, causing adverse effect on the heart. Many algorithms for ECG feature extraction had been developed. Further study is being carried out on the proper formalisation of QT interval [2].

ECG has been popularly used for diagnosing different types of cardiac symptom and diseases. The data obtained from ECG is a true record of the magnitude of electrical signals generated by repolarization and depolarization of the ventricles and atria in the human hearts. One cardiac cycle in an ECG signal consists of the P-QRS-T pattern of wave as shown in Figure 1.1.

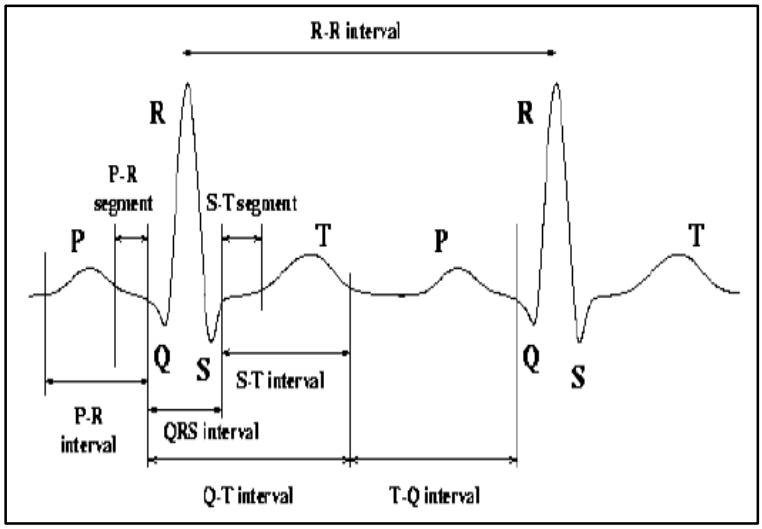


Figure 1.1 : A Sample ECG Signal showing P-QRS-T Wave [2]

Table 1 : Physiological duration of the characteristic components of an ECG patterns

Wave or interval	Guide value for the physiological duration in s
P wave	0.05 – 0.10
PQ interval	0.13 – 0.20
Q wave	< 0.05
QRS complex	0.05 – 0.10
S wave	< 0.04
QT interval	0.18 – 0.52

2. Literature Review

In the study of signal processing, many filters of different configurations and designs were used for the purpose of filtering and reducing the effect of noise from signals obtained from particular sources [25]. The Wiener filter is used to generate a desired random process by using the method of linear time-invariant (LTI) to filter off observed noisy signal, assuming known stationary signal and noise spectra.

The algorithm in the filter tries to minimize the mean square error between the estimated random process and the desired process [26]. Figure 2.1 shows the variation of amplitudes for an ECG signal with respect to the sample points.

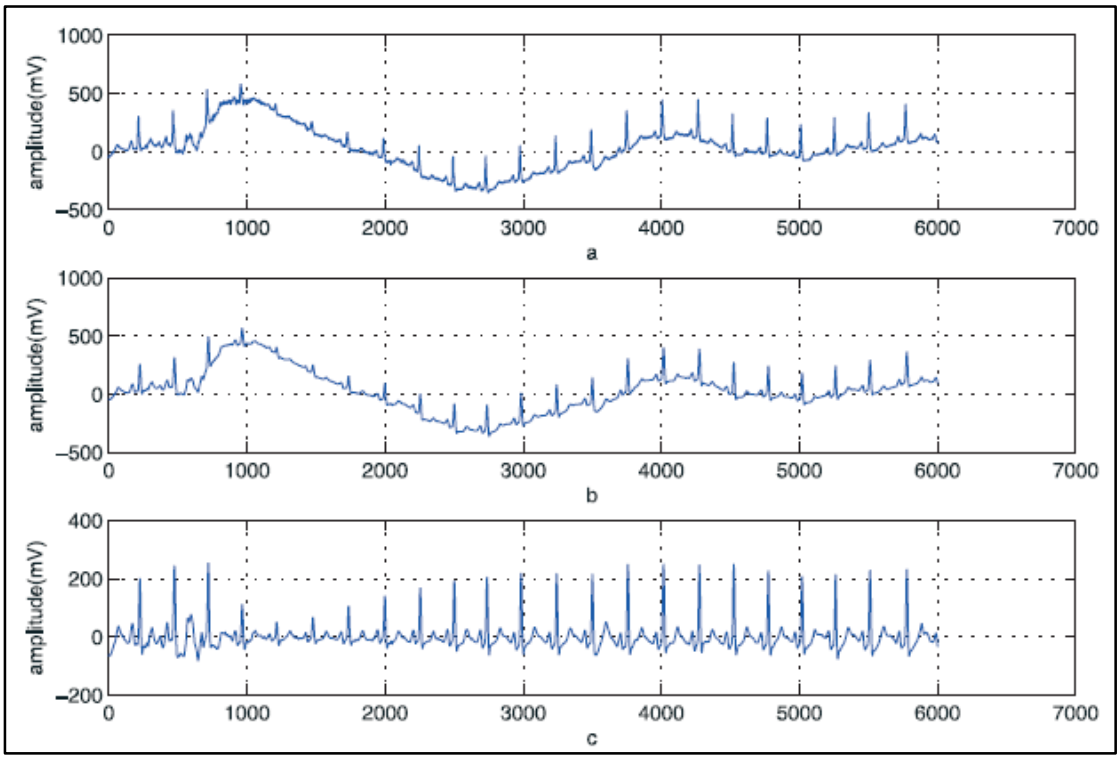


Figure 2.1 : ECG noise cancellation, (a) ECG signal with noise, (b) ECG signal after power-line noise cancellation and (c) ECG signal after power-line and base line drift noise cancellation.

2.1 Noise Filtering Using Wiener Filter

The main purpose in designing a Wiener filter is to compute a statistical estimate of an unknown signal using a known signal as an input. The filtering of the known input signal will produce the output signal. The input signal may consist of an unknown signal of interest that has been corrupted by the addition of noise [11]. The concept of the Weiner filter is based on a statistical approach like the Minimum Mean-Square Error (MMSE). It can filter off noise from the corrupted signal to provide an output signal of interest [12].

When designing a Wiener filter, it is assumed one should have the knowledge of spectral properties of original signal and noise [16]. The property of the filter is linear time-invariant which can produce an output very close to the original signal. It is frequently used in the process of deconvolution and convolution. The characteristics of Wiener filters are :

a) The signal and the noise are stationary linear stochastic processes with known spectral characteristics or known autocorrelation and cross-correlation.
b) The filter is can be constructed physically and tested to achieve the desired output.
c) The performance criterion for the filter is Minimum Mean-Square Error (MMSE).

2.2 Application of Wiener Filter

The Wiener Filters are used widely in the field of digital communication, control systems, image processing and signal processing. The filter can be used in image processing to remove noise from a picture [15]. It can also be used in signal processing to remove unwanted noise or interference. It is used to remove noise from an audio signal, especially speech, as a pre-processor before speech processing.

The wide application of Wiener filter can be grouped into the four areas as shown.

- Noise reduction
- Signal detection
- System detection and identification
- Deconvolution

2.3 Techniques And Methods Available To Filter Noise From A Signal

2.3.1 Adaptive Filter

Adaptive filter is a type of filter whereby its transfer function is controlled by variable parameters. An optimization algorithm is required to adjust those parameters [19-20]. Feedback which appears in the form of an error signal is used by the closed loop adaptive filter to refine its transfer function.

Adaptive filters are now commonly used in devices like digital camera, mobile phone and medical equipment. Figure 2.2 shows the block diagram for an Adaptive Filter.

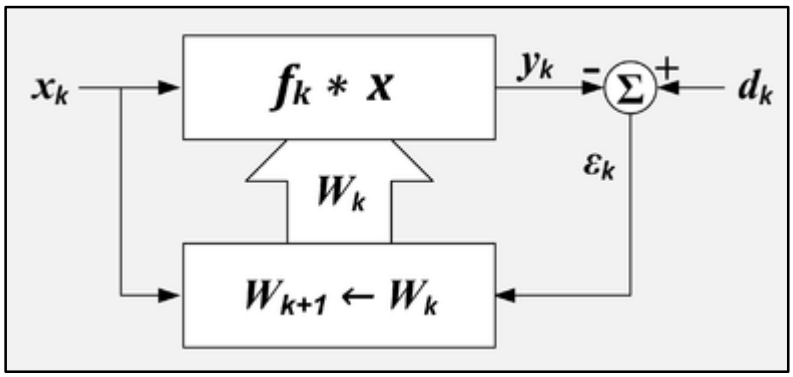


Figure 2.2 Block diagram for an Adaptive Filter [19]

2.3.2 Wiener filter

The Wiener filter [10] is used to produce a desired or target random process by linear time-invariant (LTI) filtering of an observed noisy process, assuming known stationary signal and noise spectra and additive noise. The Wiener filter minimizes the mean square error between the estimated random process and the desired process. Figure 2.3 shows the block diagram for a Wiener Filter [15].

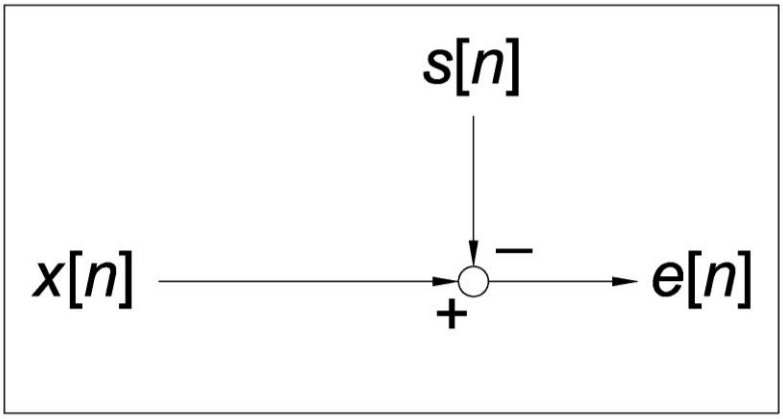


Figure 2.3 Block diagram for a Wiener Filter [10]

2.3.3 Kalman Filter

Kalman filter is a type of filter that can perform Linear Quadratic Estimation (LQE). It uses an algorithm that applies a series of measurements observed over a period of time. The measured signal contains statistical noise and other inaccuracies. It produces estimates of unknown variables that tend to be more precise than those based on a single measurement alone. The filter is named after Rudolf E. Kalman, one of the pioneer developers in this theory.

The Kalman filter has many different applications. The most common application is in guidance, navigation and control of vehicles and aircrafts. Kalman filter is widely used in the field of robotic motion planning, control and trajectory optimization. Kalman filters are also used in modelling the central nervous system encountered in control of movement. Kalman filter can provide the needed model for making estimates of the current state of the motor system and issuing updated commands.

The algorithm can process signal in steps. It is recursive and can run in real time using the present input measurements and the previously calculated state. In this process no past information is required. The assumption that Gaussian errors exist are not required in Kalman filter. The filter yields the exact conditional probability estimate that all errors are Gaussian-distributed. The underlying model is a Bayesian model where the state space of the latent variables is continuous and where all latent and observed variables have Gaussian distributions. Figure 2.4 shows the block diagram for a Kalman Filter.

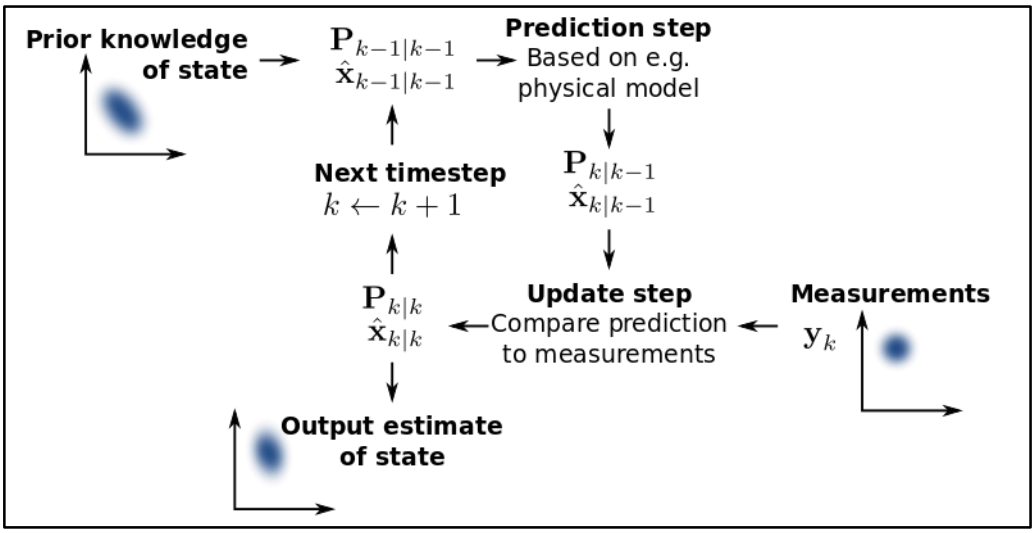


Figure 2.4 Block diagram for a Kalman Filter [28]

3. Theory and Research Methodology

3.1 Wiener Algorithm

The Wiener filter has 3 possible solution cases. The first is noncausal solution where a noncausal filter is analysed that requires an infinite amount of both past and future data. The second is a causal solution where a causal filter is used. The third is the finite impulse response (FIR) where a finite amount of past data is used [8]. The first case is simple to solve but is not realistic for real-time applications [21].

Noncausal solution

$$G(s) = \frac{S_{x,s}(s)}{S_x(s)} e^{\alpha s} \tag{3.1}$$

Where *S* are spectra. Provided that *g(t)* is optimal, then the minimum mean-square error equation reduces to

$$E(e^2) = R_s(0) - \int_{-\infty}^{\infty} g(\tau) R_{x,s}(\tau + \alpha) d\tau \tag{3.2}$$

and the solution g(t) is the inverse two-sided Laplace Transform of G(S).

Causal solution

$$G(s) = \frac{H(s)}{S_x^+(s)} \tag{3.3}$$

Finite impulse response of Wiener filter for discrete series

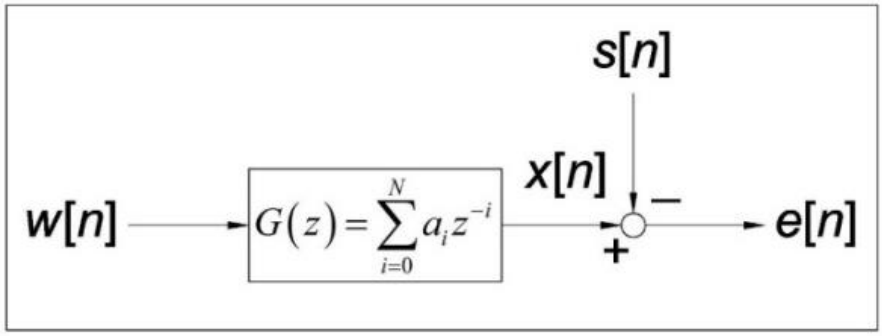


Figure 3.1. Block diagram of noise filtering**.**

Figure 3.1 shows the block diagram of the FIR Wiener filter for discrete series. An input signal $w[n]$ is convolved with the Wiener filter $g[n]$ and the result is compared to a reference signal $s[n]$ to obtain the filtering error $e[n]$.

In order to derive the coefficients of the Wiener filter, consider the signal $w[n]$ being fed to a Wiener filter of order N and with coefficients $\{a_i\}$, where i=0, 1, 2,…,N. The output of the filter is denoted $x[n]$ which is given by the expression

$$x[n] = \sum_{i=0}^{N} a_i w[n-i] \tag{3.4}$$

The residual error is denoted by $e[n]$ and is defined as $e[n]=x[n]-s[n]$. The Wiener filter is designed so as to minimize the mean square error. This can be stated as follows :

$$a_i = arg_{min} E\{e^2[n]\} \tag{3.5}$$

where $E\{\ \}$ denotes the expectation operator. The mean square error (MSE) may be written as :

$$E\{e^2[n]\} = E\{(x[n]-s[n])^2\}$$
$$= E\{x^2[n]\} + E\{s^2[n]\} - 2E\{x[n]s[n]\} \tag{3.6}$$

To find the vector $[a_0,\ldots,a_N]$ which minimizes the expression above, calculate its derivative with respect to a_i

$$\frac{\partial}{\partial a_i} E\{e^2[n]\} = 2\sum_{j=0}^{N} R_w[j-i]a_j - 2R_{sw}[j] \qquad i=0,\ldots,N \tag{3.7}$$

Letting the derivative be equal to zero results in

$$\sum_{j=0}^{N} R_w[j-1]\, a_j = R_{sw}[i] \qquad i=0,\ldots,N \tag{3.8}$$

which can be rewritten in matrix form **Ta**=**v**

$$\begin{bmatrix} R_w[0] & R_w[1] & \ldots & R_w[N] \\ R_w[1] & R_w[0] & \ldots & R_w[N-1] \\ \vdots & \vdots & \ddots & \vdots \\ R_w[N] & R_w[N-1] & \ldots & R_w[0] \end{bmatrix} \begin{bmatrix} a_0 \\ a_1 \\ \vdots \\ a_N \end{bmatrix} = \begin{bmatrix} R_{sw}[0] \\ R_{sw}[1] \\ \vdots \\ R_{sw}[N] \end{bmatrix} \tag{3.9}$$

These equations are known as the Wiener-Hopf equations. The matrix **T** appearing in the equation is a symmetrical Toeplitz matrix. Under suitable conditions on **R**, these matrices are known to be positive definite and therefore non-singular yielding a unique solution to the determination of the Wiener filter coefficient vector, $\mathbf{a}=\mathbf{T}^{-1}\mathbf{v}$. Furthermore, there exists an efficient algorithm to solve such Wiener-Hopf equations known as the Levinson-Durbin algorithm so an explicit inversion of **T** is not required.

3.2. Experimental Setup

In this experiment, the recording of signals [27] was carried out in the Hospital of Philipps-University by Professor Dr. Thomas Penzel. The laboratory technician in the public hospital will set up the necessary equipment required for

conducting the ECG signal measurement. Each set of data consists of 35 recordings. Each recording contains a single ECG signal digitized at 100 Hz with 12-bit resolution. The recording contains a set of reference annotations, one for each minute of recording. This indicates the presence or absence of apnea during that particular minute. All these reference annotations were made by human experts on the basis of simultaneously recorded respiration signals. Figure 3.2 shows the flowchart of ECG Feature Extraction Using Improved Wavelet Analysis (Wi-Wave). Figure 3.3 shows the framework of the improved wavelet (Wi-Wave).

The signals for different types of patients have been recorded and stored in proper devices. The data will be divided according to the types of signal being recorded like heart, brain, etc. Wiener filter will be used to remove the unnecessary noise in the ECG signal. Auto-correlation and Cross-correlation will be applied on the ECG signal. The filtered wave will be used for feature identification and feature extraction. If no feature can be identified, the ECG signal will be sampled and feature extraction will be carried out again. The process will stop if ECG feature is identified. The framework of this study is shown in figure 3.2. The database is derived from the patients in hospital.

Step 1 : Technician to set up ECG recording equipment in the hospital.
Step 2 : Record the particulars of patient like age, gender, heart symptom, blood pressure, cholesterol level, sugar level, pulse rate, etc.
Step 3 : Attach all the electronic probes or electrodes properly at the exact locations on the patient's body so that they can detect the sound of pulses coming from the heart.
Step 4 : Start the electronic equipment to initiate recording.
Step 5 : Verify ECG result by clinical consultant.
Step 6 : Start the electronic equipment to initiate recording.
Step 7 : Perform data identification of patient heart signals.
Step 8 : Use improved Wiener filter (Wi-Wave) Auto-correlation and Cross-correlation to process the noise.
Step 9 : Perform noise filtering and signal Auto-correlation and Cross-correlation.
Step 10 : Perform feature extraction and identification using improved wavelet analysis (Wi-Wave).

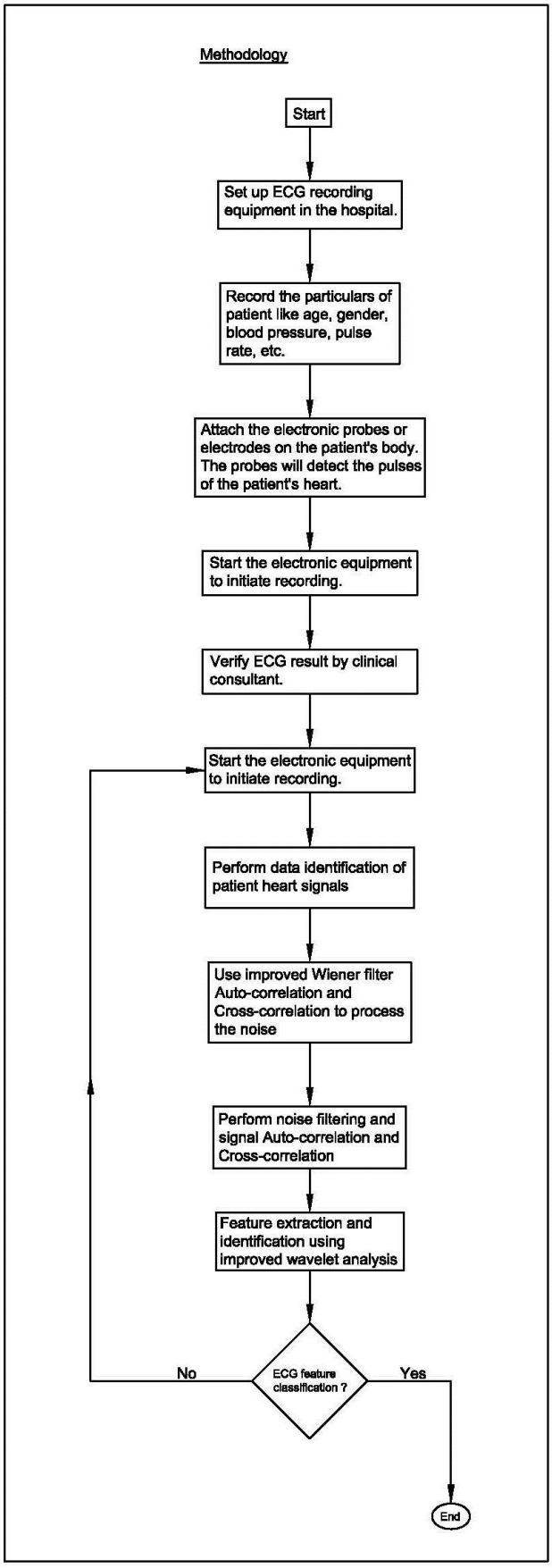


Figure 3.2 : Flowchart of ECG Feature Extraction Using Improved Wavelet Analysis (Wi-Wave)

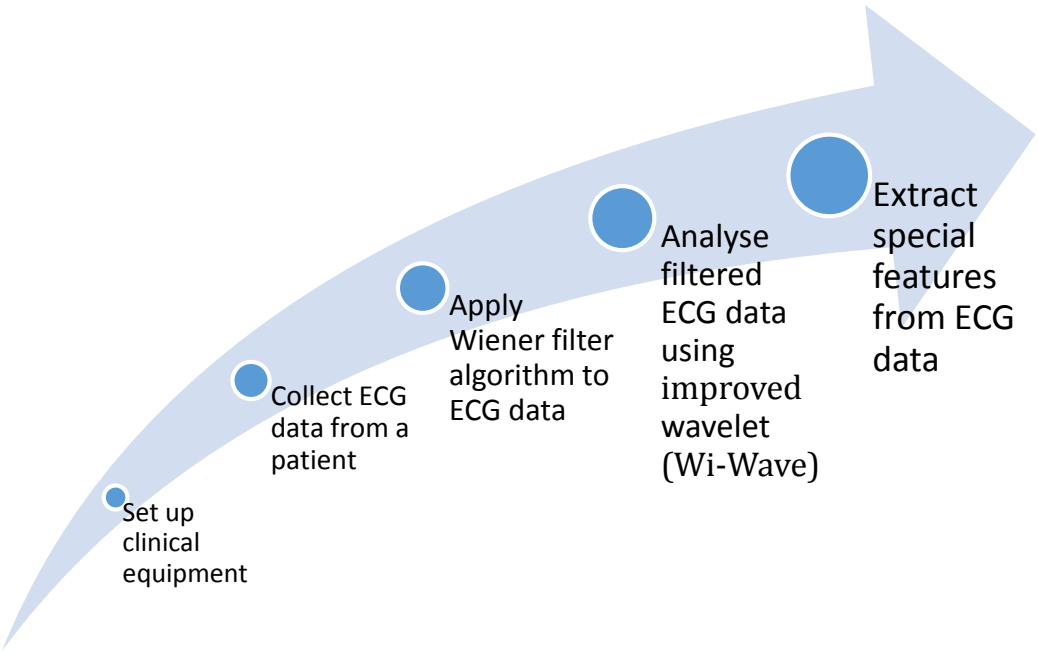


Figure 3.3 **:** Framework of the improved wavelet (Wi-Wave)

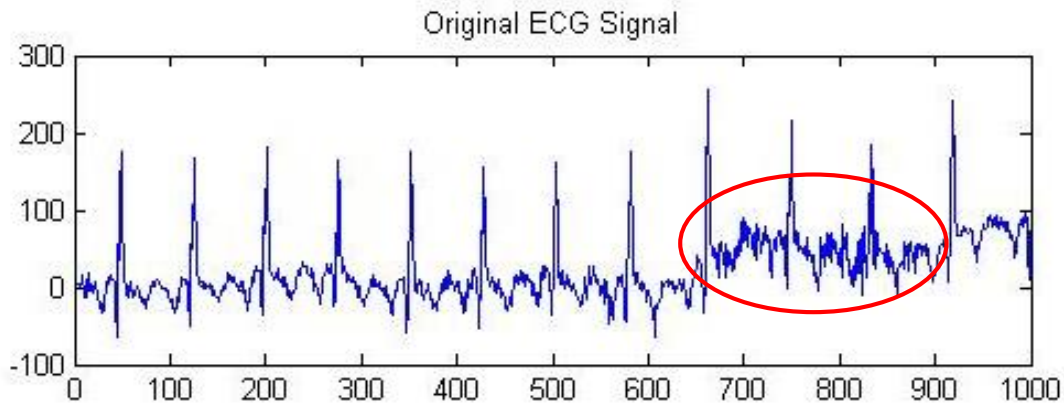
4. Results and Discussions

Several results were collected after the experiment. The figures 4.1a and 4.2a show the original ECG signal extracted from patient. The signal contains information on the abnormalities hidden in the human heart. It also contains noise and interference created from the measuring equipment.

Figures 4.1b, and 4.2b show the signal with the noise removed using the Wiener filter. The Wiener filter was applied on the original signal to remove those unwanted noise and interference. The final output was plotted out to compare with the original signal. The improved wavelet (Wi-Wave) is more flexible as it can provide more scope and level for analysis. The special feature could be extracted using improved wavelet (Wi-Wave), the results are highlighted using the square box.

The original and raw ECG signal is fed into FIR Wiener filter to obtain the filtered result. The mathematical technique will provide the algorithm to calculate the new waveforms.

(a)



(b)

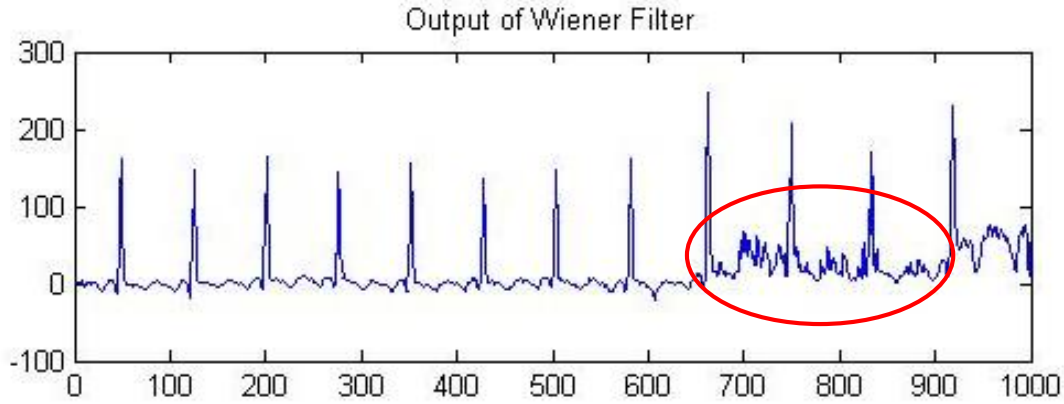


Figure 4.1 : (a) Original signal (a20m), (b) Filtered signal

Figure 4.1 (a) shows that samples 650 to 900 consist of irregularities in pattern. The shape of these patterns are distinctly different from the rest of the patterns. This was caused by interference generated as a result of noise and vibration.

(c)

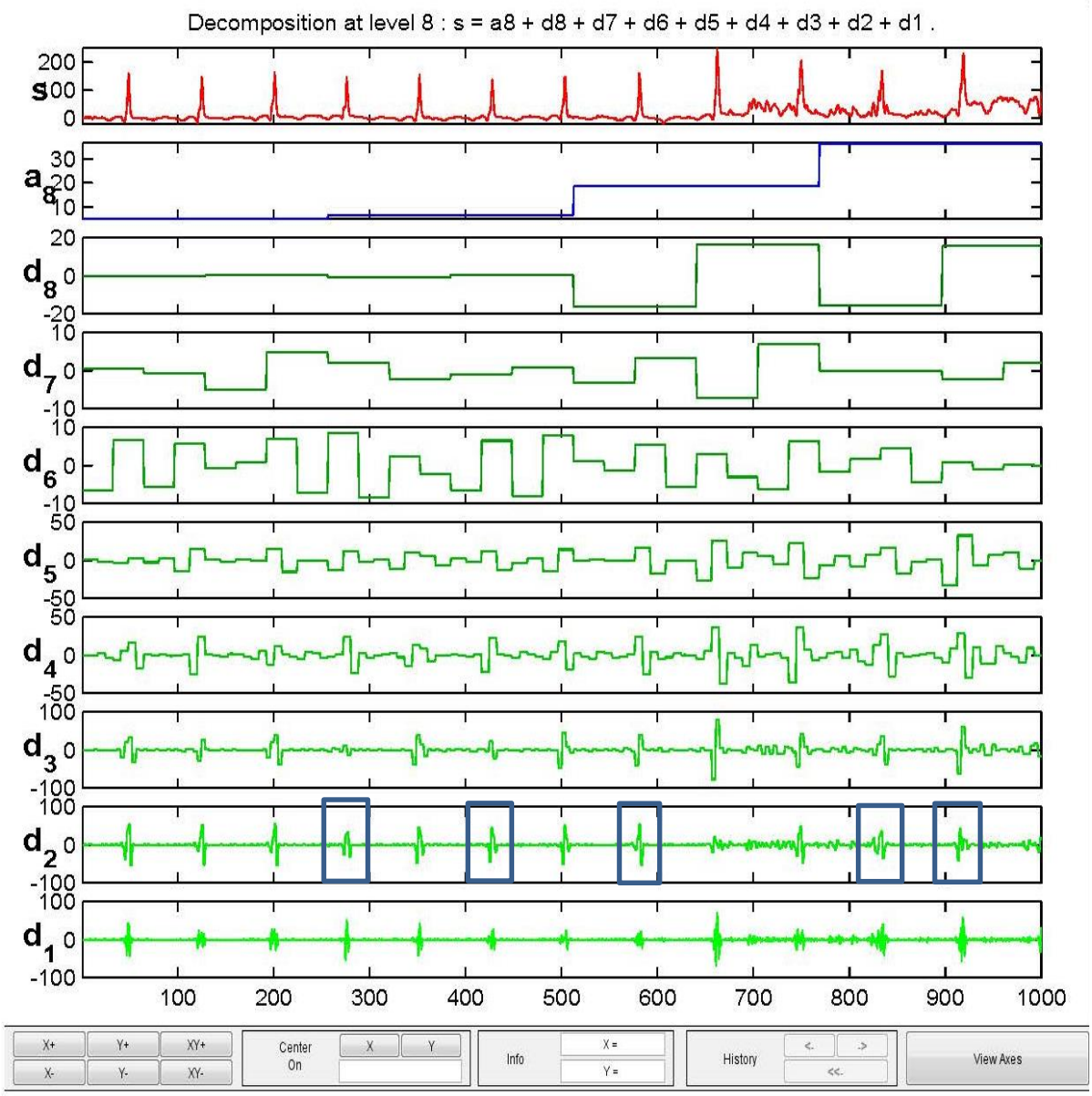


Figure 4.1(c) : Improved wavelet analysis (Wi-Wave) (Haar, Level 8) on filtered signal as shown in Figure 4.1(b)

The boxes highlighted in Figure 4.1 (c) show the features in the ECG signal.

Table 4.1 : Statistical property for the ECG signal a20m

ECG Signal Name	Mean	Variance	Standard Deviation
a20m	15.75661	992.85578	31.50961

Figure 4.1 (c) shows the experimental results using improved wavelet (Wi-Wave) for the ECG signal containing interference. The improved wavelet (Wi-Wave) plot shows many different levels. Levels d3, d2 and d1 indicate the special features in the corrupted ECG signal. The features are highlighted using boxes as shown in d2. 10 features were detected as shown in Figure 4.1 (c). Figure 4.2 shows the Histogram and Cumulative Histogram for Original Signal.

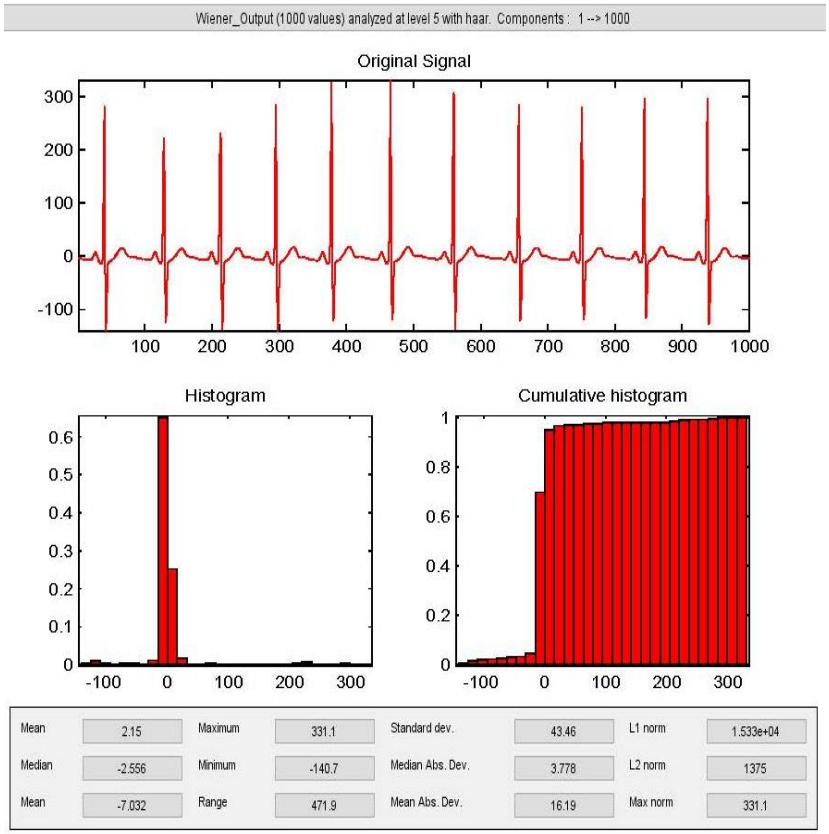


Figure 4.2 : Histogram and Cumulative Histogram for Original Signal.

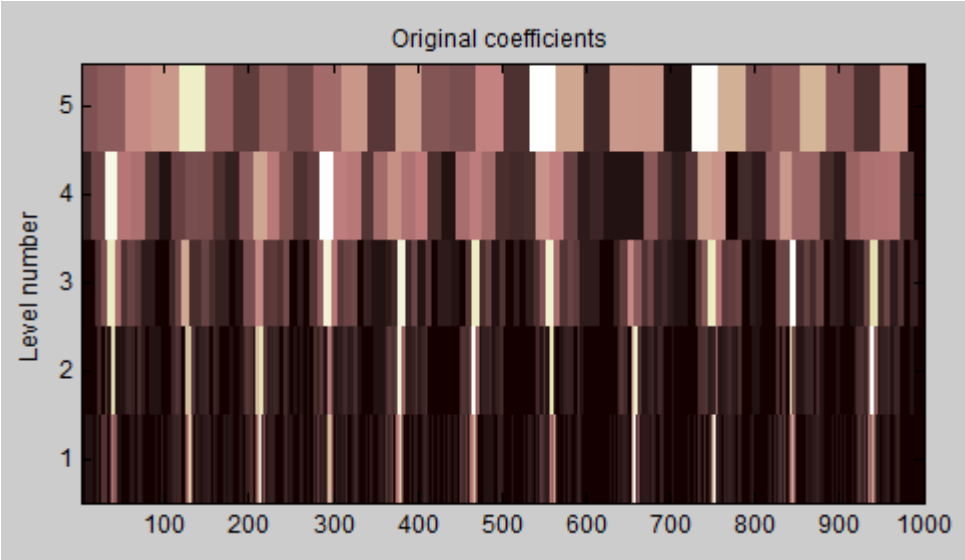


Figure 4.3 : Coefficients of ECG signal.

Figure 4.3 above shows the coefficients associated with the particular ECG signal. It is a concept derived from features extraction algorithm for ECG signal using Huang Hilbert Transform and Wavelet Transform. Based on our observation, level 5

shows the higher coefficient than level 1.

Table 2. Mean, Variance and Standard Deviation for the ECG Signal

Signal Filename	Mean	Variance	Standard Deviation
a01m	2.15040	1889.20490	43.46498
a02m	2.17313	405.09212	20.12690
a08m	14.64168	11324.44330	106.41637
a10m	-1.39727	2191.50222	46.81348
a12m	-1.74431	289.80652	17.02370
a13m	9.79765	8103.58932	90.01994
a14m	2.93584	2026.78219	45.01980
a18m	3.80798	1121.62077	33.49061
a19m	2.85703	10983.13673	104.80046
c03m	2.67132	1644.80662	40.55622

Table 2 above shows that the proper signal has a mean at about 2.15. The signal that best matched the normal ECG signal is the one having mean of 2.15 and standard deviation of 43.46.

The Mean is the sum of the sampled values divided by the number of items in the sample.

$$Mean\ \bar{x} = \frac{1}{n}\sum_{k=1}^{n} x_k \qquad (4.1)$$

The variance is the square of the standard deviation. The variance of a set of equally likely values can be written as

$$Var(x) = \frac{1}{n-1}\sum_{k=1}^{n}\left(x_k - \bar{x}\right)^2 \qquad (4.2)$$

The sample standard deviation is given by

$$\sigma = \sqrt{\frac{1}{n-1}\sum_{k=1}^{n}\left(x_k - \bar{x}\right)^2} \qquad (4.3)$$

5. Conclusion

Raw ECG signal which is contaminated with noise and interference can be made noiseless by using improved Wiener and wavelet method (Wi-Wave) created using noise filtering algorithm. Wiener filter is a type of filter that can be used to perform the function. For better result, a modified algorithm can be used to perform the filtering and extract the feature. Those noises are generated as a result of eye blink, heartbeat, equipment, human conversation, etc. High pass filter can be used to remove those noises to yield better and accurate result for analysis [23].

Many different algorithms based on diverse methods have been developed for the automated ECG feature extraction. They are efficient and characterised by a high performance and show results that fulfil the requirements for sensitivity and error ranges satisfactorily. Today, automated ECG feature extraction algorithms are standard in clinical practice and support physicians in the evaluation of ECG curves and medical diagnosis. A significant factor in this context is the saving of time which becomes more important in consideration of current changes in health care systems. Another advantage of automated algorithms is the elimination of operator-dependence which makes measurements more reproducible [24].

Nevertheless, the precise detection of ECG features is still not resolved or completed. The development of an algorithm that is able to take into account the amount of information contained in the ECG waveform is meaningful but challenging. The extensive ability of humans in pattern recognition and matching cannot be reproduced by a computer so far. Moreover, the ECG shapes show a wide variability because the anatomy, physiology and functionality of the heart are different from human to human. Patterns differing to a great extend can still be physiological instead of indicating an underlying heart disease [25].

Still, there is no gold-standard or algorithm that would give precise and always reliable results as illustrated in the study carried out by Baumert et al [1] where it turned out that none of the tested algorithms was able to detect a QT variability after the infusion of a QT prolonging drug. Moreover, these results pointed out the requirement of a high qualitative, noise free ECG recording because noise affects the performance of extraction algorithms. Especially for the QT duration the clear detection of the T wave offset which is often masked by noise is crucial because a prolongation of only a few milliseconds (in an interval of a total length of up to 500ms or more) can indicate a cardiac disorder. This fact points out the requirement of precise and exact measurements [26].

Acknowledgement

The author would like to express his appreciation to his supervisor, co-supervisor and all supporting staff for the helps and guidance provided throughout the entire research project.

Reference

[1] James H. McClellan, Ronald W. Schafer and Mark A. Yoder, "*Signal Processing First*," 1st Edition, Pearson, 2003.
[2] Alan V. Oppenheim, Ronald W. Schafer, "*Discrete-Time Signal Processing*," 3rd Edition, Pearson, 2010.
[3] Monson Hayes, "*Schaums Outline of Digital Signal Processing*," 2nd Edition, McGraw-Hill, 2011.
[4] Hwei Hsu, "*Schaum's Outline of Signals and Systems*," 3rd Edition, McGraw-Hill, 2013.
[5] Alan V. Oppenheim, Alan S. Willsky, S. Hamid, "*Signals and Systems*," 2nd Edition, Prentice Hall, 1996.
[6] John G. Proakis, Dimitris K Manolakis, "*Digital Signal Processing, Principles, Algorithms and Applications*", 4th Edition, Prentice Hall, April 7, 2006.
[7] Steven W. Smith, "*The Scientist & Engineer's Guide to Digital Signal Processing*", 1st Edition, California Technical Pub, 1997.
[8] Richard G Lyons, "*Understanding Digital Signal Processing*", 3rd Edition, Pearson, 2011.
[9] Vinay K. Ingle (Author), John G. Proakis, "*Digital Signal Processing Using MATLAB*", 3rd Edition, Pearson, 2011.
[10] Jacob Benesty, Jingdong Chen, Yiteng Huang, Israel Cohen, "*Noise Reduction in Speech Processing (Springer Topics in Signal Processing)*", 2009 Edition, Springer, 2009.
[11] Luis Chaparro, "*Signals and Systems using MATLAB*", 2nd Edition, Academic Press, 2014.
[12] Robert Grover Brown, Patrick Y. C. Hwang, "*Introduction to Random Signals and Applied Kalman Filtering*", 3rd Edition, Wiley, 1996.
[13] Jean-Claude Bertein, Roger Ceschi, "*Discrete Stochastic Processes and Optimal Filtering (Digital Signal and Image Processing)*", Wiley-ISTE, 2007.
[14] Wim C. Van Etten, "*Introduction to Random Signals and Noise*", 1st Edition, Wiley, 2005.
[15] Simon O. Haykin, "*Adaptive Filter Theory*", 5th Edition, Prentice Hall, 2013.
[16] Wilbur B. Davenport Jr., William L. Root, "*An Introduction to the Theory of Random Signals and Noise*", 1st Edition, Wiley-IEEE Press, 1987.
[17] B. Schölkopf, A. Smola and K. Müller, "*Nonlinear Component Analysis as a Kernel Eigenvalue Problem*", Neural Computation, vol. 10, no. 5, pp. 1299-1319, 1998.
[18] G. Welch and G. Bishop, "*An Introduction to the Kalman Filter*," *In Pract.*, vol. 7, no. 1, pp. 1–16, 2006.
[19] A. A. Nielsen and M. J. Canty, "*Kernel principal component analysis for change detection*," *SPIE 7109, Image Signal Process. Remote Sens. XIV*, vol. 7109, no. 10, P. 71090T–71090T–10, 2008.
[20] Analysis and Research on Combination Feature Extraction Method of EEG Signal Science Publishing Group. [ONLINE] Available at: http://article.sciencepublishinggroup.com/html/10.11648.j.acis.20150302.13.ht l. [Accessed 23 July 2015].
[21] S.Karpagachelvi, Dr.M.Arthanari, M.Sivakumar, "*ECG Feature Extraction Techniques – A Survey Approach*", (IJCSIS) International Journal of Computer Science and Information Security, Vol. 8, No. 1, April 2010.

[22] Evangelos B. Mazomenos, Dwaipayan Biswas, Amit Acharyya, Taihai Chen, "*A Low-Complexity ECG Feature Extraction Algorithm for Mobile Healthcare Applications*", IEEE TRANSCATIONS ON INFORMATION TECHNOLOGY IN BIOMEDICINE, VOL. XX, NO. XX, MONTH 201X.

[23] R. Rodrígueza, A. Mexicanob, J. Bilac, S. Cervantesd, R. Ponceb, "*Feature extraction of electrocardiogram signals by applying adaptive threshold and principal component analysis*", Journal of Applied Research and Technology 13 (2015) 261-269.

[24] C Alexakis, HO Nyongesa, R Saatchi, ND Harris, C Davies, C Emery, RH Ireland, SR Heller, "*Feature Extraction and Classification of Electrocardiogram (ECG) Signals Related to Hypoglycaemia*", Schools of Computing & Engineering, Sheffield Hallam University, Sheffield, UK, University of Bath, Bath, UK, University of Sheffield & Weston Park Hospital, Sheffield, UK.

[25] Abhilasha M. Patel, Pankaj K. Gakare, A. N. Cheeran, "*Real Time ECG Feature Extraction and Arrhythmia Detection on a Mobile Platform"*, International Journal of Computer Applications (0975 – 8887) Volume 44– No.23, April 2012.

[26] Svenja Kutscher, "*Algorithms for ECG Feature Extraction: an Overview*", Svenja Kutscher, Mälardalen University, School of Innovation, Design, and Technology, Högskoleplan 1, 72123 Västerås.

[27] Goldberger AL, Amaral LAN, Glass L, Hausdorff JM, Ivanov PCh, Mark RG, Mietus JE, Moody GB, Peng CK, Stanley HE. "*PhysioBank, PhysioToolkit, and PhysioNet: Components of a New Research Resource for Complex Physiologic Signals. Circulation 101 (23)*", [Circulation Electronic Pages; http://circ.ahajournals.org/cgi/content/full/101/23/e215]; 2000 (June 13).

[28] Zachariah, Dave; Chatterjee, Saikat; Jansson, Magnus (2012). "*Dynamic Iterative Pursuit*". IEEE Transactions on Signal Processing.

[29] Weifeng Liu; José C. Principe; Simon Haykin (March 2010). "*Kernel Adaptive Filtering: A Comprehensive Introduction*". Wiley. pp. 12–20. ISBN 978-0-470-44753-6.

Evaluation on Thoracic Trunk Shift and Coronal balance in Post-Operative Scoliosis Patients

P. Mohankumar[1*], Leong Wai Yie[2]

[1]*School of Engineering, Taylor's University, Malaysia.*
[2]*School of Engineering, Taylor's University, Malaysia.*

[*] mohankumar.palaniswamy@sd.taylors.edu.my

Abstract
Thoracic trunk shift and Coronal balance are main features to be considered while planning the treatment for scoliosis patients. Thoracic trunk shift refers to the deviation of trunk from its normal position. Coronal balance refers to the deviation of seventh cervical bone from sacrum in coronal plane. After the scoliosis patient underwent surgery, these two parameters are measured by the surgeons using radiograph images to make sure the scoliosis curve progression is stopped and whether vertebral alignment is back to normal. Since the relationship between thoracic trunk shift and coronal balance in the post-operated scoliotic patients is questionable, this study is done to find the correlation between the thoracic trunk shift and coronal balance in the thoracic scoliosis patients who underwent correction surgery at least an year before from the date of taking radiographs. Radiographs of 24 patients were collected. Statistical analysis was done using paired sample '*t*' test, with the '*p*' value of 0.05 as the level of significance. The mean millimetre measurement of thoracic trunk shift and coronal balance was found to be 27.62 mm and 10.50 mm. The results of our study showed that there is a 10.18% of relation in between the post thoracic trunk shift and coronal balance of those 24 patients.

Keywords: Vertebral fusion, Radiographs, Balance, Plumb line.

1. Introduction

Scoliosis is a medical condition in which the spine is abnormally twisted and curved. Globally scoliosis is the most common musculoskeletal disorder affecting the children ranging from 2-3%. When examining the scoliosis patients from posterior (back) view, spine looks 'C' shaped or 'S' shaped. Treatment to the scoliosis depend upon factors like Cobb angle and age. It can be treated by either cast, brace or surgery. Casting is provided for the age group between 0-3 years, bracing is provided for the children and surgery is performed if the cobb angle is more than 40 degrees. During surgery, surgeons fuse the vertebrae causing scoliosis curve, using metal implants. Since the alignment of vertebrae is affected in scoliosis, the Center of Gravity (CoG) and Line of Gravity (LoG) are also affected in the scoliosis patients. In an anatomical standing posture, the CoG and LoG lies anterior to sacrum bone (S_2). Whereas, in scoliosis patients, the CoG and LoG is altered or deviated according to the severity of scoliosis. The level of deviation can be roughly understood by measuring the Coronal balance, Sagittal balance, Thoracic trunk shift, Thoracolumbar and Lumbar sagittal alignment.

A study done by Mohsen Damavandi et al., (Damavandi, Dalleau, Stylianides, Rivard, & Allard, 2013) on head and trunk mass and center of mass position estimations in able bodied and scoliotic girls concluded that the pre-operative scoliotic girls had greater pelvic forward tilt and trunk inclination when compared with normal subjects. Whereas, another study done by Jae Yong Park et al., (Park, Park, Lee, & Lee, 2013) on the effect of scoliosis angle on center of gravity sway found that the whole body balancing abilities in the pre-operative scoliosis patients is significantly different than the normal persons. This explains the importance of pelvic tilt, center of gravity and trunk inclination in maintaining a proper posture. In scoliosis patients, since the trunk posture is altered or shifted to one side, it in turn provides more pressure to the lumbar region on the side of scoliosis curve. A conducted by Hajizadeh et al., (K, I, & G, 2013) on developing a 3D multibody model of the scoliotic spine with lateral bending motion for comparison of ribcage flexibility concluded that the load at lumbar joints in scoliosis model were higher when compared with the normal.

Even after treating the scoliosis surgically, due to the sudden upright posture caused because of stretching the scoliosis curve during surgery, patients feel a disturbance in their balance. A study by Daniela Cristina Carvalho de Abreu et al., (Carvalho de Abreu, Gomes, Rocha de Santiago, Pereira da Silva Herrero, Porto, & Luiz, 2012) on the influence of surgical treatment of adolescent idiopathic scoliosis on postural control supports this theory. They concluded that the scoliosis patients have a large center of pressure oscillation when compared with the age matched healthy adults. Even after surgery, oscillation is decreased on the initial 90 days. But later, it remained larger than before surgery. During scoliosis correction, surgeons correct the scoliosis angle by using implants, bone graft and manual pressure. Some claim that most of the curve is reduced because of the manual pressure and on the other hand, some claim its due to the vertebral fusion and metal implants. Recently, a study done by Per D. Trobisch et al., (Trobisch, Samdani, Pahys, & Cahill, 2011) on postoperative trunk shift in Lenke 1 and 2 curves concluded that the coronal balance does not correlate with thoracic trunk shift. The postoperative trunk shift is common after surgery for adolescent idiopathic scoliosis. But it occurs only in 13.6% of patients and 65% occurs as an iatrogenic (caused by surgeon). If the curve is corrected

only by manual pressure, implants can take over the vertebral fusion. Then need for fusing the vertebrae will be a questionable debate. Human spine consists of 33 vertebrae which are linked to each other through facets and ligaments. If the abnormal curve (scoliosis) leads to an altered coronal balance, sagittal balance, thoracic trunk shift, thoracolumbar and lumbar sagittal alignment, then after treating the scoliosis, these parameters must return back to normal. Hence, in order to validate this, in this study, we find the thoracic trunk shift (TTS) and coronal balance (CB) between the pre and post operated scoliosis patients. The objective of this study is to compare and find the relation between TTS and CB of pre and post-operated scoliosis using the radiographs acquired at least one year after their surgery (It takes 8 to 10 months for a complete fusion).

2. Methodology

Sampling method followed was a non-probability convenient sampling. The study design was observational cross sectional study.

2.1 Data Collection

Data collection was done at Government General Hospital, Chennai, India. Proper consent was obtained from the radiology department before collecting data. Pre and post-operative radiographs of the 24 thoracic scoliosis patients between the age group 10 to 25 years who underwent scoliosis correction surgery at least 1 year before, were obtained. Baseline assessment were done. The thoracic shift and coronal balance was measured in radiographs. Sample of 3 patient's data are provided below.

Table 1. Patient details.

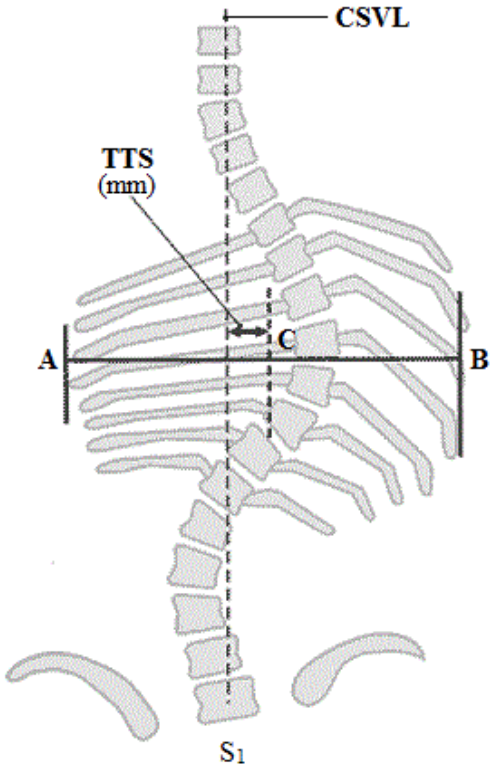
Gender	Age	TTS Pre	TTS Post	CB Pre	CB Post
F	16	28 mm	16 mm	10 mm	3 mm
F	20	51 mm	22 mm	12 mm	2 mm
M	15	31 mm	9 mm	19 mm	4 mm

2.2 Evaluation of Thoracic Trunk Shift

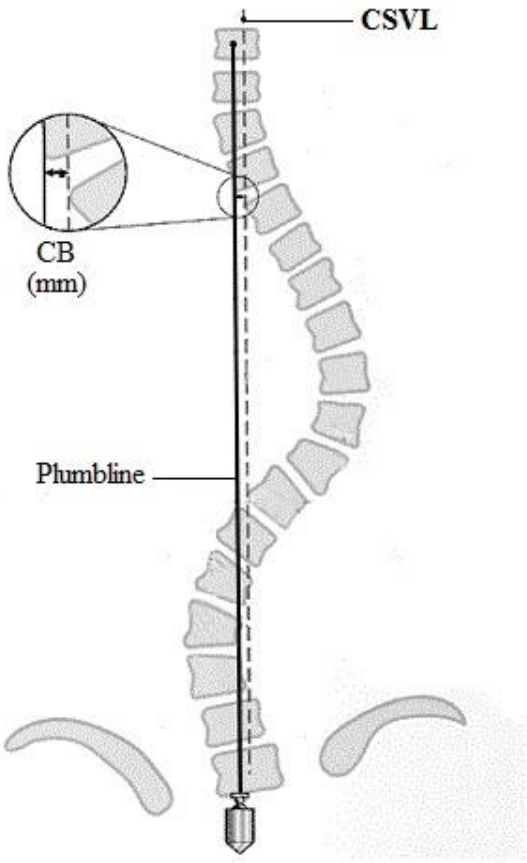
Thoracic shift is measured by first identifying the apical thoracic vertebra (the most deviated vertebra). Through the center of that vertebra, a horizontal line AB is drawn touching the boundary of the ribs on either sides. Midpoint of the line AB is calculated as point C and a vertical line, perpendicular to the line AB is drawn. Then, the center sacral vertical line (CSVL) is drawn from the midpoint of the S_1 upward and parallel to the sides of the radiograph. Now, distance between the perpendicular line through C and CSVL is measured in millimeters. (Fig. 1) This measurement refers to the thoracic trunk shift.

2.3 Evaluation of Coronal Balance

Coronal balance is measured by first identifying the C_7 bone. From the center of C_7, a vertical line drawn downward parallel to the sides of the radiograph (in other words, Plumb line). Then, the CSVL is drawn upwards. The distance between the C_7 plumb line and CSVL is measured as coronal balance. (Fig. 2) It is measured in millimeters.



• **Figure 18. Thoracic Trunk Shift.**



• **Figure 19. Coronal Balance.**

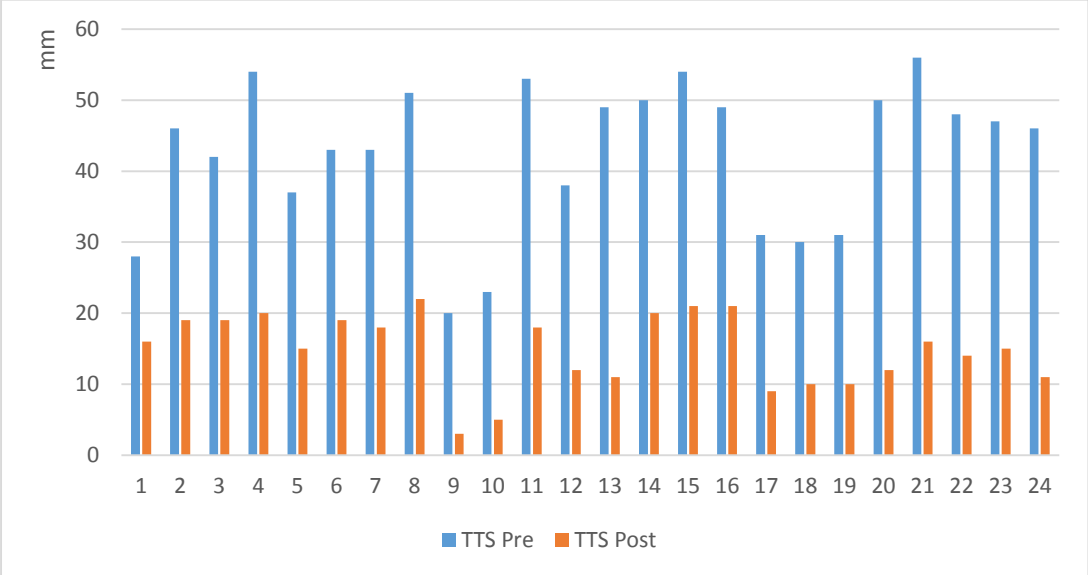
3. Results and Discussion

Out of 24 samples, 7 were males and 17 were females. Statistical analysis was done using paired sample '*t*' test, with '*p*' value set as 0.05 as the level of significance. The mean TTS of the pre and post-operated scoliosis patients was 42.45 mm and 14.83 mm. The standard deviation was ± 10.362 and ± 5.189. Whereas, the mean CB of the pre and post-operated scoliosis patients was 14.75 mm and 4.25 mm. The standard deviation was ± 4.120 and ± 1.359.

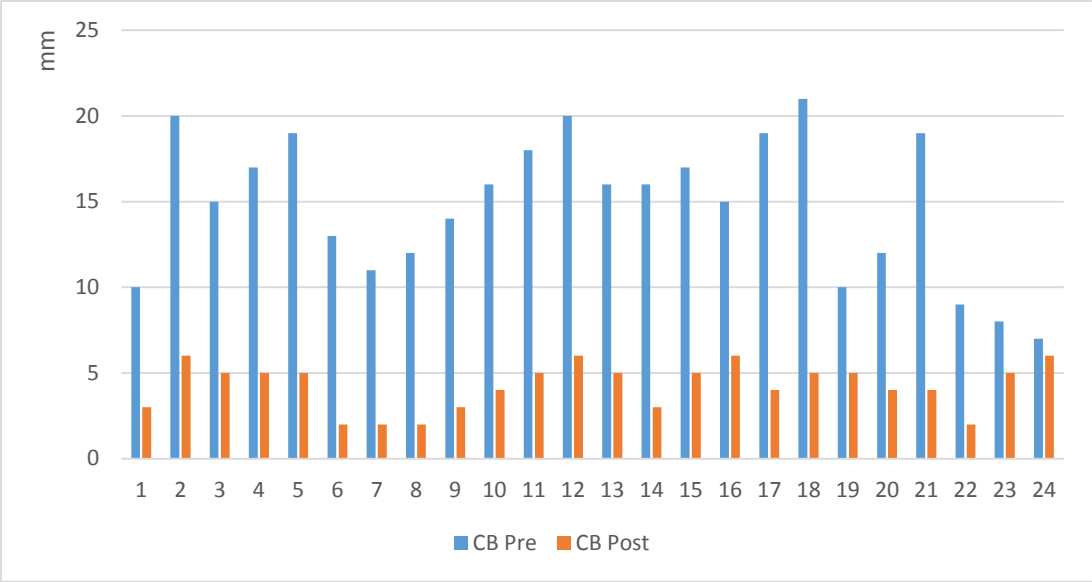
Between the pre and post TTS, mean was 27.62 mm, standard deviation was ± 7.441 with the *t* value of 18.187. While, the mean between the pre and post CB was 10.50 mm, standard deviation was ± 3.844, with the *t* value of 13.379. The results of the paired sample test of both the TTS and CB pre and post-operated scoliosis patients showed that there is a significant level of decrease with the *p* value lesser than 0.05. The mean decrease was 27.62 in TTS and 10.50 in CB, with the 95% confidence interval. Hence, we reject the null hypothesis. There is a significant difference in the TTS and CB between the pre-operative and post-operative scoliosis patients.

Table 2. Results.

	Mean	**SD**	**'*t*' value**	**'*p*' value**
TTS Pre	42.45	10.362		
TTS Post	14.83	5.189		
TTS Pre & Post	27.62	7.441	18.187	.000
CB Pre	14.75	4.120		
CB Post	4.25	1.359		
CB Pre & Post	10.50	3.844	13.379	.000



• **Figure 20. Pre and Post-Operative Thoracic Trunk Shift.**



• **Figure 21. Pre and Post-Operative Coronal Balance.**

A study done by Stephens Richards et al., (Richards, Scaduto, Vanderhave, & Browne, 2005) on assessment of trunk balance in thoracic scoliosis concluded that if the coronal balance and thoracic apical vertebral translation values are known, then the lateral trunk shift can be reliably estimated. In this study, we directly measure the thoracic trunk shift and coronal balance of the post-operated thoracic scoliosis patients. Study by Mohsen Karami et al., (Karami, Maleki, & Mazda, 2016) on the assessment of coronal radiographic parameters of the spine in the treatment of adolescent idiopathic scoliosis concluded that precise attention to the coronal balance in pre-operative is vital in prevention of post-operative decompensation. During the scoliosis correction surgery, surgeons perform osteotomy, place bone grafts in the course of scoliosis curve and fuse the vertebrae together. With the help of metal implants, bone graft and bone regeneration, curve correction occurs promptly. Another study by Ebrahim Ameri et al., (Ameri, Ghandhari, Nabizadeh, & Hesarikia, 2014) on natural history of coronal balance after spinal fusion in adolescent idiopathic scoliosis revealed that the first 12 months after posterior spinal fusion is the spontaneous improvement period for coronal balance. Following that period of time is less likely. In contrast, a study by Nicolas Siderakis et al., (Siderakis, et al., 2013) on analysis of coronal balance and last level of arthrodesis in Lenke type 5 idiopathic scoliosis concluded that the general average Apical Vertebral Translation Lumbar (AVTL) was greater in the patients whose coronal balance did not improve.

In our study, we could not able to get the patients Lenke type, as they underwent scoliosis correction surgery during the period of 2011 to 2014, only the patient's details, Cobb angle measurement, radiographs were available. Hence, such information (Lenke type) was not available at the time of data collection. But, it was evident that patients Cobb angle, TTS and CB were significantly reduced between the pre and post-operated patients. The percentage difference between the mean of pre & post TTS and pre & post CB was 89.82%. Which shows that there is a 10.18% of similarity in the relationship between TTS and CB.

4. Conclusion

Because of bone healing occurring along with vertebral fusion, most of the scoliosis correction takes place within the first 12 months itself. The results of our study clearly shows that there is a significant decrease in the thoracic trunk shift and coronal balance between the pre and post-operative thoracic scoliosis patients and 10.18% of relation between the thoracic trunk shift and coronal balance among those 28 patients.

References

1. Darabi, Z., & Ferdowsi, M. (2011). Aggregated Impact of Plug-in Hybrid Electric Vehicles on Electricity Demand Profile. *IEEE Transactions on Sustainable Energy , 2* (4), 501-508.
2. Malaysian-German Chamber of Commerce and Industry. (2011). 1st Malaysian-German Sustainable Automotive Mobility Conference. *Sustainable Mobility Conference.* Kuala Lumpur.
3. Gruber, W., Bäck, W., & Amrhein, W. (2011). Design and implementation of a wheel hub motor for an electric scooter. *2011 IEEE Vehicle Power and Propulsion Conference.* Chicago, IL.
4. Tie, S. F., & Tan, C. W. (2013). A review of energy sources and energy management system in electric vehicles. *Renewable and Sustainable Energy Reviews , 20*, 82-102.
5. Yong, J. Y., Ramachandaramurthy, V. K., Tan, K. M., Mithulananthan, & N. (2015). A review on the state-of-the-art technologies of electric vehicle, its impacts and prospects. *Renewable and Sustainable Energy Reviews , 49*, 365-385.
6. H. R. Cha, K. J. Shin and Y. J. Seo. (2011). Design of outer rotor IPM type PMSM for 3 wheel electric vehicle. *2011 International Conference on Electrical Machines and Systems.* Beijing.
7. D. Fodorean, D. C. Popa, P. Minciunescu, C. Irimia and L. Szabó. (2014). Study of a high-speed motorization for electric vehicle based on PMSM, IM and VRSM. *2014 International Conference on Electrical Machines (ICEM).* Berlin.
8. Rahman, M. A., & Masrur, M. A. (2009). Advances on IPM technology for hybrid electric vehicles. *2009 IEEE Vehicle Power and Propulsion Conference.* Dearborn, MI.
9. M. Cheng, W. Hua, J. Zhang and W. Zhao. (2011). Overview of Stator-Permanent Magnet Brushless Machines. *IEEE Transactions on Industrial Electronics , 58* (11), 50087-5101.
10. W. Xu, J. Zhu, Y. Guo, S. Wang, Y. Wang and Z. Shi. (2009). Survey on electrical machines in electrical vehicles. *International Conference on Applied Superconductivity and Electromagnetic Devices.* Chengdu.
11. Chu, C. L., Tsai, M. C., & Chen, H. Y. (2001). Torque control of brushless DC motors applied to electric vehicles. *Electric Machines and Drives Conference, 2001. IEMDC 2001. IEEE International* (pp. 82-87). Cambridge, MA: 2001. IEMDC 2001. IEEE International.
12. Ehsani, M., Gao, Y., & Gay, S. (2003). Characterization of electric motor drives for traction applications. *Industrial Electronics Society, 2003. IECON '03. The 29th Annual Conference of the IEEE. 1*, pp. 891-896. The 29th Annual Conference of the IEEE.
13. V, A. C., Norhisam, M., Aris, I., Marhaban, M. H., Ahmad, D., & Nirei, M. (2011). Double-Rotor Switched Reluctance Machine (DRSRM): Fundamentals and magnetic circuit analysis. *2011 IEEE Student Conference on Research and Development.*
14. Niu, S., Ho, S. L., & Fu, W. N. (2013). A Novel Double-Stator Double Rotor Brushless Electrical Continuously Variable Transmission System. *49* (7).
15. Griffin, M. (1990). *Handbook of Human Vibration* . San Diego: Academic Press Limited.
    I. Hostens, Y. P. (2003). A study of vibration characteristics on a luxury wheelchair and a new prototype wheelchair. *Journal of Sound & Vibration , 266*, 443-452.
16. T. Ramachandran, K. P. (2012). Review on Internal Combustion Engine Vibrations and Mountings. *International Journal of Engineering Sciences & Emerging Technologies , 3* (1), 63-73.
17. Griffin, G. P. (2009). Evaluation of Whole Body Vibration and RIde Comfort in a Passenger Car. *International Journal of Acoustics and Vibration , 14* (1), 143-149.
18. Yunhe Yu, N. G. (2001). Review of automotive vehicle engine mounting systems. *Mechanism and Machine Theory , 36*, 123-142.
19. Jasvir Singh Dhillon, P. R. (2014). Design of Engine Mount Bracket for a FSAE Car Using Finite Element Analysis. *International Journal of Engineering Reseach and Application , 4* (9), 74-81.
20. Conti, P. a. (1989). Mount Stiffness and Inertia Properties from Modal Test Data. *ASME Journal of Vibration and Acoustics, Stress and Reliability in Design , 111*, 134-141.
21. Chung-Ha Suh, C. G. (1997). Dynamic Simulation of Engine-Mount Systems. *SAE International* , 561-572.
22. Brick7. (2010). The Motorcycle Search Engine. South Africa: Brick 7.

23. Kjær, B. &. (1998). *Vibration Transducers and Signal Conditioning.* Brüel & Kjær Sound Vibration Measurement A/S.
24. Bracewell, R. N. (1989). The Fourier Transorm. *Scientific American* , 86-95.
25. S.Rao, S. (2011). *Mechanical Vibration.* Miami: Prentice Hall.
26. Frederick, J. T. (2011, March 29). *Auburn University Electronic Theses and Dissertations.* Retrieved November 20, 2016, from http://etd.auburn.edu/handle/10415/2488
27. Nolan, P. (n.d.). *Farmingdale University.* Retrieved October 31, 2016, from www.farmingdale.edu/faculty/peter-nolan/pdf/UPCh13.pdf
28. International, S. (2016). *2016 Formula SAE Rules.* SAE International.
29. Damavandi, M., Dalleau, G., Stylianides, G., Rivard, C. H., & Allard, P. (2013). Head and Trunk mass and center of mass position estimates in able-bodied and scoliotic girls. *Medical Engineering & Physics , 35*, 1607-1612.
30. Park, J. Y., Park, G. D., Lee, S. G., & Lee, J. C. (2013). The Effect of Scoliosis Angle on Center of Gravity Sway. *Journal of Physical Therapy Science , 25* (12), 1629-1631.
31. K, H., I, G., & G, L. (2013). Developing a 3D Multi-Body Model of the Scolitic Spine with Lateral Bending Motion for Comparison of Ribcage Flexibility. *International Journal of Advanced Design and Manufacturing Technology , 6* (1), 25-32.
32. Carvalho de Abreu, D. C., Gomes, M. M., Rocha de Santiago, H. A., Pereira da Silva Herrero, C. F., Porto, M. A., & Luiz, H. (2012). What is the influence of surgical treatment of adolescent idiopathic scoliosis on postural control? *Gait & Posture , 36*, 586-590.
33. Trobisch, P. D., Samdani, A. F., Pahys, J. M., & Cahill, P. J. (2011). Postoperative trunk shift in Lenke 1 and 2 curves: how common is it? and analysis of risk factors. *European Spine Journal , 20*, 1820-1828.
34. Richards, B. S., Scaduto, A., Vanderhave, K., & Browne, R. (2005). Assessment of Trunk Balance in Thoracic Scoliosis. *The Spine Journal , 30* (14), 1621-1626.
35. Karami, M., Maleki, A., & Mazda, K. (2016). Assessment of Coronal Radiographic Parameters of the Spine in the Treatment of Adolescent Isiopathic Scoliosis. *Archives of Bone and Joint Surgery , 4* (4), 376-380.
36. Ameri, E., Ghandhari, H., Nabizadeh, N., & Hesarikia, H. (2014). Natural history of coronal balance after spinal fusion in adolescent idiopathic scoliosis. *Shafa Orthopedic Journal , 1* (2), 12-16.
37. Siderakis, N., Rosado, J. P., Aguilar, A., Dinelli, D., Lutzky, L., Reviriego, J., et al. (2013). Analysis of coronal balance and last level of arthrodesis in lenke type 5 idiopathic scoliosis: Specific radiographic parameters. *Coluna/Columna , 12* (4), 296-299.

Measurement of Lumbosacral Load Using Radiographic Images

P. Mohankumar[1*], Leong Wai Yie[2], Cheah Kean How[3]

[1]*School of Engineering, Taylor's University, Malaysia.*
[2]*School of Engineering, Taylor's University, Malaysia.*
[3]*School of Engineering, Taylor's University, Malaysia.*

[*]mohankumar.palaniswamy@sd.taylors.edu.my

Abstract
Lumbosacral alignment plays a major role in the mechanical low back pain in general population. Malalignment causes increased strain to the muscles and ligaments around it which eventually leads to mechanical low back pain and discomfort. The level of strain a ligament receives in the lumbosacral junction depends upon the lumbosacral angle and the load exerted on it. If their is an easy way to find the load exerted at the lumbosacral junction, then it would be trouble free for the physicians to examine. Hence, the treatment can be planned accordingly. This study analyses the angle, net force produced and stress faced by the ligaments around the lumbosacral joint using radiographic images. Study design was analytical, observational cross sectional study. Radiographs of 30 patients suffering from low back pain were collected and one sample '*t*' test was used for data analysis with '*p*' value set as 0.05 as level of significance. The mean lumbosacral angle was found to be 44.26 degrees and the standard deviation was ± 7.8625. The results of our study showed that there is a direct relationship between the lumbosacral angle and the force exerted on the vertebrae. Also, patients suffering from low back pain had an increased lumbosacral angle.

Keywords: Lumbosacral Angle, Stress, Force, Line of Gravity.

1. Introduction

Human vertebral column consists of 33 vertebrae (24 articulating and 9 fused vertebrae). Weight from the head, arm and trunk are passed through vertebral column and transferred to the lower limbs through sacrum. Base of sacrum forms an angle with the fifth lumbar vertebrae called as Lumbosacral angle. This angle regulates the amount of load received by lower limbs. National Institute for Occupational Safety and Health guidelines for manual on lifting concluded that fifth lumbar vertebrae)L_5(and first sacral vertebrae)S_1(is the joint of greatest lumbar stress during lifting.

1.1 Lumbosacral Load

The common way of measuring lumbosacral angle was proposed by Ferguson (Hellems & Keats, 1971). He measured the angle formed between base of sacrum with the horizontal plane known as Lumbosacral angle. The optimal lumbosacral angle is approximately 30 degrees (Lippert, 2011). As mentioned above, optimal 30 degree of lumbosacral angle transfers the weight it receives to pelvis and lower limbs equally without any stress. Lumbosacral joint is stabilized by strong ligaments and facet joints, which prevents anterior shear of L_5 on S_1 (Smith, Weiss, & Lehmkuhl, 1998). There are several ways to calculate the load exerted on vertebrae like finite element analysis, pressure sensors, transducer, Hopkinson pressure bar to name a few. These techniques are time consuming and need a sophisticated instruments to carry out the study. In this paper, we use radiographs (trunk – lumbar region) to calculate the load exerted on the fifth lumbar vertebra by measuring the lumbosacral angle. Earlier, several studies have provided enough evidence that there is a strong relation between lumbosacral angle and Center of Mass (CoM).

Pasha et al., (Pasha, Aubin, Labelle, Parent, & Mac Thiong, 2015) conducted a study on biomechanical effects of spinal fusion on the sacral loading. A significant relationship was observed between sacral slope and the position of Center of Pressure (CoP) of S_1 and CoM of Trunk. As the sacral slope increases, the anteroposterior distance between CoM of Trunk and CoP of S_1 decreased significantly in postoperative subjects. Also, another study done by Nohara et al., (Nohara, et al., 2015) on lumbar disc degeneration in patients with adolescent idiopathic scoliosis with spinal fusion claims that 48% of disc degeneration occurs at L_5 – Lumbosacral (LS).

These studies give rise to the questions regarding the CoM, CoP oscillation, optimal lumbosacral angle and the net force acting on L_5 vertebra in the low back pain patients. This lead us to investigate the lumbosacral angle and load. The objective of this study is to analyse the lumbosacral load in low back pain patients using radiographs.

2. Methodology

The sampling method followed was a non-probability convenient sampling. The study design was observational cross sectional study.

2.1 Data Collection and Evaluation of Lumbosacral Angle

Data collection was done at Government General Hospital, Chennai, India. Proper consent was obtained from the radiology department before collecting data. Radiographs were took with patients in the lying position. As during standing, the patient might tilt their pelvis unknowingly. Radiographs of the 30 patients between the age group 25 to 35 years who had low back pain were obtained. Baseline assessment were done. A sample of 3 patients data are provided below (Table 1). The lumbosacral angle was measured in radiographs using the angle formed between base of sacrum with the horizontal plane (Fig. 1). Angle was measured digitaly by Sante DICOM viewer, version 5.0.4. The percentage difference while measuring the angle was found to be less than 1.6%.

Table 1. Patient details.

Gender	Age	Lumbosacral Angle
M	25	55.48
F	26	59.26
M	28	49.93

2.2 Evaluation of Force acting on Vertebra

Let us consider a rectangle placed over triangle as a lumbar vertebra over sacrum, with θ as lumbosacral angle.)Fig. 2(Now, XZY is a right angled triangle with θ at Y. Let C be the center of mass of L_5 vertebra, XY be the base of sacrum, $\overrightarrow{Fg}$ is the gravitational force or body weight acting, $\overrightarrow{Fg\|}$ is the parallel force or anterior shear acting on vertebra parallel to XY slope, $\overrightarrow{Fg^{\perp}}$ is the perpendicular force acting perpendicular to XY slope, A and B are the two points where gravitational and perpendicular force intersects XY.

$$\angle XZY = 90° \qquad (1)$$

$$\angle XYZ = \tan\theta \qquad (2)$$

Applying Trigonometric rules to find the angle in a given triangle, we get:

$$\tan\theta = \frac{Opposite}{Adjacent}$$

It is understood that, opposite to Θ is $\overline{XZ}$ line and adjacent to Θ is $\overline{YZ}$ line. So, tan Θ is $\overline{XZ}$ divided by $\overline{YZ}$.

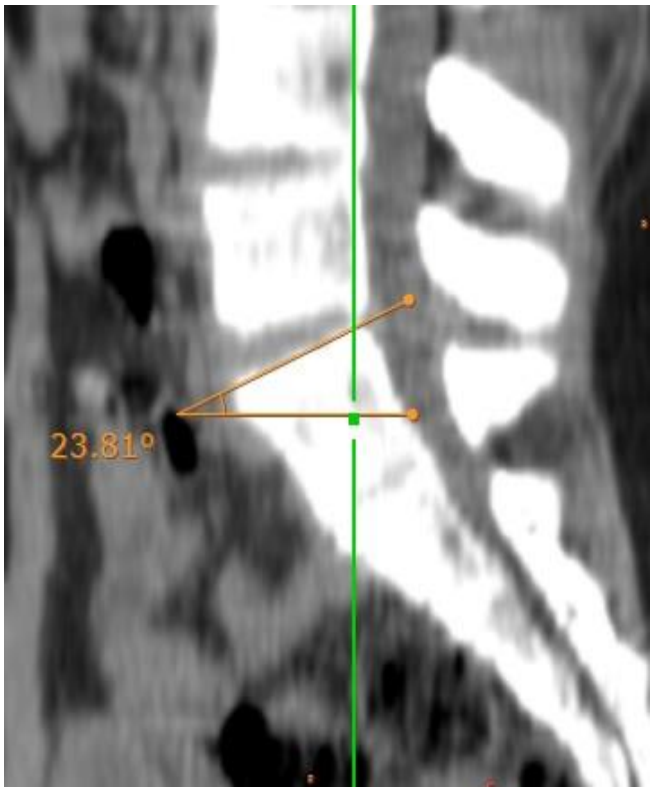
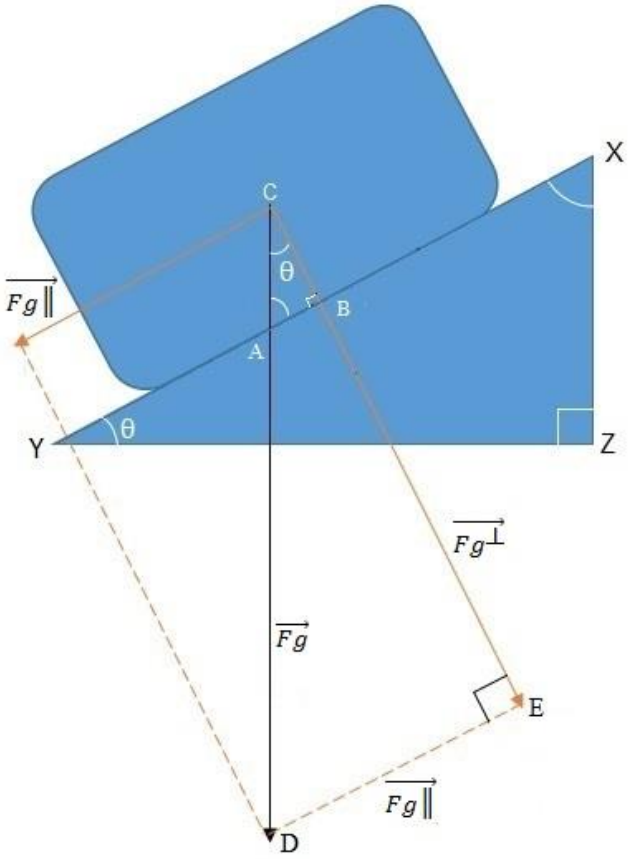


Figure 1. Lumbosacral Angle marking in Radiograph.



$$\tan\theta = \frac{\overline{XZ}}{\overline{YZ}}$$

From the above equation, Θ is derived as:

$$\Theta = \tan^{-1}\frac{\overline{XZ}}{\overline{YZ}} \qquad (3)$$

After finding the lumbosacral angle, using it, the net force exerted on the lumbosacral joint will be found. Any force directed at an angle is resolved into horizontal and vertical components. One directed parallel to the slope and another perpendicular to it.

$$\overrightarrow{Fg\|} + \overrightarrow{Fg^{\perp}} = \overrightarrow{Fg}$$

Since all the angles inside a triangle sums to 180°;

$$\angle XYZ + \angle XZY + \angle YXZ = 180°$$

Using equation 1 and 3, we can say that:

$$\Theta + 90° + (90° - \Theta) = 180° \qquad (4)$$

So, in ΔXYZ, $\angle XZY = 90°$,

Figure 22: Geometry of Lumbar Joint

$\angle XYZ = \theta, \angle YXZ = 90° - \theta$. The force vectors from the center C of L_5 vertebra, F_g and $F_{g\perp}$ passes through the slope $\overline{XY}$ at A and B. This forms another right angled triangle CBA. From geometrical rules, we know that if two parallel lines are cut by a transversal line, then alternate interior angles are congruent. Applying it here, F_g is parallel to $\overline{XZ}$ and $\overline{XY}$ acts as a transversal line. Hence:

$\angle YXZ = \angle CAB$

As mentioned earlier, since any force directed at an angle is resolved into parallel to the slope and another perpendicular to the slope, $F_{g\perp}$ is perpendicular to $\overline{XY}$, forming 90°. So, in ΔCBA, $\angle CBA$ = 90°, $\angle CAB = 90° - \theta$, $\angle BCA = U$)Unknown(. As all the angles inside a triangle sums to 180°, we get:

$\angle BCA + \angle CBA + \angle CAB$ = 180°

U + 90° +)90° - θ(= 180°

$U = \theta$)5(

Applying equation)3(in)5(, we get:

$\angle XYZ = \angle BC$

Shifting the parallel force component downward, since it is parallel to the slope $\overline{XY}$, it forms another right angled triangle CED, where its opposite side $\overline{DE}$ is formed by $F_{g\parallel}$, adjacent side $\overline{CE}$ is formed by $F_{g\perp}$, and hypotenuse side $\overline{CD}$ by F_g. Using trigonometry, the magnitude of parallel and perpendicular force due to gravity can be found. To find the magnitude of parallel component:

$$\frac{\overrightarrow{Fg\parallel}}{\overrightarrow{Fg}} = \sin\theta$$

$$\overrightarrow{Fg\parallel} = \overrightarrow{Fg}\ \sin\theta \qquad (6)$$

To find the magnitude of perpendicular component:

$$\frac{\overrightarrow{Fg\perp}}{\overrightarrow{Fg}} = \cos\theta$$

$$\overrightarrow{Fg\perp} = \overrightarrow{Fg}\cos\theta \qquad (7)$$

Since Force equals to Mass and Acceleration)$F = ma$(, the gravitational force can be resolved into mass and acceleration. Here acceleration is gravity, hence:

$$\overrightarrow{Fg} = \text{m g} \qquad (8)$$

Applying equation)8(in)6(and)7(, we get:

$$\overrightarrow{Fg\parallel} = m\ g\ \sin\theta \qquad (9)$$

$$\overrightarrow{Fg\perp} = m\ g\cos\theta \qquad (10)$$

As all the vertebrae are separated by the intervertebral discs, there is no friction produced in the lumbosacral joint. Thus the co-efficient of friction is not calculated here. In absence of friction, the acceleration of an object over an inclined

plane is the value of parallel component $(\overrightarrow{Fg\|})$ divided by mass (m). Which gives the equation:

$$a = g \sin\theta \quad (11)$$

The forces acting on vertebra are, anterior or parallel force $(\overrightarrow{Fg\|})$, downward or perpendicular force $(\overrightarrow{Fg^{\perp}})$ and upward force (opposite of $\overrightarrow{Fg^{\perp}}$) exerted on vertebra by the slope $\overline{XY}$. Net force is the vector sum of all the forces acting on the vertebra. Hence, the net force would be:

$$\overrightarrow{Fg\|} + \overrightarrow{Fg^{\perp}} - \overrightarrow{Fg^{\perp}} = \overrightarrow{Fg\|} \quad (12)$$

3. Results and Discussion

Out of the 30 samples, 14 were males and 16 were females. Since the standard normal lumbosacral angle across the population was known, comparison was made using one sample '*t*' test, with '*p*' value set as 0.05 as level of significance. The mean lumbosacral angle of the low back pain patients was 44.26 degrees and the standard deviation was ± 7.8625. The one tail critical value was 1.7108, whereas, test statistic value was 8.8269 and *p* value was less than 0.05. Since the test statistic value of 8.8269 is greater than the critical value of 1.5821 and *p* value is lesser than 0.05, as a result, we reject null hypothesis. The mean lumbosacral angle of low back pain patients is greater than 30 degrees. We calculated the net force acting on the L_5 vertebra and the forward acceleration of it over the base of sacrum. According to Aydin Tozeren weight of head, neck, trunk and upper limb weighs 63.06% of total body weight (Tözeren, 2000). Let us assume adults with optimal lumbosacral angle (30°) and 65 Kgs of weight. Therefore, the load of head, trunk and upper limb will be 40 kgs. (63.06*65/100=40.9) Using eq (9), it is found that a net force of 196 N acts on the L_5 vertebra and ligaments and muscles around the lumbosacral joint prevents the forward or anterior sliding of L_5 vertebra at the rate of 4.9 m/s^2 (eq 11). On the other hand, for low back pain patients with the lumbosacral angle of 44.26° (mean), it is found that a net force of 273.57 N acts on the L_5 vertebra and preventing acceleration of 6.8 m/s^2. For a normal adult of 45 years, with 70 Kgs weight and 1.68 m height, the intervertebral disc pressure at $L_4 - L_5$ during supine lying was found to be 0.10 MPa and 0.50 MPa during relaxed standing (Wilke, Neef, Caimi, Hoogland, & Claes, 1999). Whereas, MPa = N / mm^2. Our results showed that there is a significant difference in the lumbosacral load between the 196 N in normal (30°) and 273.57 N in low back pain patients (44.26°).

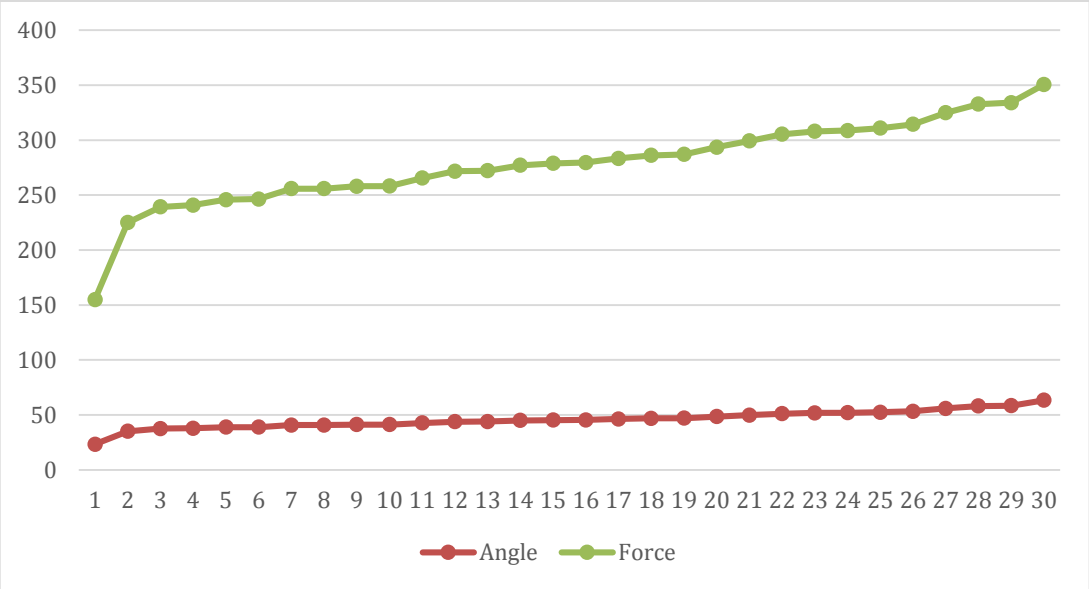


Figure 3: Lumbosacral Angle and Corresponding Force on Fifth Lumbar Vertebra.

The variation of 14.26° can be a major reason for the low back ache, sacroiliac joint dysfunction and nerve roots compression as it increases the magnitude of forces acting at the lumbosacral joint. The net force acting on L_5 vertebra is increased along with the increase in Lumbosacral angle)Fig. 3(. Both are proportional to each other. The net force of 273.57 N acting on the L_5 vertebra makes the iliolumbar and sacrolumbar ligaments to bear more stress. The L_5 - S_1 facet joints, receives excessive anterior shear of L_5 on S_1, which might make it more prone to initial area of lumbar body and disc degeneration.

4. Conclusion

This study portrays an easy method to evaluate the lumbosacral load for a given patient using their radiographs. This will be helpful for the clinicians to examine their patients lumbosacral junction load and plan the treatment accordingly. Hence allowing them to treat the low back pain along with posture correction. Changing the work place ergonomics can also be helpful for the patients suffering from mechanical low back pain.

References

1. Darabi, Z., & Ferdowsi, M. (2011). Aggregated Impact of Plug-in Hybrid Electric Vehicles on Electricity Demand Profile. *IEEE Transactions on Sustainable Energy , 2* (4), 501-508.
2. Malaysian-German Chamber of Commerce and Industry. (2011). 1st Malaysian-German Sustainable Automotive Mobility Conference. *Sustainable Mobility Conference.* Kuala Lumpur.
3. Gruber, W., Bäck, W., & Amrhein, W. (2011). Design and implementation of a wheel hub motor for an electric scooter. *2011 IEEE Vehicle Power and Propulsion Conference.* Chicago, IL.
4. Tie, S. F., & Tan, C. W. (2013). A review of energy sources and energy management system in electric vehicles. *Renewable and Sustainable Energy Reviews , 20*, 82-102.

5. Yong, J. Y., Ramachandaramurthy, V. K., Tan, K. M., Mithulananthan, & N. (2015). A review on the state-of-the-art technologies of electric vehicle, its impacts and prospects. *Renewable and Sustainable Energy Reviews , 49*, 365-385.
6. H. R. Cha, K. J. Shin and Y. J. Seo. (2011). Design of outer rotor IPM type PMSM for 3 wheel electric vehicle. *2011 International Conference on Electrical Machines and Systems.* Beijing.
7. D. Fodorean, D. C. Popa, P. Minciunescu, C. Irimia and L. Szabó. (2014). Study of a high-speed motorization for electric vehicle based on PMSM, IM and VRSM. *2014 International Conference on Electrical Machines (ICEM).* Berlin.
8. Rahman, M. A., & Masrur, M. A. (2009). Advances on IPM technology for hybrid electric vehicles. *2009 IEEE Vehicle Power and Propulsion Conference.* Dearborn, MI.
9. M. Cheng, W. Hua, J. Zhang and W. Zhao. (2011). Overview of Stator-Permanent Magnet Brushless Machines. *IEEE Transactions on Industrial Electronics , 58* (11), 50087-5101.
10. W. Xu, J. Zhu, Y. Guo, S. Wang, Y. Wang and Z. Shi. (2009). Survey on electrical machines in electrical vehicles. *International Conference on Applied Superconductivity and Electromagnetic Devices.* Chengdu.
11. Chu, C. L., Tsai, M. C., & Chen, H. Y. (2001). Torque control of brushless DC motors applied to electric vehicles. *Electric Machines and Drives Conference, 2001. IEMDC 2001. IEEE International* (pp. 82-87). Cambridge, MA: 2001. IEMDC 2001. IEEE International.
12. Ehsani, M., Gao, Y., & Gay, S. (2003). Characterization of electric motor drives for traction applications. *Industrial Electronics Society, 2003. IECON '03. The 29th Annual Conference of the IEEE. 1*, pp. 891-896. The 29th Annual Conference of the IEEE.
13. V, A. C., Norhisam, M., Aris, I., Marhaban, M. H., Ahmad, D., & Nirei, M. (2011). Double-Rotor Switched Reluctance Machine (DRSRM): Fundamentals and magnetic circuit analysis. *2011 IEEE Student Conference on Research and Development.*
14. Niu, S., Ho, S. L., & Fu, W. N. (2013). A Novel Double-Stator Double Rotor Brushless Electrical Continuously Variable Transmission System. *49* (7).
15. Griffin, M. (1990). *Handbook of Human Vibration* . San Diego: Academic Press Limited.
16. I. Hostens, Y. P. (2003). A study of vibration characteristics on a luxury wheelchair and a new prototype wheelchair. *Journal of Sound & Vibration , 266*, 443-452.
17. T. Ramachandran, K. P. (2012). Review on Internal Combustion Engine Vibrations and Mountings. *International Journal of Engineering Sciences & Emerging Technologies , 3* (1), 63-73.
18. Griffin, G. P. (2009). Evaluation of Whole Body Vibration and RIde Comfort in a Passenger Car. *International Journal of Acoustics and Vibration , 14* (1), 143-149.
19. Yunhe Yu, N. G. (2001). Review of automotive vehicle engine mounting systems. *Mechanism and Machine Theory , 36*, 123-142.
20. Jasvir Singh Dhillon, P. R. (2014). Design of Engine Mount Bracket for a FSAE Car Using Finite Element Analysis. *International Journal of Engineering Reseach and Application , 4* (9), 74-81.
21. Conti, P. a. (1989). Mount Stiffness and Inertia Properties from Modal Test Data. *ASME Journal of Vibration and Acoustics, Stress and Reliability in Design , 111*, 134-141.
22. Chung-Ha Suh, C. G. (1997). Dynamic Simulation of Engine-Mount Systems. *SAE International* , 561-572.
23. Brick7. (2010). The Motorcycle Search Engine. South Africa: Brick 7.
24. Kjær, B. &. (1998). *Vibration Transducers and Signal Conditioning.* Brüel & Kjær Sound Vibration Measurement A/S.
25. Bracewell, R. N. (1989). The Fourier Transorm. *Scientific American* , 86-95.
26. S.Rao, S. (2011). *Mechanical Vibration.* Miami: Prentice Hall.
27. Frederick, J. T. (2011, March 29). *Auburn University Electronic Theses and Dissertations.* Retrieved November 20, 2016, from http://etd.auburn.edu/handle/10415/2488
28. Nolan, P. (n.d.). *Farmingdale University.* Retrieved October 31, 2016, from www.farmingdale.edu/faculty/peter-nolan/pdf/UPCh13.pdf
29. International, S. (2016). *2016 Formula SAE Rules.* SAE International.
30. Damavandi, M., Dalleau, G., Stylianides, G., Rivard, C. H., & Allard, P. (2013). Head and Trunk mass and center of mass position estimates in able-bodied and scoliotic girls. *Medical Engineering & Physics , 35*, 1607-1612.
31. Park, J. Y., Park, G. D., Lee, S. G., & Lee, J. C. (2013). The Effect of Scoliosis Angle on Center of Gravity Sway. *Journal of Physical Therapy Science , 25* (12), 1629-1631.

32. K, H., I, G., & G, L. (2013). Developing a 3D Multi-Body Model of the Scolitic Spine with Lateral Bending Motion for Comparison of Ribcage Flexibility. *International Journal of Advanced Design and Manufacturing Technology , 6* (1), 25-32.
33. Carvalho de Abreu, D. C., Gomes, M. M., Rocha de Santiago, H. A., Pereira da Silva Herrero, C. F., Porto, M. A., & Luiz, H. (2012). What is the influence of surgical treatment of adolescent idiopathic scoliosis on postural control? *Gait & Posture , 36*, 586-590.
34. Trobisch, P. D., Samdani, A. F., Pahys, J. M., & Cahill, P. J. (2011). Postoperative trunk shift in Lenke 1 and 2 curves: how common is it? and analysis of risk factors. *European Spine Journal , 20*, 1820-1828.
35. Richards, B. S., Scaduto, A., Vanderhave, K., & Browne, R. (2005). Assessment of Trunk Balance in Thoracic Scoliosis. *The Spine Journal , 30* (14), 1621-1626.
36. Karami, M., Maleki, A., & Mazda, K. (2016). Assessment of Coronal Radiographic Parameters of the Spine in the Treatment of Adolescent Isiopathic Scoliosis. *Archives of Bone and Joint Surgery , 4* (4), 376-380.
37. Ameri, E., Ghandhari, H., Nabizadeh, N., & Hesarikia, H. (2014). Natural history of coronal balance after spinal fusion in adolescent idiopathic scoliosis. *Shafa Orthopedic Journal , 1* (2), 12-16.
38. Siderakis, N., Rosado, J. P., Aguilar, A., Dinelli, D., Lutzky, L., Reviriego, J., et al. (2013). Analysis of coronal balance and last level of arthrodesis in lenke type 5 idiopathic scoliosis: Specific radiographic parameters. *Coluna/Columna , 12* (4), 296-299.
39. Hellems, K., & Keats, T. (1971). Measurement of the Normal Lumbosacral Angle. *American Journal of Roentgenology , 113* (4), 642-645.
40. Lippert, L. S. (2011). *Clinical Kinesiology and Anatomy* (5 ed.). Philadelphia, Pennsylvania, United States of America: F. A. Davis Company.
41. Smith, L. K., Weiss, E. L., & Lehmkuhl, L. D. (1998). *Brunnstrom's Clinical Kinesiology* (1 ed.). New Delhi, New Delhi, India: Jaypee Brothers Medical Publishers (P) LTD.
42. Pasha, S., Aubin, C., Labelle, H., Parent, S., & Mac Thiong, J. (2015). The biomechanical effects of spinal fusion on the sacral loading in adolescent idiopathic scoliosis. *Clinical Biomechanics , 30*, 981-987.
43. Nohara, A., Kawakami, N., Seki, K., Tsuji, T., Ohara, T., Saito, T., et al. (2015). The Effects of Spinal Fusion on Lumbar Disc Degeneration in Patients with Adolescent Idiopathic Scoliosis: A Minimum 10-Year Follow-Up. *Spine Deformity , 3*, 462-468.
44. Tözeren, A. (2000). *Human Body Dynamics: Classical Mechanics and Human Movement.* York, Pennsylvania, United States of America: Springer.
45. Wilke, H. J., Neef, P., Caimi, M., Hoogland, T., & Claes, L. E. (1999). New In Vivo Measurements of Pressures in the Intervertebral Disc in Daily Life. *SPINE , 24* (8), 755-762.

Small Vocabulary Isolated Speech Recognition for Smart Devices

Praveen Edward James[1*], Leong Wai Yie[2], Alan Tan Wee Chiat[3], Mohsen Nabi Poor[4]

[1] *Taylors University, Subang Jaya, Selangor*

[2] *Taylors University, Subang Jaya, Selangor*

[3]*Multimedia University, Melaka*

[4] *Taylors University, Subang Jaya, Selangor*

[*]praveenedwardjames@sd.taylors.edu.my

Abstract

The features of smart devices that require complicated settings are not easily accessible to illiterate users and people with hand or vision disabilities. This paper aims to address this issue by prototypying an isolated word speech recognition system, with a vocabulary of ten words, commonly used in smart devices. The first phase of speech recognition is training the Hidden Markov Model (HMM) model. The phase involves creating HMM model with mixture coefficients, mean and covariance for each word and statistically estimating its parameters using features from speech sample. In this phase, feature extraction involves three features Linear Prediction Cepstral Coefficients with 12 coefficients (LPCC12), Mel Frequency Cepstral Coefficients with 12 coefficients (MFCC12) and Mel Frequency Cepstral Coefficients with 39 coefficients (MFCC39) by using Kulback-Liebler algorithm and simplified Expectation- Maximization (EM) algorithm on the speech samples. They were used to train the HMM to create reference models for each word. In the second phase speech recognition compares the reference models with models based on inputs captured in real-time using the same processing techniques. The comparison involves using a recursive Forward Algorithm (FA). For each word the accuracy, memory used and processing time were estimated and compared. In the estimated results, the LPCC12 based model had an accuracy 74%, MFCC12 based model had an accuracy of 76%, and MFCC39 based model had an accuracy of 86%. The recognition models are trained using the same voice and thus providing a natural security for smart devices. The results indicate that the MFCC39 based model is suitable for integrating into a continuous speech recognition system targeting smart devices.

Keywords: Speech Recognition, Isolated, Feature extraction, Preprocessing, Smart devices

1. Introduction

Speech recognition is one of the extensively researched areas in speech processing. it has evolved from being a bio-metric identification tool, to control small devices like smart phones and larger machines like automobiles. However, there are many limitations in developing a general system that can be used for controlling different devices. Only people without disabilities can use smart devices. A speech-to -text isolated word recognition addresses the difficulties of the hearing impaired by displaying them the converted text [1]. In Table 1[2], some of the existing smart device applications available commercially are given.

Table 1. Existing Speech Applications in Smart Phones [2]

No	Application	Manufacturer
1.	Voice Search	Google Inc.
2.	Vlingo Virtual Assistant	Vlingo Corporation
3.	Iris (alpha)	Dexetra
4.	Speaktoit Assistant	Speaktoit
5.	Skyvi	Blue Tornado
6.	AIVC	YourApp24
7.	Car Home	Google Inc.
8.	Dragon Search	Nuance Communications
9.	Voice Actions/ Jeanie	Pannous
10.	Everfriends	i-Free Innovations
11.	Evi	True Knowledge Ltd
12.	Andy-Siri for Android	74Technologies
13.	Edwin, Speech-to-Speech	Neureau
14.	Dragon Go	Nuance Communications
15.	Speak 4it	AT&T Interactive R&D
16.	Voice-Assistant	Quantic Apps
17.	Pocket Blonde	i-Free Innovations

18.	EVA Virtual Assistant	BulletProof
19.	Ziplocal	Phone Directories Company
20.	Chizee Your Personal Assistant	Tronton LLC

They have difficulties in handling complicated manual settings using speech. Also some of them are server based applications. A possible solution is by embedding a hardware device with a small vocabulary that can be embedded into smart devices. Since speech application can consume more hardware resources, a light-weight application would be handy.

In this paper some of the words commonly used in smart devices are used to train a Hidden Markov Model based isolated word speech recognition system. An HMM model uniquely represents a speech signal. An HMM is a finite state machine which transits between a finite number of states and generates an observation during each transition [3].

There are many types of HMM including an ergodic HMM where there can be transitions from any states, a simple left-to-right HMM where there is a fixed starting and ending state with possible transitions from left to right or back to the same state and an autoregressive model [3]. A left- to- right HMM with 5 states are shown below (Fig. 1).

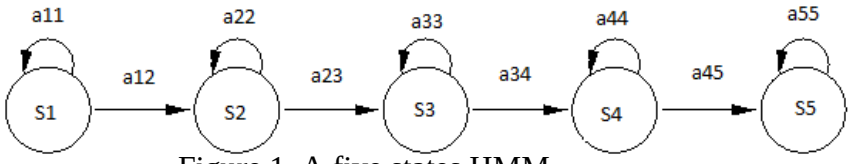


Figure 1. A five states HMM

Hidden Markov Models unlike Neural Networks trains faster and their accuracy is also comparable with the state-of-the art Neural Networks for small vocabulary applications [4].

A Speech recognition model has two phases namely training and recognition. In this paper, speech recognition models based on 3 feature extraction methods LPCC12, MFCC12 and MFCC39 feature extraction methods are implemented individually and their features are compared based on three factors namely accuracy, memory used and processing time.

2. Literature Review for HMM Based Speech Recognition

In late 1960, Rabiner introduced Hidden Markov Models (HMM) for applications in speech recognition [1]. Even today, many of the speech recognition systems that use HMM refer to this design. An efficient connected digit recognizer was modeled by Panaithep, who used Viterbi algorithm for both training and recognition [5].

Alan, Rao and Daya compared different classifiers in a subspace and the performance of Linear Prediction Cepstral coefficients (LPCC) was the highest [6]. Mark and Steve used HMM for designing a Large Vocabulary Continuous Speech Recognition system [7]. They also proposed many refinements like feature modeling, adaptation and normalization for enhancing the accuracy.

Veton and Hussein [8] proposed a hybrid feature extraction process for HMM in noisy conditions. They also compared the performance of various hybrid methods under clear and noisy conditions. The system had a recognition accuracy of 99% in a clear environment but 80% under noisy conditions. Himanshu, Kaur and Sharma designed an information system using HMM and then Neural Networks and highlighted that Neural Networks performed better [9].

Sininsa, Dragan and Ivan compared the latest speech software that are used in automobiles and smart phones [2]. They reported that the future is for smart devices that support speech. Dixit and Kau proposed a speech recognition system using stochastic approach [10]. They used two approaches namely traditional and artificial approach.

There is a large scope for improvement and HMM based systems need to satisfy constraints like, low memory, high accuracy and an optimum processing time that are the ideal requirements of small devices.

3. Design of Speech Recognition Module

The design of the speech recognition involves 2 phases namely training and recognition.

3.1 Training Speech Recognition Models

In the first phase, speech signals of isolated words are recorded, preprocessed, required features extracted from the signals and stored as templates. In addition, a reference model for each HMM model is constructed and trained. The various stages involved are presented in Fig. 2.

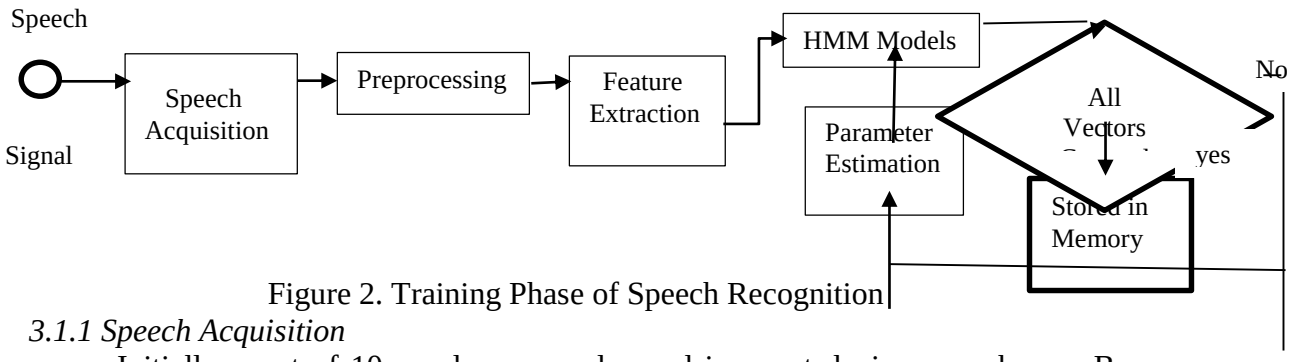


Figure 2. Training Phase of Speech Recognition

3.1.1 Speech Acquisition

Initially, a set of 10 words commonly used in smart devices are chosen. By recording each word 10 times a Speech dataset is constructed. The words are recorded, digitized with a sampling frequency of 8 KHz and a precision of 16 bits per sample and stored as wave (.wav) files.

3.1.2 Preprocessing

Preprocessing is the process of preparing the signal for further processing. It involves noise cancellation, pre-emphasis and voice activity detection.

3.1.2.1 Noise Cancellation:

Noise cancellation involves ambient noises that are mixed with the speech signal in a home or office environment [5]. Since it involves both low frequency and high frequency signals, a band pass filter is used. The digitized speech signal that has a sampling frequency of 8KHz is passed through a band pass filter with a minimum frequency of 300 Hz and maximum frequency of 3500 Hz.

The Fig. 3 and 4 show an original speech signal and the signal with its ambient noise reduced.

3.1.2.2 Pre-emphasis

This involves a high-pass filter to increase the amount of energy in the high frequencies and enabling easy access to information in the higher formants of the speech signals [5]. It enhances the phone detection accuracy. By implementing Eq. (1), a Pre-emphasis filter is designed.

$$H(z) = 1 - az^{-1} \quad (1)$$

where a is 0.95 and $H(z)$ is the filter function expressed in a Z-transform representation.

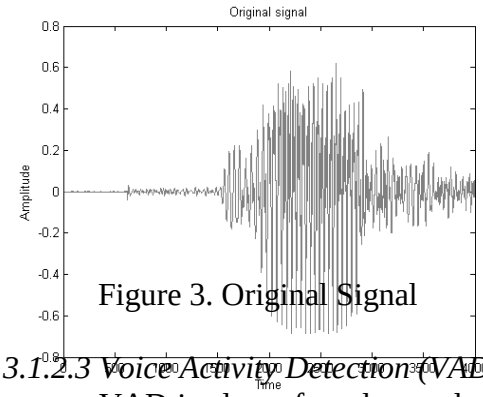


Figure 3. Original Signal

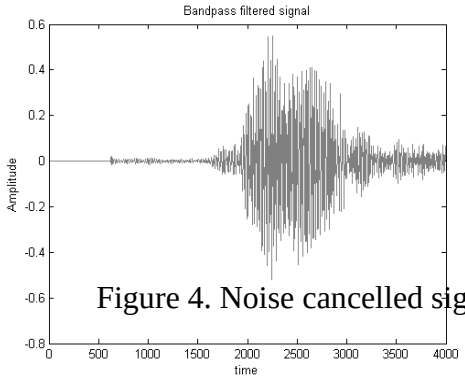


Figure 4. Noise cancelled signal

3.1.2.3 Voice Activity Detection (VAD)

VAD is also referred as end-point detection. Initially the signal is divided into equal frames. Using the sum of squares energy formula given in Eq. (2), the energy of the speech signal is calculated

$$E = \sum_{i=1}^{n} [x(i)]^2 \quad (2)$$

where i refers to the number of current vector frame, *x(i)* is the current frame of speech and n the total number of frames used to calculate energy *E*. The minimum and maximum energies of the word calculated using average of the first few frames are used to cut down the undesired parts of the signal. The output after performing pre-emphasis and voice activation detection are given below (Fig. 5 and Fig 6.) respectively.

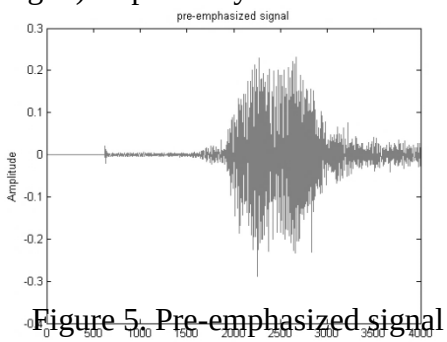


Figure 5. Pre-emphasized signal

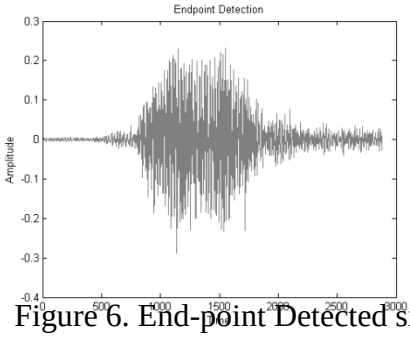


Figure 6. End-point Detected signal

3.1.3. Feature Extraction

This process involves dividing the speech signal into windows of frames and transformation of these frames into a sequence of acoustic feature vectors [11].

3.1.3.1 Windowing

A speech signal is not stationary with its properties changing in time. This limitation is overcome by extracting features from a small window of coefficients where speech is assumed to be stationary. This design uses a Hamming window function for this windowing process. The function is given by Eq. (3).

$$W(n) = \begin{cases} 0.54 - 0.46\frac{\cos(2\pi n)}{L} & for\ 0 \le n \le L-1 \\ 0 & otherwise \end{cases}$$

(3)

Where *L* is the length of the window and *n* is the number of window.

3.1.3.2 Feature Vector Transformation

The process involves implementing three types of feature transformation models namely Linear Prediction Cepstral Coefficient with 12 coefficients (LPCC12), Mel Frequency Cepstral Coefficient with 12 coefficients (MFCC) and Mel Frequency Cepstral Coefficient with 39 coefficients (MFCC39) individually. In all these models the Cepstrum is used to improve phone recognition performance. The Cepstrum (C) of a signal is the Inverse Discrete Fourier Transform (IDFT) of the log magnitude of Discrete Transform (DFT) of a signal and is given by Eq. (4).

$$C[n] = \sum_{n=0}^{N-1} log\left(\left|x[n]e^{-j\frac{2\pi kn}{N}}\right|\right)e^{j\frac{2\pi kn}{N}}\ where\ 0 \le k \le N-1 \\ and\ 0 \le\ n \le N-1$$

(4)

where *N* is the total length of the feature vector and *j* is used for representing a complex number.

3.1.3.2.1 LPCC with 12 coefficients

Linear Prediction is an estimation procedure to determine the Autoregressive Parameters (AR) from the samples of the input signal. A speech sample is an approximation of a linear combination of past p samples in a Linear Prediction model. Eq. (5). gives the coefficients involved.

$$x_{nest} = -a_1 x_{n-1} - a_2 x_{n-2} - \cdots - a_p x_{n-p}$$

(5)

where a_1, a_2 ... a_p are the prediction coefficients (12 for this model), p is the prediction order and nest stands for the predicted current speech sample. The prediction error (e_n) is calculated using equation 3.6. Identifying the system involves estimating the coefficients such that the error cost is minimized and it involves solving Eq. (5) and Eq. (6) using

$$e_n = x_n - x_{nest} \quad (6)$$

3.1.3.2.2 MFCC with 12 coefficients

Human ear is less sensitive to high frequencies. To avoid it frequencies above the DFT range are mapped to the mel scale. The mel frequency Coefficients (12 in this design) (*mel*) can be computed from the raw acoustic frequency (*f)* using the Eq. (7).

$$mel(f) = 2595 * \ln(1 + \frac{f}{700})$$
(7)

Conversion using mel scale involves creating a bank of triangular filters which collect energy from each frequency band with 10 filters spaced linearly below 1000 Hz and remaining filters spread logarithmically above 1000Hz. The mel scale to frequency plot is shown in Fig. 7 By computing the Cepstrum the MFCC coefficients are obtained.

3.1.3.2.3 MFCC with 39 coefficients

In addition to the 12 MFCC coefficients (C) the energy of the signal which correlates with phone identity is computed. For a signal *x* in a window from time sample *t*1 to time sample t2 the energy of the signal is calculated as the 13th coefficient using Eqn. (8).

$$Energy \sum_{t=t1}^{t2} x^2(t) \quad (8)$$

These 13 coefficients are used in a delta function (Δ) to identify changing features related to change in spectrum. The delta coefficients can be calculated using the delta function as shown in Eq. (9).

$$\Delta(n) = \frac{1}{\sum_{i=1}^{D} i^2} \sum_{i=1}^{D} i * [c(n+i) - c(n-i) \; where \; n = 13 \; and \; 1 \leq i \leq 3]$$
(9)

Where C refers to the existing coefficients, D is the number of coefficients used to compute Δ. D is set to 2. A set of 13 delta coefficients and then double delta coefficients (delta of delta coefficients) are calculated. Using the three sets of 13 coefficients the feature vectors with 39 coefficients are obtained.

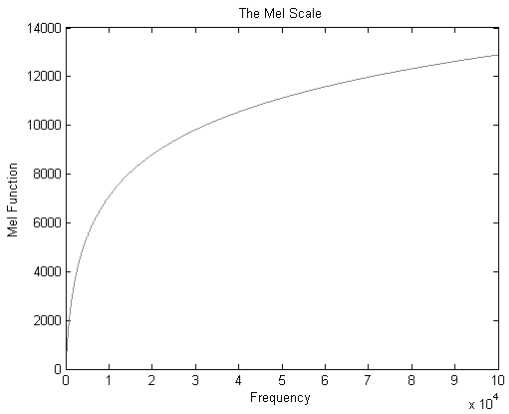


Figure 7. Mel Scale

3.1.4. Hidden Markov Models (HMM):

In HMM based modeling, the feature vectors are the observations and a spoken word usually refers to the states. This study uses the left-to-right model. Each speech sample is broken into a number of sub samples with equally spaced intervals depending upon the number of states. Using the parameters extracted from the sub vectors the HMMs are modeled. The model is then updated during training and compared with similar models of real time speech signal, during recognition.

An HMM (λ) is defined using a compact notation given in Eq. (10).

$$\lambda = (\pi, A, B) \quad (10)$$

Where $\pi = \{\pi_i\}$ the probability of being in state *i*=1 initially at time *t*=1, A refers to the state transition probability from state *i* to state *j* and is given by Eq. (11).

$$A = \{a_{ij}\} \; and \; a_{ij} = P(i_{t+1} = j | i_t = i) \quad (11)$$

Where a_{ij} refers to the probability transition to state *j* at *t*+1 from state *i* at time *t* and *B* is the probability of observing a particular symbol v_k at state j and is given by Eq. (12).

$$B = \{b_k\} \; where \; b_k = P(v_k \text{ at } t | i_t = j) \quad i = 1 \; to \; N \; and \; k = 1 \; to \; M \quad (12)$$

where *N* represents the number of states and *M* is the total number of observation symbols.

The usage of HMM in modeling real-time applications is by solving three problems namely training, decoding and evaluation. In this study these three parameters $\pi, A \; and \; B$ are calculated initially from the feature vector to create the HMM model with 5 states using K-means clustering algorithm [12].

3.1.5 Training Reference Models

Then the parameters of reference HMMs are re-estimated using a simplified Expectation-Maximization algorithm [5]. A description of the algorithm is given below. The trained HMM is stored in memory as a reference model.

3.1.5.1 Expectation Maximization Algorithm

The EM algorithm [14-19] is predominantly used for re-estimating the mean, co-variance and mixture coefficients and updating the HMM parameters to able the reference word models for robust recognition. It consists of the following steps.

Step 1: The expectation process is performed to calculate the underlying variables used for creating an HMM model. The variables are mixture coefficients (C), mean μ_i and covariance $sigma_i$

Step 2: It is the maximization process where new estimates of the mean, mixture density and covariance are used to update the observation pdf of the current HMM.
Step 3: After every iteration the change in the current iteration is used to compare with the previous iteration and a stopping criteria is calculated. The stopping criteria is compared with a threshold value and the iteration is stopped if the stopping criteria is achieved.
Step 4: The iterations are continued until the stopping criteria is achieved.

3.2 Recognition Phase

The speech signal to be recognized is recorded in real-time and preprocessed using the same techniques used in training phase and is shown in Fig. (8).

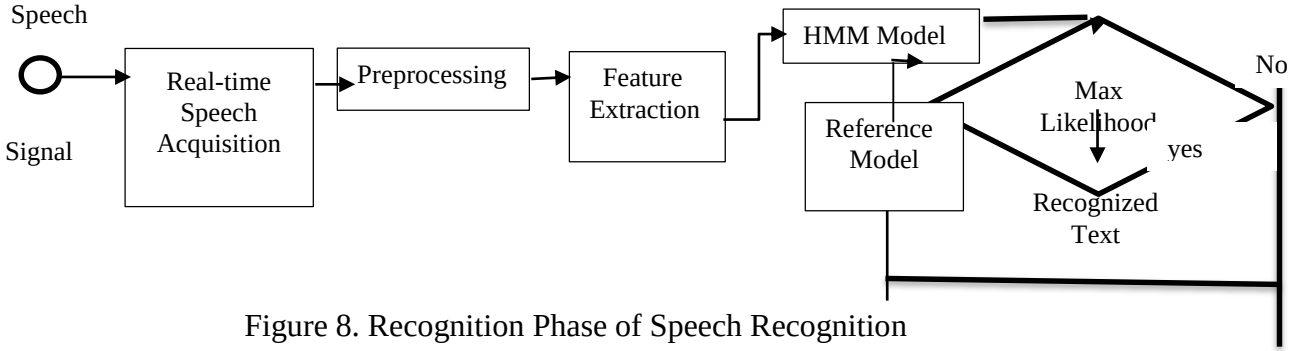


Figure 8. Recognition Phase of Speech Recognition

The waveforms of the real-time signal in various preprocessing stages are shown below (Fig. 9 Fig. 10, Fig. 11 and Fig. 12).

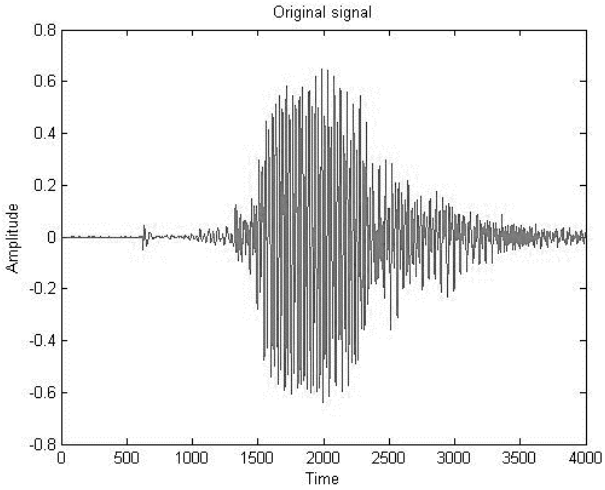


Figure ‘9. Original Signal (Good.wav)

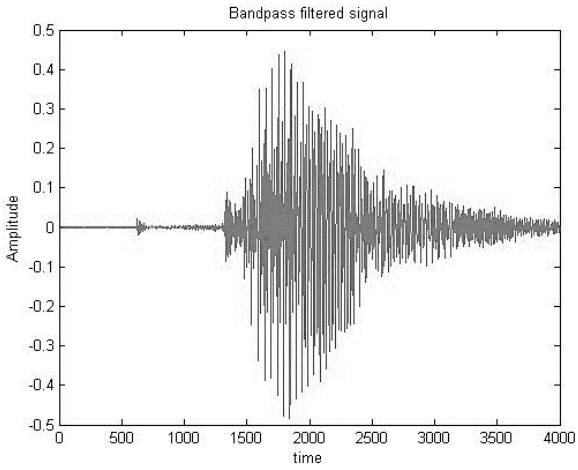


Figure 10 Noise Cancelled Signal

The feature vectors are obtained with the same techniques adopted in the training phase [3]. The likelihood of observations calculated using the forward algorithm which uses the formula given in Eq. (14).

$$\alpha_{t+1}(j) = \sum_{i=1}^{N} \alpha_t(i)\, a_{ij}\, b_j(o_{t+1}) \quad (14)$$

where $\alpha_t(i)$ is the forward variable, a_{ij} is the state transition probability and b_j is the probability of the observation in state j.

For each word the probability of observations given the model is calculated. The model with the maximum likelihood is recognized as the spoken word using Eq. (15).

$$v = \underset{1<v^*<V}{argmax}[P(O|\lambda^{v^*})] \quad (15)$$

where v^* is the recognized word, $P(O|\lambda^v)$ is the probability of observation given the model and V is the total number of words [3].

\

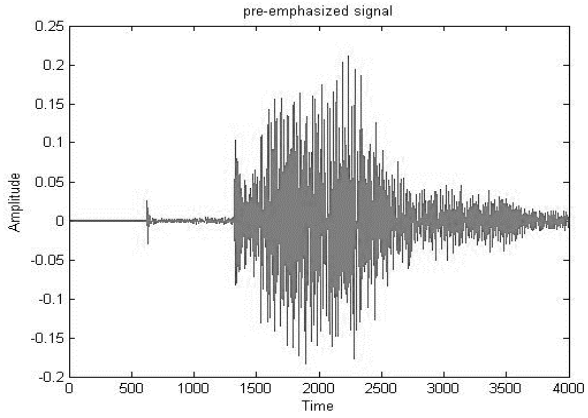


Figure 11. Pre-emphasized Signal

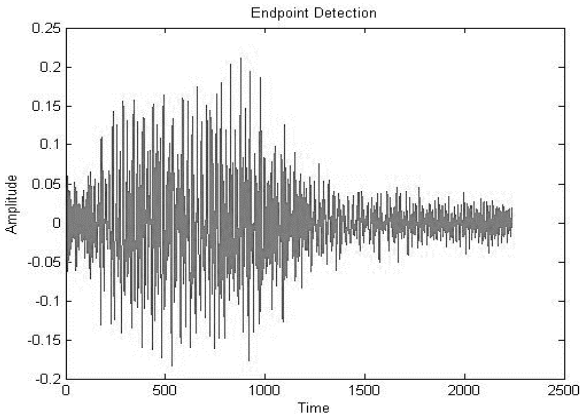


Figure 12. End- point Detected Signal

4. Results

The vocabulary of 10 words include "Call", "Praveen", "Open'', "Start", "Camera", "Turn"," On", "GPS", "Good" and "Morning". The words are spoken 10 times and so the data set contains 100 words. The three speech recognition systems are tested with the dataset sequentially to create trained HMM models. These models are compared to real time inputs to identify the spoken word. The number of times the words are recognized when spoken for 10 times is given in Table 2.

Table 2. Frequency of recognized words of the three recognition methods

	Call	Praveen	Open	Start	Camera	Turn	On	GPS	Good	Morning
LPCC 12	8	6	10	7	9	6	6	8	5	9
MFCC 12	10	9	7	6	9	6	6	8	6	9
MFCC 39	10	10	10	9	10	8	5	9	5	10

*Note: All the words are spoken 10 times and the average of the words are used for calculating the accuracy

The word accuracy of each word is calculated from Table 3. by taking the average of the recognized word. The number of times each word is recognized is shown in Fig. 13.

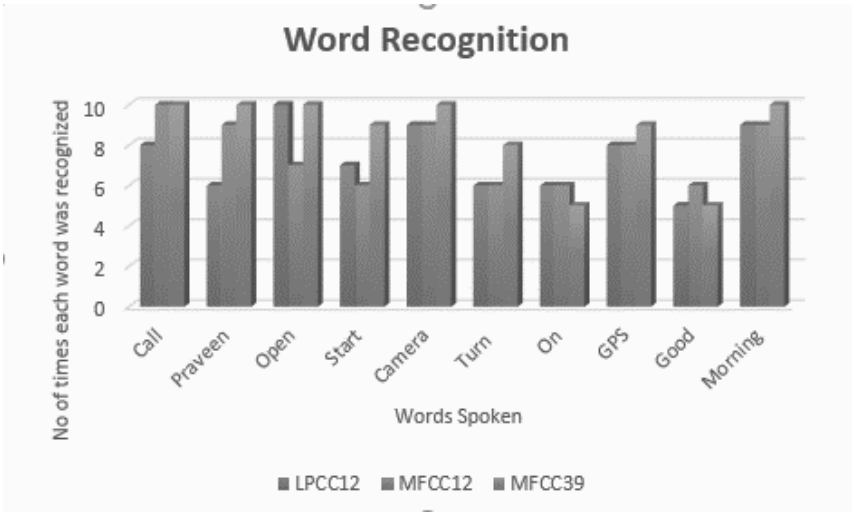


Figure 13 Word Recognition Accuracy

The memory used was obtained from the computer storage space and both these results is shown in Table 3.

Table 3. Accuracy and memory used comparison of the three recognition methods

Defining Factor	LPCC 12	MFCC 12	MFCC 39
Accuracy	74%	76%	86%
Memory Used	8.45Kb	8.86KB	10.1Kb

The processing time is calculated as training time and recognition time and the results are shown in Table 4.

Table 4. Processing time comparison of the three recognition methods

Processing Time	LPCC 12 (SEC)	MFCC 12 (SEC)	MFCC 39 (SEC)
Training Time	14.27	13.80	13.99
Recognition Time	62.45	61.90	61.98

The Accuracy, Memory used and Processing time for LPCC12 was 74%, 8.45 Kb and 76.7 seconds respectively. Similarly, the Accuracy, Memory used and Processing time for MFCC12 was 76%, 8.45 Kb and 75.7 seconds respectively. Also, the Accuracy, Memory used and Processing time for MFCC39 was 86%, 10.1 Kb and 75.9 seconds respectively. The results indicate that there is a large gain in accuracy with the model using MFCC 39 based feature vectors.

5. Discussion

The results reveal that MFCC39 has better accuracy, similar memory usage and optimum processing time. One of the limitations is that these experiments were conducted in natural environment and were subjected to noise interference. Although there are significant advancements in speech recognition using Artificial Neural Networks they have the following limitations.

i) The entire implementation of Neural Networks consumes more resources especially during training and hence high speed servers are required [4].

ii) The training time of Neural Networks is slow when compared to HMM with MFCC39 coefficients [4].

Since the HMM with MFCC39 coefficients do not require high speed servers and also operate with faster training time, they are better suited for small vocabulary applications.

6. Conclusion and Future Work

In this study, it has been revealed that HMM with MFCC39 is better suited for smart devices. This system was trained from one user and hence provides natural security for personalized devices. However, the vocabulary of words has to accommodate most of the words used in smart devices and words that represent complicated settings. The isolated word recognition model, can be integrated with other supporting modules to construct a continuous word recognition system. In future, a continuous speech recognition model targeting mobile applications for assisting people with disabilities, will be designed.

Acknowledgements

The authors wish to thank Dr. Murali for his insights on extracting information from data. The authors sincerely thank Dr. Hosseini for creating an awareness on the responsibilities of a research student.

References

[1] Ananthi, S., Dhanalakshmi, P. (2013). Speech Recognition System and Isolated Word Recognition based on Hidden Markov Model (HMM) for Hearing Impaired. *International Journal of Computer Applications*, 73(20).

[2] Husnjak, S., Perakovic, D., Jovovic, I. (2014). Possibilities of using speech recognition systems of smart terminal devices in traffic environment. *Procedia Engineering*, *69*, 778-787.

[3] Rabiner, L. R. (1989). A tutorial on hidden Markov models and selected applications in speech recognition. *Proceedings of the IEEE*, *77*(2), 257-286.

[4] Hinton, G., Deng, L., Yu, D., Dahl, G. E., Mohamed, A. R., Jaitly, N., Kingsbury, B. (2012). Deep neural networks for acoustic modeling in speech recognition: The shared views of four research groups. *IEEE Signal Processing Magazine*, *29*(6), 82-97.

[5] Srichai, P. A. (1998). Implementation of a connected digit recognizer using continuous hidden markov modeling.

[6] Tan, A. W., Rao, M. V. C., Sagar, B. D. (2007). A discriminative signal subspace speech classifier. *IEEE Signal Processing Letters*, *14*(2), 133-136.

[7] Gales, M., & Young, S. (2008). The application of hidden Markov models in speech recognition. *Foundations and trends in signal processing*, *1*(3), 195-304.

[8] Këpuska, V. Z., & Elharati, H. A. (2015). Robust Speech Recognition System Using Conventional and Hybrid Features of MFCC, LPCC, PLP, RASTA-PLP and Hidden Markov Model Classifier in Noisy Conditions. Journal of Computer and Communications, 3(06), 1.

[9] Himanshu, M., Kaur, S., & Sharma, A. (2014). Real time Information System Based on Speech Recognition. *International Journal of Advanced Research in Computer Science and Software Engineering. 4*(8), 409-414.

[10] Dixit, R. & Kau, N. (2013). Speech Recognition Using Stochastic Approach: A Review. *International Journal of Innovative Research in Science, Engineering and Technology*. 2(2). 356-361.

[11] Kumar, K., Kim, C., & Stern, R.M. (2011). Delta-spectral cepstral coefficients for robust speech recognition. *IEEE International Conference on Acoustics, Speech, and Signal Processing, May 2011, Prague, Czech Republic*.

[12] Neel, J. (2005). Cluster analysis methods for speech recognition. *Centre for Speech Technology, 17*, 44.

[13] Falkhausen, M., Reininger, H., & Wolf, D. (1995). Calculation of distance measures between hidden Markov models. In *EUROSPEECH*

[14] J. Lee, W. Liu, L. W. Tay and W. Y. Leong, "Design of Applications on Ultra-Wideband Real-Time Locating System", *The 2009 IEEE/ASME International Conference on Advanced Intelligent Mechatronics (AIM 2009)*, 14-Jul-2009 to 17-Jul-2009, Singapore, vol. FA1.4, pp. 1359-1364

[15] W. Y. Leong and D. P. Mandic,"Blind Extraction of Microsleep Events", *The 15th*

International Conference on Digital Signal Processing (DSP 2007), Cardiff, UK, 1-4 July, 2007, pp. 207-210.

[16] W. Y. Leong, D. P. Mandic and Wei Liu,"Blind Extraction of Noisy Events Using Nonlinear Predictor ", *The 32nd International Conference on Acoustics, Speech, and Signal Processing (ICASSP)*, Honolulu, United States, 15 – 20 April 2007, Vol. II, pp.657-660.

[17] R.S.Tung, W.Y.Leong, Processing Obstructive Sleep Apnea Syndrome (OSAS) Data, *Journal of Biomedical Science and Engineering*, Issue.6, pp.152-164, 2013

[18] W.Y.Leong, C. M. THAN, Features of Sleep Apnea Recognition and Analysis, *International Journal on Smart Sensing and Intelligent systems*, VOL. 7, NO. 2, MAR 2014

[19] W.Y.Leong and D. P. Mandic, "Towards Blind Separation of Post-Nonlinearly Mixed Sources: Existence and Uniqueness Analysis", *The 7th International Conference on Mathematics in Signal Processing*, pp.178-181, 17-20 December 2006 The Royal Agricultural College, Cirencester, United Kingdom.

eureca 2016 – Conference Paper
Paper Number EE_PG001

SEVEN LEVEL DIODE CLAMPED AND H-BRIDGE INVERTERS-A COMPARATIVE ANALYSIS

Suresh A[1], Rashmi M R[2], Aravind CV[3*], Dhanasekaran R[4]

[1]Professor,Department of Electrical and Electronics Engineering,
S.A. Engineering College, Chennai, India
Associate Professor, Department of Electrical and Electronics Engineering,
Amrita Vishwa Vidyapeetham, Bangalore, India
[3]Professor, Department f Electrical and Electronics Engineering,
Taylor's University, Malaysia.
[4]Professor and Director Research,
Syed Ammal Engineering College, Ramanathapuram, India

[1]drsuresha@saec.ac.in,[2]rashmi.power@gmail.com,[3,*]ChockalingamAravind.Vaithilingam@taylors.edu.my,
[4]rdhanashekar@yahoo.com

Abstract
Voltage source multilevel inverters are drawing wide attention in industry due to their high power handling capability and reduced harmonics. However, some disadvantages of these inverters are unequal current stresses, voltage balance issue, and high cost and a reduction of the reliability and efficiency of the inverter the due to increasing number of devices. To overcome the foresaid complexity, this paper proposes two types of seven levels inverter with reduced number of switches.The topologies are diode clamped and cascaded multilevel inverter (MLI). The comparative analysis is carried out between these two configurations. The simulation results and comparative analysis in terms of total harmonic distortion are presented in this paper.

Keywords:Diode clamped MLI, Cascaded MLI, Switching losses, Total Harmonic Distortion(THD).

1. Introduction

Inverters with several levels in output are replacing conventional square wave inverters in recent years. Multilevel inverters,unlike normal voltage source inverter, provides several intermediate voltage levels which improves the shape of the output voltage waveforms and almost a sinusoidal output [1]. There are several benefits of MLI, to mention few: higher voltage capability, alleviation in harmonic content of output voltage and current , high output and reduced dv/dt [2]. These inverters are mainly used in medium voltage industrial drives, as active filters for integrating renewable energy sources to the gird and in blowers, fans, traction drives, conveyors and so on. [3-7].

There are three types of MLI, viz. Diode clamped or neutral point clamped, cascaded H-bridge and flying capacitor type. The power losses are very less in Flying capacitor MLI compared to other two types. But this type of MLI is bulkier compared to the other two types since there are no clamping diodes. It is not practical to use this heavy inverter in applications that are not stable. Among all, the cascaded H-bridge MLI are simple, have the lowest weight and are economical. But this configuration is more inefficient compared to other types due to high power losses. In Diode clamped or neutral point clamped MLI, the power losses are less than the cascaded H-bridge MLI. The lowest THD is obtained in Diode clamped inverter [8-9].Various Pulse width Modulation schemes are applied to these MLIs to improve the quality of the output voltage. An analytical approach to estimate and reduce THD was proposed in [10].It uses the harmonic to calculate the inverter fundamental output, switching angles for the switches and these switching angles and the switching sequence decides the inverter voltage levels.

All the MLI are prone to large switching losses which affects the efficiency. The control algorithms are complex due to large number of devices [11-12] and voltage balancing has to be taken care. Therefore this paper presents diode clamped and cascaded MLI with reduced number of switches and the switching losses to address the foresaid problems.

In this paper Section II describes the topology of seven levels diode clamped inverter and Section III focuses on cascaded H-bridge MLI. III. The comparative results are presented in Section IV and Section V described about the conclusion.

2. Diode Clamped MLI Inverter.

In this topology, all legs share a common DC bus , therefore the number of capacitors needed are less. The voltage across non-conducting switch is limited to $V_{DC}$with the help of clamping diodes.The efficiency of the inverter can be enhanced by switching it at fundamental frequency. The efficiency of diode clamped inverter is high for fundamental switching frequency.

A seven levels diode clamped inverter is shown in Figure 1. The diode clamped multilevel inverter has only one DC source and it is split into *N* levels. For obtaining seven levels three capacitors and eight clamping diodes are required. The seven level output voltages are $\pm V_{dc}, \pm V_{dc}/3, \pm 2V_{dc}/3$ a d) V. The diodes clamp the voltage according to the DC bus voltage. The switching sequence to obtain seven level output voltage is given in Table 1.

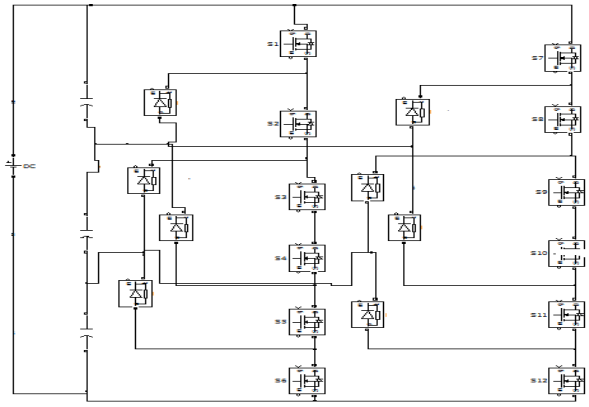


Fig 1 seven levels diode clamped inverter

Table 1: The switching states for seven level diode clamped inverter

S_1	S_2	S_3	S_7	S_8	S_9	V_{out}
1	1	1	0	0	0	V_{dc}
1	1	1	0	0	1	$2V_{dc}/3$
1	1	1	0	1	1	$V_{dc}/3$
0	1	1	0	1	1	0
0	1	1	1	1	1	$-V_{dc}/3$
0	0	1	1	1	1	$-2V_{dc}/3$
0	0	0	1	1	1	$-V_{dc}$

3. Cascaded Multilevel Inverter Topology

Seven level cascaded H-bridge MLI is shown in Figure2. This topology consists of six unidirectional power switches: Sa, Sb, SL1, SL2, SR1, SR2 and two DC voltage sources. By having unequal voltage sources, the number of levels can be increased by adding or subtracting the supply voltages. The number of switches used to generate seven level output are very less compared to the conventional topologies. The magnitudes of dc voltage source are :

$$V_{L1} = V_{dc} \text{ and } V_{R2} = 2V_{dc}$$

Table 2 shows the switching state for proposed cascaded H-bridge MLI topology.

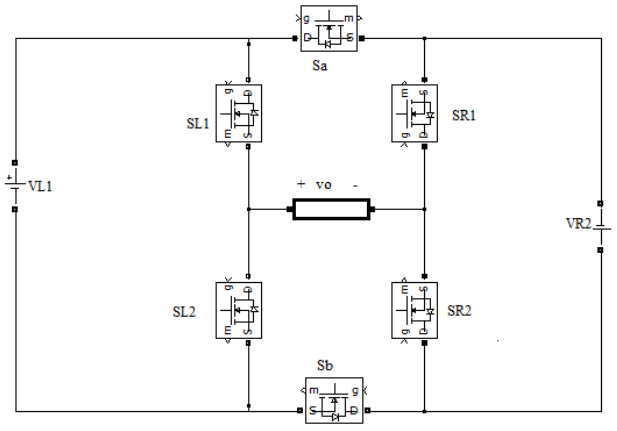


Fig 2 . Seven Levels Cascaded H-Bridge Inverter

Table 2: Switching pattern for seven level cascaded H-bridge inverter

SL1	SL2	SR1	SR2	Sa	Sb	v_o
1	0	0	1	0	1	V_{L1}
1	0	0	1	1	0	$-V_{R2}$
1	0	1	0	0	1	$V_{L1}+V_{R2}$
0	1	0	1	0	1	0
0	1	1	0	1	0	$-V_{L1}$
0	1	1	0	0	1	V_{R2}
0	1	0	1	1	0	$-(V_{L1}+V_{R2})$

4. Simulation Results

Single phase seven levels diode clamped and cascaded H-bridge inverters are simulated in Matlab/Simulink platform and the simulation results are analysed in this section. The Simulink model for conventional square wave inverter is shown in Figure3. Figure 4 shows the FFT spectra of output voltage of this inverter. The THD of the output voltage is measured and found to be 48.03%

The Simulink model for diode clamped multilevel inverter is shown in Figure 5. The input voltage is 300 V DC. The inverter output voltage is shown in Figure 6. The Simulink model for cascaded H-bridge MLI inverter is shown in Figure 7 and the load voltage is shown in Figure8

The multilevel was simulated for seven levels of output voltage with two dc sources. The FFT analysis is carried out for both the configurations. Figure 9 and Figure 10. shows the FFT spectra of a seven levels diode clamped and cascaded H-bridge inverter respectively.

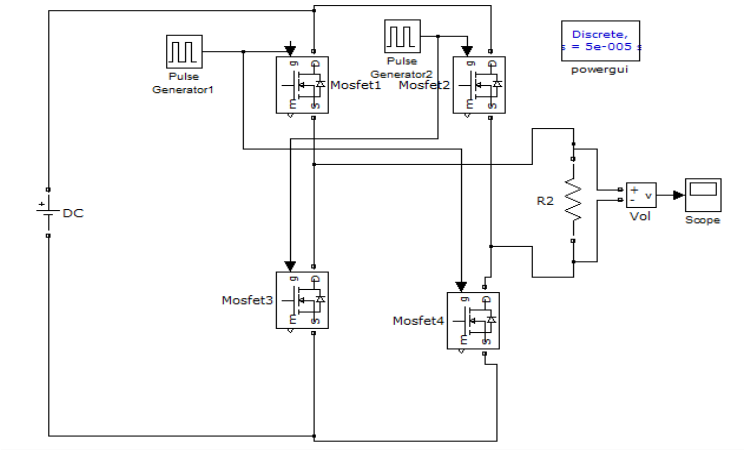


Fig 3.Simulink model for two level inverter

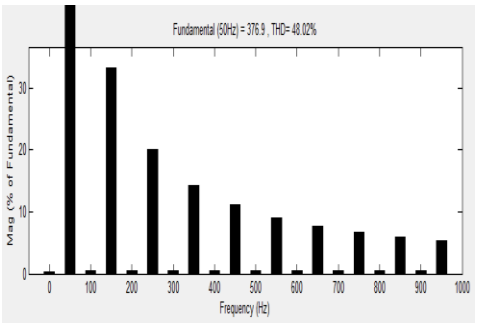


Fig 4.Harmonic Spectra of a square wave inverter

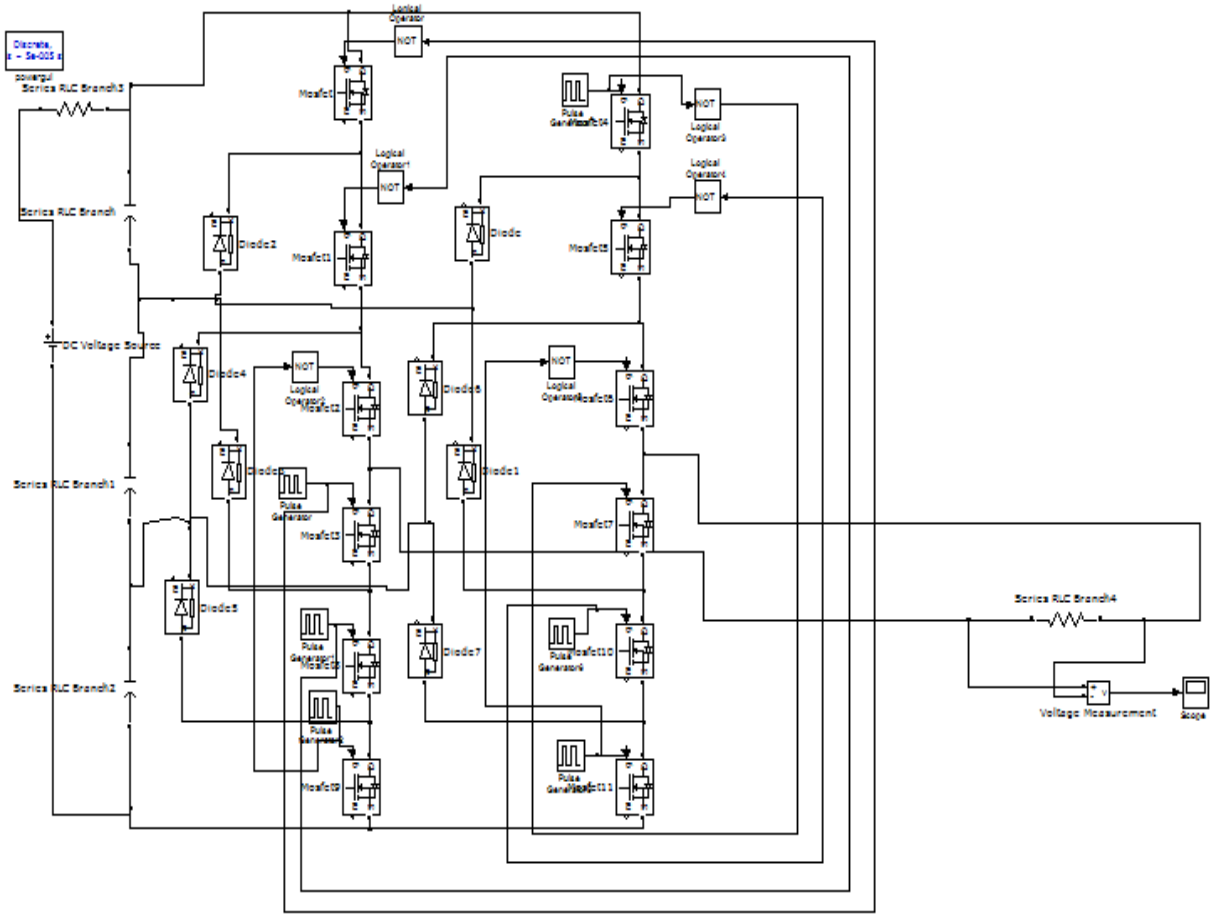


Fig 5. Simulink model for diode clamped MLI

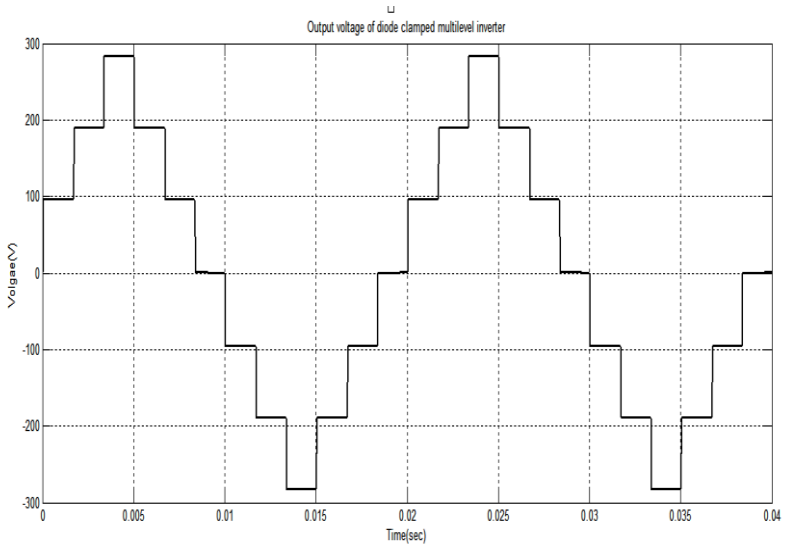


Fig 6.Output voltage of diode clamped multilevel inverter

The output voltage contains ±100 V, ±200 V, ±300 V and 0 voltage levels. Since output voltage is stepped waveform, the harmonic distortion is reduced, which is evident from the FFT spectra in Figure 9. Inorder to verify whether diode clamped MLI or cascaded H-bridge MLI performa better in reducing the harmonics, the analysis was carried out for the same voltage levels and the same load. Cascaded H-bridge MLI consists of only six switches to obtan seven levels viz. ±100 V, ±200 V, ±300 V and 0 V, in the output voltage. Therefore the control circuit is simple and switches are less compared to diode clamped MLI. From the FFT analysis of cascaded MLI shown in Figure 10, it is evident that THD is almost same as that of diode clamped MLI. Therfore cascaded H-bridge MLI is more compact and better than diode clamped inverter.

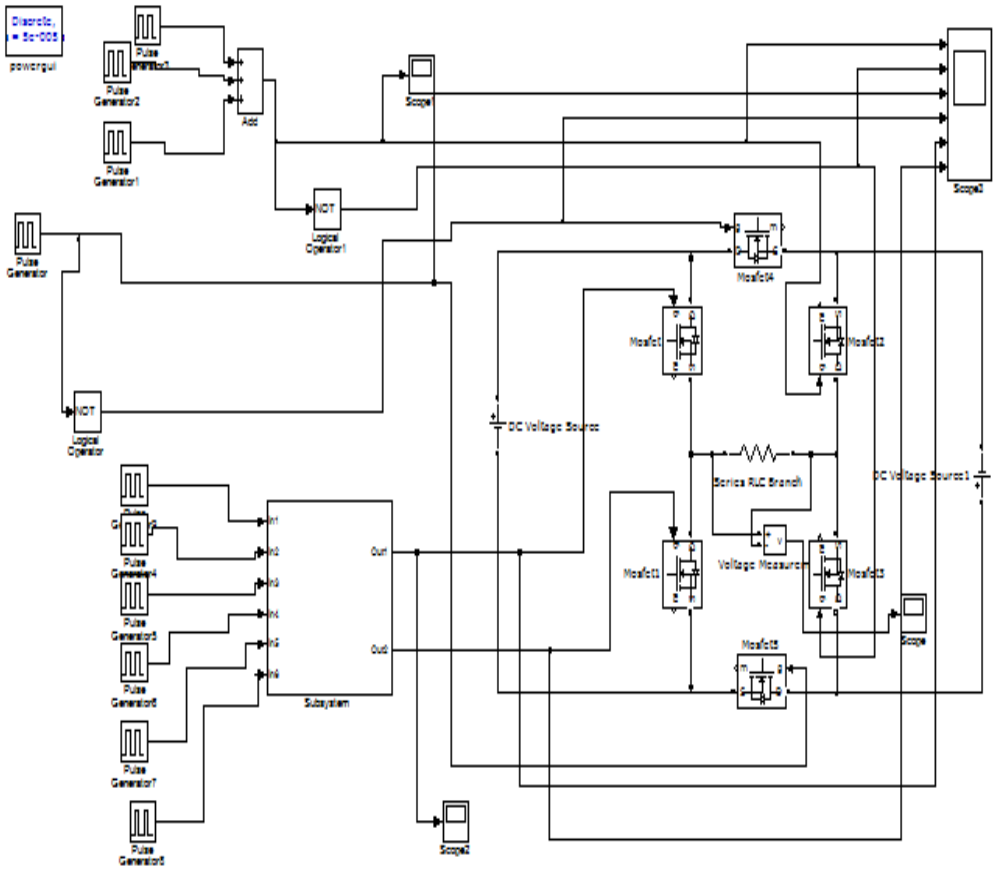


Fig 7. Simulink model for cascaded multilevel inverter

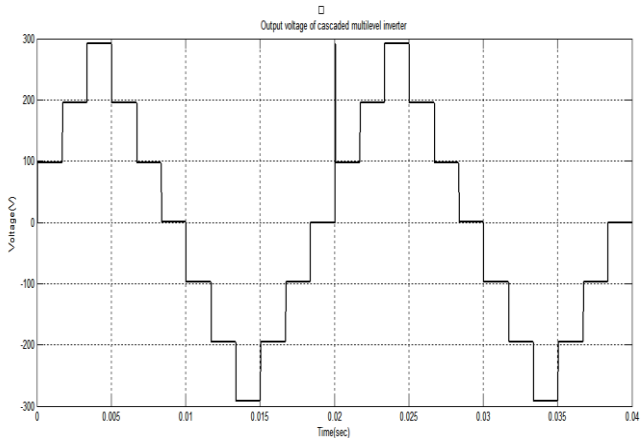


Fig 8.Output voltage of cascaded H-bridge MLI

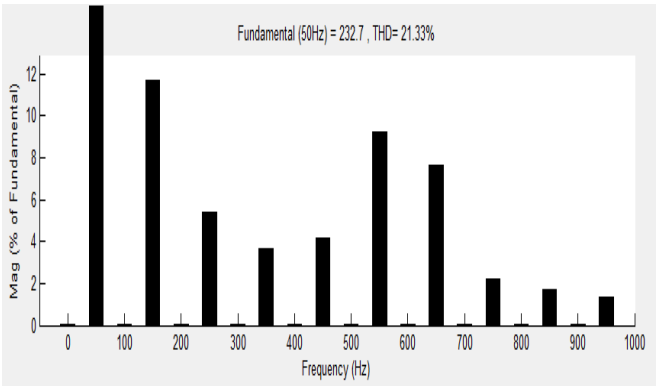


Fig 9.Harmonic spectra of output voltage- diode clamped MLI.

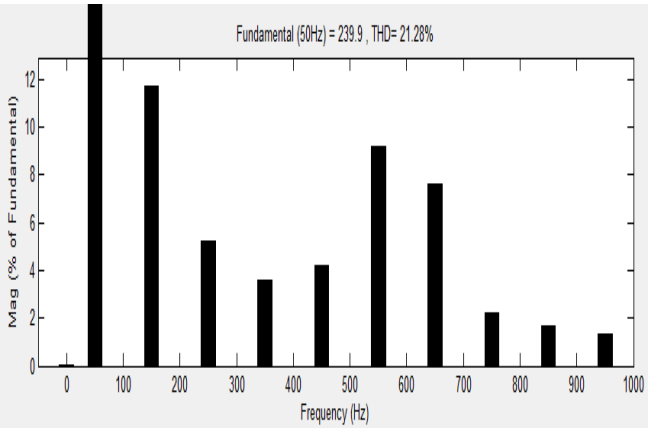


Fig 10.Harmonic spectra of the output voltage of Cascaded H-bridge MLI.

For diode clamped multilevel inverter the THD of the output voltage is measured and found to be 21.33% and for cascaded the THD is found to be 21.29%

5. Conclusion

Diode clamped inverter topology and cascaded H-bridge MLI for seven levels were considered. The cascaded H-bridge topology has few solid state devices compared to the diode clamped multilevel inverter of the same number of levels. The THD of both the configurations are almost same. The numbers of switchings per cycle in diode clamped inverter are half the number of switchings in cascaded H-bridge inverter. Therefore the switching losses are less in diode clamped inverter. Further the work can be extended on application of these inverters in power systems for power quality improvement.

References

[1] J.Rodriguez, et.al, "Multilevel inverters: A survey of topologies, controls and applications", *IEEE transactions on Industrial Electronics*,2002, Vol.49, No.4, pp.724-738.

[2] P.Panagis et.al. "Comparison of state of the art multilevel inverters," *IEEE Power electronics Specialists conference PESC 2008,* pp. 4296-4301.

[3] S. Rizzo and N. Zargari, "Medium voltage drives: What does the future hold" *4th IPEMC Conference proceedings*.,2004, vol. 1, pp. 82–89.

[4]R. D. Klug and N. Klaassen, "High power medium voltage drives-Innovations, portfolio and trends," in IEEE European Conference on Power Electronics Applications proceedings, pp. 1–10, 2005

[5] L. G. Franquelo et.al, "The age of multilevel converters arrives," IEEE Industrial electronics Magazine., vol. 2, no. 2, pp. 28–39, June 2008.

[6] J. Rodriguez, et.al, "Design and evaluation criteria for high power drives," IEEE IAS annual conference record. October 2008, pp. 1–9.

[7] M.Wenzhong and K.L.L.Yaohua, "Research on a multilevel high power

converter, "*IEEE International conference onindustrial application*, vol. 1, 2004, pp. 341-344

[8] J. Rodriguez, et.al, "Multilevel converters: An enabling technology for high-power applications," Proc. IEEE, vol. 97, no. 11, pp. 1786–1817, Nov. 2009.

[9] F. Khouchaetal., "Hybrid cascaded H-bridge multilevel inverter motor drive DTC control for electric vehicles," IEEE Proceedings of the ICEM'08, Vilamoura , September 2008.

[10] Bimal K. Bose, "Power electronics and motor drives recent progress and perspective,"IEEE transactions on industrial electronics. vol. 56, no. 2, pp. 581–588, Feb. 2009

[11] S. Kouro et.al, "Switching loss analysis of modulation methods used in cascaded H -bridge multilevel converters," IEEE Power Electronics specific conference Jun. 15–19, 2008, pp. 4662–4668.

[12] D. Andler et.al, , "Switching loss analysis of modulation methods used in neutral point clamped converters," in Proc. IEEE Energy Conv. Congress. Expo., Sep. 20–24, 2009, pp. 2565–2571

eureca 2016 – Conference Paper
Paper Number EE_PG002

Design of a Half-Bridge DC/DC Converter for Supercapacitor based Hybrid PV Storage System

Muhammad Izuan Fahmi[1,2], MD Shahrukh Adnan Khan[3], CV Aravind[4], Rajprasad Rajkumar[2*], Dino Isa[2**]

[1]*Department of Electrical and Electronics Engineering, University of Nottingham Malaysia Campus, Malaysia*

[2]*School of Electrical System, University Malaysia Perlis, Malaysia*

[3]*School of Engineering, University of Asia Pacific, Bangladesh*

[4]*School of Engineering, Taylor's University, Malaysia*

[1]*izfahmi@gmail.com*, [2]*kecx1msa@nottingham.edu.my*, [3]*aravindcv@ieee.org*,
[*]*Rajprasad.Rajkumar@nottingham.edu.my*, [**]*dino.isa@nottingham.edu.my*,

Abstract
This paper introduces a design of a DC to DC converter for hybrid energy storage system that consists of battery and Supercapacitor. The half-bridge converter used here to step-up the input voltage in the forward direction and vice versa in order to supply to the inverter and protect the storage devices. Our experiment also tested the Half-Bridge DC to DC Converter into the solar system to see the effectiveness of this type of converter and show the optimal performance of the designed converter for the Supercapacitor based PV solar system. The system was set-up and experimented at the Solar Cabin of University of Nottingham Malaysia Campus.

Keywords*:* PV Storage, Supercapacitor, DC/DC Converter, Design Optimisation.

1. Introduction

ADC to DC converter converts electronic circuit from one voltage level to another voltage level [1].These types of converters are usually used in appliance based on battery powered circuits like mobile phones. In other words, they act like a transformer but with constant voltage supplies [2].Generally, power converters used in a PV storage system have the following features namely; Bi-directional energy flow management which controls both charging and discharging process, high efficiency and withstands high peak power or providing fast response [3-5].

Furthermore, a DC to DC Converter is required to properly interface the combination of energy storage between battery and Supercapacitor. DC to DC Converter has a function to shift the voltage levels without changing power level [7]. A bi-directional DC to DC converter allows transferring power in both directions between two DC sources. For example, the usage of this application like battery charger circuit and uninterruptable power supplies works in these converters due to the reverse direction of power flow along with balanced voltage polarity [8]. All these topologies will cause an increased risk of making the circuit more complex, conduction losses and component ratings. [8] [9]. This bi-directional DC to DC converter is best for a new vehicle that are using electrical applications [10-11].In the solar system, many researchers use this type of converter. Shreelakshmi et al. [12], implement Bi-Directional DC to DC Converter for battery charging in the solar system to achieve optimised component on each step. When the load demand was less than the maximum power extracted from PV, the extra power available was used to charge the through the bi-directional DC-DC converter. Raveendhra et al. [13], proposed bi-directional DC-DC converter of solar power by using FPGA converter. This converter was designed for high gain in both buck and boost modes. The implementation of this converter was to control charging and discharging the battery storage system to increase its efficiency. In both the modes, Bi-directional DC-DC Converter was controlled with the help of voltage mode control. There are many types of circuit topologies for this kind of DC –DC Converters. Here is a list of it [14-15]:

-Non-Isolated Bi-directional DC to DC Converter (less transformer)- # Full bridge bi-directional DC to DC Converter # Half bridge bi-directional DC to DC Converter	-Isolated Bi-directional DC to DC Converter (with transformer)- # Full bridge bi-directional DC to DC Converter # Half bridge bi-directional DC to DC Converter

2. Converter Design

Briefly, the software design process included software specification, architecture and module specification. In terms of the hardware, the design associated specification, design and analysis of the highest stage system into several reduction stages of the functional block diagrams. Hardware testing was the phase where circuit and hardware had been tested, troubleshot in the case of faults or undesired results in order for them to match specifications. Software employment method involves coding of different software program modules. At the end, the system is combined as a single unit to do a testing and troubleshooting. The DC to DC Converter was placed in the solar cabin and figure 1 is the block diagram of the proposed design.

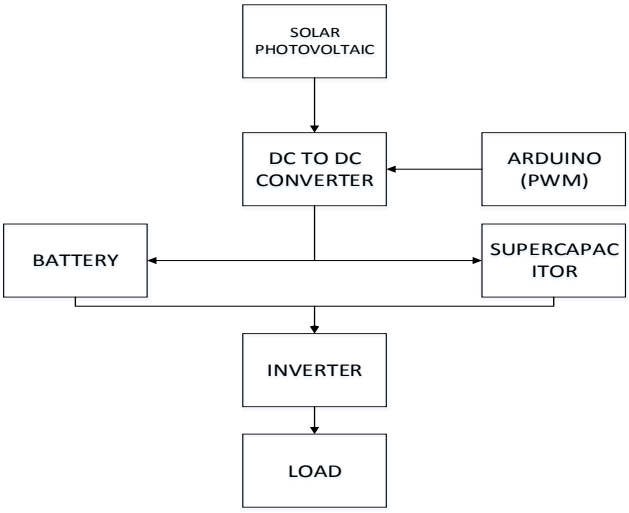


Figure 1. DC to DC Converter in Solar Cabin

The converter for operation in the solar cabin is to be designed according to the following parameters mentioned in Table 1.

Table 1: Specification of the DC/DC Converter

Minimum supercapacitor voltage	:	30V
Minimum battery DC bus voltage	:	48V
Maximum battery DC bus voltage	:	58V
Battery DC bus voltage setpoint	:	56V (when supercapacitors connected)
Minimum supercapacitor voltage	:	30V (Assuming SOC < 50%)
Maximum supercapacitor voltage	:	60V
Input power	:	2000W
Switching frequency	:	20KHz
Current ripple	:	0.2A
Voltage ripple	:	1

In order to appropriately interface the batteries and supercapacitors in the hybrid energy storage system, a DC-DC converter which has the capabilities to control power flow in two directions is required. However, since this project does not focus on design or construction of the converter, only a relatively simple yet sufficient prototype is built in order to allow further testing and data collection to take place. The converters are designed with parameters: i. Typical input voltage, Vi: 24V, ii. Desired output voltage, Vo: 48V, iii. Voltage ripple, Δ: 0.5A, iv. Current ripple, Δ: 0.5V, v. Switching frequency, fs: 30kHz

3. Half-Bridge Converter

The type of converter used in this project is non-isolated bi-directional DC-DC converter. In this project to convert the high voltage and current is more suitable to use isolated converters. The purpose for not using non-isolated DC-DC converter is due to limited budget. In order to have a better protection while using non-isolated DC-DC converter, a fuse will be used to protect the microcontroller which is used to manage the switching of MOSFET and reading of each current and voltage sensor from the bi-directional DC-DC converter circuit. Consequently, there are three type of non-isolated bi-directional buck-boost converter which is a half-bridge converter, cascaded converter and cuk converter.

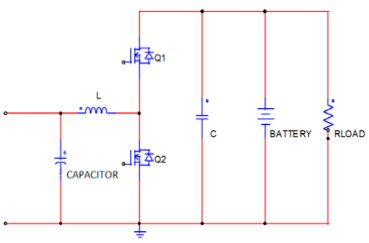


Figure 2 Circuit Diagram of Half-Bridge Conv.

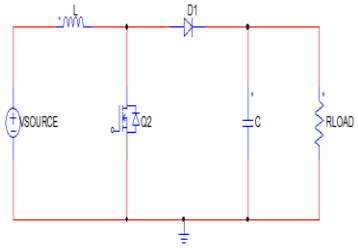


Figure 3 Circuit Diagram of a General Boost Conv.

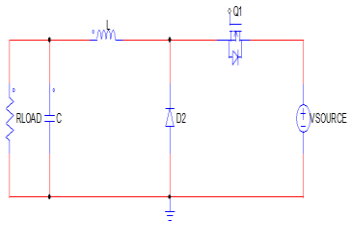


Figure 4 Circuit Diagram of a General Buck Conv.

Half-bridge converter had been chosen to use in this project. The circuit topology used for this project is a "half-bridge" converter. Due to its structure, it resembles half of that of an H-bridge shown in **Error! Reference source not found.**With the inductor connected at the input side and the capacitor connected at the output side, it is exactly identical as a boost converter as shown in **Error! Reference source not found.**3, except that the pass diode between input and output stages is replaced with a transistor switch, in this case, an n-channel MOSFET. Buck converter is shown in **Error! Reference source not found.**4, the freewheeling diode exchanged for an n-channel MOSFET transistor switch.

4. ***System Design***

This converter is designed to suit the application of interfacing supercapacitors and batteries within the hybrid energy storage system. If the half-bridge converter is regarded as a boost converter, the input side will be connected to the supercapacitors, the output is to be connected to the DC bus of the energy storage system which is also connected to the batteries and vice-versa depending on conditions. This converter aims to provide a constant output voltage even when the Supercapacitor voltage drops due to the drain of charge during discharge. Compared to others project in a review, the converter is design for a small scale and low current because tested in the laboratory. The total current for a small scale is lower than 2A compared with this system which is the highest current recorded is 10A. When running the experiment, the current is need to set the limit to protected the converter. By using steady-state analysis formula, the minimum inductor and capacitor values can be calculated. Assuming typical boost converter operation, the duty cycle operation is:

$$\frac{V_o}{V_i} = \frac{1}{1-D} \qquad (1)$$

$$\Delta i_L = \frac{V_s DT}{L} \rightarrow L = \frac{V_s DT}{\Delta L} \qquad (2)$$

During lowest supercapacitor voltage (V_i) of 30V, $V_o = 56V$ the required duty cycle D=0.4643 from **Error! Reference source not found.**. In order to limit current ripples to 0.2A, L is calculated using the following equation.This gives a minimum inductance of 3482µH. To design the appropriate value of capacitor for a boost converter, **Error! Reference source not found.** is used.

$$\frac{\Delta V_o}{V_o} = \frac{DT}{RC} \rightarrow C = \frac{DT}{R(\frac{\Delta V_o}{V_o})} \qquad (3)$$

Assuming the output of the boost converter configuration draws at most 8A, at R=7, the required output capacitance is 331.6µF. If the output voltage is exactly the same as input voltage, then there is no need for boosting characteristics of the converter, the duty cycle can be set to zero. However, due to the voltage drop at the body diode of the high side MOSFET, there will not be any output current from the converter at 0% duty cycle, hence a difference of 1.2V diode drop must be allowed. This corresponds to V_s=56V and V_o=57.2V. At this highest supercapacitor voltage

during operation, due to the architecture and design of the bi-directional DC-DC converter, D=0.0210 with the calculated inductance of 293.7µH. Output capacitor needs to be at least 15µF.Assuming typical buck converter operation, the following equations are used to calculate the required inductor and capacitor sizes:

$$L = \frac{V_o(1-D)T}{\Delta i_L} \rightarrow \Delta i_L = \frac{V_o(1-D)T}{L} \quad (4)$$

$$\frac{\Delta V_o}{V_o} = \frac{1-D}{8Lf^2C} \rightarrow C = \frac{1-D}{8Lf^2(\frac{\Delta V_o}{V_o})} \quad (5)$$

Due to the design of the converter, an essential limitation is that the output voltage will never exceed the input voltage is applicable, even at a maximum duty cycle of 100%. However, the gate driver is not able to set 100% duty cycle with the usage of bootstrap. Therefore, the maximum duty cycle is 99.75% as per the smallest division in the PWM generation of 1/400 or 0.25%. This then implies that V_s=56, D=0.9975, V_o=55.86V and so L=34.9µH and C=2.24µF. To summarise the converter design, a minimum inductance required for correct operations on both sides is 3482µH, and minimum battery side capacitance is 331.6µF. This was followed by specification of the system based on the collected data on requirements. After that, system architecture was performed in order to obtain a general concept of the overall behaviour and the structure of the system.

5.Experimental Set-up

The setup in the lab was built to overserve the DC to DC converter characteristics. This experiment also shows whether the supply was able to supply demand voltage from the solar cabin for the inverter to operate the inverter. Furthermore, the testing was to check either the bi-directional DC to DC converter was capable of operating in boost or buck operations. The DC to DC was testing on the breadboard to check the functionality of each component. **Error! Reference source not found.**5indicates testing on PCB which already done in the lab. After completed the test in the lab, the DC to DC was placed on solar cabin as shown in **Error! Reference source not found.**6.

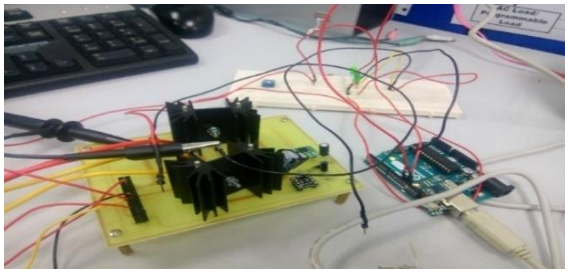


Figure 5. Test on PCB

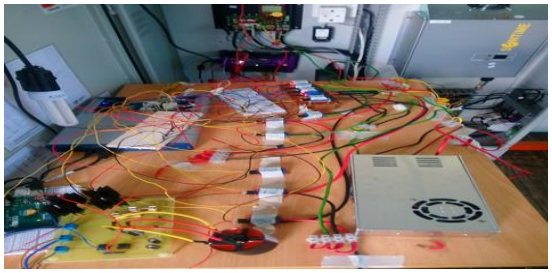


Figure 6. Connection of DC to DC Converter

6. Results and Discussion

The result of lab test for boost converter is shown in Figure 7. As expected. With the implementation of boost mode, the converter had increased its efficiency, even though the difference in voltages still increased with increasing duty cycle.

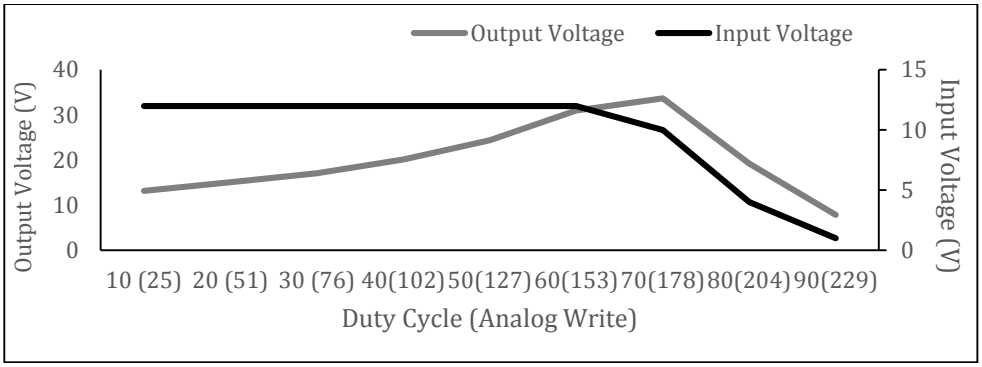


Figure 7. Output and Input Voltage Vs Duty Cycle for Boost Converter

Table 2. Boost Converter Lab Test Results

Boosting Duty cycle % (AnalogWrite)	Input voltage V	Output voltage V	Theoretical Output voltage V	Difference in voltage V
10 (25)	12	13.2	13.3	0.1
20 (51)	12	15.1	15	0.1
30 (76)	12	17.1	17.1	0
40(102)	12	20.1	20	0.1
50(127)	12	24.4	24	0.4
60(153)	12	31.0	30	1.0
70(178)	10	33.7	33.3	0.4
80(204)	4	19.2	20	0.8
90(229)	1	7.88	10	2.12

As shown in the table, the output voltage was much closer to the theoretical value compared to non-synchronous mode, as predicted. The gated MOSFET in place of forward biased body diode reduced the voltage drop across the MOSFET by a significant amount, increasing efficiency.

Table 3 Buck Converter Lab Test Results

Duty cycle % (Analog Write)	Input voltage (V)	Output voltage (V)	Theoretical Output volt. (V)	Difference in volt. (V)
10 (25)	30	3.12	3	0.12
20 (51)	30	6.18	6	0.18
30 (76)	30	9.21	9	0.21
40(102)	30	12.2	12	0.2
50(127)	30	15.2	15	0.2
60(153)	30	18.3	18	0.3
70(178)	30	21.2	21	0.2
80(204)	30	24.7	24	0.7
90(229)	30	27.7	27	0.7

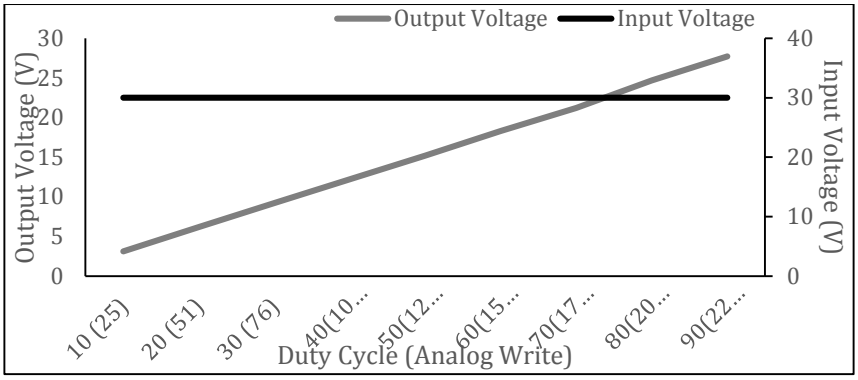


Figure 8. Output and Input Voltage Vs Duty Cycle for Boost Converter

A DC to DC Converter has been connected to the solar cabin. The 48V is downsized to 24V. The result is shown in Figure 9 which indicates that its able to run in 24V at solar cabin system and average current is 1A. For Supercapacitor part, it's able to charge and discharge directly. The result in 10has many sparks because the charge and discharge of the supercapacitor are very fast.

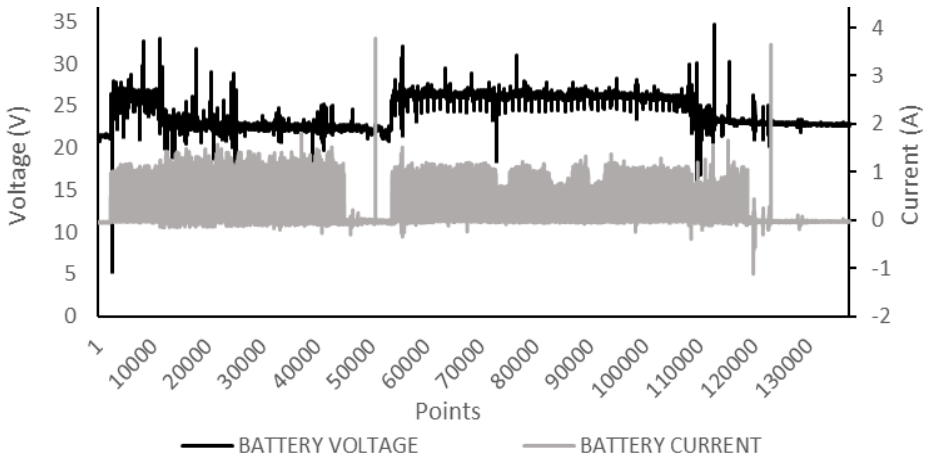


Figure 9. Battery Voltage and Current with DC to DC Converter

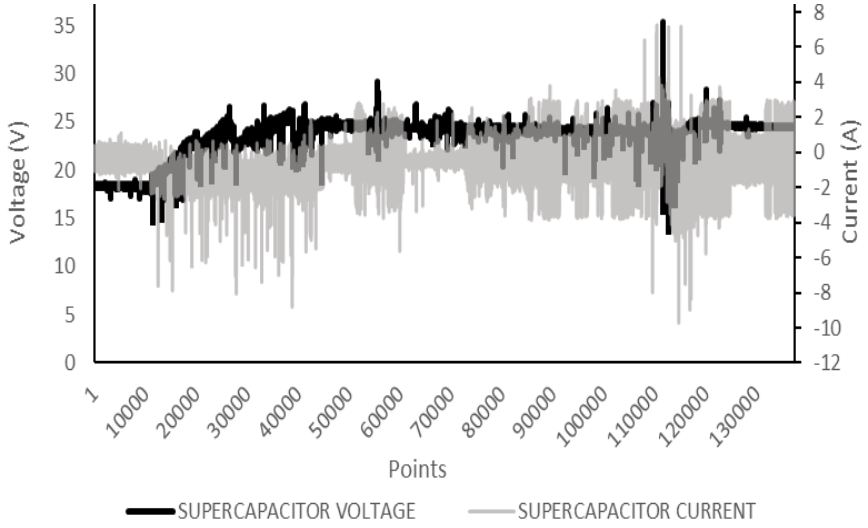


Figure 10. Supercapacitor Voltage and Current with DC to DC Converter

7. Conclusion

The Half-Bridge DC to DC converter experimenting and testing indicated successfully charge and discharge of the battery and Supercapacitor. The converter was working well in the 24V system. The DC to DC Converter results only can work in low current due to the limitation of the circuit and unable to meet energy demand from supercapacitor and load. While charging the supercapacitor in high current (>2A), the circuit discontinued operating and the results showed many sparks as the charge and discharge of the supercapacitor were very fast. Overall the experiment showed an optimal performance of the designed converter for the Supercapacitor based PV solar system.

References

[1] E. J. Yoo, T. Y. Lee, W. Y. Choi, and Y. W. Park, "Low temperature evaluation of commercial DC/DC converters for military applications," in *TENCON 2010 - 2010 IEEE Region 10 Conference*, 2010, pp. 1247–1250.

[2] F. Caricchi, F. Crescimbini, F. G. Capponi, and L. Solero, "Study of bi-directional buck-boost converter topologies for application in electrical vehicle motor drives," in *APEC '98 Thirteenth Annual Applied Power Electronics Conference and Exposition*, 1998, vol. 1, pp. 287–293.

[3] H. Martínez-García and A. Grau-Saldes, "Complex Constant Switching Frequency Control for Linear-Assisted DC-DC Switching Converters."

[4] F. C. Schwarz and J. Ben Klaassens, "A Controllable 45-kW Current Source for DC Machines," *IEEE Trans. Ind. Appl.*, vol. IA-15, no. 4, pp. 437–444, Jul. 1979.

[5] S. Vazquez, S. M. Lukic, E. Galvan, L. G. Franquelo, and J. M. Carrasco, "Energy Storage Systems for Transport and Grid Applications," *IEEE Trans. Ind. Electron.*, vol. 57, no. 12, pp. 3881–3895, 2010.

[6] Z. Amjadi and S. S. Williamson, "Novel controller design for a Luo converter electric vehicle energy management system," in *2010 IEEE Electrical Power & Energy Conference*, 2010, pp. 1–6.

[7] V. Dargahi, S. Dargahi, A. K. Sadigh, and M. Abarzadeh, "Reduced DC voltage source flying capacitor multicell multilevel inverter: analysis and implementation," *IET Power Electron.*, vol. 7, no. 2, pp. 439–450, Feb. 2014.

[8] J. G. Kassakian, "Automotive electrical systems-the power electronics market of the future," in *APEC 2000. Fifteenth Annual IEEE Applied Power Electronics Conference and Exposition (Cat. No.00CH37058)*, 2000, vol. 1, pp. 3–9.

[9] A. Rodriguez Alonso, J. Sebastian, D. G. Lamar, M. M. Hernando, and A. Vazquez, "An overall study of a Dual Active Bridge for bidirectional DC/DC conversion," in *2010 IEEE Energy Conversion Congress and Exposition*, 2010, pp. 1129–1135.

[10] G.-J. Su and F. Z. Peng, "A low cost, triple-voltage bus DC-DC converter for automotive applications," in *Twentieth Annual IEEE Applied Power Electronics Conference and Exposition, 2005. APEC 2005.*, 2005, vol. 2, pp. 1015–1021.

[11] F. H. Khan and L. M. Tolbert, "5 kW Multilevel DC-DC Converter for Hybrid Electric and Fuel Cell Automotive Applications," *2007 IEEE Ind. Appl. Annu.*

Meet., pp. 628–635, Sep. 2007.

[12] M. P. Shreelakshmi, M. Das, and V. Agarwal, "High gain, high efficiency bi-directional DC-DC converter for battery charging applications in stand-alone Photo-Voltaic systems," in *2013 IEEE 39th Photovoltaic Specialists Conference (PVSC)*, 2013, pp. 2857–2861.

[13] D. Raveendhra, P. R. ul Zaman, and K. Govind, "FPGA controlled high gain bi-directional DC-DC converter (BDC)for energy storage of solar power," in *2014 IEEE 2nd International Conference on Electrical Energy Systems (ICEES)*, 2014, pp. 300–305.

[14] N. Vasantha Gowri and G. Suresh Babu, "A novel bidirectional DC-DC converter drive," in *INTERNATIONAL CONFERENCE ON SMART STRUCTURES AND SYSTEMS - ICSSS'13*, 2013, pp. 19–23.

[15] D. Gleich, M. Milanovic, S. Uran, and F. Mihalic, "Digitally controlled buck converter," in *2004 IEEE International Symposium on Circuits and Systems (IEEE Cat. No.04CH37512)*, pp. V–944–V–947.

eureca 2016 – Conference Paper
Paper Number ME_PG01

Effect of Variable Liquid-Suction-Line Subcooler Mass Flow Rates on the Cooling Capacity and the Coefficient of Performance of an Air Conditioning System

Ali Naif[1*], Lim Chin Hong[2], Azadeh Ghadimi[3]

[1-3] *School of Engineering, Taylor's University, Malaysia*

[*]ali.naif@sd.taylors.edu.my

Abstract

Air conditioning and refrigeration systems are known to be two main culprits for about 50% of energy consumption in a household. Liquid Suction Line Heat Exchanger (LSLHX) is one of the methods to improve the cooling capacity and the Coefficient of Performance (COP) of the system. However, LSLHX also increase the compressor power consumption due to the pressure drop with in the suction line of the LSLHX. Therefore, the purpose of this paper was to investigate how variable mass flow with in the LSLHX affected the overall cooling capacity and the COP. The investigation was done by mathematically simulating the operation of the refrigerant cycle with the LSLHX using manufacturer's data. Mass flow with in the LSLHX was distributed into X and Y percentages for liquid and suction line respectively. The remaining mass in both sides was allowed to flow in the basic VCC line. For the simulations, X was tested at every 10% interval from 0% to 100%. Similarly, for every X, the Y was also tested at every 10% interval from 0% to 100%. Cooling capacity improved upto 2.94 kW and 2.83 kW or by 17.59% and 13.16% without and with the pressure drop considered respectively, as compare to the 2.5 kW the basic VCC cycle. Coefficient of Performance (COP) improved upto 3.65 and 3.54 or by 17.6% and 14.07% without and with the pressure drop considered respectively, as compare to the 2.5 kW the basic VCC cycle. Additional 6.7 W of power was required by the compressors to compensate for the 15 kPa of pressure.

Keywords: Liquid Suction Line Heat Exchanger, Coefficient of Performance, Pressure Drop, Cooling Capacity, Variable Mass Flow.

ABBRIVIATIONS

COP	Coefficient of Performance
LSLHX	Liquid Suction Line Heat Exchanger
VCC	Vapour Compression Cycle

SYMBOLS

A	Area	m^2
Cp	Specific Heat Capacity	$kJ/kg.°C$
h	Enthalpy	kJ/kg
I	Current	A
L	Difference between Condensing and Evaporating Temperatures	°C
$\dot{m}$	Mass flow rate	kg/s
P	Pressure	kPa
$\dot{Q}$	Rate of heat transfer	kJ/s
T	Temperature	°C
V	Voltage	V
W	Compressor power	W
X	Suction Line Mass Flow Percentage	%
Y	Liquid Line Mass Flow Percentage	%

GREEK LETTERS

Δ	Change
ε	Effectiveness of the Liquid Suction Line Heat Exchanger

SUBSCRIPTS

amb	Ambient
comp	Compressor
cond	Condenser
evap	Evaporator
expa	Expansion valve
in	Inlet
ll	Liquid Line
out	Outlet
ref	Refrigerant
sl	Suction Line
w	Water
1	Evaporator Exit
1'	Basic Vapour Compression Cycle Suction Line
1''	Immediate Compressor Suction
2	Compressor Discharge
3	Condenser Exit
3'	Basic Vapour Compression Cycle Liquid Line
3''	Immediate Expansion Valve Inlet
4	Evaporator Inlet
5	Liquid Suction Line Heat Exchanger Liquid Inlet
5'	Liquid Suction Line Heat Exchanger Liquid Outlet
6	Liquid Suction Line Heat Exchanger Vapour Inlet
6'	Liquid Suction Line Heat Exchanger Vapour Outlet

1. Introduction

Air conditioning and Refrigeration (ACnR) systems are used to cool or extract heat and moisture from a desired low temperature heat source and to transfer it to an external high temperature heat sink. In application for air conditioners (AC), the desired room is the heat source and the outdoor is the heat sink while for refrigerators, the food and air within the refrigerator compartment is the heat source and the kitchen air is the heat sink.

ACnR system achieve this feat by manipulating the condensing and evaporating points of the working fluid with in the closed loop of the refrigeration cycle. As the condensing and evaporating point of a fluid is dependent on the pressure, a compression device and a throttling device is used to increase and decrease the working fluid pressure respectively.

It has been found that heating, ventilation and AC systems accounts for as much as 50% of energy usage in buildings and 15% of total energy use in United States (Perez-Lombard, Ortiz, & Pout, 2008). According to the Energy Information Administration, (2005) of the United States, ACnR system are responsible for about 28% of the total residential energy consumptions. Similarly, according to the Building & Construction Authority (2007) of Singapore, with a hot and humid climate as in Singapore, ACnR system consumes about 50% of the electricity used in residential applications. However still, the demand for ACnR systems are growing as the global population is exponentially growing and the Earth's atmosphere getting warmer. Thus, to provide for the demands without negatively effecting the carbon footprint, more energy efficient ACnR systems need to be made and used. In effort to reduce the energy consumption and usage of non-renewable sources, many different types of cooling systems being studied. Coefficient of Performance (COP) is the measure of ACnR system efficiency. By definition, COP is the ratio of the cooling capacity to the power supplied in to the compressor.

$$COP = \frac{\dot{Q}'_{evap}}{W} = \frac{(h_1 - h_4)}{(h_2 - h_1)} \quad [1]$$

Most commonly probed aspect to improve the COP of ACnRs is to use an additional or intermediate component or system to increase the amount cooling capacity of the ACnR for a constant compressor power input.

$$COP \uparrow = \frac{\dot{Q}'_{evap} \uparrow}{W}$$

1.1 Subcooling

Park, et al., (2015) reviewd and categorized the technologies to improve the VCC performance into three categories; Subcooling Cycles, Expansion Loss Recovery Cycles and Multi-Stage Cycles. Subcooling cycles were further branched out to Liquid-Suction-Line Heat exchanger (LSLHX), Thermoelectric subcooler and Mechanical subcooling. Expansion loss recovery cycles were branched out to utilization of expander and ejector. And lastly, multi stage cycles were branched out to include a vapour or liquid working fluid injection cycle, or a two phase injection

cycle. Based on the findings, it was noted that multi-stage refrigerant injection cycles or saturation cycles improved the COP by 42.4 % and 38.2% using R401A and propane as working fluids. It was also found that the incoporation of LSLHX improved the COP for low and mid refrigeration applications where the evaporating temperatures fall between -30°C to -15°C and -15°C to 5°C respectively. For evaporating temperatures higher than 5°C, the COP of the system declined due to the compressors in ablitly to adapt to the pressure drop in the LSLHX.

Jiang, et al., (2015) also carried out a study to improve the COP of the two stage compression cycles with 8 different intermediate cooling setups. Intermerdiate cooling component between two compression stages were need to maintain the heat rejection at the condenser as the vapour was pressurized in stages. In this study it was found that the as the cooling capacity (heat absorption) increased at the evaporator, the heating capacity (heat rejection) at the condenser also increase. However, the rate of cooling capacity was higher than the rate of heating capacity, thus, improving the system COP.

Klein, et al., (2000) explained the negative effect of the pressure drop across the suction side of the LSLHX on the COP, which demands for more work to be done by the compressors. Eleven different working fluids were tested. Neglecting the pressure losses with in the LSLHX, system performance improvements were observed.

However, it was emphasized that the pressure drop with in the LSLHX is unavoidable in real applications. Also, it showed that the pressure drop unfavorably affected the overall COP of the system. It was explained that the density of the working fluid and the volumetric efficiency of the compressor was reduced when the working fluid pressure dropped and temperature rose, and ultimately reduced the flow rate of the working fluid.

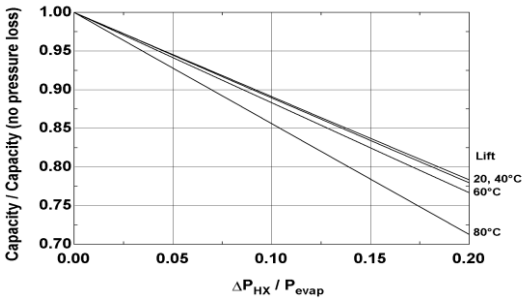


Figure 23 Correction to the relative capacity index to account for pressure loss in the low pressure leg of the liquid-suction heat exchanger.

In this particular study, an emperical model for the ratio of cooling capaity with and without pressure drop was modelled along with an emperical model for the ratio of COP with and without the pressure drop taken into cosideration. These two models are in Eq. 2 and Eq. 3 respectively.

$$\frac{Cooling\ Capacity_{\Delta P_{LSLHX}}}{Cooling\ Capacity} = 1 - (1.042 - 7.32 \times 10^{-7} L^3)\left(\frac{\Delta P_{LSLHX}}{P_{evap}}\right) \qquad [2]$$

$$\frac{COP_{\Delta P_{LSLHX}}}{COP} = 1 - (2.37 - 0.0481L + 3.01 \times 10^{-4}L^2)\left(\frac{\Delta P_{LSLHX}}{P_{evap}}\right) \quad [3]$$

It was mentioned that the comporessor power was not changed significantly to facilitate to the changes in the state of suction vapour. Amongst the 11 working fluids, R507A, R134a, R12, R404A, R290, R407C, R600 and R410A was found to have minimal pressure loss across the LSLHX as compared to R22, R32 and R717. Infact, R22, R32 and R717 had 'detrimental' effect on the COP of the cycle when used with LSLHX. However still, it was conclusive that the incoporation of LSLHX enhanced the cooling capacity significantly. But, the effect of this increase in the cooling capacity on the COP was largely hindered by the inablity of the compressor to adapt to the pressure drops and lowered refrigerant flow rate.

Similarly, Cho, et al., (2013), Navarro-Esbrí, et al., (2013) and Pottker & Hrnjak, (2015) performed a studies with and without internal subcooler with R1234yf and R134a to study the effect subcooling. Cho, et al., (2013) studied an automotive refrigeration system. Findings of Cho, et al., (2013), Navarro-Esbrí, et al., (2013) for R1234yf without and with the internal heat exchanger (IHX) as compared to the R134a cycle are summarized in Table 1 below. On the other hand, Pottker & Hrnjak, (2015) found that using condenser subcooling, COP can be improved by 18% and 9% for the R1234yf and R134a. It was also found that there is trade-off between the cooling capacity and the compressor power for a given operation condition to attain a maximum COP for the system. Additionally, Pottker & Hrnjak, (2015) also reported that a drop in COP with and without IHX for the R1234yf, but that the drop was lesser with the IHX.

Table 7 Power consumption, cooling capacity and COP changes as compared to the R134a system (Cho, et al., 2013 and Navarro-Esbrí, et al., 2013)

	Setup	**Power**	**Cooling capacity**	**COP**
Cho, et al., (2013)	R1234yf	-4%	-7%	-4.5%
	R1234yf+IHX	-2.9%	-1.8%	0.9%
Navarro-Esbrí, et al., (2013)	R1234yf	-	-6%	-13%
	R1234yf+IHX	-	-2% to 6%	-2% to 6

Studies conducted by Cho, et al., (2013), Klein, et al., (2000), Navarro-Esbrí, et al., (2013) and Pottker & Hrnjak, (2015) were performed with 100% of the working fluid mass flow into the the LSLHX or the IHX in both liquid and vapour sides. It was found in all studies that incoporating LSLHX infact did improve the cooling capacity, but the effect was hindered by reduction of the mass flow rate due to the pressure drop and the high temperatue at compressor suction. Addressing to the foresaid emperical research gap, it is worthy to study how different percentage of the total mass flow into the LSLHX effect the overall COP as it is mixed back with the remaining percentage before entering the compressor. Moreover, substituting the conventional compressor with a variable speed compressor may reduce the COP hinderance by gradually compensating for the drop in pressure and flowrate, and ultimately improve the overall system performance.

However in this study, the main focus was on the effects of different amount of subcooling on the COP by varying the amount of mass flow in the LSLHX.

Therefore, firstly the basic VCC was mathematically replicated using tested compressor operating conditions data provided by the manufacturer. Secondly, to introduce the LSLHX and investigate the effect on the COP of the steady state cycle due to different flow combinations, from 0% to 100% for both sides.

1 Methodology

1.1 Basic Vapor Compression Cycle

Vapour Compression Cycle (VCC), as shown in Figure 3, is one of the most commonly used cycles for ACnR applications. The main four components of a basic VCC are the Compressor, Condenser, Expansion valve and the Evaporator. A working fluid is used as the medium to transfer heat from the heat source to the heat sink

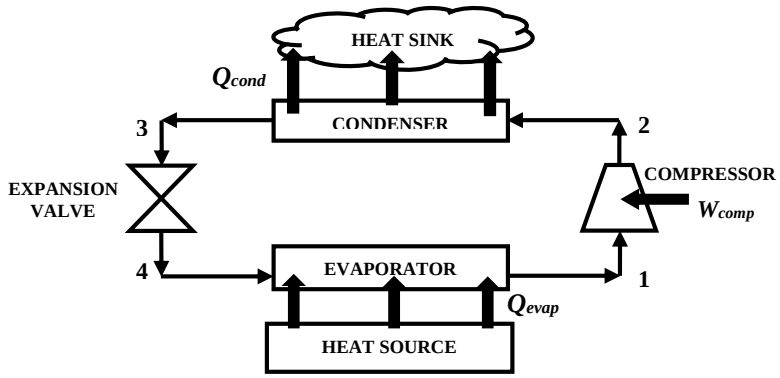


Figure 24 Basic Vapour Compression Cycle (Naif, et al., 2015)

The processes that change the physical state of the refrigerant, within the cycle are describes as:

- 1 to 2 Compression of superheated vapour
- 2 to 3 Condensation (heat rejection) of superheated vapour to saturated liquid
- 3 to 4 Expansion of saturated liquid
- 4 to 1 Evaporation (heat addition) of mixture to superheated vapour

Table 8 Basic VCC and Thermodynamic Process Formula

Component Process	Equations	
Compressor Power	$W_{comp} = \dot{m}_{ref}\ (h_2 - h_1) = VI$	[4]
Condenser Heat Load	$\dot{Q}_{cond} = \dot{m}_{ref}\ (h_2 - h_3)$	[5]
Heat Sink	$\dot{Q}_{cond,w} = \dot{Q}_{cond} = \dot{m}_w\ Cp_w\ (T_{w,out} - T_{w,in})$	[6]
Expansion Valve	$W_{expa} = 0 \quad \therefore \quad h_3 = h_4$	[7]
Evaporator Heat Load	$\dot{Q}_{evap} = \dot{m}_{ref}\ (h_1 - h_4)$	[8]
Heat Source	$\dot{Q}_{evap,w} = \dot{Q}_{evap} = \dot{m}_w\ Cp_w\ (T_{w,in} - T_{w,out})$	[9]

1.2 Operating Conditions

The compressor operating condition data used for this mathematical calculations were for the operation of Boyard HC208DC48H variable speed compressor. These operating conditions, presented in Table 3, were the result of testing performed by the compressor manufacturer. The compressor utilizes a DC inverter to vary the speed based on the cooling needed and overall system operation conditions.

Table 3 Compressor test operating conditions and outcomes obtained from manufacture for Boyard HC208DC48H variable speed compressor

Tested Operation Conditions and Outcomes		
Working Fluid	R134A	
Heat Transfer Area, **A**	0.368	m^2
Ambient Temperature, $\boldsymbol{T_{amb}}$	35	°C
Evaporating Temperature, $\boldsymbol{T_{evap}}$	10	°C
Degree of Superheat	11.1	°C
Condensing Temperature, $\boldsymbol{T_{cond}}$	54.4	°C
Subcooling Temperature, $\boldsymbol{T_3}$	46.4	°C
Cooling Capacity, $\boldsymbol{\dot{Q}_{evap}}$	2500	W
Compressor Speed, RPM	2500	RPM
Compressor Power consumption, $\boldsymbol{W_{comp}}$	800	W
Compressor Current, I	16.65	A
COP	3.1	-
Identified Operating Conditions		
Evaporating Pressure, $\boldsymbol{P_{evap}}$	1.45	MPa
Condensing Pressure, $\boldsymbol{P_{cond}}$	0.415	MPa

Evaporating and condensing pressures were identified based on evaporating and condensing temperature using the property tables for working fluid, R134a.

The test operating conditions obtained from the compressor manufacturer were applied into the condenser and evaporator simulation for the replication of the basic VCC using the heat exchanger manufacturer's data. The heat exchangers (condenser, evaporator and the LSLHX) used for this mathematical calculations were SWEP BX8THX18 plate heat exchangers.

Plate heat exchangers were used so that water could be used as heat source and heat sink. This was because water provided better control over the mass flow rate. Also, Plate heat exchangers provide a more controlled and closed volume which is influenced much less by the external environment, unlike for example using fans and air. Moreover, plate heat exchangers facilitates a constant heat exchange area.

1.3 Basic Vapor Compression Cycle Simulation

Manufacturer of the heat exchangers (condenser, evaporator, and LSLHX) provided a data system which allow to simulate the operation conditions of the condenser and the evaporator based on known parameters. Hence using the tested

compressor operation conditions, the evaporator and condenser operations were simulated.

Tables 4 and 5 shows the input conditions and the generated output conditions for the evaporator respectively. Initially, the evaporator was simulated as more input data for evaporator simulation was known.

Table 4 Input Conditions for the Evaporator.

Basic VCC - Evaporator Simulation		
Input Data		
Evaporating Temperature, $\boldsymbol{T_{evap}}$	10	°C
Subcooled liquid temperature, $\boldsymbol{T_3}$	46.4	°C
Cooling load, $\boldsymbol{\dot{Q}_{evap}}$	2500	W
Degree of super heating	11.1	°C
Evaporator outlet vapour quality	1	-
Water inlet temperature, $\boldsymbol{T_{evap,w,in}}$	28	°C
Refrigerant pressure drop, $\Delta\boldsymbol{Pd_{evap,ref}}$	15	kPa
Water pressure drop, $\Delta\boldsymbol{Pd_{evap,w}}$	15	kPa

Table 5 Generated Output Conditions for the Evaporator.

Output Data		
Evaporator inlet temperature, $\boldsymbol{T_4}$	10.41	°C
Evaporator outlet temperature, $\boldsymbol{T_1}$	21.15	°C
Water outlet temperature, $\boldsymbol{T_{evap,w,out}}$	11.6	°C
Refrigerant mass flowrate, $\boldsymbol{\dot{m}_{ref}}$	0.01681	kg/s
Water mass flowrate, $\boldsymbol{\dot{m}_w}$	0.03644	kg/s
Heat Capacity of evaporator water, $\boldsymbol{C_{p\,evap,w}}$	4.178	kJ/kg.°C

Tables 6 and 7 shows the input conditions and the generated output conditions for the condenser respectively. Then, the simulation for the condenser was performed. Condenser was simulated second because the condenser input temperature, T_2, was unknown. Once the evaporator simulation was performed and the evaporator exit temperature, T_1 was identified. Using the evaporator exit temperature, T_1, the enthalpy of state 1, h_1, was found.

Table 6 Input Conditions for the Condenser.

Basic VCC - Condenser Simulation		
Input Data		
Condensing Temperature, $\boldsymbol{T_{evap}}$	10	°C
Condenser inlet Temperature, $\boldsymbol{T_2}$	88	°C
Subcooled liquid temperature, $\boldsymbol{T_3}$	46.4	°C
Degree of subcooling	8	°C
Condenser inlet vapour quality	1	-
Water inlet temperature, $\boldsymbol{T_{cond,w,in}}$	28	°C
Refrigerant pressure drop, $\Delta\boldsymbol{Pd_{cond,ref}}$	15	kPa
Water pressure drop, $\Delta\boldsymbol{Pd_{cond,w}}$	15	kPa

Assuming compressor isentropic efficiency is 1, the compressor power was 800W and the mass flow rate to be 0.01681 kg/sec from evaporator simulation, the enthalpy at state 2, h_2, was found for the condenser pressure. Using the enthalpy at state 2, h_2, the compressor discharge (state 2) temperature, T_2, was found. Then the simulation for the condenser was performed.

Table 7 Input Conditions for the Condenser.

Output Data		
Water outlet temperature, $\boldsymbol{T_{evap,w,out}}$	50	°C
Heating load, $\boldsymbol{\dot{Q}_{cond}}$	3.32	W
Water outlet temperature, $\boldsymbol{T_{cond,w,out}}$	55	°C
Refrigerant mass flowrate, $\boldsymbol{\dot{m}_{ref}}$	0.01681	kg/s
Water mass flowrate, $\boldsymbol{\dot{m}_{w}}$	0.03644	kg/s
Heat Capacity of condenser water, $\boldsymbol{C_{p\,cond,w}}$	4.183	kJ/kg.°C

Temperatures at the evaporator input, T_4, and output, T_1, was found to be 10.41°C and 21.15°C. Using the property tables for R134a, enthalpy at the evaporator input, h_4 and the output, h_1, was found to be 266 kJ/kg and 416 kJ/kg respectively. Then, by substituting Eq. 8 in to Eq. 1, the simulated COP of the system

$$COP_s = \frac{\dot{m}_{ref}\,(h_1 - h_4)}{W} = \frac{0.01681\,(414 - 266)}{0.8} = \frac{0.0261}{0.8} \approx 3.1$$

The COP_s produced from the simulated data was equivalent to the COP provided by the manufactures testing. As the steady state basic VCC was simulated, the LSLHX was included.

1.4 LSLHX Vapor Compression Cycle

Liquid-Suction-Line heat exchanger (LSLHX) is used in a VCC to transfer heat from the high pressure subcooled liquid exiting from the condenser to the superheated vapour exiting the evaporator (or suction of the compressor) as seen in Fig. 3.

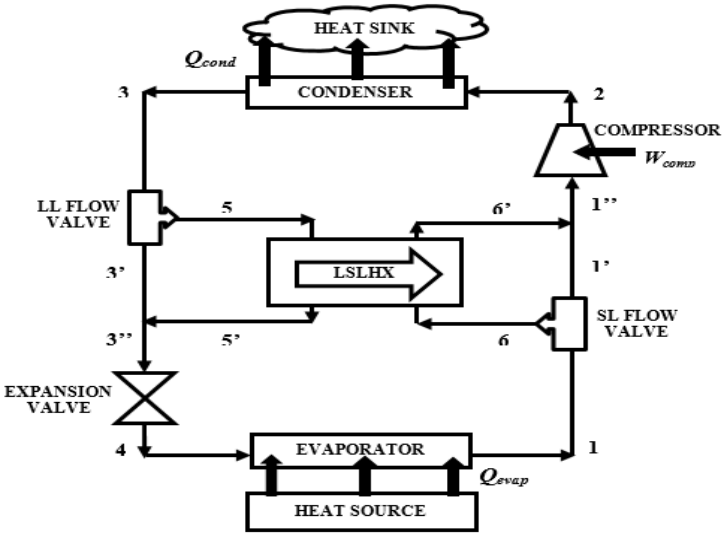


Figure 25 Liquid-Suction-Line Heat Exchanger Vapour Compression Cycle

Compressor

The rate of compressor work done or the power input to the compressor, W'_{comp}, is electrical and is as in Eq. 10.

$$W_{comp} = \dot{m}_{ref}\,(h_2 - h_{1''}) = VI \qquad [10]$$

Condenser

The rate of heat rejection, $\dot{Q}'_{cond}$, across the condenser with the LSLHX is as in Eq. 11.

$$\dot{Q}_{cond} = \dot{m}_{ref}\,(h_2 - h_3) \qquad [11]$$

The rate of heat absorbed by the heat sink water is equal to the heat rejected by the condenser, $\dot{Q}_{cond}$, across the condenser is as in Eq. 12.

$$\dot{Q}_{cond,w} = \dot{Q}_{cond}$$

$$\dot{Q}_{cond,w} = \dot{m}_{w,cond}\,C_{p\,cond,w}\,(T_{cond,w,out} - T_{cond,w,in}) \qquad [12]$$

Liquid Line Flow Distribution

The subcooled liquid at stage 3 is distributed between the main liquid line and the LSLHX liquid inlet line using the LL flow valve as in Fig. 3. Assuming X percent of the mass flow rate flows into the LSLHX liquid inlet line at stage 5 as in Eq. 13.

$$\dot{m}_{ref,5} = X\dot{m}_{ref} \qquad [13]$$

$$\dot{m}_{ref,3'} = (1 - X)\dot{m}_{ref} \qquad [14]$$

$$\dot{m}_{ref} = \dot{m}_{ref,5} + \dot{m}_{ref,3'} \qquad [15]$$

Heat transferred from the liquid line of the LSLHX is as in Eq. 16.

$$\dot{Q}_{lslhx,ll} = \dot{m}_{ref} (h_5 - h_{5\prime}) \quad [16]$$

The temperature at the expansion valve inlet, $T_{3''}$, was obtained using Eq. 17.

$$T_{3\prime\prime} = \frac{T_{5\prime} \dot{m}_{ref,5} + T_1 \dot{m}_{ref,3\prime}}{\dot{m}_{ref}} \quad [17]$$

The enthalpy at the expansion valve inlet, $h_{3''}$, is enthalpy at temperature at the expansion valve inlet, $T_{3''}$, and condenser pressure.

$$h_{3\prime\prime} = h \qquad @\ T_{3\prime\prime}\ \&\ P_{cond}$$

Expansion Valve

Assuming that the expansion process is isentropic and adiabatic, there is no work done across the expansion device. Hence, the enthalpy at the condenser exit and evaporator inlet is the same as in Eq. 18.

$$h_{3\prime\prime} = h_4 \quad [18]$$

$$W_{expa} = 0$$

Evaporator

The rate of heat absorption, $\dot{Q}_{evap}$, across the evaporator with the LSLHX is as in Eq. 19.

$$\dot{Q}_{evap} = \dot{m}_{ref} (h_1 - h_4) \quad [19]$$

The rate of heat rejected by the heat source water is equal to the heat absorbed by the condenser, $\dot{Q}'_{evap}$, across the condenser is as in Eq. 20.

$$\dot{Q}'_{evap,w} = \dot{Q}'_{evap}$$

$$\dot{Q}'_{evap,w} = \dot{m}_{w,evap} C'_{p\ evap,w} (T'_{evap,w,in} - T'_{evap,w,out}) \quad [20]$$

Suction Line Flow Distribution

The superheated vapour at stage 1 is distributed between the main liquid line and LSLHX liquid inlet line using the SL flow valve as in Fig. 3. Assuming Y percent of the mass flow rate flows into the LSLHX liquid inlet line at stage 5 as in Eq. 21.

$$\dot{m}_{ref,6} = Y\dot{m}_{ref} \quad [21]$$

$$\dot{m}_{ref,1'} = (1 - Y)\dot{m}_{ref} \quad [22]$$

$$\dot{m}_{ref} = \dot{m}_{ref,6} + \dot{m}_{ref,1'} \quad [23]$$

Heat absorbed by the suction line of the LSLHX depends on the effectiveness, ε, of the LSLHX used, which is found using the Eq. 24. The heat absorbed by the suction line of the LSLHX can also be found using Eq. 25.

$$\dot{Q}_{lslhx,sl} = \varepsilon\, \dot{Q}_{lslhx,ll}$$

$$\varepsilon = \frac{(T_{6'} - T_6)}{(T_5 - T_6)} \quad [24]$$

$$\dot{Q}_{lslhx,sl} = \dot{m}_{ref}\,(h_{1'} - h_1) \quad [25]$$

The temperature at the compressor suction, $T_{1''}$, was obtained using Eq. 26.

$$T_{1''} = \frac{T_{6'}\,\dot{m}_{ref,6} + T_1\,\dot{m}_{ref,1'}}{\dot{m}_{ref}} \quad [26]$$

The enthalpy at the expansion valve inlet, $h_{3''}$, is enthalpy at temperature at the expansion valve inlet, $T_{3''}$, and condenser pressure.

$$h_{1''} = h \qquad @\ T_{1''}\ \&\ P_{evap}$$

1.5 LSLHX Vapor Compression Cycle Simulation

The simulations for the LSLHX was performed based on the operation conditions of the steady state basic VCC. The operation conditions seen in Table 7 was simulated for the LSLHX with varying mass flow rates percentages into the liquid LSLHX line and suction LSLHX line, X and Y respectively. The remaining mass on both side flow in the basic VCC line. For the simulations, X was tested at every 10% interval from 0% to 100%. Similarly, for every X, the Y was also tested at every 10% interval from 0% to 100%. The outcome of the simulations would be elaborated in section 3.

2 Results and Discussions

Following the simulations of the LSLHX VCC operations by varying the liquid line mass flow, X, from 0-100% and for each X, varying the suction mass flow, Y, from 0-100%, the data was presented.

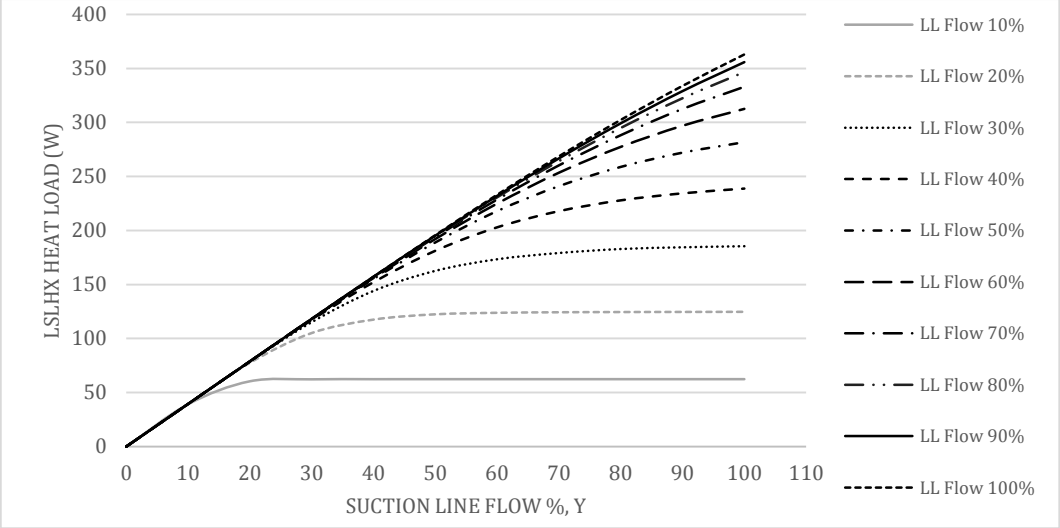


Figure 26 LSLHX Heat Load vs. LSLHX Suction Line Mass Flow Percentages

The temperatures of the working fluid entering the LSLHX at both liquid and suction line, T_5 and T_6 respectively, was kept constant during the simulations. Hence, the output temperatures, T_5' and T_6' respectively, depended solely on the mass flow with in the two channels of the LSLHX. As see in Fig. 4, the heat load across the LSLHX showed a linear behavior when liquid line flow was higher than or equal to the suction line flow ($X \geq Y$). On the other hand, it was observed that the heat load tended to approach a constant value as the liquid line flow was lower than the suction line flow ($X<Y$). This was mainly because the maximum amount of heat rejected by the liquid line at a given X percentage was constant. And therefore, as long as the liquid line flow was lower than the suction line flow ($X<Y$), the maximum heat transfer would always occur. Maximum heat load was observed at 100% flow for both X and Y. This was simply because the maximum amount of heat rejection and heat absorption dependent on the highest possible flow for both X and Y.

The effectiveness of the LSLHX also depended on the flow across both channels. The effectiveness of the LSLHX was found to be as low as 20% when the liquid line flow was minimum (X=10%) and the suction line flow was maximum (Y=100%).

The subcooled liquid temperature or the expansion valve inlet temperature, T_3'', therefore depended LSLHX liquid line flow, X. The behavior of the subcooled liquid temperature is described in Fig. 5.

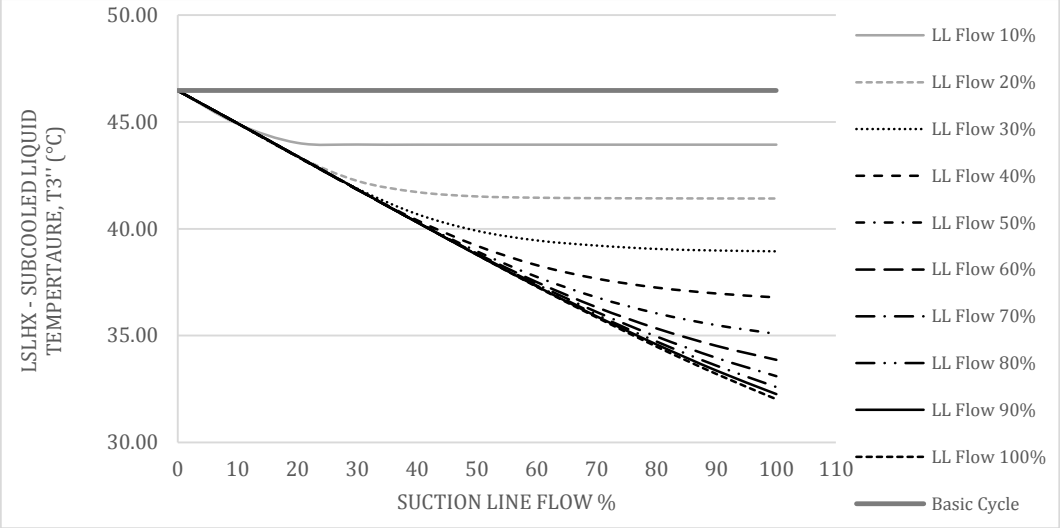


Figure 27 Expansion Inlet Temperature vs. LSLHX Suction Line Mass Flow Percentages

It was observed that the temperature of the subcooled liquid entering the expansion valve lowered linearly when the liquid line flow was higher than the suction line flow (X>Y). Subcooled liquid temperature also approaches a constant value when the suction flow rate is higher than the liquid line. This was a direct outcome of the constant maximum heat rejection possible for a given value of liquid line flow, X, which was described in Fig. 4.

Assuming a constant suction line flow, Y, the subcooled liquid temperature, T_3'', depended on the ratio of mass flow distribution between the LSLHX liquid line and the basic liquid line. Therefore, if the mass flow with the LSLHX liquid line was higher than the basic liquid line flow, (X > (1-X)), the LSLHX liquid line have a more prominent effect on the subcooled liquid temperature, T_3''. Similarly, if the mass flow with the LSLHX liquid line was lower than the basic liquid line flow, (X < (1-X)), the basic liquid line have a more prominent effect on the subcooled liquid temperature, T_3''. When X and Y was 100%, the subcooled liquid temperature dropped down to 32°C as compare to the 46.47°C of the basic VCC cycle. Additionally, as found by Klein, et al., (2000), the evaporator cooling capacity was improved in spite of the pressure drop for every combination of X and Y.

Similarly, the suction vapour temperature, T_1'', depended LSLHX suction line flow, Y. The behavior of the suction vapour temperature is described in Fig. 6.

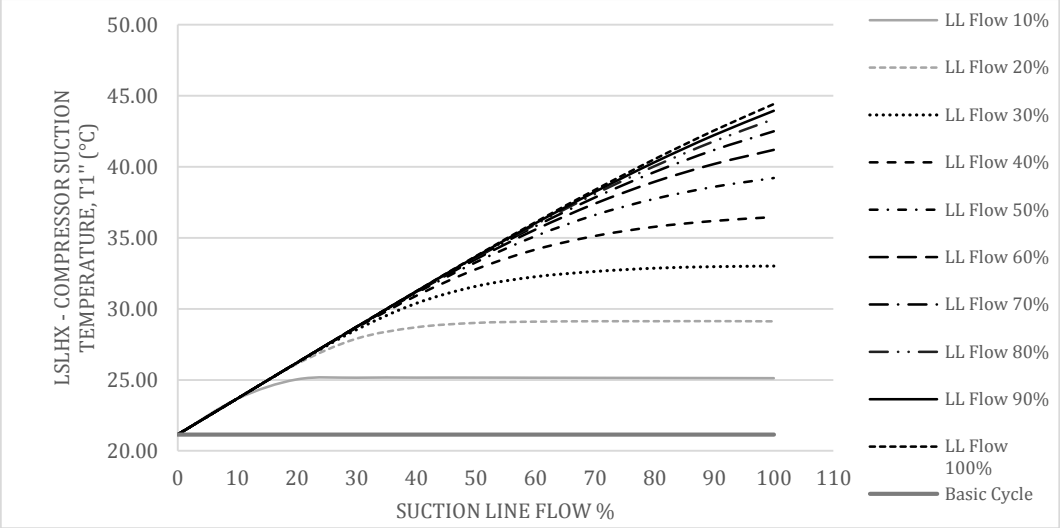


Figure 28 Compressor Suction Temperature vs. LSLHX Suction Line Mass Flow Percentages

The temperature of the suction vapour rose linearly when the liquid line flow was higher than the suction line flow (X>Y). Suction vapour temperature also approaches a constant value when the suction flow rate is higher than the liquid line. This was a direct outcome of the constant maximum heat rejection possible for a given value of liquid line flow, X, which was described in Fig. 4.

Assuming a constant liquid line flow, X, the suction vapour temperature, T_1'', depended on the ratio of mass flow distribution between the LSLHX suction line and the basic suciton line. Therefore, if the mass flow with the LSLHX suction line was higher than the basic liquid line flow, (Y > (1-Y)), the LSLHX suction line have a more prominent effect on the suction vapour temperature, T_1''. Similarly, if the mass flow with the LSLHX suction line was lower than the basic suction line flow, (Y < (1-Y)), the basic suction line have a more prominent effect on the suction vapour temperature, T_1''. When X and Y was 100%, the suction vapour temperature rose to 44.41°C as compare to the 21.15°C of the basic VCC cycle.

The pressure drop on the LSLHX vapour line was however an effecting factor to the overall COP of the system. Due to the pressure drop and rise in temperature, the mass flow of the suction vapour reduced. Klein, et al., (2000) indicated that this in fact would reduce the compressor work. However, he highlight that the net compressor work would increase due to the pressure drop increasing the compression ratio and ultimately reducing the overall COP of the system.

The Fig. 7 describes the changes in the cooling capacity for different combinations of mass flow in the liquid and suction line of the LSLHX, X and Y respectively, with and without the internal pressure drop considered.

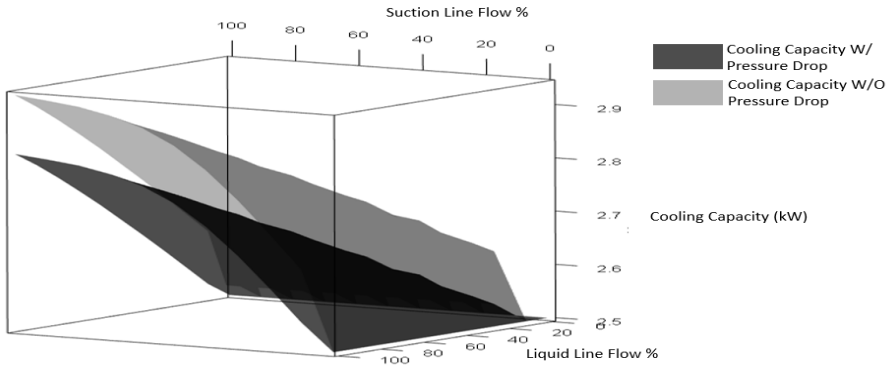


Figure 29 Effect of Pressure Drop on the Cooling Capacity with Variable Mass Flow within the LSLHX.

From the Fig. 7, it can be seen in the maximum cooling capacity improvement achieved was when both the liquid and suction line flow, X and Y respectively, was 100% despite the pressure drop consideration. The cooling capacity improvement with pressure drop considered was attained from the simulation for a constant pressure drop of 15 kPa. Neglecting the pressure drop, the achievable cooling capacity values were calculated using Eq. 2 formulated by Klein, et al., (2000).

The maximum cooling capacity achievable by neglecting the pressure drop was 2.94 kW and this was an improvement of 17.59% as compared to the 2.5 kW of the basic VCC cycle. However, taking the pressure drop into considetaion, the improvement on the cooling capacity was reduced to 2.83 kW and this was a 13.16% as compare to the 2.5 kW of the basic VCC cycle.

The Fig. 8 describes the changes in the COP for different combinations of mass flow in the liquid and suction line of the LSLHX, X and Y respectively, with and without the internal pressure drop considered.

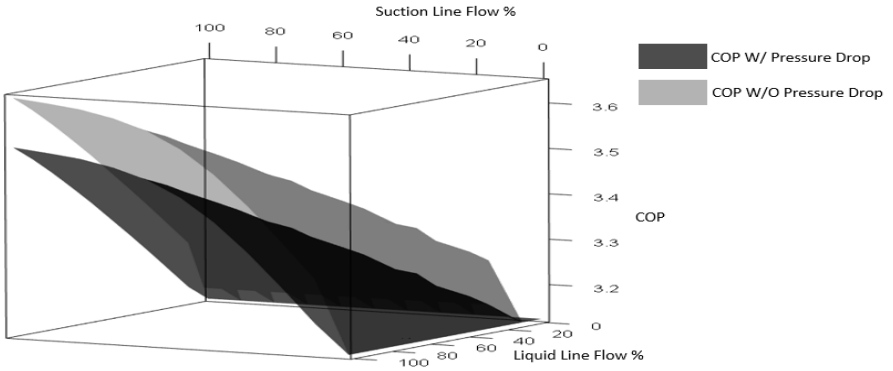


Figure 30 Effect of Pressure Drop on the Coefficient of Performance with Variable Mass Flow within the LSLHX.

From the Fig. 8, it can be seen in the maximum COP improvement achieved was when both the liquid and suction line flow, X and Y respectively, was 100% despite the pressure drop consideration. The COP improvement with pressure drop considered was attained from the simulation for a constant pressure drop of 15 kPa.

Neglecting the pressure drop, the achievable COP values were calculated using Eq. 3 formulated by Klein, et al., (2000).

The maximum COP achievable by neglecting the pressure drop was 3.65 and this was an improvement of 17.6% as compared to the 3.1 of the basic VCC cycle. However, taking the pressure drop into considetaion, the improvement on the cooling capacity was reduced to 3.54 and this was a 14.07% as compare to the 3.1 of the basic VCC cycle.

The necessary additional compressor power required to compensate for the pressure drop was calculated by diving the Eq. 3 by Eq. 2. As a result of having a fixed pressure drop, it was found that the increase in compresor power was a fixed amount of 6.4 W for all combinations of X and Y, which was only a 0.8% rise. The drop in COP was not significant when the pressure drop was taken into consideration because the pressure drop was assumed to be a constant value. However, in real life applications, the pressure drop with in the LSLHX would vary depending on the mass flow into the LSLHX. Therefore, for higher pressure drops, a higher amount of additoinal compressore would be require.

In order to further investigate the direct relationship between the pressure drop and the additional compressor power required, the this same simulation could be performed by fixating different pressure drop values for example 30 kPa, 45 kPa, etc. Additional experimental work could be performed to identify the optimal cooling capacity and power increase to achieve an optimize the COP for the overall system.

3 Conclusion

Hence, it could be concluded that varying the mass flow within the LSLHX had a positive effect on the cooling capacity of the system and the pressure drop within the LSLHX had a negative effect on the COP sure to additional compressor power required for the increased pressure ratios.

- Heal Load across the LSLHX approached a maximum when liquid line flow was equal to suction line flow (X=Y)
- Cooling capacity of the system could be improved using the LSLHX despite drop in internal pressure.
- Cooling capacity improved upto 2.94 kW and 2.83 kW or by 17.59% and 13.16% without and with the pressure drop considered respectively, as compare to the 2.5 kW the basic VCC cycle.
- Coefficient of Performance (COP) improved upto 3.65 and 3.54 or by 17.6% and 14.07% without and with the pressure drop considered respectively, as compare to the 2.5 kW the basic VCC cycle.
- Additional 6.7 W of power was required by the compressors to compensate for the 15 kPa of pressure.

References

Darabi, Z., & Ferdowsi, M. (2011). Aggregated Impact of Plug-in Hybrid Electric Vehicles on Electricity Demand Profile. *IEEE Transactions on Sustainable Energy , 2* (4), 501-508.
Malaysian-German Chamber of Commerce and Industry. (2011). 1st Malaysian-German Sustainable Automotive Mobility Conference. *Sustainable Mobility Conference.* Kuala Lumpur.
Gruber, W., Bäck, W., & Amrhein, W. (2011). Design and implementation of a wheel hub motor for an electric scooter. *2011 IEEE Vehicle Power and Propulsion Conference.* Chicago, IL.
Tie, S. F., & Tan, C. W. (2013). A review of energy sources and energy management system in electric vehicles. *Renewable and Sustainable Energy Reviews , 20*, 82-102.
Yong, J. Y., Ramachandaramurthy, V. K., Tan, K. M., Mithulananthan, & N. (2015). A review on the state-of-the-art technologies of electric vehicle, its impacts and prospects. *Renewable and Sustainable Energy Reviews , 49*, 365-385.
H. R. Cha, K. J. Shin and Y. J. Seo. (2011). Design of outer rotor IPM type PMSM for 3 wheel electric vehicle. *2011 International Conference on Electrical Machines and Systems.* Beijing.
D. Fodorean, D. C. Popa, P. Minciunescu, C. Irimia and L. Szabó. (2014). Study of a high-speed motorization for electric vehicle based on PMSM, IM and VRSM. *2014 International Conference on Electrical Machines (ICEM).* Berlin.
Rahman, M. A., & Masrur, M. A. (2009). Advances on IPM technology for hybrid electric vehicles. *2009 IEEE Vehicle Power and Propulsion Conference.* Dearborn, MI.
M. Cheng, W. Hua, J. Zhang and W. Zhao. (2011). Overview of Stator-Permanent Magnet Brushless Machines. *IEEE Transactions on Industrial Electronics , 58* (11), 50087-5101.
W. Xu, J. Zhu, Y. Guo, S. Wang, Y. Wang and Z. Shi. (2009). Survey on electrical machines in electrical vehicles. *International Conference on Applied Superconductivity and Electromagnetic Devices.* Chengdu.
Chu, C. L., Tsai, M. C., & Chen, H. Y. (2001). Torque control of brushless DC motors applied to electric vehicles. *Electric Machines and Drives Conference, 2001. IEMDC 2001. IEEE International* (pp. 82-87). Cambridge, MA: 2001. IEMDC 2001. IEEE International.
Ehsani, M., Gao, Y., & Gay, S. (2003). Characterization of electric motor drives for traction applications. *Industrial Electronics Society, 2003. IECON '03. The 29th Annual Conference of the IEEE. 1*, pp. 891-896. The 29th Annual Conference of the IEEE.
V, A. C., Norhisam, M., Aris, I., Marhaban, M. H., Ahmad, D., & Nirei, M. (2011). Double-Rotor Switched Reluctance Machine (DRSRM): Fundamentals and magnetic circuit analysis. *2011 IEEE Student Conference on Research and Development.*
Niu, S., Ho, S. L., & Fu, W. N. (2013). A Novel Double-Stator Double Rotor Brushless Electrical Continuously Variable Transmission System. *49* (7).
Griffin, M. (1990). *Handbook of Human Vibration* . San Diego: Academic Press Limited.
I. Hostens, Y. P. (2003). A study of vibration characteristics on a luxury wheelchair and a new prototype wheelchair. *Journal of Sound & Vibration , 266*, 443-452.
T. Ramachandran, K. P. (2012). Review on Internal Combustion Engine Vibrations and Mountings. *International Journal of Engineering Sciences & Emerging Technologies , 3* (1), 63-73.
Griffin, G. P. (2009). Evaluation of Whole Body Vibration and RIde Comfort in a Passenger Car. *International Journal of Acoustics and Vibration , 14* (1), 143-149.
Yunhe Yu, N. G. (2001). Review of automotive vehicle engine mounting systems. *Mechanism and Machine Theory , 36*, 123-142.
Jasvir Singh Dhillon, P. R. (2014). Design of Engine Mount Bracket for a FSAE Car Using Finite Element Analysis. *International Journal of Engineering Reseach and Application , 4* (9), 74-81.
Conti, P. a. (1989). Mount Stiffness and Inertia Properties from Modal Test Data. *ASME Journal of Vibration and Acoustics, Stress and Reliability in Design , 111*, 134-141.
Chung-Ha Suh, C. G. (1997). Dynamic Simulation of Engine-Mount Systems. *SAE International* , 561-572.
Brick7. (2010). The Motorcycle Search Engine. South Africa: Brick 7.
Kjær, B. &. (1998). *Vibration Transducers and Signal Conditioning.* Brüel & Kjær Sound Vibration Measurement A/S.
Bracewell, R. N. (1989). The Fourier Transorm. *Scientific American* , 86-95.
S.Rao, S. (2011). *Mechanical Vibration.* Miami: Prentice Hall.
Frederick, J. T. (2011, March 29). *Auburn University Electronic Theses and Dissertations.* Retrieved November 20, 2016, from http://etd.auburn.edu/handle/10415/2488
Nolan, P. (n.d.). *Farmingdale University.* Retrieved October 31, 2016, from www.farmingdale.edu/faculty/peter-nolan/pdf/UPCh13.pdf

International, S. (2016). *2016 Formula SAE Rules.* SAE International.
Damavandi, M., Dalleau, G., Stylianides, G., Rivard, C. H., & Allard, P. (2013). Head and Trunk mass and center of mass position estimates in able-bodied and scoliotic girls. *Medical Engineering & Physics , 35*, 1607-1612.
Park, J. Y., Park, G. D., Lee, S. G., & Lee, J. C. (2013). The Effect of Scoliosis Angle on Center of Gravity Sway. *Journal of Physical Therapy Science , 25* (12), 1629-1631.
K, H., I, G., & G, L. (2013). Developing a 3D Multi-Body Model of the Scolitic Spine with Lateral Bending Motion for Comparison of Ribcage Flexibility. *International Journal of Advanced Design and Manufacturing Technology , 6* (1), 25-32.
Carvalho de Abreu, D. C., Gomes, M. M., Rocha de Santiago, H. A., Pereira da Silva Herrero, C. F., Porto, M. A., & Luiz, H. (2012). What is the influence of surgical treatment of adolescent idiopathic scoliosis on postural control? *Gait & Posture , 36*, 586-590.
Trobisch, P. D., Samdani, A. F., Pahys, J. M., & Cahill, P. J. (2011). Postoperative trunk shift in Lenke 1 and 2 curves: how common is it? and analysis of risk factors. *European Spine Journal , 20*, 1820-1828.
Richards, B. S., Scaduto, A., Vanderhave, K., & Browne, R. (2005). Assessment of Trunk Balance in Thoracic Scoliosis. *The Spine Journal , 30* (14), 1621-1626.
Karami, M., Maleki, A., & Mazda, K. (2016). Assessment of Coronal Radiographic Parameters of the Spine in the Treatment of Adolescent Isiopathic Scoliosis. *Archives of Bone and Joint Surgery , 4* (4), 376-380.
Ameri, E., Ghandhari, H., Nabizadeh, N., & Hesarikia, H. (2014). Natural history of coronal balance after spinal fusion in adolescent idiopathic scoliosis. *Shafa Orthopedic Journal , 1* (2), 12-16.
Siderakis, N., Rosado, J. P., Aguilar, A., Dinelli, D., Lutzky, L., Reviriego, J., et al. (2013). Analysis of coronal balance and last level of arthrodesis in lenke type 5 idiopathic scoliosis: Specific radiographic parameters. *Coluna/Columna , 12* (4), 296-299.
Hellems, K., & Keats, T. (1971). Measurement of the Normal Lumbosacral Angle. *American Journal of Roentgenology , 113* (4), 642-645.
Lippert, L. S. (2011). *Clinical Kinesiology and Anatomy* (5 ed.). Philadelphia, Pennsylvania, United States of America: F. A. Davis Company.
Smith, L. K., Weiss, E. L., & Lehmkuhl, L. D. (1998). *Brunnstrom's Clinical Kinesiology* (1 ed.). New Delhi, New Delhi, India: Jaypee Brothers Medical Publishers (P) LTD.
Pasha, S., Aubin, C., Labelle, H., Parent, S., & Mac Thiong, J. (2015). The biomechanical effects of spinal fusion on the sacral loading in adolescent idiopathic scoliosis. *Clinical Biomechanics , 30*, 981-987.
Nohara, A., Kawakami, N., Seki, K., Tsuji, T., Ohara, T., Saito, T., et al. (2015). The Effects of Spinal Fusion on Lumbar Disc Degeneration in Patients with Adolescent Idiopathic Scoliosis: A Minimum 10-Year Follow-Up. *Spine Deformity , 3*, 462-468.
Tözeren, A. (2000). *Human Body Dynamics: Classical Mechanics and Human Movement.* York, Pennsylvania, United States of America: Springer.
Wilke, H. J., Neef, P., Caimi, M., Hoogland, T., & Claes, L. E. (1999). New In Vivo Measurements of Pressures in the Intervertebral Disc in Daily Life. *SPINE , 24* (8), 755-762.
Perez-Lombard, L., Ortiz, J., & Pout, C. (2008). A review on buildings energy consumption information. *Energy and Building , 40* (3), 394–398.
Park, C., Lee, H., Hwang, Y., & Radermacher, R. (2015). Recent Advances in Vapor Compression Cycle Technologies. *International Journal of Refrigeration , 60* (1), 118-134.
Klein, S. A., Reindl, D. T., & Brownell, K. (2000). Refrigeration System Performance using Liquid-Suction Heat Exchangers. *International Journal of Refrigeration , 23* (8), 588-596.
Navarro-Esbrí, J., Molés, F., & Barragán-Cervera, A. (2013). Experimental Analysis of the Internal Heat Exchanger Influence on a Vapour Compression System Performance Working with R1234yf as a Drop-in Replacement for R134a. *Applied Thermal Engineering , 59* (1-2), 153-161.
Pottker, G., & Hrnjak, P. (2015b). Experimental Investigation of the Effect of Condenser Subcooling in R134a and R1234yf Air Conditioning Systems With and Without Internal Heat Exchanger. *International Journal of Refrigeration , 50* (1), 104-113.
Cho, H., Lee, H., & Park, C. (2013). Performance Characteristics of an Automobile Air Conditioning System with Internal Heat Exchanger using Refrigerant R1234yf. *Applied Thermal Engineering , 61* (1), 563-569.
Jiang, S., Wang, S., Jin, X., & Zhang, T. (2015). A General Model for Two-Stage Vapor Compression Heat Pump Systems. *International Journal of Refrigeration , 51* (1), 88-102.

Naif, A., Al-Obaidi, A., & Nassir, M. (2015). Effect of Evaporator Heater Power Input and Refrigerant Flow Rate on the Performance of a Refrigerator - Developing Emipirical Model. *Journal of Mechanical Engineering and Automation , 5* (1), 20-28.
Building & Construction Authority. (2007). *Green Building Design Guide.* Singapore: Building & Construction Authority.
Energy Information Administration. (2005). *United States Household Electricity Report.* Washington DC, USA: Energy Information Administration.

eureca 2016 – Conference Paper
Paper Number ME_PG02

Multidisciplinary Engineering Design for Sustainable Development and a Learning Landscape: A critical experience from Engineering Educators

Jayasubamani Arvi N. S.Moganakrishnan[1*], Satesh Narayana Namasivayam[2], Nurhazwani Ismail[3]

[1,2,3] School of Engineering, Taylor's University Lakeside Campus, Malaysia

jayasubamaniarvismoganakrishnan@sd.taylors.edu.my

Abstract
In 2015, Malaysia experienced difficult development situations which caused public outcry for safer, healthier and protected environment due to flood disasters, air pollution from haze and alarming dengue cases. These situations have become pressing issues urging the response of better engineering solutions. Thus, it invites participation of competent engineers to help develop transformative solutions for a sustainable future. However, how have our young engineers‟ knowledge, skills and attitude been developed to participate in such platforms and present ideas in their purpose towards addressing the challenges of Malaysian society today. In this paper we address how we as engineering educators at Taylor's University School of Engineering (SOE) embrace curriculum development for sustainable development. The paper was written in critical ethnographic approach in order to express our critical experience as a creative participatory process with core interest in learning to design for SD. Details of the planning, implementation and post implementation is constructed with us detailing our experience as critically conscious educators. Our critical conscious approach drove a multidisciplinary design project from a niche to a widely participated learning landscape which could accommodate engineers and those from other discipline who are interested in the agenda of SD. For professional education linking to sustainable agency, we were able to consult by engaging with sustainable businesses in order for us to enact on our own community in Taylor's through the learning landscape initiative. Although the initiative is at early development, this paper details what forms our critical perspective and thus, paves the way for readers to understand the potential of incubated environment for personalized learning and engineering education for SD.

Keyword : engineering education, multidisciplinary, design, sustainable development

1.0 Introduction

In 2015, Malaysia experienced difficult development situations which caused public outcry for safer, healthier and protected environment due to flood disasters, air pollution from haze and alarming dengue cases [1]–[3]. These situations have become pressing issues urging the response of better engineering solutions. Thus, it invites participation of competent engineers to help develop transformative solutions for a sustainable future. Idea generation platforms involving engineering students were among the measures undertaken by the ministry to encourage participation of young Malaysian engineers in the urge to design and build technological solutions for the complex challenges [4]. However, how have our young engineers‟ knowledge, skills and attitude been developed to participate in such platforms and present ideas in their purpose towards addressing the challenges of Malaysian society today?

New generation engineers are urged to be at the forefront of solving complex societal problems but how are our educational approaches equipping them to do so? Fundamental changes have occurred in the nature of the work of engineers due to changing work circumstances [5], [6]. They are no longer technical problem solvers only [5]. Following the necessity to address the complexity of the operational dimensions have expanded their roles to accommodate the demand of the non-technical dimensions as well [5], [6]. The changes in the work situations are the result of recognizing society's biggest challenges and the respective roles that professionals and citizens have to play in the name of sustainable development (SD) [7], [8]. In recent years, SD is a global agenda addressing society's most urgent problem situations, politically providing opportunities for the development of engineering solutions for human well-being [9]. As a result, there must be implications on the education system of engineers with pressure for the development of the new kind of engineer to play roles in these unfamiliar realms [9], [10].

Engineering Education for Sustainable Development (EESD) community have raised concern with regards to understanding of broad and varied content as well approaches pertinent to development of change agents in the engineering curriculum [9], [11], [12]. Thus, as engineering educators, how have we embraced the challenge of bringing imperative changes to our curriculum with regards to valuing and playing various roles in the complex context of SD?

Global SD goals and Grand Challenges of Engineering represent the global agenda for engineering education in the context of sustainable development. More design oriented curriculum have been suggested as the pathway particularly in order to cross boundaries of work in which we locate ourselves in situations where beyond engineering solutions are needed [11]. Thus, curriculum changes as we note in literature suggest the pathway from multidisciplinary cooperation to transdisciplinary collaboration for addressing a common issue of SD [11]. However, it is not discussed in terms of a bottom's up approach to construct a link from local efforts to a global agenda [13]. We lack experts on EESD within our community and thus, we lack critical understanding with regards to the kind of situations and issues which has formed this agenda and lack ability to be stewards for SD. We acknowledge ourselves as new players and thus have adopted changes as part of a bigger initiative (i.e conceive design implement operate (CDIO) initiative). Nevertheless, we wanted to be

able to seek a cause in SD which we could be involved in order to explore on what our role demanded through our education system.

The engineering module in Taylor's SOE which the curriculum development changes is envisioned is Multidisciplinary Engineering Design (MED). The module is semester three undergraduate engineering students who have prior engineering design learning experience in the previous two semesters. Thus, despite the grandeur of the task, as we seek more equitable opportunity to learn engineering, we find establishing a cause through participation could make our relationship with our students more meaningful as our students are centered. We also seek this cause in order for students to learn more than the traditional economic value bound designing of product.

Multidisciplinary engineering design within practice from literature are projects that require the cooperation of engineering students from multiple disciplines [14], [15]. The cooperation is necessary in order to coordinate the development of a project in which they work in parallel towards project completion. Learning from participation is contextual with the values innate to the situation. Within our experiences, we gather understanding on how some students value the design experience and others who value the connections they made while designing.

Within this paper, the creative process of linking SD goals and Grand Challenges of Engineering to a Multidisciplinary Engineering Design project is presented in its details. The process was undertaken within the current settings of curriculum at Taylor's School of Engineering. The following sections will detail the process leading to development of understanding with regards to establishing the link which has been identified imperative for EESD. The details of the process will be presented in the form of action and reflection in which we identify the educative content which could act as a heuristic to understanding the link between global agenda of SD for engineers and specific engineering learning area (i.e. multidisciplinary engineering design). We present a critical ethnographic study on the development of understanding leading to the learning to design for SD through participation in our local context.

1.1 Development of critical aim and methodology for this paper

This paper is written based on understanding derived from the engineering education research undertaken in the area of EESD. The research approach used is qualitative approach based on critical perspective [16]–[20]. Within this research process, we asked many critical questions [19] through ethnographic style [21]–[23] with regards to the practice in which both engineering educators and students participate to learn engineering design with the theme of SD. Ethnography is found useful when depicting details in cultural stance [21] which we could transfer from literature as audiences from a process perspective. This is appropriate for this study due to the nature of engineering design which is process based and reflects culture of engineers with regards to global engineering practice [24]. These were essential questions [25] that guided us to bigger questions in the political context on the use of engineering design to address grand problems in Malaysian society. A bigger identified question was "What is the value of multidisciplinary engineering design to the future of students who participate in this limited context ". The critical stance on the value of the design module to undergraduate engineering students has led to the consideration of changes on approaches within practice in order for us to 'think

globally and act locally'. We identified the following essential question in which we ask "In what context can we learn to design and recognize the far reaching consequences to global SD agenda from acting locally ". We used the concept of critical consciousness [19] as engineering educators who are responsible for education and change for SD as well as reflexively [26] considering our role as agents of SD in higher education context with regards to our community and the industry. The details on the participation in the process of implementing design for SD that undertook in our practice will be detailed in paper.

The aim of the paper is to detail the use a situational perspective in order to answer deeper questions on our educational practice. We refer to the understanding provided by Case & Light [27] in terms the importance of using qualitative approach to answer deeper questions about engineering education. As we explore the critical perspective through participatory research [28], [29] , we found value in being able to understand improvement through a communal understanding as we learn from participation with engineering educators and students [21].

2.0 Implementation of a multidisciplinary engineering design project and personalizing learning for SD

This section has been written to represent the process of planning, implementation and finally post implementation in which a learning landscape was identified for a common concern.

Learning landscape [30] in this context is a platform where students and educators articulate beyond engineering and business value on designing for a common concern in society in a multidimensional space. Within this study, teaching and learning spacious through the Great Toilet initiative being developed as post implementation strategy. We built an evolving vision to represent the total context of student and educator learning experience in the space of this initiative, a toilet in Taylor's University.

A common concern is referred to a social or environmental concern when a product is used in which for this study, it is about the vulnerability of cleaners and overconsumption of water as great sanitation problem [31]. We proceeded through the phases by raising essential questions in light of exploring the link with global agenda of SD. The final outcome provided an opportunity for us the educators to consider the building of partnership with community and industry through institutional effort [32].

2.1 Pre- implementation stage (contextualized planning)

Translating SD agenda into educative context requires a practical approach due to the contextualization of SD issues. Learning within this context is participatory [33] in which we situationally learn 'with and from each other'. Participation in this context was driven by bottom up approach [28] from the involvement of us as those concerned with vulnerability of human health and resource conservation within our institutional context.

a) Participation for SD

The dimensions of SD that is relevant to EESD is the operational [9]. Within the operational dimension, in terms of our social and cultural understanding of engineering identified with technology we are familiar with the concept of innovation and environmental sustainability with the advent of green technology and manufacturing [34]–[36]. However, we lack understanding in human-technological interface which form the social aspect of the operations for SD [9], [37]. We consider this limitation as an impediment to our conceptualization of being instrumental for SD as we are not familiar on proceeding to design and build in a context which is of multidisciplinary nature as well there is stake on the value for clients.

Thus, the first area of consideration was the context of the problem and our participation with client in order to define the problem with sensitivity towards what is valued within the context [38]. We considered the problem of cleaning as hazardous and physically straining activity for janitors in the con text of Taylor's SOE who participated with us and our students to convey what they are value in a tool that they could work with.

Participation is a common feature on engineering design which are contextualized [39]. A context such as the toilet accommodates and interact with many agents. As in our case, we chose the toilet and cleaners as those we would like to participate with. Through this project, we intend to serve the underserved community with better tools for productivity, health and safety. Developmental work is needed in this area they engaged in a participatory effort to understand "who to engage, why we need to engage, how we need to engage'. This is possible through the use of transdisciplinary perspective [40]–[42] when designing in which the design experience is contextualized to address specific user groups in a specific situation. This participatory effort is necessary to guide our brainstorming of project idea reflecting the agenda of SD.

Participation to understand project ideas however, was not a new addition to the culture of educational practice at Taylor's SOE. Thus, with the supportive embedded practice of continuous improvement processes (CQI) to ensure quality of education, we were able to embrace the newly arising challenges for learning through participation. In the CQI document for project idea proposal, an explicit link for Grand Challenges of Engineering has already been embedded in order to ensure projects are linked to the mentioned agenda. However,

b) Concern for sustainability and the multidisciplinary context

For EESD project idea development, we started with a broader concern relating to sustainability. Designing for sustainability identifies concern in terms of social and environmental aspects in a problem context where a technological solution is potentially feasible [38]. Sustainability problems ae complex and by nature, require explicit discussion on the disciplines involved and how they may contribute [9].

Multidisciplinary engineering design created the possibility of engaging students from different disciplinary background in addressing a common concern in parallel [14], [43], [44]. A more product and service oriented economy in which the

use of multidisciplinary engineering design has provided avenue for engineering schools to explore technological development areas as in innovation and product development [45]. The engineering practice of product development contribute to our understanding on parallel contribution of multiple disciplines which requires operationalization at the conceptual level [46].

Thus we question "How we can understand operationalization of various disciplines in addressing a social or environmental concern? We started with understanding how it was operationalized through various case studies on EESD in practice [12], [47], [48]. In practice however, we are limited in terms of our understanding on how our students would be able engage and enact from their disciplinary background in their effort to be instrumental for SD [49].

We agreed with the use of one article which was experimental setup for multidisciplinary collaboration provided us the ground to understand the nature of cooperation we are expecting from each discipline. This article was on a coffee maker and how mechanical, chemical and electrical aspects of the product could be understood in the way the product functions [50][51]. Our current setup in terms of discipline is similar to the case in this article and thus, the details of the engineering science through an experiment was a learning platform on developing understanding systemic contribution of various disciplines to a specific product development.

From the learning process, we asked "How to link a social concern to a multidisciplinary engineering design project that would be of value for all the disciplines". Literature on Education for Sustainable Development (ESD) identifies the link between being instrumental in which the agent understand how he can take informed action based on his competence is important for participation of change agents [12], [32], [52]. Thus, from our discussion, recognizing the potential contribution of each discipline is vital for the cause to be shared and cooperation to develop into collaboration. The lack of fundamental engineering knowledge within a multidisciplinary context is another reason why student cooperation may not lead to professional meaningful roles[53]. Continuous reflection and discussion provided insights into how we can broaden our perspective and thus, critically be of help to the student as a guide to reflect upon the potential they see in which they could contribute. In Figure 2.0 below, the summation of our discussions on brainstorming a project idea through practically relating multidisciplinary engineering design is related in a model to find an equitable role prior to implementation.

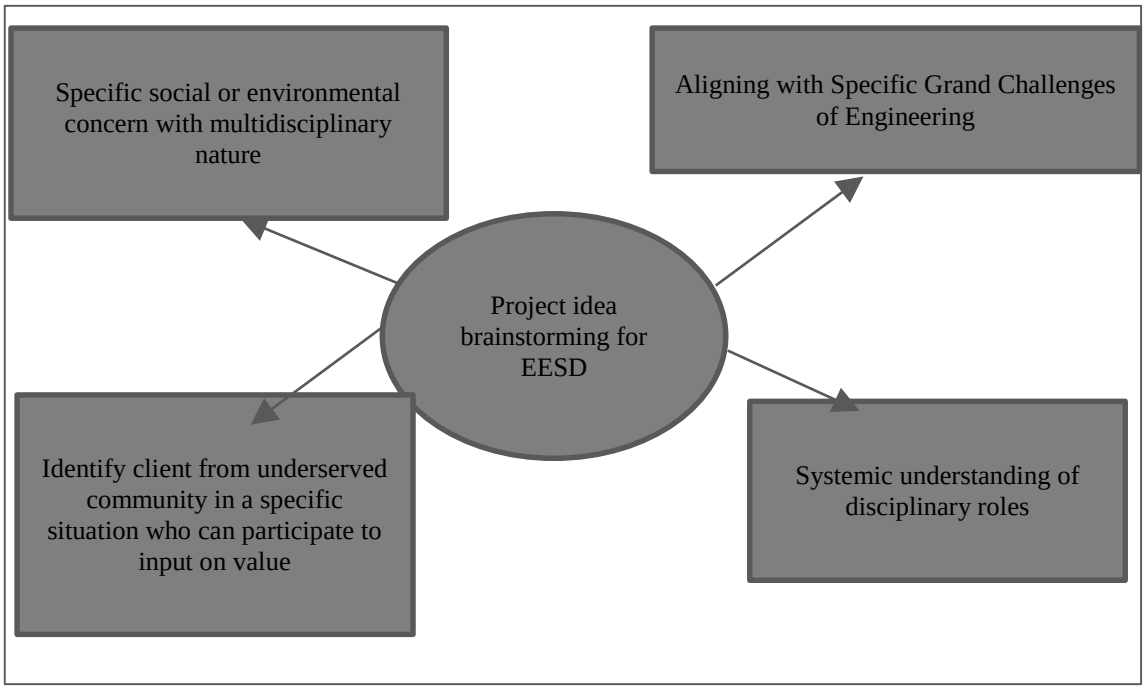


Figure 2.0. Figure showing the various consideration which form the conceptualization of project idea

2.2 Implementation stage (facilitation)

The societal problem which we are designing solution for is targeted towards challenges in the cleaning of toilets in large context like universities in which janitors are subjected to chemical and physical harm from work. Harm from cleaning work has been identified as a contributor in which janitors develop occupational disease such as eczema and asthma from the use of inappropriate tools usually meant for less demanding context such as the home [31].

Cleaning is described mainly as chemical and mechanical based activity and thus, the material context is important to provide us with the understanding on how cleaning is performed [54]. From our initial discussion we could understand that the process of cleaning is imbued with many assumptions. We were varied in the way we make sense of the activity of cleaning. We used an empathic approach in which we observed and discussed what we considered the most critical area which requires address of improvisation to reduce the risk of damage from work [55], [56].

Emphatic design are referred to design that center on user feeling towards the product [56]. In terms of developing tools for janitors, we found that janitors are emotional bonded with their tools. Tools not only help them to achieve the visual quality of cleaning. Due to the social and environmental burden on them from society as agents responsible for hygiene, a good tool is more of an ‘ally to combat with dirt” than a support which means they are extremely choosy in order perform better. However, they did not recognize impact of the tool in limiting them as it was intended for more domestic purposes.

For two consecutive semesters, we participated in understanding how to design a technical solution which can improve the working condition of janitors in our institution as a whole. These discussions undertook amidst engineering design students from different engineering disciplines using conceive -design- implement-operate (CDIO) [57] initiative framework in learning to design and build.

We realized through our discussion we been ignorant of some values as it is embedded but hidden from the social reality [58]. We need to make a choice to include it or it could be rationalized as invaluable to the design. We led the students into meeting the janitors at their work while I kept closer interaction in other context outside their work context. Two janitors were part of our discussion and were both females from different cultural background. They shared personal stories of what this work means to them apart from us observing and conversing with them on specific cleaning work processes. These stories were important for our reflection on what we were empathetic to and in what way we could be instrumental based on our discipline.

A good example of how we led our empathy to guide design was when we could relate to an electrical aspect within our design. We decided to avoid automation or use of servo which we felt was a redundant addition due to our understanding on the value the janitors prescribed to manual work. They liked manual work and preferred the image of hard worker then an effective cleaner. They also saw fear in the loss of their job if we decided to use automation. However, a critical reflection exercise led us to move from functionality to other aspects such as safety functions. We could relate to inclusion of safety function like alarms for to buzz if cleaner needs help and tracing capability as this has now become more valuable. Figure 2.1 are pictures showing outcomes from interactions which representation of work and tool context and systems thinking drawing which resulted from our conceptualization of design with janitors for the two consecutive semesters.



Figure 2.1. Pictures of outcome from student interaction with are representation of work tools, tool testing and systems thinking development

2.3 Post implementation stage: Development of a learning landscape and a multidisciplinary engineering design project for personalized learning

This project was repeated for two semesters and due to the nature of the project, we found that the project had many negative reviews as many of its audience suggested that

i. it was more of a design project rather than an engineering project in which no engineering parameters were tested , and
ii. it lacked business value in which a commercial entity could be interested to invest

Limited resources and limited time for project driven by empathetic recognition of problem areas was identified as the main cause for the outcome of the project to be of not satisfactory. In terms of facilitation, it was also recognized that apart from emphasizing on the instrumental involvement, product development in engineering requires testing and validation. In terms of CDIO initiative, our emphasis lacked in terms Implementation and Operation in which the sustainability of maintaining the artefact was not addressed. We recognized understanding on sustainable of manufacturing practices such as closing of loop in product operations with regards how a product is made and product attributes is an area which needs emphasis [59]. Skill development on decision making for product tests to assess functionality and sustainability are among the identified pathways to facilitate for better implementation and operation of product.

However, it indeed had a noticeable negative impact towards our team, especially our students. When observing the assessment process by the industry representatives, apart from the business value, they could articulate other important values such as value for low end workers and how they saw value in their design. In one assessment, our engineering students unsatisfied with the comment of assessors on the value of their product reached out to their friends from the Business School to understand business value from the perspective of ‘others’. Upon our reflection, we recognize “some of us use the traditional capitalistic definition in assessing business value but often do not realise that there is a view that business need to consider social value as part of the value embedded in their product apart from profit making. However, our understanding on marketing the product is also not grounded in the scenario of market conditions with regards to this product. Products needs demand as well as usability and our understanding is limited to the functionality and service without considering competitive advantage [45].

However, as engineering educators, we feel compelled through critical consciousness [16] to provide a platform for our students to articulate value for their work in more depth than what we are prepared to listen to. The following semester, we engaged in the development of an integrated project idea which brought environmental and social value to the context of toilet. The negative image of toilets is also as an impediment to value these design and thus, to plan sustainability, we saw a potential of a learning conceptualization [60] to be embedded in the toilet (i.e learning space).

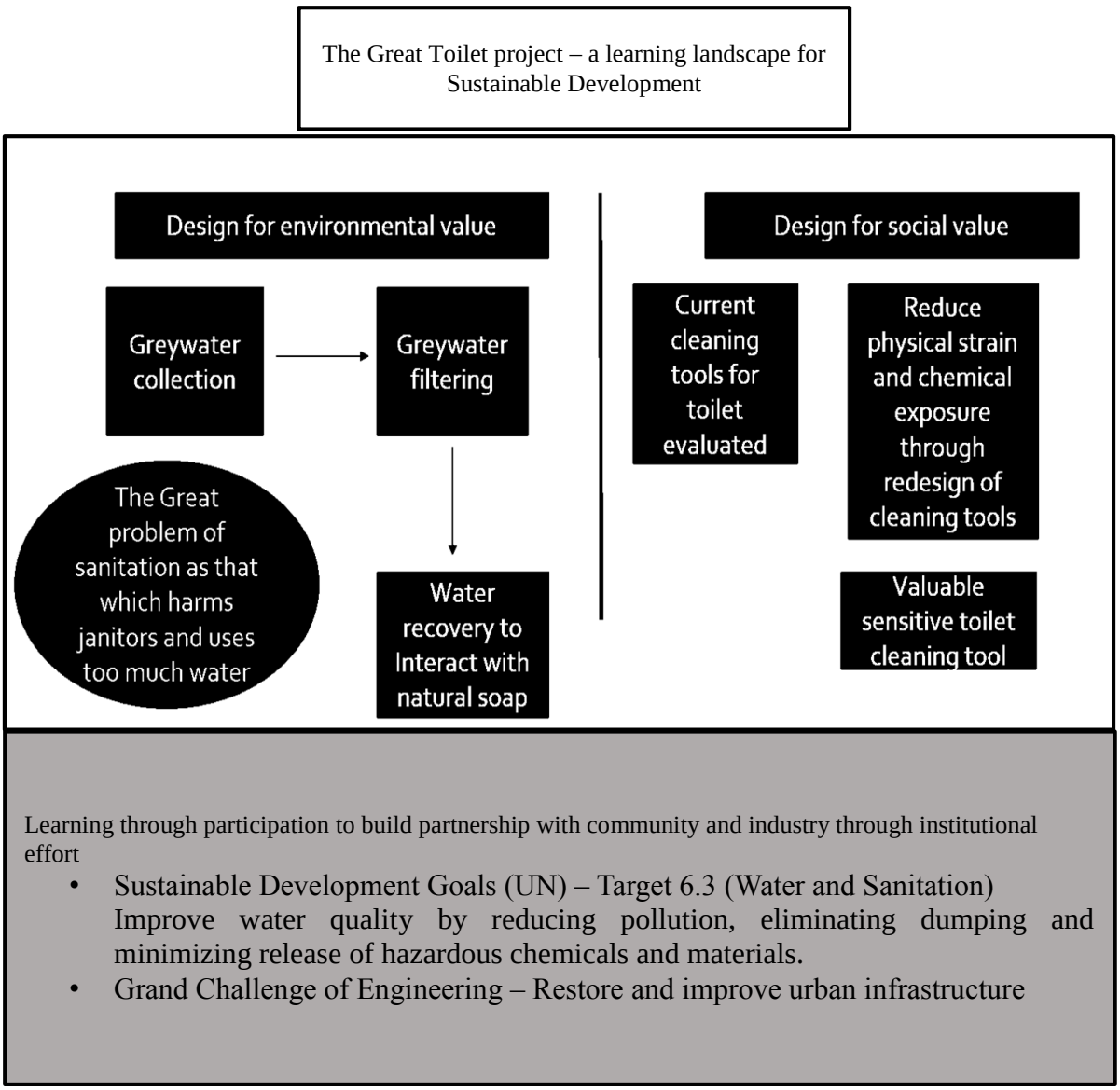


Figure 2.2 The Great Toilet Project as a learning landscape for Sustainable Development

We used the concept of a learning landscape [30] to integrate the cleaning tool with a greywater recovery system which recover water for reuse and repurpose the water to mechanically dispense natural soap. Figure 2.2 and 2.3 are compilation of what kind of value is brought to learning about SD for engineers tackling the problem of water and sanitation. In Figure 2.3, we increased the participatory context to find value for more agents who interact with the context of toilets. Various value to stakeholders [45] across the water cycle is mapped to four agents which includes users of toilet as well as the owner of the toilet. Through this landscape, we are able to relate a multidimensional aspect in which we see a rich context that could maximize encounter of ideas and people [30], [61].

In order to initiate the use of the learning landscape as a platform to learn integrated technology, we consulted sustainable business partners to guide our new conception in terms identifying potential challenges in moving forward. The Great

Toilet project initiative is at developmental stage. Malaysia's first green hotel owner has lend his views with regards to the challenges we potentially face With experiences in water recovery systems using green practices , he was able to shed light on appropriate technology for use within this context. In turn we approached the facilities management of Taylor's to present our intention to collaborate for community development project in terms of sustainability with the advent of the learning landscape as impetus for discussion. The Great Toilet project is thus intended as an exhibition for participation on integrative solution for water and sanitation as potential initiative for Taylor's SOE. In Figure 2.2, we relate to the SD goal which is Target 6.3 on water and sanitation in which we could address all aspects of the target as well as improving urban infrastructure under the Grand Challenges of Engineering.

As personalized learning emphasizes the need to consider diversity of value in the context of learning through participation, thus, we were able to construct a platform in which various values on engineering design and beyond was accessible to learners who intend to interact with us and the project. The learning landscape design specifically addresses professional development to value social and economic perspectives of a design through sustainable agency. As our ethical understanding on design broaden to incorporate macro and microethics in terms of SD [62], young engineers require the incubated [9] experience of dialogue with regards to sustainability values in design .

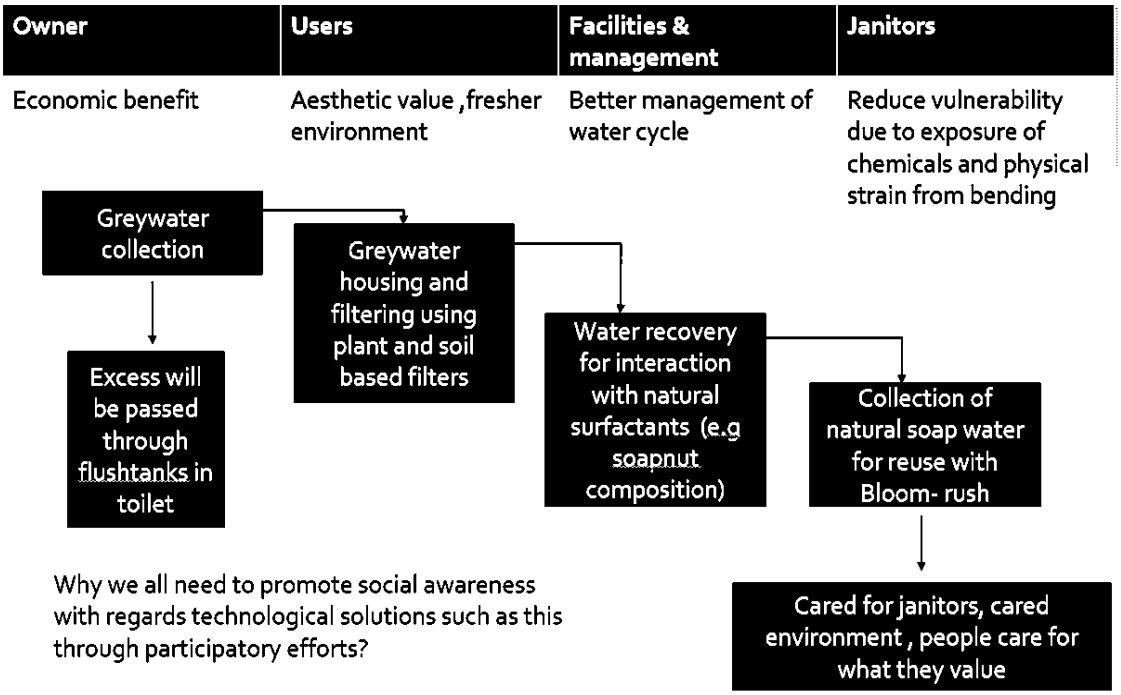


Figure 2.3. Figure showing the extended participatory context to show value of the learning project for all agents who interact with the toilet

3.0 Conclusion

This paper has been written with the critical aim to make a case for the critical experience of engineering educators for EESD. The core of the paper was written to

detail the critical questioning as well as the processes which undertook within the context. Using the platform of engineering education research, we used an ethnographic approach [41] to critically make a case for participation to mutual learning for EESD. Through the project, we were able to address the component requirement of the taxonomy for EESD [32] through an institutional effort as shown in Figure 3.0 . The integrated design which incorporates the environmental design of greywater reuse to supplement the functioning of the sensitively designed cleaning tool as shown in Figure 2.3. This forms the background for the development of the Great Toilet initiative in the form of a learning landscape which addresses raising of awareness with regards to development of these technologies. In our effort, we have outreached to industrial representatives from sustainable businesses to empower us to enact on our own community. With many milestones reached within this project which translated into a learning landscape to raise awareness on sustainable technologies and design in underserved domain, this initiative has been noted by participants from non-engineering disciplines as that which has far reaching consequences where voices of working communities form the core of the project. The employment of critical conscious as the threading process in which we could trail forward in which the value of our cleaners to the context of sanitation is heard. This has been a project which could address equity issues across domains in an incubated environment for our students. Thus, we would to respond to question by Ashford [9] raised in his article and inspired us. Does EESD require an incubated environment and what is the possibility in doing it [9]? The understanding derived from our critical experience provided insights to the possibilities of answering this question.

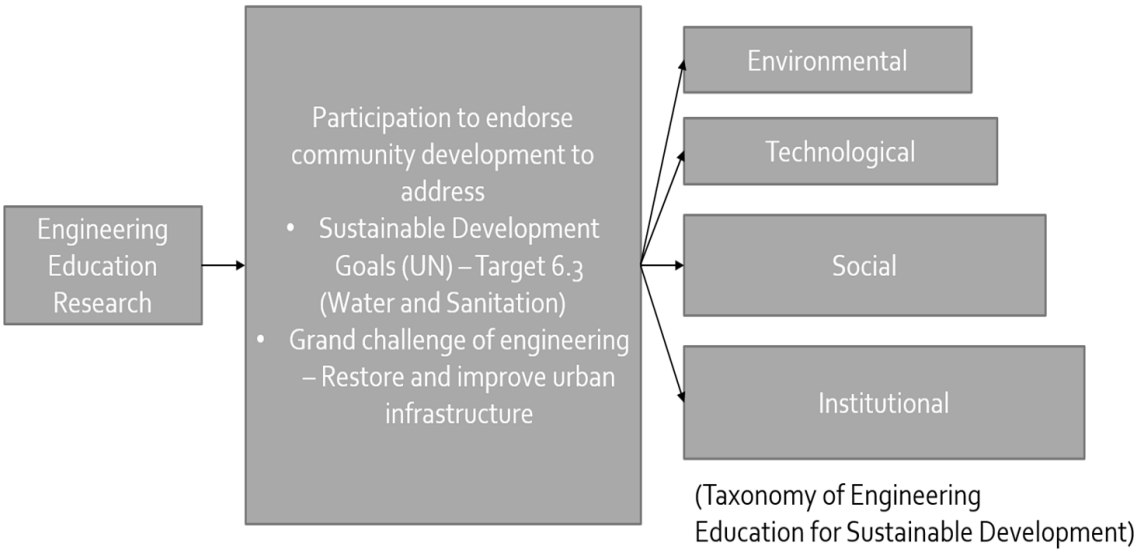


Figure 3.0. Linking global SD agenda to EESD at the local level through engineering education research

References

[1] M. Sahani *et al.*, "A case-crossover analysis of forest fire haze events and mortality in Malaysia," *Atmos. Environ.*, vol. 96, pp. 257–265, Oct. 2014.
[2] K. Maree, H. M. Radzi, S. Sipon, K. Othman, N. N. N. N. Nazli, and Z. A.

Ghani, “2nd World Conference on Psychology and Sociology, PSYSOC 2013, 27-29 November 2013, Brussels, BelgiumDemographic Influence on Muslim Flood Victim Wellbeing in Flood Prone Districts in Malaysia,” *Procedia - Soc. Behav. Sci.*, vol. 140, pp. 488–492, 2014.

[3] M. S. Mia, R. A. Begum, A. C. Er, R. D. Z. R. Z. Abidin, and J. J. Pereira, “Trends of dengue infections in Malaysia, 2000-2010,” *Asian Pac. J. Trop. Med.*, vol. 6, no. 6, pp. 462–466, 2013.

[4] L. Ismail, “Students from five universities compete for RM43,500 seed fund Read More : http://www.nst.com.my/news/2015/11/students-five-universities-compete-rm43500-seed-fund,” *2015-11-12*, 2015. [Online]. Available: http://www.nst.com.my/news/2015/11/students-five-universities-compete-rm43500-seed-fund. [Accessed: 13-Jul-2016].

[5] G. Downey, “Are Engineers Losing Control of Technology?,” *Chem. Eng. Res. Des.*, vol. 83, no. 6, pp. 583–595, 2005.

[6] G. L. Downey *et al.*, “The Globally Competent Engineer: Working Effectively with People Who Define Problems Differently,” *J. Eng. Educ.*, vol. 95, no. 2, pp. 107–122, Apr. 2006.

[7] J. Pritchard and C. Baillie, “How can engineering education contribute to a sustainable future?,” *Eur. J. Eng. Educ.*, vol. 31, no. 5, pp. 555–565, 2006.

[8] P. T. Robbins, “The reflexive engineer: perceptions of integrated development,” *J. Int. Dev.*, vol. 19, no. 1, pp. 99–110, 2007.

[9] N. a. Ashford, “Major challenges to engineering education for sustainable development: What has to change to make it creative, effective, and acceptable to the established disciplines?,” *Int. J. Sustain. High. Educ.*, vol. 5, no. 3, pp. 239–250, 2004.

[10] H. J. Cruickshank and R. A. Fenner, “The evolving role of engineers: Towards sustainable development of the built environment,” *J. Int. Dev.*, vol. 19, no. 1, pp. 111–121, 2007.

[11] K. Kastenhofer, A. Lansu, R. van Dam-Mieras, and M. Sotoudeh, “The Contribution of University Curricula to Engineer ing Education for Sustainable Development,” *GAIA-Ecological Perspect. Sci. Soc.*, vol. 19(1), pp. 44–51, 2010.

[12] C. J. Desha, K. Hargroves, and M. H. Smith, “Addressing the time lag dilemma in curriculum renewal towards engineering education for sustainable development,” *International Journal of Sustainability in Higher Education*. Emerald Group Publishing Limited, 12-Apr-2013.

[13] J. R. Mihelcic, L. D. Phillips, and J. David W. Watkins, “Integrating a Global Perspective into Education and Research: Engineering International Sustainable Development,” *http://dx.doi.org/10.1089/ees.2006.23.426*, 2006.

[14] K. Wolffa and K. Lucke, “Integrating multidisciplinary engineering knowledge,” *Teach. High. Educ.*, vol. 18, no. 1, pp. 78–92, 2013.

[15] A. Christy and M. Lima, “Developing creativity and multidisciplinary approaches in teaching Engineering problem-solving,” *Int. J. Eng. Educ.*, vol. 23, no. 4, pp. 636–644, 2007.

[16] E. Frydaki and E. Katsarou, “The dialogic practices of educational action research participants as a means of supporting or undermining its critical orientation,” *Action Res. Educ.*, vol. 4, 2013.

[17] J. Asghar, “Critical Paradigm: A Preamble for Novice Researchers,” *Life Sci.*, vol. 10, no. 4, pp. 3121–3127, 2013.

[18] I. Thomas, “Critical Thinking, Transformative Learning, Sustainable Education,

and Problem-Based Learning in Universities," *J. Transform. Educ.*, vol. 7, no. 3, pp. 245–264, Jul. 2009.

[19] Apple, Education, and Power, "Teachers as Researchers Routledge Education Classic Edition Series," *Autism Learn. Teach. Music Music. Crit. Incidents Teach.*, 1982.

[20] P. Reason and H. Bradbury, *The Sage handbook of action research participative inquiry and practice*. SAGE Publications, 2008.

[21] N. K. Denzin and Y. S. Lincoln, *The Sage handbook of qualitative research*. Sage, 2011.

[22] G. del Cerro Santamaría, "Transdisciplinary technological futures: An ethnographic research dialogue between social scientists and engineers," *Technol. Soc.*, vol. 40, pp. 53–63, 2015.

[23] C. Ellis, T. E. Adams, and A. P. Bochner, "Autoethnography: An Overview," *Forum Qual. Sozialforsch. / Forum Qual. Soc. Res.*, vol. 12, no. 1, 2010.

[24] L. L. Bucciarelli, *Engineering philosophy*. Delft, The Netherlands: DUP Satellite, 2003.

[25] A. Zmuda and M. Tomaino, *The competent classroom : aligning high school curriculum, standards, and assessment- a creative teaching guide*. NEA, 2001.

[26] C. A. Barry, N. Britten, N. Barber, C. Bradley, and F. Stevenson, "Using Reflexivity to Optimize Teamwork in Qualitative Research," *Qual. Health Res.*, vol. 9, no. 1, pp. 26–44, Jan. 1999.

[27] J. M. Case and G. Light, "Emerging Research Methodologies in Engineering Education Research," *J. Eng. Educ.*, vol. 100, no. 1, pp. 186–210, Jan. 2011.

[28] E. D. G. Fraser, A. J. Dougill, W. E. Mabee, M. Reed, and P. McAlpine, "Bottom up and top down: analysis of participatory processes for sustainability indicator identification as a pathway to community empowerment and sustainable environmental management.," *J. Environ. Manage.*, vol. 78, no. 2, pp. 114–27, Jan. 2006.

[29] G. W. White, M. Suchowierska, and M. Campbell, "Developing and systematically implementing participatory action research11No commercial party having a direct financial interest in the results of the research supporting this article has or will confer a benefit upon the author(s) or upon any organizatio," *Arch. Phys. Med. Rehabil.*, vol. 85, pp. 3–12, Apr. 2004.

[30] S. Dugdale, "Space Strategies for the New Learning Landscape.," *Educ. Rev.*, vol. 44, no. 2, p. 50, 2009.

[31] M. Medina-Ramón *et al.*, "Asthma, chronic bronchitis, and exposure to irritant agents in occupational domestic cleaning: a nested case-control study.," *Occup. Environ. Med.*, vol. 62, no. 9, pp. 598–606, Sep. 2005.

[32] J. Segalàs, K. F. Mulder, and D. Ferrer-Balas, "What do EESD 'experts' think sustainability is? Which pedagogy is suitable to learn it?," *Int. J. Sustain. High. Educ.*, vol. 13, no. 3, pp. 293–304, Jul. 2012.

[33] A. Johri and B. M. Olds, "Situated Engineering Learning : Bridging Engineering Education Research and the Learning Sciences," *J. Eng. Educ.*, vol. 100, no. 1, pp. 151–185, 2011.

[34] I. Nair, "Life Cycle Analysis and Green Design: A Context for Teaching Design, Environment, and Ethics," *J. Eng. Educ.*, vol. 87, no. 4, pp. 489–494, Oct. 1998.

[35] U. Diwekar, "Green process design, industrial ecology, and sustainability: A systems analysis perspective," *Resour. Conserv. Recycl.*, vol. 44, no. 3, pp. 215–235, Jun. 2005.

[36] A. Smith, J.-P. Voß, and J. Grin, "Innovation studies and sustainability transitions: The allure of the multi-level perspective and its challenges," *Res. Policy*, vol. 39, no. 4, pp. 435–448, May 2010.
[37] A. El-Zein, D. Airey, P. Bowden, and H. Clarkeburn, "Sustainability and ethics as decision-making paradigms in engineering curricula," *Int. J. Sustain. High. Educ.*, vol. 9, no. 2, pp. 170–182, 2008.
[38] V. M. Novak, "Design management of sustainability values: a learning organization perspective.," *Archit. Eng. Des. Manag.*, vol. 10, no. 3/4, pp. 218–232, 2014.
[39] A. M. Lopes, D. Fam, and J. Williams, "Designing sustainable sanitation: Involving design in innovative, transdisciplinary research," *Des. Stud.*, vol. 33, no. 3, pp. 298–317, 2012.
[40] J.-Y. Park, "Transitioning toward Transdisciplinary Learning in a Multidisciplinary Environment," *Int. J. Pedagog. Learn.*, vol. 6, no. 1, pp. 82–93, 2010.
[41] G. del Cerro Santamaría, "Transdisciplinary technological futures: An ethnographic research dialogue between social scientists and engineers," *Technol. Soc.*, vol. 40, pp. 53–63, Feb. 2015.
[42] D. J. Lang *et al.*, "Transdisciplinary research in sustainability science: practice, principles, and challenges," *Sustain. Sci.*, vol. 7, no. S1, pp. 25–43, Feb. 2012.
[43] D. Parent and L. Speer, "Advances in Engineering Education A Case Study of a Co-instructed Multidisciplinary Senior Capstone Project in Sustainability," pp. 1–30, 2014.
[44] D. Sobek and C. Plumb, "Using The Engineering Design Process To Re Envision Multidisciplinary Educational Experiences For Engineering Students," in *2007 Annual Conference & Exposition*, 2007, p. 12.1570.1-12.1570.14.
[45] W. Yan, C.-H. Chen, D. Chang, and Y. T. Chong, "A stakeholder-oriented innovative product conceptualization strategy based on fuzzy integrals," *Adv. Eng. Informatics*, vol. 23, no. 2, pp. 201–209, Apr. 2009.
[46] I. De Vere, G. Melles, and A. Kapoor, "Product design engineering - a global education trend in multidisciplinary training for creative product design," *Eur. J. Eng. Educ.*, vol. 35, no. 1, p. 33, 2010.
[47] E. J. Coyle, L. H. Jamieson, and W. C. Oakes, "Integrating Engineering Education and Community Service: Themes for the Future of Engineering Education.," *J. Eng. Educ.*, vol. 95, no. 1, pp. 7–11, 2006.
[48] M. K. Watson, C. Noyes, and M. O. Rodgers, "Student Perceptions of Sustainability Education in Civil and Environmental Engineering at the Georgia Institute of Technology," *J. Prof. Issues Eng. Educ. Pract.*, vol. 139, no. 3, pp. 235–243, 2013.
[49] P. Vare and W. Scott, "Learning for a Change: Exploring the Relationship Between Education and Sustainable Development OPINION ESSAY," vol. 1, no. 2, pp. 191–198, 2015.
[50] S.-M. Cheah and C. H. T. Ng, "Integrating Design Thinking into Chemical Product Design – An Initial Experience," *Proc. 14th Asia Pacific Confed. Chem. Eng. Congr.*, 2012.
[51] R. P. Hesketh and C. S. Slater, "Demonstration of Chemical Engineering Principles to a Multidisciplinary Engineering Audience."
[52] M. Svanström, U. Palme, M. K. Wedel, O. Carlson, T. Nyström, and M. Edén, "Embedding of ESD in engineering education: Experiences from Chalmers University of Technology," *Int. J. Sustain. High. Educ.*, vol. 13, no. 3, pp. 279–

292, 2012.

[53] E. Tsang, J. van Haneghan, B. Johnson, E. J. Newman, and S. Van Eck, "A report on service-learning and engineering design: Service-learning's effect on students learning engineering design in 'Introduction to Mechanical Engineering,'" *Int. J. Eng. Educ.*, vol. 17, no. 1, pp. 30–39, 2001.

[54] J. Makhoul, R. Nakkash, T. Harpham, and Y. Qutteina, "Community-based participatory research in complex settings: clean mind-dirty hands.," *Health Promot. Int.*, vol. 29, no. 3, pp. 510–7, Sep. 2014.

[55] C. Hopkins and R. McKeown, "Education for Sustainable Development: past experience., present action and future prospects," *Educ. Philos. Theory*, vol. 33, no. 2, pp. 231–244, 2001.

[56] D. Leonard and J. F. Rayport, "Spark Innovation Through Empathic Design Harvard Business Review."

[57] "Multi-Disciplinary Design-Build PBL As An Introduction to Engineering | Worldwide CDIO Initiative." [Online]. Available: http://www.cdio.org/knowledge-library/documents/multi-disciplinary-design-build-pbl-introduction-engineering. [Accessed: 12-Feb-2016].

[58] Y. Hurol, "Ethical considerations for a better collaboration between architects and structural engineers: design of buildings with reinforced concrete frame systems in earthquake zones.," *Sci. Eng. Ethics*, vol. 20, no. 2, pp. 597–612, 2014.

[59] C. Rusinko, "Green Manufacturing: An Evaluation of Environmentally Sustainable Manufacturing Practices and Their Impact on Competitive Outcomes," *IEEE Trans. Eng. Manag.*, vol. 54, no. 3, pp. 445–454, Aug. 2007.

[60] T. Meppem and R. Gill, "Planning for sustainability as a learning concept," *Ecol. Econ.*, vol. 26, no. 2, pp. 121–137, Aug. 1998.

[61] M. Savin-Baden, "The Problem-Based Learning Landscape," *Planet*, no. 4, pp. 4–6, Nov. 2001.

[62] J. Herkert, "Professional societies, microethics, and macroethics: product liability as an ethical issue in engineering design," *Int. J. Eng. Educ.*, vol. 19, no. 1, 2003.

eureca 2016 – Conference Paper
Paper Number ME_PG03

Numerical and Experimental Investigation of NACA0012 Wing Geometry Aerodynamic Efficiency at Low Reynold's Number

Shahrooz Eftekhari[1*], Abdulkareem Sh. Mahdi Al-Obaidi[2]

School of Engineering, Taylor's University, Malaysia[1]

[*]shahroozeftekhari@sd.taylors.edu.my

Abstract

Recent developments in aerial vehicles such as unmanned aerial vehicles (UAVs) and also research and developments on the aerodynamics of flying birds/insects has attracted the aerodynamicists attention and increased the urge to study the aerodynamic characteristics of wings at low subsonic speeds. The aerodynamic characteristics of a NACA0012 wing geometry at a low Reynold's number of 129000 and angle of attack ranging from **0**° to **20**° are investigated and evaluated in this study. Numerical simulations as well as experiments are conducted throughout the study. The numerical investigations are conducted through 3-D simulation using ANSYS FLUENT. The numerical results are then validated by the experimental results that are obtained utilizing utilizing a custom designed test rig which has been design, implemented and installed on Taylor's University subsonic wind tunnel. It is observed form the results of the study that the aerodynamic performance of the NACA0012 wing is improved as the angle of attack is increased from 0° to 10°. However, further increment of angle of attack from 10° to 20° results in early flow separation at the leading edge of the wing, transition of laminar flow to turbulent flow, vortex formation and increase in form drag coefficient; hence the drag coefficient exponentially increases which results in drastic reduction in aerodynamic efficiency of the wing.

Keywords: NACA0012, Wing, Aerodynamic efficiency, Low Reynolds number.

1. Introduction

Throughout the past century, researches and developments have been conducted on wings which contributes a constructive role in designing wind turbines, ship rudder, missiles and aviation industries. NACA0012 is a well-known airfoil that is utilised in academic researches as well as industrial applications such as Mini-UAV(MUAV). The MUAVs fly at low velocity and small length scale which put them in low wing chord Reynold number flight regime ranging from 15000 to 500,000 [1] which is below that of conventional aircrafts. The aerodynamic performance of MUAVs is critically dependant on the lifting surface of the aircraft which is the wing. Ahmed et al [2] numerically examined the behavior of lift and drag coefficients of NACA 0012 at 0° to 50° angle of attack. The study was conducted using ANSYS FLUENT. The turbulence model utilized in the study was k-ω shear stress transport model (SST). In order to obtain results with high accuracy, the number of nodes was increased to reach a cell number of 120000 to have a satisfactory mesh size. The obtained results at 0°,10° and 15° angle of attack were then compared and benchmarked with NASA's Langley Research Centre Validation Case for validation purposes [3]. The results obtained from the experiment show that for a Mach number of 0.2 and 10° angle of attack, the lift and drag coefficients are 0.019 and 0.001 respectively. On the other hand, by increasing the angle of attack to50°, the lift coefficient drops to 0.015 while the drag coefficient increases to 0.006. An experimental study was conducted by Zhou et al. [4] to measure the mean forces acting on NACA0012 at angle of attack ranging from 0° to 90° and low Reynolds number of 5.3×10^3 and 5.1×10^4. A closed loop water tunnel consisting airfoil support, torque resisting system and load cell was the apparatus utilized in the experiment. The force measurements were obtained using a load cell at angle of attack varying with 5° increment for angle of attack less than 20° and 10° increment for angle of attack between 20° and 90°. The results were then compared with Devinant et al. [5] test data for 0° to 90° angle of attack. As the results of experiment explains, lift and drag coefficients are strongly dependant on the angle of attack for high Reynold's number while at low Reynold's numbers the lift and drag coefficients do not experience significant variation. It can be understood from the data that the lift coefficient increases as angle of attack increases from 0° to 15°. Further increments of angle of attack results in decrements in lift coefficient until it reaches 0.1 at 90° angle of attack. However, the increments of drag coefficient is linear and relatively small for angle of attack less than 15° and it starts to have a sudden increment at 15° angle of attack until it reaches 2.1 at 90°. In another study, Zhang et al. [6] numerically studied the flow field of NACA 0012 at 0° to 180° using C-type grid with 360 cells, H-type grid with 200 cells and O-type grid with 320 cells. The Mach number and Reynold's number were set to 0.15 and 0.5×10^6 respectively. The simulation was performed for angle of attack ranging from 10° to 70° utilizing Spalart-Allmaras, standard k-ε, RNG k-ε as well as SST k-ω turbulent model. The simulations were conducted for 0° to 180° angle of attack on the NACA 0012 utilizing Spalart-Allmaras turbulent model. Comparison between the lift and drag coefficient obtained from the simulations show that C-type grid has the best fit to the experimental results while coefficients obtained from the H-type and O-type grid show a great scatter at angle of attack. Hence the C-type grid was found to be a more reliable grid type compared to O-type and H-type. However, simulation results also show a stall angle of 16° while based on experimental results the airfoil should experience stall at 14°

angle of attack. Shukri et al. [7] conducted a 2-D numerical analysis on the flow separation around NACA 0012 . The lift and drag coefficient variation behaviour with changes of angle of attack were studied during the analysis. The analysis studied different angle of attack ranging from 0° to 20° for turbulent and incompressible flows. The numerical solutions were obtained using the k-ε turbulent model. The results from the analysis shows that increasing the angle of attack results in high separation level and therefore high turbulence. The flow is understood to be laminar below 10° angle of attack. From 0° to 10° angle of attack there is no separation and lift coefficient increases while the drag coefficient is nearly constant. Increments after 10° results in increase of adverse pressure gradient on the upper surface which causes turbulence. It was also found that the lift coefficient increases until 12° angle of attack without significant change in drag coefficient and the separation happens at the tail of the airfoil. The separation continues growing until a critical angle of attack (stall angle) of 15° in which the flow is fully separated from the upper surface of airfoil and the lift coefficient increases slowly while the drag coefficient increases dramatically. Owen & Owen [8] investigated the flow quality in a wind tunnel by reviewing different techniques for turbulence measurement. Tests techniques were illustrated using data obtained through turbulence assessment experiments in a number of wind tunnels. The results of the experiments show the urge for the design and development test techniques and instruments to reduce the turbulence and noise which are the major flow disturbance in wind tunnel, hence the flow disturbances which cause turbulence in the test section. Hence, the efficiency and performance of the wind tunnel has improved. Also, the accuracy of the results obtained from experiments have been improved.

Previous studies have numerically and experimentally examined the aerodynamics of NACA0012 airfoil and infinite wing geometries at different angle of attack. However, the available data for finite wing aerodynamic characteristics are limited and this study is another effort to provide a better understanding of the aerodynamic characteristics of a finite wing geometry at low Reynold's number of 129000.

2. Numerical Simulation

Numerical simulations have recently developed a good reputation in engineering researches. Computational Fluid Dynamics (CFD) is utilized in this research to expedite the research process and to reduce the cost of prototypes and experiments. In order to achieve reliable results through simulation process, it is important to apply the right meshing method and boundary conditions. The numerical simulation in this project has been performed using ANSYS FLUEN 15.0.

2.1 Geometry

The NACA0012 wing geometry as well as the fluid boundary domain (Fig. 1) is modelled in FLUENT DESIGN MODELLER. The boundaries are set to have a distance of 20 chord lengths from the wing geometry [9]. The coordinates of the NACA0012 airfoil is obtained using the formula in Eq. (1) below.

$$\pm y_t = \frac{t}{0.2}(0.2969\sqrt{x} - 0.1260x - 0.3516x^2 + 0.2843x^3 - 0.1015x^4 \quad (1)$$

where x is coordinates along the length of the airfoil, from 0 to c (which stands for chord, or length), y is the coordinates above and below the line extending along the length of the airfoil, these are either y_t for thickness coordinates or y_c for camber coordinates, t is maximum airfoil thickness in tenths of chord, m is maximum camber in tenths of the chord and p is position of the maximum camber along the chord in tenths of chord.

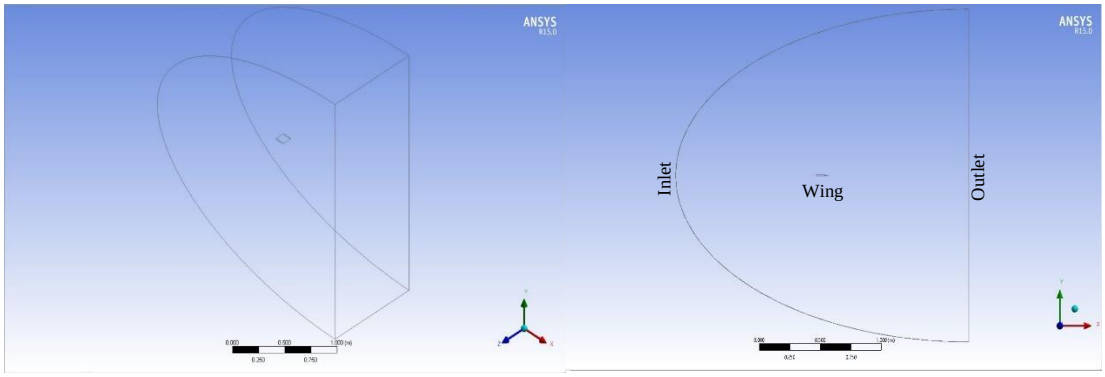


Figure 31. Wing geometry in the fluid domain (left) The boundary named selection.

2.2 Mesh

A fine mesh is one the requirements to achieve accurate simulation results. The C-type grid topology is utilised in this research as it is the found to be the efficient meshing method for wing geometry based on literature [10]. A fine mesh (Fig. 2) is achieved and implemented in this study by defining edge sizing and inflation layers on the edge of the wing geometry and sweeping the achieved mesh along the wing span.

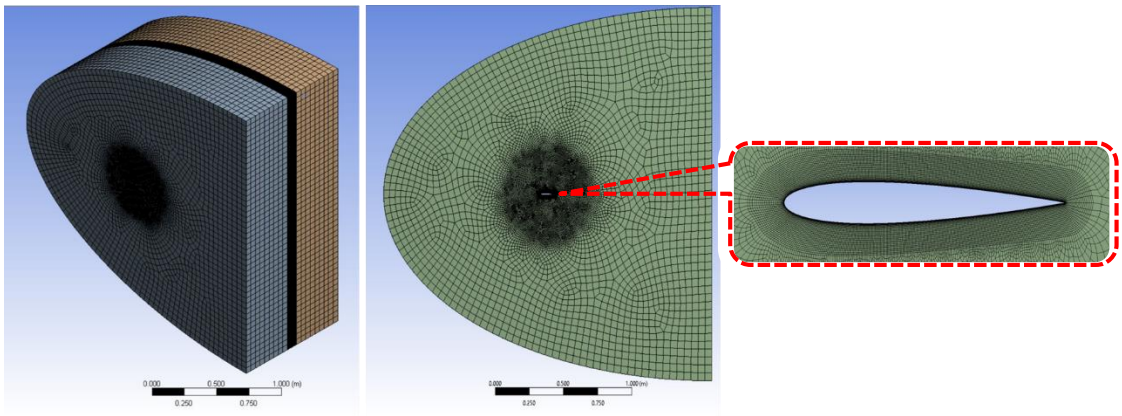


Figure 32. Mesh of the fluid domain.

In order to achieve the efficient mesh, different mesh edge sizing and inflation layers were generated and simulations were conducted with different cell numbers ranging from 60000 cells to 1.3 million cells. Based on the convergence time, achieved wall Y+ and accuracy of the results obtained from simulations, the following (Table 1) geometry mesh characteristics are selected.

Table 9. Mesh characteristics.

Mesh Control	Location	Size
Entire Fluid Domain	Wing center	$1e^{-2}$
Edge Sizing	Wing edge (Airfoil)	$5e^{-4}$
Surface Inflation	Fluid surface around the wing	$1e^{-5}$ (First layer thickness)

2.3 Numerical Setup

The flow is considered to be incompressible since the Mach number is less than 0.3. A pressure based solver is selected and the velocity of the flow is set to 18.256 $\frac{m}{s}$ to achieve the Reynold's number of 1.29×10^5 for validation of the numerical results with wind tunnel experimental results. The properties of the fluid are presented in Table 2. The Spalart-Allmaras turbulence model is selected for the simulations as it was investigated by Lei [11] and it is found to be the efficient and applicable turbulent model for wing simulations at low speed.

Table 10. Simulation fluid properties assumptions

Fluid Properties			
Fluid	Temperature	Density ($\frac{kg}{m^3}$)	Viscosity ($\frac{kg}{ms}$)
Air	20°	1.225	$1.7894e^{-5}$

3.0 Experimental

3.1 Experimental Apparatus

The results obtained through simulations on the wing are validated by experimental results. The wing geometry is fabricated using Taylor's University utilising 3D printing machine. The precision of the manufactured wing geometry is evaluated by comparing the model with printed technical drawing of the wing model prepared using Solidworks 15. The precisely evaluated wing models are installed in the Taylor's University low speed wind tunnel test section to conduct experiments. Taylor's University wind tunnel (TUWT) is an open subsonic wind tunnel model with 3:4:1 contraction ratio (Fig. 3). The test section of the wind tunnel is rectangular with a square cross section of 0.303 m × 0.303 m and length of 0.885 m. A Gamma DAQ F/T transducer is utilised to collect force and moment data. The force and moment readings from the transducer sensor are accurately measured and displayed using a PCI DAQ card model of NI PCI-6220 installed in the computer. The flow is created using a fan having a diameter of 0.63 m, 3 hp and 4145 V.50 Hz.

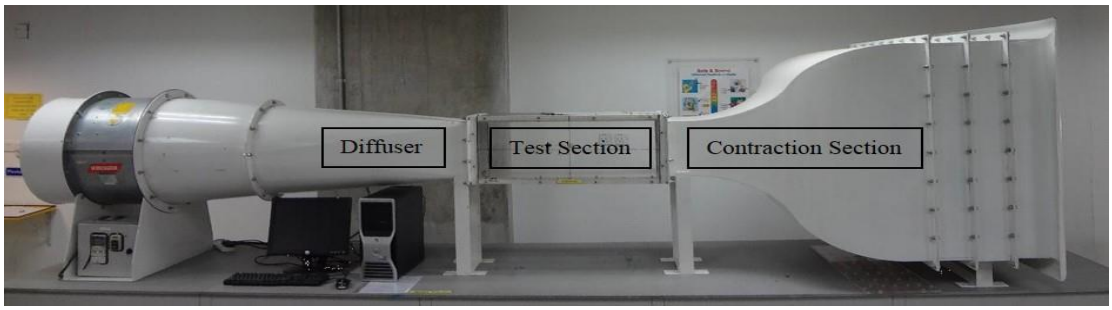


Figure 33. Taylors University Subsonic Wind Tunnel.

3.2 Experimental Setup

A force measurement mechanism is designed, calibrated and installed on the Taylor's University wind tunnel prior to experiments conduction. The mechanism consists of the following components (Fig. 4):

1. Heavy base
2. Tool side fixture shaft
3. 6 axis transducer (GAMMA ATI)
4. Model mounting adaptor
5. Model mounting strut
6. Base stand

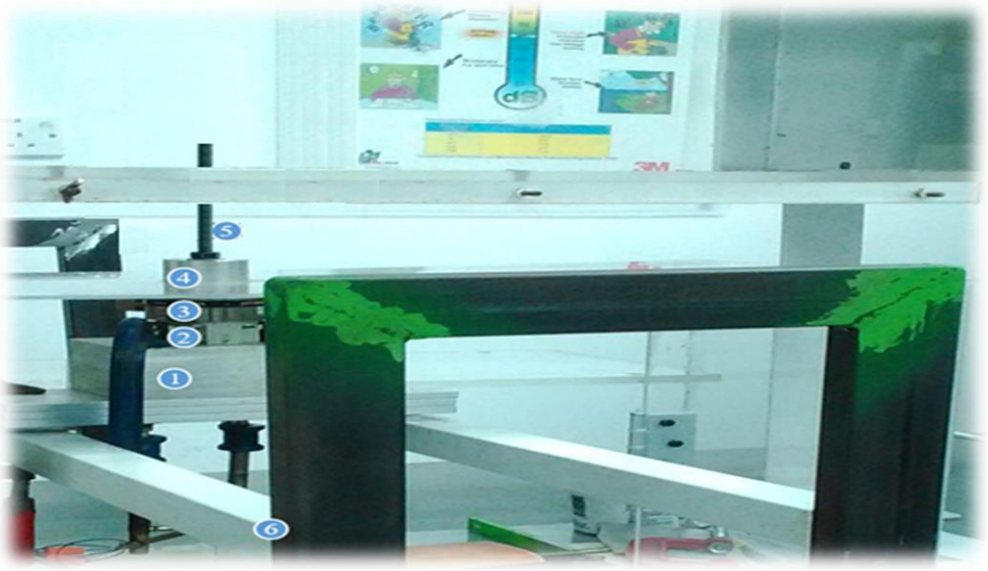


Figure 34. Manufactured force measurement mechanism

The load cell is fixed on a base through its tool side as suggested in the load cell's technical manual. The aluminium fixture shaft is custom designed and manufactured utilising CNC machine. The base is mounted on a stand which is fixed to the floor. This is done to avoid any vibration caused by the operation of wind tunnel. The custom model mounting geometry is manufactured and attached to the mounting adaptor plate. The model mounting part enables the installation of model struts on the load cell. The strut holds the wing model inside the wind tunnel test section as shown in (Fig. 5) and transfers the forces acting on the wing to the load cell. The load cell is connected to a DAQ system which collects the data and transfer to computer. The collected data will be shown in an excel sheet and various graphs for different aerodynamic characteristics such as lift and drag forces is plotted. In order to validate the experimental set up, experiments will be conducted at different angle of attack on NACA0012 wing and the results obtained from the experiments will be compared with experimental data publish by Kwanchai et al. [12]. The operating speed of the wind tunnel is to be adjusted to achieve the similarity. For physical similarity, Reynolds number (Re) is to be maintained the same as the published data. The operational speed is calculated using the following equation:

$$\mathrm{Re} = \frac{\rho V l}{\mu} \tag{2}$$

where, ρ and μ are the density and kinematic viscosity of air respectively, l is the chord length of the wing and V is the velocity of the flow.

3.3 Wing Model

The experiments have been conducted on the NACA0012 wing model with chord length of 0.15 m and aspect ratio of 1. The wing is installed through its aerodynamic center [12]. The aerodynamic center of the wing is calculated using the Eq. 3:

$$AC = \frac{C}{4} \tag{3}$$

Where AC is the aerodynamic center from the leading edge and C is the chord length of the wing.

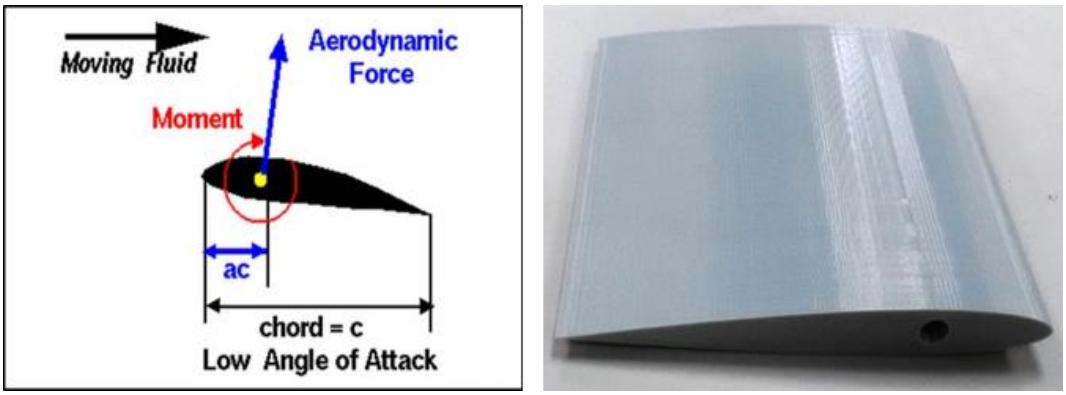


Figure 35. Aerodynamic center of wing (left) and NACA0012 wing(Right)

4.0 Results and Discussion

4.1 Numerical

The simulations are conducted for 0° to 20° angle of attack to evaluate the behaviour of the flow separation and aerodynamic characteristic at different angle of attack and low Reynold's number. The numerical results are compared with Kwanchai et al. [12] published experimental results for validation. As it shown in figures below (Fig. 6) and (Fig. 7), the lift and drag coefficients obtained from simulations complement the published experimental results with minor error of 3% at angle of attack less than 15°. However, at 20° angle of attack, the simulation results differ from published experimental results by 19% which is caused by increased wall Y+ at the leading edge of the wing (Fig. 7). This is caused by the flow separation at leading edge due to high angle of attack. Further refinement of the mesh around the wing's leading edge helps reducing the percentage error obtained.

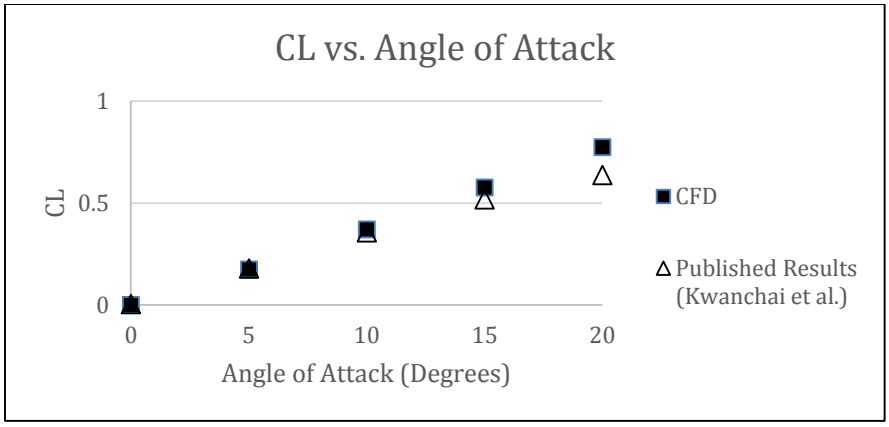


Figure 36. Lift coefficient at different angle of attack.

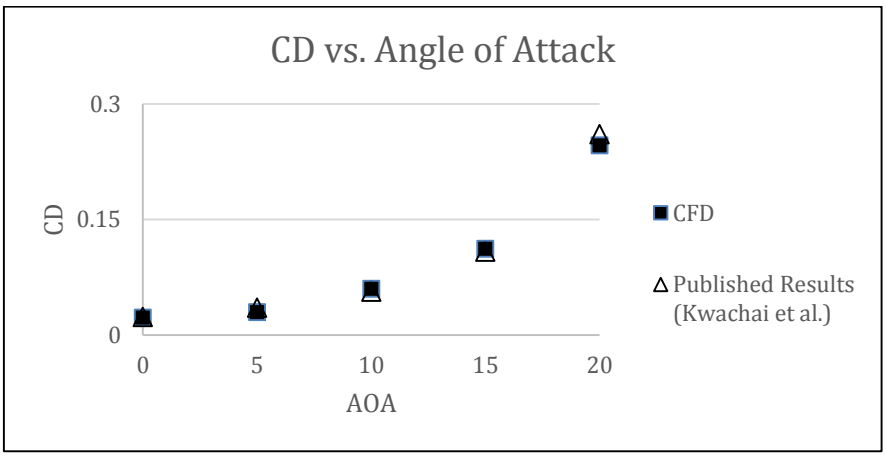


Figure 37. Drag coefficient at different angle of attack.

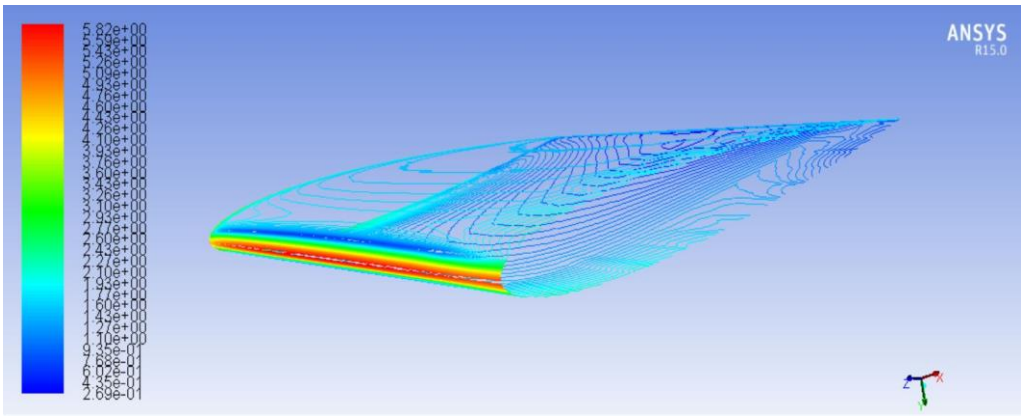


Figure 38. Wall Y+ at 20° angle of attack

The stream flow analysis provides a better understanding of the pressure distribution around the airfoil at different angle of attack. As it can be seen in (Fig. 9), the flow stream sticks to the airfoil surface at 0° angle of attack. As the angle of attack increases to 5° the stream starts to separate from the airfoil's upper surface, and the separation moves towards the leading edge of airfoil by increasing the angle of attack. Separation of the flow from the airfoil results in the formation of eddies starting from where the flow is separated towards the trailing edge of airfoil as the flow tends to stick back to the airfoil's surface. Formation of eddies causes chaos, therefore the flow loses its laminar characteristics as since the flow path line is not predictable anymore. Increasing the angle of attack results in more separated region from the

airfoil surface hence more turbulence. Flow stream in (Fig. 9) shows that the flow stream is symmetry at 0° angle of attack and the velocity of the upper and lower surface of the airfoil are equal, while increasing the angle of attack from 0° to 20° results in higher flow velocity on the upper surface compared to lower surface of the airfoil. Based on Bernoulli's principle, air flows at higher speed through regions with lower pressure. Therefore, it can be said that the pressure at the upper surface of the airfoil is less than the lower surface airfoil since the upper surface velocity is higher than the velocity at lower surface (Fig. 9). The pressure difference between the lower and upper body of the airfoil results in lift force which is caused by increasing the angle of attack from 0° to 15°. This results in pressure increment on the lower surface of the airfoil hence increment in lift force as the angle of attack increases.

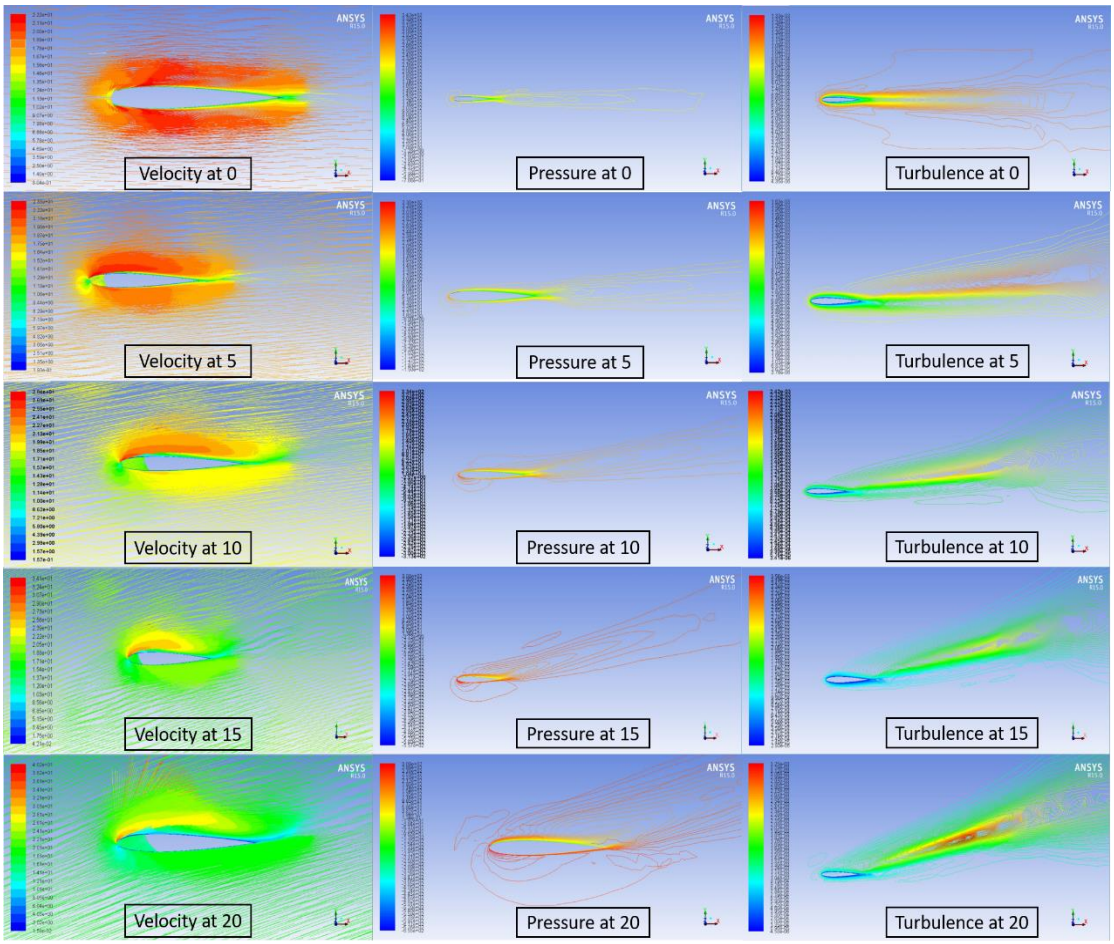


Figure 39. Velocity stream(left), Pressure contour(middle) and turbulence contour(right)

4.2 Experimental

The wind tunnel speed was to 13.1 $\frac{m}{s}$ to meet achieve the Reynolds number of 1.29×10^5. The lift and drag coefficients for 0° to 20° angle of attack obtained from the experiments are compared with the numerical results and Kwanchai et al. [12] published data to evaluate the accuracy of the experimental results obtained from wind tunnel experiments as shown in (Fig. 10) and (Fig. 11). The error analysis of the test setup converges that the largest percentage error of the lift coefficient and drag coefficients obtained from the experiment are 13% and 14% respectively which

corresponds to 20° angle of attack. This error has occurred due to the sensitivity of the load cell to vibration of the test rig while the wind tunnel operates. However, the trend of the results obtained from the experiments are in a complement with numerical results the published experimental data.

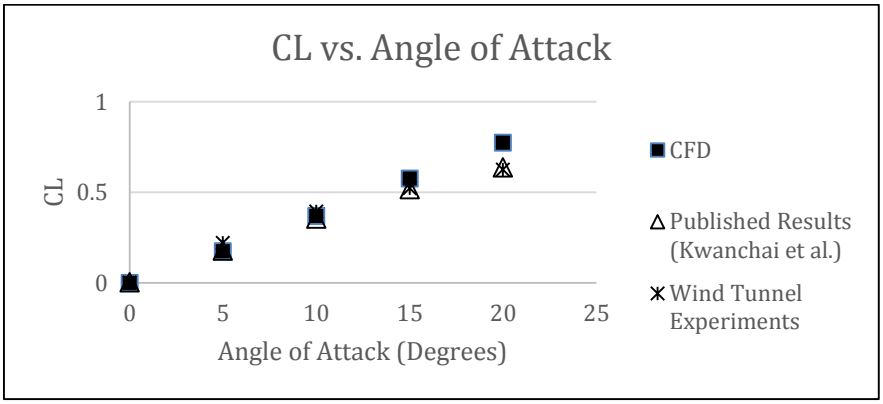


Figure 40. Lift coefficient comparison.

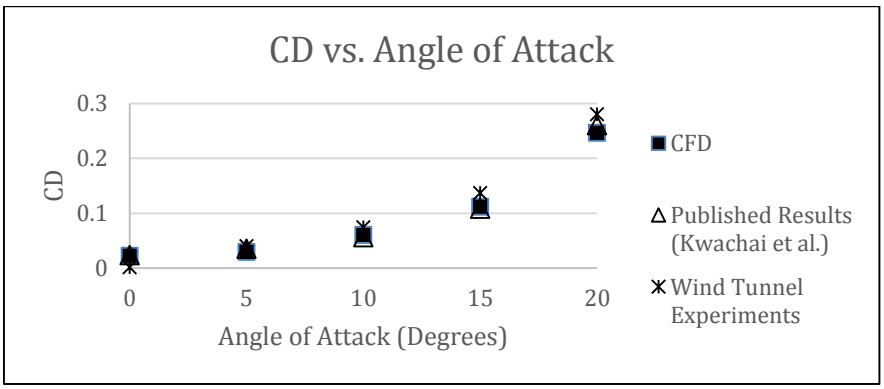


Figure 41. Drag coefficient comparison

The aerodynamic performance of NACA0012 wing in terms of it's aerodynamic efficiency is evaluated using the graph shown in (Fig. 12). As it can be seen, the aerodynamic efficiency of the wing increases as the angle of attack increases from 0° to 10°. While with further increment of angle of attack from 10° to 20°, the aerodynamic efficiency slope starts to reduce which is cause by simultaneous reduction in lift and increment in drag. This is due to increase of the form drag that is resulted by vortex formation after the separation of the flow near leading edge of the wing.

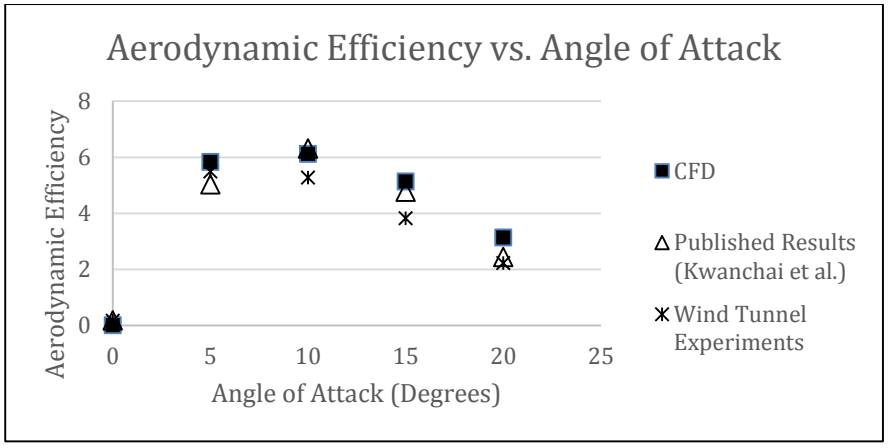


Figure 42. Aerodynamic efficiency of NACA0012 wing at different angle of attack

5. Conclusion

In conclusion, the numerical and experimental results of this study shows that increasing the angle of attack from 0° to 20° results in linear increase in lift coefficients. The drag force acting on the airfoil increases linearly as the angle of attack is increased from 0° to 10°, while further increment of the angle of attack results in dramatic increase in drag forces which is caused by separation of the flow at the leading edge and change of laminar flow to turbulent flow. Therefore, the aerodynamic efficiency is observed to be reduced as the drag coefficient is exponentially increased with further increment of angle of attack from 10° to 20°.

References

[1] Chahl. (2015). 'Unmanned Aerial Systems (UAS) Research Opportunities', Journal of Aerospace.
[2] T. Ahmed, M. Tanjin, S. Rafiul Islam and S. Ahmed. (2014). "Computational study of flow around a NACA 0012 wing flapped at different flap angles with varying mach numbers", *Global journal of researches in engineering*.
[3] I. H. Abbott and A. E. Von Doenhoff. (1959). Theory of Wing Sections, Including a Summary of Airfoil Data. New York, Dover Publications.
[4] Y. Zhou, M. Alam, H. Yang, H. Guo and D. Wood. (2011). "Fluid forces on a very low Reynolds number airfoil and their prediction", *International Journal of Heat and Fluid Flow*.
[5] P. Devinant, T. Laverne and J. Hureau. (2009)"Experimental study of wind-turbine airfoil aerodynamics in high turbulence", *Journal of Wind Engineering and Industrial Aerodynamics*.
[6] P. Zhang, A. Liu and J. Wang. (2009). "Aerodynamic modification of NACA 0012 airfoil by trailing-edge plasma gurney flap", *AIAA Journal*.
[7] I. Ali and S. Ahmed. (2011). "Modeling of turbulent separation flow", *World Academy of Science*.
[8] F. Owen and A. Owen (2008). "Measurement and assessment of wind tunnel flow quality", *Progress in Aerospace Sciences*.
[9] H. Shah, S. Mathew and C. Lim. (2015). "Numerical simulation of flow over an airfoil for small wind turbines using the γ - Re θ model", *Int J Energy Environ Eng*.
[10] T. Ahmed, M. Tanjin, S. Rafiul Islam and S. Ahmed. (2014). "Computational study of flow around a NACA 0012 wing flapped at different flap angles with varying mach numbers", *Global journal of researches in engineering*.

[11] Z. Lei. (2005). "Effect of RANS turbulence models on computation of vortical flow over wing-body configuration", *Transactions of the japan society for aeronautical and space sciences.*
[12] K. Chinwicharnam, D. Ariza, J. Moschetta and C. Thipyopas. (2013). "Aerodynamic characteristics of a low aspect ratio wing and propeller interaction for a Tilt-Body MAV", *International Journal of Micro Air Vehicles*.